

SKYLAB

Explores The Earth

NATIONAL AERONAUTICS
AND SPACE ADMINISTRATION

(NASA-SP-380) SKYLAB EXPLORES THE EARTH
(NASA) 512 p MF A01; SOD HC \$16.50 CSCI 08B

N82-12492
THRU
N82-12509
Unclas
02222

H1/43



30W 15W 0 15E 30E 45E 60E 60N 75E

Current

Benguela Current

West Wind Drift Current

| Explanation | |
|-------------|------------------------------|
| | African drought |
| | Deserts |
| | Geology |
| | Volcanoes |
| | Manicouagan impact structure |
| | Ice |
| | Snow |
| | Oceans |
| | Coastal sediments |
| | Cloud features |
| | Atmospheric pollution |
| | Cultural features |
| | Vegetation patterns |
| | Ocean surface circulation |
| | Tropical storm |



Major tectonic features of mountain ranges in Wyoming, Idaho, and Montana are greatly enhanced by snow cover and a low Sun angle. Yellowstone Lake is readily seen within the dark, heavily forested Yellowstone National Park. This view, taken during the Skylab 4 mission in January 1974, represents one of many areas of the Earth observed and photographed by Skylab crewmen for the Visual Observations Project.

ORIGINAL PAGE IS
OF POOR QUALITY

Skylab Explores the Earth

**ORIGINAL CONTAINS
COLOR ILLUSTRATIONS**

Skylab Explores the Earth

Prepared by
NASA Lyndon B. Johnson Space Center



Scientific and Technical Information Office
NATIONAL AERONAUTICS AND SPACE ADMINISTRATION
Washington, D.C.
1977

Library of Congress Cataloging in Publication Data

Main entry under title:

Skylab explores the earth.

(NASA SP ; 380)

1. Geophysics--Remote sensing--Addresses, essays, lectures. 2. Skylab Program--Addresses, essays, lectures.
I. Lyndon B. Johnson Space Center. II. Series: United States. National Aeronautics and Space Administration. NASA SP ; 380.

QC808.5.S48 550 77-829

For sale by the Superintendent of Documents,
U.S. Government Printing Office
Washington, D.C. 20402

Stock Number 033-000-00674-8

Foreword

DURING THE PAST TWO DECADES, achievements in space exploration have made dreams become real, have strengthened many scientific theories and revealed others as myths, and have provided both matter and thrust for new dreams. Men have landed and walked on the Moon, have observed and recorded many of its exposed features, and have collected samples of its materials. The surfaces of the Moon, Mars, Venus, Mercury, and Jupiter have been photographed, and displays of the Sun's energy have been recorded from a manned Earth-orbiting space station. Nor has Earth itself been neglected in the excitement of these and other successes, for there has been much effective "looking back" at our own planet from vantage points in space.

Earth is not yet fully explored, even at the surface, and certainly it is not yet fully understood as a complex and highly active macrosystem. However, we do know many useful things about it and about the complex interactions among its atmospheric, oceanic, and lithospheric systems. We know enough, for example, to at least partly characterize these systems; to recognize some important empirical relationships within and among them; and to formulate, for future testing, concepts concerning their origins, life histories, sources of energy, and present functioning. Much of this knowledge is a cumulative product derived from centuries of painstaking Earth-based studies, but an astonishingly large addition has been made in recent years through the use of optical and electronic sensors on manned and unmanned Earth-orbiting satellites.

Throughout the entire history of effective Earth exploration, the common denominator has been observation combined with documentation. Man has moved from place to place, often at considerable inconvenience, to observe more and more of this planet and variously to fortify his visual observations with written descriptions, sketches and maps, and photographs or other imagery. The Earth has been thus observed and studied scientifically at many scales, first with growing appreciation of the occasional synoptic view (the "big look" of the geoscientist) and later with more deliberate efforts to obtain and record such views. To see much from one place at one time can be of great value, whether the target is a static section of rocks across a deep canyon or a moving pattern of clouds just below a mountain top. And to document the view can be equally important, whether to demonstrate its existence or to record transitory relationships. A century ago, for example, it required the superb photographs of William H. Jackson to convince a doubting public that reported thermal features of "Colter's Hell" were real, and to persuade the Congress to make Yellowstone our first national park. Today similar doubts remain about the existence or significance of other reported Earth features, and still others doubtless remain to be observed. Less than 5 years ago, it was shown that successive synoptic images from geosynchronous satellites can contribute vitally to refined tornado warnings.

The individual scientist has long recognized the challenges of scale, beginning with his own position in effect as a mite on a mountain, and his imaginative responses toward understanding the Earth have been remarkably successful. As he has explored the lands and oceans and has assimilated the results of the Hayden, Powell, *Challenger*, and many other expeditions, he has been inescapably attracted to observation points above the Earth's surface. With kites, balloons, airplanes, rockets, and satellites, he has sought and obtained the "big look," at times personally and at times in surrogate fashion.

The interrelationships of land, air, and sea phenomena have become increasingly evident as observations have improved with the application of scientific ingenuity and technological refinement. Thus, meteorological satellites permitted for the first time a global view of the relationship between oceanic features and weather conditions, and space exploration has provided new insight into phenomena such as duststorms, drought, snowfall, oceanic currents, icepack movements, coastal sedimentation, volcanic and earthquake activities, and air and water pollution. It also has been of value in such diverse areas as resource inventories, crop and forest management, and wide-ranging geological studies. From today's technological and scientific accomplishments has come further realization of the magnitude of the tasks that man faces in his efforts to understand the Earth's systems.

William H. Jackson, in his 1875 visit to examine the Mesa Verde cliff dwellings in Colorado, required three mules to carry him and his 50- by 60-cm (20 by 24 in.) camera and glass plates. The Skylab Earth-orbital exploratory mission of 1973-74 had far greater requirements and far more extensive objectives. As in Jackson's expedition, it embodied the advantages of direct observation, decisionmaking, and action by man; but, in this instance, from the especially advantageous position of a space platform carrying sensors that span the radio to ultraviolet portion of the electromagnetic spectrum. It provided a new kind of information source, systematic in concept and specifically directed but under the control of those in a position for complementary viewing. The human abilities to see, comprehend, interpret, discriminate, and integrate are unique; from a space platform, they can be focused toward new insights into the features and phenomena of the Earth's land, ocean, and atmosphere systems. This document addresses some of these insights. It may also convey some notion of further opportunities to be provided by the Space Shuttle Program, a scientific study of the Earth in which man again will be the direct and principal agent.

RICHARD H. JAHNS
Stanford University
Stanford, California

December 1976

Preface

THE SKYLAB 4 VISUAL OBSERVATIONS PROJECT was one of our most personally satisfying efforts. We had some unforgettable views of Earth and were able to record some of them to share with our colleagues on the ground. The meager 20 hours we spent in discussions with the 19 discipline scientists before the mission was a small investment that yielded a large return. The men and women who supported this effort can indeed be proud of their participation.

I think that we have discovered a new national resource. With better equipment and more sophisticated training, space observers can capitalize on their initiative, discrimination, and judgment to obtain information to better understand and manage our environment and to conduct Earth science experiments from space. Our 84 days in space (even though we had extremely limited training and simple photographic tools) rewarded us with many spectacular scenes such as the luminescent red, green, and blue plankton blooms in the intertwining ocean currents off the coasts of Argentina and New Zealand and the variety of shapes and colors that define agricultural patterns in many countries. Our knowledge of the planet Earth increased during the mission, and we began to realize the full impact of the scientific briefings we received. We were able to gather new information on many changing features and phenomena. We photographically recorded the eruption of the volcano Sakura-zima in Japan and the vast extent of red dust clouds generated from the Sahara. Within a matter of hours, we were able to compare the color of and photograph all the major sand seas of the world, thereby adding to the knowledge of the deserts. In a similar manner, we observed the ever-changing appearance of the wind-driven ice patterns in the Gulf of St. Lawrence. The direct relation of ice movements to coastal shipping became immediately apparent to us. These are only a few examples of what we recorded verbally, visually, and photographically during the Skylab 4 mission.

When one realizes the vastness of the Earth, the complex interrelations of oceans, land, and atmosphere, and the abundance of information required to understand and manage our environment, it is obvious that the "game is just beginning" and that man will play an important role in the data-gathering and interpretation phase of a total space system. In looking back on Skylab 4, one realizes that a definitive role of man in Earth observations has developed from this mission. Looking forward to the Space Shuttle, which will have better equipment and more sophisticated training, space observers can capitalize on this multimission Earth-orbiting platform to seek answers to many problems about the Earth and its processes.

GERALD P. CARR
Commander, Skylab 4

December 1976

Contents

| | Page |
|--|------|
| INTRODUCTION <i>Verl R. Wilmarth, John L. Kaltenbach, and William B. Lenoir</i> | xi |
| 1. SUMMARY <i>Verl R. Wilmarth</i> | 1 |
| 2. DESERT SAND SEAS <i>Edwin D. McKee, Carol S. Breed, and Steven G. Fryberger</i> | 5 |
| 3. GLOBAL TECTONICS: SOME GEOLOGIC ANALYSES OF OBSERVATIONS AND PHOTOGRAPHS FROM SKYLAB <i>W. R. Muehlberger, P. R. Gucwa, A. W. Ritchie, and E. R. Swanson</i> | 49 |
| 4. GEOLOGICAL FEATURES OF SOUTHWESTERN NORTH AMERICA <i>L. T. Silver, T. H. Anderson, C. M. Conway, J. D. Murray, and R. E. Powell</i> | 89 |
| 5. SKYLAB 4 OBSERVATIONS OF VOLCANOES | |
| PART A. VOLCANOES AND VOLCANIC LANDFORMS <i>Jules D. Friedman and Grant Heiken</i> | 137 |
| PART B. SUMMIT ERUPTION OF FERNANDINA CALDERA, GALAPAGOS ISLANDS, ECUADOR <i>Tom Simkin and Arthur F. Krueger</i> | 171 |
| 6. THE MANICOUAGAN IMPACT STRUCTURE OBSERVED FROM SKYLAB <i>M. R. Dence</i> | 175 |
| 7. SNOW-MAPPING EXPERIMENT <i>James C. Barnes, Clinton J. Bowley, J. Thomas Parr, and Michael D. Smallwood</i> | 191 |
| 8. CULTURAL FEATURES IMAGED AND OBSERVED FROM SKYLAB 4 <i>Robert K. Holz</i> | 225 |
| 9. VEGETATION PATTERNS <i>David M. Carneggie and Brian T. Fine</i> | 243 |

| | |
|--|-----|
| 10. REPORT ON THE SKYLAB 4 AFRICAN DROUGHT AND ARID LANDS EXPERIMENT <i>N. H. MacLeod, J. S. Schubert, and P. Anaejionu</i> | 263 |
| 11. VISUAL OBSERVATIONS OF THE OCEAN <i>Robert E. Stevenson, L. David Carter, Stephen P. Vonder Haar, and Richard O. Stone</i> | 287 |
| 12. AN ASSESSMENT OF THE POTENTIAL CONTRIBUTIONS TO OCEANOGRAPHY FROM SKYLAB VISUAL OBSERVATIONS AND HANDHELD-CAMERA PHOTOGRAPHS <i>George A. Maul and Michael McCaslin</i> | 339 |
| 13. VISUAL OBSERVATIONS OF FLOATING ICE FROM SKYLAB <i>W. J. Campbell, R. O. Ramseier, W. F. Weeks, and J. A. Wayenberg</i> | 353 |
| 14. QUANTITATIVE ANALYSIS OF ATMOSPHERIC POLLUTION PHENOMENA <i>Darryl Randerson</i> | 381 |
| 15. METEOROLOGICAL APPLICATIONS OF SKYLAB HANDHELD-CAMERA PHOTOGRAPHS <i>W. C. Skillman and William E. Shenk</i> | 407 |
| 16. SOME ASPECTS OF TROPICAL STORM STRUCTURE REVEALED BY HANDHELD-CAMERA PHOTOGRAPHS FROM SPACE <i>Peter G. Black</i> | 417 |
| 17. MESOSCALE WAKE CLOUDS IN SKYLAB PHOTOGRAPHS <i>T. Theodore Fujita and Jaime J. Tecson</i> | 463 |
| 18. MESOSCALE CLOUD FEATURES OBSERVED FROM SKYLAB <i>David E. Pitts, J. T. Lee, J. Fein, Y. Sasaki, Kit Wagner, and R. Johnson</i> | 479 |
| APPENDIX A—GLOSSARY | 503 |
| APPENDIX B—STANDARD WEATHER SYMBOLS | 509 |
| APPENDIX C—PHOTOGRAPH INDEX | 511 |

Introduction

OBSERVING THE EARTH was an important part of crew activities during Project Mercury and the Gemini and Apollo Programs, and many spectacular photographs of the land, oceans, and atmosphere were obtained. With the exception of the photographic experiments on Apollo 7 in 1968 and Apollo 9 in 1969, observations were made and photographs were taken at the discretion of the individual crewmember. Nevertheless, the Earth-orbital photography from the manned programs provided geologists and geomorphologists a new perspective for the study of Earth terrain features. The practical applications of space synoptic photography in geology have already been demonstrated.

The successful launch of the Skylab workshop on May 14, 1973, enabled man to observe and study the Earth for periods of 28, 59, and 84 days during the Northern Hemisphere summer, fall, and winter seasons. The following table shows the scheduling of the Skylab missions.

| <i>Mission no.</i> | <i>Crew</i> | <i>Lift-off date</i> | <i>Splashdown date</i> | <i>Days in space</i> |
|--------------------|----------------------------|----------------------|------------------------|----------------------|
| 1 | Unmanned | May 14, 1973 | — | — |
| 2 | Conrad Kerwin Weitz | May 25, 1973 | June 22, 1973 | 28 |
| 3 | Bean Garriott Lousma | July 28, 1973 | Sept. 25, 1973 | 59 |
| 4 | Carr Gibson Pogue | Nov. 16, 1973 | Feb. 8, 1974 | 84 |

The repair of Skylab during the first manned mission reduced the crew's opportunity to study the Earth. However, the crew of the second manned mission observed and photographed 35 land, ocean, and atmosphere sites on instructions from the mission support team at the NASA Lyndon B. Johnson Space Center (JSC). The objectives were to determine what types of features the crew could discern and identify and to determine the composition of onboard data required to perform these observations. From results obtained during this mission, a visual observations experiment was planned for the third manned mission of 84 days. The purpose of this experiment was to determine the quality and the quantity of photographic and observational data that could be acquired by the crew of the many types of Earth features when supported by multidisciplinary scientific training before lift-off, by real-time science mission planning, and by a comprehensive onboard set of procedures, maps, and photographs.

The objectives of the visual observations experiment were as follows:

1. To determine the types of surface, air, and water phenomena the crew could visually identify from the Skylab orbit
2. To determine what visual observations, supplemented by photography, could be accomplished to support scientific investigations
3. To explore the use of several data parameters in the study of multidisciplinary areas
4. To determine the type of crew training necessary to perform the visual observations desired by scientists

From the Skylab 3 experience, it was recognized that additional scientific and operational training was required for the crew to undertake a multidisciplinary visual observations experiment. However, limited time was available for experiment discussion and training with the crew, and only 20 hours of briefings by a team of 19 scientists were completed. From lectures on such diverse subjects as global tectonics, hurricanes, snow mapping, deserts and arid lands, ocean phenomena, sea-ice dynamics, vegetation and cultural patterns, air and water pollution, and mesoscale weather features, the crew gained insight into the significance of the observational data and an awareness of the type of photographs and verbal descriptions needed for specific studies.

During the 84-day mission, communication with the crew was accomplished daily through the Mission Control Center at JSC. The JSC operations team selected and scheduled the observation sites, made recommendations on photography, maintained a status log of photographic and visual accomplishments, and conducted a weekly review with the crew on the status and accomplishments of the experiment. The individual discipline scientists received copies of the crew's daily voice report, which provided them with information for recommendations to the JSC team regarding scheduling of sites and changes or additions to the type of information desired. Upon completion of the mission, the debriefing sessions among the crew, the scientists, and the JSC operational team provided detailed information on specific sites or features described and photographed; they also provided a critique on the operational procedures and utility of the cameras, film, and viewing devices.

During the 84-day Skylab 4 mission, the crew verbally described more than 850 features and phenomena and took approximately 2000 photographs to document their observations. The initial results of the experiment were published in 1974* and included detailed descriptions of crew training and mission operations and preliminary analyses of selected photographs. The integration of the detailed analyses of approximately 600 photographs with the observational data has subsequently been completed, and the results are presented in the individual sections of this document. The maps that form the inside covers indicate the locations of the sites that are discussed herein.

VERL R. WILMARTH,
JOHN L. KALTENBACH, and
WILLIAM B. LENOIR
NASA Lyndon B. Johnson Space Center

* J. L. Kaltenbach, W. B. Lenoir, M. C. McEwen, R. A. Weitenhagen, and V. R. Wilmarth, eds., "Skylab 4 Visual Observations Project Report," NASA TM X-58142, 1974.

1

Summary

VERL R. WILMARTH^a

DURING THE 84 days the Skylab 4 crew orbited the Earth at 435 km (235 n. mi.) above the surface, they conducted an experiment to determine the role of man in observing the Earth on future Earth-orbital missions. The preflight training for the crew consisted of 20 hours of lectures by 19 discipline scientists and was designed to provide the astronauts with an insight into the scientific significance of a feature or phenomenon, the type of information desired by the scientist, and the procedures for observing and photographing. The scientists and the NASA Lyndon B. Johnson Space Center Visual Observations Team, operating through the Mission Control Center, scheduled daily sites for the crew to observe. An onboard data book and a world map showing the site locations were used by the astronauts as background information for the 165 features and phenomena that were identified by the scientists during premission training. Although the time available for the crew to observe and photograph features of interest was limited, more than 850 verbal descriptions were made and approximately 2000 photographs were returned by the Skylab 4 astronauts. The Skylab 4 visual observations, in combination with the handheld-camera photographs from the other Skylab missions, have resulted in new information on (1) Earth features and processes, (2) operational procedures and constraints in observing and photographing the Earth, and (3) the use of man in the real-time analysis of oceanic and atmospheric phenomena.

Binoculars (10×) and handheld Hasselblad (70 mm) and Nikon (35 mm) cameras were the principal instruments used by the crewmen. The camera and lens com-

binations provided wide, medium, and narrow fields of view. Color exterior Ektachrome film was used almost exclusively for photography; the few frames of Ektachrome color-infrared film that were exposed for specific features were generally not as satisfactory as natural color.

Skylab 4 has shown that the study of Earth features can be most effective under specific lighting and surface conditions. The crew observed and photographed the Earth over the entire range of Sun angles from low twilight to local noon and over a range of viewing angles from nadir to high oblique when the Earth's horizon appeared in the scene. Because Skylab 4 was flown in the winter months over the Northern Hemisphere, snow cover enhanced many land features. With the combinations of Sun and viewing angles and the variation in surface conditions, some unusual photographs of the Earth's surface were obtained and are discussed in the individual sections of this report.

High Sun angles (more than 50° from the horizontal) were found to be best for making color discriminations, whereas low Sun angles (less than 20° from the horizontal) were best for detection of topographic and meteorological relief. In general, viewing near the nadir is most desirable; however, oblique views are helpful for discerning the regional framework. It was found that conditions such as haze and cirrus clouds are not as serious a detriment to crew observations as had been anticipated. Regular patterns and bright colors can be detected and classified through as much as 75-percent cloud cover because of the "picket fence" effect.

The use of sunglint was found to be an extremely productive method for observing the surface texture of the oceans and rivers of the Earth. Many photographs and observations were recorded by the crew of large-

^aNASA Lyndon B. Johnson Space Center.

scale dynamic ocean features such as currents and associated eddies, internal waves, upwellings, and coastal sediment transport. Current boundaries and upwellings were easily observed because of color contrasts and the local occurrence of plankton blooms. The boundary features and the current rings caused by the confluence of the Falkland Current and the Brazil Current were observed for more than 3500 km (1900 n. mi.) in the South Atlantic Ocean. Before the mission, these features were largely unstudied. From analysis of Skylab 2 and 3 photographs, eddies as large as 56 km (30 n. mi.) in diameter were identified by color contrast and the occurrence of circular cumulus cloud formations around the periphery. Based on these data, the crew identified similar eddies in ocean currents in the Coral Sea, in the North and South Equatorial Pacific Ocean, and in the South and West Atlantic Oceans. Upwelling areas, particularly along the Chilean and Portuguese coasts, were identified by the dark-blue color and the distinctive surface patterns developed by wind. Of the many ocean features seen by the crew, the location and shape of internal waves were most easily identified in sunglint. A photograph of the Gulf of Nicoya, Costa Rica, contained an internal wave field that was used in analysis of tidal effects. It is these results that suggest the surface manifestation of major ocean events can be studied from manned orbital platforms.

Analyses have been made of the handheld-camera photographs and crew observations of deserts, global tectonic features, the southwestern United States, northwestern Mexico, volcanic regions, and the Manicouagan impact crater in Canada. The Skylab data have been used in worldwide desert research to confirm a global classification of eolian sand deposits and have provided information for preparation of maps that show the relationship of sand deposits to natural barriers, sand sources, rainfall patterns, and surface winds. From Skylab, the crewmen were able within a few hours to compare such features as color and landforms that are important factors in the study of worldwide desert formation.

The synoptic view from Skylab afforded the crew opportunities to observe and photograph many types of global tectonic features under varying Sun angle and

scene conditions. In the southwestern United States and adjacent Mexico, the crew observations were an integral part of a geological experiment that resulted in the recognition of major fault zones in Baja California, southeastern California, and adjacent Sonora, Mexico. Field studies resulting from the crew observations led to the discovery of regionally significant stratigraphic units. The complexity of global tectonic features such as the Alpine Fault in New Zealand, the Atacama Fault in Chile, the African rift zone, Guatemala fault zones, and the Caucasus and Zagros Mountains in Asia is vividly shown in many handheld-camera photographs. Analysis of the photographs revealed new fault patterns and relative ages of crustal movements that pertain to current concepts of plate tectonics.

An unusual oblique photograph of the Manicouagan impact structure in Quebec, Canada, provided the first clear indication of a disturbed zone 150 km (80 n. mi.) from the center that represents the outer limit of disruption from the meteor impact. Concepts derived from this information can be applied to the study of similar landforms on the Earth, Moon, and planets. Oblique photography is an example of how man's capabilities can be used to obtain new scientific information about surface features.

The Skylab 4 crewmen achieved a space "first" by obtaining stereophotographs of the eruption sequence of the Sakura-zima Volcano in Japan. Quantitative analysis of these data combined with upper atmospheric radiosonde data showed that the eruption plume did not penetrate the tropopause and thereby create a stratospheric dust veil.

In the Southern Hemisphere, the crewmen observed the harvesting and subsequent replanting of cereal crops. These observations indicate that a space-based crewman can classify areas of bare soil, bright-green young plants, mature green crops, and crops being harvested. Recording these vegetational patterns and variability within croplands can be accomplished through as much as 75-percent cloud cover. Crop damage was not discernible, but the extent of flood conditions could readily be resolved. In areas of sparse vegetation (such as arid lands), the condition of the foliage could not be ascertained. In general, low-contrast

areas (e.g., ancient cities in arid terrain such as Addis Ababa) were much less discernible than high-contrast areas (e.g., newer cities such as Phoenix). Color contrast is best perceived in near-nadir features that are illuminated by high Sun angle. In postflight viewing of the Skylab 4 photographs, the crew noted reduced details and color discrimination in the photographs compared to what they observed from space.

This mission afforded an excellent opportunity to observe and photograph sea-ice development in the Gulf of St. Lawrence. The observational data, supported by many photographs, have provided information on the rapid variability in ice features over very brief intervals, on the morphological change as new ice forms and old ice thickens, and on the overall extent and character of the ice sheet from beginning to maximum coverage. This information can be used directly for routing ships, relating weather to ice extent, and studying the thermodynamics of ice and seawater.

Although discrimination of snow from clouds is a difficult task from space imagery, the crew readily identified the occurrence and relative depth of snow. They observed that the reflectance of a forest area markedly decreased a short time after a snowstorm because snow did not stay on the trees. They reported that snow cover greatly enhances land features such as city patterns, highways, timber-harvested areas, drainage patterns, and topographic forms. In the winter wheat areas, the crew detected areas of snowfall and areas of early melting that exposed the plants to killing frost. These observations, in conjunction with local weather data, can be important in crop predictions.

In repeated observations of the African Sahel, the crew recorded the occurrence of major duststorms, extensive burning of foliage, the low color contrast of the region, and the widespread occurrence of traditional subsistence (cellular) land use patterns in regions adjacent to the Sahel. Data from Skylab, Landsat, and field studies have shown that destructive agricultural land use practices are warning signs of aridification—a precursor to desert formation, loss of productivity, and mass starvation. The synoptic view from a space platform has enabled man to observe parameters that are useful in the study of the cause of the Sahelian drought.

Of the many meteorological phenomena described

and photographed, those unresolvable in meteorological satellite images are particularly important for understanding the relationship of such features to weather conditions and predictions. The stereophotographs are valuable in determining the heights of multilayered clouds and the details of cloud structure. An analysis of handheld-camera photographs and upper atmosphere data has shown that in a stable atmosphere Kármán vortex streets form downwind of large islands when the wind velocity ranges from slow to medium, whereas wake waves occur downwind of a small island under medium to fast flow. Analysis of photographs of cloud streets and local weather data has revealed that cloud streets occur in an unstable atmosphere with a medium to slow wind velocity and are indicative of low-level windflow as possible clues for developing cyclonic systems.

Important observations and photographs made by the Skylab crewmen have aided in the recognition of small features such as persistent convective overshoot regions and concentric waves in developing tropical storms; the existence of outward-tilting eyewall clouds in some quadrants of mature tropical storms; and the existence of overshooting convective turrets, internal gravity waves, and transverse waves near the center of mature tropical storms. These results require new thinking in tropical storm studies, including modification of current computer models to include the possibility of sloping eyewalls.

Photographs and observational data of manmade and natural atmospheric pollution indicate that observations of such features from space can be useful. Descriptions and photographs of many different sources of atmospheric contamination were made that permit postflight analysis of wind conditions and of the size, shape, extent, and textural variations of the pollutant. As a result of further detailed analyses, source features, atmospheric conditions, diffusion, and other parameters possibly can be related to the occurrence and distribution of the pollutants.

The major limitations on the results of this project were the extremely tight scheduling of the crew's time and the lack of preflight crew training in rapid site recognition and observation.

2

Desert Sand Seas

EDWIN D. MCKEE,^a CAROL S. BREED,^b AND STEVEN G. FRYBERGER^b

A WORLDWIDE SURVEY of desert sand seas using mosaicked false-color imagery from the unmanned Earth resources technology satellite (Landsat-1) as a map base was initiated in 1972. Imagery data were combined with data from ground-based studies of climate and from field studies of the internal structures of eolian sand deposits. To obtain detailed information concerning the origin, movement, and distribution of the world sand seas, the Skylab 4 crewmembers were asked to make observations and to obtain handheld-camera color photographs of 18 important locations. The formally designated areas were those sand seas that are most difficult to study using conventional means, either because reliable maps and aerial photographs are not available or because the region is inaccessible for political reasons.

The usefulness of manned observations and handheld-camera photographs from space is confirmed by the immediate application of Skylab 4 data to the study of sand seas. The Skylab 4 crew provided information that (1) confirms a tentative global classification of eolian sand deposits based on observed similarities in most of the major deserts of the world; (2) allows the preparation of maps that show the relationships of sand deposits to each other, to sand source areas, to natural sand distribution barriers, and to human land use; and (3) allows the regional patterns of large-scale dune morphology to be studied in relation to rainfall distribution and surface winds.

The data provided by the Skylab 4 crew, when combined with further ground-based work both in the laboratory and in the field, should have long-range applications to geologic and geographic research in at least the following five areas.

1. Geologic interpretation of environments of deposition of eolian sandstones. The effects of primary sedimentary structures that control migration of oil, water, or other fluids can be better evaluated.

2. Understanding dune movement. Control of dune movement is important in areas subject to sand inundation, such as the Sahelian Zone of northern Africa and the Thar Desert of India and Pakistan.

3. Prediction of future environments of sand deposition in areas of drought, as in parts of India, Australia, and northern Africa.

4. Exploration for wind-concentrated mineral deposits.

5. Interpretation of exotic environments of wind deposition, such as those believed to exist on Mars, by comparing Martian sand seas with sand seas on Earth.

The sites chosen for handheld-camera photographs and visual observations included four in the Sahara and sub-Sahara of northern Africa, four in the Namib and Kalahari Deserts of southern Africa, two in the Empty Quarter of Saudi Arabia, five in the Takla Makan and Gobi Deserts of China, and three in the trans-Caspian deserts of the U.S.S.R. Additional areas in northern Africa, India, Mexico, and Australia were recommended as optional sites.

The Skylab 4 crew succeeded both in obtaining photographs and in making visual observations of most of the formally designated areas of study and many of the optional sites (fig. 2-1).

^aU.S. Geological Survey, Denver, Colorado.

^bU.S. Geological Survey, Flagstaff, Arizona.

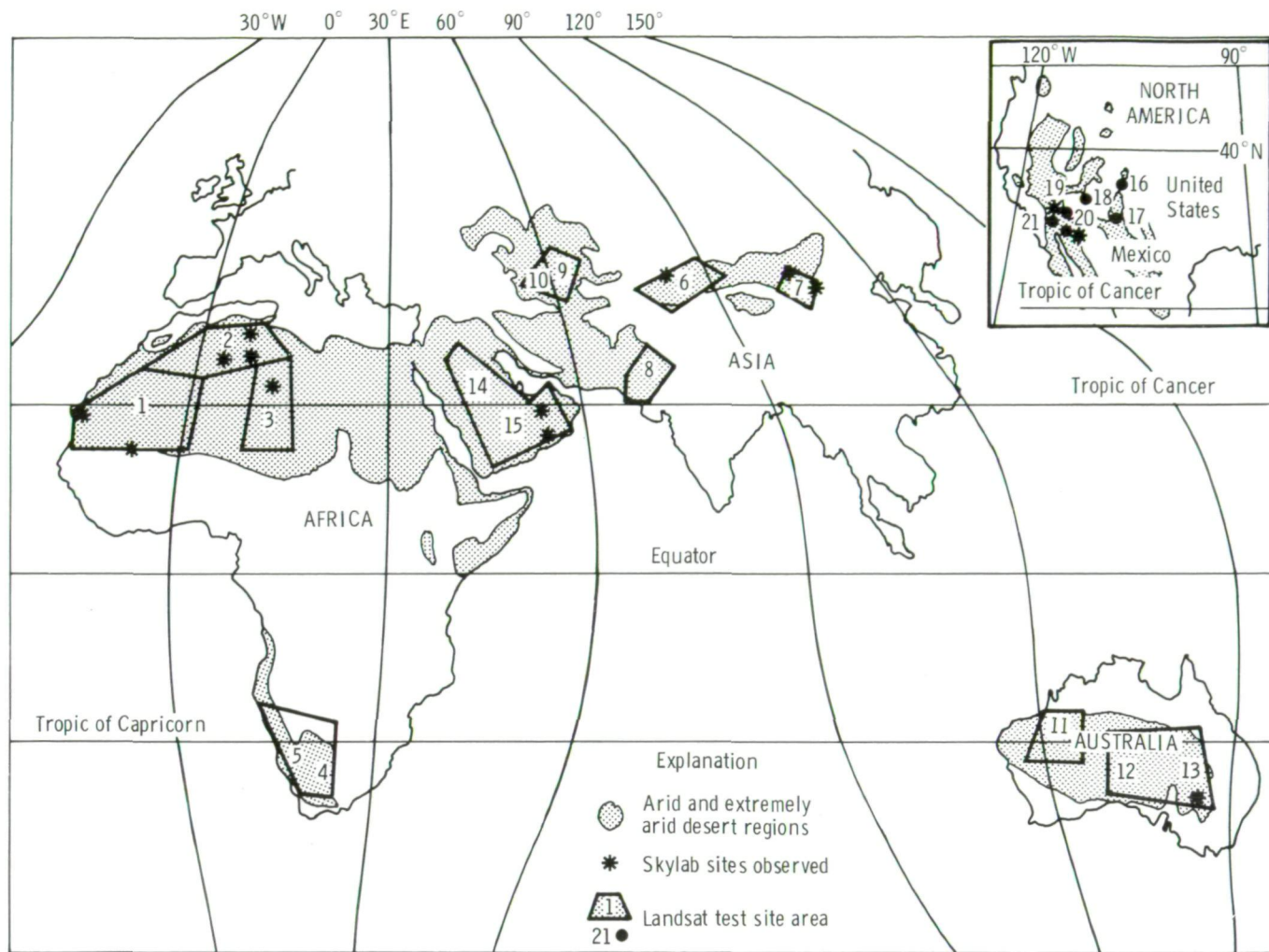


FIGURE 2-1.—Index map of principal desert and semiarid regions showing Landsat-1 test site areas and Skylab handheld-photograph sites in the sand seas of Asia, Africa, Australia, and North America. Numbers on the map correspond to the following areas: (1) Mauritania, Mali; (2) Great Western and Great Eastern Ergs, Algeria; (3) Libya, Niger, Chad; (4) Kalahari Desert, South Africa; (5) Namib Desert, South West Africa; (6) Takla Makan Desert, China; (7) Gobi Desert, China; (8) Rajasthan-Thar Desert, India and Pakistan; (9) Kyzylkum Desert, U.S.S.R.; (10) Karakum Desert, U.S.S.R.; (11) Great Sandy Desert, Australia; (12) Great Victoria Desert, Australia; (13) Simpson Desert, Australia; (14) An Nafud, Saudi Arabia; (15) Empty Quarter, Saudi Arabia; (16) Sand Hills, Nebraska; (17) White Sands, New Mexico; (18) Great Sand Dunes, Colorado; (19) Navajo Country, Arizona; (20) Gran Desierto, Mexico; (21) Algodones Desert, California.

GLOBAL CLASSIFICATION OF EOLIAN SAND DEPOSITS SEEN FROM SPACE

Terminology

The Skylab 4 crewmembers provided the first test of a preliminary, large-scale classification of eolian sand deposits. The need for an objective global definition of dune forms is desirable because earlier work has been limited mostly to local studies in single desert regions.

The great number of these local studies has resulted in a multiplicity of names for eolian sand deposits. Furthermore, the dune terminology of local studies could not be transposed from region to region because many of the older categories (e.g., transverse, longitudinal) carried genetic implications. Early in this project, an objective classification was developed that was based on major sand-sea patterns as seen on Landsat imagery. The validity of this system for inventorying large sand deposits from space was confirmed by the observations

TABLE 2-I.— Global Classification of Eolian Sand Deposits Seen From Space

| <i>Large-scale eolian sand deposits</i> | | | <i>Figure no.</i> | <i>Major areas of occurrence</i> |
|---|---|--|-------------------------|---|
| <i>Dune pattern</i> | <i>Dune description</i> | <i>Form</i> | | |
| Parallel straight | Has length many times greater than width, regular spacing, dune/interdune area ratio approximately 1:1 | Simple | 2-2(a) | Simpson, Great Victoria, and Great Sandy Deserts, Australia |
| | | Compound | 2-2(b) | Kalahari Desert in South Africa; Sahara, northern Africa; Navajo Country, United States |
| | | Widely spaced (with dune/interdune area ratio less than 1) | 2-2(c) | Sahara, northern Africa |
| | | Complex, with incipient radial (star) dunes on crests (transitional to star dunes alined on sub-parallel linear ridges to form chains) | 2-2(d) | Namib Desert, South West Africa |
| Parallel wavy | Composed of crescentic segments each with the width equal to or nearly equal to the length, to form wavy ridges that have all major slipfaces on one side | Simple | 2-3(a) | White Sands, New Mexico; Sand Hills, Nebraska; Karakum and Kyzylkum Deserts, U.S.S.R.; Sahara, northern Africa; Empty Quarter, Saudi Arabia; Namib Desert, South West Africa; Thar Desert, India and Pakistan |
| | | Simple | 2-3(b) | Empty Quarter and An Nafud, Saudi Arabia; Thar Desert, India and Pakistan; Libyan Desert, northern Africa |
| | | Giant crescent | 2-3(c) | Saudi Arabia; Algodones Desert, California; Sonora Desert, Mexico; Atacama Desert, Peru |
| | | Chevron | 2-3(d) | Takla Makan Desert, China |
| Star | Sand mountains with segments radiating from the centers of the complexes in pinwheel fashion | Scattered | 2-4(a) and 2-4(b) | Great Eastern Erg, Algeria; Empty Quarter, Saudi Arabia; Gobi Desert, China; Namib Desert, South West Africa |
| | | Star dune alined on sub-parallel linear ridges to form chains | 2-4(c) and 2-4(d) | Great Eastern and Great Western Ergs, Algeria; Empty Quarter, Saudi Arabia; Sonora Desert, Mexico |
| | | | | |
| | | | | |
| Parabolic (U-shaped) | U-shaped dunes with elongate arms at least partly fixed by vegetation | Simple form with two arms | 2-5(a) | White Sands, New Mexico |
| | | Compound clusters of coalesced parabolic dunes with several arms; commonly several kilometers in size | 2-5(b) | Thar Desert, India and Pakistan |
| Sheets and stringers | Eolian sand deposits without slip-faces but with distinct geographic boundaries (may include bed forms below resolving power of Skylab photographs) | Large | 2-6(a) | Sahara, northern Africa; southern Kalahari Desert, South Africa |
| | | Small | 2-6(b) | An Nafud, Saudi Arabia; Mojave Desert, California; Painted Desert, northern Arizona |

of the Skylab 4 crew and documented by their photographs.

The morphologic classification shown in table 2-I applies to large-scale dunes called draa by some investigators. These large dunes may be composed of numbers of smaller dunes and, depending on type, commonly are 2 or 3 km in diameter from front to back or from horn to horn. In many regions, also, the dunes are separated from each other by flat, windswept interdune corridors or hollows (called couloirs, bahirs, gassis, fuljes, feidj, and other local names). (For a glossary of related terms, see appendix A.) These interdune features are an integral part of the overall pattern of a sand sea. An understanding of the characteristics of the interdune areas is important to an understanding of the internal structures of eolian sandstones discussed in the latter part of this section.

Although most sand seas display several characteristics and distinctive dune types, sufficient similarities among regional sand patterns have been seen from space to place all dunes in one of five major pattern categories: (1) parallel straight, (2) parallel wavy, (3) star, (4) parabolic, or (5) sheets and stringers. Within each major pattern, varieties or subtypes result from the interaction of several different influences. Principal controls on regional dune patterns are variations in wind regime, position or topographic barriers, rainfall, vegetation, changes of elevation within depositional basins, and distance downwind from the sources of sand. The major types of eolian sand patterns as seen and photographed from Skylab are shown in figures 2-2 to 2-5 and are briefly described in table 2-I.

Sand Patterns

Parallel straight dunes (fig. 2-2), whether simple or compound, are many times greater in length than in width. In most (perhaps all) areas, the straight sand ridges have slipfaces along both sides. Dunes of this type have been called longitudinal dunes (refs. 2-1 to 2-4), sand ridges (refs. 2-5 and 2-6), draa (refs. 2-7 and 2-8), and seif chains or seifs (refs. 2-9 to 2-11). A relatively simple type of parallel straight dunes makes a distinctive pattern in the Simpson Desert of Australia

(fig. 2-2(a)). Very large compound dunes of this type that extend 1000 km from east to west are present in the Empty Quarter of Saudi Arabia (fig. 2-2(b)). A wide spacing of parallel straight dunes (fig. 2-2(c)) occurs in the western Sahara of northern Africa, and a complex variety occurs in the Namib Desert of South West Africa (fig. 2-2(d)). In the Namib, the crests of parallel ridges have been modified into incipient star dunes, and a complex dune variety is formed that is intermediate between the parallel straight and the star dunes. Another variety (not illustrated in this report) is the feathered seif, which may be classified as a compound parallel straight dune.

Parallel wavy dunes (fig. 2-3) are composed of individual arc-shaped (crescentic) segments, each having a width equal to (or almost equal to) the length. Typically, the segments are aligned in wavy ridges that are asymmetrical in plan view, and the ridges have all the major slipfaces on one side. The most common development of this type is the transverse or barchanoid ridge with open interdune corridors, described by McKee (ref. 2-10) at White Sands, New Mexico, and now recognizable (in Landsat imagery and Skylab photographs) in many deserts throughout the world. A small-scale example of transverse ridges is illustrated in the aerial photograph of White Sands, New Mexico (fig. 2-3(a)).

Parallel wavy dunes that have fully enclosed interdune spaces have been called peak and fulje (ref. 2-12), compound transverse dunes (ref. 2-13), and akle (refs. 2-14 and 2-15). An example of the parallel wavy patterns occurs near Ghat in the Libyan Desert (fig. 2-3(b)).

A compound form of the parallel wavy dune type that has been called giant crescent (ref. 2-16) occurs in the Empty Quarter of Saudi Arabia (fig. 2-3(c)). The giant crescentic dune, shown joined in chains in figure 2-3(c), has a single major slipface and many smaller crescentic dunes on its windward slope. This dune form occurs in the Algodones Desert of California and Mexico where it has been called megabarchan (ref. 2-17). The giant Pur-pur dune of Peru (ref. 2-18) and dunes around the Pinacate Mountains of northern Sonora, Mexico (fig. 2-4(d)), are other examples of giant crescent dunes.



FIGURE 2-2.—Parallel straight dune patterns. (a) Simple, Simpson Desert (SL4-143-4637). (b) Compound, Empty Quarter, Saudi Arabia (SL4-143-4643). (c) Widely spaced, Sahara, northern Africa (SL3-28-365). (d) Complex, Namib Desert, South West Africa (SL4-137-3693).

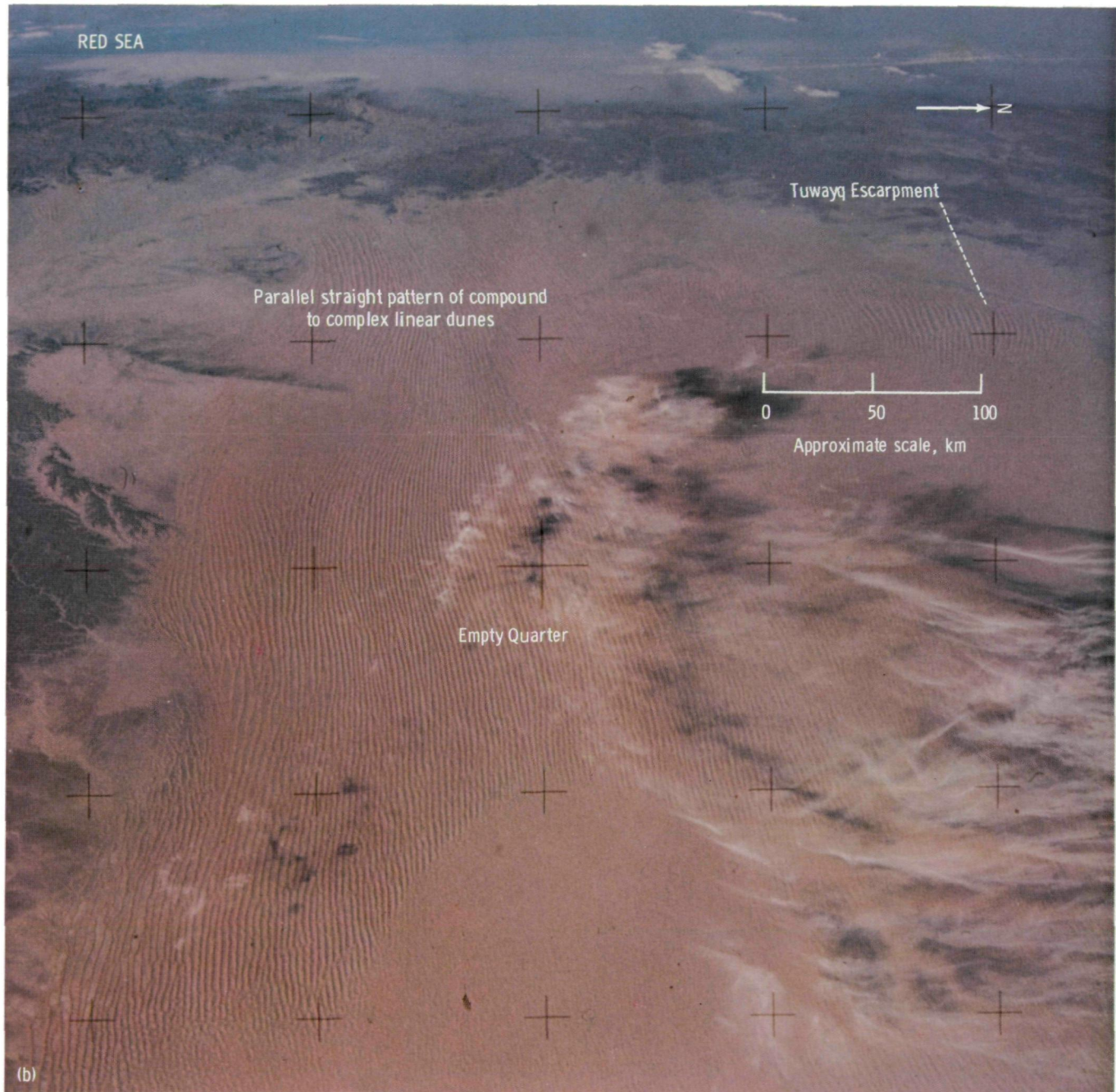


FIGURE 2-2.—Continued.

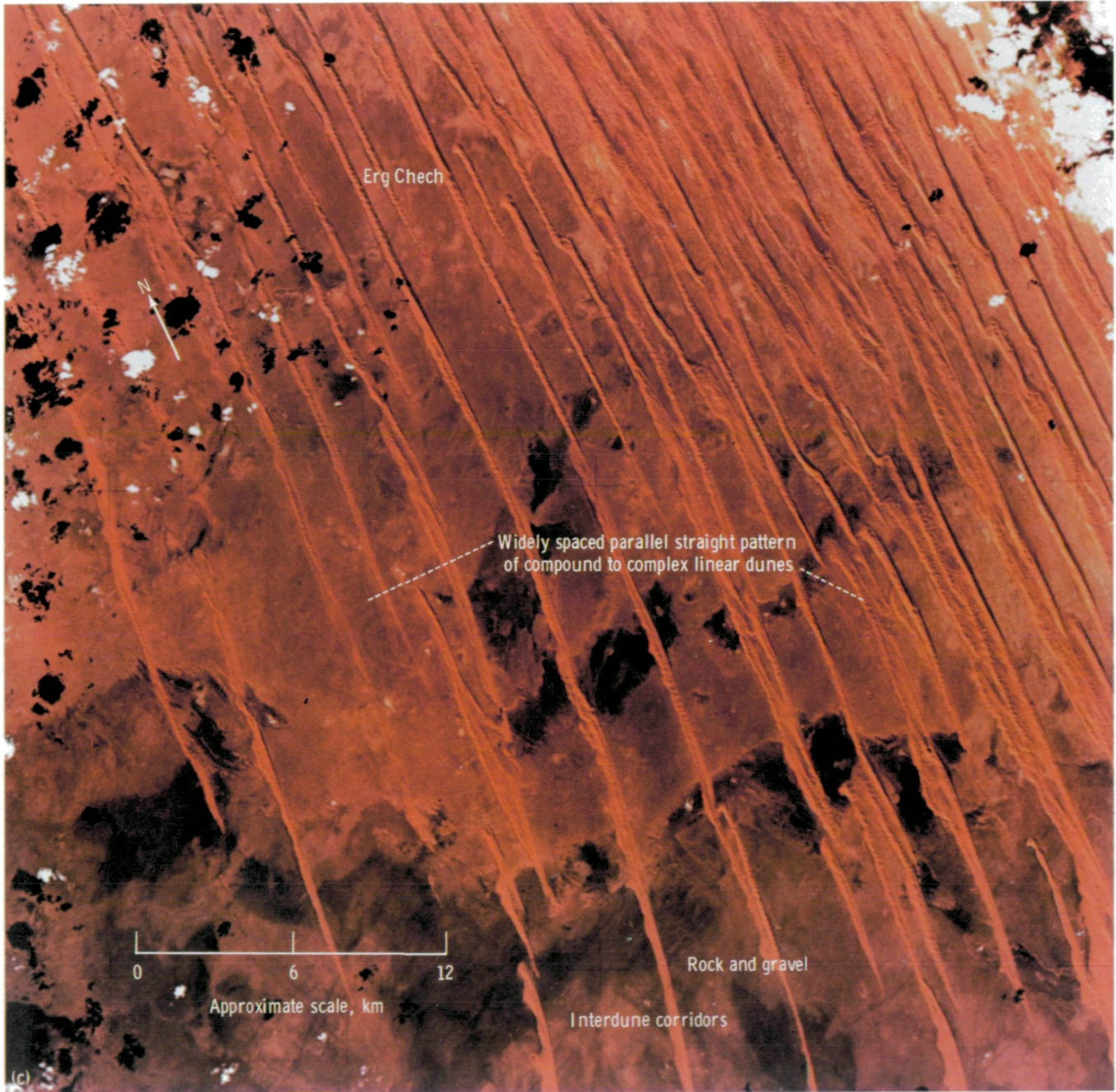


FIGURE 2-2.—Continued.

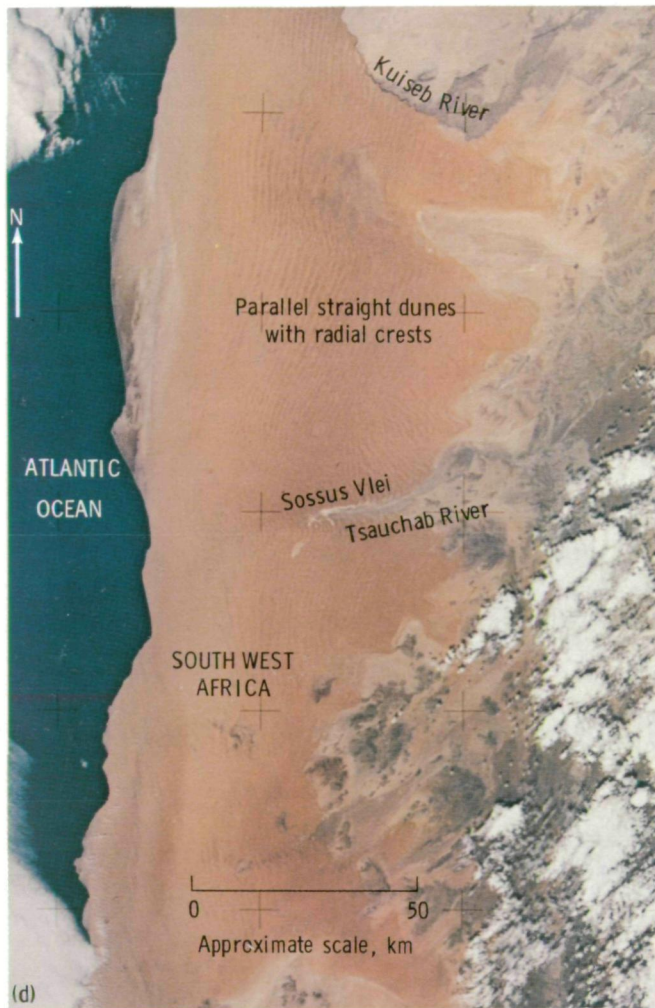


FIGURE 2-2.—Concluded.

Oblique-angle photographs were taken by the Skylab 4 crew of a variety of the parallel wavy dune pattern that has only been observed in the Takla Makan Desert of northern China (fig. 2-3(d)). In the Takla Makan Desert, rows of dune ridges and interdune areas are offset and form a chevron or herringbone pattern first described by Hedin (ref. 2-19). Because it is both physically remote and politically inaccessible, the Takla Makan Desert is known to western geologists scarcely better now than in Hedin's time. Thus, photographs and images from space are especially valuable.

Star dunes (fig. 2-4) have segments or arms that radiate from the high center part of the dune complex in pinwheel or starlike fashion and constitute mountains of sand. These huge features have been called rhoursds or polypyramids (ref. 2-20); mastodons (ref. 2-21); oghurds (refs. 2-4 and 2-22); khurds (ref. 2-7); pyramidal dunes (ref. 2-16); draa peaks or stellate roses (ref. 2-23); and star dunes (ref. 2-10). Different patterns are formed by random scattered star dunes and star dunes alined in chains. Scattered star dunes, most of them more than 200 m high (ref. 2-24, p. 99), occur in the Erg Oriental of Algeria (fig. 2-4(a)).

In South West Africa, scattered star dunes near the dry river valleys of the northern Namib Desert were photographed by the Skylab 4 crewmen and are shown in figure 2-4(b); star dunes in this desert are reportedly as high as 270 m (ref. 2-25, p. 133).

Star dunes on linear ridges and alined in chains in the southwestern part of the Erg Oriental, Algeria (fig. 2-4(c)), were observed by the Skylab crew. The highest dune in this part of the erg is 320 m, according to Wilson (ref. 2-24, p. 93).

Star dunes in chains that are smaller than the Algerian star dunes but identical to them in form can be discerned in Skylab photographs of the Sonoran Desert approximately 100 km west of the Pinacate Mountains in northern Mexico (fig. 2-4(d)). The previously described giant crescent dunes are also shown in figure 2-4(d). Linear distribution of star dunes was identified in northern Sonora early in 1973. These are the only star dunes observed to date in space imagery of North American deserts and are, therefore, prime targets for field studies of the internal structure of star dunes. Preliminary studies of structures in star dunes near Zalim, Saudi Arabia, were made by McKee (ref. 2-10).

Parabolic dunes (fig. 2-5) are U- or V-shaped dunes (called upsiloidal dunes by Smith in ref. 2-13) that are greatly elongated in plan view. Although not implicit in the definition of parabolic dunes, the arms of most of these dunes are partly anchored by vegetation and extend upwind. Simple parabolic dunes that developed along the downwind margins of White Sands National Monument, New Mexico (fig. 2-5(a)), were studied in the field by McKee and others during the years 1964 to 1967 and 1972 to 1973.

Compound parabolic dunes in which multiple extended arms form complexes as long as 40 km occur in the Thar Desert of India and Pakistan (ref. 2-26, p. 210, and ref. 2-27). The parabolic dune patterns of this region, shown in a Landsat image (fig. 2-5(b), upper right), probably contain the largest individual dunes of this type in the world. However, no Skylab photographs of this desert were taken, and no parabolic dunes were

observed by the crew in any of the deserts over which they orbited.

Sheets and stringers of sand as seen on space imagery are relatively flat-appearing deposits that have well-defined geographic boundaries. An example of sheets and stringers of sand in the northwestern part of the Sahara in Africa is shown in figure 2-6(a). The relationship of the sand streaks in this photograph to the wind

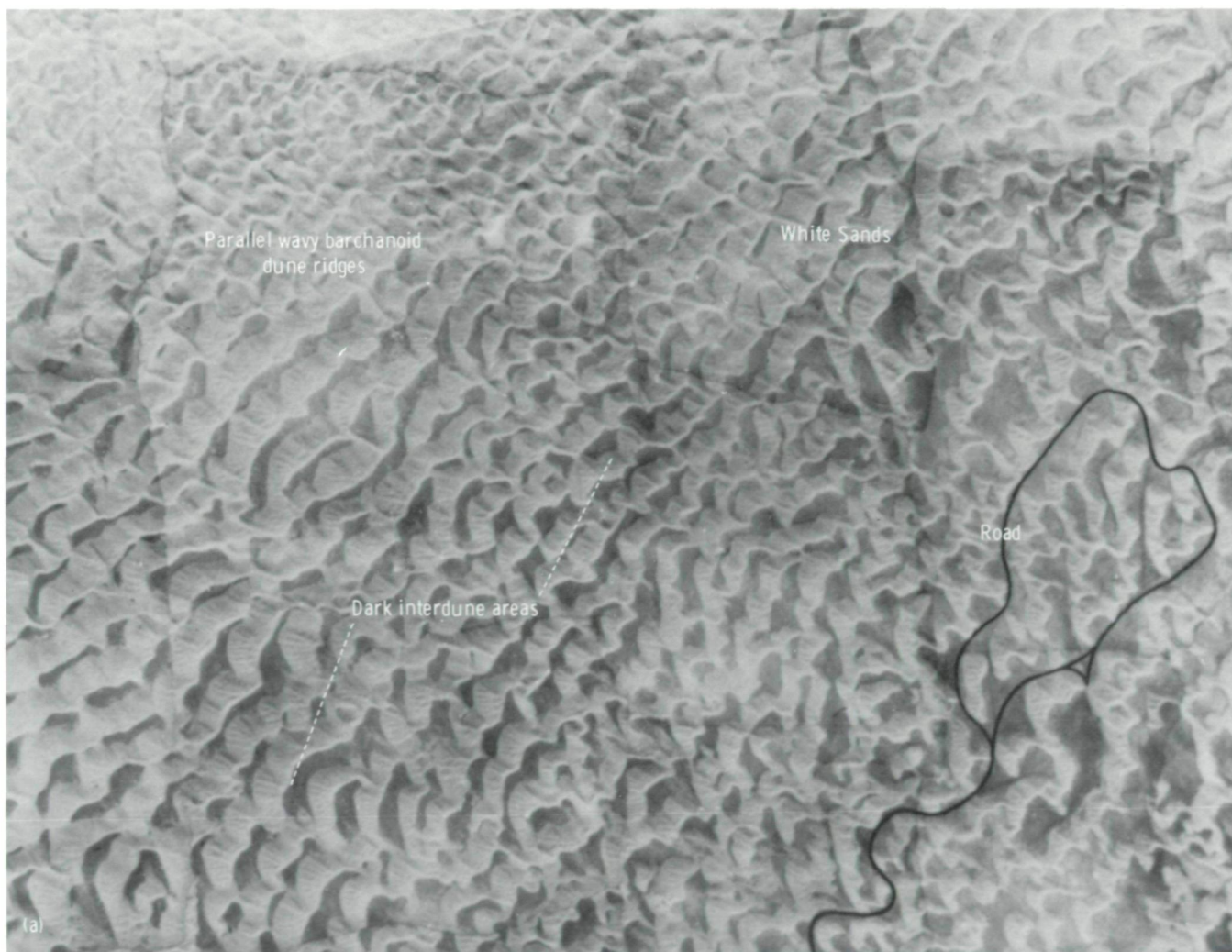


FIGURE 2-3.—Parallel wavy dune patterns. (a) Simple, White Sands, New Mexico (aerial photograph). (b) Simple with full enclosure of interdune areas, Marzūq Sand Sea, Libya (SL4-141-4354). (c) Giant crescent, Empty Quarter, Saudi Arabia (SL4-141-4255). (d) Chevron, Takla Makan Desert, China (SL4-136-3389).

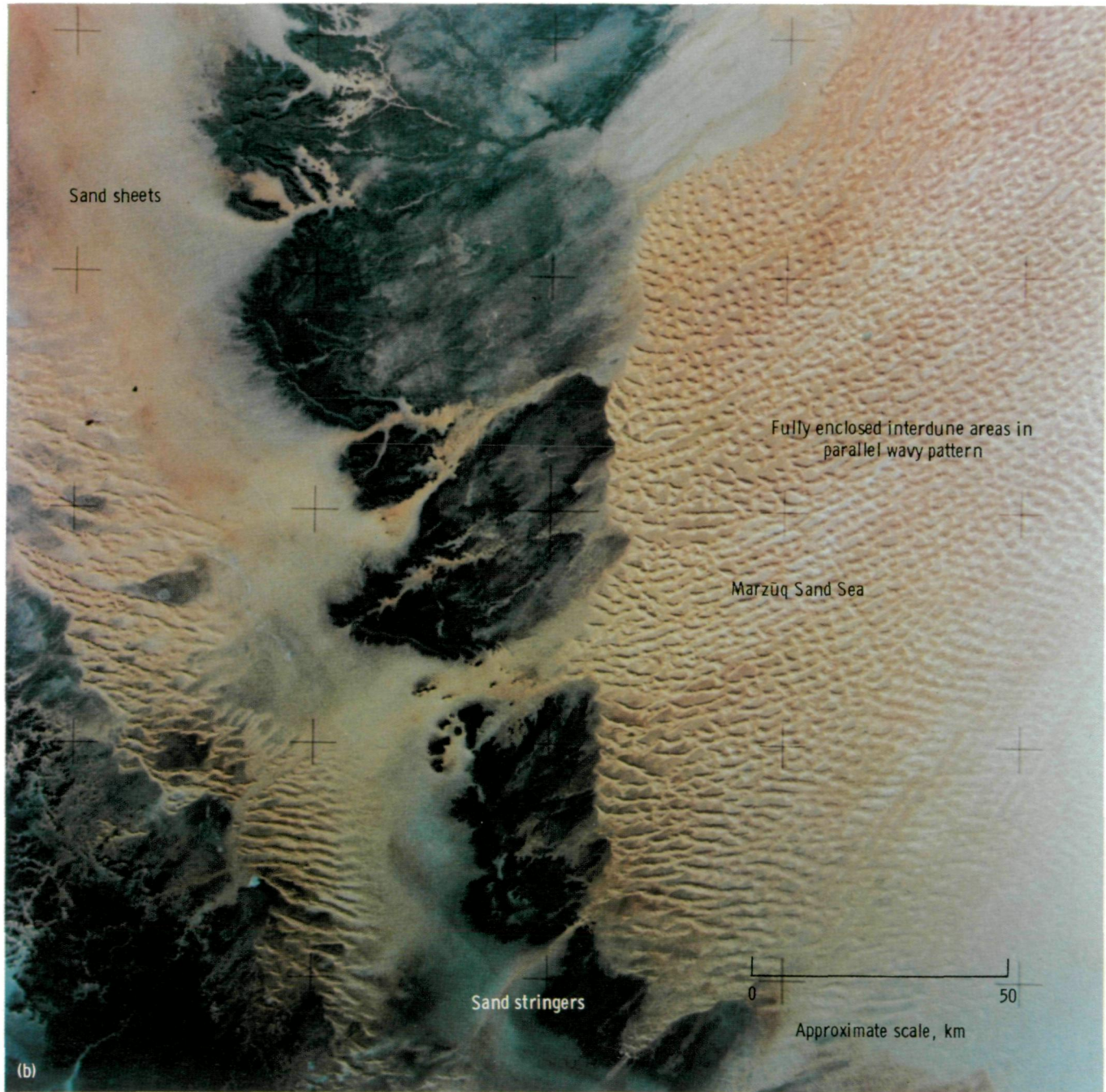


FIGURE 2-3.—Continued.

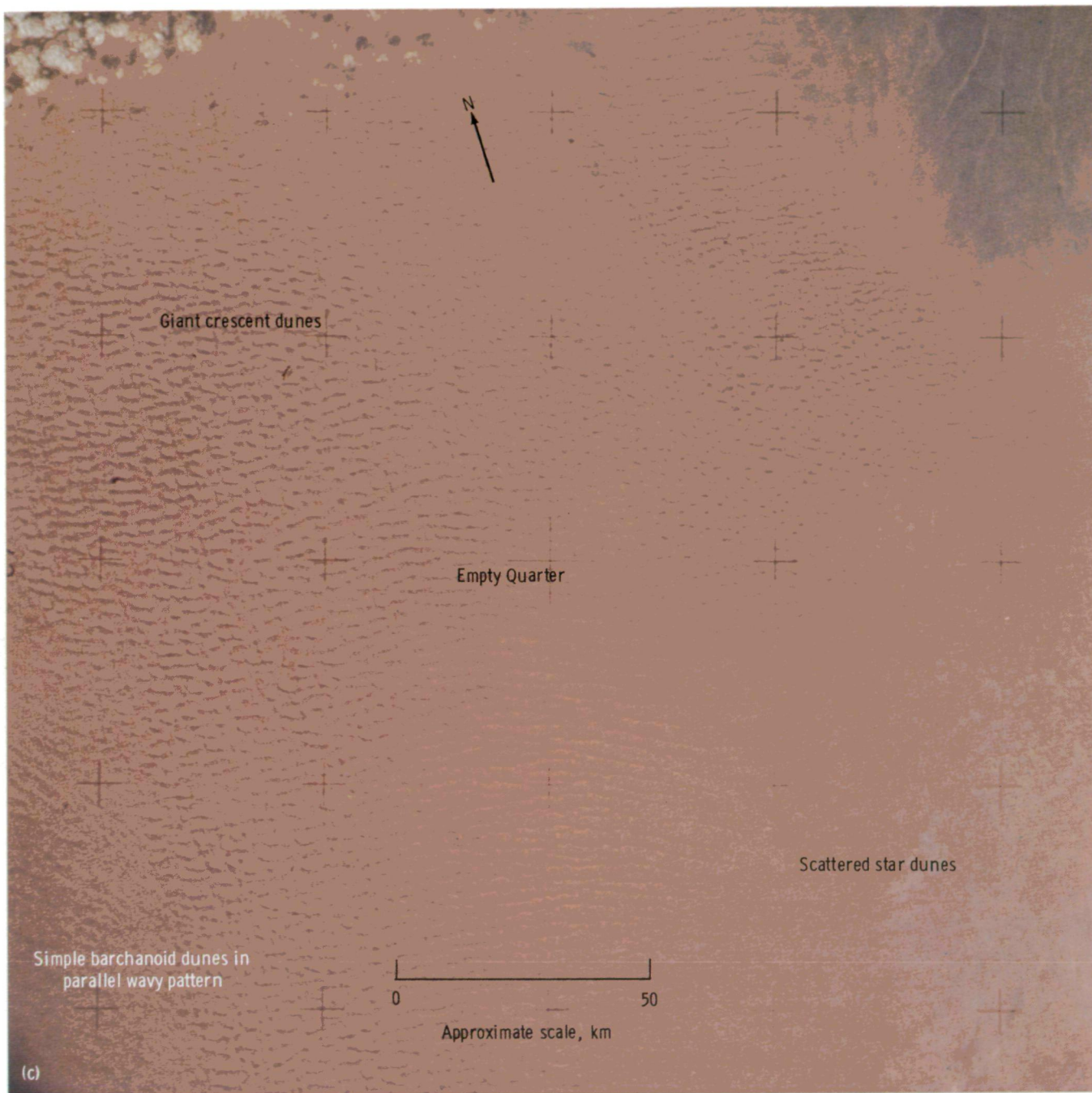


FIGURE 2-3.—Continued.

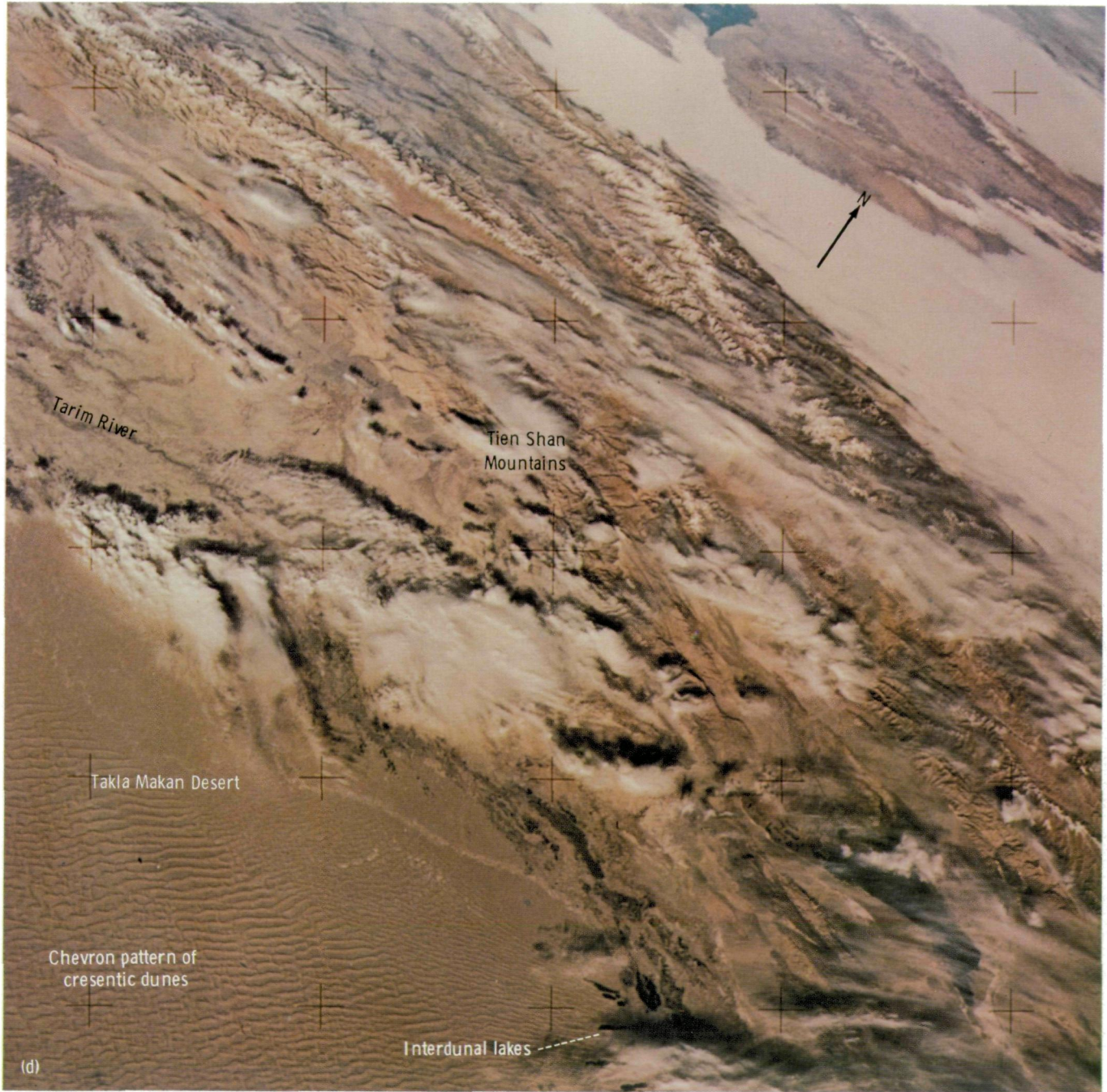


FIGURE 2-3.—Concluded.

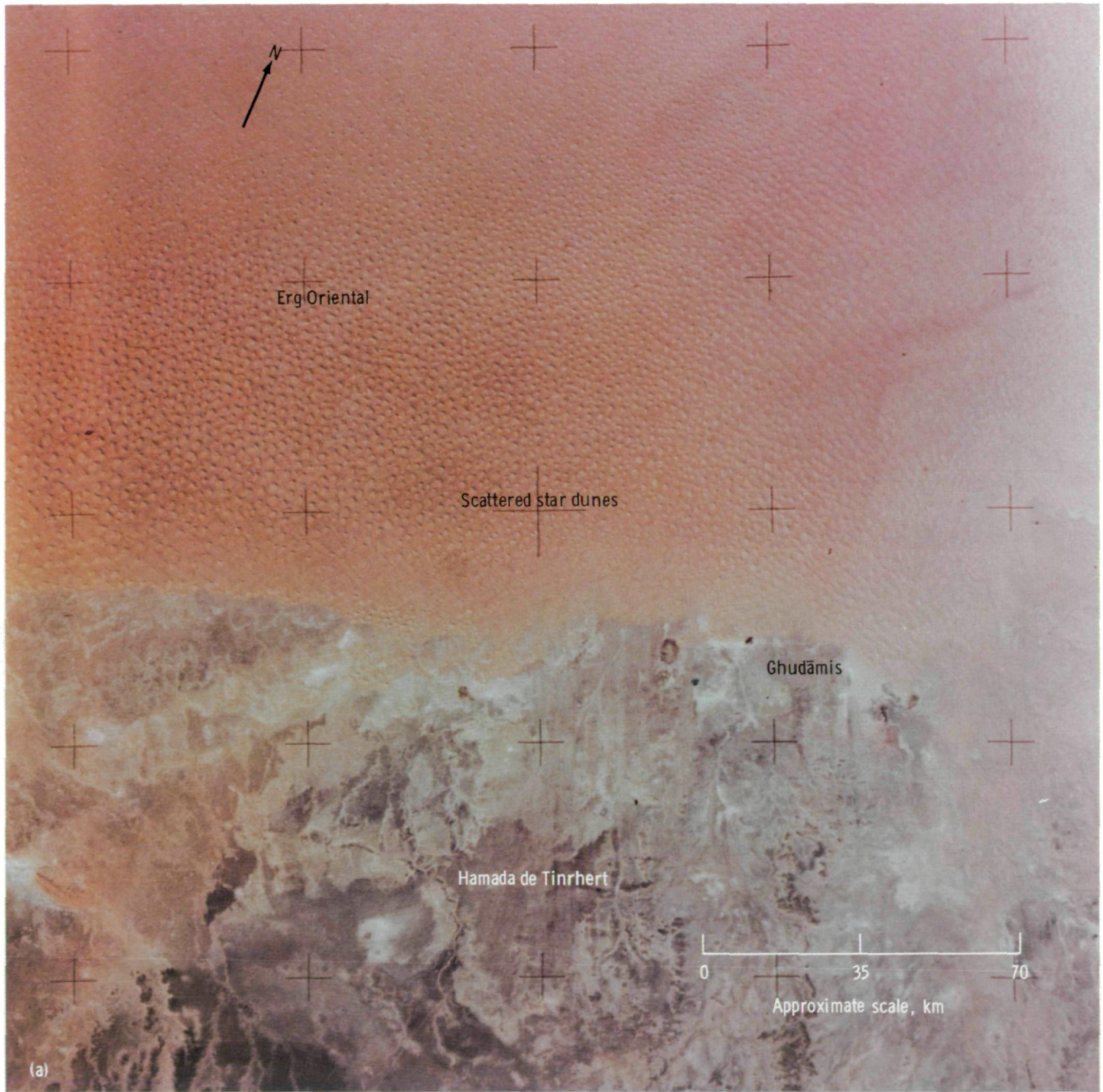


FIGURE 2-4.—Star dune patterns. (a) Scattered, Erg Oriental, Algeria (SL4-139-3900). (b) Scattered, Namib Desert, South West Africa (SL4-207-8074). (c) Star dunes in chains, Erg Oriental, Algeria (SL4-138-3885). (d) Star dunes in chains, Sonora, Mexico (SL4-140-4131).

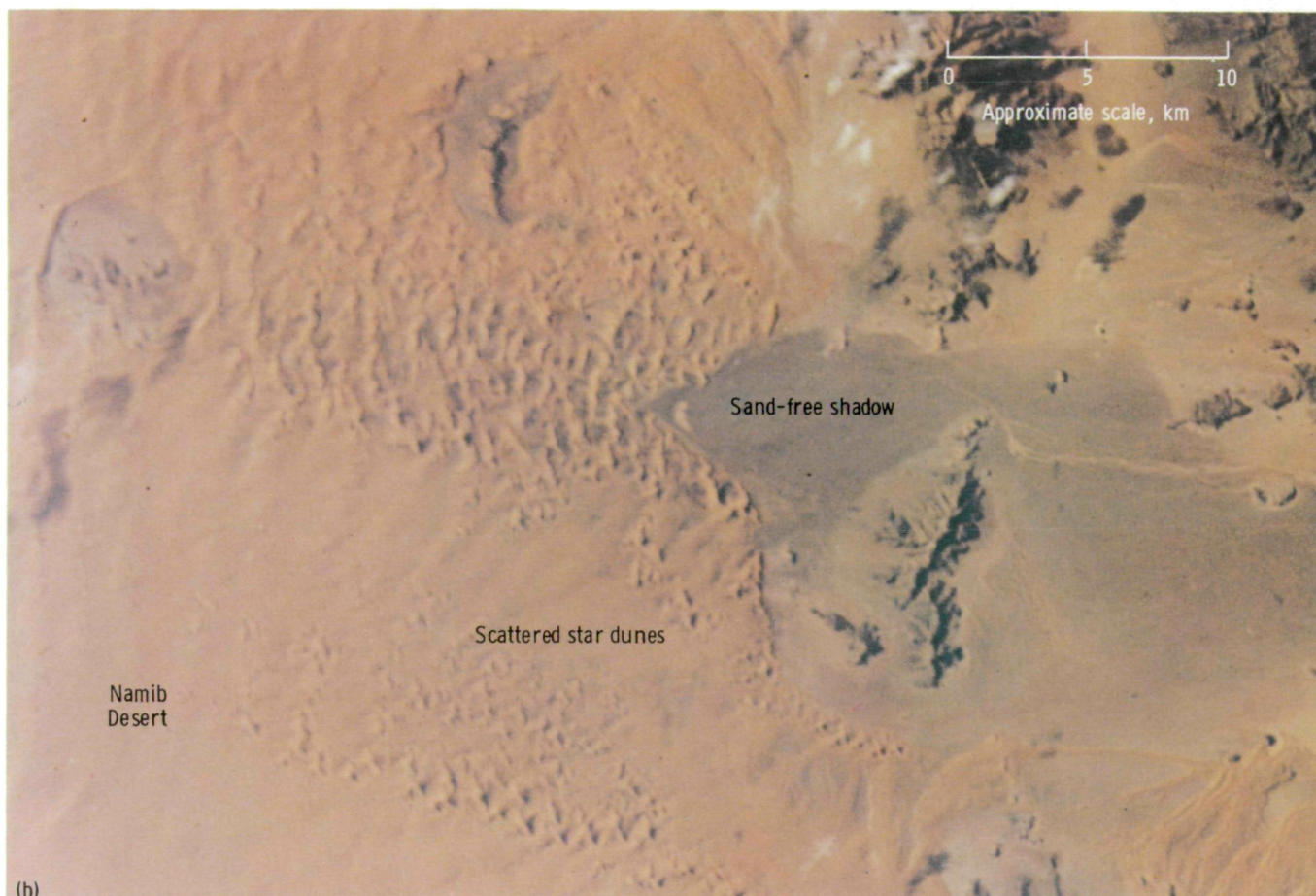


FIGURE 2-4.—Continued.

regime of northwestern Africa is discussed in the section entitled "Relationship of Sand Distribution to Surface Wind Regimes."

Sheets and stringers of sand may include eolian forms that are too small to be resolved on space photographs or imagery. Sand stringers in Landsat imagery of northern Arizona are shown in figure 2-6(b). These sand stringers were examined in the field and found to consist of elongate sheets of sand on which many small dunes (domes and barchans) had formed.

The classification summarized herein was confirmed and refined by the work of the Skylab 4 crewmen, whose observations and photographs of eolian sand bodies were accommodated by the outlined classifica-

tion. A field examination of some of the basic dune types conducted by the senior author is summarized elsewhere in this section. Some field work remains to be done to test hypothetical relationships among types of dune patterns seen from space, the internal structures of specific dune types, and the relationship of these depositional features to surface wind regimes. Areas in which hypotheses might readily be field tested include the area in southern California and northern Sonora near Yuma, Arizona, where two of the major eolian sand dune patterns (parallel wavy and star aligned on parallel straight ridges) have been identified both in Skylab photographs and in Landsat imagery.

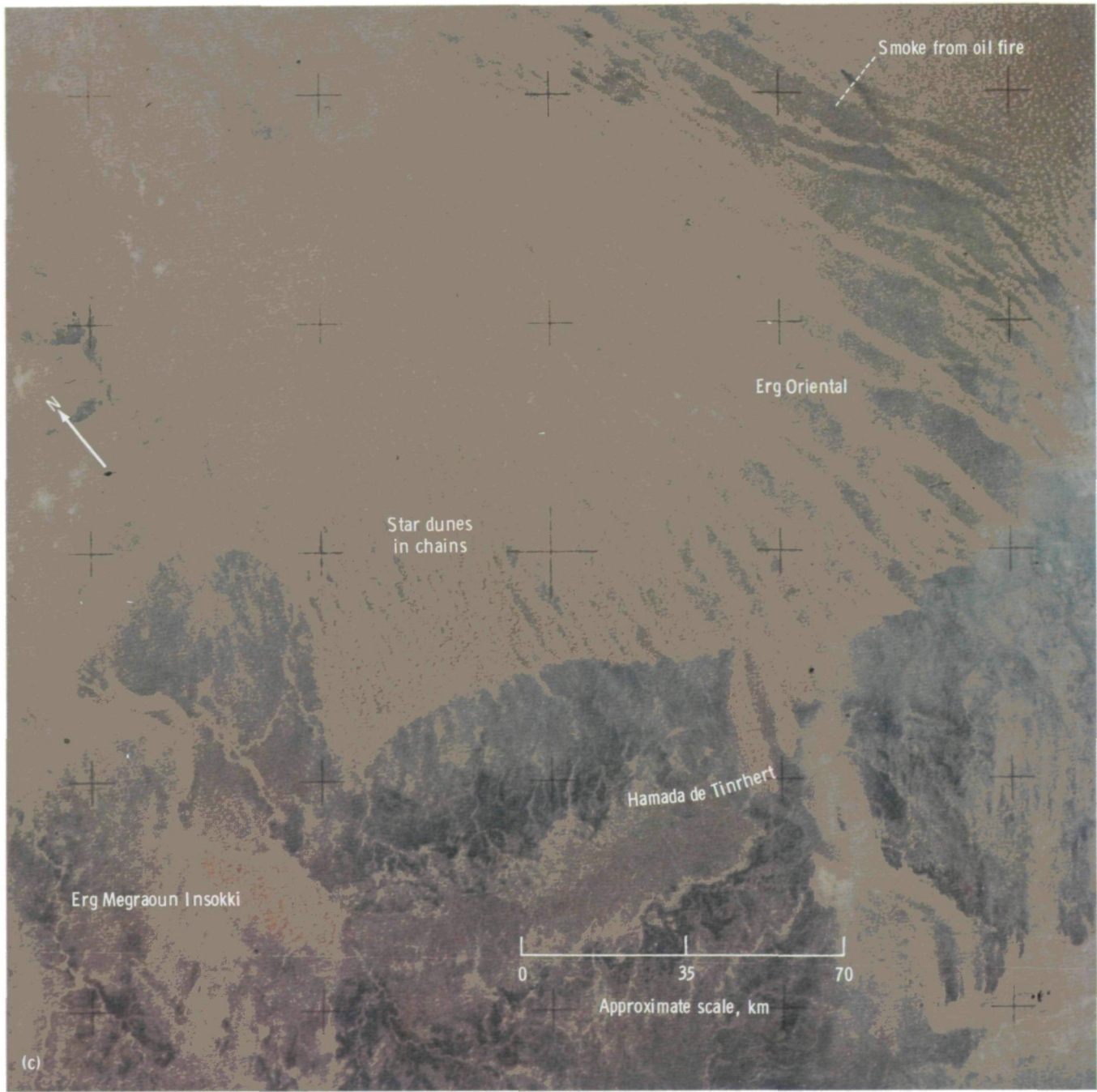


FIGURE 2-4.—Continued.

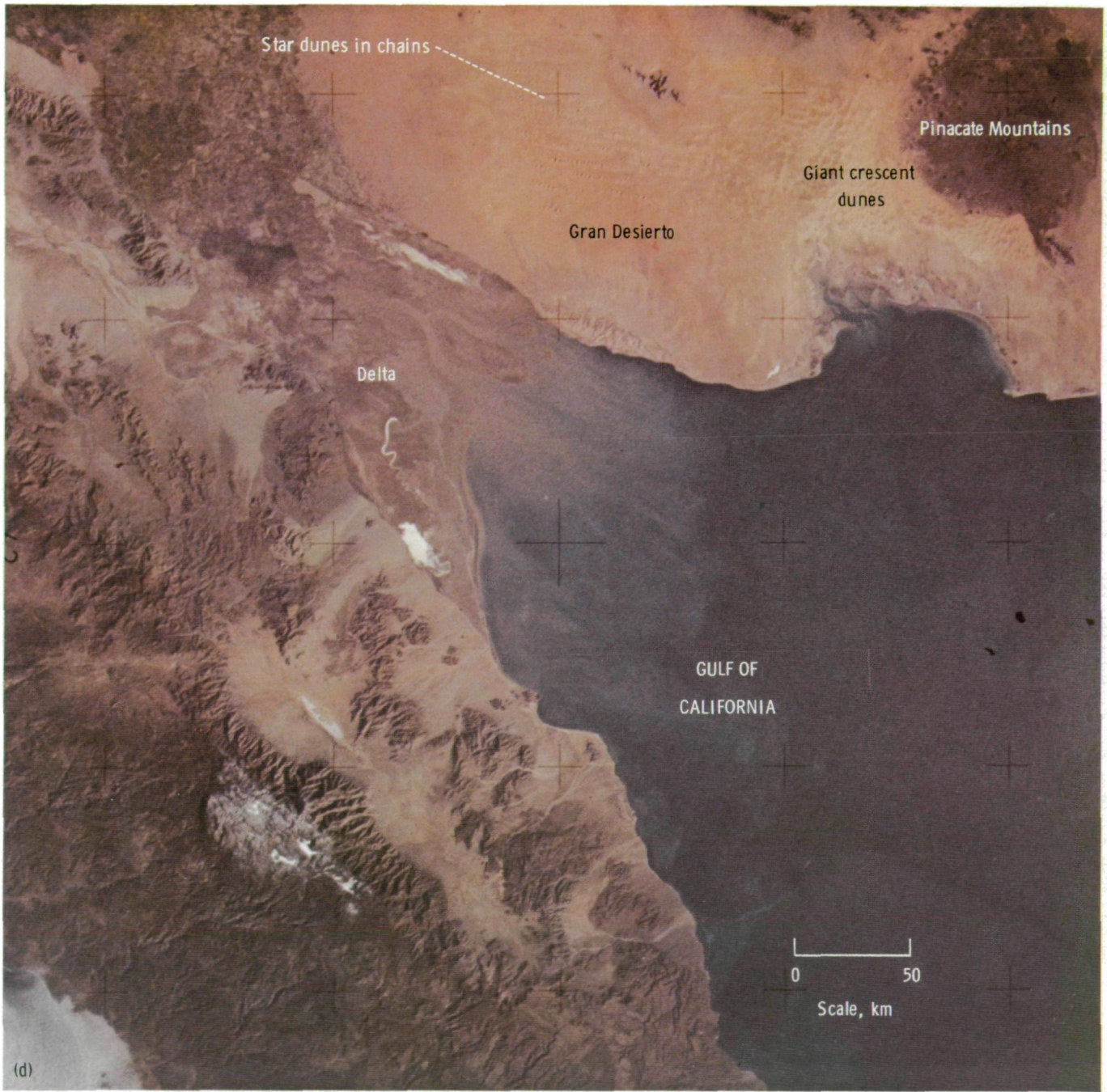


FIGURE 2-4.—Concluded.

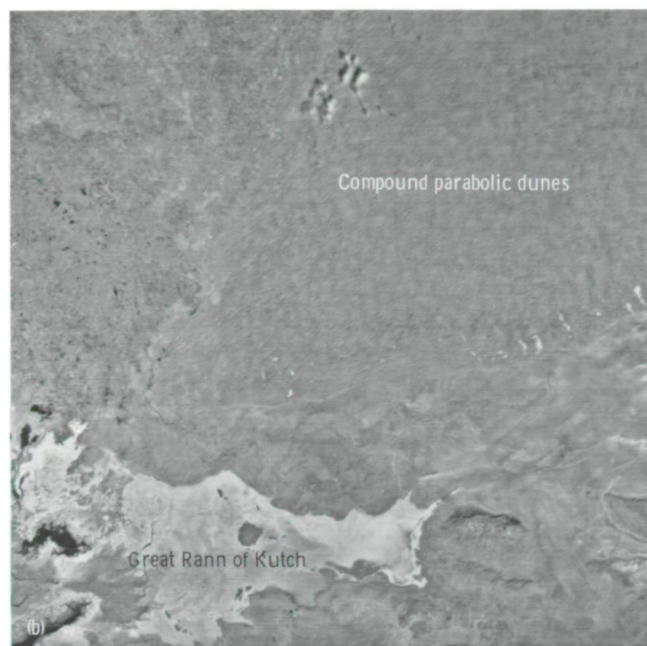
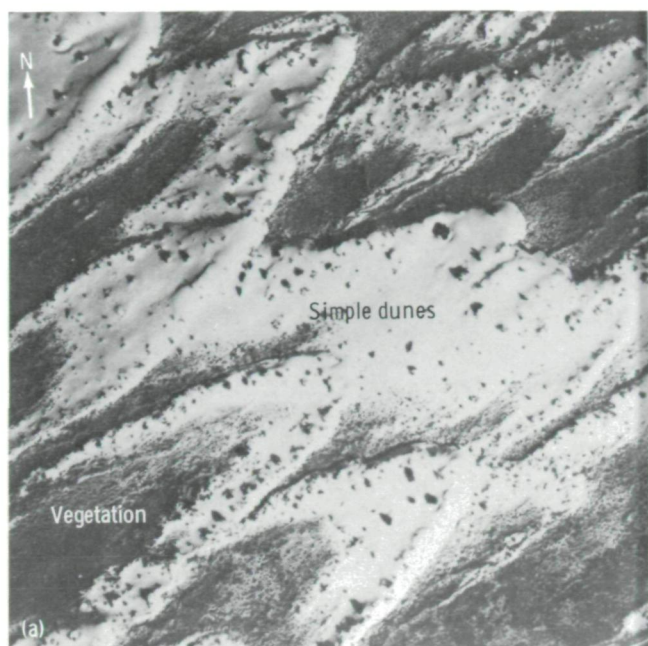


FIGURE 2-5.—Parabolic dune patterns. (a) Simple parabolic, White Sands, New Mexico (aerial photograph). (b) Compound parabolic, Thar Desert, Pakistan (Landsat image E1173-05211).

DEPOSITIONAL ENVIRONMENTS OF EOLIAN SAND BODIES: SAND-DISTRIBUTION MAPPING

Skylab high-resolution color photographs, especially those near-vertical views obtained with the 300- or 100-mm lenses, permit detailed mapping of desert sand deposits. Sand surfaces are easily discerned on the Skylab photographs because of their characteristic brightness, texture, color, and patterns. The locations of sand deposits of various types and the positions of these deposits relative to each other; to vegetation patterns; to natural barriers such as rivers, hills, and shorelines; and to climatic factors such as surface winds and rainfall regimes can be studied best from the regional viewpoint provided by space photographs and imagery. The following two examples illustrate the kinds of studies that can be made by combining Skylab photographs and visual observations data with Landsat imagery and with various kinds of ground-based data.

Eolian Sand Deposits in the Sahelian Zone of Northern Africa

A map prepared by Frances Lennartz from two Skylab photographs (fig. 2-7) shows the area between Tombouctou and Mopti around the Inland Delta of the middle Niger River in Mali. The size and spatial relationships of eolian sand deposits are shown on this map. The area lies within the climatic zone known as the Sahel, between the Sahara and the Sudanese savanna zone of northern Africa. The Sahel is a region on the desert margin in which human survival is currently a matter of much concern. Increasing aridity and severe drought, in the Sahelian Zone and in other parts of the world adjacent to major deserts, are thought by some investigators to result from poor agricultural and grazing practices and thus to be amenable to corrective measures. Others attribute increasing drought conditions to general climatic change. The Skylab photo-

graphs, together with other evidence (ref. 2-28), may indicate several changes of climate in this region during geologically recent time.

More than one period of aridity greater than the present period seems to be indicated in the middle Niger River basin by the relationships of sand bodies seen in Skylab photographs. Two sets of sand dunes that differ from each other in size, color, and orientation can be discerned easily. Previous maps of sand deposits in this area, drawn from conventional aerial photographs (ref. 2-14, p. 27; ref. 2-15, p. 286; refs. 2-29 and 2-30; and ref. 2-31, p. 200), have shown all dunes with a single general orientation to belong to the same category and thus, presumably, to represent uniform conditions of sand deposition.

Skylab photographs have provided cloud-free pictures of the dune shapes and sand distribution (as seen in fig. 2-7(a)) in true Earth colors; Landsat images have provided definitive evidence of bedrock surfaces, vegetation patterns, and surface water in relation to the sand deposits. When considered together, the Skylab photographs and Landsat images reveal at least two generations of major linear dunes and a pattern of sand sheets or stringers that obliterates much of the underlying topography.

The most obvious landforms on the map are large linear dunes in a parallel straight pattern oriented east-west across the course of the Niger River. The grayish tone, the rough surface texture, and the blurred outlines of these Niger dune ridges on the Skylab photographs are attributed to their modification by erosion and to the presence of vegetation, although the crests of the dunes may be composed of free sand. The dune ridges have an average width of approximately 2 km and are separated by interdune spaces averaging approximately 1.5 km in width. The area covered by this dune field is approximately 16 500 km². These fixed and eroded dunes are similar in form and size to active dunes in the Sahara to the north. Development of dunes of this magnitude may indicate a period of extreme aridity, although that assumption is questioned by some workers (ref. 2-31, pp. 201 and 202).

Many of the spaces between dune ridges shown on figures 2-7(b) and 2-7(c) are occupied by interdune



FIGURE 2-6.—Sheets and stringers of sand. (a) Large sand stringers and sheets, Sahara, northern Africa (SL4-138-3756). (b) Small sand stringers, Painted Desert, Arizona (Landsat image E1193-17324).

lakes and tributaries of the Niger River. The adjustment of the Niger and its tributary streams to the positions of the dune ridges has resulted in a trellis drainage pattern. Thus, the adaptation of the course of the Niger and its tributaries to the pattern of dunes occurred after emplacement of a sizable sand sea composed of large, probably linear dunes.

The stabilization of the dunes by vegetation and the presence of numerous lakes in the interdune spaces would seem to indicate a present period of lesser aridity than existed during the time of dune emplacement.

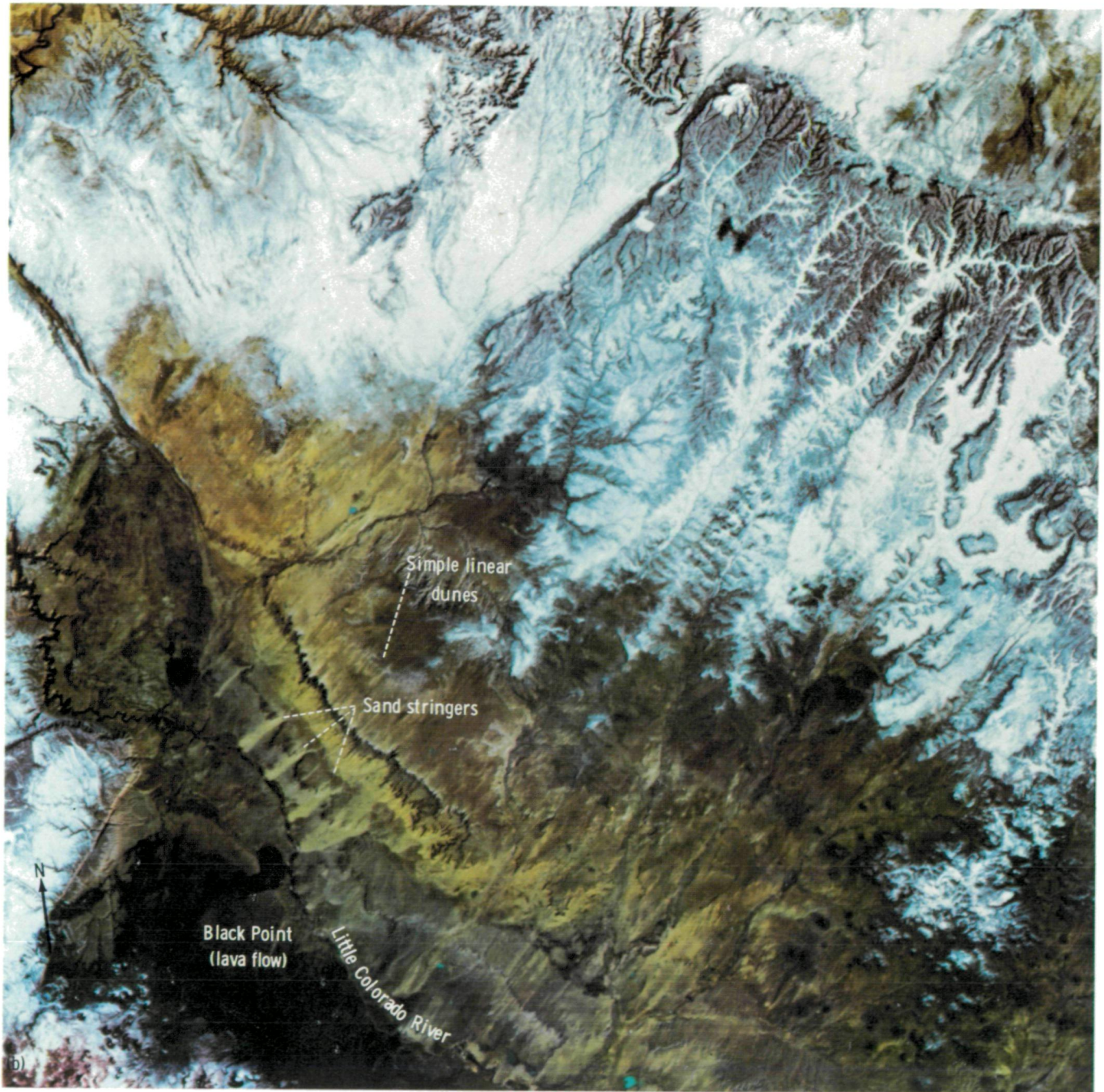
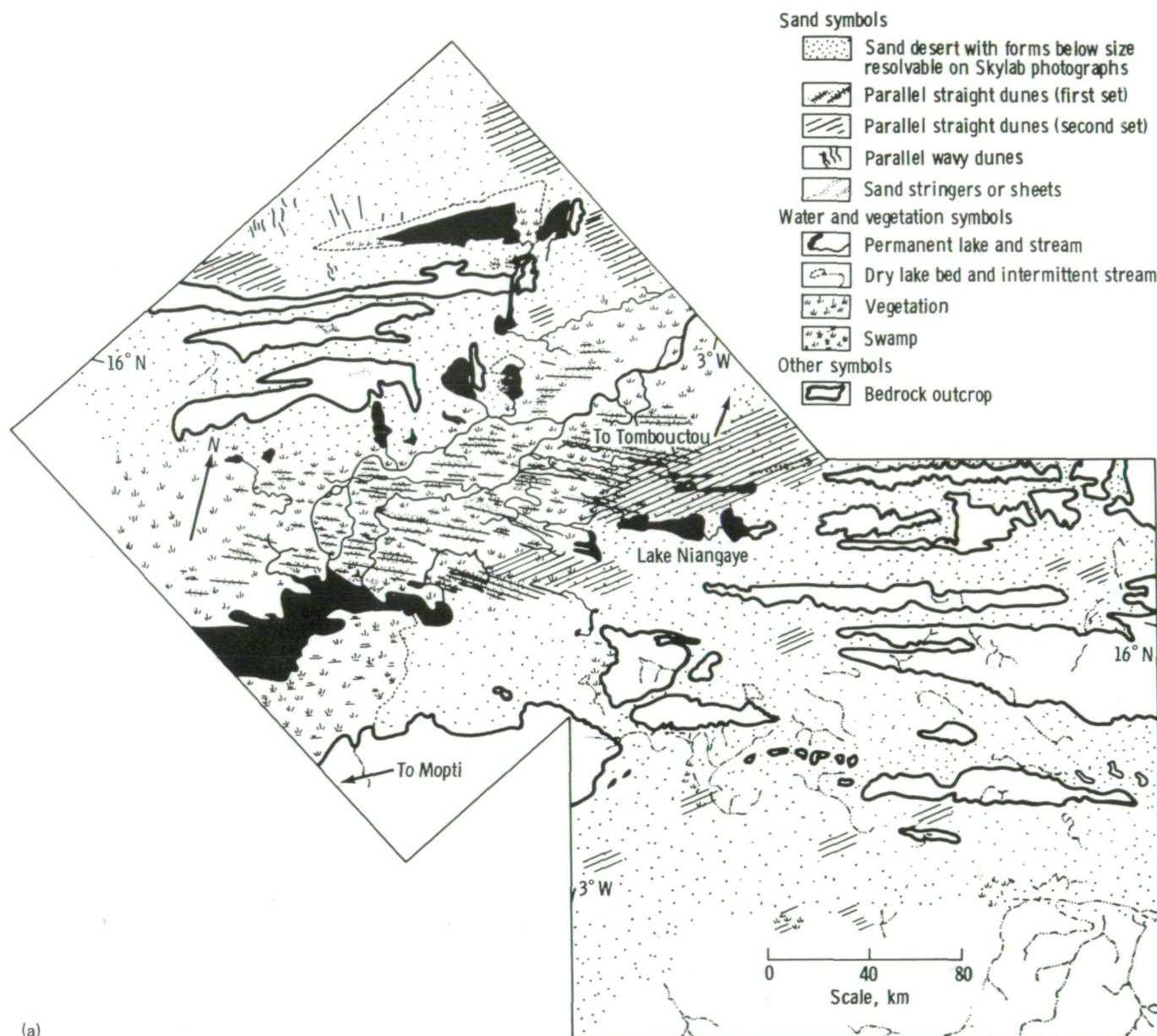


FIGURE 2-6.—Concluded.



(a)

FIGURE 2-7.—Eolian sand deposits in the middle Niger River basin, Mali. (a) Map of eolian sand deposits derived from figures 2-7(b) and 2-7(c). (b) Skylab photograph SL4-141-4361. (c) Skylab photograph SL4-136-3381.

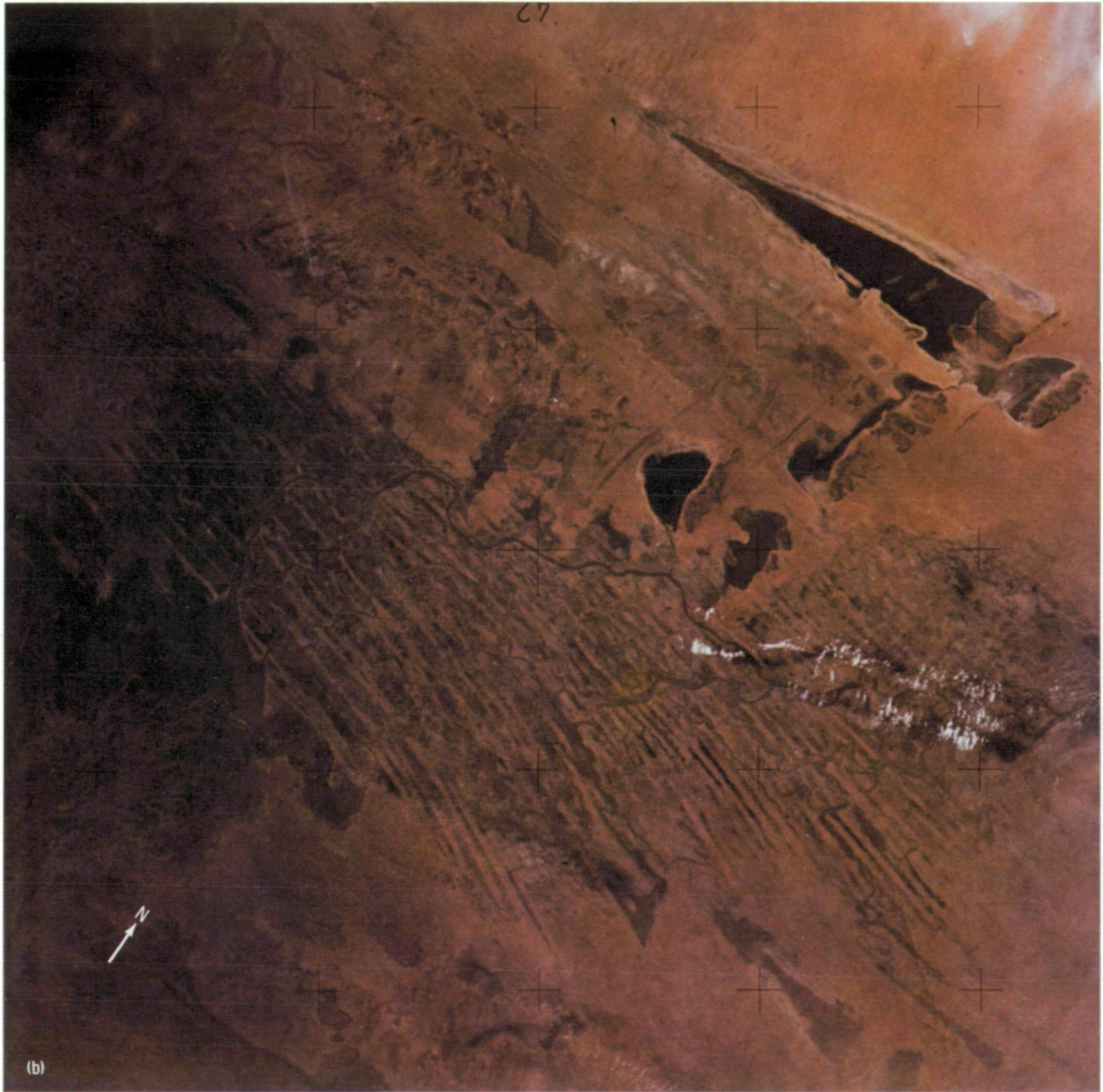


FIGURE 2-7.—Continued.



FIGURE 2-7.—Concluded.

The second set represents the parallel straight dune pattern and appears bright pink on the Skylab photographs. The dunes of the second set trend northeast-southwest and cross parts of the first (east-west trending) set of large dunes. In the area near Lake Niangaye, which is south of Tombouctou, the second set of dunes crosses some of the tributary drainage to the Niger River. Such a relationship seems to indicate that the second set of parallel straight dunes formed in this area after development of the larger (first) set and after adjustment of the Niger River drainage to the first set. During emplacement of the second set of dunes, conditions apparently were favorable for the movement of differently oriented, small linear sand dunes into the area. The dunes and the interdune spaces of the second set each have an average width of approximately 1 km, half the width of the dunes of the first set.

Another type of eolian sand deposit in the middle Niger region forms subparallel broad stringers that extend for hundreds of kilometers in a northeast-southwest direction. These deposits, which seem to be sand sheets, are light pink in Skylab photographs and seem to lack vegetative cover. No surface drainage occurs on the sand bodies; however, bedrock, vegetated surfaces, and remnants of intermittent drainage systems can be seen between the broad patches of sand-covered terrain. Similar stringers of sand have been seen (on Landsat imagery) in several parts of sub-Saharan northern Africa; the relationship of these stringers of sand to other sand deposits and to surface wind regimes needs further study with the aid of higher resolution photography and field examination.

These tentative conclusions indicate that the Skylab photographs and Landsat imagery of the Sahelian Zone should provide sufficient coverage to complete a comprehensive regional study of eolian sand deposits along the southern margin of the Sahara. The results of this study should be directly applicable to problems of land use in the region.

Eolian Sand Deposits in the Namib Desert in South West Africa

Skylab photographs of the Namib Desert illustrate barriers to sand deposition, dune and pattern types, color distribution, and postulated relative ages of eolian sand deposits. Data concerning this desert are especially valuable because much of the Namib is not accessible by conventional air or ground survey.

Many types of dunes occur in the Namib Desert. A map of the various dune patterns (fig. 2-8) has been derived from analysis of Landsat imagery (ref. 2-27). A part of the interior of the Namib Desert is shown in detail in a Skylab photograph (fig. 2-9). The significant effect of various physical barriers on the distribution of sand deposits is illustrated in figures 2-4(b) and 2-9.

An area to the north of that shown in figure 2-4(b) is shown in figure 2-9. Disrupted dunes occur around the Sossus Vlei, a playa into which the Tsauchab River intermittently flows westward from the Great Western Escarpment. The dunes in this area range from complex linear forms (fig. 2-9) to randomly scattered star dunes near the Sossus Vlei, where the dune pattern ends abruptly. Observations and photographs confirm that the trough formed by the dry Tsauchab River Valley has a significant effect on sand-transporting winds in this vicinity.

The most widespread dune pattern in the Namib (fig. 2-2(d)) is parallel straight composed of complex forms which are attributed by Logan (ref. 2-25, p. 136) to the combined effects of an onshore wind blowing northeastward and a "berg" (east) wind blowing westward from the interior highlands. The funneling and deflecting of winds by troughs and topographic highs may be a major cause of the peculiar distribution of the complex linear dunes and the star dunes in this desert, as indicated by examination of the effects of the vleie (playas) and other barriers seen in Skylab photographs and Landsat imagery.

Wind as a controlling factor in sand distribution is discussed in the section entitled "Relationship of Sand Distribution to Surface Wind Regimes." Although surface wind data for areas within the main body of the Namib Desert are not available, data for some peripheral areas have been summarized recently (ref. 2-27) and apply to this discussion.

At Aus, which lies south of the area shown in figure 2-4(b), winds capable of transporting sand blow in any of three directions, depending on the time of day. The trimodal wind regime measured at this locality is in agreement with McKee's hypothesis of a shifting wind direction in the formation of star dunes (ref. 2-10). Figure 2-4(b) shows numerous star dunes. The distribution of the star dunes seems to be affected by the positions of mountain barriers, which are numerous along the inland boundary of the Namib.

A second effect of the barriers shown in figure 2-4(b) is the association of relatively sand-free "shadows" between the mountains and the sand deposits hundreds of

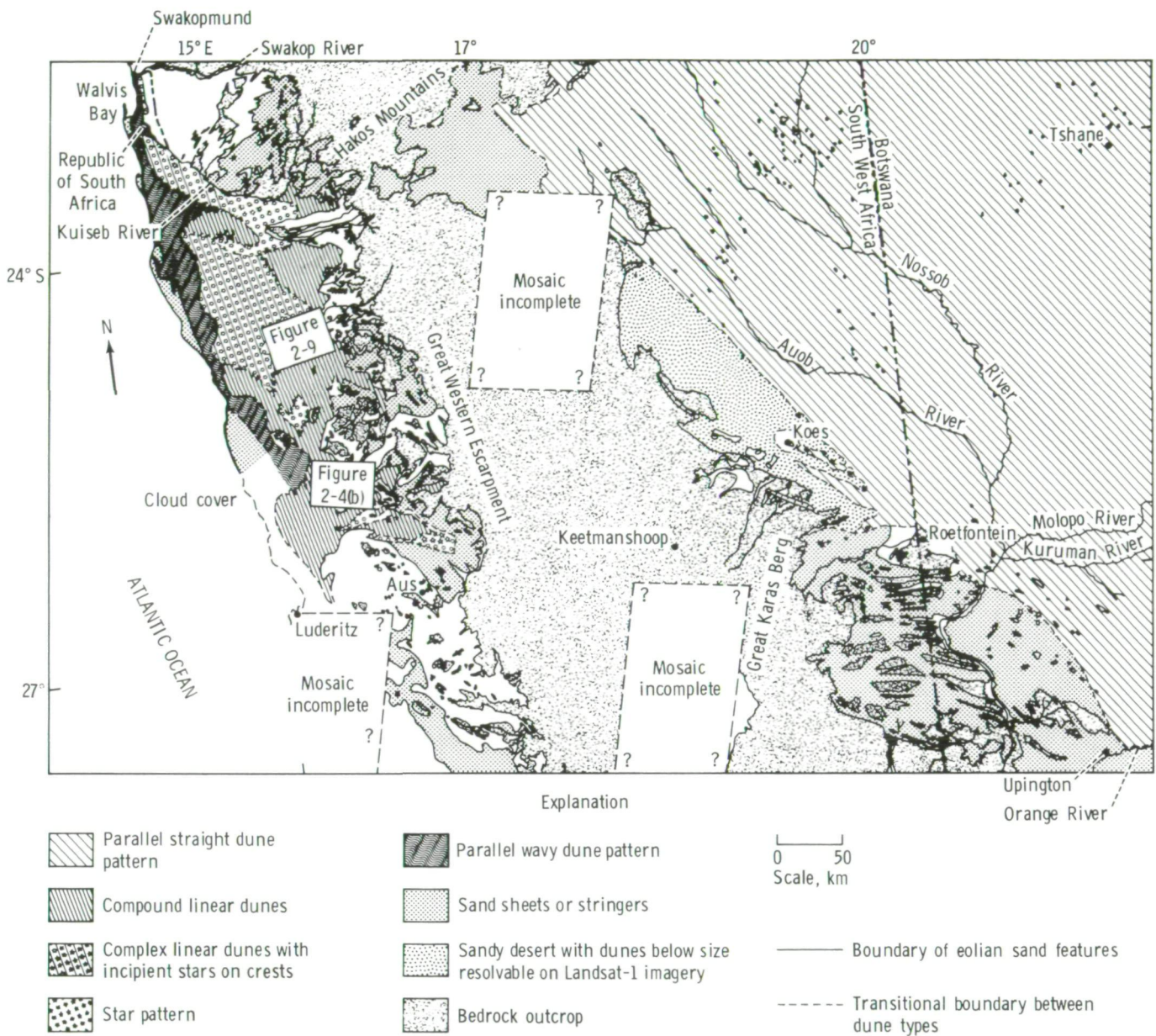


FIGURE 2-8.—Map of patterns and distribution of eolian sand in the Namib Desert of South West Africa.

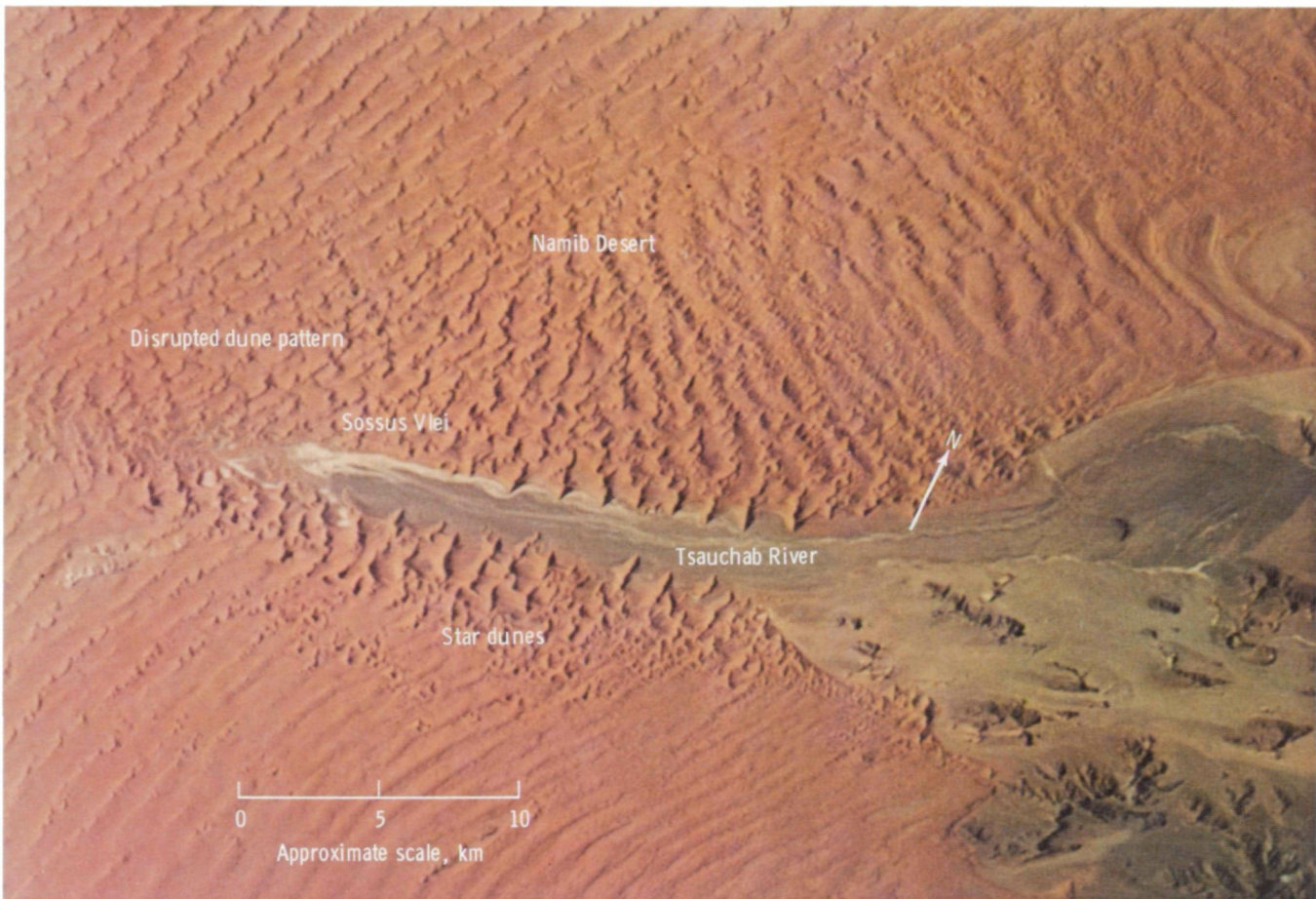


FIGURE 2-9.—Skylab vertical photograph taken with a 300-mm lens on the Nikon camera, showing disrupted dune pattern around the Sossus Vlei, Namib Desert (SL4-207-8073).

meters high that begin abruptly at a given distance from the barriers. Examination is needed to test the relationships of size, shape, and orientation of barriers to corresponding features of the sand-free shadows.

Sand deposits in most of the world's middle-latitude deserts have a distinctly reddish hue on Skylab photographs. Within each such red desert, particular hues and intensities of red seem to correlate with the occurrence

of particular dune types and their geographic position relative to boundaries of the dune field. This phenomenon is well illustrated by the color distribution in photographs of the Namib (fig. 2-2(d)). Simple dunes that make the parallel wavy pattern near the Atlantic coast are pale pink; dunes of the parallel straight pattern farther inland are mostly red, and complex dunes of the parallel straight pattern and star dunes farthest inland

are deep red. These observations seem to apply to the entire Namib sand sea and concur with the observation by Logan (ref. 2-25, p. 136) that "the farther inland a dune is located, the redder is its color This difference in color is believed to be the result of the greater age of the inland dunes which has allowed greater oxidation of the iron components within the sand."

The significance of reddening of dune sands is problematical. If relative redness within an erg can be used as a measure of relative age of eolian accumulation of dune sands, then the observations from space of the large-scale distribution of red coloration could be useful in tracing the growth and movement of sand within a sand sea. Degrees of redness could be used in distinguishing areas of relative stability from areas of change and interpreting the controls on sand transport, deposition, and erosion within a desert.

RELATIONSHIP OF SAND DISTRIBUTION TO SURFACE WIND REGIMES

Surface Wind Data

Sources of information.—Information concerning surface winds was acquired from three principal sources: (1) N-Summaries of surface winds from the National Climatic Center in Asheville, North Carolina, (2) general works describing the climate of certain deserts, and (3) the literature concerning sand dunes.

The N-Summaries were used as the data base for the computations of sand-moving winds, and the literature concerning climate and dunes contributed descriptions and interpretations from previous studies.

Computation of sand roses.—The sand-moving potential of winds of differing velocities, from any number of directions, may be computed (eqs. (2-5) to (2-8) of the appendix to this section) if the percentage occurrence both by velocity and by direction is known. Numerically, the magnitude of the vector that represents the sand-moving potential of wind from a given direction is the sum of the several products of weighted values for wind velocity categories and percentage occurrence within those categories. The construction of circular histograms that represent the potential of the wind to move sand at a given station and that are called sand roses or sand-movement roses (by analogy with wind roses) consists of the following steps.

1. Wind velocity groups are weighted to express sand-movement potential. This factor is expressed numerically by $v - v_t$ in equation (2-7) in the appendix and is figured by averaging the limits of the velocity group, subtracting from this average the value of v_t (4.63 m/sec for first calculations in this section), and cubing the result.

2. The percentage occurrence of winds in a given velocity group from a given direction is multiplied by the weighted value for the velocity group calculated in step 1. This gives the value of

$$\sum_{i=1}^n (v_{(i)} - v_t)^3 t_p$$

of equation (2-7) when the resulting products are added and yields a magnitude for that vector which represents the potential amount of sand transported across the station from a given direction, relative to that transported from other directions.

3. The amount of energy available for sand movement within a sand sea varies widely from station to station. Numerical values for vector totals computed by the method described above range from 5×10^5 to 5×10^2 units, although most stations will show individual directional totals in the low thousands and multidirectional totals from 7000 to 10 000. The vector totals may be divided by a suitable power of 10 to express the values for length of sand-rose arms in millimeters to facilitate the plotting of sand roses.

Arms of sand roses were plotted extending in the direction from which sand would drift (in keeping with a similar practice in the plotting of wind roses), but resultants (representing the net effect of drift from different directions) were plotted pointing down-drift.

Computation of resultants.—The theoretical sand-movement potentials included in the sand-rose computations are resolved trigonometrically into a resultant for the time period of all the measurements. All the vectors are resolved into their X and Y components on a pair of Cartesian coordinate axes, and these components are added to obtain the coordinates of the resultant. The magnitude of the resultant is equal to the square root of the sum of the squares of the X and Y components.

Assumptions of the wind data analysis.—The following four assumptions were used in processing the data.

1. The surface of the ground was the same at all stations, which would mean that the surface roughness

factor K' (also defined as turbulent flow; see appendix to this section), the average grain size, and the grading of the sand surface are uniform throughout the study area. In addition, the factor K' includes the assumptions that no vegetation interferes with the surface windflow and that the flow is over a flat surface. These factors are more important when stations are compared than when resultants for different directions at a single station are compared.

2. The wind sample compiled by the National Climatic Center is representative of the wind regime at the locality.

3. Anemometer heights above the surface are the same at all stations. National Climatic Center data are derived from World Meteorological Organization (WMO) stations that, according to instructions in "Guide to Meteorological Observing Practices" (WMO No. 8 TP-3), should have anemometers mounted at a standard height of 10 m.

4. A particular value was assumed for threshold velocity v_t for initiation of sand movement by prevailing winds at all stations.

An important factor that may affect the results of computations, and particularly the directions of resultants, is the value assigned to v_t , the threshold velocity of wind at which sand grains of a given diameter are set in motion. This factor is especially important in computing sand roses for stations at which relatively strong winds come from quarters different from those of relatively moderate winds.

Although wind threshold velocity values for a height of measurement of 1 m or less have been measured in laboratory studies, little work has been done in the field to evaluate threshold velocities under various wind and surface conditions. Therefore, even for a known grain size, the threshold velocity is difficult to predict in a field situation.

The application of equation (2-1) to experimental data gathered in both the laboratory and the field by Bagnold (ref. 2-9, pp. 60 and 82) indicates a v_t of 61.2 and 79.7 m/sec at a 10-m height for sand grains of "average" diameter 0.25 and 0.33 mm, respectively. The range of these values places v_t within the 57- to 87-m/sec velocity group of the National Climatic Center data. Brookfield (ref. 2-32) and other writers, however, have used 46 m/sec as the threshold velocity for a 10-m height of measurement. This value was chosen as the assumed threshold velocity.

Values derived from the equation represent only potential sand movement at a station. If there is no sizable

sand source upwind, there will be little sand movement from that direction. Moreover, regional rates of mass transport may vary depending on the barrier effect of the dunes themselves. Rivers and other barriers may permit flow past a particular point only during certain seasons or only in one direction.

Finally, whereas monthly changes in wind direction are evident, the diurnal and very-long-term fluctuations (more than 10 years) are not explicitly evident in the data.

Interpretation of Skylab Photographs in Relation to Measured Surface Winds

Sand sheets and stringers in the northwestern Sahara.—The northwestern coast of Africa, including parts of Mauritania and Spanish Sahara, is shown in figure 2-6(a). Pink areas that are highly reflective are interpreted as eolian sand deposits and are distributed in the following manner.

Near the top center of the photograph, grayish-pink linear features extend from Cape d'Arguin northward beyond the image area. The orientation of these features is approximately N 7° E.

In the center of the photograph are three broad bands containing subparallel pink sand stringers that are aligned N 45° E to N 50° E. Within the sand stringers are groups of closely spaced linear dunes that trend approximately N 25° E to N 30° E, so that the trend of the dunes intersects that of the sand stringers at angles of 15° to 20°. The dunes within the sand stringers in the center part of the desert have an unvegetated appearance.

Other closely spaced dunes extend from the coast at Cape Timiris inland approximately 100 km. These dunes are oriented approximately N 22° E. The dark tone indicates that the dunes are probably covered by vegetation.

At the bottom center of the photograph, both the sand stringers and the linear dunes within the sand stringers swing southward to an orientation of approximately N 60° E to N 65° E.

Little background information about this part of the Sahara has been found in the literature, although some information is available about the dune areas south of Nouakchott and around the Sénégal River (refs. 2-30 and 2-33).

Sand roses and annual wind resultants were constructed, by using the methods described earlier in this

section, from N-Summaries of surface winds measured at stations in and around the area shown in figure 2-6(a). The sand roses and annual wind resultants, and the lines of postulated sand drift calculated from them, are plotted on the map in figure 2-10. As a corollary to these efforts, the lines of postulated sand "flow" from Wilson's map of "Sand Flow in the Sahara" (fig. 5 of ref. 2-34) were added to figure 2-10, as were Wilson's wind resultants, which were derived from an earlier study by Dubief (ref. 2-35).

A formula for calculating wind results used by Dubief (ref. 2-35, p. 143) is similar in principle to that used in this section, although he set the threshold velocity slightly higher to make it equivalent to 5.7 m/sec at a 10-m height. Dubief's raw wind data, however, were composed of observations in the Beaufort scale. The Beaufort scale consists of 12 levels of wind force, but the Beaufort value assigned to a wind depends on a subjective estimate by the observer. The wind measurements supplied to this project by the N-Summaries of the National Climatic Center are based on readouts from equipment that must meet the relatively strict standards of the WMO. Therefore, some of the differences in interpretations of wind regimes in the Sahara by Dubief and Wilson and in this section may be due to differences in basic data. The use in this section of direct measurements of wind velocities from WMO stations is believed to represent considerable progress in the study of surface winds in deserts, although WMO stations are still sparsely located in sand-sea areas.

The sand-moving potential of the measured surface wind is depicted on the map (fig. 2-10) from which the following interpretations are drawn.

1. In the northern coastal part of the area (north of 20°30' N and west of 16° W), sand drift is from approximately N 7° E.

2. At Atar and at Fort Gouraud in the eastern part of the area, sand drift is from approximately N 65° E.

3. Near the coast at Cape Timiris, a southward curvature in the postulated sand drift becomes noticeable, and this southward curvature becomes more pronounced in the areas east and south of the cape.

Comparison of the observed orientation of features in the Skylab photograph (fig. 2-6(a)) with the postulated orientations derived from wind data (fig. 2-10)

shows the following:

1. Parallel linear features in the area from Cape d'Arguin northward are alined N 7° E, exactly the postulated direction of sand drift there.

2. Alinement of the broad bands of northeast-trending, subparallel sand stringers in the center part of the photograph agrees with the winter resultant direction of postulated sand drift in that part of the desert. However, the alinement of groups of closely spaced linear dunes within the sand stringers generally agrees with the annual resultant direction of postulated sand drift.

3. The observed southward curvature of the sand stringers and linear dunes in the southernmost band shown in figure 2-6(a) agrees closely with the southward curvature shown clearly on the map (fig. 2-10) by the measured wind data. Curvature shown by these calculations differs considerably from the more westward direction of sand "flow" shown by Wilson in figure 5 of reference 2-34 and illustrated in figure 2-10 in this section.

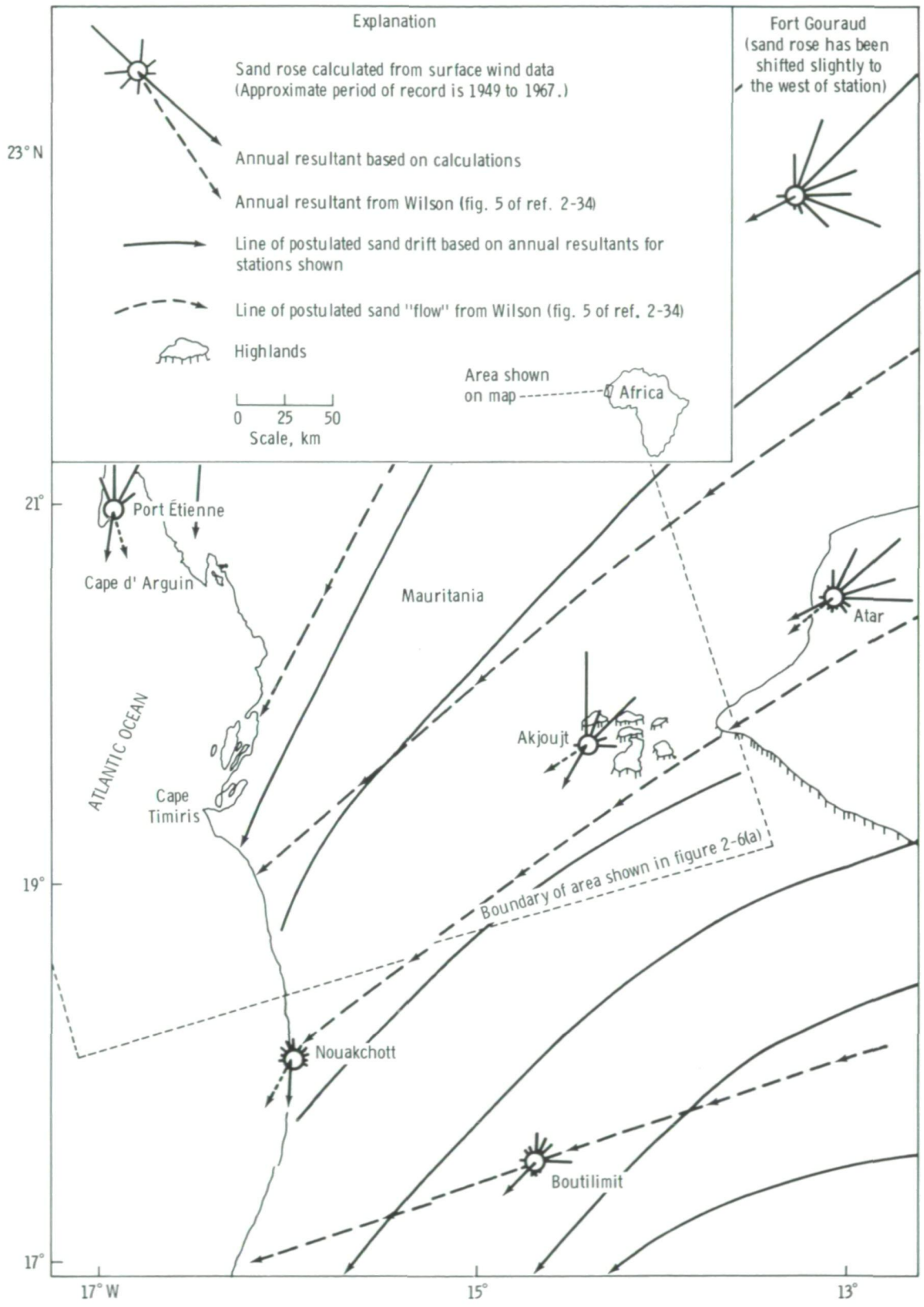
The apparent conclusion that all the observable sand features on the Skylab photograph except the very prominent large stringers parallel the resultant effect of present-day sand-moving winds in the northwestern Sahara raises some interesting questions.

The reason why sand stringers alone, among all the sand features observed, do not entirely follow the trend of present-day winds can only be speculated without field data. Several possible explanations might be tested.

One hypothesis is that sand stringers were deposited by winds of an earlier (Pleistocene?) regime, and now the sand of the stringers is a source for the formation of dunes, which parallel the resultants of present-day winds. One test of this idea would be to observe the areas of stringers at long intervals to see if and where sand movement is occurring.

A second hypothesis is that the orientation of the stringers corresponds only to the direction of the high-speed components of the present wind regime. To test this idea, some calculations were made that, by theoretically raising the threshold windspeed in the annual resultants to 7.7 m/sec, in effect eliminated from the resultants all winds in the lower category of sand-moving effectiveness. Recalculation of the annual

FIGURE 2-10.—Map of the northwestern Sahara showing sand roses, annual wind resultants, and postulated sand drift. →



resultants at Boutilimit and at Akjoujt by this method changed resultants by only approximately 4°. Present-day high-speed winds thus do not seem to account for the difference between the orientation of sand streaks and that of the annual wind resultant.

A third hypothesis is that the orientation of the sand stringers corresponds to a seasonal component of the wind regime. Analysis of wind data for Akjoujt suggests that the orientation of the stringers is controlled by the winter and spring winds. Dunes within the stringers, on the other hand, may have developed their orientation in response to the total wind regime.

A fourth possible explanation for the anomalous orientation of sand stringers is grain size distribution, the method by which Wilson (ref. 2-24, p. 105) and Warren (ref. 2-6, pp. 165 and 166) explain the variations among sand features of different sizes and orientations within an erg. Assemblages of sand of a certain grain size would be affected by winds of a certain speed range, whereas other assemblages of sand of different grain sizes would be affected by other components of the wind regime. Sand samples from a number of different types of eolian sand deposits must be systematically collected and analyzed to test whether certain sand features are indeed formed of sand grains of a certain size range.

Results of the Skylab experiment, though not complete, indicate that observations and photographs from space, together with ground-based data such as wind measurements and laboratory work with sand samples, provide a regional view from which it can be determined whether the actual patterns of sand deposition seen from space agree with the hypothetical determinations of sand movement in remote, poorly known desert regions.

Star dunes in chains and in "random" patterns in the Erg Oriental, Algeria.—Isolated star dunes are seen in seemingly random distribution in the eastern part of the Erg Oriental (fig. 2-4(a)) and alined in chains on sand ridges in the western part (fig. 2-4(c)). In particular, chains of star dunes were observed by the Skylab 4 crew because color and texture contrasts between brick-red sand deposits and gray bedrock and gravel interdune surfaces give a bizarre appearance to this part of the Sahara.

Little information is available on scattered star dune patterns in the eastern part of the erg, although a reconnaissance by Capot-Rey (ref. 2-7) gives a general

description of the area. More recent work by Wilson (refs. 2-24, 2-34, and 2-36), mostly in the northern and central parts of the erg, provides some measurements of dune size and distribution, presumed grain size distribution, depths to bedrock at selected points, etc. However, for many of his measurements, Wilson (ref. 2-24, p. 90) relied on topographic maps and aerial photographs. He did not have the advantage of the view from Skylab, which, together with the measured wind data subsequently presented in this section, provides new interpretations of sand drift that differ considerably from results of earlier work in this area.

The following features are shown in figure 2-4(c).

1. In the main erg, chains of star dunes are alined on sand ridges that are subparallel and that have a roughly north-south trend; these ridges end abruptly at the Hamada [plateau] de Tinrhert. Another smaller group of star dunes in chains forms the Erg Megraoun Insokki (fig. 2-11). Southward in the main erg, chains are progressively wider and farther apart, and the star dunes gradually increase in size. The southern sand deposits are darker and redder than the northern sand deposits. These color, size, and spacing changes are not effects of perspective but are true changes with distance from north to south and are confirmed by Landsat images (vertical views) of the same area.

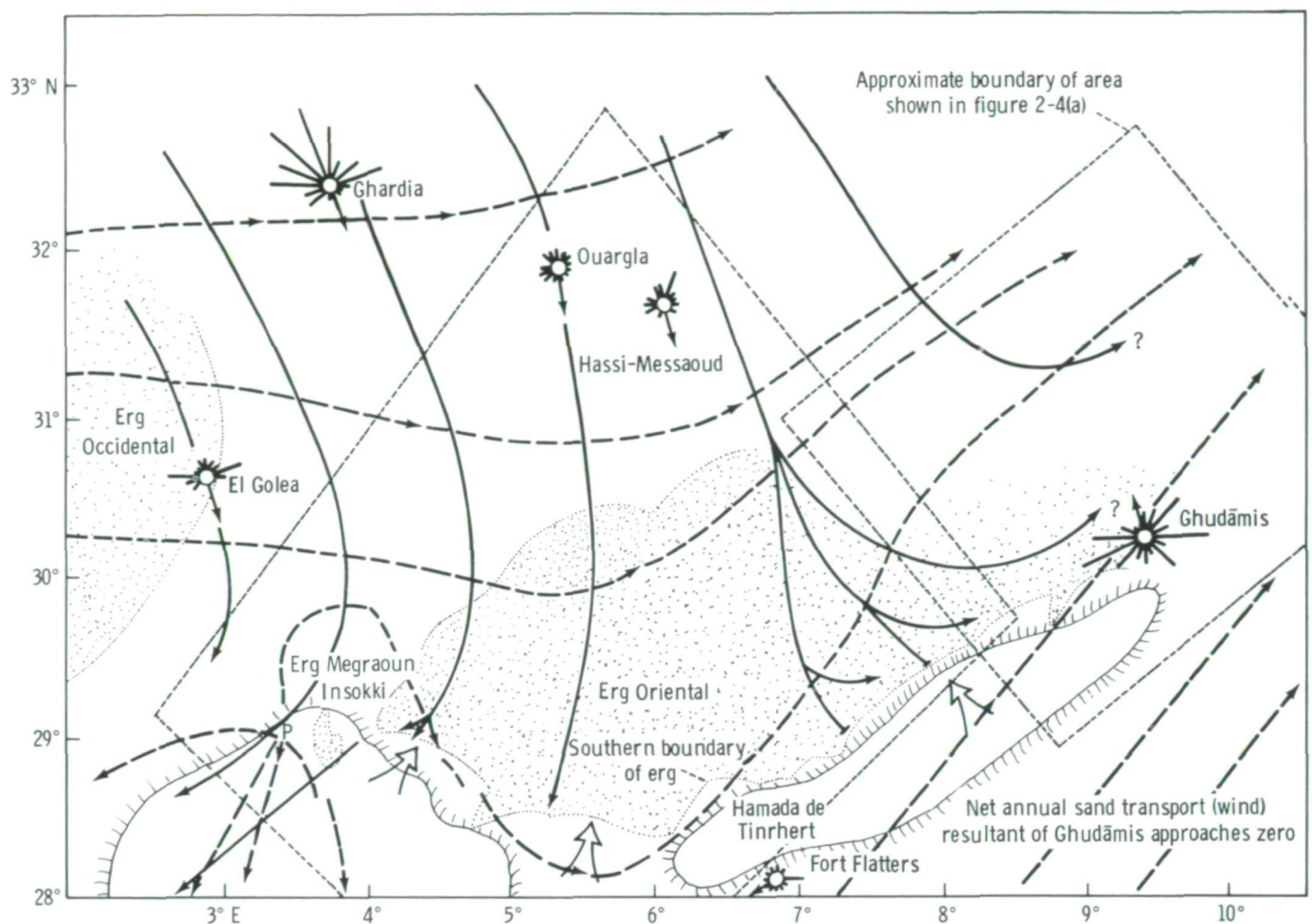
2. Light-gray to white subparallel stringers are visible among areas of dark bedrock in the lower right corner of the photograph. The white stringers extend approximately 50 km and trend northeast. These stringers are believed to be eolian erosional features.

3. A light reddish haze, presumably a thin cover of sand, in the left third of the photograph, crosses the gap between the dunes of the main erg and those of the Erg Megraoun Insokki.

4. Four (possibly five) dark smoke plumes are visible near the upper part of the photograph and indicate that a surface wind was blowing generally from north to south when the photograph was made.

Sand roses and annual wind resultants for the north-eastern Sahara were calculated using the methods described earlier in this section and are plotted in figure 2-11. The postulated sand drift directions are based on surface wind measurements from the stations shown. Analysis of these data suggests the following.

1. Sand drift in the western part of the Erg Oriental is from the north and northwest, with sand being deposited along the southwestern margin of the Erg



Explanation

 Sand rose calculated from surface wind data (Approximate period of record is 1949 to 1967.)

 Annual resultant based on calculations

 Line of postulated sand drift based on annual resultants for stations shown

 Line of sand flow derived by Wilson (fig. 3 of ref. 2-34) from Dubief (ref. 2-35)

 Highlands

 Erg or sand sea

 Direction of sand transport by wadis

P Sand-flow peak number 1 of Wilson (ref. 2-34)

0 25 50
Scale, km



FIGURE 2-11.—Map of the northeastern Sahara showing sand roses, annual wind resultants, and postulated sand drift.

Oriental, or drifting into the Erg Megraoun Insokki, and then to the southwest.

2. Sand drift in the eastern part of the Erg Oriental differs from that in the western part. The sand drift resultant at Ghudāmis near the southern margin of the dunes approaches zero but favors a net transport toward the northeast. The most significant aspect of wind regime in this part of the Sahara may be that sand drift into this part of the Erg Oriental seems to exceed the drift leaving; therefore, sand would tend to accumulate in a kind of sand trap.

As with the northwestern Sahara wind data, a test was conducted to determine whether considering high-speed winds in calculations of the annual resultants would produce a different direction of sand drift in the area. In the northeastern Sahara test, raising threshold windspeed theoretically to 7.7 m/sec resulted in a swing of annual resultants for the northern stations counterclockwise approximately 10°, emphasizing the eastward sand drift direction, and, at Ghudāmis in the eastern part of the field, emphasizing the northeastward sand drift trend.

Interpretation of the Skylab photograph relative to measured wind data gives the following results. Subparallel straight dune ridges along which star dunes are aligned are parallel to the postulated direction of sand drift resultants. These sand drift directions and their relationships to dune orientations contradict some earlier work in the Sahara (refs. 2-24 and 2-34). Postulated directions of sand drift derived from the WMO wind measurements used in this section differ from postulated sand "flow" directions derived by Wilson (fig. 3 of ref. 2-34) from Dubief's "formula" resultants and "sandstorm" resultant (ref. 2-35) and are shown in figure 2-11. Dubief's data (ref. 2-35, p. 144) for the western part of the Erg Oriental agree well with measured wind data from this work, but the map of sand "flow" that Wilson derived from Dubief's data does not agree (as fig. 2-10 shows). Wilson apparently based his conclusions not only on Dubief's wind data but also on his own ideas (refs. 2-23, 2-24, and 2-34) about the relationship of "bed form" (dune) distribution to size distribution of sand grains within a sand sea. Furthermore, Wilson obtained the orientation of slipfaces on several large dune features that he called "sym-

metrical transverse bed forms" from maps and aerial photographs (ref. 2-34, p. 185) and used these orientations in his analysis of sand flow.

Various hazards are inherent in a genetic classification of dune forms, such as used by Wilson, particularly if the assignment is based on a rendition of dune forms on topographic maps (ref. 2-34, p. 185). This study indicates that many maps (U.S. Air Force Operational Navigation Charts J-2, J-3, J-4, and Army Map Service series 1301, NH32, NH31) of various parts of the Sahara show dune forms that are fanciful. Use of aerial and ground photographs to obtain slipface orientations may be valid for learning the effects of various components of the wind regime on sand distribution locally, but the view from space provided by Skylab photographs and Landsat images provides a regional frame of reference essential in seeing the entire pattern of slipface orientations over an entire sand sea and in determining the relationships, if any, of these patterns to regional wind regimes.

The Skylab 4 crew observed smoke and dust plume wind indicators in the north African region that agree with the measured wind data. Furthermore, the elongate areas of high reflectance within the area of reddish haze (left side of fig. 2-4(c)) parallel the sand drift direction there. The extension of the area of high reflectance to the southwest of the eastern edge of the Erg Megraoun Insokki seems to be a downwind sand drift from that erg, because no body of sand occurs directly to the southwest that might have supplied the sand from that direction.

From the foregoing evidence, the major sand features of this region (ridges that are subparallel and along which star dunes are aligned) clearly are not "transverse" features but rather lie parallel to the resultant direction of net sand drift in the northeastern part of the Sahara. Furthermore, the concentration of very large dunes along the southern margin of the Erg Oriental is probably a result of accumulation of sand over a long span of time. Downwind increase in size and spacing of ridges and of star dunes aligned on the ridges may be related to changes in wind with distance and to relative ages of sand accumulations. These factors were discounted in the earlier work by Wilson (ref. 2-24, p. 94).

Skylab photographs and visual observations of the northeastern Sahara have been very useful; the need now is for high-resolution vertical color photographs of specific parts of this erg to be acquired, preferably as stereopairs, so that accurate measurements of dune size distribution and slipface orientation within the entire erg can be made.

APPLICATION OF SAND STUDIES TO INTERPRETATION OF EOLIAN SANDSTONES

Relationship of Dune Type to Internal Structures

The principal types of dunes that coalesce to form patterns as recognized in this study are represented by

distinctive and characteristic internal structures, especially cross-stratification. Investigations of these structures must necessarily be made on the ground by trenching or digging test pits. Initial trenching studies have been conducted with the examination and analysis of four dune forms at White Sands National Monument, New Mexico (ref. 2-10), an isolated barchan dune in Arizona (ref. 2-3), a reversing dune at Great Sand Dunes, Colorado (ref. 2-10, p. 61), a seif dune in Libya (ref. 2-37), and a star dune in Saudi Arabia (ref. 2-10, pp. 65 to 68).

The major varieties of stratification represented in dune sections have been recorded for a few areas, and some representative samples are illustrated in figures 2-12 to 2-15. Major differences can be seen between each of the dune types, but much more field work must

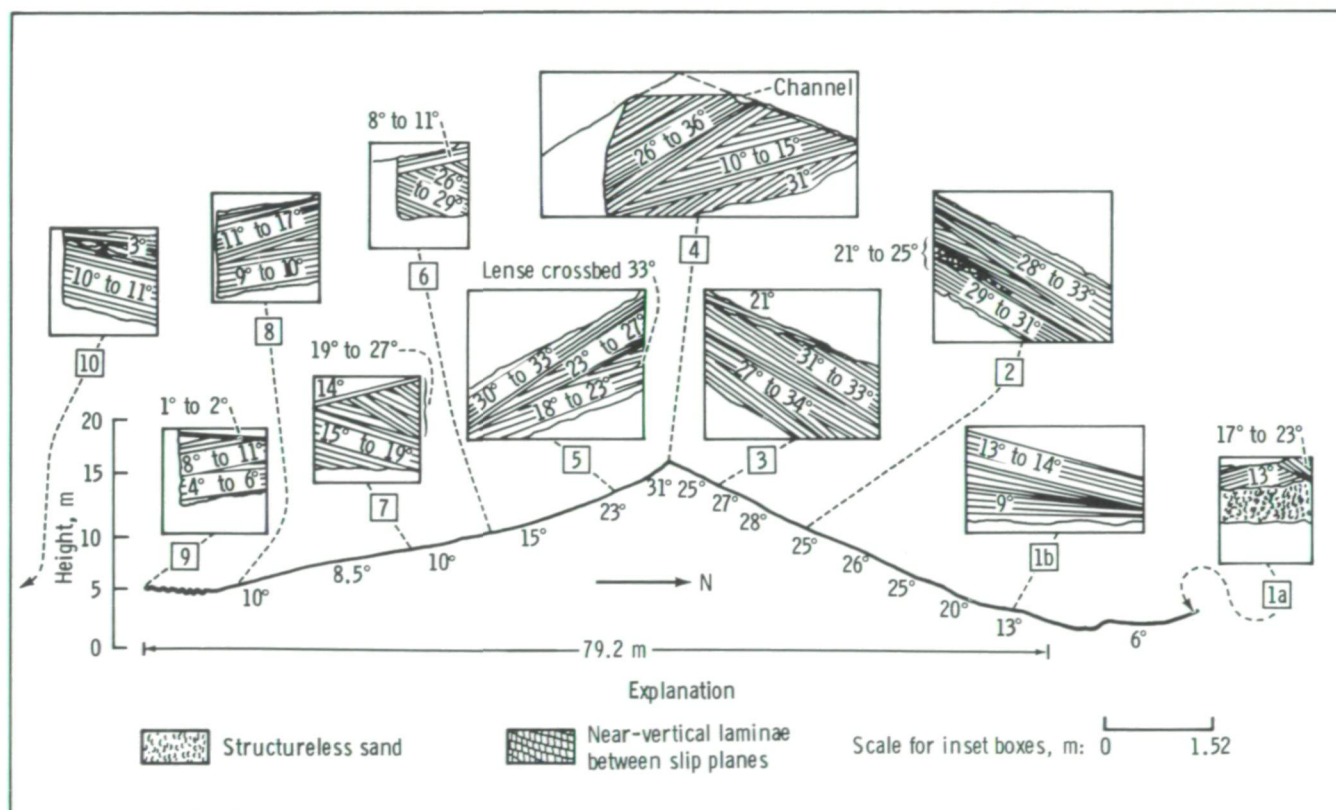


FIGURE 2-12.—Internal structures of seif dune: parallel straight dune pattern, Sebham, Libya (modified from fig. 6 of ref. 2-37).

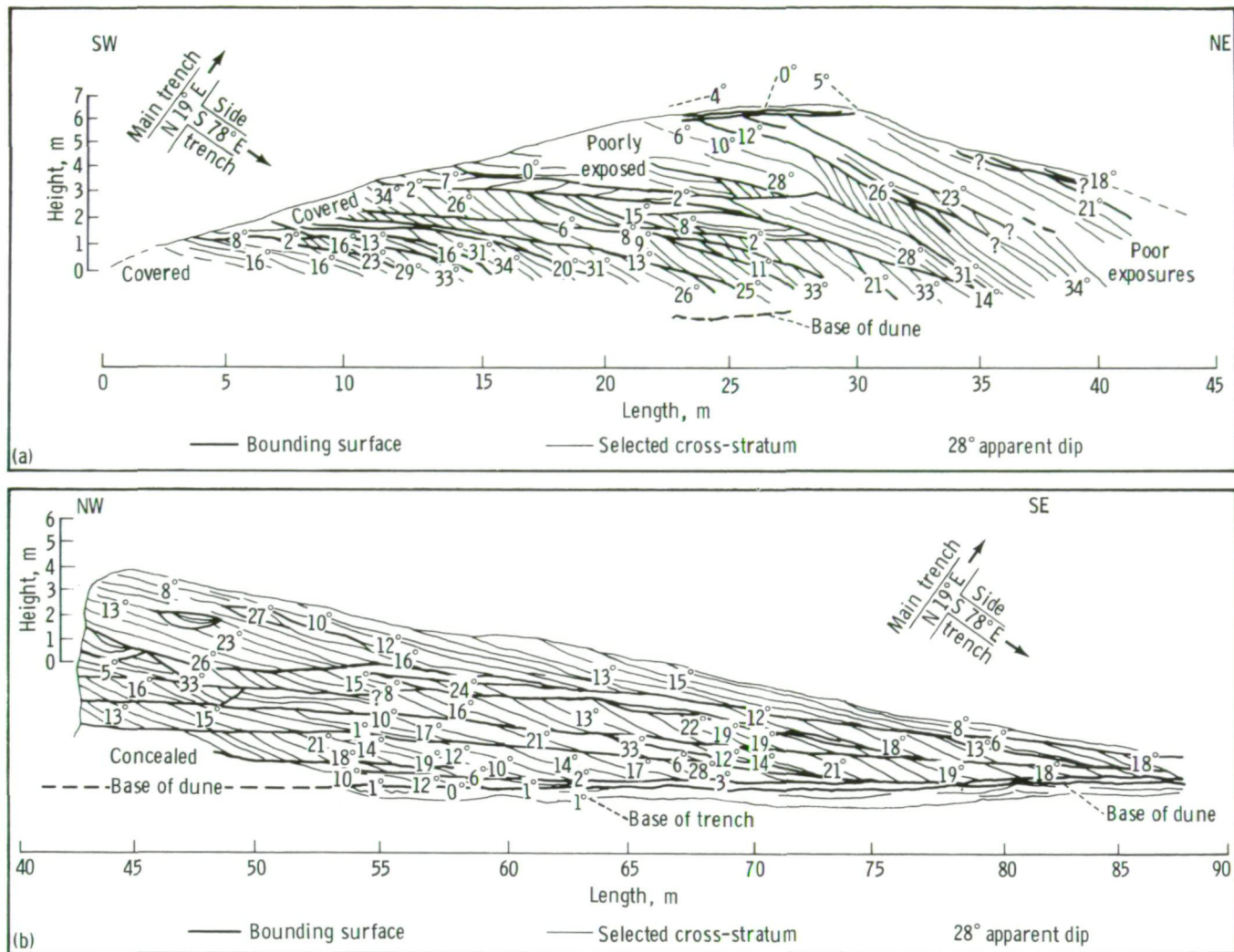


FIGURE 2-13.—Internal structure of barchanoid dune: parallel wavy dune pattern, White Sands, New Mexico (modified from fig. 7 of ref. 2-10). (a) Main trench. (b) Side trench.

precede a meaningful worldwide comparison of structures. Ultimately, data of this kind should permit an accurate interpretation of dune forms as found in ancient rocks and an understanding of the relationship of primary structures to permeability, porosity, and fluid movement in the rocks under consideration.

Significance of Interdune Areas

An especially important contribution by the Skylab 4 mission consists of information, accumulated both

through handheld-camera photography and by direct observation, on the nature and extent of interdune areas. These areas appear as conspicuous features among dunes in most sand-sea patterns and differ from sand masses in several significant respects.

Interdune deposits are generally darker than dune sands and thereby are readily recognized and delineated from the air. Furthermore, interdune deposits differ from dunes in texture in that they usually contain a large percentage of fine, dust-sized material; thus, they are usually much more poorly sorted than dunes. In most deserts, interdune areas consist of unconsolidated

sediment, but, in some areas, bedrock is exposed or interdune areas contain bodies of water or scattered vegetation.

Recent ground studies at White Sands, New Mexico (ref. 2-38), have demonstrated through core drilling and trenching that interdune surfaces are actually parting planes that separate sets of dune strata and therefore have important stratigraphic significance. While one part of a thin sheet or layer of sediment is being developed on an interdune surface, another part of the same layer is being buried by an advancing dune; eventually, a gently dipping plane surface or a thin layer of sediment is formed within the sand body across an entire area.

Because dunes of different patterns represent various types of movement or migration, characteristics of interdune surfaces differ greatly from one region to another. Clearly, surfaces surrounding star dunes, in which movement varies widely and growth is more vertical than horizontal, are very different from surfaces formed by the forward migration of barchanoid dunes. Thus, the nature of interdune surfaces and their relationship to the overall structure of an extensive sand body is complex and poorly understood, even though economic implications demand an understanding of the relationship.

Economic Benefits of Research on Structures of Eolian Sandstones

A long-term objective of this study is to obtain an understanding of the overall structures in sand seas and thereby to differentiate among various types of dunes. Field documentation, in conjunction with the Skylab 4 project on sand-sea studies, has revealed some basic principles related to dune structures or cross-stratification that tend to modify earlier concepts regarding accumulation of desert sand bodies. In the past, dunes were thought to be the result of sand migration by the processes of saltation and avalanching under the influence of "prevailing" wind. After a study of sand patterns derived from Landsat imagery and further analysis using Skylab and aerial photographs, it seems clear that in many regions unimodal and bimodal regimes of effective wind result in forward migration of sand in crescentic or linear dunes, which are grouped in characteristic patterns that are usually parallel. In other places, however, more complex wind regimes (involv-

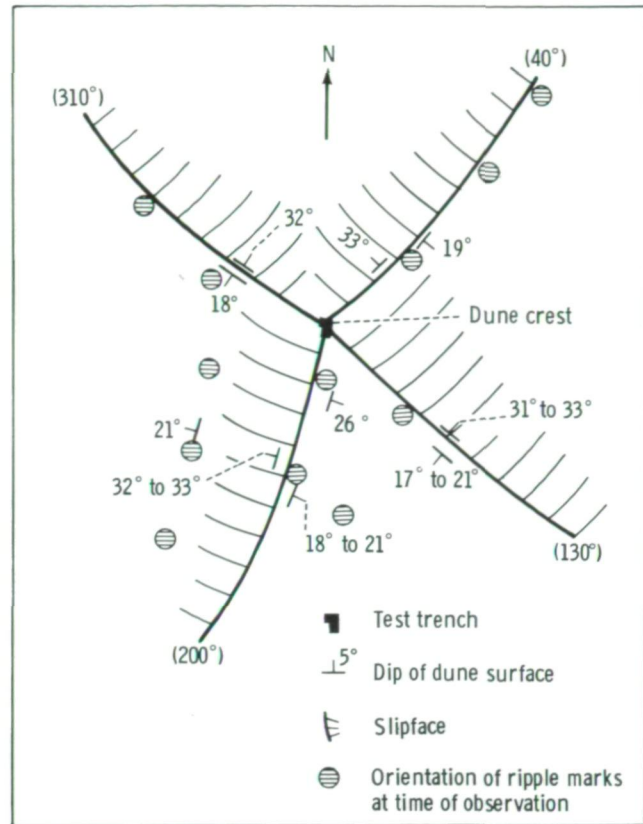
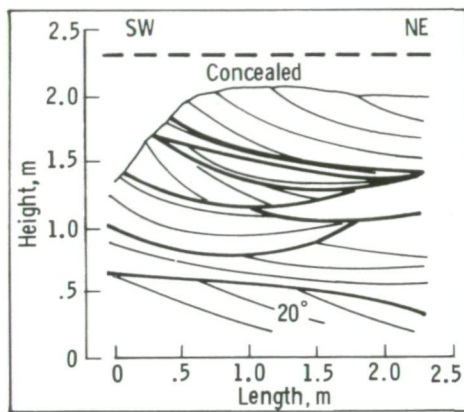
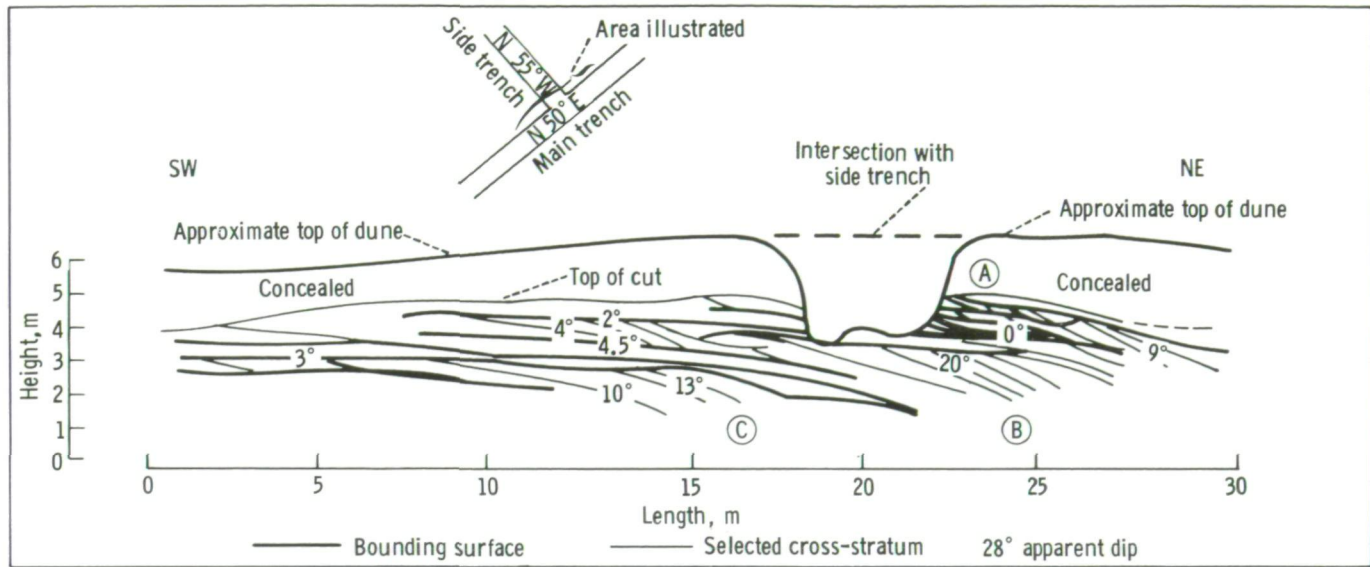


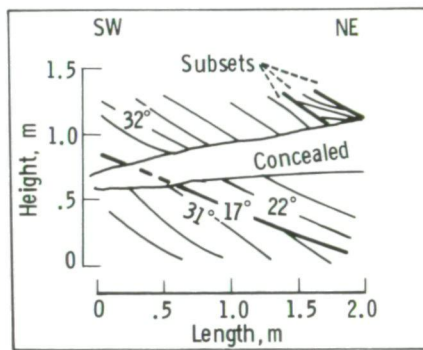
FIGURE 2-14.—Plan view of high star dune illustrating nature of internal structure in star pattern, Zalim, Saudi Arabia (modified from fig. 10 of ref. 2-10).

ing rotation, reversal, and other motions) result in other dune types and often highly complex dune patterns. The resultant internal structures differ very much from one dune type to another, and recognition of such differences should assist greatly in understanding structures that control fluid migration and reservoir quality in ancient rocks.

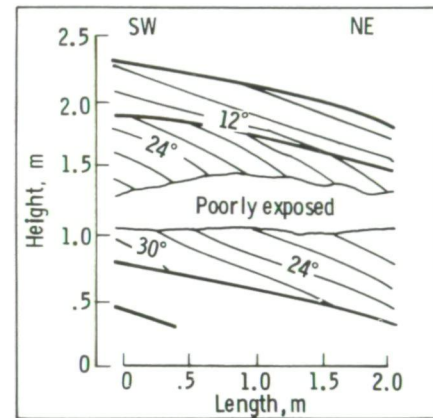
Some quartz sandstones of the type commonly interpreted by geologists as eolian have large-scale, high-angle cross-stratification and fine-grained, well-sorted sand with no matrix. In contrast, interdune deposits generally are poorly sorted, horizontally bedded, and variable in matrix content, all of which probably have a deleterious effect on the potential reservoir quality of eolian deposits. Well-known examples of ancient dune sands are the Coconino sandstone of Permian age in Arizona, the Navajo sandstone of Triassic(?) and Jurassic age in Arizona and Utah, and the Lyons



Detail at point (A)



Detail at point (B)



Detail at point (C)

FIGURE 2-15.—Internal structures of parabolic dune, White Sands, New Mexico (modified from fig. 9 of ref. 2-10).

sandstone of Permian age in Colorado. Additional examples of eolian-type sandstones are in England, Germany, and other parts of the world.

In general, the aforementioned sandstones are highly permeable aquifers. Both the Coconino and the Navajo sandstones are important sources of ground water in Arizona, and the Navajo sandstone locally contains copper deposits, apparently accumulated from percolating waters. The large-scale, southward-dipping foresets in both the Coconino and the Navajo formations obviously are major factors in determining the direction and rate of movement of water, oil, and other gases and liquids. These foresets are believed to be the slipfaces of ancient wind-formed dunes.

ECONOMIC BENEFITS AND APPLICATIONS OF SAND-SEA RESEARCH

Application to Land Use in Deserts

Agricultural and pastoral land use.—Erosion and deposition of sand and dust by wind have economic impact wherever arid regions are used for growing crops or grazing animals. Inappropriate agricultural practices and the overgrazing of animals in areas of fixed dunes may disrupt a stabilizing cover of vegetation. Sand thus freed is transported by wind; it may choke water-courses, encroach on fertile land, or threaten the existence of villages. Problems of this nature are cur-

rently being experienced in the Sahelian Zone of northern Africa and in the Rajasthan-Thar Desert settlements of India and Pakistan. In Punjab and western Uttar Pradesh, India, windblown sand is encroaching on fertile, cultivated land at an annual rate of as much as 130 km² (refs. 2-39 and 2-40).

Urban and industrial land use.—Invasive sand threatens land use in the oil-producing countries of northern Africa and the Arabian Peninsula where sand seas commonly surround towns, oil wells and refineries, and transportation facilities. Eolian sand movement and deposition may be controlled around these installations (ref. 2-41). Regional-scale analysis of the relationship of sand distribution and movement to sand source areas, topographic barriers, and wind regimes is made possible by observations and photography from space.

Surface winds can be used as a power energy source, a development of great importance to the energy-deficient desert areas. Surface wind regimes of the more remote areas under study in this project—such as the Arabian Peninsula, southwestern Africa, much of northern Africa, and the deserts of northern China and eastern Russia—have not been systematically studied by meteorologists. Meteorological studies have concentrated on higher level winds (at least 1000 m above the surface). The N-Summaries of the National Climatic Center provide a data base that is the first comprehensive compilation of surface wind regimes for many of the deserts where sand seas are being studied. From these data, information on regional surface wind distribution patterns is being developed.

Application to the Exploration of Mars

Martian bright and dark albedo markings, which change both seasonally and secularly, are generally attributed to sand and dust transported by wind. The concept of eolian transport as a dominant process on Mars was pioneered by McLaughlin in the mid-1950's and confirmed by observations from Mariner 9 (refs. 2-42 to 2-44). The global study of sand seas on Earth, based on observations and photographs from space, results in a definitive survey of eolian deposits that, by analogy, may aid in the interpretation of morphologically similar deposits on Mars.

Dunes are suspected components of several parts of the Martian landscape, and, almost certainly, dunes

form an 1800-km² mass on the floor of a crater at 331°, 47.5° S, in the Hellespontus region (refs. 2-43 and 2-45). The Hellespontus dunes are comparable in size and wavelength to dunes which form many of the parallel wavy patterns seen in Landsat images and Skylab photographs of several deserts on Earth. Martian dune patterns are markedly similar to those of terrestrial dune fields whose margins, like those of the Hellespontus dune field, are probably topographically controlled. In such terrestrial dune fields, the positions of the topographic boundaries seem to control the locations of dunes of different types and sizes.

A streaked pattern of light and dark material extends from topographic protuberances on the Martian surface (ref. 2-43). The Martian streaks strongly resemble streaks and sheets of sand that are seen in Landsat images and Skylab photographs to extend outward several kilometers from rock outcrops such as ridges and volcanic craters, particularly in deserts where effective winds are dominantly unidirectional (fig. 2-6(a)).

USEFULNESS OF SPACE OBSERVATIONS AND HANDHELD-CAMERA PHOTOGRAPHS FOR DESERT SAND-SEA STUDIES

Visual Observations

Types of useful visual data.—The practical use of a viewpoint from space for pinpointing areas of wind erosion caused by inappropriate land use has recently been demonstrated (ref. 2-46). The Landsat imagery was used to locate sources in the Mojave Desert from which plumes of blowing dust were moving across southern California. Duststorms cause considerable economic damage to crops and property during the Santa Ana wind season. However, fixed automated sensors, such as Landsat, do not have the capabilities of human observers in space to search for sources of moving sand or to relate evidence of eolian transport to changes on the land surface.

The Skylab 4 crew demonstrated the ability to observe blowing dust in the Sahara, to estimate the size of dust clouds, and to record the precise location and direction of dust cloud movement relative to the deserts and water bodies. Figure 2-16 shows dust moving from the northwest Sahara outward over the Atlantic Ocean. The dust cloud is 300 km wide, from Cape Timiris to the Sénégal River. Such dust clouds have been suggested as

ORIGINAL PAGE IS
OF POOR QUALITY

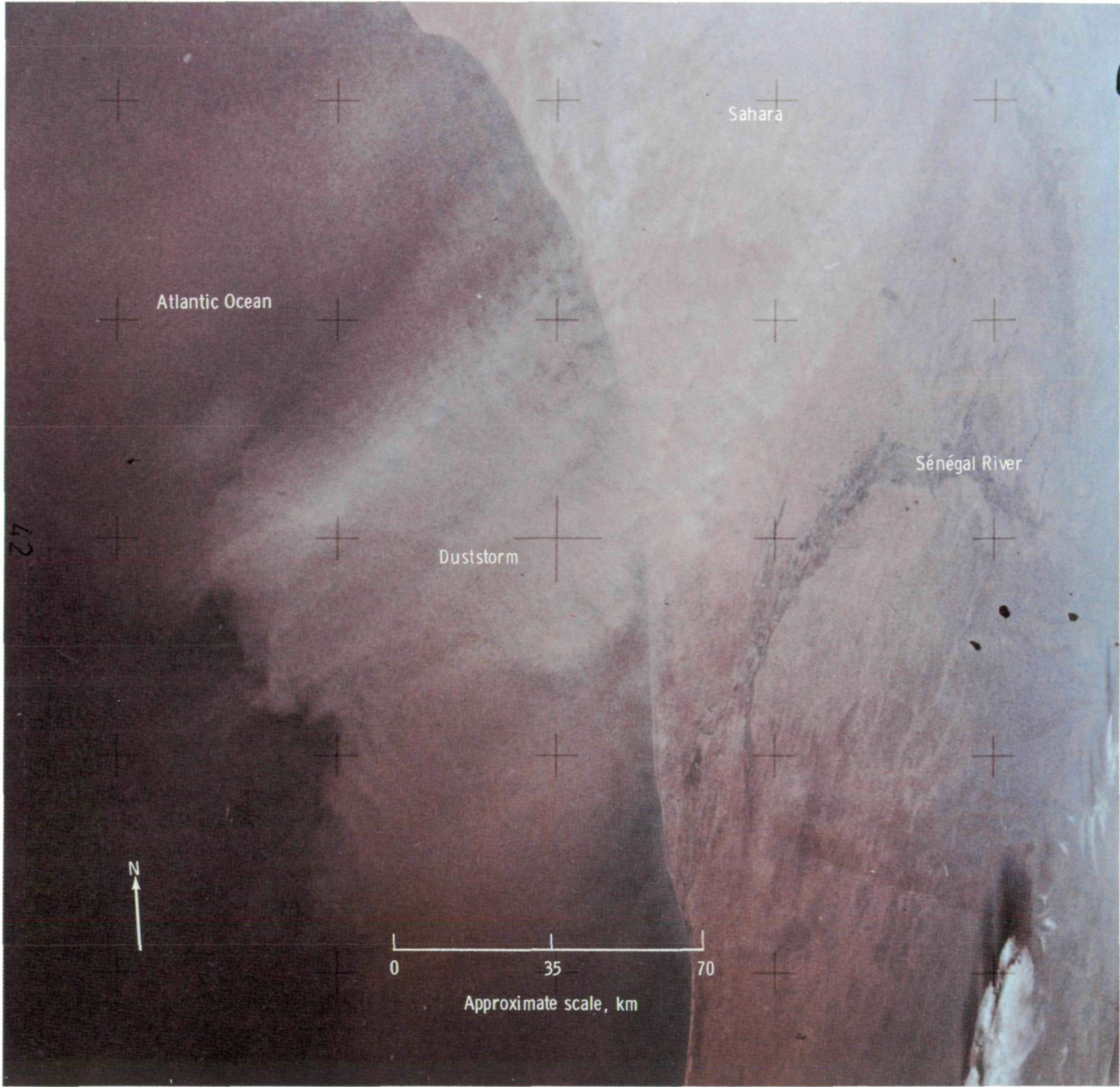


FIGURE 2-16.—Photograph showing duststorm over the northwestern Sahara and the Atlantic Ocean (SL4-140-4227).

a cause of the 10- to 15-percent reduction in the solar energy that reaches the surface in the tropical Atlantic. Saharan duststorms are being studied in the Global Atlantic Tropical Experiment (GATE) of the Global Atmospheric Research Program (GARP) (ref. 2-47).

The human eye may be more sensitive to differences of color than aerial film, as suggested by the crew's postmission comments concerning the colors recorded on their photographs. Although certain color differences on handheld-camera photographs of deserts could be presumed to be real and significant, confirmation of the true range of color and intensity came from the visual observations of the crew.

Suggested training and equipment for future visual observations.—The Skylab 4 crew made many good observations of desert phenomena, but they did not always know what they were observing, why they were observing it, or how best to describe the features. Familiarization with Earth features from orbit required time but was necessary before specific observations could be made. Skills should be acquired in training that would enable the crew to become thoroughly familiar with and able to describe Earth features as they appear from space.

Familiarity with the orbital view of Earth geography could be accomplished in training by having the crew examine and describe strips of space photographs or imagery in a context of scale and time sequence that would closely simulate the view from orbit. Excellent Landsat imagery is now available for nearly all parts of the Earth and could be viewed in proper geographical sequence. The crew would then be ready to examine in detail individual photographs of specific areas and to learn the necessary vocabulary for describing relevant features during the lecture and discussion periods with investigators.

If visual observations are to be recorded, an onboard set of color standards, such as a color wheel showing Earth colors as seen from space, is needed. The Munsell system is an almost universal color-description system and forms the basis for the Universal Color Language, Inter-Society Color Council/National Bureau of Standards (ISCC/NBS) method of describing colors. A set of

250 color chips calibrated to the ISCC/NBS system of color designations is available in the American Society of Photogrammetry "Manual of Color Aerial Photography." Twenty-four colors could be chosen that would adequately represent the colors of both land and water features as they appear from orbit.

A size and distance scale should also be readily available to quantify visual observations. Verbal descriptions of features need to be quickly quantified for later comparison with other observations and photographs. Before lift-off, practice might be devised to aid crewmen in observing and quickly describing features flashed on a screen for a few seconds.

Handheld Cameras

Handheld-camera photography is a necessary complement to visual observations from space. Handheld-camera photographs document the phenomena that the human observer judges to be worth recording; as such, the photographs are not substitutes for systematic, objective, uniform photographic coverage from an automated satellite such as Landsat. However, handheld-camera photography permits the deliberate acquisition of certain types of photographs, such as stereopairs, which the observer deems best for recording and measuring specific objects.

Stereophotographic pairs with 25° separation are needed for automatic stereoplotting of the features under study. The distribution of dune heights (reportedly as much as 320 m in some desert areas) may be significantly related to distance from sources of sand, topographic barriers, boundaries, and time.

Vertical true-color photographs from which areal and linear measurements of sand features can be obtained are valuable, particularly for analyzing regional distribution of dunes of different types. Oblique photographs are useful as general illustrations of the regional settings in which deposition of eolian sand occurs.

CONCLUDING REMARKS AND RECOMMENDATIONS

Data furnished by the Skylab crewmen, both from the verbal descriptions and from the handheld-camera photographs, constitute an essential ingredient for the global study of sand seas. The information is intermediate in scale between that furnished by Landsat images from an altitude of approximately 900 km and that derived from detailed ground studies, including trenching, coring, and laboratory analysis.

Skylab photographs of sand seas are essential to interpretation of various depositional forms observed in the patterns of Landsat images. Many details that blend together and lose their identity at the scale of Landsat images can be visually distinguished and recognized in

the Skylab photographs; thus, components of each pattern can be separated into discrete objects subject to classification and analysis.

Advancing the investigation of sand structures still further, including the interpretation of genesis, requires a supporting program of ground studies. Systematic sampling to determine characteristics of texture and composition can be accomplished readily, but essential studies of structure based on trenching and drilling are more difficult.

Methods of determining structural patterns by sectioning dune deposits with pits or trenches are well known but involve many physical difficulties. Nevertheless, a program is needed to systematically test principal dune types if further progress is to be made in understanding sand-sea environments.

Appendix

Summary of Equations Used to Compute Sand Roses

Wind velocity during sand driving increases as the logarithm of increasing height above the ground (ref. 2-9, p. 58). Regardless of how great a velocity is measured at any given height z , a level of zero velocity will exist at some small height above the surface.

During sand driving across a given surface, and at an exact height K' , which Bagnold (ref. 2-9, p. 68) named the "focus," all lines that depict vertical velocity gradients converge on a graph of velocity plotted against the logarithm of the height. This point also corresponds to the threshold velocity v_t described subsequently.

The rate of velocity increase with the logarithm of height above height K' is called the drag velocity V'_* . This value is numerically equal to the increase in wind velocity between any two measurement levels differing by 0.174 in logarithms of height (ref. 2-9, p. 53).

If the wind velocity as measured at height z is known and if a height between 0.3 and 0.8 cm (for uniform and mixed sand, respectively) for K' may be assumed from experience, then the velocity v at any height z can be found from the following equation (ref. 2-9, p. 61).

$$v = 5.75V'_* \log \frac{z}{K'} + v_t \quad (2-1)$$

In this equation, v_t is the minimum wind velocity (usually in centimeters per second) as measured at height K' required to maintain sand movement. This value approximates 360 cm/sec at K' . Because of the logarithmic distribution of wind velocity with height, the definition of v_t may be extended to include that wind velocity as measured at a given height necessary to maintain sand flow.

The rate q at which sand is driven by the wind when the threshold velocity for a given height of measurement is surpassed is shown (ref. 2-9, p. 67) to be equal to

$$q = C \sqrt{\frac{d}{D} \frac{\phi}{g}} (V'_*)^3 \quad (2-2)$$

where d is the average diameter of surface sand at the locality, D is the average diameter of most desert sands (0.25 mm), and ϕ/g is the ratio of the density of air to the gravitational constant and is equal to 1.25×10^{-6} in the cgs system. The constant C takes into account the effect of the degree of sand sorting and is empirically determined to be between 1.5 and 2.8 (ref. 2-9, p. 82).

The rate at which sand is driven by the wind, once the threshold velocity for a given height of measurement has been surpassed, is shown (ref. 2-9, p. 69) to be equal to

$$q = \alpha C \sqrt{\frac{d}{D} \frac{\phi}{g}} (v - v_t)^3 \quad (2-3)$$

where $v - v_t$ is the difference between wind velocity as measured at height z and threshold velocity for that height, and α is an empirical constant resulting from replacement of V'_* by $v - v_t$ and is equal to

$$\left[\frac{0.174}{\log\left(\frac{z}{K'}\right)} \right]^3$$

Equation (2-3) represents the substitution of $v - v_t$ for V'_* . A similar substitution for computing the sand-movement vectors is described subsequently. The preceding equations make it possible to substitute measurements of wind velocity made at a known height for V'_* ; substitution is desirable because wind summaries are published with wind velocities measured at some fixed height, usually 10 m.

The total sand movement m across a given small area from a given direction is shown (ref. 2-9, p. 184) to be equal to

$$m = b V'^3 t \quad (2-4)$$

where b is an empirical constant and t is the time during which wind blows steadily. If wind velocity is measured at a given height, then the expression $v - v_t$ may be substituted for V'_* (ref. 2-9, p. 67) in equation (2-4) as follows:

$$m = b (v - v_t)^3 t \quad (2-5)$$

The common meteorological practice is to divide the wind velocity as measured at a fixed height into velocity categories for purposes of summarizing observations.

Most, if not all, of the original observations at the stations used for this report were recorded to the nearest 10° direction and nearest knot (1-minute average) following the standard procedure of the WMO. The N-Summaries contain these original data condensed into 16 categories of direction corresponding to the 16 points of the nautical compass and into 10 velocity categories as follows: calms, 0.5 to 1.5 m/sec (1 to 3 knots); 2.1 to 3.1 m/sec (4 to 6 knots); 3.6 to 5.1 m/sec (7 to 11 knots); 5.7 to 8.2 m/sec (11 to 16 knots); 8.7 to 10.8 m/sec (17 to 21 knots); 11.3 to 13.9 m/sec (22 to 27 knots); 14.4 to 17 m/sec (28 to 33 knots); 17.5 to 20.6 m/sec (34 to 40 knots); and greater than 20.6 m/sec (40 knots).

Assuming the compartments of the N-Summary are small enough, then the average of the two velocities defining the compartment may be taken as the average wind velocity of all occurrences in the compartment and

$$m \approx \sum_{i=1}^n b (v_{(i)} - v_t)^3 t \quad (2-6)$$

where $v_{(i)}$ is the average velocity of the (i) th velocity category.

If the percent occurrence of observations falling within a certain velocity category for a certain direction may be considered approximately proportional to the actual occurrence of winds of the given velocity group from the given direction at the station (assuming observations are frequent enough and well distributed in a 24-hour time period and the period of record is sufficiently long), then

$$m \propto \sum_{i=1}^n (v_{(i)} - v_t)^3 t_p \quad (2-7)$$

where t_p is the time during which wind in a given velocity category blew, as represented by percent occurrence in observations. Equation (2-7) was used to evaluate the relative power of the wind from a given direction.

It follows that the total sand transport potential of wind from all directions M is the sum of all the potentials from the individual directions

$$M = \sum_{j=1}^{\eta} m_{(j)} \quad (2-8)$$

where $m_{(j)}$ is the transport potential of wind from the (j) th direction. Equation (2-8) was used to evaluate the power of winds from all directions at a station. If the height above the ground at which the wind was measured may be assumed to be equal for all stations, then the expression for sand movement potential may also be thought of as an approximate indication of the amount of energy available at the site for the movement of sand, whether or not this movement occurred.

ACKNOWLEDGMENTS

Acknowledgment is gratefully made to Dr. Harold L. Crutcher, Scientific Advisor, National Climatic Center, Asheville, North Carolina, and to Dr. Richard G. Layton, Physics Department, Northern Arizona University, Flagstaff, Arizona, for reading this section and making numerous helpful suggestions. The authors also thank Gary Dean for his assistance in the preparation both of the section entitled "Relationship of Sand Distribution to Surface Wind Regimes" and the appendix.

REFERENCES

- 2-1. Aufrère, L.: L'Orientation des Dunes Continentales. Proceedings of the 12th IGU Congress, Cambridge, 1928, pp. 220-221.
- 2-2. Hack, John T.: Dunes of the Western Navajo Country. Geog. Rev., vol. XXXI, 1941, pp. 240-263.
- 2-3. McKee, E. D.: Primary Structures in Some Recent Sediments. Bull. American Assoc. Petrol. Geol., vol. 41, no. 8, Aug. 1957, pp. 1704-1747.
- 2-4. Folk, Robert L.: Genesis of Longitudinal and Oghurd Dunes Elucidated by Rolling Upon Grease. Bull. Geol. Soc. America, vol. 82, no. 12, Dec. 1971, pp. 3461-3468.
- 2-5. Madigan, C. T.: The Australian Sand-Ridge Deserts. Geog. Rev., vol. 26, 1936, pp. 205-227.
- 2-6. Warren, Andrew: Dune Trends and Their Implications in the Central Sudan. Ann. Geomorph. (Z. Geomorph.), Suppl. 10, Piedmont Plains and Sand-Formations in Arid and Humid Tropic and Subtropic Regions, 1970, pp. 154-180.
- 2-7. Capot-Rey, R.: Dry and Humid Morphology in the Western Erg. Geog. Rev., vol. XXXV, no. 3, 1945, pp. 391-407.
- 2-8. Lelubre, Maurice: Une Reconnaissance Aérienne sur l'Édeyen de Mourzouk (Fezzan): Travaux de l'Institut de Recherches Sahariennes, vol. 5, 1948, pp. 219-221.
- 2-9. Bagnold, Raymond Alger: The Physics of Blown Sand and Desert Dunes. Methuen and Co. (London), 1954.
- 2-10. McKee, E. D.: Structures of Dunes at White Sands National Monument, New Mexico (and a Comparison With Structures of Dunes From Other Selected Areas). Sedimentology, vol. 7, no.1 (spec. issue), 1966.
- 2-11. Glennie, K. W.: Desert Sedimentary Environments. Developments in Sedimentology, vol. 14, Elsevier Publishing Co., 1970.
- 2-12. Melton, Frank A.: A Tentative Classification of Sand Dunes—Its Application to Dune History in the Southern High Plains. J. Geol., vol. 48, no. 2, Feb.-Mar. 1940, pp. 113-174.
- 2-13. Smith, H. T. U.: Dune Morphology and Chronology in Central and Western Nebraska. J. Geol., vol. 73, no. 4, July 1964, pp. 557-578.
- 2-14. Monod, Théodore: Majâbat al-Koubrâ. Contribution à l'Étude "L'Empty Quarter" Ouest-Sahara: Mémoires de l'Institut Français d'Afrique Noire, no. 52, 1958.
- 2-15. Cooke, R. U.; and Warren, Andrew: Geomorphology in Deserts. Univ. of California Press, 1973.
- 2-16. Holm, Donald August: Desert Geomorphology in the Arabian Peninsula. Science, vol. 132, no. 3437, Nov. 1960, pp. 1369-1379.
- 2-17. Norris, R.; and Norris, K.: Algodones Dunes of South-eastern California. Bull. Geol. Soc. America, vol. 72, 1961, pp. 605-620.
- 2-18. Simons, Frank S.; and Ericksen, George E.: Some Desert Features of Northwest Central Peru. Soc. Geol. Peru Bol., vol. 26, 1953, pp. 229-246.
- 2-19. Hedin, Sven: The Scientific Results of a Journey in Central Asia, 1899-1902 — Vol. 1, The Tarim River. Lithographic Institute of the General Staff of the Swedish Army, Stockholm, 1904-1905.
- 2-20. Aufrère, L.: Morphologie Dunaire et Météorologie Saharienne. Bull. l'Ass. des Géographes Français, vol. 56, 1932, pp. 34-47.
- 2-21. Price, W. Armstrong: Saharan Sand Dunes and the Origin of the Longitudinal Dune: A Review. Geog. Rev., vol. XL, no. 3, 1950, pp. 462-465.

- 2-22. Gautier, E. F. (Dorothy F. Mayhew, transl.): Sahara—The Great Desert. Columbia Univ. Press, New York, 1935.
- 2-23. Wilson, Ian G.: Aeolian Bedforms—Their Development and Origins. *Sedimentology*, vol. 19, no. 3/4, Dec. 1972, pp. 173-210.
- 2-24. Wilson, Ian G.: *Ergs. Sed. Geol.*, vol. 10, no. 2, 1973, pp. 77-106.
- 2-25. Logan, R. F.: The Central Namib Desert, South West Africa. *Natl. Acad. Sci./Natl. Research Council Pub.* 758, 1960.
- 2-26. Verstappen, H. Th.: On the Origin of Longitudinal (Seif) Dunes. *Z. Geomorph. (Ann. Geomorph.)*, Band 12, Heft 2, June 1968, pp. 200-220.
- 2-27. McKee, E. D.; Breed, C. S.; Fryberger, S. G.; Gebel, Dana; and McCauley, E.: A Synthesis of Sand Seas Throughout the World: Photosaics of Africa, Asia, and Australia. Type III Final Report for July 1, 1972, to March 31, 1974, NASA Earth Resources Survey Program, 1974.
- 2-28. Bryson, Reid A.: A Perspective on Climate Change. *Science*, vol. 184, no. 4138, May 1974, pp. 753-760.
- 2-29. Grove, A. T.: The Ancient Erg of Hausaland and Similar Formations on the South Side of the Sahara. *Geog. J.*, vol. 124, 1958, pp. 526-533.
- 2-30. Grove, A. T.; and Warren, A.: Quaternary Landforms and Climate on the South Side of the Sahara. *Geog. J.*, vol. 134, pt. 2, 1968, pp. 194-208.
- 2-31. Prescott, J. R. V.; and White, H. P.: Sand Formations in the Niger Valley Between Niamey and Bourem. *Geog. J.*, vol. 126, pt. 2, 1960, pp. 200-203.
- 2-32. Brookfield, Muriel: Dune Trends and Wind Regime in Central Australia. *Ann. Geomorph. (Z. Geomorph.)*, Suppl. 10, Piedmont Plains and Sand-Formations in Arid and Humid Tropic and Subtropic Regions, 1970, pp. 121-153.
- 2-33. Tricart, J.; and Brochu, M.: Le Grand Erg Ancien du Trarza et du Cayor (Sud-Ouest de la Mauritanie et Nord du Senegal). *Rev. Géomorph. Dynamique*, vol. 6, no. 4, 1955, pp. 145-176.
- 2-34. Wilson, Ian Gordon: Desert Sandflow Basins and a Model for the Origin of Ergs. *Geog. J.*, vol. 137, pt. 2, June 1971, pp. 180-199.
- 2-35. Dubief, Jean: Le Vent et le Déplacement du Sable au Sahara. *Travaux de l'Institut de Recherches Sahariennes*, vol. VIII, 1952, pp. 123-164.
- 2-36. Wilson, Ian: Journey Across the Grand Erg Oriental. *Geog. Mag.*, vol. 43, 1971, pp. 264-270.
- 2-37. McKee, Edwin D.; and Tibbitts, Gordon C., Jr.: Primary Structures of a Seif Dune and Associated Deposits in Libya. *J. Sed. Petrol.*, vol. 34, no. 1, Mar. 1964, pp. 5-17.
- 2-38. McKee, E. D.; and Moiola, R. J.: Geometry and Growth of the White Sands Dune Field, New Mexico. *J. Res. U.S. Geol. Survey*, vol. 3, no. 1, Jan.-Feb. 1975, pp. 59-66.
- 2-39. Seth, S. K.: A Review of Evidence Concerning Changes of Climate in India During the Protohistorical and Historical Periods. *Changes of Climate, Proceedings of the Rome Symposium Organized by UNESCO and the World Meteorological Organization, Arid Zone Research Series*, vol. 20, 1963, pp. 443-454.
- 2-40. Raheja, P. C.: Research and Development in the India Arid Zone. *Arid Zone (UNESCO Newsletter)*, no. 15, 1962, pp. 7-12.
- 2-41. Kerr, Richard C.; and Nigra, John O.: Eolian Sand Control. *Bull. American Assoc. Petrol. Geol.*, vol. 36, no. 8, Aug. 1952, pp. 1541-1573.
- 2-42. McCauley, John F.: Mariner 9 Evidence for Wind Erosion in the Equatorial and Mid-Latitude Regions of Mars. *J. Geophys. Res.*, vol. 78, no. 20, 1973, pp. 4123-4137.
- 2-43. Cutts, J. A.; and Smith, R. S. U.: Eolian Deposits and Dunes on Mars. *J. Geophys. Res.*, vol. 78, no. 20, 1973, pp. 4139-4154.
- 2-44. Sagan, Carl: Sandstorms and Eolian Erosion on Mars. *J. Geophys. Res.*, vol. 78, no. 20, 1973, pp. 4155-4161.
- 2-45. McCauley, J. F.; Carr, M. H.; Cutts, J. A.; Hartmann, W. K.; Masursky, Harold; et al.: Preliminary Mariner 9 Report on the Geology of Mars. *Icarus*, vol. 17, 1972, pp. 289-327.
- 2-46. Bowden, Leonard W.; Huning, James R.; Hutchinson, Charles F.; and Johnson, Claude W.: Satellite Photograph Presents First Comprehensive View of Local Wind: The Santa Ana. *Science*, vol. 184, no. 4141, June 1974, pp. 1077-1078.
- 2-47. Sahara Dust, Tropical Weather, Pollution, and Solar Energy Balance Linked. *Mariner's Weather Log, NOAA Environmental Data Service*, vol. 18, no. 2, Mar. 1974, pp. 103-104.

3

Global Tectonics: Some Geologic Analyses of Observations and Photographs From Skylab

*W. R. MUEHLBERGER,^a P. R. GUCWA,^a A. W. RITCHIE,^a
AND E. R. SWANSON^a*

THE PRESENT model of mountain building involves the interaction of rigid plates of the Earth's crust as they move relative to one another. The major mountain chains of the world are the result of complex interactions of these moving plates with deformation concentrated near the plate boundaries. The three principal types of deformation caused by relative plate movement are described in the following paragraphs.

Spreading zones generally correspond to midocean ridges. These areas are (1) above sea level in Iceland (too far north for observation by the Skylab crewmen) and (2) the length of Africa as long, linear, fault-bounded valleys from Mozambique in the south through the East African rift valleys and up the Red Sea to the Gulf of Suez.

Transform faults are formed when plates slide horizontally past each other, as illustrated by the San Andreas Fault of California, the Alpine Fault of New Zealand, and the Dead Sea rift zone.

Subduction occurs when one tectonic plate is thrust under an adjacent plate. Subduction zones are associated with ocean deeps, chains of volcanoes, and complex fault patterns, such as those in Central America and, more complexly, by the Atacama Fault of Chile and the Philippine Fault of the Philippine Islands.

Skylab crew observations and handheld-camera photographs of the regional patterns of fault traces and related branch faults, together with synoptic photographs from space, should assist in evaluating present analyses as well as in integrating the results of ground observations in widely separated areas.

In repeated passes over the same regions, even though at 5-day intervals, the crew remembered previous observations and were able to integrate this knowledge and improve on earlier observations and photographs. In addition, the crew identified and commented on major fault zones and anomalous-appearing regions that had not been discussed during briefings or during the missions, such as faults parallel to the Brazilian coast north of São Paulo and Rio de Janeiro, faults bounding the Deccan Plateau of west-central India, and a circular feature in southern Wisconsin.

This section contains the results of the authors' geologic studies of Skylab photographs to date. Most of the work has centered around Skylab 4 handheld-camera photographs and crew observations. A premission briefing of global tectonic features and patterns focused the crew's attention on some tectonic problems of worldwide interest and significance. This section includes both expansions of observations reported in the "Skylab 4 Visual Observations Project Report" (ref. 3-1) and new studies.

^aThe University of Texas at Austin.

NEAR AND MIDDLE EAST

According to plate-tectonics theory, the juncture of three radially symmetrical rift systems is interpreted as an early stage in crustal separation (ref. 3-2). The Afar triple junction, or Afar depression, is an example of this relationship and occurs at the junction of the Red Sea, the Gulf of Aden, and the East African rift systems (fig. 3-1). The spreading associated with this triple junction has been most active in the Red Sea and the Gulf of Aden arms and has resulted in the separation and

northeastward translation of the Arabian plate from Africa. Movement of the Arabian plate is associated with the opening of the Red Sea and Gulf of Aden, left-lateral strike-slip faulting along the Dead Sea rift, and the convergence of the Arabian plate with Eurasia, which leads to the development of complex structures in Iran and Turkey.

TABLE 3-1.—Index of Near and Middle East Photographs

[See figure 3-2]

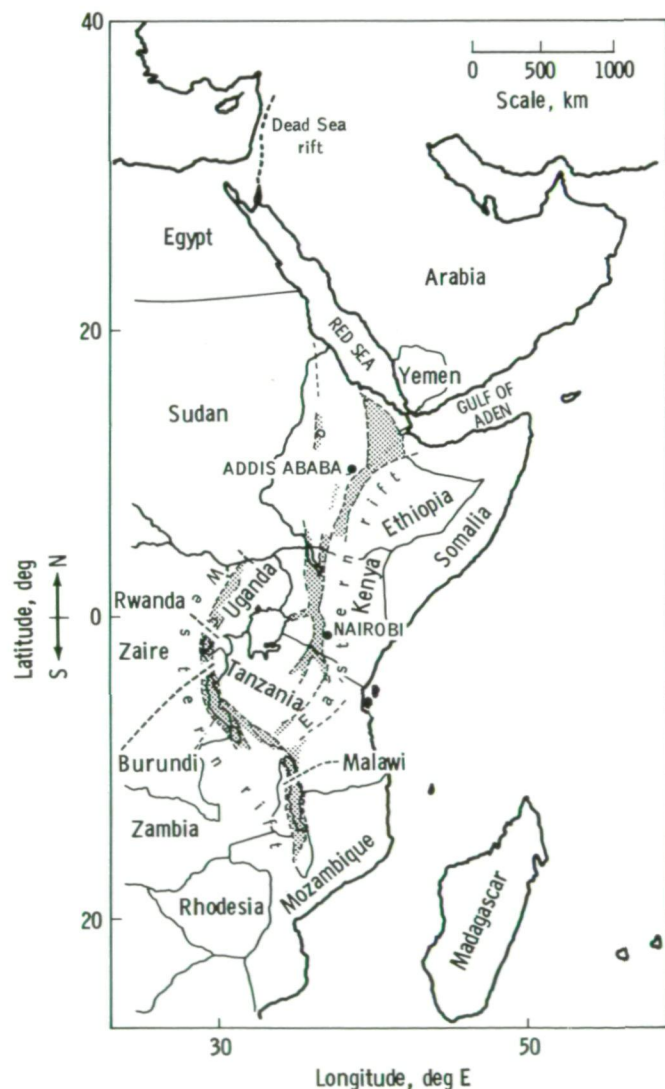


FIGURE 3-1.—Afro-Arabian rift system. Continental depressions are shaded. The Afar triangle is the shaded area west of the junction of the Red Sea and the Gulf of Aden (modified from ref. 3-3).

| Area | Area no. | Skylab photograph no. |
|--|----------------|-----------------------|
| Caucasus (C) | 1 | SL4-139-3904 |
| | 2 | SL4-138-3871 |
| | 3 | SL4-138-3870 |
| | 4 | SL4-138-3872 |
| | 5 | SL4-138-3873 |
| | 6 | SL4-139-3905 |
| | 7 | SL4-138-3817 |
| | 8 | SL4-138-3819 |
| | 9 | SL4-138-3818 |
| Sinai, Red Sea, Dead Sea, and western Saudi Arabia (S) | 1 | SL4-194-7262 |
| | 2 | SL4-194-7261 |
| | 3 | SL4-194-7256 |
| | 4 | SL4-194-7259 |
| | 5 | SL4-194-7254 |
| | 6 | SL4-194-7257 |
| | 7 | SL4-194-7260 |
| | 8 ^a | SL4-190-6993 |
| | 9 | SL4-138-3749 |
| | 10 | SL4-138-3750 |
| | 11 | SL4-138-3751 |
| | 12 | SL3-46-209 |
| Afar (A) | 1 | SL4-137-3586 |
| | 2 | SL4-137-3719 |
| | 3 | SL4-137-3718 |
| | 4 | SL4-137-3697 |
| | 5 | SL4-141-4294 |
| | 6 | SL4-141-4295 |
| | 7 | SL4-141-4296 |
| | 8 | SL4-141-4297 |
| | 9 | SL4-137-3708 |
| | 10 | SL4-137-3709 |
| | 11 | SL4-137-3585 |
| | 12 | SL4-137-3584 |
| | 13 | SL4-191-7059 |
| | 14 | SL4-191-7056 |
| | 15 | SL4-191-7057 |
| | 16 | SL4-191-7055 |
| Iran and Oman (I) | 1 | SL4-141-4252 |
| | 2 | SL4-141-4251 |
| | 3 | SL4-141-4278 |
| | 4 | SL4-141-4257 |
| | 5 | SL4-141-4257 |
| | 6 | SL4-141-4276 |

^aThe following photographs were also taken in the area of SL4-190-6993: SL4-190-6994, SL4-194-7219, SL4-194-7220, SL4-194-7221, SL4-138-3815, SL4-138-3771, SL4-138-3772, SL4-138-3773, SL4-138-3790, SL4-138-3815, SL4-138-3869.

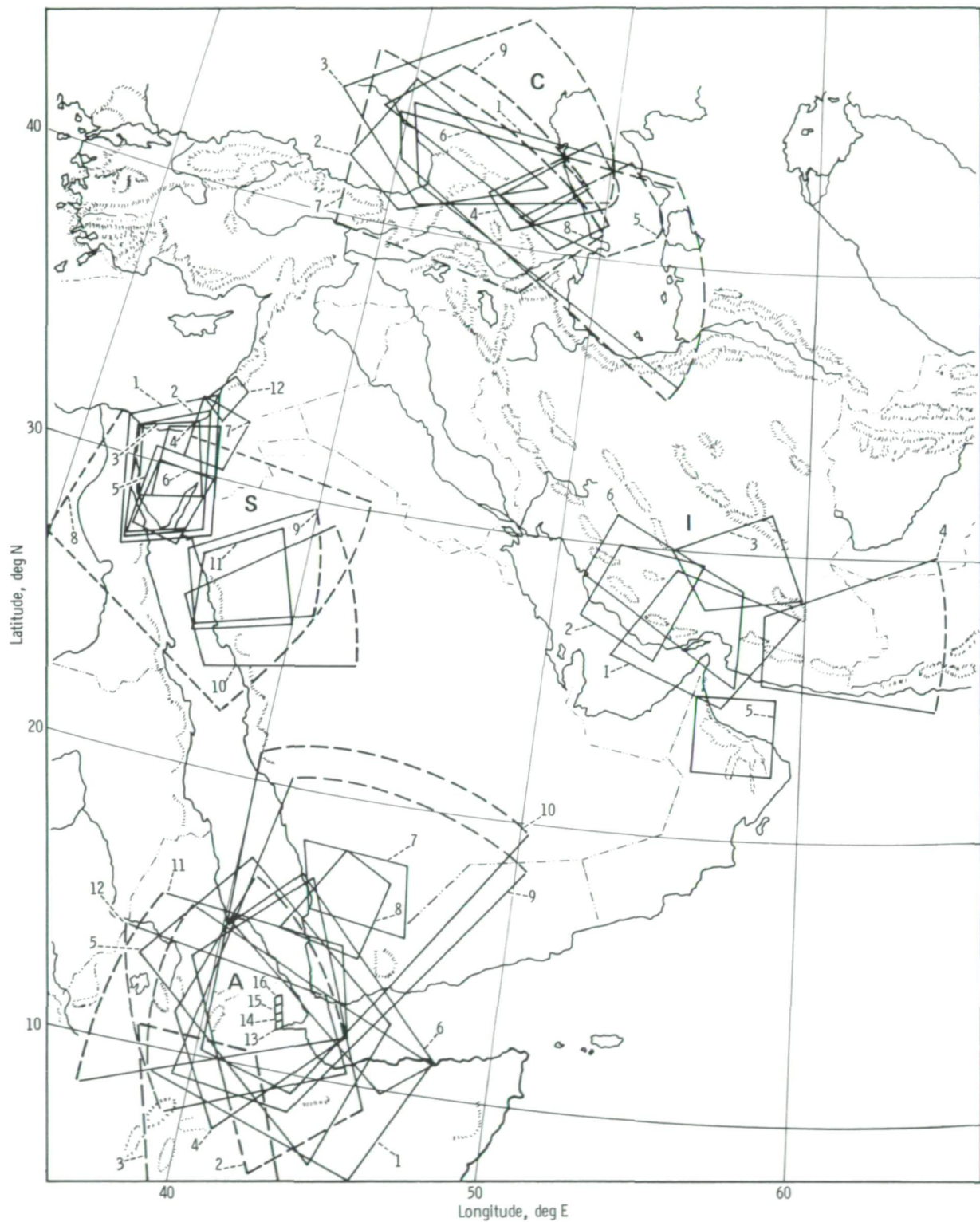


FIGURE 3-2.—Location of the Skylab 4 photographs of the Near and Middle East that were studied. Numbered areas are indexed in table 3-1.

Geologic studies of these areas are often too detailed in a small region to recognize a rigid plate character or, conversely, unknown over a sufficiently large area to show the internal and external features of plate interaction. Space photographs provide an excellent means of investigating the relationships between structures and analyzing the regional significance. The Skylab 4 crew photographed areas of the Near and Middle East that represent each of the main types of relative plate motion. Zones of divergence, or pull-apart areas, are represented by the Afar depression, the Red Sea, and the Gulf of Aden; a zone of transform motion is represented by the Dead Sea rift; and a zone of convergence is represented by the belt of the Zagros Mountains of southeastern Iran. The Skylab 4 photographs of these areas are indicated in figure 3-2 and indexed in table 3-1.

The African rift system, one of the few major rift systems above sea level, extends the length of the eastern side of Africa from Mozambique to the Red Sea. At approximately latitude 10° N, the main Ethiopian rift widens northward to form the Afar depression.

The Afar depression is structurally complex. An excellent discussion of the geology of this region is contained in "Geology of the Eastern Rift System of Africa" (ref. 3-3), and the following summary is taken largely from this work.

In the Afar depression, Late Mesozoic to Early Tertiary downwarping, accompanied by the emplacement of the Trap Series basalts, was followed by local upwarping in the Late Tertiary period. The first major period of rift faulting appears to have begun in the mid-Miocene. Strong graben faulting occurred in late Pliocene/early Pleistocene and was followed by intense faulting during the mid-Pleistocene. Each of these periods of faulting was accompanied by volcanic activity. Evidence that the tectonic activity has continued into the Holocene is found in seismic data, the occurrence of Quaternary volcanic activity, and zones of Recent faulting.

The tectonic history of Afar is dominated by graben faulting and volcanic activity. The deformation has been intermittent since its initiation approximately 80 million years ago and has continued to the present. Published fault maps of Afar (fig. 3-3) indicate the northern half is dominated by northward trends, whereas, in the southern half, northwestward and north-northeastward trends are more apparent. All the Skylab photographs of the Afar area show these features. Figure 3-4 is one example of the Skylab 4 photography of the Afar depression. Bannert (ref. 3-4) used Apollo 9 photographs to supplement earlier

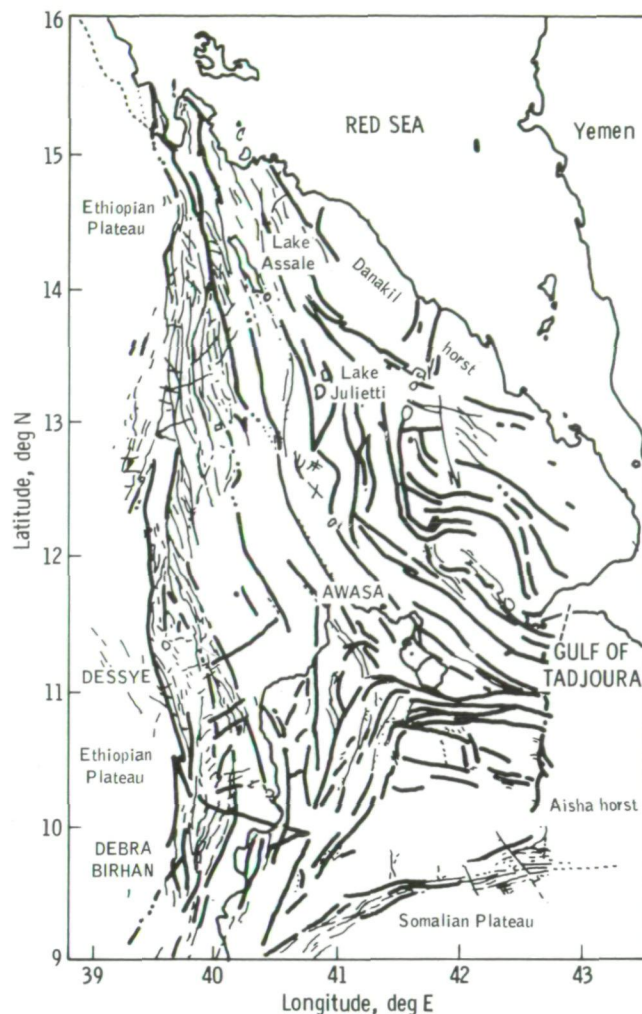
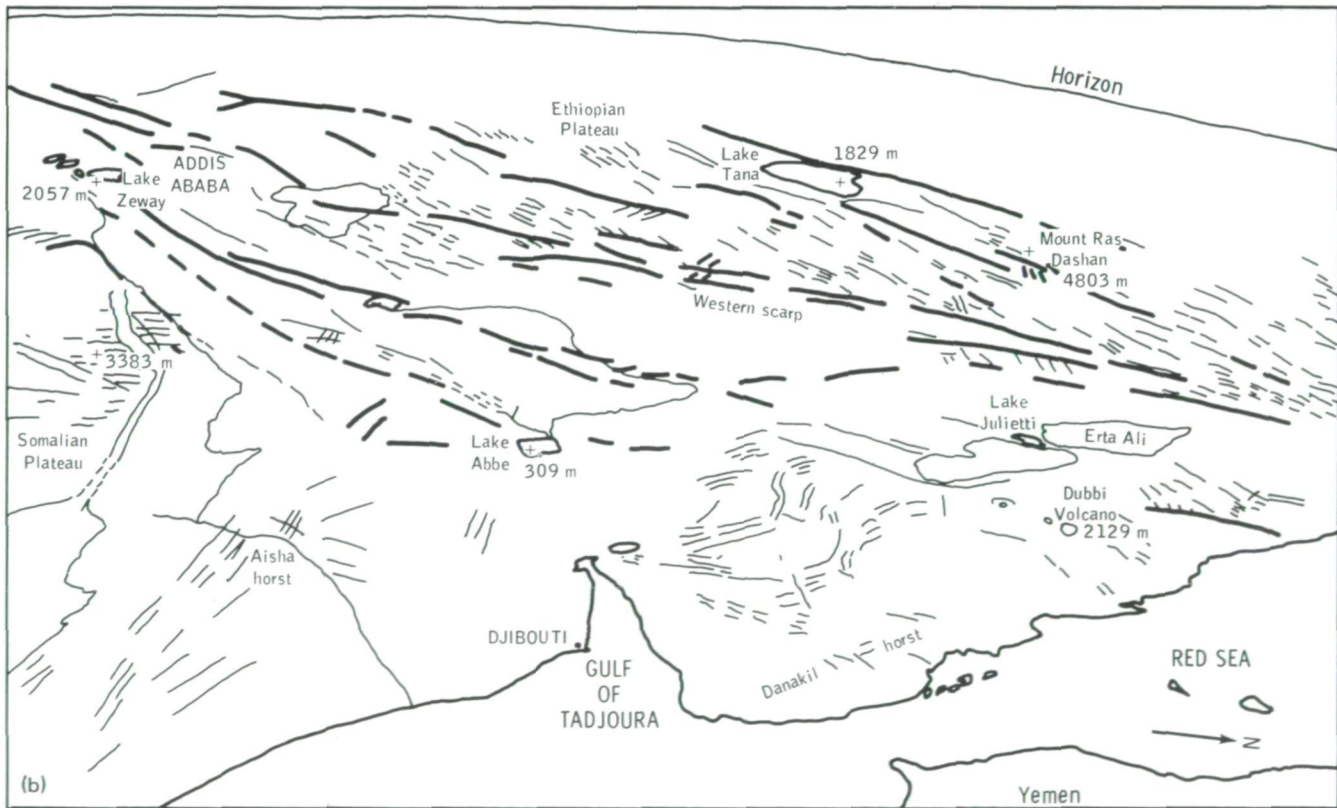


FIGURE 3-3.—Major faults of the Afar triangle (modified from ref. 3-3).

FIGURE 3-4.—View west across the Afar triangle. (a) Mosaic of photographs SL4-137-3584 and SL4-137-3585. (These two photographs also make a useful stereopair.) (b) Sketch map to locate major structural and topographic features. The Danakil horst is a basement block apparently separated from the Ethiopian Plateau during the opening of the Red Sea. The complex character of the western scarp and the continuation of the north-northeastward trend (Wonji Fault belt) as discontinuous segments from Lake Zeway to the Red Sea near the Dubbi Volcano are noteworthy. →



ORIGINAL PAGE IS
OF POOR QUALITY

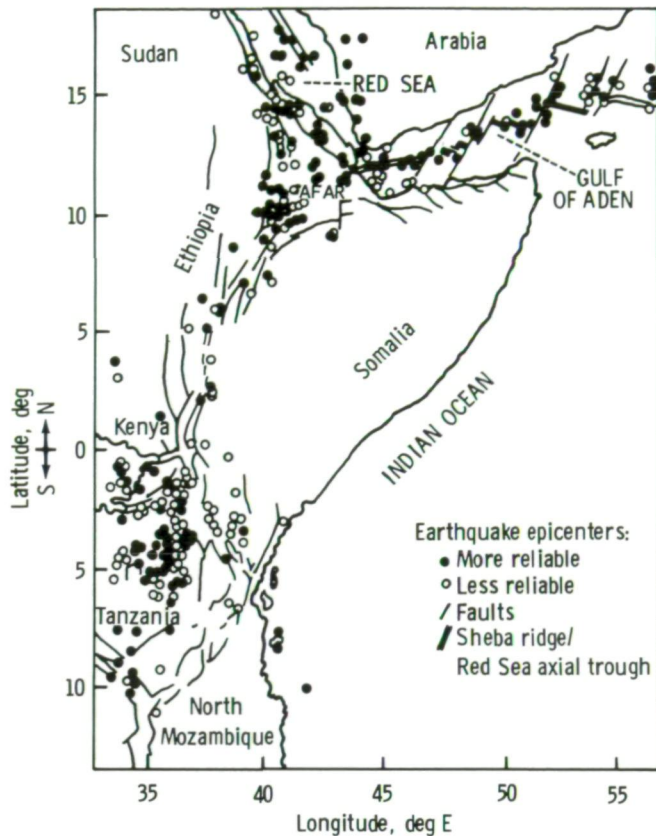


FIGURE 3-5.—Seismicity of the eastern rift and the Gulf of Aden (from ref. 3-3).

ground and photographic studies. Although he could distinguish in the space photographs between two basalt units that could not be divided on conventional photographs, the small scale of the space photographs eliminated some critical details visible on the lower level aerial photographs. An additional advantage of space photographs, Bannert noted, was the synoptic view of large areas.

Some controversy has arisen over the relationship of the East African rift system with the Afar depression. Tazieff et al. (ref. 3-5) argue that the continuation of the African rift system represented by the Wonji Fault belt cannot be traced north of Lake Abbe (figs. 3-3 and 3-4). The offset of the Red Sea rift at approximately 15° N latitude and the deformation observed in northwestern Afar are related according to Tazieff et al. to the rotation of the Danakil horst away from the Ethiopian Plateau along the southern continuation of the Red Sea rift that turns eastward and merges with the Gulf of Aden rift (fig. 3-3). Seismic data (fig. 3-5) do not support these concepts but suggest a north-northeastward

continuation of the African rift trend along the same zone suggested by Baker et al. (ref. 3-3) from geologic data. Moreover, figure 3-4(b) indicates the presence of discontinuous linears along this trend.

As previously mentioned, rifting and spreading have been more active along the Gulf of Aden and the Red Sea arms of the Afar triple junction. Spreading of these two areas was accompanied by the northward translation and counterclockwise rotation of the Arabian plate. Much of the relative displacement was accomplished by left-lateral strike-slip faulting along the Dead Sea rift. Geological and geophysical data suggest considerable overlap of Yemen (fig. 3-3) into the Afar depression in pre-Miocene time (ref. 3-6). Laughton (ref. 3-7) suggests that, since the Miocene epoch, Arabia has drifted away from Africa in a counterclockwise direction approximately 250 km at 15° N latitude consequent to the opening of the Gulf of Aden. He further states that a large part of the crust beneath Afar has formed since this drifting. Because Red Sea trends can be traced directly from Arabia into Africa in pre-Miocene reconstructions, Laughton's theory represents a late stage in the opening of the Red Sea. This interpretation is partly supported by the following model for the opening of the Red Sea. Girdler (ref. 3-8) suggests a separation of approximately 240 km at 15° N latitude with the amount of separation decreasing to the north. The model is based on a northward translation of Arabia of 100 km and a counterclockwise rotation of 7°. The 100-km northward translation at the north end of the Red Sea is interpreted from the left-lateral offset along the Dead Sea rift, which Freund et al. (ref. 3-9) have documented as 105 km since the Cretaceous. The article by Freund et al. contains an excellent geologic review of the Dead Sea rift and is summarized in part in the following paragraphs.

Although there is some controversy concerning the exact nature of the Dead Sea rift, the argument for 105 km of left-lateral shear is convincing. Restoration of the suggested displacement places more than 20 equivalent features in adjacent positions without creating a single anomaly, which thereby provides a single explanation for the observed features. All pre-Tertiary marker horizons resume a reasonable paleogeographic configuration when restored, which implies that the shear is post-Cretaceous. The offset of Miocene rocks, 40 to 45 km, leaves approximately 60 km to pre-Miocene displacement. Quennell (ref. 3-10) had earlier (1956) assigned 45- and 62-km displacements, respectively, to the two stages of movement.

The Dead Sea rift fault is not a single fault but, like many large transcurrent faults, is a complex fault zone. Freund (ref. 3-11) suggests that much of the complexity is due to secondary adjustment of an originally non-linear fault. Some complex fault patterns associated with this shear in the southern part of the Dead Sea rift are shown in figure 3-6 for comparison with figure 3-7, a published fault map of this area. Skylab 4 photographs did not include the northern part of the Dead Sea rift in Israel except in highly oblique photographs. Part of this area was photographed during the Skylab 3 mission, and the interesting features of this part of the fault zone are illustrated in figure 3-8. North of the Sea of Galilee, the fault begins splaying into several pronounced arcuate faults. The features observed in figure 3-8 suggest that some of the displacement along the Dead Sea rift fault might be accounted for by deformation in this zone. Freund et al. (ref. 3-9) report that, north of Lebanon, 80 km of displacement can be attributed to the Dead Sea rift fault; furthermore, they suggest a 20- to 25-km overlap in the area north of the Sea of Galilee. Freund (ref. 3-11) interprets the Dead Sea rift fault as a transform fault that extends from the extensional zone of the Red Sea rift to the compressional zone of the Taurus-Zagros trend of Turkey and Iran.

The Skylab 4 crew was asked to photograph any anomalous features on either side of the Red Sea that might suggest deformation of Saudi Arabia other than that paralleling the Red Sea opening. The crew identified and photographed an area along the northern Red Sea margin of the Arabian Peninsula (fig. 3-9) that is broken by a complex network of faults, both parallel and oblique to the coast. Many of the linears in figure 3-10 are part of a coastal fault system that extends for some distance along the western Arabian margin. Many of the faults have been mapped as Precambrian (refs. 3-12 to 3-16), but the presence of lines of Late Cenozoic fissure basalts and the prominence of some of the linear elements indicate the strong possibility that some of these faults have been reactivated. The continuation of some of the linears with mapped faults well into the Arabian platform suggests that perhaps not all the displacement of the Arabian plate is represented along the Dead Sea rift. Thus, much deformation may have been absorbed internally along fault systems such as these.

Several authors have interpreted much of the structural complexity of Iran as resulting from the collision and subduction of the Arabian plate beneath Eurasia (refs. 3-17 to 3-19). Iran can be divided into many distinct geologic structural zones (ref. 3-17). Takin (ref.

3-18) has suggested that the structure of many of these zones is related to the closing of the Tethyan Sea by the northeastward translation of Africa and Arabia. Of particular interest in this discussion are the folded belt of the Zagros Mountains, the Zagros thrust zone, and the southern side of the Sanandaj-Sirjan ranges. The location of these zones is shown schematically in figure 3-11. The following summary is taken mostly from Stöcklin (ref. 3-17) and Haynes and McQuillan (ref. 3-19).

The folded belt of the Zagros Mountains extends along the southwestern border of Iran. From the Infracambrian to mid-Triassic, this area was a relatively stable platform. In the Triassic, the character of the area changed to that of a trough, the axis of which has gradually shifted southwestward to its present position in the Persian Gulf. The Infracambrian Hormuz salt is present in this folded belt and appears to be restricted to the Zagros fold belt (fig. 3-11, region 2). Deformation in this zone appears restricted to the Plio-Pleistocene.

The Zagros thrust zone is a narrow zone in which Paleozoic to Early Cenozoic rocks were thrust southwestward over the folded belt. Although there is evidence for some deformation as early as Infracambrian, the main period of deformation appears to have been Late Cretaceous to Plio-Pleistocene.

Both the Zagros fold belt and the Zagros thrust are interpreted to be part of the Arabian plate. The main Zagros thrust is interpreted to separate the Arabian plate to the southwest from the Iranian platform to the northeast. The Sanandaj-Sirjan ranges are thought to represent the southwest edge of the Iranian platform.

The Skylab 4 photographs of Iran that were studied were mostly of the Zagros fold belt. The compressional features and salt structures in this area are illustrated in figure 3-12.

The question of the amount of deformation internal to plates is also illustrated in the Skylab 4 photographs of the Caucasus Mountains. Photographs of this area (such as fig. 3-13) show a set of previously unrecognized north-northwestward-trending linears transverse to the range. The greater abundance and closer spacing of the linears at the bends in the Caucasus system and the almost right-angle relationship to the length of the range are similar to the transverse faults crossing the bend of a single fold but on a much larger scale. Such features were expected but had never been photographed or documented before. The snow and cloud cover in the photographs prohibits an interpretation of the regional significance of these features.

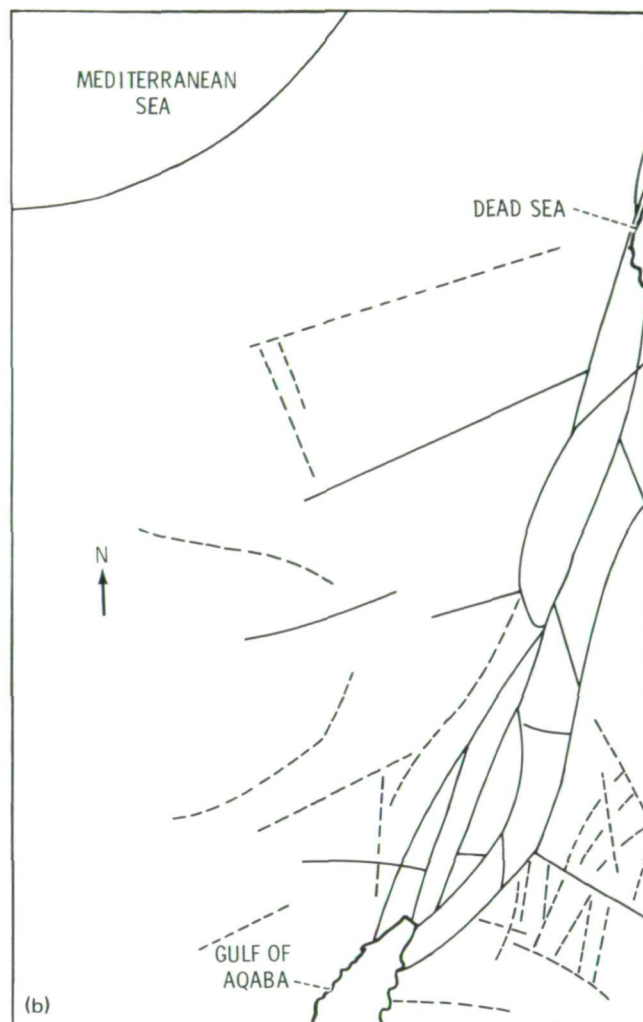


FIGURE 3-6.—The region between the Gulf of Aqaba and the Dead Sea. (a) Photograph (SL4-194-7259). (b) Sketch map. Solid lines are prominent linears, probably faults; dashed lines are other linears, possibly faults. See figure 3-7 for comparable features and scale. (Figure 3-6(a) was taken at an oblique angle; therefore, the scale is variable.)

The Skylab 4 photographs of the Near East and Middle East provide excellent examples of the types of deformation associated with extensional, transform, and compressional plate boundaries. The photographs also illustrate deformation internal to the plates. Thus, they can be used both for illustrative and teaching aids and as a basis for understanding relationships between deformed zones in the Earth's crust. More specifically, the style of deformation of each zone is distinct and

complex. In places, plate boundaries appear to overlap (African rift against the Red Sea trend in the Afar area), or some deformation may be distributed to the "rigid" plate in areas not considered in a strict sense to be a plate boundary (Dead Sea rift fault north of the Sea of Galilee). In addition, whereas lithospheric plates may be rigid with respect to the plate boundaries, deformation internal to the plate related to plate motion is not unexpected.

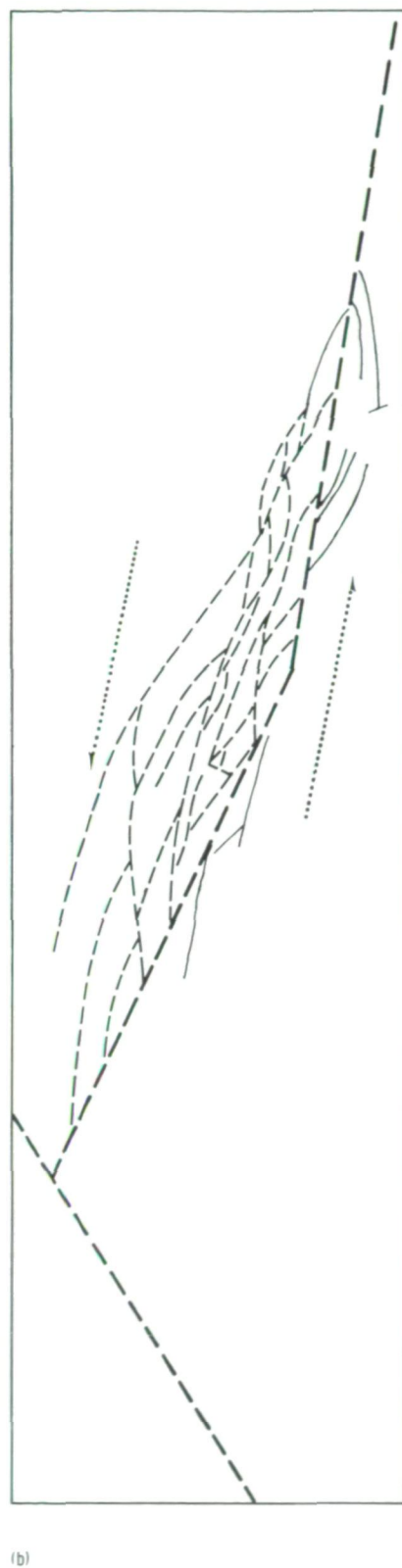
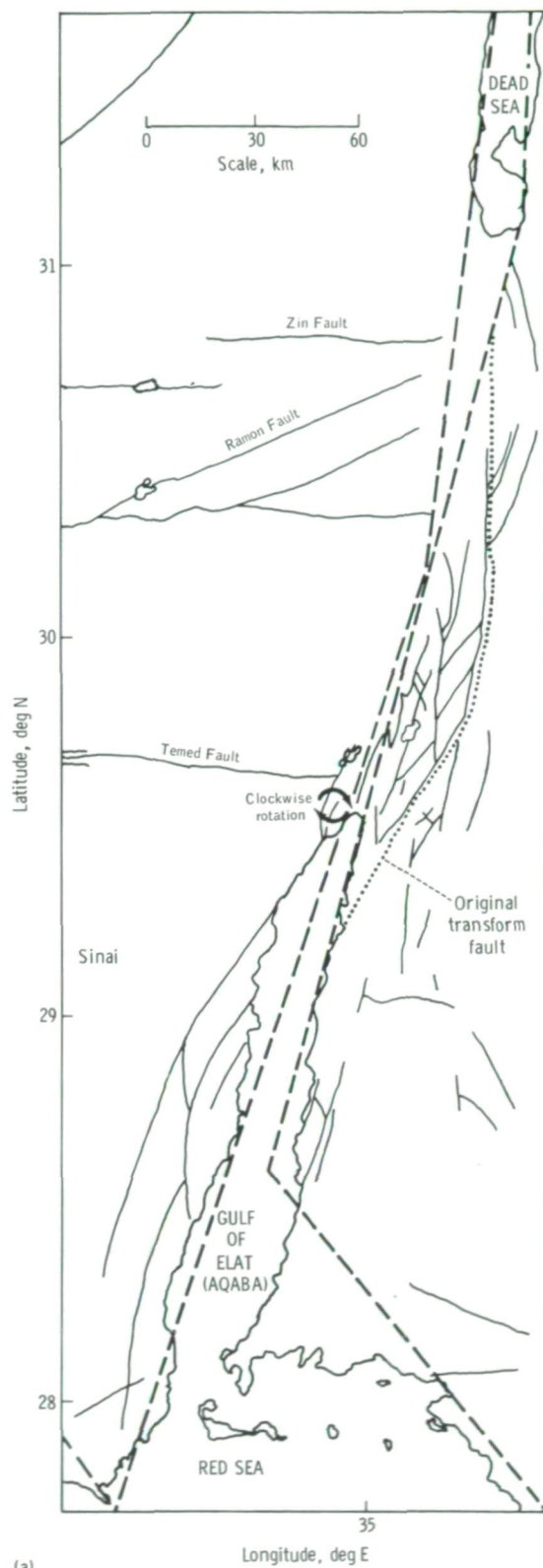
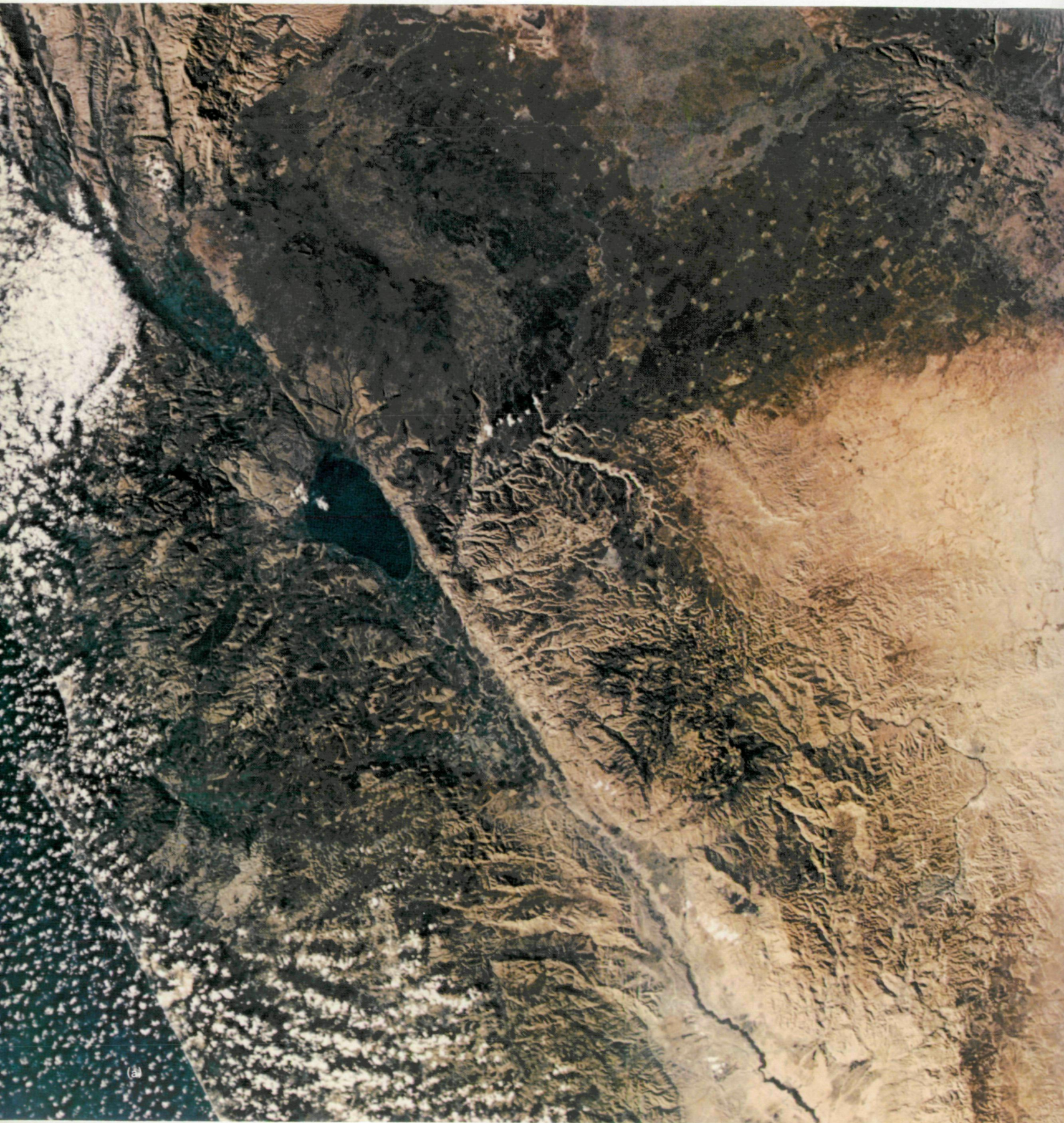


FIGURE 3-7.—Strike-slip faults associated with the southern part of the Dead Sea rift (from ref. 3-11). (a) Fault pattern as presently observed. (b) Restored pattern eliminating the strike-slip displacement.



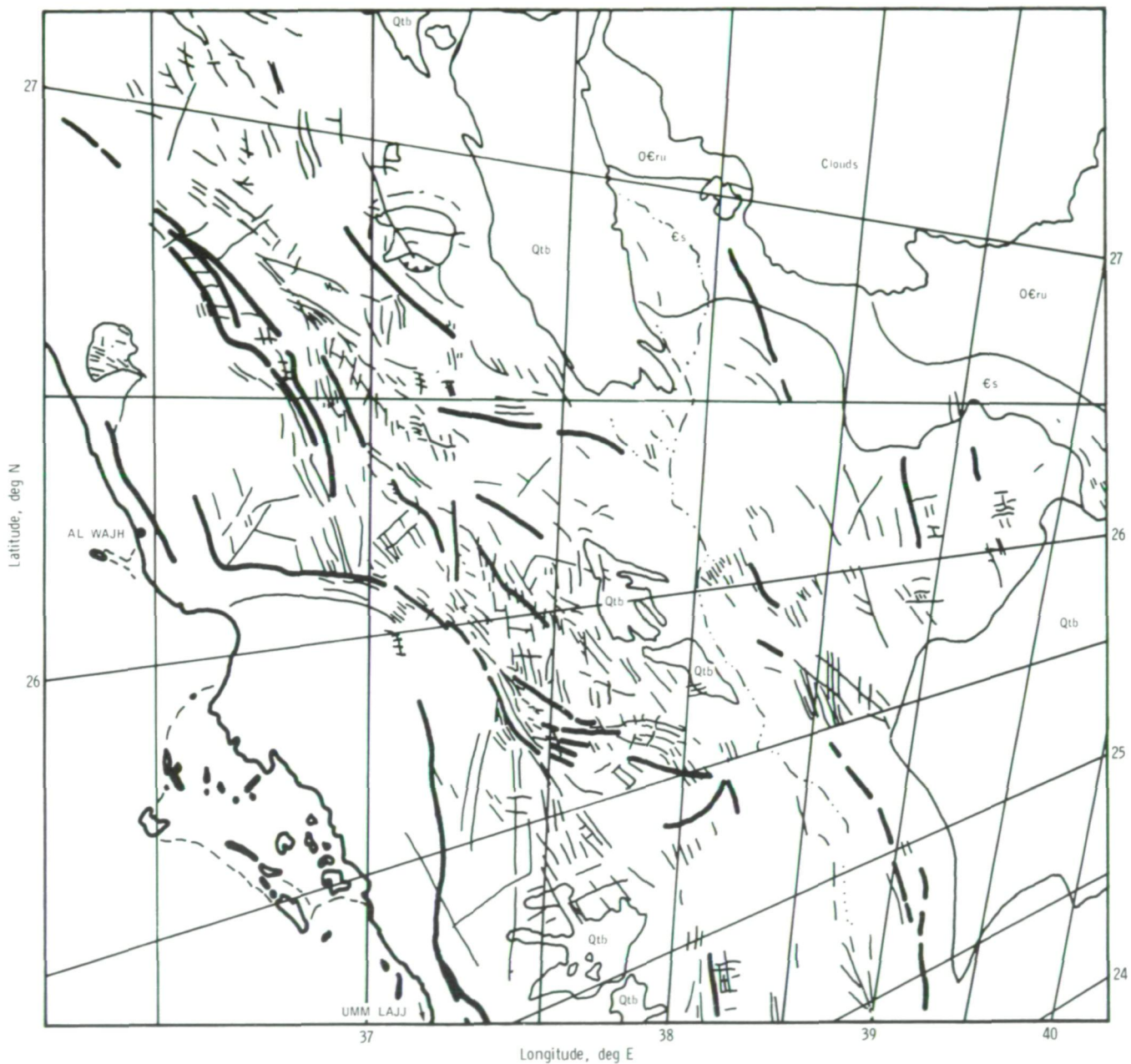
ORIGINAL PAGE IS
OF POOR QUALITY



FIGURE 3-8.—Sea of Galilee region. (a) Color frame taken with multispectral S190A camera system (SL3-46-209). (b) Sketch map showing photolinears. Solid lines are probable faults; dashed lines are possible faults; circles northeast of the Sea of Galilee are volcanoes along the Golan Heights.



(a)



(b)

Qtb Quaternary basalt and andesite
 OErU Cambro-Ordovician sandstone
 Es Cambrian sandstone

FIGURE 3-9.—Al Wajh region, Saudi Arabia. The Skylab 4 crewmen recognized this area as having anomalous trends compared with structures paralleling both sides of the Red Sea. (a) Photograph (SL4-138-3751). (b) Sketch map. Heavy lines are prominent photolinears (faults), and photolinears (faults?) are shown with light lines.

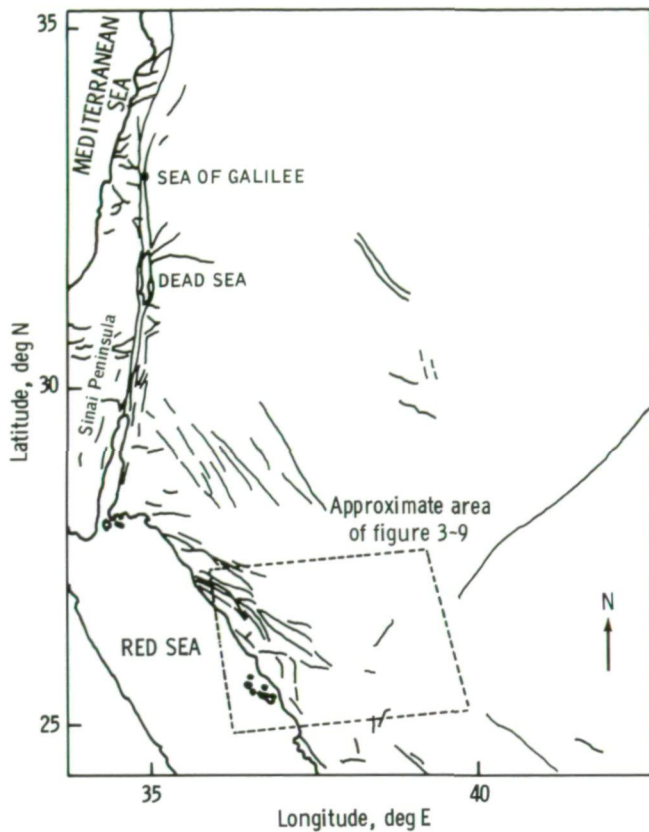


FIGURE 3-10.—Tectonic sketch map of part of Arabian Peninsula showing distribution of mapped faults (from ref. 3-16).

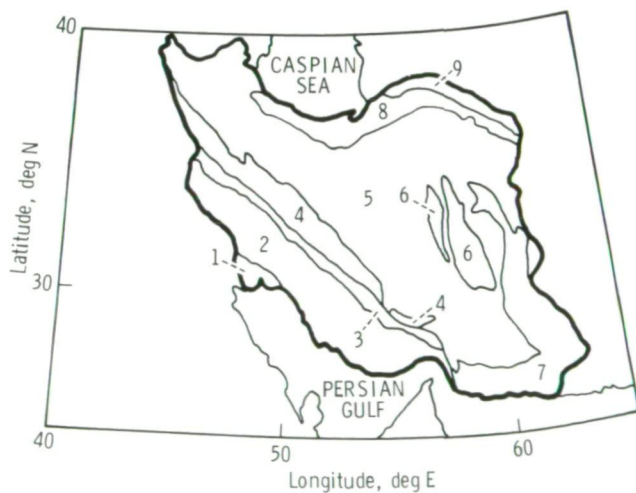


FIGURE 3-11.—Sketch map showing generalized tectonic provinces of Iran as follows: Arabian platform (1); Zagros fold belt (2); Zagros thrust belt (3); Sanandaj-Sirjan ranges (4); central Iran (5); Lut block (6); East Iran-Makrin Ranges (7); Elburz Mountains (8); Kopet-Dag Mountains (9) (modified from ref. 3-17).

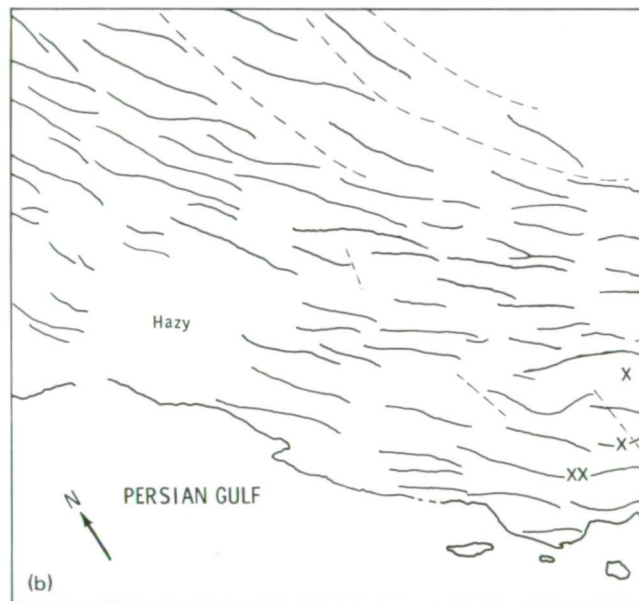


FIGURE 3-12.—Zagros Mountains fold belt, southwest Iran. (a) Photograph (SL4-141-4251). (b) Sketch map. Solid lines are fold axes; dashed lines are possible faults; and "X" indicates possible salt diapirs.

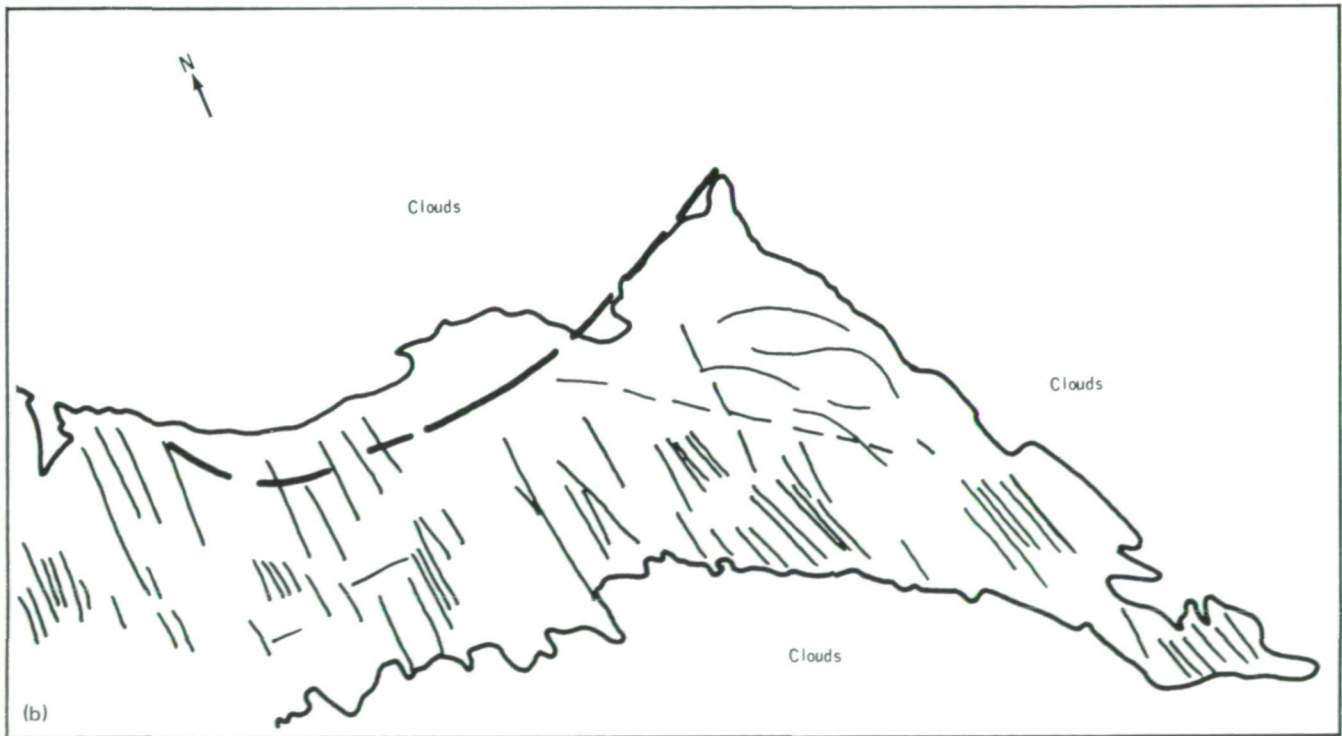
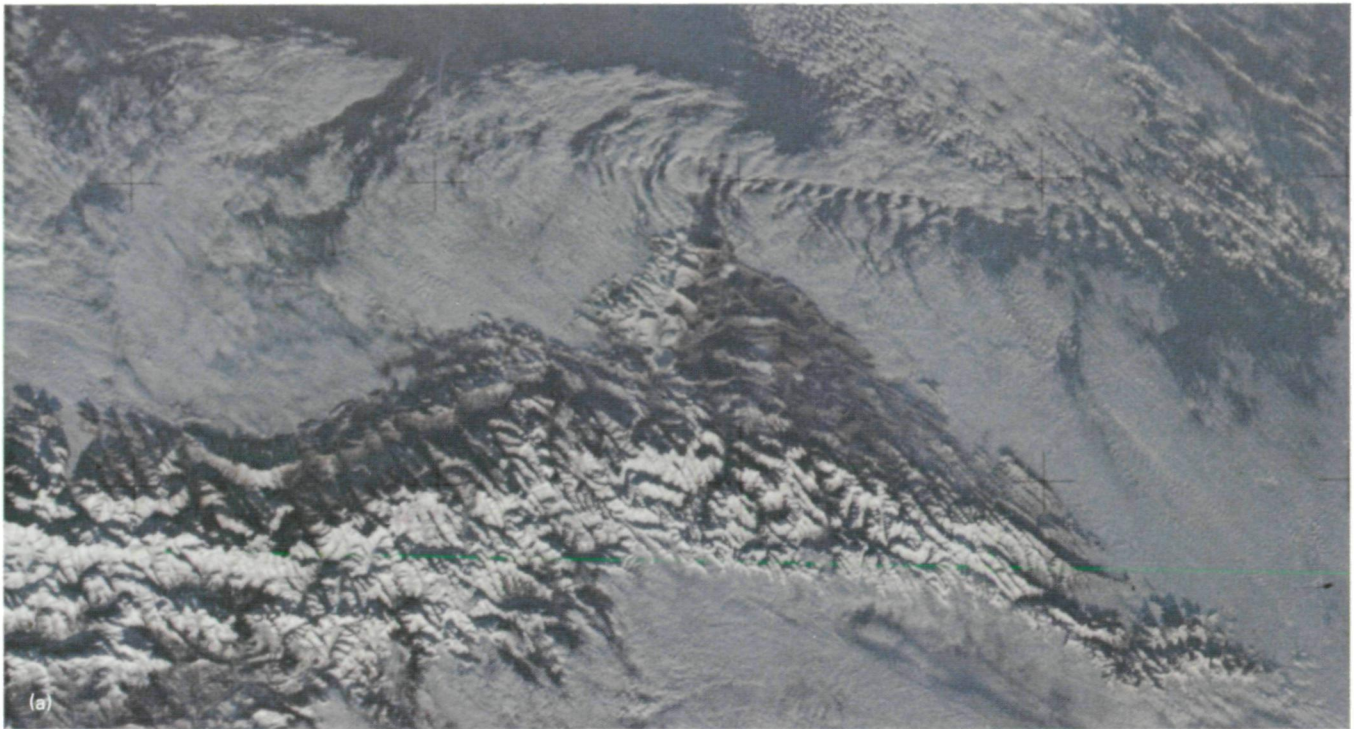


FIGURE 3-13.—A portion of the eastern Caucasus Mountains, U.S.S.R. (a) Oblique view (SI.4-138-3872). (b) Sketch map. Prominent linears are interpreted as cross faults; heavy dashed line is a linear that corresponds to a mapped fault shown on the "Geologic Map of the Russian Platform and Its Surrounding Areas," scale 1:1 500 000, Moscow, 1970.

ATACAMA FAULT, CHILE

The Atacama Fault is a poorly understood linear feature that parallels the coast of northern Chile for more than 1000 km (fig. 3-14). On the western margin of South America, the Pacific Ocean floor is being thrust under South America along the Peru-Chile trench. Before the beginning of underthrusting approximately 200 million years ago, the western coast of South America was the site of accumulation of sedimentary rocks. Subduction (underthrusting) began and folded the older rocks and produced magmas that formed a volcanic arc and associated batholiths. Later, a second volcanic arc began to form east of the first arc. Rising magma produced the volcanic and intrusive rocks that form the foundation of the western cordillera of the Andes. Approximately 15 million years ago, explosive volcanic activity began, followed closely by the eruption of andesitic lavas, which form the volcanoes (some still active) that dominate the Andes (refs. 3-20 and 3-21).

In southern Chile, the central valley is an actively subsiding graben that separates the low coastal ranges to the west from the high Andes to the east. In northern Chile, the tectonic setting west of the Andes is not as simple. A poorly defined topographic depression, the Pampa del Tamarugal, is oblique to the coast and reaches the Pacific Ocean at Arica. This depression may be a northern analog of the central valley to the south (ref. 3-22). The coastal ranges are separated to the west of this valley by the presently active Atacama Fault.

Historically, the Atacama Fault has been considered to be a right-lateral strike-slip fault, an analog to the well-known San Andreas Fault of California. Field evidence for the strike-slip nature of the Atacama Fault includes (1) the linearity of the fault for hundreds of kilometers, (2) rift topography with no consistent differential elevation across the fault, (3) dextral stream offsets near Salar Grande, and (4) widespread horizontal slickensides with rakes averaging 29° (ref. 3-23). However, the most recent activity along the Atacama Fault has been normal, as indicated by small fault scarps in recent alluvium. Conjugate northeast-trending left-lateral strike-slip faults break the Atacama Fault at several locations, most notably along the Camarones Fault and associated faults between Arica and Iquique. A left-lateral offset of the Atacama Fault also occurs along the northwest-trending Taltal Fault farther south (fig. 3-14). The largest demonstrable recent lateral offsets are on the northeast cross faults: 0.4 km of

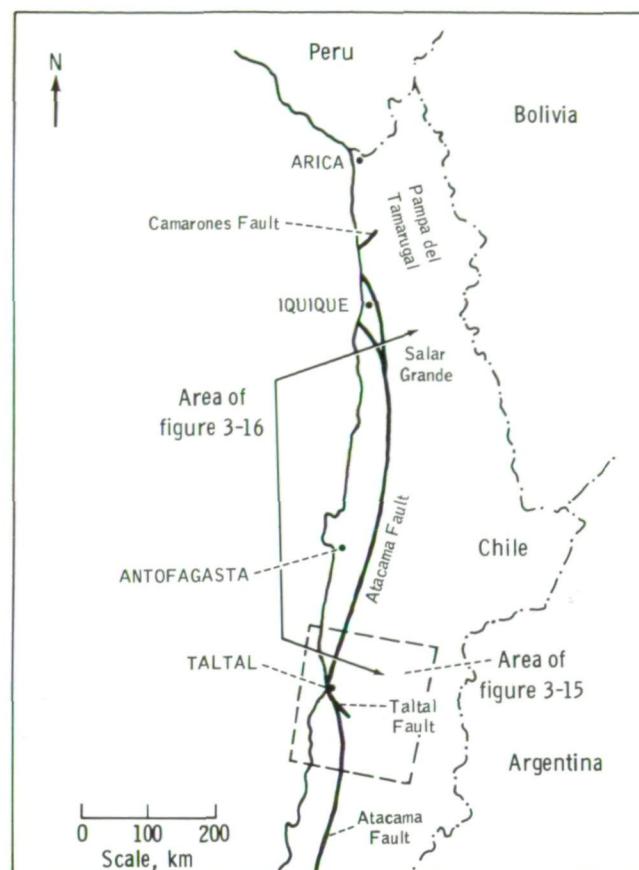


FIGURE 3-14.—Principal geographic features of northern Chile.

sinistral stream offset along the Camarones Fault and 1.5 km along a parallel fault 10 km to the east (ref. 3-23).

The Skylab 4 crewmen observed the Atacama Fault to determine the exact nature of the fault; that is, to map its position, direction and amount of movement, and interrelationships with other faults. Examination of the Skylab 4 photographs has revealed the following information concerning the Atacama Fault.

1. Possible Andean frontal faults (figs. 3-15 and 3-16), previously unknown in northern Chile, can be seen on the photographs and were very conspicuous to the crewmen. Such Andean frontal faults, possibly normal, may represent the eastern side of a central-valley-type graben in northern Chile similar to the Central Valley graben of central and southern Chile. The western side of the graben may be marked by either the Atacama Fault or by the northeast-trending photo-linears between the frontal faults and the Atacama Fault (fig. 3-16).

2. In the area immediately north of Antofagasta (fig. 3-16), the Atacama Fault appears to be discontinuous; that is, comprised of a series of en echelon segments. Such discontinuity makes large-scale recent lateral movement on the fault unlikely.

3. Photolinears where no linear features had previously been mapped can be seen crosscutting or trending such that the extensions would crosscut the Atacama Fault in the vicinity of Taltal. These photolinears may be additional cross faults displacing the Atacama trend. Analysis of the attitude of these features and their offsets should facilitate an analysis of the stress patterns of northern Chile.

4. Some of these observations independently confirm the results of extensive field work done by Arabasz (ref. 3-24). The interpretation of the Skylab 4 photographs agrees with the locations of many of the faults in the vicinity of Paposo (fig. 3-15), such as the Sierra el Jote Fault.

5. The crewmen were unable to identify the Taltal Fault, even though they specifically and repeatedly searched for it. However, the approximate location of this important cross fault can be inferred from figure 3-15 in which the Atacama Fault trace is bent to the northwest near the town of Taltal.

6. The crewmen had difficulty recognizing and photographing the Atacama Fault. However, considering their observations and recent knowledge concerning this fault zone (ref. 3-24), it can be said that this fault is not a simple, continuous strike-slip fault zone such as the San Andreas Fault of California. On the contrary, the Atacama Fault is today being fragmented by other faults of different trends and displacements.

ALPINE FAULT ZONE, NEW ZEALAND

One of the primary sites for geologic observations by the Skylab 4 crewmen was the Alpine Fault of New Zealand, regarded as one of the great strike-slip faults of the world (refs. 3-25 to 3-29). It was expected that a fault of this magnitude would be visible from orbit and that the Skylab 4 crewmen would be able to photograph and observe it. The crew described the fault and also obtained coverage of the entire area of North and South Islands with approximately 60 photographs with varying Sun angles, viewing angles, and cloud cover.

The locations of the vertical or near-vertical Skylab 4 photographs of New Zealand that are almost cloud free are shown in figure 3-17. A location map of vertical or

near-vertical photographs that are mostly clear but contain some cloud cover is given in figure 3-18. Many other photographs were taken of New Zealand on all the Skylab missions but most are too oblique or contain too much cloud cover to be of geologic value. However, some of these photographs are extremely useful for specific areas.

The Alpine Fault has a demonstrable 480-km right-lateral strike-slip displacement (ref. 3-26). With the development of plate-tectonics concepts, the Alpine Fault is now considered to be a portion of the Indian-Pacific Plate boundary. The fault is believed to be a transform fault between the westward-dipping Tonga subduction zone to the north and the eastward-dipping Macquarie subduction zone to the south (refs. 3-30 and 3-31). Recent field studies have not entirely supported such a simple explanation but reveal a more complicated picture of rapid vertical motion along the Alpine Fault where it bounds the Southern Alps and counterclockwise rotation of fault blocks in northern South Island (refs. 3-11, 3-32, and 3-33). The latest interpretation (ref. 3-33) describes tectonic patterns in South Island as evolving in response to a rotation of the Indian-Pacific slip vector from parallel to the Alpine Fault to the present position approximately parallel to the Hope Fault (fig. 3-19). This rotation produced a series of faults splaying from the Alpine Fault to the northeast. Initial movement along the northeast-trending faults was strike-slip, but an increasing component of dip-slip motion occurred as the slip vector changed. The change to dip-slip motion is evident in the recent rapid uplift of the Southern Alps.

Skylab photographs generally support the interpretation of Scholz et al. (ref. 3-33). A photograph of the central portion of South Island is shown in figure 3-19. The scene was described by the Skylab 4 commander from orbit as follows.

The Sun angle was quite low; it was shortly after sunrise. I would estimate the Sun angle to be maybe 20°. The Alpine Fault down New Zealand was very, very easy to see — quite clear We were crossing the northern end of South Island looking to the south, and you could see a fault line all the way from the very northern end of South Island until it disappeared under the clouds. The weather is just perfect, and the Sun angle is perfect.

This remarkable photograph shows many significant features which indicate that motion along the Alpine



(a)

ORIGINAL PAGE IS
OF POOR QUALITY



(b)

Approximate scale, km

FIGURE 3-15.—Taltal region, Chile. (a) Photograph (SI4-138-3794). (b) Sketch map of photolinears and correlation with faults in the Taltal region showing the complex nature of the Atacama Fault Zone.



(a)

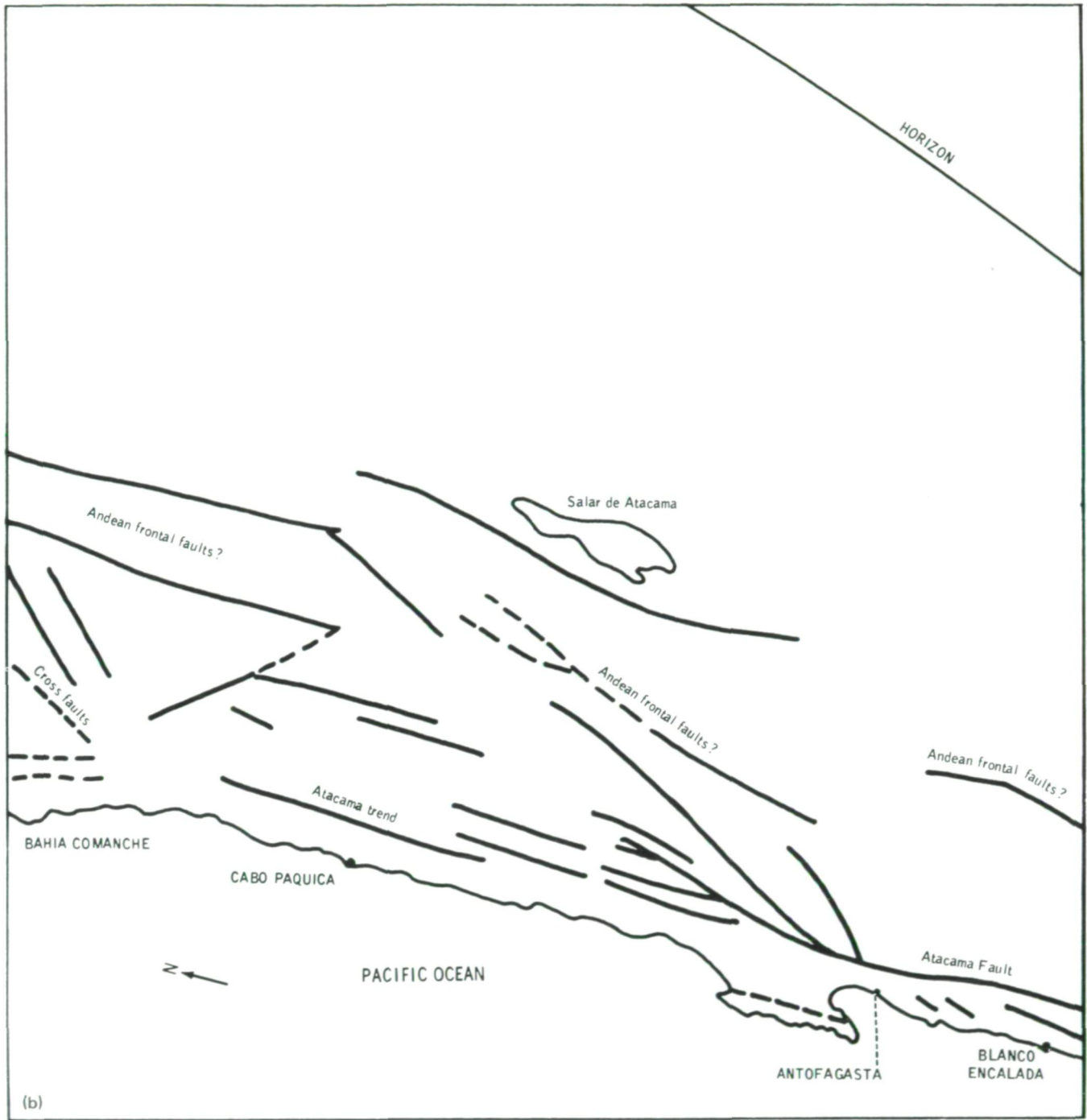


FIGURE 3-16.—Antofagasta region, Chile. (a) Photograph (SL4-137-3711). (b) Sketch map of photolinears and correlation with faults in the region, showing the Atacama and related faults. Dashed lines are poorly defined photolinears.

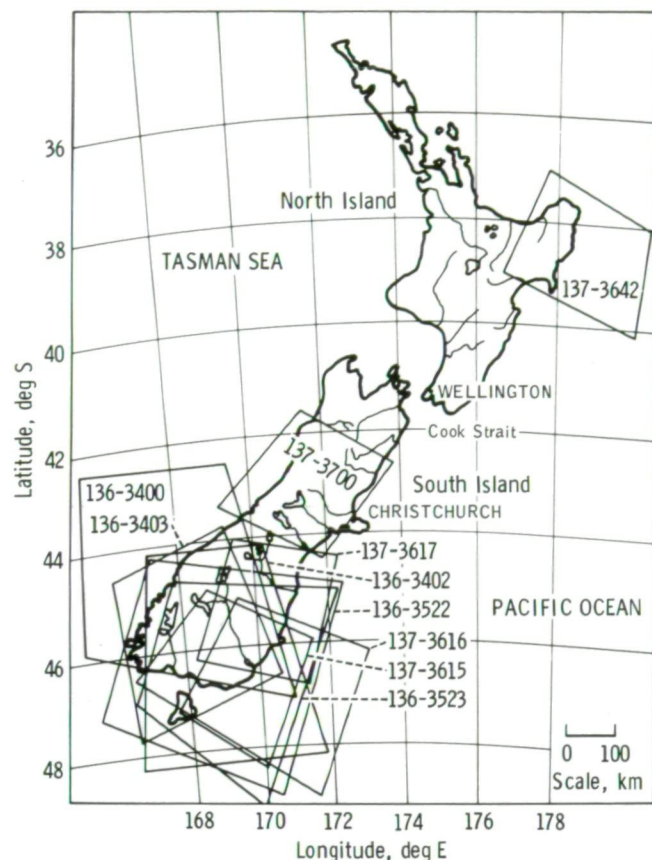


FIGURE 3-17.—Location map of vertical or near-vertical (almost cloud-free) Skylab 4 photograms of New Zealand.

Fault has not been entirely strike-slip movement. Traced northward, the Alpine Fault can be seen to be offset or bent to the right in several localities. Some of these offsets coincide with the termination of the northeast-trending fault valleys that are presently the prominent strike-slip faults of South Island. At the top of the photograph, the Alpine Fault appears to terminate; the fault actually bends sharply northwest before it continues its northeasterly trend to the north end of the island. This sharp bend shows that strike-slip motion along the Alpine Fault is sharply inhibited and that dip-slip motions are now dominant. The uplift of the east side results in the spectacular Southern Alps.

The fault splays extending northeastward are the principal linear trend in north-central South Island. These faults are well displayed in other oblique views. However, north-trending cross faults subdivide the region into a mosaic of large rhombs and parallelograms

the angles of which are the common 60° to 120° conjugate fault set of structural analysis. The northeast-trending faults have demonstrable right-lateral slip (refs. 3-34 to 3-36), a slip sense consistent with counterclockwise rotation of the whole region; the twisting is shown by the sharp left bend of the Alpine Fault near the top of figure 3-19. (For a smaller scale version of the same type structure, see figure 3-8, immediately north of the Sea of Galilee where the prominent strike-slip faults are bent.) The coincidence of known faults with the photolines suggests that many of these linears are indeed faults. The abundance of linears seen from Skylab indicates that many more faults exist in this part of New Zealand than have been mapped. Photointerpretive studies combined with field work should produce rapid advances in the knowledge of the structure of New Zealand.

The Skylab 4 crewmen also commented on linear features diverging at a low angle from the southern end of the Alpine Fault (fig. 3-20). The scientist pilot described the southern portion of the fault as follows.

The rivers and water-erosion areas are very discernible on the west side and on the east, and there does appear to be a preferred orientation of these relative to the fault line However, as far as identifying these as other faults, that's hard to say You can identify these features—they're linear—but to call them a fault is—I find from observations from here—very difficult.

The scientist pilot also was able to contrast the broad coastal valleys from those east of the Alpine Fault where valleys are deeply incised into the Southern Alps (fig. 3-19).

I counted rather quickly up to around 50 [that] I'd call fairly major ravines or river channels leading out to the ocean, running from the fault zone itself, and their orientation could be very clearly delineated. I could not see where these picked up on the other side of the fault zone at all.

Although part of the main Alpine Fault zone was partly covered by clouds, figure 3-21 shows the magnitude of strike-slip displacement as shown by the ultramafic belts, one of several offset units used to demonstrate the 480 km of right slip along the fault zone. Kingma in a well-illustrated book shows (ref. 3-37, fig. 12) all Lower Permian igneous rocks of South Island in their present geographic distribution. The Red Hills, a large mass of ultramafic rocks, are prominent in the left

foreground because of the reddish color and lack of vegetation in a heavily vegetated area. The ultramafic rocks extend in discontinuous masses (including Dun Mountain, under clouds, the type locality of dunite) onto the island at the clouds near the lower left of the photograph. The Wairau River marks the northern continuation of the Alpine Fault (Wairau Fault). The right-slip offset is shown by the ultramafic mass comprising Red Mountain at the upper right. The Red Mountain region is shown from a better vantage point in figure 3-20.

The Skylab 4 crew observations and photographs of the Alpine Fault zone demonstrate that the ability to recognize both probable extensions of faults and relationships between major crustal blocks in an already extensively studied area can be significantly improved. This technique should be of even more value in remote, unfamiliar regions.

SIERRA MADRE OCCIDENTAL, MEXICO

The Sierra Madre Occidental is an elevated plateau of Tertiary volcanic rock that forms the western portion of the central upland of Mexico. This province contains one of the most extensive volcanic fields of the Earth and has been an important source of precious and base metals for hundreds of years. Despite the economic importance of the area, the vastness and inaccessibility of the area have impeded detailed mapping. Skylab photographs are valuable for reconnaissance mapping and for deriving regional interpretations from small areas mapped in detail. Two areas covering approximately 50 000 km² of the Sierra Madre Occidental (fig. 3-22) will be discussed in this section. The Durango area (fig. 3-23) is crossed by Federal Highway 40, along which students at the University of Texas at Austin have mapped. The general geology of the Durango area is known from these studies. The Chihuahua area (fig. 3-24) was mapped by photointerpretation followed by field checking in June 1974 by Swanson (ref. 3-38).

Basement rock in the Durango area is largely composed of andesite of Late Cretaceous to Early Tertiary age, which has been introduced by a batholithic complex with major pulses at 90, 70, and 50 million years ago. The andesite is unconformably overlain by as much as 1 km of ash-flow tuff of Late Oligocene to Early Miocene age (refs. 3-38 to 3-40). In places, alkali basalt of Late Miocene age unconformably overlies the ash-flow tuff (refs. 3-38 and 3-39).

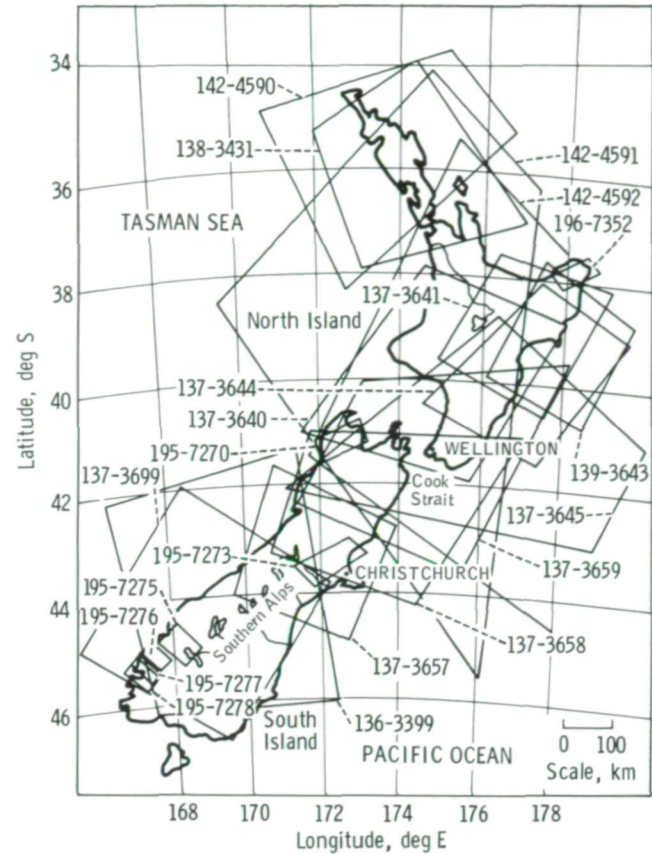


FIGURE 3-18.—Location map of vertical or near-vertical Skylab 4 photographs of New Zealand that contain a small amount of cloud cover.

Calderas related to ash-flow volcanism are undoubtedly numerous, but only one such caldera has been recognized by field geologic studies (refs. 3-38 and 3-39). This caldera, which contains the city of Durango, is associated with economically important iron and tin mineralization and is the source of several major ash-flow units. The curved lineaments west of Durango (fig. 3-23) are faults related to the collapse of the caldera. West of the city of Mezquital, tributaries of the Rio San Pedro have eroded headward forming a moat around a large domal structure. The dome, approximately 35 km in diameter, may be a resurgent caldera. Two smaller, less dissected topographic domes that also may be resurgent calderas can be seen in the northern part of the photograph. Volcanic rock units in the vicinity of El Salto are extremely thick and contain abundant epiclastic rock suggesting infilling of a topographic low.



(a)

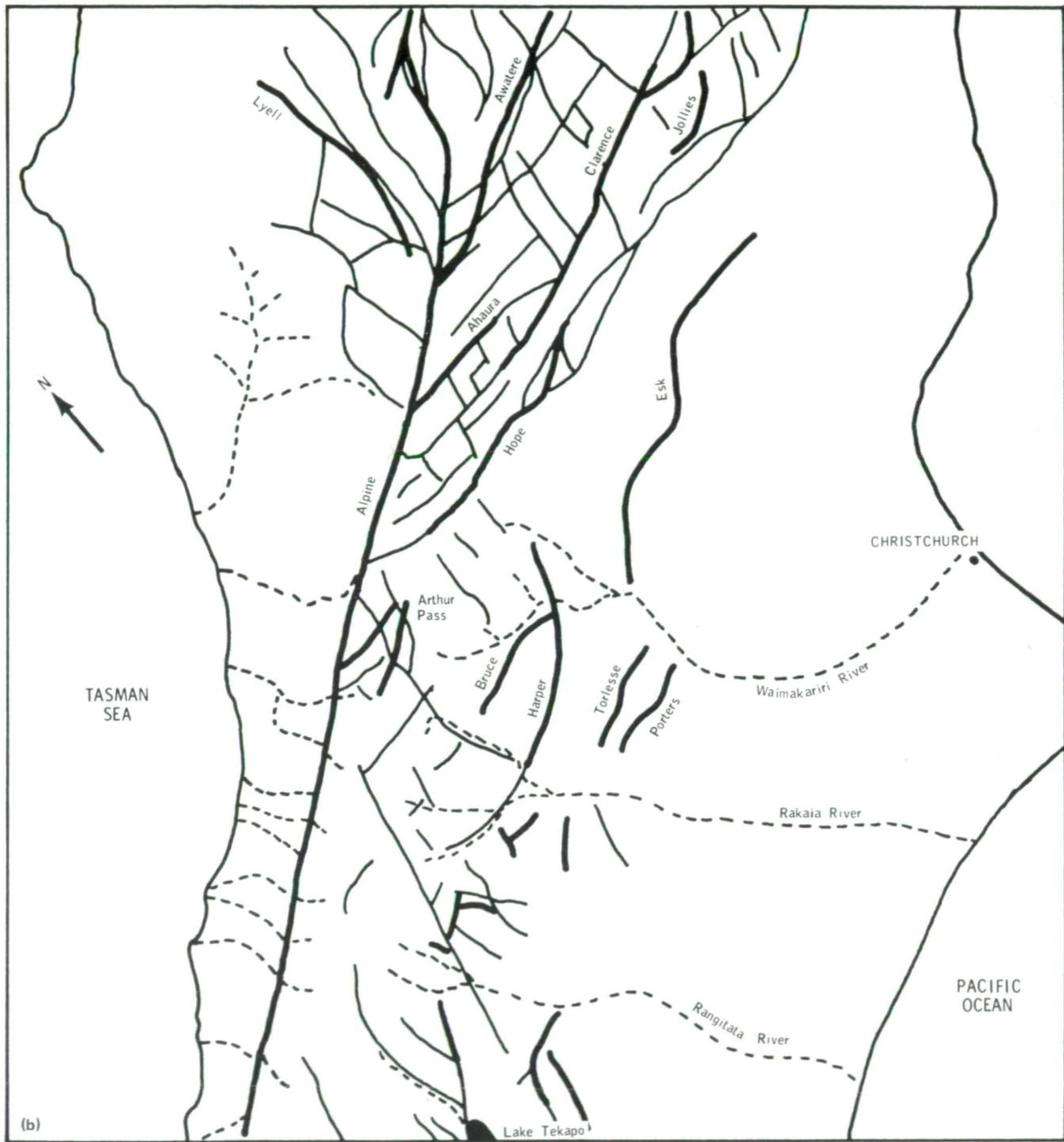
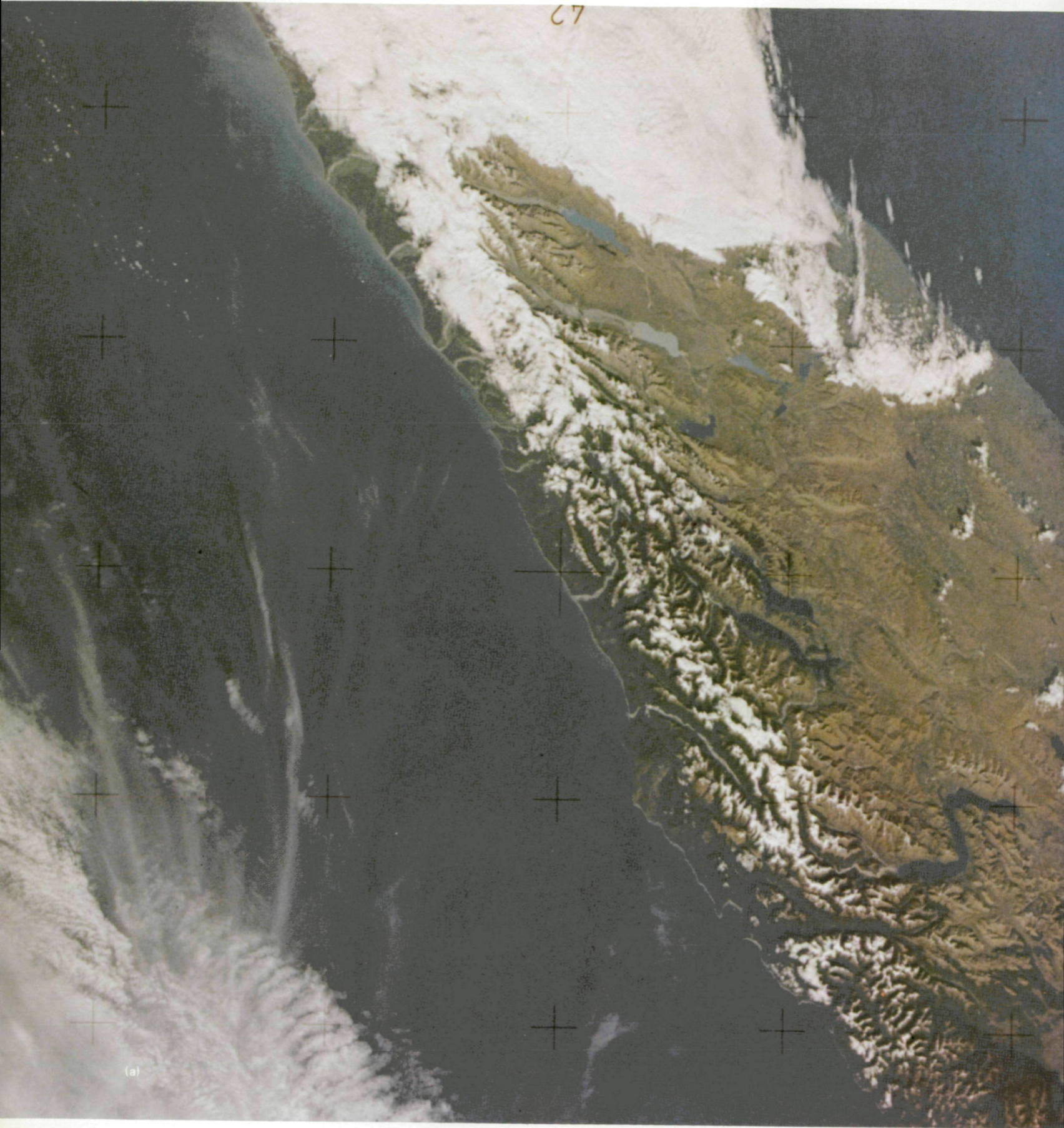


FIGURE 3-19.—Near-vertical view of central South Island, New Zealand. (a) Photograph (SL4-137-3700). (b) Sketch map of linear features. Heavy solid lines are mapped faults; light solid lines are photolinears (probable faults); and short dashed lines show drainage patterns.

27



(a)

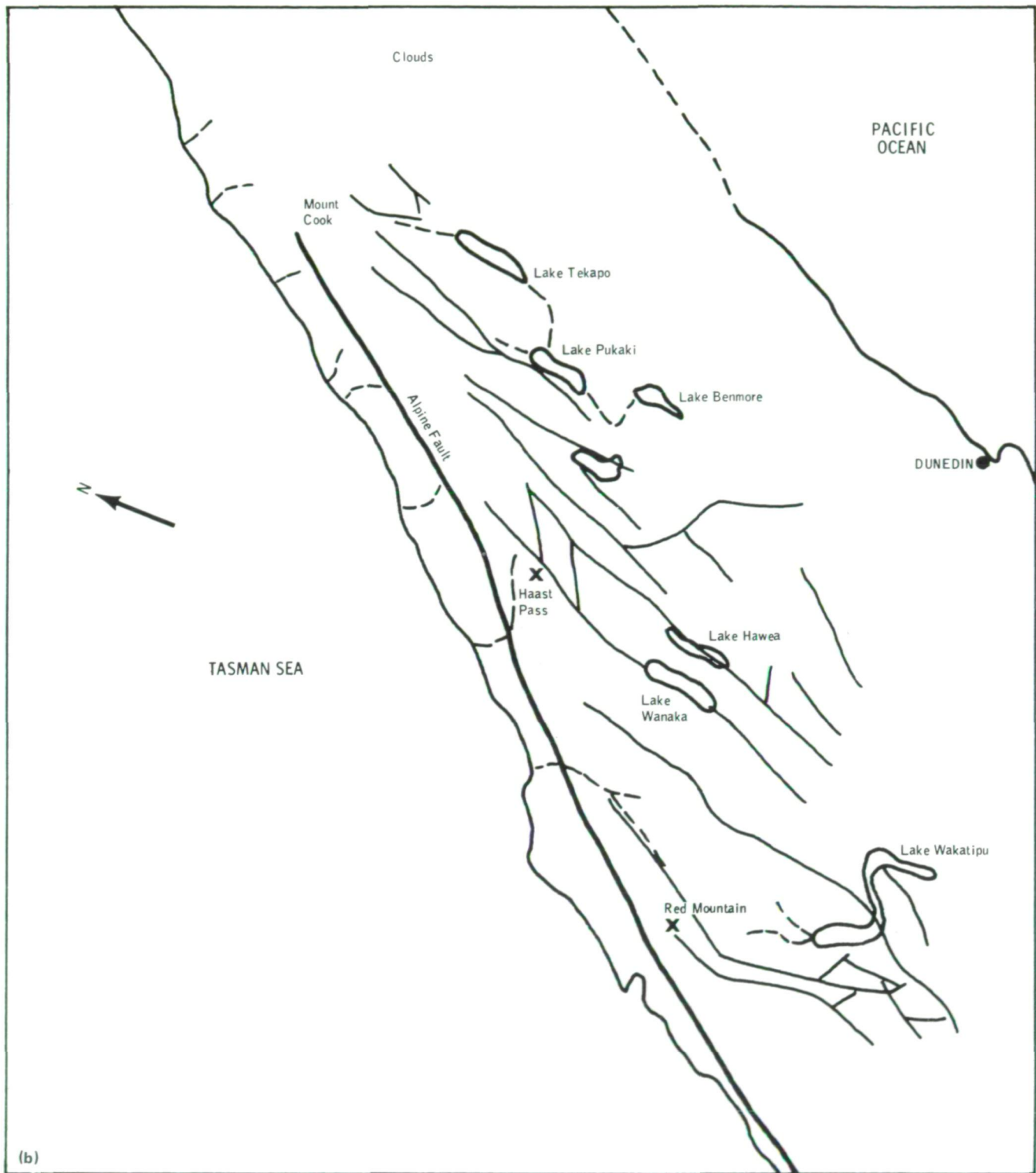


FIGURE 3-20.—South-central South Island, New Zealand. (a) Photograph (SI4-136-3399). (b) Sketch map. Solid lines are interpreted as faults; short dashes are drainage.



(a)



FIGURE 3-21.—View south across South Island, New Zealand. (a) Photograph (SI4-136-3531). (b) Sketch map. Red Hills and Red Mountain are ultramafic masses on opposite sides of the Alpine Fault. These features are two of several units correlated across the fault that indicate a right slip of 480 km.

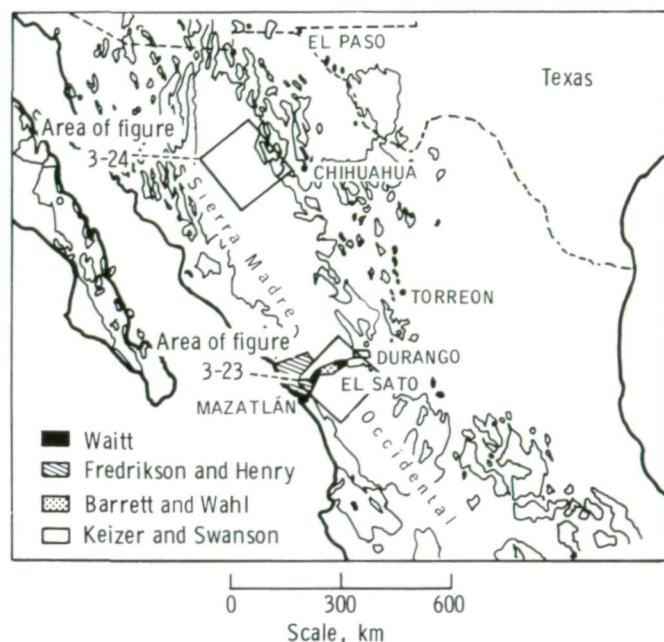


FIGURE 3-22.—Distribution of Tertiary volcanic rocks (outlined areas) in the Sierra Madre Occidental and adjacent regions of Mexico. Patterns indicate areas mapped by University of Texas graduate students. Large squares are areas of Mexico photographed from Skylab and interpreted for this report. (Modified from refs. 3-38 and 3-39.)

Arcuate lineaments suggest that this low may be a large caldera or caldera complex that became a trap for eolian and fluvial sediments. The circular features seen in the Skylab photographs are prime areas for further study.

In the western part of the photograph (fig. 3-23(a)) (under clouds), normal faults trending generally northward cut the deep canyon country. Displacement on many of these faults is at least 1 km. Geologic mapping along Highway 40 and on this Skylab photograph reveals that faulting in the high plateau near Durango is relatively minor. The photograph shows, however, that faulting along the western margin of the plateau has been more extreme. Faults over the entire region trend generally northward except where affected by local structures.

Alkali basalt, capping the ash-flow tuff, crops out in several places along Highway 40 between Durango and El Salto. The alkali basalt, which appears reddish brown in the photographs (figs. 3-23(a) and 3-24(a)), was erupted approximately 12 million years ago contemporaneously with faulting of the area (refs. 3-38 and 3-39). Similar-appearing areas form the caps of much of

the Sierra Madre Occidental northwest of Durango and beyond the areas studied in the field. The Skylab photographs provide the first indication that alkali-basaltic volcanism may have been an event of regional significance late in the volcanic history of the Sierra Madre Occidental.

A handheld-camera photograph of part of western Chihuahua (fig. 3-24; see fig. 3-22 for location) shows the extent to which Skylab photographs can aid the researcher interested in a remote area. Figure 3-24 is a photograph of a transitional area between the high plateau area to the south and the basin and range region that extends northward into the western United States. The large basins generally conform with normal faults that trend northwestward, the dominant structural direction in the area. Of particular interest is a group of remarkably straight valleys northwest of La Junta. These lineaments, interpreted as fault valleys, conform with the regional fault pattern but curve anomalously eastward west of La Junta. South of this faulted area is a dark topographic dome with a surrounding moat. The dark area is a latite porphyry intrusive body. Streams have eroded along the contact between the porphyry and surrounding ash flow and epiclastic rock, producing a topographic dome. A similar porphyry crops out in many other places, which suggests that this intrusive body underlies a large region. Fault trends in the vicinity may have been influenced by this large intrusive mass. The abundance of intrusive rock, the irregular volcanic stratigraphy, and the abundance of large granitic and andesitic lithic fragments in the tuff suggest that this area was a major eruptive center (possibly a caldera). This photograph (fig. 3-24) and subsequent field reconnaissance permitted rapid delineation of the major geologic problems and problem areas not possible with conventional techniques because of the extreme relief, limited access, and extensive forest cover.

In addition to these local structural and stratigraphic problems, Skylab photographs have made it possible to pinpoint areas of regional stratigraphic importance. Existing geologic maps of western Chihuahua show the area (fig. 3-24) to be covered by Tertiary volcanic rock. Although Tertiary igneous rock does appear to cover the entire area, the outcrop can be divided into two major sequences. Several relatively undissected dark areas are in contrast to their surroundings. Field investigation of two of the largest areas has confirmed that they are recent fields. Similar basalts were noted by Weed (ref. 3-41) capping rhyolite in southern Chihuahua. These

basalts lack any fresh volcanic landforms but unconformably overlie the ash-flow tuff. The petrographic similarity of these basalts to basalt in West Texas (ref. 3-42) and to the basalts in the Sierra Madre Occidental near Durango suggests that they are part of a major basin-range basaltic event.

In summary, study of figures 3-23 and 3-24 together with reconnaissance field checking has greatly facilitated the initiation of detailed ground study in the Sierra Madre Occidental area. A possible eruptive center and a structural anomaly have been pinpointed west of La Junta, and large areas of basaltic volcanic rock have been delineated for the first time. These important areas, which may have remained unnoticed for many years, are now being studied in detail.

CARIBBEAN/AMERICAS PLATE BOUNDARY, GUATEMALA AND SOUTHERN MEXICO

A major fault zone the name of which changes from west to east, the Cuilco-Chixoy-Polochic Fault, crosses Guatemala and extends into southern Mexico (fig. 3-25). The parallel Motagua Fault immediately to the south is easily identifiable in central and eastern Guatemala. Both these faults have been projected into the Caribbean to become faults of the Bartlett or Cayman Trough (ref. 3-43).

The currently accepted interpretation of plate boundaries and motions as presented by Molnar and Sykes (ref. 3-44) is given in figure 3-25. This interpretation indicates that the Cocos plate is moving northeastward from the spreading center of the eastern Pacific rise and is being subducted under the Americas and Caribbean plates along the Middle America Trench. The Caribbean plate is moving eastward, sliding past the Americas plate on the north along the left-lateral Bartlett Trough and the Motagua/Polochic Fault system and on the south along a series of right-lateral faults in northern Venezuela and Colombia. On the eastern margin, the Caribbean plate is overriding the Americas plate.

Kesler (ref. 3-45) proposed that the Cuilco-Chixoy-Polochic Fault is the Cenozoic plate boundary and that the left-lateral offset along this zone is less than 150 km. If this hypothesis is correct, this offset severely limits proposed plate motions (e.g., ref. 3-46) and makes understanding the complex wedge-shaped region of the Caribbean plate between the Americas and Cocos plates

(southern Guatemala, western Honduras, and El Salvador) even more important.

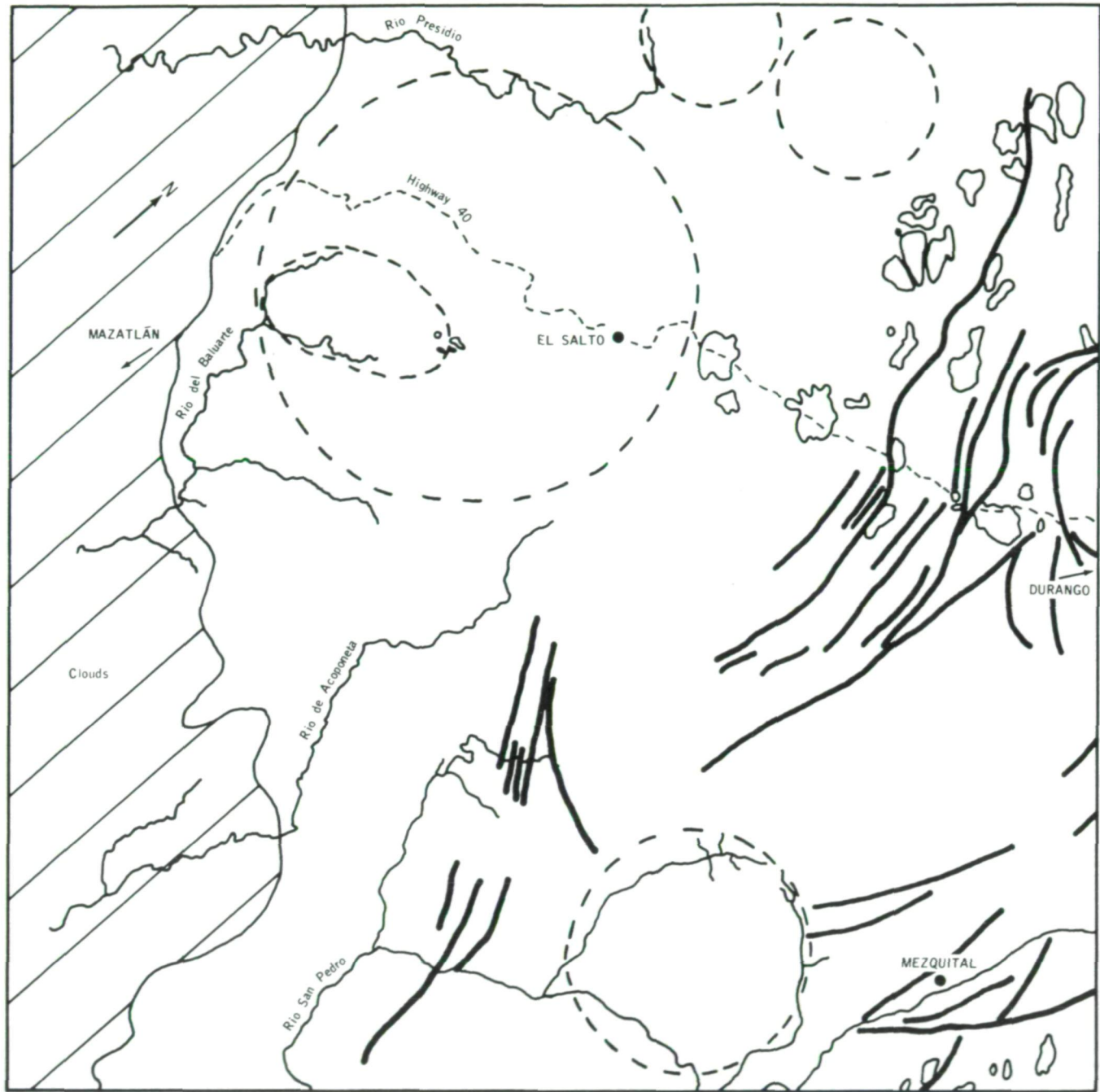
Donnelly (ref. 3-47) and his coworkers find little evidence for strike-slip displacement along the Motagua Fault but, instead, find much evidence for north-south compression that has generated a number of imbricate thrust sheets rooted in the Motagua Fault zone. A Skylab 4 photomosaic (fig. 3-26) shows prominent linears crossing Guatemala; the most prominent of these is the Cuilco-Chixoy-Polochic Fault, which extends nearly due east from southernmost Mexico across Guatemala to the southwestern corner of Lago de Izabal (Lake Izabal). This lake is bounded by a pair of N 60° E striking faults that abut the eastern end of the Polochic Fault (fig. 3-27). The angular intersection seen on the photographs is in contrast to earlier reconnaissance studies (refs. 3-48 to 3-50), which show one fault curving into the trend of the other. The northeast-trending valley (Izabal graben; see ref. 3-48) containing Lake Izabal might be a zone of extension similar to that proposed by Dillon and Vedder (ref. 3-51) for the deep troughs offshore from Belize (formerly British Honduras). In this scheme, the Polochic is still assumed to be left-lateral, and the northeast-trending faults bounding Lake Izabal are assumed to have oblique offsets with the valley being a downdropped block. Similar parallelogram-shaped depressions can be interpreted for the Motagua Valley south and east of Lake Izabal.

The Cuilco Fault forks at its western end in Mexico, and a prominent branch, possibly a transform fault, extends southwestward to the coastal plain. The existence of a faint set of linears in the coastal plain suggests that the fault might extend southwestward to the coastline; if so, the fault could then be projected toward a prominent submarine canyon on the inner wall of the Middle America Trench (ref. 3-52). The other branch of the Cuilco Fault extends westward as a series of en echelon left segments that are also traceable to the inner margin of the coastal plain. North of this area to the Gulf of Tehuantepec, the inner edge of the coastal plain is bordered by escarpments that appear to be the result of down-to-the-west fault movement. The landward margin of the coastal plain is a remarkably straight line on these photographs. Farther inland, the lower mountains appear to be separated from the high plateau in long, angular segments, which suggests that the boundary is fault controlled.

The Motagua Fault is prominent from the Caribbean coast westward to northeast of Lake Atitlán (approximately 91°00' W). West of this point, faint linears in



(a)



(b)

0 10 20 30
Scale, km

FIGURE 3-23.—Region west of Durango, Mexico. (a) Photograph (SI2-04-155). (b) Sketch map showing interpretation of Durango region. Heavy dashed lines indicate the location of circular structures, possibly calderas; heavy solid lines are photolinears interpreted as faults; light solid lines are interpreted as outcrops of alkali basalt.





FIGURE 3-24.—Region west of Chihuahua, Mexico. (a) Photograph (SL3-40-163). (b) Sketch map showing principal towns, roads, geographic features, faults, and areas of basalt and latite porphyry.

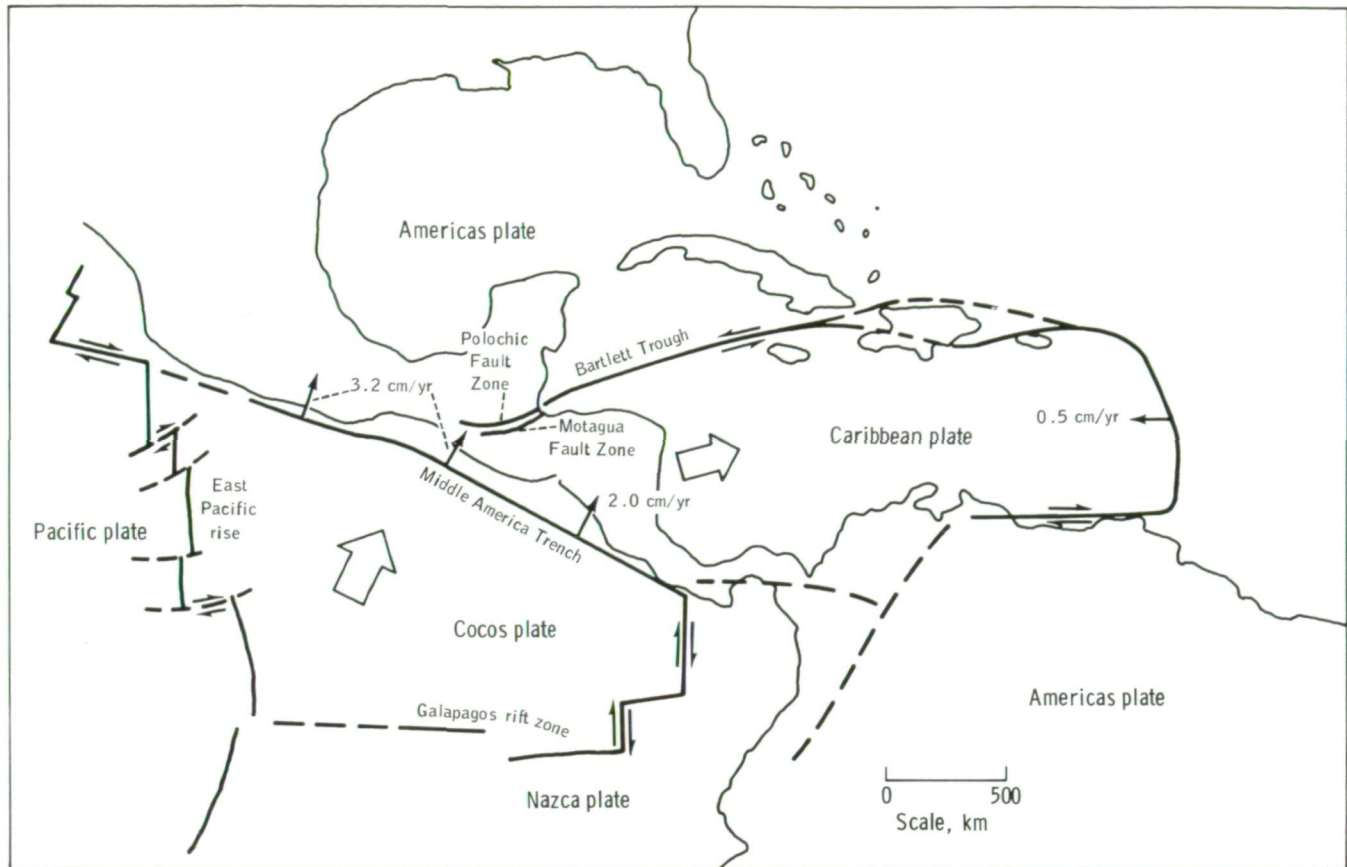


FIGURE 3-25.—Generalized current plate tectonics of the middle America and Caribbean regions, showing rates and directions of motion relative to a fixed Americas plate (adapted from ref. 3-44).

the Cenozoic volcanic cover suggest that the fault continues westward to the inner margin of the coastal plain. A northwest-trending linear extends from this latitude to the Cuilco Fault.

These data together with published geologic maps suggest a succession of plate boundary faults from south to north. The sequence is (1) the Jocotán-Chamelecón-La Ceiba Fault (not visible on these photographs), which is parallel to and south of the Motagua Fault and extends from Guatemala City across northwestern Honduras and which is now offset by north-trending faults (i.e., the Guatemala City graben and the Ulua graben of Honduras); (2) the Motagua Fault, which may now be inactive in its western portion; and (3) the Cuilco-Chixoy-Polochic Fault, the presently active plate boundary. The western end of the Cuilco-Chixoy-Polochic Fault apparently forks into a southwest-trending fault and a northwest-trending fault to separate the coastal plain from the mountains of

southern Mexico; the eastern end of the fault terminates against a N 60° E zone of extension.

The Jalpatagua Fault (a prominent linear on the Skylab 4 photographs) extends from south of Guatemala City to northwest El Salvador. No active volcanoes are present along the Jalpatagua Fault trace, but, at the northern termination, Volcan Fuego is presently active. Volcan Fuego is at the junction of three geologic features: the southern end of the Guatemala City graben, the northwestern end of the Jalpatagua Fault, and the southeastern end of the line of volcanoes that extends northwest to the Mexican border. On the ground, the Jalpatagua Fault appears to be a high-angle,

FIGURE 3-26.—Major fault zones (valleys) that cross Guatemala are centered in this photographic mosaic. Figure 3-27 shows the major features of these photographs on an orthogonal geographic base. (Mosaic of (left to right) SL4-201-7666, SL4-201-7667, and SL4-201-7668.)

ORIGINAL PAGE IS
OF POOR QUALITY



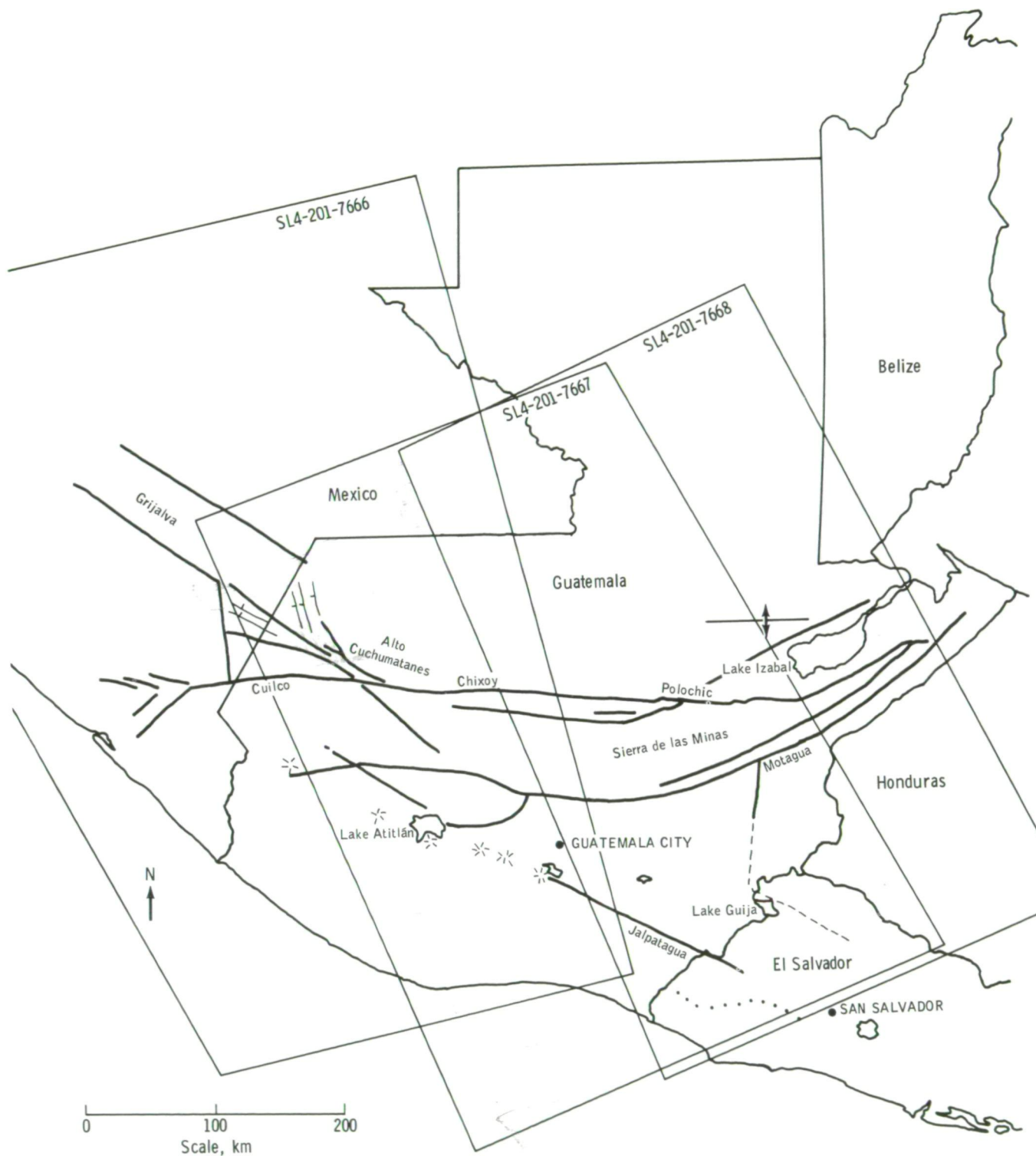


FIGURE 3-27.—Principal structural features of Guatemala and adjacent countries identifiable on the mosaic in figure 3-26. (El Salvador and western Honduras are also covered in photographs SL4-201-7669 and SL4-201-7670.) Solid lines are photolines, mostly known faults; stars are prominent volcanoes; dotted line in northwestern El Salvador is summit of volcanic range; dashed line marks eastern edge of lowlands; anticline symbol shows trend of folded mountains north of Lake Izabal.

C-2

strike-slip fault because of the linearity, freshness, and rift topography. The valleys and lines of volcanoes in El Salvador trend more westerly and are not straight lines (fig. 3-27) as the corresponding features in both Guatemala and Nicaragua are. The recent volcanic belt of El Salvador opens northward into Guatemala to include much of the triangular wedge east of Guatemala City and north of Lake Guija.

The splintering of this region can be better understood by noting that the wedge-shaped region of the Caribbean plate is at the junction of the Americas and Cocos plates (fig. 3-25), each of which has different amounts and directions of movement. To judge from the fault pattern, the wedge is extending along an east-west line, and each block, at least along the southern part (El Salvador), is twisting in a counterclockwise direction.

SUMMARY

The examples in this section illustrate some of the uses of Skylab handheld-camera photographs in the analysis of major regional geologic features. Oblique views from many directions emphasize large-scale linear trends not easily recognizable on conventional vertical photographs (taken from either aircraft or spacecraft). These photographs also display the interrelationships between small, well-known areas within a generally poorly known area and thus rapidly guide the reconnaissance geologist to the major areas that need to be analyzed to understand the region. Furthermore, these photographs provide a synoptic view that can improve or suggest alternative syntheses of structural provinces.

These data are extremely important as teaching aids. These photographs have already made a significant impact and will continue to make major revisions both in teaching format and in student understanding of regional structural patterns and their significance.

REFERENCES

- 3-1. Kaltenbach, J. L.; Lenoir, W. B.; McEwen, M. C.; Weitenhagen, R. A.; and Wilmarth, V. R., eds.: Skylab 4 Visual Observations Project Report. NASA TM X-58142, 1974.
- 3-2. Burke, Kevin; and Dewey, J. F.: Plume-Generated Triple Junctions: Key Indicators in Applying Plate Tectonics to Old Rocks. *J. Geol.*, vol. 81, no. 4, 1973, pp. 406-433.
- 3-3. Baker, B. H.; Mohr, P. A.; and Williams, L. A. J.: Geology of the Eastern Rift System of Africa. *Geol. Soc. America Special Paper* 136, 1972.
- 3-4. Bannert, Dieter: Afar Tectonics Analyzed From Space Photographs. *American Assoc. Petrol. Geol. Bull.*, vol. 56, no. 5, 1972, pp. 903-915.
- 3-5. Tazieff, H.; Varet, J.; Barberi, F.; and Giglia, G.: Tectonic Significance of the Afar (or Danakil) Depression. *Nature*, vol. 235, Jan. 21, 1972, pp. 144-147.
- 3-6. Laughton, A. S.: The Gulf of Aden, in Relation to the Red Sea and the Afar Depression of Ethiopia. *The World Rift System*, T. N. Irvine, ed., *Geol. Survey of Canada Paper* 66-14, 1965.
- 3-7. Laughton, A. S.: The Gulf of Aden. *Phil. Trans. Roy. Soc. London, Ser. A*, vol. 259, 1966, pp. 150-171.
- 3-8. Girdler, R. W.: The Role of Translational and Rotational Movements in the Formation of the Red Sea and Gulf of Aden. *The World Rift System*, T. N. Irvine, ed., *Geol. Survey of Canada Paper* 66-14, Sept. 1965.
- 3-9. Freund, R.; Garfunkel, Z.; Zak, I.; Goldberg, M.; et al.: The Shear Along The Dead Sea Rift. *Phil. Trans. Roy. Soc. London, Ser. A*, vol. 267, 1970, pp. 107-130.
- 3-10. Quennell, A. M.: Tectonics of the Dead Sea Rift. *Asociación de Servicios Geol. Africanos, Cong. Geol. Int. XX*, Mexico D. F., 1959, pp. 386-403.
- 3-11. Freund, R.: Kinematics of Transform and Transcurrent Faults. *Tectonophysics*, vol. 21, 1974, pp. 93-134.
- 3-12. Brown, G. F.; Jackson, R. O.; Bogue, R. G.; and Elberg, E. L., Jr.: Geologic Map of the Northwestern Hijaz Quadrangle, Kingdom of Saudi Arabia. *U.S. Geological Survey Misc. Geol. Investigations Map* I-204A, Scale 1:500 000, 1963.
- 3-13. Brown, G. F.; Layne, N.; Goudarzi, G. H.; and MacLean, W. H.: Geologic Map of the Northeastern Hijaz Quadrangle, Kingdom of Saudi Arabia. *U.S. Geological Survey Misc. Geol. Investigations Map* I-205A, Scale 1:500 000, 1963.
- 3-14. Hadley, D. G.: Geology of the Sahl Almatran Quadrangle, Northwestern Hijaz, Kingdom of Saudi Arabia. *Kingdom of Saudi Arabia Ministry of Petroleum and Mineral Resources Geologic Map* GM-6, 1973.
- 3-15. Johnson, R. F.; and Trent, V. A.: Mineral Reconnaissance of the Al Jizl Quadrangle, Northwest Hijaz. *Kingdom of Saudi Arabia Ministry of Petroleum and Mineral Resources, Mineral Investigations Map* MI-10, 1967.
- 3-16. Geologic Map of the Arabian Peninsula. *U.S. Geological Survey Miscellaneous Geol. Investigations Map* I-270A, Scale 1:2 000 000, 1963.
- 3-17. Stöcklin, Jovan: Structural History and Tectonics of Iran: A Review. *American Assoc. Petrol. Geol. Bull.*, vol. 52, no. 7, July 1968, pp. 1229-1258.

- 3-18. Takin, Manoochehr: Iranian Geology and Continental Drift in the Middle East. *Nature*, vol. 235, Jan. 21, 1972, pp. 147-150.
- 3-19. Haynes, Simon J.; and McQuillan, Henry: Evolution of the Zagros Suture Zone, Southern Iran. *Geol. Soc. America Bull.*, vol. 85, no. 5, May 1974, pp. 739-744.
- 3-20. James, David E.: Plate Tectonic Model for the Evolution of the Central Andes. *Geol. Soc. America Bull.*, vol. 82, no. 12, Dec. 1971, pp. 3325-3346.
- 3-21. James, David E.: The Evolution of the Andes. *Sci. American*, vol. 229, no. 2, Aug. 1973, pp. 61-69.
- 3-22. Cristi, Jorge Munoz: Chile. Handbook of South American Geology, William Furness Jenks, ed., *Geol. Soc. America Memoir* no. 65, 1956, pp. 187-214.
- 3-23. St. Amand, P.; and Allen, C. R.: Strike-Slip Faulting in Northern Chile (abs.). *Geol. Soc. America Bull.*, vol. 71, 1965.
- 3-24. Arabasz, Walter Joseph, Jr.: Geological and Geophysical Studies of the Atacama Fault Zone in Northern Chile. Ph. D. Thesis, California Institute of Technology, 1971.
- 3-25. Wellman, H. W.; and Willett, R. W.: The Geology of the West Coast From Abut Head to Milford Sound, Part 1. *Roy. Soc. New Zealand Trans. & Proc.*, vol. 71, pt. 4, 1942, pp. 282-306.
- 3-26. Wellman, H. W.: The Alpine Fault in Detail: River Terrace Development at Maruia River. *New Zealand J. Sci. Technology, Sec. B*, vol. 33, 1952, pp. 409-414.
- 3-27. Wellman, H. W.: Data for the Study of Recent and Late Pleistocene Faulting in the South Island of New Zealand. *New Zealand J. Sci. Technology, Sec. B*, vol. 34, 1953, pp. 270-288.
- 3-28. Wellman, H. W.: New Zealand Quaternary Tectonics. *Geol. Rundschau*, vol. 43, 1955, pp. 248-257.
- 3-29. Wellman, H. W.: Rate of Horizontal Fault Displacement in New Zealand. *Nature*, vol. 237, June 1972, pp. 275-277.
- 3-30. Le Pichon, Xavier: Sea-Floor Spreading and Continental Drift. *J. Geophys. Res.*, vol. 73, no. 12, June 1968, pp. 3661-3697.
- 3-31. McKenzie, D. P.; and Morgan, W. J.: The Evolution of Triple Junctions. *Nature*, vol. 224, Oct. 1969, pp. 125-133.
- 3-32. Freund, R.: The Hope Fault, A Strike Slip Fault in New Zealand. *New Zealand Geol. Surv. Bull.*, new series, vol. 86, 1971.
- 3-33. Scholz, Christopher H.; Rynn, John M. W.; Weed, Robert W.; and Frohlich, Cliff: Detailed Seismicity of the Alpine Fault Zone and Fiordland Region, New Zealand. *Geol. Soc. America Bull.*, vol. 84, no. 10, Oct. 1973, pp. 3297-3316.
- 3-34. Richter, C. F.: *Elementary Seismology*. W. H. Freeman and Co., 1958.
- 3-35. Lensen, G. J.: Elastic and Non-Elastic Surface Deformation in New Zealand. *Bull. New Zealand Soc. Earthquake Eng.*, vol. 3, 1970.
- 3-36. Johnson, Tracy; and Molnar, Peter: Focal Mechanisms and Plate Tectonics of the Southwest Pacific. *J. Geophys. Res.*, vol. 77, no. 26, Sept. 1972, pp. 5000-5032.
- 3-37. Kingma, Jacobus T.: *The Geological Structure of New Zealand*. John Wiley & Sons, 1974.
- 3-38. Swanson, E. R.: *Petrology and Volcanic Stratigraphy of the Durango Area, Durango, Mexico*. M.A. Thesis, University of Texas, 1974.
- 3-39. Keizer, R. P.: *Volcanic Stratigraphy, Structural Geology, and K-Ar Geochronology of the Durango Area, Durango, Mexico*. M.A. Thesis, University of Texas, 1974.
- 3-40. McDowell, F. W.; and Clabaugh, S. E.: *Edades Potasio-Arگون de Rocas Volcánicas en la Sierra Madre Occidental, Noreste de Mazatlán*. *Soc. Geol. Mexico, IIA, Convención Nacional, Memoria*, 1972, pp. 182-185.
- 3-41. Weed, W. H.: Notes on a Section Across the Sierra Madre Occidental of Chihuahua and Sinaloa, Mexico. *American Inst. Min. Eng., Trans.*, vol. 32, 1902, pp. 444-458.
- 3-42. Dasch, E. Julius; Armstrong, Richard L.; and Clabaugh, Stephen E.: Age of Rim Rock Dike Swarm, Trans-Pecos, Texas. *Geol. Soc. America Bull.*, vol. 80, no. 9, Sept. 1969, pp. 1819-1823.
- 3-43. Hess, Harry H.; and Maxwell, John C.: Caribbean Research Project. *Geol. Soc. America Bull.*, vol. 64, 1953, pp. 1-6.
- 3-44. Molnar, Peter; and Sykes, Lynn R.: Tectonics of the Caribbean and Middle America Regions From Focal Mechanisms and Seismicity. *Geol. Soc. America Bull.*, vol. 80, no. 9, Sept. 1969, pp. 1639-1684.
- 3-45. Kesler, Stephen E.: Nature of Ancestral Orogenic Zone in Nuclear Central America. *American Assoc. Petrol. Geol. Bull.*, vol. 55, no. 12, Dec. 1971, pp. 2116-2129.
- 3-46. Pinet, Paul R.: Diapirlike Features Offshore Honduras: Implications Regarding Tectonic Evolution of Cayman Trough and Central America. *Geol. Soc. America Bull.*, vol. 83, no. 7, July 1971, pp. 1911-1922.
- 3-47. Donnelly, T. W.: *Geological Study of Motagua Fault Zone*. Paper presented at IV Reunion de Geólogos de America Central, Tegucigalpa, Honduras, June 1974.
- 3-48. Bonis, Samuel B.: *Geologica Reconnaissance of the Alta Verapaz Fold Belt, Guatemala*. *Geol. Bull. 5, Inst. Geog. Nacional, Guatemala*, 1967.
- 3-49. Dengo, Gabriel: *Estructura Geológica, Histórica Tectónica, y Morfología de America Central*. Centro Regional de Ayuda Técnica, Mexico, 1968.
- 3-50. Bonis, Samuel; and Bohnenberger, Otto: *Mapa Geológico de la Republica de Guatemala*. Scale 1:1 500 000, *Inst. Geog. Nacional, Guatemala*, 1970.
- 3-51. Dillon, William P.; and Vedder, John G.: Structure and Development of the Continental Margin of British Honduras. *Geol. Soc. America Bull.*, vol. 84, no. 8, Aug. 1973, pp. 2713-2732.
- 3-52. Fisher, Robert Lloyd: Middle America Trench — Topography and Structure. *Geol. Soc. America Bull.*, vol. 72, no. 5, May 1961, pp. 703-720.

4

Geological Features of Southwestern North America

*L. T. SILVER,^a T. H. ANDERSON,^a C. M. CONWAY,^a
 J. D. MURRAY,^a AND R. E. POWELL^a*

THE SKYLAB 4 crewmen conducted visual observations of seven designated geological target areas and other targets of opportunity in parts of southwestern United States and northwestern Mexico. The experiments were designed to determine how effectively geologic features could be observed from orbit and what research information could be obtained from the observations when supported by ground studies. For the limited preparation they received, the crewmen demonstrated exceptional observational ability and produced outstanding photographic studies. They also formulated cogent opinions on how to improve future observational and photodocumentation techniques.

Significant research contributions to ongoing field investigations were obtained from the photographs and observations. These contributions were integrated into other aspects of the ground investigations to (1) identify and evaluate zones of major faulting in southeastern California, Baja California, and northwestern Sonora; (2) develop a new key to the regional stratigraphy of the prebatholithic rocks of northern Baja California; (3) discover the most southwesterly known occurrence of Precambrian crystalline rocks in North America; (4) discover a previously unmapped section of Mesozoic (?) volcanic rocks in southeastern California; and (5) contribute important overview perspectives to many regional geologic problems.

^aCalifornia Institute of Technology.

The experimental data and the demonstrated crew capabilities justify planning future geology visual observation experiments for manned Earth-orbiting programs such as the Space Shuttle. Both professional scientist-observers and astronaut-observers can make contributions if properly prepared and equipped. The experiments should be closely coordinated with active surface research investigations. The emphasis should be on selecting important problems and objectives and integrating orbital observations and ground studies, not on prospecting for isolated spectacular discoveries.

INTRODUCTION

Man's role as a direct and discriminating observer of geologic features on the Earth's surface as seen from the vantage point of an orbiting platform was tested formally for the first time during the third manned visit to Skylab. The great value of unmanned Earth-orbital photographic and other remote-sensing techniques in Earth science studies had been clearly established before the Skylab missions. However, the potential of man in real-time, dedicated, terrestrial geological observation activities had not been previously investigated. With the obvious future requirement for a better geological understanding of the Earth, man's capability to meet these needs in various space-flight applications deserves thorough consideration and evaluation.

To provide relevance, there are two general conceptual areas in which the objectives and implementation

of the Skylab geology observation experiments should be considered.

1. What are man's inherent capabilities as a geological observer from a satellite? What orbital conditions, equipment, and techniques and what ground-based activities can provide the most effective use of these capabilities?

2. What are the types of geologic problems and scientific questions to which man in orbit can make superior or unique observational contributions? Are the problems and his contributions of sufficient scientific value to justify the use of man in this space activity as compared to other functions he can perform? As compared to other approaches to the same problems?

The Skylab visual observations experiments provided useful data and experience pertaining to these questions. In addition, photographic and visual observations data that are valuable to geological research in a number of areas in southwestern North America were obtained.

Approximately a month before the Skylab 4 mission, the senior author participated in the preparation of a visual observations program in which the crewmen would examine and photograph selected geological areas in southwestern North America (fig. 4-1). A series of seven operational exercises and study areas in the southwestern United States and northwestern Mexico was discussed during a 1-hour briefing for the astronauts. For each exercise, a photograph from Apollo or earlier Skylab missions illustrated the feature to be studied. These photographs were included in the on-board data package for use by the astronauts.

During the mission, the crew made extensive visual observations in almost all the geological study areas of southwestern North America and collected a comprehensive photographic record of their observational opportunities. The results of these efforts are contained in table 4-1 and figure 4-2.

On March 12, 1974, the crew participated in a 4-hour geology debriefing conducted by the principal investigators of the geology experiments. Included in the debriefing were a brief review of the available handheld-camera photographs and discussions of the observational opportunities, conditions, and equipment and of the construction of the exercises. The transcript of this debriefing was used in the preparation of this report. Photographic transparencies and a limited number of photographs of the experiment sites and nearby areas were analyzed. Field studies to verify the photogeologic interpretations were carried out from April to December 1974. Field work and photointerpretation were done

by the various authors: Arizona, C. M. Conway and L. T. Silver; southern California, R. E. Powell and L. T. Silver, Baja California, J. D. Murray and L. T. Silver; and Sonora, Mexico, T. H. Anderson and L. T. Silver. Dayna Salter assisted in the study of structural lineaments in southern California.

PLANNED GEOLOGY VISUAL OBSERVATION EXPERIMENTS

The geology experiments were designed with dual objectives: to determine how effective an orbiting observer could be in the context of the Skylab flightpath, flight time, and facilities and to determine the type of scientific yield that could be obtained from analysis of the crewmen's observations and photographic products when supported by ground studies.

The assigned exercises are shown in figure 4-1. Because of time constraints, the preflight briefing was minimal, and the crewmen's understanding of the experiment objectives was obtained only from discussions with the senior author. The general orbital tracks shown in figure 4-1 show the types of northeast and southeast passes during which the crewmen made their observations.

Each exercise was designed around a geological problem or group of problems with which the senior author and his colleagues were concerned. In each area, extended field work had been carried out before the Skylab 4 mission and considerable familiarity with ground truth had been established. Therefore, some questions were designed to test the crewmen's observations of known phenomena. Nevertheless, substantial scientific questions remained in each area for which it was hoped that the astronauts' observations would make significant contributions. Further ground-verification activities were intended to be a part of these studies.

DATA PRODUCED BY THE EXPERIMENTS

The direct results of the observational experiments take three forms.

1. The in-flight verbal commentary by crewmembers as they conducted their observations was recorded and subsequently transcribed.

2. Crewmembers used a handheld Hasselblad 70-mm camera with a 100-mm lens and a Nikon 35-mm

camera with 55- and 300-mm lenses to photograph sites and features. Both cameras were used for all sites designated for this study under a variety of observing positions and lighting conditions. Also photographed were "targets of opportunity" (i.e., geological features that the astronauts believed to be noteworthy but that had not been included in the assigned exercise). A total of

more than 400 photographs was taken during the mission as part of these experiments. A tabulation of the photographs according to geographical area is given in table 4-I. A geographical map index showing photographic coverage and photographic orientation is presented in figure 4-2.

3. Postmission crew debriefing and individual crew-

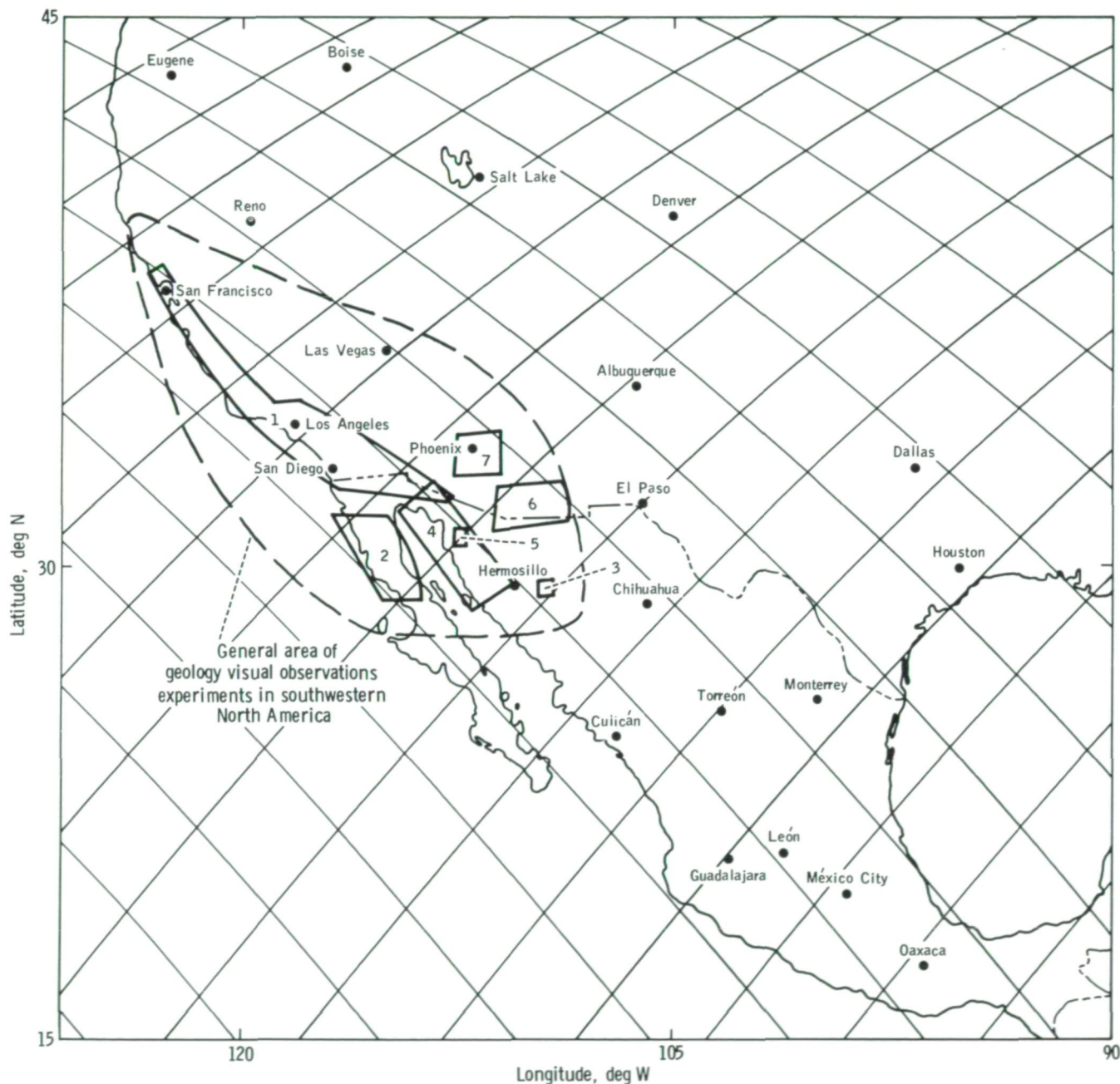


FIGURE 4-1.—Skylab 4 orbital track map showing the general region and the seven study areas involved in this experiment.

TABLE 4-1.—Index of Skylab 4 Handheld-Camera Photographs
of Southwestern North America

| Area | Photograph no. | |
|--|--|--|
| | Nikon 35-mm camera | Hasselblad 70-mm camera |
| Baja California and Gulf of California | SL4-152-5186 SL4-156-5294 and 5295 SL4-191-7036 to 7040 SL4-193-7187 to 7190 SL4-194-7234, 7235, and 7238 SL4-195-7325 SL4-196-7371 and 7372 SL4-197-7426, 7428, and 7429 SL4-199-7552 and 7553 SL4-202-7718, 7725, and 7732 SL4-203-7807 to 7813 and 7816 to 7819 SL4-204-7870 and 7882 to 7885 SL4-206-7967 and 7970 | SL4-136-3385, 3409, 3410, 3437 to 3439, and 3479 to 3481 SL4-137-3727 SL4-138-3807 to 3810, 3827 to 3829, 3860, 3861, 3880, and 3881 SL4-140-4126 to 4140, 4154 to 4156, 4197, and 4198 SL4-142-4486 to 4489, 4544 to 4550, 4552 to 4554, 4562 to 4565, and 4581 SL4-143-4603 to 4607 |
| Sonora, Mexico | SL4-156-5294 and 5295 SL4-193-7154 and 7155 SL4-194-7236, 7237, 7239, and 7240 SL4-196-7355, 7356, 7363, 7371, and 7372 SL4-197-7429 to 7431 SL4-199-7558 to 7580 SL4-200-7619 to 7622 SL4-202-7725 to 7745 SL4-203-7807 to 7825 SL4-204-7870 SL4-206-7970 and 7989 SL4-207-8034 to 8056 SL4-209-8199 to 8201 | SL4-136-3409 and 3410 SL4-139-3983 and 4062 to 4064 SL4-140-4130 to 4141, 4154 to 4156, 4186 to 4188, 4197, and 4198 SL4-141-4390 to 4401 SL4-142-4547 to 4554 SL4-143-4603 to 4607 and 4616 to 4622 |
| Arizona | SL4-156-5294 to 5297 SL4-191-7008, 7009, and 7019 SL4-193-7192 SL4-194-7216 and 7217 SL4-196-7371 SL4-197-7429 SL4-199-7552 to 7557 SL4-202-7719 to 7724, 7726, and 7730 SL4-203-7800, 7806, 7812 to 7815, and 7820 | SL4-138-3808 to 3812, 3860, 3861, and 3881 SL4-139-4034 to 4037 SL4-140-4132, 4134, 4135, 4137 to 4141, 4157, and 4185 SL4-141-4385, 4386, 4390, and 4391 SL4-142-4435 to 4440, 4474, 4477, 4564, 4565, 4580, and 4581 |
| San Andreas and related faults | SL4-156-5294 and 5295 SL4-193-7191 SL4-194-7212 to 7214 SL4-196-7354, 7361, and 7362 SL4-197-7426 to 7431 SL4-199-7552 to 7557 SL4-203-7784 to 7825 SL4-204-7879 to 7885 SL4-206-7961 to 7972 and 8009 to 8019 SL4-207-8026 to 8033 and 8086 SL4-208-8116 to 8120 and 8123 to 8126 SL4-209-8192 to 8196 | SL4-136-3406 to 3408 and 3437 to 3439 SL4-138-3807 to 3810, 3828, 3829, 3843, 3860, and 3861 SL4-139-4033 SL4-140-4130 to 4141 SL4-141-4377, 4378, 4381 to 4384, and 4387 to 4389 SL4-142-4482 to 4487, 4520 to 4523, 4530 to 4547, 4551, and 4558 to 4565 SL4-143-4615 |
| California, Nevada, Utah, Colorado, and New Mexico | SL4-156-5296 and 5297 SL4-191-7004 and 7019 SL4-192-7091 SL4-193-7151 and 7197 SL4-199-7552 to 7557 SL4-202-7716 to 7726 SL4-204-7870 SL4-206-7961 to 7969, 7972, and 8009 to 8019 SL4-207-8081 and 8082 | SL4-138-3811, 3812, 3844, 3845, 3875, and 3881 SL4-139-4034 to 4040 and 4047 to 4049 SL4-140-4086, 4157 to 4159, 4167, 4168, 4185, 4211, 4231, and 4232 SL4-141-4258, 4259, 4371 to 4376, and 4379 to 4386 SL4-142-4430 to 4437, 4580, and 4581 |



FIGURE 4-2.—Geographical map index showing selected photographic coverage and photographic orientation used in this report.

man communications provided opportunities for the crewmen to synthesize and summarize their impressions of the actual observing conditions, of the art of observation, and of the scientific subjects explored by them and to offer their recommendations for future improvements. The discussions with the Skylab 4 crew have been useful in completing this report.

CREW EFFECTIVENESS

Our preliminary assessment of crew effectiveness in conducting geology experiments from space (ref. 4-1) has been reinforced during the completion of the report. The effectiveness of a visual observations program depends on many key factors, such as the interest, scientific training, observational powers, and preflight preparation of the personnel involved. The Skylab 4 crew demonstrated a high degree of interest in the general visual observations program and in the specific geologic questions that concerned the related sites. This interest and an obvious enjoyment of Earth observation were manifested both during and after the mission. The scientific background of the crewmen indicated that they clearly understood the nature of observational techniques and the associated inductive logic. The crewmen did not receive extensive familiarization with geologic phenomena, and they recognized that a longer geological training program would have been beneficial.

The observational powers of the crewmen were exceptional. Combined with their interest and enthusiasm, these capabilities have produced some outstanding photographs of geologic phenomena. The contribution of the verbal commentary is subordinate to these photographs because of the general tendency of the crew to depend on their photographic documentation. This tendency may reflect a lack of confidence in their command of the diverse scientific subject matter. The fact that the crewmembers quickly recognized and identified the geological features in the designated sites reinforces the belief that more extensive preflight preparation would have enhanced the total scientific yield of the visual observations.

The crew developed many new and significant impressions of visual observation and photographic techniques. For example, they have stressed one important factor: no photograph can match the effectiveness of the human eye in perception of color, texture, and form of surface phenomena. During the debriefing session,

the commander made the following comment:

I think there is one fallacy we fell to, and that was the tendency to depend on the photographs. We've gotten back and we've looked at this photography now. It doesn't capture everything that's there and I think you guys understand that. I don't think we understood it as well as we should have before we left. Some of the stuff we have looked at just does not hold a candle to what you can really see with the old MK-VIII eyeball. And this is something we are going to have to do in future programs, and that is either to get better photography or start training a little bit more towards being able to get verbal descriptions of what you're looking at, because these pictures just don't have all of it at all.

In summary, the observational performance of the crew was outstanding. On the basis of the photographic documentation and results from discussions with them, we believe that they have made a convincing argument for future geological visual observations experiments from Earth orbit. Such experiments should continue to test and compare the effectiveness of manned visual observations with other approaches. They should be designed, however, as part of ongoing research programs with the orbiting observer (astronaut or scientist) as an active participant in the research. The criteria for effectiveness should include measures of steady research contribution as well as the opportunities for unexpected discovery.

DISCUSSION

The observations made by the astronauts, particularly their photographic record, were deliberately directed to areas where regional research investigations were being actively pursued by various members of this team. Our studies have shown that the selective photography is a rich reservoir of new information and insight.

Totally new, unsuspected major geologic features have rarely been found although there are innumerable new data points. Invariably, it has been found that space photography has given a new perspective to each research problem in which the geography and geometry of the diverse geologic elements of a region hundreds of kilometers in dimension fall into obvious spatial relation. This is not simply a result of having a new

horizontal map base; it demonstrates that space photographs help to establish the color, texture, structure, and form of surface features on a scale and with an orientation that was not previously available.

From previous work and postmission field studies, we have learned to be cautious of oversimplifying the significance of many apparent photographic relations. At the same time, several large-scale relationships that were suspect but that had not been properly integrated into the regional framework because of the lack of a documented overview have been confirmed.

For a region as geologically well known as southern California, the photographs from the Skylab 4 handheld camera appear to make their greatest research contribution when used in conjunction with other diverse approaches in developing a more complete understanding of large-scale features. In this application, the usefulness of the photographs is more steady and pervasive if less spectacular.

In more unfamiliar regions such as northwestern Mexico, there is a greater potential for exciting discoveries, and it is believed that some of the results from the Skylab 4 experiments will help achieve this result. However, it is in precisely this type of situation that premature generalization without adequate ground studies for confirmation can obscure the potential. The extent of our efforts has not been such as to provide thorough testing of most of the important possibilities inferred from the studies of the Skylab photographs and crew commentary.

This section contains some of the many promising (and sometimes enigmatic) research results that have been derived and will continue to be derived from the visual observation efforts of the Skylab 4 crew.

San Andreas Fault System and the Architecture of Southern California

The remarkable control exerted by the San Andreas Fault system on the topographic character of southern California was explicitly documented by the Skylab 4 astronauts. From a striking series of oblique handheld-camera photographs, a photomosaic (fig. 4-3(a)) has been constructed that captures the continuity and the relationship of the principal active faults of this system and the Gulf of California. The principal elements of this fault system are identified in figure 4-3(b).

Most of the fault structures are well known and have

been intensively studied. The crew's attention was directed to them as perhaps the best examples of fault-line features from which they could establish their observational criteria for fault recognition. The Skylab 4 photographic record has provided, in turn, an unparalleled overview of the fault system. From a significant number of relevant applications to southern California geology, three diverse examples that illustrate the great potential of the Skylab 4 handheld-camera photographs are presented.

East-west lineaments.—A profound geologic and physiographic break in the general northwest-southeast trends of California and Baja California is formed by the east-west structural grain of the Transverse Ranges. The tectonic significance of this unique transverse province in western North America is not fully understood in terms of the timing of structural events and the definition of structural elements. Skylab 4 handheld-camera photographs have provided an excellent overview of the Transverse Ranges province (fig. 4-3) and an opportunity to further delineate some of its structural elements.

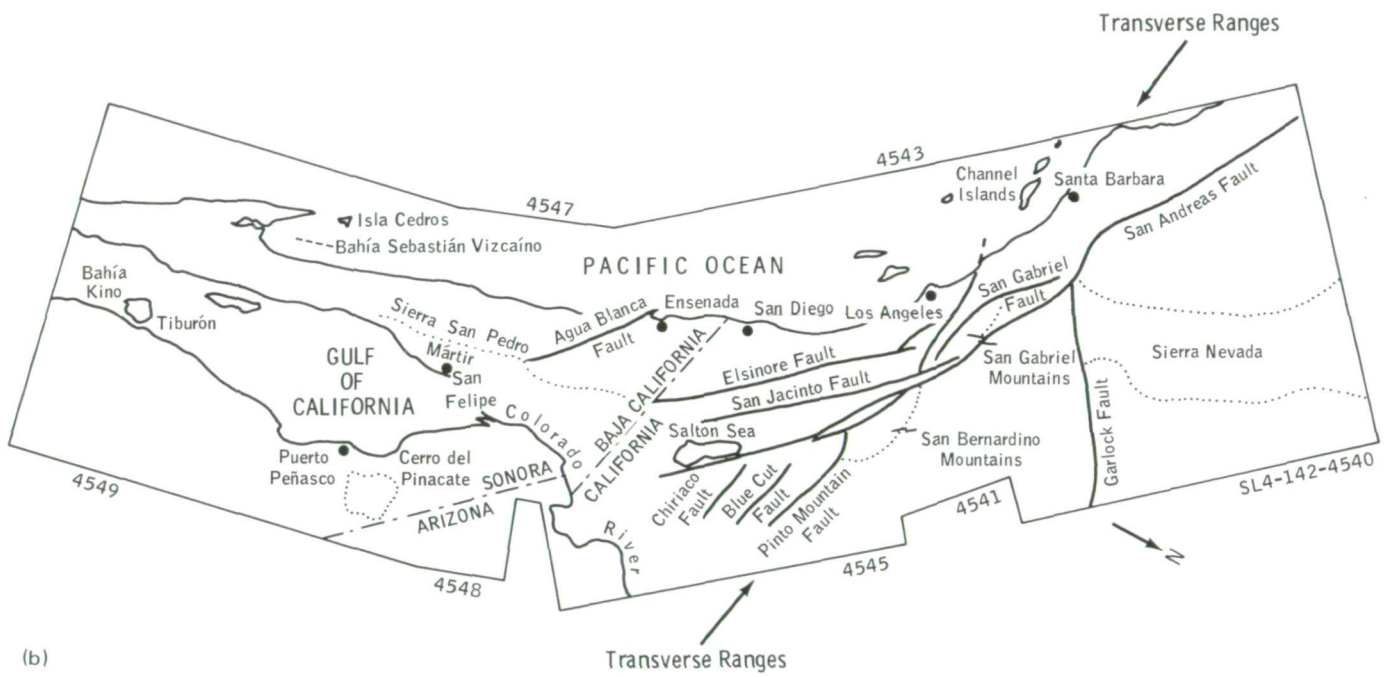
The eastern Transverse Ranges are distinguished by several east-west faults along which left-lateral displacement has been documented (refs. 4-2 and 4-3). These faults, including the Pinto Mountain, Blue Cut, and Chiriaco Faults (fig. 4-4), define prominent linears on Skylab 4 handheld-camera photographs. The Pinto Mountain, Blue Cut, and a few smaller faults were known to have left-lateral displacement before the Skylab 4 mission.

Based on ground verification of the in-flight observations of the Skylab 4 crewmen, 11.3 km of left-lateral movement has been demonstrated along the eastern half of the Chiriaco Fault (fig. 4-5(b) and ref. 4-4). The offset lithologic units cannot be resolved on the Hasselblad photographs, but areas for comparison and possible correlation are suggested and are detectable on the Nikon 300-mm photograph (fig. 4-5(a)).

The study of Skylab 4 handheld-camera photographs has resulted in the recognition of additional east-west linears south of the Chiriaco Fault. Left-lateral displacement has been established on two of these linears. An important goal for continued research is to determine whether the remaining linears are controlled by left-lateral faults. Recognition of the distribution of east-west linears on Skylab 4 photographs, followed by documentation of fault control and timing of fault motion, will increase understanding of the mechanical evolution of the Transverse Ranges structural province.



(a)



(b)

FIGURE 4-3.—Overview of major fault systems in southern California and northwestern Mexico. (a) Photomosaic. (b) Sketch map.



FIGURE 4-4.—Major linear features in southern California. (a) Photograph (SL4-142-4545). (b) Sketch map showing major east-west and northwest-southeast linears. Arrows indicate the direction of relative motion on opposite sides of faults. (c) Prominent conjugate linears in the northern Peninsular Ranges.

ORIGINAL PAGE IS
OF POOR QUALITY

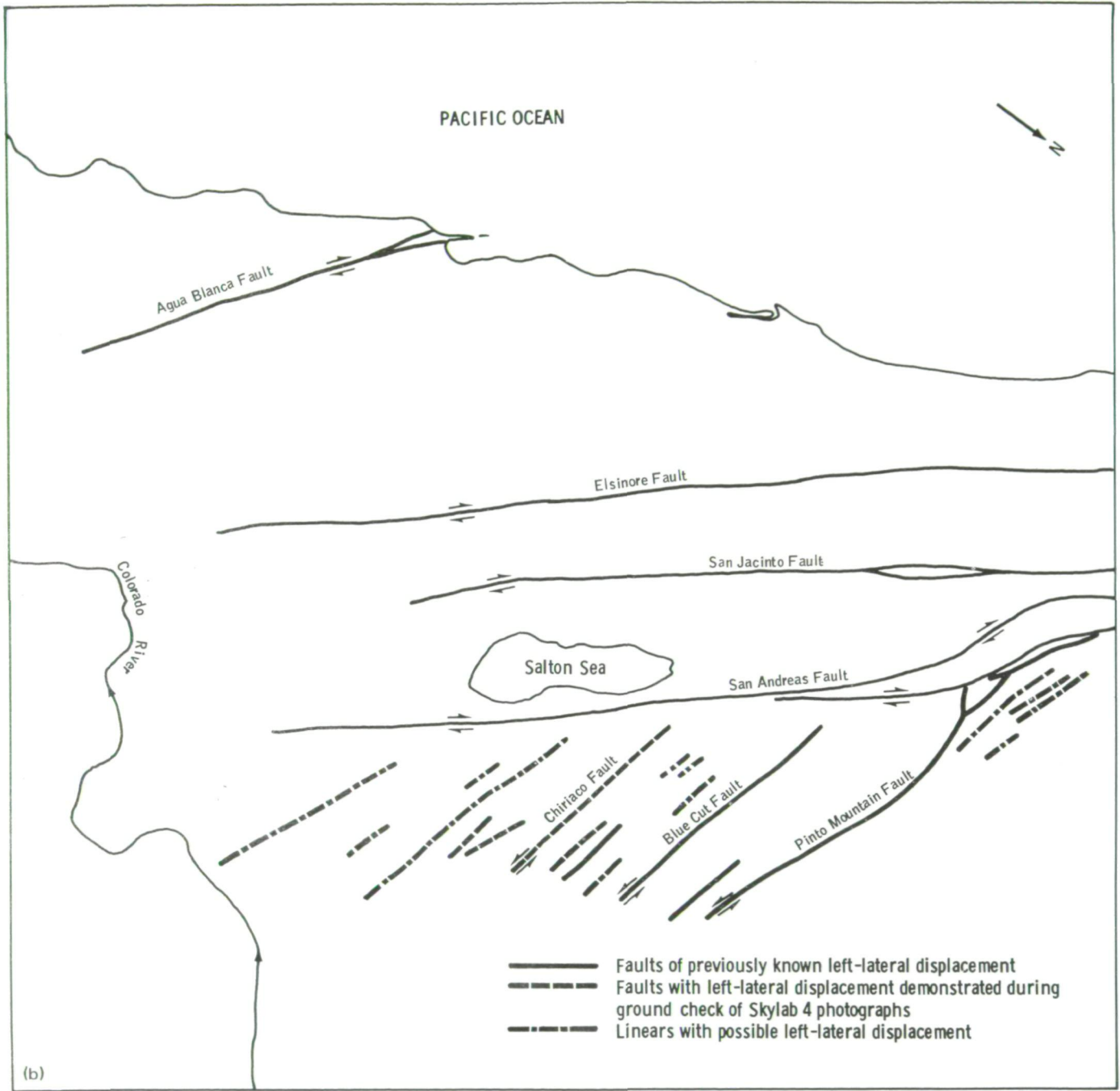


FIGURE 4-4.—Continued.

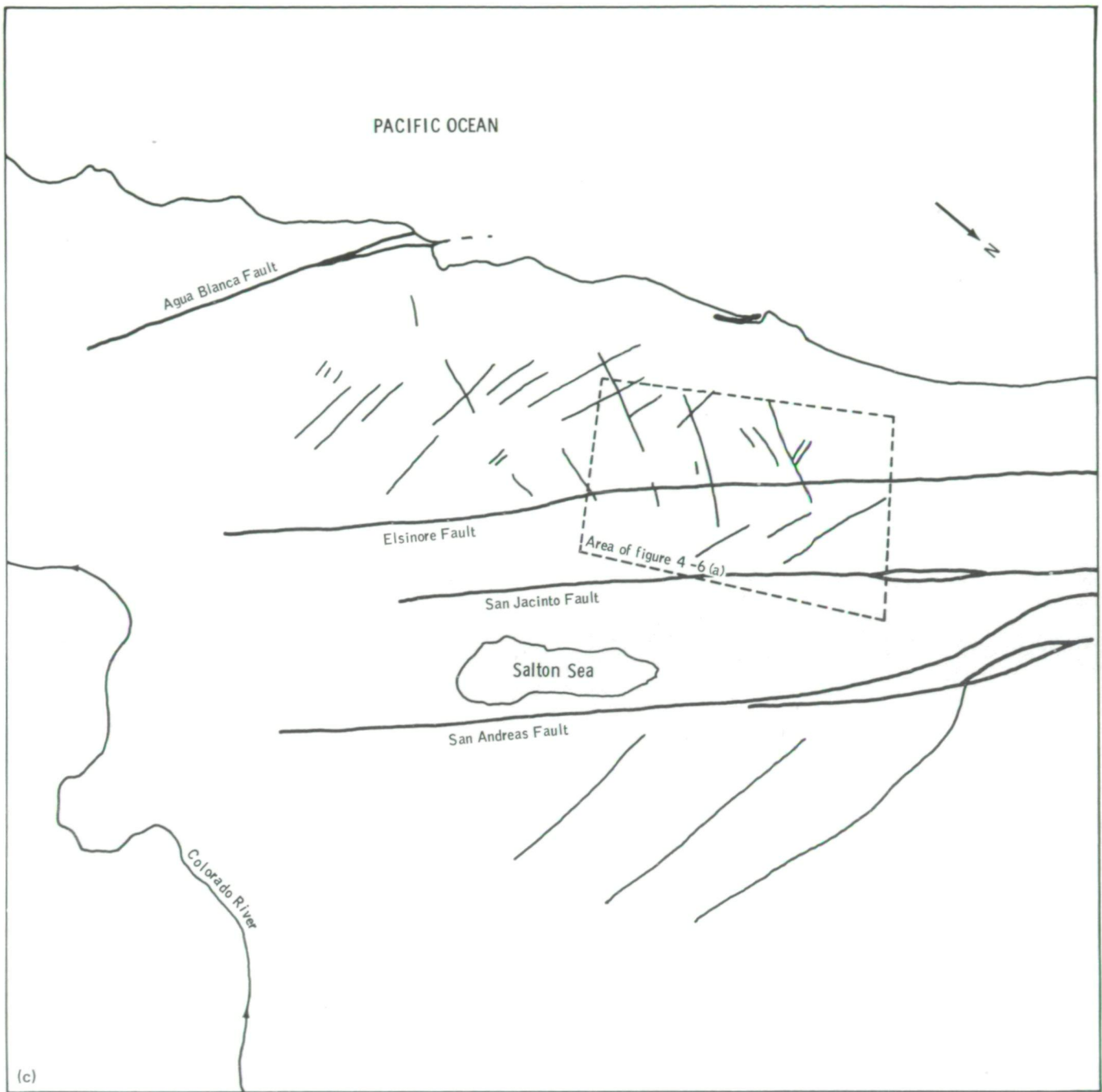


FIGURE 4-4.—Concluded.

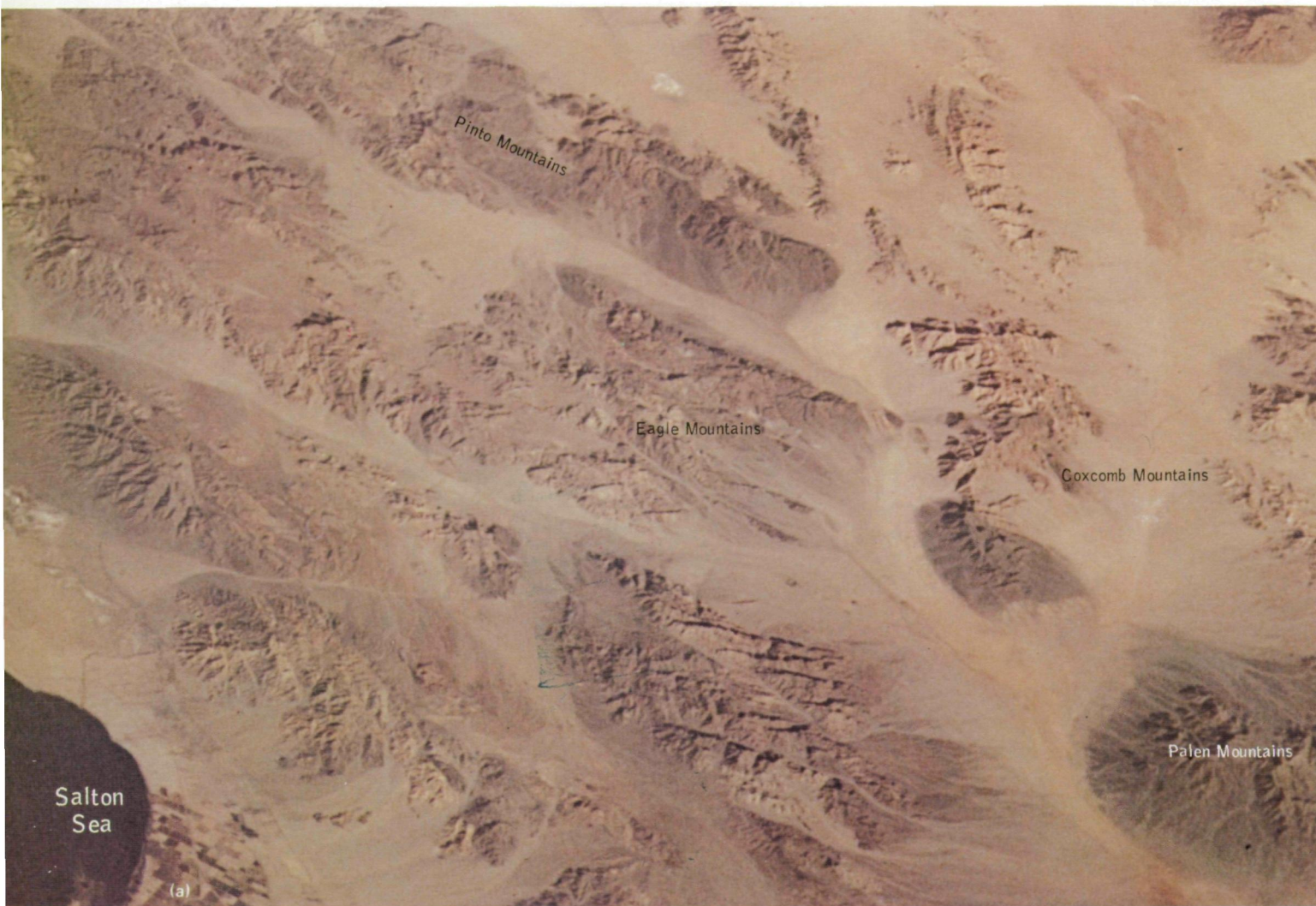


FIGURE 4-5.—The area northeast of the Salton Sea. (a) Photograph (SL4-203-7804). (b) Sketch map showing prominent east-west linears northeast of the Salton Sea. Distance from A to A' indicates 11.3 km left-lateral displacement on the Chiriaco Fault. (c) Geologic map based on combined photointerpretation and field reconnaissance. Regions indicated as alluvium contain clastic debris derived from the bedrock units shown.

Conjugate fracture systems in the Peninsular Ranges.—Two prominent sets of linears are recognized in the Peninsular Ranges of southern California and Baja California in the Skylab 4 handheld-camera photographs. Southwest of the Elsinore Fault, these sets strike N 15° to 35° E and N 70° to 80° W (figs. 4-4(a), 4-4(c), and 4-6). Northeast of the Elsinore Fault, the linear sets strike N 20° to 30° E and N 60° to 70° E. The geometric pattern of the linears suggests that they may be conjugate fracture sets that have been superimposed on the batholithic terrane, transgressing but not con-

finied to individual plutons. The fractures have been identified throughout the length of the Peninsular Ranges covered by the Skylab 4 photographs (see section entitled "Northern Baja California"). Other structural linears are present but are considered as separate phenomena.

If the conjugate fracture system is interpreted as a conjugate shear system, then the axis of maximum principal (compressional) stress is oriented approximately N 65° E or roughly perpendicular to the main structural, petrologic, geochemical, and geophysical

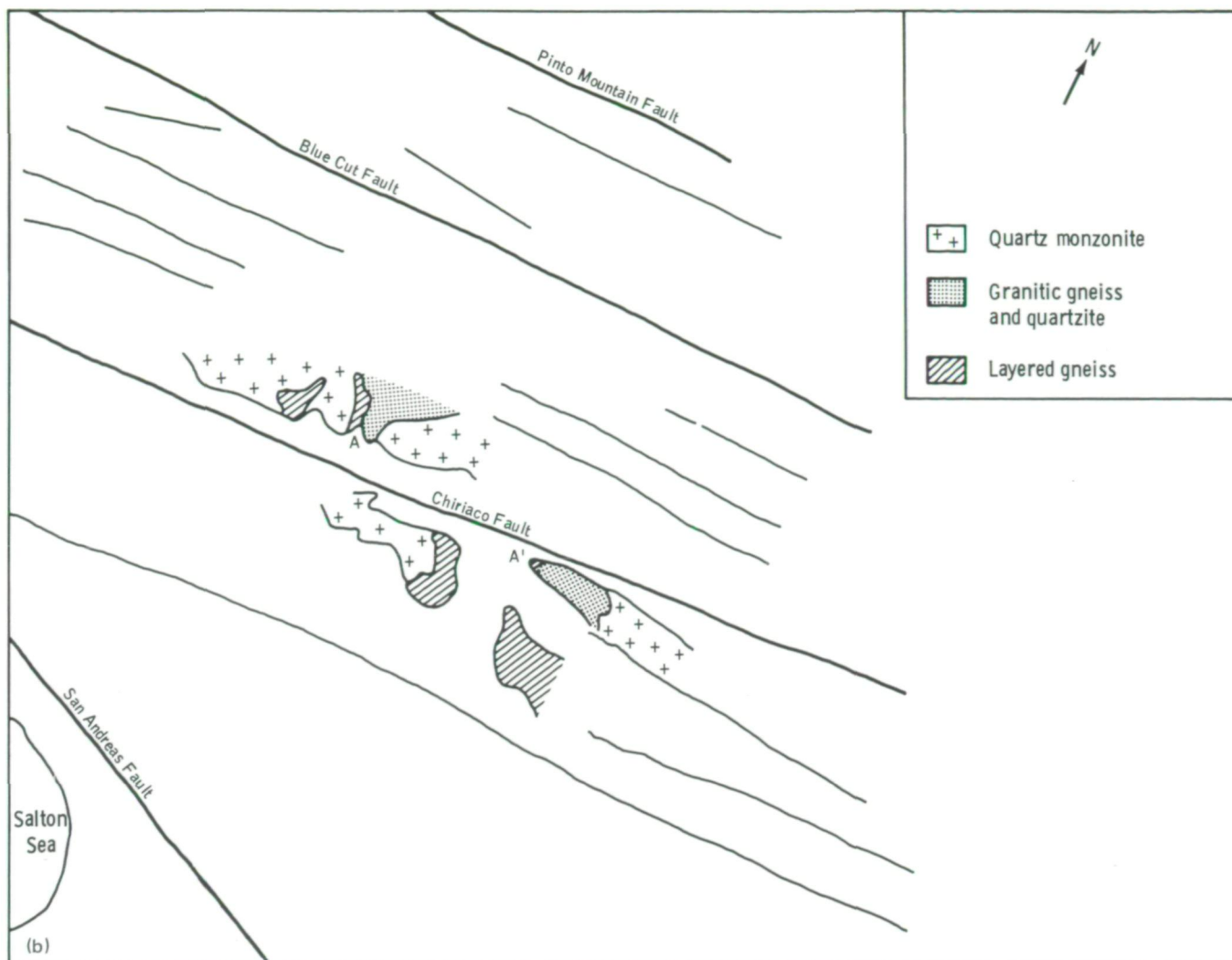


FIGURE 4-5.—Continued.

trends of southern California and Baja California. The slightly different orientation of the fracture pattern northeast of the Elsinore Fault may reflect a variation in local stress field across one of the major faults of the Peninsular Ranges or a superimposed rotational effect produced by later movements on the Elsinore and San Jacinto Faults. The conjugate fracture pattern may represent a response of the peninsula to compressional stresses imposed on the peninsular block during the opening of the Gulf of California or to regional stresses developed on a more extensive area of southwestern North America shortly before the rifting of the Gulf. It does not appear to be related directly to the San

Andreas stress system. A similar pattern of fracturing appears to be present in the southern Sierra Nevada, as shown faintly in figure 4-3(a) and very distinctly in figure 4-7, centered on Lake Isabella, California.

The overview of these regional fracture patterns provided by the Skylab photographs suggests the possibility of an integrated crustal response to tectonic strain on a scale that has not previously been observed and appreciated. It appears that within the inventory of Skylab mapping and handheld-camera photographs are the resources for an extended investigation of these phenomena and their broad geologic implications.

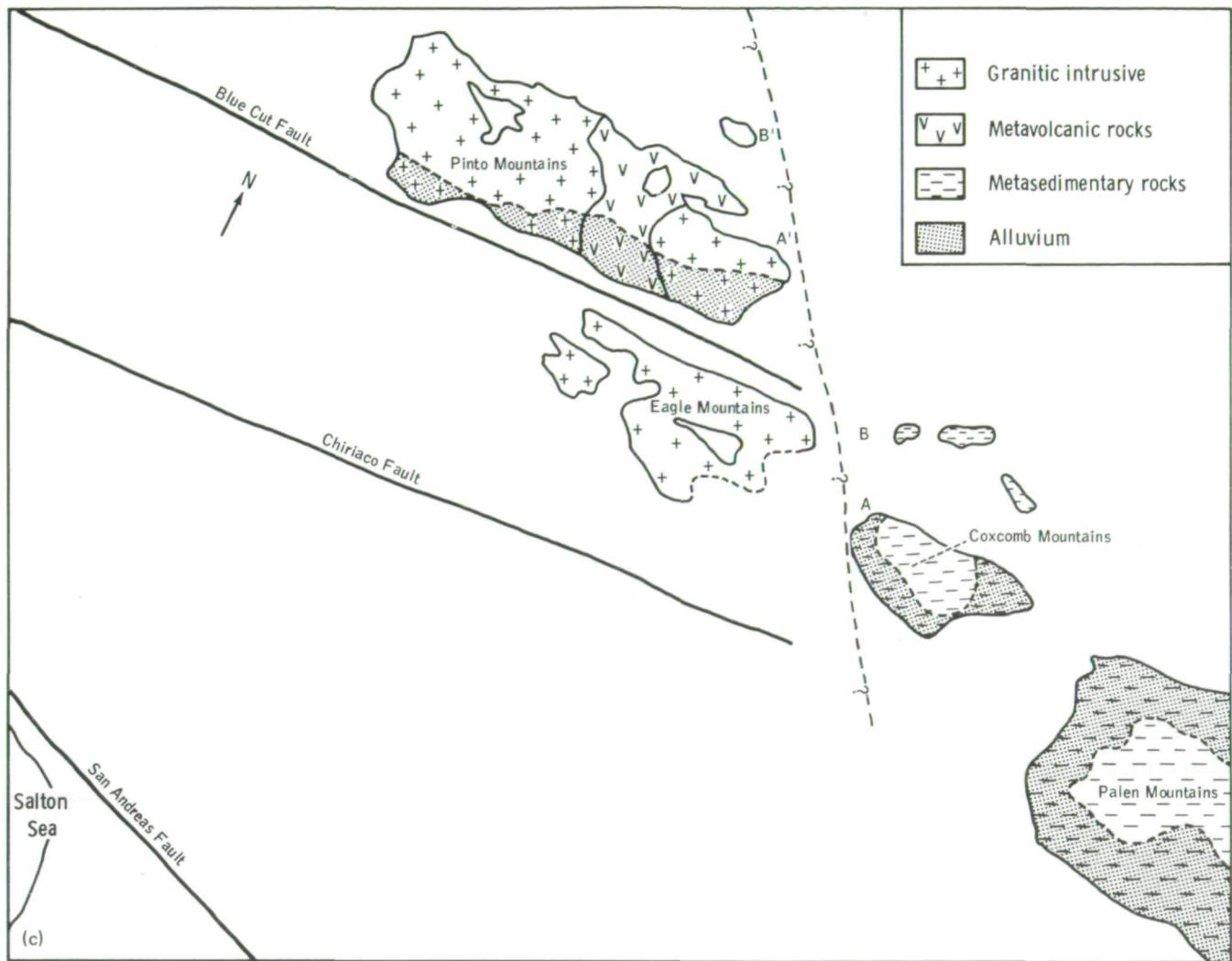


FIGURE 4-5.—Concluded.

A test of color values for lithologic correlations.—The value of Skylab handheld-camera color photographs for identifying and correlating lithologic units on a regional scale is potentially great, although reliable use requires a thorough understanding of color values and the factors that influence them. Color differences between rock types of varying lithologic composition are modified by such parameters as Sun angle, desert varnish, surface texture of bedrock and debris, and vegetation. Ambiguity in photointerpretation arises when some or all of these factors combine to give different lithologies similar color values. Resolution of the ambiguity re-

quires an interplay of photointerpretation and field work. A cross-check of this type was conducted in an area northeast of the Salton Sea (figs. 4-5(a) and 4-5(c)).

Existing field and photointerpretive maps represent the eastern Eagle and Pinto Mountains as granitic intrusive rocks and the southern Coxcomb and Palen Mountains as volcanic-derived metasedimentary rocks. However, the color values of the eastern Pinto, southern Coxcomb, and Palen Mountains in figure 4-5(a) are very nearly the same, which suggests the possibility that existing maps are inaccurate and that the dark color values are reflected from equivalent

lithologies. On the basis of these color values, a possible right-lateral offset of approximately 32 km along the dashed line in figure 4-5(c) was postulated. This line represents the eastern physiographic limit of the Transverse Ranges as well as a consistent local geologic discontinuity. In the use of Skylab 4 handheld-camera photographs for photogeologic interpretation, a correlation of dark-color-valued units intersecting the queried line at points A and B with those at A' and B' was postulated. Field reconnaissance has indicated that there is in fact a significant area of unmapped volcanic rocks in the eastern Pinto Mountains, although it is subordinate to the granite intrusives (fig. 4-5(c)). However, the dark color values do not represent equivalent lithologic units, so the suspected fault displacement was not confirmed. The dark units in the eastern Pinto Mountains are metavolcanic and granitic intrusive rocks, whereas volcanic-derived metasedimentary rocks comprise the southern Coxcomb and Palen Mountains.

There are several points to note in figure 4-5(a) with respect to photointerpretation of the dark color values. First, this particular granitic rock in the Pinto and Eagle Mountains is deeply colored by desert varnish; thus, its color value in the eastern Pinto Mountains is difficult to distinguish from that of the lithologically darker metasedimentary and metavolcanic rocks. Second, the texture and the color of the alluvial material derived from the granitic unit are distinct from those derived from the sedimentary and volcanic units. In particular, the freshly broken stream material is lighter colored in granitic-derived fans than in fans derived from metavolcanic or metasedimentary rocks. This contrast probably reflects primary lithologic color differences unbiased by desert varnish. Third, metasedimentary and metavolcanic rocks are indistinguishable on the basis of color value. Fourth, the texture and the color of the alluvium derived from metasedimentary and metavolcanic sources are indistinguishable.

The geologic usefulness of the Skylab photographs of southeastern California is constrained by the overlap of color value contributed by lithology and that contributed by desert varnish. The usefulness may, however, be enhanced by coordinating photointerpretation and field study. Comparison of photographs taken of a single area with visible and infrared film and at different Sun angles might further help to distinguish lithologic units.

Northern Baja California

Northern Baja California was divided into five specific sites (fig. 4-8(b)) and objectives, and the detail of photography, visual observations, and commentary varied greatly among these sites. The crew focused particularly on the Agua Blanca Fault zone (site 3) but also addressed themselves directly to the other sites. A total of 58 Hasselblad and 44 Nikon 55- or 300-mm photographs of the test area was obtained.

The geology of Baja California has not been studied in great detail, and the potential yield from satellite-based observations and photographs in terms of geologic reconnaissance is therefore high. The overall objective of the experiment was to identify (1) major patterns in the folded strata, (2) the occurrence of granite plutons, and (3) the location of major faults and conspicuous recent geological features. The photographs provide an overview of large areas of the peninsula that cannot be obtained from conventional aerial photographs; they are therefore especially useful for observation and integration of large-scale structural patterns.

The results are discussed under four major topics: (1) observation and interpretation of the significance of a 200-km-long light-colored stripe (site 1) and associated linear features, (2) recognition and mapping of igneous intrusive bodies (plutons), (3) observations of the Agua Blanca Fault zone and related features, and (4) photogeologic mapping of major fracture patterns in the northern part of the peninsula. The crewmen also photographed and discussed the young volcanic features at San Quintín and farther south (site 5). Apparently, the cinder cones were more clearly visible to the naked eye than they are in the photographs. Little detail of the volcanic construction is visible in the photographs, despite the fact that the photographs are of as good quality as any of the others.

The light-colored stripe and associated linear features.—The objectives of the Skylab 4 crewmen for sites 1 and 4 were to photograph and trace the extension of two major linear features (A and B in figs. 4-8(a) and 4-8(b)). The goal was to map these features, to identify patterns or differences in the rocks or vegetation on either side of these features, and to search for evidence relating to their geologic nature.

Numerous photographs show both features clearly, especially the light-colored stripe (A). The crewmen

were able to recognize this stripe for a distance of approximately 45 km southward from a point just south of the San José pluton. In figure 4-8(a), the stripe can be traced much farther, for a distance of nearly 100 km southeastward from Arroyo Calentura. North of the San José pluton, the stripe is less well defined than it is farther south, and it may, in fact, consist of two sub-parallel stripes that possibly combine near the northern end of the pluton. Near B in figure 4-8(b), the light-colored stripe merges with a region of arcuate patterns. Because it is generally exposed on westward- or

southward-facing slopes, the stripe is most clearly visible when illuminated by midday or afternoon Sun.

Field studies at four localities (fig. 4-8(b)) indicate that the light-colored stripe is principally the expression of a specific stratigraphic zone in the prebatholithic section, at least along a 15-km-long segment north and east of the San José pluton. The light color is due to (1) the paucity of brush and the smoothness of the ground surface underlain by this unit, (2) the light color (tan) of the rock and its derivative soil, and (3) the fissile (platy and chippy) nature of the rock that partially covers the

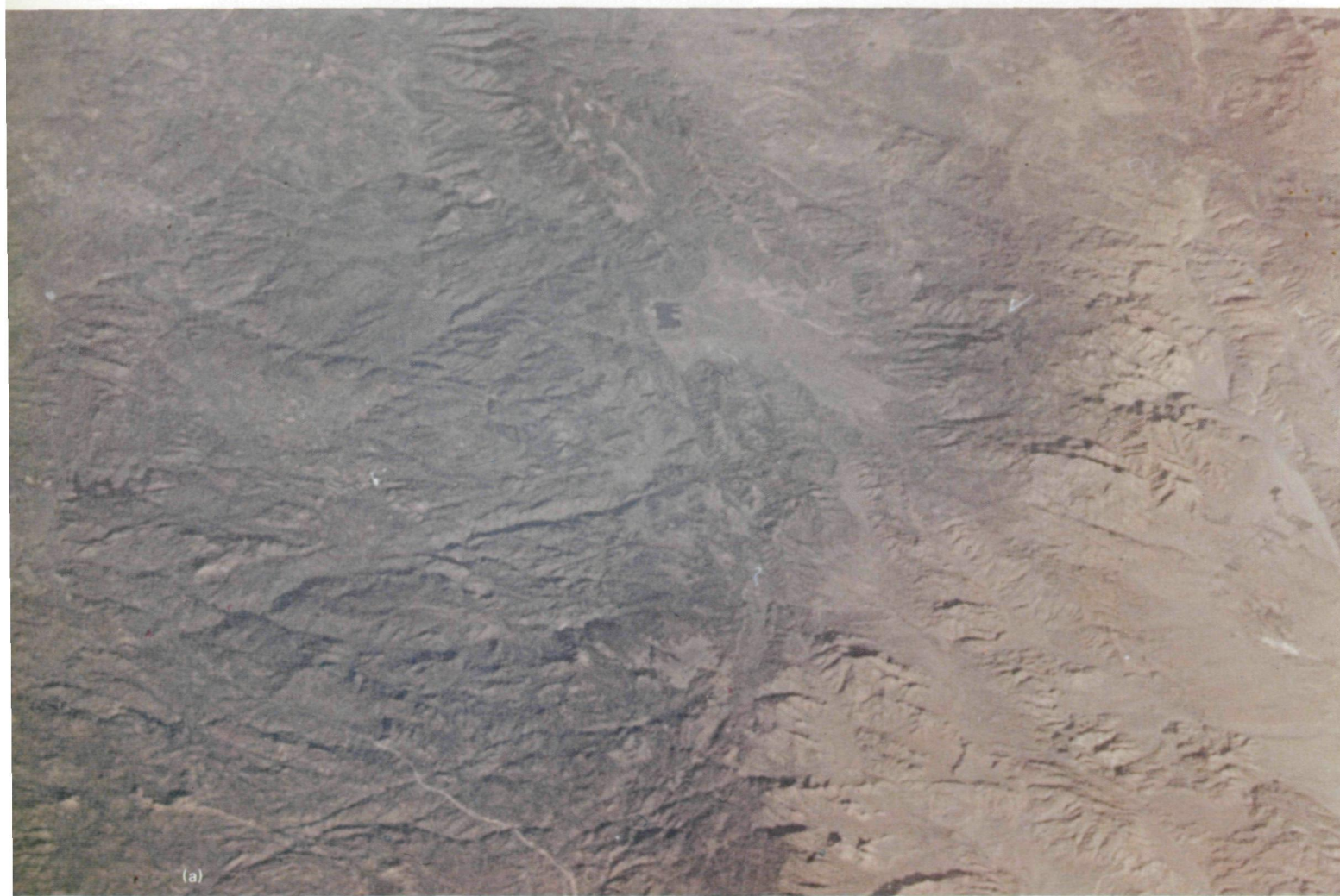


FIGURE 4-6.—Conjugate linear fractures in the north-central Peninsular Ranges. (a) Photograph (SL4-203-7802). (b) Sketch map.

slope with small reflective platy chips lying parallel to the ground surface. However, for a 2-km distance between the two northernmost field sites, the stripe coincides with a steep southward-facing reflective slope in the southern margin of a light-colored granitic (tonalite) pluton. Farther south, a 15-km portion of the stripe (near A on fig. 4-8(b)) appears on the photographs to coincide with the western escarpment of the Sierra San Pedro Mártir. In the latter area, the light-colored stripe may be a manifestation of the same stratigraphic zone, or it may be due to reflection off a steep westward-

facing slope that possibly coincides with the western margin of a large mass of granitic rock underlying much of the sierra (the largest stippled area in fig. 4-8(d)). Thus, although evidence suggests that the light-colored stripe defines the distribution of a single stratigraphic zone, it is not known that this condition exists along its entire length. Field studies at additional localities along the stripe are required to resolve this question.

The recognition that the stripe is related to a stratigraphic unit provides new and extremely valuable information on the regional stratigraphy and structure



in the prebatholithic rocks. For the first time, it appears that a single stratigraphic zone can be traced from a region west and northwest of the San José pluton, where the age and general structural characteristics are fairly well known, into a little-explored area southeast of the pluton. Northwest of the pluton, the light-colored stripe is part of a section known from the work of Silver

et al. (ref. 4-5) to be part of the Alisitos formation of upper Lower Cretaceous age. In reference 4-5, it was shown that this section can be traced from the Pacific coast just south of the Agua Blanca Fault zone southeastward for 110 km to the San José pluton. Little information exists for the area southeast of this point. The trace of the light-colored stripe now suggests that, east

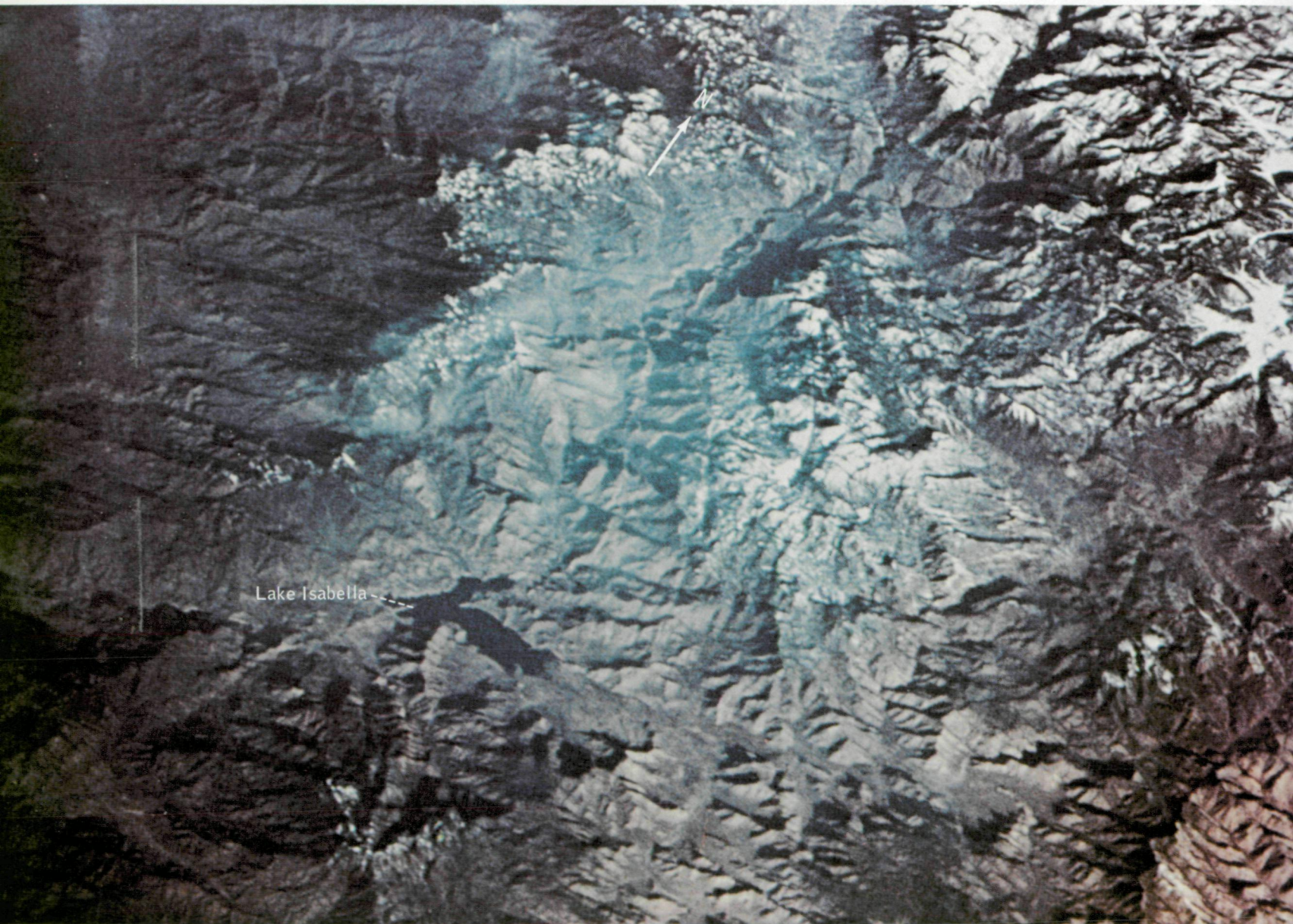


FIGURE 4-7.—Fracture patterns in the granitic rocks of southern Sierra Nevada around Lake Isabella (SL4-203-7787).



(a)

FIGURE 4-8.—Northern Baja California. (a) Photograph (SL4-197-7428). (b) Trace of linear features A (light-colored stripe) and B and the intervening region of arcuate patterns. Small X's denote locations of ground study. (c) Overview of the Agua Blanca Fault zone and associated fractures. (d) Principal sharp linear features and several prominent plutons (stippled). Lines are dashed where defined only by vague color change or where continuity is probable but uncertain.

and southeast of the pluton, the Alisitos formation swings abruptly to a more southerly trend and can be projected with reasonable confidence for another 55 to 60 km parallel to the trend of the Sierra San Pedro Már-

tir. This projection, however, should be tested by more extensive ground observations, particularly concerning the validity of the identification of the light-colored stripe as the trace of a single stratigraphic zone.

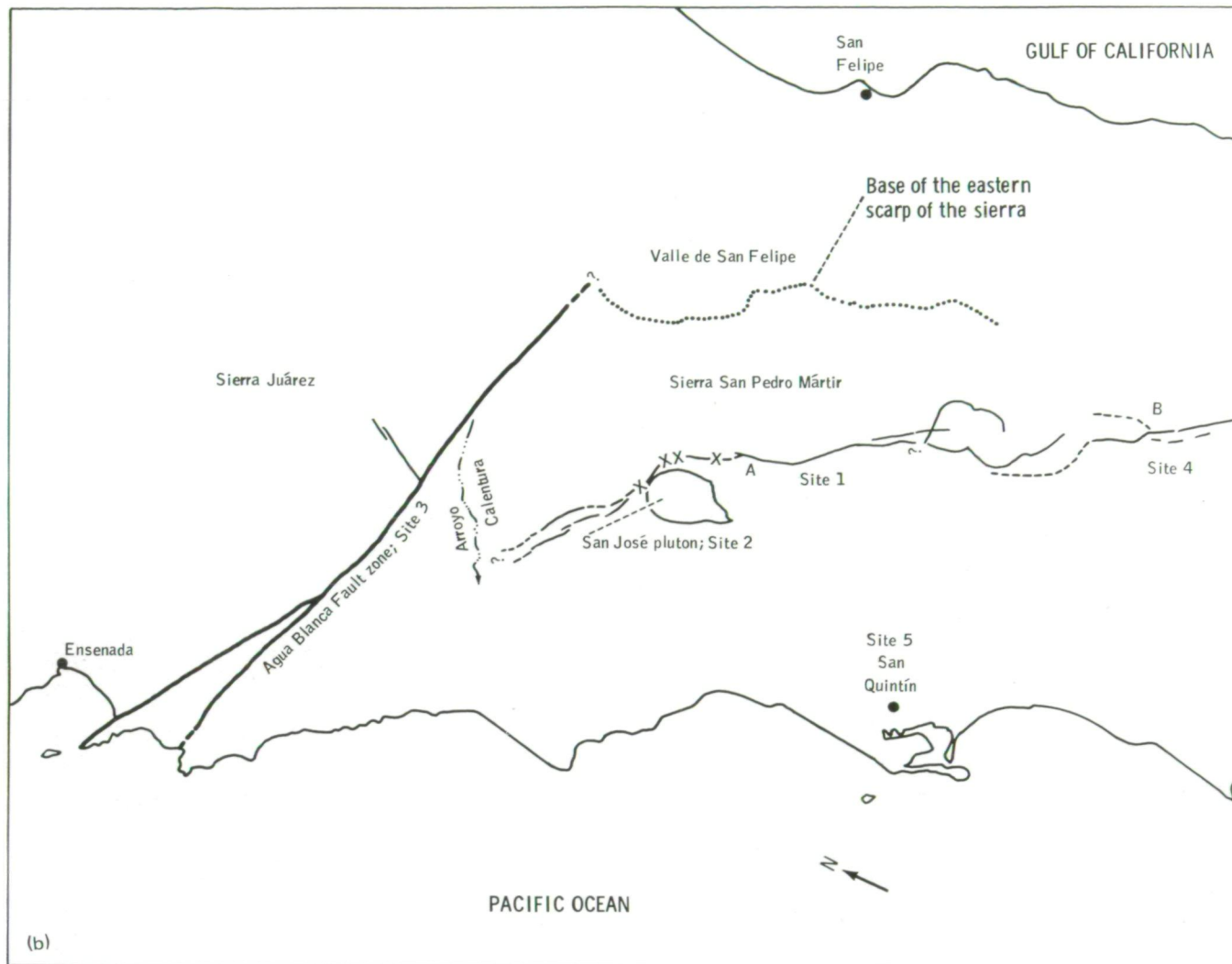


FIGURE 4-8.—Continued.

Near the San José pluton and in much of the area to the west and northwest, the Alisitos strata are known to be tightly folded, but the structure of this region has not been mapped. Near Arroyo Calentura, the occurrence of two light-colored stripes may be a manifestation of this folding. Folding may also account for the apparent discontinuity of the stripe east of the San José pluton. Recognition of the stripe has thus provided a geologic feature that can be mapped and used to decipher the complex structures of the region.

At feature B on figure 4-8(b) is the northernmost and least well defined portion of a major linear feature. Although the trend of this linear is parallel to and along

the projected extension of the light-colored stripe (A), it is separated from the stripe by a 25-km-long area dominated by complex arcuate rather than linear patterns. The photographic coverage of the linear feature at B did not result in new information on the nature or the structural or stratigraphic relationship of the feature to the light-colored stripe.

Recognition and mapping of igneous intrusive bodies.— The crewmen were asked to describe and photograph igneous intrusive masses (plutons) with particular emphasis on their size and distribution and their relationship to layering in the surrounding rocks. The San José pluton (figs. 4-8(a), 4-8(b), and 4-8(d)) served as a

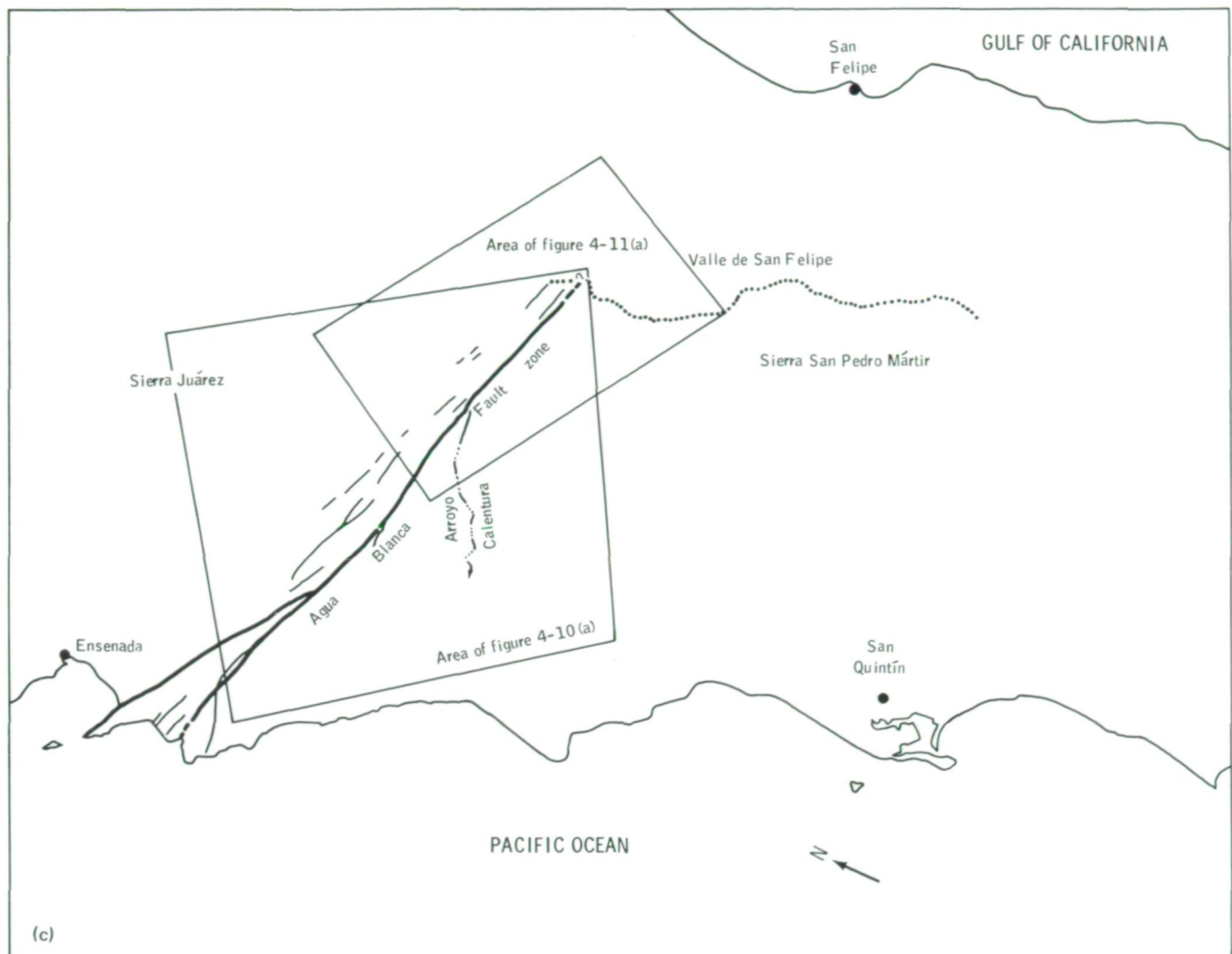


FIGURE 4-8.—Continued.

readily visible and identifiable reference. Other plutons are also visible on many photographs, yet comparatively few of the plutons known to exist are actually recognizable. However, the crewmembers have emphasized that the plutons, especially the San José pluton, were much more clearly visible to the naked eye than they are in the photographs.

The identification of plutons on Skylab photographs appears to be dependent on Sun angle, density of vegetative cover, and atmospheric clarity. An oblique view of an area also may aid or hinder the identification of plutons. Arcuate patterns associated with known or possible plutons are shown in figure 4-9(a), a Nikon

300-mm oblique photograph taken in the early morning. These patterns have been traced on the sketch map in figure 4-9(b). The plutons are revealed principally by their topographic expression enhanced by the low Sun angle. The color and the albedo contrast between the plutons and their surrounding rocks are subdued, partly because illumination is not uniform at a low Sun angle and partly because, under these lighting and viewing conditions, vegetation is especially effective in masking color variations.

Contrast figure 4-9(a) with figure 4-8(a), which is a near-vertical Nikon 55-mm photograph taken at a high Sun angle (about 11:30 a.m. local time). Color and

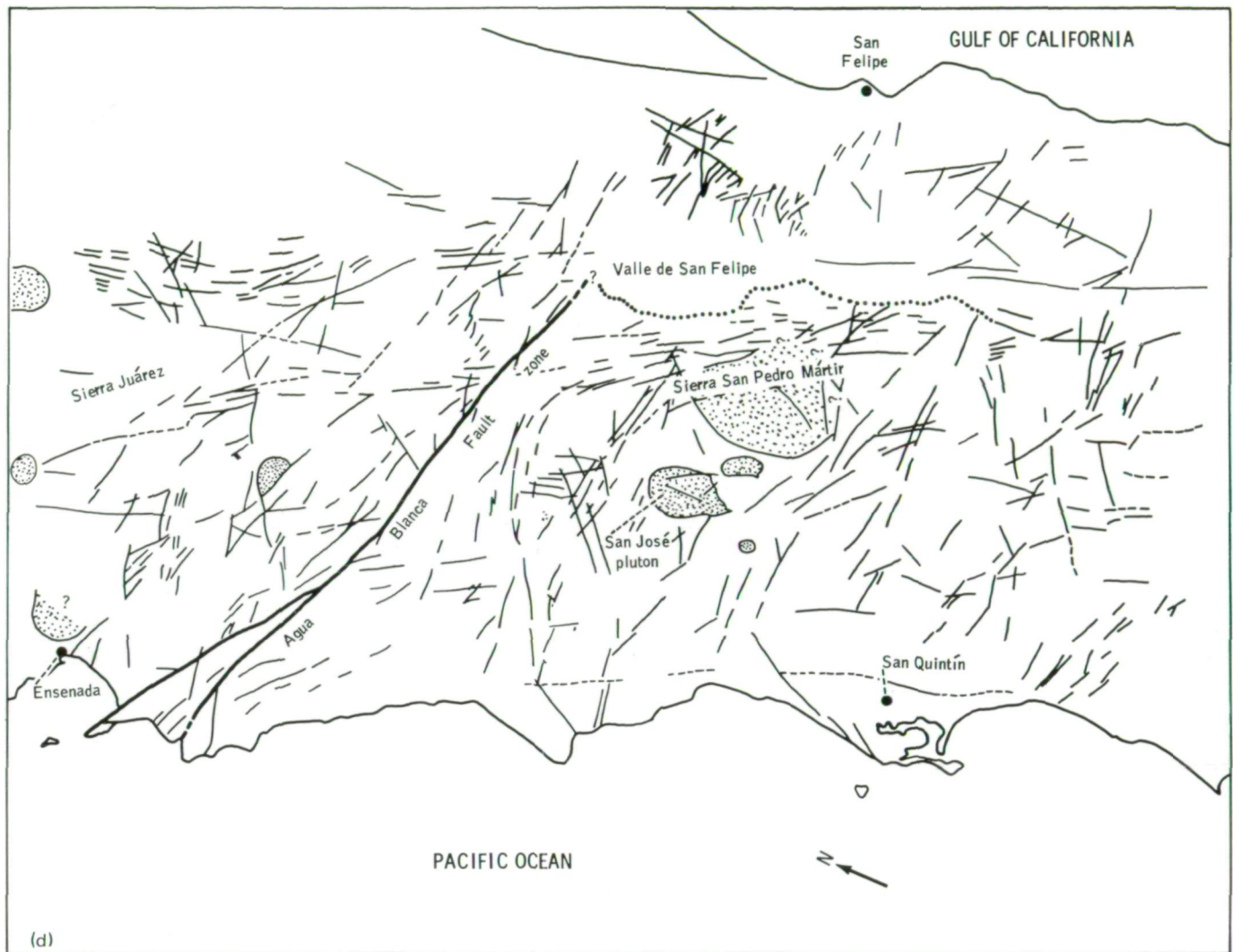


FIGURE 4-8.—Concluded.

albedo contrast are enhanced in the latter photograph, but topographic expression is less pronounced. Several prominent plutons recognized in figure 4-8(a) have been outlined in figure 4-8(d). The San José pluton and a smaller pluton several kilometers to the southeast are strikingly visible in figure 4-8(a), principally because of their high albedo. Unlike the plutons visible in figure 4-9(a), these two bodies become less visible (although still distinct) at low Sun angles. Thus, the ideal Sun angle for satellite observation and photography of plutonic bodies varies, depending on whether the bodies are best distinguished by their topographic ex-

pression or by their color and albedo contrast with adjacent rocks.

Many more plutons are known to exist in the area shown in figure 4-8(a) than are indicated on figure 4-8(d). Some can be distinguished vaguely on the photograph, but many cannot. Although the effect of vegetation is minimized by the high Sun angle and the near-vertical view, vegetation still is an important factor in masking color and albedo contrast between the plutons and their adjacent rocks. In addition, atmospheric haze has probably reduced both spatial resolution and color and albedo contrasts. In the absence of clouds, the

effects of haze are not obvious. The ability of the crewmembers to see plutons more clearly than they appear on the photographs is due to an observer's ability to mentally compensate to some degree for obscuring effects such as haze and shadows.

Despite the difficulties in recognizing many plutons on the Skylab 4 photographs, it is clear from figures 4-8(a), 4-8(d), 4-9(a), and 4-9(b) that a combination of low- and high-Sun-angle photographs and visual observations could contribute significantly to reconnaissance geological mapping in unexplored areas, particularly where conventional aerial photographic coverage is not available. For problems requiring maximum color and albedo contrast, high-Sun-angle vertical-view photographs are essential.

Agua Blanca Fault zone and associated fractures.—

The greatest part of the crew's effort in northern Baja California was directed toward the Agua Blanca Fault zone (site 3). In addition to general observation and photography of the fault zone, the investigation of the site involved two principal questions. How far east can the fault be traced? Can offset streams or other features indicative of the relative motion on opposite sides of the fault be recognized by the crew or on photographs? The astronauts' verbal commentary concentrated on (1) the striking physiographic expression of the fault — especially the appearance of a "k" shape defined by the intersection of Arroyo Calentura with a canyon from the north and a canyon along the fault trace (figs. 4-8(a) and 4-10(a)); (2) the eastern limit of the fault zone— whether or not it crosses Valle de San Felipe and reaches the Gulf; and (3) suggestions of offset along the fault zone. Twenty photographs with the fault as the principal target were obtained by the crewmen.

In figures 4-8(c), 4-10(b), and 4-11(b), the known trace of the fault breaks as mapped by Allen et al. (ref. 4-6) has been drawn, together with some of the more prominent subparallel lineaments. The correspondence between the fault trace and the topography is obvious.

The astronauts looked repeatedly but saw no evidence that the fault zone crosses the Valle de San Felipe to the Gulf of California. Several excellent photographs (e.g., fig. 4-11(a)) reveal only faint lineaments east of the end of the mapped trace of the fault zone, and most of these lineaments stop at the western edge of the valley. Physiographic evidence of a major fault appears to terminate at the end of the mapped trace of the fault zone. Thus, the photographs and crew observations

offer no contradiction to the ground-based interpretation that the fault zone ends west of the Valle de San Felipe. The objectives of this aspect of the site 3 study were very successfully completed.

An important goal at site 3 was to determine whether or not small-scale fault features such as offset streams could be recognized from Skylab. The commander (at 18:46:07 GMT, Dec. 7, 1973) interpreted the "k" pattern as a "cross-fault" offset in a left-lateral sense by movement on the Agua Blanca Fault zone (fig. 4-10). He also inferred (02:31:24 GMT, Jan. 20, 1974) a left-lateral offset of a stream crossing the fault zone just west of the "k." However, detailed ground studies of this region by Allen et al. (ref. 4-6) have shown that the direction of relative motion on the fault zone is right-lateral. The suggested left-lateral stream offset described by the commander is indicated in the rectangular area outlined in figure 4-10(b). In figure 4-10(a), a drainage (A, fig. 4-10(b)) enters the fault zone from the northeast, appears to be diverted approximately 4 km southeastward along the fault zone (B), and then turns abruptly southwestward away from the fault. Field data have shown that the drainage is actually diverted approximately 6 km northwestward (C) along the fault zone (fig. 4-10(b)). A low drainage divide (not distinguishable on the photograph) would not permit the drainage from northeast of the fault to connect with the drainage that intersects this fault at B on figure 4-10(b).

Two points should be emphasized concerning the use of offset streams as evidence of fault motion. First, such offsets are generally small-scale features. Second, reliable interpretation of relative motion from such offsets requires observation of numerous offsets with consistent direction. Sharp jogs in drainage traces may result from processes other than fault motion and may even be in the direction opposite that of the true relative motion. The true relative fault movement is indicated only when there is a pattern of many consistent offsets. Allen et al. (ref. 4-6) observed numerous right-lateral stream offsets along much of the length of the Agua Blanca Fault zone, but the offsets are generally on the order of tens to hundreds of meters. One offset identified by Allen et al. can be seen, although in a distorted and unconvincing view, in figures 4-10(a) and 4-10(b) (the feature labeled "O.S."). Fault offsets of the magnitude of the Agua Blanca Fault zone can be identified by crewmen and in satellite-based photographs. The crew emphasized that the details along this fault zone

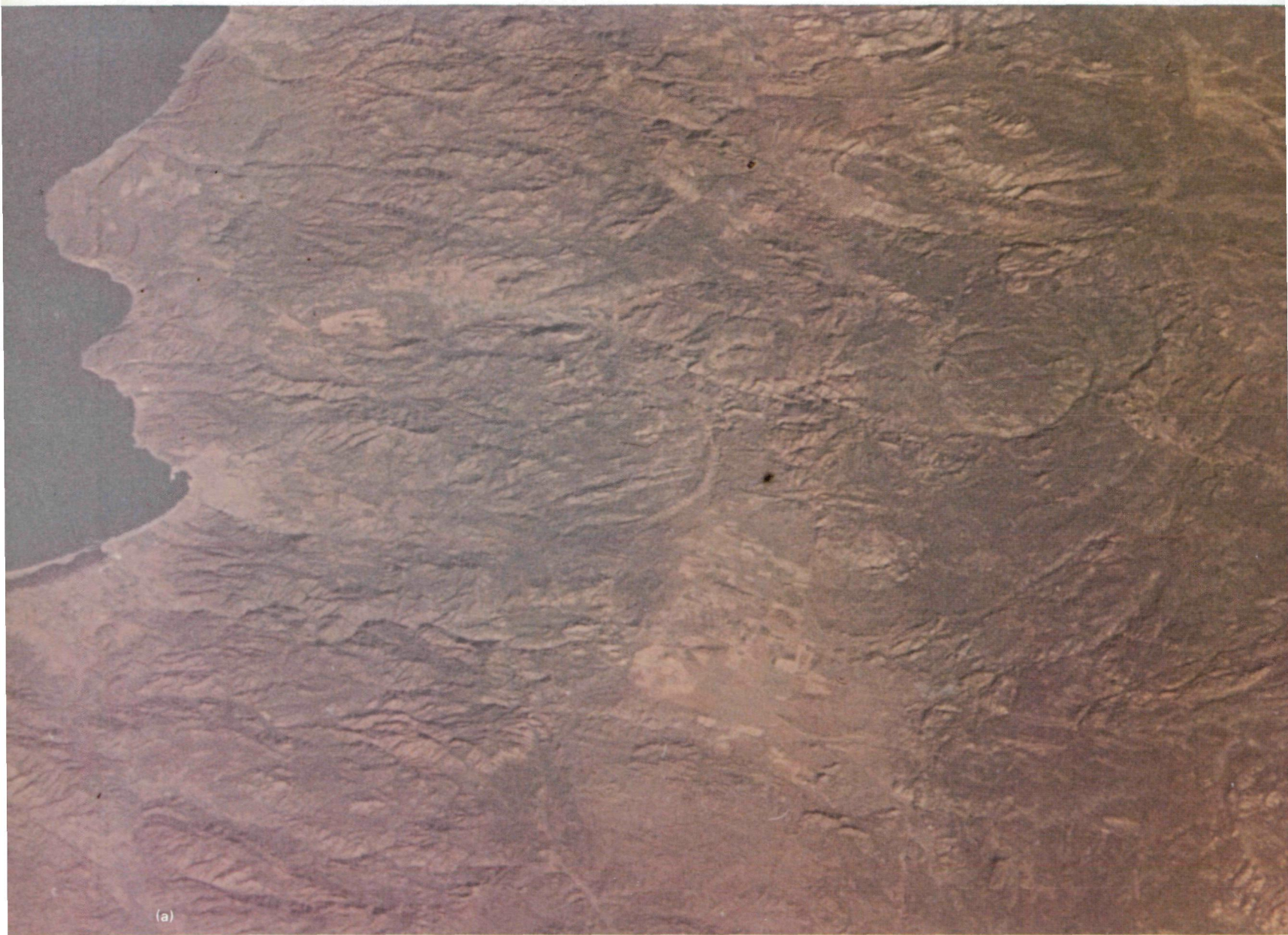


FIGURE 4-9.—Arcuate features associated with known or possible granitic intrusive bodies in northern Baja California. (a) Photograph (SL4-203-7808). (b) Sketch map.

were more distinct to the naked eye than in the photographs. The most effective photographs for study of fault features are those taken as vertical or slightly oblique views perpendicular to the length of a fault zone, particularly at low Sun angles.

In summary, the Skylab 4 crew commentary and the handheld-camera photographs have shown that

satellite-based observations and photographs have definite potential for discovery and reconnaissance mapping of faults of the magnitude of the Agua Blanca Fault zone and associated small structures.

Fracture patterns in northern Baja California.—The Skylab 4 photographs are particularly useful in providing the basis for an integrated analysis of the fracture



systems in northern Baja California. Figure 4-8(d) is a sketch map of the principal sharp linear features that are visible in figure 4-8(a), a photograph of most of northern Baja California. Several prominent plutons visible in figure 4-8(a) are traced in figure 4-8(d). The sketch map reveals the principal fault and fracture patterns in the region. With similar photographs of the entire peninsula, a photolineament map could be constructed that would be extremely useful in geologic analysis.

Nearly all the linear features in figure 4-8(d) are part of three well-defined sets: (1) a set that is subparallel to the Agua Blanca Fault zone and generally strikes $N 70^{\circ}$ to 90° W but extends to $N 80^{\circ}$ to 90° E; (2) a set that strikes $N 25^{\circ}$ to 35° W parallel to the high mountain ranges and to the axis of the peninsula; and (3) a less well developed set that strikes $N 30^{\circ}$ to 55° E. The remaining lineaments generally strike $N 60^{\circ}$ to 80° E.

The linear set that strikes $N 70^{\circ}$ to 90° W tends to be concentrated in discrete zones such as those just north and south of the San José pluton. North of the Agua Blanca Fault zone, some of the linears have been previously identified as faults and others are probably major fractures or fracture zones without significant offset. Major faults that parallel this trend have not been recognized south of the Agua Blanca Fault zone.

The $N 25^{\circ}$ to 35° W set is very strongly developed along and parallel to the eastern escarpments of the Sierra Juárez and Sierra San Pedro Mártir. East and west of this zone of maximum development, parallel lineaments are sparse. Some of these linears may reflect major faulting parallel to the escarpments.

A series of aligned short features suggests the possibility of a major throughgoing linear feature that extends $N 30^{\circ}$ W from just east of the largest pluton across the Agua Blanca Fault zone and to the northern

edge of the map. This zone is especially striking in the photograph (fig. 4-8(a)); if it is continuous, it suggests that no major lateral offset has occurred along the eastern part of the Agua Blanca Fault zone since the development of this N 30° W structure.

The N 30° to 55° E set is sparsely developed throughout the area and is the least consistent in trend of the three main sets. Neither it nor the N 60° to 80° E set is parallel to any other obvious geographic or geologic features in the area. At present, there is no evidence of major faulting parallel to these fractures.

Sierra Mazatan, Sonora, Mexico

The Sierra Mazatan in Sonora was selected as an important geological subject for study from Skylab because it is topographically distinctive, geologic information is sparse, and detailed topographic maps and aerial photographs are not available. The small mountain range is composed almost entirely of intensely deformed granite that can be distinguished chemically and structurally from adjacent rocks. The crewmen were asked to consider the possibility that the entire

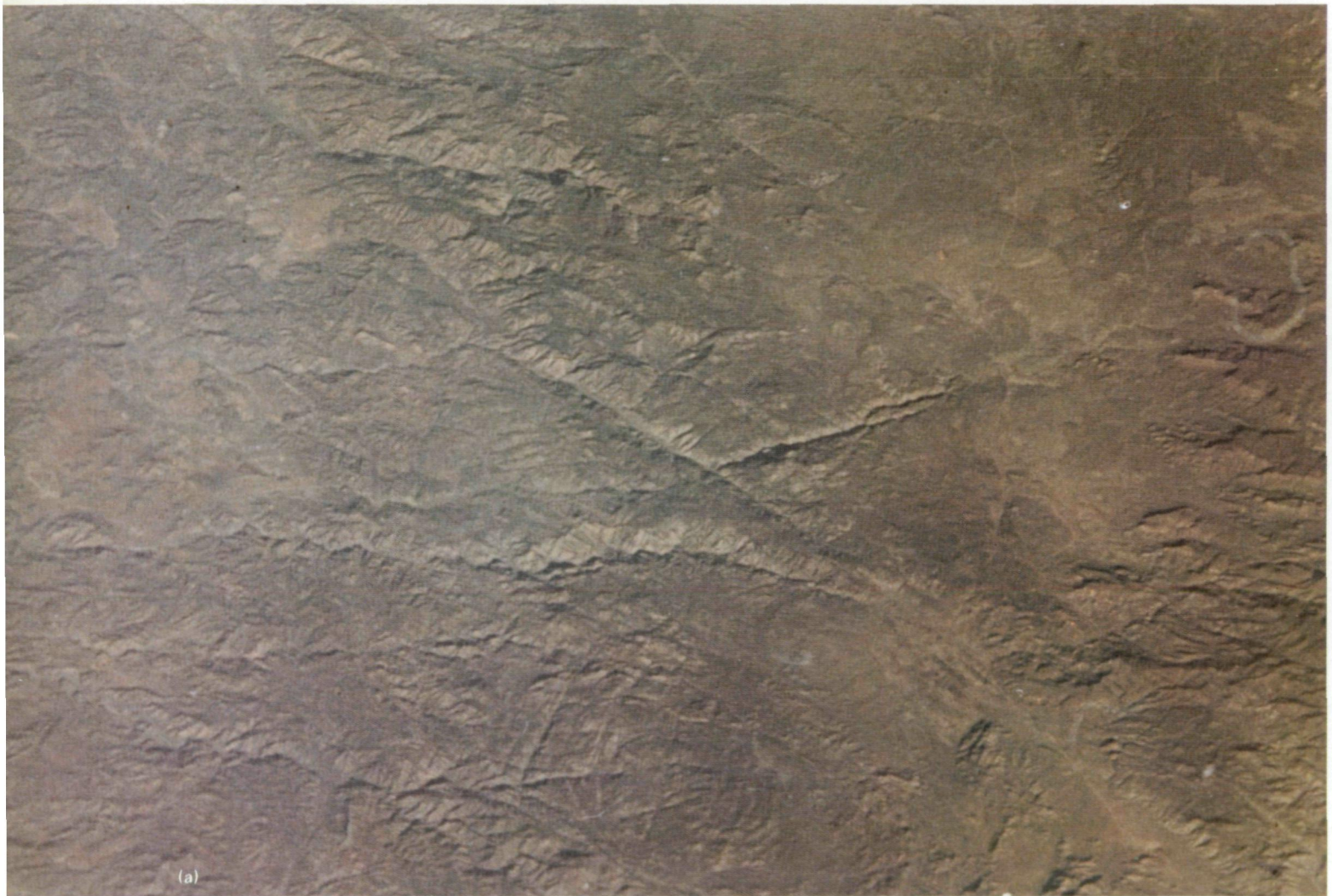


FIGURE 4-10.—Central and eastern portions of the Agua Blanca Fault zone. Letters in inset are explained in text. (a) Photograph (SI4-203-7809). (b) Sketch map.

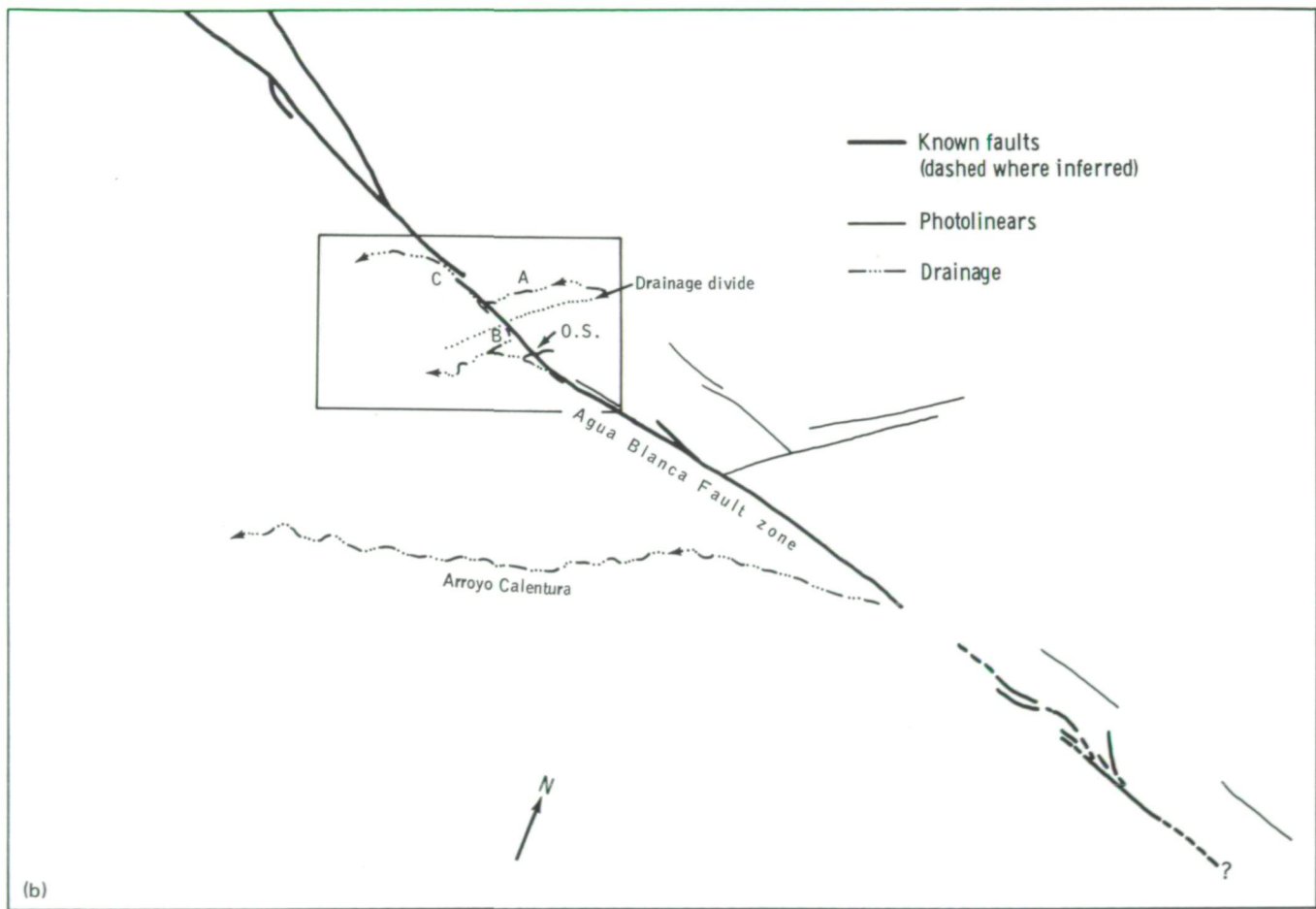
mountain range may have been brought to its present site by profound faulting. They were requested to observe and photograph linear features that might represent such fault systems and to search in the mountainous region surrounding Sierra Mazatan for topographic characteristics similar to those of the range.

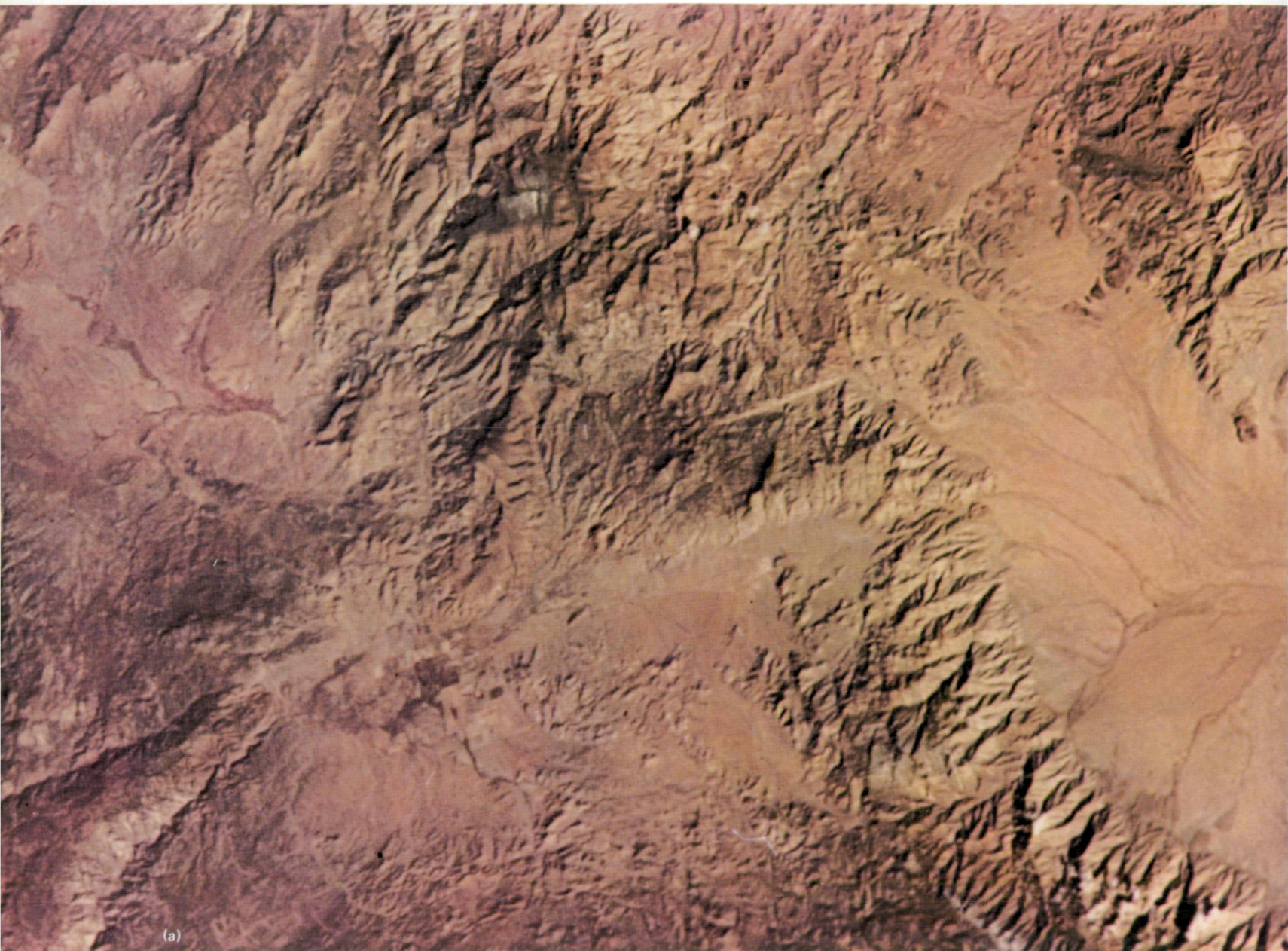
The Sierra Mazatan region was thoroughly photographed, without commentary, by the Skylab 4 crewmen. Inspection of the photographs (e.g., fig. 4-12(a)) has not revealed features similar to Sierra Mazatan within a radius of 50 km. In regard to major fault systems, the Skylab 4 photographs and postmission field studies have identified a north-trending linear feature that passes a few kilometers east of Sierra Mazatan (figs. 4-12(a) and 4-12(b)). This feature may represent a suture structure and can be traced for more

than 100 km south toward Ciudad Obregon and about the same distance to the north. Further field studies are necessary to determine whether this is a significant structural feature related to the origin of Sierra Mazatan.

Northwestern Sonoran Coast Fault Zones

The evolution of the continental margin in northwestern Sonora has been investigated by the senior author for several years. Along the coast between Puerto Libertad and Bahía Kino (fig. 4-13), northwest-trending faults that parallel the coast have been mapped. Associated with the region of faulting is the termination of the older crust (Precambrian and



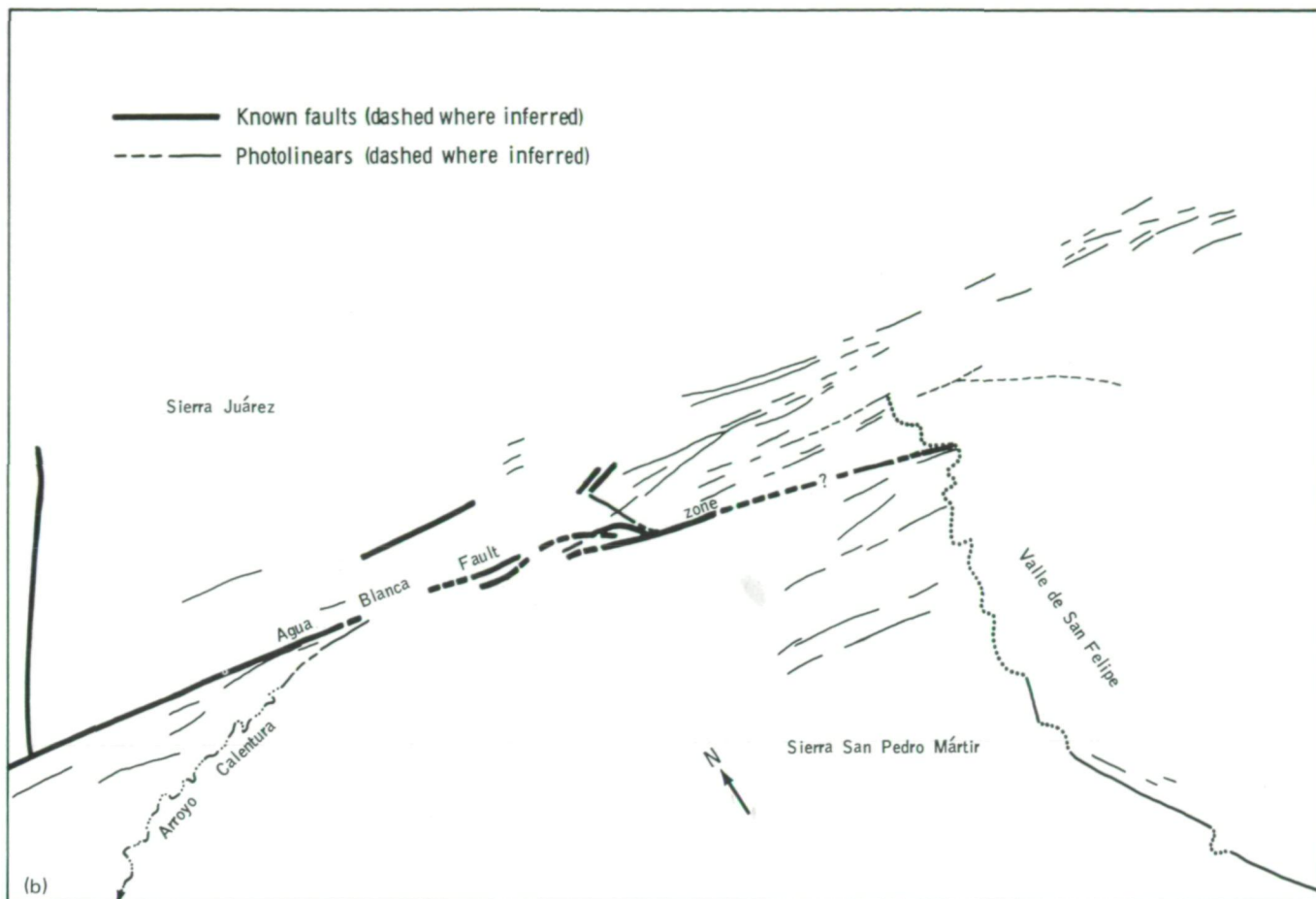


(a)

FIGURE 4-11.—Known faults and parallel lineaments at the eastern end of the Agua Blanca Fault zone. (a) Photograph (SL4-193-7190). (b) Sketch map.

Paleozoic rocks) against younger crust (middle and late Mesozoic volcanic and granitic rocks). The Skylab 4 crewmen were requested to search for linear trends in the coastal desert as possible expressions of major fault zones, both active and inactive, that might have modified the continental margin.

An excellent folio of photographs of the Sonoran coast was obtained. Analyses of these photographs have confirmed the presence of throughgoing fault zones. In figure 4-13(b), the general dimensions of the fault zone are visible from north of Puerto Libertad to south of Bahía Kino. In figure 4-14, numerous linear features are



visible in the bedrock that forms the Sierra Seri and Sierra Bacha.

The photographs and ground studies reveal that, in general, there is little evidence of recent fault movement and displacement of the surface. Only at a point just north of Puerto Libertad and east of the tied island of Punta Tepopa were there possible suggestions of active faults. Several major and many minor drainages cross the fault zone without indication of fault offset. The principal fracture systems offset middle (?) to late (?) Tertiary volcanic and nonmarine sedimentary rocks. It is inferred that movement along the major fractures of these zones occurred in the Miocene or Pliocene with perhaps some recent reactivation locally.

The evidence indicates that the coastal structural zone developed before the establishment of the presently configured Gulf of California, which is estimated to be 4 to 5 million years old. The structural zone may be related to the development of a protogulf, a series of

elongate marine basins that preceded the throughgoing Gulf of California rift system (ref. 4-7). The sense and magnitude of displacement on the structural zone has not yet been established. As indicated in figure 4-13(b), the fractures parallel the presently known southwestern limit of the older continental crust and are approximately 30 km from the nearest Precambrian rock exposures. An important possibility is that the fractures identified in the Skylab photographs constitute part of a late Tertiary strike-slip fault zone along which two dissimilar crustal blocks have been juxtaposed. This would imply a possible correlation with early movements on the larger San Andreas/Gulf of California transform fault system.

In summary, the visual observations and photographs have provided an integrated view of the Sonoran coastal fault system that emphasizes its regional significance and that will guide future research programs.



(a)

ORIGINAL PAGE IS
OF POOR QUALITY

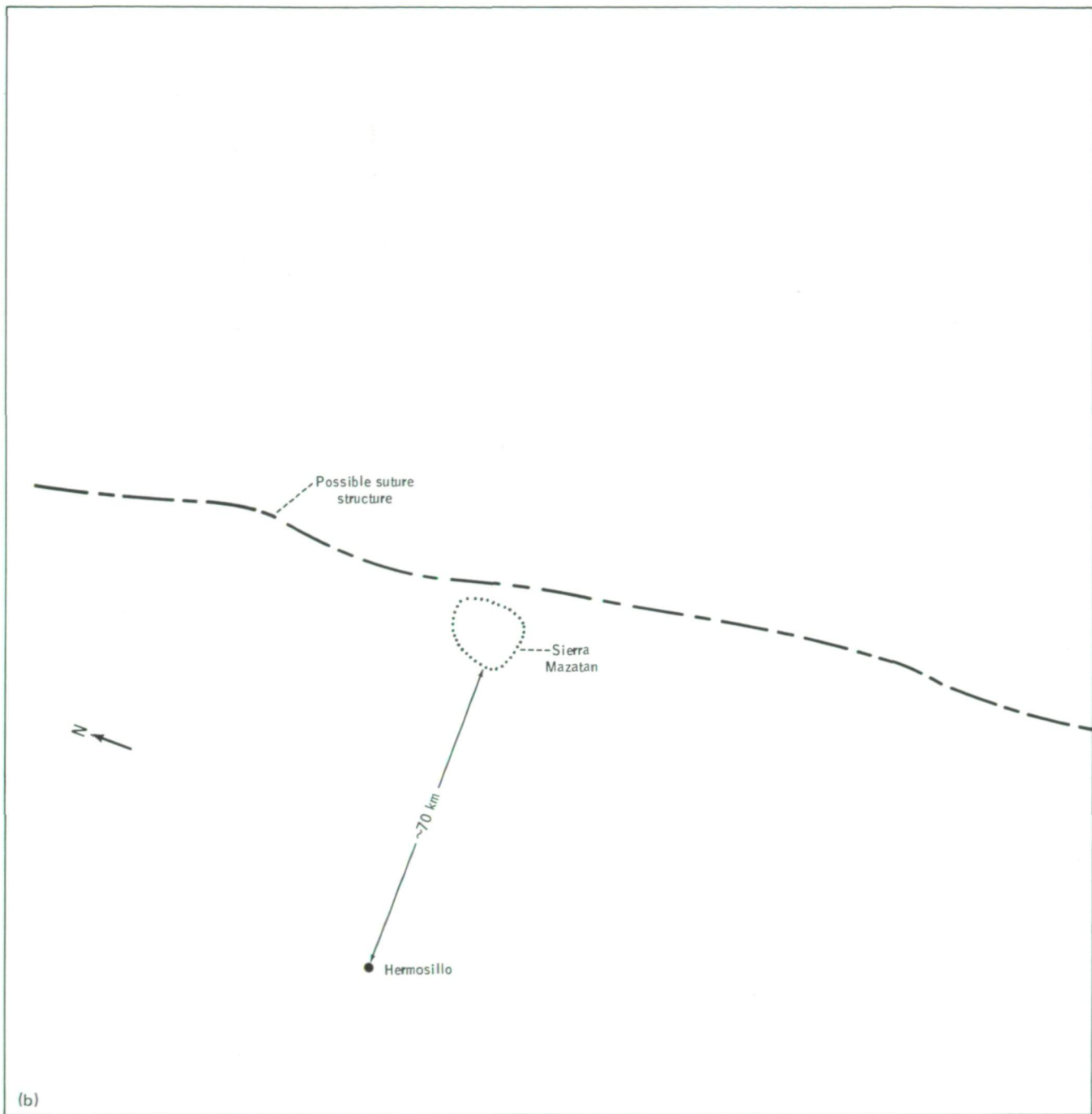


FIGURE 4-12.—The Sierra Mazatan in northwestern Sonora, Mexico, an anomalous mountain range of deformed granite the structural position of which may be related to a possible north-trending fault suture to the east of it. (a) Photograph (SL4-141-4398). (b) Sketch map.



(a)



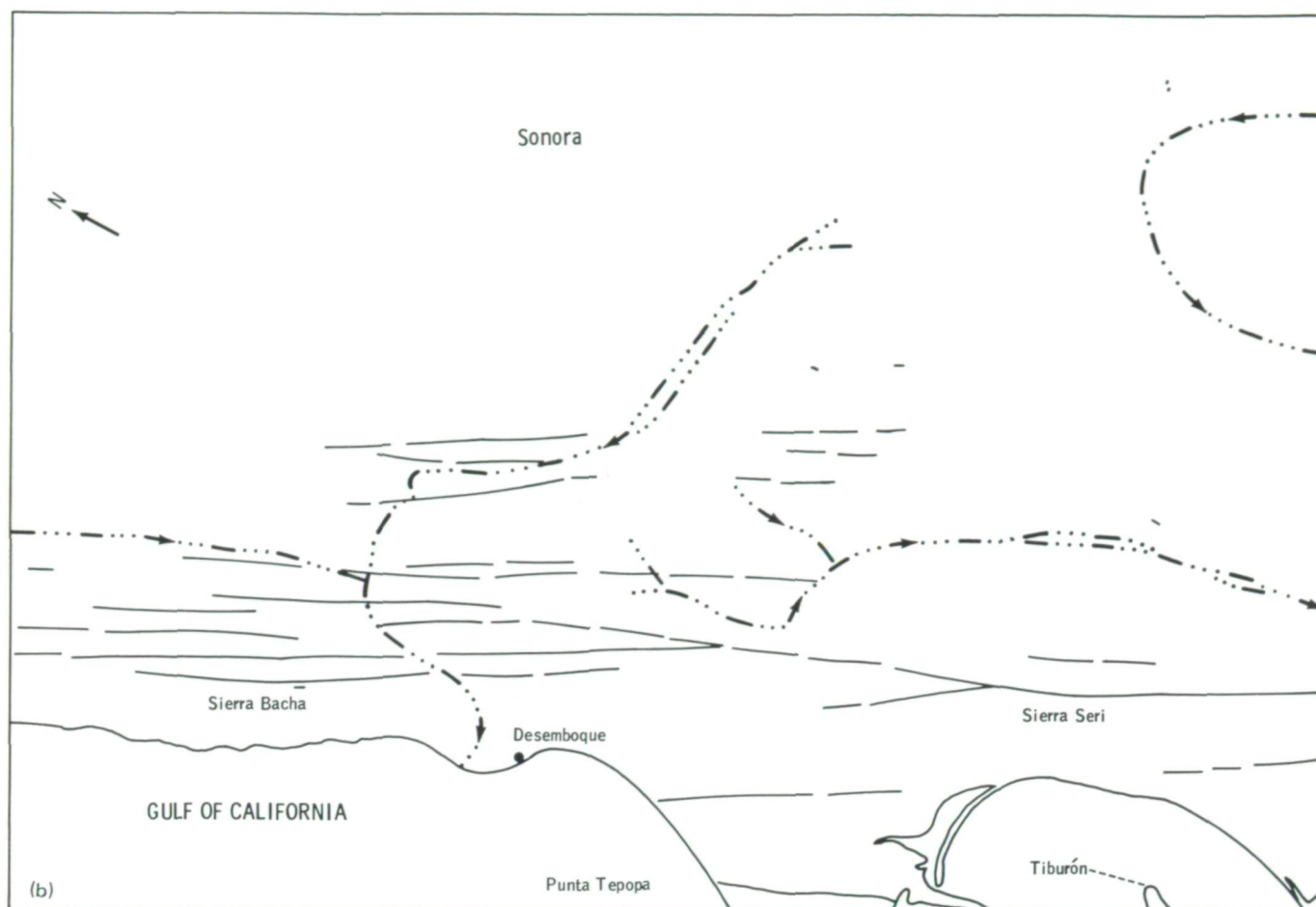
(a)
FIGURE 4-14.—The coastal fracture zones of Sonora, Mexico. (a) Photograph (SL4-194-7236). (b) Sketch map showing details of the coastal fracture zones of northwestern Sonora, Mexico.

Sierra del Alamo, Sonora, Mexico

The color contrasts in the Sonoran desert strikingly reflect the diversity of geologic formations and rock types exposed in the region, despite the homogenizing effects of desert varnish. For this region, the Skylab 4

crewmembers were asked to observe and photograph distinct color and textural units in the Sierra del Alamo and adjacent ranges to the south.

Analysis of one of these photographs (fig. 4-15) revealed the occurrence of previously unrecognized Precambrian “basement” rocks south of Sierra del



Alamo in the northern and central region of Sierra Viejo. The dark zone adjacent to the granitic terrain was found to contain a variety of metamorphic rocks including granitic gneisses and metasedimentary schists. South of the granitic rocks, a complex structural belt of late Precambrian and early Paleozoic sedimentary rocks extends to the southern tip of the range. The combination of Precambrian and Paleozoic formations in the Sierra Viejo represents the most southwesterly extension of the North American craton (older crust) identified thus far (fig. 4-13(b)).

Arizona

The yield of observational data for the Arizona region, although less extensive than for the other study areas, included excellent photographs of the Colorado River system. The erosional features and the principal

structures of the Grand Canyon and the adjacent plateaus were captured by the astronaut photographers in a remarkable demonstration of man's ability to optimize an opportunity for obtaining unique photographic data of the Earth's surface. Two areas in Arizona to which the Skylab 4 handheld-camera photographs have contributed new geologic insight are discussed in the following sections.

Central Arizona.—Linear or arcuate features, due primarily to faulting, have been identified in the photographs of the central Arizona study area. Some of these features were known faults, some are extensions or connections of known faults, and some were previously unrecognized.

Of specific interest are the arcuate features. Conway (ref. 4-8) has mapped a system of northeast-southwest faults in northern Gila County, some of which swing around to the north to trend north-south. A very similar arcuate feature is one of the salient features of the

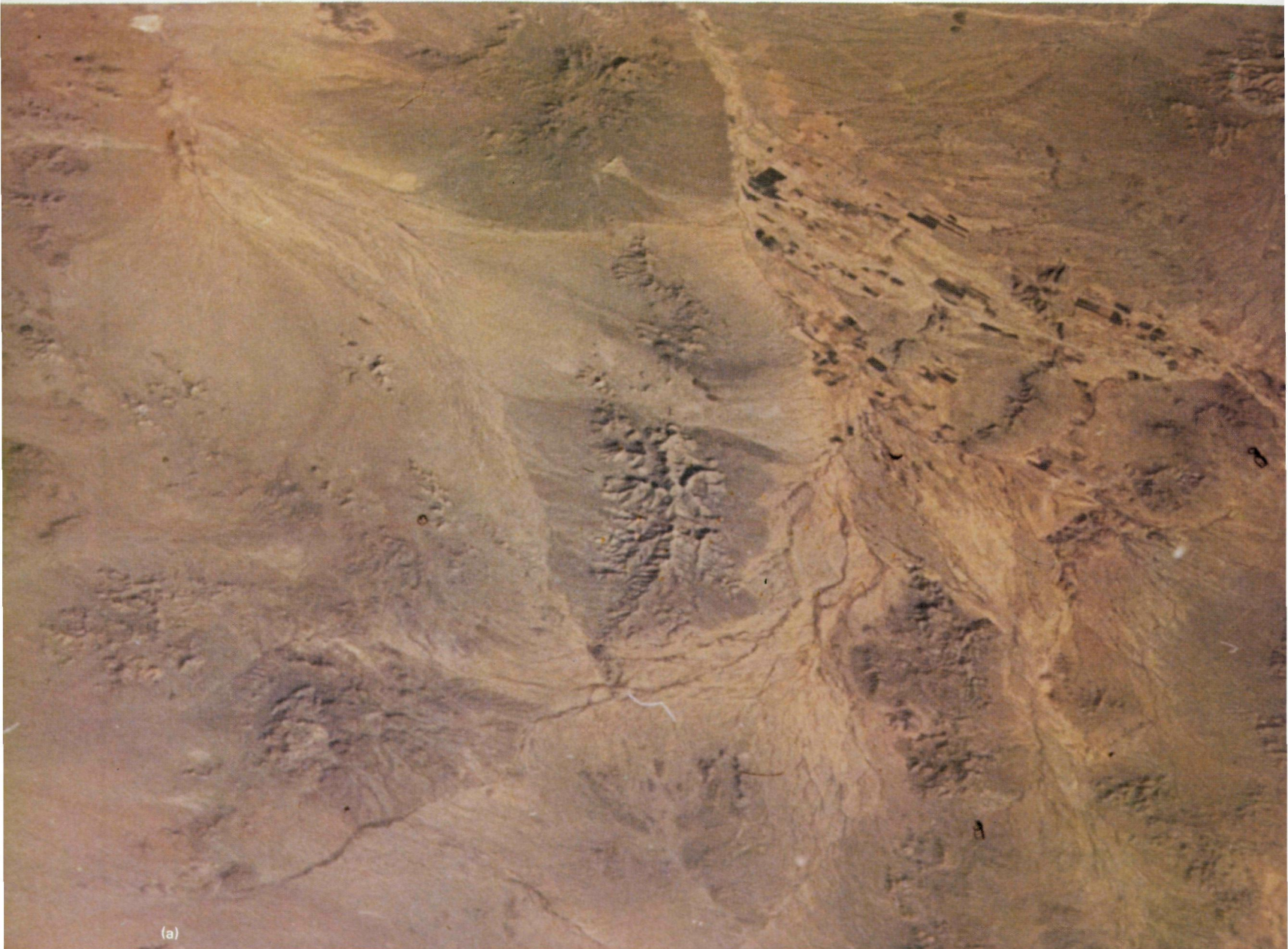
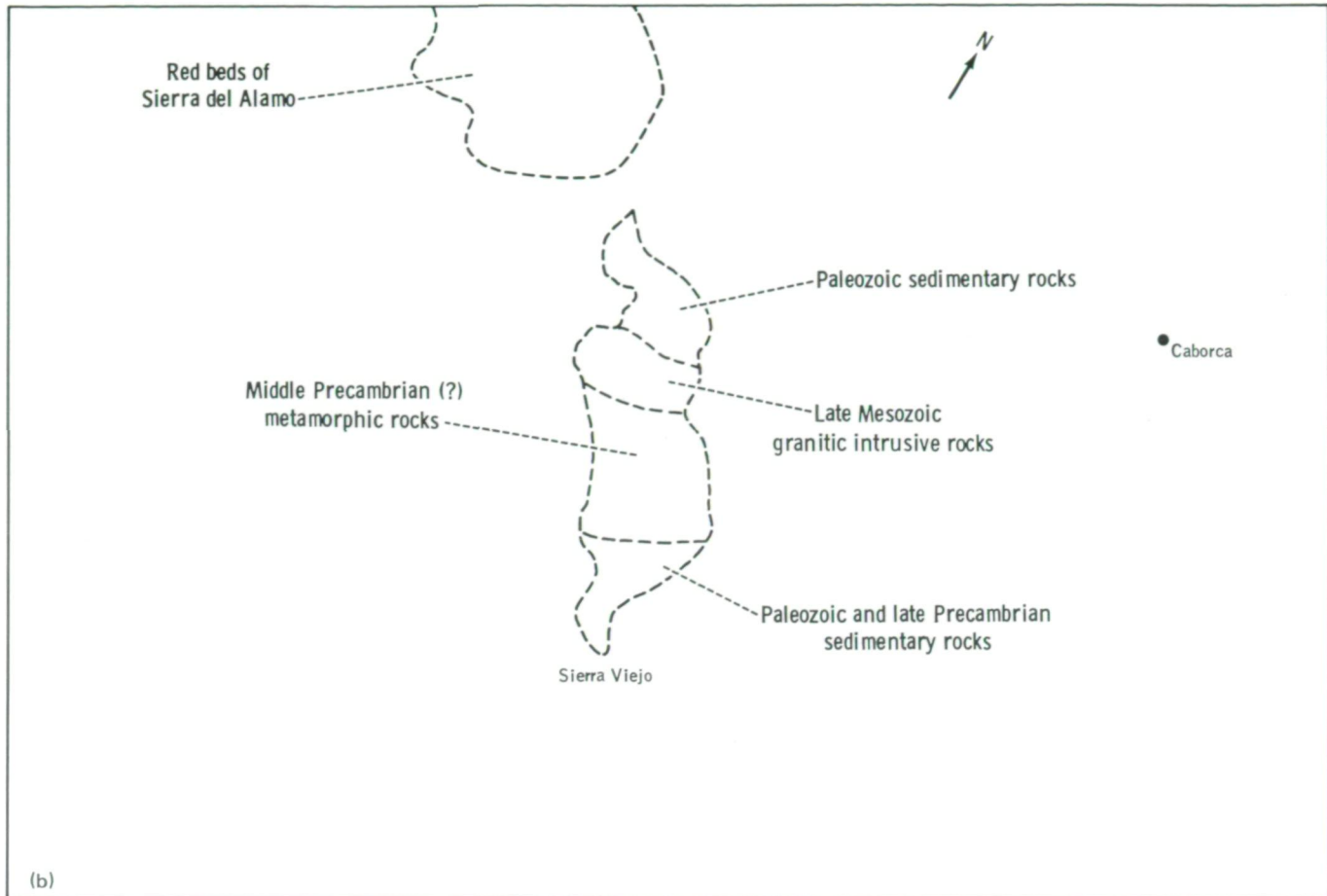


FIGURE 4-15.—Sierra Viejo in northwestern Sonora, Mexico. (a) Photograph (SL4-203-7821). (b) Sketch map showing geologic subdivisions.

northern Mazatzal Mountains (fig. 4-16). A part of this feature was earlier mapped (ref. 4-9) as an almost straight fault, the Deadman Fault. This entire arcuate feature is almost certainly a fault and probably of the same origin as the arcuate faults first identified only 32 km to the east by Conway. There are much weaker suggestions of other such arcuate features. Recognition in

the photographs of arcuate faults, and possible arcuate faults, in a much broader area than that in which similar features were first mapped is very exciting. Further search for and confirmation of these features in Skylab Earth resources experiment package (EREP) photographs is important; understanding such a distinctive regional fault system will have significant implications



for the nature of the tectonic regime in which this old portion of the Earth's crust was both formed and subsequently modified. Work is proceeding on this project.

In regard to Precambrian structures, the northeast-southwest grain was noted throughout the Sierra Ancha-Mazatzal Mountains area (fig. 4-16), thus confirming and clarifying what has been noted by many geologists over the years. The usefulness of the photographs in this regard is the identification of lineations in areas where detailed mapping has not yet been done. This will aid the future determination of the nature and extent of faulting. There are suggestions of continuation of faults only partly mapped in earlier studies.

Tertiary faulting in the Sierra Ancha-Mazatzal Mountains area has extensively modified the Precambrian terrain. These faults are more difficult to see in the photographs than the Precambrian structures but are nevertheless decipherable. One probable Tertiary

fault is newly identified in figure 4-16. This fault is a prominent linear feature that runs northwest-southeast for more than 24 km in the northern Mazatzal Mountains and is on trend with the central Verde Valley to the northwest. There are numerous other lineations of similar trend and probably of related Tertiary origin.

The understanding of Tertiary structure in this area is exceedingly important because it would provide clues to the nature of the profound transition from the thick, relatively undeformed Colorado Plateau crustal block to the much thinner, structurally complex Basin and Range crustal block. Understanding the nature of this transition is particularly important in understanding geologically recent crustal activities that have been (and still may be) modifying the southwestern North American crust and that have played an important role in the origin of some metallogenic processes.



(a)

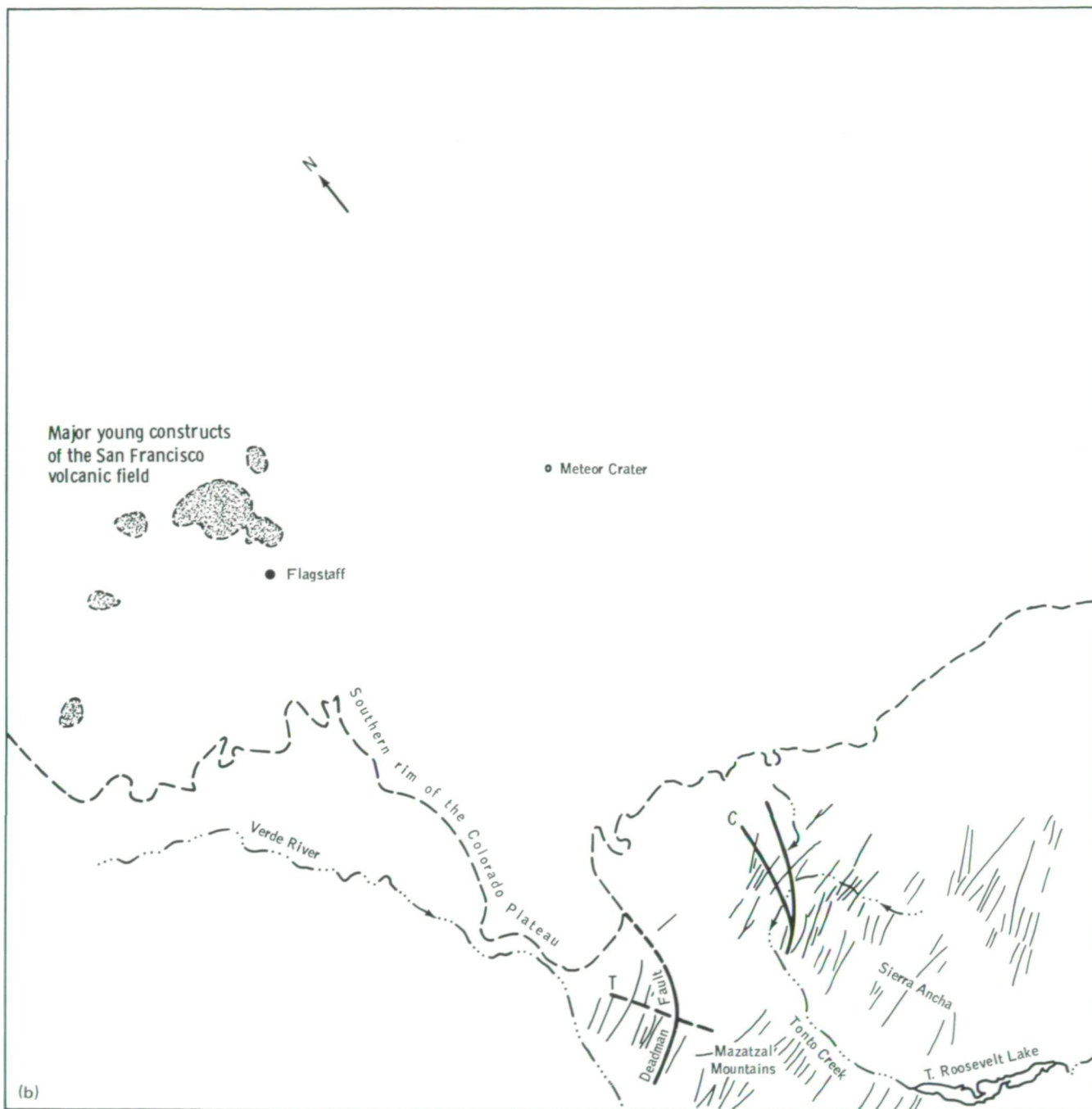


FIGURE 4-16.—The northern Sierra Ancha and the Mazatzal Mountains. (a) Photograph (SI4-142-4438). (b) Sketch map showing northeast-southwest structural grain and major northward-curving faults. The straight northeast-southwest segment of the Deadman Fault was mapped by Wilson (ref. 4-9), but the northward-curving extension is a new suggestion based on figure 4-16(a). Arcuate faults (C) were mapped by Conway (ref. 4-8), and a probable Tertiary fault (T) is parallel to the projected extension of the central Verde Valley.

Northern Arizona linear features.—Skylab 4 photographs of the Grand Canyon area of northern Arizona (figs. 4-16(a), 4-17, and 4-18(a)) are remarkable in clarity, resolution, and color contrast. The conditions that prevailed during photography (early to midafternoon winter Sun, excellent visibility, cloudless skies, and light snow cover at higher elevations (greater than 1525 to 1825 m)) combined to make these photographs unusually valuable to the geologist. Although the Grand Canyon was extensively photographed by the Skylab 4 astronauts, the other photographs do not compare in quality.

The light snow cover is particularly helpful in enhancing some linear features and in providing contrasts both in elevation and in vegetation cover. For example, the unforested areas and drainage bottoms are sharply defined in white. Abundant lineations, which reflect faulting, jointing, and monoclinical flexing (all only partly mapped) are spectacularly highlighted on the photographs. Some structural features, however, are not visible under the conditions in which these photographs were taken. In the summer or in morning light, other lineations might appear and some that are visible in these photographs would disappear.

All lineations suggestive of jointing, folding, or faulting were determined from analyses of figures 4-16(a), 4-17, and 4-18(a) and were compiled on topographic maps. As an example, figure 4-18(b) was compiled from a Skylab 4 photograph (fig. 4-18(a)) and illustrates the technique and the detail in which throughgoing lineation systems can be seen. Only a few of these features correlate with structures shown on the geologic map of Arizona (ref. 4-10). These include a few discontinuous major north-south faults that are irregular in trend. In a recent structural study of a central portion of this area (fig. 4-18(b)), Lucchitta (ref. 4-11) has mapped numerous north-south faults. The lineaments traced from the Skylab photograph correspond well with the faults shown on this map.

Lucchitta hypothesized that the straight portion of the Grand Canyon from the mouth of Kanab Creek (A, fig. 4-18(b)) southwest to the first major southward bend of the river (B) is a structurally controlled segment. He also noted on a Landsat image a zone of lineaments that trend northeast. A major discovery from analysis of the Skylab photograph (fig. 4-18(a)) is a pronounced set of lineaments along, and particularly on trend to the southwest of, the straight segment of the canyon. This documentation supports Lucchitta's sug-

gestion of structural control for this segment of the river.

Shoemaker et al. (ref. 4-12) compiled a structural map of northern Arizona (fig. 4-19) from published sources and Landsat imagery. A mosaic of lineaments from the photographs was prepared from figures 4-16(a), 4-17, and 4-18(a) and generally there is good agreement between the two maps. As expected, many faults shown in figure 4-19 were not detected in the Skylab photographs. Conversely, a surprising number of Skylab photograph lineaments was found to be without analogs in figure 4-19. Skylab photograph lineaments that do not correspond to faults on the map by Shoemaker et al. are shown in figure 4-20. Most pronounced are the northeast-southwest lineations that are best shown in the western part of the Grand Canyon. Numerous faults of this trend are shown by Shoemaker et al. in the far eastern part of the Grand Canyon in and near the Bright Angel Fault system and farther south and east in the Mesa Butte Fault system, but the lineation system seen so clearly to the west in the Skylab photographs has essentially no fault representation on their map. The Skylab data show quite clearly a strong structural trend in near coincidence with, though perhaps displaced to the north of, a structural zone inferred by Shoemaker et al.

Fault offset has not been demonstrated on the newly discovered lineaments and, if present, may be very minor. Fault offset on the Sinyala Fault is only approximately 5 m on the bend of the river (attenuating upward to less than 1.5 m in the highest strata of cuts), but the fault is continuous for 48 km and profoundly influences topography (ref. 4-13, p. 331).

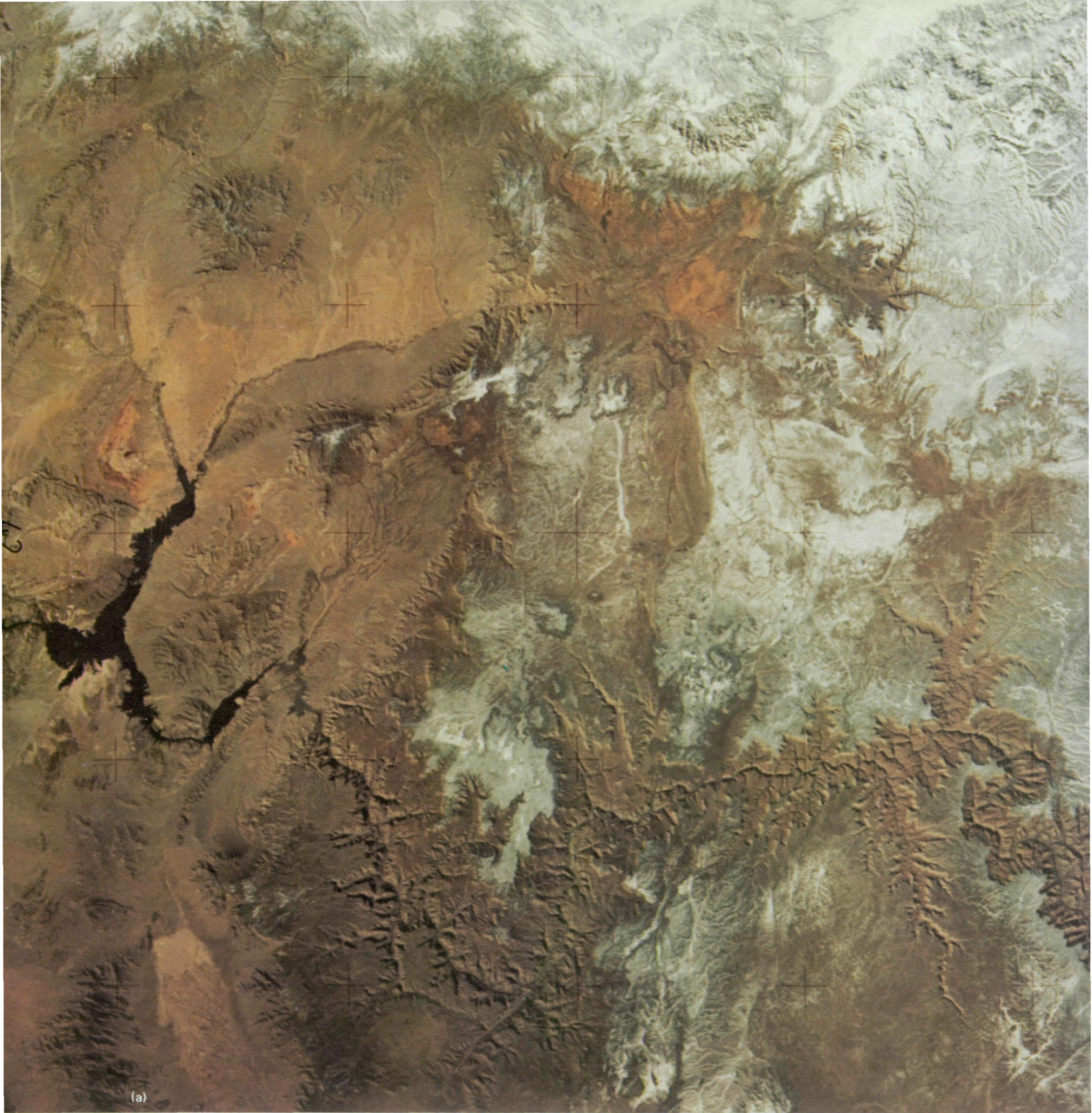
Rejuvenation of motion along old Precambrian fault lines is well documented (refs. 4-12 and 4-13) for faults cutting Paleozoic strata of the Grand Canyon area. This is particularly true for those faults trending northeast-southwest, and Shoemaker et al. suggest that the Mesa Butte, Bright Angel, and Sinyala systems are developed on great Precambrian fault zones.

It is well known that the Precambrian basement of Arizona has a strong northeast-southwest structural grain. Skylab photograph lineaments strongly support the suggestion of a Sinyala system and add significantly to the overall northeast-southwest fault pattern. Apparent concentration of these lineaments in the deeper portions of the Grand Canyon area may further support the idea of reactivation on Precambrian faults.



FIGURE 4-17.—The Grand Canyon area of northern Arizona (SI4-142-4436).

ORIGINAL PAGE IS
OF POOR QUALITY



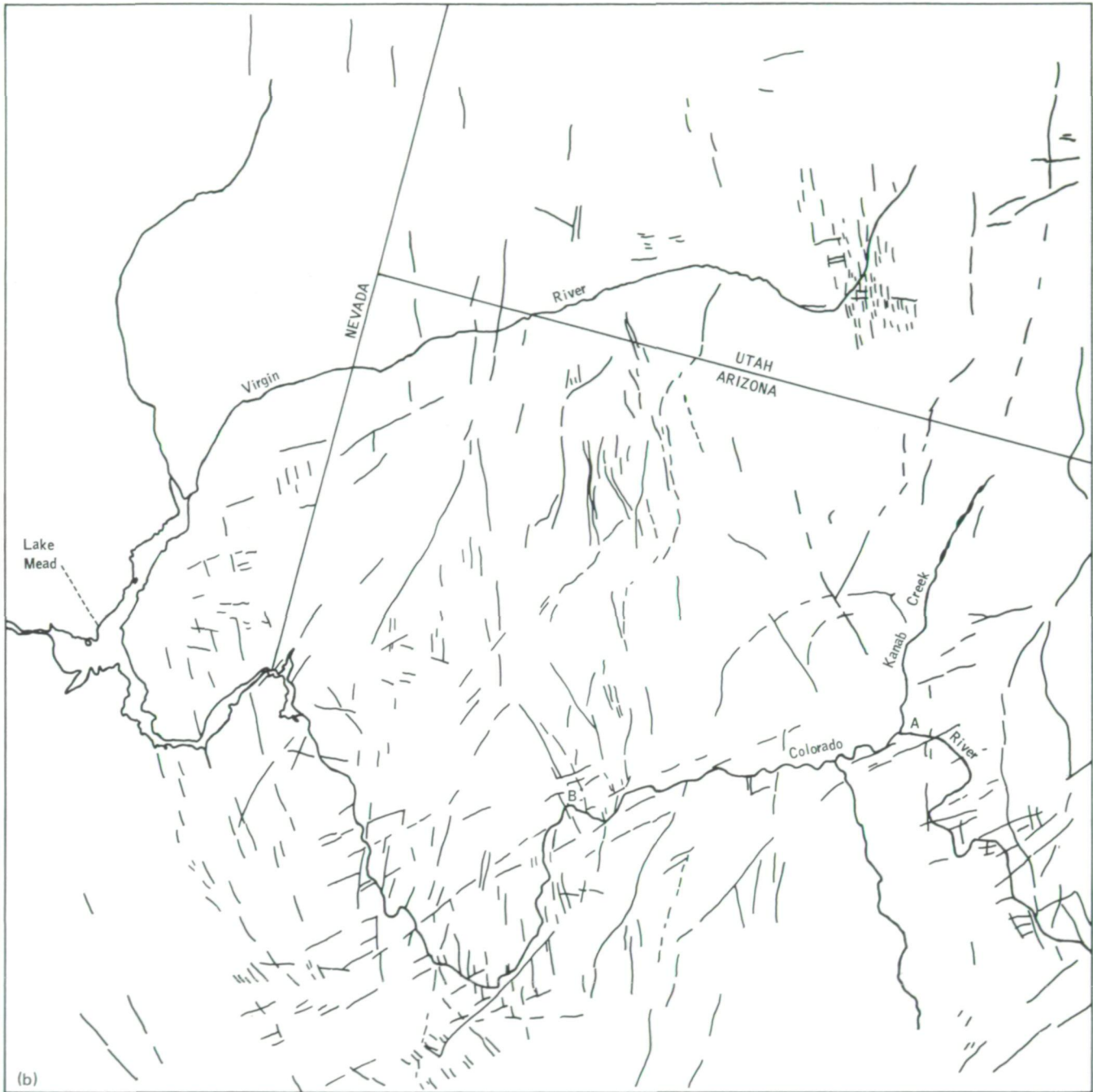


FIGURE 4-18.—The northern Arizona area. (a) Photograph (SL4-142-4435). (b) Sketch map showing linear fractures developed in the surface strata of the Colorado Plateau in the vicinity of the Grand Canyon as revealed in the photograph.

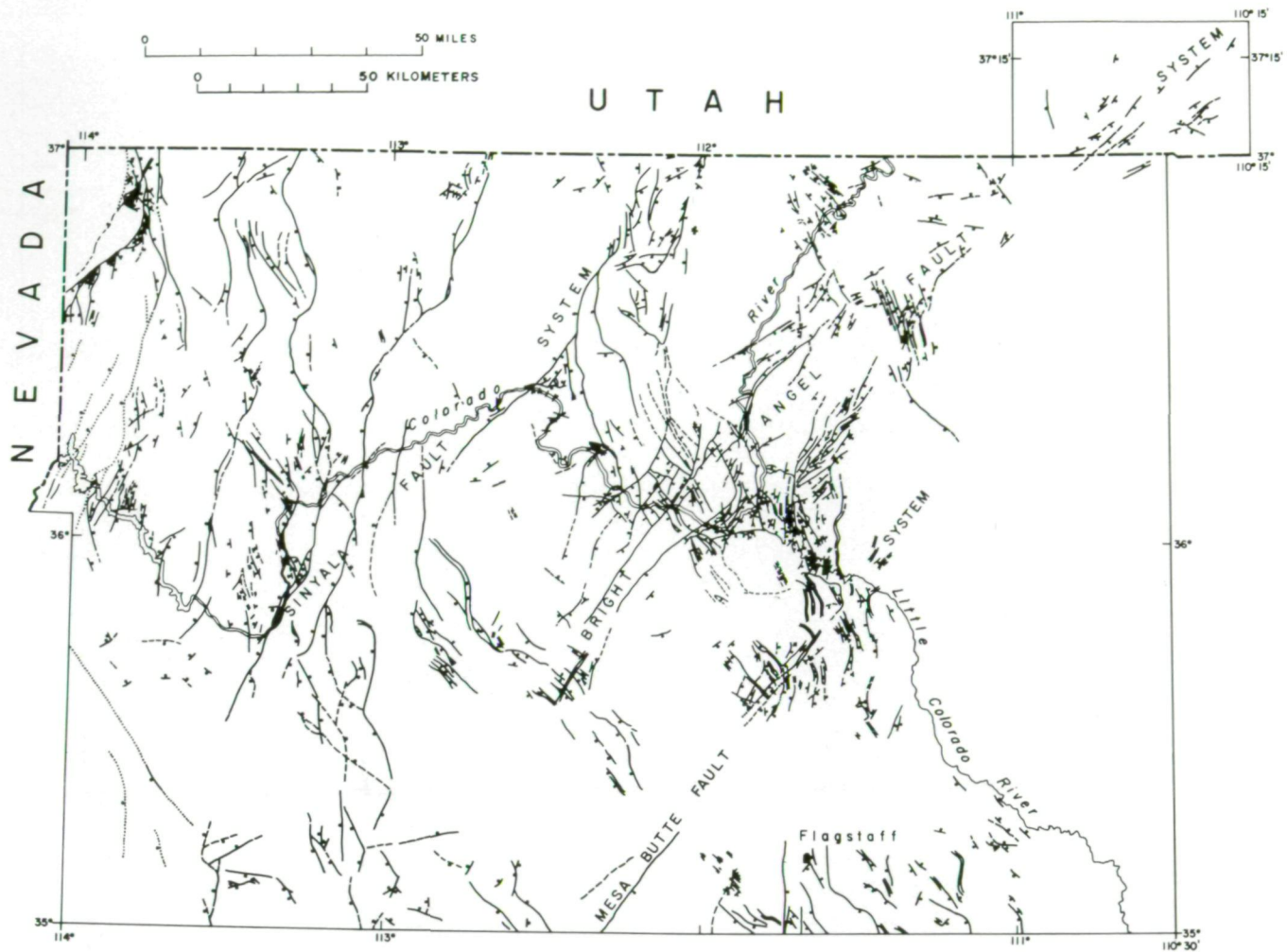


FIGURE 4-19.—Map of faults in northwestern Arizona. Most faults shown are normal faults; bar and dot on downthrown side (from ref. 4-12).

SUMMARY OF SIGNIFICANT RESULTS

The Skylab 4 geologic investigations have yielded the following geologically significant results.

1. Demonstration of an 11-km left-lateral displacement on the Chiriaco Fault zone and of the presence of other previously unidentified faults of similar orientation and sense in the Colorado Desert of southern California

2. Evidence of a previously unrecognized major northwest-trending shear zone on the northwestern coast of Sonora, Mexico

3. No evidence that would dispute the abrupt eastern termination of the Agua Blanca Fault zone in northern Baja California

4. Recognition of the extensive nature of conjugate linear fracture systems in the crystalline rocks of peninsular California over a distance of more than 644 km

5. Identification of a continuous stratigraphic reference zone in the prebatholithic rocks of northern Baja California

6. Discovery of the most southwesterly known occurrence of Precambrian crystalline rocks in the North American continent

7. Discovery of a previously unmapped section of Mesozoic (?) volcanic rocks in the Pinto Mountains of southeastern California

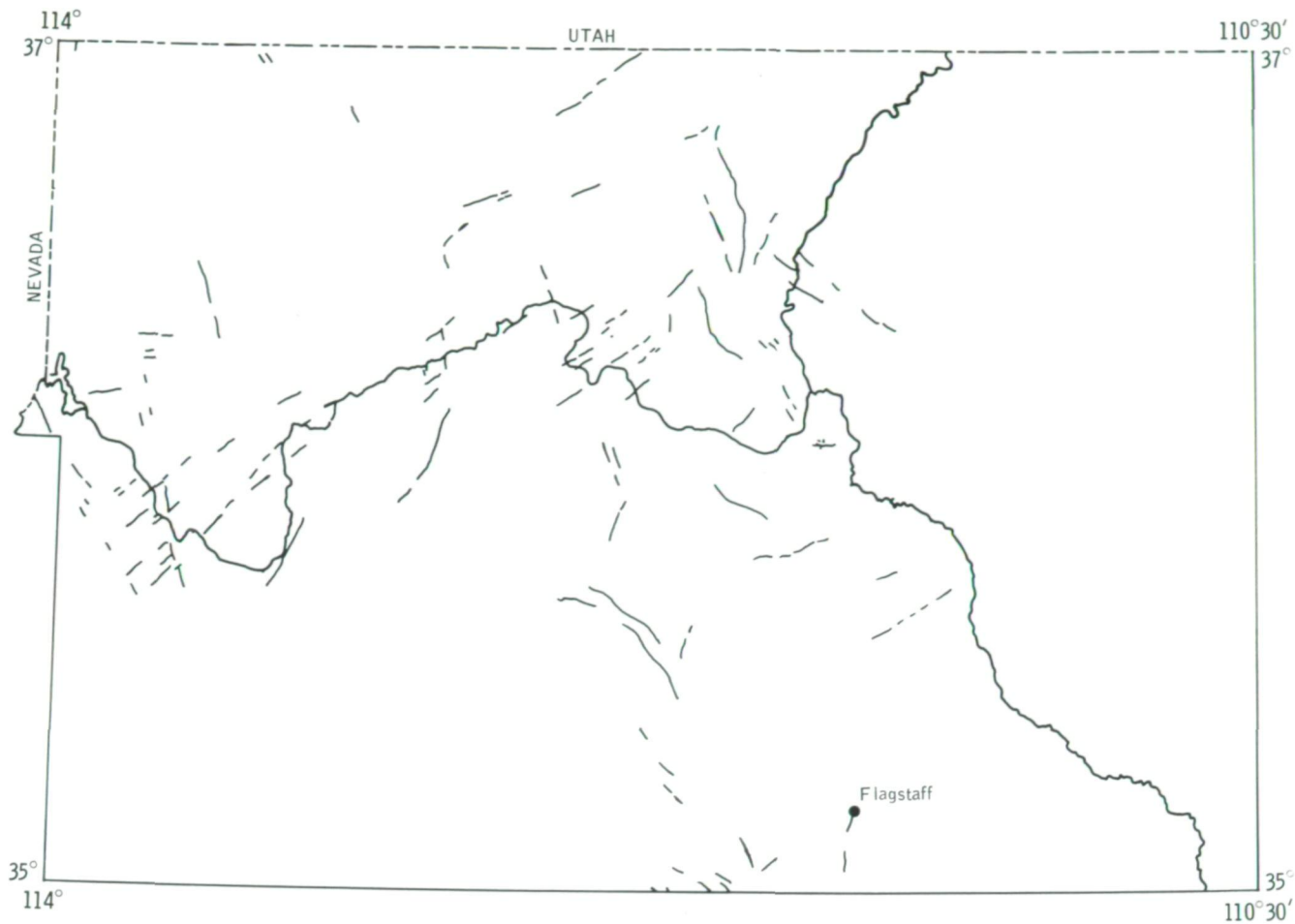


FIGURE 4-20.—Sketch map showing previously unrecognized fracture systems in northern Arizona revealed by the Skylab 4 handheld-camera photographs.

RESEARCH VALUE OF SKYLAB 4 GEOLOGICAL OBSERVATIONS

The research reported herein represents the integration of the orbital observation data with extensive ground studies. These studies were supplements to ongoing long-term research programs, which provided a background of problem awareness for the recognition of research potential in the Skylab 4 observations. It is desirable to establish as clearly as possible the direct research value of these observations.

The primary contribution is in the form of excellent photographs that could be applied in photogeologic appraisals of the several regions. As noted previously, verbal commentary by the astronauts was largely limited to

establishing subject, time, and photographic conditions. However, the debriefing indicated a much greater potential in terms of crew awareness and sensibilities than was recorded in real time or than was translated and focused in postmission contacts. It was only in the inspection of the eastern terminus of the Agua Blanca Fault zone that the crew positively verbalized their research conclusions. Our ground studies supported their validity.

The great value of the photographs is in the effective selection of a view of the subject in which lighting and camera position, as well as other transient conditions, permit the geologically significant aspects of the subject to be photographed. This requires a value judgment on the part of the operator of the handheld camera, which

distinguishes his work from mapping-camera photography. There is a tendency to view geological subject material as static and therefore automatically capturable. This is erroneous. Informative photographs of geological features are the result of an educated photographer recognizing an effective opportunity.

The astronaut photography was very effective for the majority of the designated sites and for the opportunity sites, which confirms that the astronauts were able to perceive the spatial and geometric relations under consideration. The effectiveness of the photography increased as the mission progressed. Even without seeing their photographic product, the astronauts seemed to learn to appreciate and document the better perspectives of their subject matter. An outstanding example is the sequence of oblique photographs of the California fault systems from which the mosaic in figure 4-3 was created.

There were several sites (e.g., the plutons of the peninsular batholith) in which the camera failed to capture what the astronauts could clearly discriminate. These discrepancies must reflect our lack of understanding of all the factors by which the human eye and brain exceed the camera and film in perception. It is clear that the training of the astronauts for handheld-camera photographic documentation was more or less perfunctory and that the equipment which they carried was good but not optimal.

The photographic product that was introduced into our research, then, was an astronaut-selected view of the Earth from which an attempt was made to recognize the important geological patterns bearing on the research objectives. The scale of the features observed, the ability to interrelate large features in areas measuring 10 000 to 100 000 km², and the unexpected revelations about the organization in the surface patterns are contributions almost unique to these types of data. The color values, when the lighting and photographic processing were optimal, were also unprecedented in our experience.

Essentially, this visual information has provided a large-scale framework on which the details derived from surface studies can be organized. In the best circumstances, local investigations can be expanded much more confidently to their proper regional significance.

An appropriate example can be drawn from a recent research report (ref. 4-14) in which it was tentatively concluded that an enormous fault zone, active about 150 to 200 million years ago, sliced northwest-southeast across southwestern North America from California to

Mexico and displaced the crust at least 800 km. This was an unsuspected structure the existence of which explained many first-order plate tectonics problems in continental evolution. The research leading to this conclusion was at least 6 years in progress. In the spring and summer of 1974, the implications of the research became apparent, but the regional dimensions seemed too vast to obtain extensive confirmation easily. By the spring of 1974, the handheld-camera photographs of Skylab were available. Although the coverage could not be complete, it provided many clues to important surface sites for detailed inspection and study in California, Arizona, and Sonora. The additional information supported our hypothesis, and it was accordingly reported. The Mojave-Sonora megashear has received much recent attention. If it survives independent scrutiny, the excellent Skylab 4 photographs must be recognized as a valuable source of perspective in refining the final hypothesis. In the studies of coastal Sonora that are reported herein, the possibility exists that still other important features related to the growth and modification of the continental margin can be recognized.

Numerous other observations made by the astronauts or developed from these studies of the photographs also have the potential for significant research yield. It is emphasized that the most effective use of the Skylab 4 data will be made in the course of its continued incorporation and application in ongoing research at the ground level. Until new programs of directed visual observations are initiated, only by additional surface investigations and by ground-truth tests to follow up the many interesting implications of the existing photographs can more of this potential science be realized.

RECOMMENDATIONS

1. The Skylab 4 geology experiment has yielded data of significant scientific value, and the Skylab 4 crewmen have shown that there is still greater potential in this approach. Accordingly, future orbital missions should include plans for manned visual observations of Earth.

2. To achieve the potential yield, a comprehensive planning, facility preparation, and training program is necessary. A basic design for such a program should be considered sufficiently soon so that the Skylab experiences will not be forgotten.

3. An Earth-orbiting observatory on the Space Shuttle may be manned by a professional scientist.

Nevertheless, Shuttle astronaut crews should be given training in geology and other Earth sciences so that their natural observational talents can be directed toward appropriate problems and targets of opportunity.

REFERENCES

- 4-1. Silver, L. T.; Anderson, T. H.; Conway, Clay; and Murray, Jay: Preliminary Report on Geologic Investigations of Southwestern North America. Skylab 4 Visual Observations Project Report. NASA TM X-58142, 1974, pp. 7-1 to 7-8.
- 4-2. Dibblee, T. W., Jr.: Evidence of Major Lateral Displacement on the Pinto Mountain Fault, Southeastern California. Special Paper 115, Geol. Soc. America Abs., 1967, p. 322.
- 4-3. Hope, Roger A.: The Blue Cut Fault, Southeastern California. Professional Paper 650-D, U.S. Geol. Survey, 1969, pp. D116-D121.
- 4-4. Powell, R. E.: The Chiriaco Fault: A Left-Lateral Strike-Slip Fault in the Eastern Transverse Ranges, Riverside County, California. Geol. Soc. America Abs., vol. 17, no. 3, 1975, p. 362.
- 4-5. Silver, L. T.; Stehli, F. G.; and Allen, C. R.: Lower Cretaceous Pre-Batholithic Rocks of Northern Baja California, Mexico. American Assoc. Petrol. Geol. Bull., vol. 47, no. 12, 1963, pp. 2054-2059.
- 4-6. Allen, Clarence R.; Silver, Leon T.; and Stehli, Frances Greenough: Agua Blanca Fault — A Major Transverse Structure of Northern Baja California, Mexico. Geol. Soc. America Bull., vol. 71, no. 4, 1960, pp. 457-482.
- 4-7. Moore, David G.: Formation and Crustal Growth, Gulf of California Structural Province. Geol. Soc. America Bull., vol. 84, 1973, pp. 1883-1906.
- 4-8. Conway, C. M.: Petrology, Structure, and Evolution of a Precambrian Volcanic and Plutonic Complex, Tonto Basin, Gila County, Arizona. Ph. D. Dissertation, California Institute of Technology, 1976.
- 4-9. Wilson, Edward Dewey: Pre-Cambrian Mazatzal Revolution in Central Arizona. Geol. Soc. America Bull., vol. 50, no. 7, July 1, 1939, pp. 1113-1164.
- 4-10. Wilson, Eldred D.; Moore, Richard T.; and Cooper, John R.: Geologic Map of Arizona. Arizona Bur. Mines and U.S. Geol. Survey Coop. Project, 1969.
- 4-11. Lucchitta, Ivo: Structural Evolution of Northwest Arizona and Its Relation to Adjacent Basin and Range Province Structures. Geology of Northern Arizona, Part I — Regional Studies. Northern Arizona University/U.S. Geol. Survey, 1974, pp. 336-354.
- 4-12. Shoemaker, E. M.; Squires, R. L.; and Abrams, M. J.: The Bright Angel and Mesa Butte Fault Systems of Northern Arizona. Geology of Northern Arizona, Part I — Regional Studies. Northern Arizona University/U.S. Geol. Survey, 1974, pp. 355-393.
- 4-13. Huntoon, Peter W.: Synopsis of Laramide and Post-Laramide Structural Geology of the Eastern Grand Canyon, Arizona. Geology of Northern Arizona, Part I — Regional Studies. Northern Arizona University/U.S. Geol. Survey, 1974, pp. 317-335.
- 4-14. Silver, L. T.; and Anderson, T. H.: Possible Left-Lateral Early to Middle Mesozoic Disruption of the Southwestern North American Craton Margin. Geol. Soc. America Abs., vol. 6, no. 7, 1974, pp. 955-956.

APPENDIX

SOURCES OF INFORMATION

The principal sources of information used for preparing this report are as follows.

1. Skylab 4 Visual Observations Flight Book
2. Transcript of Skylab 4 crew comments
3. Skylab 4 handheld-camera photograph logs
4. Skylab 4 summary of completed visual observations and handheld-camera photographs
5. Skylab 4 orbital track map, starting November 10, 1973
6. Skylab 4 indexes of handheld-camera photographs by geographic location
7. Earth-looking video tapes (SL4-165, SL4-175, and SL4-186)
8. Skylab 4 crew debriefing, March 12, 1974
9. Skylab 2, 3, and 4 handheld-camera photographs (Hasselblad (70 mm) and Nikon (35 mm) cameras)
10. Apollo 6, 7, and 9 and Skylab Earth resources experiment package (EREP) photographs
11. Field investigations by the authors
12. Informal discussions with the Skylab 4 crew

D4

N82-12496

5

Skylab 4 Observations of Volcanoes

THE 84-DAY SKYLAB 4 MISSION provided repeated opportunities for the three crewmen to observe and photograph terrestrial volcanic features under a variety of viewing conditions and Sun angles. These observations and photographs have provided new information on two volcanic eruptions, on geologic settings of several remote volcanic regions, and on specific volcanic landforms and have thus yielded observational results that aid in the study of volcanism from space. This section includes a discussion of each of these

aspects together with information obtained from crew descriptions and from analytical studies of selected handheld-camera photographs. Where appropriate, the discussion includes a review of the geology of the volcanic features, primarily from published literature, but with special emphasis on the landforms and structures visible in the Skylab 4 images. New information or evidence for new interpretations derived from analyses of Skylab photographs is stressed.

Part A

Volcanoes and Volcanic Landforms

JULES D. FRIEDMAN^a AND GRANT HEIKEN^b

VOLCANIC ERUPTIONS

Two significant volcanic eruptions in the circum-pacific belt of volcanism were observed and documented by the Skylab 4 crewmen. Sakura-zima, in southern Kyūshū Island, Japan, was observed and photographed repeatedly by the crewmen during its eruption in December 1973 and January 1974. Their observations, together with concurrent ground observations and meteorological measurements, constitute a rare documentation of several entire eruption clouds.

A major eruption occurred at the remote Fernandina Volcano in the Galapagos Islands. The crewmen were able to observe the eruption because of a fortuitous combination of events; that is, cloud cover was light, the orbital path crossed the volcano during daylight hours, and the crewmen were stationed at a window to make a scheduled observation of the volcano. The results of the observations of the Sakura-zima and Fernandina eruptions are reported in this section.

Volcanoes of Kyūshū, Japan

Many of the volcanoes off Kyūshū, southernmost of the Japanese islands, have had recorded eruptive activity since A.D. 742. Consequently, this island was one

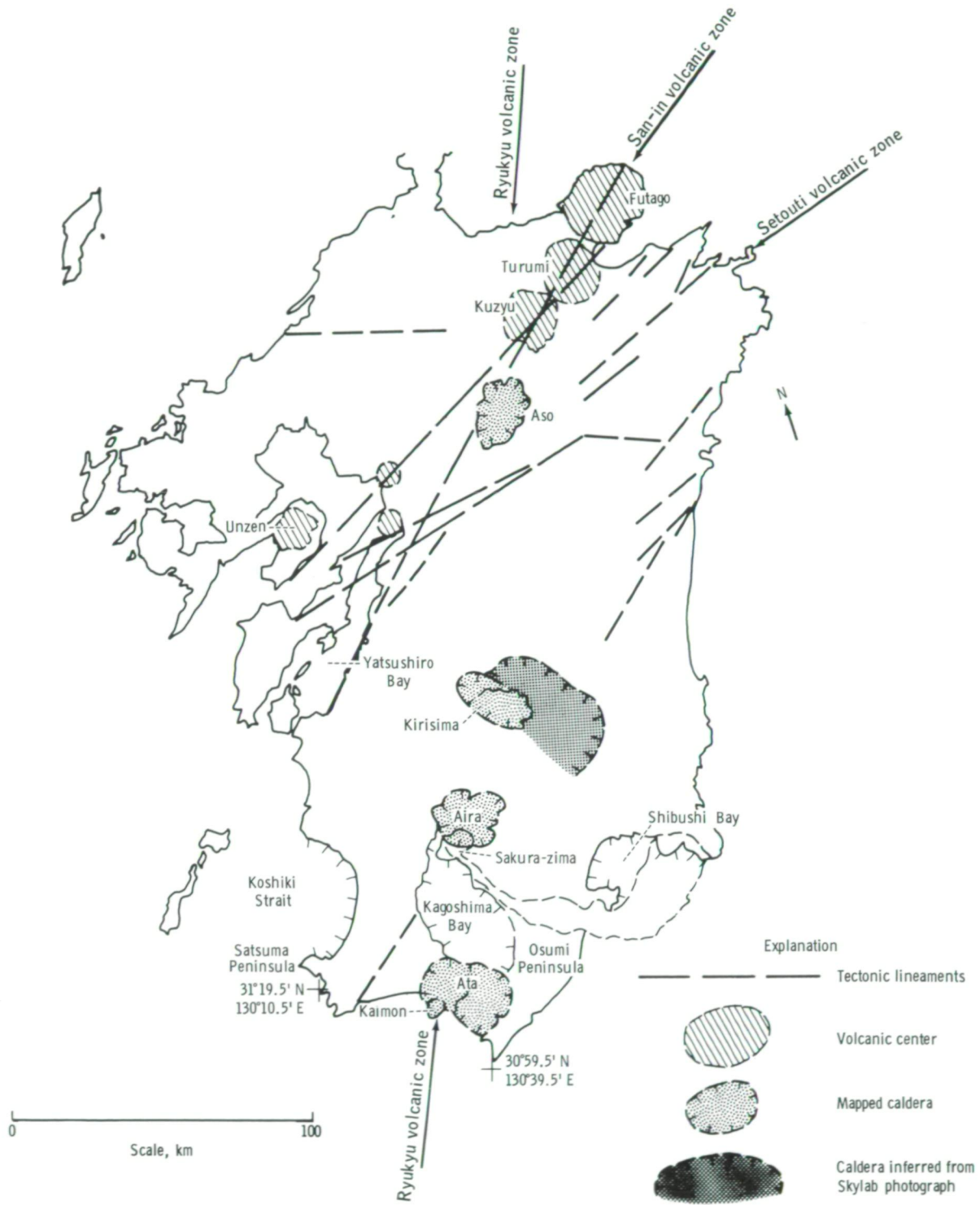
^aU.S. Geological Survey, Denver, Colorado.
^bLos Alamos Scientific Laboratories, Los Alamos, New Mexico.

PRECEDING PAGE BLANK NOT FILMED



FIGURE 5-1.—Island of Kyūshū, Japan, showing numerous Quaternary volcanoes. (a) Sakura-zima Volcano emitting an eruption cloud can be seen at the lower center of this photograph taken on January 7, 1974 (SL4-139-3942). (b) Sketch map of Kyūshū, Japan, showing distribution of tectonic lineaments, volcanic centers, calderas, and volcanic zones.

ORIGINAL PAGE IS
OF POOR QUALITY



(b)

of the primary sites investigated during the Skylab 4 mission. As a result, this selection yielded more detailed photographs of a single volcanic eruption sequence than had ever been taken from space. The volcanic plume of Sakura-zima and the location of the Quaternary volcanoes Turumi, Kuzyu, Aso, Unzen, Kaimon, and Sakura-zima are shown in figure 5-1(a). A sketch of the island (fig. 5-1(b)) identifies the volcanoes and volcanic structures. Turumi and Kuzyu are in solfataric or fumarolic stage with no known historical eruptions (ref. 5-1), whereas Aso, Kirisima, Unzen, Kaimon, and Sakura-zima have a long historical record of eruptions. The major volcanic zones that cross Kyūshū, from oldest to youngest, are the Setouti, San-in, and Ryukyu.

The Setouti volcanic zone (ref. 5-2) is represented by tectonic lineaments, alinement of landforms, and extinct volcanoes. The Setouti zone trends northeast and in the past may have extended completely across the island. The shoreline segments along the northern part of the Yatsushiro Bay (fig. 5-1(a)) are alined along the trend of the zone, which suggests that the zone once extended to western Kyūshū.

San-in, a second prominent volcanic zone (ref. 5-2), trends northeast across the island and is indicated by the alined and somewhat overlapping volcanic masses of Turumi, Kuzyu, Unzen, and Futago. Of these volcanoes, only Unzen has erupted since 1700. This zone profoundly affects the topography and shoreline of Kyūshū and combines with the Setouti zone to contribute to the geomorphology of Yatsushiro Bay.

The youngest and most active volcanoes occur in the north-trending Ryukyu zone that includes the Aso, Kirisima, Aira, and Ata caldera complexes. The Aso caldera, 25 km in diameter, was the focus of 111 eruptions between A.D. 796 and 1958 (ref. 5-3, p. 429). The last eruption was in 1970 (ref. 5-4). The small white plume scarcely discernible in figure 5-1(a) is interpreted as an indication of continuing, powerful fumarolic activity from one or more of the many craters within the Aso caldera. Vast quantities of ash-flow tuffs surround the caldera and occupy the valleys that radiate from the caldera (ref. 5-2). The Aso caldera is the northernmost active volcano of the Ryukyu zone, the most significant tectonic trend visible in the Skylab photographs. South along this zone is the major Kirisima volcanic field that has had 50 eruptions between A.D. 742 and 1959 (ref. 5-3), 19 of which have occurred since 1700 (ref. 5-4). The Kirisima caldera complex (40 by 30 km) is considerably more obvious in the Skylab photograph than on current geologic maps. Matumoto (ref. 5-5) terms

the Kirisima complex a cryptocaldera primarily because it is characterized by the absence of distinct pyroclastic deposits. The Ryukyu volcanic zone at the southern end of Kyūshū consists of overlapping calderas of the Aira group, which includes the modern volcano Sakura-zima.

The zone terminates on southern Kyūshū with the Ata caldera complex, which contains the young Kaimon Volcano. The Ata caldera (25 by 12 km) is a tectonically complex caldron-subsidence structure that formed by several stages of subsidence and the extrusion of three large ash-flow tuff sheets (ref. 5-6). Peripheral volcanoes, including Kaimon, developed at a later stage. The caldron, on the whole, resembles the Phlegrean Fields of Italy (ref. 5-2, p. 38; cf. fig. 5-21).

Kagoshima Bay links the Aira and Ata calderas and is regarded by Matumoto (ref. 5-2, pp. 43 to 52) as a linear hollow of volcano-tectonic origin, formed by roof collapse following eruptions from the Aira and Ata calderas. The Skylab 4 photograph (fig. 5-1(a)) provides a synoptic view of the landforms in relation to size and shape of the known volcanic centers. The shoreline and steep slopes that form Kagoshima Bay appear to be made up of intersecting concave segments that, if projected into the bay, would form a chain of overlapping rings similar in form and size to the overlapping segments of the Aira caldera. Thus, these landforms may represent the remnants of a chain of individual calderas rather than a linear collapse structure. Similarly, the crescentic outlines of the Satsuma shoreline of Koshiki Strait and Shibushi Bay also suggest volcano-tectonic collapse structures. If the Satsuma shoreline of Koshiki Strait is indeed of volcano-tectonic origin, it would represent a ring 40 km in diameter, which is the same order of magnitude as the depression containing the Kirisima volcanic field.

Sakura-zima Eruption

Among the most valuable photographs of volcanic activity ever made from Earth orbit are those obtained by the Skylab 4 crewmen that show the active volcano Sakura-zima. Sakura-zima (fig. 5-1(a)), identified by the white eruptive cloud, occurs along one of the boundary faults of the Aira caldera (ref. 5-4). Activity has been recorded at this volcano since A.D. 708; sequential explosive activity has dominated recent eruptions at Minami-dake (south peak), where several eruptions each day occurred in 1973 and 1974 interspersed with

the quiet release of fume clouds. The maximum elevation reached by the tephra clouds during the 1973-74 eruptions was 3.4 km above the vent (fig. 5-2 and ref. 5-7). An isthmus, formed in 1914 by lava flows, connects Sakura-zima with Kyūshū (fig. 5-3). Since the 1914 eruption, the activity has shifted to and has been localized at the summit of Minami-dake, as shown in figure 5-3. However, during the Pleistocene epoch, the volcanic activity of proto-Sakura-zima occurred at a point 10 km northeast of the present Sakura-zima Volcano. The semicircular form of the northeastern

shoreline of Kagoshima Bay may represent the outline of the older caldera formed before the present Sakura-zima. The Skylab photographs thus aid in the study of the landforms that resulted from the southwestward shift in focus of volcanic activity now concentrated at the Minami-dake summit of Sakura-zima.

The recorded history of Sakura-zima indicates that the volcano is characterized by paroxysmal eruptions. During 1973 and 1974, 385 explosions occurred from the Minami-dake Crater at approximately 1118 m above sea level (ref. 5-7). Some of these were accompanied by

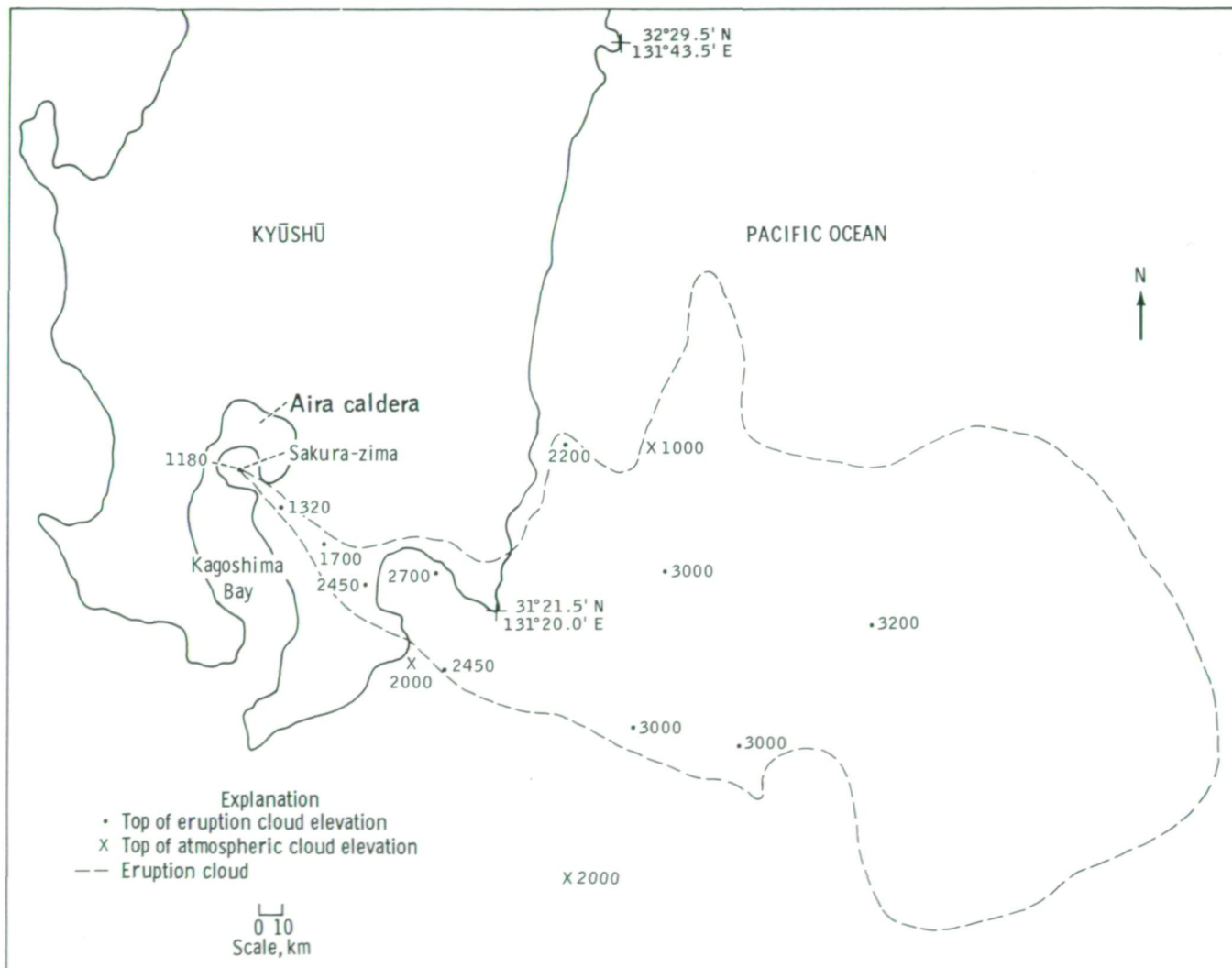


FIGURE 5-2.—Planimetric map of diffused eruption cloud of Sakura-zima on January 8, 1974, based on figure 5-5. Elevations of clouds are given in meters.

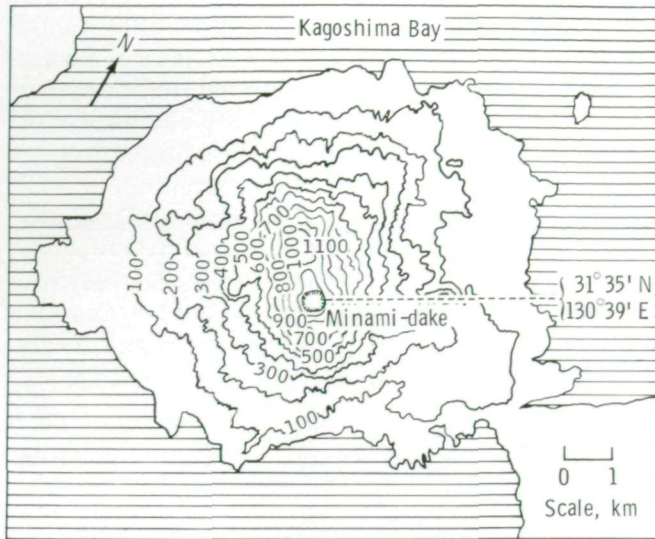


FIGURE 5-3.—Topographic map of Sakura-zima Volcano.

relatively minor amounts of tephra ejected onto the flanks of the volcano. Light tephra fall amounting to approximately 4000 m³ total outfall in May 1974 reached Kagoshima City and surrounding agricultural areas.

The Skylab 4 crewmen observed and photographed Sakura-zima on December 1, 1973, and on January 7 and 8, 1974. On December 1, a volcanic plume appeared as a narrow band that extended southward over Kagoshima Bay (fig. 5-4). On January 7, the Skylab 4 crewmen observed that Sakura-zima was erupting and subsequently described and photographed (fig. 5-1(a)) the entire eruption cloud. Control of the eruption-cloud movement by winds was evident in the following description by the commander: "The smoke was flowing straight southeast from the volcano over the southeast corner of Kyūshū. As soon as it reached the ocean, it began to diffuse and billow." The eruption cloud was not continuous but was a series of "puffs" possibly corresponding to paroxysms spaced a few seconds apart. After crossing the Osumi Peninsula and reaching the ocean, the cloud moved northeast and was dispersed by strong winds. The width of the plume pattern appears to be 2 to 3 times that of the white cloud.

On January 8, 24 hours after the initial description of the Sakura-zima plume, the commander photographed the plume again (fig. 5-5) and described it as "diffused, covering a much larger area." The plume pattern was similar to that observed on January 7; the crewmen estimated that the white or tan cloud was approximately 240 km long.



FIGURE 5-4.—Sakura-zima eruption cloud. (a) Photograph taken on December 1, 1973, at approximately 01:55 GMT with the Nikon camera using a 300-mm lens (SL4-196-7340). (b) Planimetric map of Sakura-zima eruption cloud. Elevations of clouds are given in meters.

A detailed study of the photographs was undertaken with an analytical stereoplotter to determine the size, shape, and altitude of the eruptive clouds. On December 1, the eruptive cloud formed a continuous plume

that was approximately 4 km wide at the source and reached a maximum width of 10 km over the coastline (fig. 5-4). Maximum elevation of the cloud top was 1560 ± 150 m. More intense eruption on January 7 and



FIGURE 5-5.—Extent of eruption cloud from Sakura-zima on January 8, 1974 (SL4-139-3971).

8 is evident by the increase in the size of the cloud. Stereoanalysis indicates that the eruptive cloud of January 7 was divided into three segments (fig. 5-6). Near the vent, the smoke plume formed a narrow cloud with tops at 2.5 km. As the cloud became dispersed over the coastline, the maximum plume elevation was 3.38 km (fig. 5-2). On January 8, 1 day later, the volcanic cloud was continuous until it reached the ocean, turned northeast, and was dispersed (fig. 5-2). The length of the visible cloud in figure 5-5 is estimated to be 285 km. The degree of dispersion is evident in the width of the cloud. Near the vent, the cloud was approximately 4 km wide, whereas at 172 km from the vent, it was approximately 85 km wide and was dispersed into 1- to 8-km-wide parallel bands. The maximum altitude of the dispersed part of the plume was 3.2 km (fig. 5-2).

The Skylab photographs are significant in that they record synoptically the characteristics and extent of several entire eruption clouds as viewed from Earth or-

bit. The curling, twisting clouds visible in the photographs taken on January 7 and 8 suggest that previous models of tephra fall following parabolic or elliptical outfall sectors with near-linear axes may not always apply.

The results of stereoplotter analysis have also provided information relating the intensity of Sakura-zima volcanic explosions to contamination of the upper atmosphere. To create a stratospheric dust veil, penetration of the tropopause by an eruption column is necessary. The analytical plots of the stereographic images from January 7 and 8 show that the eruption cloud did not penetrate the tropopause, and therefore a dust veil in the upper atmosphere was not formed. This conclusion is in accord with radiosonde data (table 5-I) recorded by the Japan Meteorological Agency at the Kagoshima station for January 6 to 8, 1974. These data indicate that the southeast-trending part of the plume is aligned with tropospheric wind directions.

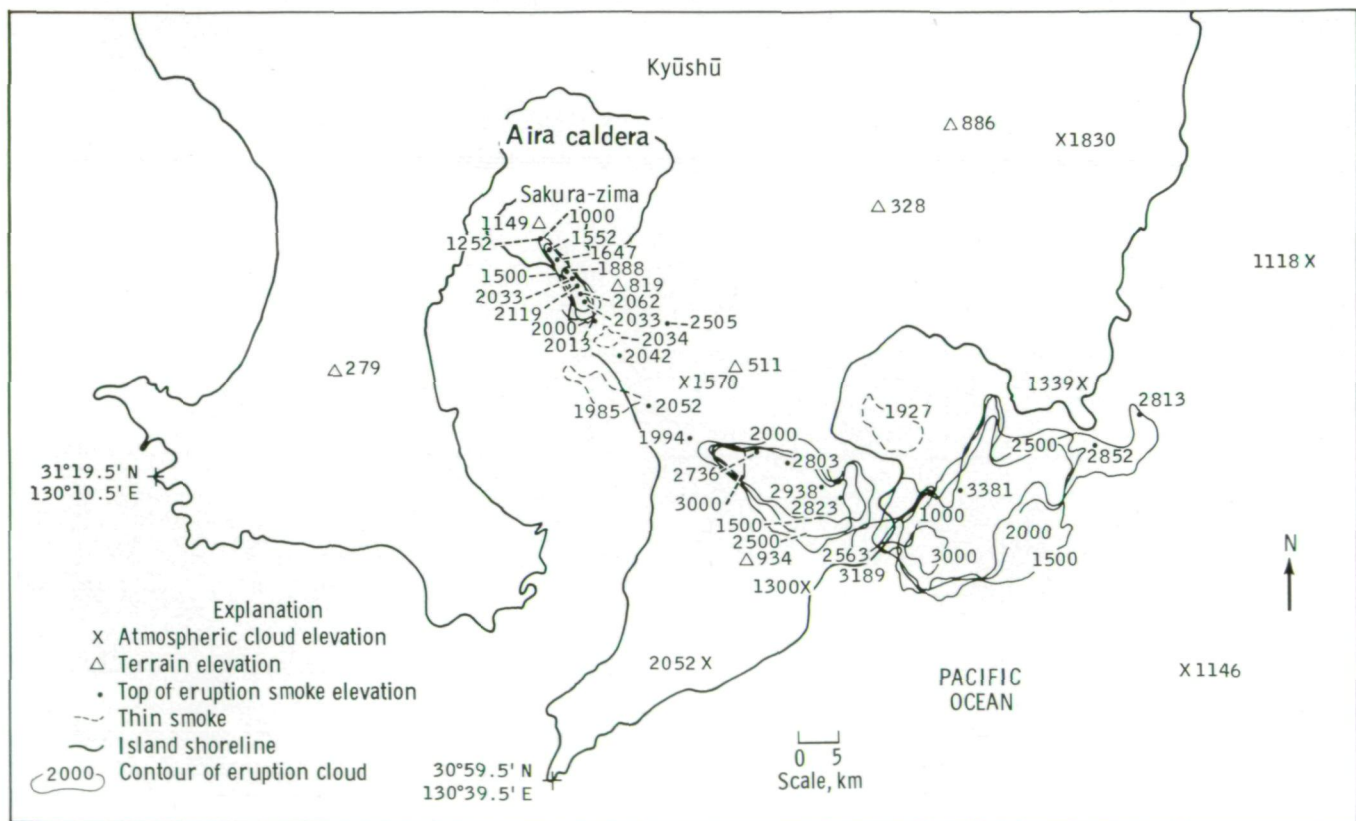


FIGURE 5-6.—Planimetric map of Sakura-zima eruption cloud on January 7, 1974, based on figure 5-1. Elevations of clouds are given in meters.

TABLE 5-1.—Upper Wind Conditions in the Kagoshima Area

| Date and time, GMT | Standard atmospheric height, m | Atmospheric pressure level, kPa (mb) | Wind direction, deg | Windspeed, m/sec (knots) |
|-----------------------|--------------------------------|--------------------------------------|---------------------|--------------------------|
| Jan. 6, 1974 00:00 | 1 458 | 85 (850) | 250 | 4.1 (8) |
| | 3 014 | 70 (700) | 290 | 10.8 (21) |
| | 5 578 | 50 (500) | 285 | 19.0 (37) |
| | 7 190 | 40 (400) | 280 | 27.8 (54) |
| | 9 170 | 30 (300) | 270 | 36.0 (70) |
| | 10 370 | 25 (250) | 265 | 44.7 (87) |
| | 11 792 | 20 (200) | 265 | 49.9 (97) |
| Jan. 7, 1974 00:00 | 13 618 | 15 (150) | 270 | 46.8 (91) |
| | 16 171 | 10 (100) | 275 | 37.0 (72) |
| | Tropopause | 85 (850) | 305 | 5.1 (10) |
| | | 70 (700) | 285 | 8.7 (17) |
| | | 50 (500) | 290 | 23.1 (45) |
| 40 (400) | | 285 | 24.2 (47) | |
| 30 (300) | | 280 | 38.1 (74) | |
| 25 (250) | | 275 | 50.9 (99) | |
| Jan. 8, 1974 00:00 | 20 (200) | 280 | 54.0 (105) | |
| | 15 (150) | 275 | 54.0 (105) | |
| | 10 (100) | 280 | 38.1 (74) | |
| | Tropopause | 85 (850) | 305 | 7.2 (14) |
| | | 70 (700) | 260 | 14.9 (29) |
| | | 50 (500) | 285 | 18.0 (35) |
| | | 40 (400) | 300 | 27.8 (54) |
| 30 (300) | | 300 | 44.2 (86) | |
| 25 (250) | | 290 | 54.0 (105) | |
| Jan. 8, 1974 00:00 | 20 (200) | 285 | 62.2 (121) | |
| | 15 (150) | 285 | 50.9 (99) | |
| | 10 (100) | 285 | 32.0 (62) | |

In 1956, the daily kinetic energy yield of paroxysmal eruptions from the Minami-dake summit crater was approximately 10^{11} J (10^{18} ergs) (fig. 5-7; ref. 5-1, pp. 25 to 32). If the 1973-74 eruptions are indeed similar in magnitude to those of 1956, the cumulative kinetic energy yield of the pyroclastic activity may be approximately 4×10^{13} J (4×10^{20} ergs). For comparison, the kinetic energy yield associated with the pyroclastic activity of the great 1914 eruption of Sakura-zima was 7.5×10^{15} J (7.5×10^{22} ergs), and the thermal energy yield was 6.2×10^{17} J (6.2×10^{24} ergs) (Matuzawa in ref. 5-3). If the 1973-74 eruptions can be considered to be of the same scale as the 1956 eruptions, a volcanic explosion energy yield of 10^{11} J (10^{18} ergs) at latitude 31° to 32° N may be too small to penetrate the tropopause and create a stratospheric dust veil.

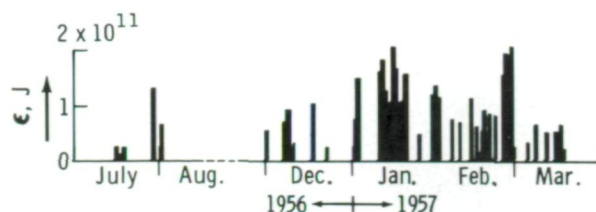


FIGURE 5-7.—Daily kinetic energy of the paroxysmal eruptions from Minami-dake Crater (Sakura-zima) in 1956-57.

The size of an eruption cloud is measured by the dust veil index (DVI) and depends on many factors, such as the kinetic energy yield associated with the explosive phase, the composition of the lava, the height of the eruption column in relation to the tropopause, and the total volume of particulate matter injected into the upper atmosphere. In the 1914 eruption at Sakura-zima, the DVI ranged from 2 to 12 and was associated with an outfall of 620 m^3 (ref. 5-3). In contrast, the 1973-74 eruptions produced only 4000 m^3 of tephra with a DVI of less than 2. For comparison, the classical Krakatoan eruption of 1883, which had a total energy yield of 10^{18} J (10^{25} ergs) and a kinetic energy yield of 10^{17} J (10^{24} ergs), had a DVI of 1000 (ref. 5-8). Assuming a similar ratio between kinetic and thermal energy yield for the Sakura-zima pyroclastic activity of 1973-74, the cumulative thermal energy yield associated with pyroclastic activity from 1973 through June 1974 would be approximately 2.5×10^{15} J (2.5×10^{22} ergs); this amounts to a small- to medium-scale eruption.

VOLCANO-TECTONIC LINEAMENTS OF ISABELA AND FERNANDINA ISLANDS

In addition to the active, plume-emitting eruption from the summit caldera of Fernandina shield volcano, the six major calderas of Isabela Island (Volcan Ecuador, Wolf, Darwin, Alcedo, Sierra Negra, and Cerro Azul) are discernible in the Skylab photograph (fig. 5-8(a)) and are shown on the sketch map (fig. 5-8(b)). They display some of the most outstanding examples of circumferential structures around summit calderas and radial fracture systems on their flanks (ref. 5-9, p. 99) but are similar to Mauna Loa on Hawaii in other aspects of volcanogenesis (i.e., age and composition of volcanic products). The Galapagos calderas differ from the Mauna Loa summit caldera in that the striking circumferential structures in the Galapagos examples are the dominant structures associated with caldera collapse.



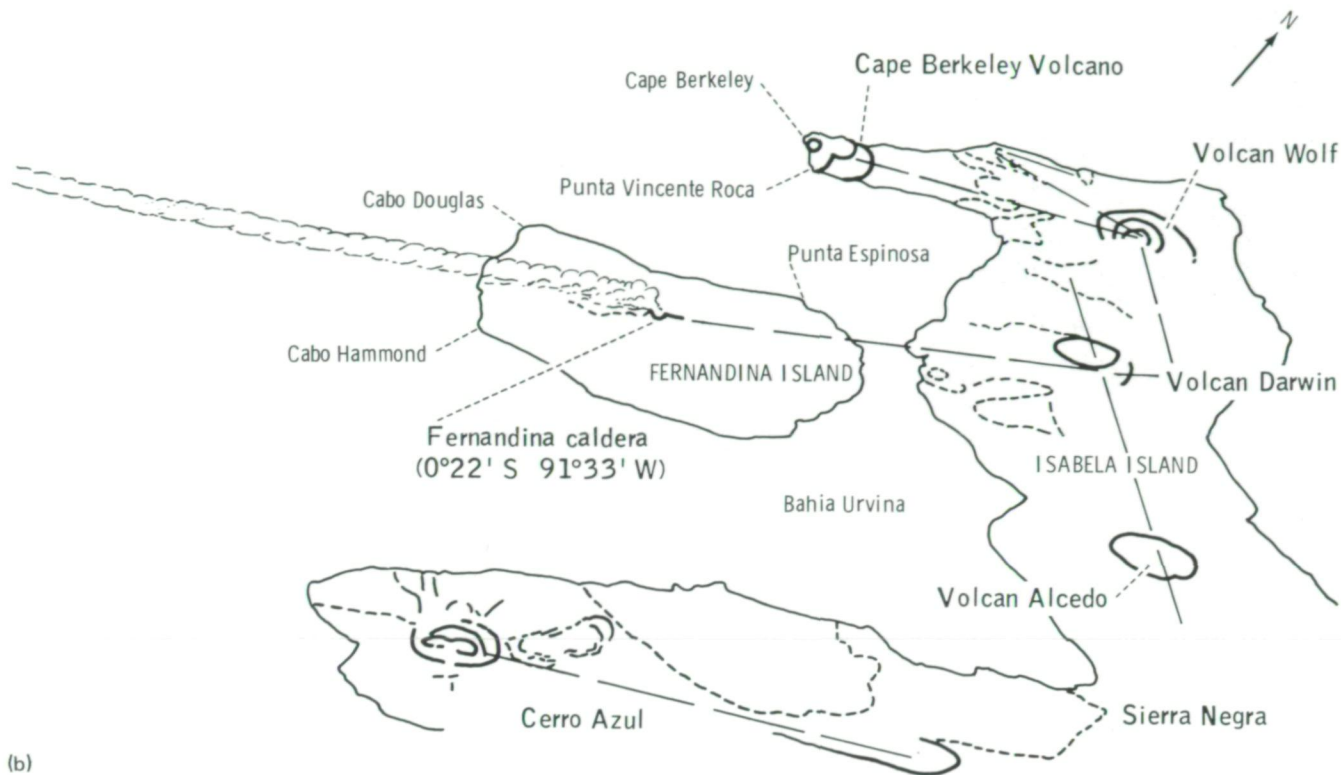
FIGURE 5-8.—Eruption cloud from Fernandina Volcano in the Galapagos Islands. (a) Photograph taken on December 11, 1973, at approximately 15:16 GMT (SL4-195-7299). (b) Sketch map of Fernandina and Isabela Islands showing large calderas and tectonic lineaments (dashed lines).

The arrangement of the volcanoes suggests an orthogonal northwest and northeast tectonic pattern with the volcanoes occurring at intersections (fig. 5-8(b)). The tectonic pattern was first recognized by Darwin and subsequently recognized on the ocean floor by McBirney and Williams (ref. 5-9). That the Galapagos Islands are situated in a zone of active sea-floor spreading was first recognized in the 1960's (refs. 5-10 and 5-11). Much current work is in the process of clarifying the plate-tectonic setting of these islands.

Another feature of interest to be seen in figure 5-8 is the fairly uniform spacing of the major calderas on Isabela Island. Friedlander (ref. 5-12) noted that the great calderas of Isabela and Fernandina are approximately 34 to 39 km apart; these estimates were confirmed by subsequent mapping.

REMOTE VOLCANIC REGIONS

One objective of the Skylab 4 mission was to obtain information on types of volcanic features observable from Earth orbit at an altitude of 450 km and to document these features photographically for further analysis. To accomplish this task, the crewmen were requested to observe volcanic regions that are not only remote and inaccessible but also geologically complex and about which insufficient information is available. It was hoped that the crewmen could obtain additional data on regional geologic features at such sites as the Tibesti Massif (including the Emi Koussi caldera), Chad; Kamchatka Peninsula, U.S.S.R.; and the neovolcanic zone of the southeastern central plateau in Mexico. During the prelaunch training, the crewmen



(b)

were provided with summary data on the appearance of volcanic areas and landforms and volcanic processes of scientific interest. Using this basic knowledge, the crewmen photographed a poorly known and remote volcanic area, the altiplano volcanic field in Argentina, Bolivia, and Chile, and obtained new and significant photographic information on the landforms in this region.

Tibesti Volcanic Massif and Emi Koussi Caldera, Chad

The Tibesti Massif is a major topographic feature in northern Chad and includes the prominent Emi Koussi caldera. The geology of the region has been described by Geze et al. (ref. 5-13) and consists of early Paleozoic to Mesozoic sedimentary sections as much as 2000 m thick intruded and uplifted by igneous rocks. Approximately

70 million years ago, volcanic eruptions began and formed the vast basaltic shield that surrounds the Emi Koussi caldera.

The Skylab 4 photograph in figure 5-9 is a low oblique view of the southern part of the Tibesti Massif. A prominent feature in this photograph is the recently extinct Emi Koussi caldera, which is 12 to 15 km in diameter and is the highest point (3415 m) of the massif. The adjacent mountains, Tarso [Mount] Tiéroké and Tarso Ahon, are also visible.

The Emi Koussi shield, consisting mostly of ash-flow tuffs, surrounds the caldera and is 60 by 80 km in diameter. The caldera and shield deposits overlie reddish Paleozoic and Mesozoic sandstones, as can be inferred northeast and west of Emi Koussi where erosion of the overlying volcanics has exposed the underlying sandstones. These underlying beds were uplifted as much as 4000 m; the uplift resulted in the formation of



FIGURE 5-9.—Tibesti Massif and Emi Koussi caldera, Chad (SL4-138-3789).

a domelike structure before the extrusion of the volcanic sequence of the shield (ref. 5-13).

Prominent northeast-trending linear features of the Plains of Borkou, seen most clearly in the southeast (lower right) quadrant of figure 5-9, are composite linear sand dunes and wind-eroded grooves developed largely on Paleozoic and Mesozoic sandstones (ref. 5-14, p. 43). As determined by Pesce (ref. 5-15, p. 67) and Lowman and Tiedemann (ref. 5-14, p. 43), these linear features of the Plains of Borkou are actually concentric to the Tibesti Massif around Emi Koussi as the approximate center of curvature. The best interpretation (ref. 5-14, p. 43) seems to be that these concentric lineations were controlled by tension fractures related to the uplift of the Tibesti Massif. Exploitation of the original fractures by streams, and later wind erosion and sand accumulation (ref. 5-12, p. 30), enhanced the pattern.

The prominent circular feature in the lower left center of figure 5-9 was noted on earlier Gemini photographs (ref. 5-14) and interpreted as the surface expression of an unmapped igneous intrusion.

The synoptic view from Skylab (fig. 5-9) reveals the major tectonic patterns developed on the Emi Koussi shield and aids in defining the structural features in the caldera. According to Gèze et al. (ref. 5-13), the caldera appears to consist of two calderas, one nested in the other, that have depths of 300 and 200 m, respectively. A crescentic sliver of the outer caldera is visible on the north-northeast side in the Skylab photograph (fig. 5-9). Explosion craters, as well as ash-flow tuffs and basalt flows, occur within the inner caldera (ref. 5-13); the largest of these craters, the Trou au Natron du Koussi, is 2 by 3 km and appears as a white spot southeast of the center of the inner caldera. According to Gèze et al. (ref. 5-13), the basalt flows of the outer caldera appear older than those of the inner caldera, which suggests that the basalt flows occurred in at least two stages, with or related to collapse of the outer and inner calderas at different times. The explosion craters are intermediate in age.

The oldest volcanic rocks of the Emi Koussi Massif are andesites grading into porphyritic basalt of Tertiary age. The upper parts of the outer caldera consist of alkalic rhyolites (ref. 5-13).

Gèze et al. postulated that vast laccoliths emplaced at medium depth during the tectonic phase affected the Nubian sandstone and resulted in the formation of the Tibesti Mountains. Shortly afterward, in the Tertiary period, volcanism began in the distended zones of the bedrock cover over the laccoliths (ref. 5-13, p. 168). This action gave rise to the oldest ignimbrites (rhyolite and trachyte flows and, later, basalt and andesite flows). These events were followed by subsidence or collapse of the summit of the Emi Koussi Massif that first produced the outer caldera and then the inner caldera and related smaller eruption craters and flows within the inner caldera.

Figure 5-9 shows the somewhat radial dissection of the Emi Koussi shield, characteristic of the erosion pattern developed on a rising dome. This photograph also reveals the dendritic erosion of the volcanic flows to the northeast, which has exposed the underlying sandstones and revealed the relative thinness of the carapace formed by ignimbritic and other volcanic flows over older, prevolcanic bedrock. This erosion pattern, visible in figure 5-9, is characteristic of crustal doming and thus supports the hypothesis of Gèze et al. that the Emi Koussi caldera had a tectonic origin and is similar in origin to other calderas characterized by collapse following discharge of colossal volumes of pyroclastic (i.e., ignimbrite) flows from arcuate fissures unrelated to preexisting volcanoes (ref. 5-4, p. 308).

Altiplano Volcanic Field of Bolivia, Argentina, and Chile

The altiplano, or high plateau, volcanic field in the Andes Mountains straddles the boundaries of Argentina, Bolivia, and Chile (fig. 5-10). The Andes constitute an orogenic system noted for the exceptionally powerful andesitic volcanism that occurred during the eugeosynclinal phase. This volcanism is primarily represented by the Araucanian volcanoplutonic belt in the western cordillera of the Chilean-Argentine Andes. This belt was formed in the Early Cretaceous after a short stage of geosynclinal subsidence (ref. 5-16). Subsequent evolution of the region occurred under continen-

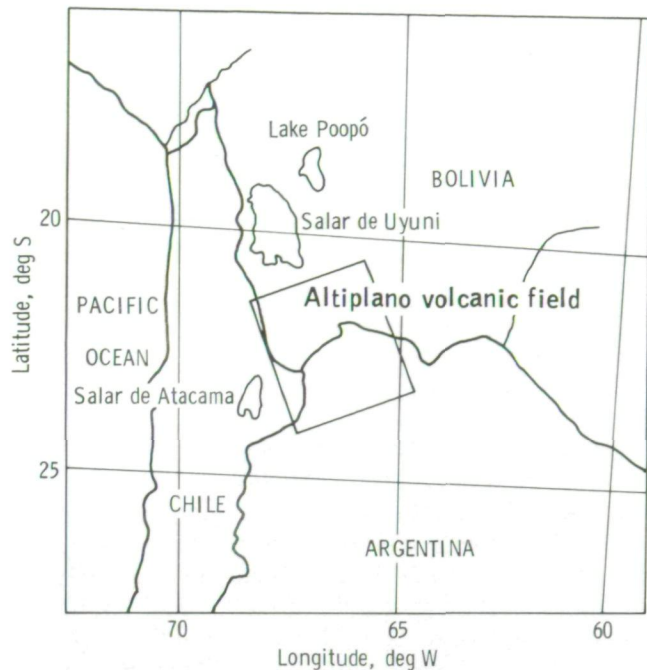
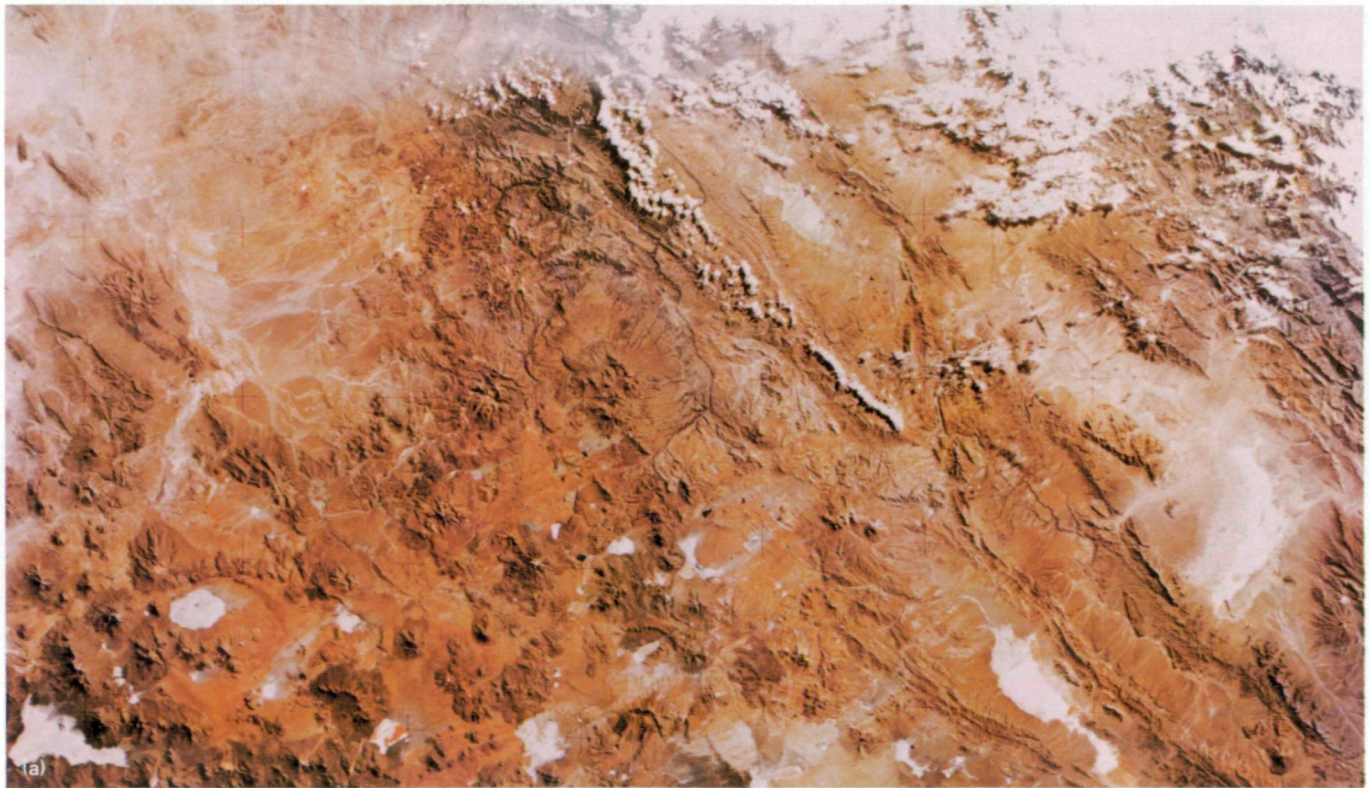


FIGURE 5-10.—Index map of Argentina, Bolivia, and Chile showing location of altiplano volcanic field.

tal conditions, and with time the volcanism migrated eastward.

The altiplano field separates the Araucanian volcanoplutonic belt of the western cordillera and the ranges of the eastern cordillera. During the late Mesozoic and Cenozoic eras, the altiplano was a depositional basin for continental sediments derived from both cordilleras. The Cenozoic sequence of the Bolivian altiplano may be as much as 15 km thick (ref. 5-17). Cenozoic volcanism occurred in the altiplano and the western flank of the eastern cordillera. Structural compression that occurred in the Miocene and Pliocene epochs produced eastward-directed folding and thrust faulting that affected the altiplano and eastern cordillera and possibly coincided with Pliocene-Pleistocene volcanism. Then, in late Quaternary time, the waning of igneous activity corresponded to the relaxation of compressive stresses, and graben structures were formed within the altiplano (ref. 5-17).

The synoptic views obtained by the Skylab 4 crewmen have provided new information on the topographic and geologic features of this isolated and inaccessible region. A photomosaic of the area (fig.

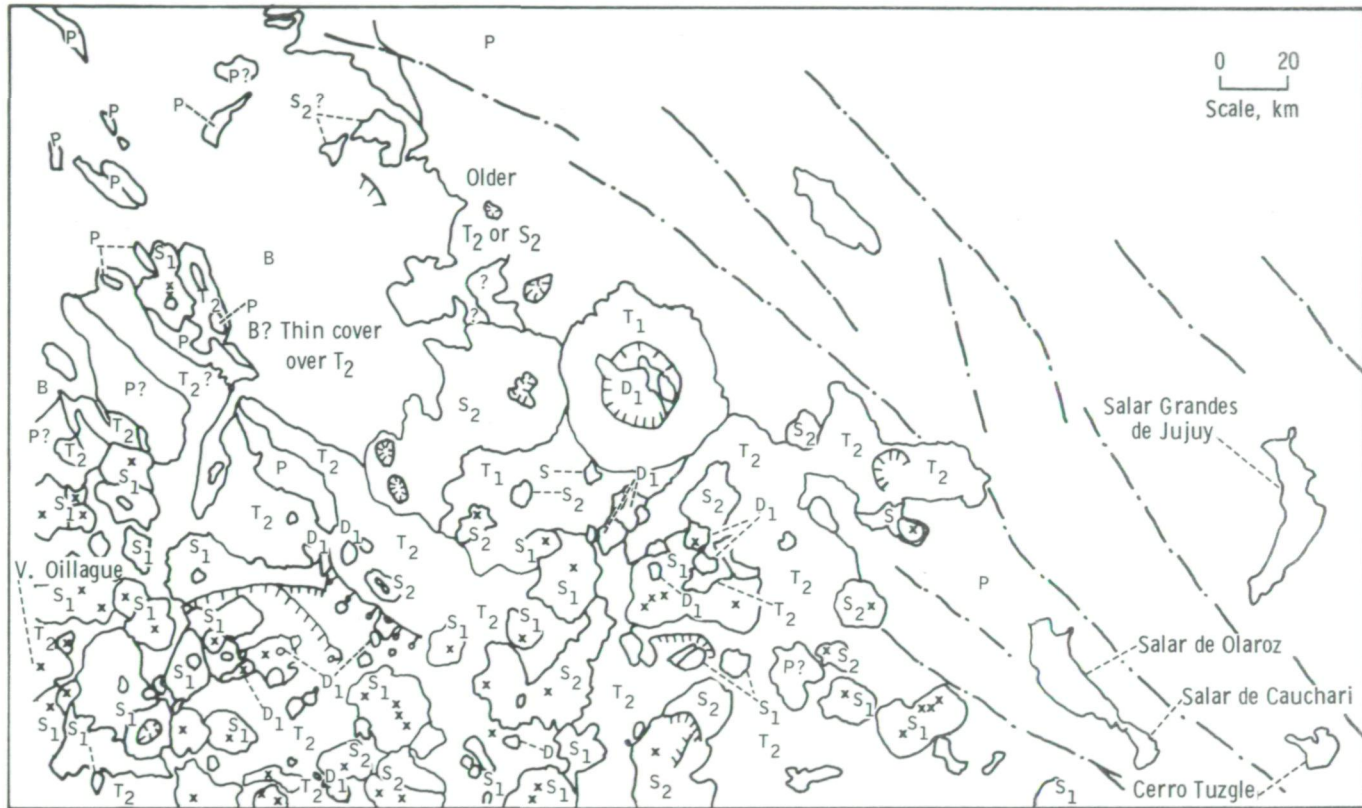


5-11(a) illustrates the diversity of landforms that occur, including the numerous and prominent dry lakes. An analysis of the photographs is shown in a sketch map of the region (fig. 5-11(b)).

Within the region shown in figure 5-11(b), the prevolcanic terrain of Ordovician through Paleocene rocks is cut by north-south-trending block faults. The intermontane basins formed by this faulting have been

partly filled by late Cenozoic sedimentary and pyroclastic rocks and lava.

The "base" on which most of the younger volcanic rocks rest is a plateau that apparently consists of ash-flow tuffs (T_2) and older stratovolcanoes that have been heavily dissected and partly buried. The plateau is characterized by flat depositional surfaces that seem to fill and smooth the prevolcanic topography. Near the



Explanation

- | | | | |
|-------------|---|----------------|--|
| x | Volcanic peaks | S | Salar |
| ⊖ | Crater or caldera rim | S ₁ | Recent stratovolcanoes |
| — — — | Fault (bar and ball on downthrown side) | B | Intermontane basin fill (sediment, pyroclastic detritus, lava flows) |
| — · — · — · | Structural trend of prevolcanic terrain | D ₁ | Recent domes and thick, short lava flows |
| | | T ₁ | Ash-flow tuffs of the "border" caldera |
| | | S ₂ | Older, partly buried, and heavily dissected stratovolcanoes |
| | | T ₂ | Ash-flow tuff plateaus |
| | | P | Pre-late Cenozoic rocks |

(b)

FIGURE 5-11.—Altiplano volcanic field of Argentina, Bolivia, and Chile. (a) Photomosaic (SL4-137-3674 and SL4-137-3675). (b) Sketch map of the altiplano volcanic field.

center of figure 5-11(a), the ash-flow tuffs may be roughly correlated with the 4.8-million-year-old tuffs that crop out near Salina de Rincon, Argentina, several kilometers south of the area visible in this photograph (ref. 5-18). The burial of irregular terrain by ash-flow tuffs, as interpreted from figure 5-11(a), is consistent with the observation by Schwab and Lippolt (ref. 5-18) that there is a pronounced nonconformity here between Paleocene sedimentary rocks and late Cenozoic sedimentary and volcanic rocks.

In the left center of figure 5-11(a), a prominent circular ash-flow tuff deposit (T_1) approximately 50 km in diameter is shown sloping away from a central caldera 23 km in diameter. The caldera is nearly filled with younger domes (D_1) and flows. Several semicircular depressions (lower left, fig. 5-11(b)) are also interpreted as partly buried calderas.

Throughout the western part of the volcanic field and overlying the ash-flow tuff plateau are abundant stratovolcanoes (S_1), cinder cones, and some spectacular intermediate or silicic flows (andesite or dacite(?)). Cerro Tuzgle, in the lower right of figure 5-11(b), has latite flows 0.1 ± 0.3 million years old (ref. 5-18). Compared to Cerro Tuzgle, most of the stratovolcanoes shown in figure 5-11 are younger.

Figure 5-12(a) is an oblique, south-facing photograph of the Andean highlands from approximately latitude 24° S to 28° S. The width of the area photographed near the middle of the frame is approximately 250 km. Most of the area is within Argentina, but the Chilean border is located near the left (western) edge of the photograph. In this area, the plateau seems to consist mainly of pyroclastic rock (ash-flow tuffs) overlying folded and faulted older rocks. Much of the plateau appears to be block faulted. Near the lower left edge of the photograph, the ash-flow tuffs are blocked by north-trending mountain ranges. The locations of all major features in figure 5-12(a) are shown in a sketch map (fig. 5-12(b)).

Salar de Antofalla, the prominent 160-km-long depression in the center of figure 5-12, might be a graben. The Salar and the bordering terrains consist of the following three separate physiographic units.

1. East of Salar de Antofalla, the nearly flat-lying ash-flow tuff plateau is approximately 80 to 100 km wide. Much of the north-trending pre-ash-flow topography appears to be buried. The plateau is relatively free of young volcanoes with only a few widely spaced basaltic(?) shields, cones, and flows. A 20- to 30-km-wide caldera, which may be a source for some of the

voluminous pyroclastic deposits present in the Andean highlands, is near the center of the plateau.

2. Along the Salar de Antofalla depression, ash-flow tuffs and possibly sediments and other pyroclastic rocks are cut by normal faults. The dark shieldlike masses along the edges of the depression may be basaltic flows. Immediately west of the depression near the center of the area photographed is a long, narrow depression tapering toward both ends that may be simply an eroded anticline or an elongate volcanic depression.

3. West of Salar de Antofalla, the terrain appears to be a plateau of ash-flow tuffs(?) overlain by a myriad of late Cenozoic to Holocene volcanoes. Almost 200 cones, depressions, or craters and domes are visible in the western third of the area photographed. Stratovolcanoes appear to be the most dominant volcanic landform.

Kamchatka Peninsula, U.S.S.R.

A magnificent oblique view of the southern half of the Kamchatka Peninsula (fig. 5-13(a)) was obtained during the Skylab 4 mission. Snow cover, particularly in the uplands, enhanced volcanic landforms, drainage systems, and linear features.

Kamchatka is within the circumpacific belt of volcanism and forms part of the Kamchatka-Kuril arc, one of a larger system of arcs bordering the Asian continent. The Asiatic part of the circumpacific belt is connected by the Aleutian arc to the American Pacific belt. The Aleutian and Kamchatka-Kuril arcs interlock almost at right angles (ref. 5-19, p. 7).

The oblique synoptic view of the Kamchatka Peninsula (fig. 5-13(a)) aids in defining the relationship of the tectonic systems and the volcanoes. Figure 5-13(b), a sketch based on the Skylab photograph, indicates the distribution of linear features and volcanoes. Because of the oblique view, distortion and foreshortening are inherent in this photograph, and a single azimuthal trend appears differently in different parts of the frame; hence, the strike of lineaments cannot be plotted accurately. Many linear features coincide with apparent consequent drainage courses across the Sea of Okhotsk coastal plain and continue to the northeast across the axes of several mountain ranges. Such linear drainage courses associated in their headwater regions with

linear tectonic trends are commonly structurally controlled.

The near-longitudinal Kamchatka tectonic trend, the northwesterly Aleutian trend (refs. 5-19 and 5-20), and another northeasterly tectonic trend appear to control the distribution of volcanoes on Kamchatka. Lineaments following both trends probably reflect fault dislocations and are discernible in figure 5-13(a). The volcanoes along the Aleutian trend are transverse to the longitudinal distribution of major volcanic centers. The Aleutian tectonic pattern apparently does not terminate where it intersects eastern Kamchatka near the Klyuchevskaya volcanic massif but is reiterated in lineaments across the southern part of the peninsula and perhaps onto the continental shelf of the Sea of Okhotsk.

The northeasterly tectonic trend appears in figure 5-13(a) as a set of lineaments crossing the peninsula from the southwestern coastal plain of the Sea of Okhotsk. Faults following this trend generally are not shown on recent Soviet tectonic maps (ref. 5-21). Several of the longer lineaments that follow this northeasterly trend appear to coincide with deep faults located heretofore by geophysical data and hidden by sedimentary deposits, effusive rocks, or water. These faults control the distribution of plutons of ultrabasic composition, as shown on recent Soviet tectonic maps (ref. 5-21). Even these map symbols are terminated on the southwest, short of the coastal plain of the Sea of Okhotsk. The synoptic, low-angle coverage of the snow-covered terrain of southern Kamchatka afforded by the Skylab photographs may be the first known view of these long-continuing lineaments as mappable surface features. Moreover, figure 5-13(a) provides evidence that several of these deep-seated structures may cross the continental shelf of the Sea of Okhotsk.

On Kamchatka, there are 100 to 150 volcanoes of which approximately 20 may be considered active (ref. 5-19, p. 7). Early stages of Kamchatka volcanism apparently involved regional effusive activity (ref. 5-19). More recently, and up to the present, the distribution of volcanoes has been controlled by the tectonic trends previously mentioned. A western longitudinal zone of generally older, inactive volcanoes occurs along the Sredinny Khrebet (fig. 5-13). Other active Pleistocene-Holocene volcanoes are longitudinally distributed along the eastern (Kumroch) ranges to form a zone of intensive contemporary volcanism.

The western (Sredinny Khrebet) zone of generally

extinct volcanoes is separated from the eastern volcanic zone of Kamchatka by a tectonic depression of the graben or rift type, which extends north-south along much of the peninsula (ref. 5-19, p. 6; fig. 5-13(a)). The Kamchatka River and Yelovka River valleys occupy this depression, which can be seen in the Skylab photograph. The origin of the vast, effusive eruptions of low albedo (dark area of photograph) was linked to the formation of large faults bordering the central Kamchatka graben in pre-Quaternary time. The Klyuchevskaya group of volcanoes, including Bezymianny, can be seen in figure 5-13(a) at the northern end of the tectonic depression between the Sredinny Khrebet and the Kumroch Range. The Klyuchevskaya volcano group was built up on a mosaic of block mountains, uplifted under Klyuchevskaya Sopka [volcano] (ref. 5-20) and may represent the triple-junction point between the Aleutian and Kamchatka-Kuril structural arcs.

The dissected caldera of Opala Khrebet (fig. 5-13(a)) is one of the most obvious volcanic features to be seen in the Skylab photograph. The active volcano Opala is located on the northern rim of this caldera, one of the largest calderas of Kamchatka outside the zone of active volcanoes.

The volcano groups of Avacha, Avinchinskaya Sopka, and Koryakskaya Sopka (fig. 5-13(a)), controlled by Aleutian or northwest-trending faults, are visible in the eastern zone north of the city of Petropavlovsk-Kamchatskiy. Avachinskaya Guba, a circular bay that is the result of continuing volcano-tectonic subsidence (ref. 5-19, p. 6), can also be seen. Farther south, volcanoes of the Gorely Khrebet are also controlled by northwest-trending structures.

Volcanoes of the Kambal'naya Sopka group near the southern tip of Kamchatka are aligned along a north-northeast-trending lineament that also passes through the center of Ozero [lake] Kuril'skoye; the three craters of Kambal'naya fit on this line (ref. 5-19, pp. 137-138). The active Koshalev Volcano and associated geothermal area are located northwest of Kambal'naya Sopka on a transverse fissure similar to that noted in the distribution of the volcanoes of the Avacha and Koryaka groups (ref. 5-19, p. 142).

From analysis of the Kamchatka photograph, the pronounced relationship between tectonic features (linear on the photograph) and volcanic areas appears to support the concept that the location of virtually all volcanoes is controlled tectonically (Gorshkov and Piip in ref. 5-19, p. 3).

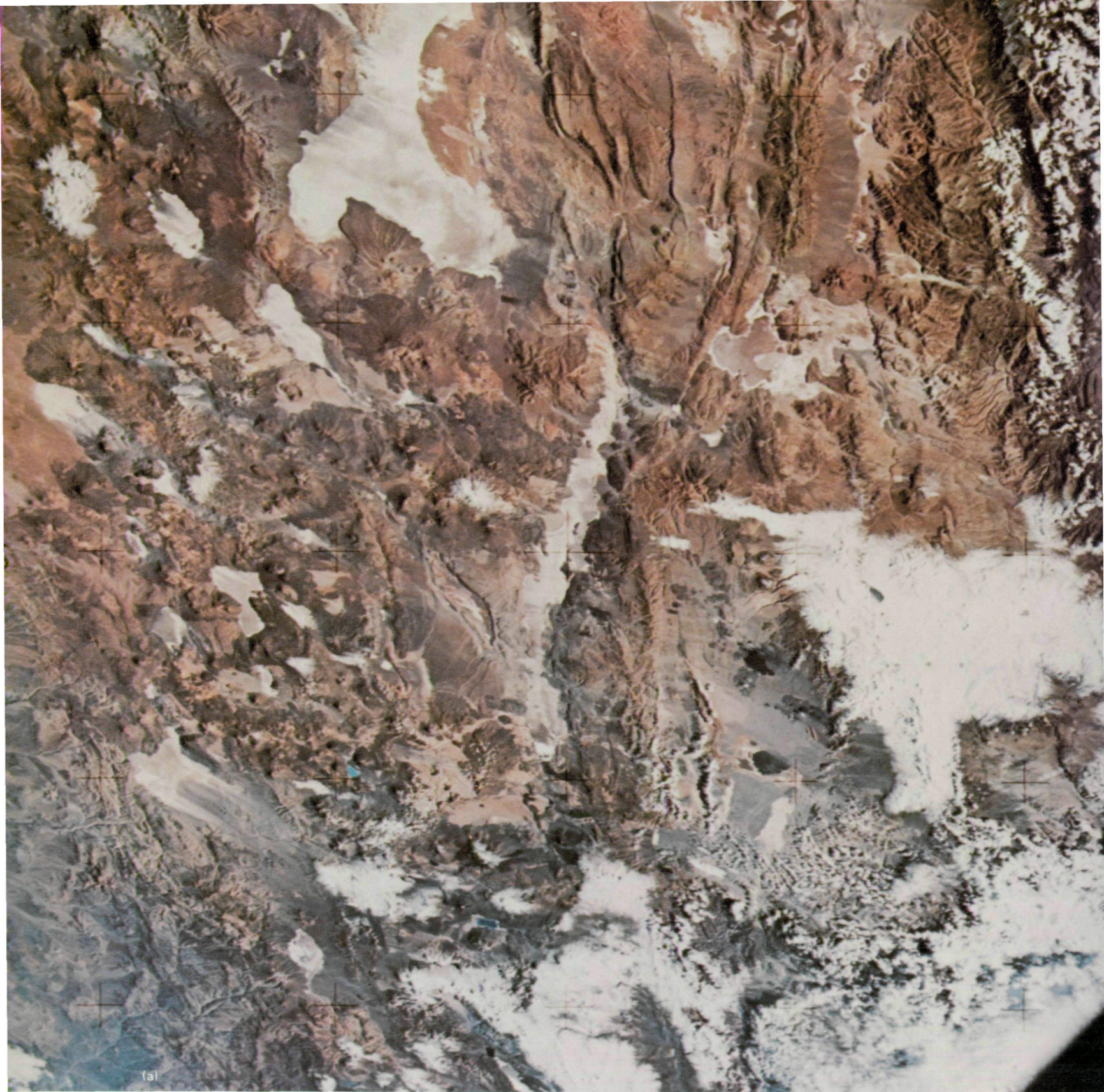


FIGURE 5-12.—Part of the altiplano volcanic field. (a) Photograph (SL4-137-3676). (b) Sketch map.

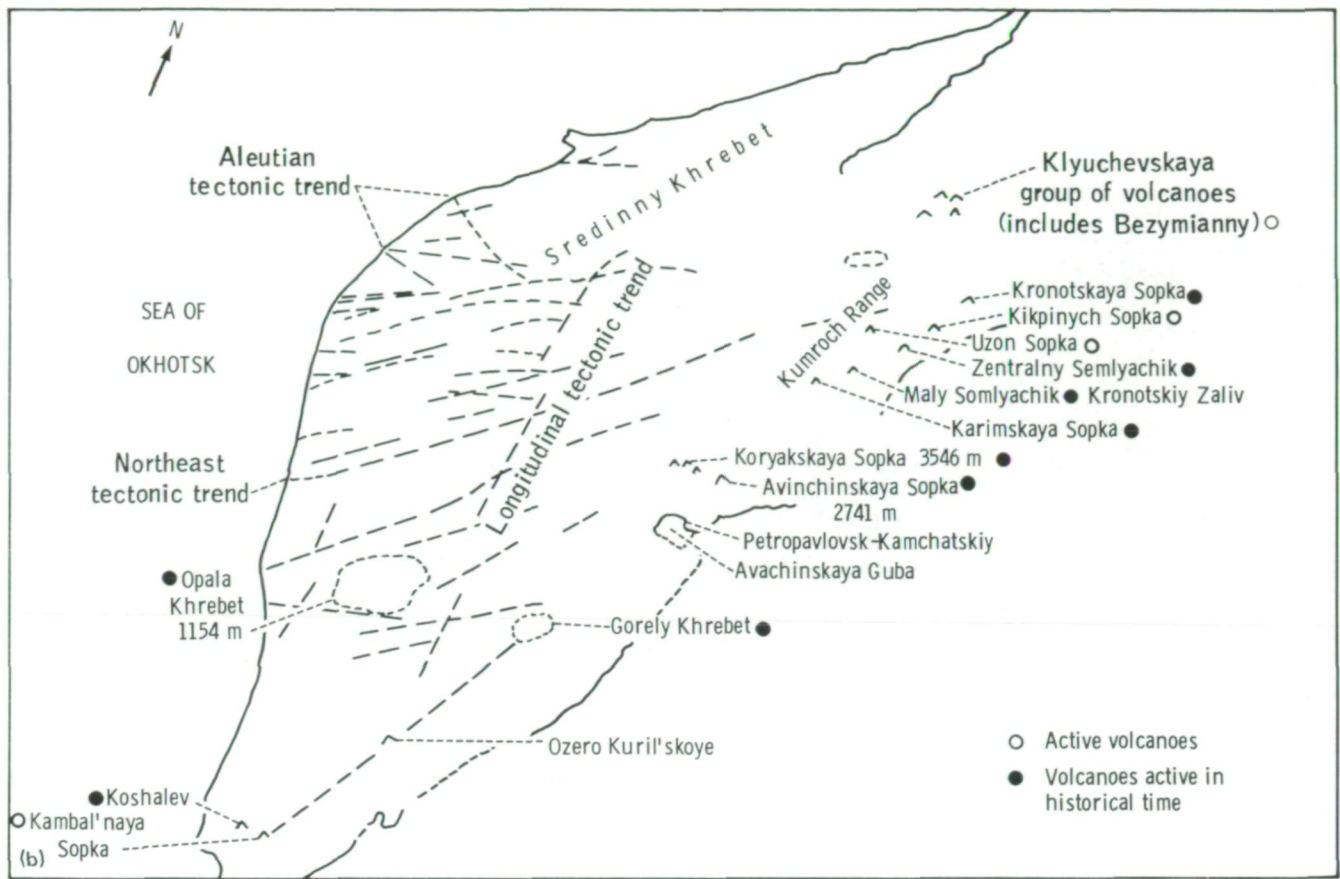


Explanation

- | | | | | | |
|---|---|---|--|---|---|
| o | Volcanic peaks | S | Salar | T | Ash-flow tuff plateaus |
| | Crater or caldera rim | V | Younger volcanic terrain, including stratovolcanoes, domes | P | Pre-Cenozoic volcanic terrain |
| | Structural trend of prevolcanic terrain | D | Dome-flow clusters or groups | B | Inter montane basin fill (sediment, pyroclastic detritus, lava flows) |
- (b)



(a)
FIGURE 5-13.—Southern half of Kamchatka Peninsula, U.S.S.R., showing volcanic landforms and lineaments. (a) Photograph (SL4-141-4273). (b) Sketch map.



Southeastern Central Plateau of Mexico

A Skylab photograph of the volcanic highlands east of Puebla, Mexico, shows several large circular features that may be calderas (fig. 5-14(a)). Although maars or explosion craters near Puebla have been described, the authors have not found in the published literature a description of the large circular structures seen on the Skylab photograph. A sketch map of this area prepared from the Skylab photograph gives the location of the major volcanic features (fig. 5-14(b)).

Figure 5-14(a) is an oblique view of the Mexican highlands from the La Malinche Volcano east to the Gulf of Mexico, a distance of approximately 210 km. Features on the photograph are identified as follows.

1. A shallow, nearly circular depression (14-km diameter) with lava flows radiating from the rim, suggesting a caldera origin. Of the circular structures visible on the photograph, this structure is the least eroded.

2. Two shallow, overlapping depressions that may be partly buried calderas. The westernmost depression is approximately 12 by 28 km, and the remnants of the eastern structure indicate that it might have been as much as 15 km in diameter.

3. A circular, highly dissected structure (possibly a caldera) 30 km in diameter. The western edge and part of the central section of the structure consist of light-colored, yellowish-brown rock that might be hydrothermally altered.

4. Clusters of small volcanoes within a basin (former lake basin(?)).

5. Stratovolcanoes.

6. La Malinche Volcano.

7. Ixtaccihuatl Volcano.

Figure 5-15 is a southeast-looking oblique photograph of volcanoes Popocatepetl and Ixtaccihuatl, Mexico. Popocatepetl is an active, young stratovolcano located at the southern end of a north-trending chain of

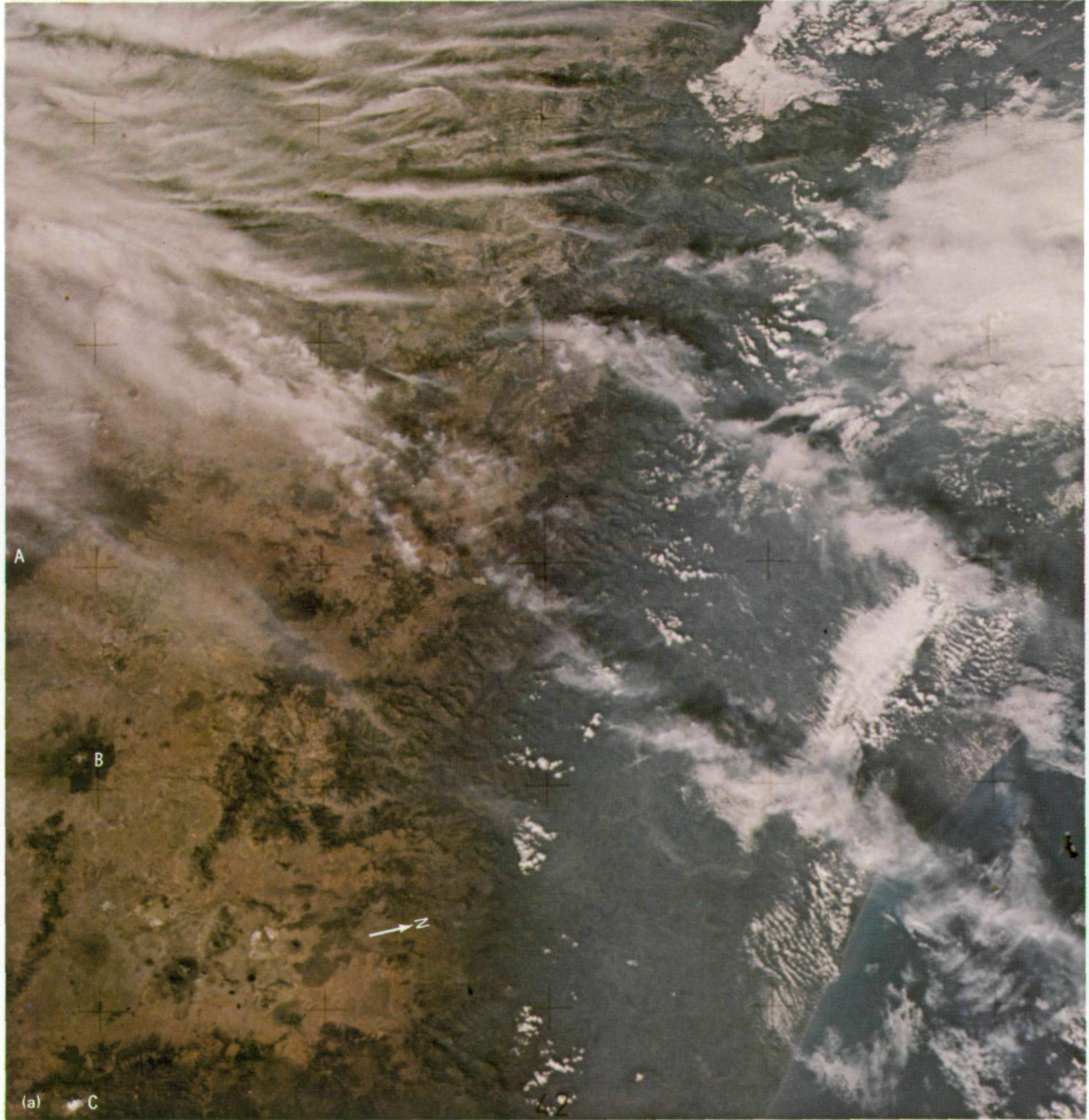
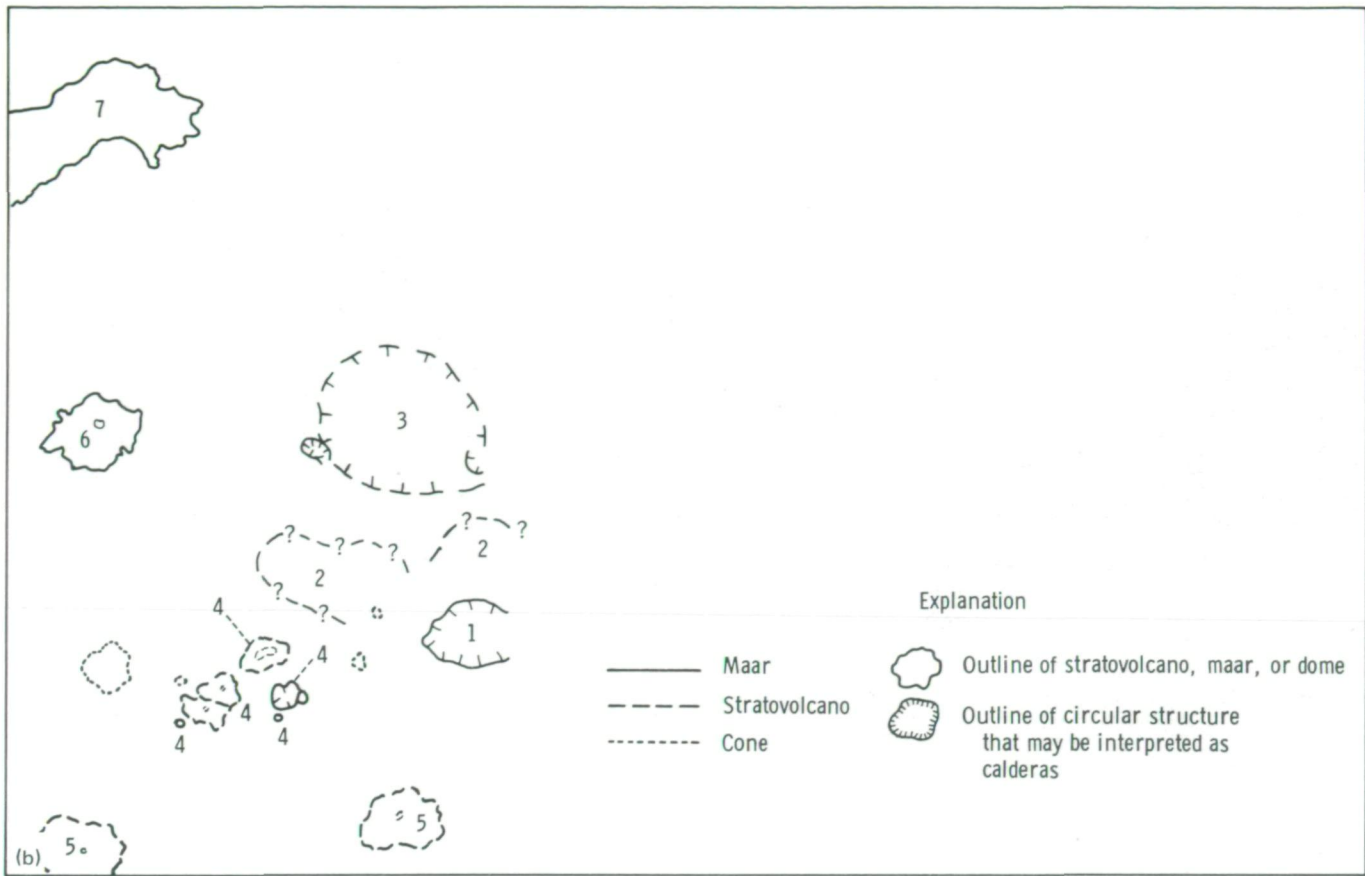


FIGURE 5-14.—Mexican highlands from Ixtaccihuatl Volcano east to the Sierra Madre Oriental. "A" is San Nicolas, "B" is La Malinche, and "C" is Rico de Orizaba. (a) Photograph (SL4-139-4064). (b) Sketch map of eastern segment of neovolcanic zone of Mexico. See text for explanation of numbers.



volcanoes of the eastern segment of the neovolcanic axis separating the valleys of Mexico City and Puebla (fig. 5-16). The upper slopes of the volcano appear to be mainly pyroclastic rock, whereas thick andesitic(?) flows are visible extending from the base.

Ixtaccihuatl is more complex. The hummocky appearance of the lower slopes is caused by a series of short, thick andesitic(?) lava flows. This volcano is older than Popocatepetl and is highly dissected by stream valleys.

Synoptic views such as figures 5-14(a) and 5-15 are useful in the study of large-scale structures that might not be recognized in aerial photographs or mapped in ground surveys. The circular structures tentatively identified in Skylab photographs as calderas may be source vents for the pyroclastic deposits of the central Mexican plateau. Because ore deposits are commonly associated with the boundary faults of calderas, these structures should be studied in detail by ground survey teams.

LANDFORMS OF VOLCANIC PROVINCES

A variety of photographs of the volcanoes in Hawaii, Italy, the Aleutian Islands, and Oregon and Washington was obtained by the Skylab 4 crewmen. The published literature contains many reports that define the geologic settings of these volcanic regions, and the Skylab photographs provide an interesting regional view of these volcanic areas.

Hawaii

The island of Hawaii, as seen in a Skylab photograph (fig. 5-17(a)), is a major basaltic shield volcano composed of five distinct volcanoes (fig. 5-17(b)): Mauna Kea, 4273 m in elevation and snowcapped in the Skylab photograph; Mauna Loa, 4240 m and snowcapped; Kilauea, 1252 m; Kohala, 1720(?) m; and Hualalai, 2584(?) m. The volcanic shield of Hawaii rises 9144 m

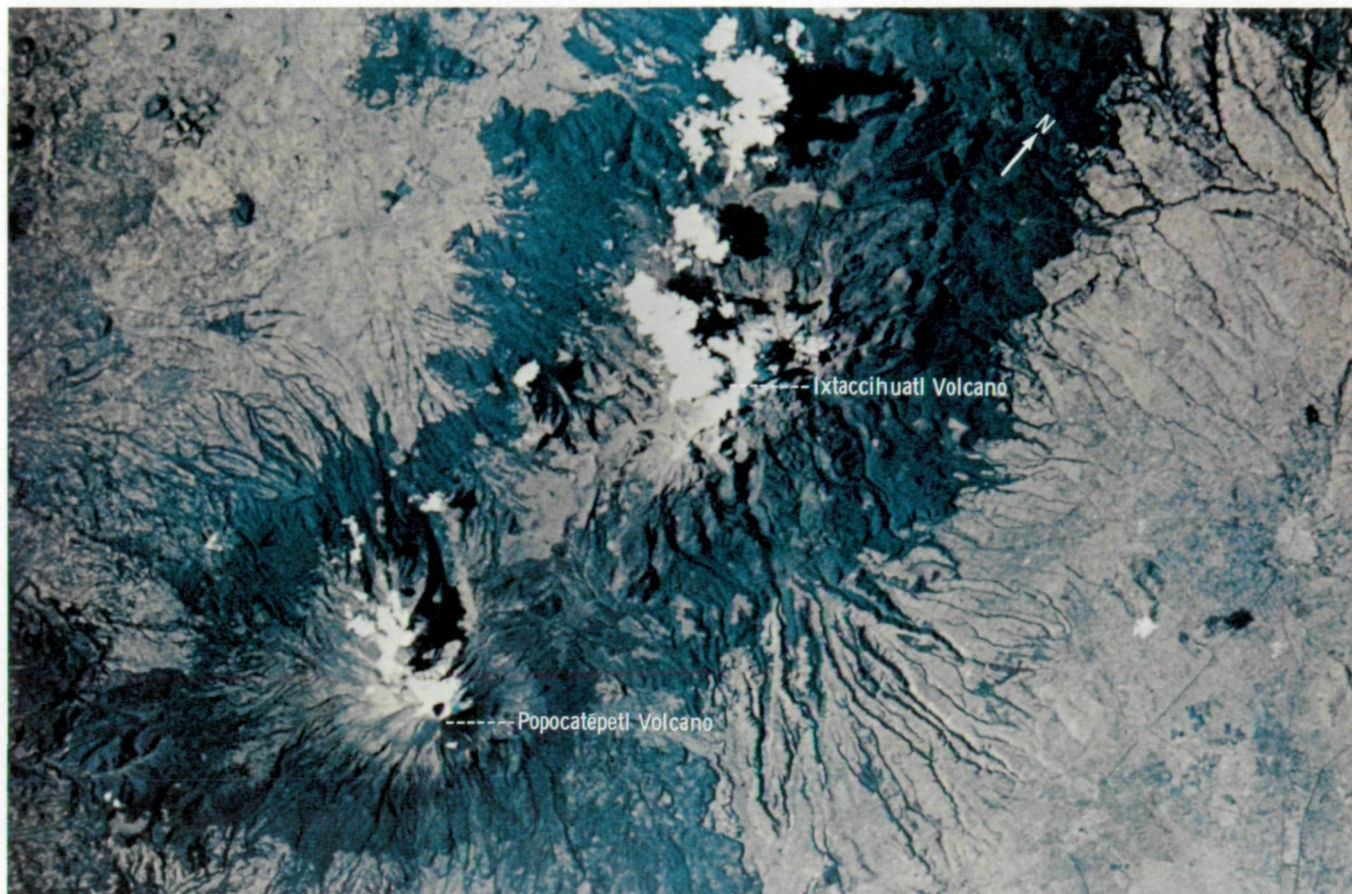


FIGURE 5-15.—Nikon photograph taken with 300-mm lens showing the volcanoes of Popocatepetl and Ixtaccihuatl near Mexico City (SL4-207-8056).

from the ocean floor to the summit of Mauna Loa and Mauna Kea and in this sense could be considered the highest mountain on Earth (ref. 5-4).

The shield has been built up largely by effusive eruptions from a system of fissures that form rift zones. At each volcanic edifice, one or two of the three rift zones tend to be dominant. The trigonal ground plan of the entire island, obvious in the Skylab photograph, is the result of the geometric arrangement and development of the dominant rift zones. The rift zones of each volcano converge in summit calderas at 120° . The most prominent of these is the Mokuaweoweo caldera of Mauna Loa. The ribbonlike historical flows (i.e., those of low albedo, not significantly covered by vegetation) extend downslope from the rift zones to the coast. This configuration can be seen in detail in figure 5-17.

Mauna Kea.—A snowcap in the Skylab photograph

marks the summit of Mauna Kea (fig. 5-17(a)), the highest point on the island of Hawaii. The Mauna Kea dome, 50 km in diameter, is coalescent with Mauna Loa and Kohala. Lavas of the Laupahoehoe volcanic series that overlie glacial deposits indicate that Mauna Kea became extinct in the Holocene epoch (ref. 5-22). In figure 5-17(a), the absence of low-albedo lava flows on Mauna Kea contrasts sharply with the presence of these flows on Mauna Loa and also suggests the lack of historical lava-flow activity.

Kohala.—Kohala Volcano is an extinct volcano that forms the northwestern peninsula of Hawaii. Clouds obscure the volcano in figure 5-17(a). A summit caldera 3.3 by 5.0 km long has been filled by lavas (ref. 5-22).

Hualalai.—Hualalai Volcano, 28.4 km in diameter, dominates the Kona coast, is built over a dominant northwest rift zone, and was last active in 1800-1801

when the voluminous Kaupulehu flows erupted from a long crack on the northwestern flank (ref. 5-22). The low-albedo Kaupulehu flows can be seen clearly.

Mauna Loa.—The Mauna Loa dome measures 100 by 50 km and is capped by the Mokuaweoweo caldera, which measures 6.0 by 2.8 km. It can be identified under the southern snowcap in figure 5-17(a). Mauna Loa has well-defined southwest and northeast rift zones and a weakly developed north rift zone (ref. 5-22). The southwest rift zone and the northeast zone are the sources of hundreds of historical, voluminous, ribbonlike, low-albedo lava flows that are clearly visible in the Skylab photograph. Several circular pit craters located near the summit calderas perforate the rift zones of Mauna Loa (ref. 5-4). Of these, North Pit and South Pit on Mokuaweoweo caldera and Lua Hou (only 460 m

in diameter and approximately 1 km south of South Pit) are visible in the Skylab photograph as dark spots in the area of the snowcap.

Kilauea.—Kilauea, on the southeastern flank of Mauna Loa, probably lies at the termination of the feeder rift system that passes through Kohala and Mauna Kea (ref. 5-23). The summit caldera is 4.9 km long and 3.3 km wide. Kilauea has two dominant rift systems: the southeast rift zone, marked by a chain of recently active pit craters, and a southwest rift zone, marked by fissure eruptions along dilation fissures, such as the Great Crack, which is more than 13 km long (ref. 5-4). Both the summit caldera and the southeast rift zone activity have in recent years been marked by lava-lake development as well as lava effusions from rift zone fissures.

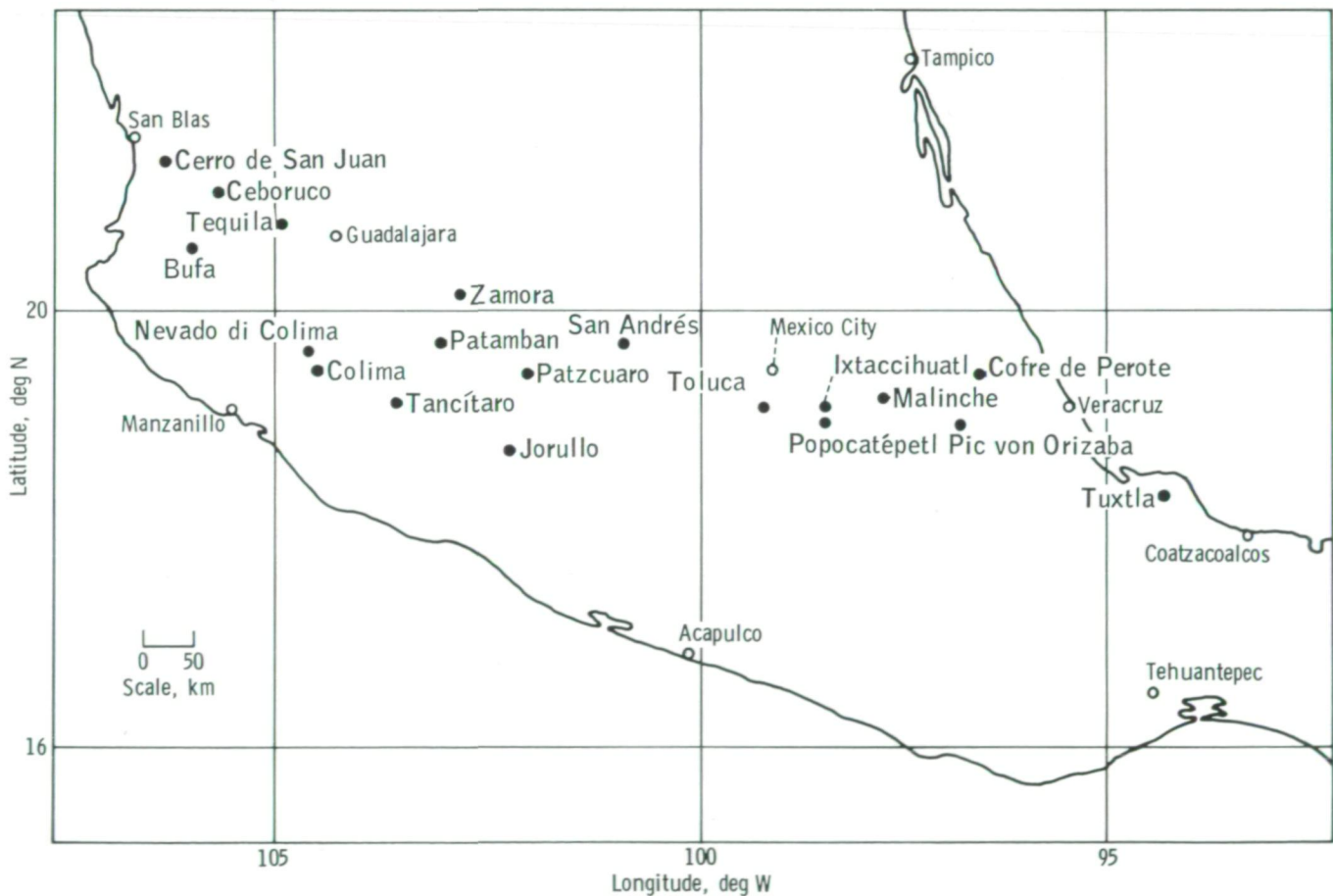


FIGURE 5-16.—Map showing location of active volcanoes in Mexico. The distribution of these volcanoes outlines the neovolcanic axis of Mexico.

ORIGINAL PAGE IS
OF POOR QUALITY

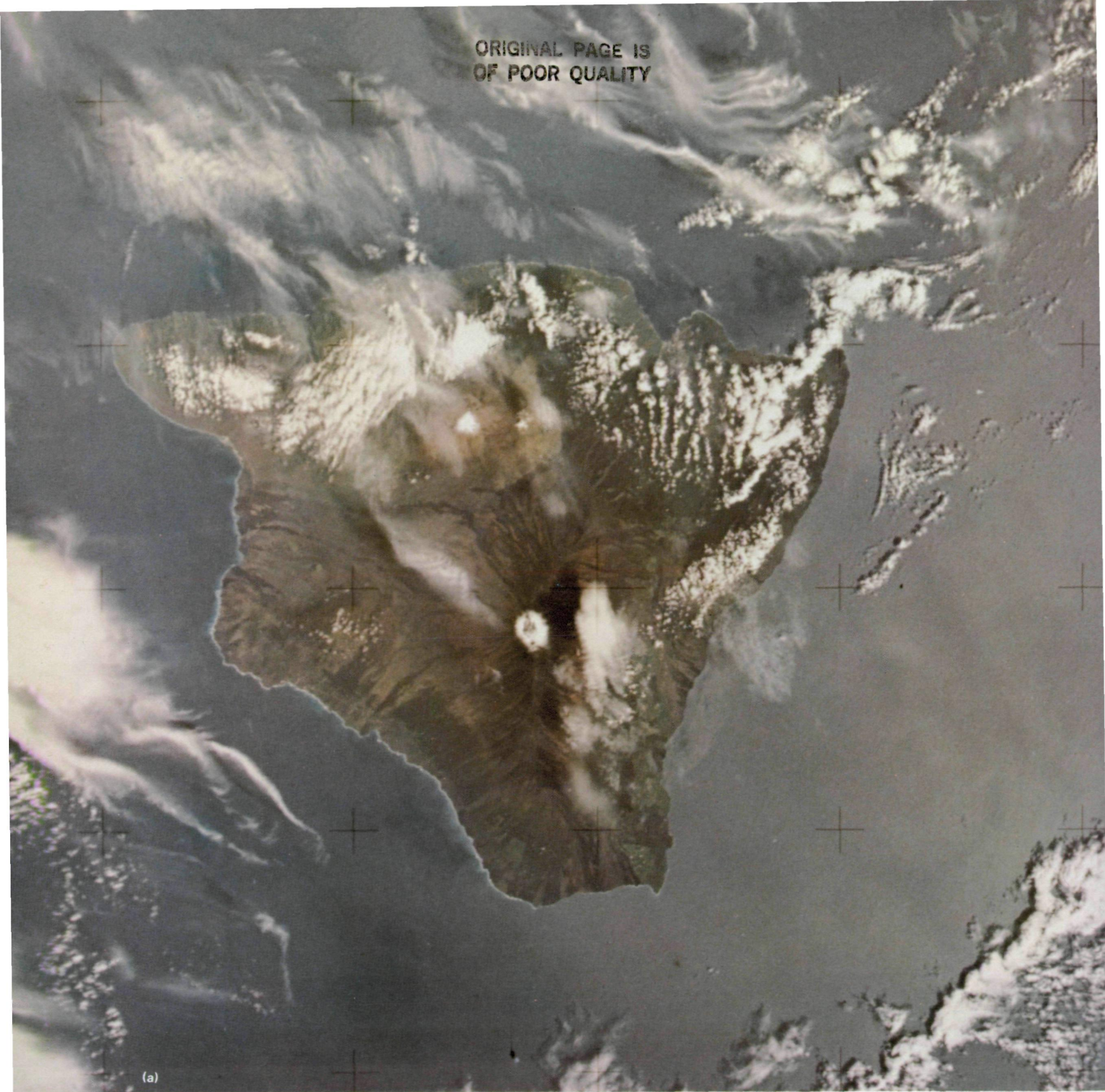
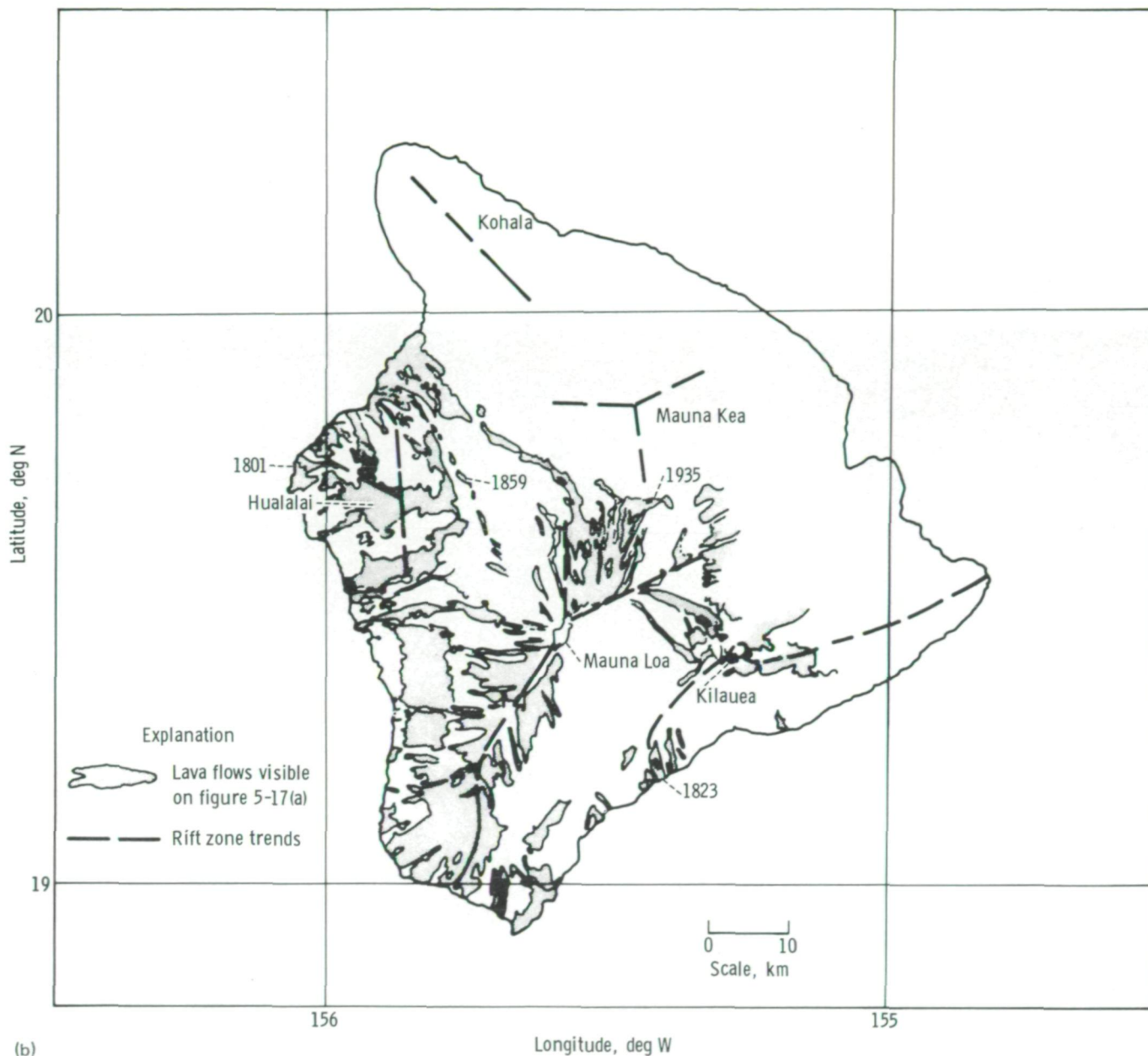


FIGURE 5-17.—Island of Hawaii. (a) Photograph (SL4-139-3997). (b) Planimetric sketch map of Hawaii showing major configuration of lava flows of low albedo.



The chief contribution of the Skylab photograph (fig. 5-17(a)) is the synoptic view showing in one frame the cloud-free areas of virtually all historical lava flows from Mauna Loa and Kilauea. Such a view is primarily useful as a reference for continued investigations of Hawaiian volcanoes.

Aleutian Islands and Alaska Peninsula

The Aleutian Island chain and the Alaska Peninsula fringe the North Pacific with 76 major volcanoes, half of which have erupted since 1860 (ref. 5-24). Approximately half of the volcanic arc was photographed by

the Skylab 4 crewmen, from Mount Cleveland at latitude 52°49' N, longitude 170° W, to the northeastern end of the Alaska Peninsula at approximately 156° W, 57° N (fig. 5-18).

The stratovolcanoes Maushin, Akutan(?), Fisher, Pogromni, Westdahl, Shishaldin, Isanotski, and Frosty are visible as snowcapped points from the bottom of the photograph to almost the middle of the frame. All these volcanoes except Westdahl and Frosty have been active since 1860 with "smoke" (fume or ash cloud) or short,

thick lava flows emanating from the craters (ref. 5-24). Northeast of Frosty, cloud cover obscured the volcanoes of the Alaska Peninsula. Several very large stratovolcanoes on the horizon may be Katmai, Mageik, and Denison in the Katmai National Monument.

The historical value of handheld-camera photographs in the panoramic study of volcanic terrain is illustrated in figure 5-18, which shows 11 volcanoes that are inaccessible most of the year.

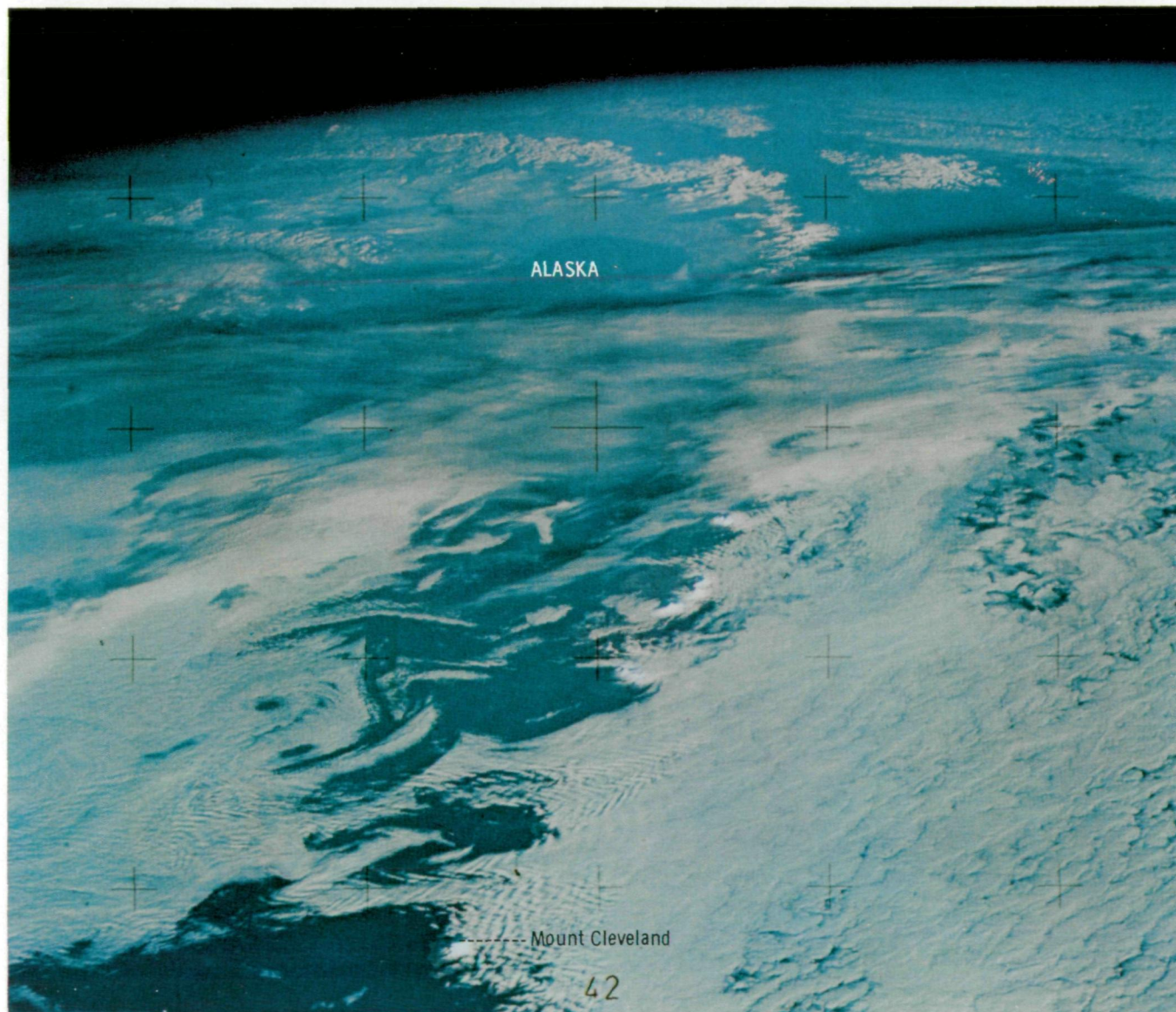


FIGURE 5-18.—Part of the Aleutian Island volcanic arc (SL4-140-4089).

Oregon and Washington

Oblique Skylab photographs were taken over the Cascade Range and adjacent high plateaus from the California-Oregon border to southern Canada. In figure 5-19, the Crater Lake caldera is easily identified. Continuing north from Crater Lake, the high Cascade volcanoes (enhanced by snow cover) are visible. These volcanoes include Three Sisters, Mount Jefferson, Mount Hood, Mount St. Helens, Mount Adams, and Mount Rainier (fig. 5-20). East of the Cascade Range, the relatively smooth terrain is the surface expression of Pliocene basalt flows (right side of fig. 5-19). The plateau basalt flows are cut by normal basin-and-range faults that control both the topography and location of many Pleistocene and Holocene volcanoes in south-central Oregon. The white areas in figure 5-19 are dry lakebeds. Older volcanic landforms that support forests are masked by snow.

In south-central Oregon, snow cover is not extensive, and the basalt flows at Lava Mountain and Green Mountain (right center) are visible, as are numerous small cones and domes (upper right).

Southern Italy

The volcanic region near Naples, Italy, was an investigative site for the Skylab 4 crewmen. The major volcanic features of the Bay of Naples area, visible on figure 5-21(a), a low-oblique photograph, are the volcano-tectonic horst block of Ischia and associated islands (including Procida), the Phlegrean Fields volcanic system west of Naples, and the Somma-Vesuvius stratovolcano. Ischia, the Phlegrean Fields, and Vesuvius are volcanically active. Farther north, the Tertiary volcanic landforms of Mount Roccamonfina are also visible.

Ischia.—Ischia (lat. 40°44' N, long. 13°53' E) is a volcano-tectonic horst complex cut by near-vertical faults that have channeled lava and geothermal vapors from a large underlying magma chamber. Volcanic activity at Ischia may have begun in Miocene time and later extended northeast to the Phlegrean Fields and the Somma-Vesuvius region (ref. 5-25, p. 20). Today, Ischia is tectonically and volcanically connected to Procida and the Phlegrean Fields by a N 52° E-trending fault zone, part of the Tyrrhenian fracture system, which extends at least from the isthmus of San Angelo (fig. 5-21(b)) through a vale between the horst blocks of

Mount Epomeo and Mount Campagnano on southeastern Ischia, and then through Procida and the Phlegrean Fields to Benevento (ref. 5-25, p. 20). This Tyrrhenian fracture system is marked by the alignment of several craters too small to be seen on the Skylab photograph and by the volcanic domes San Angelo (fig. 5-21(a)) and Castle of Ischia. Eruptions in the Ischia volcano-tectonic system occurred between the second and fifth centuries B.C. (ref. 5-25, pp. 22-23). The last eruptive activity occurred in A.D. 1301, but seismic activity accompanied by uplift and subsidence on Ischia and in the Phlegrean Fields volcanic area has occurred as recently as the 1970's. In addition, fumarolic activity and thermal springs along the beach zone east of San Angelo outline the position of the Tyrrhenian fracture system on the southern coast of Ischia. The San Angelo dome, which marks this same fracture zone, is sodalite-phonolite in composition and represents differentiated lavas from the highest part of the underlying magma chamber.

Phlegrean Fields.—The Phlegrean Fields west of Naples (lat. 40°50' N, long. 14°08' E), visible in figure 5-21(a) as a circular area 15 to 20 km in diameter, are the caldera remnant of a polygenetic volcano. Several craters and crater remnants 3 to 4 km in diameter are visible within the larger circle. The Phlegrean volcanic zone continues offshore and includes the submarine Shoal of Pampano, probably a remnant of a crater, and a submarine terrace east of Procida, which includes the volcanic remnant of Miseno and the Benda Palummo shoals (ref. 5-25, p. 2). These volcanic features are aligned along the eastern segment of the same Tyrrhenian (east-northeast to west-southwest) fracture system that controlled the location of the San Angelo dome and other domes along the southern coast of Ischia.

Phlegrean eruptive activity is thought to have begun in Pliocene time, with magma being channeled to the surface along faults aligned along the Tyrrhenian fracture zone (ref. 5-25). Ultimately, a major stratovolcano was built up and later destroyed in the area of the present Phlegrean Fields circle—which represents the caldera infrastructure.

The only certain historic eruption in this area occurred in A.D. 1538; the present Mount Nuovo cinder cone was formed in the first two days of the eruption (ref. 5-25, p. 2). An earlier historic eruption may have occurred at Solfatara in A.D. 1198; but, in any case, relatively deep-seated fumarolic activity, sometimes accompanied by seismic and bradyseismic activity, and emergence and subsidence of the volcanic area at the



FIGURE 5-19.—Cascade Range and adjacent high plateaus from the California-Oregon border to southern Canada (SL4-139-4048).

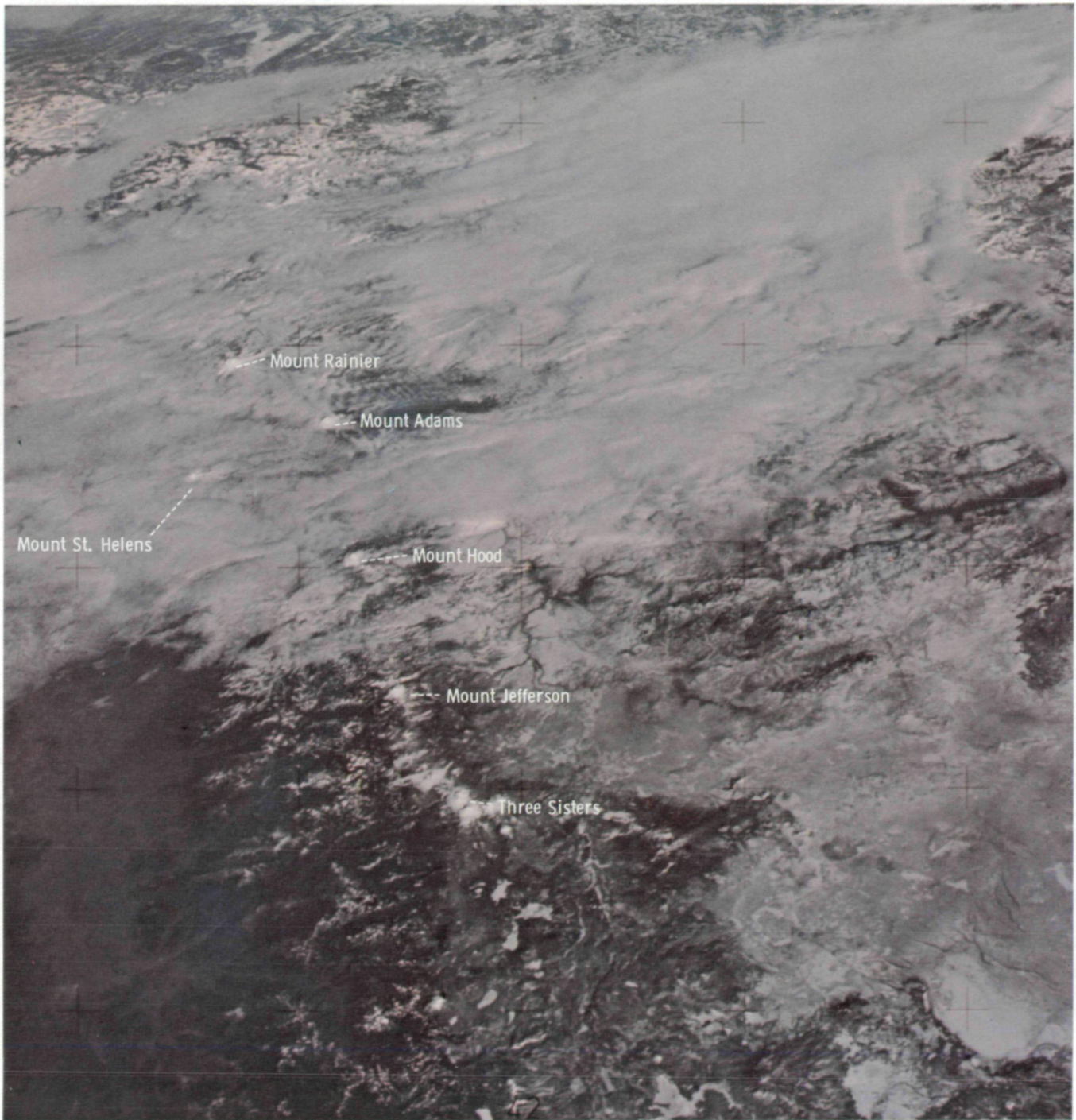
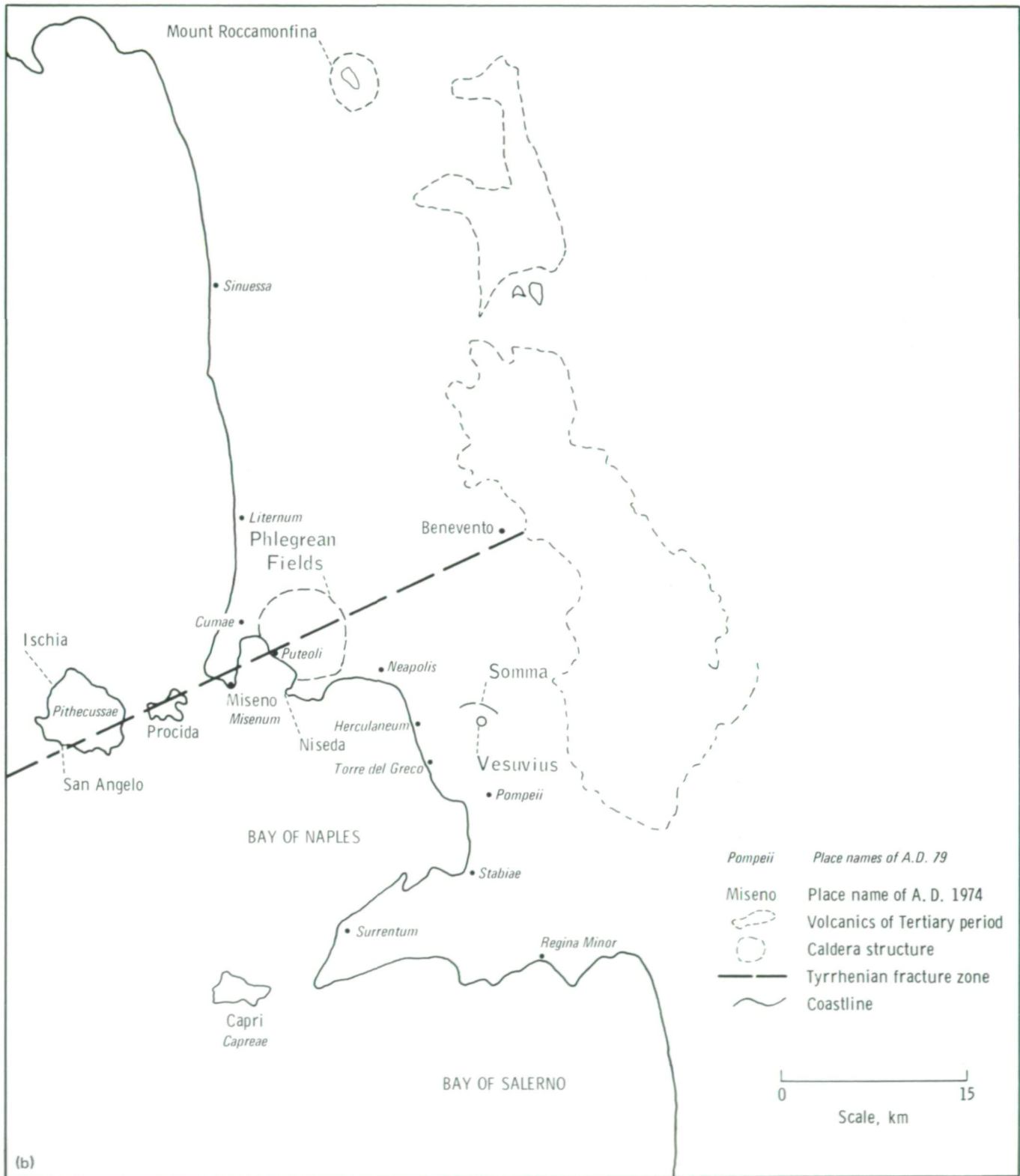


FIGURE 5-20.—Cascade Range and adjacent high plateaus (SL4-139-4047).



FIGURE 5-21.—Volcanic features in southern Italy. (a) Photograph (SL4-141-4288). (b) Sketch map of the Bay of Naples region.



edge of the Bay of Pozzuoli in relation to sea level have continued since at least the second century B.C. (ref. 5-25, p. 4).

Somma-Vesuvius.—The ring remnant of the polygenetic stratovolcano Somma and the present Vesuvius (lat. 40°49' N, long. 14°26' E) is clearly recorded in figure 5-21(a). Located on the middle-east shore of the Bay of Naples in the Campanian Plain, the Somma-Vesuvius volcanic complex marks the site of the classical Plinian eruption of A.D. 79. The narrow bow-shaped Valle del Gigante that separates the two volcanic structures is also visible. The Valle del Gigante is divided into parts: the Atrio del Cavallo on the west and the Valle del Inferno on the east.

The eruptive history of Somma-Vesuvius has been complicated and can be divided into four cycles of activity separated by long periods of quiescence: (1) the Pre-Somma cycle, during which a cone of trachyte ash and pumice were erupted 10 000 years ago (ref. 5-26); (2) Older Somma, represented by an acid tephrite cone that buried the trachyte cone; (3) Younger Somma, the eroded, vegetation-covered volcano known to the ancient Romans and thought by Strabo (ca. A.D. 20) to be extinct (ref. 5-4, p. 232), represented by a leucite tephrite cone that replaced Older Somma; and (4) Vesuvius (the present cycle), which was built up starting with an eruption in A.D. 172 in the caldera of Younger Somma.

The present ring of Somma represents the northern and eastern remnant of the caldera rim that remained after the collapse of Younger Somma. The collapse followed the paroxysmal Plinian eruption of A.D. 79, which destroyed Pompeii and Herculaneum.

Interestingly, the eruptive axes of Somma and Vesuvius do not coincide (ref. 5-25, p. 8). The present axis, represented at the surface by the present crater (fig. 5-21(a)) and conduit, visible in the Skylab photograph as a dark spot, is inclined northeastward and shifted approximately 700 m south-southwestward in relationship to the eruptive axis of Younger Somma (ref. 5-25, p. 7). South of Vesuvius is a slightly darker zone, indicating the area covered by the extrusive volcanic products of both Younger Somma and modern Vesuvius; this includes the pumice and ash that destroyed Pompeii and the volcanic mudflow deposits that destroyed Herculaneum in A.D. 79.

The Skylab photograph (fig. 5-21(a); also see fig. 5-21(b)) of volcanic landforms of the Bay of Naples region, Italy, indicates the linear alignment and possible genetic relationship of the following volcanic features

along the east-northeast-trending Tyrrhenian fracture system: (1) San Angelo sodalite-phonolite volcanic dome on the southern coast of Ischia, (2) a zone of geothermal emission on the southern coast of Ischia, (3) an east-northeast-trending linear topographic depression bounding the Ischia volcano-tectonic horst block, (4) the volcanic island of Procida, and (5) the Phlegrean Fields volcanic area (which appears as a distinct caldera on the Skylab photograph).

OBSERVATIONAL RESULTS

Eruptive clouds are perhaps the most dynamic terrestrial features seen from space. However, the Skylab 4 crewmen were unable to identify motion within the Sakura-zima plumes during a single overflight (30 to 40 seconds), but on successive passes they found that the movement of the Sakura-zima plume could be determined relative to ground features.

Color contrasts and shape variations seen by the crewmen from orbit may not be discernible in the transparencies. However, the transparencies have the advantage of availability for extended quantitative study. The color of volcanic features recorded on film depends on a variety of factors (e.g., lighting conditions). The color shown in the photographs may or may not accurately reproduce that actually seen from Skylab. The crewmen commented that pronounced "streaking" (i.e., albedo and color differentiation) between young (dark) lava flows and old (tan brown) flows on Hawaii was readily apparent. In contrast, the volcanoes in Central America were difficult to discern, and even the dark lava flows were not visible.

The level of detail seen from orbit was equivalent to that seen in the stereophotographs. Gross features of volcanic regions are recognized from orbit, but the size and shape of small-scale features, such as craters and cones less than 1 km in diameter, are not visible. A Sun angle of 20° or less is optimum for viewing and photographing volcanic surface features and eruption clouds. The low Sun angle enhances low-relief features, whereas a high Sun angle and low phase angle provide optimum definition of color contrasts.

CONCLUSIONS

Analysis of handheld-camera photographs of volcanic processes and landforms obtained during the

Skylab 4 mission of 1973-74 suggests at least four categories of scientific investigations that may be made using observations and photographs from manned spacecraft.

1. Determination of the characteristics of volcanic eruption columns, clouds, and plumes in terms of penetration of the tropopause and creation of stratospheric dust veils. Confirmation of volcanic penetration of the tropopause is a logical first step in making a numerical assessment of the dust veil index. The eruptions of Sakura-zima and Fernandina Volcanoes are examples.

2. Observation of volcanic ring infrastructures and caldera landforms by using synoptic photographs that show subtle differences in coastal landforms, topographic textures, relief, drainage pattern, albedo, or color and thus show previously unobserved relationships between geomorphology and structure. Examples described are the Aira, Ata, and Kirisima calderas of Kyūshū and the Phlegrean Fields caldera of the Bay of Naples, Italy.

3. Observation of previously unmapped tectonic lineaments that may represent structural control of volcanic features. Such observations are enhanced by low Sun angles, snow-covered terrain, oblique angles of view, and the linear alinement of topographic details. Examples of such tectonic lineaments were observed on the Kamchatka Peninsula.

4. Stratigraphic or relative age distinctions between partly overlapping basaltic flows made on the basis of albedo variations and cutting relationships. Hawaii would be an example.

ACKNOWLEDGMENTS

The authors thank George Ulrich and his coworkers of the U.S. Geological Survey, Flagstaff, Arizona, for the analytical stereoplotter analyses of the Sakura-zima photographs and the Japan Meteorological Agency and the U.S. National Climatic Data Center, Asheville, North Carolina, for tabulated radiosonde data on upper winds over Sakura-zima, Japan.

Part B

Summit Eruption of Fernandina Caldera, Galapagos Islands, Ecuador

TOM SIMKIN^a AND ARTHUR F. KRUEGER^b

On December 10, 1973, a large summit eruption began on Isla Fernandina (lat. 0°22' S, long. 91°33' W), an uninhabited basaltic shield volcano in the Galapagos Islands, Ecuador. The eruption was first recognized by analyses of National Oceanic and Atmospheric Administration (NOAA) 2 satellite images. On December 11, at approximately 15:16 GMT, the Skylab 4 crewmen observed the eruption and obtained the photograph shown in figure 5-8(a).

The eruption might have been triggered by an earthquake with a magnitude of 4.2 that occurred at 01:55 GMT on December 10 along a prehistoric caldera-boundary fault that had been reactivated in 1968 when the caldera floor dropped 350 m. A large lake was formed subsequently in the caldera (ref. 5-27). In the 1973 eruption, at least 130 000 m³ of lava (equivalent to a thermal energy yield of approximately 1.8×10^{16} J (1.8×10^{23} ergs)), from vents located midway between the caldera rim and floor, poured into a large caldera lake that had formed at the time of the 1968 collapse.

On the first day of the eruption, December 10, a prominent vapor plume extended 200 km west-southwest from the caldera and was perpendicular to the prevail-

^aSmithsonian Institution, Washington, D.C.

^bMeteorological Satellite Laboratory, NOAA, Washington, D.C.

ing surface winds. The plume was approximately 15 km wide at 50 km distance. The volcano, however, is on the western side of the archipelago and therefore was not visible from inhabited islands. Thus, the eruption was not recognized locally until the night of December 11.

On December 11, the second day of the eruption, an oblique 35-mm photograph (fig. 5-8(a)) was taken by the Skylab 4 crewmen from nearly 1000 km east-southeast of the eruption. This low-oblique image provides valuable information on the condition of the plume approximately 24 hours before the first ground-based photographs were obtained. Billowing white clouds rose approximately 2.7 km above the vents (3.4 km above sea level). Immediately to the west, however, the narrow cloud descended several hundred meters and was swept to the caldera rim (approximately 1.3 km above sea level). This plume was above the trade-wind inversion, as determined by previous studies of 1968 radiosonde data. As seen in the Skylab photograph, the plume on December 11 had a vertical extent of ≤ 2 km and a horizontal extent of 5 km at a distance of 50 km from the vent.

On December 12, the third day of the eruption, 24 hours after the Skylab 4 photograph was taken, the first ground-based photograph of the cloud indicated that the initial cloud height had decreased and was approximately 2.4 km above sea level (less than 1000 m above the caldera rim). Survey parties from the Charles Darwin Research Station reported that the eruption apparently ended on December 15; ground inspection on December 17 showed that the level of the caldera lake, steaming from the addition of hot lava, was dropping rapidly.

ACKNOWLEDGMENT

The authors are grateful to D. Lyons of the NASA Lyndon B. Johnson Space Center for photogrammetric measurements of the eruption cloud.

REFERENCES

- 5-1. Kuno, Hisashi: Catalogue of the Active Volcanoes of the World, Including Solfatara Fields. Part XI, Japan, Taiwan, and Marianas. Intern. Volc. Assoc. (Rome), 1962.
- 5-2. Matumoto, Tadaiti: The Four Gigantic Caldera Volcanoes of Kyūshū. Japan J. Geol. Geogr., vol. 19, 1943, p. 57.
- 5-3. Rittmann, Alfred: Les Volcans et Leur Activité, Édition Française à Partir de la Deuxième Édition Originale, Établie et Introduite par Haroun Tazieff. Masson et Cie, Éditeurs (Paris), 1963.
- 5-4. Macdonald, G. A.: Volcanoes. Prentice-Hall, 1972.
- 5-5. Matumoto, Tadaiti: Calderas of Kyūshū. Transactions of Lunar Geology Field Conference (Bend, Oregon), 1966, pp. 15-20.
- 5-6. Aramaki, Sigeo: Pyroclastic Flows, Calderas, and Other Depressions in Southern Kyūshū, Japan. Abstracts of IAVCEI Symposium on Volcanoes and Their Roots, Oxford Univ., 1969, pp. 77-78.
- 5-7. Japan Meteorological Agency: Sakurazima Volcanic Activity. Smithsonian Center for Short-Lived Phenomena, Card No. 1886, 1974.
- 5-8. Lamb, H. H.: Climate: Present, Past and Future. Vol. I, Methuen & Co., Ltd. (London), 1972.
- 5-9. McBirney, A. R.; and Williams, Howel: Geology and Petrology of the Galapagos Islands. Geol. Soc. America Mem., no. 118, 1969.
- 5-10. Wilson, J. Tuzo: Continental Drift. Sci. American, vol. 208, no. 4, 1963, pp. 86-100.
- 5-11. Menard, Henry W.: Marine Geology of the Pacific. McGraw-Hill (New York), 1964.
- 5-12. Friedlander, Immanuel: Regelmässigkeit der Abstände Vulkanischer Eruptionszentern. Z. Vulk., vol. 4, 1918, pp. 15-32.
- 5-13. Gêze, B.; Hudeley, H.; Vincent, Pl.; and Wacrenier, P. H.: Les Volcans du Tibesti (Sahara du Tchad). Bull. Volc., ser. 2, vol. 22, 1969, pp. 135-172.
- 5-14. Lowman, Paul D.; and Tiedemann, Herbert A.: Terrain Photography From Gemini Spacecraft—Final Geologic Report. NASA TM X-65451, 1971.
- 5-15. Pesce, Angelo: Gemini Space Photographs of Libya and Tibesti, A Geological and Geographical Analysis. Petroleum Exploration Society of Libya, Tripoli, 1968.
- 5-16. Lomize, M. G.: Araukanskiy Vulkanicheskiy Poyas; Andy (Araucanian Volcanic Belt; the Andes). U.S.S.R. Academy of Sciences, vol. 213, no. 5, 1973, pp. 1147-1150.
- 5-17. James, David E.: A Plate Tectonic Model for the Evolution of the Central Andes. Geol. Soc. America Bull., vol. 82, no. 12, 1971, pp. 3325-3346.
- 5-18. Schwab, Klaus; and Lippolt, Hans: K-Ar Mineral Ages and Late Cenozoic History of the Salar de Cauchari Area (Argentine Puna). Paper presented at IAVCEI Symposium Internacional de Volcanologia (Santiago, Chile), Sept. 9-14, 1974.
- 5-19. Zavaritsky, A. N.: The Volcanoes of Kamchatka. Academy of Sciences, U.S.S.R., Laboratory of Volcanology, Bulletin of the Volcanological Station, no. 10, 1955.

- 5-20. Sviatlovskii, Aleksandr Evgen'evich: On the Volcano-Tectonics of the Klyuchevskaya Group of Volcanoes on Kamchatka. Academy of Sciences, U.S.S.R., Laboratory of Volcanology, Bulletin of the Volcanological Station, no. 26, 1957, pp. 114-120.
- 5-21. Krasnii, L. I., ed.: Structure Formation Map of the North-western Part of the Pacific Mobile Belt (Within the U.S.S.R.). Scale, 1:1 500 000, Russia Ministerstvo Geologii, Moscow, 1972.
- 5-22. Stearns, Harold T.: Geology of the Hawaiian Islands. Hawaii Territory, Department of Public Works, Division of Hydrography, Bull. 8, 1946.
- 5-23. Stearns, H. T.; and Clark, W. O.: Geology and Water Resources of the Kau District, Hawaii. U.S. Geol. Survey Water-Supply Paper 616, 1930.
- 5-24. Coats, Robert: Volcanic Activity in the Aleutian Arc. U.S. Geol. Survey Bull. 974-B, 1950.
- 5-25. Imbo, G.: Catalogue of the Active Volcanoes of the World. Part XVIII, Catalogue of the Active Volcanoes and Solfatara Fields of Italy. Intern. Volc. Assoc. (Rome), 1965.
- 5-26. Rittmann, A.: Die geologisch bedingte Evolution and Differentiation des Somma-Vesuvsmagmas. Zs. Vulkanol., vol. 15, 1933, pp. 8-94.
- 5-27. Simkin, Tom; and Howard, Keith A.: Caldera Collapse in the Galapagos Islands, 1968. Science, vol. 169, no. 3944, July 1970, pp. 429-437.

Page intentionally left blank

Page intentionally left blank

6

The Manicouagan Impact Structure Observed From Skylab*

M. R. DENCE^a

AMONG THE MOST striking topographic features of the Canadian Precambrian shield is the circular ring outlined by the waters of the Manicouagan Reservoir in Quebec. The center of the ring is approximately 200 km northwest of Port Cartier on the St. Lawrence River, in the rugged terrain of the Grenville geologic province.

Initial studies of the structure led to a volcanictectonic interpretation of its origin (ref. 6-1). Modifications of this theory have been followed by some later investigators (refs. 6-2 to 6-4). However, since 1954, the structure has been under consideration as a possible major meteorite impact site. Early geophysical investigations were inconclusive (ref. 6-5), but discoveries of breccias, pseudotachylyte veins (ref. 6-6), and shock metamorphic effects, including an exceptionally fine development of maskelynite (ref. 6-7), have established the Manicouagan structure as a probable impact site (ref. 6-8). As such, the structure continues to be the object of detailed study as an analog for large, circular features on other planetary bodies.

SKYLAB OBSERVATIONS

Regional Setting

Skylab photographs provide a clear indication of the size of the Manicouagan structure and its setting within the Canadian shield. The Daniel Johnson Dam can be

seen (fig. 6-1) 60 km south of the circle formed by the enlargement and junction of former Manicouagan Lake and Lake Mouchalagane. The circle thus completed has an outer diameter averaging 65 km, within which is an irregular plateau with elevations generally 200 to 300 m above the level of the reservoir. A massif with a 15-km diameter forms a central peak complex almost 600 m higher than the water level. This feature, however, is not visible in figure 6-1. To the east, fresh snow caps an adjacent range of mountains that are 100 to 200 m higher.

The view from the west (fig. 6-2) shows the central position of the structure in the northeastern part of the Grenville province, a 400-km-wide belt of generally high-grade metamorphic rocks that have potassium-argon (K-Ar) radiometric ages of approximately 1 billion years. Field studies in this part of the Grenville province have delineated a number of massive gabbroic-troctolitic-anorthositic intrusions, one of which underlies the snowcapped mountains immediately east of the Manicouagan ring. The broad structural pattern of the Grenville province apparent in figure 6-2 is composed of large massifs cut by long lineaments that form deep valleys filled by lakes and rivers draining to the south. By contrast, the older (more than 2.5 billion years) Superior province to the northwest, although also underlain by crystalline rocks of moderate to high metamorphic grade, has more subdued relief and less pronounced structures. In figure 6-2, this province appears as a patchwork of snow-covered areas resulting from an irregular network of lakes and muskeg swamps. The boundary between the two provinces, the Grenville front, is partly defined by two regions of

*Earth Physics Branch contribution number 544.

^aEnergy, Mines and Resources Canada, Ottawa, Canada.



(a)

**ORIGINAL PAGE IS
OF POOR QUALITY**



FIGURE 6-1.—The Manicouagan ring. The St. Lawrence River near Sept-Iles is in the lower left. Left of center, the valley of the south-flowing Manicouagan River leads from the Daniel Johnson Dam, behind which the Manicouagan Reservoir is impounded. Snow covers heights rising more than 1 km above sea level. A distinct circumferential depression at twice the radius of the main ring marks the outer limits of structural disturbance. (a) Photograph (SL3-122-2628). (b) Sketch map.

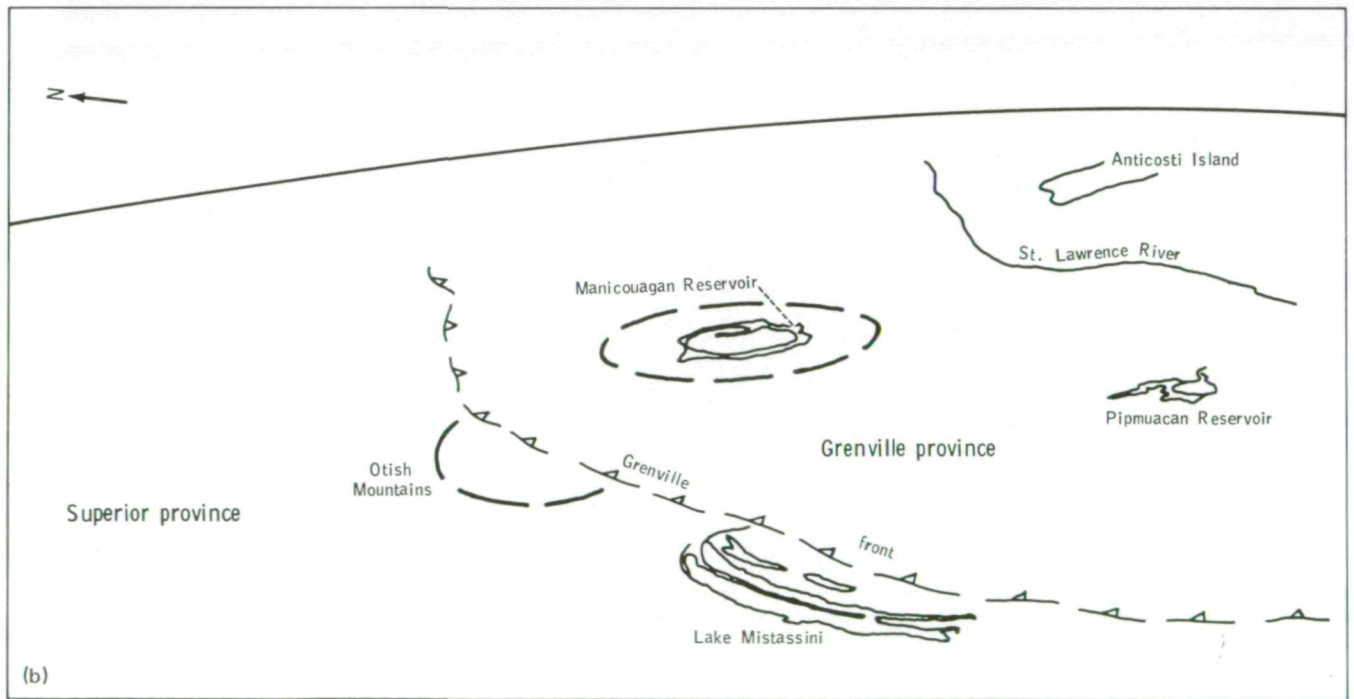


FIGURE 6-2.—View looking east showing the regional setting of the Manicouagan ring. (a) Photograph (SI.4-140-4173). (b) Sketch map.

faulted but only weakly folded and metamorphosed sedimentary rocks of Lower Proterozoic age (probably between 2.5 and 2.0 billion years). These rocks crop out around the prominent arc of Lake Mistassini in the foreground and in the snowcapped Otish Mountains farther northeast. To the southeast, the clouds and ice covering the St. Lawrence River are broken by the long, subdued profile of Anticosti Island that marks the gently dipping Ordovician and Silurian rocks of the Anticosti basin on the northern margin of the Appalachian Mountain system.

From over the Appalachians near the Maine-Quebec border, the view north to the Manicouagan ring includes three other roughly circular structures in the Grenville province (fig. 6-3). The Charlevoix structure on the northern shore of the St. Lawrence River is similar in form to the Manicouagan structure and includes a central peak and a peripheral trough 35 km in diameter, which is outlined by snow-covered fields and small lakes. Shatter coning (ref. 6-9) and other indications of shock metamorphism (ref. 6-10) identify the Charlevoix structure as another impact structure. This site has been shown to be almost twice the age of the Manicouagan structure (ref. 6-11) and is correspondingly more deeply eroded and affected by later tectonic events. The other two features have also been suggested to be impact structures, but available data support alternative explanations. Lake St. John, an elliptical depression around which flat-lying Ordovician sedimentary rocks are preserved, lies within the graben formed by the Saguenay River fault zone, which has associated small Cambrian carbonatitic intrusions. The circular feature largely surrounded by Pimouac Reservoir is a granitic intrusion of Grenville age.

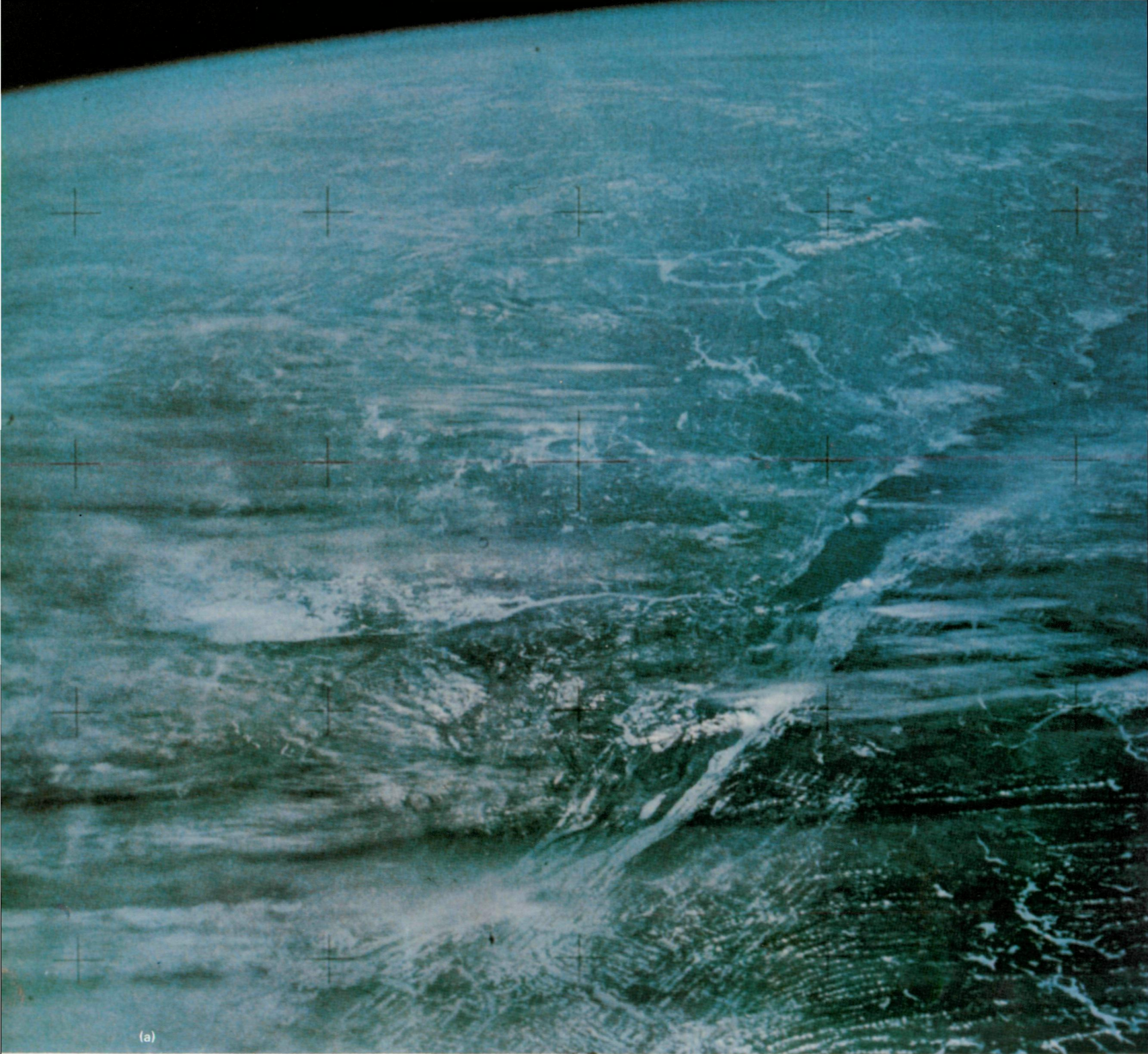
North of Manicouagan (fig. 6-4), the most conspicuous feature is the snowcapped ridge that defines the boundary between the iron formations and other rocks of the Proterozoic Labrador Trough to the east and the older Superior province to the west. The Grenville front north of the Manicouagan structure is not so readily traceable (except at the Otish Mountains) because it is defined by a metamorphic boundary rather than by a change in rock units. Superior and Labrador Trough rocks continue southward across the boundary, notably in the vicinity of Wabush where metamorphosed iron formations are mined. Some indication of this is apparent in this photograph from topographic similarities on both sides of the boundary.

Manicouagan Structure

The synoptic view of the Manicouagan feature (fig. 6-1) reveals more clearly than other means the full extent of the Manicouagan disturbance. The apparent outer limit can be traced in the photograph as an almost complete, circular system of valleys with a radius of approximately 70 km, twice that of the main reservoir-filled trough. Thus extended, the Manicouagan structure has a distinct multi-ring form with five major elements (fig. 6-5): the outer circumferential depression, the outer disturbed zone, the peripheral trough, the inner plateau, and the central region (including the central peaks).

The particular contribution of the Skylab observations is the recognition of the outer circumferential depression. The size of the Manicouagan structure, its moderately deep level of erosion, and especially the complexity of the country rocks make the depression difficult to identify in topographic maps or lower altitude photography. Previously, outer depressions of similar relative dimensions have been identified at several smaller Canadian craters. The clearest examples are at moderately eroded craters with central uplifts, notably Deep Bay (refs. 6-12 and 6-13) and the two Clearwater Lake Craters (ref. 6-14). In these examples, the circumferential depression is more visible partly because variations in country rock lithology and in regional topographic relief are less pronounced than in the Manicouagan region. At the Manicouagan structure, the outer circumferential depression is most apparent on the western side where the rocks are mainly gneisses of amphibolite grade and the topography is relatively uniform. On the northern and southern margins of the crater, the depression is partly obscured by glacial deposits, the most recent direction of regional glaciation having been from north to south. However, the depression can be traced eastward into a series of valleys cutting the higher grade gneisses and basic rock complexes on the eastern side of the crater.

The zone between the circumferential depression and the reservoir appears relatively heavily forested in most of the Skylab views because there are few open bodies of water. However, the zone is cut by a considerable number of narrow finger lakes and long arms of the reservoir. In effect, the terrain has been rejuvenated locally with a concurrent increase in the intensity of jointing (ref. 6-15). At the other craters previously



(a)

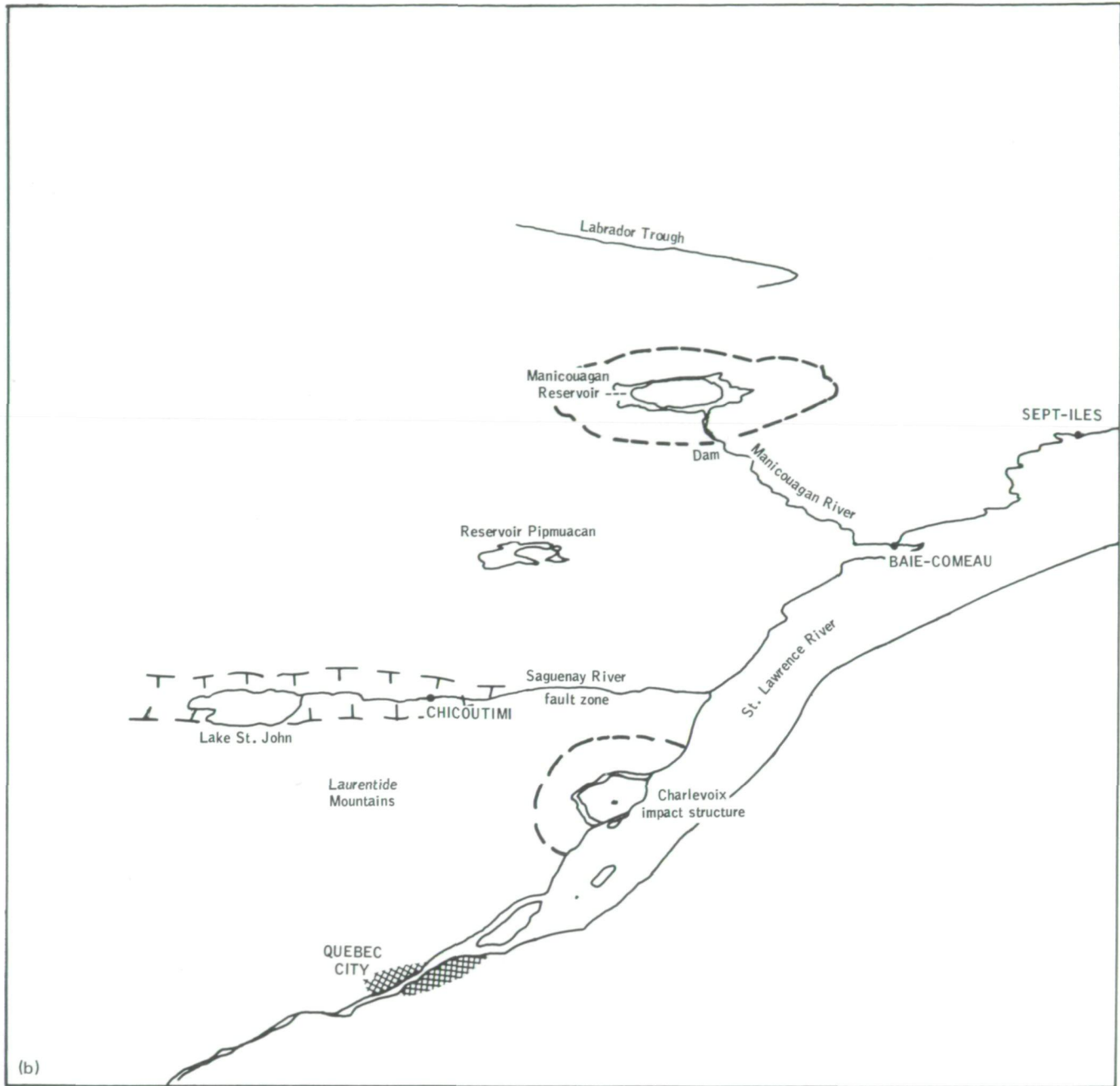
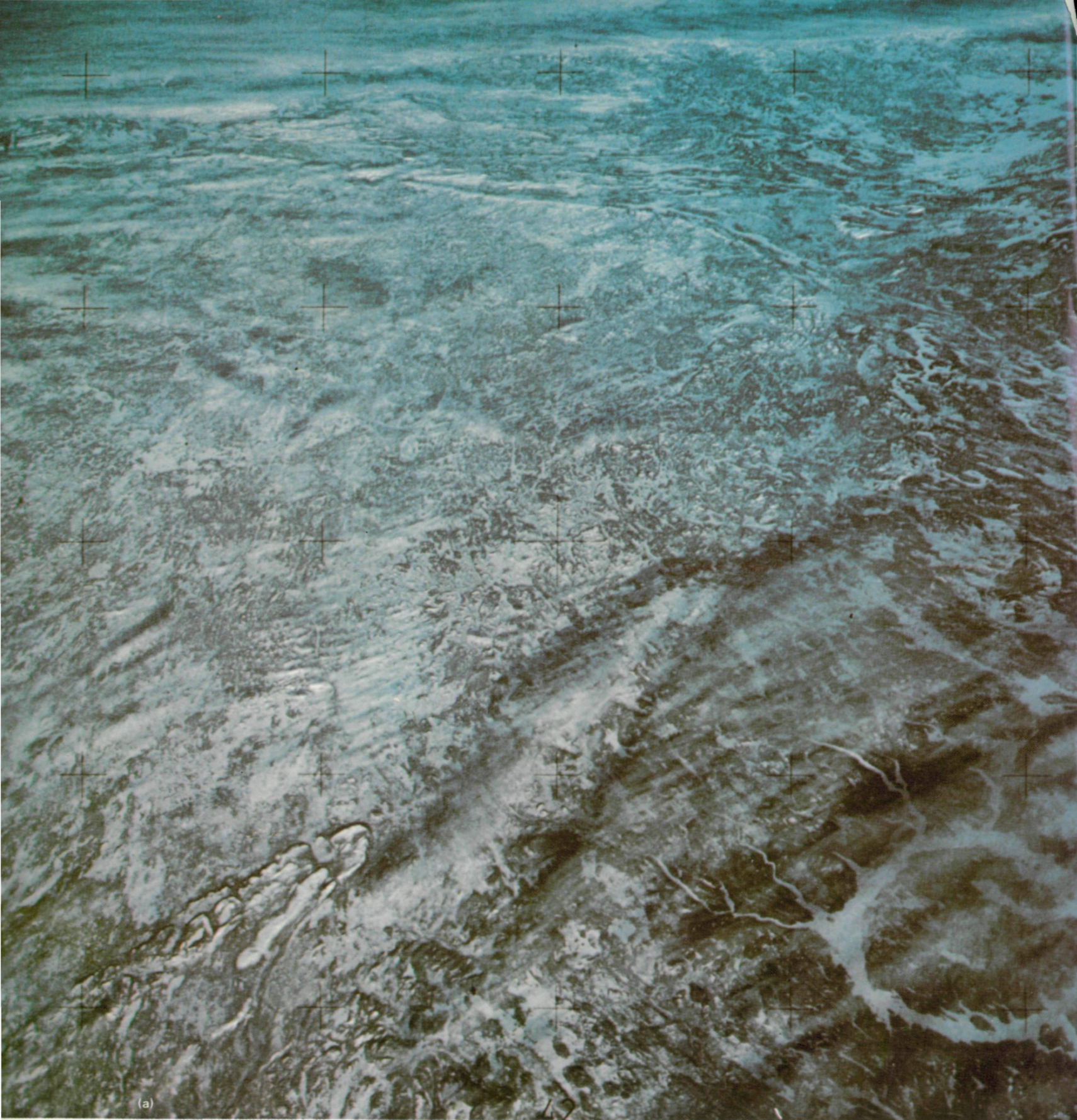


FIGURE 6-3.—Circular features south of Manicouagan looking north from the vicinity of the Maine-Quebec border. Quebec City is in the foreground. (a) Photograph (SL4-138-3897). (b) Sketch map.



(a)

ORIGINAL PAGE IS
OF POOR QUALITY

C-3

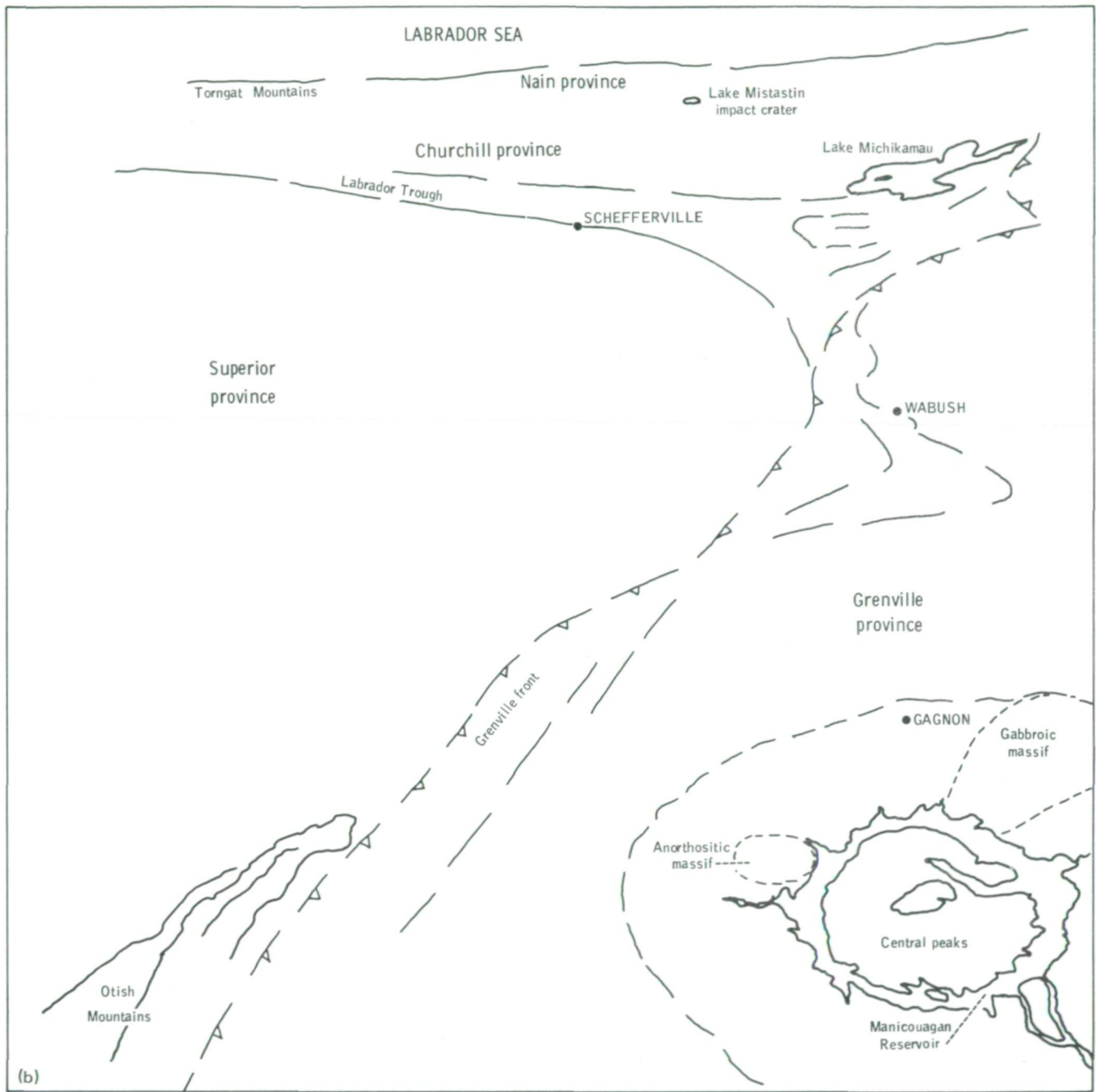


FIGURE 6-4.—Major features of the region north and east of the Manicouagan ring. Parts of four provinces of the Canadian shield are visible, including most of the iron-ore-producing regions of Quebec and Labrador. Within the Manicouagan structure, snow cover outlines the central region including the central peaks. (a) Photograph (SL4-139-4044). (b) Sketch map.

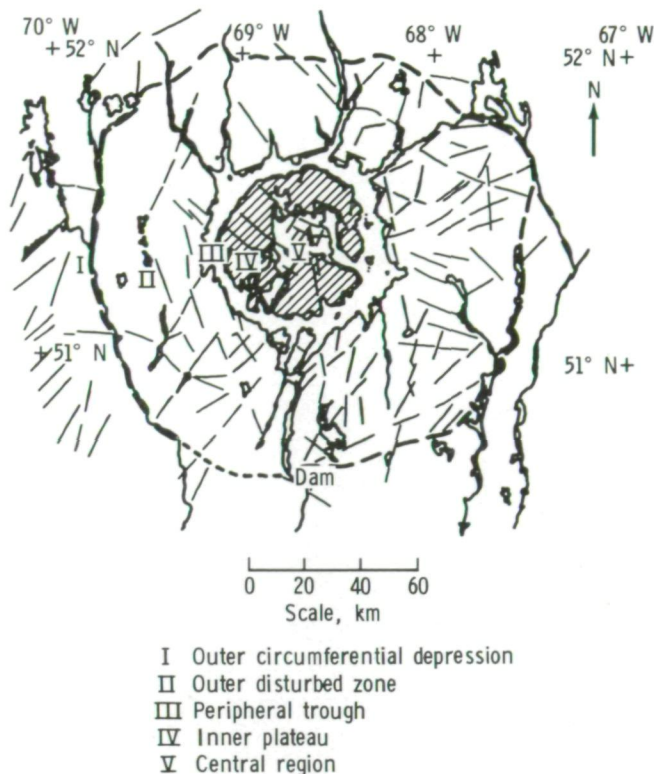


FIGURE 6-5.—Sketch map of lineaments and principal structural features of the Manicouagan ring. Exposures of melt rocks on the inner plateau and central region are found in the shaded area.

mentioned, this outer disturbed zone is elevated slightly above regional levels, but irregularities of the topography obscure any evidence of a similar effect at the Manicouagan structure. Although difficult to prove in crystalline rock terrains, the outer disturbed zone probably has been tilted and uplifted during crater formation. The outer circumferential depression can be interpreted as the fracture zone marking the boundary between disturbed and essentially undisturbed country rocks.

The basic structure of the reservoir-filled peripheral trough has been established by ground observations made before flooding began. The trough is essentially a graben ring bounded on the outside by steeply dipping normal faults. Approximately 20 exposures of folded, faulted, and locally brecciated lower Paleozoic limestones and shales, as thick as several tens of meters, were visible along or near the shorelines of the former lakes and are interpreted as relics of cratonic cover deposits that overlay the Precambrian basement at the time of crater formation. The nearest rocks of similar age and lithology crop out discontinuously along the

northern shore of the St. Lawrence River north of Anticosti Island (fig. 6-2) approximately 350 km from the Manicouagan ring. The folding of the sedimentary rocks at the Manicouagan structure indicates an initial compression deformation occurred before later downfaulting (moving mainly on preexisting regional planes of weakness) dropped the rocks 1 km or more. Regional trends thus control the form of the trough, giving it a distinctly polygonal outline in the map view.

Fracturing and local brecciation also affect basement crystalline rocks exposed in the peripheral trough and along valleys toward the center of the structure. The patchy exposures of basement rocks provide evidence of a general increase in the intensity of shock metamorphism toward the center (ref. 6-16) and of an extensive development of pseudotachylite dikes and veins. The zones of shock metamorphism developed in the basement rocks are similar to those mapped at the more deeply eroded and more completely exposed Charlevoix structure (ref. 6-10).

In the inner plateau, the basement, and near the peripheral trough, the Paleozoic rocks are largely covered by an extensive sheet of flat-lying to gently dipping and undulating melt rocks. The preserved thickness of these rocks is 100 to 200 m; the thickness before erosion was considerably greater as the matrix increases in grain size from the base to the top, with the coarsest grained rocks at the highest exposures. At the base, the rocks are underlain by mixed breccias or large blocks of fractured country rocks, in places cut by dikes of breccia or fine-grained to glassy melt rocks. The lower part of the melt unit commonly contains 15 to 30 percent of inclusions of country rocks, some of which are highly deformed. The most prominent set of inclusions are recrystallized anorthositic rocks similar to the rocks of the central peak. With increasing grain size of the melt matrix, inclusions become less apparent and the coarsest grained rocks appear to have a uniform igneous texture featuring blades of pyroxene as long as 1 cm. Changes in matrix grain size are abrupt in some cases, which suggests more than one generation of melt. Although variations in composition (ref. 6-4) point to the same conclusion, the lack of chilled contacts and of obvious crosscutting relationships within the melt unit indicate emplacement at the same time. Paleomagnetic studies (refs. 6-17 and 6-18) indicate that the melt rocks behaved as a single cooling unit. Textural variations may thus reflect factors such as differences in content of inclusions or volatiles.

Systematic studies of compositional variations in the melt rocks are in progress, but early studies (refs. 6-4 and 6-19) indicate that the average composition closely approximates that of a mixture of the country rocks. Indeed, certain basement granulites (mangerites) exposed near the center of the structure are chemically almost identical to the mean composition of the bulk of the igneous rocks (ref. 6-4). In this respect, as in their distribution and structural relationships, the Manicouagan melt rocks are larger versions of similar rocks exposed at West Clearwater Lake, Lake Mistastin, and other craters (refs. 6-20 and 6-21). In all examples, the melt rocks can be interpreted as impact melts, which were generated by intense shock compression near the point of impact and spread over the crater floor during crater growth, engulfing less strongly shocked rocks in the process. Although only a portion of the total melt generated would remain within the crater, the volume is nonetheless impressive. At the Manicouagan structure, the volume preserved from erosion is approximately 150 km³ of melt and inclusions; the original amount within the crater before erosion must have been at least three to four times as great. The K-Ar age of the melt rocks is 210 ± 4 million years (ref. 6-22), which can be taken as dating the time of impact.

The transition from the plateau to the central region is marked by a number of lake-filled depressions, including the arm of the reservoir covering former Lake Memory on the eastern side of the crater. These depressions result mainly from deep gouging by glaciers deflected in part around the central peaks. The central region is not well defined topographically but may be taken as the inner area with a radius of approximately 12 km.

A high-resolution photograph of the central region shows three topographic highs, two to the north rising approximately 600 m above the reservoir level and a more subdued high to the south with an elevation of 435 m above the reservoir (fig. 6-6). The more massive northern mountains, together measuring 15 by 7 km, are commonly referred to as the central peaks of the crater. These peaks consist almost entirely of anorthositic rocks that have been shocked to grades corresponding to shock pressures of 20 to 30 GN/m². Many of the anorthositic rocks have been altered to zeolites and other secondary minerals but, in places, have yielded fresh maskelynite, the glassy shock-produced form of plagioclase (ref. 6-7). Patches of melt are present at the base and on the sides of the massif,

but the presence of still vitreous maskelynite suggests that the higher parts were never covered by melt rocks. The southern, more subdued high, however, is still covered by a thick blanket of melt rocks, patches of which are scattered throughout the lower lying remainder of the central region.

The differences in elevation correlate closely with changes in Precambrian rock types in the central region. Whereas the anorthosites stand high, the lower lying areas are underlain by mixed garnetiferous gneisses, which are usually rich in pyroxene, hornblende, and biotite. These more mafic gneisses are also shocked to approximately maskelynite grade and, in places, contain relatively crude shatter cones.

Differences in basement rock types in both the central region and the outer zone are matched by strong geophysical field variations giving complex regional Bouguer gravity and magnetic fields, which are difficult to interpret. Clearly, there is a gravity low over the peripheral trough and a rise in both gravity and magnetic fields toward the center with maximums corresponding to the central area of mafic garnetiferous gneisses. A distinct local negative gravity anomaly exists over the anorthositic massifs of the central peak, with the associated magnetic field being subdued. The general rise toward the center is in contrast to the Bouguer gravity fields at such craters as those at Clearwater Lake (refs. 6-14 and 6-23) and suggests that mafic rocks extend to considerable depth in the center of the Manicouagan structure.

Several sets of lineaments cutting both the inner plateau and the central region are also delineated in the detailed Skylab photograph of the center of the crater (fig. 6-6). A number of these lineaments are also apparent on Landsat imagery, on which some can be traced across the peripheral trough into the regional country rocks (fig. 6-5). Most prominent is a set of lineaments trending northwest-southeast across the center of the structure, with a second set trending north-northeast, and a third slightly west of north, almost parallel to the direction of glacial scour. These directions correspond to major regional trends and indicate that, despite the effects of shock metamorphism and other structural complexities, even the center of the structure largely conforms to the regional pattern. This situation contrasts that of volcanic features such as the Timber Mountain, Nevada, resurgent caldera that some investigators have suggested to be a structural analog (ref. 6-4). At Timber Mountain, the uplifted central

peak consists of early volcanic units rather than pre-existing basement and has a distinctly different structural style (dominated by extension faulting) from that of the region (refs. 6-24 and 6-25).

Inasmuch as the lineaments crossing the central region and interior plateau of the Manicouagan ring appear to cut the melt rocks as well as the basement, one or more episodes of lineament development or redevelopment appear to have occurred since the crater was formed. There is little indication of either lateral or vertical displacement of crater units since formation; thus, the lineaments may be interpreted as joints. Some may have been initiated during cooling of the crater floor, but it seems likely that regional vertical displacements, such as those that occur during glacial loading and unloading, were a major factor in the development of the observed pattern.



DISCUSSION

Enhanced definition of the multi-ring structure of the Manicouagan Crater through Skylab photographs emphasizes its similarity to other large multi-ring impact structures on Earth and to comparable features on the Moon, Mars, and Mercury. The more than 50 terrestrial hypervelocity impact structures (ref. 6-8) provide evidence for changes in crater morphology with size and rock type and offer insight into the underlying structural differences. For craters formed in essentially massive crystalline rocks, the transition from simple bowl-shaped to complex central-uplift form occurs at approximately 4 km diameter, whereas prominent ring structure is evident in structures more than 25 km across. Where sedimentary rocks form all or an important part of the target, the transition diameters are smaller by a factor of as much as 3.

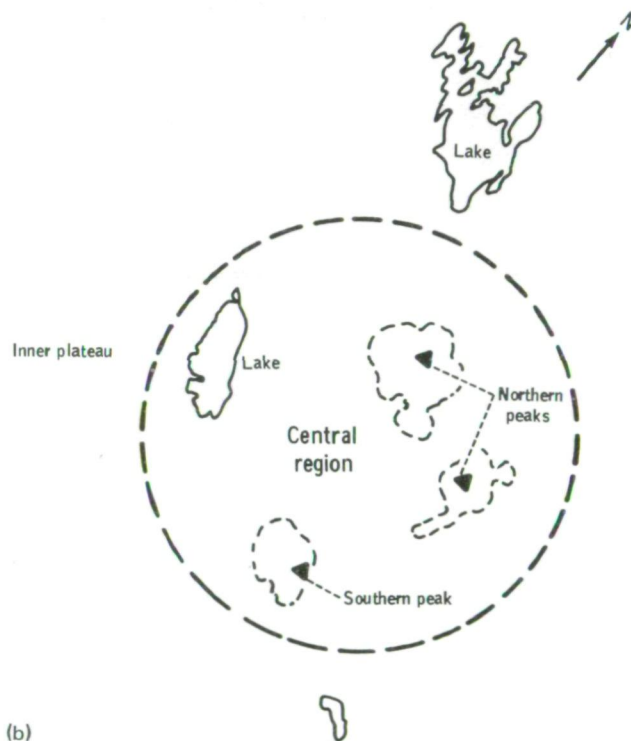


FIGURE 6-6.—View from Skylab of details of the inner plateau and center of the Manicouagan structure. Direction of glacial scour is from north to south and clearly influences both hill topography and lake shorelines. The central peaks of shock-metamorphosed anorthosite lie just north of center. The most prominent northwest-southeast lineament bisecting the crater south of the central peaks marks the approximate boundary between basic rocks underlying the northern half of the crater and mixed gneisses underlying the southern half. (a) Photograph taken with a 35-mm Nikon camera with a 300-mm lens (SI.4-192-7093). (b) Sketch map.

As several authors have noted, comparable changes, with attendant changes in depth/diameter ratio, occur on the Moon at diameters of approximately 20 and 150 to 250 km, respectively (refs. 6-26 to 6-28), and similar transitions have been noted on Mars (refs. 6-29 and 6-30) and Mercury (ref. 6-31). These observations have led to the suggestion that the size at which changes occur in crater morphology, with scatter caused by factors such as variation in rock properties, is related to gravitational acceleration g by $D_c \propto 1/g$, where D_c is the characteristic diameter (ref. 6-32). This supports the suggestion that slumping under gravity (ref. 6-33), rather than interactions between shock compression and rarefaction waves (ref. 6-34), is the principal factor in determining final crater form.

Because of the effects of erosion, especially on terrestrial structures, morphological comparisons are difficult to make. Positive topographic features such as rim crests, commonly used in the characterization of structures on other planets, are particularly vulnerable to erosion on Earth and are rapidly modified. At Manicouagan, the initial appearance and position of the rim can be only roughly estimated, but some guidance can be gained by comparisons with other terrestrial craters, especially two only slightly eroded large craters, the Ries Crater in Germany (ref. 6-35) and the Popigay Crater in Siberia (refs. 6-36 and 6-37). The peripheral trough at Manicouagan probably corresponds to the structurally complex outer zones immediately inside the rim at the Ries and Popigay Craters. On this basis, a conservative estimate for the diameter of the fresh Manicouagan basin is 75 to 80 km, compared with 22 to 24 km at the Ries Crater and 95 to 100 km at the Popigay Crater. Assuming similar rock properties and gravitational scaling, the Manicouagan ring can be considered a structural analog of 200-km-diameter ring structures on Mars and Mercury and 400- to 500-km lunar basins.

Howard et al. (ref. 6-28) have noted that, at this size lunar basin, there is an apparent transition from smaller ring structures, the rings of which are spaced at intervals of 2, to larger structures, for which the factor is approximately $2^{1/2}$. Although degraded, the positive features at the Manicouagan structure appear to conform to the spacing factor 2: the diameter of the outermost margin of the outer depression is approximately 150 km; the preerosion rim is 75 to 80 km; and a subdued inner ring, traced from local heights of land in the inner plateau, is 35 to 40 km. Little evidence exists for

intermediate positive features that could conform to the $2^{1/2}$ spacing, although the inner plateau rises slightly toward its outer margin, which has a diameter of 50 to 55 km.

The 35- to 40-km inner ring at Manicouagan can be compared with the island ring at West Clearwater Lake. In both rings, there are small exposures of Paleozoic limestone—the remnants of the cratonic cover rocks present at the times of impact—near the crest of the ring. No Paleozoic rocks are present closer to the center. The crest of the ring, therefore, may be taken as the approximate position of the rim of the transient cavity (refs. 6-20 and 6-33) as initially excavated before uplift of the center and downdrop of the rim. In this interpretation, the present peripheral trough corresponds to the subsided outer slope of the transient cavity rim.

This model for Manicouagan favors interpretations of lunar rings as essentially slump structures. The frozen wave or tsunami model (refs. 6-38 and 6-39) finds little support in the Manicouagan data because no evidence exists of effects such as fluidization by strong shock (more than 30 GN/m^2) in the basement rocks inside or outside the peripheral trough. Shock-melted materials are confined to the relatively thin sheet lying on the inner plateau and acted merely as a superficial blanket covering the basement rocks as the later slumped inward and, in the center, upward.

The central uplift at the Manicouagan structure provides further data that may have general application to large basins on other planets. Whereas the large blocks of anorthosite at Manicouagan are high, much of the central region is lower than the inner ring. The resulting multiple peak form is reminiscent of multiple peaks at many large, fresh lunar craters. Popigay Crater, however, has a central depression with no apparent peaks. Central peak development is probably a function of both crater size and bedrock type and homogeneity. The Manicouagan structure provides an example of strong differences in rock composition and physical properties.

The depth of origin of the rocks in the center of Manicouagan is also of interest. If the transient cavity conformed to the parabolic shape suggested by Dence (ref. 6-40), the cavity would have been approximately 14 km deep; however, this theory cannot be determined directly from available data. The rocks now exposed in the central region were originally deeper than this limit and may well incorporate material from the lower crust, which in this area lies below a discontinuity averaging

20 km in depth (ref. 6-41). Uplift of deep crustal material may therefore account for the previously noted central geophysical anomalies, and possibly for the unusual seismic results recorded there (ref. 6-5). If so, the structural pattern of the Manicouagan ring supports models for the Orientale and Imbrium basins in which central uplift is shown as bringing lunar mantle to the surface (refs. 6-28, 6-42, and 6-43).

SUMMARY

From the comprehensive views of eastern Canada provided by the Skylab oblique photographs, major provinces and subprovinces of the Canadian shield can be delineated, and the main elements of the multi-ring Manicouagan structure can be defined. Abundant ground observations of shock metamorphism establish the probable hypervelocity impact origin of the Manicouagan structure, which when fresh had a rim diameter of 75 to 80 km. An inner ring of half this diameter is interpreted as the collapsed rim of the initial transient cavity, whereas an outer ring approximately 150 km in diameter is considered to be a fault zone marking the outer limit of disturbance.

The Manicouagan structure, by gravitational scaling, is an analog for 200-km-diameter ring structures on Mars and Mercury and 400- to 500-km basins on the Moon. These structures also have rings spaced at intervals of 2. Because most larger structures on these other planets have rings with $2^{1/2}$ spacing, it is of particular interest to see whether current work at the Manicouagan structure can lead to the identification of rings with intermediate spacing.

REFERENCES

- 6-1. Hammond, W. P.: Geology of the Mouchalagane Lake Area, Saguenay County, Quebec. M.A. Thesis, Univ. of Toronto, 1946.
- 6-2. Rose, E. R.: Manicouagan Lake, Mushalagan Lake Area, Quebec. Geol. Survey Canada, Paper 55-2, 1955.
- 6-3. Currie, K. L.: On the Origin of Some "Recent" Craters on the Canadian Shield. *Meteoritics*, vol. 2, no. 2, 1964, pp. 93-110.
- 6-4. Currie, K. L.: Geology and Petrology of the Manicouagan Resurgent Caldera, Quebec. Geol. Survey Canada Bull. No. 198, 1972.
- 6-5. Willmore, P. L.: The Seismic Investigation of the Manicouagan-Mushalagan Lake Area in the Province of Quebec. *Pub. Dominion Obs.*, Ottawa, vol. 27, no. 6, 1963, pp. 325-336.
- 6-6. Dence, M. R.: A Comparative Structural and Petrographic Study of Probable Canadian Meteorite Craters. *Meteoritics*, vol. 2, no. 3, 1964, pp. 249-270.
- 6-7. Bunch, T. E.; Cohen, Alvin J.; and Dence, M. R.: Natural Terrestrial Maskelynite. *American Mineralogist*, vol. 52, nos. 1 and 2, Jan.-Feb. 1967, pp. 244-253.
- 6-8. Dence, M. R.: The Nature and Significance of Terrestrial Impact Structures. *Planetology. International Geological Congress*, no. 24, sec. 15, 1972, pp. 77-89.
- 6-9. Rondot, Jehan: Nouvel Impact Météoritique Fossile? La Structure Semi-Circulaire de Charlevoix. *Canadian J. Earth Sci.*, vol. 5, no. 5, 1968, pp. 1305-1317.
- 6-10. Robertson, P. B.: La Malbaie Structure, Quebec—A Paleozoic Meteorite Impact Site. *Meteoritics*, vol. 4, no. 2, 1969, pp. 89-112.
- 6-11. Rondot, Jehan: Géologie de la Structure de Charlevoix. *Planetology. International Geological Congress*, no. 24, sec. 15, 1972, pp. 140-147.
- 6-12. Innes, M. J. S.; Pearson, W. J.; and Geuer, J. W.: The Deep Bay Crater. *Publ. Dominion Obs.*, Ottawa, vol. 31, no. 2, 1964, pp. 19-52.
- 6-13. Dence, M. R.; Innes, M. J. S.; and Robertson, P. B.: Recent Geological and Geophysical Studies of Canadian Craters. *Shock Metamorphism of Natural Materials. Mono Book Corp.* (Baltimore, Md.), 1968, pp. 339-362.
- 6-14. Dence, M. R.; Beals, C. S.; and Innes, M. J. S.: On the Probable Meteorite Origin of the Clearwater Lakes, Quebec. *J. Roy. Astronom. Soc. Canada*, vol. 59, 1965, pp. 13-22.
- 6-15. Roy, D. W.: Étude de la Fracturation dans la Partie Ouest de la Structure Circulaire de Manicouagan. M.S. Thesis, Univ. of Montreal, 1969.
- 6-16. Murtaugh, John G.: Shock Metamorphism in the Manicouagan Cryptoexplosion Structure, Quebec. *Planetology. International Geological Congress*, no. 24, sec. 15, 1972, pp. 133-139.

- 6-17. Robertson, W. A.: Manicouagan, Quebec, Paleomagnetic Results. *Canadian J. Earth Sci.*, vol. 4, no. 3, 1967, pp. 641-650.
- 6-18. Larochelle, A.; and Currie, K. L.: Paleomagnetic Study of Igneous Rocks From the Manicouagan Structure, Quebec. *J. Geophys. Res.*, vol. 72, no. 16, Aug. 1967, pp. 4163-4169.
- 6-19. Currie, K. L.: Origin of Igneous Rocks Associated With Shock Metamorphism as Suggested by Geochemical Investigations of Canadian Craters. *J. Geophys. Res.*, vol. 76, no. 23, Aug. 1971, pp. 5575-5585.
- 6-20. Dence, Michael R.: Impact Melts. *J. Geophys. Res.*, vol. 76, no. 23, Aug. 1971, pp. 5552-5565.
- 6-21. Grieve, R. A. F.: Impact Melt at Mistastin Lake, Labrador (abs.). *EOS*, vol. 55, no. 4, 1974, p. 336.
- 6-22. Wolfe, Stephen H.: Potassium-Argon Ages of the Manicouagan-Mushalagan Lakes Structure. *J. Geophys. Res.*, vol. 76, no. 23, Aug. 1971, pp. 5424-5436.
- 6-23. Dence, M. R.: The Extraterrestrial Origin of Canadian Craters. *Geological Problems in Lunar Research*, vol. 123, art. 2, 1965, pp. 941-969.
- 6-24. Christiansen, Robert L.; Lipman, P. W.; Orkild, P. P.; and Byers, F. M., Jr.: Structure of the Timber Mountain Caldera, Southern Nevada, and Its Relation to Basin-Range Structure. *U.S. Geol. Survey Prof. Paper 525-B*, 1965, pp. B43-B48.
- 6-25. Cummings, David: Mechanical Analysis of the Effect of the Timber Mountain Caldera on Basin and Range Faults. *J. Geophys. Res.*, vol. 73, no. 8, Apr. 1968, pp. 2787-2794.
- 6-26. Quaide, W. L.; Gault, D. E.; and Schmidt, R. A.: Gravitative Effects on Lunar Impact Structures. *Ann. New York Acad. Science*, vol. 123, 1965, pp. 563-572.
- 6-27. Pike, Richard J.: Schroeter's Rule and the Modification of Lunar Crater Impact Morphology. *J. Geophys. Res.*, vol. 72, no. 8, Apr. 1967, pp. 2099-2106.
- 6-28. Howard, K. A.; Wilhelms, D. E.; and Scott, D. H.: Lunar Basin Formation and Highland Stratigraphy. *Rev. Geophys. Space Phys.*, vol. 12, 1974, pp. 309-327.
- 6-29. Wilhelms, Don E.: Comparison of Martian and Lunar Multiringed Circular Basins. *J. Geophys. Res.*, vol. 78, no. 20, July 1973, pp. 4084-4095.
- 6-30. Hartmann, William K.: Martian Cratering, 4, Mariner 9 Initial Analysis of Cratering Chronology. *J. Geophys. Res.*, vol. 78, no. 20, July 1973, pp. 4096-4116.
- 6-31. Murray, B. C.; Belton, M. J. S.; Danielson, G. E.; Davies, M. E.; Gault, D. E.; et al.: Mercury's Surface: Preliminary Description and Interpretation From Mariner 10 Pictures. *Science*, vol. 185, 1974, pp. 169-179.
- 6-32. Hartmann, William K.: Interplanet Variations in Scale of Crater Morphology—Earth, Mars, Moon. *Icarus*, vol. 17, 1972, pp. 707-713.
- 6-33. Dence, M. R.: Shock Zoning at Canadian Craters—Petrography and Structural Implications. *Shock Metamorphism of Natural Materials*. Mono Book Corp. (Baltimore, Md.), 1968, pp. 169-184.
- 6-34. Milton, Daniel J.; and Roddy, David J., Jr.: Displacements Within Impact Craters. *Planetology*. International Geological Congress, no. 24, sec. 15, 1972, pp. 119-124.
- 6-35. Preuss, Ekkehard; and Schmidt-Kaler, Hermann: Das Ries. *Geologie, Geophysik und Genese eines Kraters*. *Geologica Bavarica*, no. 61, 1969.
- 6-36. Masaytis, V. L.; Mikhaylov, M. V.; and Selivanovskaya, T. V.: The Popigay Meteorite Crater. *International Geology Rev. (transl.)*, vol. 14, no. 4, Apr. 1972, pp. 327-331.
- 6-37. Masaytis, V. L.; Mikhaylov, M. V.; and Selivanovskaya, T. V.: The Popigay Basin; An Explosion Meteor Crater. *Akad. Nauk SSSR, Dokl.*, vol. 197, no. 6, 1971, pp. 1390-1393.
- 6-38. Van Dorn, W. G.: Lunar Maria: Structure and Evolution. *Science*, vol. 165, no. 3894, Aug. 1969, pp. 693-695.
- 6-39. Baldwin, Ralph B.: The Tsunami Model of the Origin of Ring Structures Concentric With Large Lunar Craters. *Physics of the Earth Planetary Interiors*, K. E. Bullen, S. K. Runcorn, and D. W. Collinson, eds., North-Holland Publ. Co. (Amsterdam), vol. 6, 1972, pp. 327-339.
- 6-40. Dence, M. R.: Dimensional Analysis of Impact Structures (abs.). *Meteoritics*, vol. 8, 1973, pp. 343-344.
- 6-41. Berry, Michael J.; and Fuchs, Karl: Crustal Structure of the Superior and Grenville Provinces of the Northeastern Canadian Shield. *Bull. Seismological Soc. America*, vol. 63, no. 4, Aug. 1973, pp. 1393-1432.
- 6-42. Wise, Donald U.; and Yates, M. T.: Mascons as Structural Relief on a Lunar "Moho." *J. Geophys. Res.*, vol. 75, no. 2, Jan. 1970, pp. 261-268.
- 6-43. Dence, M. R.; and Plant, A. G.: Analysis of Fra Mauro Samples and the Origin of the Imbrium Basin. *Proceedings of the Third Lunar Science Conference*, *Geochim. Cosmochim. Acta Suppl.* 3, vol. 1, 1972, pp. 379-399.

Page intentionally left blank

Page intentionally left blank

Snow-Mapping Experiment

JAMES C. BARNES,^a CLINTON J. BOWLEY,^a
J. THOMAS PARR,^a AND MICHAEL D. SMALLWOOD^a

SNOW HAS AN enormous effect on the large-scale geophysical environment of the Earth. Seasonal changes in snow cover produce significant variations in the albedo of the land areas. These albedo variations strongly influence the radiation balance at the surface, which, in turn, influences both short- and long-term weather conditions. In many regions, such as the western United States, snow also has a direct economic impact. The snowmelt runoff is used for irrigation, industrial production, power generation, municipal water systems, and recreation. However, too much runoff may produce destructive flooding.

Snow was one of the first terrestrial water resources to be observed from space. Approximately 15 years ago, snow in eastern Canada was detected in images from TIROS-1, the first weather satellite launched by the United States. Since then, increasing use has been made of satellite data to map snow cover (ref. 7-1). Recently, the results of studies using data from the first Earth resources technology satellite (Landsat-1) and from the Skylab Earth resources experiment package (EREP) have demonstrated that spacecraft observations have substantial practical application to snow hydrology (refs. 7-2 and 7-3).

One of the objectives of the Skylab 4 Visual Observations Project was to observe and photograph snow cover in specified test sites, primarily in the western United States. The crewmen were able to select and observe specific test areas and to make observations at various viewing angles that enabled detection of

features not readily apparent in vertical-view photographs. Knowledge gained through the analysis of the resulting sample of color photography will help to improve satellite snow-mapping methods and eventually lead to a more cost-effective means for monitoring snow cover distribution.

DATA SAMPLE

As a part of the Skylab 4 Visual Observations Project, the crewmen took more than 300 handheld-camera photographs (about 250 with the Hasselblad and 75 with the Nikon) showing snow cover, mostly over the United States and Canada. The remaining photographs show snow in the European Alps, the Caucasus and Himalaya Mountains, the Pacific coastal areas of the U.S.S.R., and New Zealand. Because of lighting conditions, the entire data sample over the United States was taken during January and February 1974.

The handheld-camera photographs cover most parts of the United States in which snow existed during the mission and include the Sierra Nevada in California, the Salt-Verde Watershed in central Arizona, the Rocky Mountains in Colorado, Great Salt Lake and Yellowstone Park in Utah and Wyoming, the Cascade Range in Washington and Oregon, the Black Hills in South Dakota, the Central Plains, and the Great Lakes. Thus, the sample includes snow cover in both mountainous and relatively flat terrain.

The time of the Skylab 4 mission was opportune for crewmen to observe snow cover over a large part of the United States and, more importantly, to observe changes in snow extent. Much of the western and

^aEnvironmental Research & Technology, Inc., Concord, Massachusetts.

central United States received substantial snowfalls in late December and early January. In the Far West, snow was reported in some of the southern California desert areas; in the Central States, snow existed in early January as far south as the Texas Panhandle. A general warming trend occurred in January, and much of the snow cover in the Central Plains had disappeared by the end of the month.

Overall, the quality of the handheld-camera photographs, particularly the 70-mm Hasselblad photographs, is excellent. Over broad snowfields, where the albedo is high, nearly all the photographs had correct exposures. Some smearing is evident in the 35-mm Nikon photographs, especially those taken with the 300-mm lens. Approximately 40 percent of the Hasselblad and 70 percent of the Nikon photographs are from a vertical or near-vertical viewing angle. Of the total data sample, approximately 25 usable stereopairs were obtained. In nearly every instance, the photographs are sufficiently cloud free to enable positive identification of snow.

WESTERN UNITED STATES TEST SITE AREAS

Sierra Nevada (California)

The Sierra Nevada in California was one of the western United States test site areas observed by the Skylab 4 crewmen. In the southern part, snow hydrology is of vital concern and satellite observations have been shown to have particular application for snow mapping (ref. 7-2). This region is not as heavily forested as are some mountains, such as the Cascade Range, and it has a relatively high incidence of cloud-free weather during the snowmelt season, from late March through June. Figure 7-1 is a map of the Sierra Nevada region, showing the location of river basins.

Figures 7-2 and 7-3 are photographs taken over the central Sierra Nevada on January 21 and 22, 1974. In figure 7-2, only the western slope of the mountains near Lake Tahoe is visible; in figure 7-3, the area from Lake Tahoe to south of Mono Lake is viewed. A photograph of the southern Sierra Nevada, taken on January 27 at 11:00 local time (fig. 7-4), illustrates the contrast of the brown tones of the desert in the background against the white, snow-covered mountains.

The series of photographs taken by the crewmen as the Skylab spacecraft crossed the Sierras on January 21 includes several excellent opportunities for stereoview-

ing. For example, an excellent stereopair of the Kern River Basin on the same pass (about 14:00 local time) is shown in figure 7-5.

The snow-covered terrain can be readily identified because of its high albedo. The crewmen reported that the contrast in albedo between snow- and non-snow-covered terrain is so marked that there was never any doubt in their minds as to the location of snow boundaries. They also reported that color aided in the identification of snow. The crewmen indicated that the contrast they actually saw between the white snow and the surrounding terrain was often more distinct than that recorded on film.

The irregular snowline along the western slopes of the Sierra Nevada (figs. 7-2 and 7-3) results from the numerous river valleys remaining snow free. In figure 7-3, areas of little or no snow to the east of Lake Tahoe and Mono Lake and in the Owens Valley can be

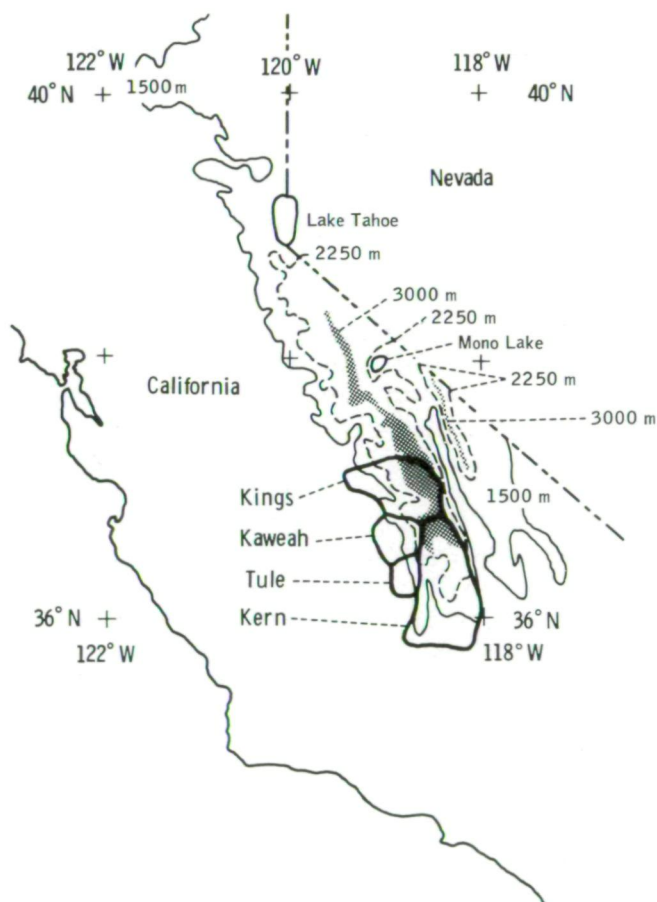


FIGURE 7-1.—Map showing the river basins in the southern Sierra Nevada site area.

detected. In the view of southern California (fig. 7-4), snow can be seen in the Coast Range and in the San Gabriel Mountains. Earlier in January, the crewmen detected snow in parts of the Mojave Desert that resulted from an unusual snowfall at the low elevations in southern California.

In figure 7-4, some mountain shadows are evident in the Kings and Kern River Basins. The shadows are not as distinct as those observed in Landsat images, however, and apparently are not as troublesome in identifying snow. The combination of high Sun angle (i.e., the handheld-camera photographs were taken nearer local noon than were the Landsat-1 images) and color (as compared to the Landsat single-band black-and-white imagery) appears to reduce the shadow effect considerably.

The Skylab 4 crewmen emphasized that they could detect no significant difference in the appearance of snow from one area to another; in other words, the snow-covered Sierra Nevada does not appear uniquely different, for example, from the snow-covered Cascade Range or the Colorado Rockies.

Differentiation between snow and clouds has been a problem since attempts were first made to map snow boundaries in satellite photographs. However, the problem is less severe when using high-resolution data, such as Landsat imagery or Skylab photography, because patterns can be mapped in more detail and because natural and manmade features not visible in lower resolution data can be detected.

The crewmen were confident that they could distinguish between snow and clouds in most instances and reported that snow was generally brighter than clouds except at low Sun angles. They also indicated features could be identified that might not be detectable in photographs. The recognition of these features, such as small clear-cut swaths from timbering operations, aided in determining cloud-free areas. The crew also could "integrate" through partial cloud cover to identify snow. The crewmen concurred that distinguishing between snow and clouds is most difficult when a layer of thin cirrus exists over a large, uniform snowfield.

The availability of repetitive observations of the same area, as illustrated in figures 7-2 and 7-3, helps in the identification of clouds. By comparing these two photographs, a viewer can positively identify the cloud just south of Lake Tahoe and map the correct snowline. Some of the clouds with lesser definition in figure 7-3 are more difficult to detect from a single photograph, but their general "fuzzier" appearance is different from

the more distinctly defined snow features. Cloud shadows, especially when cumulus cells occur, are also good indicators; the shadow of a cloud can be seen just south of Lake Tahoe.

In figure 7-5, stereoviewing aids in the delineation of the snow extent. In these photographs, stereoscopy enhances the cumulus cells over the Mojave Desert (located on the right side of the frame). On the left side of the frame, stereoscopy aids in the distinction between the altocumulus and cumulus clouds and the snow-covered terrain below the clouds. Examples of this distinction are the small cumulus cells rising over the larger mountain peaks in the Kern River Basin; these cellular clouds are difficult to see when the photographs are viewed monocularly. In the upper left of these frames, the eastern portion of the Kern River Basin shows up very clearly. Stereoscopic viewing provides a more accurate indication of topographic relief than does monocular viewing and therefore enables a more accurate measurement of the snow cover extent.

In discussion of their snow observations, the crewmen pointed out that in the Sierra Nevada, as well as in other western United States test sites, the high conical peaks were definitely brighter than the lower snow-covered terrain. It was not possible to determine visually whether this difference resulted from greater snow depths or from vegetation effects. Analysis of the photographs together with comparative snow depth measurements indicates that the observed brightness variations are due principally to the influence of forest cover, not snow amount.

Snow depth measurements plotted in figure 7-3 were provided by the California Department of Water Resources. The snowline derived from the photograph is also indicated. The snow course data were collected during the last week of January and thus corresponded closely to the time of the Skylab observations. These measurements indicate snow depths from 100 to 230 cm in the areas of highest reflectance in the photograph. Snow depths of 15 to 50 cm were reported in the mottled gray areas along the western slopes and surrounding Lake Tahoe. Similarly, in the Kern River Basin, snow depths to 230 cm were reported in the areas of highest reflectance (fig. 7-4).

Substantial snow did exist in some of the areas that appear dark in the photographs. The darker patterns, which are well defined along the lower slope of the Sierra Nevada (fig. 7-2), correspond closely to the areas known to be more heavily forested. Charts of California forest types indicate that the commercial timber

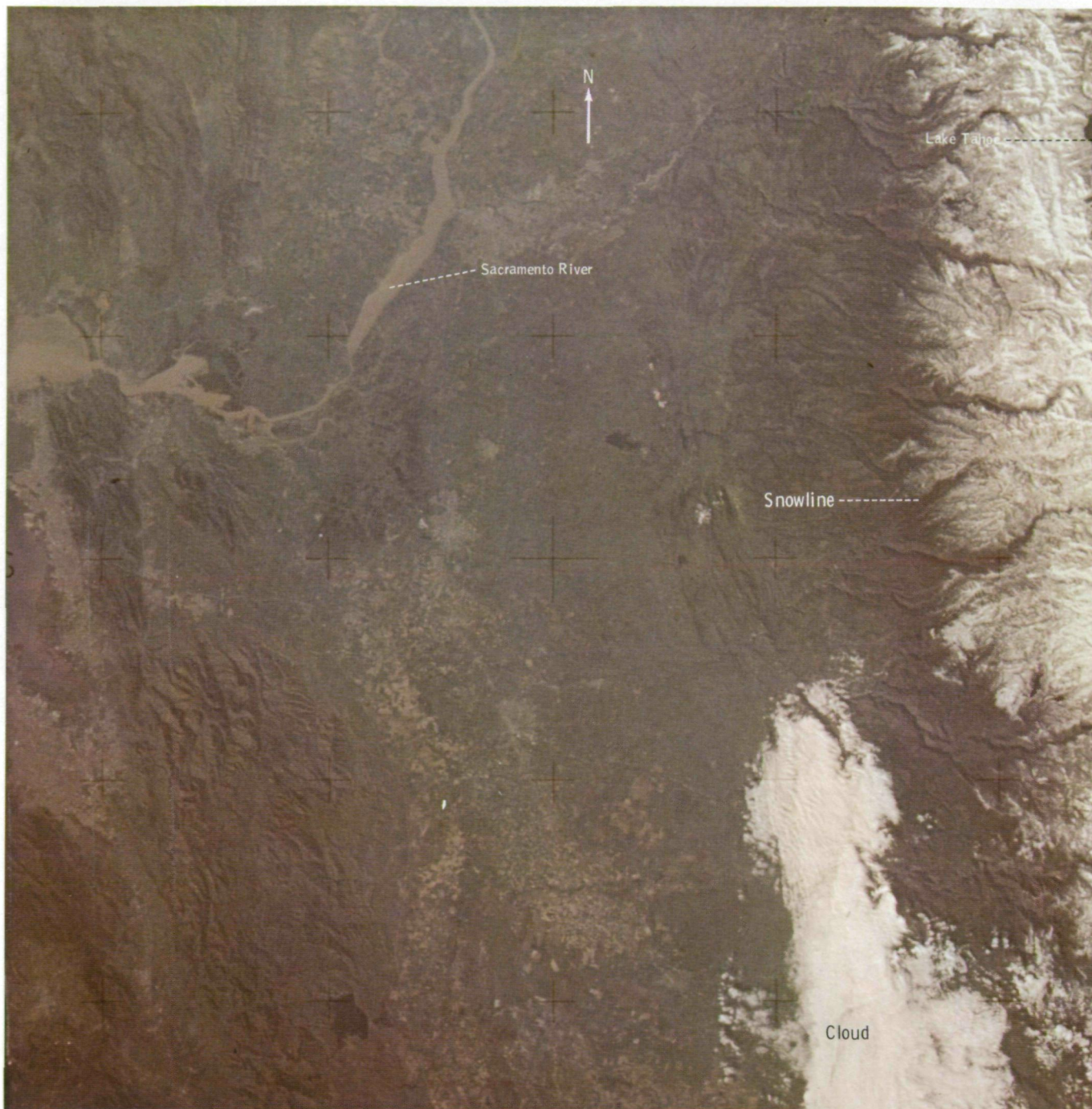
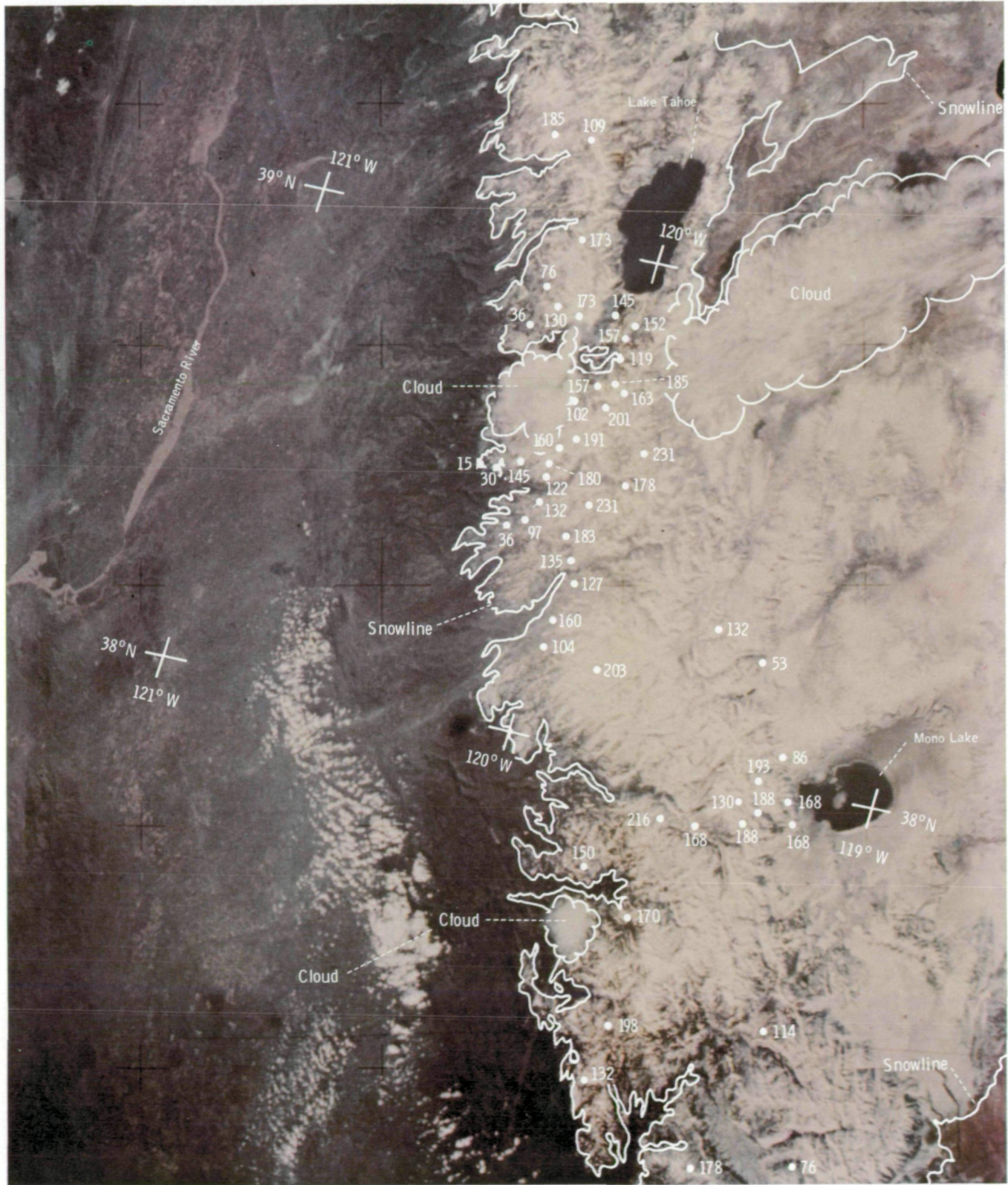


FIGURE 7-2.—Snow cover on January 21, 1974, along the western slope of the central Sierra Nevada in California. The photograph was taken with the Hasselblad camera and a 100-mm lens (SL4-141-4374).

FIGURE 7-3.—Snowline and snow depths (in centimeters) are plotted on this photograph of the central Sierra Nevada, taken 1 day later (January 22, 1974) than the photograph in figure 7-2. Snow measurements were made by the Cooperative Snow Survey Program of the California Department of Water Resources during the last week of January (SL4-142-4434). →

ORIGINAL PAGE IS
OF POOR QUALITY



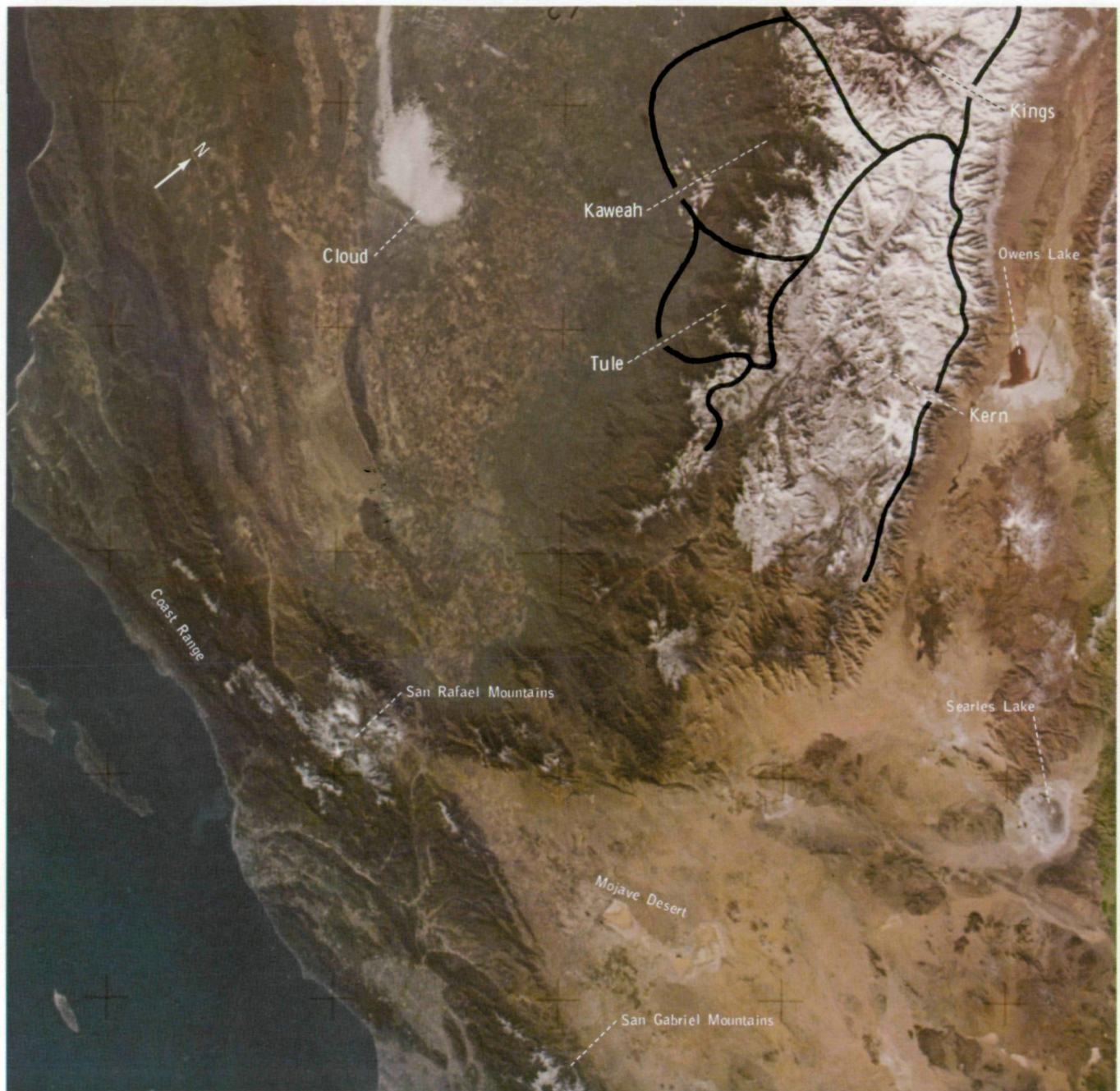


FIGURE 7-4.—Snow cover on January 27, 1974, in the southern Sierra Nevada. The Kern, Tule, and Kaweah River Basins, as well as part of the Kings River Basin, are outlined (SL4-142-4540).

zone in the central Sierra Nevada is between the 600- and 2500-m levels along the western slopes of the mountains; the higher terrain and the eastern slopes are sparsely vegetated. A recent study using digitized data from the visible channel of the National Oceanic and

Atmospheric Administration satellite NOAA-2 very-high-resolution radiometer has shown that reflectance increases as snow depths increase to approximately 25 cm; but as snow amounts increase beyond 25 cm, no further increase in reflectance occurs.

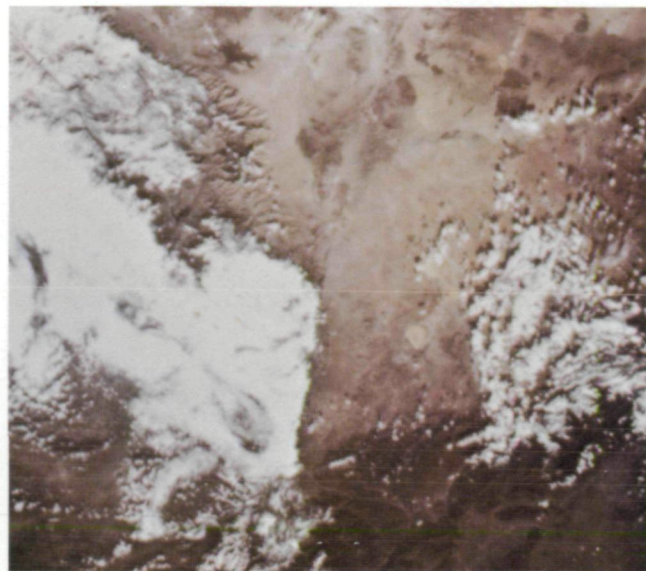
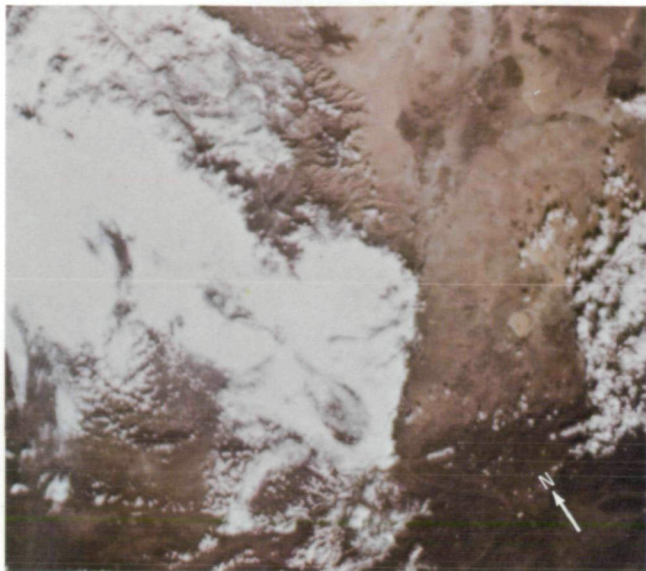


FIGURE 7-5.—The southern Sierra Nevada is shown in this stereopair of photographs taken on January 21, 1974. Clouds obscure part of the area, but snow is visible in the Kern River Basin. Stereoviewing aids in distinguishing snow from clouds and in determining topographic relief (SL4-141-4381 and SL4-141-4382).

Salt-Verde Watershed (Arizona)

The Salt-Verde Watershed in central Arizona is another drainage area in which the accumulated winter snowpack is of great hydrologic interest (fig. 7-6). The snowpack in Arizona, however, is generally much less extensive and much more transient than the Sierra Nevada snowpack.

Two handheld-camera photographs of the central Arizona area are shown in figures 7-7 and 7-8. In these and other photographs taken over Arizona, a reddish hue was dominant. In the debriefing discussion, the crewmen explained that they had not seen the reddish color and that it may have been caused by the low Sun angle at the time the photograph was taken. This color discrepancy indicates that the human observer is a better discriminator of color than is the camera. Other investigators have also found this to be the case (ref. 7-4).

The Skylab 4 crewmembers observed the central Arizona area on several passes and reported that they could detect gross changes in the snow extent as the mission progressed. The two photographs, taken on January 14 (fig. 7-7) and January 22 (fig. 7-8), illustrate the retreat in snow cover that was observed. On each date, central Arizona was cloud free and useful snow-cover information was obtained for all but the extreme

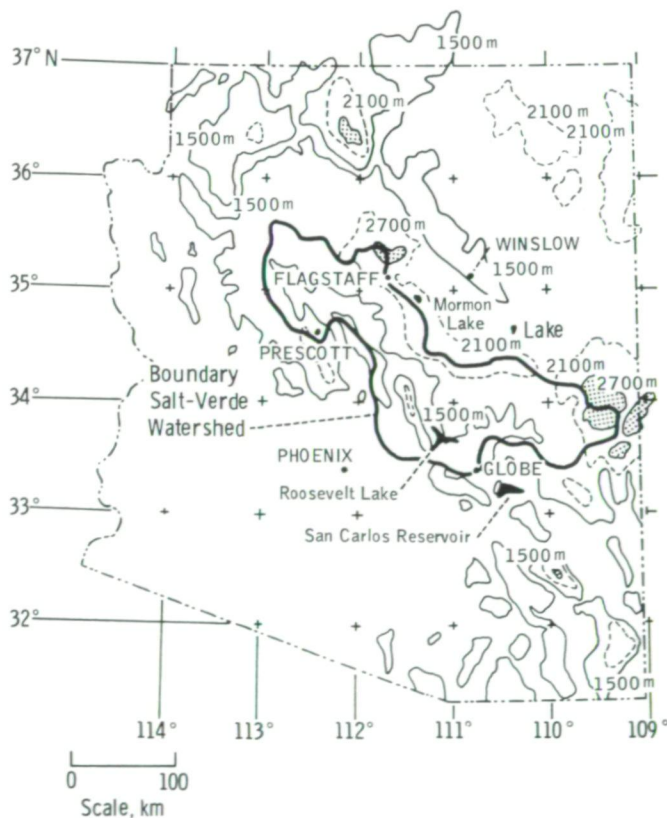


FIGURE 7-6.—Map showing the Salt-Verde Watershed in Arizona.

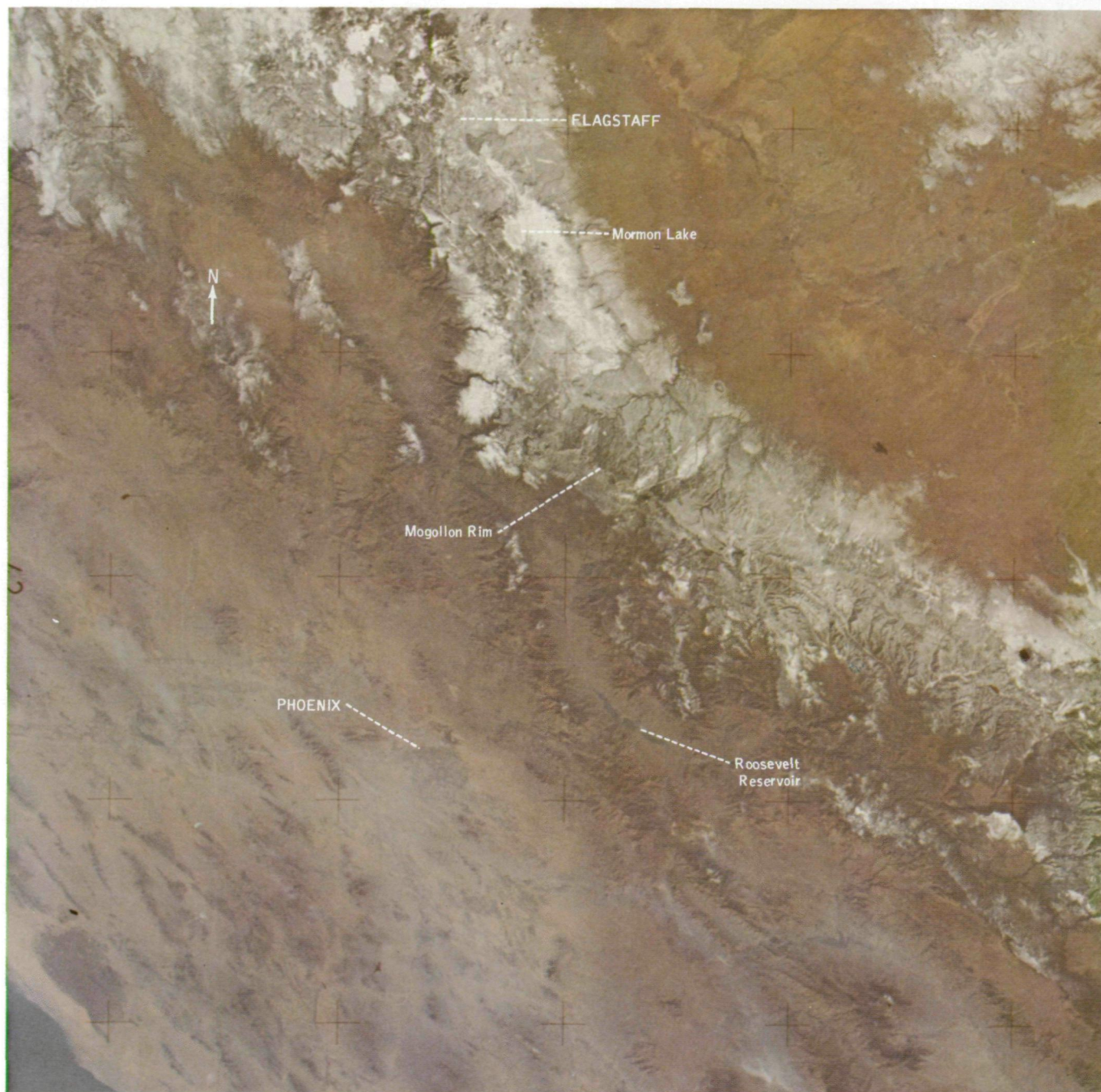


FIGURE 7-7.—Photograph of central Arizona, including the Salt-Verde Watershed, showing snow cover on January 14, 1974 (SL4-140-4141).

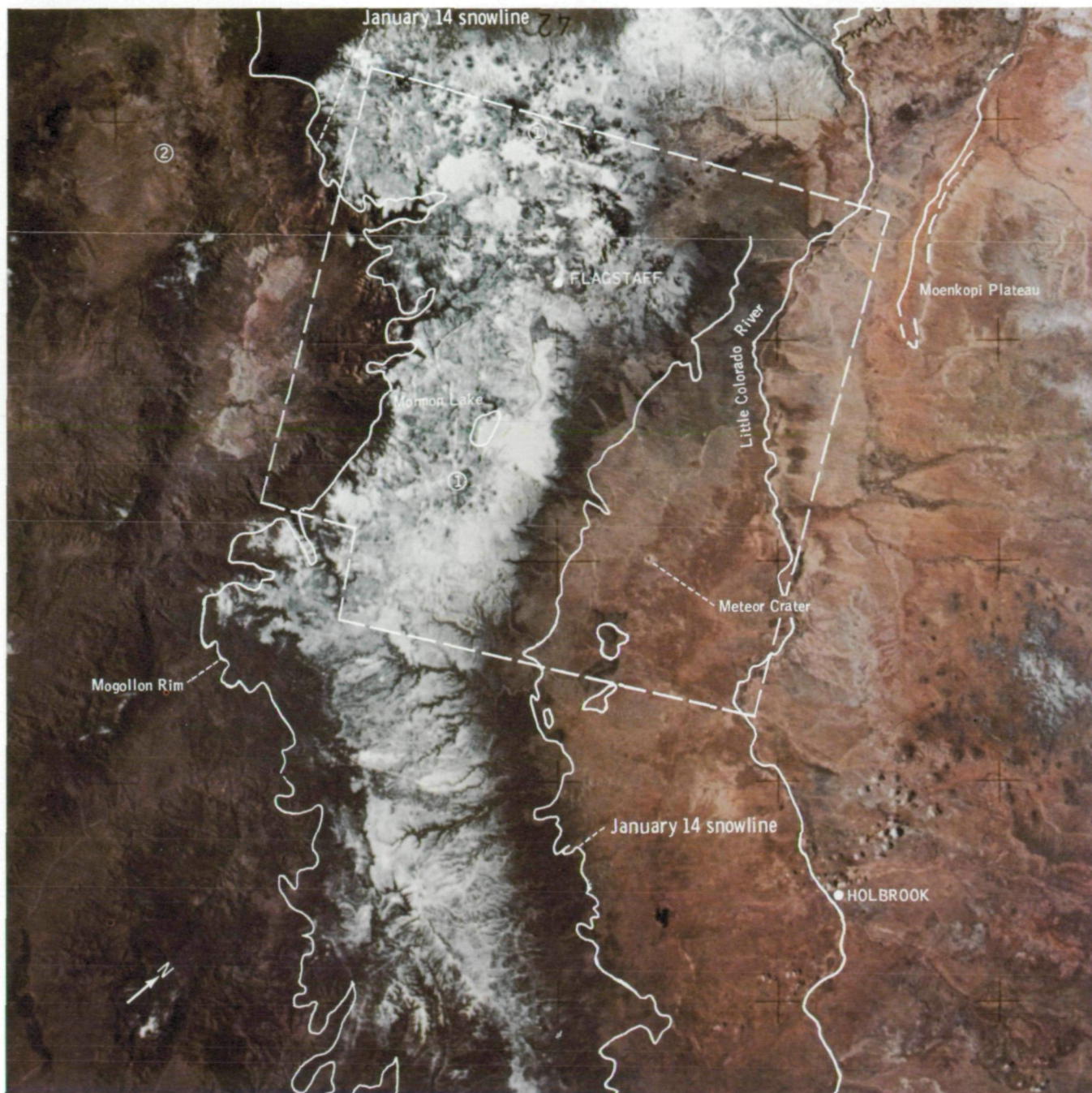


FIGURE 7-8.—Photograph showing the January 22, 1974, snow cover of central Arizona. The January 14 snowline from figure 7-7 is shown, indicating the 8-day snowmelt. Along the southern edge of the watershed, the difference is as much as 3 to 4 km; to the north, as much as 10 km. The broken line encloses the area shown in figure 7-10. Volcanic craters are easily seen in contrast to snow (1) but are less visible against dark landforms (2) (SL4-142-4438).

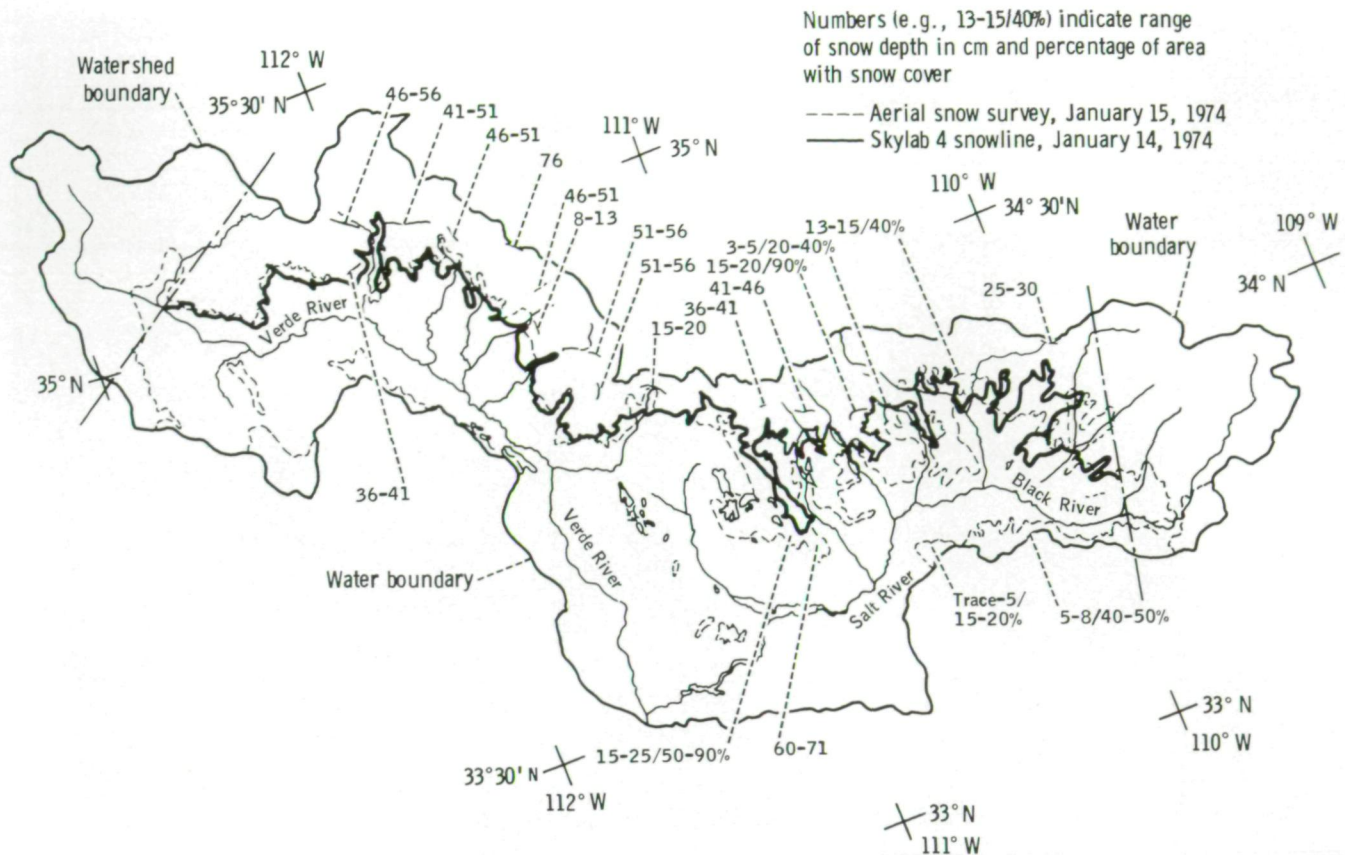


FIGURE 7-9.—Snowlines for the Salt-Verde Watershed mapped from the Skylab photograph (fig. 7-7) and from an aerial survey snow chart. The aerial survey was flown 1 day after the Skylab observation. Snow depth in centimeters and snow cover in percentages, as estimated by the aerial observer, are indicated.

eastern and western limits of the watershed. The comparison reveals that a significant retreat in snow extent had occurred during the 8-day interval.

Weather records for the period indicate that considerable snowmelt had taken place. At Flagstaff (elevation 2100 m), substantial snowfall occurred from January 5 to January 10. Thereafter, a warming trend began, with daytime temperatures as high as 289 K; as a consequence, the snow depth was reduced from 43 cm on January 14 to 13 cm on January 22. To the west of Flagstaff at the town of Williams (elevation 2025 m), the reported snow cover dropped from 28 to 3 cm during the same period.

Because of the transient characteristics of the snowpack in the Salt-Verde Watershed, aerial surveys are flown by the Salt River Project Office at approximately 2-week intervals throughout the winter season; one such survey was flown on January 15. For a quantitative evaluation of the difference between the Skylab

handheld-camera photograph and the aerial survey, the percentage of snow cover was computed from data obtained through planimetry. Figure 7-9 is a map showing the snow extent derived from the Skylab photograph (fig. 7-7) and as depicted on the aerial survey chart. Snow depth estimates made from the aerial survey (through visual sightings of markers and other indicators) are also plotted.

The computations were performed for the portion of the watershed covered in the Skylab photograph (all but the easternmost and westernmost extremes). The measured snow cover for the aerial survey observation is 39 percent; for Skylab, 32 percent. The 7 percent less snow cover derived from Skylab data is consistent with the mean difference in snow cover of 7 percent obtained from analysis of seven Landsat-1 images (ref. 7-2). As was true with Landsat data, it appears that more detail in the snowline can be mapped from space than can be mapped visually by the aerial observer. The



FIGURE 7-10.—The same area of the Salt-Verde Watershed shown in figures 7-7 and 7-8 is visible in this Skylab EREP S190B photograph taken on EREP pass 83, January 14, 1974. Color infrared film was used. Flagstaff, Arizona, had 43 cm of snow on the ground on this date (SL4-93-067).

discrepancies are most significant in the area north of Roosevelt Lake, in which the greatest discrepancies also were found in the Landsat study. Since the reported snow amounts are light in this area, it may be that the aerial observer somewhat overestimates the snow cover because of his oblique viewing angle. However, some of the areas of thin snow cover may not be detectable from space data.

Data across central Arizona were also collected with EREP along the Skylab groundtrack on January 14. It is possible, therefore, to compare the handheld-camera photographs with photographs from the multispectral cameras (S190A) and the Earth terrain camera (S190B). Aircraft photography of this test site was also collected on January 14 in support of the EREP program. The

EREP photography covers only the western third of the watershed. Figure 7-10 is an S190B photograph of part of the western watershed.

A comparison between the January 14 handheld-camera photograph (fig. 7-7) and the corresponding EREP data (fig. 7-10) indicates that although many small features are visible along the snowline in the EREP pictures, the handheld-camera photographs adequately define the major snow boundary. Because the handheld-camera photographs may not be taken at the nadir, using them to determine the geographic gridding and, therefore, to precisely map the snowline location is more difficult.

Variations in the reflectance within the snow-covered area are visible in the handheld-camera and

EREP photographs. Previous investigators (ref. 7-2) have concluded that the varying reflectance is due primarily to forest effects. The very bright patches, such as those near Mormon Lake, are flat mesa-type land, which is not forested as are the surrounding slopes. The crewmen confirmed that these areas did appear flat and were not characteristic of the highly reflective conical peaks that were observed in the Sierra Nevada and Cascade Ranges.

For distinguishing forested terrain, color photography does not appear to offer significant advantages over black-and-white imagery. However, color infrared film, such as used in the S190B camera (fig. 7-10), may be used to distinguish between forested terrain and terrain that has only a light snow cover. In figure 7-10, the area north of Mormon Lake (just beyond the very bright mesa land) appears gray, whereas the area south of Mormon Lake has a reddish tone. A comparison of the January 14 views (figs. 7-7 and 7-10) with the later observation (fig. 7-8) indicates that the snow cover in the more northerly area disappeared during the 8-day interval, but no change occurred in the other area. These data indicate that the terrain to the north is not heavily vegetated and was covered by only a light amount of snow, whereas south of Mormon Lake, the terrain is forested and was covered by as much as 75 cm of snow (fig. 7-9).

Great Salt Lake Area (Utah)

The Great Salt Lake area in Utah afforded the crewmen the opportunity to observe dynamic changes in snow cover. In the photography log for January 8, the crewmen wrote, "Comparison for snowmelt from previous day's pictures: snow is starting to melt." The snowmelt that was apparent by January 8 continued for most of the month. The melting trend, especially in the area immediately south and west of Great Salt Lake, is evident in the photographs taken on January 8 and 16 (figs. 7-11 and 7-12, respectively).

Weather maps for January indicate that as much as 25 cm of new snow had fallen in northern Utah during the period of January 5 to 7. Temperatures remained

relatively low (daytime high values near 270 K) until January 12, when a significant warming trend developed. Daytime maximum temperatures rose to more than 280 K on both January 13 and 14 and to more than 285 K on January 15 and 16. Daily reports of snow depth indicate that in the Great Salt Lake area, an average of 18 cm of snow melted during this 8-day period.

Reported snow depths northeast of Great Salt Lake on January 8 ranged from 36 cm in the flat terrain areas to 90 cm in the higher terrain of the Wasatch Range, and significant snow cover was still evident in this region on January 16. However, one well-defined snow-free pocket, not visible in the earlier imagery (fig. 7-11), is visible near the western slope of the mountains in figure 7-12. The crewmen reported this changing pattern, which was later identified as a lake bounded on the west by salt flats. Probably, a thin layer of frazil ice or slush was coated with new snowfall when the earlier photograph was taken; after the week of warm weather, much of the lake was again open water.

Reported snow depths on January 8 in the flat terrain regions south and west of Great Salt Lake ranged from 8 to 24 cm. At Salt Lake City, the snow depth dropped from 24 cm on January 8 to 7 cm on January 16. Even on the earlier date, urban areas could be detected because of the slightly lower reflectance. On the later date, Salt Lake City, Ogden, and smaller urban areas appeared much darker in tone; therefore, cultural features such as intersecting dark roads were detected easily.

Mapping of Seasonal Changes in Snow Extent

Observations made by the Skylab 4 crewmen can be compared with the observations made by the crewmen of the two earlier missions to map seasonal changes in snow extent. One area that was photographed on both the Skylab 2 and Skylab 4 missions was Yellowstone National Park and the adjacent portions of Wyoming, Montana, and Idaho. The photograph taken in January 1974 is shown in figure 7-13 and the previous photograph from June 1973 in figure 7-14.

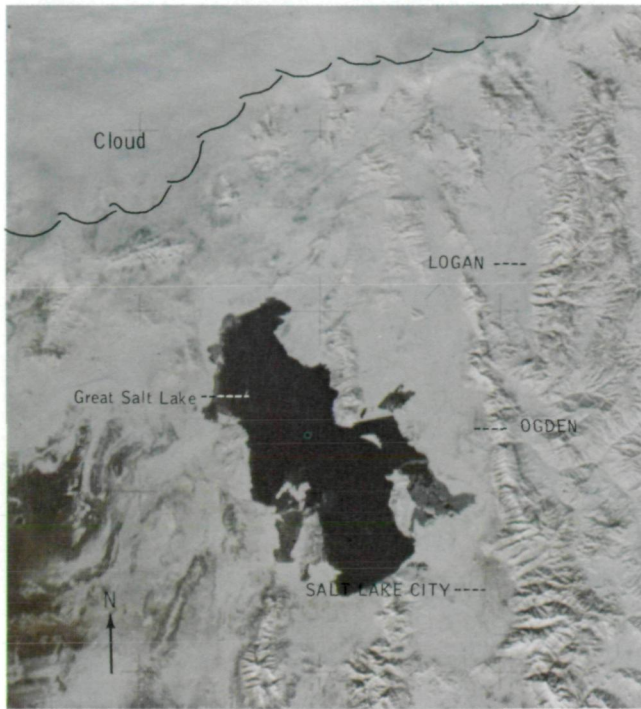


FIGURE 7-11.—Photograph of Great Salt Lake area in Utah taken on January 8, 1974, showing the terrain covered with snow except for an area southwest of the lake (SL4-139-3992).

The Skylab 4 photograph (fig. 7-13) covers probable maximum snow extent over the region of Yellowstone National Park, including the Absaroka, Wind River, Salt River, Wyoming, and Gros Ventre Ranges and the Teton, Owl Creek, and Big Horn Mountains. The Yellowstone Park area had the lowest reflectance in the photograph and in the crewmen's observations. The dark pattern extends beyond the area of geothermal activity in Yellowstone Park, and the boundaries correspond closely with those of forested land on land use maps. Therefore, the dark pattern is inferred to be the dense forest of Yellowstone National Park rather than a snow-free area possibly resulting from geothermal activity.

Within the forested region, bright areas such as Yellowstone Lake, small lakes to the west, and a large

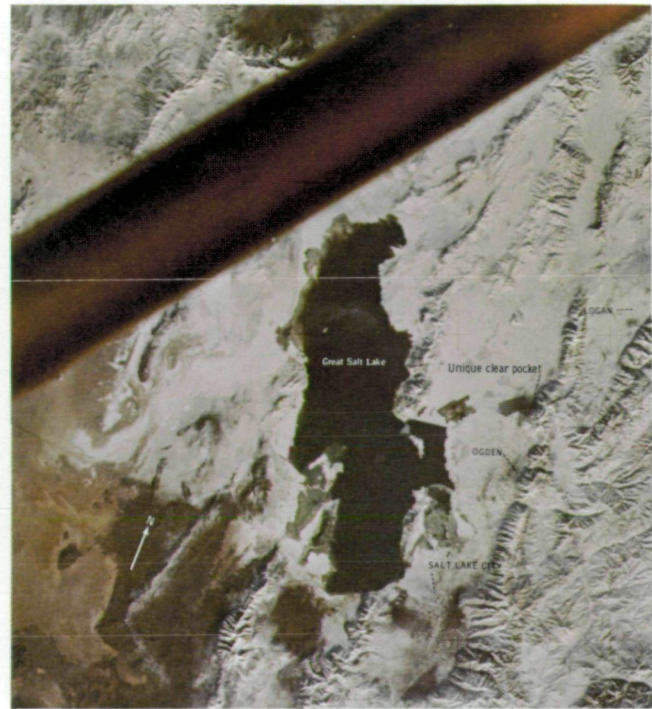


FIGURE 7-12.—The decrease in snow cover of the Great Salt Lake area is evident in this photograph taken on January 16, 1974. The snow-free area east of Great Salt Lake (not visible in fig. 7-11) is a lake which may have had a layer of ice covered by new snow at the time of the earlier picture (SL4-140-4167).

open meadow or grassland north of Yellowstone Lake indicate that snow cover did exist. The areas of highest reflectance within the mountainous terrain were generally confined to the maximum elevations above the tree line. Nonforested terrain such as the Snake River Plain and the relatively flat basin areas between the mountain ranges appeared uniformly bright. An area of lower reflectance in the nonforested zone was noted along the southern slope of the Owl Creek Mountains, near the southern end of the Big Horn Mountains. This is apparently an area of lesser snow amount, which may be the result of locally strong surface winds removing the snow from the relatively flat, unvegetated land. Figure 7-14 is a Skylab 2 photograph showing the Yellowstone Park area in June. The snow cover was confined to the terrain above the tree line. The heavily



FIGURE 7-13.—Northwestern Wyoming, completely covered by snow, is shown at 16:00 local time on January 1, 1974. The dark pattern in the upper part of the photograph is the forested land of Yellowstone National Park. The nonforested Snake River Plain (upper left) and flat basin areas between the mountain ranges and above the tree line display the most reflectance (SL4-138-3846).

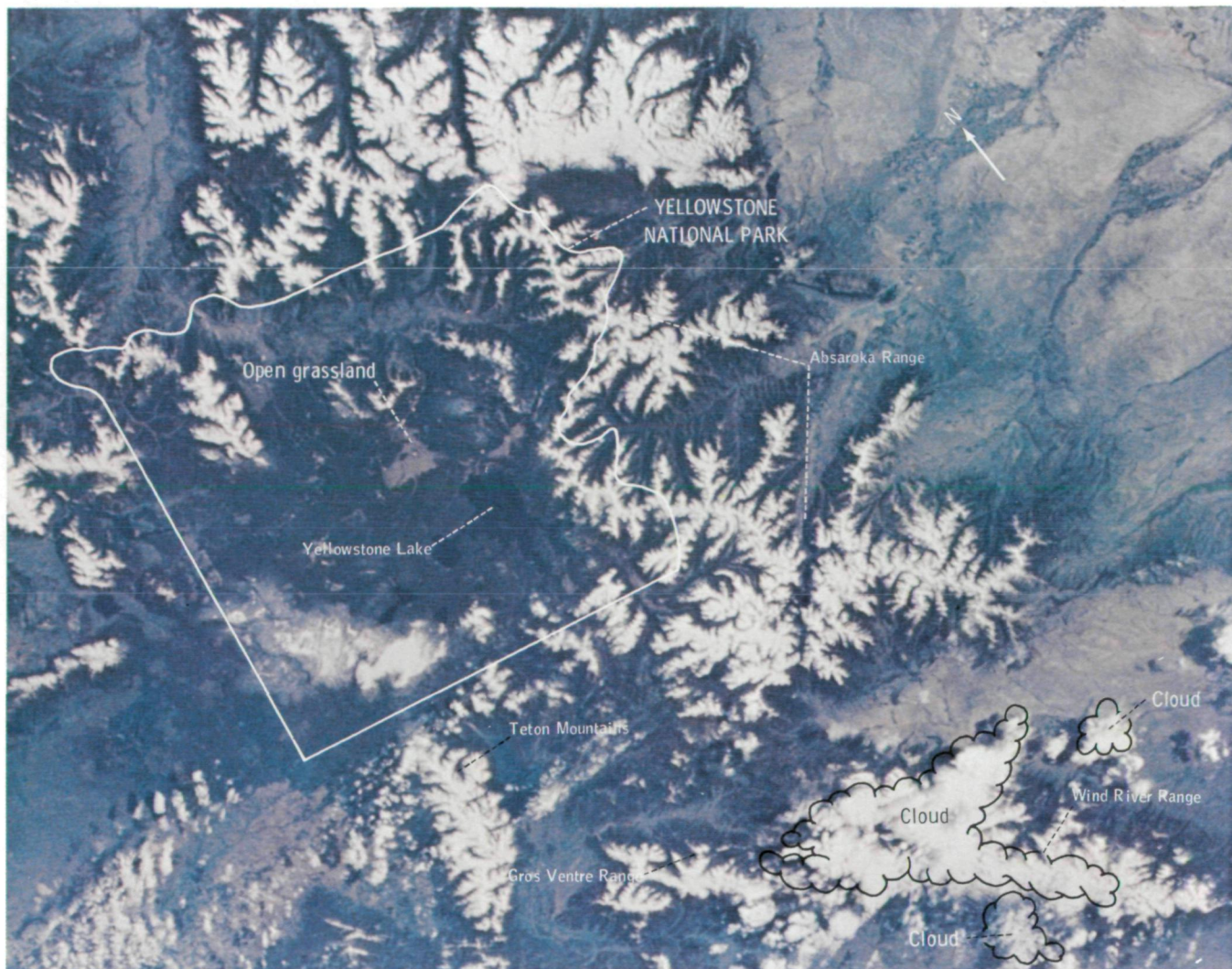


FIGURE 7-14.—Northwestern Wyoming as it appears in early summer is shown in this Skylab 2 photograph taken on June 9, 1973, with a Nikon camera. Snow cover exists above the timberline (above approximately the 3000-m level). The forested land appears darker than the non-forested areas (SL2-105-1084).

forested lower elevations of the mountains and the forested land of Yellowstone Park appear in dark contrast to the surrounding nonforested land. At the western edge of the park, the forest boundary coincides closely with the boundary of the dark pattern in the wintertime observation (fig. 7-13). The forest boundary along the eastern slope of the Absaroka Range is well defined; in the winter photograph, this area was partially obscured by clouds and by mountain shadows.

Although the vegetation patterns evident in the June observation (fig. 7-14) are useful for interpreting the snow distribution in the January observation (fig. 7-13),

to detect snow within the dense forest of Yellowstone Park is difficult. By comparison, even with a substantial snow cover, the densely forested terrain appeared darker than the forested areas of the southern Sierra Nevada (figs. 7-2 to 7-4) and of the Salt-Verde Watershed (fig. 7-7).

Mountain shadows are evident in the January photograph (fig. 7-13) of the Yellowstone area, which was taken in the late afternoon. Although shadows tend to enhance some geological aspects of mountain structures, they present problems for snow mapping. In the handheld-camera photographs of the Yellowstone area,

no evidence can be found of features that could conclusively be associated with geothermal activity.

Skylab 2, 3, and 4 handheld-camera photographs of a portion of the Colorado Rocky Mountains have provided the information for comparing the seasonal extent and effect of snow cover on various terrestrial features, including rock surfaces above timberline, forested areas, grassland basins, valleys, and urban areas. The early morning oblique image of June 9, 1973 (fig. 7-15), sharply defines the snow cover in the Colorado mountains. The snow cover was well illuminated as a result of the low Sun angle and was confined to the higher elevations. The boundary of the forested areas,

which appear dark, is sharply defined and allows identification of the relatively flat grassland basins. Some signs of urban development and agriculture are evident in the mottled area east of the Front Range. Denver appears somewhat lighter in tone than does the surrounding area.

The low-oblique view provided by the Skylab 3 image of September 20, 1973 (fig. 7-16), reveals that considerable snowmelt had occurred since June in the mountainous areas also seen in figure 7-15. Isolated snow patches are visible along the highest elevations of individual ridges and at the peaks of higher mountains. The high reflectance of the snow-free rock surfaces

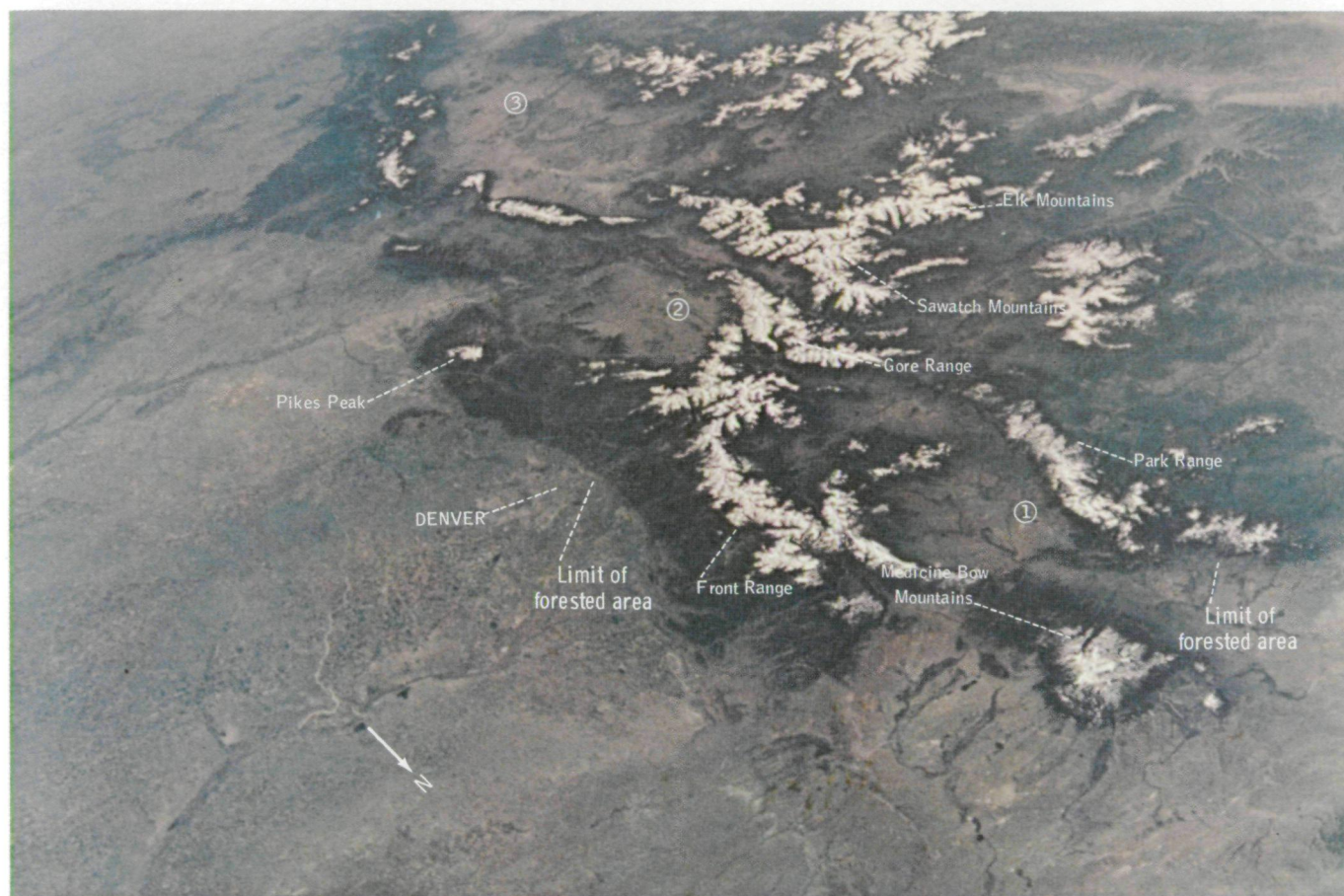


FIGURE 7-15.—The Colorado Rocky Mountains as they appeared on June 9, 1973, are shown in this Skylab 2 photograph taken with a Nikon camera. Snow cover is visible at higher elevations. The forested areas appear dark in contrast to flat grassland basins, such as North Park (1), South Park (2), and San Luis Valley (3) (SL2-105-1087).

ORIGINAL PAGE IS
OF POOR QUALITY



FIGURE 7-16.—This view of the Colorado Rockies was taken on September 20, 1973, on the Skylab 3 mission. Limited snow cover is visible only at the highest elevations (above 4000 m). The grasslands at (1) and (2) are still identifiable as they were in June (fig. 7-15) (SL3-122-2583).



FIGURE 7-17.—Photograph of the Colorado Rockies taken on January 3, 1974, with the entire area covered by snow. Identification of the flat grasslands at (1) and (2) is made easier by the snow cover (SI4-138-3875).

above the timberline is in contrast to the dark background of the heavily forested areas; the nonforested grassland basins are also evident. In addition, small lakes and river valleys not apparent in the Skylab 2 oblique image obtained 3 months earlier are plainly visible in this image.

The Skylab 4 photograph of the same area on January 3, 1974 (fig. 7-17), shows substantial snow cover in the Colorado mountain region and in the plains region east of Denver. This image clearly displays that even with maximum snow cover, identification of the major terrestrial features observed in the summer and fall photographs is possible. The snow cover appears to enhance some features in the higher terrain areas (such as plateaus and ridges). The highest reflectance was confined to the regions of maximum elevation above the timberline, where as much as 64 to 127 cm of snow was reported on this date. Although depths of 25 to 30 cm were reported at lower elevations within the forested areas, these areas had low reflectances because



FIGURE 7-18.—The snowline is indicated on this Skylab 2 photograph of Mount Rainier in Washington taken on June 11, 1973, using a 300-mm lens on a Nikon camera (SL2-104-1023).



FIGURE 7-19.—Mount Rainier had snow cover only on the permanent snowfields at its peak when this photograph was taken on September 12, 1973, 3 months later than the photograph in figure 7-18. This Skylab 3 photograph was taken with a 300-mm lens on the Nikon camera (SL3-119-2260).

the snow does not accumulate on the trees, which are predominantly conifers. The presence of snow aids in the identification of the flat grassland basins and enhances some of the relatively small isolated areas at higher elevation. Although urban areas such as Denver and Greeley, Colorado, and Cheyenne, Wyoming, reported snow depths from 8 to 12 cm, these cities can be located because of their significantly lower albedo.

Peaks in the Cascade Range in Washington were photographed on all three Skylab missions. The photographs of Mount Rainier on June 11 (fig. 7-18), September 12 (fig. 7-19), and January 11 (fig. 7-20) are shown. (Figure 7-20 appears to be somewhat smeared because of camera movement.)

The snow pattern on each of these photographs was mapped onto a transparent, fine-mesh grid overlay and then transferred to a 1:250 000-scale topographic map.



FIGURE 7-20.—This view of Mount Rainier was taken during the Skylab 4 mission on January 11, 1974, using a 300-mm lens on the Nikon camera. The high reflectance of the clear-cut areas indicates that snow cover exists at those elevations even though the forested land appears dark (SL4-192-7080).

In the June 11 photograph (fig. 7-18), the mean snowline elevation was measured at the 1525-m level, slightly above the timberline. By September 12 (fig. 7-19), the mean snowline elevation had retreated to the 2130-m level, well above the timberline; in this photograph, considerable bare rock surface is apparent below the snowline, which essentially defines the permanent snowfields of the mountain. The winter observation (fig. 7-20) shows the boundary of the very bright snow cover near the 1375-m level; however, the visible boundary defines the limit of the dense coniferous forest rather than the snowline because snow can be seen in timber-cut open areas at much lower elevations.

CENTRAL UNITED STATES TEST SITE AREAS

Central Plains

Two examples of snowlines in the Central Plains of the United States are shown in Skylab 4 handheld-camera photographs of January 6 and 23, 1974. The early January photograph (fig. 7-21) shows a well-defined snowline oriented approximately east-west near the Kansas-Oklahoma border. Although reports of snow depths were rather widely scattered over this region, depths within the brighter pattern north of the snowline ranged from 8 to 13 cm. The area of higher reflectance appears overall to represent snow depths greater than approximately 2.5 cm. A lower albedo is observed in the area of Wichita, Kansas, where 10 cm of snow was reported.

The late January photograph (fig. 7-22) shows a snow boundary in southeastern Iowa and west-central Illinois. Reported snow depths in the brighter region north of the snowline ranged from 2.5 to 8 cm. Again, the high reflectance appears to indicate the area with snow depths exceeding 2.5 cm. Drainage patterns are evident throughout the snow-covered area because of tree growth along the streams. Also, a sharp lowering of the snow albedo is observed in the urban areas of Cedar Rapids and Waterloo, Iowa, and Rockford, Illinois.

South Dakota

An oblique photograph taken on January 8 (fig. 7-23) includes the region extending from the Black Hills eastward across South Dakota. The Black Hills, because of the heavy forest cover, appear very dark even though the snow depths within this area were greater than those reported in the surrounding, nonforested terrain. The Skylab 4 crew observed the Black Hills immediately after a snowfall and reported that the area looked somewhat brighter, but quickly returned to the more characteristic dark pattern. This observed change in reflectance implies that some of the fresh snowfall remained on the tree canopy briefly but disappeared rapidly because of wind action, melting, or ablation.

Of particular interest is the area of low reflectance approximately 70 to 90 km northeast of the Black Hills. Because the central portion of South Dakota is essentially nonforested, this darker pattern indicates little or no snow cover. A review of weather records for South Dakota during December and January shows that the

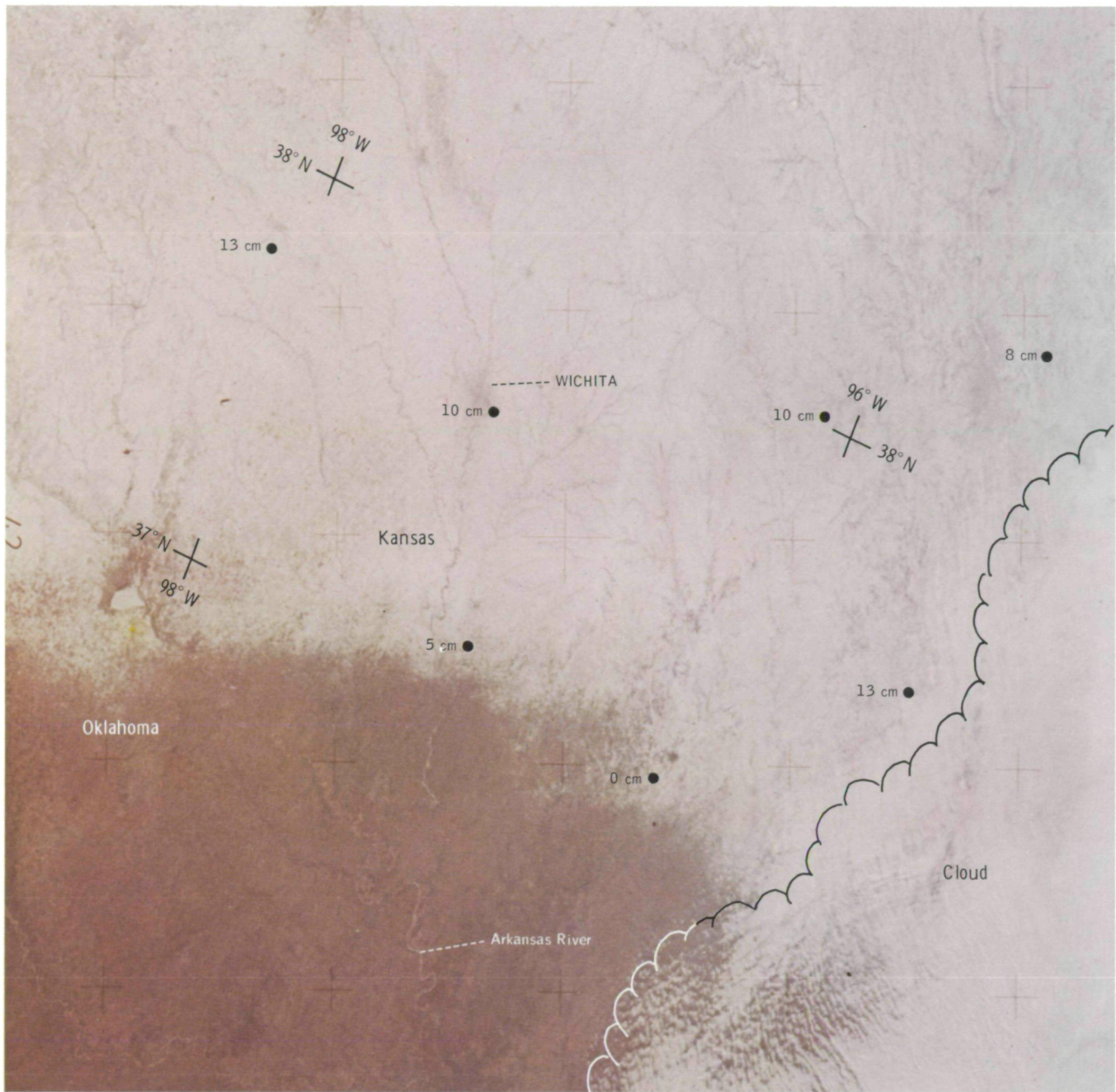


FIGURE 7-21.—Snow cover in the Kansas-Oklahoma area on January 6, 1974, is shown with snow depths plotted in centimeters (SL4-139-3928).

snow-free band is not the result of snowmelt but instead of the overall lack of substantial snowfall. The surface weather charts for late December and early January indicate that during that period, light snowfalls of relatively short duration were generally reported

throughout this area of lower albedo, whereas heavier snowfalls of longer duration were reported by stations in the surrounding areas. This condition is confirmed by the snow depth reports for January 8 of substantial amounts throughout the Northern Plains (as much as

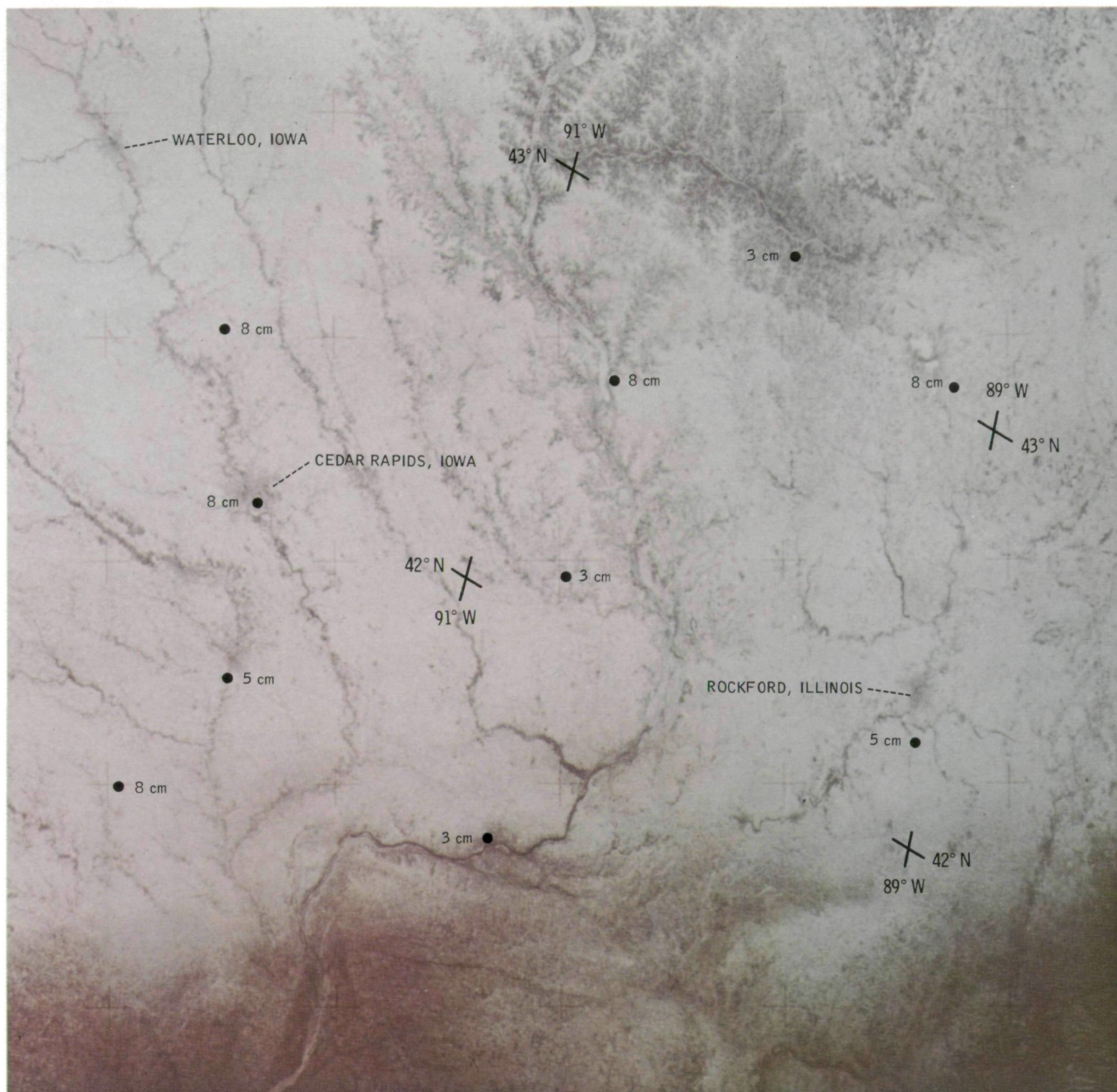


FIGURE 7-22.—Snow cover in eastern Iowa on January 23, 1974, is shown with snow depths plotted in centimeters (SL4-142-4466).

20 cm in eastern South Dakota, 23 cm in North Dakota, 40 cm in Nebraska, and 15 to 30 cm throughout the Black Hills); at the same time, considerably lower snow depths (5 to 10 cm) were reported in the region im-

mediately surrounding the darker snow-free belt. Milesville, South Dakota, the single reporting station within the area of low reflectance, reported only a trace of snow on the ground.

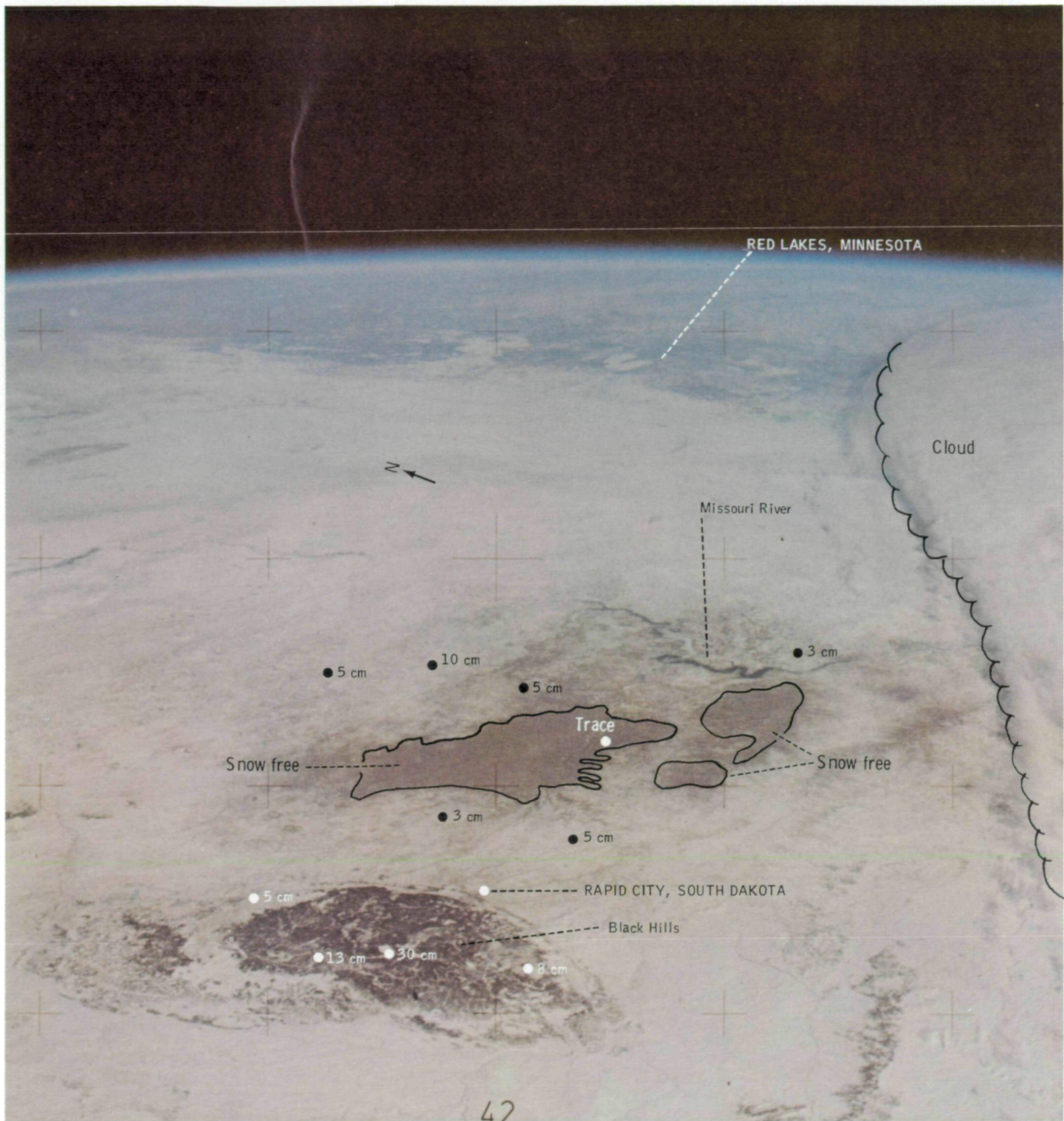


FIGURE 7-23.—This oblique photograph was taken on January 8, 1974, looking east across South Dakota. The forested Black Hills appear dark but are snow covered. A snow-free area is visible in central South Dakota. The bright spots within the Black Hills correspond to areas known to be grasslands or lakes. Snow depths are shown in centimeters (SL4-139-3994).

Linear Snow Pattern (Kansas-Iowa)

An unusual linear snow pattern was observed and photographed by the crewmen on January 22 (fig. 7-24). This pattern extended east-northeasterly from near Tuttle Creek Reservoir in Kansas (outside the photograph) to near Des Moines, Iowa, a distance of approximately 300 km. As discussed in section 14, enhancement of precipitation by thermal pollution or frictional convergence cannot account for this snowfall pattern. Review of weather conditions that had occurred just before the Skylab observation leads to consideration of the possibility that this unique pattern resulted from a band of freezing rain, sleet, and possibly wet snowfall associated with a storm system that had moved through the area.

The surface weather maps of January 22 show that a weak frontal wave disturbance had tracked rapidly northeastward out of Texas, across extreme southeastern Oklahoma and central Missouri and into northern Illinois. Although this system remained relatively weak (central pressure 101.3 kPa), the advection of warm, moist, tropical air flowing northward out of the Gulf of Mexico spread precipitation well to the north of the center; light rain was reported throughout most of Kansas, Missouri, and Illinois, whereas light snow was reported across northern Kansas, Iowa, northern Illinois, and Wisconsin. The east-northeast orientation and the location of the linear snow pattern observed from Skylab coincides with the orientation and mean location of the rain/snow boundary depicted on the surface weather charts. In addition, a narrow band of freezing rain and sleet in the area of the unique snow pattern occurred during a 6-hour period (03:00 to 09:00 GMT) before a change to light snow. The snowfall distribution is plotted on the photograph in figure 7-24.

Based on the known weather conditions before the Skylab observation, a probable explanation for the unique linear snow pattern is that a narrow band of sleet and freezing rain coated the ground and vegetation with an ice layer. The high albedo along this band resulted from the ice and subsequent very light snowfall and was greater than the albedo just north of the band, where only a trace of new snow fell following a period of light rain, and south of the band, where the precipitation was in the form of rain.

The observations over the central United States test site areas show that snow amounts of as little as 2.5 cm produce a significant increase in albedo. With a few centimeters of snow on the ground (as much as 10 cm),

features such as vegetated drainage systems and checkerboard road patterns, common in the Midwest, can be detected. Even when as much as 10 cm of snow is reported, urban areas have a significantly lower albedo than does the surrounding countryside.

The analysis of the photographs taken by the Skylab 4 crewmen indicates that snowfall patterns that may be undetectable at the scale of the reporting station network can be mapped accurately from space observations. In addition to the hydrologic implications, the snow cover distribution in Midwestern States can have a drastic influence on crop production. This influence is also considered in section 9. For example, an area such as that in South Dakota (fig. 7-23), which remains free of snow cover for a substantial period in midwinter, would freeze to a greater soil depth than the surrounding snow-covered areas and would have a moisture deficiency at the end of winter. These conditions could have a detrimental effect on crop production in the following growing season.

EFFECTS OF URBAN AREAS ON SNOW COVER

In nonforested regions, urban areas can be readily identified when snow is on the ground because of their reduced reflectance. The reflectance rapidly decreases after a snowfall because of contamination by pollutants, snow removal from roads, and increased rate of snowmelt due to the higher temperatures associated with heated buildings, industry, transportation networks, and the close-knit structure of the urban core. The reduced reflectance of urban areas was readily apparent to the Skylab 4 crewmen, who reported that they could see the cities "grow" as the snow melted.

The two photographs of the Great Salt Lake area (figs. 7-11 and 7-12) are examples of the effects of urban areas on snow reflectance. The January 8 photograph (fig. 7-11) was taken when a rather uniform snow cover was reported in the Salt Lake City area. Even though the Salt Lake City station reported a snow depth of 25 cm, the reflectance in the immediate vicinity of the city was lower than in the surrounding area. The major highways extending south from the city appear darker than the adjacent terrain, probably because of snow plowing and traffic. The January 16 photograph (fig. 7-12) shows the core of Salt Lake City had a reflectance as low as the snow-free areas west of Great Salt Lake even though the land around the city was still white. The lower albedo of other cities, such as Ogden and Logan, is also evident.

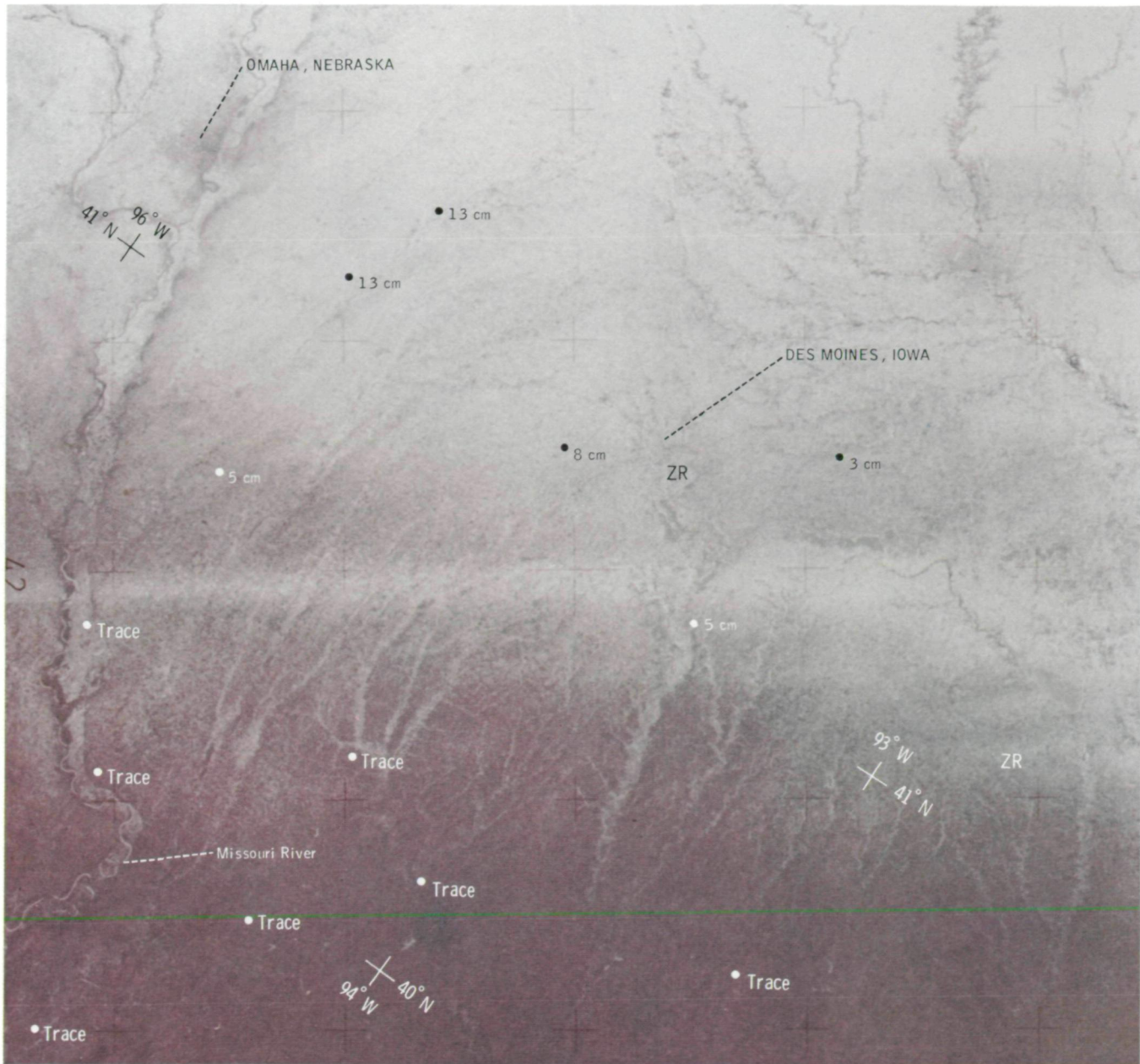


FIGURE 7-24.—An unusual linear snow pattern in southwestern Iowa is shown in a January 22, 1974, view. Snow depths are plotted in centimeters; ZR indicates freezing rain (SL4-142-4467).

Another urban area monitored repeatedly by the crewmen was Denver, Colorado. The city can be identified in the figure 7-17 photograph, taken on January 3. A photograph of the city taken 1 day later (fig. 7-25) shows the urban structure in detail. On this date, 11

days after the most recent heavy snowfall, 17 cm of snow was reported on the ground at the Denver airport.

Chicago and the other urban areas along the shore of Lake Michigan had a low reflectance which aids in their identification in the photograph taken on January 7 (fig.

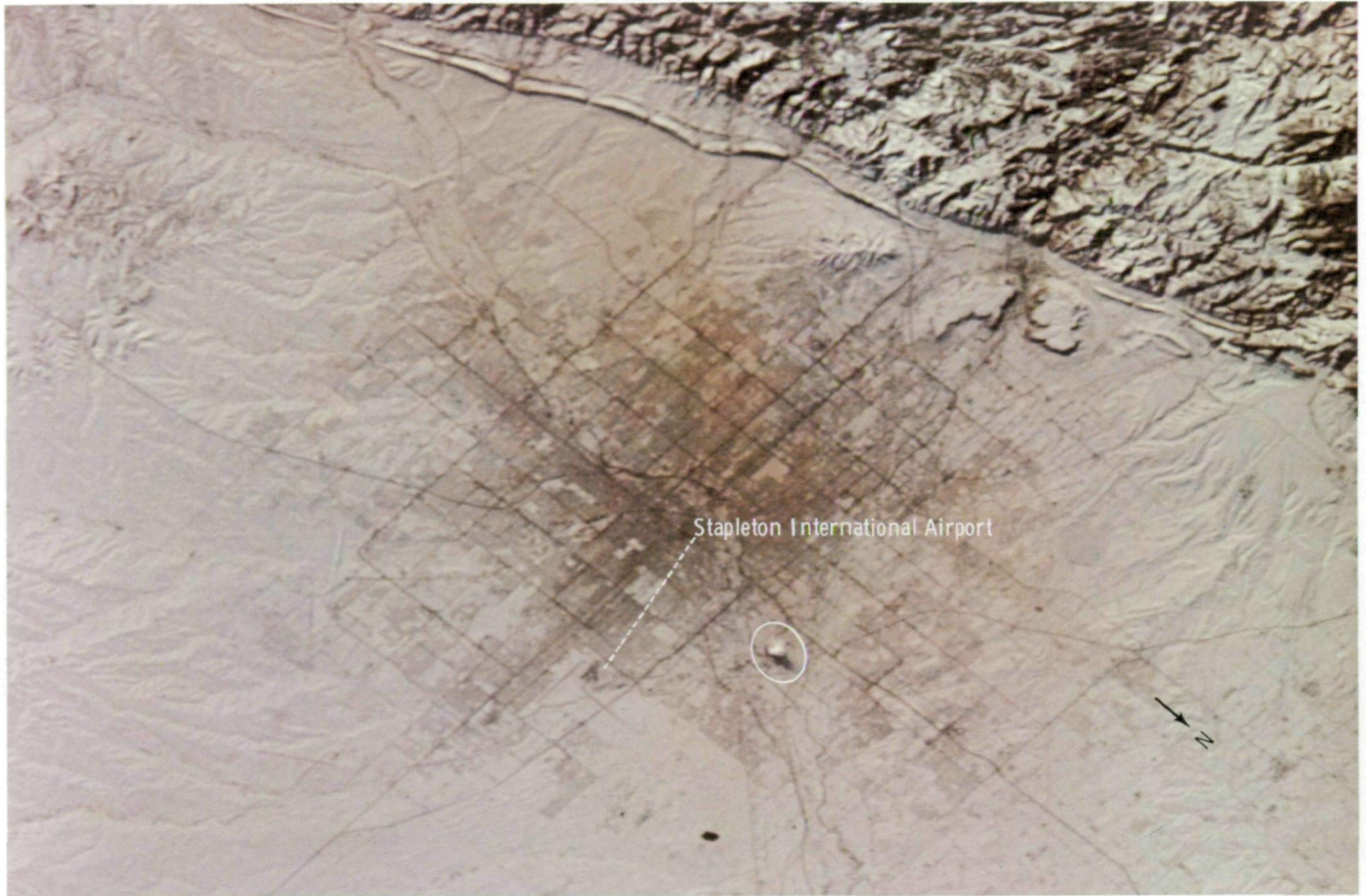


FIGURE 7-25.—Denver, Colorado, had 17 cm of snow on the ground when this photograph was taken with the Nikon camera and 300-mm lens on January 4, 1974. The bright feature in the circle is believed to be a condensation plume from a steam electric generating station cooling tower (SL4-193-7151).

7-26). Snow depths in the area of highest reflectance in this photograph ranged from 8 to 15 cm, whereas only 2.5 cm of snow was reported in Chicago. Section 8 includes a discussion of the effect of snow on cultural features.

The observations made by the Skylab 4 crewmen confirm that urban areas have an enormous impact on snow cover. The reflectance of a snow cover not only drops rapidly but the snow also melts at a much faster

rate than in the surrounding countryside. As a result, the snow depth measurements made at National Weather Service reporting stations in or near cities may be very unrepresentative of the overall snow conditions in the region. Observation from space provides information for monitoring the urban influence on snow cover and for study of urban growth features, which are often enhanced by snow cover.

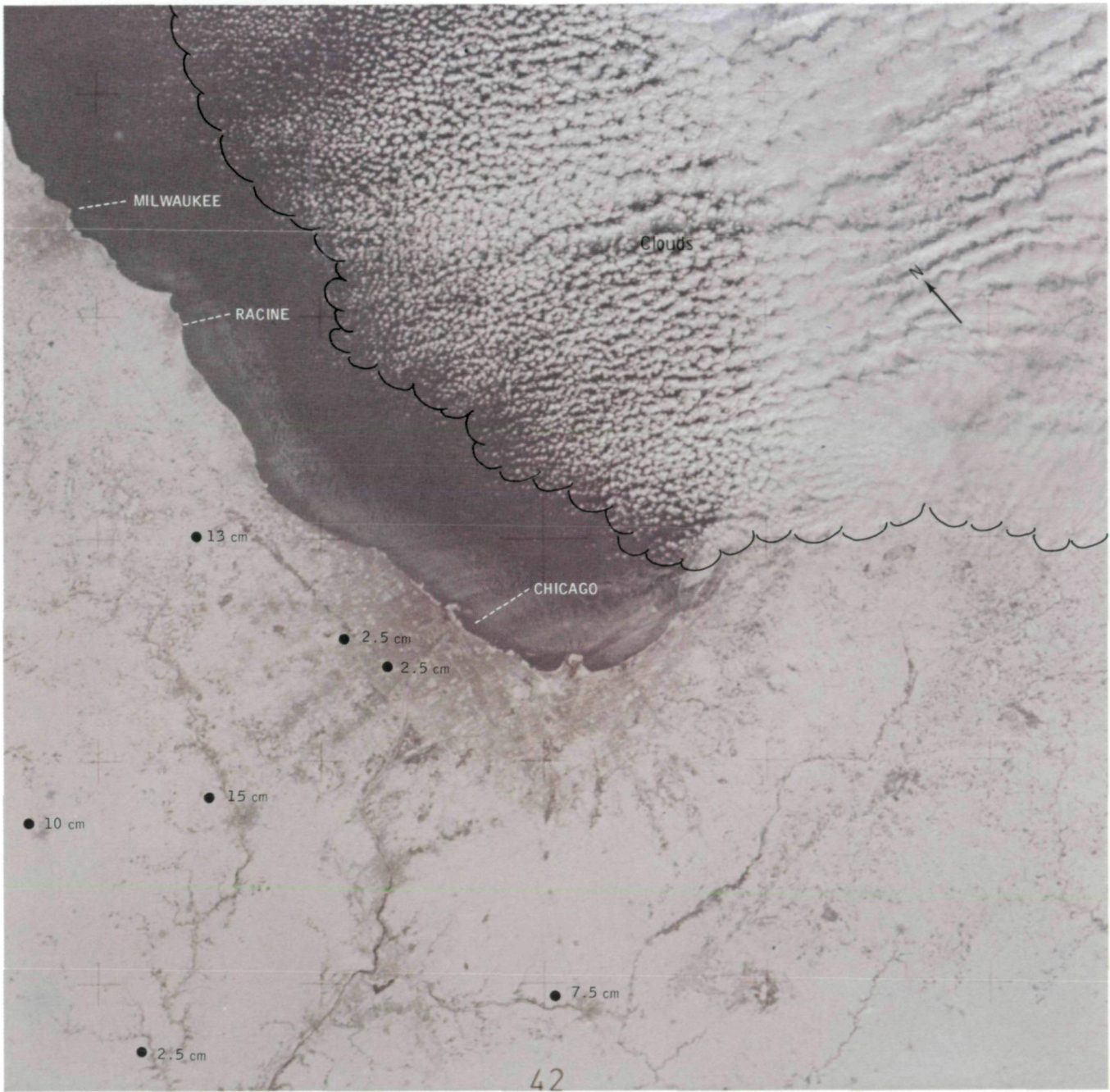


FIGURE 7-26.—The low reflectance of snow-covered urban areas is illustrated in this photograph of the western shore of Lake Michigan taken on January 7, 1974. Snow depths are in centimeters (SL4-139-3954).

SNOW COVER EFFECTS IN GEOLOGY

A blanket of snow can aid geologic and related investigations by enhancing rock features and associated landforms. During review of the Skylab 4 crewmen's observations and photographs obtained for the snow-mapping experiment, several examples were identified in which land features were intensified by the snow cover. These photographs are included to illustrate how space imagery obtained under a variety of viewing angles and solar illuminations can supplement geologic studies using conventional aerial image analysis techniques.

The photographs of central Oregon (figs. 7-27 and 7-28) show characteristic snow patterns in the Cascade Range and Columbia River drainage system. As part of the Skylab 4 crew debriefing, the nature of the two pronounced linear features on the photograph (fig. 7-27) was discussed. Each feature is longer than 100 km, and, by comparison with topographic maps of this region, the linears correspond to the valleys formed by the John Day River and Mountain Creek. Figure 7-28, a near-vertical view of the region, shows the limit of snow cover and the resulting enhancement of the dark, snow-free valleys. These photographs illustrate the general thesis that the visibility of drainage patterns is

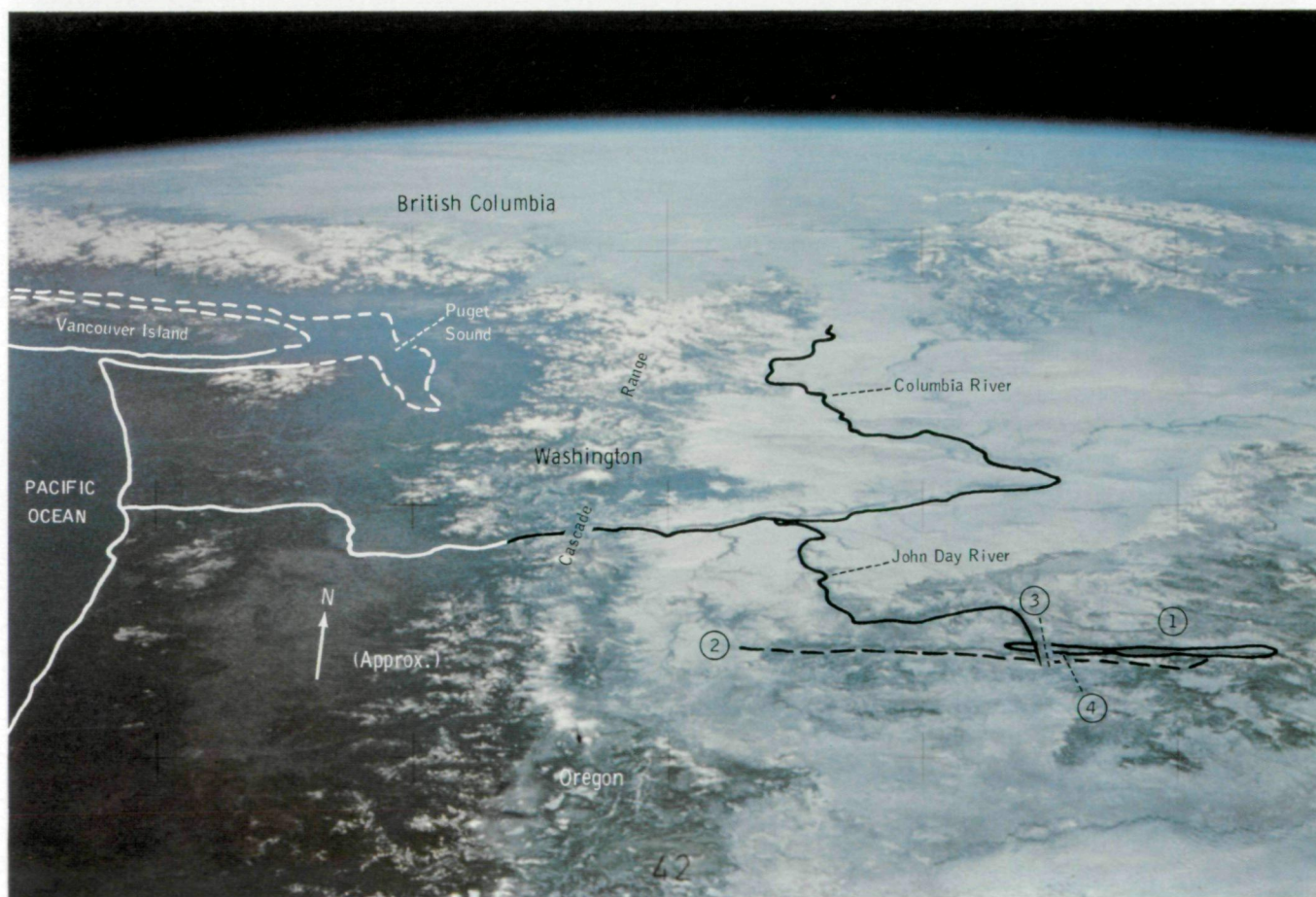


FIGURE 7-27.—Oblique photograph of Washington, Oregon, and British Columbia taken on January 6, 1974. Linear features at the lower right are marked by snow cover. The linear at point 1 correlates with the valley formed by the John Day River and Mountain Creek. The linear at point 2 is more sinuous. North-south linears are formed by the alinement of the John Day River with Cottonwood Creek (3) and the trend of the South Fork of the John Day River (4) (SL4-139-3935).

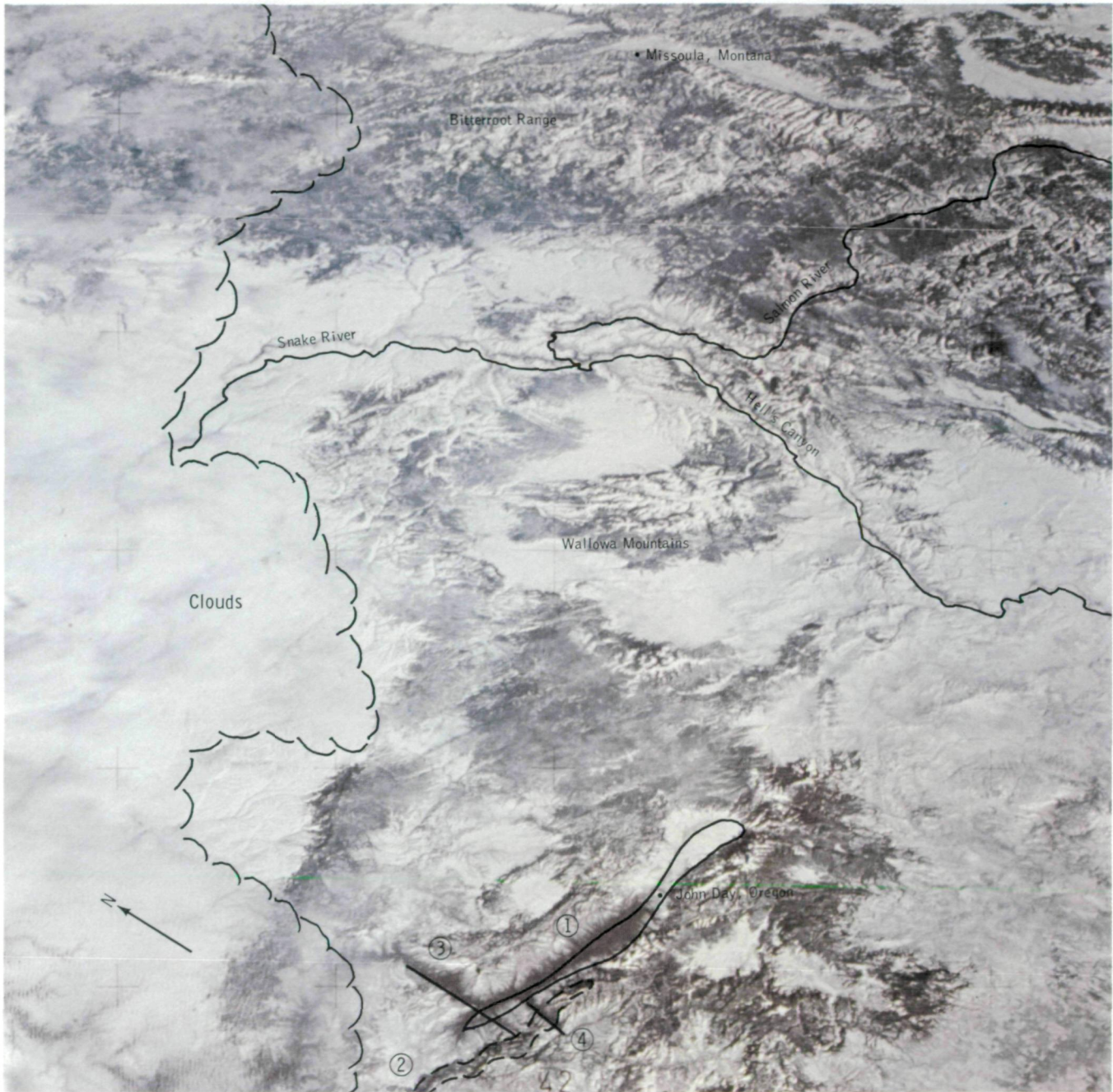


FIGURE 7-28.—This oblique photograph, taken on January 9, 1974, covers Washington, Idaho, and Western Montana. The linears visible in figure 7-27 (1, 2, 3, 4) are also seen in this photograph (SI4-139-4013).

enhanced by snow cover. Further, the patterns are generally controlled by structural features such as the John Day River Valley that parallels the John Day Fault, a regional structure in the Blue Mountains of Oregon.

The handheld-camera photograph of the Flagstaff, Arizona, region (fig. 7-8) was taken on January 22; on the following day, the snow depth was reported to be 13 cm and restricted to the higher elevations. As was seen in the photographs of the Cascade Range of Oregon, the drainage pattern is accentuated especially where the stream valley is prominent in the snow-covered area. Volcanic craters and cones are common landforms in the Flagstaff area. Enhancement of volcanic features through snow cover of moderate depths is useful in geologic reconnaissance surveys.

Another winter scene obtained by the Skylab 4 crewmen illustrates the enhancement of topographic and geologic features in a photograph taken at high-oblique, low-Sun angles of an area having extensive snow cover. Figure 7-13, taken over northwestern Wyoming, demonstrates the enhancement by snow of both geological lineaments and other bedding and structural characteristics. This enhancement is particularly evident in the Wyoming and Salt River Ranges, the Gros Ventre Range, the southern half of the Absaroka Range, and along the margins of the Wind River Range. The snow appears to reduce the spectral noise of vegetation and cultivation and provides a surface of more nearly uniform reflectivity against which relief and shadowing emphasize structural and coarse textural features. The strength of this effect can be seen by comparing the lineaments resolved in the Gros Ventre and Absaroka Ranges in figure 7-13 with the lack of information revealed in figure 7-14 under conditions of greatly reduced snow cover. The geologist familiar with the region will notice a similar enhancement of structural and intrusive features in the central and southern Colorado Rockies in figure 7-17. Snow cover does decrease the tonal information where the bedrock or soil is relatively bare; however, structural information is enhanced and offsets the discrete data on color variations which may be indicative of rock distribution.

In summary, crewmen of Skylab 4 were able to observe selected areas, taking full advantage of changing solar illumination (Sun elevation and azimuth), varying degrees of obliqueness, and shifts in line-of-sight azimuth. Geologically, this target-of-opportunity capability is very useful because one particular combination of viewing angle and illumination may provide

the key to recognizing new features in well-mapped terrain. Photography of such features cannot be planned because their enhancement frequently depends on a unique combination of factors. Snow cover may often be significant in enhancing certain structural and textural characteristics, and melting patterns may be useful in delineating some stratigraphic units.

OBSERVATIONS OF SNOW COVER IN AREAS OUTSIDE THE UNITED STATES

More than 75 photographs of snow-covered areas outside the United States or Canada were taken by the Skylab 4 crewmen. One area observed on several Skylab passes was the European Alps (fig. 7-29). Although no exhaustive snow-mapping effort was conducted using this photograph, a cursory analysis comparing the snow extent with topographic charts indicates an average snowline elevation of 1375 m.

The entire length of the Caucasus Mountains is observed in the figure 7-30 photographs. In these two photographs, the southern slopes of the mountains appear to have more extensive snow cover than the northern slopes; however, the darker tone of the northern slopes is probably due to a combination of shadow and vegetation effects rather than to a lesser snow amount. Extensive mountain shadows exist in these late afternoon photographs; also, stratus clouds in the valleys obscure the snowline at several locations.

In figure 7-31, a stereopair of photographs taken over the southern tip of Sakhalin Island, U.S.S.R., is shown. Snow on both mountainous and level terrain is visible. The cities of Korsakov and Yuzhno Sakhalinsk can be identified because of low reflectance. These photographs also show the distribution of sea ice in Zaliv Terpeniya (Terpeniya Bay), east of the island. A narrow band of mostly open water is apparent along the eastern coastal area, extending southward to a highly reflective zone of fast ice at the northern end of Mys Aniva (Cape Aniva). To the east of the open water area, variations in reflectance enable easy identification of zones of different ice types, ranging from newly formed gray ice to areas of medium to thick first-year ice. The application of the Skylab observations to sea ice studies is discussed in section 13.

In several photographs of this area, a small-scale feature of possible significance has been detected in a small bay or inlet along the west coast of Mys Aniva, Sakhalin Island. In figure 7-32, a large area of open

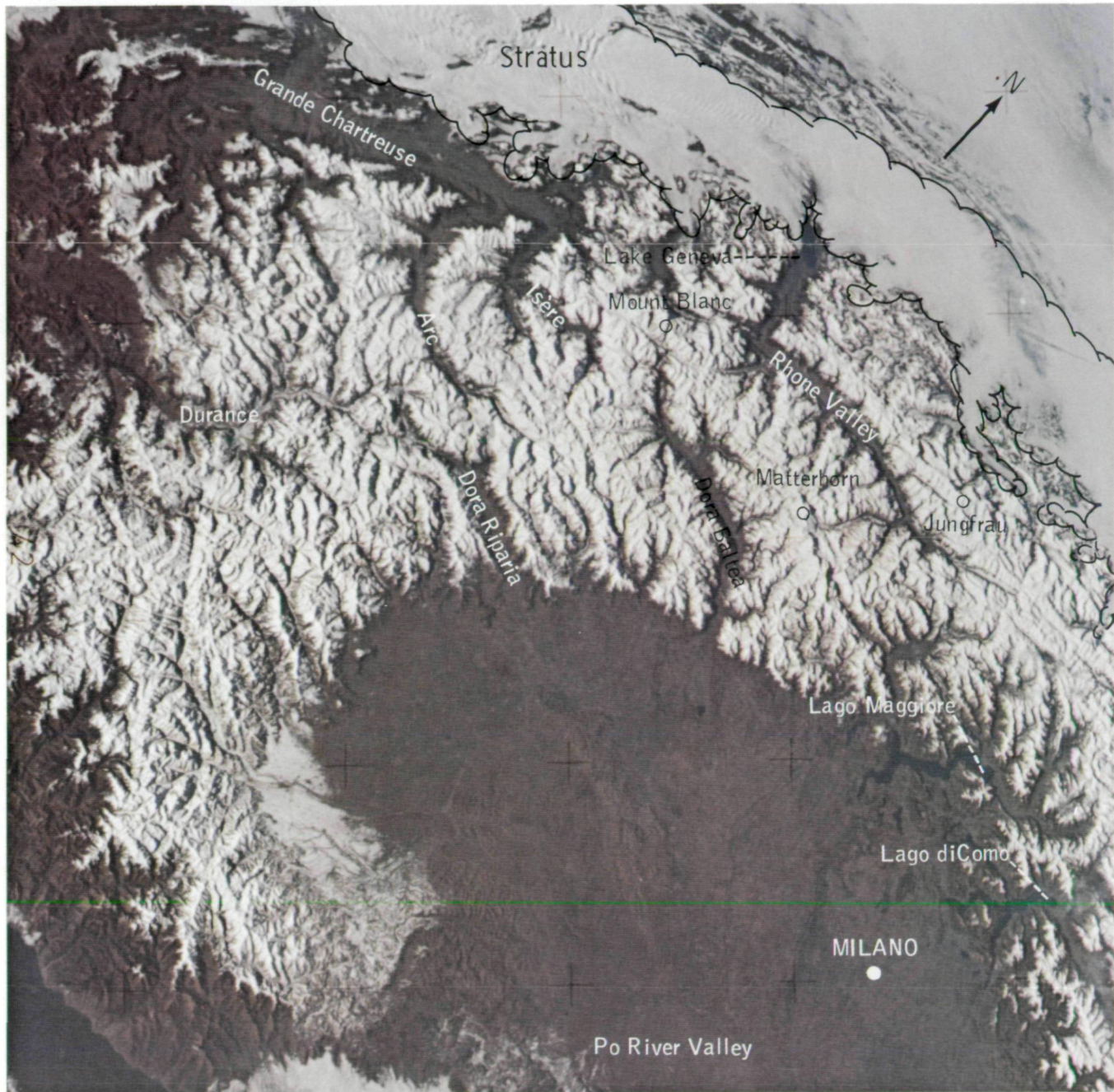


FIGURE 7-29.—Major geographical features are indicated on this view of the European Alps taken on January 20, 1974 (SI4-141-4283).

water surrounded by fast ice is visible in the center of the bay, and a long, narrow linear channel of open water extends northward from the open water area to a position very near the coast. This feature, apparently man-made, may result from the use of icebreakers or some

other means of maintaining access to the ice-free waters of Zaliv Aniva (Aniva Bay). A narrow, ice-free inlet linking Zaliv Aniva with the open water within the smaller bay is also visible.



FIGURE 7-30.—These oblique photographs of the Caucasus Mountains in the U.S.S.R. were taken looking north on January 3, 1974. (a) Western part (SL4-138-3871). (b) Eastern part (SL4-138-3872).



FIGURE 7-31.—The southern part of Sakhalin Island (U.S.S.R.) is shown in this stereopair taken on January 21, 1974. The view is unusual because it includes proximate snow, ice, clouds, and open water (SL4-141-4336 and SL4-141-4337).

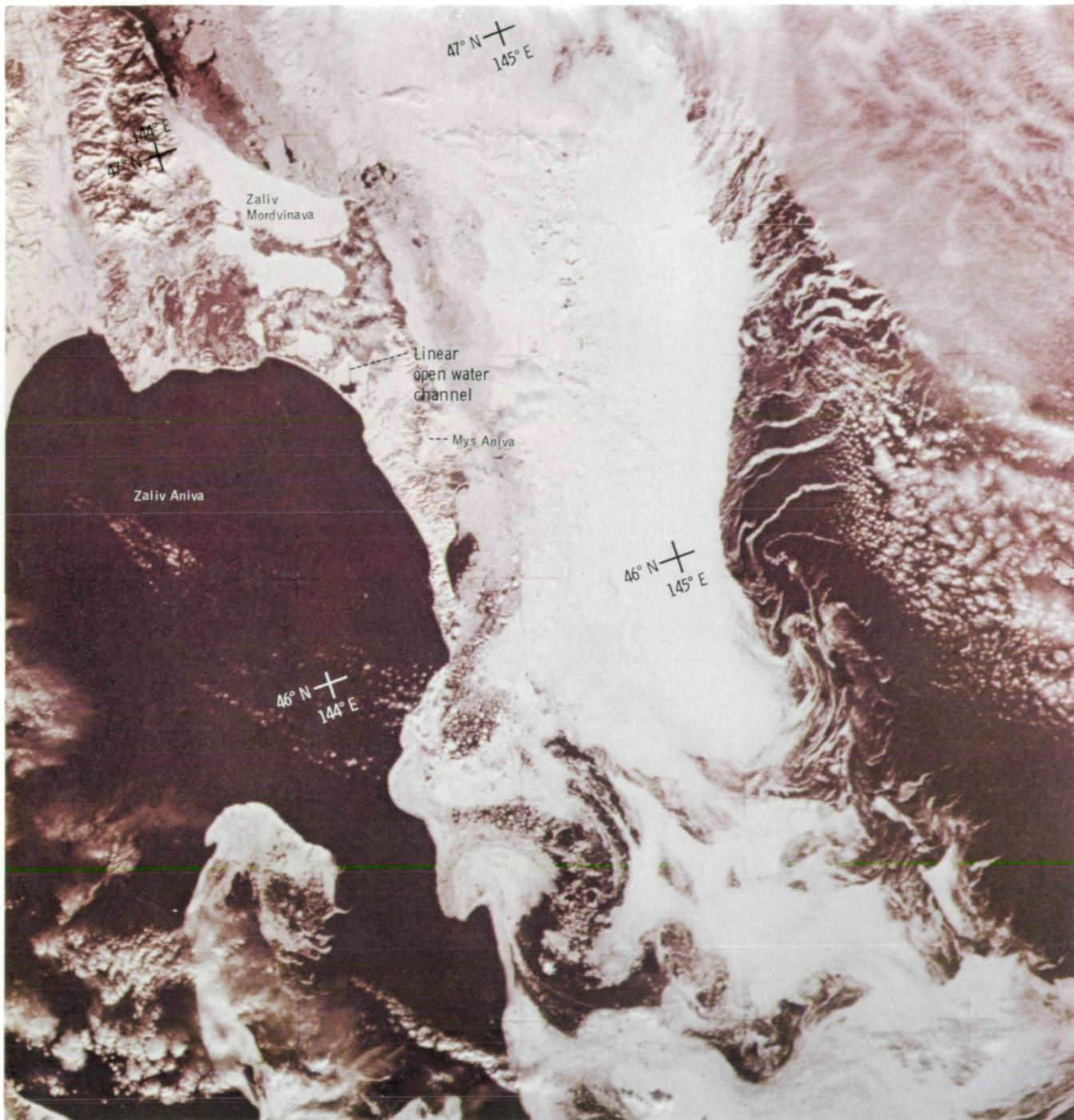


FIGURE 7-32.—The location of a linear open water channel is indicated on this view of the southern part of Sakhalin Island taken on January 21, 1974. A large area of open water surrounded by ice is visible (SI4-141-4339).

CONCLUSIONS

The Skylab 4 Visual Observations Project has provided a substantial amount of information that can be applied to snow-mapping studies. The Skylab 4 crewmen observed the United States during a favorable period because a general snowmelt trend in the central and western part of the country followed the widespread snowfalls in late December and in early January.

In summary, the crewmen experienced no problem in identifying snow, even at great distances from the subpoint of the spacecraft. The results of the Skylab 4 experiment indicate that a space observer can, in some instances, identify snow that photointerpreters cannot distinguish on a photograph of the same area; in particular, a crewman can integrate through partial cloud cover to view the terrain, whereas the interpretation of a photograph with the same cloud cover would be difficult. A person can also select the optimum viewing angle and Sun angle and the appropriate film and filter combination to ensure acquisition of the best possible data. This flexibility has particular application for observing geological structures enhanced by snow cover when a proper combination of viewing angle and solar illumination may permit the discovery of a previously unknown feature. The uncertainty in optimum viewing angle, illumination, and snow cover for a geological study of any particular area places a significant emphasis on the role of the crewman in selecting targets and maximizing the data collection.

The ability of a person in space to identify snow and to point a camera at a specific target, together with the orbiting track of a spacecraft, would permit the observation of a specific drainage basin more frequently and more reliably during a critical snowmelt period than is currently possible from unmanned satellites providing high-resolution data. There may be situations in which high data rates, limited field of view, and data processing considerations may make it imperative to point a camera at specific targets during cloud-free periods, rather than to obtain continuous data coverage. A manned, multipurpose Earth resources space laboratory provides this capability.

Snow can be identified in high-oblique photographs; however, for purposes of mapping the extent of snow cover in specific drainage basins, photographs taken at or near the vertical viewing angle are desired. A low-oblique viewing angle may sometimes be necessary to photograph an entire drainage basin.

Snow mapping is not a new application of space technology. Investigations have shown that the Landsat and NOAA unmanned satellites can provide the hydrologist with substantial practical data. Some snow cover maps derived from the NOAA very-high-resolution radiometer are currently supplied to hydrologists.

Unmanned satellites can best fulfill operational snow-mapping requirements. Observations from manned satellites can provide information that can be used to gain a better understanding of the problems inherent in mapping snow from space and to improve satellite snow-mapping methods. The flexibility of manned space flights in the Space Shuttle era will undoubtedly enable the collection of data to augment those from unmanned satellite systems.

ACKNOWLEDGMENT

The work described in this section was performed by Environmental Research & Technology, Inc., for the NASA Lyndon B. Johnson Space Center under contract NAS 9-13974. The snow survey data used in the study were provided by the Salt River Project Office in Arizona and by the California Department of Water Resources.

REFERENCES

- 7-1. McClain, E. P.: Snow Survey From Earth Satellites. World Meteorological Organization, pub. no. 353, Geneva, Switzerland, 1973.
- 7-2. Barnes, James C.; Bowley, Clinton J.; and Simmes, David A.: The Application of ERTS Imagery to Mapping Snow Cover in the Western United States. (Final report, NASA contract 5-21803, Environmental Research & Technology, Inc., Concord, Mass.) NASA CR-137223, 1974.
- 7-3. Barnes, James C.; Bowley, Clinton J.; and Smallwood, Michael D.: A Study To Develop Improved Spacecraft Snow Survey Methods Using Skylab/EREP Data; Demonstration of the Utility of the S190 and S192 Data. (Interim report, NASA contract 9-13305, Environmental Research & Technology, Inc., Concord, Mass.) NASA CR-138687, 1974.
- 7-4. Kaltenbach, John L.; Lenoir, William B.; McEwen, Michael C.; Weitenhagen, Ronald A.; and Wilmarth, V. Richard: Skylab 4 Visual Observations Project Report. NASA TM X-58142, 1974, pp. 5-1 to 5-4.

8

Cultural Features Imaged and Observed From Skylab 4

ROBERT K. HOLZ^a

THE STUDY of man's impact on the land is important, useful, and significant for space scientists. The many elements of cultural patterns observed and photographed from a space platform provide a synoptic view that is a powerful tool for the scientific community to use in seeking answers to vexing and vital environmental problems. To prepare for visual assessment of man's traces on Earth, the Skylab 4 crewmen were briefed on the characteristic features of cultural patterns in physiographic provinces of the United States, on the variations in structures of metropolitan complexes, and on special topics such as the location and appearance of geometric patterns on the plains of Nazca, Peru. An important objective of this mission, therefore, was to determine the crewmen's capabilities to discern and describe and to obtain photographs that documented the salient points of these patterns. The results of the analyses of the observational and photographic data obtained by the crewmen during the Skylab 4 mission are presented in this section.

MAN'S ROLE IN CHANGING THE EARTH SURFACE

Near the turn of the century, geographers in the United States became increasingly concerned with the impact of man on the land; eventually, this interest evolved into a branch of geography that sought to increase the knowledge of man's relationship with the land (ref. 8-1). For many decades, geographers had ex-

pressed concern about the effects of man living on and using the land, and these studies undoubtedly influenced the scope of research in America (ref. 8-2).

Modification of the Earth by man is the predominant component of the landscape in many areas in the world (ref. 8-3). For example, in the eastern United States, in western Europe, and in parts of the Middle East, northeastern Asia, and eastern Australia, the dominant features of the landscape are manmade or considerably modified by man. A large area of significant man-induced change is seen in the low-oblique photograph of southeastern Australia taken by the Skylab 4 crewmen (fig. 8-1). Even remote areas of the world have not escaped the influence and activities of modern man. For example, roadways have been cut through remote and inaccessible parts of the world, such as the upper reaches of the Amazon River in western Brazil. Glaciers in Antarctica have traceable amounts of radioactive fallout, and considerable quantities of equipment and materials are evidence of numerous exploratory and scientific expeditions.

Substantial information exists in the published literature on the types of Earth science data that can be extracted from space imagery of the Earth (ref. 8-4). The intent of this section is to describe, through the use of the crewmen's visual observations and analyses of selected handheld-camera photographs, the cultural features or traces of man on the Earth surface that are observable from near-Earth orbit and to discuss the observational tasks man can perform from space to study and analyze cultural features (ref. 8-5).

During the Skylab 4 mission, the crewmen described and photographed many patterns developed by man to

^aUniversity of Texas at Austin.

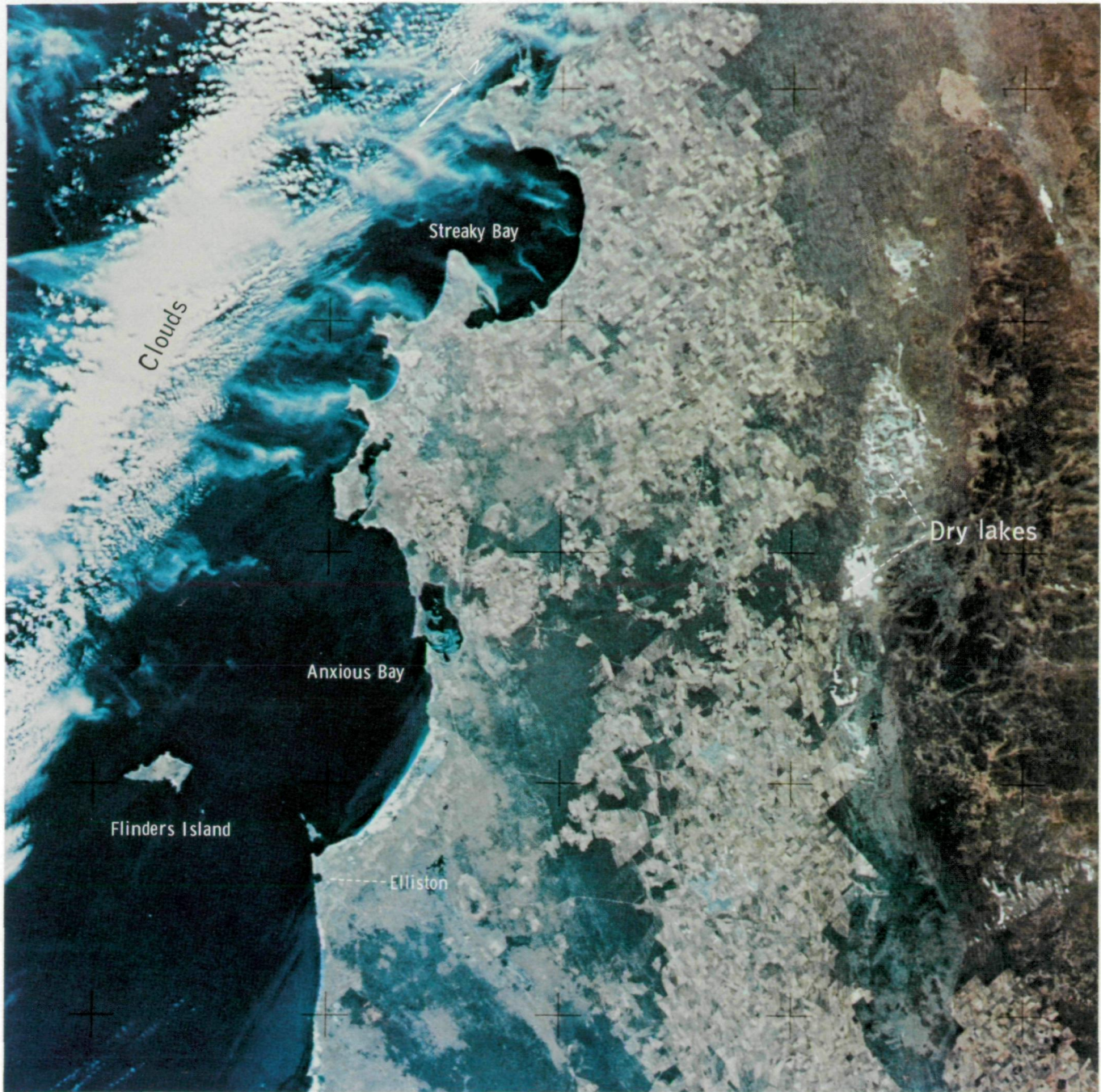


FIGURE 8-1.—Handheld-camera photograph showing an area of intensive commercial agriculture in southeastern Australia (SL4-137-3572).

meet his specific needs for economic development (metropolitan complexes), mobility (transportation systems), food (agriculture), and building materials (lumbering).

METROPOLITAN COMPLEXES

The geometric configuration of metropolitan complexes reflects the historical development, the geographic location, and, in part, the cultural heritage of the society. Analyses of space photographs have shown that the land use and growth trends of individual metropolitan areas can be defined and the results used in comparative studies of city patterns (ref. 8-6). To assess the use of handheld-camera photographs and crew observations in urban area structure studies, the Skylab 4 crewmen were requested to describe and photograph 20 cities situated in or near mountains, coastal areas, deserts, plains, or rivers and river deltas (table 8-I). In accomplishing this task, the Skylab 4 crewmen also obtained 89 handheld-camera photographs of 47 cities in the United States and 11 other countries (table 8-II). In the following paragraphs, the discussions are directed to visual observations results and to conclusions gathered from analyses of the handheld-camera photographs.

Observations

Large cities of the western industrialized nations are clearly visible from space. The development and growth of such cities as Dallas and Fort Worth, Texas (fig. 8-2), significantly change the environment and produce a new signature on the landscape. The Skylab 4 crewmen described western cities, particularly those in the United States, as having the appearance of gray, unhealthy-looking areas. Discussion with the Skylab 4 crewmen has shown that, as the city size decreases, as the climate becomes more humid, or as the society becomes less industrialized, it becomes increasingly difficult to discern urban areas and to identify internal

TABLE 8-I.—Metropolitan Areas Scheduled for Observation From Skylab

| <i>Environment</i> | <i>City</i> |
|--------------------|--|
| Mountainous | La Paz, Bolivia Mexico City, Mexico Bogotá, Colombia Addis Ababa, Ethiopia Katmandu, Nepal |
| Desert | Antofagasta, Chile Khartoum, Sudan Phoenix, Arizona |
| Coastal area | Rio de Janeiro, Brazil Vera Cruz, Mexico Manila, Philippines Marseilles, France |
| Plains | Fort Worth and Dallas, Texas Omaha, Nebraska Brasília, Brazil |
| River | Kisangani, Zaire Iquitos, Peru St. Louis, Missouri |
| Delta | Calcutta, India New Orleans, Louisiana |

TABLE 8-II.—Skylab Photographs of Metropolitan Complexes

| <i>Continent</i> | <i>Number of cities</i> | <i>Number of photographs</i> |
|----------------------------|-------------------------|------------------------------|
| North America ^a | 29 | 60 |
| Europe | 4 | 4 |
| Asia | 2 | 7 |
| South America | 9 | 13 |
| Africa | 2 | 4 |
| Australia | 1 | 1 |
| Total | 47 | 89 |

^aOf the North American cities, 26 of the 29 observed were U.S. cities; 57 of the 60 photographs taken were of the United States.

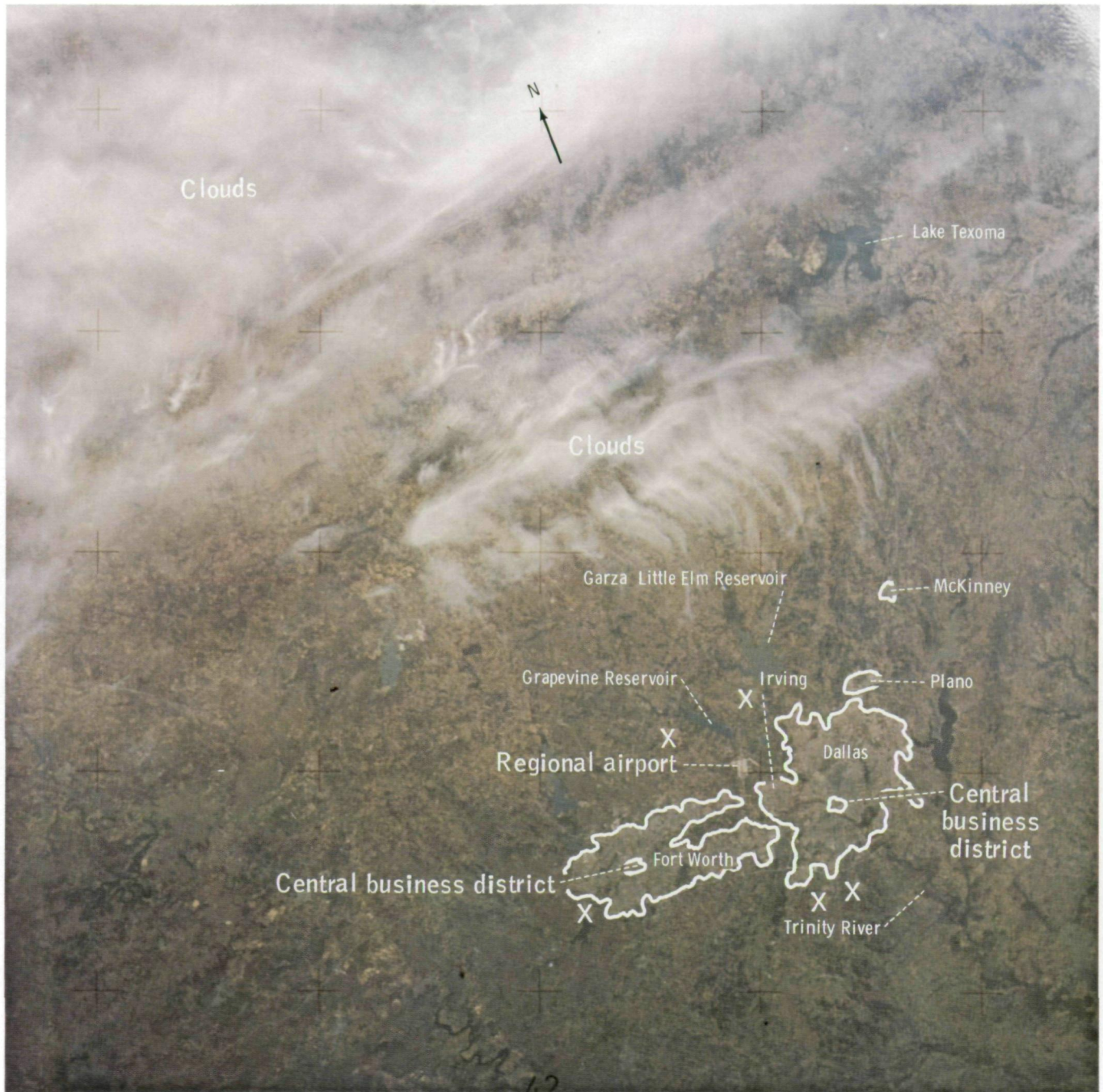


FIGURE 8-2.—A low-oblique photograph of Dallas and Fort Worth, Texas. Note the bright arrowlike signature of the new regional airport just north of the two cities (SL4-139-3950).

detail within the built-up portion of the urban area. An exception to these generalizations is that city patterns are enhanced when a light snow cover blankets an area; even small central places populated by only several hundred can be identified against this strong contrast.

Twice during the Skylab 4 mission, the crewmen's schedule, optimum weather conditions, and the spacecraft orbital path allowed nighttime viewing of the California coastal regions and of Florida. The crew commented that the lights of major arteries, major cities, and small towns were prominent. The night view of Florida was similar to a roadmap pattern. Although city lights were clearly visible, internal structures of the urban areas were not readily apparent.

The reasons some cities can be more easily identified and observed than others are still being examined. The Skylab 4 crewmen could not locate such large cities as Brasilia, Addis Ababa, and Marrakech. Although these cities were observation sites, repeated attempts to locate them failed, even with the aid of 10× binoculars. Cities such as Rio de Janeiro, Mexico City, San Francisco, and Acapulco were easily observed and photographed from space. The size (spatial extent) of the cities was an important factor in locating them, but other environmental and cultural factors may be more significant. For example, Addis Ababa and Marrakech are large but are not as industrialized as other large cities of the world. These two cities are characterized by the absence of tall buildings and large paved areas. Open spaces are common within the urban areas, and the cities blend gradually into the countryside. In contrast, western cities such as Dallas and Fort Worth have created a manmade urban environment and a cultural signature that differs greatly from the surrounding landscape (fig. 8-2). Non-western cities are more integrated into the landscape. They are generally constructed from locally available natural materials, such as clay or mud brick. Figure 8-3 is a 35-mm aerial photograph taken near Marrakech that shows the red clay and alluvial soils typical of the Haouz Plain on which the city is located. Marrakech, sometimes called Red City, is constructed almost exclusively from red mud brick made locally; its buildings and walls, therefore, have a photographic signature much like that of the surrounding countryside. Figure

8-4 is a Skylab 4 photograph of the northwestern coast of Africa. Marrakech is located in the lower left corner of this photograph, to the northwest of the snow-covered Grand Atlas Mountains. Because it blends into the rural surroundings, it is not easily discerned, even with the aid of photographic enhancing and enlargement techniques. Study of such metropolitan complexes in subtle "natural" environments by future space observers will require (1) onboard maps showing precise location in relation to natural landmarks, (2) special prelaunch training, and (3) the capability to gather data of selected ground sites with high-resolution instruments.

Observing very humid areas of the Earth's surface from space is generally difficult. Clouds, haze and other atmospheric pollutants, and the presence of dense, healthy vegetation give these regions a faded blue-green appearance that obscures surface details. Cities, especially those with a considerable amount of vegetation within the built-up areas, tend to assume the same general signature as the surrounding landscape. In rapidly growing cities, the older areas usually have more vegetation, particularly trees that are large and rise above the general level of the building roofs. Although these older areas are sometimes difficult to distinguish



FIGURE 8-3.—A low-level high-oblique aerial photograph near Marrakech, Morocco. Note the reddish cast to the plain in the background.

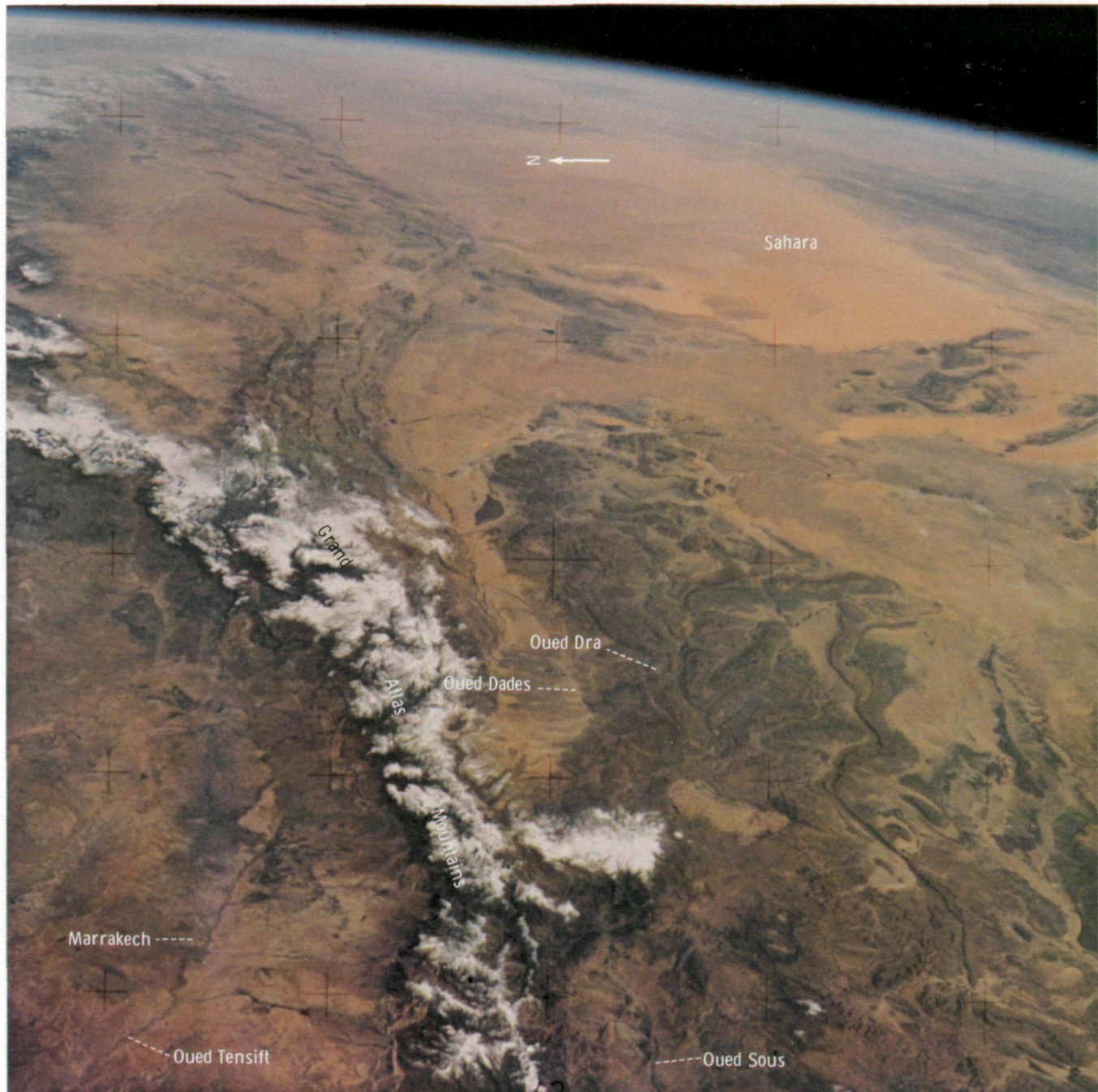


FIGURE 8-4.—This high-oblique photograph taken over southern Morocco looks across the snow-covered Grand Atlas Mountains to the Sahara and the horizon in the background. Marrakech is near the snow-covered area in the lower left (SL4-139-3910).

from the rural countryside, they provide the careful interpreter with some insight into the age and perhaps the quality of housing in various parts of built-up urban areas (ref. 8-7).

Interurban features such as transportation systems and airports were identified from Skylab, especially in western cities; however, the Skylab 4 crewmen reported that they were unable to identify individual buildings such as the Pentagon in Washington, D.C., or the pyramids in Egypt with the aid of binoculars. Nevertheless, large facilities such as the NASA John F. Kennedy Space Center and the NASA Lyndon B. Johnson Space Center were discerned when viewing toward the west with an early morning Sun. The crewmen described their view of urban areas as approximating the informational content contained in the 1:1 000 000-scale (11.4 cm) contact photograph from the Skylab Earth terrain camera. The photograph of the Chicago region (fig. 8-5) shows the view from Skylab 3 of this metropolitan complex. The major features discerned by the Skylab 4



FIGURE 8-5.—Skylab 3 photograph of Chicago, Illinois, taken with the Earth terrain camera in September 1973 (SL3-88-222).

crewmen were the transportation routes (white lines), urban areas, rectangular land use pattern, and the near-shore light-blue sediment-laden water in Lake Michigan.

From a 430-km orbit, the view provided human observers is primarily regional or small scale. The Skylab 4 crewmen demonstrated that observational data of metropolitan complexes are limited to detection of the city outline, major transportation arteries, suburban built-up areas, overall textural patterns of the city compared to those of adjacent regions, and color or albedo. Consequently, for future Earth-orbit missions, little can be gained from observation of the detailed internal morphology of cities unless the crewmen are equipped with instruments capable of resolving details of urban areas.

Image Analysis

An important objective of the Skylab 4 study of metropolitan complexes was to determine the type of information obtainable from analysis of color photographs taken under a variety of ground conditions and Sun and viewing angles.

Screening of the 89 handheld-camera photographs has shown that the western industrial cities appear as scars on the landscape and produce a stronger image signature than nonwestern cities. Cities in semiarid regions are in sharp contrast to the surrounding terrain, whereas, in humid regions, factors such as atmospheric haze and abundance of vegetation tend to obscure the urban areas. Equally as important as the contrast between city and surrounding terrain is the size of the metropolitan area; large cities are easier to locate and to photograph.

The regional views of the handheld-camera color photographs are of primary use in the identification of the built-up areas. The most useful photographs were those taken from near nadir and when there was little atmospheric moisture (clouds, haze) and urban pollution. For example, in the Skylab 4 handheld-camera photograph of San Diego, California (fig. 8-6), urban details such as parks, airports, major new transportation



FIGURE 8-6.—Low-oblique view of San Diego, California. (a) Photograph (SL4-196-7354). (b) Areal map.

routes, the central business district, other commercial nodes, new suburbs, and the limits of the built-up occupied area are discernible. However, complex detail or large-scale information (such as type of dwellings, minor street patterns, and quality of housing) is not visible in such photographs.

The near-nadir view of Miami, Florida, shown in figure 8-7 illustrates the effects of clouds and humidity on observing details of urban areas. The major outline of the city is apparent; however, the internal patterns are not discernible.

For selected cities, the Skylab photographs were

analyzed and an assessment was made of the image quality, resolution, viewing angle, and surface condition for defining the texture and patterns in the city. Although the Skylab 4 crewmen could not determine large-scale internal patterns of metropolitan areas with the aid of binoculars, the photographs they obtained are historical documents that provide information on the regional cultural patterns. To assess the use of such photographs in the study of urban area patterns, analyses of photographs taken of Denver, San Antonio, and San Diego were completed and are included in this section.

PACIFIC
OCEAN



Chicago, Illinois.—The Skylab 4 mission was flown during the winter season in the United States, and photographs of urban areas with extensive snow cover were obtained. One such photograph of the Chicago area illustrates the enhancement of some land use and cultural features against a strong background contrast (fig. 8-8). In this color image, approximately 100 000 square kilometers of the Chicago region are shown. The dominant cultural feature is the metropolitan area that extends along the shores of Lake Michigan from Milwaukee, Wisconsin, to Gary, Indiana. In metropolitan Chicago, the older central core (A) appears much

darker than the suburbs primarily because the “heat island” of the inner city has large buildings, less green or unoccupied space, and more pollution of the snow cover, thereby reducing the effect of the white background. In the darker areas, open spaces such as parks, golf courses, airports, and other land use areas with a low building density are identified by lighter tones. In the most densely built-up part of the city, major lineaments or arteries that represent major transportation routes (streets, highways, railroads, and pipelines) and drainageways (rivers and canals) are visible. For example, the Chicago River canal appears as a dark line near



FIGURE 8-7.—Photograph of the southern tip of Florida (SL4-139-3982).

the center of the city. Locally dark tones occur that are probably caused by dense cover (trees and brush) and other changes in land use that mask the snow cover. This same effect is observable on the rural landscape where the major drainage lines of the region are easily traced.

Urban researchers have identified three basic types of city growth: concentric, nodal, and sectorial. Examination of figure 8-8 reveals elements of all three growth patterns. The densely built-up inner city (A) is surrounded by zones B and C, which are characterized by a decrease in the intensity of land use; however,

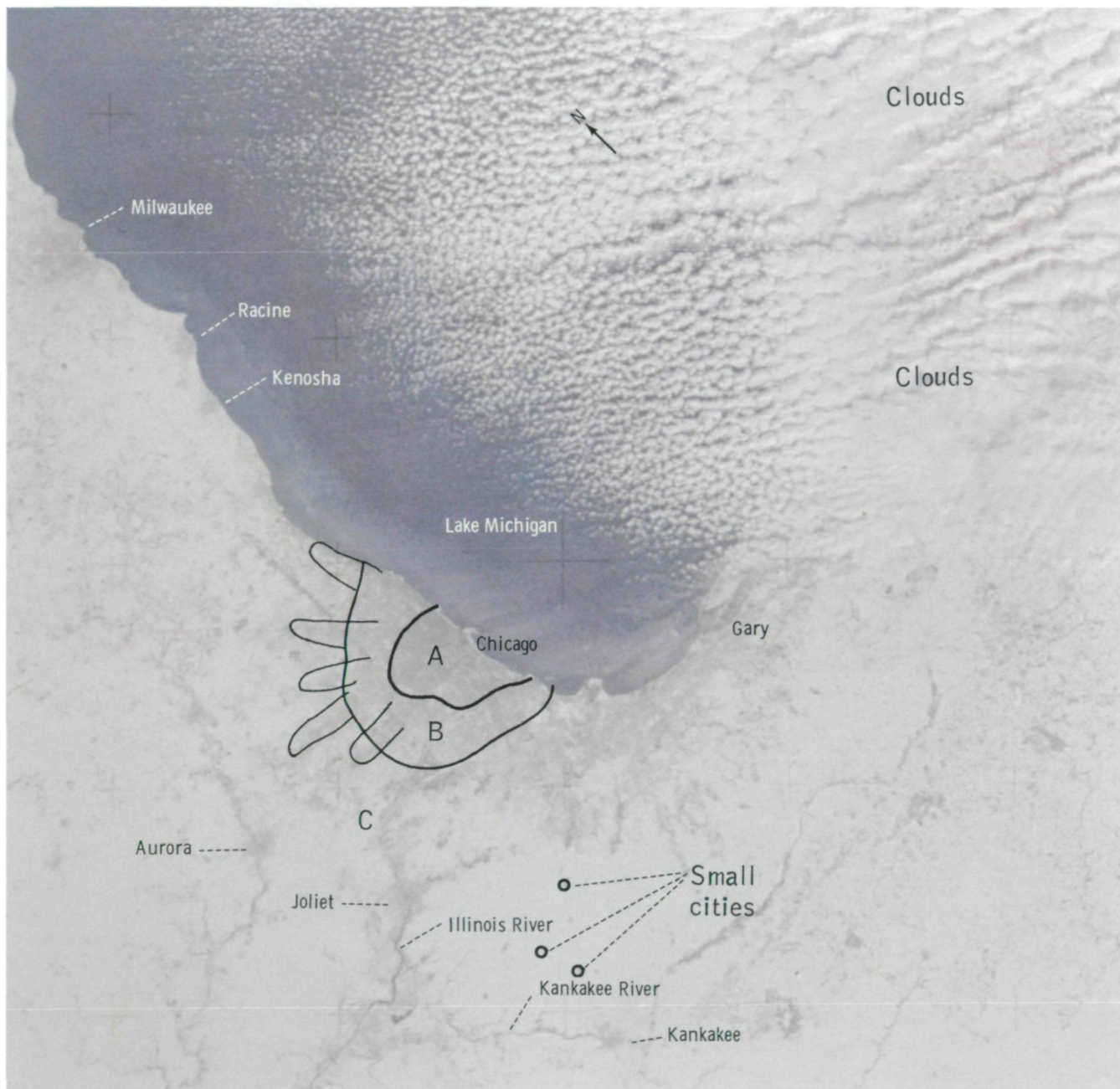


FIGURE 8-8.—A low-oblique photograph taken over east-central Illinois. Chicago is at the center. A light snowfall covers the area, and a cloud bank to the northeast obscures southern Michigan (SL4-139-3954).

nodes of concentrated human activity are indicated as dark areas. Tendrils that follow transportation routes into the suburban fringe are characteristic features of the Chicago growth patterns. Major urban development has occurred along the sectors that appear as dark areas to the northwest, to the south, and in two lines to the

west. Within these sectors, nodes of more intense development appear darker in the photograph. This pattern suggests that sectors grow by outward directional expansion of previously existing nodes. Nearer to the core of the city, the zones between the sectors have been occupied. If the majority of metropolitan com-

plexes follow this pattern of urban growth—the filling in of unoccupied land between built-up sectors—the growth patterns of cities can be predicted.

Dallas and Fort Worth, Texas.—Dallas and Fort Worth, Texas, exhibit some aspects of the Burgess hypothesis of city growth by concentric zones, although the pattern is better developed in the northeastern and eastern parts of Dallas (fig. 8-2). Growth of the urban areas between Dallas and adjacent suburban cities to the northeast has resulted in the expansion of Dallas since the 1968 Apollo 6 photograph shown in figure 8-9 (ref. 8-6). The extent of this expansion is shown by a comparison of figures 8-2 and 8-9. The 1974 Skylab 4 photograph (fig. 8-2) reveals the development of non-contiguous series of small central places. These urban places already show evidence of linear growth toward each other and could form the next concentric zone still farther from the central cities of Dallas and Fort Worth.

Social studies of metropolitan complexes have indicated that cities tend to grow in specific patterns. These patterns may be associated with types of social organizations, and their development may occur in sectors around nodes or in concentric zones. On the Skylab photograph of the Dallas-Fort Worth area (fig. 8-2), the elements of the three growth patterns that can be identified include the concentric pattern illustrated by the central business district surrounded by a major urban area. Sectors are indicated by the elongation of the urban area northward from Dallas and the eastward extensions from Fort Worth toward Dallas. Several small urban centers (marked "X") probably developed as residential or industrial centers and represent the outward extension from the metropolitan complex.

Denver, Colorado.—Denver developed on the piedmont of the Great Plains and is bounded on the west by the Front Range of the Colorado Rocky Mountains. Major expansion of the city to the west has reached the first outliers (hogbacks) of the Front Range. Figure 8-10(a) is a photograph obtained by the Skylab 4 crewmen in which a light snow cover combined with a relatively low Sun angle produced a shadow and a strong target to background contrast. The result is excellent topographic detail of the mountains and enhancement of city detail.

The built-up urban area consists of a dense zone (dark) and a sparse zone (light) (fig. 8-10(a)). The

zones are not discrete entities but merge gradually into one another. The dark tone is the city of Denver (the South Platte River effectively divides the city into two units), although there are tendrils and/or islands of dark tones that occur within some of the suburban areas. The light tone forms a fringe around the dark core; however, within the fringe, numerous parks and open areas appear white in contrast. The light tone is the result of less building density, more open spaces, less snow removal, and snowmelt.

Features identified on the photograph and plotted on an areal map of the region (fig. 8-10(b)) include the grid pattern formed by major streets and highways (dark lines), parks (white snow cover), the sinuous trace of the Platte River, and the location of a powerplant (smoke plume).

Perhaps the most valuable lesson to be gained from studying figure 8-10(a) is that urban detail is very apparent when seen in the high-contrast background provided by the snow cover. Normally, after the passage of a snowstorm, there is a clearing effect as drier, colder, more stable air from an anticyclone (high pressure) moves into an area. These clear atmospheric conditions allow a space observer to easily discern or photograph an urban environment. For future space missions, the study of urban or other cultural features under these weather conditions should be considered.

San Antonio, Texas.—San Antonio, with a population of approximately 750 000, developed on the break between the Texas Hill Country and the Gulf Coast Plains. The city's northern environs now extend into the hills as builders seek new areas to develop. The Skylab 4 crewmen obtained a low-oblique photograph (fig. 8-11(a)) to determine its utility in the study of structural features of this plains city. Analysis of the photograph resulted in a sketch map of the San Antonio region (fig. 8-11(b)). Although the internal structures of the city are somewhat obscured, the major urban buildup is readily apparent in the photograph and is shown on the accompanying sketch map.

The San Antonio urban areas have a gray signature on the interface between the Hill Country and the blackland prairie. The central business district is a somewhat lighter blue than the rest of the city, which may be a function of recent development and construction resulting in the concentration of commercial nodes



FIGURE 8-9.—An Apollo 6 photograph of the Dallas and Fort Worth area (AS6-2-1462).

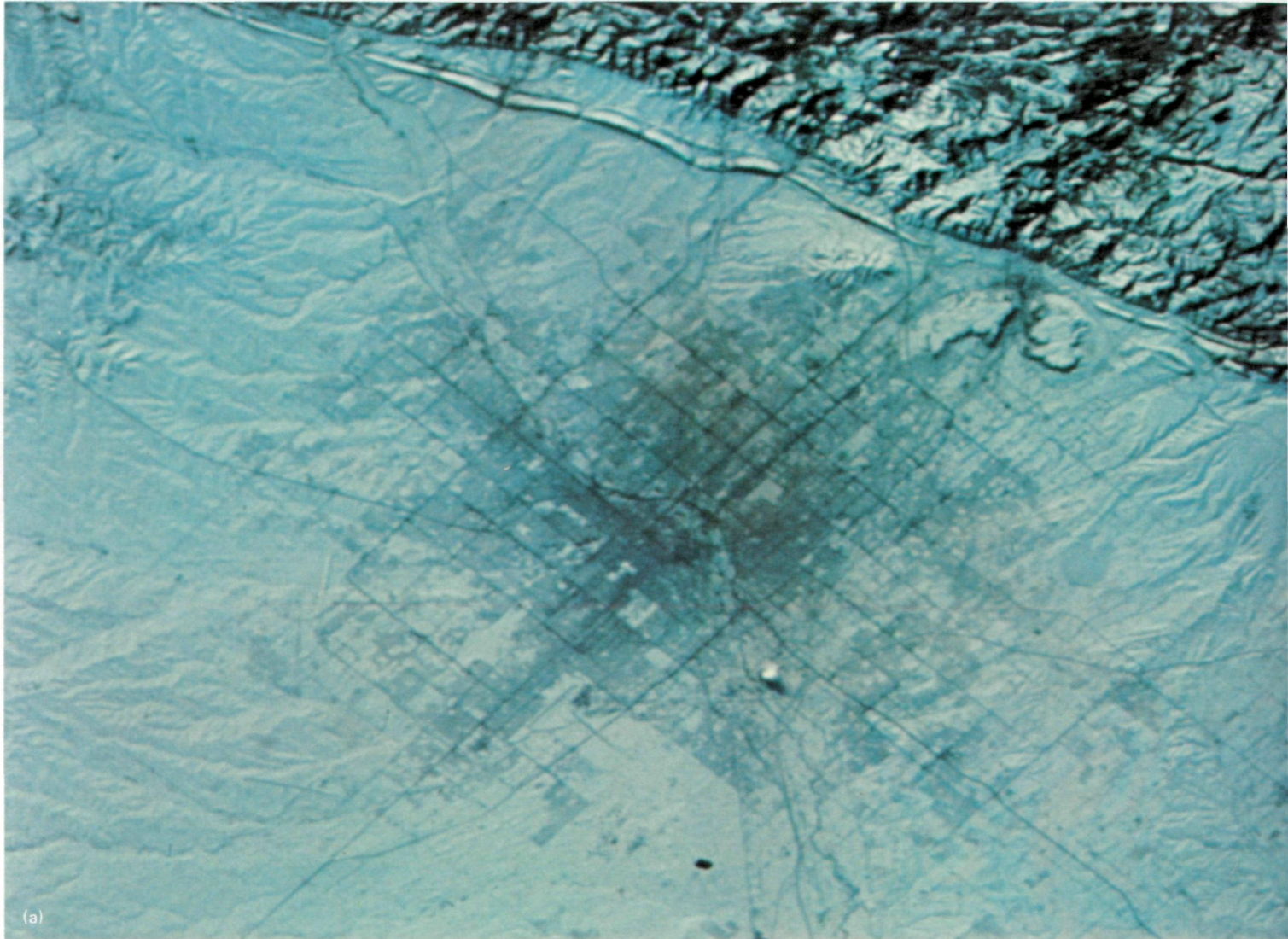


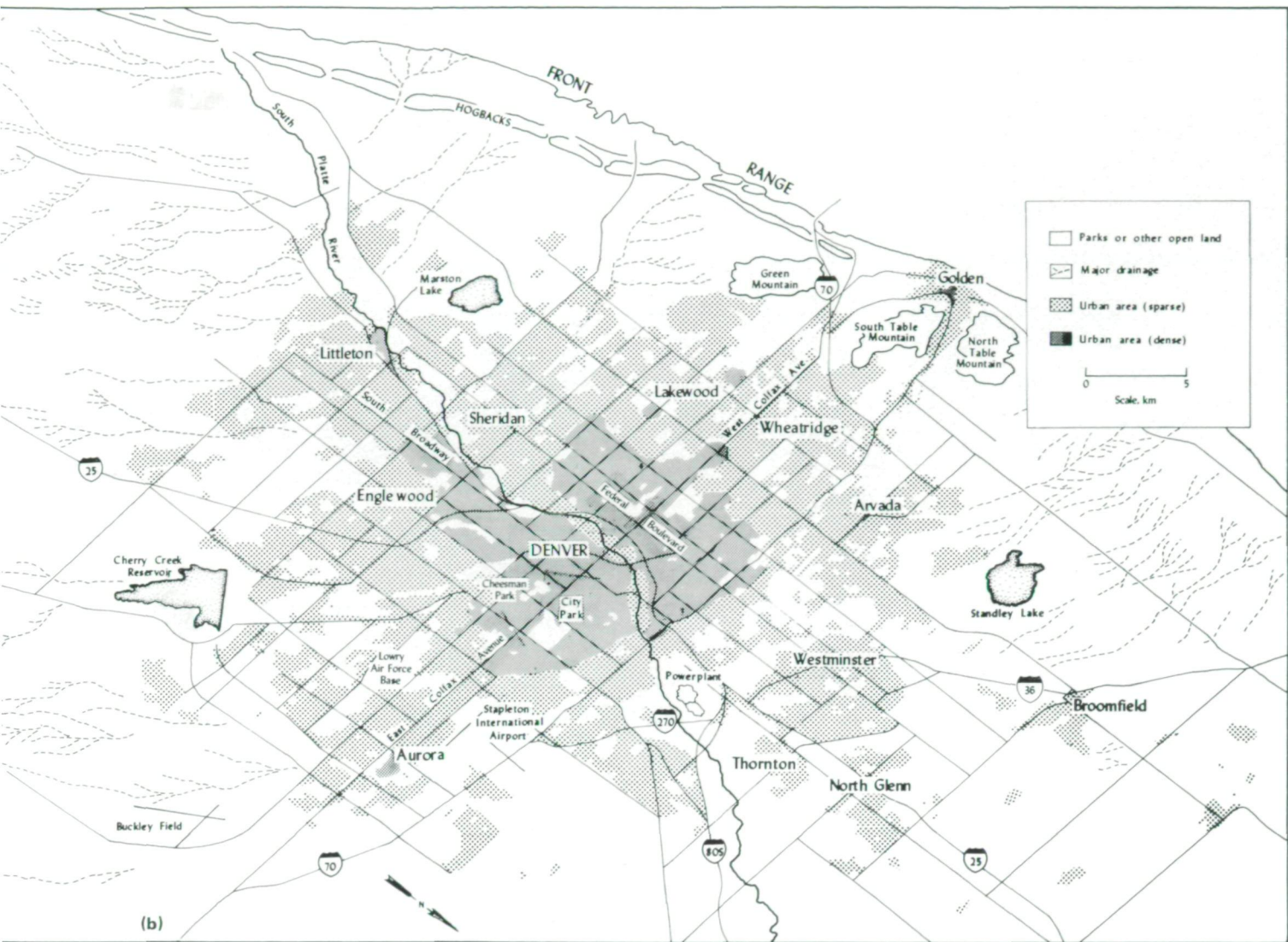
FIGURE 8-10.—A low-oblique view of Denver, Colorado. (a) Photograph (SL4-193-7151). (b) Areal map.

in this area. San Antonio has a rectangular appearance in figure 8-11(a); however, a general north-south vector is apparent in the developing pattern. The city is ringed by a belt route with urban growth pushing out to the inner margins of this highway system. Considerable space exists for future urban expansion and growth, especially in the southwestern portion of the city. San Antonio is a unique metropolitan area because few satellite cities have developed around it.

The vegetation patterns visible in figure 8-11(a) reflect to a major degree the soil types. From north to

south, there are four distinct vegetation zones (fig. 8-11(b)), each with a different overall signature: (1) grazing land and scrub oaks (the Hill Country), (2) agricultural areas (the sharp break along the Balcones Fault escarpment to blackland prairie), (3) the Carrizo Sands hardwood scrub forest area, and (4) the cultivated zone. Poor photographic resolution prohibits further definition of land use practices.

Major transportation systems and airports, river courses, and limestone mines that appear as bright irregular areas are also visible in figure 8-11(a). The pri-



mary value of this oblique photograph is the synoptic view that presents the relation of the city complex to various geomorphic landforms.

San Diego, California.—San Diego, California, has developed on an emerging coastline backed on the landward side by the hills and steep-sided erosional canyons of the Coast Ranges. San Diego Bay, one of the best natural harbors on the western coast, is the focal point around which the city has developed (fig. 8-6). Although the bay is a focal point for urban concentration, the steep topography of the Coast Ranges and the bay itself restrict urban development.

In the near-vertical view of San Diego shown in figure 8-6(a), the urban areas are gray and contrast

sharply with the dark-green vegetation along the drainage features. Although a definite central business district is not discernible, the airports are prominent, as is the rectilinear pattern of the docks along San Diego Bay. Figure 8-6(a) shows the interesting relationship between Interstate Highway (IH) 5 and U.S. Highway 805 and the built-up areas. The 5-year-old IH5 is almost indiscernible. The U.S. Highway 805 is obscured in some urban areas and in others is a pronounced white line. Extensive landscaping and aging of the concrete reduce the overall visibility of the roadways. At the southern end of San Diego Bay, the photograph shows an obscured land/water boundary and a different signature than the rest of the bay. The signature change is

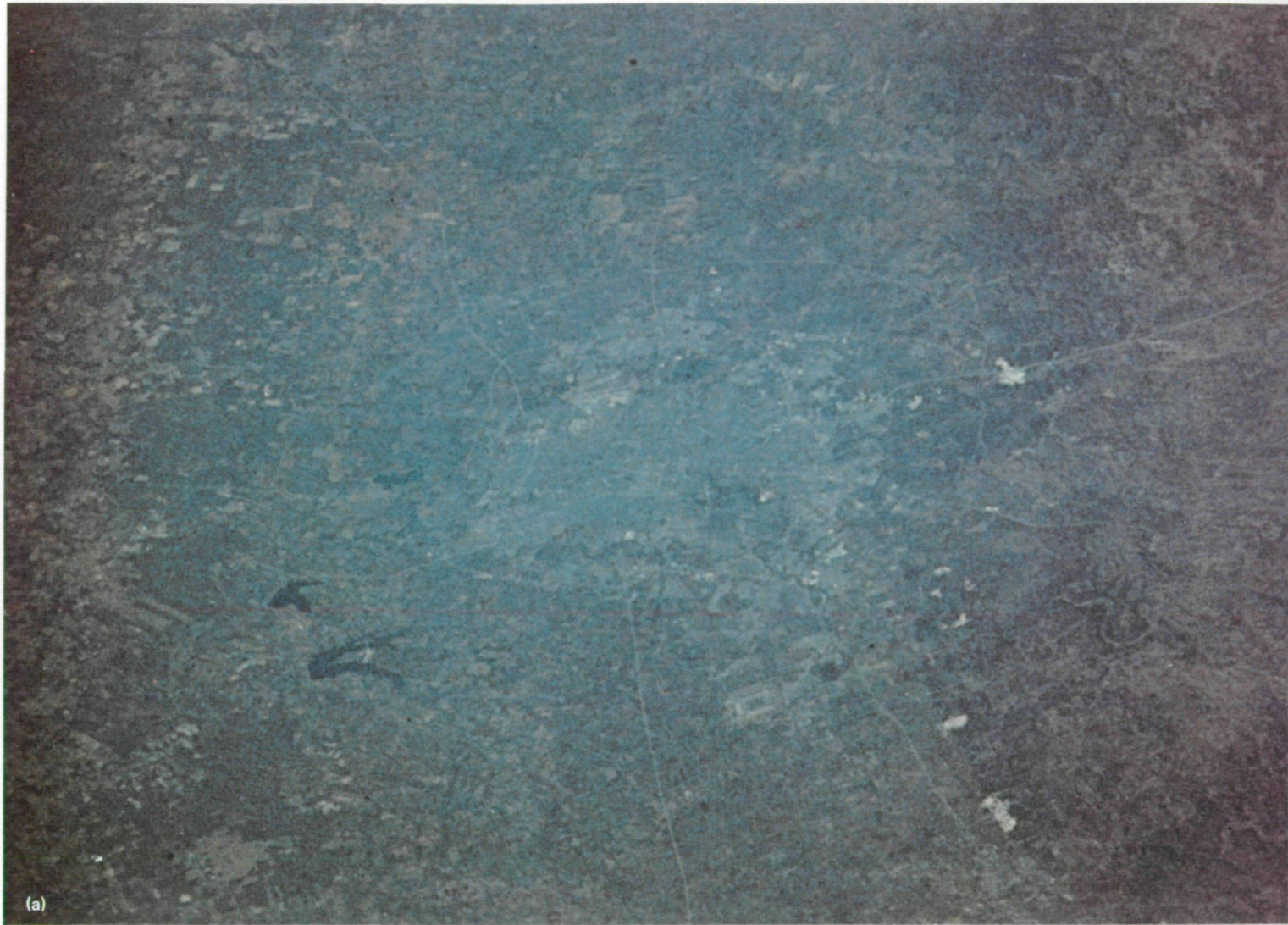


FIGURE 8-11.—A low-oblique view of San Antonio, Texas. (a) Photograph (SL4-203-7773). (b) Areal map.

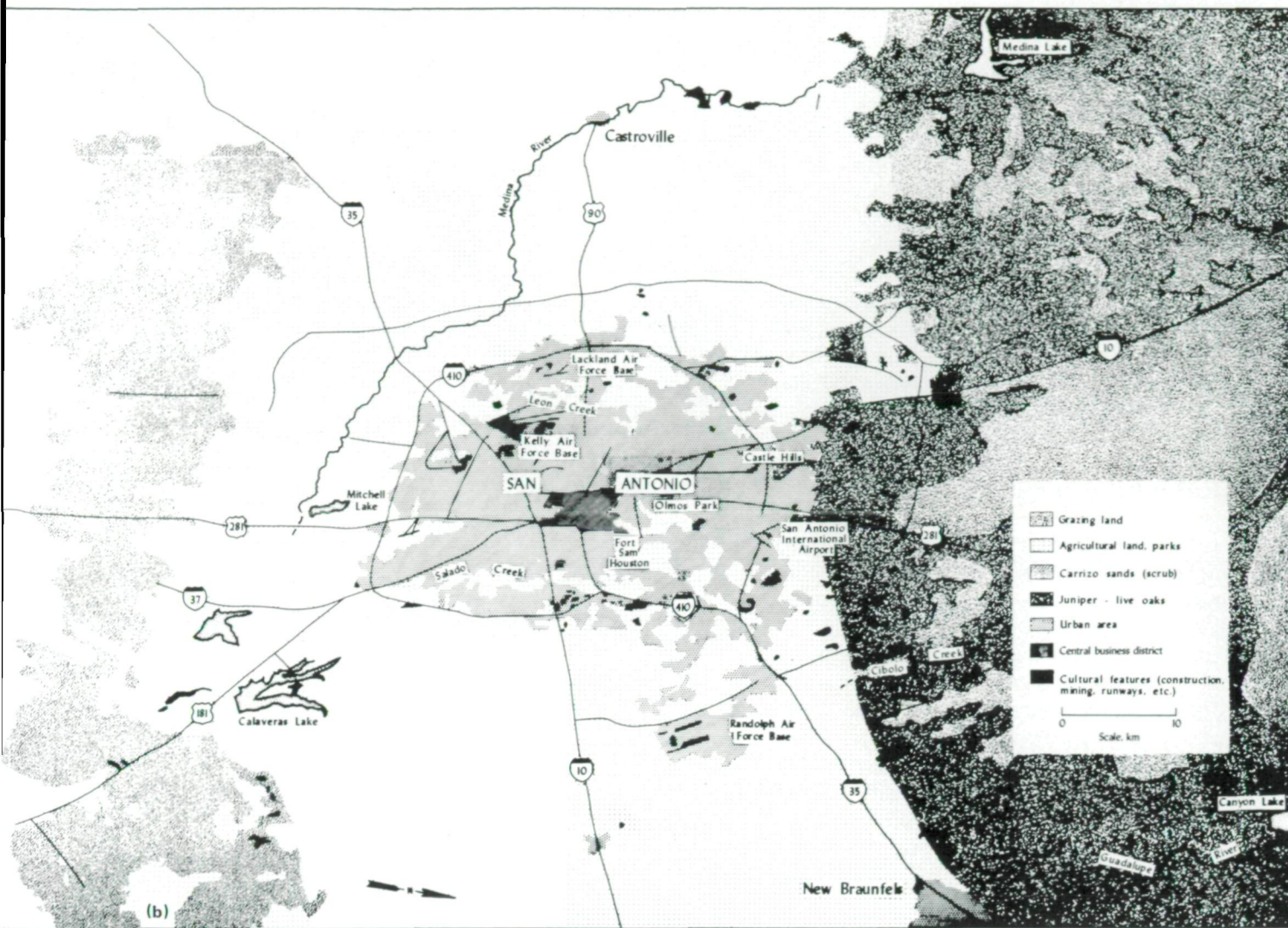
probably due to sedimentation, although no ground observations were obtained during overflight to verify this theory. Such timely observations could aid in effecting ground investigations for study of environmental conditions in the bay.

VEGETATION PATTERNS

One of the most pronounced patterns that can be observed in space imagery is that created by man's agricultural activities (ref. 8-8). Typical agricultural pat-

terns in major cereal crop areas are rectilinear, such as those in southeastern Australia (fig. 8-1). Photographs from previous manned space missions indicate a wide range in the size, shape, and distribution of agricultural patterns. Because the Skylab 4 crewmen were in orbit for a long period of time, they were able to monitor changes in texture and color of the agricultural areas and to document these changes on film for the first time. Such data are a source of information for study of regional environments.

From Skylab orbital altitudes, the crewmen could readily identify forest regions of the Earth because of



the blue-green signature, but they reported that detailed information on the specific forest type could not be determined. Areas of timber harvest were readily discernible and were clearly distinct in the Skylab 4 handheld-camera photographs. Transportation networks on the rural landscape were generally observable from space, but their signature is subject to many variables that mask them on space photographs. Size is one factor that aids in the identification of roads from space and in photographs. An interstate highway is more visible than an unpaved country road. A transportation route that bends at an angle across the "grain" of the rural land use pattern is more visible than one that does

not. Dense vegetation, particularly forests, may obscure a transportation system. Interestingly, the age of a transport route can determine its visibility from space. A transportation route entering a city is generally lost to view in the urban buildup, a fact reported by early researchers working on photographs taken from space (ref. 8-9). The known exceptions are newly constructed routes or road systems enhanced by a light snow cover. Especially in arid or semiarid regions, disturbance of the soil during construction or mining exposes subsurface materials that have a high albedo and produce a bright (almost white) spectral signature on the imagery.

CONCLUDING REMARKS AND RECOMMENDATIONS

The Skylab 4 mission demonstrated that man can obtain unique and useful photographs and observational data of cultural features from near-Earth orbit. The information gained is primarily small scale or regional in scope.

The Skylab observations and photographs of cultural features were favorable when the site or feature was exposed to view (i.e., when it was not hidden by clouds, pollution, shadows, vegetation, or the darkness of nighttime); when the site or feature was strongly contrasted (high albedo) to its surroundings; and when the site or feature was of sufficient size to register within the minimum resolution capability of the sensor being used. The capability of the sensor depends on the orbital altitude of the space platform: the farther the platform is from Earth, the larger an object on the ground must be to be observed or imaged. The Skylab crewmen, for example, could not see large individual buildings even though they looked for them with the aid of optical devices.

Study of the Skylab 4 imagery of metropolitan complexes has shown that western industrial cities scar the land and produce a stronger image signature than do nonwestern cities. In general, western cities in semiarid to arid regions are easier to observe than those in more humid areas. The viewing angle and atmospheric conditions determine how much internal urban detail an observer can interpret; that is, a near-vertical view of a city provides more urban detail than an oblique view. Land/water boundaries in urban areas aid in providing image detail.

Future space missions should be designed to result in a more comprehensive determination of the extent of man's role as an observer and scene selector. The Skylab 4 mission provided only a primitive beginning to the investigation of the potential of man's role in acquiring data and performing analyses of cultural features from a space platform.

For future missions, it is recommended that a manned Earth-orbiting laboratory be developed to

allow observations and remote sensing of the Earth over an extended period of time. A prime task for the orbiting observatory would be to gather accurate information on the color of the Earth during seasonal changes. During the Skylab 4 mission, the crewmen could recognize land masses by color because each continent has a unique color tone. The preparation of a map that depicts the natural colors of the Earth surface is an important task for future missions. Such a map would serve as a teaching aid for schools, as an operational and training tool for space missions, and as an important data source for Earth investigations.

REFERENCES

- 8-1. Sauer, Carl O.: The Fourth Dimension of Geography. *Ann. Assoc. American Geog.*, vol. 64, no. 2, June 1974, pp. 189-192.
- 8-2. Hartshorne, Richard: *Perspective on the Nature of Geography*. Rand McNally and Company, 1959.
- 8-3. Thomas, William Leroy, ed.: *Man's Role in Changing the Face of the Earth*. Univ. of Chicago Press, 1956.
- 8-4. Holz, Robert K., ed.: *The Surveillant Science: Remote Sensing of the Environment*. Houghton Mifflin Co., 1973.
- 8-5. Shahrokhi, F., ed.: *Remote Sensing of Earth Resources*. Univ. of Tennessee Space Institute, vol. I, 1972.
- 8-6. Holz, Robert K.; and Boyer, Robert E.: Patterns From Apollo VI Photos. *Photogram. Eng.*, vol. XXXVIII, no. 10, Oct. 1972, pp. 974-984.
- 8-7. Tuyahov, A. J.; Davies, S.; and Holz, Robert K.: Detection of Urban Blight Using Remote Sensing Techniques. *Second Conference on Earth Resources Observation and Information Analysis System*. Univ. of Tennessee Space Institute, vol. II, 1973, pp. 213-226.
- 8-8. Colwell, Robert N.: Remote Sensing of Natural Resources. *Sci. American*, vol. 218, no. 1, Jan. 1968, pp. 54-69.
- 8-9. Simonett, David S.; Henderson, Floyd M.; and Egbert, Dwight D.: On the Use of Space Photography for Identifying Transportation Routes: A Summary of Problems. *Sixth International Symposium on Remote Sensing of Environment (Michigan)*, vol. II, 1969, pp. 855-877.

9

Vegetation Patterns

DAVID M. CARNEGIE^a AND BRIAN T. FINE^b

BECAUSE MAN is dependent on vegetation for food and fiber to sustain himself, he must acquire sufficiently detailed information regarding this important renewable resource to conserve, manage, and use it for his benefit. In the past, vegetation resource information has been acquired through conventional ground and aerial survey techniques. In many instances, these techniques have been adequate for providing information regarding the kind, quantity, quality, distribution, and availability of vegetation resources. In other instances, however, conventional inventory techniques have not provided information that was either timely enough or accurate enough for intensive management purposes. Within the last several years, therefore, manned and unmanned satellite systems have emerged as new tools for rapidly acquiring information about vegetative resources on a global basis.

This section includes an analysis of visual observations and handheld-camera photographs of vegetative resources obtained by the Skylab 4 crew. A primary objective of the Visual Observations Project is to determine man's role in acquiring timely information from Earth-orbiting satellites regarding vegetative resources.

PREPARATION AND TRAINING

Two training sessions were held before the Skylab 4 mission. At the first session, the crewmen were introduced to the importance of making observations of

vegetation. Primary emphasis was given to the recognition of factors that cause problems and damage of economic importance to vegetation in forest, range, and agricultural environments. Early detection of such damaging factors as fire, flood, insects, and diseases is important for minimizing economic losses; thus, it is important to learn the extent to which a trained observer in an Earth-orbiting satellite can detect these damage-causing agents. Secondary emphasis was directed to observing significant changes in vegetation appearance that result from either normal plant development or disturbance factors. By determining the location and time of these changes in appearance of crops and range forage, for example, a trained observer in space might provide clues to the identity of vegetation types and conditions. The relative productivity of the crop might also be inferred, based on the point in plant development that the observed changes occurred. To aid the crewmen, a handbook of specific observations to be made in preselected locations throughout the world was provided. During the second training session, the handbook was reviewed with the crew to answer last-minute questions regarding observations of vegetative phenomena.

DATA INPUTS FOR VEGETATIVE ANALYSIS

Throughout the 84-day mission, the verbal descriptions of forest, range, and agricultural vegetation by the crewmen were transcribed and made available to the Visual Observations Team for evaluation. Such transcripts helped the team to learn which features

^aThe University of California at Berkeley.

^bThe University of California at Davis.

could be observed from space. In many instances, more detailed questions were relayed to the crew during the mission to test the limits of their observational capability. Concurrent with the orbital observations, both vertical and oblique space photographs were taken of vegetation within prescribed observation sites. Examples of these photographs (taken with Nikon and Hasselblad cameras) are used in this section to illustrate many of the vegetation phenomena observed from orbital altitudes.

A 3-hour postmission debriefing was conducted to question the Skylab 4 crew regarding their visual observations and to review the transcripts of verbal descriptions and the available photographs acquired in space. The information derived from the debriefing together with the analysis of the available photographs and the transcripts forms the basis for this section. Two subjects are treated separately: (1) the factors affecting a person's ability to observe various features of forest, range, and agricultural vegetation, and (2) the important characteristics and conditions of these vegetative resources that can be observed.

FACTORS AFFECTING VISUAL OBSERVATIONS OF VEGETATION FROM ORBITAL ALTITUDES

The primary factors affecting a person's ability to observe vegetation on the surface of the Earth from orbital altitudes are characteristics of spacecraft windows, atmospheric conditions, time of day, viewing angle, spacecraft speed, kind and color of vegetation, size of the area observed, distance between the area observed and the observer, and amount of background or training the observers have regarding vegetative phenomena.

Spacecraft Windows

The observation windows aboard Skylab varied in size and in thickness of glass. The crewmen expressed concern that observations of features viewed at an angle through such windows are affected by optical and reflective distortions. Although important, information was not available concerning the extent to which the observation windows may have been tinted, and to what extent this tinting may have varied from window to

window. To remove any variable attributed to differences in window characteristics for future observation satellites, consideration should be given to standardizing the characteristics of observation windows or to providing one specific window that is not tinted and that is free from optical and reflective distortions. Moreover, all precautions should be taken to minimize external contamination of the window by residue emission during lift-off.

The Skylab 4 crew stated that the special window used for the Earth resources experiment package (EREP) was the best for their visual observations because it provided a good vertical view of the Earth. The science pilot (SPT) noted that there were problems in making observations through other windows:

Two things that limited us are looking at high [oblique] angles [of the Earth] or very low angles . . . because you might get glint off the outside. There was a little layer or coating on the outside [window] and if you got the Sun angle right, it was tough to see through it. Also looking out the . . . window just didn't allow you to have a good field of view; you'd be looking at a lot of structures.

Atmospheric Conditions

The three major atmospheric factors that influence a person's ability to make observations from an Earth-orbiting platform are percentage of cloud cover, amount of haze, and presence of smoke.

Cloud cover frequently prevented the crewmen from determining the vegetation types and conditions. The commander (CDR) noted that agricultural areas can be seen through as much as 75 percent cloud cover because of the distinctive "checkerboard" pattern. In the natural vegetation areas, geometric patterns and sharp contrasts are much less common, and hence the crewmen could distinguish only clouds and a dark region below. The extent to which visual observations of vegetation patterns can be made through broken cloud cover is also affected by time of day. At low Sun angles, cloud shadow will obscure additional areas beyond those obscured by clouds.

A higher frequency of haze was observed over heavily vegetated areas, such as tropical zones, than elsewhere. "You never had a clear shot at the jungle like

you did the desert areas," stated the CDR at the postmission debriefing. The adverse effect of haze on the ability to discriminate among types and colors of vegetation became more pronounced as the angle of viewing increased from the vertical. The SPT stated that haze did not affect his ability to discriminate between features or colors when his viewing angle was vertical, but that both haze and smoke did influence his ability to observe features at what he called "slant range."

The main effect of haze was the difficulty it imposed in discrimination among shades of colors. During most of the mission, the crewmen were able to distinguish between light and dark greens. As the haze increased, however, the ability to discriminate between shades decreased. The crew observed that haze usually increases during the day and becomes most severe during middle to late afternoon, local time.

Haze had a greater effect on photographic image quality, and thus on subsequent interpretation, than it had on visual observations. In viewing numerous photographs taken from space, the crewmen observed that haze had reduced detail and color discrimination compared to what they had actually seen. This finding is significant because it indicates that human eyes may be superior to cameras for discriminating colors and discerning ground details through moderate amounts of haze and smoke.

Time of Day: Sun Angle

The Skylab 4 crewmen considered noon local time to be the optimum time for discerning and describing vegetation types and conditions. Without exception, a high Sun angle increased the crew's ability to discriminate vegetation on the basis of color. The SPT stated, "You've got to see a lot of reflection." A high Sun angle enabled the crew to see and contrast the colors and various shades of vegetation.

The pilot (PLT) noted the problem of haze when he was using binoculars to observe wheatfields in South America and Australia; he could not make a positive determination, and stated that, late in the day, the effect was the same as "looking through a dark, dirty glass."

When Sun angle was relatively high, the crewmen detected sunglint from standing water that was near the flightpath. The relationship between Sun angle and

viewing angle, which permits Sun reflection from water to be seen, can be exploited to verify the presence of standing water. This technique may be particularly valuable in assessing the availability and distribution of water in rangeland and drought-affected portions of little-known areas, such as the Sahel section of Africa, and, to a limited extent, in assessing flood damage in agricultural and other vegetated areas.

Angle of View

Although observations are more easily made at the nadir, the crew could discern features and patterns at a distance of 480 km on either side of the flightpath. However, oblique photographs that showed land features out to this distance were generally poor and of low contrast and therefore difficult to interpret. The primary cause for the poor quality was atmospheric effect on color films. The crewmen also acknowledged that a slight color variation is inherent in visual observations because of the viewing angle but that the eye compensates for most of this change.

Rate of Movement

The rapid speed of the spacecraft caused the crewmembers some problems in detecting details within the vegetation complex early in the observation program. They had approximately 30 seconds to locate a specific area and make observations; hence, only generalized observations were made. Later in the program, the crewmen became more familiar with specified sites and were able to observe more details about the vegetation. Occasionally, binoculars with image-motion compensation were used to extend slightly the viewing period of pinpoint objects and to make more detailed observations. The CDR summarized the effect of the rapid speed of the spacecraft over the target area:

. . . you could not zoom in and make some sort of . . . verbal . . . description or analysis anywhere near as accurately as you could just find that location and bring some sensors to bear and take photographs that can be evaluated.

Color and Pattern of Vegetation

From space, the Skylab crew could distinguish agricultural land from forest and rangeland by the color, density, and pattern of the vegetation. While looking at the agricultural lands of the world, the crewmen made repeated reference to the patterns that were the primary identifying feature they used in their assessments of agricultural land with such comments as "The agricultural areas are like checkerboards," and "You begin to get this cellular or honeycomb effect."

The crewmen said that the regular patterns that are characteristic of agricultural areas were the most obvious indication of farming. No textural details were discerned to permit discrimination among basic agricultural types such as cereal crops, truck crops, orchards, and vineyards.

Within the wildland vegetative environments, distinguishing between certain kinds of rangeland and forest land was difficult. Generally, forested land appeared very dark green. Variations of types of forests within forest land could not be detected. However, within rangeland environments, greater color variation was discernible. In the semiarid and arid environments, vegetation was sparse, and determining if and where it existed became increasingly difficult. These findings demonstrate that many questions relating to the extent to which man can discern specific vegetation types within forest and rangeland environments may not receive conclusive answers until space observers have either more training or a greater background in observing vegetative resources.

Dark colors were more difficult to differentiate than light colors. The range of colors used by the crew to describe agricultural crops in various stages of development included "light green, much lighter green, brilliant green, healthy green, deep green, dark green, very dark green, brown, dark brown, black, light tan, yellow, straw colored, and gold-tan." The lighter and brighter greens and the light tans and yellows were easier to detect and to separate than were the darker greens, blacks, and

browns. Despite the difficulty of discriminating dark colors, the crewmen were usually able to agree among themselves on the color of an object. However, they also agreed that color standards should be developed for future space experiments to reduce the subjectivity associated with color descriptions. A color standard such as the Munsell system would also be very useful for describing colors under haze conditions, when the observers have indicated that color discrimination is much greater with the eye than is possible from space photographs. As has been indicated, the ability to discriminate colors is reduced with low Sun angle.

Altitude and Scale Effects

Insufficient evidence exists to determine whether lower orbital altitudes would significantly increase the amount of detail that crewmen could see within the vegetation complex. The crewmen indicated that texture was not an important identifying characteristic in discriminating vegetation type or condition. However, it is significant that the crewmen could observe considerably greater detail with the use of binoculars. For example, one of the crewmen, in describing the terrain over northern Australia, indicated that the only location where green vegetation could be seen was along the watercourse. Upon inspection with binoculars, the green vegetation was found to be an area of concentrated truck-farming crops. Also with the use of binoculars, the crewmen could see greater variations within fields. This trade-off between what a space observer can see with and without binoculars may be extended to imply that an observer at a considerably lower orbital altitude could see much greater detail with the unaided eye. Agricultural land in the Imperial Valley of California is shown in figures 9-1 and 9-2. Figure 9-1 was taken with a 100-mm lens on the 70-mm Hasselblad camera, whereas figure 9-2 was taken with a 300-mm lens on the 35-mm Nikon camera. The difference in detail seen in



FIGURE 9-1.—Photograph of the Imperial Valley, California, taken with a 100-mm lens on a Hasselblad camera (SL4-141-4388). Compare detail of individual fields in this photograph with that in figure 9-2.

these two photographs simulates the difference in detail that the crewmen observed while using unaided vision and when viewing through binoculars.

Familiarity and Training

The crewmembers expressed the need for more intensive and comprehensive training concerning the evaluation of vegetation. They believed that their analyses would have been much more meaningful and precise if they had been familiar with various agricultural practices throughout the study areas. In summarizing the crew's concern, the CDR stated:

He must have more training and more background information in order to make any sort of a judgment. He can give you data; he can give you color data, if you give him the proper tools. He can make a color wheel and tell you what the colors are. You need to know a little bit about what's going on on the ground and understand how people operate, and then you can take samples through clouds and generalize them, if you know enough about how people operate.

Another important factor that would increase the usefulness of trained observers in space would be to familiarize the crewmembers with the important features as part of an intensive training program. If crewmen could preview on the ground what they were going to see from space, they would be better equipped to provide useful resource information. The SPT stated:

You've really got to know what you're after. You've got to be familiar with the areas and anticipate what you are going to see in general in terms of the geography and know what you're after . . . and be able to rapidly find the area you want investigated with a few specific questions in mind.

A more comprehensive training program is recommended for future missions. Such training should emphasize the land use and management practices in specific geographical locations and stress those factors that affect the distribution and appearance of vegetation.

ORIGINAL PAGE IS
OF POOR QUALITY



FIGURE 9-2.—Photograph of the area outlined in figure 9-1 taken with a 300-mm lens on a Nikon camera. The large, square fields are 647.5 m². Variations in the appearance of this area are the result of crop type, stage of development, plant density, soil type, et cetera. Even with this much detail, it would be difficult to detect and identify variations caused by crop-damaging agents (SL4-207-8033).

OBSERVABLE CHARACTERISTICS AND CONDITIONS WITHIN VEGETATION ENVIRONMENTS

During the Skylab 4 mission, specific observations were made of both natural and agricultural vegetation. The crew was asked to observe and photograph the following observation sites and features: wheat in Australia, Argentina, and the United States; rangeland in Australia, Africa, and the United States; land use in Malaysia; vegetation in New Zealand; agriculture in the State of California; drought in northern Australia; insect and disease damage in any of the sites; and forest and range fires wherever found.

After the mission, the CDR summarized the crew's ability to observe the two major vegetation classes within the test sites:

It is easier to see man's influence on the Earth, on the vegetation, than it is to find natural vegetation differences.

Agriculture

During the 84-day mission, the crewmen became more aware of their ability to observe changes in the tonal characteristics of the agricultural fields. The CDR noted:

It was amazing to see over a 6-week period the field color change from tan and gold, sort of uncolored, to various greens . . . from chartreuse to a deep rich green.

While observing wheat-producing areas in Argentina, the CDR made the following observations over a period of time. On November 28, 1973, he stated that "the colors of the fields in the agricultural area varied from light tan to a very dark green." On December 19, he observed no "great change in color as yet. There's a lot of green and a lot of gold-tan." On December 21, the CDR stated:

I estimate that about 25 to 30 percent of the squares that I saw . . . were a dark green, indicating fresh vegetation; I'd say 20 to 25 percent of the area looked to be brown, probably plowed ground. And the remainder was various different colors between the dark green and the brown, just

sort of tan and a little bit toward the yellow, and some very light green indicating what I considered would probably be fresh growth.

Finally, on December 30:

I do believe I see more light green fields and the overall general color is the tan and the browns and the very dark green occasionally. But when I begin to look at it a little more closely with the binoculars, I can see more light green coming in, which indicates they've got a crop getting started. I noticed this time a scattering of nice brilliant green fields, not the very dark green indicating older vegetation.

From these descriptions, it is easy to infer that the CDR observed the cereal crops progress through their normal drying phase and new crops become established on those fields that had earlier supported a cereal crop. In making comparisons of crop development over a period of time, or between two areas, the crew cautioned against differences attributable to different soil color and to the proportion and stage of development of natural vegetation that may be intermixed in the cereal cropland.

In the Southern Hemisphere, progressive drying of cereal crops followed by harvesting and replanting was observed by the Skylab crewmen. An area of wheat crops in Victoria, Australia, in early January and February is shown in figures 9-3 and 9-4. While discussing the photographs of January (fig. 9-4) and February (figs. 9-3 and 9-5), one of the crewmen made the comment:

This is where I started really talking up the light greens, where we really begin to feel like we'd seen a change over December. . . . My subjective opinion was that between about December (the last time we got a good look at Australia) and then at our first opportunity again in early February that this whole portion [southeastern part] of Australia had greened up considerably.

The CDR quantified the proportion of wheatfields that contained green mature plants, exposed soil, bright green fields of juvenile plants, and dry plants or plants in harvest stage. When asked if they could differentiate between mature crops, which appear dark green, and recently plowed or irrigated fields, which also appear very dark, the response was that "there is no way to tell the difference unless you have some sort of special instrument."

2

Desert Sand Seas

EDWIN D. MCKEE,^a CAROL S. BREED,^b AND STEVEN G. FRYBERGER^b

A WORLDWIDE SURVEY of desert sand seas using mosaicked false-color imagery from the unmanned Earth resources technology satellite (Landsat-1) as a map base was initiated in 1972. Imagery data were combined with data from ground-based studies of climate and from field studies of the internal structures of eolian sand deposits. To obtain detailed information concerning the origin, movement, and distribution of the world sand seas, the Skylab 4 crewmembers were asked to make observations and to obtain handheld-camera color photographs of 18 important locations. The formally designated areas were those sand seas that are most difficult to study using conventional means, either because reliable maps and aerial photographs are not available or because the region is inaccessible for political reasons.

The usefulness of manned observations and handheld-camera photographs from space is confirmed by the immediate application of Skylab 4 data to the study of sand seas. The Skylab 4 crew provided information that (1) confirms a tentative global classification of eolian sand deposits based on observed similarities in most of the major deserts of the world; (2) allows the preparation of maps that show the relationships of sand deposits to each other, to sand source areas, to natural sand distribution barriers, and to human land use; and (3) allows the regional patterns of large-scale dune morphology to be studied in relation to rainfall distribution and surface winds.

The data provided by the Skylab 4 crew, when combined with further ground-based work both in the laboratory and in the field, should have long-range applications to geologic and geographic research in at least the following five areas.

1. Geologic interpretation of environments of deposition of eolian sandstones. The effects of primary sedimentary structures that control migration of oil, water, or other fluids can be better evaluated.

2. Understanding dune movement. Control of dune movement is important in areas subject to sand inundation, such as the Sahelian Zone of northern Africa and the Thar Desert of India and Pakistan.

3. Prediction of future environments of sand deposition in areas of drought, as in parts of India, Australia, and northern Africa.

4. Exploration for wind-concentrated mineral deposits.

5. Interpretation of exotic environments of wind deposition, such as those believed to exist on Mars, by comparing Martian sand seas with sand seas on Earth.

The sites chosen for handheld-camera photographs and visual observations included four in the Sahara and sub-Sahara of northern Africa, four in the Namib and Kalahari Deserts of southern Africa, two in the Empty Quarter of Saudi Arabia, five in the Takla Makan and Gobi Deserts of China, and three in the trans-Caspian deserts of the U.S.S.R. Additional areas in northern Africa, India, Mexico, and Australia were recommended as optional sites.

The Skylab 4 crew succeeded both in obtaining photographs and in making visual observations of most of the formally designated areas of study and many of the optional sites (fig. 2-1).

^aU.S. Geological Survey, Denver, Colorado.

^bU.S. Geological Survey, Flagstaff, Arizona.



FIGURE 9-3.—A high-oblique photograph showing the agricultural lands along the Murray River (lower right) in the Australian states of Victoria, New South Wales, and South Australia (SL4-143-4639).

**ORIGINAL PAGE IS
OF POOR QUALITY**



FIGURE 9-4.—Near-vertical photograph taken on January 1, 1974, showing agricultural land around Lake Tyrrell (arrow) in the state of Victoria, Australia (SL4-138-3835).

**ORIGINAL PAGE IS
OF POOR QUALITY**



FIGURE 9-5.—Low-oblique photograph taken with a 300-mm lens on a Nikon camera in early February showing the greening of the cereal crop area near Lake Tyrrell, Australia. The greening of the crops planted after the wheat harvest is evident when this photograph (SL4-200-7638) is compared with figure 9-4.

It is apparent from these observations that space observers are capable of describing and contrasting the stages of crop maturity within a region. These types of observations are perhaps the most significant because they demonstrate that the human space observer can efficiently acquire timely data regarding the development and condition of cereal crops on a global basis. This information can provide inputs for determining the availability and perhaps the productivity of cereal crops.

In the Northern Hemisphere, winter wheat either was being or had been seeded at the time of the Skylab 4 mission. Recently seeded fields were discernible as were the area of snowfall and the relative amount of snow on the wheatfields. Moreover, the crewmen could easily detect areas where early snowmelt could expose wheat plants to killing frost. These observations regarding snowmelt patterns are especially important within regions where protective snow cover is critical for the insulation and survival of the plants. Observations regarding the timing of snowmelt also can be correlated with local weather conditions that affect plant growth. Figure 9-6 illustrates the ease of detecting areas with and without snow cover.

Throughout the mission, the crewmembers failed to observe variations within fields that could be attributed to insect or disease damage. They indicated that the fields would have to be large (at least 2.6 km^2) and variations very distinctive for human observers to recognize damage. As field size increased, the crewmen's ability to detect variations that could affect crop productivity would also increase. The use of binoculars could also assist in evaluating crop-damaging agents. Finally, and of singular importance, specific observations could be made if the crewmen were told precisely where to look for the feature to be recorded.

Several floods were observed. Each time, the crewmen were able to observe the extent of the flooded area and the type of land use affected. In the northern Sacramento Valley of California (fig. 9-7), in the Mississippi Valley, and in eastern and central Australia, agricultural land was inundated by floodwaters. Suspended silt in nearby water bodies was the telltale sign of flood used by the Skylab 4 crew.

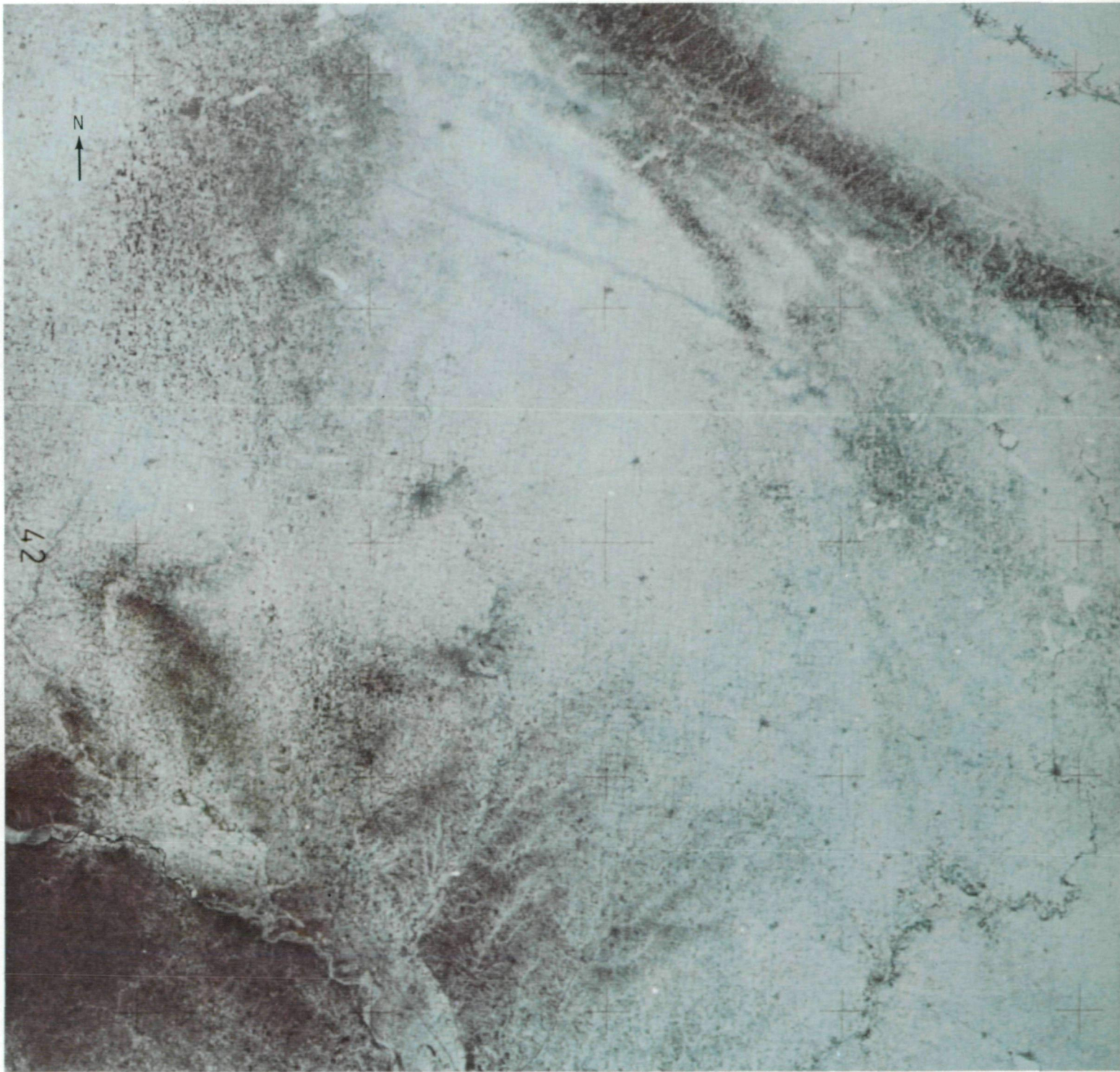


FIGURE 9-6.—Photograph of South Dakota, Minnesota, and Iowa showing the uneven distribution of snow cover that could be critical for survival of the winter wheat (SL4-142-4465).



FIGURE 9-7.—Visual observations and later photointerpretation show that the Sacramento River in the Sacramento Valley of California was in flood stages at the time this photograph was taken. The dotted line indicates the normal river channel. The land use being affected is agricultural (SL4-142-4432).

Regarding the flooding that occurred in central and northern Australia in late January, the CDR stated:

We saw the wetting up of central Australia. We saw it very, very dry . . . but sunglint kind of told . . . that there was water down there. . . . In late January after the big rains and the floods . . . we saw all the silt out to sea . . . and there was more extensive wet areas in central/north-central Australia. . . . These are just general things we can say. As far as getting . . . details, I don't think we can. That's what we have to reserve photographic evidence for.

In summary, space observers have very little difficulty determining the location and distribution of agricultural land. The color, shape, and size of the field and the linearity of field boundaries contribute to this ease of identification. Although agricultural field patterns and field sizes were seen to vary considerably, most agricultural land could be detected. Within regions characterized by small fields, the crewmen could not detect variations within fields that could be associated with factors causing damage or loss of production to crops. No specific examples were noted of damage-causing agents within large agricultural fields. Although binoculars were often used to see more details of agricultural land, the crewmen did not think crop types could be determined.

An interesting and potentially promising observation made by the crew dealt with changes in the appearance of wheatfields in Argentina and Australia. Space observers apparently can determine various growth stages of crops by recognizing distinctive field colors. By observing changes in field colors during a period of time, they can assess the rate and the timing of various plant development stages. Other crops that progress through distinctive color changes as they develop can also be monitored in stages of planting, maturity, and harvest.

It seems uncertain whether crop-damaging agents such as insects, disease, and wind can be identified. However, some of the variations detected within large fields in the Skylab 4 experiment might have been caused by these damaging agents. If space observers knew the location of suspected outbreaks, they could

use additional equipment (photographs, high-powered binoculars, etc.) to assess the extent of the damage. Agricultural land that is subject to floods or fire can also be assessed by space observers. The occurrence of floods or fire and the type of land affected can be readily assessed by an orbiting crew.

Rangeland Environments

Rangeland environments are extremely variable in appearance. They can vary from dense grasslands, which may appear from space like shrubland or forest land, to desert or semiarid ranges characterized by sparse vegetation. Rangelands generally support native forages for grazing livestock and wildlife. Although rangeland may be fenced to control animal movement, such land generally is not irrigated or cultivated. Unless there is a sharp difference in forage use across a fence line, the presence of such a line would not be readily discernible by space observers. Grazing land use was recognized by the crewmen in rangeland environments where paddock or pasture boundaries could be detected because the extent of grazing on one side of the boundary differed significantly from that outside or adjacent to it. Such fence-line boundaries were particularly distinctive in parts of Australia. In areas where these features could not be detected, the primary land use was not obvious.

Rangeland areas along the southern coast of Western Australia are shown in figure 9-8. This land was fenced for grazing only 10 years earlier, and the paddock boundaries are clearly evident, indicating the differing amounts of grazing inside and outside the paddocks. Not only are the fence-line boundaries clearly evident on the photograph, but the locations of watering points within the paddock are also easily detected. Watering points appear light in tone because the concentrated livestock use around the water removes the vegetative cover and exposes the more reflective soil surfaces. In instances where suspected water points can be detected, space observers could exploit sunglint to determine whether water was available for livestock use. Because the existence of water is most important in achieving



FIGURE 9-8.—A portion of the Nullarbor Plain along the southern coast of Western Australia. Fenced paddock boundaries are visible (areas 1 and 2) because grazing has reduced plant cover within paddocks. At areas around watering holes (area 3), the vegetation cover is nearly gone (SL4-137-3630).

proper use of rangelands, the ability to detect its presence and distribution is also very important. Detection of known watering points may be a useful method for determining whether rangelands are experiencing drought conditions and, if so, the extent or severity of the drought.

Describing rangelands in Australia, the CDR observed that the land was flatter and that there were some areas of green along the river. The land appeared changed by human interference in that, although not all the land was rectangular, some regularity was present.

There are some very light greens . . . but the land for the most part was tan to red. . . . In general, I would say the Australian rangeland . . . looks quite red. It is not what you could call very green at all. The grazing areas are not very rectangular. There are a few straight lines seen which are probably fence lines; the patterns of the grazing land are rather irregular, indicating that the cattle . . . range pretty much free, and stay where the vegetation is.

From these comments and from subsequent debriefing sessions, it became apparent that the Skylab crew had difficulty determining the presence of green, healthy vegetation in rangeland environments where vegetation was sparse.

Throughout the mission, the crew watched for areas where the forage either greened or dried. The CDR recalled that in northern and southwestern Australia, the rangeland appeared greener later in the mission than earlier. The SPT commented that space observers could follow color changes that correspond with forage development if properly trained in specific areas.

Numerous range fires were sighted throughout South America, Africa, and Australia. In some instances, fires had been accidentally ignited or resulted from lightning. Most of the fires, however, were probably intentionally ignited because fire is an important tool in many rangelands for controlling shrub invasion and the tsetse fly and for improving forage quality (fig. 9-9). Where smoke did not obscure observations of the ground, the crewmen could usually determine whether the vegeta-

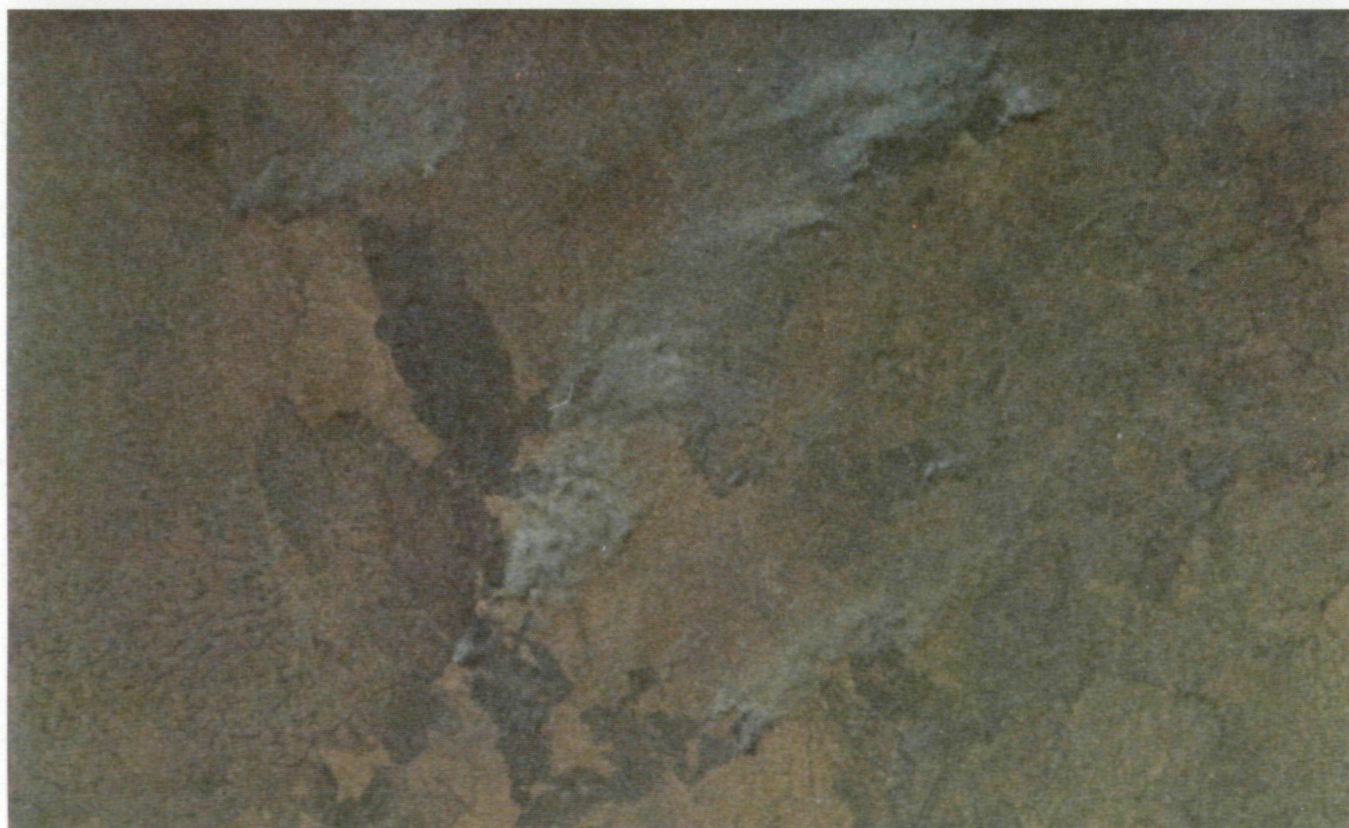


FIGURE 9-9.—Fires in a wildland area of Sudan are shown in this photograph taken with a 55-mm lens on a Nikon camera (SL4-208-8140).

tion that was burning was grassland, shrubland, forest land, or agricultural land. The smoke color also helped identify the type of material that was burning. While

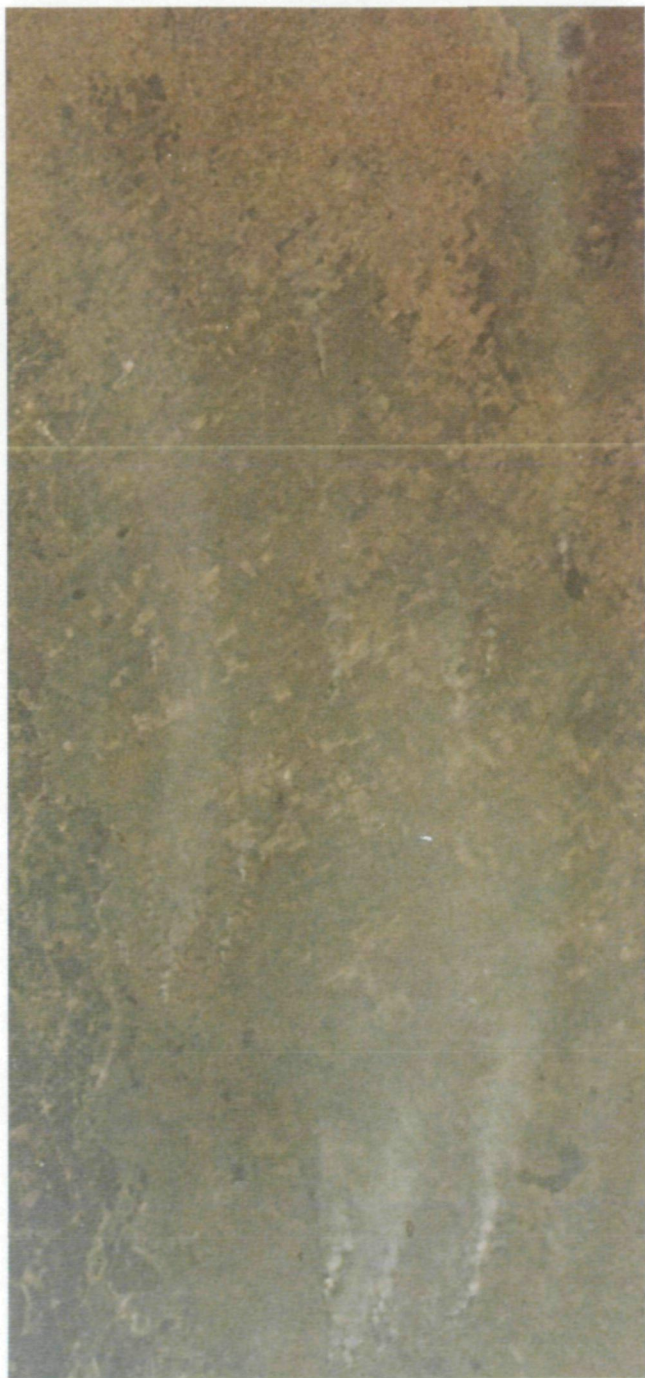


FIGURE 9-10.—This photograph of Argentina, taken with a Nikon camera and a 55-mm lens, shows the whitish smoke color typical of that produced by burning vegetation (SL4-197-7443).

passing over Argentina, the crewmen noticed a string of rangeland fires that exhibited a whitish or grayish smoke plume (fig. 9-10). Then, on a pass over the Algerian part of the Sahara, they observed an oil well fire. The black smoke associated with this fire is the result of a carbon flame.

In summary, it appears that space observers can recognize rangeland environments despite their variable appearance. Moreover, grazing land use can be determined when fence-line boundaries are detected. In many arid or semiarid environments, the Skylab crewmen could not positively determine the presence of healthy vegetation or forage. However, they identified water or sunglint from standing water; therefore, it appears feasible that space observers can determine to some extent the availability and distribution of water that livestock require to uniformly use rangeland. In addition, the crewmen could assess the extent and severity of drought-affected regions of the world. Range fires were also readily detected (but, unless manmade structures or valuable forage sources are threatened, these fires are generally not harmful).

Forest Land

Although the crewmen expressed difficulty in distinguishing different forest cover types, they could usually determine when they were observing a forest environment. Forest land with a complete canopy cover generally appeared very dark green or black. Where clear cutting is used as the method for timber harvest, regular boundary lines could be detected. In particular, in Washington State (fig. 9-11) and in New Zealand (fig. 9-12), Douglas fir and Monterey pine in plantations are removed by clear cutting, thus producing blocks that form a distinctive pattern within the forest environment.

No specific sightings were made of damaging agents such as disease or insects within forest land. However, variations caused by old fires were detected in Australian eucalyptus forests. The Skylab crewmen had no difficulty locating fires. Thus, one of the important observations space observers could make in forest environments includes detecting fires, describing the direction of burn, and assessing the value of resources that could be consumed if control were not effected. These data have particular significance in the resource management of remote and thinly populated regions.



FIGURE 9-11.—A Nikon photograph taken with a 300-mm lens of Mount Adams (1) and Mount St. Helens (2) in the state of Washington. Clear-cutting blocks (3), which are evidence of commercial timber harvesting, are easily visible on the slopes of Mount St. Helens because of snow cover (SL4-192-7081).

USER REACTION TO SKYLAB PHOTOGRAPHS

Selected handheld-camera photographs from Skylab 4 were sent to resource scientists in Australia and New Zealand for their reaction regarding the value of space observations and photographs for assessment of vegetation resources.

Dr. G. Ross Cochrane of the Geography Department at the University of Auckland in New Zealand reported that the Skylab handheld-camera photographs sent him were

fantastic They offer a remarkable range of information for mapping land use, extent of forest milling, demarcation of indigenous and exotic forest areas, indication of regional pasture productivity, drought effects, and patterns of coastal currents and shore sediment drift. The South Island photograph [fig. 9-13] additionally affords a sharp picture of different farming types, the extent of piedmont fans and their relationships to farming practices, the different classes of hill and mountain landforms, drainage basin networks, extent of snow cover, stream sediment discharge plumes, contrasts in water quality of glacier-fed and river-fed lakes, and numerous categories of natural vegetation I've already used them [Skylab handheld-camera photographs] to update a vegetation map of New Zealand being prepared for a New Zealand atlas.

Dr. Cochrane also indicated that the Skylab photographs would provide an excellent method of improving knowledge of New Zealand's resources and greatly aid many aspects of resource management, namely forestry, land use, farming, hydrology, geomorphology, and oceanography.

It is apparent from Dr. Cochrane's statements that the information derived from the photographs is extremely important for updating resource inventories in New Zealand. Based on the lists of tasks for which this information might be used, it appears equally apparent that space observers could provide timely observations concerning pasture condition and productivity and drought effects.

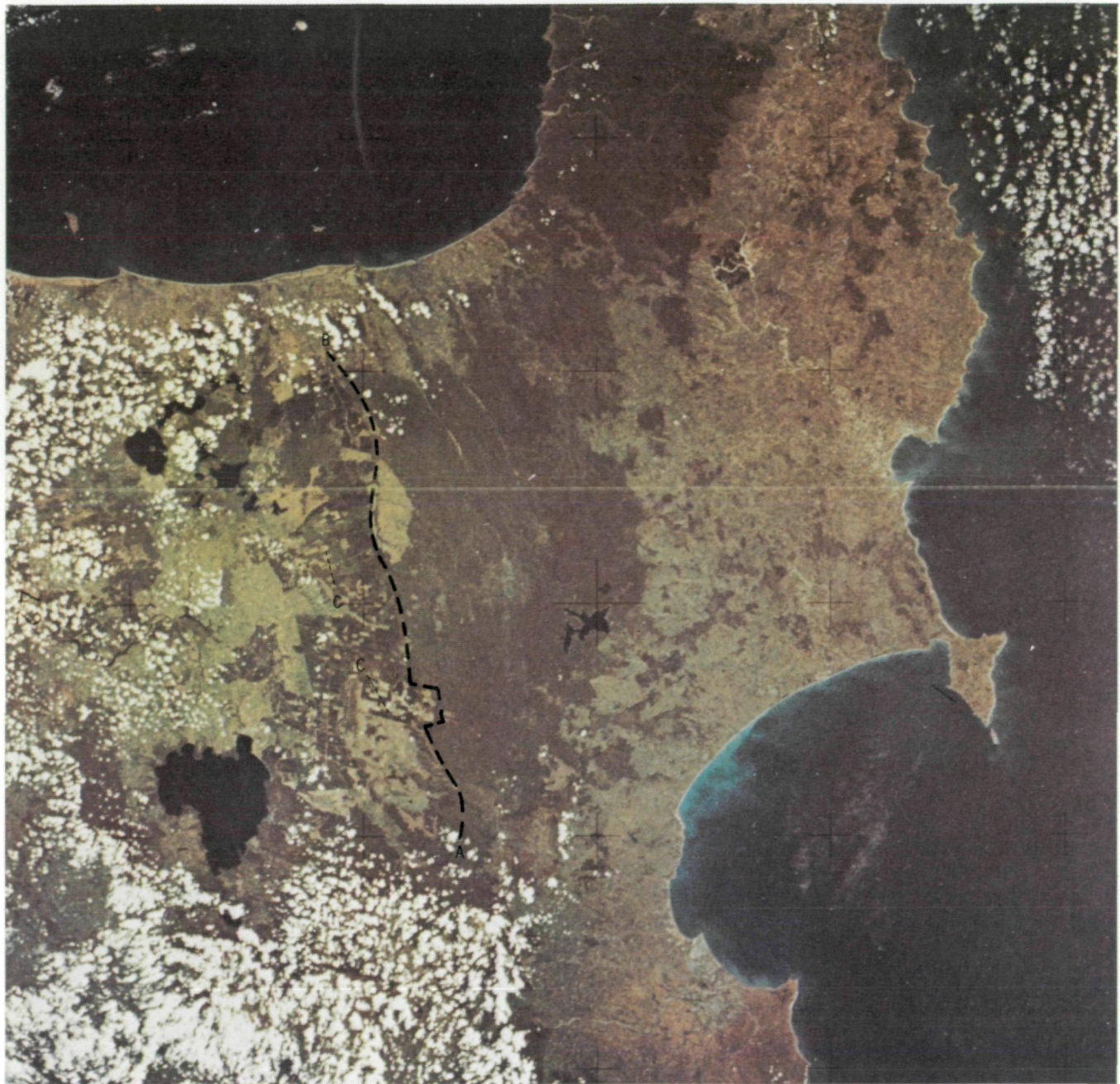


FIGURE 9-12.—Hasselblad photograph of North Island, New Zealand, showing a boundary between the indigenous vegetation and the introduced Monterey pine plantations, right and left, respectively, of the dotted line extending from A to B. Clear-cutting blocks can be seen in the plantation area (C) (SL4-137-3641).

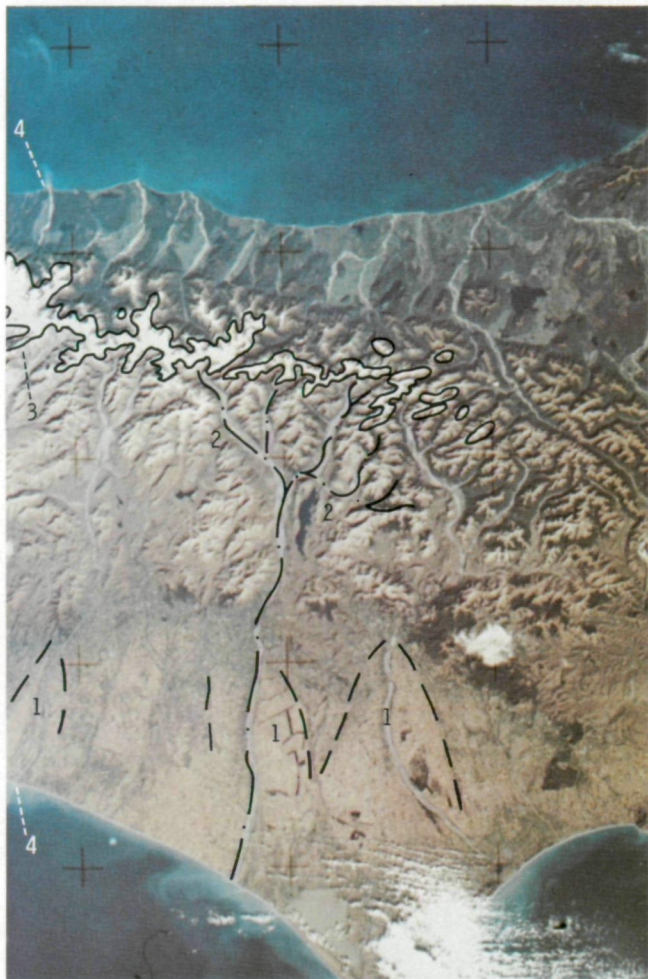


FIGURE 9-13.—Photograph of South Island, New Zealand, showing piedmont fans (1), drainage basin networks (2), extent of snow cover (3), and stream sediment discharge plains (4) (SL4-137-3700).

David G. Wilcox, who works for the Department of Agriculture of the State of Western Australia, reported:

... we were impressed with the clarity and the detail available from the image [Skylab handheld photograph]. We found that it was possible to obtain all types of information by continued searching of the print We were fortunate in that we received a print of the Nullarbor

Plain [fig. 9-8] since we have just recently spent some time out there. The print showed the station [ranch] development with amazing clarity . . . this area was only recently leased, the oldest properties along the transline [railroad and highway] being only 10 years old. It was possible for us to distinguish fence-line effects, paddocks, watering points, railroad, and highway. The unfenced country stood out in stark relief to that which wasn't used [grazed] and the gradations of use away from the watering points were incredibly clear. We have made an overlay of this area in acetate, and it provides the most compelling evidence of overuse and mismanagement of the resource. I think that interpretation of photographs like this in areas where these distinctions are so clear will prove invaluable to administrators I believe that the information is of immense value in inventory and, provided that there is adequate ground information, we could use such images with real purpose.

Mr. Wilcox, in comparing photographs of the rangeland on the Nullarbor Plain with those of rangeland in west-central Western Australia, could not see grazing effects so readily on the latter. He speculated that this was because of the uniform misuse and the relatively low percentage of vegetative cover. This observation is consistent with those made by the Skylab crewmen, who expressed difficulty in discerning even the presence of vegetation and certainly could not determine the condition of the range.

Referring to Skylab handheld-camera photographs of agricultural land in Western Australia, Mr. Wilcox wrote:

... we were most impressed with the clarity and with the potential provided for assessing cleared areas, disposition of lakes, roads, amount of uncleared land

The statements by Dr. Cochrane and Mr. Wilcox demonstrate that resource users can and will profitably use space photographs to gain a better knowledge of the resources they manage. It is significant that Mr. Wilcox

suggested that the space photographs provide compelling evidence of overuse and mismanagement of rangelands. The evidence presented in such space photographs could lead administrators to take appropriate corrective actions. Similarly, space observers could aid in this information-gathering chain by initially detecting problem areas and then taking appropriate photographs that could be further analyzed to assess management problems.

PHOTOGRAPH QUALITY EVALUATION

Color positive film was used to photograph most of the vegetation sites during the Skylab 4 mission. Such variables as lighting and atmospheric conditions, photographic experience, and film storage and processing resulted in photographs of varying quality and directly affected the interpretability of the space photographs for vegetation analysis.

Many of the photographs were of good quality, but many others were of no value for vegetation analyses because of improper exposure or focusing, low Sun angle, or adverse atmospheric conditions. The exposure and focusing problems occurred because the crewmen were inexperienced in taking photographs under such a variety of photographic conditions.

Because positive film was used, developing did not cause variation in image quality between rolls of film. The quality of prints from a transparency, however, may be variable. Prints are often fourth-generation images. This multiple reproduction results in a loss of resolution and contrast of the features. To attain the best print, the variable factors must be reduced to a minimum. The most critical factor is the variation in the colors acquired during printing. These subtle variations in photographic quality are highly important for vegetation analysis. Color contrast and proper exposure during developing must be maintained so that interpreters can acquire the most information about the vegetation complex.

Both vertical and oblique photographs were taken during the Skylab 4 mission. A few of the differences

between these view angles have been mentioned in the section entitled "Angle of View." Oblique photographs exhibit poorer detail and color contrast and a darker density because of atmospheric conditions. Haze and smoke contribute most to the degradation of image quality. Dr. Dean Gretz of the Rangeland Research Unit of the Commonwealth Scientific and Industrial Research Organization in New South Wales, Australia, analyzed oblique photographs of New South Wales and commented:

I am sorry to say it is our general opinion that such imagery obtained by orbiting astronauts would probably be of little benefit to resource monitoring and management in Australia on a systematic basis. We have arrived at this conclusion because of the poor colour balance (affected by atmospheric haze), the oblique nature and the irregular supply.

Dr. Cochrane of the University of Auckland also commented on the lack of usefulness of oblique photographs. Although Dr. Gretz and Dr. Cochrane both indicated there is little need for oblique photographs, they said vertical imagery is useful for resource monitoring. Dr. Cochrane stated:

The nearer vertical they are the better, because it obviates the need for major rectification before they can be used [for mapping].

Although oblique photographs are poor for detailed information, they are valuable for reconnaissance of flooded areas, for fire monitoring, and for water detection. They also provide an overview of the area around and within the vegetation environment of interest.

SUMMARY

The important factors that governed the ability of the Skylab 4 crew to make meaningful observations of vegetation resources were angle of view from the spacecraft, atmospheric conditions and Sun angle, speed of the spacecraft, characteristics of natural and culti-

vated vegetation, and familiarity of the crew with the phenomena to be observed.

The crewmen believed that their observations were more reliable when they were viewing toward the nadir through a window perpendicular to the line of sight. Increased obliquity of view caused features to appear darker and decreased color contrast. This obliquity and atmospheric haze and smoke are major factors that were found to cause a reduction in the quality of both the visual observations and the handheld-camera photographs acquired by the crew. Although haze and smoke affect oblique observations, they have relatively less influence on vertical observations. The ability to differentiate light and dark shades of a color was influenced by the amount of haze and smoke. Cloud cover over an agricultural area could be as high as 75 percent and the crew could still distinguish between agriculture and natural vegetation. After the vegetation type was established as being agricultural, the crewmembers' ability to make evaluations of color and condition of crops was increased. To make visual observations of natural vegetation conditions, however, the cloud cover had to be well below 75 percent.

Atmospheric conditions also affected photographic quality. When either oblique or vertical photographs were taken through haze, the photographs appeared washed out and feature discrimination was reduced. Cloud cover frequently was the cause for improperly exposed photographs of ground features.

To ensure optimum conditions for analysis of vegetation, visual observations or photographs should be acquired under a high Sun angle. Shadows (caused by low Sun angle) are important in landform analysis but do not enhance assessment of vegetation features.

During the mission, the crewmen had approximately 30 seconds to locate, observe, and photograph a specific site. Because of the rapid rate of movement of the spacecraft, the crew at times could only make very general observations of vegetation types and conditions. One of the major problems involving the rapid movement past the point of interest was locating the area. The crewmen stated that if they were familiar with an area, they could pinpoint it faster and have more time for observations or photography. Also, greater

familiarity with ground areas would make their observations more accurate. The speed of the spacecraft did not enable the crew to detect variations within agricultural fields or to accurately estimate the amount of natural vegetation present. Binoculars provided a means for observing greater ground detail, but speed remained a limiting factor.

The Skylab 4 crewmembers were asked to make observations of two vegetation types, natural (rangeland, forest land, arid) and agricultural (wheat in the United States, Argentina, and Australia). They were able to discern changes in the color of fields in wheat-producing cropland associated with crop development. They also observed differences in the crop cycle between the Northern and Southern Hemispheres and distinguished differences in the timing of crop development between countries in the Southern Hemisphere. Because disease and insect damage was not on a catastrophic scale, the crew was not able to detect evidence of damage-causing agents. Natural vegetation assessments were limited to the recognition of paddocks (caused by overgrazing), watering holes, clear-cutting patterns in timber, and fires.

Most of the potential users of space-acquired data (range specialists, water quality scientists, forest specialists, agriculturists) favor the acquisition and interpretation of high-quality photographs or images. Photographs taken at a vertical angle are preferred for mapping and inventory work; oblique views would be useful only for reconnaissance surveys that require a minimum of quantitative assessment. Visual observations and descriptions of vegetative resources from space, however, have limited application. General assessments of crop development, forage condition, and available moisture in drought-affected areas are among the few important tasks that orbital observers could perform to provide real-time information to wildland managers. Man's most valuable role in space, for vegetation analysis, appears to be determining the appropriate conditions (time, atmosphere, and lighting) and choosing the appropriate sensing device for acquiring the high-quality imagery necessary for assessing vegetation resource conditions and management problems.

10

Report on the Skylab 4 African Drought and Arid Lands Experiment

N. H. MacLEOD,^a J. S. Schubert,^a and P. ANAEJIONU^a

THE HANDHELD-CAMERA photographs and visual observations returned by the crew of Skylab 4 and the usefulness of this information in the analysis of phenomena related to the African drought and arid lands are examined in this section. The crew and the scientists-analysts on the ground worked through an analytical process that resulted in new knowledge and perspectives, and an attempt is made to make that epistemological process clear in this report. This process through which new insight into the arid lands systems was gained should be useful in future manned missions and should lead more directly from sensor development and space observations to new knowledge of other terrestrial systems and to the application of the new knowledge in resolving the social and physical problems besetting Spacecraft Earth and its crew.

The objective of this section is to make explicit the process of concept formulation and application that was derived from the Skylab 4 experiment. This process involved shifts and modifications in the perceptions of the causes, consequences, and possible cures of the drought/arid conditions in the Sahel (fig. 10-1) before, during, and after the Skylab 4 African drought and arid lands visual observation team (VOT) experiment.

During the period from 1969 to the present, our knowledge of the African Sahel changed from a state of

little familiarity to an understanding sufficient to formulate a general set of ideas concerning the dynamics of the Sahelian zone; after the preliminary VOT report, a more useful set of ideas was incorporated into two new concepts—potential agricultural zone (PAZ) and climax agriculture (CA). These concepts and others given in table 10-I are defined in the following subsections. Table 10-I outlines the process involving the Skylab 4 contribution to the conceptualization of the Sahelian aridification process. The epistemological process may be traced from our initial understanding of the Sahelian drought conditions, initially believed to be sand accumulation or encroachment (hence, desertification), to the understanding, through field observations and space data analysis, that widespread destructive land use activities contributed to the then prevalent arid conditions.

CONCEPTS

The terms used in this section to describe arid land processes and phenomena are crucial to the experiment because they are the means of expressing both old and new perspectives. Therefore, the terms are defined as follows.

Desertification: The process of desert formation (generally desert encroachment into land used for food production); also, the making of a dust bowl, often

^aDrought Analysis Laboratory, American University, Washington, D.C.

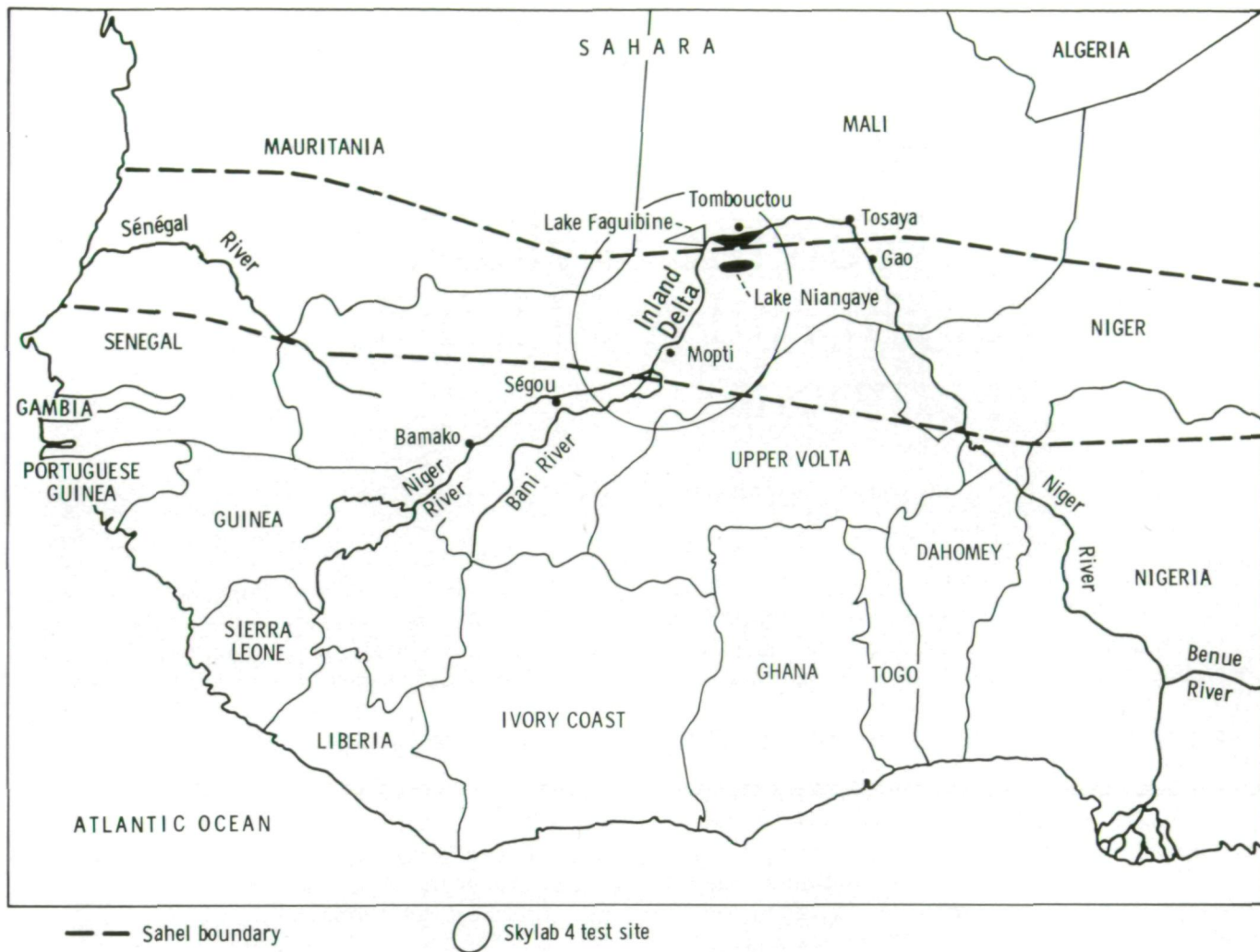


FIGURE 10-1.—Index map of West Africa showing location of the Sahel zone and the Skylab 4 test site.

thought to be due to climatic change or overuse of land. The process occurs in arid and semiarid regions.

Aridification: The process of human or cultural creation of dry land through removal of vegetation, burning, overgrazing, overcropping, and even urbanization. The process can occur in any ecological zone. The end point or extreme result is a desert.

Drought: A lack of rainfall or period of below-normal precipitation during a season in which rainfall normally occurs. Causes of drought are unknown; suggested causes are changes in climate, in location of jet streams, in regional land surfaces and their use, or in solar activity.

Potential agricultural zones (PAZ): Food production

zones geographically equivalent to ecosystems (zones of similar ecological phenomena). The agricultural productivity of a PAZ is defined not by present productivity but by the productivity maximum inherent in the ecosystem in a mature and stable state.

Climax agriculture (CA): Agricultural management systems in which economic plants (crops) replace the natural vegetation of mature ecosystems to re-create the geometry of the climax plant community canopy. This replacement of economic life forms for natural climax life forms creates the environmental and ecological conditions for maximum productivity and land stability. Perennial surface cover and crop diversity are characteristic of CA; monoculture and open fallow are not.

TABLE 10-1.—*Skylab 4 Contributions to the Concepts of Aridification and Climax Agriculture*

| Concept | Date | Information | Data source |
|----------------------------|--|---|--|
| Desertification | Pre-1973 | Sahara enlarging Underdevelopment of sub-Sahara water resources | Refs. 10-1 to 10-3 ^a Nimbus III images Landsat-1 images Field studies |
| Drought effects | Feb. 1973 | Decrease in rainfall and food production | Refs. 10-1 to 10-3 ^a Field studies |
| | Aug. 1973 (crew briefing) | Desertification parameters to observe/photograph: Sand accumulation Interdunal features Changing patterns of vegetation Soil erosion Massifs drainage systems, including dried-up channels | Principal investigator |
| | Nov. 1973 to Feb. 1974 (Skylab 4 mission) | Crew reported: Duststorms Extensive fires Smoke plumes Blandness of region Changing color of delta lakes Recognition of land use patterns | Crew observations |
| | Mar. 1974 (crew debriefing) | Crew confirmed: Extensive fires in Sahel Similarity of land use patterns in West Africa Periodic restricted observation of surface Vastness of duststorms | Principal investigator/crew interaction |
| Aridification, PAZ, and CA | Postmission to present | Systematic description of Sahelian natural resources and their uses | Skylab 3 and 4 photograph analysis and crew observations Landsat-1 image analysis Extended field studies and local reports |

^aData also obtained from A. T. Anderson and N. H. MacLeod, "Measurement of Annual Flooding of the Niger River Inland Delta From Space Observations," Goddard Space Flight Center, 1972.

GEOGRAPHIC AREA OF THE SAHEL

The Sahelian zone extends from the Red Sea on the east to the Atlantic Ocean on the west, a broad band of transition from the Sahara Desert to the sub-Saharan savanna. The transitional nature of the Sahel (Sahel means border or shore in Arabic) makes it difficult to define its northern and southern extent. Using annual precipitation, it is possible to define the zone as that sub-Saharan region of either 200 to 500 mm or 300 to 700 mm annual precipitation; both amounts are used to locate the Sahel. However, the rainfall in the zone is unpredictable because it is highly variable in both amount and time. This variability led to great difficulty in realizing that a drought had been in progress from

1969 through 1974; not all weather reporting stations experienced the same lack of rainfall during this period.

Precipitation occurs in the summer months, especially as squalls along the Intertropical Convergence Zone (ITCZ) where a moist southwest wind meets a dry northeast wind (the harmattan) in the easterlies trough. The zone moves north in the summer and south in the winter, in reaction to the apparent motion of the subsolar point on the surface of the Earth. The most northerly position is above the latitude of Tombouctou (about 16°40' N); the most southerly position is along the coast of the Gulf of Guinea, which receives rain during all 12 months.

Thus, the rainfall, while regular in season, is sporadic in occurrence, torrential when it comes, and crucial to

life in the Sahel. In the northern Sahel, when rainfall is scanty, there is famine, and the people of the Sahel are familiar with drought and famine. Before colonial times (late 19th century), the nomadic way of life was well adapted to the climatic variability. With increasing westernization, that adaptation was lost, and refugee camps are now filled with nomads, a sight not seen before in the Sahel (ref. 10-1).

A second means of geographic definition of the Sahel is through the location of plant communities existing in the north-south transition. At the desert or northern border, one finds scattered *Acacia* but little other perennial vegetation. At the savanna or southern border, one finds a rather complete canopy of grass (predominantly *Andropogon*) and scattered trees of several genera, but *Acacia* again is probably the most common. This method of defining the Sahel is more successful because perennial plants tend to integrate or "average" the effects of climatic variability; it is less frequently used, however, because, until Nimbus III, no opportunity existed to view the Sahel in its entirety.

In the Sahel, one sees only disturbed plant communities; those stressed by overgrazing, burning, or overcultivation. All Sahelian plant communities have undergone a high degree of aridification, which also has led to the formation of dunes. This stressed condition gives rise to great confusion about the location of the desert border, the rate of desert encroachment into the Sahel, and even the validity of the concept of a permanent Sahel.

Geologically, the region is a series of ancient sedimentary beds overlying the continental mass. It is generally flat, with occasional mountains of intrusives (the Tibesti, the Air, the southern Ahaggar, and the Adrar des Iforas). Rising in these mountains are ancient drainage systems, now only an occasional source of surface water but a frequent source of artesian and other near-surface water. Three major tectonic basins, each associated with a major river system, are found within the Sahel: the Sudd in Sudan, associated with the Nile; Lake Chad, associated with the Chari and, at high lake levels, with the Benue; and the Inland Delta of the Niger River in Mali. A similar basin may be said to exist along the Sénégal River, the fourth major river of the Sahel. The basins are large, shallow, and marshy. The water is generally of good quality, although this resource has not been fully developed. There are indications that the water resources were more intensively developed in the past.

PRE-SKYLAB 4 MISSION CONTRIBUTIONS

Nimbus III Investigation and Apollo 9 Photography

With the launch of Nimbus III in April 1969, a daily view of the entire Earth was made available with the high-resolution infrared radiometer (HRIR) and the image dissector camera system (IDCS). For the first time, there was sufficient geometric resolution (10 km) to permit study of such large surface features as rivers, large lakes and inland seas, mountain ranges, and the major ecological zones of the entire Earth.

With Nimbus III satellite data, the authors were able to study for the first time an anomalous feature located at the border of the Sahara and the Sudanic savanna south of the Sahara; that is, in the Sahel. The feature was the growth and passage of the flood in the Inland Delta of the Niger River in Mali. Associated with the flood were the seasonal growth of Sahelian pasture outside the Inland Delta and the movement of water along ostensibly dry channels from the Niger River near Ségou, Mali (upstream and west of the delta), to the Hodh depression in southeastern Mauritania (i.e., northwest of Nioro du Sahel, Mali).

In viewing this feature in Nimbus III HRIR data obtained from April to December 1969, the movement of the Intertropical Convergence Front (ITCF), whose clouds obscured the view of the Sahel during the summer, became evident. Examination of each day's imagery showed the broad northward penetration of the squall lines and the occasional movement of weather fronts across the Sahara to the Mediterranean Sea.

The Nimbus imagery made available a means of viewing many aspects of the Sahel: the soils, plant growth, pattern of river flow, flood and ebb, as well as unusual features such as the subsurface watering of ostensibly dry river channels. The view, a daily and regional or synoptic one, permitted the integration of several features, thus revealing the dynamic aspects of the Sahel as a functional system. It is interesting to note that, in subsequent work, 1969 is given as the first year of Sahelian drought; but, by the definition of drought given previously, 1969 was a normal year with a slight tendency to droughtiness at most stations.¹

¹A more detailed discussion of the findings of this investigation is given in reference 10-2.

In addition to the usual visual analysis of Nimbus imagery, digital analysis techniques were being developed to extract the maximum information from the HRIR data and to present feature classifications based on rectified imagery in an image format. The purpose was to prepare for Landsat-1² data; however, in the course of this work, reports were also made on flooding and land classes in the Inland Delta.³ Furthermore, spectrophotometric analyses were being made of plants and soils in the laboratory and in the field to form a basis for objective interpretation of multiband imagery (ref. 10-3).

Nimbus III gave a broad and dynamic view of the Sahel—indeed, of all Africa—a view that opened a vista of unending questions. The historical, political, ecological, and geological literature on West Africa provides sparse but intriguing evidence pointing to enormous and continuing change. Because a regional view had been almost impossible to obtain before the advent of Earth-observing spacecraft, earlier studies dealt with isolated West African phenomena. One can read the travelers' tales of Ibn Battuta, Leo Africanus, René Caillié, Mungo Park, and Heinrich Barth (refs. 10-4 to 10-8), all of whom traveled in the Inland Delta region, and glean a sense of the dynamic characteristics of the people, the vegetation, and the Niger River and life along it; a sense of continuous changes through the centuries.

The photograph of the northern Inland Delta and the arrowhead-shaped Lake Faguibine taken by the Apollo 9 crew in April 1969 encapsulates and illuminates the view reported by those earlier observers of the Sahel.

In the Apollo 9 photograph, three dune formation sequences, all including the town of Tombouctou, are apparent. One can see how far Tombouctou is from the river today, or wonder why Lake Faguibine is so little discussed. The lake is a large body of freshwater for which the northern shore is the Sahara itself. There are reports of the Canal du Sali (named after a Malian emperor) that was opened in the 13th century to accommodate water transport and trading links from Ségou to Tombouctou. In the Apollo 9 photograph, the waterway is seen at the western end of Lake Faguibine. At its

²Formerly designated as the Earth Resources Technology Satellite (ERTS).

³A. T. Anderson and N. H. MacLeod, "Measurement of Annual Flooding of the Niger River Inland Delta From Space Observations," Goddard Space Flight Center, 1972.

prime, Tombouctou had a population of 25 000. It now has approximately 5000 people and is surrounded by desert. These populations seem too small to require a transportation route better than the present-day journey through the Inland Delta interior.

Examination of Nimbus imagery taken over the Inland Delta indicates the watering of northwestward-trending channels that are now dry. The existence of these dry channels, the regional extent of which has been revealed from satellite data, substantiates information in Ptolemy's (A.D. 150) map (ref. 10-9) as well as accounts from Leo Africanus⁴ (ref. 10-10) and from Malian oral historians that the Niger once flowed to the west. Topographic maps of the regions show the westward flow to be more likely, if based on hydrographic gradients, than the present easterly flow.

If it is true that the Niger flowed to the west in the historical past, it flowed through what is now a desert filled with sand dunes, desert pavement, and bare rock. Could and should a diversion of the Niger River be made to rewater the desert of that area? How did that desert form? Paleoecological studies and floristic analysis of the Ahaggar in the central Sahara demonstrate the actuality of a more mesic (wetter) past in the Sahara. Rock paintings and carvings, as well as fossil studies, show the presence in the Sahara of animals usually found in tropical regions of moderate rainfall. Pastoral scenes are depicted in the more modern rock paintings. Do these studies and ancient artists point to a time of a green Sahara? Did the climate change?

The very tenuous evidence indicates profound changes in the Sahel in the last 5000 years and very rapid change in the last 200 years. The formation of the Sahara as a desert may have accompanied a reversal of the Niger's direction of flow. The prosperous capitals of Sahelian empires were founded and flourished in areas that today are unwatered, unvegetated, and unpopulated. Was the pastoral Sahara overgrazed?

Landsat-1 Contribution

In August 1972, the senior author joined an Agency for International Development (AID) team visiting the Republic of Mali to discuss the probable usefulness of

⁴Leo Africanus was an educated and widely traveled man of the Mahgreh, a slave of Pope Leo who valued Leo precisely because of his accurate reporting.

Landsat data to Mali. The team was briefed by the Government on the major development problems of Mali, which were (1) desertification, (2) development of the Niger River water resources, (3) agricultural development, (4) improvement of livestock production, and (5) development of mineral resources. The Government was fully aware of the progress of desertification and the devastation that this process was causing. People in the Sahel recognized the deterioration of their ranges and the lower production of their farms, as well as the potential of the region's water resources. The deficiency most clearly perceived was the lack of comprehensive resource information. The AID team concluded from its visit that Landsat might help.

The first Landsat images of the Sahel included the southern Inland Delta, the Office du Niger (a 200 000-hm² irrigation scheme), and the Snake River valley. In these first views of Mali, both the modern and old (dry) river systems were clearly visible, evoking the comment⁵ that "of course the Snake River used to flow north and then west to the S n gal River." That ancient course of the Snake River has since been traced in Landsat-1 imagery.

The Bambara farmlands and villages near the Inland Delta were also apparent in space imagery, although, at that time, it was not known how to estimate the intensity of land use in relation to the time necessary for recovery of the soil fertility. In the past, a fallow period was adequate and formed a basis for a stable slash-and-burn farming system. At the present time, the fallow is simply inadequate to restore fertility; the land is often continuously cultivated and erosion is serious. These relations were determined from a simple model generated by analysis of Landsat-1 data.

During 1973, the realization that a major drought was occurring in the Sahel became worldwide. Livestock surveys by the United Nations in February and March 1973 indicated that a devastation of Sahelian herds had occurred and that surviving cattle had been moved far south of the normal winter season pastures. As a result of concern about determining both the causes and the effects of drought on the Sahelian resource system, the Drought Analysis Laboratory was established at the Goddard Space Flight Center (GSFC) collaboratively with GSFC, the American University, and the Catholic University of America. Its function was to archive, analyze, and interpret Sahelian Landsat-1 data and to

⁵Personal communication from M. Robert N'Daw, Malian Minister of Public Works.

provide that information to the Sahelian governments. In this work, vegetation types, water quality, soil types, and occupational patterns of sedentary regions were classified.

During this period, the Landsat-1 data of the 110 000-hm² Ekrafane Ranch in western Niger were studied. The ranch stood out as a vegetated region in the midst of the barren Sahel. On a field trip to the ranch, investigators found that the process of desertification appeared to have been reversed through simple pasture management procedures, and that the reversal had occurred during the years of drought.

In late August of 1973, these findings were reported to the Niger Government. Based on the field trips and the analysis of the Landsat-1 imagery, the study indicated that desertification had been reversed at Ekrafane Ranch through a process which could be repeated throughout the Sahel. Also, the ancient natural drainage systems in the Sahara and the Sahel were still working and had near-surface water in association with irrigable soils. These soils could be located by use of Landsat-1 data and could be used for immediate production of food.⁶

By this time, then, the new view from space had transformed our understanding of the Sahel from a state of little knowledge about a static situation to a perception of the diurnal and seasonal interaction of climate, soils, vegetation, and people on their farms or with their herds. There were still many puzzling questions, including the process by which deserts formed and the meaning of desertification.

INVESTIGATION OBJECTIVES AND ASSUMPTIONS

The basic objective of the Skylab 4 mission over the Sahara-Sahelian regions of Africa was to observe and photograph features and phenomena affecting the natural resource base of the area. Specific study objectives concerned vegetation patterns, flooding, soil erosion, interdunal water accumulation, natural drainage systems, and drainage patterns in the Black Volta and White Volta River basin. The Niger Inland Delta in Mali was selected as a test area to investigate the distribution and the changing patterns of vegetation and

⁶N. H. MacLeod and D. Randall, American University, preliminary report to President Diiori Hammani, Republic of Niger, 1973.

flooding of the major freshwater resources in the drought-prone Sahel.

To study the effect of soil erosion on agricultural production, two test sites were selected: one in Niger between Niamey and Filingué, the other in Mali between Bamako and Ségou. Two test sites, one north of Lake Faguibine in Mali and one north of Lake Chad in Chad, were selected to observe and map interdunal vegetation and the associated interdunal water accumulation. Test areas were selected in Mali and Niger for identification of major ancient drainage systems so that soil and water sources useful to the expansion of irrigation agriculture could be located and mapped. The drainage basin of the Black and White Volta Rivers in Upper Volta was the test area for observing and mapping the drainage patterns and conditions conducive to the black fly, which is known to cause river blindness.

For this investigation, the Skylab 4 crewmen were instructed to obtain information on such features and phenomena as dust and cloud movement, vegetational patterns, land surface features, color and distribution of surface water, and conditions (color changes) of lakes within the drought zone. A particularly important task for the crewmen was to determine the "greening" of areas for near-real-time planning of grazing herd distribution.

To become familiar with the type of features seen from Skylab, the Skylab 4 crewmen viewed a video tape obtained during a Skylab 3 pass over the Sahel. The salient features of the region, such as prominent landmarks and land use color and patterns, were identified and the type of information needed was described. Supplemented by detailed descriptions of the test sites in the onboard data book, this video tape was the information used to aid the crewmen in observing and photographing the Sahelian drought zone.

Assumptions underlying the briefing instructions to the crew included the following: (1) that arid lands problems, including drought, were considered an integral part of desert encroachment on agricultural land; (2) that desertification was primarily defined in terms of desert invasion, and that investigators were dealing with factors of desertification which the astronauts could observe and photograph; (3) that a cloud-free atmosphere over the Sahelian zone would provide extended unobstructed regional viewing conditions; and (4) that the crewmen could observe regionally distributed small-scale features and patterns.

Crew observations proved the last two assumptions incorrect and provided a basis for modifying the first

two. The difference between the premission understanding of the processes of desertification and drought and the postmission appreciation of the associated factors and processes, including the conceptualization of the aridification process, should again be pointed out.

The Skylab 4 crew made several passes over the Sahara-Sahelian region of Africa during which they observed and photographed scenes of the region's resource base. A total of 33 Hasselblad (70 mm) and Nikon (35 mm) images were obtained of related features. A summary of the crew observations is given in table 10-II.

TABLE 10-II.—*Skylab 4 Sahel Drought Observations*

| <i>Category</i> | <i>Number of observations</i> |
|---|-------------------------------|
| Dust, including storms, clouds, sand movements | 9 |
| Sand and dunes | 18 |
| Smoke and fires | 12 |
| Vegetation patterns and color | 4 |
| Weather conditions | 9 |
| Wind directions | 13 |
| Lake conditions | 4 |
| Other, including land use patterns and surface textures and color | 12 |
| Total | 81 |

OBSERVATIONS

Some of the phenomena that have large-scale and global significance in arid land research and that were observed by the Skylab 4 crewmen are occurrence of burning, dusty clouds and duststorms, bland appearance of the Sahel, and land use patterns.

Burning

An example of man's correlative abilities to observe and to integrate information is the discovery of the source of smoke clouds over the Indian Ocean. By observing on successive passes at different times of the day, the crewmen were able to identify the burning practices in Tanzania and Kenya as the source of some of the clouds. Discovery of the cloud sources was based on two separate types of observation. First, the crewmen observed that the clouds, though similar to cirrus formations, appeared to be darker. Cloud height information, which would have aided in defining the relation

of the clouds to land features, was not available to the crew.

The second type of observation was the crew's discovery of firelines (approximately 650 km long) in Nigeria, Cameroun, and the Central African Republic that appeared bright at night. By day, this strip was obscured by dark plume patterns that were determined by the commander to be smoke produced by the fires seen at night. In addition, because of the extent of fires and their proximity to what was identified as vegetation, it was concluded that the fires associated with the slash-and-burn farming practice or with game flushing occurred on a scale never before recognized.

Another particularly interesting observation of burning was in the Gourma region of southeastern Mali, where the fires appeared to occur in an area devoid of vegetation. This apparent absence of vegetation was due to the similarity in the colors of the soil and the dried-out vegetation, resulting in the lack of tonal contrasts when viewed from Skylab.

In Australia, Argentina, and East and West Africa, both visual observations and handheld-camera photography were used to observe large-scale burning. The extent of burning in arid and semiarid regions (both developed and developing) is surprising. The enormous extent of burning in sub-Saharan Africa is slowly being

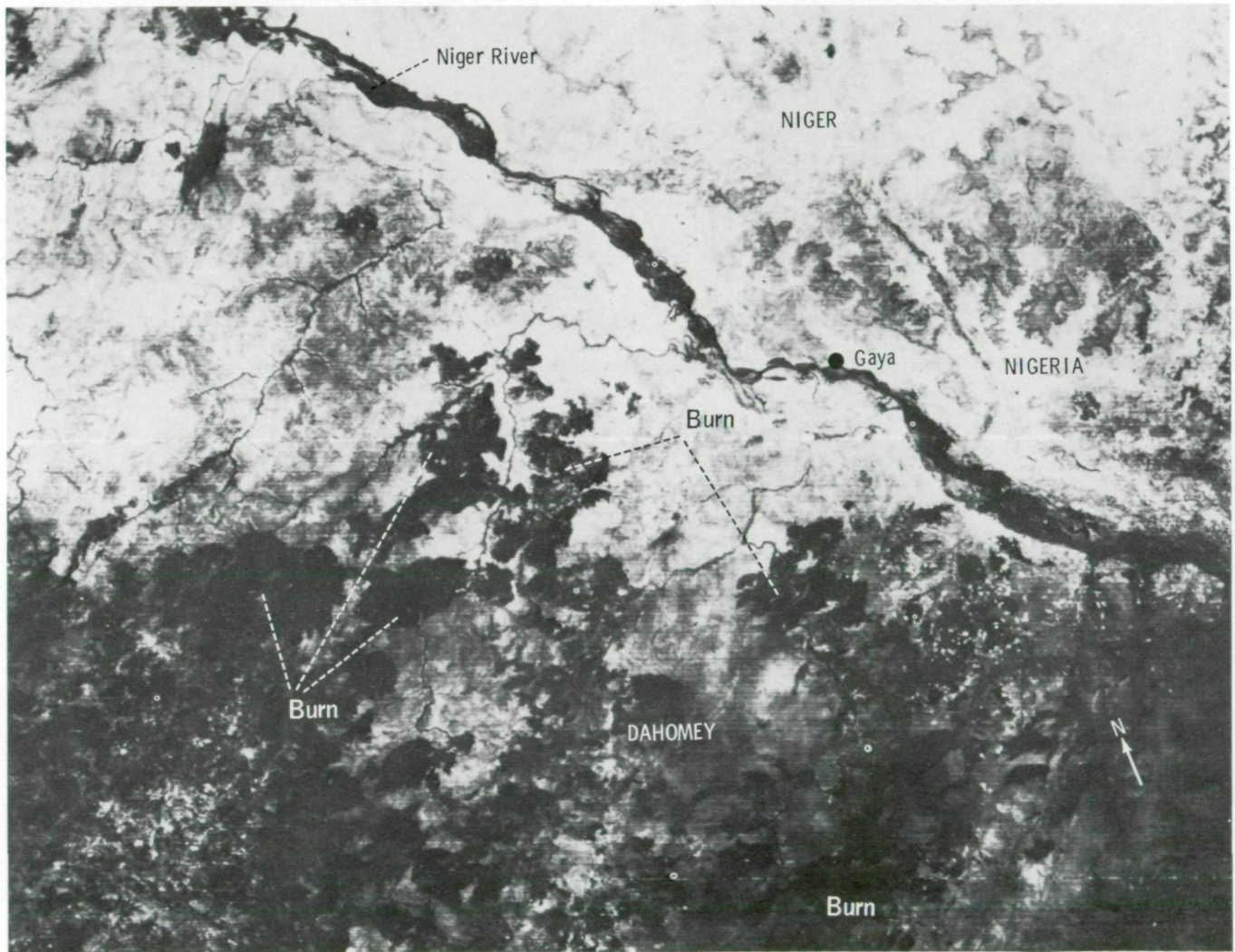


FIGURE 10-2.—The striking land use pattern shown in this Landsat image is the effect of "bush" burning within forest areas. Burns appear black and show the vast expanse of land where vegetation has been removed (E1487-09350).

recognized from the Skylab 4 visual and photographic documentation, Landsat-1 imagery, and other sources. Landsat imagery has been used by Deshler (ref. 10-10) and Anaejionu (ref. 10-11) to classify and estimate areas covered by concentrated burning patterns in the region from West to East Africa where the Skylab 4 crewmen observed long firelines. This region was not

previously classified as having high-intensity burning, although it was observed as such from Skylab 4. Figure 10-2 shows portions of the zone in West Africa that exhibits concentrated burning patterns.

Although burning does increase mineral availability to plants, reduce insect populations, selectively maintain resistant plant species, and simplify clearing ac-

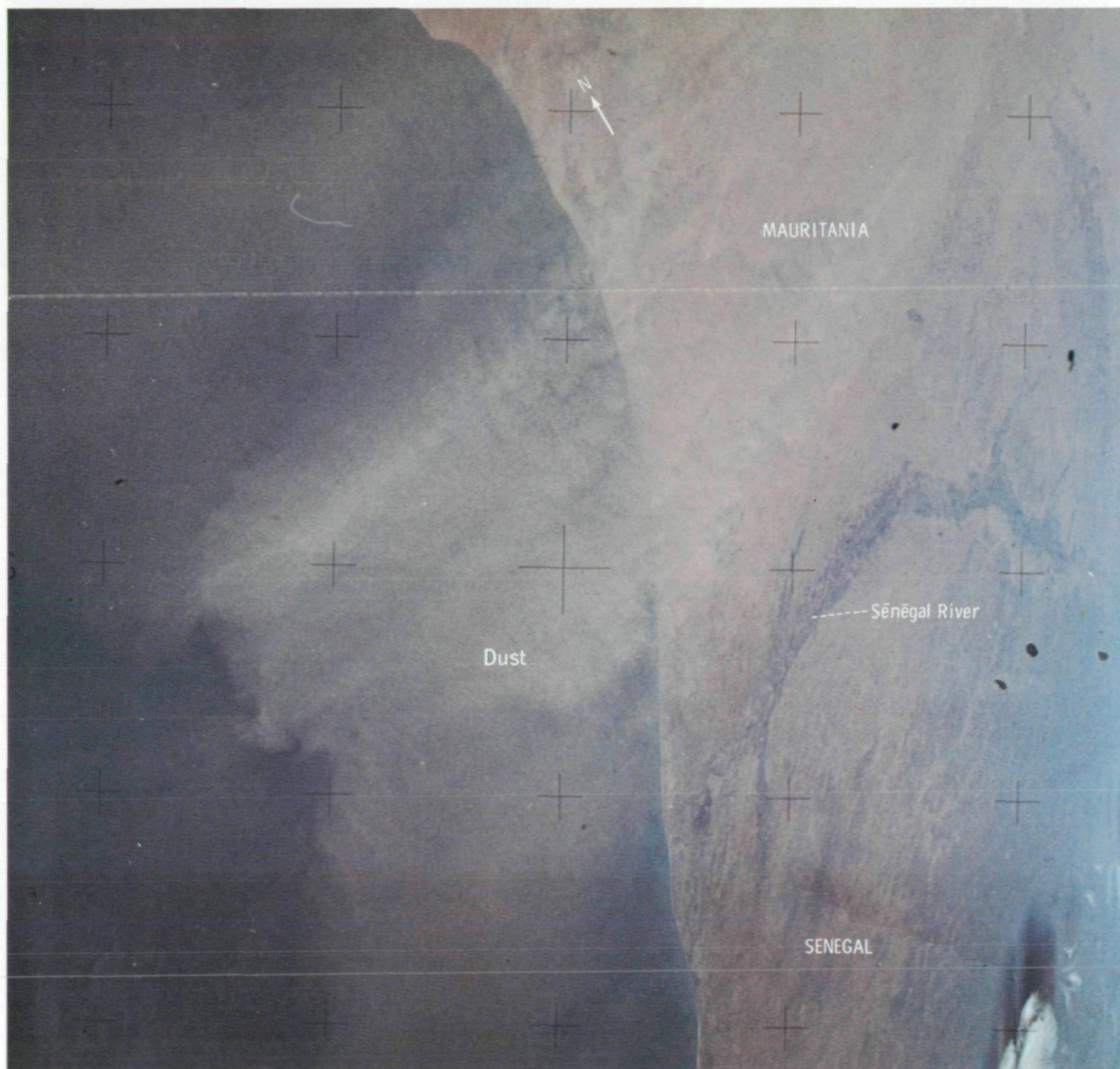


FIGURE 10-3.—Duststorm photographed by the Skylab 4 crewmen over Mauritania (SL4-140-4227).

tivities, there are negative aspects. The most harmful result of burning is the removal of vegetative cover during the hottest and windiest season. This practice increases the susceptibility of the land to wind erosion. Burning also reduces the organic matter of the soil, which is already badly depleted in the Sahel. Organic matter is important in the maintenance of good soil physical properties, available minerals, and plant litter that moderate the surface microclimate of the soil. Although the burning of rangeland traditionally results in new grass growth, burning destroys bushes and trees that are important forage producers in the Sahel where cattle are well adapted to this particular feed source.

A widely held concept is that burning occurs in the Sahel just before the rainy season and therefore results in minimum harm and maximum benefit. The Skylab 4 observations, however, clearly indicate that the burns occur at the worst time; that is, just after the rainy season ends. Destruction of grass cover by burning at this time of the year exposes the soil surface to heavy erosion by the northeasterly, dry harmattan winds, thus further reducing the productivity of the land and extending the drought region.

Dusty Clouds and Duststorms

Very significant observations of cloudiness in Africa were made by the Skylab 4 crewmen as they described and differentiated these "smoky" or "dusty" clouds from white clouds. Based on observations during successive passes, the pilot described the smoky or dusty clouds on January 22, 1974, as follows:

I've noticed it on 2 days running, and this is a pervasive and extensive cirrus development—which extends from off of the coast of Somalia and the southern end of the Arabian Peninsula out into the Indian Ocean, for 1500 to 2000 miles. As far as you can see. The peculiar character of the cirrus clouds is that they are dirty looking, and appear much darker than the other clouds in the same area.

The cirrus clouds I saw today at Sokoto, Nigeria, had that same appearance. They had a striated texture of a cirrus cloud, the fine, delicate structure of a cirrus cloud, but were dirty. It looked like a jet streamer path. It didn't seem to be associated in any way morphologically with the lower clouds that were in the area.

The crewmen observed the movement of these smoky or dusty cloud systems into the Atlantic and Indian Oceans from West, Central, and East Africa (fig. 10-3). The significance of the observations is twofold. First, the crewmen were able to identify and differentiate the smoky or dusty clouds from normal clouds. Second, this information enabled the crewmen to locate the cloud source and to observe the distribution and fate of the clouds as the systems moved on a continental scale far into adjacent oceans.

Discerning the relationship between the fires and the smoky clouds is the type of correlative integration of information that may always be unique to man. The crewmen, ignoring gaps in the data, followed the smoky clouds on successive passes and determined their sources. Without this correlative ability of man from space, detection of the widespread circulation of smoky clouds would not have been possible at this time.

Investigations at the National Oceanic and Atmospheric Administration (NOAA) and analysis of Landsat-1 data taken over West Africa support the dusty-cloud-movement observations made by the Skylab 4 crewmen. Figure 10-4 is a Landsat-1 image of the Senegalese coast showing windblown dust over the Atlantic Coast. The NOAA studies have shown that the cloud systems moving from West Africa into the Atlantic Ocean reduce solar irradiation of the ocean surface by 25 percent. The systems retain their identity as a stable inversion layer as far as the Caribbean Sea, and this

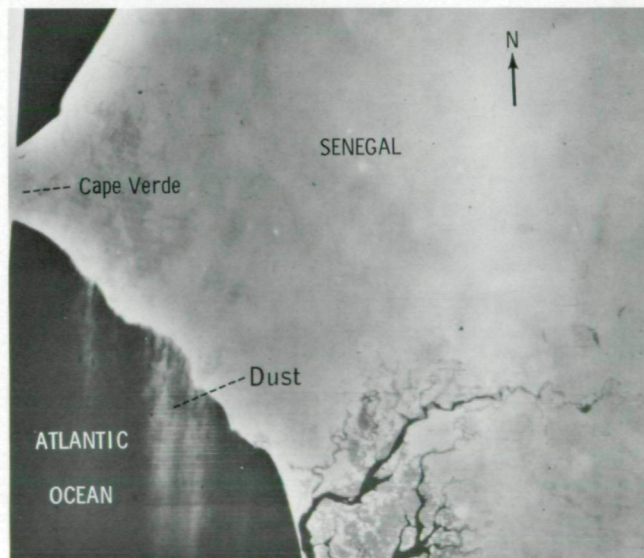


FIGURE 10-4.—Dust blowing off Senegal coast (E1267-10574).

layer suppresses cumulus cloud formation (i.e., the normal exchange of water and energy between atmosphere and ocean does not occur).

The ability of the crewmen to classify the cloud systems and to note their extent should lead to further analysis of the effect of African dust and smoke on global weather events. If the devegetated Sahel is a significant source of dust and smoke and if these aerosols are affecting both energy balance and regional hydrologic cycles, the Skylab 4 observations should stimulate action to undertake further studies of the regional occurrences and distribution of dusty and smoky clouds and to rehabilitate the dust source regions.

Bland Appearance of the Sahel

The crewmen's description of the West African surface as bland was puzzling at first. In other regions, they were able to discern details in land use and hydrologic features that were as new to their eyes as the drought-afflicted Sahel. The Inland Delta test site was readily identified by using the unique arrowhead shape of Lake Faguibine as a conspicuous marker for orientation. In considering the bland appearance of the Sahel region to the crew, a review of onsite field reports obtained during the Skylab 4 mission and an examination of Landsat-1 and Skylab photographs have shown that the crew observations of the Sahel were almost continuously obscured by dust in the atmosphere. This dustiness was not due to duststorms that obscure the surface but is a significant and persistent component of the atmosphere south of the ITCZ. It has been determined that this dustiness extends to the tropopause, is composed of fine particles, and is a daily feature of the modern Sahelian climate. The dustiness is well distributed in the troposphere, unlike the streams of sand described in the following paragraphs.

Sand, moving in coherent streams in western Niger and eastern Mali, was recorded on Landsat-1 images (e.g., image 1523-29331) obtained in December 1973. The occurrence of the moving sands, which covered many thousands of square kilometers, indicated that the deterioration of the soil and vegetation may have passed a critical point and a vast "dust bowl" was developing. The Landsat-1 images showed that the sand plumes on the surface were often more than 150 km in length. Correlation of the features observed in the Landsat-1 images with surface field conditions in Niger

was undertaken. Unprecedented sandstorms and duststorms were reported in this region where sand movement was observed in the images. Extensions of sand dunes were found in the Tchén Tabaraden area of Niger, and much deflation of silts occurred in basins. These are indications that soils protected from wind erosion by vegetated covering had lost their protection and had become unstable (ref. 10-12).

A major task for the Skylab 4 crewmen was to visually determine changes in the permanent lakes in the Inland Delta and to document these changes with photographs. A major problem under study was the reported disappearance of vegetation and, consequently, color changes in lakes such as Faguibine, Do, Niangaga, Débo, and Aougoundou. The loss of vegetation may be a factor in changes in the seasonal amplitude and period of the Niger River flood crest. This relationship between loss of vegetation and flooding periods is significant because, in this region, floodwaters are used for irrigating rice downstream. Consequently, devegetation diminishes the food-production capacity of the region. The removal of vegetation in the delta is thought to have resulted in a more rapid and a higher flood that lasted 1 month instead of 3 months. In 1973 and 1974, for instance, the flood arrived at Niamey, Niger, 2 months early, which drastically affected vegetable, rice, and other irrigated crop production in that area.

From Skylab, the crewmen observed the lakes from early November of 1973 to January 21, 1974, and recorded the following information. On November 11, 1973, the commander described the area under cloudless conditions as follows:

The lakes were quite clear, and I did not have time to really look at the difference in color between the different lakes, but my general impression was that the lakes were all about the same color. The old dune area was quite visible. . . . Just to the west and slightly south of the dune area is a very large green area, apparently very well vegetated and considerably more green in color than the surrounding area.

Another observation by the commander on January 1, 1974, indicated color changes in the lakes:

Faguibine is a very dark-green-looking lake, and smaller lakes nearby have sort of a background of dark . . . green. But then, there is a lot of lighter green colors in those lakes. The colors vary from a light green in some areas to a tan. In one or

two of the lakes, the tan was obviously sedimentation. In one lake, it was difficult to say exactly what the tan was. It did not have the telltale pattern of silt. It was sort of a cellular-type pattern, which indicated that maybe it was dead vegetation; vegetation greens ranged from a very light green to an emerald green. And we noticed that

the Niger River—beginning upstream where there is a sort of a dam-like-looking area with very well cultivated fields off to the north [referring to the Niger Office]—there, the river turns very bright green and stays green all up through the Inland Delta area and around the hump as it moves on down toward Nigeria.



FIGURE 10-5.—Photograph of the Dogondoutchi region of Niger showing the cellular land use patterns (light tones) developed around the villages and settlement areas (SL4-93-299).

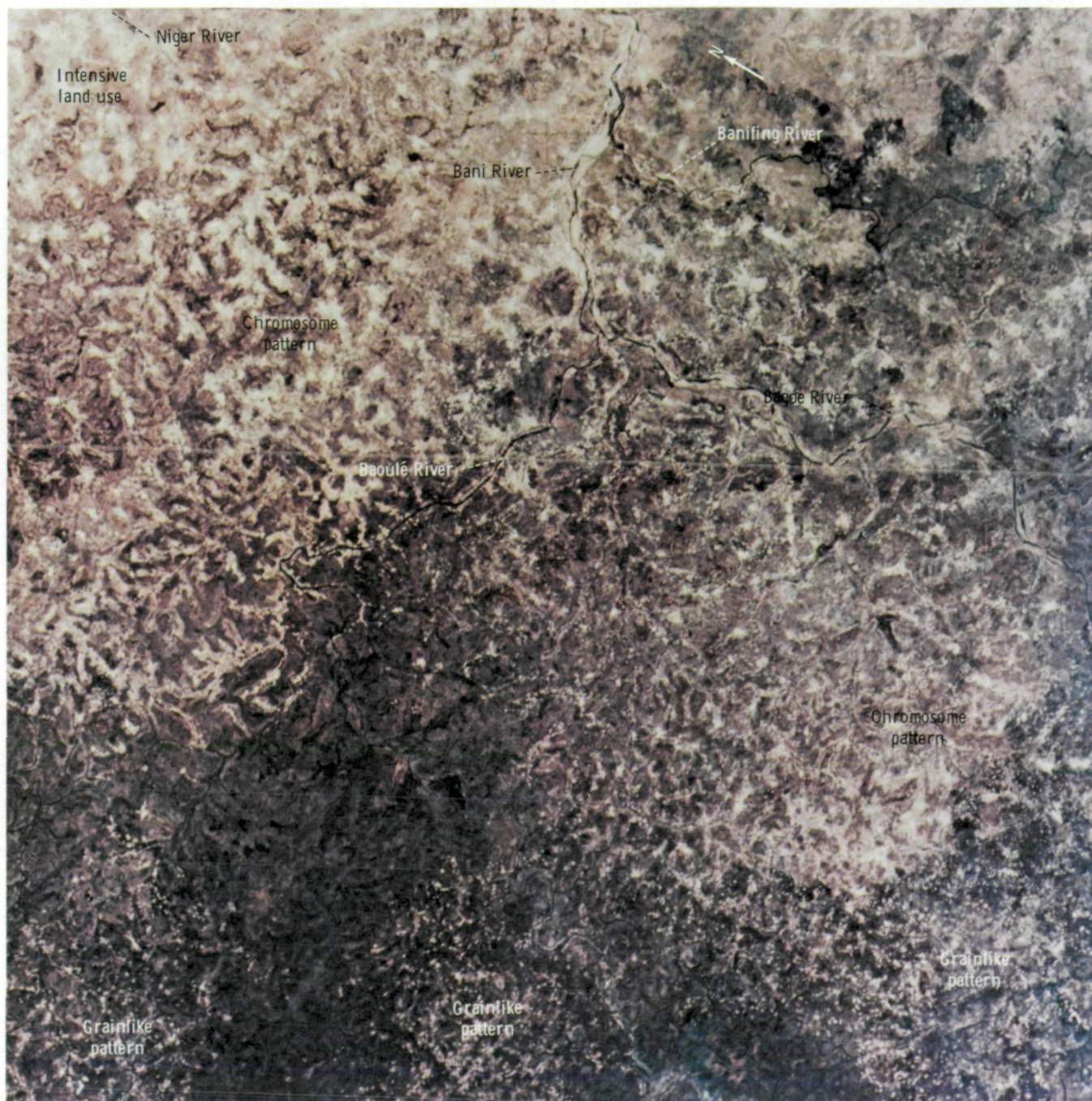


FIGURE 10-6.—Photograph of southern Mali showing variations in cellular land use patterns: extensive cultivation (white) near the Niger River, a chromosome land use pattern near the Baoulé River, and the grainlike pattern of discrete villages (white dots) in the southern part (SL4-58-233).

The last observation of the lakes in the delta region was on January 1, 1974, when the commander reported:

I got a picture of Lake Faguibine in the Niger Inland Delta. I noticed the light coloring, that most of the lakes were a darker green. One of the larger lakes was a lighter green. But most of the interdunal lakes now look like they've got some rain there—and look like a very chalky green. Rather peculiar. I guess that's an indication of a lot of algae in the lake.

In regard to the vegetation patterns, the crewmen gave the following description of the flood plains bordering the Niger River near Bamako on January 6, 1974:

There's quite a few little cultivated areas in there that look like, to the naked eye, just like little salt veins; but looking at it through the binoculars, you can see these areas have a rather rectilinear shape to them and the color of all these nice green ones, indicating lush vegetation.

During the period of progressive Inland Delta flooding (November and December 1973) and then in January and February 1974, the major change in the Inland Delta recorded by the crewmen was the change in color of the lakes. The dominant green of the permanent lakes in the late months of 1973 changed to a light green or tan. This color change is an indication of increased sediment content associated with water runoff. The interdunal lakes also became chalky green as the flood level, and the amount of vegetation, in the lakes increased.

Land Use Patterns

A particularly informative learning cycle occurred for the Skylab 4 crewmen in observing and recognizing the rectilinear land use patterns of western agriculture in arid regions in contrast to the traditional patterns found in Africa. Over Tanzania, the commander described the scene as

a rather peculiar land pattern which was obviously a land use pattern. There was also quite a bit of flash burning going on. And I noticed that there is little or none of the rectilinear patterns

that we usually see in cultivated areas. The land use patterns in this particular area were very much cellular. They obviously followed the topography rather than following the drainage

The cellular land use patterns shown in figures 10-5 to 10-7 are typical of those observed by the crewmen in parts of the Sahel and in Angola, Zaire, and Uganda.

In briefings to the astronauts before the mission, the authors described the general land use problem in the Sahel as overexploitation of the dwindling arable zone. These discussions did not include, however, a description of the characteristics of associated land use patterns because the appearance of such patterns from space was not known by the authors. Fanale (ref. 10-13) analyzed Landsat images and described these structures as concentric zones of traditional agriculture. At the village level, the concentric or subsistence land use patterns characterize settlement areas that are surrounded by cultivation and fallow zones. In parts of the Bandiagara Plateau of Mali (fig. 10-8), for example, the subsistence land use patterns identify the villages on the Gondo plains. Both the Skylab photographs and the Landsat images of this region show areas near population centers where the land is used intensively. In the Dogondoutchi region of Niger (fig. 10-5), intensively used areas appear as light-toned dots intermixed with mottled patterns. The Skylab 4 crewmen independently determined that the circular or cellular patterns they observed were local patterns of cultivated lands. These patterns, when viewed from space, provide a regional perspective of traditional African land use patterns. Interpretation of satellite data by the author has shown that, in parts of the Sahelian countries, villages and overused zones can be mapped from Landsat imagery. However, the Skylab 4 observations and photographs of the cell-like land use patterns in Tanzania, Zaire, Angola, and Uganda and in the Sahel are new information that can contribute to our understanding of the major similarities and differences between regional land use patterns in Africa where people engage in subsistence agriculture.

The Skylab photograph (fig. 10-6) shows clearly that variations exist in the subsistence land use patterns in the region south of Ségou in Mali drained by the Niger, Bani, Banifing, and Baoulé Rivers. Settlements are more concentrated near the Niger River than in areas drained

C-4

by the Bagoé River at the southeast corner of the photograph. Several villages shown in the southern portion of figure 10-6 appear as light-toned tiny dots.

Near the Niger River, intensive land use is indicated by the extensive white areas that grade into a pattern that is designated chromosomelike near the Baoulé River. Land use is less extensive in these areas and grades into a grainlike pattern where cultivation is restricted to small areas surrounding the villages. The appearance of the grainlike pattern is similar to that of cell nuclei seen through an electron microscope. This pattern is dominant in three distinct clusters in figure 10-6.

The factors that result in differences in land use patterns include topography, drainage patterns, cultural differences, land use activities (crops or animal raising), surface and ground water, and vegetative cover. The effect of drainage pattern on land use is illustrated in the Skylab 4 photograph (fig. 10-7) taken northwest of Lake Victoria between Zaire and Uganda. The intensive land use patterns seen in West Africa are not evident in this photograph. The type of land use activity carried on in this region of East Africa and the apparent density of vegetation in this area may explain the difference. Because much of this region is reserved for game parks, the land is not used extensively for cultivation.

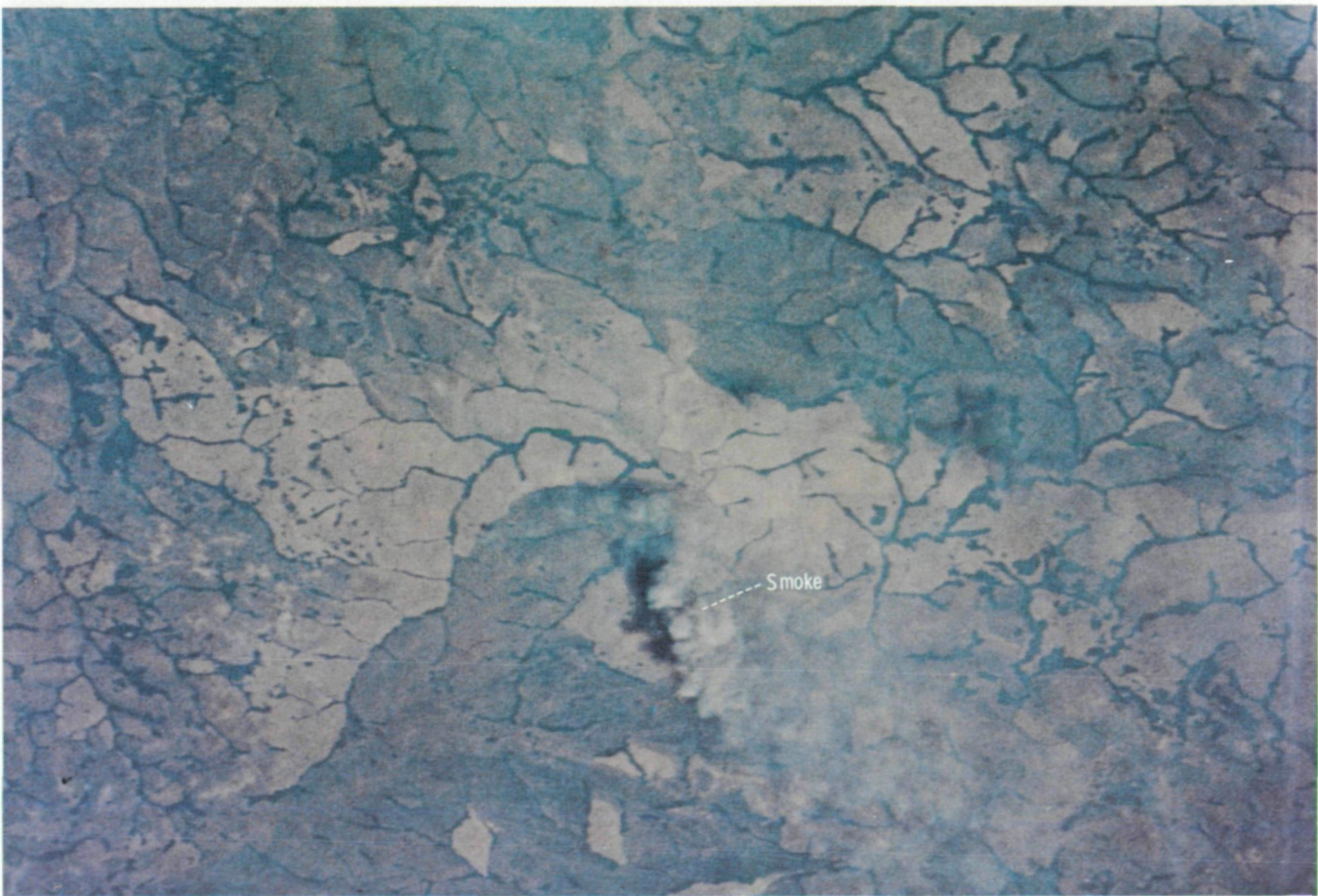


FIGURE 10-7.—Oblique color photograph of an area northwest of Lake Victoria, Uganda, showing the cellular land use patterns associated with dendritic drainage systems (SL4-209-8157).

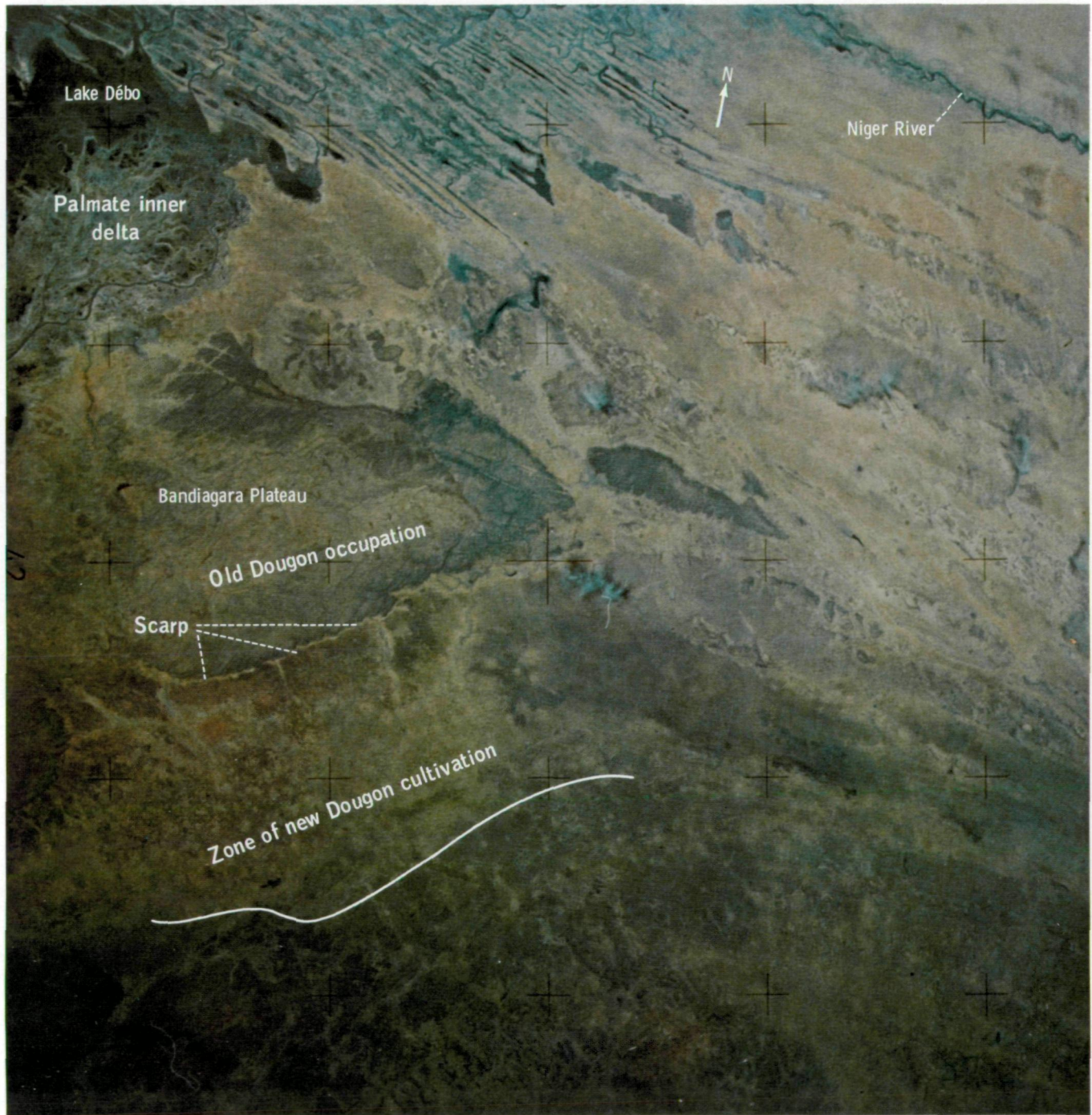


FIGURE 10-8.—An oblique color photograph of a portion of the Niger Inland Delta, Mali. The dominant structural trend is east-west and is most evident in the outcrops of the Bandiagara Plateau. A complementary set of features trends north. Sand dunes trend east-northeast (SL4-142-4497).

SKYLAB CONTRIBUTIONS TO ARID LAND RESOURCE MANAGEMENT

Two significant results that have been identified from the Skylab 4 Sahelian drought observational and photographic experiment include the development of a new dimension in the astronaut-observer/scientist-analyst team system for Earth observations and the formulation of the CA concept, a rehabilitative agricultural management process.

Evolution of the observer/scientist team system can be best illustrated by examples of the effect of crew observations on the development of the concept of aridification. The basic process of the experiment consisted of crew briefings, crew observations and data acquisition, postflight crew debriefings, and concurrent research activities that included field studies by the science analysis group at the Drought Analysis Laboratory.

The specific experiment objectives were to acquire data on Sahelian land use, hydrologic conditions (especially in the Inland Delta of the Niger River), and soil erosion and to identify the resolving capabilities of the crewmen to discern features in the Sahel. In pre-mission briefings, geographically small and specific features and phenomena for observations and photography were presented and discussed. As determined from postmission analysis, these requests for specific data were not satisfied fully by the crew because of unusually difficult viewing conditions during the mission and because of our lack of understanding of the crewmen capabilities. The role of the astronaut-observer was both active and passive; active in the perception and description of land-ocean-atmospheric systems and passive in the acquisition of requested photographs and observations (i.e., acting the role of a part of the remote-sensing equipment). The role of the scientist-analyst was similar, providing knowledge in a passive role and conceptualizing systems in an active role. The interaction of the two groups is crucial to optimize the process for Earth studies.

Also important was the role of the people of the Sahel. Their input was perceived in two modes: the evolution of present land use practices and personal interactions with the scientist-analysts. Government officials, politicians, nomadic and sedentary leaders, and, most of all, the many citizens who discussed the past, their present problems, and their aspirations and

perspectives have enlightened the scientist-analysts' understanding of the human aspects of the Sahel. This was not always an informed, scientific understanding, although cultural anthropologists are part of the Drought Analysis Laboratory. Instead, there has developed a realization of the cultural strength of the Sahelian people. Their culture is a crucial guide to rehabilitation programs, and only the Sahelian people can provide that guidance to their own future and to our understanding of appropriate measures to assist them in rehabilitating their region. The scientist-analysts can only assist them by providing insight about science and technology and information about the scientific aspects of the Sahel (i.e., mensuration of its climate, description of soils and vegetation, or regional nature of the Sahelian phenomena) to which neither they nor anyone else had access before the space age.

As a case in point, the authors were able to view the flood of the Inland Delta from Nimbus, the uniformity of the landscape from Skylab 4, and the geologic structure from Landsat-1 and Skylab 4 observations. As a result of observing Ekrafane Ranch from Landsat-1, replication of the ranch in similar regions was recommended, but these recommendations were transformed into a more acceptable cultural mode in which fences were virtually eliminated and the practice of transhumance (seasonal migration of cattle) was enhanced and stabilized. The transformation was based on the encounters with the people of the Sahel. Information was provided on the regional scale of resource phenomena. The people of the Sahel transformed the technical recommendations into their own cultural modality and then proceeded with implementation.

The contributions of three groups (the astronaut team, the research scientists, and the Sahelian resource users) to a useful definition of a dynamic natural resource base should be recognized. In this regard, the role of the astronaut team is vital; it demonstrates that neither the perceptions of the scientists nor the perceptions of the resource users provide information that is adequate to accurately describe and delimit the natural resource systems of a region. This contribution demands that, before making recommendations to solve resource management problems such as desertification, erosion, and silt accumulation in rivers and lakes, scientists must consider not only the perceptions of potential and actual users of resources but also the perceptions of "objective" observers, such as those from space.

At the time of the Skylab 4 crew briefing in August 1973, the generally accepted definition of desertification involved a gradual process of removal of vegetation and exposure of soil surface (ref. 10-14). Field studies in 1972 indicated the desertification process, as understood in Mali, was sand movement into cultivated fields; the perceived process was actual growth of the desert. By mid-1973, a very serious and extended drought was in progress in Africa. Although primary attention was focused on the Sahelian zone, there was an awareness of the need to consider climatic and other ecologic interactions between the Sahel, the Sahara, and the Sudanic savanna at the southern border of the Sahel. This was a limited view that was particularly changed through the Skylab 4 experiment observations.

Field studies had indicated that the Sahelian zone was "devastated" not by drought but by soil erosion. Through analyses of Landsat-1 data, the African village patterns were defined, but these occupancy patterns had not been related to the drought. Burning was known to be widespread in West Africa but was considered to be a localized phenomenon (i.e., the fire effects had a geographic scale identical to the fire itself).

Because of the premission concepts that (1) soil erosion was the principal observable feature set related to desertification, (2) the nature of the water resources in the northern Sahel was important for cattle production, and (3) dry river channels were possible areas for food production in a time of acute food shortage, the crewmen were requested to acquire data over Mali, and the Inland Delta in particular, that could be used directly. This was an error because it had been assumed that the Skylab 4 crew would see the surface as the scientist-analysts saw it and that the observing conditions would permit photographs of the clarity of Landsat-1 imagery but with better resolution. It was also assumed that the crew would see land use patterns as viewed from the surface and by Landsat-1.

Results from the mission have shown that, first, visual observations were hampered by fine dusts in the Sahelian atmosphere. The persistence and the opacity of the dust were, in combination, surprising and important. The significance emerged only after much discussion of the crewmen's commentary on the "blandness" of the Sahel. Observations from aircraft and field studies had shown that the Sahel was full of contrast, not bland. Second, viewing conditions presumably also prevented observations of contrasting plant communities, such as scrub or forest or cultivated fields. The crew's observations of vegetation and erosion pat-

terns in the Sahelian region provided the following three contradictory results.

1. West of the Inland Delta, the crew frequently and correctly identified the 200 000-hm² irrigated region of the Office du Niger as green and lush with huge western-type fields. Adjacent to the Office du Niger are large areas of traditional cultivation that were consistently not identified, although, on the Landsat-1 images of the area, the traditional land use patterns were identified for the crewmen during the briefing sessions.

2. The crewmen, as part of their onboard experience, devised a method for identifying the traditional land use patterns in other parts of Africa, with a direct result that similar patterns are now known to be far more extensive than previously thought. With this information and with field surveys to correlate satellite and ground data and the recognition of the extent of drought-affected regions, there emerged an understanding that the traditional land use pattern identified by the crew was indicative of a region in serious trouble. A premission review of the Skylab 3 television clip of Nigeria and Niger showed that the traditional land use pattern extended from the desert to the coast. Aridification was occurring not just in the Sahel but throughout West Africa and in the other African regions that the crew had observed.

3. The soil erosion features as observed on the ground were too complex and too small to be seen from Skylab. Instead, the crew observed sediments derived from soil erosion in the Niger River and erosion-related phenomena such as widespread burning, sandstorms, and dustiness. Actually, the crew was observing erosional activity *as it was occurring*, whereas the premission request was for them to observe erosion *after* it had occurred. The crew observed burning over much of East, Central, and West Africa, even in places where there was no apparent vegetation to burn (e.g., Mali); they saw the tan colors of sediment-laden rivers, noting the points of origin and extent of transport; and they saw sandstorms and duststorms in progress.

Although it was known that the West African atmosphere was dusty, and probably getting more so, it was not previously recognized that the source of the dust was not only the Sahara and the overgrazed Sahel but also the savanna and adjacent forested areas to the south. Crew nighttime observations of long firelines in Cameroun, Chad, and the Central African Republic together with daytime observations of smoke in the same regions emphasized the destruction of vegetation cover at the beginning of the dry season, opening enor-

mous areas to wind erosion for several months. Additionally, the crew reported the large-scale movement of smoke and dust north and south of the Equator. The occurrence and distribution of dust and smoke on a continental scale were new and significant contributions of Skylab in the study of arid lands.

In essence, the crew observations were anomalous in relation to the premission experiment objectives. An assessment of these anomalies led to a revision of the significance of processes or systems being observed and the interrelation of such processes that underlie the dynamics of Earth resources systems. By integrating the crew observations with scientific knowledge of the process or system (i.e., Sahelian drought), there emerged a global view of arid land dynamics and reordering of the importance of large-scale (dust, land use patterns, burning) and small-scale (surface water features) phenomena in the study of dynamic Earth systems.

The Skylab 4 crew observations, together with field studies, were used in the reassessment of the interaction between drought and land use management practices and, particularly, of the role of such practices in areas more humid than the Sahel. From crop and range management rehabilitation studies in the Sahel, it was deduced that such investigations should be extended throughout the West African zones where the climate is humid as well as arid.

Arid land research has been restricted, to a large degree, to the study of phenomena and processes within the desert itself. From Skylab, however, the discovery of widespread dust and smoke clouds and of the similarity of land use patterns adjacent to the Sahelian drought zone has led to the formulation of two closely related concepts: PAZ and CA.

The PAZ concept was developed from viewing Apollo 17 Earth entry photographs of Africa; from the mosaics of West African Landsat-1 imagery; from the Skylab 3 television clip of Nigeria, Niger, and Libya; from the early Nimbus III HRIR data; from the isohyets of Sahelian precipitation; and from vegetation maps. From these data, the clear sequence of desert, Sahel, Sudanic savanna, and Guinean savanna ecological zones emerges. The Skylab 4 crew observations provided the scope of dynamic interactions among the zones. From the work of Küchler (ref. 10-15), the concept of potential natural vegetation maps is derived. The classic works of Clements (ref. 10-16) and Shantz and Marbut (ref. 10-17) provided the ideas of climax vegetation and climatically controlled soil and plant for-

mations, respectively. From concepts used to define the idea of the potential productivity of the climax community, the potential agriculture concept is derived.

In the summer of 1974, analysis of Landsat-1 imagery in Niger resulted in the identification of four land use classes that corresponded to ecosystems. These classes were pastoral, mixed agriculture, sedentary, and intensive. For each of the use classes, a set of agricultural management techniques was recommended that corresponded to the capability of the ecosystem to sustain production of crops and livestock. Inherent in the recommendations was the concept of potential productivity based on the observations and concepts stated in the previous paragraph.

The process is not inherently different from the type of agricultural management recommendations made in the United States, where individual soil types and capabilities form the basis for management. There is, however, a significant difference. In the United States, agricultural management recommendations are based on the existing level of soil fertility; fertilization, crop protection, and cultivation recommendations are designed to overcome deficiencies in soil fertility and other environmental factors.

In the case of PAZ, management can be directed toward re-creation of the original level of fertility (i.e., that of the climax community). The climax community has a particular set of microenvironments that, in sum, is the climax environment; the climax environment forms the physical surroundings in which maximum sustained productivity occurs in nature. PAZ management is directed toward reconstitution of the climax environment through use of economic species (crop plants) that are physically similar to the species occurring in the natural climax community. When the replacement of natural species with economic crops is accomplished by man, the result, without fertilizers or crop-protection measures, is a severalfold increase in yield. This management process or technique is called CA (climax agriculture). Examples of the application of CA in the Sahel include range management at the Ekrafane Ranch, millet production in Niger, and peanut production in Senegal. To date, these have had inadvertent or unplanned results. (The CA concept is presented for the first time in this report.)

African land use patterns and their distribution provided a second major information parameter. The Skylab 3 television coverage along a north-south strip extended from the woodlands of Nigeria to the deserts of Niger and showed, for the first time, the surprising

uniformity in the appearance of cultivated areas despite the very real differences in rainfall. As the Skylab 4 crewmen became more familiar with the appearance of traditional agriculture patterns, they identified this pattern beyond West Africa in Central and East Africa. This particular pattern of land use, observed on a broad scale by the Skylab 4 crewmen and identified on a local scale in Landsat-1 imagery, is the pattern of stress and represents low productivity, whether induced by drought, overpopulation, or other causes. It represents a warning signal to those who rely on the agricultural subsistence system for food. In areas where such a land use pattern exists, widespread suffering from long-term lack of food may be expected. The pattern indicates that aridification is well underway. Both space observations and field studies show aridification to be a global process. Aridification is enhanced by devegetation, a process in which the vegetation is removed by cutting and burning. The vegetation is replaced only locally in national forests or on modern ranches.

On the basis of Skylab imagery analysis, the land use patterns that are warnings of advanced aridification can be identified in other arid regions and discriminated from those regions from which vegetation has completely disappeared. It may be possible, through examination of the space imagery of presently arid or desert regions, to discriminate between manmade deserts (where an end point of aridification has been reached) and natural deserts. In recognizing the traditional land use patterns in space imagery as indicative of aridification, the application of the CA concept to global studies can be undertaken.

The evolution of the Niger River Delta exemplifies the relation of land use patterns to aridification and desert formation. Historically, farming has been conducted in the upper Niger River basin for at least 5 millennia (ref. 10-18). In considering the long-term effects of land clearing for agriculture, particularly in a tropical region, one of the first is the loss of soil stability through loss of organic matter and a trend to reduction of permeability of tropical soils through formation of iron oxide concretions, as well as the loss of fine particles to windblown dusts and coarse particles through water erosion. The eroded soils lose their sediments to small streams and then to the Niger River. If there is more sediment than the river can carry, levee buildup begins and the channel bottom rises, as has happened

with the Yellow River in China. Eroding soils are infertile, and, where they exist, farmers must increase the size of the cultivated area to maintain the level of production, thus making soils susceptible to further loss of fertility. It is quite possible that Malian farmers, over the centuries, have lost sufficient soil to the Niger to raise the level of the channel and the bordering natural levees to significantly change the hydraulic gradient in the stream between Bamako and Ségou. The present hydraulic gradient between Ségou and Gao is less than 40 m in 1000 km of river, a very small amount. The topographic gradient from Ségou to the northwest is much steeper, and a river would easily flow in that direction.

Some evidence that this did occur is seen in figure 10-9, a Skylab photograph that shows a definite line linking Segala on the Niger River with Niono on the channel in the Office du Niger. A canal was constructed from the Niger River at Markala to Niono to allow Niger River water into the irrigation systems of the Office du Niger. Above the canal junction are numerous meanders in the northwest-trending stream. On the left side of the photograph is the trace of a dry river valley, the Vallée du Serpent. This valley can be traced on Landsat-1 imagery to a confluence with the Sénégal River. If the line between Segala and Niono was a former course of the Niger River and was blocked by levee building, the Niger River would flow past Ségou and into the Inland Delta. This is the present course, in fact. Because the Niger transports vast quantities of sediments, a young delta (such as the palmate delta inside the Inland Delta north of Mopti) could be formed (fig. 10-8). An ultimate effect of erosion and river sedimentation would be a reversal in the direction of flow of the Niger River, with subsequent migration of Sahelian peoples and extension of the Sahel zone of aridification.

The opening of new lands in the Sahel is still proceeding. A Skylab 4 photograph (fig. 10-8) shows the palmate inner delta and the Bandiagara Plateau where the Dougon people have lived for centuries. Approximately 75 years ago, they began to cultivate the Gondo plain to the east and are still expanding their cultivation in the plain. The zone of Dougon cultivation in figure 10-8 appears as a network of villages and fields. The fields are tan because of the large amount of open soil in cultivated areas as compared to the dark, vegetated

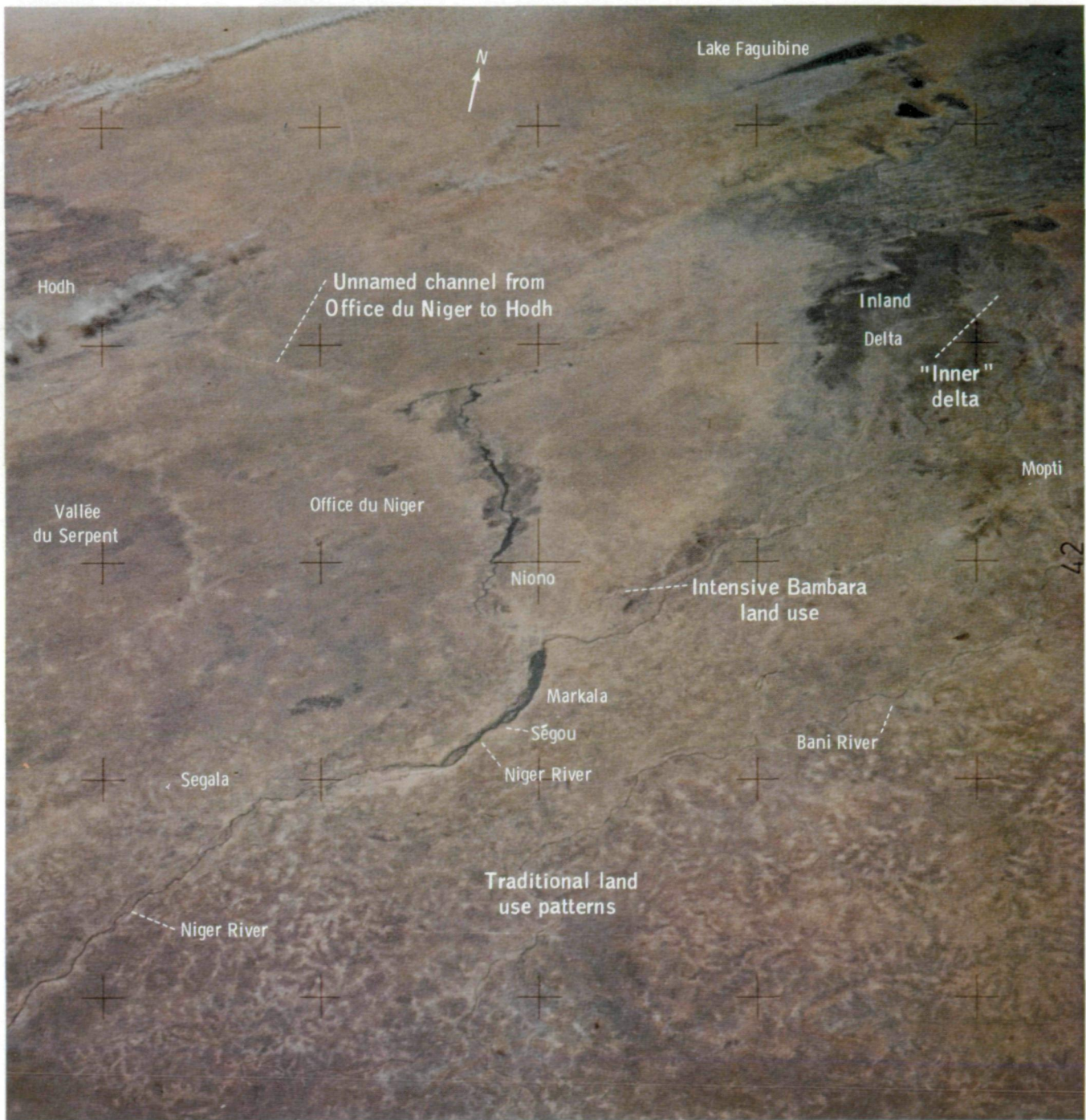


FIGURE 10-9.—An oblique handheld-camera color photograph of a portion of southern Mali. The Niger River is seen flowing northeastward into the Inland Delta at the upper right of this view, with Lake Faguibine immediately north of the Delta. Office du Niger, a cultivated region (left center), is irrigated by water from the Niger River (SI4-142-4579).

land. Villages appear as dark dots surrounded by fields. The frequency of villages decreases to the east; the decrease is an expression of "a new occupancy gradient." The forests are disappearing, and even the Dougon, reputed to be the best farmers in Mali, must now struggle with more arid conditions than were known to their fathers. In this photograph are seen the processes of new land opened for cultivation, of vegetation removal, of increased soil erosion, and of delta

sedimentation. These are the same processes that may have caused the Niger River to flow east, not west.

The significance of such a change in land use and subsequent river flow is that, in a region where there is now insufficient water for men and animals, there were once large cities, such as Kumbi-Selah, the capital of the ancient empire of Ghana, and other competing Saharan cities located in the deserts of southeastern Mauritania. Kumbi-Selah is said to have been a well-watered and



FIGURE 10-10.—A low-oblique color photograph of the Inland Delta of the Niger River in southern Mali. Lake Faguibine and several smaller lakes are just north of the Delta. The dominant structural trend is east-west, which is most evident in the central part of this view. Rock outcrops are seen between Lake Faguibine and the Niger River and in the Bandiagara Plateau (lower-right corner) (SL4-141-4361).

prosperous center of trade and agriculture. Today it is covered with Saharan sands. Can and should water be brought to that region again? Perhaps the first step is to stabilize (revegetate) the land again so that improvements will be permanent.

Skylab photographs provide other evidence that the flow of the Niger River has changed. The photograph in figure 10-10 shows that the fossil sand dunes of the northern delta are not dunes generated by the prevalent northeast wind (harmattan) system. In particular, the southernmost line of dunes extends to the east and the west of the delta and is aligned geographically with known regional tectonic lineations. These dunes do not have the fine structure of sand dunes observed in space imagery and instead may be sand accumulations controlled by tectonic faulting. These features are older than the present course of the Niger River, as indicated by their transection by the river. In contrast, at the southern end of the delta, sediment has filled and formed the braided river channels; that is, the sediments are younger than the channel (which is also structurally controlled).

In summary, the Skylab 4 study of arid lands has formed a framework in which the regional-scale processes of aridification can be determined. The linkage of humid area land use practices to the stability of arid regions is dramatically shown by the smoke and dust clouds originating not only in the desert but also in regions of tropical rain forest. The pattern of land use recognized by the Skylab 4 crewmen is now considered to be a warning sign of environmental problems and of immediate hazards for the practice of traditional subsistence agriculture and food production and survival.

In these analyses, there is an emerging awareness of the possibility of determining those deserts of the world that are natural and those that are the result of man's cultural action. The occurrence of dry valleys, as discerned from space imagery, can provide clues to desertification and associated aridification when integrated with analysis of land use patterns.

RECOMMENDATIONS

In future manned Earth-observing missions, the definition of systems that include a variety of problems and factors must be a primary concern. Development of a dynamic systems view of the Earth will require a dedicated, trained crew observer to record anomalous information, identify system interactions, and review and in-

tegrate with the scientist-analyst the concepts, the data acquisition priorities, and the planned observational and photographic program. The result will be the improvement in knowledge that the Skylab 4 experience proved possible.

Crewmen training for observations on Shuttle missions should include intensive training in ecological subjects. Such training will provide them with an understanding of the interrelationships of soil, water, vegetation, and human occupation patterns that is essential for making correlative and interpretive observations. These interrelationships are expressed as subtle but recognizable differences in the land surface. In addition to such training, sensors for direct use by crewmen should be developed to permit observations of phenomena outside the visible spectrum. Further, a major effort should be made to integrate data from unmanned satellites and to provide observers in orbit with the output from resource information systems now being developed. The Skylab 4 crewmen demonstrated clearly that the synthesis of information by orbiting observers does lead to new and important insights regarding the condition of the surface of the Earth. Further training, special sensors, and a continuous information linkup will provide the capability for man in space to exploit his special abilities.

REFERENCES

- 10-1. MacLeod, N. H.: Can the Sahel Be Saved? War on Hunger, vol. 8, no. 6, 1974, pp. 9-13.
- 10-2. MacLeod, N. H.: Observations of the Inland Delta of the Niger River by Nimbus 3 High-Resolution Infrared Radiometer (HRIR). NASA TM X-65469, 1970.
- 10-3. MacLeod, N. H.: Spectral Reflectance Measurements of Plant-Soil Combinations. Fourth Annual Earth Resources Program Review, Vol. I, Manned Spacecraft Center, Houston, Texas, 1972, pp. 6-1 to 6-11.
- 10-4. Ibn Battuta (H. A. R. Gibb, transl.): Travels in Asia and Africa, 1325-1354. G. Routledge (London), 1953.
- 10-5. Leo Africanus, Joannes: The History and Description of Africa. English translation in 1600, Robert Brown, ed., The Hakluyt Society (London), 1896.
- 10-6. Caillié, René: Travels in Central Africa to Timbuctoo and Across the Great Desert to Morocco, Performed in the Years 1824-1828. Barnes and Noble, 1968.
- 10-7. Park, Mungo: Travels in Africa. Nelson (Edinburgh), 1841.
- 10-8. Barth, Heinrich: Travels and Discoveries in North and Central Africa. Vols. 1 to 3, Harper & Bros. (New York), 1859.

- 10-9. Ptolemaeus, Claudius (Edward Luther Stevenson, transl.): *Geography of Claudius Ptolemy*. New York Public Library, 1932.
- 10-10. Deshler, Walter: *An Examination of the Extent of Fire in the Grassland and Savanna of Africa Along the Southern Side of the Sahara*. Proceedings of the Ninth International Symposium on Remote Sensing of Environment, Vol. 1, Environmental Research Institute of Michigan, 1974, pp. 23-30.
- 10-11. Anaejionu, P.: *African-American Investigations of Resources Development Problems in West Africa Using Satellite Data*. Resources Analysis Laboratory, American University, 1975.
- 10-12. MacLeod, N. H.: *Use of ERTS Imagery and Other Space Data for Rehabilitation and Development Programs in West Africa*. Paper presented at the Seminar on Space Applications of Direct Interest to Developing Countries, São José dos Campos, Brazil, June 1974.
- 10-13. Fanale, Rosalie: *A Utilization of ERTS-1 Imagery in the Analysis of Settlement and Land Use of the Dogon in Mali*. M.S. Thesis, The Catholic University of America (Washington, D.C.), 1975.
- 10-14. Aubréville, André: *Climats, Forêts et Désertification de l'Afrique Tropicales*. Société d'Éditions Géographiques, Maritimes et Coloniales (Paris), 1949.
- 10-15. Kùchler, August Wilhelm: *Vegetation Mapping*. Ronald Press Co., 1967.
- 10-16. Clements, F. E.: *Experimental Vegetation, the Relation of Climaxes to Climate*. Pub. No. 355, Carnegie Institution of Washington, 1924.
- 10-17. Shantz, H. L.; and Marbut, C. F.: *The Vegetation and Soils of Africa*. Published jointly by National Research Council and American Geographical Society (New York), 1923.
- 10-18. July, Robert W.: *A History of the African People*. Second ed., Scribners, 1974.

11

Visual Observations of the Ocean

ROBERT E. STEVENSON,^a L. DAVID CARTER,^b
STEPHEN P. VONDER HAAR,^c
AND RICHARD O. STONE^c

THE CAPABILITIES and techniques of observing the ocean from space by the three Skylab 4 astronauts (Col. Gerald Carr, Col. William Pogue, and Dr. Edward Gibson) have been compared to the interpretations by the authors (Stevenson, Carter, Vonder Haar, and Stone) of the same or similar features, from photographs taken by the crewmen. This analysis showed that men with only a cursory knowledge of the ocean, backed by scientists listening and advising from the ground, can indeed make visual observations that accurately describe major dynamic conditions of the sea. Furthermore, the Skylab 4 crewmen were able to see colors, subtle textural differences, and ocean/atmospheric manifestations of the sea surface that cannot be seen in the best space photographs. However, there are some conditions of the ocean that are not suited to visual observations. These are ocean features that are either too small or near shorelines where they become "lost" among the multitude of coastal features. These are more easily interpreted from photographs than from visual observations.

The observational capabilities of men in orbit substantiate the contention that the sea surface reflects major dynamic motions in the upper ocean. In the late 1960's, Dr. Gifford C. Ewing made the analogy (ref.

11-1) that the classic technique of studying the ocean by lowering sampling equipment on lines from ships into the depths was like reading the Sunday edition of The New York Times by laying it flat on the living room floor, sticking it with pins, and laboriously reconstructing the ink stains on the pins into the words and sentences hidden in the pages. Clearly, years would be spent in such an attempt, and there would be an overwhelming number of possible letter and word combinations to consider. When a logical story finally could be established for any given section or layer, the "news" would long since have become outdated.

The obvious question was, therefore, "Why not read the front page (the sea surface)?" One would at least know the major "news stories" (ocean features) and have a hint of what was inside (in deeper layers). Before the Skylab missions, the answer was, "Whether there is enough information on the front page is not known, and what is there appears as nearly undecipherable hieroglyphics." In other words, scientists could not read the "front page"; the sea surface was a mystery.

As with all unknown languages, translations can be constructed cipher by cipher. The interpretation of Gemini and Apollo photographs was providing some clues, but one could not be sure whether or not all the ciphers had been recorded (i.e., whether or not all the sea-surface features had been photographed). The coordination of visual observations and photographs from Skylab could provide, therefore, a concentrated translation effort, a chance to make a real advancement in reading the surface of the sea.

^aOffice of Naval Research Branch Office, Pasadena, California.

^bU.S. Geological Survey, Menlo Park, California.

^cDepartment of Geological Sciences, University of Southern California, Los Angeles, California.

For a century, oceanographers were constrained by the limited mobility of their prime sampling platform, the research vessel. This limitation required that scientists emphasize features spread over degrees of latitude and make conclusions based on a concept of an ocean "frozen in time" (refs. 11-1 and 11-2). Obviously, only the gross anatomy of the ocean could be recognized; its turbulent rhythm remained virtually unknown. Early investigators had to be satisfied, though frustrated, with sampling frequencies measured in days, years, and even decades and over intervals of tens to hundreds of kilometers.

A vast change has occurred in the past two decades from the leisurely sampling of pre-1950 days. New measuring devices, sensors measuring the sea in several spectral bands, and the adaptation of computer technology have permitted measurements to frequencies as high as kilohertz and lengths short enough to approach molecular dimensions (refs. 11-3 and 11-4). Together with these capabilities has come the recognition that the stratified ocean contains a spectrum of highly anisotropic turbulence with scales of eddies extending from near molecular dimensions to essentially global. The key to reliable forecasts of the ocean and the atmosphere lies in knowing how energy is exchanged up and down the scale of turbulence (ref. 11-5).

By the late 1960's, it was evident that new data collection and analysis techniques were required to study the energy fluxes through these scales of turbulence. Furthermore, investigators knew they must study the scales of motion "in concert," not in isolation. It would be of particular importance to establish the quantitative relations between the various scales, because in those quantities lie the basic variations in weather and climatic changes.

At about the same time, the world's climate became a topic of discussion and concern. To many people came the news that climates change, that our grandfathers really did struggle through deeper snows than those of today or drier, dustier streets, as the case may be, and that civilization may face similar conditions once again. The reality of climatic change became a subject for national and international concern. From that concern have come the beginnings of organized research experiments directed toward a clear knowledge of energy transfer in the ocean and atmosphere. An example is the North Pacific Experiment, in which 50 scientists

from 7 universities have begun efforts to establish the relationship between the Pacific Ocean and weather systems over the North American continent.

Also, in the late 1960's, a few hydrodynamicists studying turbulence in air and water had come to a unique conclusion on the origin of eddies (ref. 11-6). Ironically, the most significant observations in their research were made visually rather than with sophisticated electronic instrumentation and computer techniques (ref. 11-7). The essence of these observations is that turbulent flows are not chaotic as presumed heretofore. There is order in the motion with an observable and repeatable chain of events. Furthermore, it was ascertained that the vortexes retained their coherence downstream (coalesced, in fact), implying a strong conservation of vorticity.

This revelation resulted in many new experiments. By mid-1973, it was known that such turbulent features could be reproduced in air and water along boundaries of currents that have differing velocities, differing densities, or differing temperatures. That such turbulence could be formed and maintained in the ocean was yet to be established (refs. 11-8 and 11-9).

It was in this "atmosphere" of research activity that the Skylab missions were flown. The time was perfect for the ocean data gathered by the crew to be readily incorporated into ongoing research. Such a quick integration of unique data into the general flow of scientific information is unusual. More commonly, a decade passes before new ideas are accepted. The Skylab Program, however, came at a propitious time; a time in oceanography when major efforts were being made to establish a firm understanding of the ocean's role in worldwide climate.

Even though laboratory studies had now defined the origins of many turbulent eddies, until November 1973 there was no clear, convincing evidence that similar vortexes, formed by shear stresses along the boundaries of currents, existed in the open ocean (ref. 11-10). Some 30 years before, Spilhaus (ref. 11-11) had encountered distributions of water temperatures in the Gulf Stream which he thought could be the result of eddies 15 to 40 km in diameter. There was no further study to confirm his thoughts. A number of scientists have surveyed eddies forming from loops in major ocean currents (such as the Gulf Stream and Kuroshio), but these are not

formed as a result of a sequential turbulence regime (ref. 11-12). Then, in 1973, Bernstein, in evaluating hydrographic data gathered by personnel of the Bureau of Commercial Fisheries during expeditions in the trade

winds off Hawaii, interpreted periodic water temperature changes as eddies with diameters of 100 km or larger (ref. 11-13). There were no data showing continuity or persistence, but he suggested that continuity

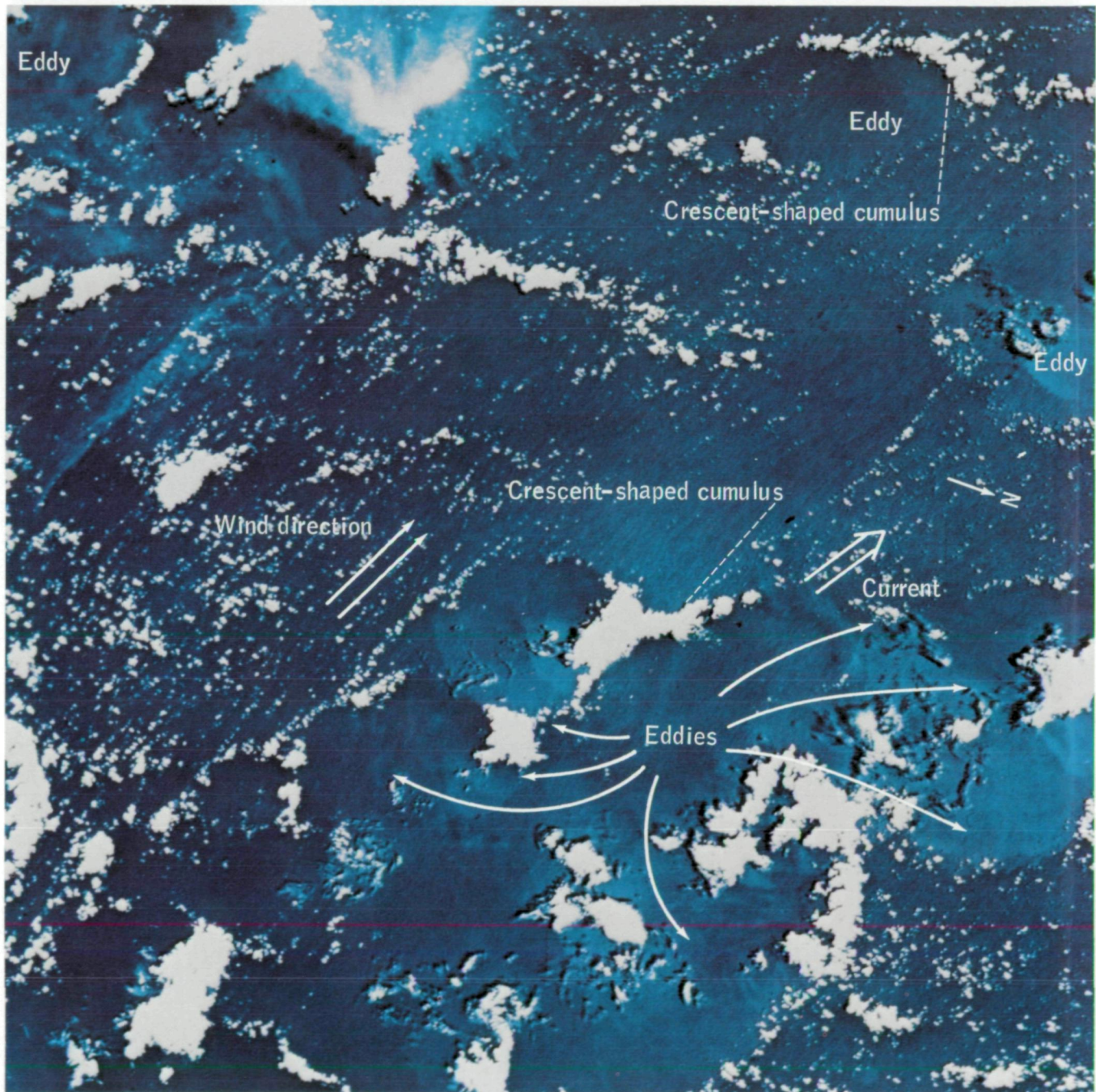


FIGURE 11-1.—The northwestern Caribbean Sea, photographed in the summer of 1973, had linear cloud streets, oriented with the southeast trade winds, interrupted by oval-shaped clear patches of sky. Circular ocean eddies are clearly defined in the cloudless areas (SL2-10-072).

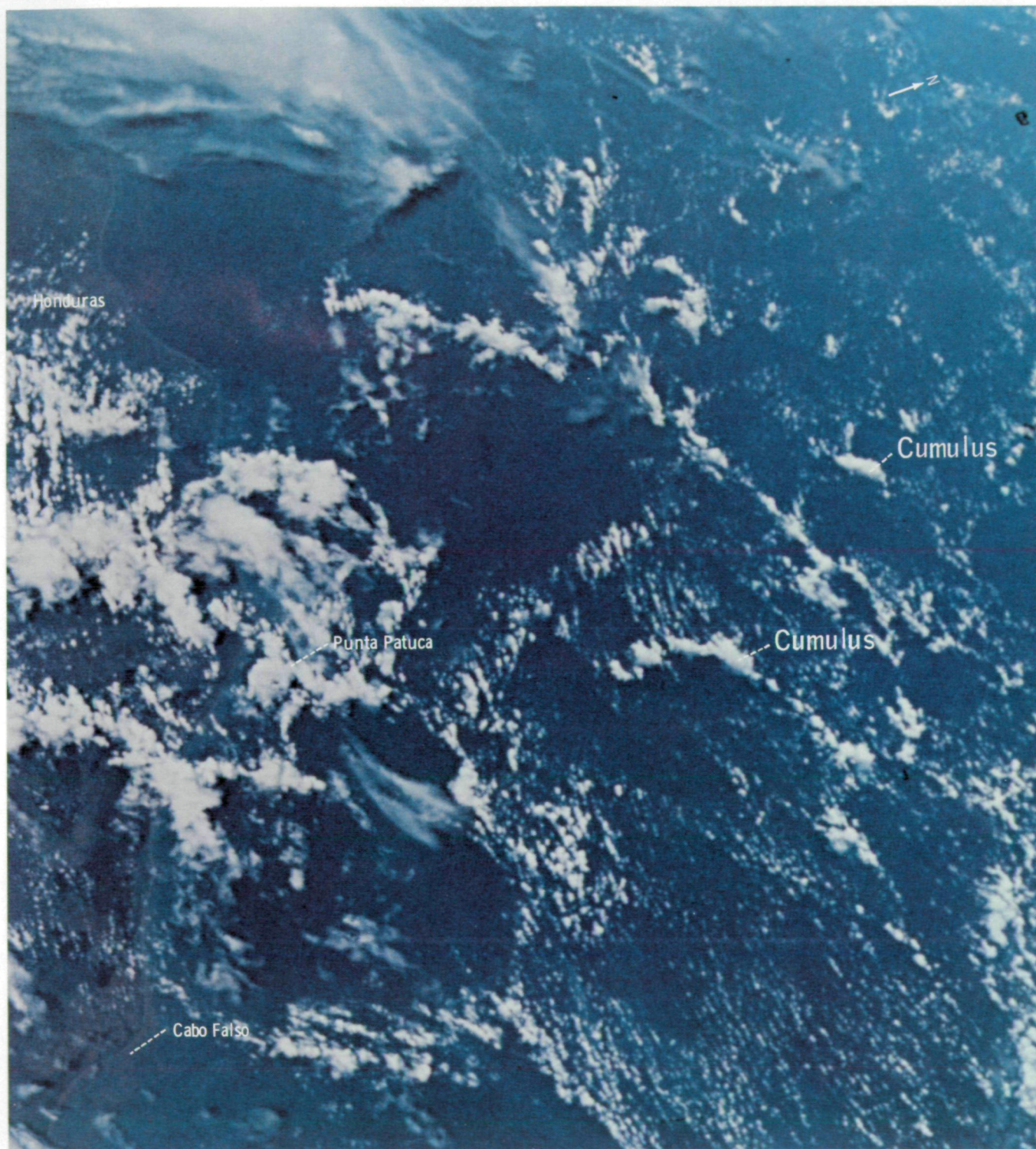


FIGURE 11-2.—Skylab 4 crewmen were unable to see the ocean surface expression of cold-core eddies on December 6, 1973, when this photograph was taken over the northwestern Caribbean Sea. The typical crescent-shaped towering cumuli were visible, however, east of Honduras (SL4-196-7384).

could be defined from time-series data taken at several fixed ocean stations (such as buoys or weather ships). None of these scientists had any opportunity to acquire and evaluate data of coherent turbulence along the boundaries of currents. There was a rapidly growing recognition, however, that turbulence of all scales might extend throughout the ocean. Consequently, the discovery of cold-core eddies in warm-water currents, interpreted from Skylab photographs, was significant (ref. 11-14).

From stereophotographs taken during the Skylab 2 mission (May and June 1973) over the northwestern portion of the Caribbean Sea (fig. 11-1), elliptical features that looked like pockmarks on the sea surface were noted by the senior author. To the left of the current axis were what appeared to be cyclonic vortexes that ranged in diameter from 5 to 30 km. There was (1) a smoother sea surface within the eddies than outside, (2) a disruption of the wind-driven Langmuir circulation in the sea surface and the overlying atmosphere, (3) towering cumulus arranged in a crescent shape over the down-current boundary, and (4) clear skies over the eddies. These conditions indicated that the surface water temperatures in the eddies were cooler than the surrounding water temperatures of the current and that waters warmer than those of the open current were on the down-current border.

On December 5, 1973, a message was transmitted to the Skylab crewmen in which the eddies and their associated cloud features were described. The crewmen were requested to make visual observations early the next morning as the spacecraft crossed the Caribbean Sea. At 7:30 a.m. local time on December 6, the characteristic clouds were indeed seen by all three crewmen, but the Sun angle was too low to permit examination of the ocean surface in the Sun's reflection (fig. 11-2). The following day, on a parallel orbital pass 330 km to the east, the onboard television scanned the Caribbean Sea, and the crescent-shaped clouds associated with the eddies were monitored from Cuba to the coast of Colombia.

A message was subsequently transmitted to the Skylab crewmen suggesting six other ocean areas where they should observe and obtain photographs of cyclonic eddies. As a result, the turbulent features were observed in four of the six areas (Coral Sea, North and South Equatorial Pacific, western South Atlantic); the other two being omitted because of crew sleep cycles and the low Sun angle for observations. In addition, eddies with similar surface manifestations, but without the tower-

ing cumulus, were observed east of New Zealand and in the Pacific north of the Hawaiian Islands. These latter observations confirmed the concept that eddies of such magnitudes would be present wherever there were conditions suitable to their formation, regardless of water temperature, and that eddies in warm currents were simply easier to see (and photograph) because of the associated cumulus clouds.

There were yet no definitive data of the water temperatures, depth in the water to which the eddies extended, or the magnitude to which the eddies modified the ocean temperatures. Consequently, on January 24, 1974, a long-range aircraft from the Navy's Weather Reconnaissance Squadron Four flew over the northwestern Caribbean Sea, dropping air expendable bathythermographs (AXBT's) along two lines, each approximately 300 km long. Heading south, the aircraft followed a flight line directly beneath the orbital track of Skylab (the spacecraft was over the area just as the first AXBT was dropped) and over waters on the left side of the core of the Caribbean Current (fig. 11-3). An AXBT was dropped every 15 km (about once every 3 minutes of flight time) on both tracks. After completing the first leg, the pilot flew the plane to the east 90 km and then followed a northerly course over the axis of the current.

The temperature profiles (fig. 11-4) indicated eddies along the length of the first flight line and a deeper thermocline and eddies of lesser intensity along the "current-core" flight line. Although there were distinct differences in surface temperature, the greatest change in the ocean's thermal structure was the vertical displacement of the typically flat, deep-lying thermocline.

Turbulence in currents does not form spontaneously, as was pointed out by Defant (ref. 11-15) in 1961, so it was logical to consider the possible origin of the eddies. The two most likely possibilities were (1) sea-floor irregularities projecting into the surface layers and (2) shear stresses along discontinuities in the current.

Because the eddies were seen, and photographed, in ocean currents flowing in great depths of water, it seemed most probable that the turbulence originated from shear stresses across the velocity profile of the currents. In every ocean current where the eddies have been observed, the current velocity diminishes sharply over distances of but a few kilometers from that in the current core. Furthermore, the eddies are always noted on the side where rotation would produce cold water in the center of the eddy. (There should, of course, be eddies formed on the opposite side of the current, but the

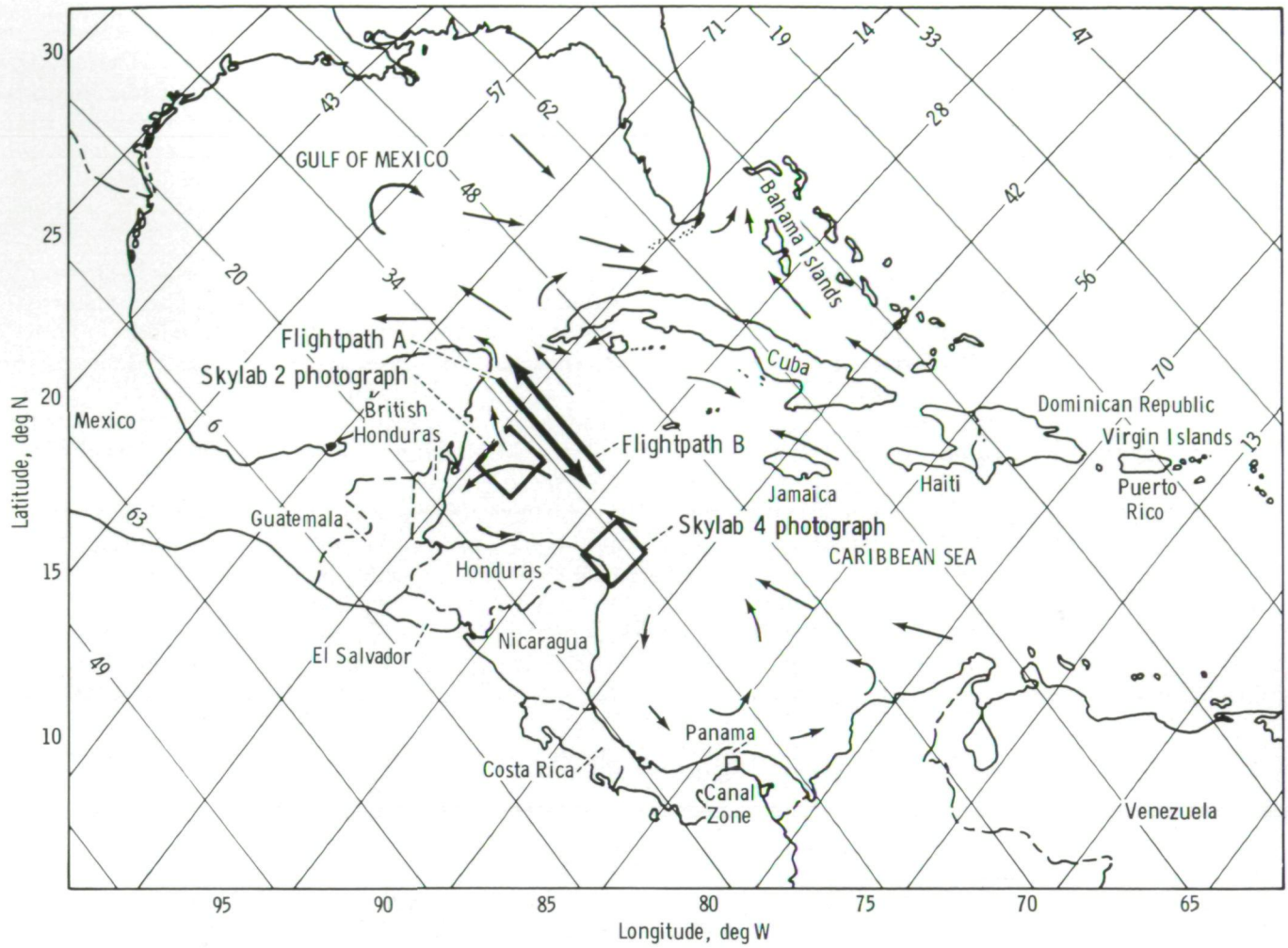


FIGURE 11-3.—Map showing surface currents in the Caribbean Sea and the Gulf of Mexico. Also included are the flightpaths of the aircraft which dropped AXBT's. Skylab orbits are shown by numbered lines.

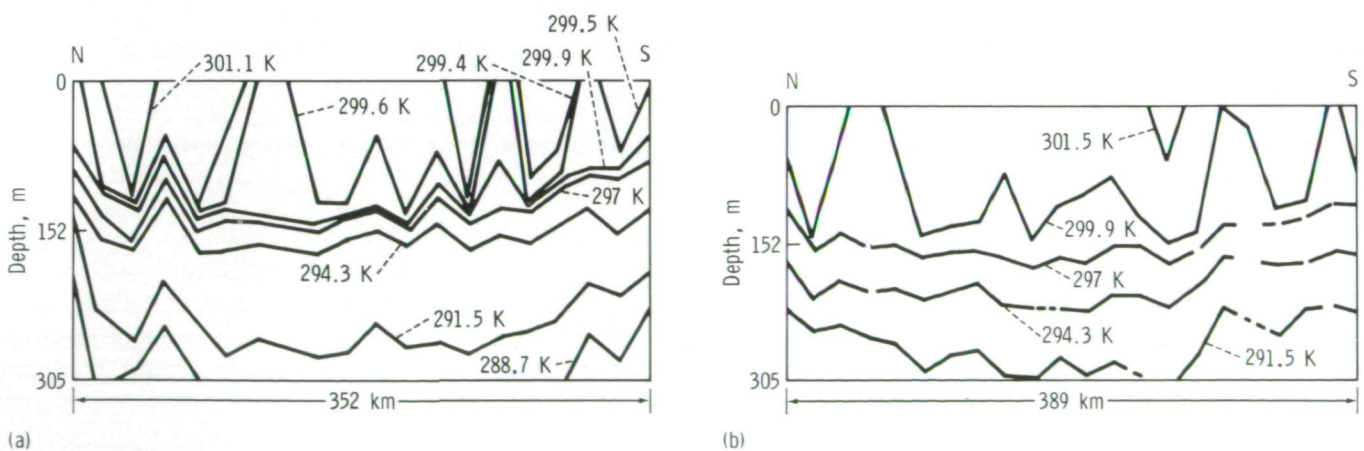


FIGURE 11-4.—Profiles of water temperatures in the northwestern Caribbean Sea developed from AXBT's dropped January 24, 1974. (a) Flightpath A (18:20 to 20:01 GMT). (b) Flightpath B (20:25 to 21:38 GMT).

cores would be warm and at that time the cloud forms that would be associated with warm-core eddies had not been defined. That was to come later, in 1975, through the work of Dr. Paul Scully-Power and Paul Twitchell (ref. 11-16.)

All the evidence seemed to point to an origin similar to the turbulent features studied in the laboratory by Liepmann (ref. 11-17) and, most recently, Brown and Roshko (ref. 11-7). The development and growth of the eddies as they move downstream in the laboratory (fig. 11-5) seemed to correspond with the Skylab observations. Should the Yucatan-type eddies be of this origin, then they must be expected to decrease in number and increase in size in a down-current direction; conserving vorticity through the sequence.

Such data were not obtained from the Skylab missions. What was learned from this experiment, however, is that definitive observations of the dynamic ocean can be accomplished from orbital heights, and that scientists on the ground and crewmen in space can communicate in a ready, timely fashion so that unique oceanographic events can be examined from the space laboratory.

ANALYSIS OF THE SKYLAB 4 OBSERVATIONS

More sea observations were made during the Skylab 4 mission than during all previous manned space flights. A compilation of 11 oceanic features seen by the crewmen (table 11-I) indicates that 70 percent of the observations were of currents, eddies, and sediment moving along coasts or entering an ocean from rivers. Of that 70 percent, currents accounted for 41 percent of the observations, eddies 16 percent, and sediment 13 percent.

The repeatability of the visual observations during the entire 84-day mission, even though there was a wide geographic range of observations, is shown in table 11-II. For example, using table 11-II and starting on the subtotal line, on 17 occasions observation of a given area was repeated twice for a specific ocean feature; three times for sediments, on four occasions for eddies, three times for waves, etc. The three sediment locations were the Mississippi Delta, the Bay of Fonseca, and the Rio de la Plata. A resulting "couplet" would be

FIGURE 11-5.—Eddy sequence formed from a velocity shear at the highest Reynolds number ever attained in a flume. The work was done at the California Institute of Technology, and the photograph was taken by Dr. Anatol Roshko (ref. 11-7). →



TABLE 11-I.—Skylab 4 Crewmen's In-Flight References to Oceanic Features

| Feature mentioned | Total sightings recorded |
|---|--------------------------|
| River and coastal sediment entering ocean | 28 |
| Volcanic sediment entering ocean | 6 |
| Duststorm sediment entering ocean | 5 |
| Seamounts | 4 |
| Atolls and shoals | 4 |
| Island wakes | 14 |
| Eddies | 39 |
| Distinct wave patterns | 15 |
| Currents | 93 |
| Upwelling | 15 |
| Unexplained major turbulence | 2 |
| Subtotal | 225 |
| Additional coastal and ocean areas (mentioned by name but no details presented) | 180 |
| Total | 405 |

coastal sediment/Mississippi Delta. Repeated observation of a given couplet ideally would occur 10 or more times, but a more realistic goal for a future space flight is 4 observations. These repeated couplets form the building blocks for understanding dynamic ocean processes.

Clouds obscured oceanographic targets in 15 instances during the Skylab 4 flight. However, on 15 other occasions, the crewmen cited clouds as being associated, and perhaps dynamically linked, with ocean features. Sunlight was reported 33 times as a useful tool for observation of ocean surface textures.

The orbital characteristics of the Skylab spacecraft increased the opportunity for repeated crew observations of specific sites. For example, the converging orbital paths between latitudes 40° and 50° S increased the crewmembers' data-gathering time over the region of the Falkland Current. Review and evaluation of the 38 observations of this current system indicate that the quality and usefulness of visual observations increased with additional time for observations and with growing crew familiarity with the feature.

While in space, the crewmembers had only a limited amount of time allocated for visual observations; thus, they emphasized the description and location of individual features. During the debriefing, however, it was learned that the crewmen were actually able to synthesize descriptions of features and to suggest possible origins. Table 11-III is a summary of 28 different oceanographic features emphasized by the crewmen during debriefing.

Examination of the photographs was done in two steps. Initially, each transparency was scanned (refs. 11-18 and 11-19) to permit the investigators to become completely familiar with the general content of the im-

TABLE 11-II.—Index of Repeated Observations for Ocean Feature/Location Couplets

| Specific location/ocean feature | Number of observations and citations | | | | | | | | | | | |
|---|--------------------------------------|----|----|---|---|---|---|---|----|----|----|----|
| | 1 | 2 | 3 | 4 | 5 | 7 | 8 | 9 | 10 | 11 | 12 | 38 |
| Sediment along coasts and entering from rivers | 17 | 3 | 2 | — | — | — | — | — | — | — | — | — |
| Eddies | 17 | 4 | 1 | — | — | — | — | — | — | 1 | — | — |
| Waves | 15 | 3 | 1 | 1 | — | — | — | — | — | — | — | — |
| Seamounts, atolls, and shoals | 6 | 1 | — | — | — | — | — | — | — | — | — | — |
| Island wakes | 10 | 2 | — | — | — | — | — | — | — | — | — | — |
| Volcanic sediment entering ocean | 1 | — | — | — | 1 | — | — | — | — | — | — | — |
| Duststorm sediment entering ocean | 5 | — | — | — | — | — | — | — | — | — | — | — |
| Unexplained major turbulence | 2 | — | — | — | — | — | — | — | — | — | — | — |
| Currents | 17 | 4 | — | 1 | — | — | 1 | 2 | — | — | — | 1 |
| Subtotal | 90 | 17 | 4 | 2 | 1 | 0 | 1 | 2 | 0 | 1 | 0 | 1 |
| Oceanic location mentioned but not coupled to a feature | 45 | 17 | 7 | 4 | 7 | 2 | 0 | 0 | 1 | 1 | 1 | 1 |
| Total | 135 | 34 | 11 | 6 | 8 | 2 | 1 | 2 | 1 | 2 | 1 | 1 |

ages, scale variations, cloud appearances, subtleties of color and tone changes on water, and the range and type of features that can be recognized. The preliminary study was followed by detailed examination of the photographs using (1) a light table and a hand magnifying glass, (2) a projector to view the images on a screen, and (3) a binocular microscope with a special light arrangement and a zoom lens (magnification $\leq 30\times$). As the work progressed, the first and third techniques were found to be the most effective. In the later stages of the work, investigators used the light table and magnifying glass almost exclusively.

During the examination, the oceanographic phenomena that could be discerned from the transparencies were recorded without reference to the visual observations data. Then, transcripts pertinent to each photograph were read, and the visual observations data were compared to the written analysis of the features in the photograph. In this way, investigators could evaluate both separately and comparatively the quality of the data present in both the photographs and the transcripts.

A comparison of the photographs with the crewmen's in-flight descriptions makes it evident that the crewmen were able to distinguish details and to discern color differences not apparent on the photograph. They confirmed this ability during the debriefing when they stated that photographs did not adequately record the colors and details observed from orbit. For example, on December 10, 1973, the Skylab 4 science pilot described in detail the upwelling along the coast of Chile. He was able to determine on the basis of color contrasts produced by plankton concentrations that circulation was away from the coast. As the water moved away from the coast, the science pilot could see eddies and thin, tenuous arms and stringers because of the color contrasts. On the photographs, one prominent eddy is visible, but the detailed information contained in the crewman's description is not evident. Had the photographic system been equal to the eyes of the crewman, an accurate map of the turbulent features of upwelling and offshore moving water could have been made.

The potential value of handheld-camera photography in conjunction with descriptions from visual observations is threefold:

1. As a permanent record of the features observed
2. As a base for accurate mapping of observed features
3. As a source of data for features not described but within the field of the photographs

For the realization of this potential, a manually controlled photographic system comparable to the multispectral cameras flown in the Skylab Earth resources experiment package (EREP) is necessary.

STUDIES OF OCEAN RESOURCES AND DYNAMICS

The following selected examples illustrate the contributions and potential contributions of Skylab 4 visual observations and handheld-camera photography to studies of ocean resources and dynamics. Most of the examples are of concurrent visual observations and photography; the greatest potential for data acquisition is in the combined use of these two methods. However, visual observations alone can provide valuable information, and photographs are useful data sources even without visual observations. Examples of contributions to both regional and topical studies are included. In general, the topics correspond closely to observation experiments established before the flight.

New Zealand Region

Skylab 4 visual observations and photographic data of oceanic features in the vicinity of New Zealand were recorded on 12 days in December 1973 and January and February 1974. During this period, currents, eddies, upwelling, plankton, internal waves, coastal-sediment plumes, and the Subtropical Convergence were described and/or photographed.

Observations of the coastal and offshore regions of New Zealand were recorded 21 times by the flightcrew, and 12 observations were accompanied by detailed descriptions. Information compiled from the crewmen's observations is generalized in figure 11-6. Oceanic features were described as manifested by contrasts in water color except in early February, when the D'Urville Current through Cook Strait was viewed in sunglint. With one exception, the observed flow patterns conform to the published circulation chart of the New Zealand region (fig. 11-7), but the color contrasts are of special interest because blue-green streaks and blotches offshore possibly indicate the presence of plankton.

The D'Urville Current flows eastward between North and South Islands and was described in five instances by the crewmen. In each case, the color pattern

TABLE 11-III.—Skylab 4 Debriefing Comments About Ocean Features

| Feature | Process | Occurrence |
|--|---|--|
| Surface Texture | | |
| Linear features (streamlines and streamline flow patterns) | Ocean current | Between North and South Islands, New Zealand Between Tiburon Island and Mexican mainland, in the Gulf of California |
| Curved, arching lines | Current boundary or interface; possibly associated with turbulence | |
| Ropy, intertwining, stringy Eddies | At a current contact Formed within currents Formed by peeling or being shed off a current or by pinched-off intertwining currents | Falkland and South Equatorial Currents Humboldt off western coast of South America Bay of Fonseca, Gulf of California, southern portion of Falkland Current, in Falkland and South Equatorial Currents |
| Smooth or slick topped | Perhaps associated with wind and/or upwelling; usually in lee of islands; perhaps a diffused wake, not an interface | |
| Sinuuous to linear "demarcation," 115 km long, commonly shorter | Unknown | |
| Cusps (roughening or smoothing of ocean surface) | Often associated with cumuli | |
| Round structure: approximately 160 km diameter | Unknown | In Gulf of Fonseca |
| Vortexes | Current intersections and intertwining | Falkland and South Equatorial Currents |
| Sinuuous, serpentine patterns; streamings, figures "8" and "S" | Current intersections and intertwining | |
| "C" eddies (mustache pattern) | Turbulence in lee of an island | Chatham Island |
| Sharp linear or nearly linear interface in open ocean or near land | Possibly due to wind effect | Near Kangaroo Island |
| Albedo | | |
| Albedo difference in lee of islands | Unknown | New Guinea and northwestern Australia |
| Wakes | | |
| Wake in water | Island disrupting current flow, usually a simple wake relative to atmospheric wakes | Solomon Islands, Furneaux Island Group, Antipodes, Bougainville, and New Hebrides |
| Wave patterns | | |
| "Corduroy sea," very fine, always present, hundreds in number | Surface swell overlying internal waves | |
| "Rug effect," width-to-length ratio of about 5 to 10, parallel | Unknown | In Atlantic Ocean |
| Arcuate-shaped sets of 6 or 7 | Internal waves | |
| Sets of 7, 4, etc., always adjacent to a sharp boundary | Unknown (likely internal waves) | Worldwide |
| In lee of islands | Current disrupted by islands | Antipodes |

TABLE 11-III.—Concluded

| <i>Feature</i> | <i>Process</i> | <i>Occurrence</i> |
|---|--|--|
| Color differences | | |
| Darker water in lee of islands | Possible upwelling | Cape Verde, Chatham Island, and Falkland Islands |
| Darker water always between mixing portions of currents | Unknown | Off Brazil, Argentina, and New Zealand |
| Sediment | | |
| Moving along coast | Possibly alongshore transport | To north from Amazon and Orinoco Rivers |
| Not mixing with plankton | Unknown current | Offshore Brazil |
| Sharp interface of sediment-laden river water and ocean | Sediment precipitation (electrolytic flocculation) | Rio de la Plata, Argentina, Uruguay |
| Plumes and streaks adjacent to shores | Perhaps due to river flooding Shifting patterns | Mississippi River, Sacramento River In Mobile Bay and off the Mississippi River delta; minimal amount off Congo River; huge quantities in Yellow Sea region |
| Caught up in violent weather | Sandstorms | Into the Arabian Sea and between Tunisia and Sicily |
| Bottom topography | | |
| Perhaps through 6 to 15 m of water | Clear water | Around Bahamas and Ulithi Atoll |

was seen to extend at least 150 km east of New Zealand. On December 16, the pattern observed in Cook Strait was seen extending to approximately 750 km east of New Zealand, where eddies were visible. In this area, the crewmen indicated that color contrasts could represent the confluence of waters coming from the north and south. Seven days later, on December 23, the crewmen reported seeing a "mustache," or eddy-shaped plankton streaks, indicated by a distinct color contrast, extending from 80 to 250 km east of Cook Strait and representing the flow between the islands on this date.

In a sequence of observations beginning on January 30, 1974, the Skylab 4 crewmen observed an east-west current pattern with eddies extending from Cook Strait toward Chatham Island. On February 1, the current between the islands was seen in sunglint, and pale blue-green streaks of plankton in the current patterns were observed approximately 250 to 350 km east of New Zealand. On February 2, a prominent long-wave pattern, probably internal waves, east of Cook Strait was de-

scribed. The observations indicate that, during this particular southern summer, the Canterbury Current, a north-flowing current of sub-Antarctic water, did not extend north of Cook Strait (refs. 11-20 and 11-21).

East of North Island, diffuse patches and northwest-trending wisps and sinuous streaks of blue-green water, probably representing plankton concentrations, were viewed during the period December 16 to 19 from 60 to 75 km northeast of Chatham Island. These features were tentatively interpreted as an indication of upwelling, in which southeast-flowing water is forced upward as it encounters the Chatham Rise. Generally, the diffuse and wispy plankton patterns provided little indication of flow direction, but the presence of a meandering, streamlike pattern was interpreted as indicating a southeasterly flow. On December 19, spinoff eddies and one large clockwise eddy were observed by the flightcrew near the Chatham Islands and alongside the apparent main stream of the flow.

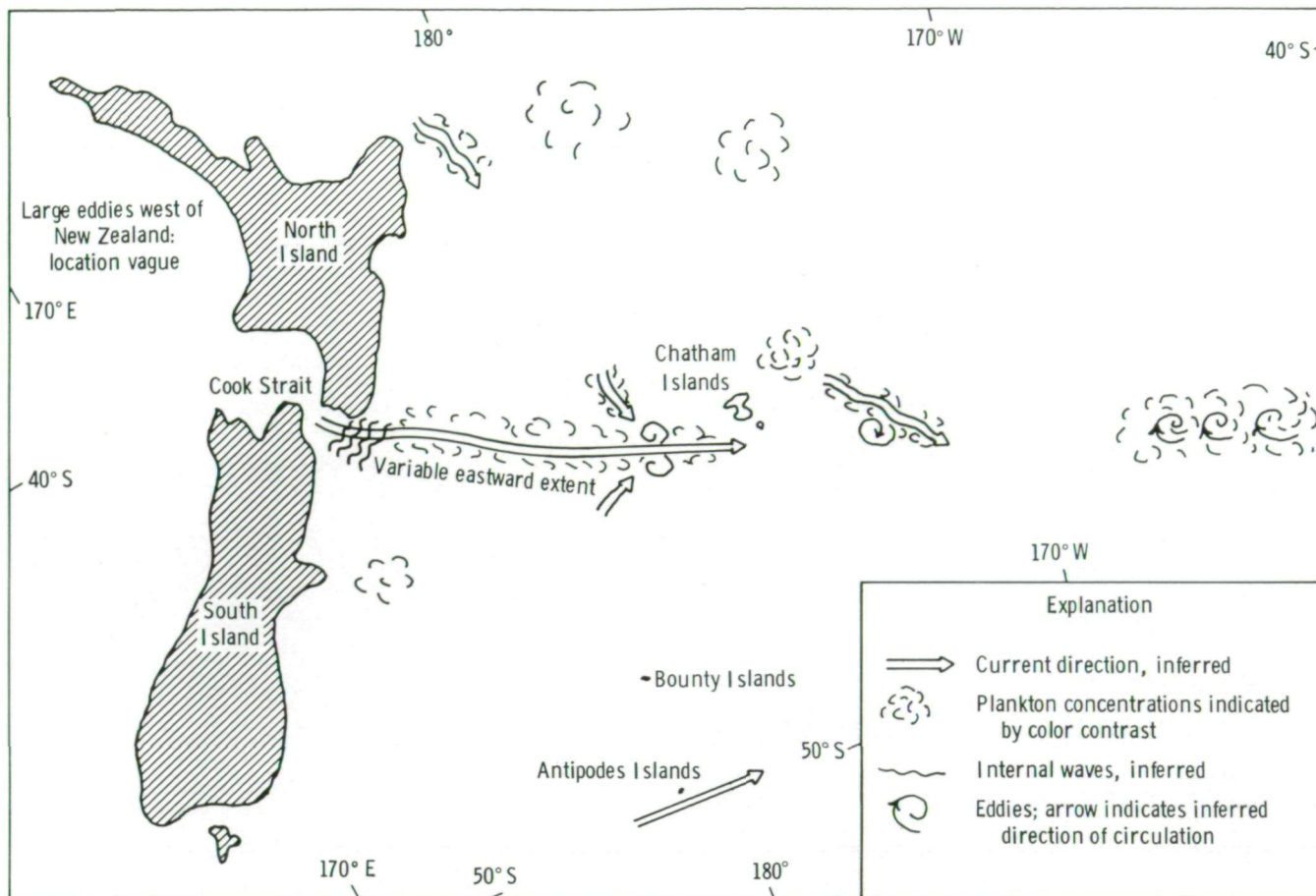


FIGURE 11-6.—Generalized oceanographic chart of New Zealand drawn from visual observations made by the Skylab 4 crewmen.

On January 30, the commander observed and described an area of blooming (blue-green water), approximately 850 to 1000 km east of the Chatham Islands, associated with curly, parallel, C-shaped eddies that trend east with their open sides facing eastward. The eddies are apparently embedded in eastward-flowing, warm, subtropical water, and the description of their shape suggests clockwise circulation with cold upwelling water in the low-pressure eddy cores. The association of blooming with these eddies is thus reasonable. No photographs were taken of these features.

The West Wind Drift southeast of New Zealand was manifested as a bow wave emanating from the Antipodes Islands. On December 19, 1973, the science pilot photographed the wave (fig. 11-8). He also noted the blue-green coloration from plankton in sub-Antarctic water near New Zealand off Christchurch on December 17. Plankton in this position may be nourished by upwelling induced as the Canterbury Current ap-

proaches the Chatham Rise. Alternatively, however, upwelling and plankton growth could indicate that a clockwise eddy is occasionally present at this location.

Data gathered by photointerpretation of Skylab 4 handheld-camera photographs are summarized in figure 11-9. The photographs generally confirm the crew observations. In particular, the photographs show eastward flow through Cook Strait toward the Chatham Islands (fig. 11-10). This current is joined by a moderately distinct flow from the north (fig. 11-11). Several of the excellent descriptions by the crewmen were not accompanied by photographs; therefore, mapping of the features is difficult. During one of the early observations of ocean surface features in the Chatham Islands area, the pilot described the occurrence of blue-green plankton eddies and inferred current flow patterns. Figure 11-12 is a photograph of this region. The patterns that indicate turbulence can be seen in figure 11-10 adjacent to Cook Strait and along the eastern coasts of both

North and South Islands. This turbulence is apparently generated by the eastward flow of Tasman Sea water moving away from the coast and may indicate coastal upwelling.

Directions of littoral drift are inferred from the shape of coastal-sediment plumes; littoral drift, in turn, may be an indication of coastal current direction (fig. 11-9). Along the western coast of North Island, littoral drift was southward along the coast from Reef Point for 300 to 350 km. To the south, sediment plume shapes were ambiguous but could indicate northward flow. Southward drift below Reef Point is compatible with the presence of the West Auckland Current, which previously was determined on the basis of drift-card measurements (ref. 11-20). Northward drift north of Cape Egmont is accounted for by the north-flowing Westland Current. Along the eastern coast of North Island, southward drift is indicated south of Hawke Bay. This drift reinforces the conclusion that the Canterbury Current did not extend north of Cook Strait during the period of observation. Northward littoral drift from Jackson Bay along the western coast of South Island probably reflects the north-flowing Westland Current. Along the eastern coast, south of Banks Peninsula, northward drift is apparent in response to the north-flowing Southland Current.

The position of the Subtropical Convergence and the presence of the Southland Current east of South Island can be inferred on the basis of atmospheric conditions (fig. 11-13). Under the proper conditions, the presence of the Subtropical Convergence is indicated by a cloud boundary, with stratus clouds present over the cool water on the southern and western sides of the convergence (ref. 11-22). Such conditions apparently existed on December 8, and the northern limit of stratus clouds in figure 11-13 marks the convergence. On this basis of identification, cool water does not extend northward to Cook Strait; therefore, the conclusion that the Canterbury Current did not extend that far north during this particular summer is confirmed. The cloud-free areas along the coast south of Banks Peninsula are interpreted as indicating the presence of the warm Southland Current.

Coastal Suspended Sediment

Skylab 4 observations of suspended sediment in coastal waters were made 29 times. Examination of the descriptions and the photographs leads to the conclu-

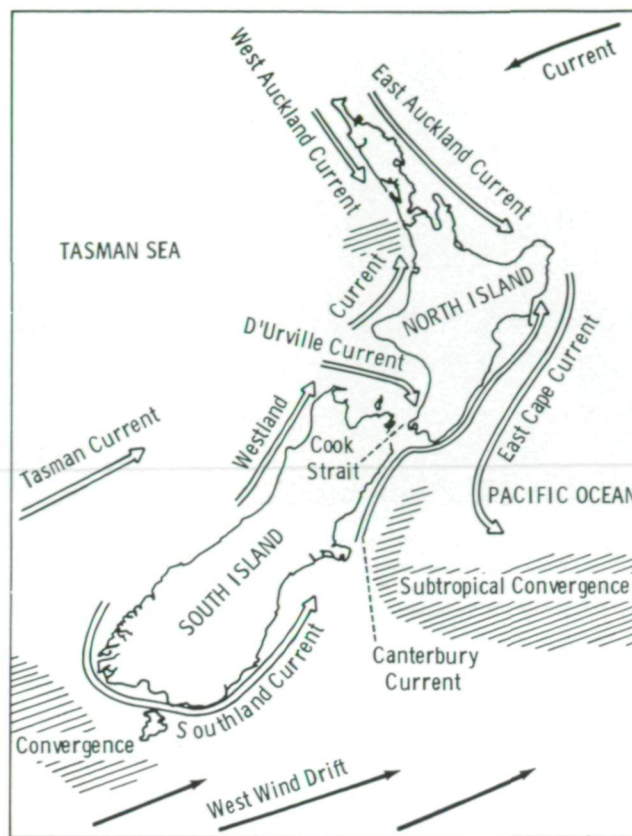


FIGURE 11-7.—Coastal current patterns around New Zealand derived from drift-card paths (ref. 11-11).

sion that such observations can yield contributions in the following studies:

1. Character of the dominant type of suspended load contributed by a river
2. Types of coastal sediment transport mechanisms
3. Paths of sediment dispersal
4. Variability of sediment contribution to the ocean basins

On several occasions, the crewmen were able to observe the estuary of Rio de la Plata between Uruguay and Argentina. On each occasion, the boundary between sediment-laden water and normal ocean water was sharply defined (fig. 11-14). On February 1, 1974, the commander described the boundary as resembling a meniscus. He also noted that, within the estuary, the boundary occurred in different positions, but it was never observed seaward of the river mouth. The rapid decrease in suspended sediment concentration indicated by the abrupt boundary is probably a result of flocculation and subsequent settling of clay-sized particles at the interface between freshwater and saltwater.

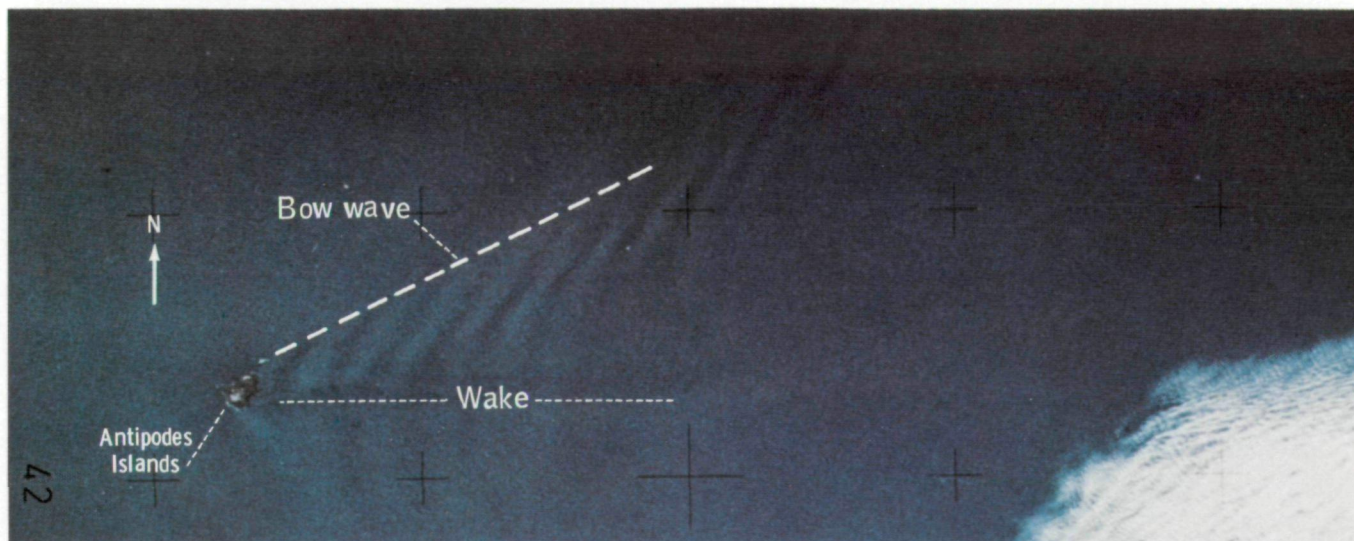


FIGURE 11-8.—A bow wave and a wake visible behind the Antipodes Islands, southeast of New Zealand, give an indication of the West Wind Drift of the Antarctic Ocean (SL4-137-3655).

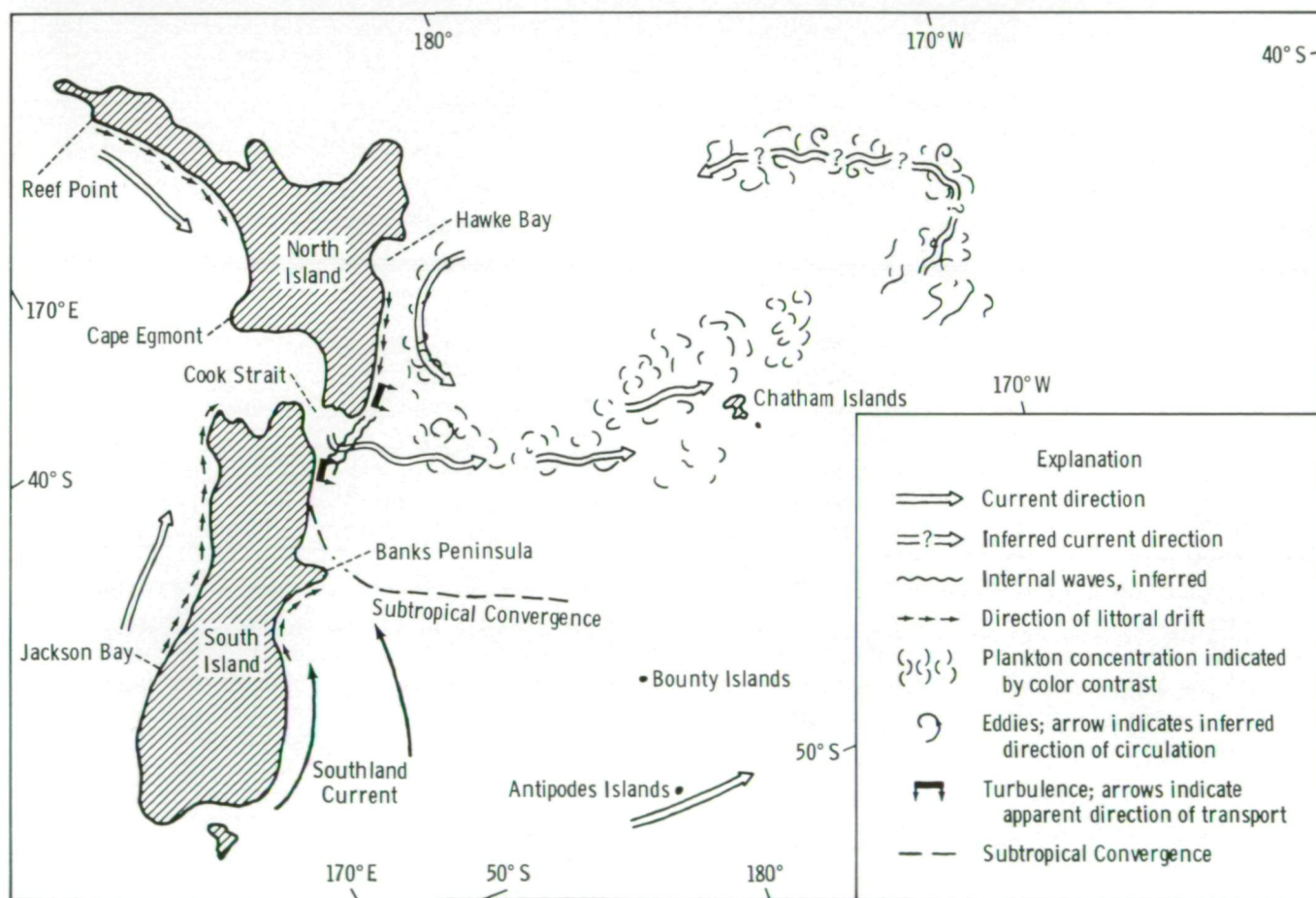


FIGURE 11-9.—Generalized oceanographic chart of New Zealand drawn from interpretation of handheld-camera photographs taken during the Skylab 4 mission.

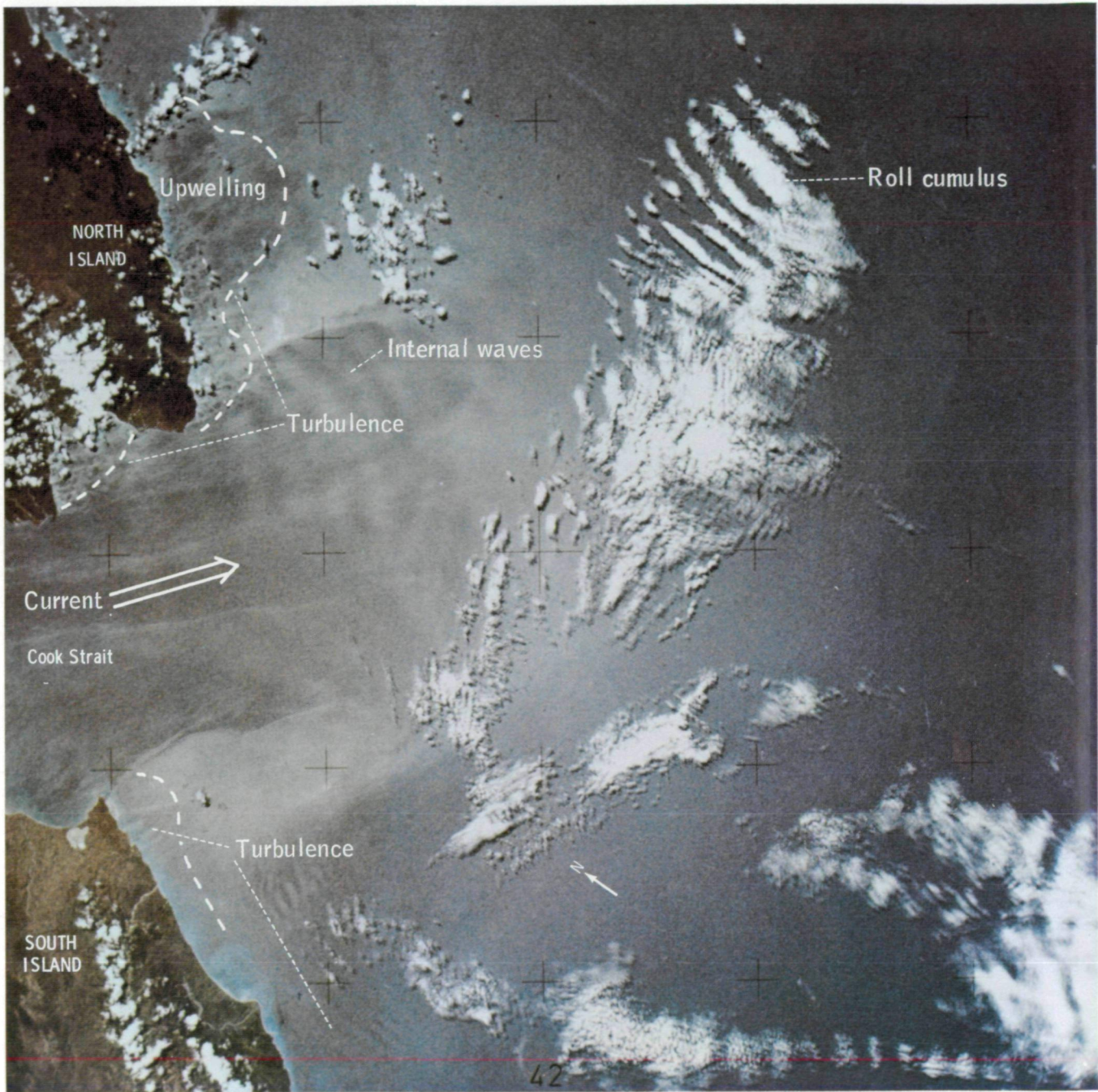


FIGURE 11-10.—The eastward flow of water through Cook Strait, New Zealand, is visible in solar reflection from the sea surface (SL4-137-3725).

ORIGINAL PAGE IS
OF POOR QUALITY

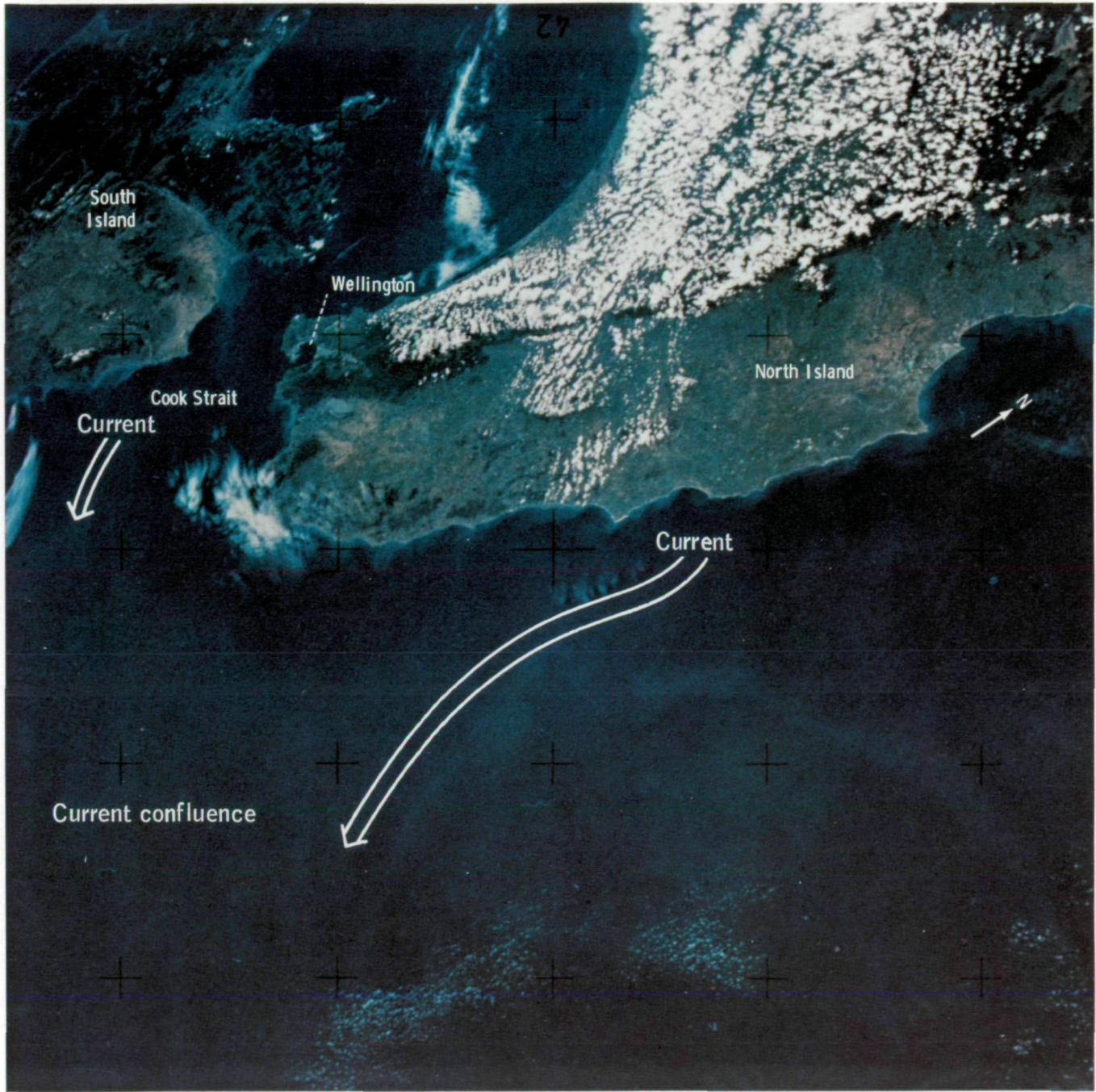


FIGURE 11-11.—The southward-flowing current can be traced by the light blue discoloration of the waters off the eastern coast of North Island, New Zealand (SL4-137-3645).

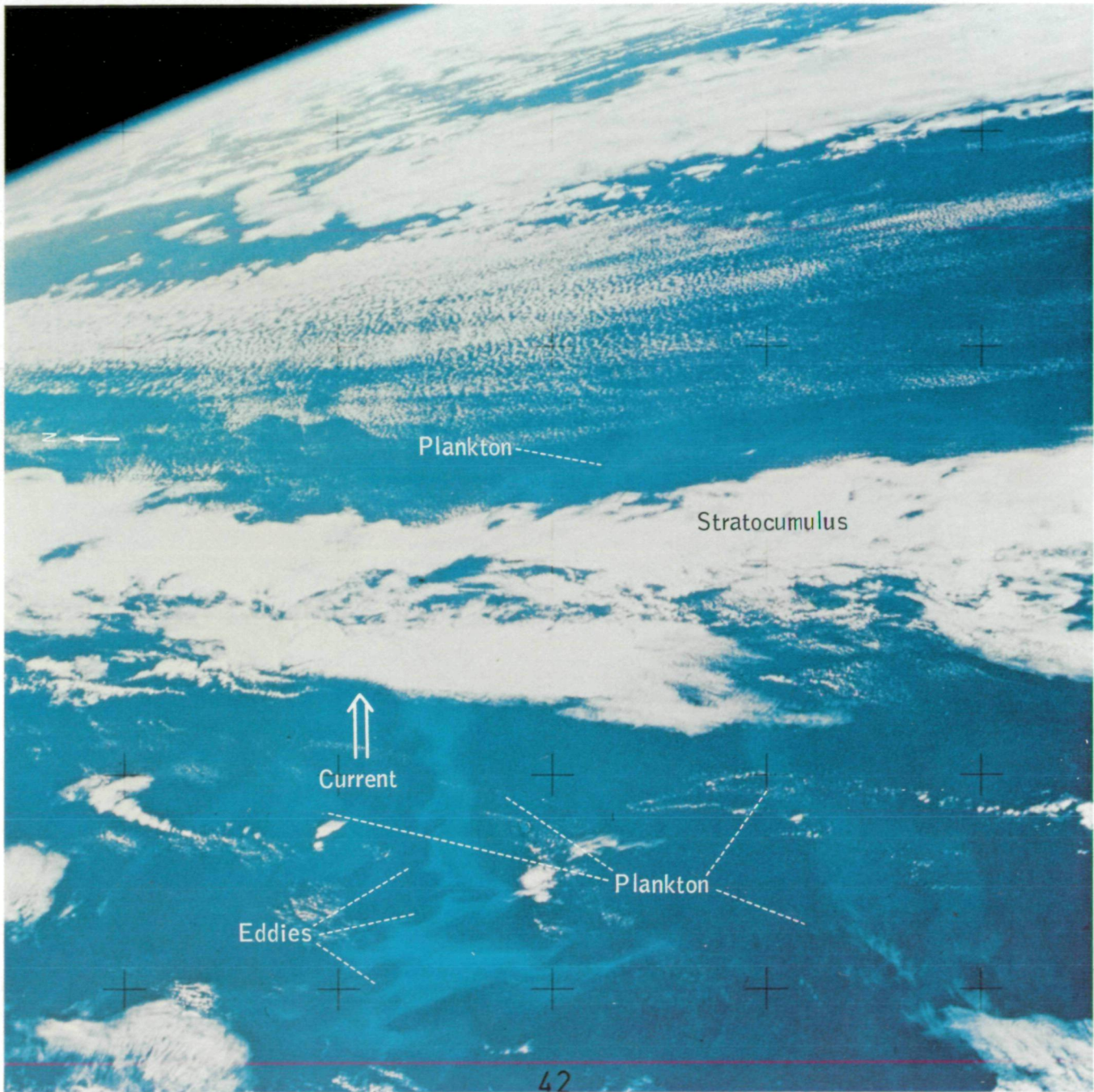


FIGURE 11-12.—The eastward-flowing current can be traced for several hundred kilometers east of Chatham Island (lat. 43° S, long. 177° W) by the pale blue-green water, discolored by blooms of plankton. Several streams of discolored water were present; the most intensely colored stream extends beyond the band of stratocumulus (SL4-136-3446).

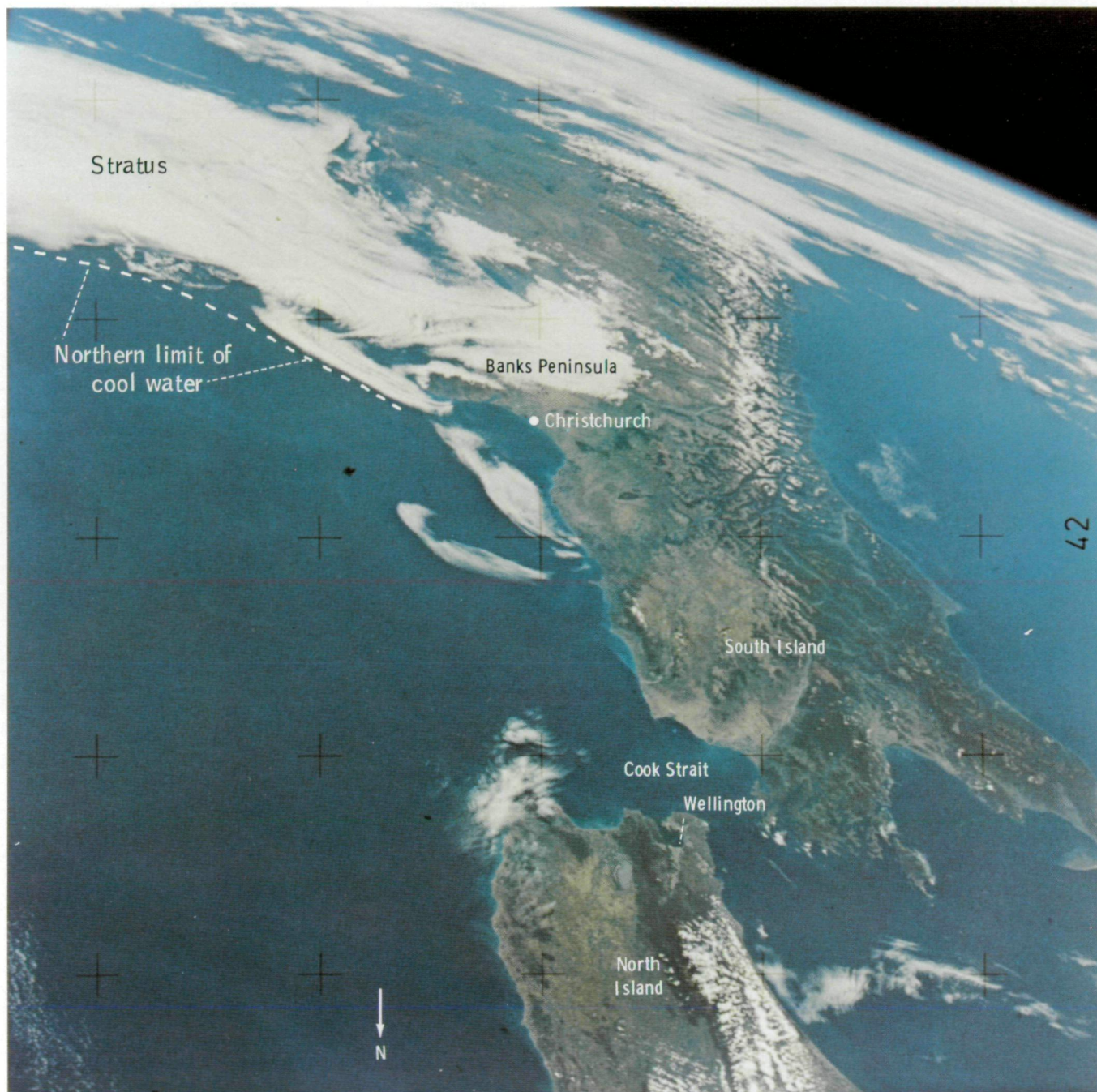


FIGURE 11-13.—Thick stratus east of South Island, New Zealand, marks the Subtropical Convergence and the Southland Current in this photograph taken on December 8, 1973 (SL4-137-3646).

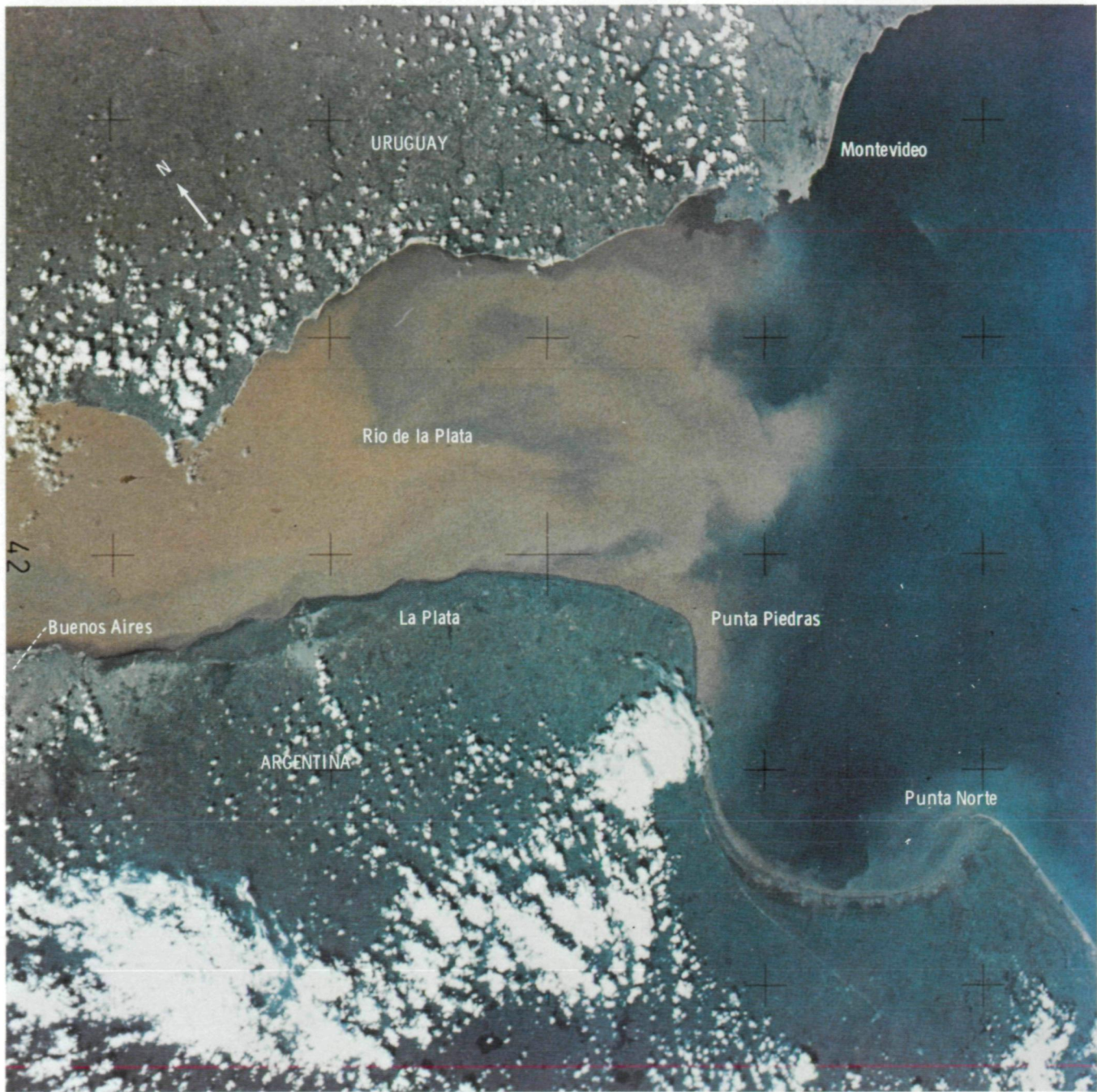


FIGURE 11-14.—Reddish-brown sediment discolors the water in the Rio de la Plata estuary between Uruguay and Argentina (SL4-143-4608).

The clarity of the water seaward of the interface suggests that clay-sized particles comprised the dominant portion of the suspended load of Rio de la Plata.

In contrast, no apparent rapid diminution of sediment load occurs where turbid waters of the Yün Ho and Yellow Rivers enter the Yellow Sea from China (fig. 11-15). There, the change from turbid to relatively clear ocean water is transitional. These observations indicate that silt-sized, rather than clay-sized, particles predominate in the suspended load of both Chinese rivers. The character of the interface between turbid and clear water and the degree of expulsion of sediment-laden water into the sea may be useful criteria, therefore, in estimating the particle size of the river-borne load.

Wind and current are the two types of sediment

transport that were distinguished on the basis of descriptions by the crewmen or analysis of handheld-camera photographs. Clear examples of sediment transport in water moved by wind along the Atchafalaya coastal region of Louisiana are illustrated in figures 11-16 and 11-17 and were described by the crewmen. On December 7, 1973 (fig. 11-16), sediment entering the Gulf of Mexico from the Atchafalaya Bay was transported seaward and dispersed by strong offshore winds. A turbid eddy was visible offshore. On January 30, 1974 (fig. 11-17), winds were onshore; sediment remained close to the coast and was carried westward by the coastal current. These photographs also illustrate the diversity in the paths of sediment dispersion when wind is the dominant mechanism (ref. 11-23).

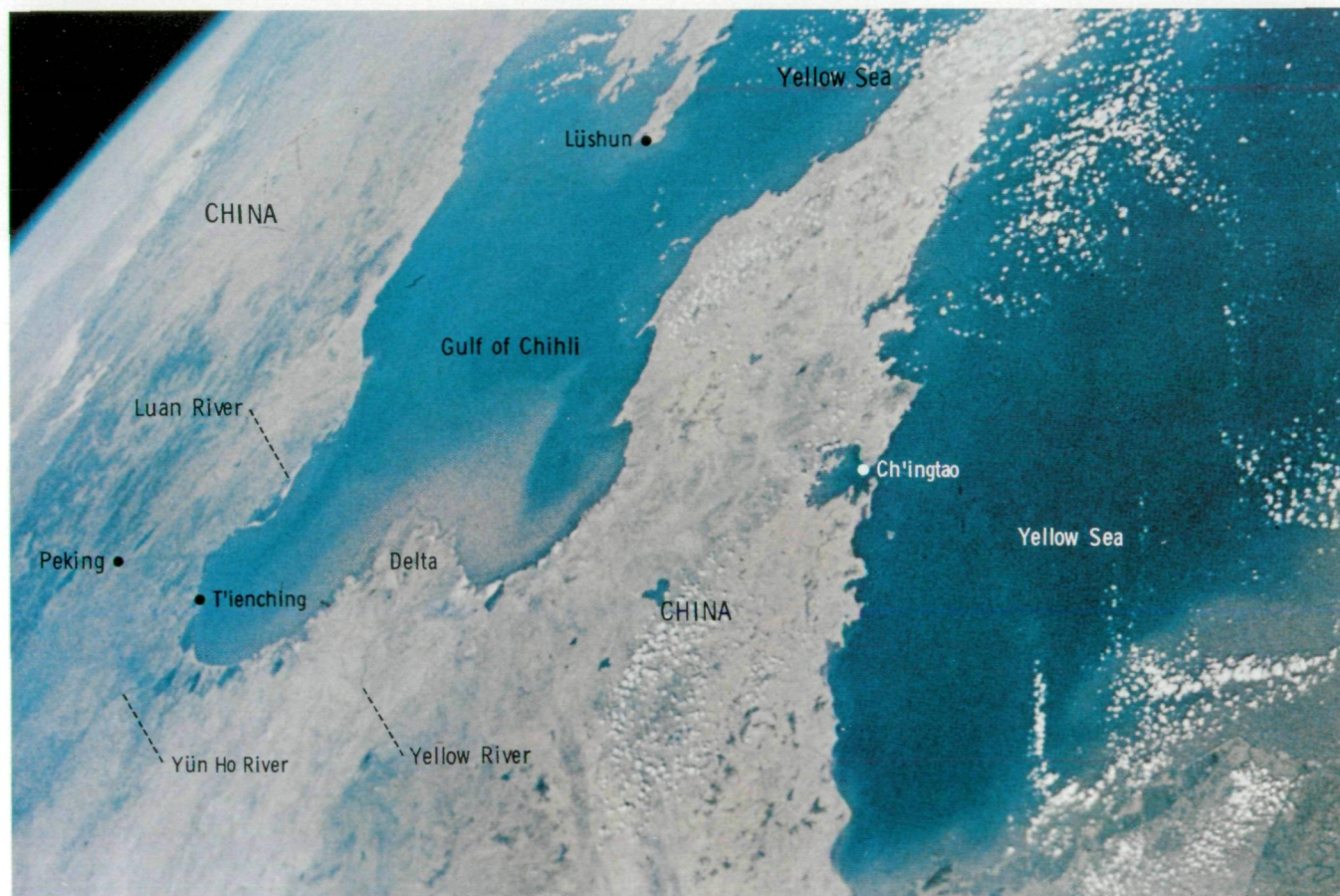


FIGURE 11-15.—Yellowish-brown water laden with sediment empties into the Yellow Sea from the Yün Ho and Yellow Rivers (SL4-197-7423).

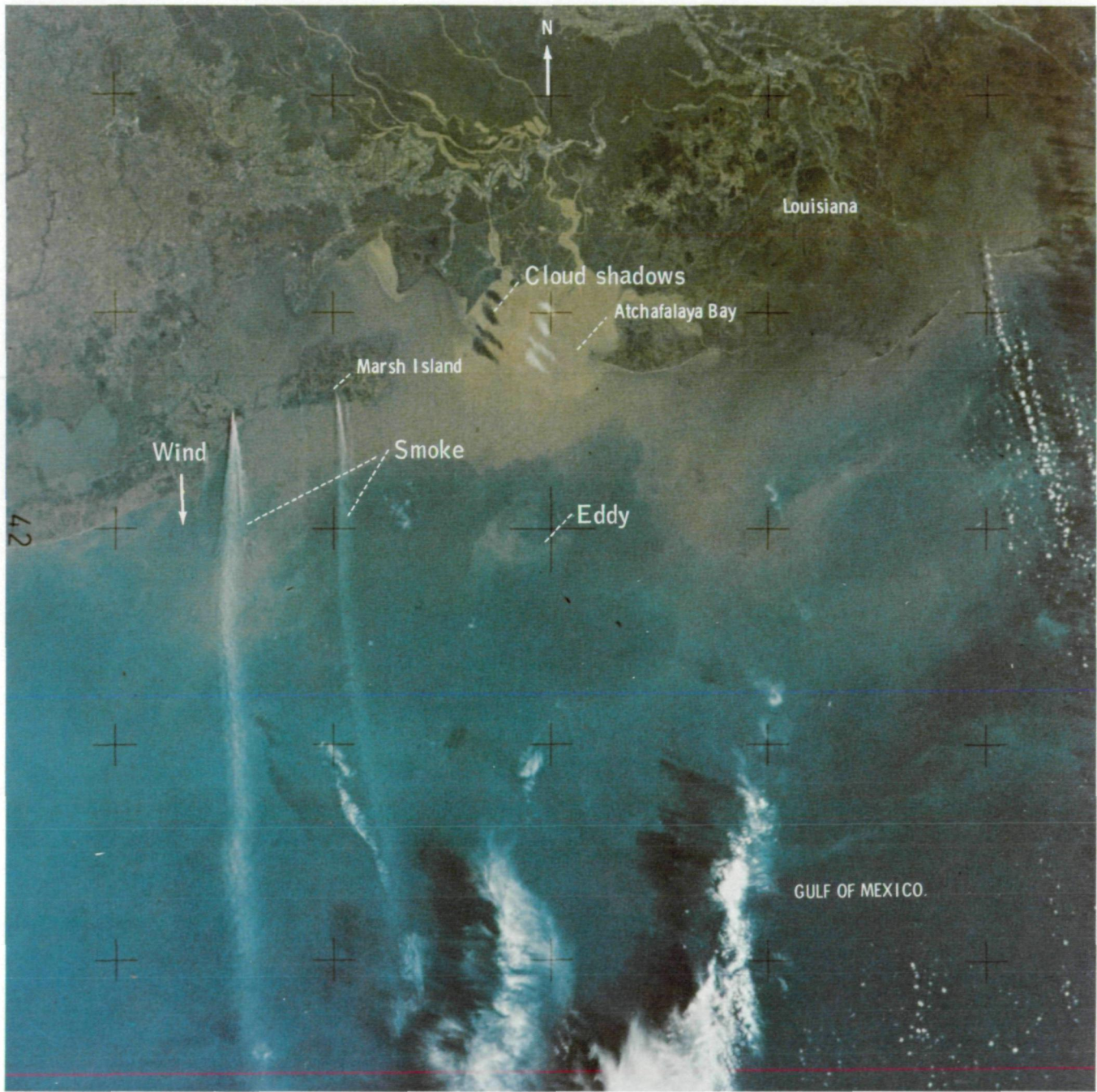


FIGURE 11-16.—Reddish-brown water laden with sediment was flowing through the Atchafalaya Bay and into the Gulf of Mexico under the influence of strong north winds on December 7, 1973. The wind direction is clearly marked by the long smoke plumes extending south over the Gulf of Mexico (SL4-136-3475).

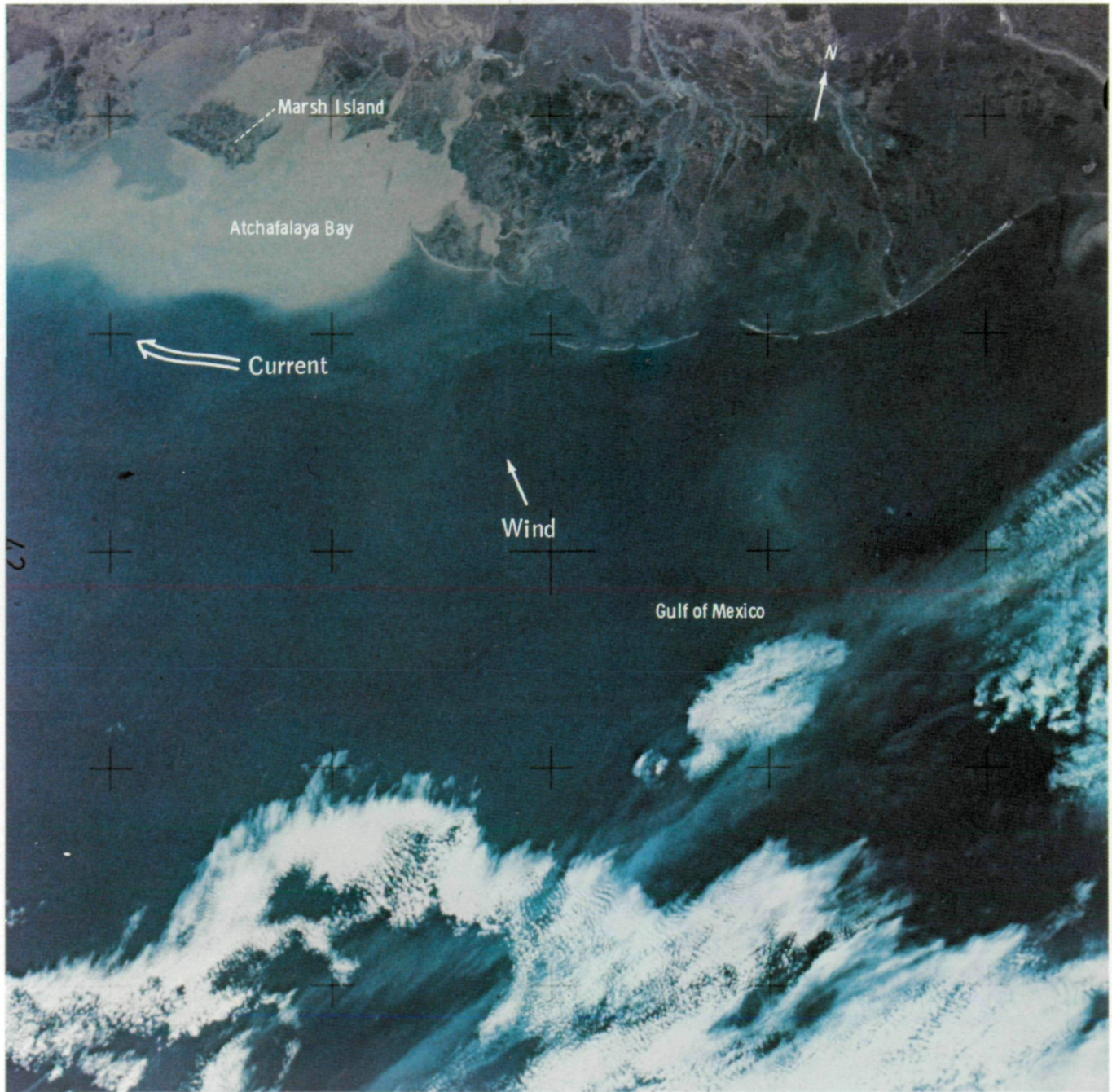


FIGURE 11-17.—A mass of light-brown sediment-laden water was observed by the Skylab 4 crew on January 30, 1974, as it spread along the Louisiana coast from Atchafalaya Bay (SL4-143-4600).

The entrainment and transportation of sediment by ocean currents is vividly illustrated by photographs of Rio Magdalena in Colombia (fig. 11-18) and Rio São Francisco in Brazil (fig. 11-19). Figure 11-18, a photograph taken on January 6, 1974, shows that the sediment from Rio Magdalena was entering the ocean and being entrained by a northwest-flowing current. The Skylab 4 crewmen observed a similar pattern of movement. The photograph of Rio São Francisco (fig. 11-19), taken on November 30, 1973, illustrates the sediment delivered to the sea being carried southeast along the coast under the influence of strong current flow. On January 24, a similar condition was observed by the science pilot and described: "The sediment carried out by the river was quickly carried to the south by what looked like a relatively strong current." Such observations indicate the influence of the north and south equatorial currents on sediment transportation along these portions of the South American coast.

The previous examples illustrate the ease of discerning sediment concentrations and directions of transport from space and therefore the potential for monitoring paths of sediment transport. Another example is shown in figure 11-20, a view of the coast of Albania. North of Vlorë, sediment movement is southward along the coast. At Vlorë, the direction of transport changes, and sediment is moved offshore toward the northwest and into the Adriatic Basin.

Descriptions by the Skylab crewmembers show that the variability in the characteristics of sediment contributions to coastal waters can be determined and therefore monitored from space. The crewmen were able to distinguish between rivers that constantly carry large loads of sediment to the sea and rivers in which sediment influx to the sea is episodic. Among the discharge areas in which turbid water was repeatedly ob-

served were the Yellow Sea (fig. 11-15), the northern coast of Korea, the mouth of the Mississippi River (fig. 11-21), the Atchafalaya Basin (figs. 11-16 and 11-17), the Rio Magdalena (fig. 11-18), and the Rio São Francisco (fig. 11-19). Areas where episodic influxes of sediment were observed included portions of the coast of Oregon and northern California and Monterey Bay in California.

Ocean Turbulence Observed From Skylab

The realization that eddies of several kilometers in diameter could be observed easily and regularly from orbital altitudes spurred the attempt for visual examination of turbulence of other scales. The authors' working hypothesis was that cold-core eddies, as in the Yucatan Current, were early stages of the sequence described by Brown and Roshko (ref. 11-7) and Winant and Browand (ref. 11-24). It seemed likely that any eddies larger than those observed off Honduras would not exist farther north because of the constriction of the current between the Yucatan Peninsula and Cuba. Furthermore, the observation of such features had not been part of the preflight briefing. It was not prudent, therefore, to request the crew to look for eddy growth or decay. Instead, the Flight Plan was modified to include new observational areas in hopes that the crew would report turbulence of scales different from those in the northwestern Caribbean Sea.

During the debriefing session in March 1974, the pilot reported that he had been continuously intrigued by Langmuir cells at the sea surface (table 11-IV). These turbulent phenomena are semiorganized, horizontal, helical vortexes in the mixed layer of the ocean (ref. 11-25). This mixing process is not known well, but theories and observations have been presented

TABLE 11-IV.—Turbulence Observable From Manned Orbits

| <i>Feature</i> | <i>Scale, km</i> | <i>Comments</i> |
|-----------------------|---|---|
| Langmuir cells | 0.01 to 1 | Observed and photographed; diameter never greater than 200 m |
| Mesoscale eddies | 1 to 100 | Observed and photographed; none interpreted larger than 55 km |
| Synoptic-scale eddies | 100 to 1000 | Observed and photographed in part, never seen in toto; assumed sizes of 500 km |
| Large-scale eddies | 1000 and larger Rossby and inertial waves | Never recognized in photographs or observations; visible fronts may be boundaries |

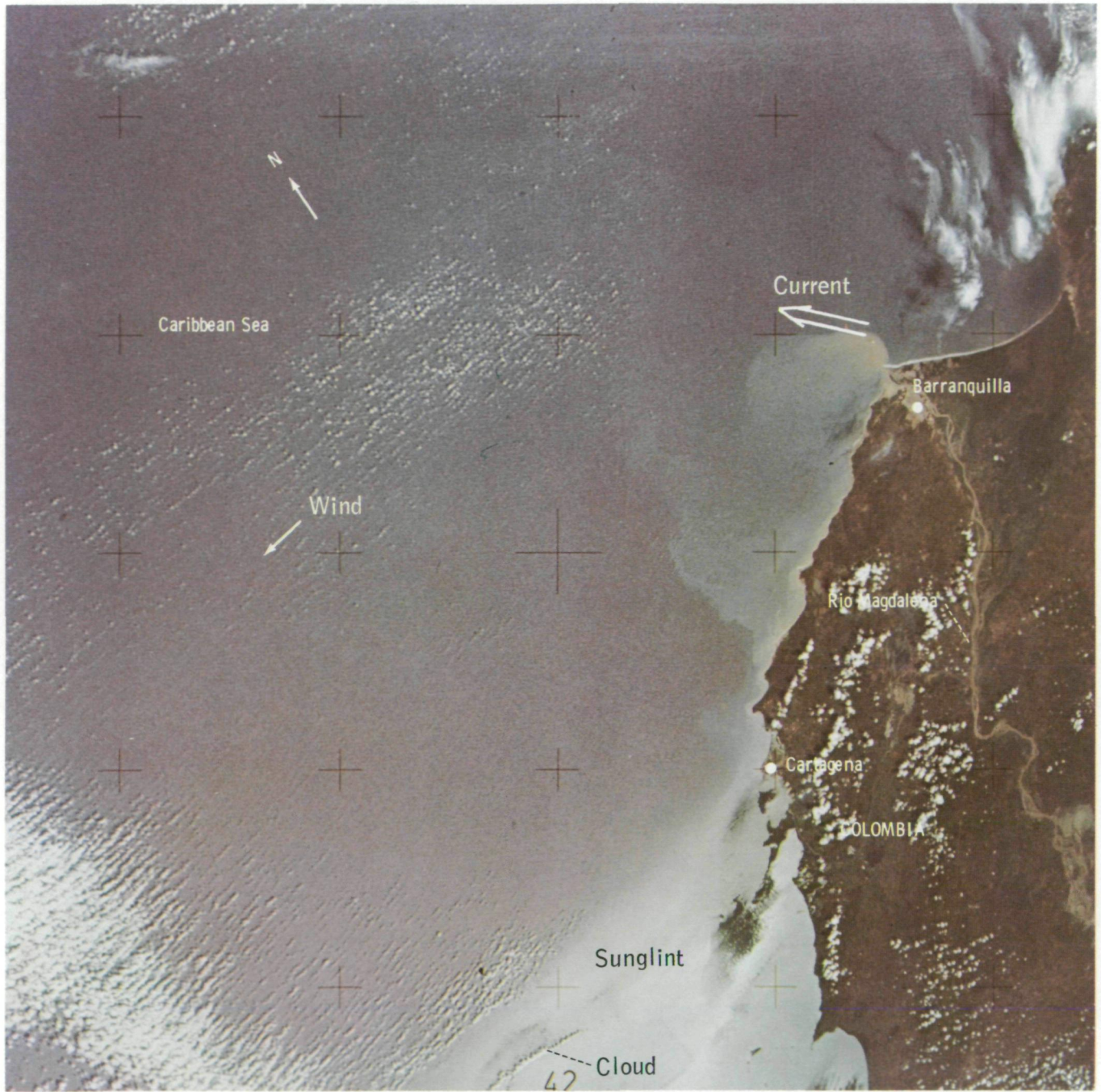


FIGURE 11-18.—Sediment-laden water entering the Caribbean Sea from the Rio Magdalena of Colombia is transported southwestward by the coastal current. Along the coast farther south, the solar reflection on the sea surface highlighted smooth waters and wakes behind headlands and offshore islands, as seen in this photograph taken on January 6, 1974 (SL4-139-3914).

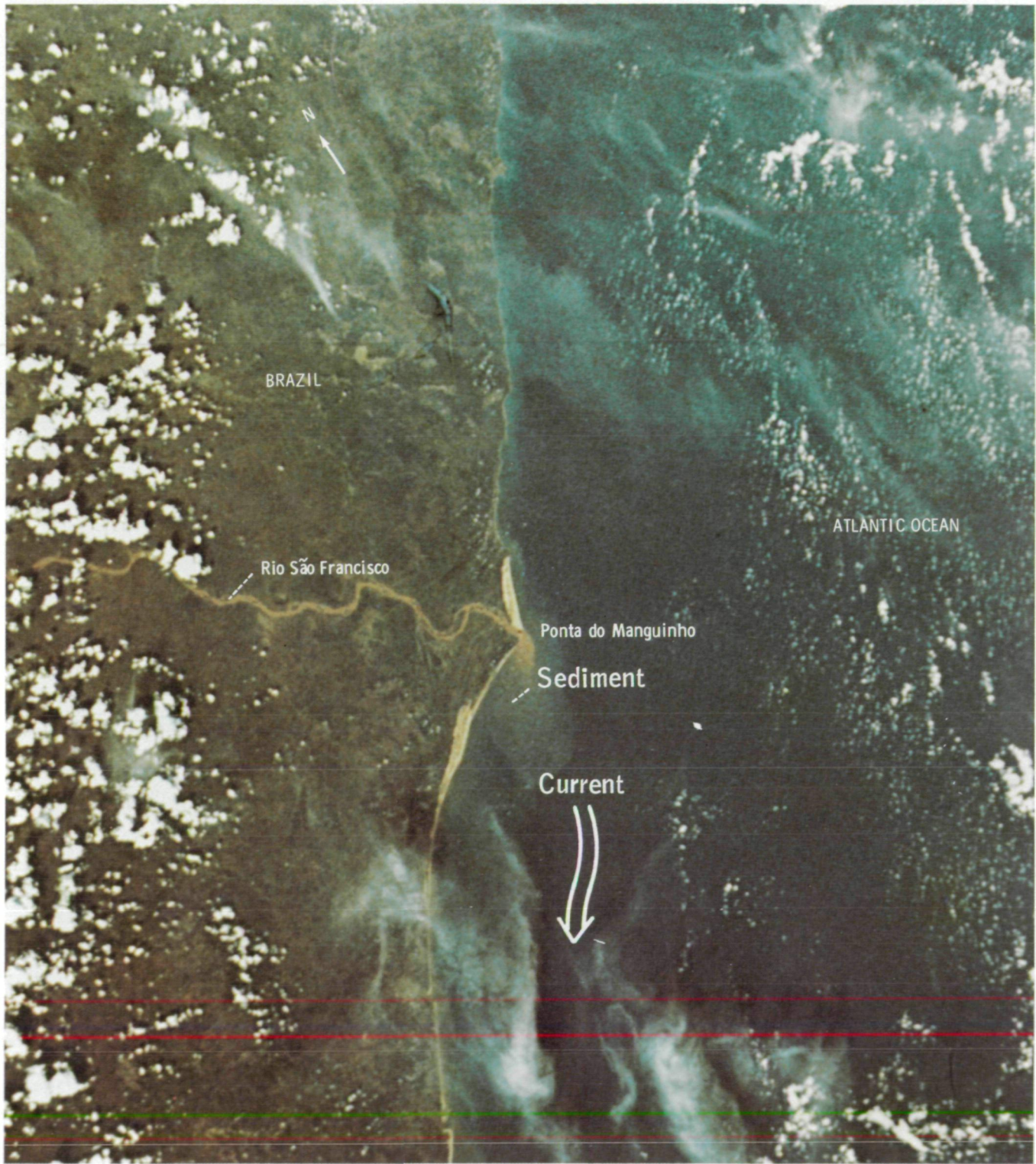


FIGURE 11-19.—The current along the southern Brazil coast flowing strongly to the south was clearly seen on November 30, 1973, as the sediments were swept away from the mouth of the Rio São Francisco (SL4-197-7416).

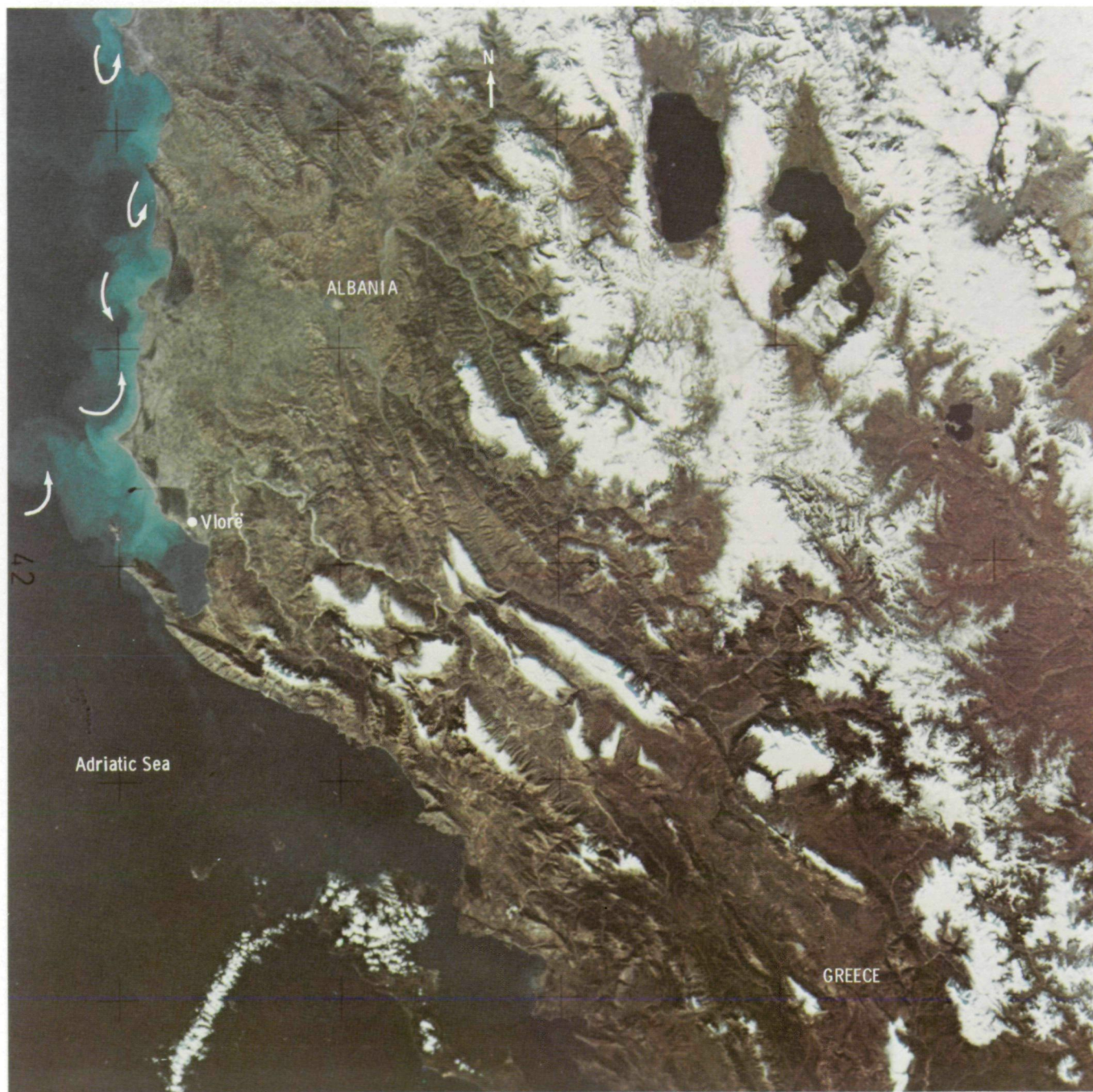


FIGURE 11-20.—A winter scene over Albania shows clear skies, mountain tops deep in snow, and ice-free lakes. Along the Adriatic Coast, nearshore waters, laden with suspended sediments, were useful to the Skylab 4 observers in tracing the movements of the alongshore currents (SL4-141-4408).

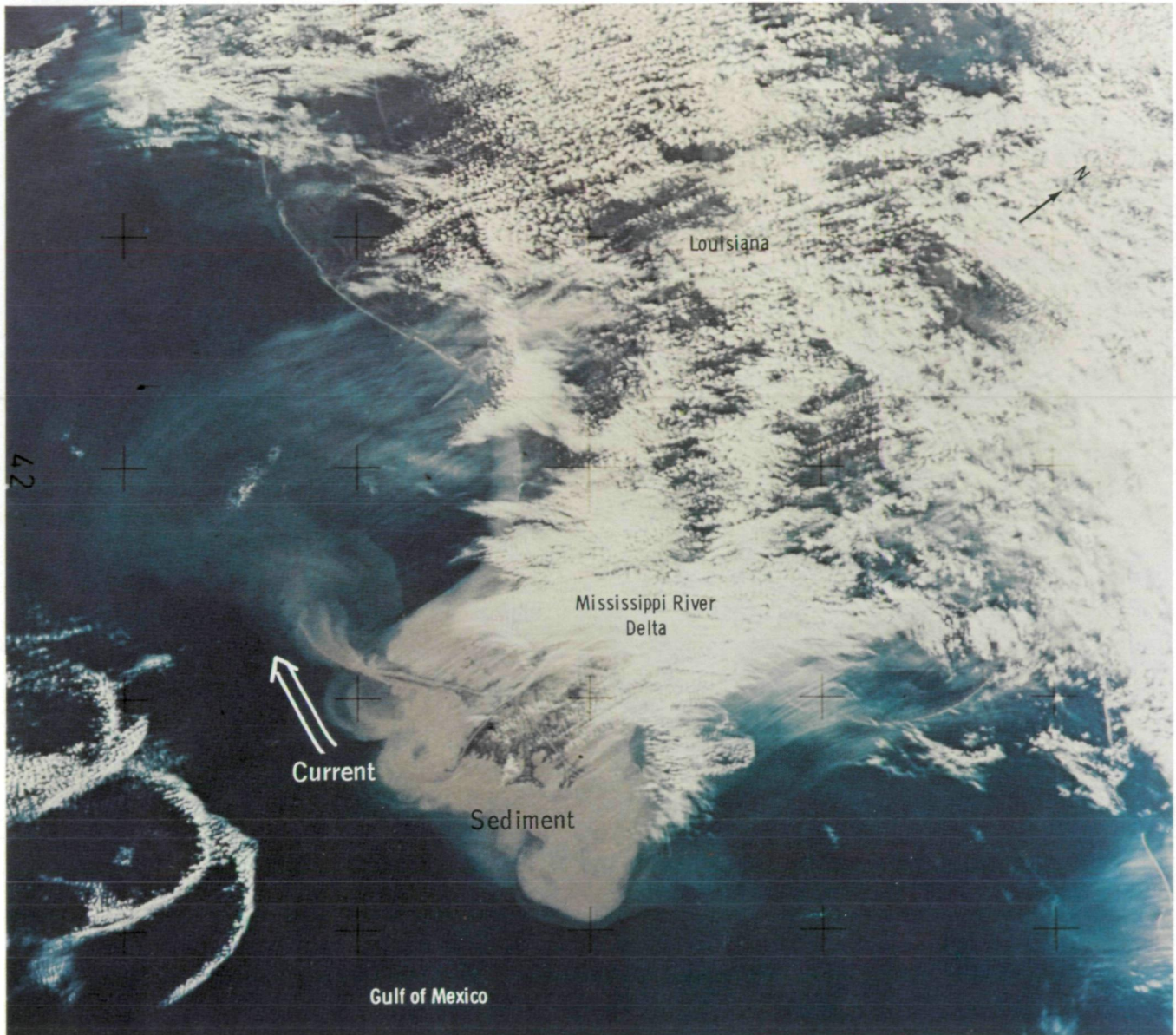


FIGURE 11-21.—Although most of the coasts of Louisiana and Mississippi were covered with cumulus and stratocumulus when this January 1974 photograph was taken, the delta of the Mississippi River was clearly visible. The great sediment load carried by the river forms a distinct pattern as it enters the Gulf of Mexico, showing sequential, concentric sediment fronts and the influence of the current flowing westward (SL4-139-4032).

that indicate the close association with winds (ref. 11-26). The importance of these cells in transporting energy from the sea surface down to the ocean's thermocline (50 to 150 m) seems clear (refs. 11-27 to 11-29). The processes by which this energy transfer takes place should be learned, however, because the Langmuir circulation probably feeds into larger, convective-scale

systems which in turn lead into synoptic-scale turbulence (ref. 11-15). This sequence is considered a key factor in the development of our weather and climate (ref. 11-30). The capability of routinely observing and photographing Langmuir cells (fig. 11-22), thereby allowing quantitative evaluations of their size, persistence, and extent, was welcomed by oceanographers.



FIGURE 11-22.—Typical cumulonimbus overlay land in this summer 1973 photograph of the western end of Puerto Rico, and scattered cumuli and cloud streets extended over the Caribbean Sea. The southeast trade winds, blowing from the upper right in this view, created the streaky sea surface, an indication of Langmuir cells. Cold-core eddies, with associated crescent-shaped cumuli, were also well defined (SL2-10-181).

Synoptic Scale

The synoptic scale (table 11-IV) is most closely connected with the practical day-to-day forecasting of the weather and of ocean conditions. Even though meteorologic measurements over land have been routine for more than a century, there is a clear limit to the predictability of the atmosphere if it is considered a static system, as such measurements do. The growing weather disturbances seemed to be caused by interaction of smaller scales of motions—scales not being measured in a time or space sequence by our meteorologic network. Consequently, they are not easily included in numerical predictive schemes.

Furthermore, the certainty that heat transferred from the sea to the air is a primary factor in the development of storm systems of all magnitudes has been firmly established (refs. 11-31 and 11-32). There is, however, a huge gap in daily weather reporting because of the lack of continuous observations from the world ocean. Consequently, the constant daily effects of the ocean on the atmosphere are really not known.

It is easy to imagine, therefore, the interest among marine meteorologists and oceanographers when it was learned that the Skylab 4 crewmen had visually observed eddies of mesoscale size (fig. 11-23). Such turbulent features could be, it was conjectured, the “feeders” of synoptic-scale eddies that are presumed to exist in the ocean as well as in the atmosphere. And, although schemes have been devised to measure such eddy systems, using ships and moored buoys (fig. 11-24), a real understanding of sizes, persistence, and frequencies of all eddies in the ocean was needed so the sampling platforms could be properly located. The visual observations of eddies provided scientists with the very information needed.

After the Skylab 4 crewmen had observed the cold-core eddies in the Caribbean Sea, they were asked to look for systems with diameters larger than 10 to 30 km. On February 6, 1974, a large loop, or eddy, was observed west of South Georgia Island, South Atlantic Ocean, in an east-west trending current (the Antarctic West Wind Drift). This sighting was a culmination of five observations in January and early February by the Skylab 4 crew; all sightings were of fairly subtle surface expressions of such eddies (fig. 11-25).

In the Solomon Sea, where warm water flows to the northwest, a series of mesoscale and somewhat larger eddies was photographed and described by the Skylab 4 commander during a descending orbital pass to the southeast. The smoother-than-usual water was noted in the Sun's reflection together with some typical cumulus cloud boundaries. The commander noted during debriefing, “I don't remember seeing much that wasn't in the sunglint [in the Solomon Sea].”

A less distinct but definite boundary in the ocean surface can be seen in a photograph taken of the equatorial Pacific Ocean 1000 km northeast of New Guinea (fig. 11-26). This dim feature was described by the pilot as “large surface features, sort of circular, and periodically stretched out.” The science pilot commented further that he could see curved, arching boundaries but “never get the complete picture.”

The inherent advantage of viewing large-scale features in their entirety can be noted in a photograph of the western Mediterranean Sea, the Strait of Gibraltar, and the eastern Atlantic Ocean (fig. 11-27). In the western Mediterranean Sea, clouds were in the shape of two major eddy patterns on this day. During winter in these waters, the association of clouds with sharp temperature boundaries in surface water is strong because the general distribution of cumulus clouds is at a minimum. Thus, it is likely that the clouds in the photograph were manifestations of eddies in the sea, similar to the eddies that were forming June 2, 1973, south of Spain (fig. 11-28).

Such an interpretation is supported by available oceanographic data. Temperature data gathered by scientists at Woods Hole Oceanographic Institution from the western Mediterranean Sea between Spain and Algeria (fig. 11-29) show an upward bowing of isotherms that reach the surface (stations 6015 to 6017) (ref. 11-33). This profile suggests that warm-core eddies may be present from time to time embedded in the east-flowing surface current of the western Mediterranean Sea. In contrast, data from transect 24, which crosses the Mediterranean Sea farther east, between France and Algeria, indicate relatively uniform surface temperatures and suggest that eddies are uncommon in these waters. Indeed, cloud lines indicative of eddies have not been observed or photographed in this area.

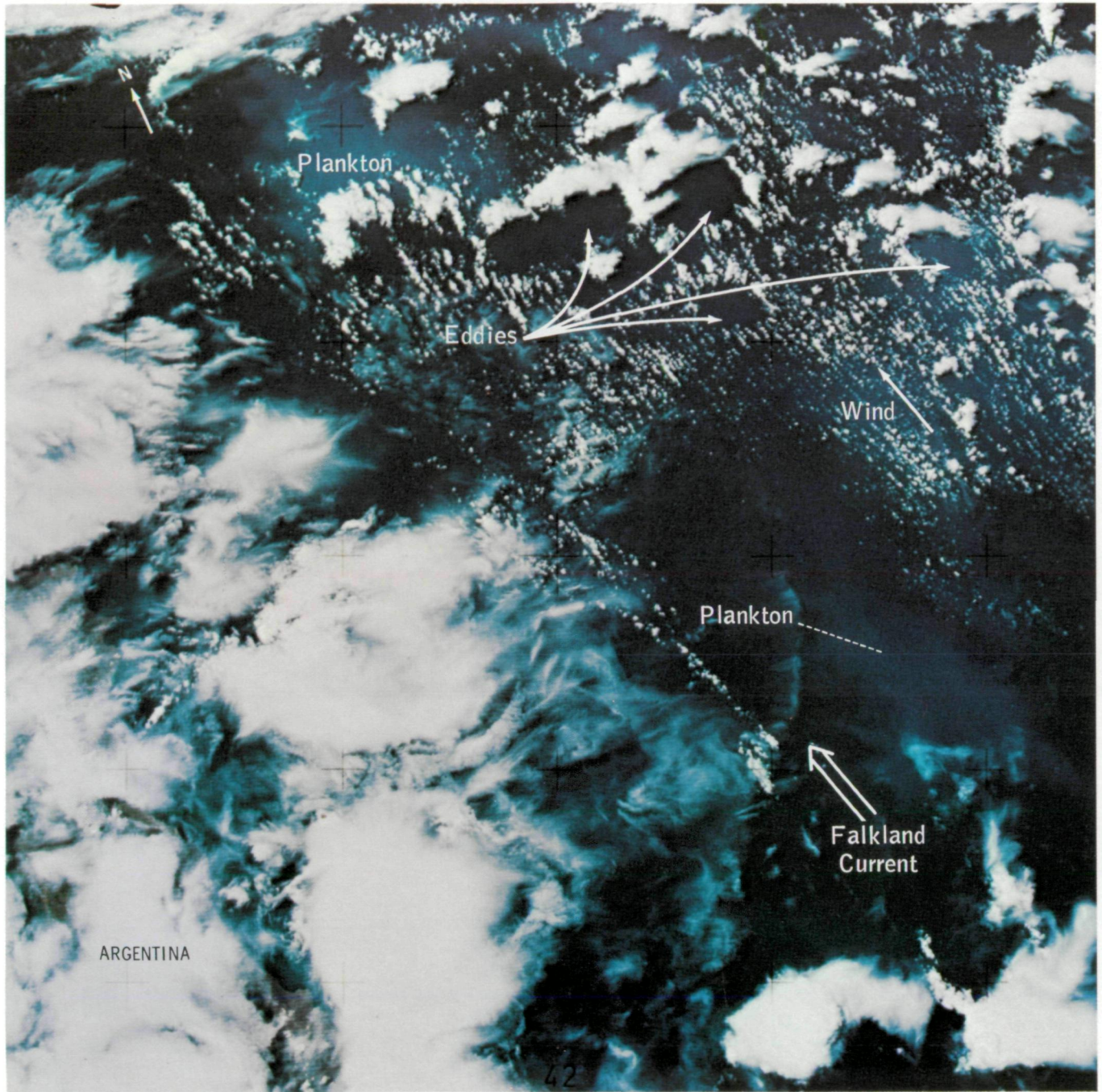


FIGURE 11-23.—An expansive development of crescent-shaped cumuli, characteristic of cold-water eddies, was apparent in the warm waters intruding from the South Equatorial Current. The crewmen reported cumuli spread over a wide area around the Falkland Current east of Argentina when this photograph was taken (SL4-137-3608).



FIGURE 11-24.—Ocean-data station DANA, operated by General Dynamics under contract with the Office of Naval Research, under tow off the California coast by the RV Agassiz, Scripps Institution of Oceanography.

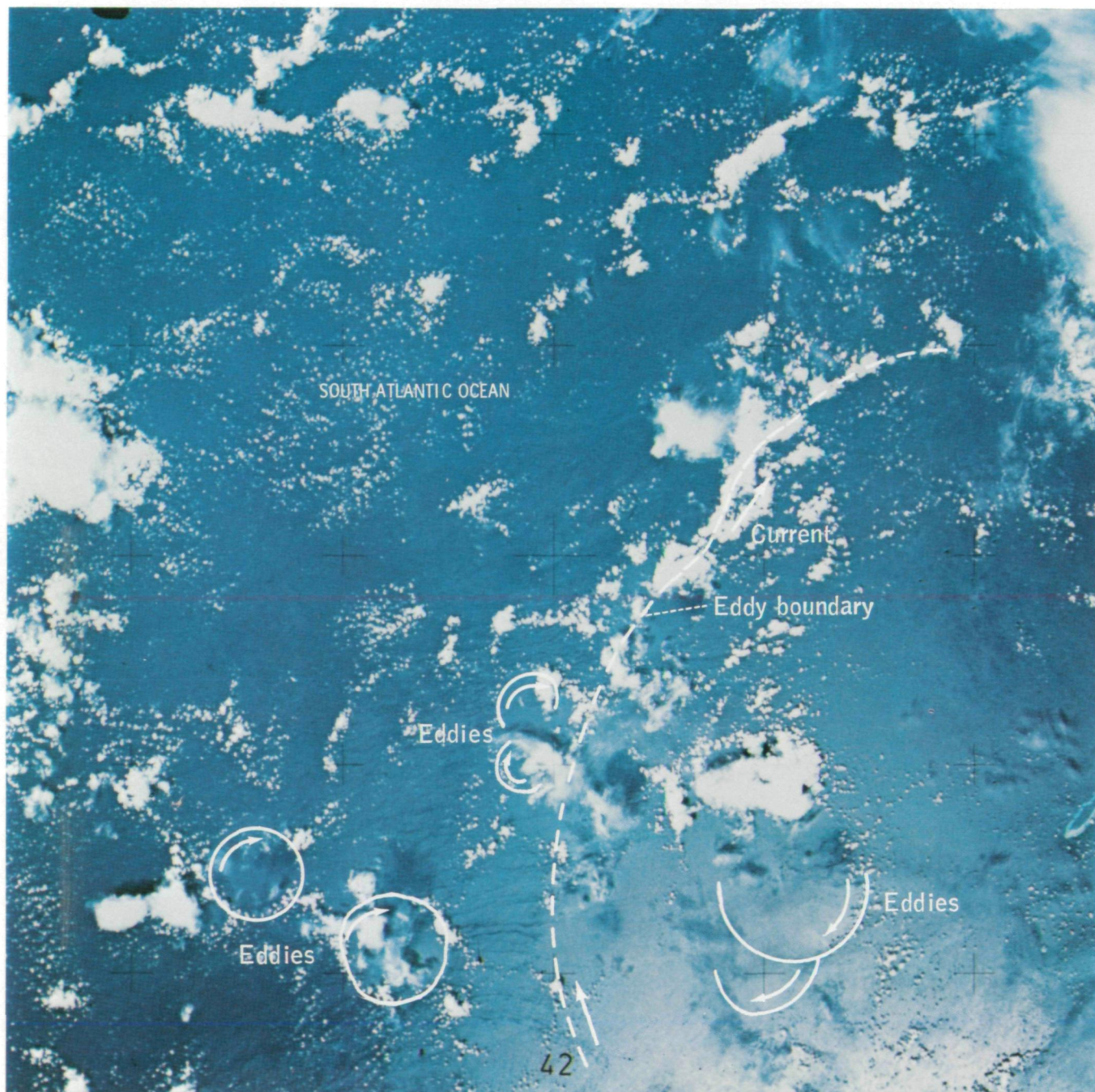


FIGURE 11-25.—Between South Georgia Island and the Falkland Islands, the West Wind Drift turns northeast and brings cool Antarctic waters into the South Atlantic Ocean. However, the water is warmer than the overlying air, which is blown from the south. Consequently, as this photograph shows, cumuli appear to outline some of the boundaries of eddies formed on the sea surface (SL4-138-3782).

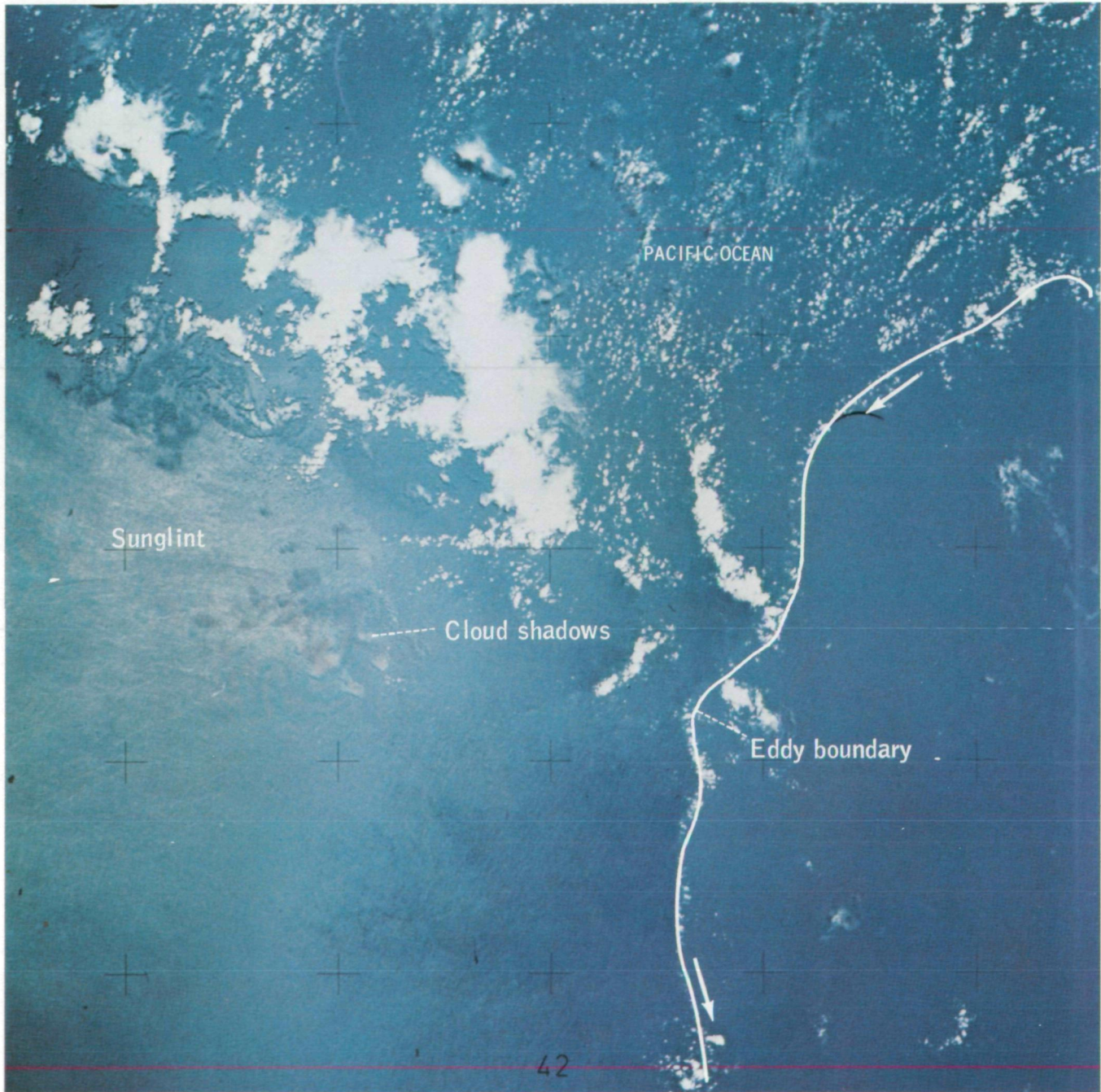


FIGURE 11-26.—Approximately 1000 km northeast of New Guinea, the equatorial countercurrent of the tropical Pacific Ocean flows easterly through Micronesia. Turbulence of various scales occurs, and tropical cumuli respond to slight differences in water temperature. This condition appeared visible to the Skylab 4 crewmen as they searched for large eddies (SL4-138-3761).

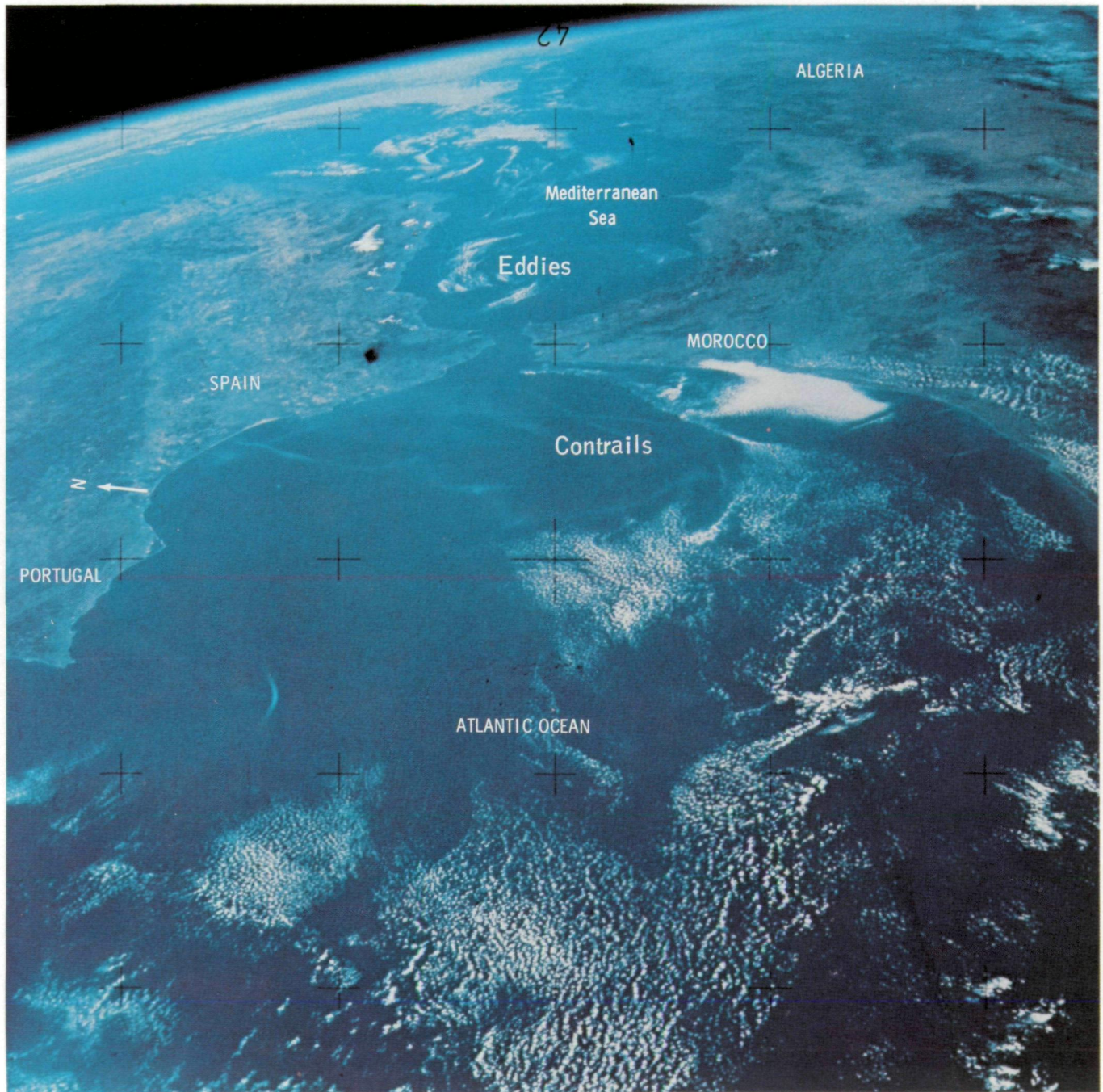
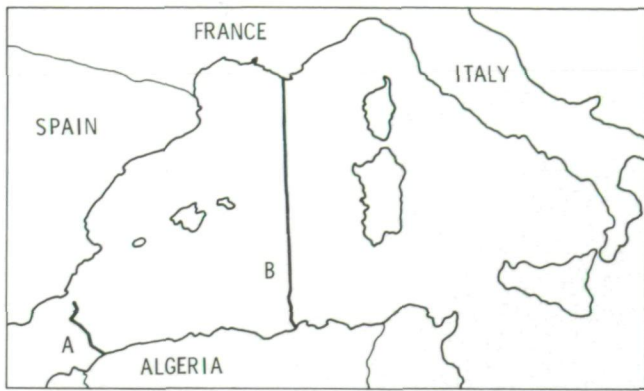


FIGURE 11-27.—The entire western core of the former Saracen Empire (southern Spain, Morocco, and Algeria) was visible under clear skies. Over the western Mediterranean Sea, cumuli are arranged in a series of large eddies (SL4-141-4415).

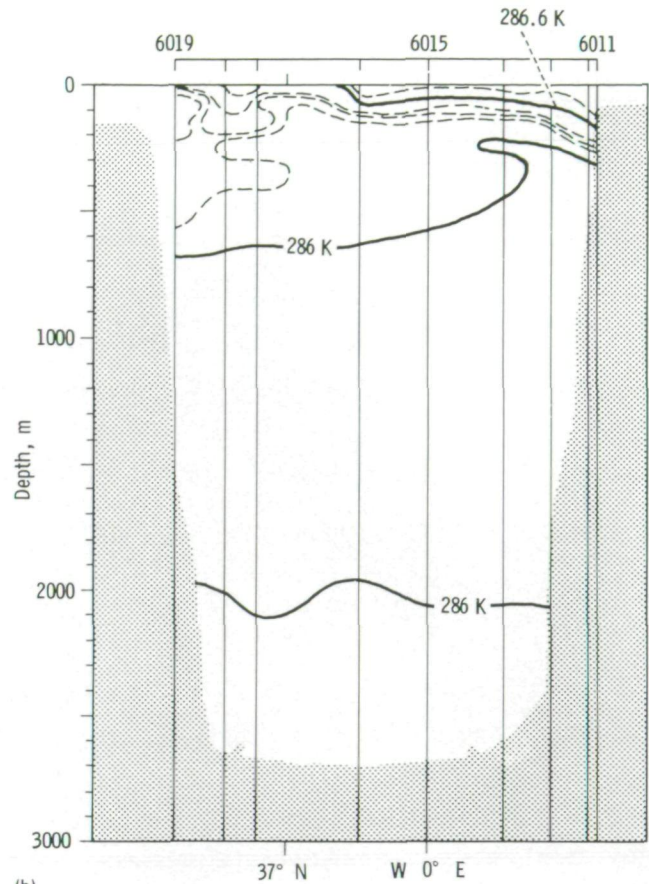


FIGURE 11-28.—The northern edges of two large eddies are clearly visible in sunglint in this summer view of Spain, Morocco, and Algeria (SL2-5-370).

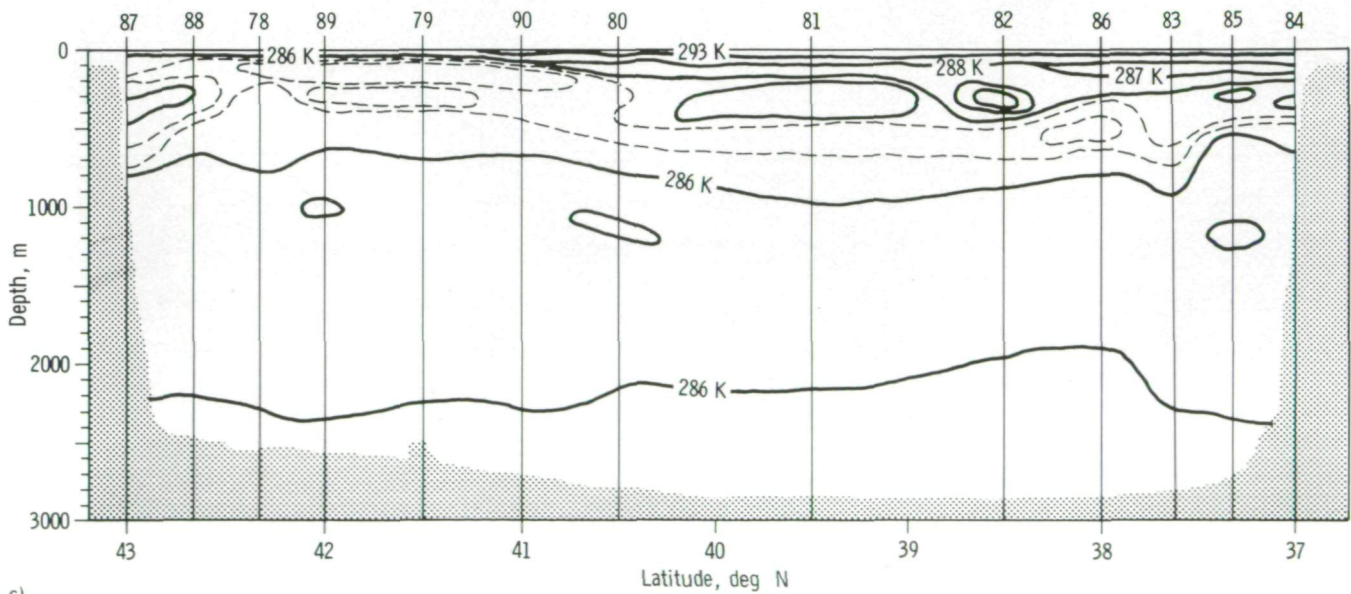


(a)

FIGURE 11-29.—Water temperature profiles taken along two lines in the western Mediterranean Sea (figs. 11-27 and 11-28). Numbers at the top are station numbers. Data from Woods Hole Oceanographic Institution. (a) Profile location map. (b) Profile A. (c) Profile B.



(b)



(c)

Upwelling and Turbulence

The process of coastal upwelling falls within the synoptic scale of turbulence in the sense that the sea is modified over areas of tens of thousands of square kilometers. The mechanism by which coastal upwelling is induced is fairly simple. Winds blowing parallel to, or slightly offshore from, a coastline (the shore being to the left looking downwind in the northern hemisphere; to the right in the southern) cause the warm surface waters to move seaward. To replace that loss, waters from some depth in the ocean move towards the coast and rise to the surface. Such subsurface water is always cooler and contains more nutrients than the departed surface water. The consequence is that coastal regions adjacent to upwellings are bathed with cooler-than-usual air and water, are covered by low clouds, and have a coastal fishery more abundant and concentrated than in other parts of the sea.

The crew was conscious of the importance of upwelling to world fisheries and spent some time looking for its manifestations. Mainly, they looked for water near the coast that was darker blue than that farther offshore. As the commander noted during debriefing, after looking at a photograph of the Chilean Coast (fig. 11-30), "That is what I intuitively called upwelling because it was a darker blue color and it looked slicker—a little bit smoother than the other water."

Most of the time, the Skylab 4 crewmen were looking for colors that they thought were caused by differences in plankton content (the more plankton, the greener the water). Indeed, they frequently observed such differences associated with the Falkland Current and waters around New Zealand. However, along the Chilean coast, the color distinctions were caused by differences in roughness of the sea, as seen in figure 11-30.

In some areas, the upwelling waters were more turbulent than in others because of the irregularities of the coastline and the occurrence of strong winds at the time of the observation. These two conditions combined to provide the view in January 1974 of the coast at the Peru-Chile border (fig. 11-31). On January 22, the pilot observed "a large circulation eddy—about 250 km in diameter" approximately 200 km off the western coast of Guatemala. He commented that "its shape was that of a swirling back hook," and it appeared to have "broken off" from the coastal current.

The crew was well prepared, therefore, to examine the coastal current off Chile and Peru, which is similar

to that off Guatemala except that it flows north rather than south. Large embayments and adjoining headlands act in concert with turbulence in the current to produce the large eddies seen along the arid Chilean coast. Overlying the 60- to 80-km-wide eddies on their shoreward edge are water-surface areas covered by a lacelike pattern of wind-induced, small-scale turbulence. The larger of the two areas in this scene, which was a vivid display in the Sun's reflection from the sea surface, occurred off the nearly straight coast terminating at Punta Coles. That straight coast interacts with air blowing at speeds greater than 13 m/sec from inland to create the turbulence. Such lacelike turbulent vortices are well known from wind-tunnel experiments (ref. 11-6) and were described 50 years ago by Theodore von Kármán. This photograph was the first from Skylab to show such turbulence in coastal seas.

A much different upwelling system occurs off the coast of Portugal (fig. 11-32). Cumulus cloud streets indicate winds blowing from the north. Water moved away from the coast by these winds meets the offshore water at a scum line which is perpendicular to the cloud streets. This nutrient-rich upwelling water supports the anchovy population that is a mainstay of Portugal's fishing industry.

These examples of synoptic-scale eddies in coastal oceans, where they are usually easier to study than in the open ocean, show that the various scales of turbulence described by Roll (ref. 11-5) do indeed exist in the ocean. It seems certain, therefore, that many of the physical processes involved in energy transfer can be studied in coastal waters. Furthermore, because of these impressive observations from the Skylab 4 crewmen of the magnitude of turbulence along the coasts of the world, there is now a much better understanding of the manner in which open-ocean eddies may be destroyed by interaction with the land boundaries.

Large-Scale Eddies

Large-scale circulation in the ocean and atmosphere includes systems that vary in time from weeks to several decades. It is the latter scale that is called climatic change, although it should be recognized that it is a variation, for there is no real evidence of permanent changes. Nonetheless, the fact that variations of considerable magnitude do take place (such as the ice ages) establishes the desirability of recognizing the causes and signs of approaching departures from long-term

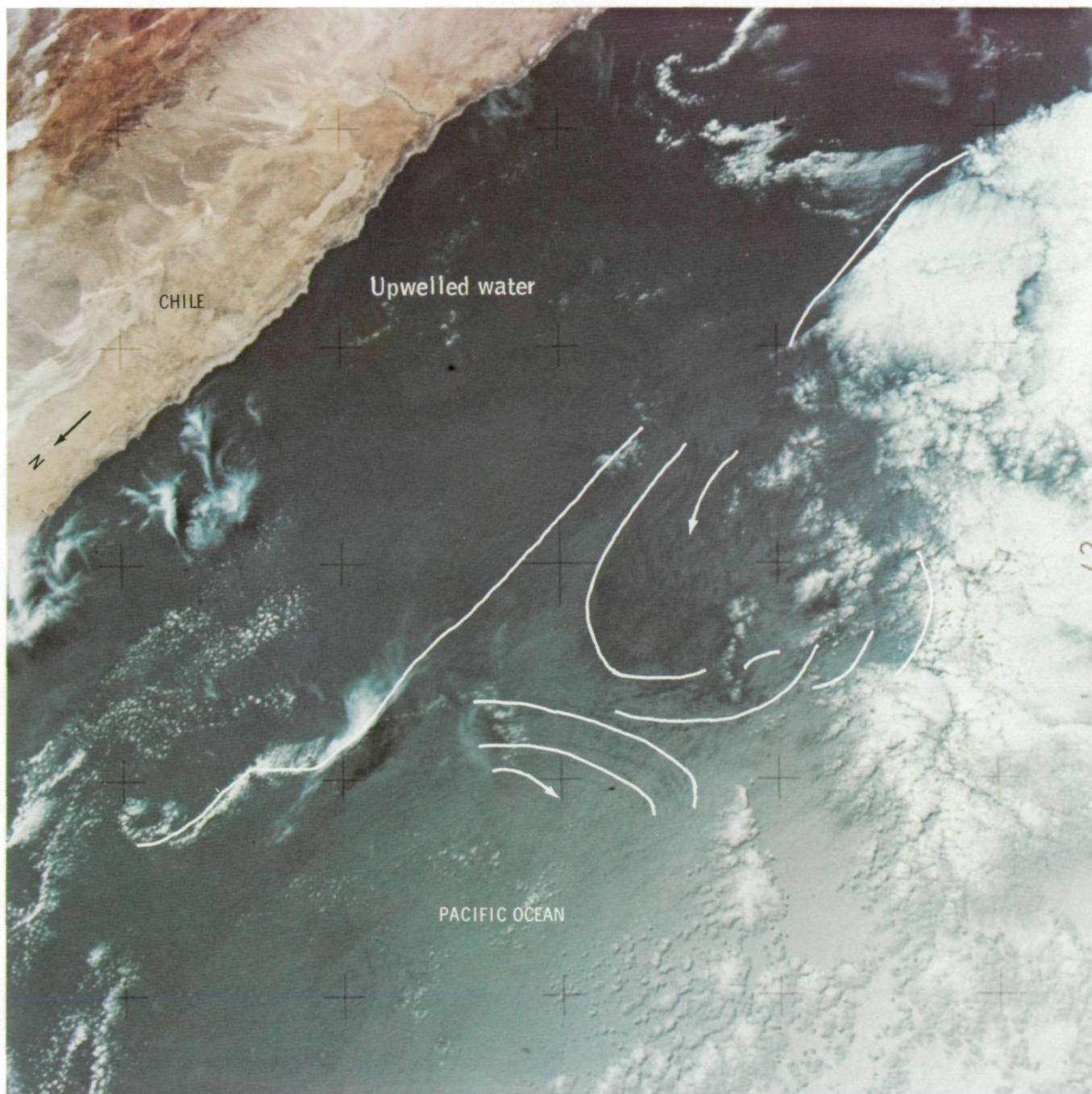


FIGURE 11-30.—Adjacent to the coast of Chile, the sea surface appears smooth compared to the surface offshore beneath the scattered stratocumuli. The coastal waters are darker blue than those in the more diffuse reflection from the seaward surface. Two large (100 km) eddies are visible because of these surface texture differences (SL4-138-3854).

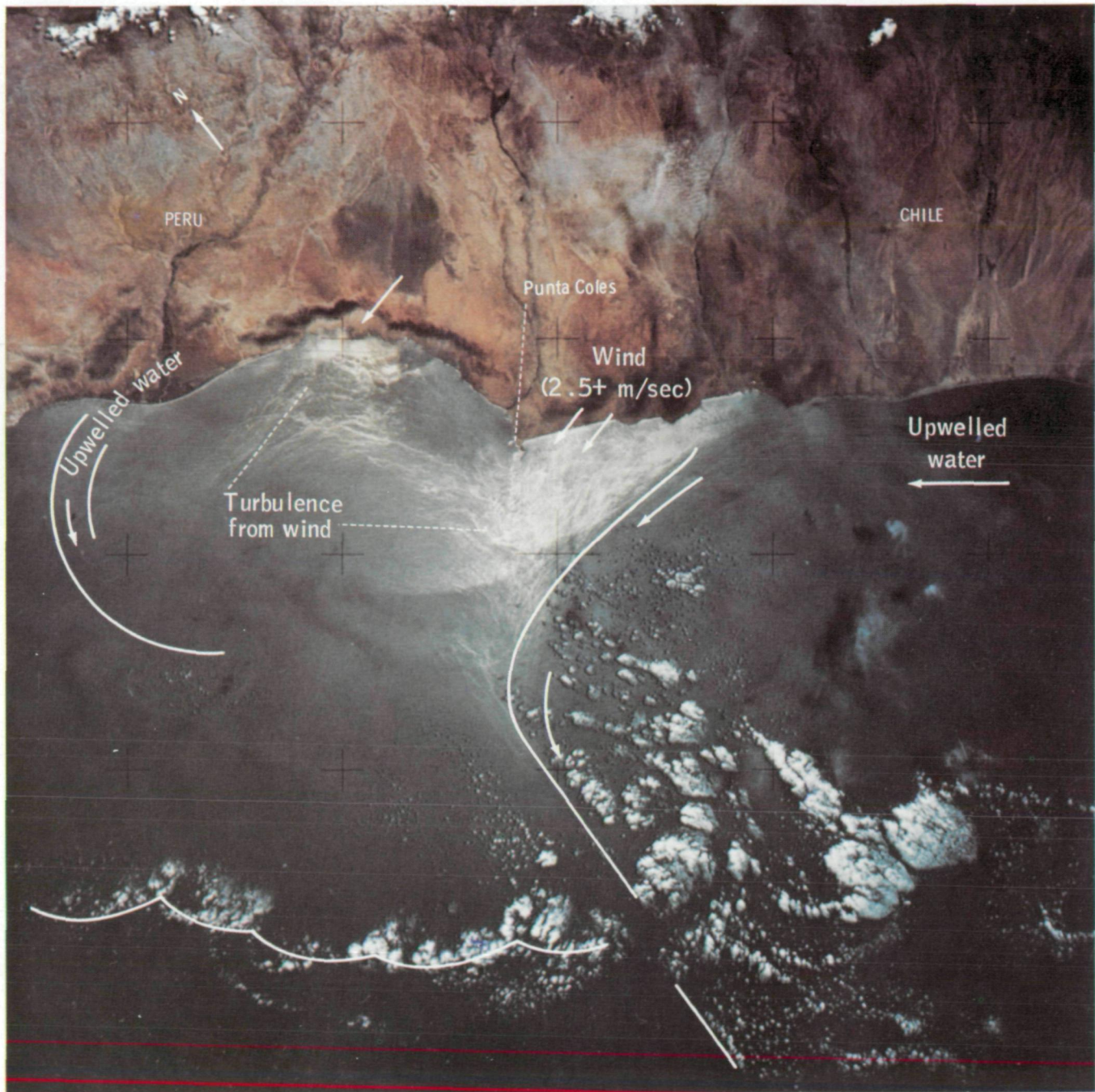


FIGURE 11-31.—Along the coastline of Peru and Chile, solar reflection illuminates lacelike patterns of turbulence and large (100 to 200 km) eddies driving the waters offshore (SI.4-138-3858).

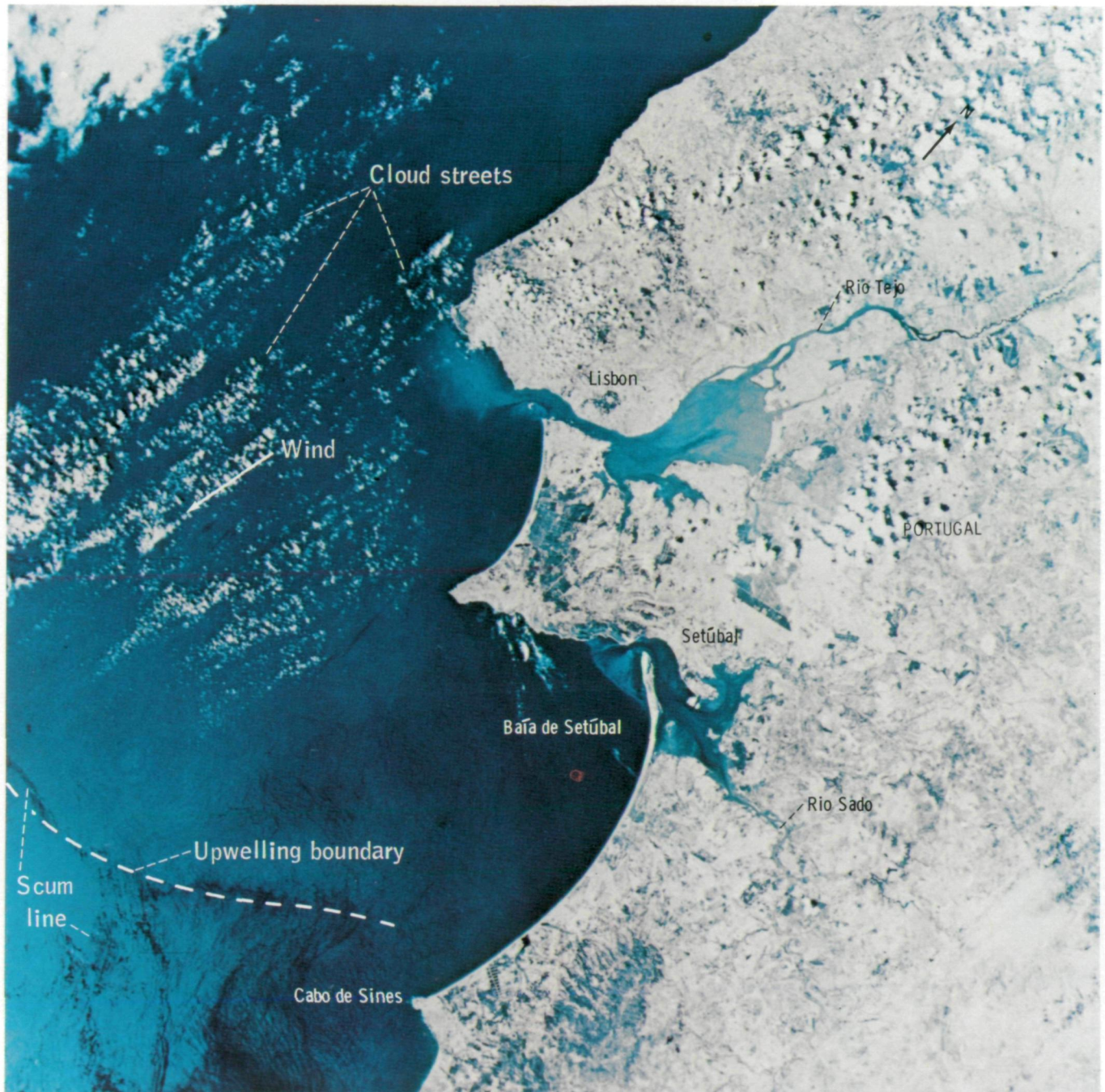


FIGURE 11-32.—Heavy sediment flowing into the Rio Tejo estuary and along the coast of Portugal is depicted in this vertical photograph taken by the EREP multispectral camera. In contrast, the Rio Sado is carrying light sediment into the Baía de Setúbal. Offshore, cumulus streets aligned with the northerly winds indicate the area of upwelling typical to this coast. Water temperature in the area of the photograph was measured earlier in the summer of 1973; upwelled water was 7 K cooler (288 K) than the waters 80 km from shore (295 K) (data from Woods Hole Oceanographic Institution). Concentrated off Lisbon, the southern boundary of upwelling is marked by a line extending from just north of Cabo de Sines westward out of the field of view (SL3-34-317).

climatological conditions. To do this, an understanding is needed of how energy transferred through the scales of turbulence interacts with the deepest parts of the ocean. This understanding is similar to the desire to understand the eddy systems of smaller size, but now the concern is for systems covering the entire width of a major ocean.

Again, the necessity of measuring the different scales throughout the ocean is clear. Fortunately, as with the coastal ocean, the visual observations and photographs from the Skylab 4 mission have provided a basis by which logical measurement schemes can be devised. Constantly, over most of the ocean, the crewmen saw what they called "the predominant surface texture" overlying features that were (1) "arc-shaped," (2) "parallel to one another, but not linear," (3) with "width to diameter ratios of 5 to 10," and (4) "stacked up all the way along." An interesting example was observed and photographed west of the Galapagos Islands (fig. 11-33). Although the fine texture (surface wind waves and long, parallel ocean swell) is not visible in the photograph, what the commander and the science pilot called their "corduroy sea" and "denim sea," the scales of turbulence similar to those noted off the Chile-Peru coasts, provided a spectacular display. The lacelike, wind-driven turbulence is seen as a texture overlying at least five eddies with 50- to 60-km diameters all convex to the left of the field of view. These in turn overlie a boundary of a much larger system (with a diameter of at least 500 km) with differing current velocities on either side (at the bottom of the field of view). The shear in the middle-sized eddies is not only clear in the photograph but was noted by the crewmen as an "interference pattern."

The photographs and observations do not clarify the question of the origin of the eddies. Are they the direct result of the overlying winds, or are they formed in the ocean's major circulation system? The likelihood is that both modes of origin exist with those exemplified in figure 11-33 formed by shears in ocean currents and those seen responding as cloud features (fig. 11-34) formed by wind reacting to the interference of the flow by islands.

The winds were from the south in January 1974 when the Skylab 4 crew passed over the Hawaiian Islands. Clouds were seen banked against the southern coasts of Lanai, Maui, and Hawaii with large cumulus forming over Mauna Loa (north of the snow ring around the crest) and Mauna Kea of the Big Island.

Cloud lines and eddies were building to the north of the islands, but to the south, semicircular rings of cumulus were forming, probably along boundaries of large ocean eddies.

The boundaries of eddies with diameters of 500 to 1000 km were visible to the crewmen in many parts of the ocean and were denoted by several features: clouds, shears, differences in surface texture, and color. All three crewmen became quite adept at distinguishing such features even though, as the commander noted, "The system does not come out totally," and the pilot added, "Looking straight down, all you can do is get a piece of it."

One such "piece" was observed south of Australia (fig. 11-35). The gently curving, sharp boundary extended more than 400 km, 200 of which were photographed. The wind was blowing toward the brightly reflecting water indicating the relative motion—the bright, shiny water moving into the wind.

Interaction of Ocean Waves and Currents

While describing his "corduroy sea" (parallel ocean swells), the commander pointed out how persistent the pattern was across the ocean until Skylab passed over an ocean current and there the "texture" (of the sea) just seemed to disappear. The implication was that the ocean swells on the surface of the sea were "absorbed," or blotted out, by the flow of the current. The commander stated that he saw this phenomenon frequently but thought that this interaction between ocean swells and currents was common knowledge among oceanographers. His observations were of great importance. Although oceanographers and seamen had long known of the interaction of wind waves and currents (ref. 11-34), attempts to verify any interaction between ocean swells and currents have been fruitless (ref. 11-35). Although no pictures of this phenomenon were taken by the Skylab 4 crewmen, a chance photograph taken during the Skylab 3 mission caught a swell/current interaction (fig. 11-36). A small "corduroy" pattern does not extend across the sharp, current boundary. Less easily seen is another wave system that was moving from the upper left. Because this wave system did not fully cross the boundary, an irregular "confused" wave field within the mainstream of the current resulted.

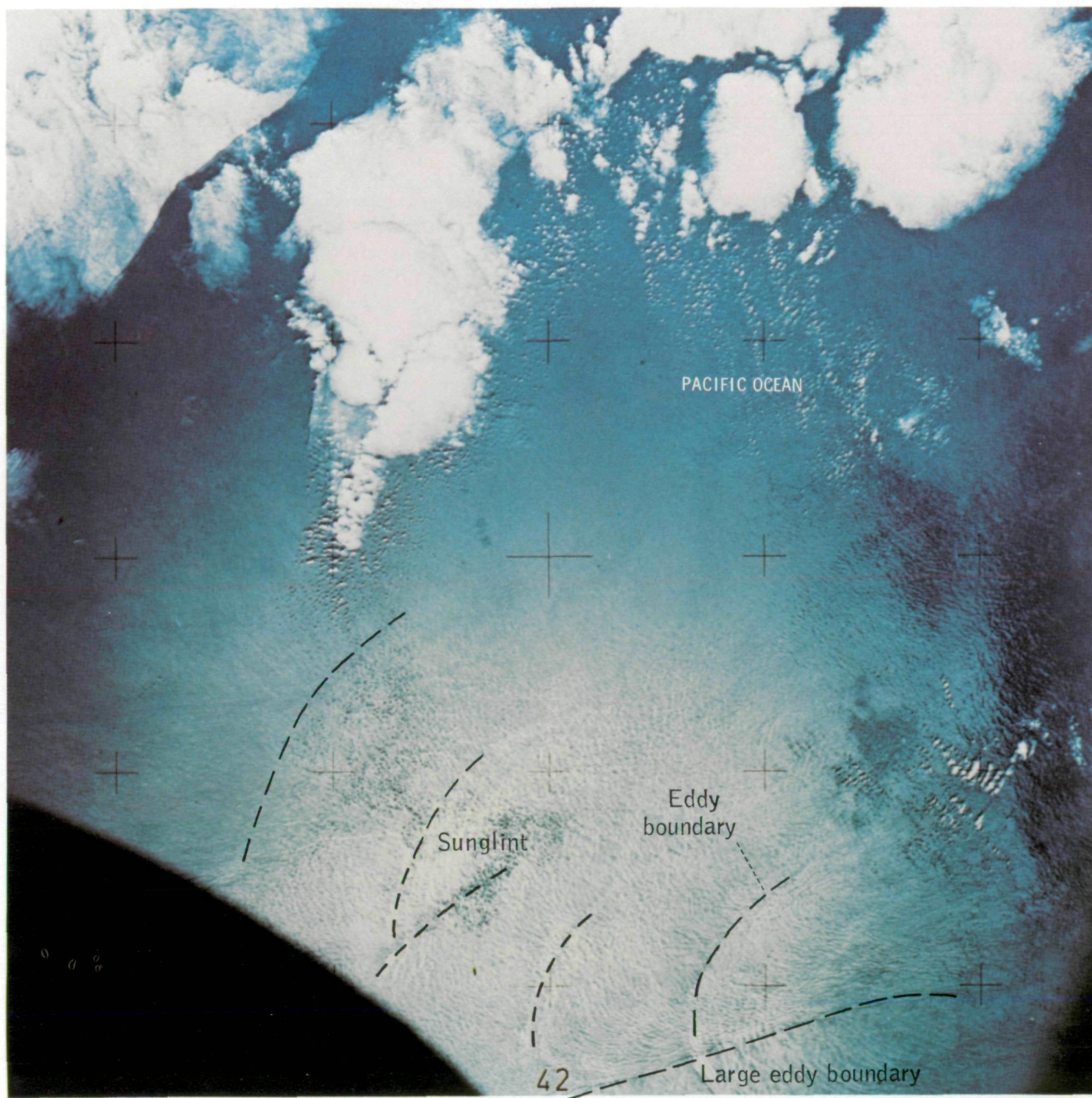


FIGURE 11-33.—Lacelike, wind-driven turbulence, 100-km-diameter eddies, and a major shear boundary near the bottom of the field of view are visible in sunglint on the Pacific Ocean west of the Galapagos Islands (SI.4-138-3842).



FIGURE 11-34.—South of Hawaii, huge rings of cumuli, like a chain, establish a pattern indicating large-scale turbulent eddies. The contrail of a jet aircraft is also visible (SL4-138-3865).

ORIGINAL PAGE IS
OF POOR QUALITY

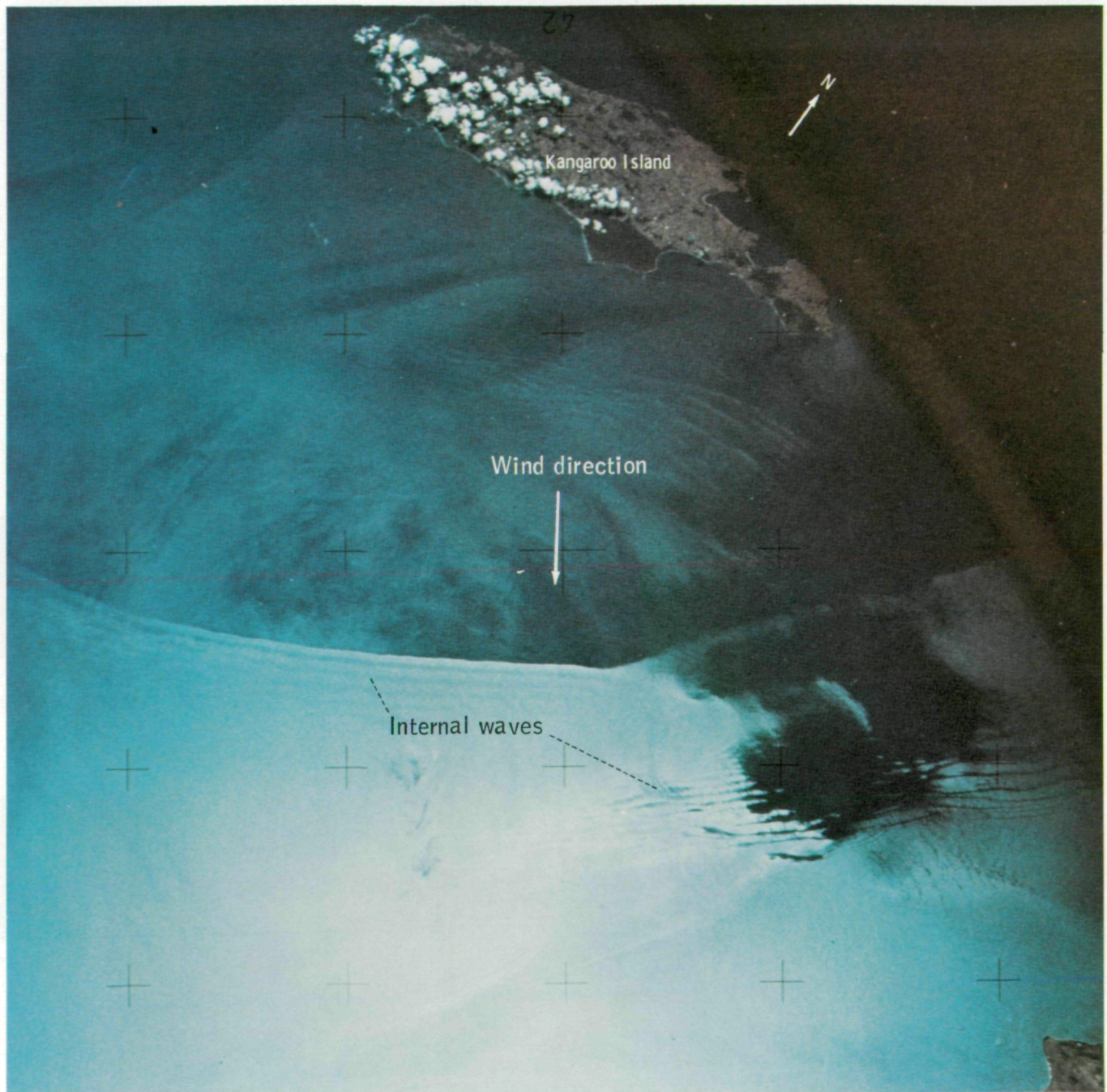


FIGURE 11-35.—An unusually well-defined water mass boundary was seen by the Skylab 4 crew near Kangaroo Island, off the southern coast of Australia. The specular point of the sun glint pattern is near the bottom of the scene, where waveforms 5 to 10 km long are visible. The regularity indicates internal waves. No waves are noted north of the boundary (SL4-137-3564).

FIGURE 11-36.—The Skylab 3 multispectral camera photographed this water boundary in the Atlantic Ocean approximately 300 km south of Bermuda. Ocean swells entering the field of view from the top of the photograph did not cross the boundary (SL3-28-050). →

ORIGINAL PAGE IS
OF POOR QUALITY

Ocean Currents

Ocean currents were identified by the crewmen on the basis of surface texture, atmospheric effects, and water color. Current boundaries may be marked by abrupt changes in surface texture, because patterns of rough and/or slick water occur within the current in contrast to the more uniform texture of adjacent water. Surface texture is best viewed in the Sun's reflection, often with striking visual effects. The Humboldt Current, for example, was recognized on this basis. Figures 11-30 and 11-31 illustrate the patterns associated with the current on January 2, 1974. At that time, the interaction of the current with the western-curving South American coast could be detected.

As air moves across water-mass boundaries, temperature differences between the water masses sometimes produce visible atmospheric effects. The crewmen recognized such an effect on January 11, as they were observing the western Pacific current near Luzon. The pilot reported:

This appears just to be northeast of Luzon probably on the order of 150 miles [278 km]. And the thing that's so significant about this is that the path—there's a clear path in the clouds that corresponds apparently to a current path in the surface of the water. You can actually see . . . the streaks and striations and the countereddies in the water, and it was very apparent to Jerry [commander] in the binoculars as he was looking at it.

Differences in water color, useful as current indicators, are usually caused by concentrations of plankton of various colors (fig. 11-37). Such concentrations act as natural tracers that outline current paths and eddies. Because of the prolific plankton growth, the surface circulation system of the southwestern Atlantic Ocean was spectacularly displayed to the orbiting observers. Comments of the crewmen in flight and during debriefing form the basis for the following analysis of the ocean current in this area.

The Falkland Current could be seen extending from near the Falkland Islands, off the Strait of Magellan, to Montevideo, a distance of approximately 2500 km. As the current flowed around the Falkland Islands, it split into two eddying portions but then merged in the lee of the islands before continuing northward. The main current that came from the southwest appeared strong and substantial, and an offshoot that angled off toward the northeast also appeared strong.

As the main body of the current moved northward, some eddies seemed to peel off or to be shed in a southerly direction. One such eddy became trapped in the Golfo San Jorge for several days. Another eddy that had a counterclockwise rotation entered the northern end of the Golfo San Jorge, and an additional current offshoot moved into the Golfo San Matias. In those places, the main current was 65 to 80 km off the Argentine coast.

The Brazil Current, flowing to the south from the bulge of Brazil, was difficult to detect more than 240 to 320 km north of Montevideo but could be observed easily where the Falkland and Brazil Currents met. In the region off the Rio de la Plata, there was no apparent mixing of the two currents but rather they intertwined, often into numerous "S" and figure "8" shapes. The westernmost portion of the confluence was notable for a large eddy or eddy system. At the confluence, the vortexes did not shed down into smaller and smaller ones, confirming the concept that such turbulence grows by coalescing eddies.

In one instance, a huge clockwise-rotating eddy broke off and started to move to the south-southeast only to come back and remix farther to the south with the Falkland Current.

As the intertwined currents moved from near the Rio de la Plata to the southeast for 3000 to 5000 km, the bright colors dimmed but with an occasional bright plankton streak. Some of the streamings from the currents reached large amplitudes and formed a sinuous-serpentine pattern; in some cases, the waveforms became unstable and eddies were detached. The boundaries of these currents were complex and curved and exhibited considerably stringy texture. As they neared the African coast, the visible discoloration in currents disappeared before the current turned to the north.

Windborne Sediment Entering the Ocean

One of the curiosities of sediments on the sea floor is the large percentage of windborne dust and volcanic ash. Assessments of these sedimentary constituents were of interest to but a small community of scientists until the early 1970's when atmospheric pollution became a public concern. Shortly thereafter came the growing discussion regarding worldwide climatic variations, especially as they relate to social growth. Most research into climatic change has centered around



FIGURE 11-37.—The Skylab 4 flightcrew was especially intrigued by the multicolored plankton blooms that extend over the length of the Falkland Current. Crewmembers said the colors they saw were even brighter than those in this photograph (SI4-196-7350).

prehistoric climate cycles, with much of the data coming from a study of windborne dust contained in deep-sea sediments. Consequently, the observations of dust clouds made by the Skylab 4 crewmen were of interest to oceanographers, marine geologists, and environmentalists.

The Skylab 4 crewmen made repeated observations of windblown dust from desert regions, and of smoke

and dust from a volcanic eruption, that were carried over portions of the sea. As indicated in table 11-I, six observations of volcanic ash and five of terrestrial dust carried seaward were recorded.

A dust cloud from the Sahara region (fig. 11-38) was described that extended approximately 120 km seaward from the Mediterranean coast, and on another occasion, one was observed that spread seaward approximately 50

km from an area near Algiers. Dimensions, color, and associated meteorological fronts were noted, including the streaks that trailed behind the main dust head. During debriefing, an additional dust cloud was described that had been observed moving from the Iranian Deserts over the Arabian Sea.

Winds of considerable force and duration blowing from arid regions seaward are particularly dominant in the African, Middle East, and central Asian deserts; sufficiently so that in a number of instances they have been given distinctive names (ref. 11-36). In Egypt, there is the Haboub and the Khamsin (winds of 50 consecutive days); the Sirocco, a hot desert wind from the Sahara and particularly from Syria and Israel, blowing

from the desert over the Mediterranean Sea; and in Iran, the Seistan, a strong seaward-directed wind, is also known as the "wind of 120 days." Even though these winds occur regularly and have an unquestioned dust-carrying ability, little valid data exist on the volume of sediment transported seaward.

There is no agreement on the magnitude of the contribution of windblown silt and clay to the marine environment. Biscaye (ref. 11-37) largely discounts the contributions of windborne sediment to deep-sea clays, but Windom (ref. 11-38) suggested that globally transported dusts may comprise from 25 to as much as 75 percent of the detrital phases of marine sediment in the North and South Pacific and Central Atlantic



FIGURE 11-38.—Algiers, a port on the Mediterranean, lies amidst the paths of frequent Saharan dust clouds. An extensive seaward protrusion of such a cloud is shown in this photograph taken by the Skylab 4 crewmen (SL4-140-4163).

Oceans (ref. 11-39). More recently, Kukal and Saadallah (ref. 11-40) proposed that as much as 2.1 cm of atmospheric dust fallout may occur in a single year.

Skylab 4 crewmen were able to visually differentiate among duststorms, cloud cover, volcanic eruptions, and smoke (refs. 11-41 and 11-42 and table 11-I). In this manner, the areal extent of duststorms can be accurately delineated. If, during future manned flights, simultaneous sampling could be accomplished by support aircraft at several elevations within the dust cloud and at several positions in its horizontal extent, the first even moderately quantitative data on the volume of sediment transported by a given storm could be obtained. These data would then be used to determine approximate volumes of sediment removed from desert regions and to make a more precise evaluation of windblown fallout.

An interesting dividend might then accrue from the work of Parmenter and Folger (ref. 11-43) who, using the amount of wind-carried biogenetic detritus (as diatoms) in deep-sea sediments, related higher-than-normal dust concentrations in equatorial marine sediments during cool climatic periods to increased desiccation in the Saharan regions.

CONCLUSIONS

The Skylab 4 mission allowed large-scale, dynamic ocean features such as ocean currents and associated eddies to be observed, described, and photographed repeatedly. Such synoptic study is vital to the understanding of these features and was accomplished by visual observations and handheld-camera photography (ref. 11-44). The flexibility and advantages unique to this method were demonstrated by the Skylab crewmen and can be summarized as follows.

1. Crewmen were able to choose direction and angle of observation so that they made the maximum number of possible observations of a single site. Further, sites of opportunity were selected with increasing care as the flight progressed. This selectivity increased the use that could be made of the reflection of the Sun where current boundaries, turbulence, and slicks are best observed.

2. Crewmen were able to take selected oblique photographs. In this way, systems that were 300 km or more in diameter could be photographed.

3. Visual observations could be made when cloud

cover or haze precluded photography. The crewmen were able to look through small clear areas and thin cirrus overcasts and describe features that they were unable to photograph.

4. There were wind conditions that created cloud patterns useful in detecting certain ocean features. Such conditions were recognized, described, and easily photographed by crewmen.

5. The crewmen provided a real-time capability; data could be discussed and transmitted as they were gathered so that existing conditions could be provided to any user within minutes.

6. The detailed examination of the photographs subsequent to the flight, together with pertinent oceanographic, meteorologic, and visual observation data, added significant information to the frequencies of motion in the ocean.

7. For some features, it will be possible to amend existing charts of ocean currents on the basis of visual observations and photographs.

8. Observations from space are capable of contributing to the following sediment studies: (a) character of the dominant type of suspended load contributed by a river; (b) types of coastal-sediment transport; (c) paths of sediment dispersal; and (d) variability of sediment contribution.

RECOMMENDATIONS

The successful visual observations of the ocean made during the Skylab mission clearly indicate that man in space plays a key role in acquiring useful Earth resources information. To put this capability into an operational mode, there must be an appropriate data gathering and analysis system aboard the space laboratory. From such requirements come these recommendations.

There should be sufficient onboard computer capability to conduct analysis of multispectral data and display the results. This capability is essential to the concept of site and data selection. It will be possible, therefore, to transmit "answers" to ground stations based on the onboard processing results, thereby reducing data rates by one to two orders of magnitude.

A wide-band uplink and downlink video transmission capability is essential. Only in this way can effective testing and verification of the real-time objectives be accomplished.

Sensors

All sensors must be boresighted; that is, the resolution element for any sensor must be able to be overlaid in the image plane by another resolution element from any other sensor. This is achievable partly by hardware and partly by software. It will permit the crewman to describe any Earth feature in the ultraviolet, visible, reflected, thermal infrared, and microwave frequencies. The intensity of the signal as a function of wavelength can be recorded thusly, and the record processed to provide information on shape, color, thermal radiation, dielectric constant, and polarization effects.

The geometry of all sensor records must be able to be reformatted to represent the true geometry of the scene. At least one sensor record will provide stereoscopic coverage.

The sensors must be designed with ease of maintenance as an important consideration. Experience has shown that man can make good use of even marginal equipment if he has the opportunity to make repairs and modify equipment operation.

Sensor System Control

The required hardware and circuit logic has been implemented for most sensors so that the crewman can have the option of frequency selection, format control (tape or film), and sensitivity selection.

Sensor attitude control is also essential, although the problem is more complex than that for sensor switching. A trade-off must be made between vehicle attitude and sensor-platform attitude. Probably, sensor-platform attitude implementation with stellar reference would be the best answer in view of the basic requirement of the spacecraft systems for a solar reference attitude. A gimbaled platform may be the best solution to this problem.

There is a requirement for the crewman to monitor the analog signal generated by the sensors and, in the case of image-forming devices, to examine the image quality. These displays should be an integral part of a calibration and sensor control panel.

Onboard Analysis

All sensors that record the scene in electronic form should be provided with A-scopes and a color cathode-ray-tube (CRT) display. The CRT should be designed

so that the scene is displayed continuously in a moving format. The scope should permit the crewman to monitor the full voltage range of the scene without an arbitrary baseline.

A multichannel oscilloscope should be incorporated in the display panel and should be computer driven. In this manner, scene redundancy can be analyzed and only spectral differences displayed in the multichannel unit.

Two analytical display units with a color output are desirable for both visible and microwave data analysis. Both displays should be computer driven because there would be a requirement for the multifrequency data to be reformatted, registered, stored, and analyzed for redundancy. The computer is required to have sufficient core to handle normal cross correlation and second- and third-order statistical analysis algorithms.

Sensor Payload Control

A pointing and tracking telescope is the heart of the sensor system, the device by which the crewman may make a major contribution. The telescope would be used as follows.

1. A high-resolution optical sensor. This is a requirement of all Earth-resource disciplines. With a telescope equipped with dichroic optics between the objective and eyepiece, one can simultaneously view and photograph the Earth. More important, the crewman can precisely point the telescope and, with the drive assembly, can select the sensor coverage and be assured that the feature is located at nadir on all sensors.

2. A sensor that need not make a record. The crewman can evaluate the scene and determine whether sensor coverage or visual observations would be the most suitable.

3. An onboard ground-truth device. Because the sensors will be equipped with image-forming displays and a clear relationship exists between the visible and other parts of the spectrum to be recorded, it will be possible to view the scene in high resolution through the scope and then refer to the displayed image. By this means, the maximum possible contrast record can be acquired.

Training

Crewmembers will need special training in sensor operation, calibration, and recording functions; in data

analysis; and in the Earth-science disciplines. Based on the experience of the Skylab 4 crewmen, it is clear that such a combined effort to observe and report on oceanographic features would be of measurable benefit to a multitude of seafaring groups.

REFERENCES

- 11-1. Ewing, Gifford C.: Current and Future Needs for Remotely Sensed Oceanographic Data—A Speculation. Proceedings of the Fourth Symposium on Remote Sensing of Environment, University of Michigan, 1966, pp. 7-11.
- 11-2. Ewing, Gifford C.: On the Design Efficiency of Rapid Oceanographic Data Acquisition Systems. *Deep-Sea Res.*, vol. 16, 1969, p. 35.
- 11-3. Yentsch, Charles S.: Measurement of Visible Light Absorption by Particulate Matter in the Ocean. *Limnol. Oceanog.*, vol. 7, no. 2, Apr. 1962, pp. 207-217.
- 11-4. McAlister, E. D.: Infrared Optical Techniques Applied to Oceanograph-1 Measurement of Total Heat Flow From the Sea Surface. *Appl. Optics*, vol. 3, no. 5, May 1964, pp. 609-612.
- 11-5. Roll, Hans U.: Problem Areas in Air-Sea Interaction. *Studies in Phys. Ocean.*, Science Pubs., vol. 1, 1972, pp. 63-72.
- 11-6. Laufer, J.: New Trends in Experimental Turbulence Research. *Ann. Rev. of Fluid Mech. Annual Reviews, Inc.*, vol. 7, 1975.
- 11-7. Brown, Garry L.; and Roshko, Anatol: On Density Effects and Large Structure in Turbulent Mixing Layers. *J. Fluid Mech.*, vol. 64, pt. 4, July 24, 1974, pp. 775-816.
- 11-8. Patzert, William C.: Current Meter Data: An Indication of Either Subtropical Counter Current or Anticyclonic Island Circulation. *J. Geophys. Res.*, vol. 78, no. 33, Nov. 20, 1973, pp. 7919-7922.
- 11-9. Scully-Power, P. D.: Coral Sea Flow Budgets in Winter. *Aust. J. Freshwat. Res.*, vol. 24, 1973, pp. 203-215.
- 11-10. Favorite, Felix; and McLain, Douglas R.: Coherence in Transpacific Movements of Positive and Negative Anomalies of Sea Surface Temperature, 1956-60. *Nature*, vol. 244, no. 5412, July 20, 1974, pp. 139-143.
- 11-11. Spilhaus, A. F.: A Detailed Study of the Surface Layers of the Ocean in the Neighborhood of the Gulf Stream With the Aid of Rapid Measuring Hydrographic Instruments. *J. Marine Res.*, vol. 3, 1940, pp. 51-75.
- 11-12. Stommel, Henry: *The Gulf Stream*. Second ed. University of California Press (Berkeley), 1965.
- 11-13. Bernstein, Robert L.: Mesoscale Ocean Eddies in the North Pacific Ocean: Westward Propagation. *Science*, vol. 183, no. 4120, Jan. 11, 1974, pp. 71-72.
- 11-14. Stevenson, Robert E.: Observations From Skylab of Mesoscale Turbulence in Ocean Currents. *Nature*, vol. 250, no. 5468, Aug. 23, 1974, pp. 638-640.
- 11-15. Defant, Albert: *Physical Oceanography*. Pergamon Press (New York), 1961.
- 11-16. Scully-Power, P.; and Twitchell, P.: Satellite Observation of Cloud Patterns Over East Australian Current Anticyclonic Eddies. *Geophys. Res. Letters*, vol. 2, Mar. 1975, pp. 117-119.
- 11-17. Liepmann, H.: Free Turbulent Flows. *The Mechanics of Turbulence. Int. Symp. Natl. Sci. Res. Ctr.*, 1961, pp. 211-227.
- 11-18. Carter, Louis D.; and Stone, Richard O.: Interpretation of Orbital Photographs. *Photogram. Eng.*, vol. XL, no. 1, Jan. 1974, pp. 193-197.
- 11-19. Vonder Haar, S. P.; and Stone, R. O.: Oceanographic Analysis of Orbital Photographs of the Upper Gulf of California. *Photogrammetria*, vol. 29, Apr. 1973, pp. 45-61.
- 11-20. Brodie, Jonathan W.: Coastal Surface Currents Around New Zealand. *N.Z. J. Geol. Geophys.*, vol. 3, 1960, pp. 235-252.
- 11-21. Stanton, B. R.: Circulation Along the Eastern Boundary of the Tasman Sea. *Oceanography of the South Pacific*, New Zealand National Commission for UNESCO, 1972, pp. 141-147.
- 11-22. Heath, R. A.: Low Cloud Boundaries Coincident With Oceanic Convergences. *N.Z. J. Marine Fresh Water Res.*, vol. 3, 1973, pp. 209-216.
- 11-23. Stevenson, R. E.: Space Photos Detect Changing Currents Along the Texas Coast. *Ocean Industry*, 1969, pp. 39-40.
- 11-24. Winant, C. D.; and Browand, F. K.: Vortex Pairing: The Mechanism of Turbulent Mixing-Layer Growth at Moderate Reynolds Number. *J. Fluid Mech.*, vol. 63, pt. 2, Apr. 3, 1974, pp. 237-255.
- 11-25. Langmuir, Irving: Surface Motion of Water Induced by Wind. *Science*, vol. 87, Feb. 1938, pp. 119-123.
- 11-26. Faller, Allen J.; and Woodcock, Alfred H.: The Spacing of Windrows of Sargassum in the Ocean. *J. Marine Res.*, vol. 22, no. 1, 1964, pp. 22-29.
- 11-27. Welander, Pierre: On the Generation of Wind Streaks on the Sea Surface by Action of a Surface Film. *Tellus Stockholm*, vol. 15, no. 1, Feb. 1963, pp. 33-43.
- 11-28. Faller, A. J.: The Angle of Windrows in the Ocean. *Tellus Stockholm*, vol. 16, 1964, pp. 363-370.
- 11-29. Scott, Jon T.; Myer, Glenn E.; Stewart, Ronald; and Walther, Eric G.: On the Mechanism of Langmuir Circulations and Their Role in Epilimnion Mixing. *Limnol. Oceanog.*, vol. 14, no. 4, July 1969, pp. 493-503.
- 11-30. National Academy of Science: *Understanding Climatic Changes*. National Research Council, Washington, D.C., 1975.
- 11-31. Namais, Jerome: Space Scales of Sea-Surface Temperature Patterns and Their Causes. *U.S. National Marine Fisheries Service Fishery Bull.*, vol. 70, no. 3, 1972, pp. 611-617.
- 11-32. Namais, J.: Longevity of a Coupled Air-Sea-Continent System. *Monthly Weather Review*, vol. 102, no. 9, 1974, pp. 638-648.

- 11-33. Miller, A. R.; Tchernia, P.; and Charnock, H.; Mediterranean Sea Atlas. WHOI Atlas Series, vol. 3, 1970.
- 11-34. Sugimori, Yasuhiro: Dispersion of the Directional Spectrum of Short Gravity Waves in the Kuroshio Current. *Deep-Sea Res.*, vol. 20, no. 8, Aug. 1973, pp. 747-756.
- 11-35. Kenyon, Kern E.: Wave Refraction in Ocean Currents. *Deep-Sea Res.*, vol. 18, no. 10, Oct. 1971, pp. 1023-1034.
- 11-36. Stone, R. O.: A Desert Glossary. *Earth Science Rev.*, vol. 3, no. 4, 1967, pp. 211-274.
- 11-37. Biscaye, P. E.: Mineralogy and Sedimentation of Recent Deep Sea Clay in the Atlantic Ocean and Adjacent Seas and Oceans. *Geol. Soc. America Bull.*, vol. 76, 1965, pp. 803-832.
- 11-38. Windom, Herbert L.: Atmospheric Dust Records in Permanent Snowfields: Implications to Marine Sedimentation. *Geol. Soc. America Bull.*, vol. 80, no. 5, May 1969, pp. 761-782.
- 11-39. Griffin, John J.; Windom, Herbert; and Goldberg, Edward D.: The Distribution of Clay Minerals in the World Ocean. *Deep-Sea Res.*, vol. 15, Apr. 1968, pp. 433-459.
- 11-40. Kukal, Z.; and Saadallah, A.: Aeolian Admixtures in the Sediments of the Northern Persian Gulf. *The Persian Gulf*. B. H. Purser, ed., Springer-Verlag, 1973, pp. 115-121.
- 11-41. Randerson, Darryl: Preliminary Analysis of the Skylab 4 Imagery of Atmospheric Pollution. Skylab 4 Visual Observations Report. NASA TM X-58142, 1974.
- 11-42. MacLeod, N. H.; and Schubert, J. S.: African Drought and Arid Lands. Skylab 4 Visual Observations Report. NASA TM X-58142, 1974.
- 11-43. Parmenter, Carol; and Folger, D. W.: Eolian Biogenic Detritus in Deep Sea Sediments: A Possible Index of Equatorial Ice Age Aridity. *Science*, vol. 185, no. 4152, Aug. 23, 1974, pp. 695-698.
- 11-44. Garriott, Owen K.: Skylab Report: Man's Role in Space Research. *Science*, vol. 186, no. 4160, Oct. 18, 1974, pp. 219-226.

12

An Assessment of the Potential Contributions to Oceanography From Skylab Visual Observations and Handheld-Camera Photographs

GEORGE A. MAUL^a AND MICHAEL McCASLIN^a

FOR 84 days, the Skylab 4 crewmen had the opportunity to observe the oceans from a unique vantage point. The breadth and frequency of the survey provides a valuable and distinct view of this subject in a science long limited to a few ships for vast seas. The record of their observations gives not only improved insight into the detailed characteristics of oceanic features but also insight into the possible role space observers have in oceanographic experimentation.

This section will examine these roles by considering what has been learned in oceanography from space observations. Specifically, several interesting ocean photographs and visual observations made during the Skylab 4 mission will be discussed. Consideration of the uses and limitations of these photographs has produced a set of recommendations that the authors believe will optimize the information obtained from a space crew. The section will discuss that optimization compared to possible alternative systems for gathering the same type of data.

^aNational Oceanic and Atmospheric Administration; Atlantic Oceanographic and Meteorological Laboratories, Miami, Florida.

OBSERVATIONS

The Gulf of Nicoya on the Pacific coast of Costa Rica was photographed on January 28, 1974, at 12:25 local standard time (18:25 Greenwich mean time (GMT)) (fig. 12-1). This photograph is particularly useful because it shows detailed ocean features and includes land areas so that they can be located on a chart. The ability to determine the geographical coordinates and the time of a photograph is important in oceanography. Although a photograph demonstrates the types of features that can be seen from space, it is rarely useful for photointerpretation without such positioning information.

The striking feature of figure 12-1 is the apparent internal wave field, organized into at least three distinct packets, which can be seen on the left side of the photograph. These are interfacial waves that occur at density boundaries between layers within the water. When close enough to the surface, they may appear as parallel "slicks" on the water that move with the same velocity as the waves.

Historical surveys in this region have determined the existence of a density discontinuity at a depth of approximately 30 m. Measurements from the photograph

ORIGINAL PAGE IS
OF POOR QUALITY

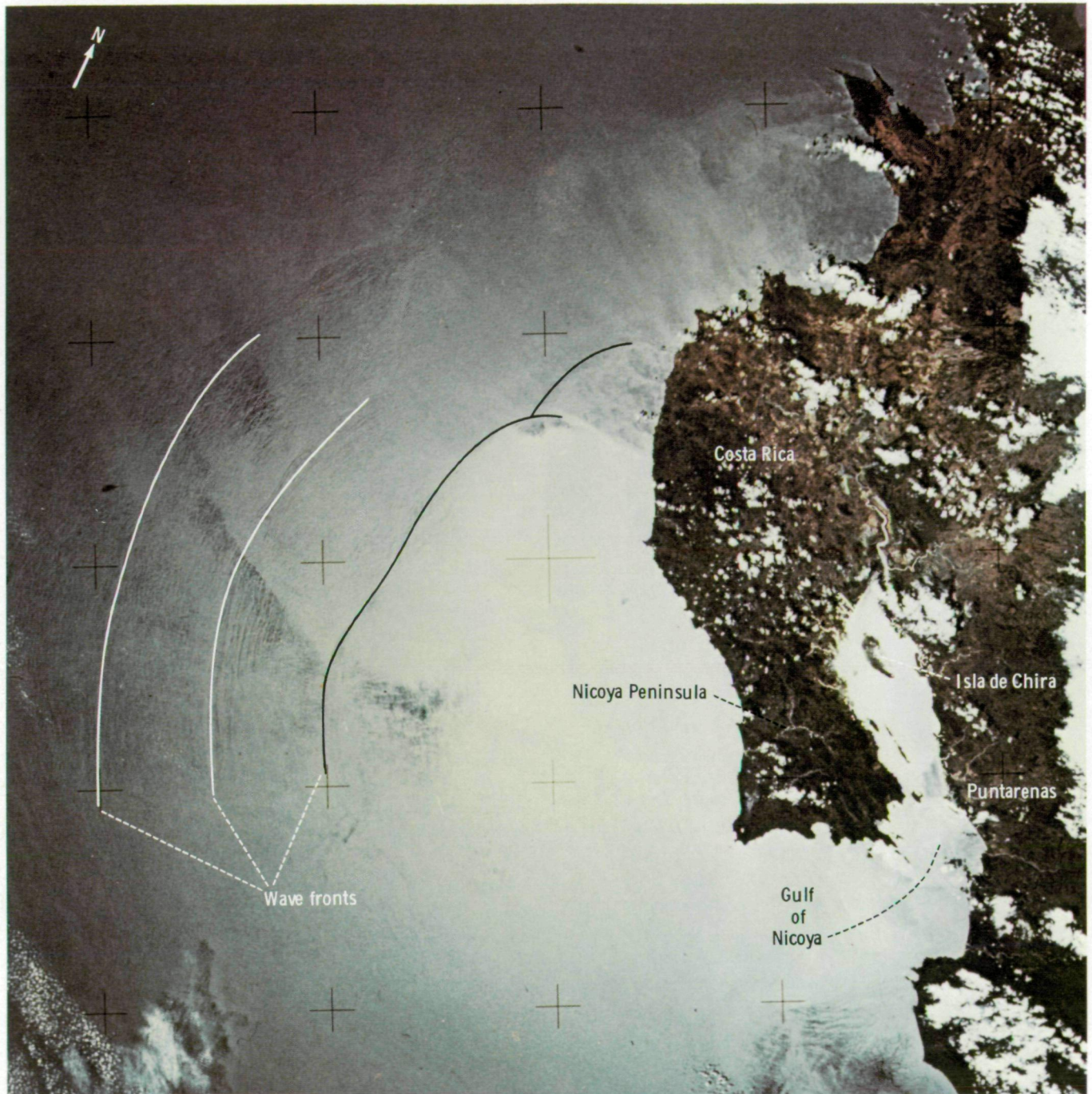


FIGURE 12-1.—Internal wave packets in the Pacific Ocean off the coast of Costa Rica. The leading edges of the three packets are identified by lines. Changes in apparent water color are due to specular return of sunglint caused by changes in capillary wave slopes. This 70-mm photograph was taken January 28, 1974, at 18:25 GMT (SL4-142-4567).

give a wavelength λ for the field of approximately 1000 m, with approximately 31 km between the fronts of the different packets. For a two-layer model:

$$C = \left[\frac{g}{k} \left(\frac{\rho - \rho'}{\rho \coth kh + \rho' \coth kh'} \right) \right]^{1/2} \quad (12-1)$$

where C = speed of the waves, ρ = density of the lower water layer, ρ' = density of the upper water layer, $g = 9.8 \text{ m sec}^{-2}$, h' = thickness of the upper water layer, h = thickness of the lower water layer, and $k = 2\pi/\lambda$. From equation (12-1), the wave speed is 69 cm sec^{-1} , which is within the expected range. With this speed and the distance of 31 km between packets measured on the photograph, the time between passage of the packets is 12.5 hours. This time corresponds very closely to the interval of the semidiurnal tide cycle dominant in this area, as shown by records from the tide station at Puntarenas. Such a finding supports the concept that internal or surface gravity waves are important in the dissipation of tidal energy, a parameter that affects the rotation of the Earth.

The wave fronts are curvilinear features, as revealed in the photograph. The bottom topography in this region has a U-shaped shoal that extends southwest from the Nicoya Peninsula and is a major cause of the refraction pattern seen in the photograph. Thus, the energy from the tide is transformed into internal waves that propagate into the coastal zone, where their energy is dissipated in turbulent diffusion and contributes to vertical mixing of the water.

Figure 12-1 is an example of an oceanographic feature made visible by sunglint. Ordinarily, sunglint is avoided in overwater photographs because color information is lost in the specular reflection. The Skylab 4 crewmen, however, reported that additional information could be obtained when observing and photographing the sea surface in sunglint. Sunglint covers an area of the sea surrounding the solar reflection point, which appears to be at the large island (Isla de Chira) in the Gulf of Nicoya. Within the specular region, the capillary wave facets may be tilted by the slope of the surface gravity waves such that the surface gravity wave patterns appear to be reflected.

Figures 12-2 and 12-3 are nearly consecutive photographs taken off the coast of the Republic of South Africa on December 7, at approximately 13:00 local

standard time. The important features are two large-scale eddies in the left central part of figure 12-2 and an apparent water boundary visible as a color change in the center of figure 12-3. Figure 12-4 represents the best fit of these features to a Chamberlin trimetric projection. Location of the features is approximate because of the distortion in the high-oblique photograph (fig. 12-2); the small amount of land in figure 12-3 makes positioning difficult. Obliqueness in space photography involves major trade-offs between the relative ease of mapping from near-vertical images and the greater coverage and interesting angles available in oblique views. Whenever possible, land should be included in the photograph for orientation, and obliqueness may be desirable if it is necessary to include sufficient land in the picture.

An eddy with an anticyclonic rotation is shown on charts of oceanic sea-surface currents, north of the Subtropical Convergence zone between the West Wind Drift and the current systems of the central South Atlantic. (See inset to fig. 12-4.) Data taken in 1925 by the research vessel *Meteor* expedition were used to construct the charts of this region, which has few hydrographic stations. Analysis of figure 12-2 suggests that this region indeed may be one in which eddies are frequently formed; however, the sense of rotation in the Skylab data appears to be cyclonic. The color changes in the eddies indicate that the centers contain water different from the outer portion of the circulation, which is analogous to the Gulf Stream eddies observed off New England. Unfortunately, it is not possible to make quantitative measurements from the photograph to determine the water composition.

The water boundary shown in figure 12-3 exhibits the meandering sometimes characteristic of current boundaries and appears to be the Subtropical Convergence associated with the Agulhas Current. This current flows southwestward down the east coast of South Africa until it encounters the West Wind Drift zone off the Cape of Good Hope. Some idea of the flow possible in this region can be gained from the track of a free-drifting buoy that was deployed between July and October 1973 (fig. 12-4). The ability to plot the Agulhas Current and the eddies on a regular basis would be helpful to ships, particularly supertankers, that travel around the Cape of Good Hope. Westbound ships would use the current to gain extra speed, and eastbound ships would avoid the current.

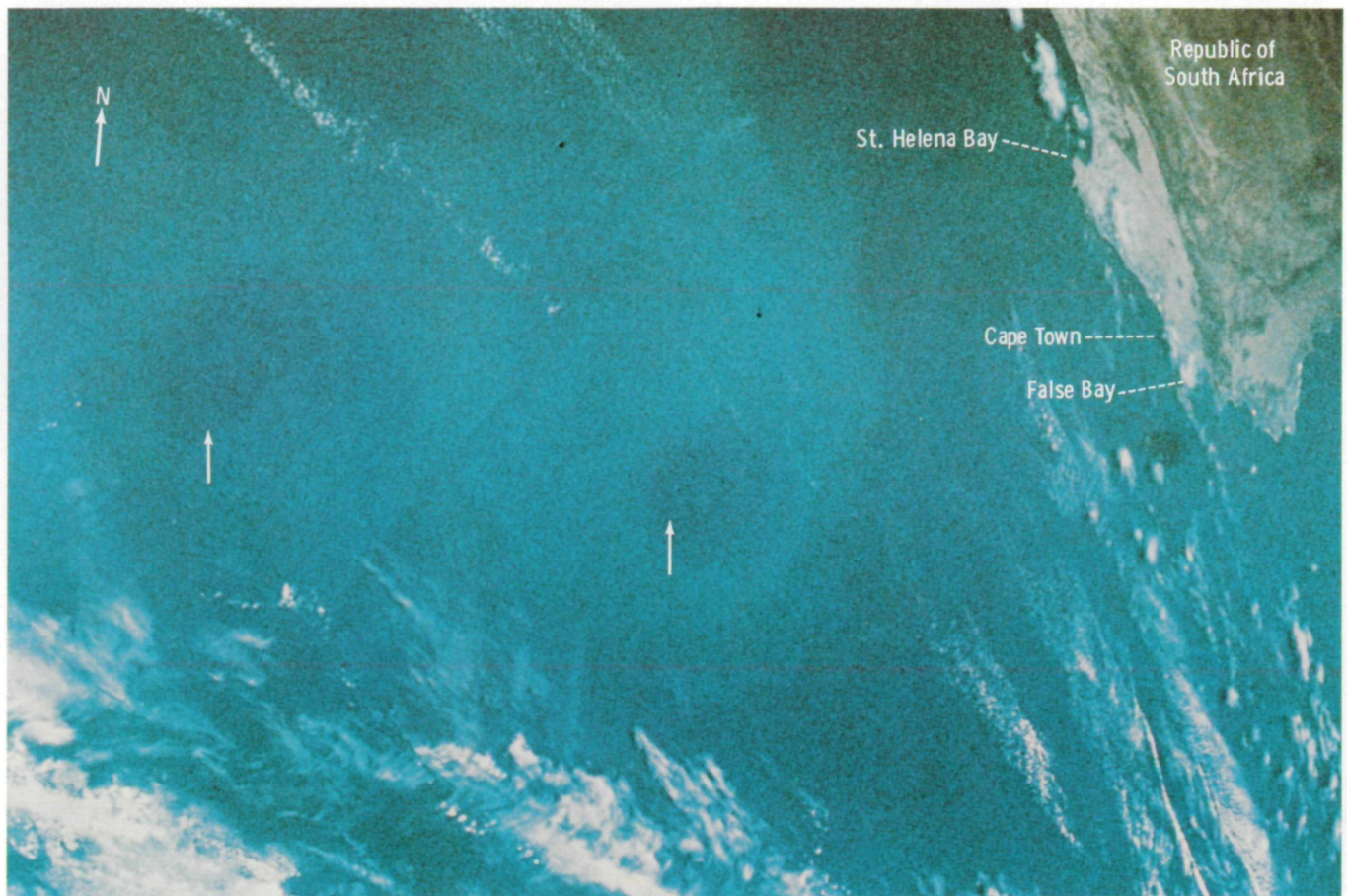


FIGURE 12-2.—Nikon 35-mm photograph showing two large eddies off the southwestern coast of South Africa (arrows pointing toward the blue water in the center). These features are 200 to 300 km in diameter and are probably cyclonic. These eddies are sketched in figure 12-4 (SI.4-196-7387).

The Skylab 4 crewmen indicated that the color of the handheld-camera photographs did not reveal the detail or the vividness of their sightings. They indicated that the Skylab Earth terrain camera (S190B) photographs were more representative of what they actually saw. For example, the commander remarked that the ocean had a fine texture that resembled corduroy material. Only in examining the S190B photographs with a magnifier could he detect this common pattern, which is probably a manifestation of surface gravity waves.

The crewmen remarked that binoculars were used for at least half of their observations. This fact may explain their disappointment with the handheld-camera 70-mm photographs and the reason that the S190B products were much closer to the detail actually seen.

The long focal length of the S190B camera more closely parallels their observations with binoculars. Many of the descriptions were given while using binoculars, and the relatively wide field of view of the 70-mm camera, which was used without a viewfinder, did not reproduce the observation.

Examples of colored water that may be caused by plankton, which occurs where surface water is rich in life-sustaining nutrients, are shown in figures 12-5 to 12-7. In each of these photographs, the color contrast outlines the boundary of water flow. Figure 12-5, taken on December 19 at 15:42 local standard time, shows the confluence of the Falkland Current and the Brazil Current off the east coast of Argentina. The discoloration in the Falkland Current (on December 25 at 11:03 local standard time) is shown in figure 12-6. Whether the red-

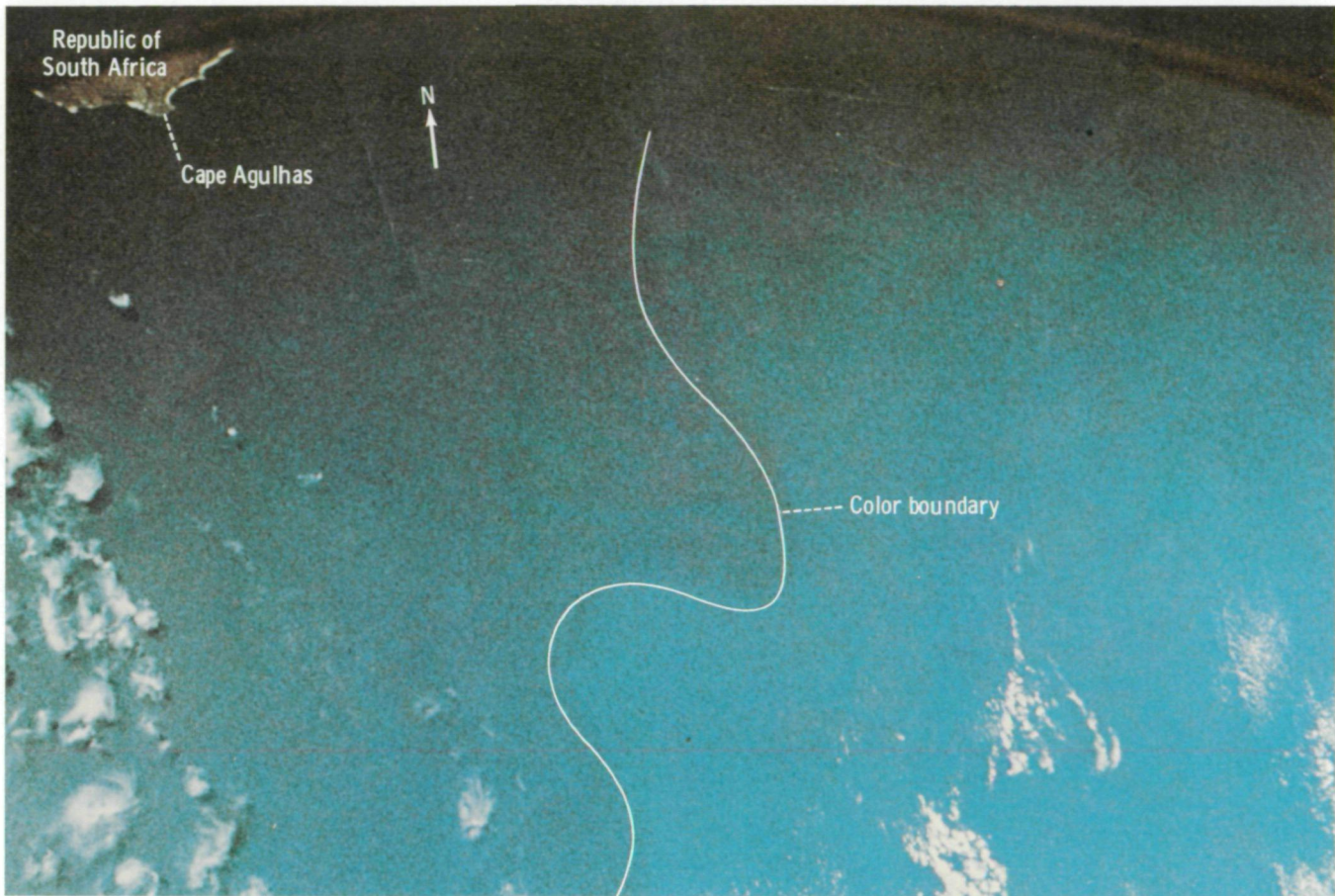


FIGURE 12-3.—Nikon 35-mm photograph showing boundary between water masses off South Africa. This color difference probably delimits the blue waters of the Agulhas Current, which has a tropical origin in the Indian Ocean, and the West Wind Drift, which has a sub-Antarctic origin. Wavelike features may grow and detach to form the eddies seen in figure 12-2, which was taken during the same overflight (SI4-196-7389).

dish color is terrigenous or biogenic is not certain, but it is known that large patches of lobster krill, common in this region at this time of year, can discolor the water. That the Falkland Current would appear bright green as it flowed northeast from Cape Horn, past the Falkland Islands, and eventually east into the South Atlantic Ocean was totally unexpected. The Skylab 4 crewmen reported that the boundary of the warm Brazil Current and the cool Falkland Current could be followed visually more than 3500 km and that the two currents formed intertwining serpentine paths, yet never showed mixing across the boundary. The growth and separation of meanders and current rings were not observed by the Skylab crew in this South Atlantic analog to the Gulf Stream-Labrador Current system. The combination of orbital groundtrack convergences at latitude

50° S permitted repeated observations of the currents during January 1974.

Unfortunately, sufficient information does not exist to orient all the photographs to a common projection and thus to construct a time series of the current. Such a time series, with the detail provided by these photographs, could be one of the most informative products of space photography. In addition, new observations by the crewmen of what appear to be plankton blooms may provide biological oceanographers with further insight into the spatial and temporal extent of these organic discolorations.

Figure 12-7 was taken at 13:23 local standard time on December 7, over the South Pacific Ocean east of New Zealand. The lower half of the picture shows a streaming event of light-colored water in the center and more

diffused patches on each side. Although there are no named currents in this region, the apparent eddying and general configuration of the central band is indicative of current activity and is probably associated with the Subtropical Convergence that passes between North Island and South Island, New Zealand.

Space photographs may prove useful in determining the occurrence and distribution of plankton blooms. Measuring the ratio of blue transmission to that of green on the color transparencies and correlating these data with surface observations may provide tools to determine plankton concentrations from space. Plankton, the base link in the oceanic food chain, is a prime indicator of areas potentially rich in sea life. In-

formation concerning plankton distribution is important to fishermen and marine biologists.

Transmission ratios for figures 12-6 and 12-7 are given in table 12-I; each value is the mean of several individual measurements taken by a spectromicrodensitometer from different locations in the appropriate water zone. The large standard deviations are due to patchiness in the water. If other conditions (sea state, sunlint, oceanic particulates, and atmospheric scatterers) that affect the upwelling radiance from the ocean can be determined, it is possible that these ratios can be evaluated in terms of chlorophyll-a concentrations. Thus, if the photographs are calibrated in a few areas, the isopleths of the blue/green ratio may be used

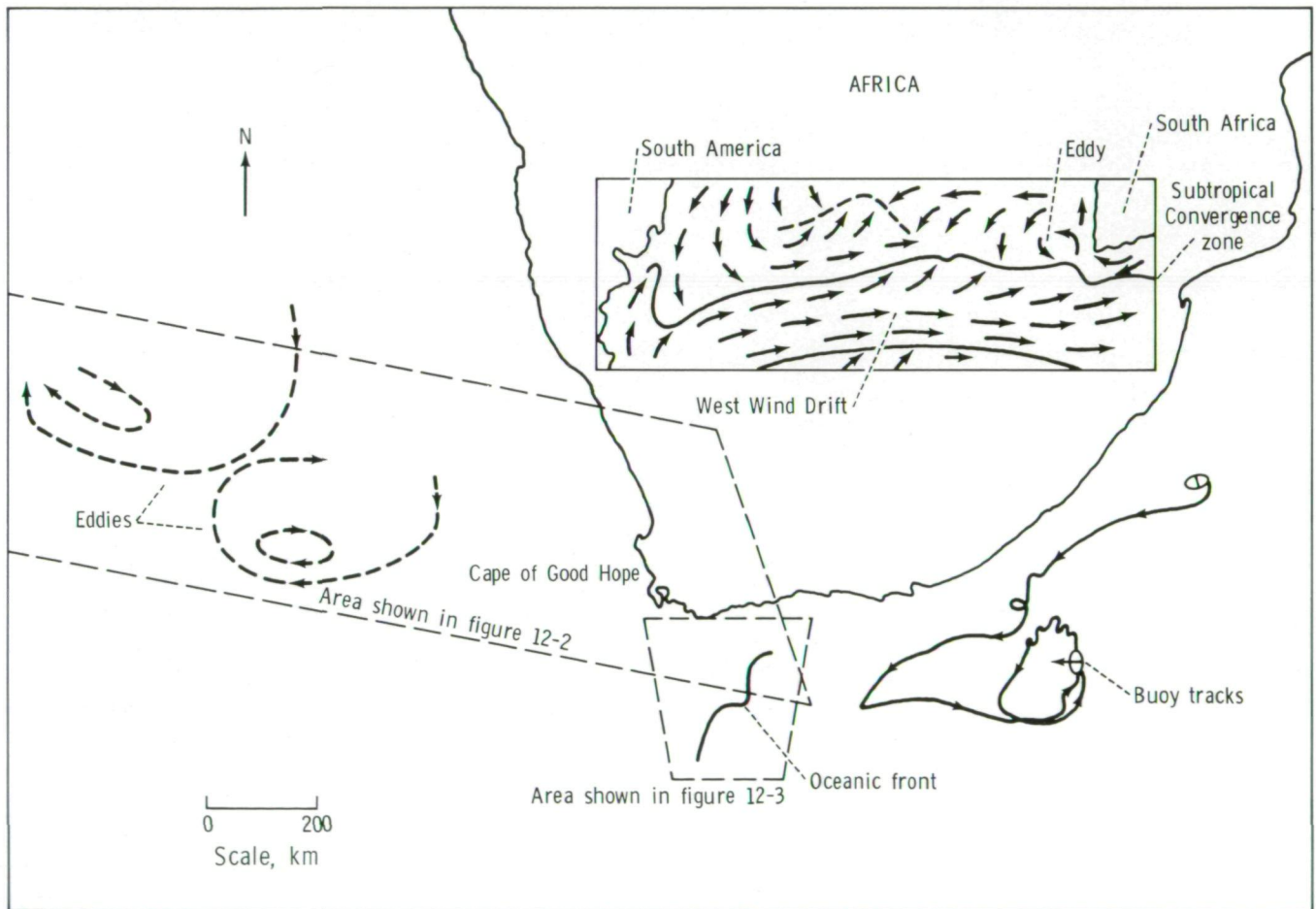


FIGURE 12-4.—Sketch of the South Atlantic Ocean off the Cape of Good Hope showing the features photographed in figures 12-2 and 12-3. The buoy track by Stavropoulos and Duncan in the Agulhas Current was made by using satellite tracking and is an indicator of representative trajectories. The boundary labeled from figure 12-3 is probably the Subtropical Convergence. Inset is a schematic map of surface currents in the South Atlantic Ocean; the solid line is the Subtropical Convergence zone.

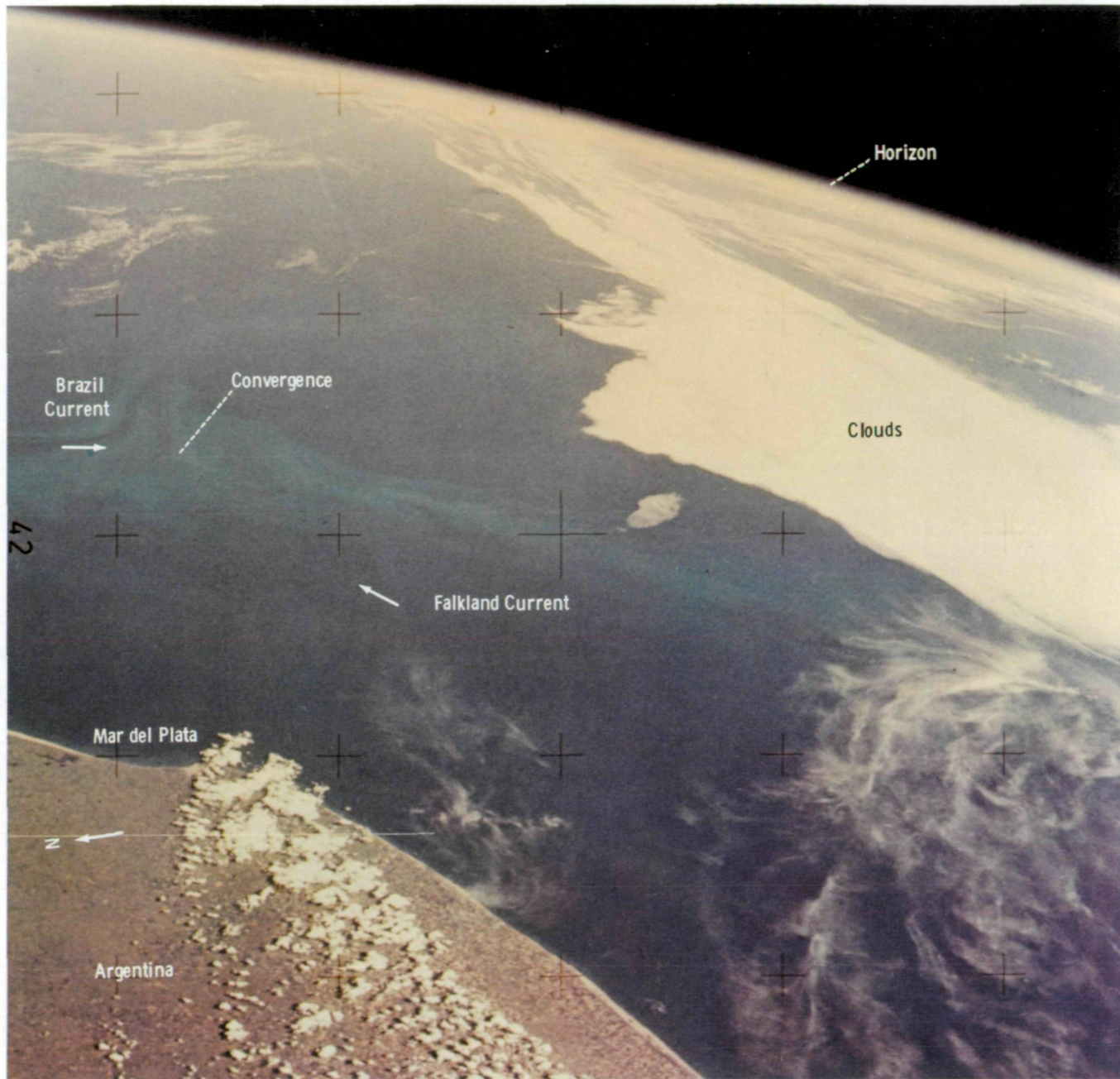


FIGURE 12-5.—East-looking view from Mar del Plata, Argentina, of the confluence of the north-flowing Falkland Current and the south-flowing Brazil Current. The light-green streaming probably marks the right-hand edge (facing downstream) of the currents and, hence, is the inshore boundary of the Brazil Current and the offshore edge of the Falkland Current (SIA-137-3690).

able as contours of pigment concentrations, which are proportional to phytoplankton populations.

Other measurements made from photographs taken by wide-angle aerial lenses have revealed a vignetting problem that seriously affects the ratios. If this problem

exists, an adjustment curve must be obtained to rectify the numbers by obtaining values from a photograph of a uniform color field with the same lens. An example of such a curve is given in figure 12-8. The Skylab photographs that have been analyzed herein were taken with

TABLE 12-I.—Transmission Ratio Measured From Two Skylab Photographs^a

| Region | Transmission ratio |
|----------------------------|--------------------|
| Figure 12-6 (SL4-137-3721) | |
| Front | 1.57 ± 0.14 |
| Surrounding water | 2.33 ± 0.02 |
| Plankton bloom | 2.29 ± 0.06 |
| Figure 12-7 (SL4-136-3446) | |
| Front | 2.33 ± 0.07 |
| Surrounding water | 3.13 ± 0.51 |

^aThe percent transmission is measured with a spectromicrodensitometer, which uses an irradiance receptor. White light is passed through the filter, then through the transparency for measurement. (Blue filter: Wratten no. 94, 455 nm; green filter: Wratten no. 93, 540 nm.)

a Hasselblad camera using various lenses, and there is no indication of any serious vignetting effect. This problem, however, should be considered in future flights, and an adjustment curve for each lens-filter combination should be prepared before the flight.

An example of mesoscale ocean eddies observed in the sunglint of a vertical photograph of the Gulf of Mexico taken on August 4 at 13:35 local standard time is shown in figure 12-9. These eddies are associated with the Loop Current in the eastern Gulf of Mexico, and their location has been correlated with the known position of this Gulf Stream-like flow. This view illustrates the important discovery that ocean features can be seen in images obtained by a seldom-used photographic technique and also provides a means of searching for other examples of eddies for a frequency-of-occurrence evaluation. In addition, air-sea interaction studies may be enhanced by studying sunglint patterns and relating them to the wind-stress vector in the atmospheric boundary layer. The photograph in figure 12-9 is one of a stereographic pair that enabled positive identification of the ocean surface features and clouds. Many potentially useful photographs have questionable value because oceanic and atmospheric features cannot be differentiated; stereophotographs or a stereographic camera would eliminate such doubts.

DISCUSSION

The usefulness of manned space vehicles to science, particularly in the area of flexibility of observation programs and routines, has been demonstrated. Communications between scientists on the ground and observers in space can significantly improve the usefulness of space observations by improving site choices and techniques. The capability to voice record the human observations gives to the scenes a perspective otherwise not available. This perspective is valuable because of the observer's visual acuity and ability to change quickly from a detailed observation to a general large-area survey. Furthermore, the relative motion of the vehicle and the Earth is a reliable aid to depth perception; for the scientists, one of the most valuable aspects of debriefing was watching the television tapes to learn how the Earth appears from orbit.

From the standpoint of oceanography, however, the space observations have not reached the full potential of their usefulness because many of the photographs cannot be geographically positioned. This limitation is critical because it prevents accumulation of time-series data, which, because most ocean features change relatively quickly, are important tools in understanding ocean dynamics. The ability to take high-oblique shots is sometimes a distinct advantage but can cause difficulty in mapping an area from the photograph. One possible approach to the problem of mapping is to try to match the photograph to weather-satellite imagery. Attempts by the authors, who used the standard archived product of the National Oceanic and Atmospheric Administration (NOAA) weather satellite NOAA-2, have not been successful because of the fairly low resolution of the satellite images (fig. 12-10) and the time difference between observations by the satellite and by the Skylab crewmen. Very-high-resolution instruments exist on the NOAA-2 satellite, however, and can be activated if sufficient warning is given. The polar-orbiting satellites are not as useful for ocean-dynamics studies as the high-resolution sensors on geosynchronous vehicles because the time difference between each observation is critical when clouds are used as common locators in manned photography and imagery.

The documentation, awkward to use and occasionally incomplete, has been one of the major problems with the Skylab photographs. The crewmen were

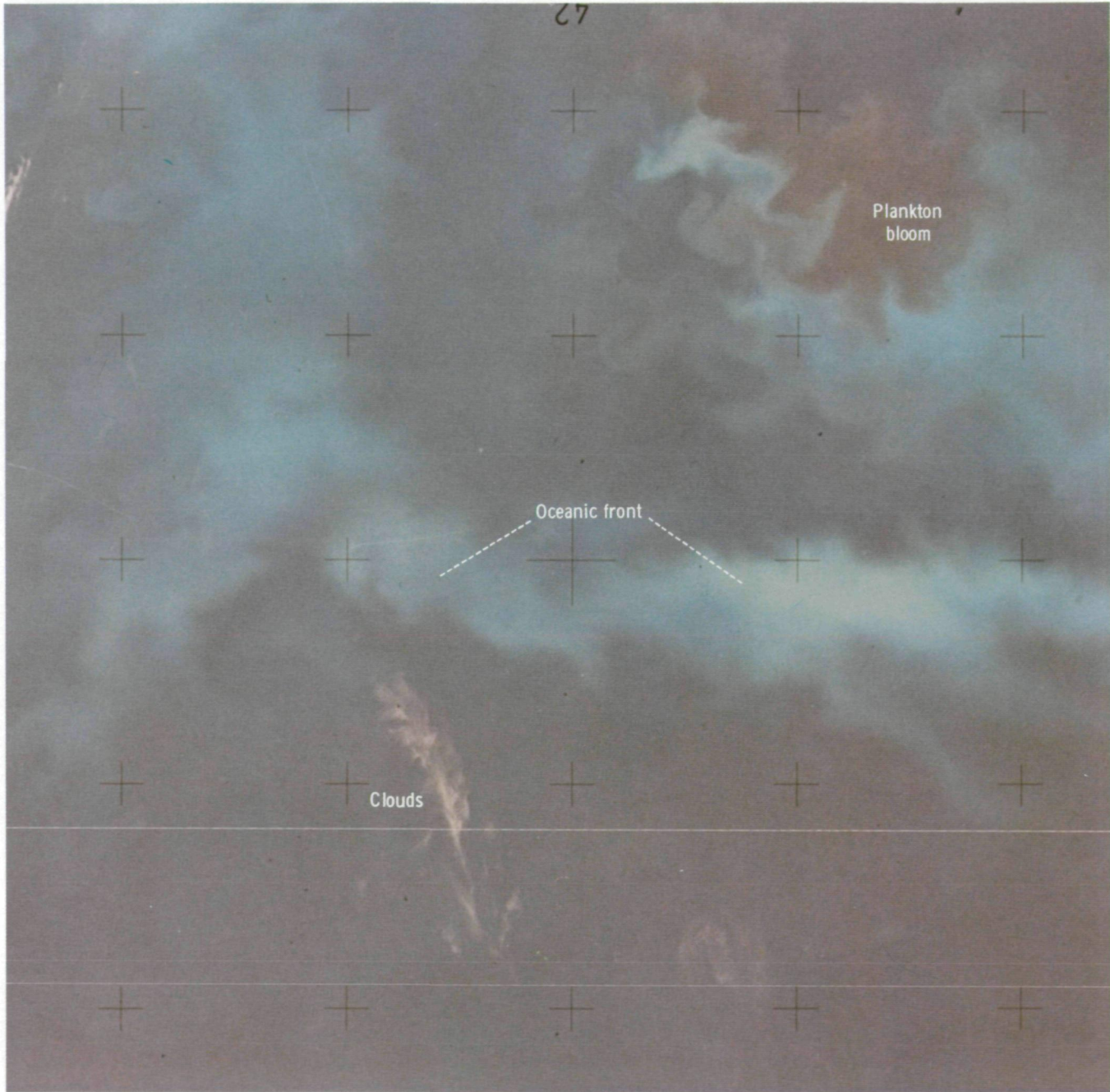


FIGURE 12-6.—Near-vertical photograph showing reddish discoloration embedded in the Falkland Current that is probably biogenic material. The offshore edge of the current appears as a bright green lineation, then a dark-blue zone separating the green from a lighter blue region, which is dominated by eddies approximately 15 to 20 km in diameter (SI4-137-3721).



FIGURE 12-7.—High-oblique view east of New Zealand. The light-blue meandering flow (arrow) is near the historical position of the Subtropical Convergence zone and demonstrates horizontal shear-flow instability (SL4-136-3446).

required to record their descriptions and log information such as time, camera, and lens types. This procedure hampered activities in space as well as on the

ground. The technology exists to annotate each frame automatically with information such as date and time as it is taken. This automation would relieve crewmen of

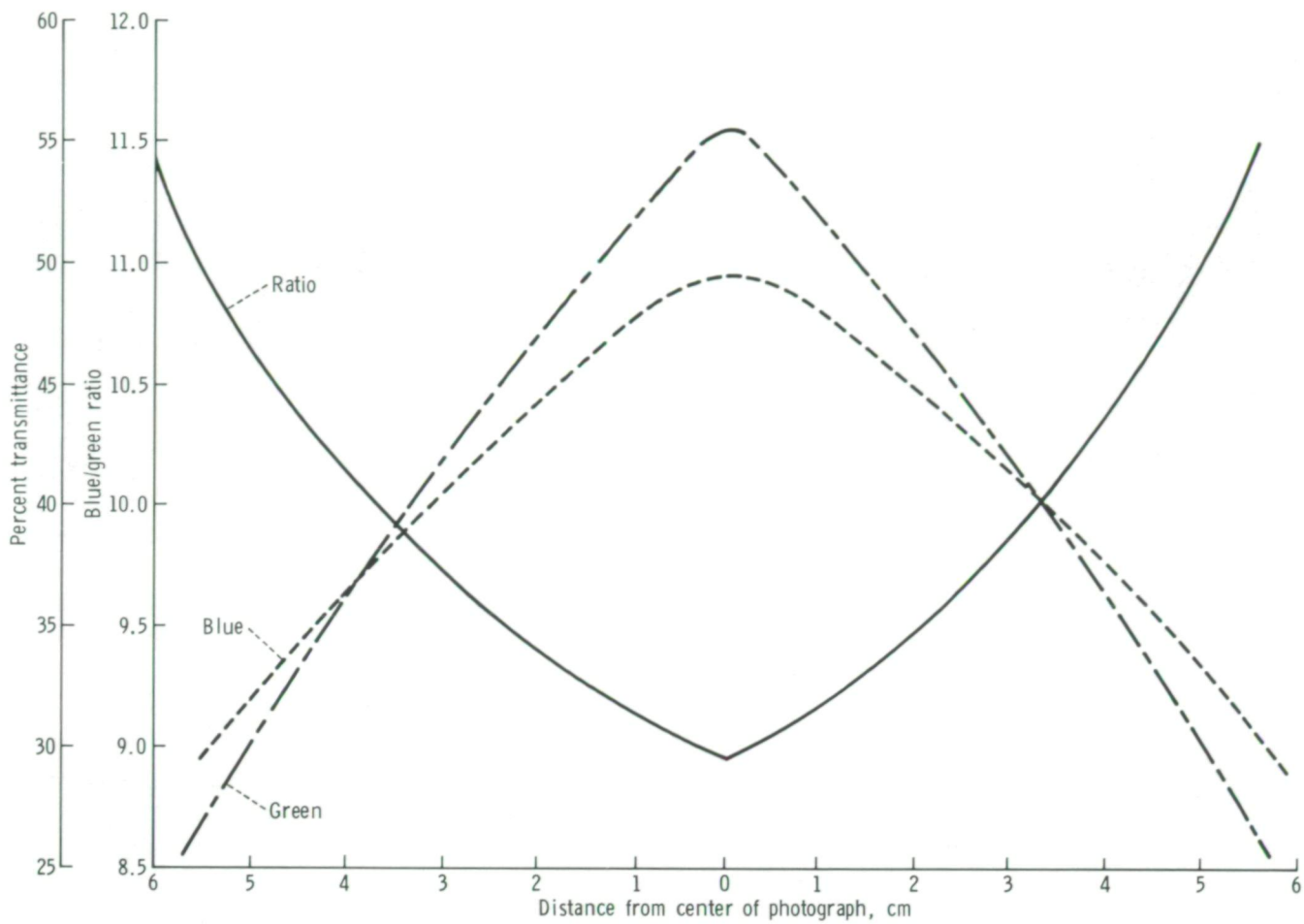


FIGURE 12-8.—Example of vignetting causing significant changes in the blue/green ratio of transmitted light measured over a uniformly blue ocean target. This result from an aircraft transparency shows that a significant correction may be necessary when using blue/green transmission ratios to assess the chlorophyll concentration in water (private communication from S. Baig).

much of their logging responsibilities and facilitate use of the photographs later. Consideration should be given also to recording other numbers such as f-stop, shutter speed, magazine and frame number, and as much other pertinent information as possible.

In addition, the camera should have a zoom lens to eliminate lens changes and should be of the single-lens reflex type. Ideally, the camera would include the functions of a pair of binoculars. Filters should be quick and easy to exchange, and the film advance should be motorized to facilitate stereophotography. Because good depth perception is important in photointerpretation, all space photographs should be taken in stereopairs. Vignetting curves should be obtained for all combinations of lenses and filters, for uniform color fields at 455, 540, and 670 nm to conform with the appropriate

Wratten filters. With few exceptions, 35-mm photographs were not as interesting as 70-mm photographs, and the crew apparently found the 35-mm camera more difficult to use. Having exchangeable film packs or magazines would permit more flexible use of different film types for each photographic situation. Much research is underway in developing films for oceanographic photography; specialized alternatives to a standard color film should be investigated.

The formidable ergonomics of such a photographic system may indicate that a very-high-resolution television system would be superior. A ground-based television receiver accessible in real time could give scientists the depth perception inherent in the spacecraft motion and the sense of "being there," which cannot be obtained from a photograph. The overflights could be



FIGURE 12-9.—Vertical photograph in the eastern Gulf of Mexico showing eddies 12 to 32 km in diameter observed in the sunlint pattern. These shear-flow instabilities are not associated with any color boundary because the eddies are in the main body of the Gulf Loop Current. The serpentine feature is probably an oil slick because it is along the main shipping route to New Orleans (SI.3-22-124).

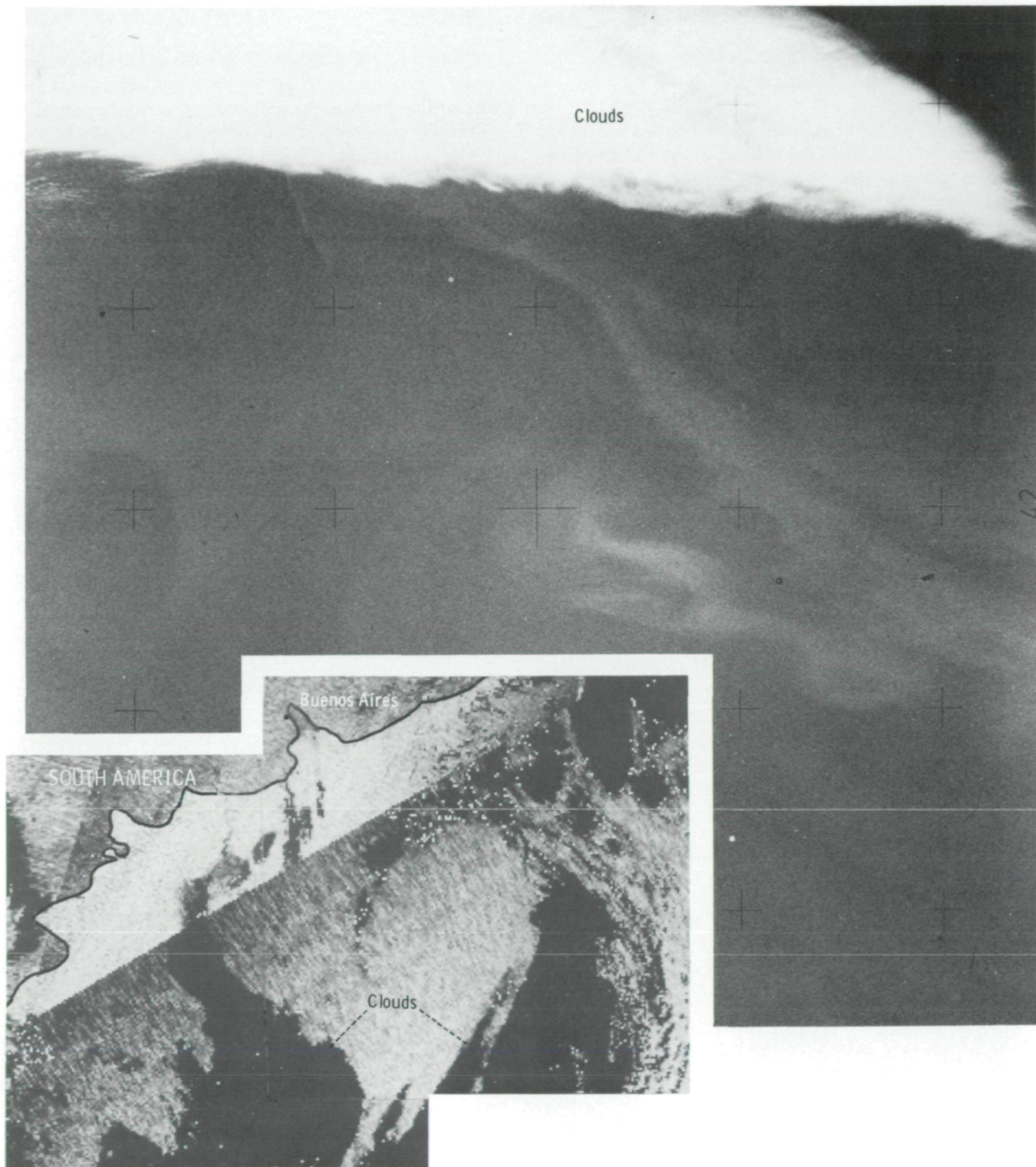


FIGURE 12-10.—Oblique photograph of the Falkland Current. Computer-enhanced inset is the NOAA-2 scanning radiometer archived visible image taken the same day as the photograph. Correlation of the cloud feature in the photograph with the image is not possible for several reasons: insufficient image ground resolution, insufficient field of view in photograph, and timelag between observations. Without the ability to locate each ocean photograph, the value of the photograph is significantly diminished (SI.4-143-4610).

video taped, and photographic copies of important scenes from the television image should be easy to produce.

The Skylab 4 crewmen spent several days learning to identify their location at any time over the Earth. More intensive geographical training before the mission should reduce the length of this orientation period. The experience of the Skylab 4 crewmen may be the most important link in such a training procedure and could be their most important long-term contribution to space science. Crew training for future flights should include simulated identification of ocean features at the same scale as those seen in orbit. Such simulation can be accomplished by flying aircraft missions that duplicate the resolution and color observed from space (i.e., aircraft missions can be flown without the astronauts to gather the simulated data for later instruction sessions), and by reviewing photographs and television tapes from previous space flights.

CONCLUDING REMARKS

One of the obvious characteristics of oceanographic features is that they are in constant motion. Among the dominant natural phenomena of the Earth, only meteorological events occur more rapidly than oceanographic events; Gulf Stream features, for example, may shift position significantly in 1 or 2 days. Because of these rapid, highly variable motions, an ocean observation needs to be one of a series to provide

a clear idea of the dynamics involved. Identification of water types, plankton distribution and types, and other discernible parameters will become possible only if the observations are on a well-calibrated quantitative basis.

Oceanographic observations from space are useful because they provide a much-needed opportunity to survey the ocean on a scale and with a regularity that cannot be duplicated in any other manner. Handheld-camera photography has a distinct role in reconnaissance, but it cannot surpass the quantitiveness of a multispectral observation from a known attitude. Significantly, many of the most interesting ocean scenes were taken by the S190B camera, which produced very-high-resolution photographs taken from a vertical position. From the standpoint of long-term oceanographic research from space, quantitative observations are needed with accurate geographical positioning, and concurrent ocean surface observations are needed to correlate the data. The space observer can significantly augment these needs by real-time interaction with earthbound scientists in a coordinated effort of discovery and exploration.

ACKNOWLEDGMENTS

The authors express appreciation to Dr. S. Baig, who graciously provided the spectro-microdensitometer measurements, and to Dr. S. Q. Duntley, who critically reviewed the manuscript.

13

Visual Observations of Floating Ice From Skylab

*W. J. CAMPBELL,^a R. O. RAMSEIER,^b W. F. WEEKS,^c
AND J. A. WAYENBERG^a*

THE LAKE and sea ice visual observation experiment performed during the Skylab 4 mission was very successful. In the initial experiment design, the Gulf of St. Lawrence and Lake Ontario were chosen as prime sites at which ground-truth measurements and aircraft remote-sensing data were to be obtained. In addition, the Skylab 4 astronauts obtained excellent photographs of sea ice in the Sea of Okhotsk and in the James Bay portion of Hudson Bay and of icebergs in the Southern Ocean. Some of the sequential photographs contain very useful broad-scale information on the distribution of ice and ice types, the overall deformation patterns, and the amount of relative ice motion. Information obtained from this experiment will be invaluable for interpreting the Skylab Earth resources experiment package data, the aircraft remote-sensing data acquired from four aircraft which participated in the experiment, the ground measurements acquired from a ship in the Gulf of St. Lawrence, and the data obtained from a helicopter and from hovercraft in Lake Ontario.

^aU.S. Geological Survey, Tacoma, Washington.

^bDepartment of the Environment, Ottawa, Ontario.

^cCold Regions Research and Engineering Laboratory, Hanover, New Hampshire.

GULF OF ST. LAWRENCE

Fortunately for the sea ice experiment, the winter of 1974 was one of heavy ice conditions in the Gulf of St. Lawrence, and a variety of ice types was observed. The Skylab visual observation data provide excellent information on the rapidly varying ice conditions caused by high winds (≤ 90 km/hr) during the study period. The morphological changes that occur during this period of rapid ice growth were also observed. The Skylab satellite observations were obtained between January 6 and 21. Between January 9 and 15, surface observations were conducted in the Gulf of St. Lawrence by the Canadian Oceanographic Ship *Dawson*, operated by the Bedford Institute of Oceanography. Originally, these observations were planned to last through January 21, but the cruise had to be terminated early because of a malfunction of the ship steering system.

The first useful Skylab 4 photograph (fig. 13-1), taken on January 6, clearly reveals several features characteristic of the early ice growth period in the Gulf of St. Lawrence. The heaviest ice conditions are found in the western portion, where the pack is quite open. The heaviest ice appears to be gray-white and is particularly abundant along the southern side of the gulf. Near the northern shore, gray ice becomes the predominant ice type with an open lead persisting along the northern



FIGURE 13-1.—Skylab near-vertical photograph of the northwestern part of the Gulf of St. Lawrence on January 6, 1974, showing concentrations of heavy (gray-white), thin (gray), and fast (gray) ice along the coast of Quebec, Canada. The heavy ice is predominant (SL4-139-3934).

coast. This ice thickness distribution reflects the general ice drift pattern to the south and east into the central gulf. Also notable are indications of pronounced ice divergence during this drift that results in as much as 25 percent open water. The only ice visible near Anticosti Island consists of some plumes off the southwestern coast. Also, fast ice is only partly developed in the bays on the eastern part of the Gaspé Peninsula.

Surface photographs are shown in figures 13-2 and 13-3 of the two principal ice types present in the Gulf of St. Lawrence in early January. Figure 13-2 illustrates a field of consolidated pancake ice near the southern coast of the St. Lawrence River estuary; figure 13-3 shows the typical newly formed gray-white ice near the northern shore. Pressure ridging associated with differential ice motion was quite common in the heavier ice (fig. 13-4).

On January 11, the Skylab crewmen obtained a photograph (fig. 13-5) of the ice distribution in the vicinity of the northeastern portion of the Gulf of St. Lawrence. Note that only lightly developed ice is present southwest of the Strait of Belle Isle and that the thickest ice occurs just southwest of the neck of the strait. The most striking features in this photograph are the ice plumes that occur to the east of Newfoundland



FIGURE 13-2.—Surface photograph of pancake ice near the southern coast of the St. Lawrence River estuary, on or about January 6, 1974.



FIGURE 13-3.—Surface photograph of gray ice near the northern shore of the St. Lawrence River estuary, on or about January 6, 1974.

and Labrador. Figure 13-6 is a surface view of these types of plumes, in which the ice is unconsolidated frazil that is kept from congealing by the continuous passage of waves through the plumes. These features characteristically appear to form at the edge of the pack



FIGURE 13-4.—Surface photograph of pressure ridging in the Gulf of St. Lawrence, on or about January 6, 1974.

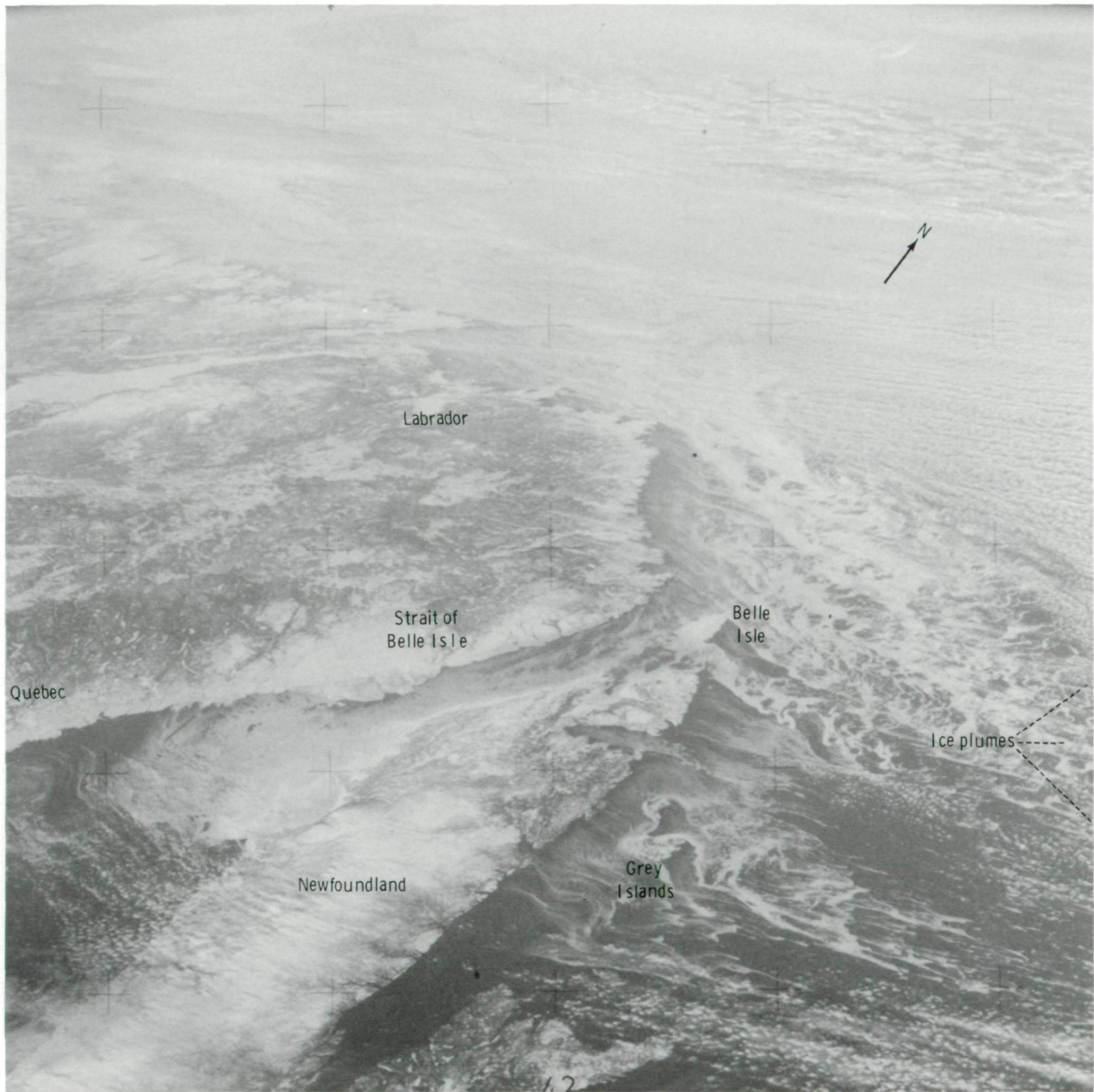


FIGURE 13-5.—Skylab oblique photograph of the northeastern part of the Gulf of St. Lawrence on January 11, 1974, showing the development of ice southwest of the Strait of Belle Isle and ice plumes east of Newfoundland and Labrador. The plumes are composed of unconsolidated frazil ice and are oriented parallel to the surface wind direction (SI.4-139-4072).

during periods of high winds. They can best be described as having a vortex type of structure. In figure 13-5, the vortex lines flow around Belle Isle and the Grey Islands. The small plumes are composed of slush and are elongated parallel to the surface wind directions, which were determined by shipboard observations.

The next cloud-free Skylab 4 photograph of this area was taken on January 19. The most striking feature of this photograph (fig. 13-7) is the strongly developed plume structure near Newfoundland. The marked difference in the structure of these plumes compared with the ones discussed earlier is that these later plumes are elongated perpendicular to the surface wind direction as deduced from the stratocumulus bands. The investigators suggest that whereas the earlier plumes were composed of slush, this orientation change indicates that the later plumes are composed of deformed pack ice. The presence of open water and gray ice in the lee of Newfoundland and of Belle Isle and the Grey Islands is due to the combined effects of the offshore surface winds and the southerly flowing surface currents.

Figure 13-8, obtained on January 20, shows the further development of the area of thick ice just west of the Strait of Belle Isle. When the open water along the Quebec shore and the pattern of the leads are considered, it appears that a recent advection of the ice in the northeastern gulf toward the southwest has occurred. In figure 13-8, the ice appears to be thinner just west of the strait; in figure 13-9, taken later on the same orbit, the presence of thin ice in this region is clearly evident. These observations suggest that no pronounced flux of ice occurred northeastward through the Strait of Belle Isle. The fact that the zone of heavier ice remains relatively static at the southwestern end of the strait also suggests the lack of a strong flux of ice at the time of the photograph from the Labrador Sea through the strait into the gulf.

The ice patterns in the general area of the Gaspé Peninsula were photographed on January 18 and 20 (figs. 13-10 and 13-11, respectively). These two photographs show the most rapid period of ice growth observed in this experiment. In particular, note the dramatic increase in ice thickness in the Baie des Chaleurs. Also note the advection of heavier ice through the



FIGURE 13-6.—Surface photograph of ice plumes near the edge of the St. Lawrence icepack, on or about January 6, 1974.

Gaspé Passage into the area to the east of the Gaspé Peninsula. Figure 13-11 also shows a large open lead along the northern bank of the St. Lawrence River. This feature was commonly observed by the crewmen and photographed during the Skylab 4 mission. The fairly constant surface winds from the north during this period brought about the advection of ice away from the coast and thus caused this zone to be one of strong ice production. During the period between January 6 and January 20 (figs. 13-1 and 13-11, respectively), extensive fast ice developed in the Baie de Gaspé.

The behavior of the ice in the vicinity of Anticosti Island is well illustrated in the Skylab 4 photographs taken on January 18 and 20 (figs. 13-12 and 13-13). Again, note the presence of the shore lead along the entire northern shore of the Gulf of St. Lawrence extending as far east as the heavy ice zone at the neck of the Strait of Belle Isle (see also fig. 13-9). During this period of pronounced ice growth, the entire northern edge of the gulf served as a source area for ice, which was subsequently redirected to the south. The lead patterns in figure 13-13 show a generally extending flow of ice into the southern gulf, except in the Jacques Cartier Passage, where blockage of this flow by Anticosti Island results in north-south leads produced by the local compressional flow. This condition causes lateral divergence to the east and the west. The chevron pattern in the lead

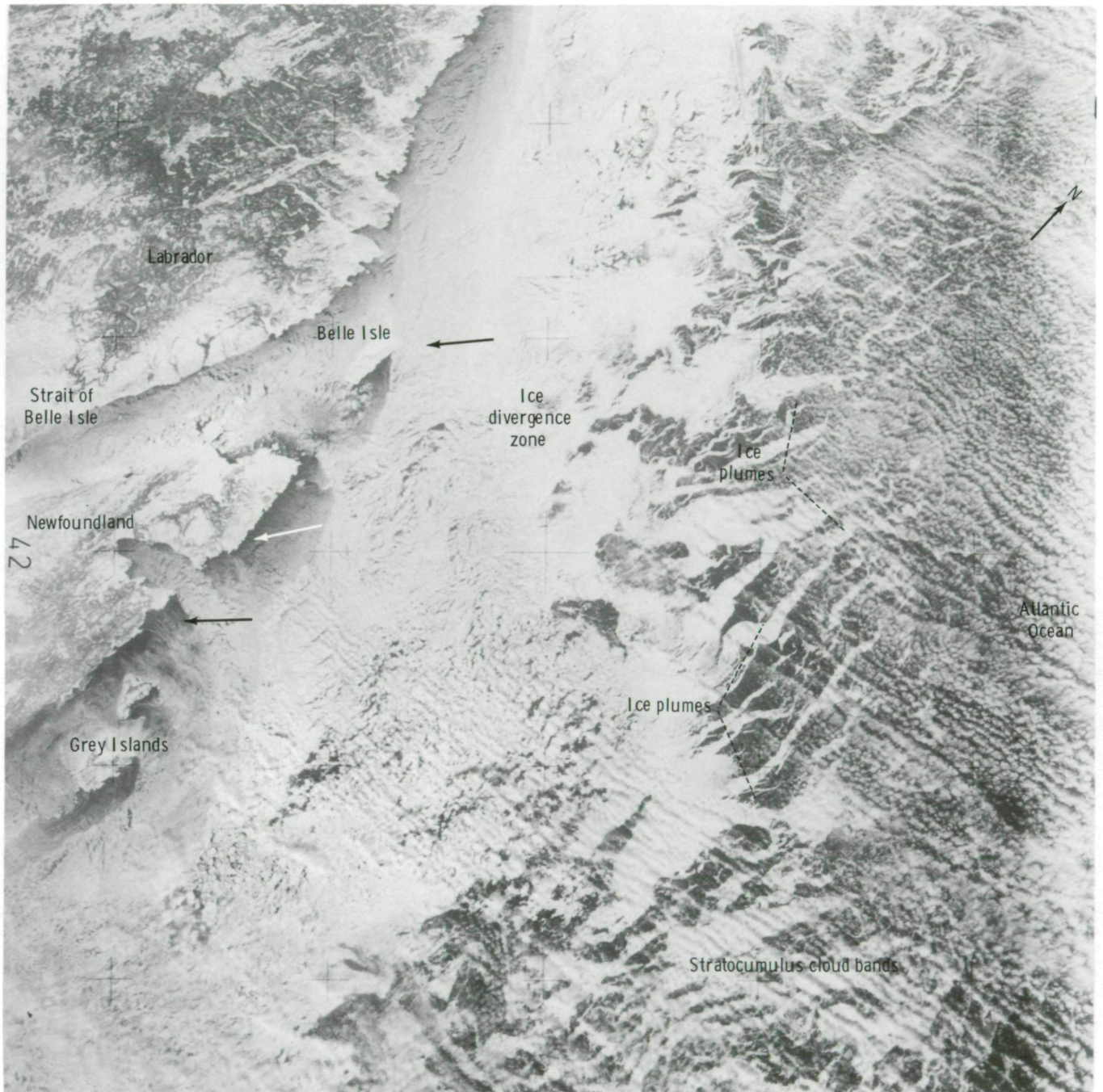


FIGURE 13-7.—Skylab near-vertical photograph of the Atlantic Ocean off Labrador and Newfoundland on January 19, 1974, showing ice plumes composed of deformed pack ice oriented perpendicular to the easterly flowing surface winds. Note the ice divergence zones in the lee of Belle Isle and at the tip of Newfoundland (SL4-141-4263).

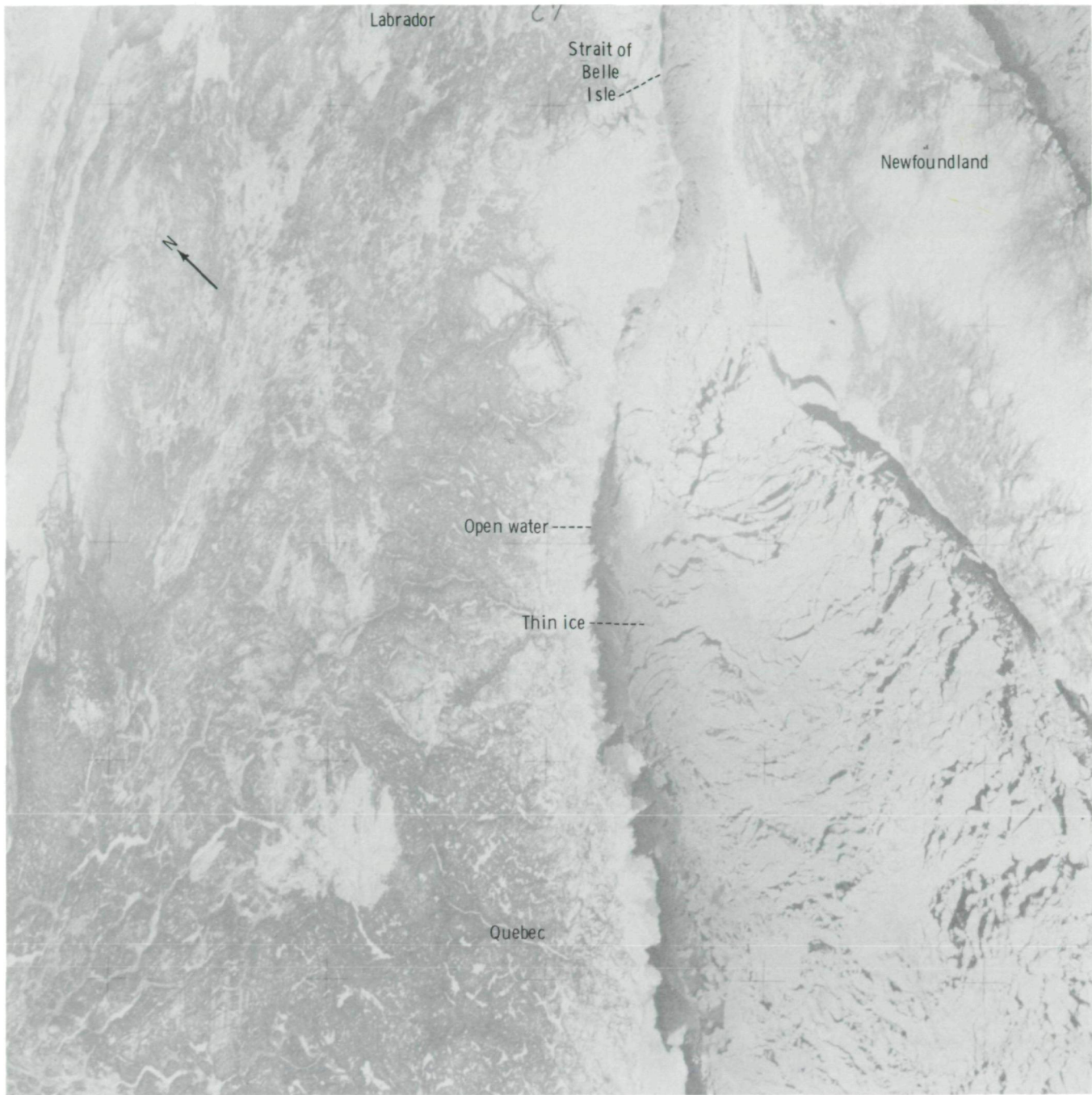


FIGURE 13-8.—Skylab oblique photograph of the northeastern part of the Gulf of St. Lawrence on January 20, 1974, showing the ice in and west of the Strait of Belle Isle. An open lead can be seen along the Quebec shoreline, as well as a patch of thin gray ice just west of the strait. Fracture patterns (leads) suggest a southwestern movement of the icepack (SI4-141-4326).

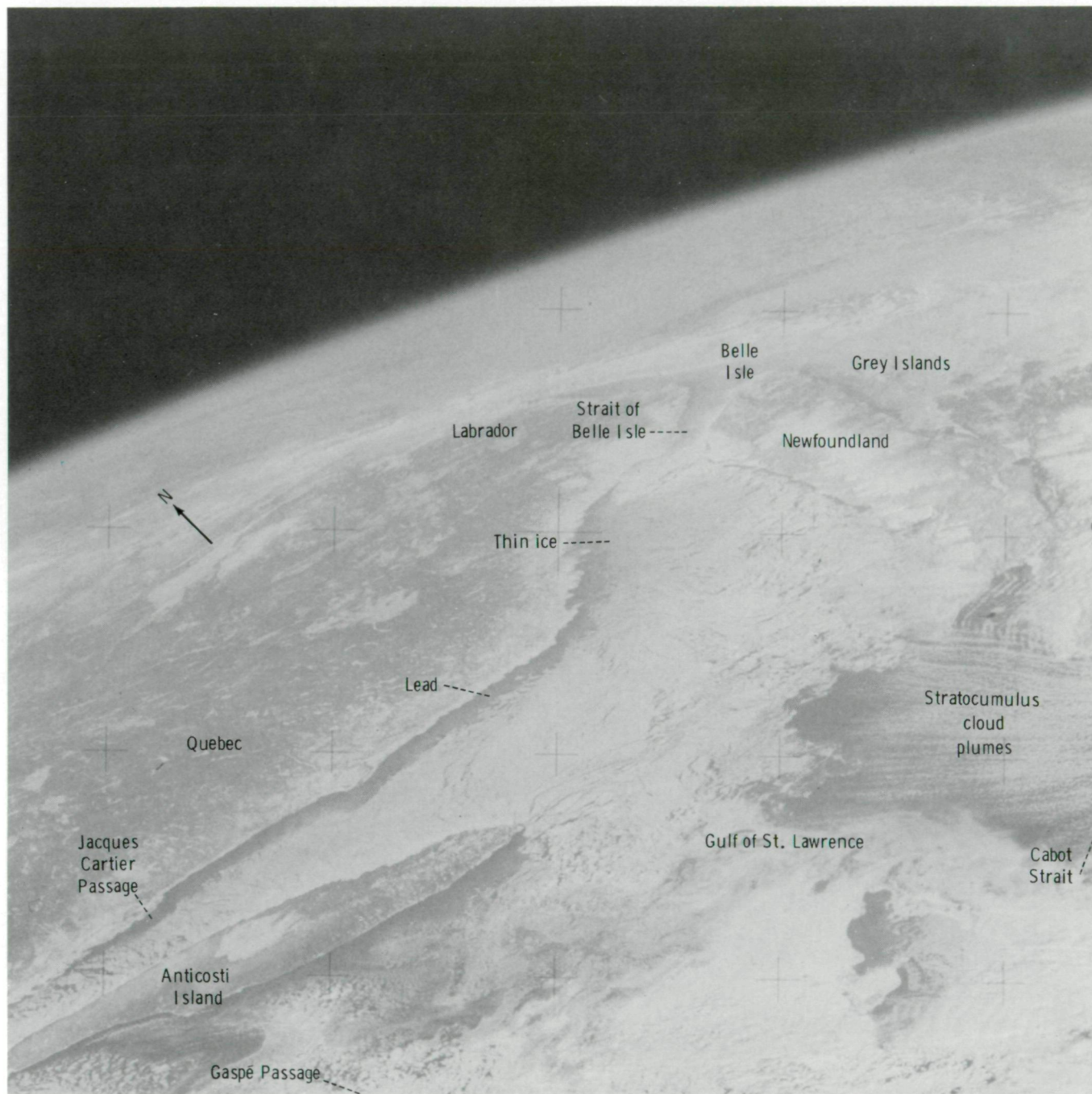


FIGURE 13-9.—Skylab oblique photograph taken on January 20, 1974, during the same orbit as figure 13-8, of the northern part of the Gulf of St. Lawrence showing the lead along the Quebec shoreline and the patch of thin gray ice west of the Strait of Belle Isle. Note stratocumulus cloud plumes in the area of Cabot Strait (SL4-141-4331).

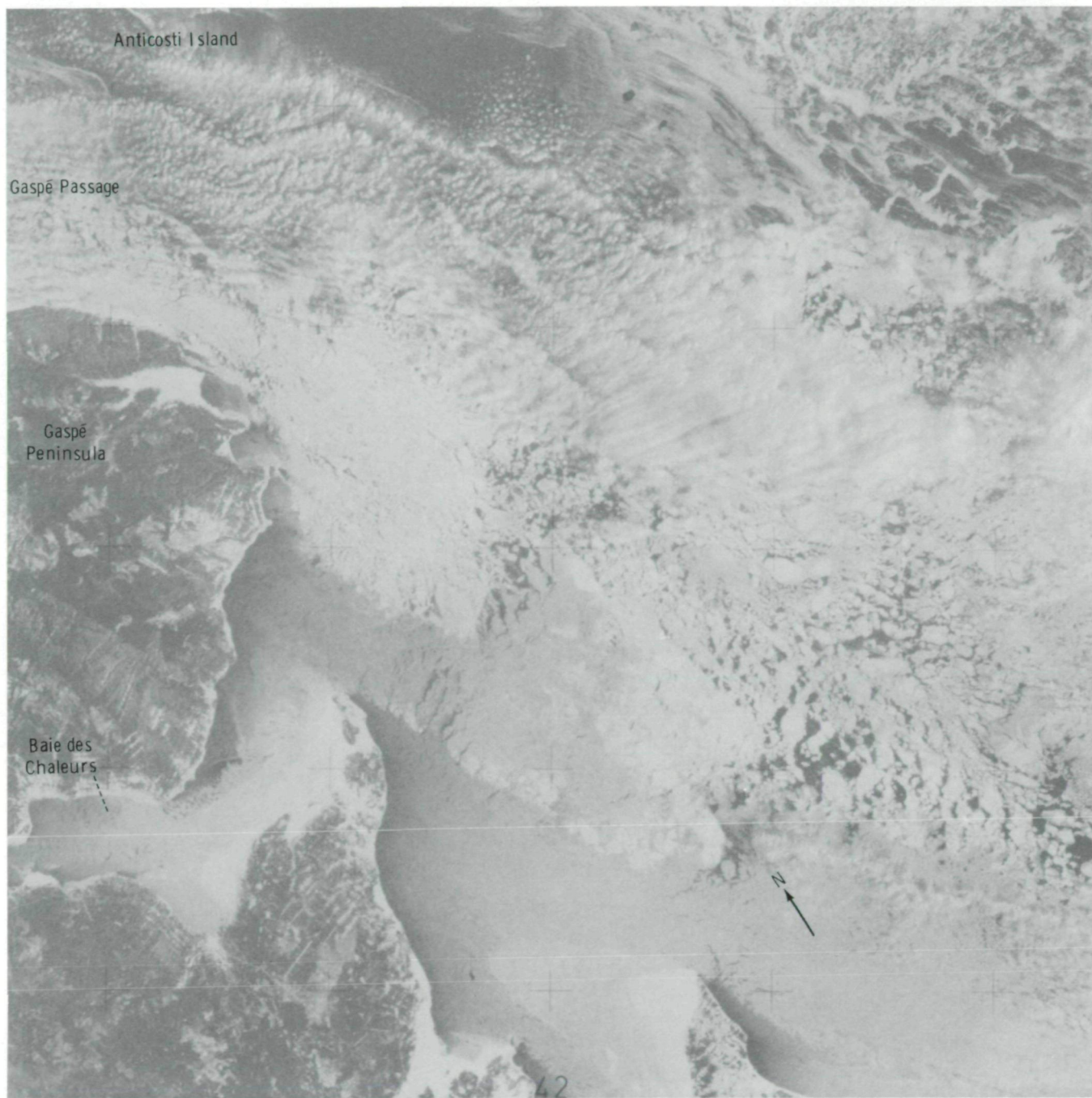


FIGURE 13-10.—Skylab near-vertical photograph of the northwestern Gulf of St. Lawrence and the mouth of the St. Lawrence River on January 18, 1974, showing the ice patterns in the vicinity of Gaspé Passage. Note the ice growth in the Baie des Chaleurs (SL4-140-4215).

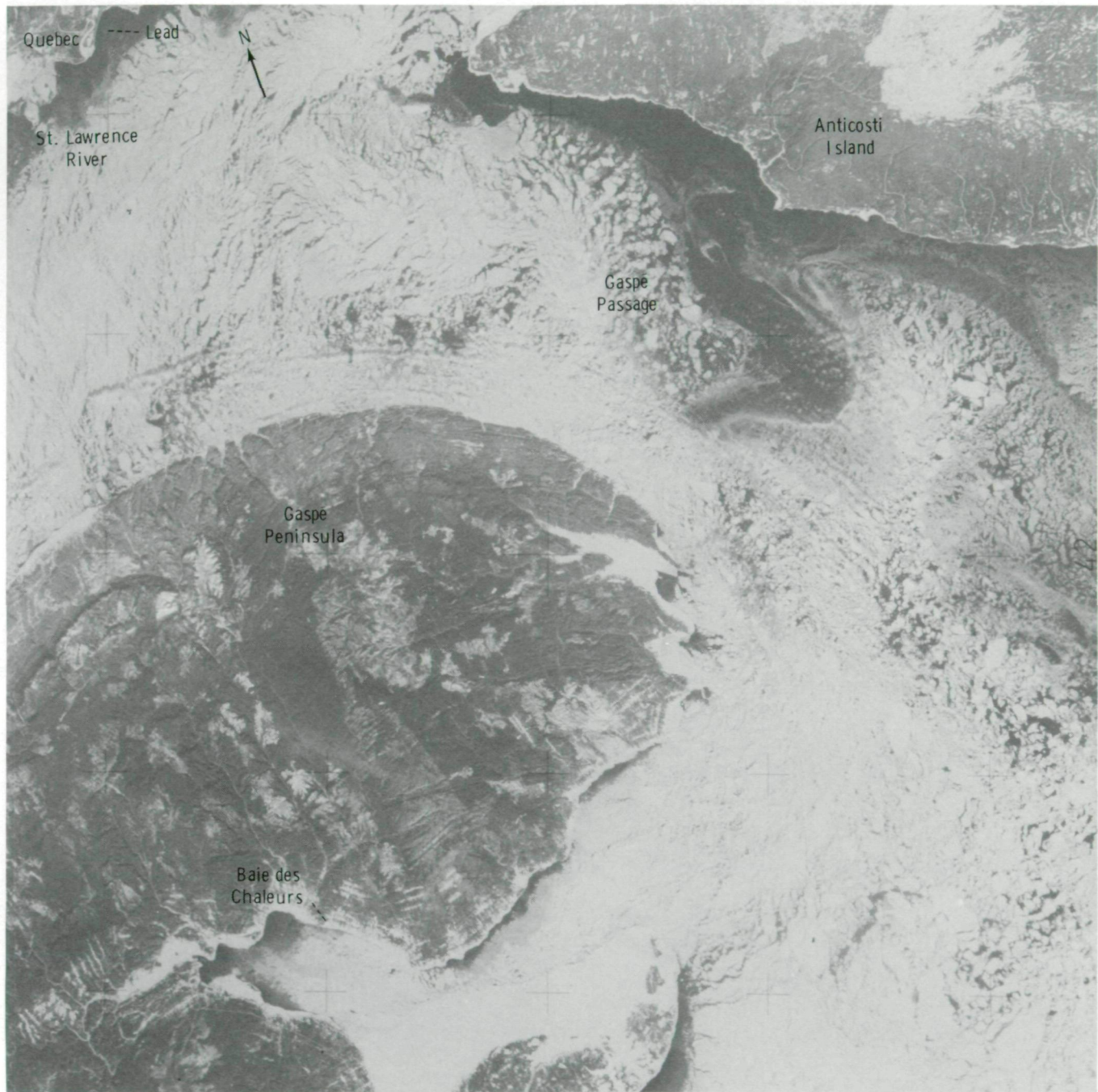


FIGURE 13-11.—Skylab near-vertical photograph of the northwestern Gulf of St. Lawrence and the mouth of the St. Lawrence River on January 20, 1974, showing the distribution of ice in the vicinity of Gaspé Passage. (See fig. 13-10.) Note the ice growth in the Baie des Chaleurs and the lead along the northern shore of the St. Lawrence River (SI4-141-4321).

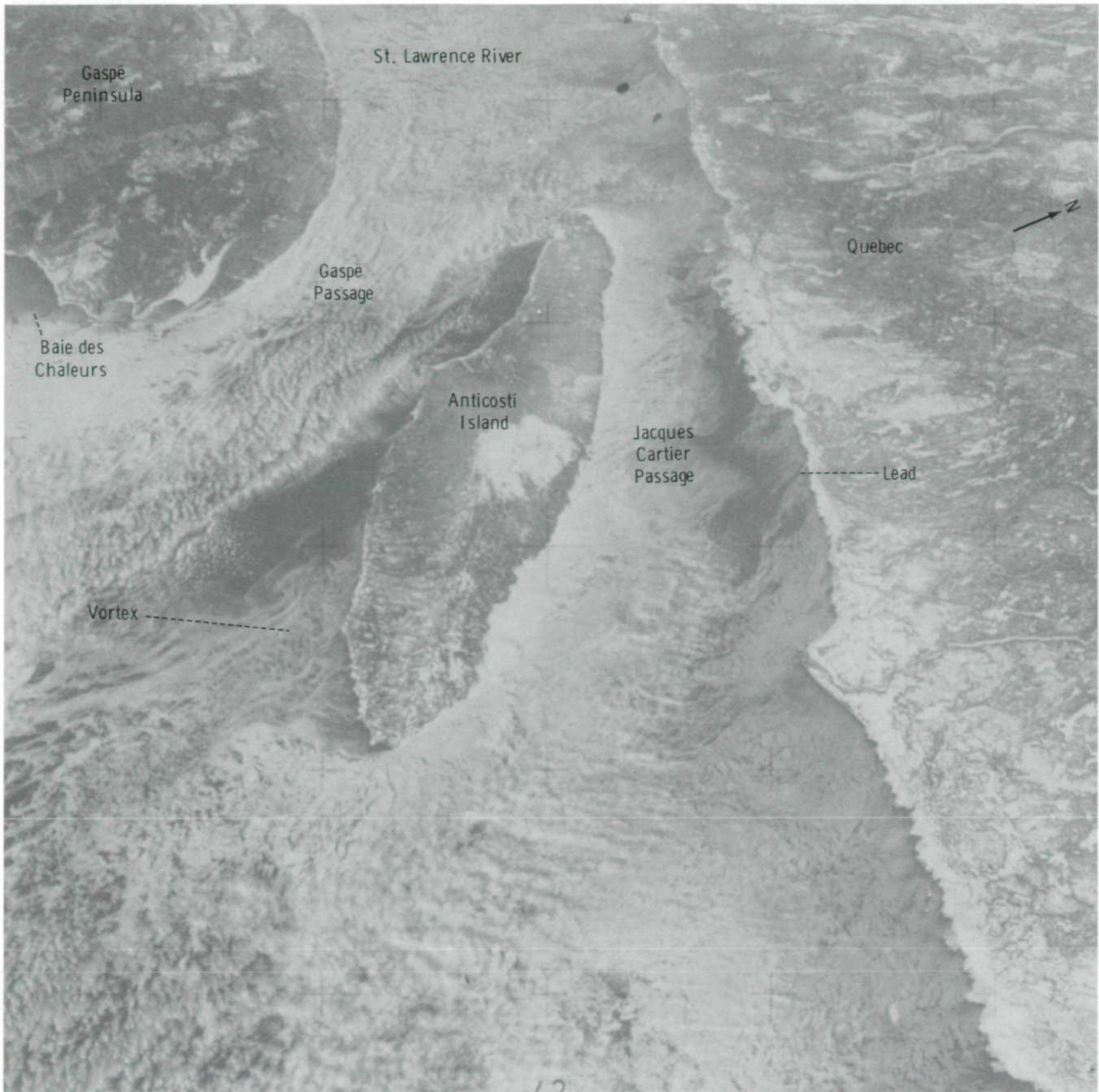


FIGURE 13-12.—Skylab oblique photograph of the northern Gulf of St. Lawrence on January 18, 1974, showing the distribution of ice and open water in the area. Note vortex pattern in ice south of Anticosti Island (SL4-140-4216).

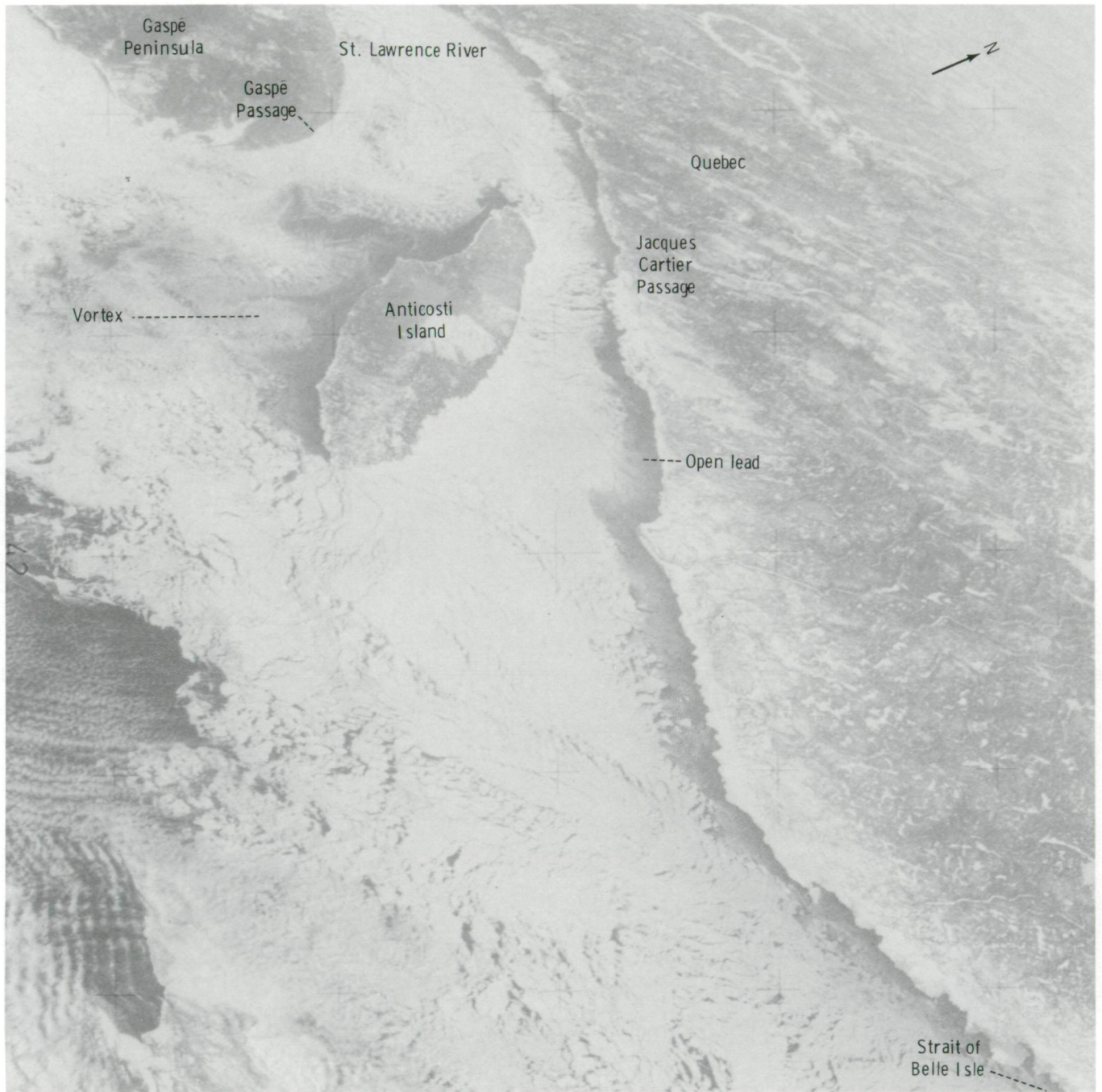


FIGURE 13-13.—Skylab oblique photograph of the northwestern part of the Gulf of St. Lawrence on January 20, 1974, showing the distribution of the icepack and the lead pattern. A southern flow of the pack is suggested. A chevron pattern can be seen in the leads north of Anticosti Island, and a vortex pattern can be seen in the ice south of the island (SI.4-141-4327).

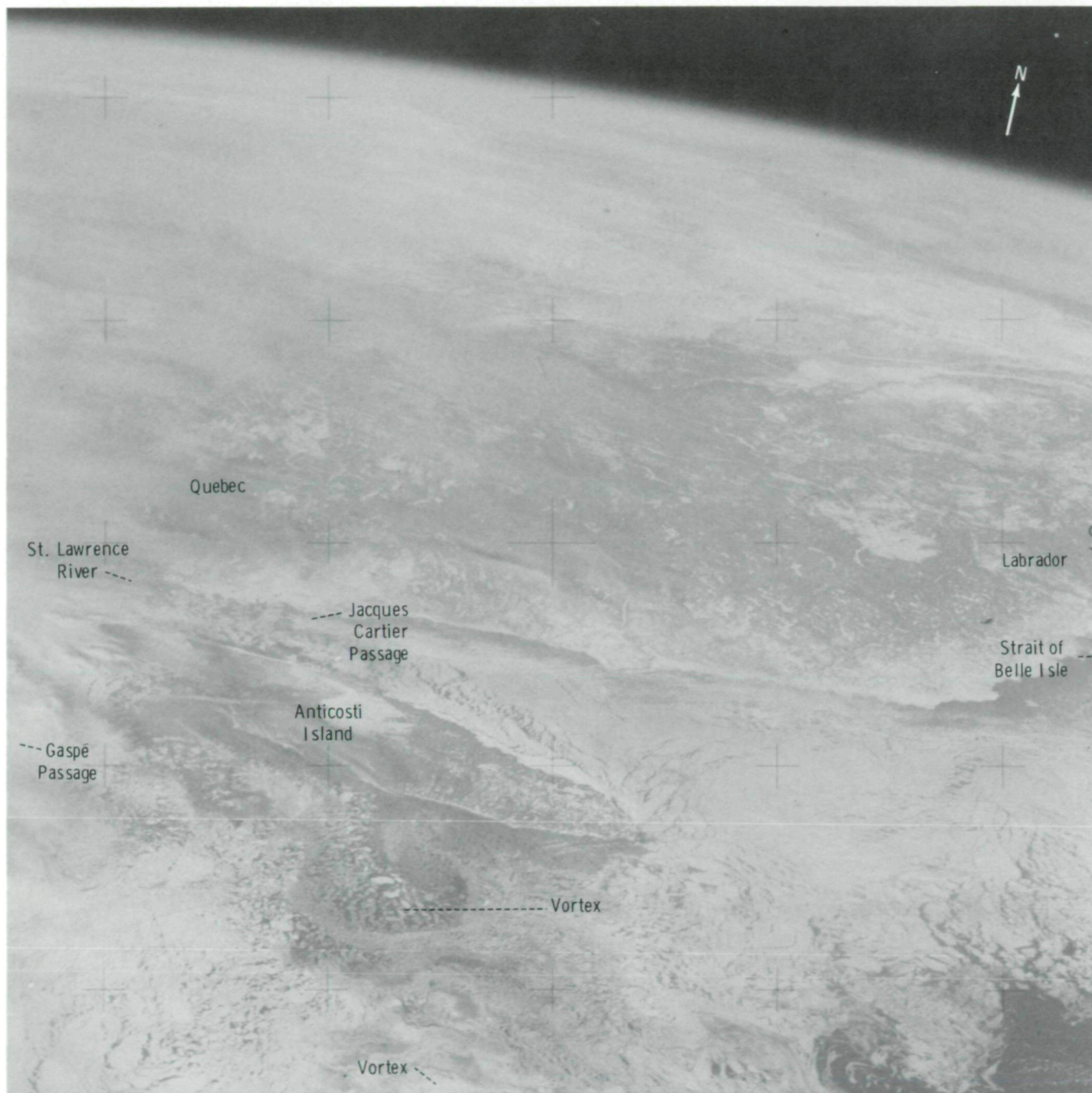


FIGURE 13-14.—Skylab oblique photograph of the northern Gulf of St. Lawrence on January 20, 1974, showing the distribution of the pack ice. The shore lead along the northern coast of the Jacques Cartier Passage has been partly closed. Note the vortex pattern in the ice south of Anticosti Island (SL4-141-4366).

structure northeast of Anticosti Island is a result of the blocking effect of the island.

Perhaps the most striking ice feature in the vicinity of Anticosti Island is the vortex structure that forms in the lee (to the south) of the island. The development of the vortex pattern can be seen in figures 13-12, 13-13, and 13-14, which indicate that a fairly unperturbed flow of ice progressed into one with large perturbations (≈ 150 km) in the period of 3 days. During the 3 weeks in which the Skylab crewmen observed the Gulf of St. Lawrence, this vortex feature was continuously developed in an area of constant ice production. In figure 13-9, an excellent example is seen of the development of stratocumulus plumes as the cold surface air flows from the ice over the open water area in the vicinity of Cabot Strait. The manner in which the entire pack rapidly adjusts to changes in wind direction can be seen in figures 13-9 and 13-14. On January 20, surface winds from the north acting on the pack (fig. 13-9) changed directions during the night and partly closed the shore lead along the Jacques Cartier Passage (fig. 13-14).

LAKE ONTARIO AND ST. LAWRENCE RIVER

During the 1974 ice growth period, the ice extent in the Gulf of St. Lawrence was greater than normal. However, the ice coverage on Lake Ontario was significantly less than normal; in fact, on January 20, the east end of Lake Ontario was covered by the lowest percentage of ice (70 percent) in the previous 7 years. On January 8, Lake Ontario and the Thousand Island regions were ice-free, and ground observations confirmed the absence of ice in the St. Lawrence Seaway (fig. 13-15). At this time of year, the ice normally would extend approximately 2 km offshore from Long Point in Lake Erie and from Wolfe Island in Lake Ontario, and the possibility of a full lake ice cover would exist as far as Main Duck and Galloo Islands in the eastern end of Lake Ontario.

On January 13, the ice covered the seaway and had an opaque white appearance (fig. 13-16). A near-surface photograph of this area taken on this day is shown in

figure 13-17. Before January 13, an intense cooling period occurred and resulted in the formation of ice 10 to 28 cm thick on the seaway. A snow layer 3 to 5 cm thick covered approximately 85 percent of the ice area. Surface observations confirmed that black ice occurred westward from an opaque white ice boundary that occurred on both sides of Wolfe Island. This ice, which had formed more recently than the white ice, extended beyond the island chain and filled the eastern end of the lake. The black ice was between 3 and 11 cm thick at this time. Figure 13-18 is a near-surface photograph of this ice type. In a vertical section, snow ice (white) overlies columnar (black) ice; in thin section, the detailed textures of these types of ice are distinctly different (fig. 13-19). The upper part of the white ice sample (fig. 13-19(a)) shows the presence of snow ice that formed when the water froze in the snow on top of the underlying columnar ice. The columnar ice below the snow ice (fig. 13-19(b)) occurs with its crystals elongated parallel to the direction of heat flow. The thin black ice westward of Wolfe Island is composed of columnar ice the origin of which is similar to that of the columnar ice below the snow ice.

When compared to the dynamic sea ice of the Gulf of St. Lawrence, the lake ice of Lake Ontario is classified as static. However, photographs of the edge of the cohesive ice cover made on successive Skylab 4 orbits provide valuable data on the rapidly changing ice extent. The extent of the ice cover has, in turn, a direct influence on the temperature of the water entering the St. Lawrence River. During cold periods, a small area of ice coverage will cause supercooling of the water entering the St. Lawrence River. Figure 13-20 includes a water temperature-time curve for the St. Lawrence River of data taken at a depth of 8 m at Alexander Point on Wolfe Island in the seaway. The times of intense supercooling correlate with the combined conditions of minimal ice extent and cold surface air. This supercooling enhances the formation of frazil ice in the western end of the river. Conversely, the presence of a large, well-developed ice cover prevents the formation of frazil ice in the head of the river. Morphological changes that occur in the ice cover downstream in the St. Lawrence River can therefore be inferred from satellite photography of the ice cover.

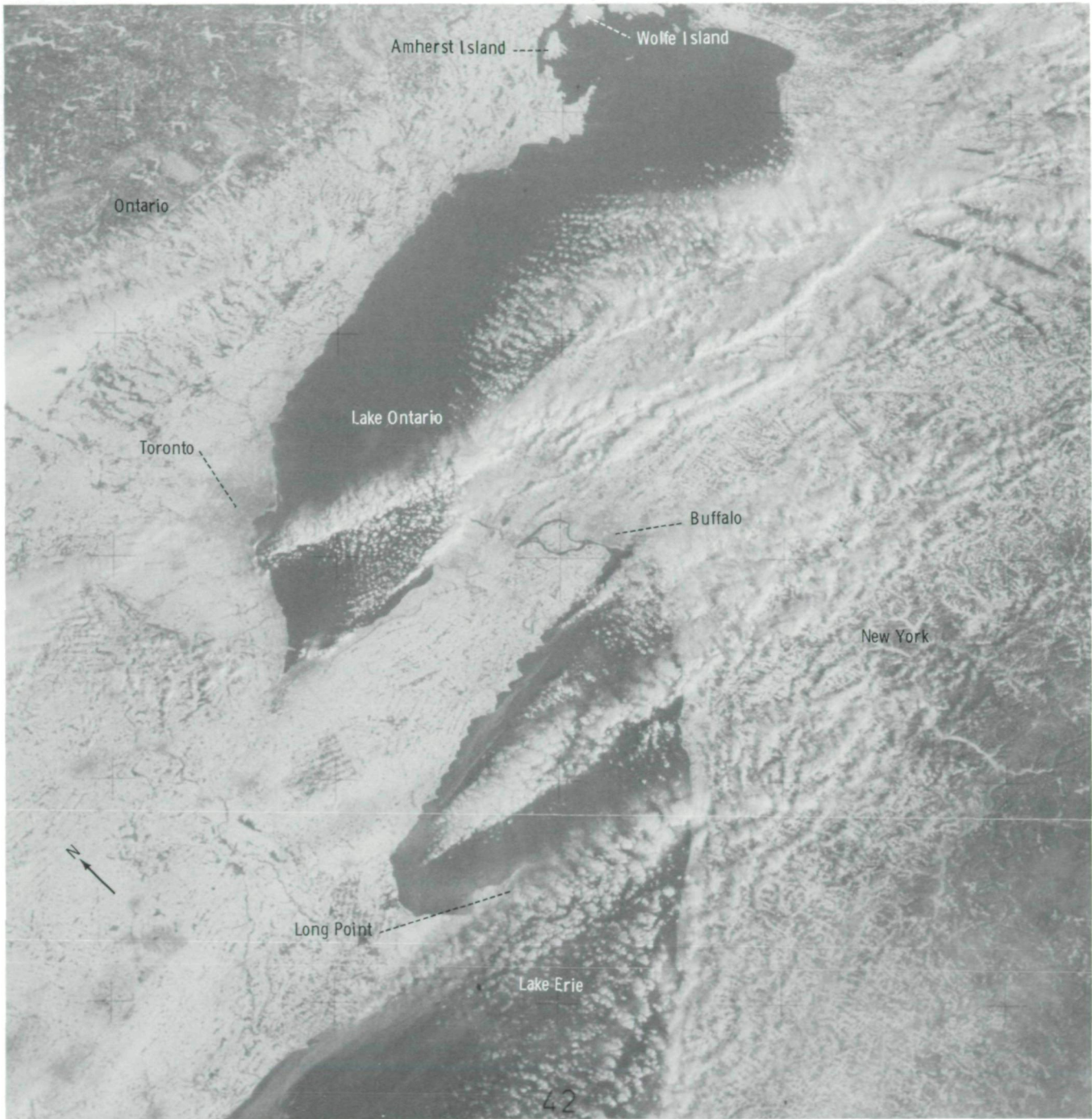


FIGURE 13-15.—Skylab 4 oblique photograph of the Lake Erie/Lake Ontario region on January 8, 1974, showing the absence of white opaque ice in the vicinity of Wolfe Island and at the entrance to the St. Lawrence Seaway (SL4-139-3989).

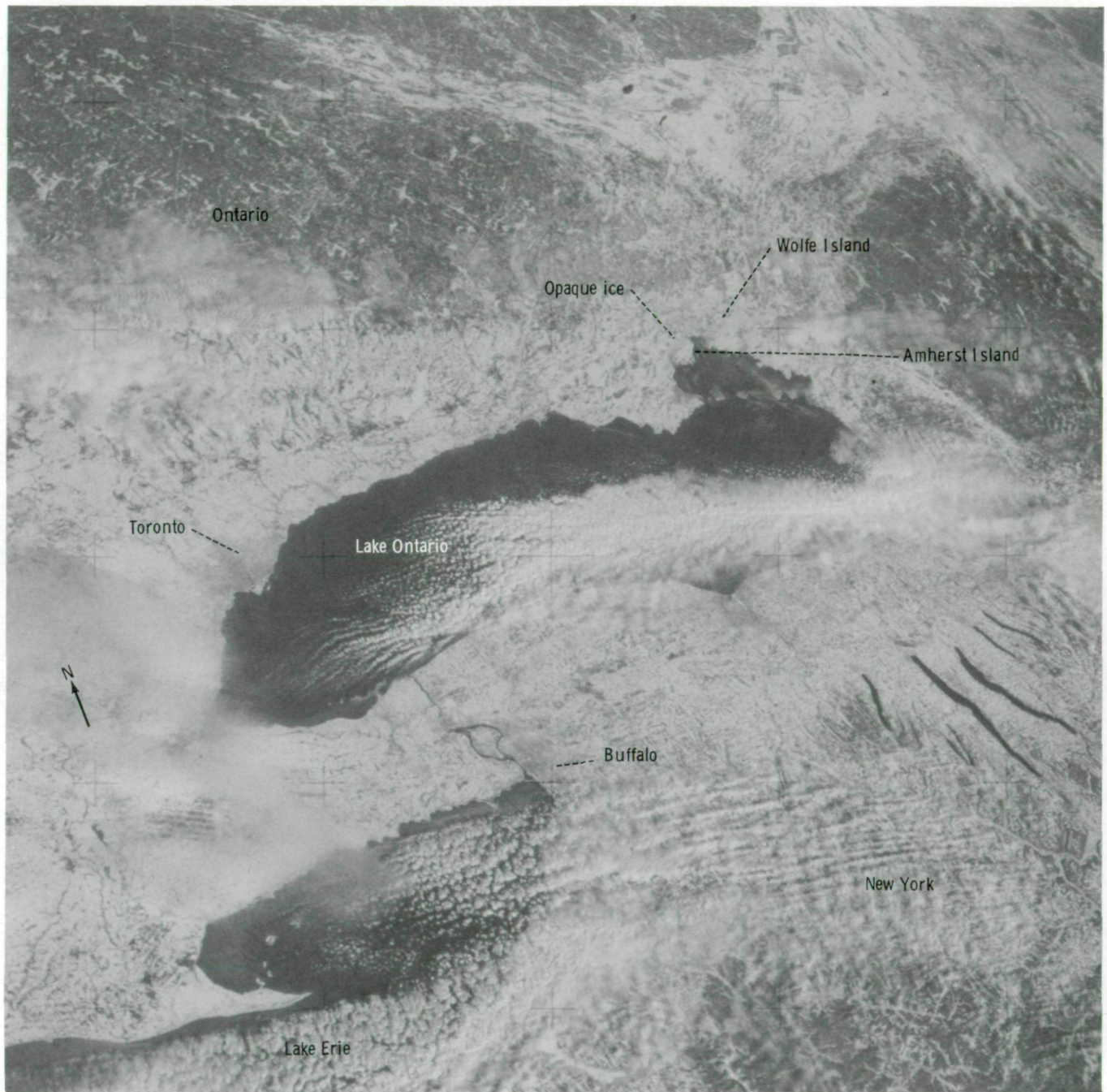


FIGURE 13-16.—Skylab 4 oblique photograph of the Lake Ontario/Lake Erie region on January 13, 1974, showing the presence of white opaque ice in Lake Ontario in the vicinity of Wolfe and Amherst Islands (SL4-140-4097).



FIGURE 13-17.—Aerial photograph of the snow and ice cover in the St. Lawrence River on January 13, 1974.



FIGURE 13-18.—Aerial photograph of the black ice cover in the St. Lawrence River on January 13, 1974.

JAMES BAY

Another interesting target of opportunity photographed during the Skylab 4 mission was the James Bay region of southern Hudson Bay. Figures 13-21 and 13-22 are two views of this region taken on January 13 and 17, 1974, respectively. When these two figures are compared, many differences in ice structure can be noted. On January 13, the surface wind was strongly to the east, as indicated by the low-level stratocumulus clouds. During the following 4-day period, the surface wind shifted and a strong southerly flow fragmented the

James Bay pack and caused it to diverge and to develop many open leads (fig. 13-22).

The motion of an individual ice floe of old shorefast ice can be measured by comparing these two photographs (figs. 13-21 and 13-22). The large (1 by 2 km) floe floating within the newly forming ice off the eastern coast of Akimiski Island on January 13 moved 18 km to the south during the 4 days between observations.

Another dynamic feature observed is the change of the shorefast ice edge on the western side of James Bay and on Akimiski Island. The southerly flowing pack

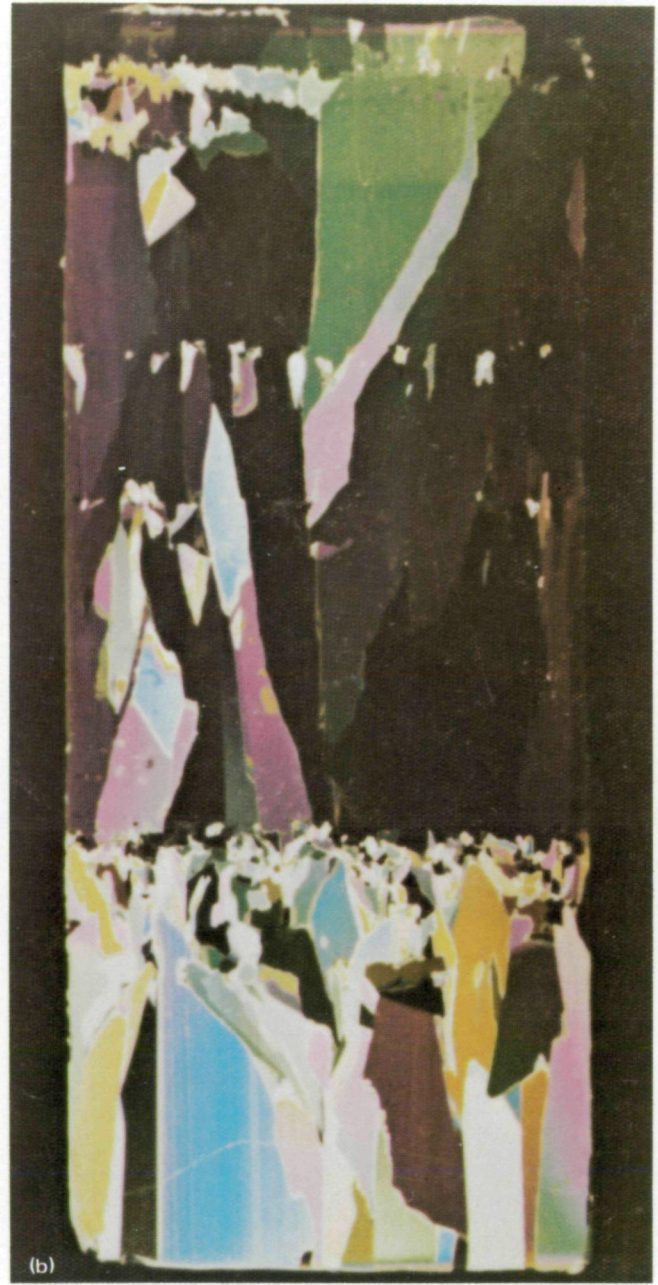


FIGURE 13-19.—Thin-section photomicrographs of two St. Lawrence River ice samples. (a) Snow ice over columnar (black) ice. (b) Columnar (black) ice.

C-5

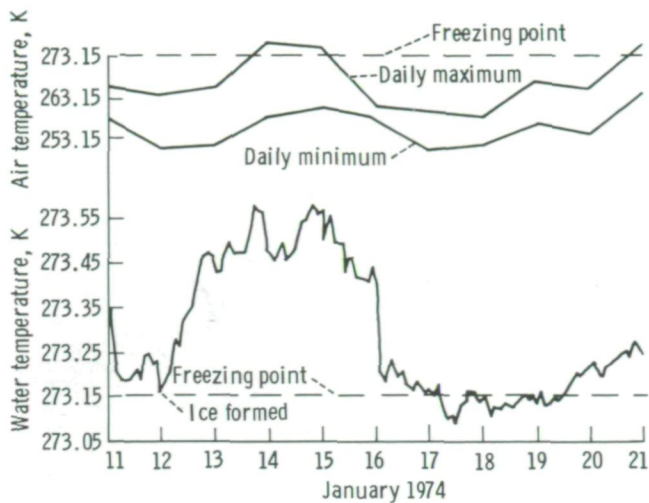


FIGURE 13-20.—Temporal plots of water and air temperatures measured at the entrance of the St. Lawrence River in January 1974.

removed sections of shorefast ice from the coast of James Bay north of Akimiski Island and from the northern and eastern coasts of Akimiski Island, whereas only minor changes in the shorefast ice occurred south of Akimiski Island. The major deformation of the pack occurred between Akimiski Island and Charlton Island to the east.

HOKKAIDŌ AND SAKHALIN

Several excellent photographs were obtained of the ice in the Okhotsk Sea. These photographs clearly demonstrate the extreme complexity and the dynamic nature of the icepack in this region. An excellent pair of sequential photographs (January 21 and 24, 1974) of the northern coast of Hokkaidō are shown in figures 13-23 and 13-24. On the earlier date, the ice off Abashiri is consolidated for a distance of 45 km from the coast.

Three days later, this ice has broken into a series of large, irregular, discrete ice floes that have been redirected eastward.

Other striking features of this pack are the number of large ice eddies and plumes. The eddy between Abashiri and Mombetsu, Hokkaidō, Japan, has a diameter of roughly 50 km and a distinct spiral structure (fig. 13-24). The ice plumes that occur farther off the coast toward the edge of the pack are as long as 50 km. Based on the investigators' observations at other locations such as the Bering Sea and the Gulf of St. Lawrence, these plumes suggest strong surface winds at the time of the photograph. Two distinct classes of ice thickness are clearly discernible in the large eddy in the January 24 photograph. Generally, ice in this area has a thickness of less than 50 cm at this time of year. These images will provide information for use in evaluating and expanding the coverage of the ice radar system that is operated along the Hokkaidō coast between Esashi and Abashiri by the Institute of Low Temperature Science at Hokkaidō University (ref. 13-1).

Figure 13-25 (January 21) shows the ice distribution farther to the north along the eastern coast of Sakhalin Island, U.S.S.R. The width of the pack ice belt here is approximately 65 km. A comparison of figures 13-23 and 13-25 reveals readily identifiable identical ice features (points A, B, and C). Advection of this ice is continuously southward toward the coast of Hokkaidō. Fast ice occurs in the bay east of Yuzhno Sakhalinsk, whereas a large amount of thin, newly formed gray and gray-white ice is formed along the coast just to the north. The general presence of thin ice along the coast indicates a general recent motion of the pack away from the coast. This suggestion is also supported by the presence of massive and highly developed ice plumes extending eastward from the edge of the pack as far as 30 km. The presence of these plumes also indicates a strong surface wind from the west.

Skylab 4 photographs taken on January 21 contain no evidence of ice in the Sea of Japan (higher water temperatures) or in the nearby Pacific Ocean (deeper, more saline water).



FIGURE 13-21.—Skylab oblique photograph of James Bay and Akimiski Island on January 13, 1974, showing the well-formed shorefast ice and deformational lead patterns in the pack ice. A large (1 by 2 km) floe of old shorefast ice (white) occurs in the pack ice just east of Akimiski Island (SL4-140-4101).

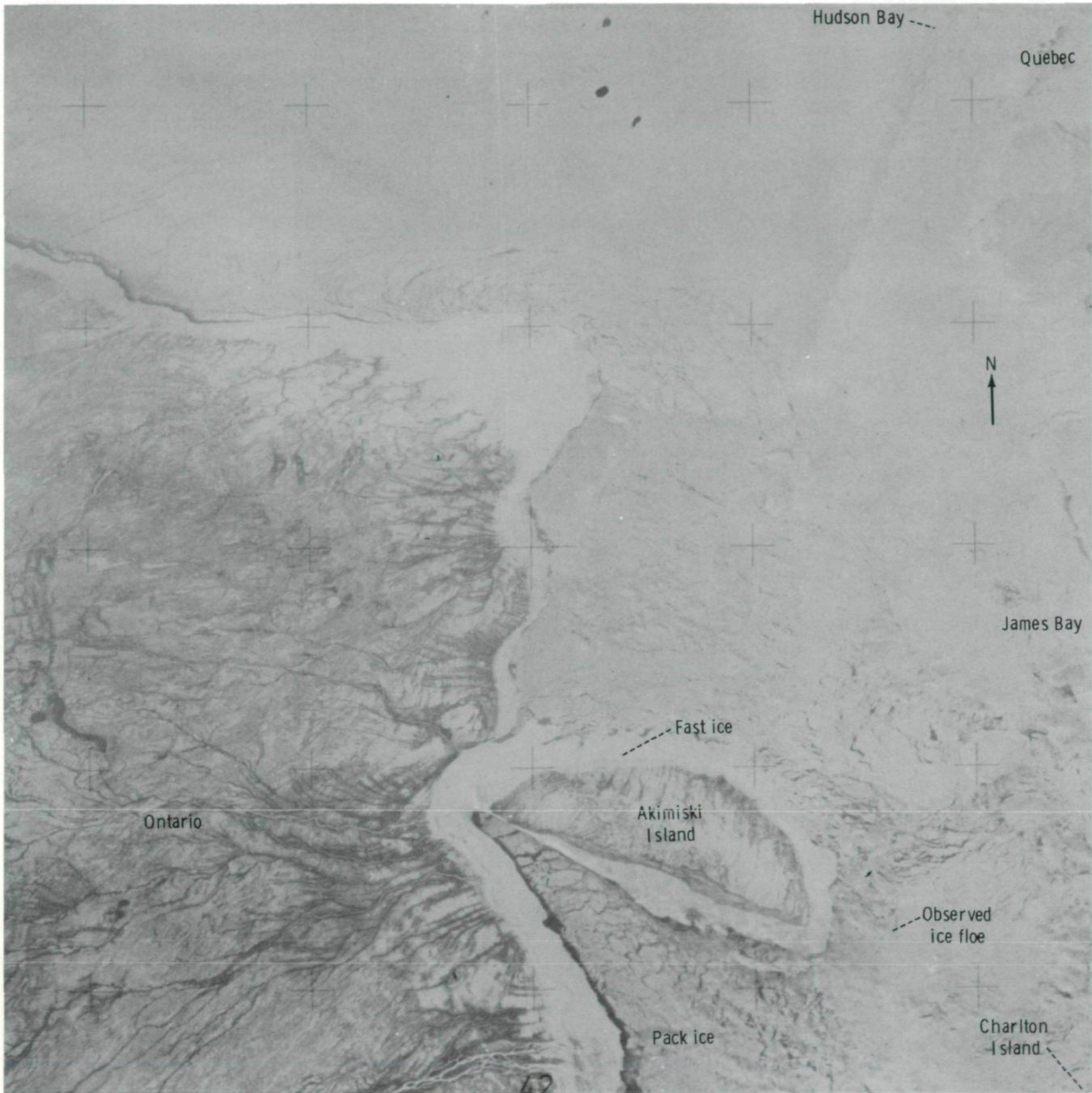


FIGURE 13-22.—Skylab oblique photograph of James Bay and Akimiski Island on January 17, 1974, showing the shorefast ice and the pack ice 4 days after the time of figure 13-21. The large floe noted in figure 13-21 is in the pack ice east of Akimiski approximately 18 km south of its position in figure 13-21 (SL4-140-4206).



FIGURE 13-23.—Skylab near-vertical photograph of the northeastern coast of Hokkaidō, Japan, on January 21, 1974, showing the consolidated pack ice off Abashiri. Ice plumes as long as 50 km are visible off the coast, and large ice eddies occur in the pack between Abashiri and Esashi (SL4-141-4340).

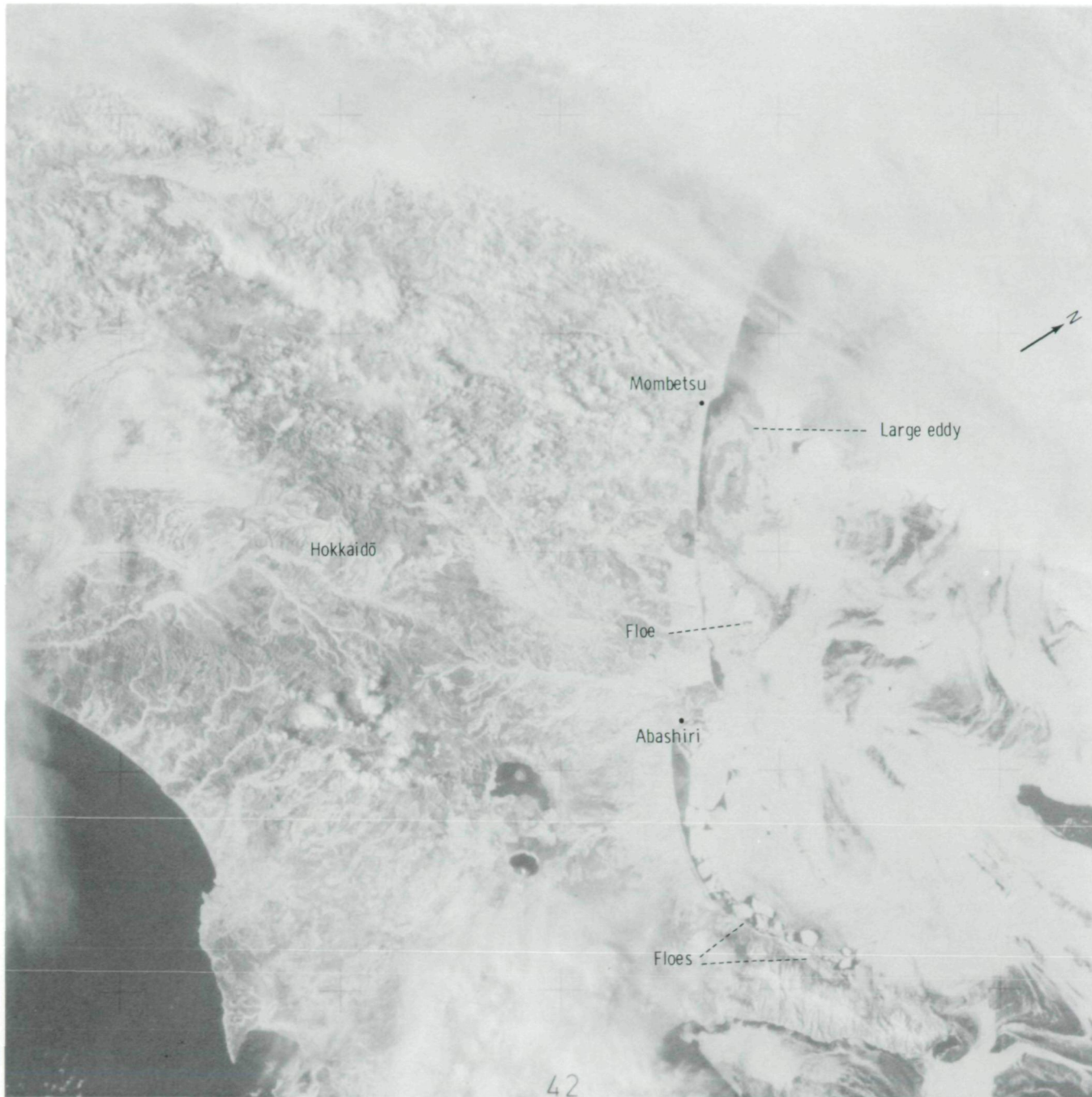


FIGURE 13-24.—Skylab near-vertical photograph of the northeastern coast of Hokkaidō, Japan, on January 24, 1974, showing breakup of the icepack into large, angular floes. Many plumes and eddies occur in the icepack, including a well-formed spiral eddy between Abashiri and Mombetsu in which the bands of thick ice (white) and thinner ice (gray) are easily discernible (SI.4-142-4490).

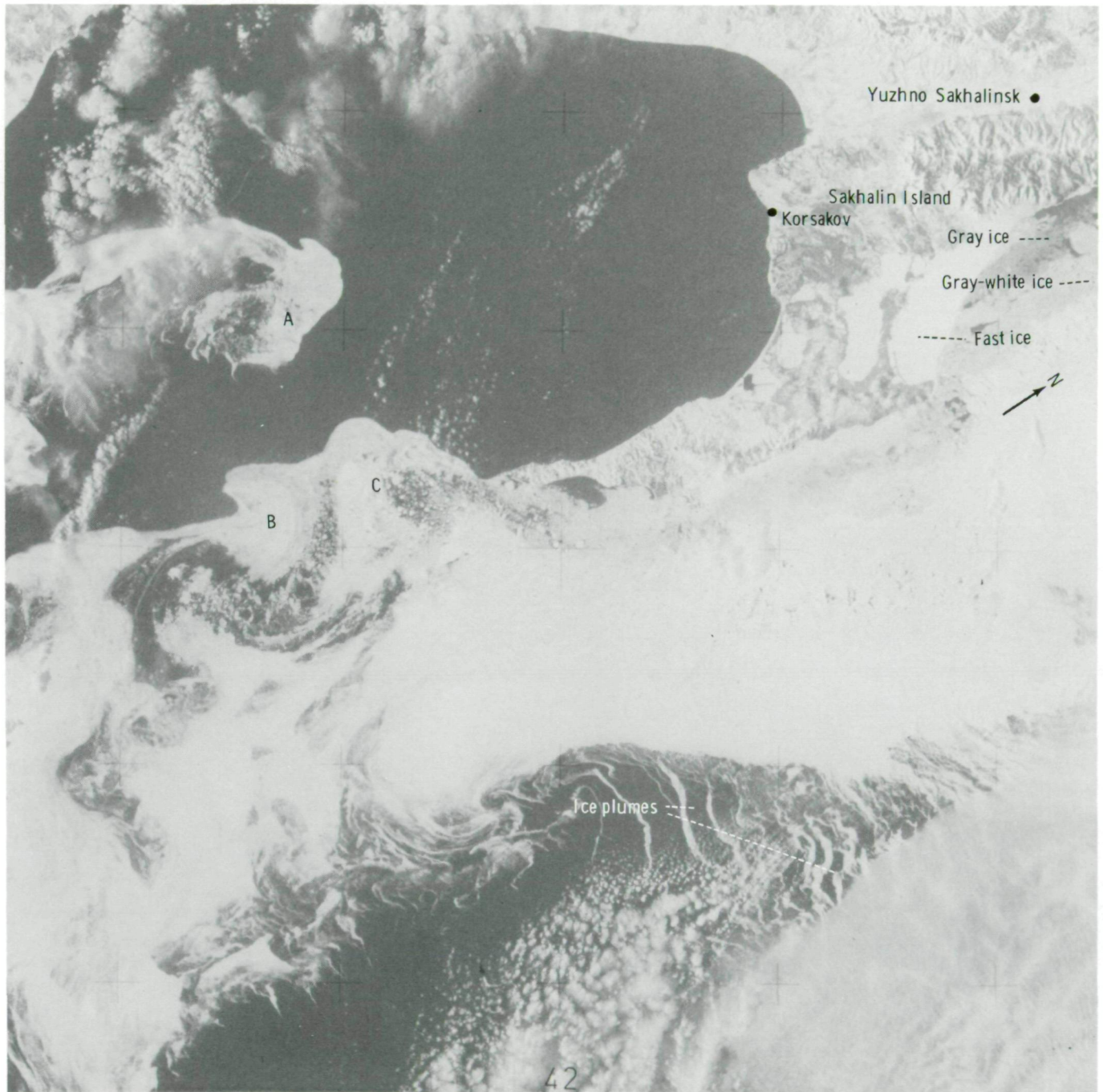


FIGURE 13-25.—Skylab near-vertical photograph of southeastern Sakhalin Island, U.S.S.R., on January 21, 1974, showing the icepack on the eastern coast of the island and the plumes and eddies extending south and east. Fast ice occurs in the bay east of Yuzhno Sakhalinsk, and newly formed gray and gray-white ice occurs along the coast to the north (SI4-141-4339).

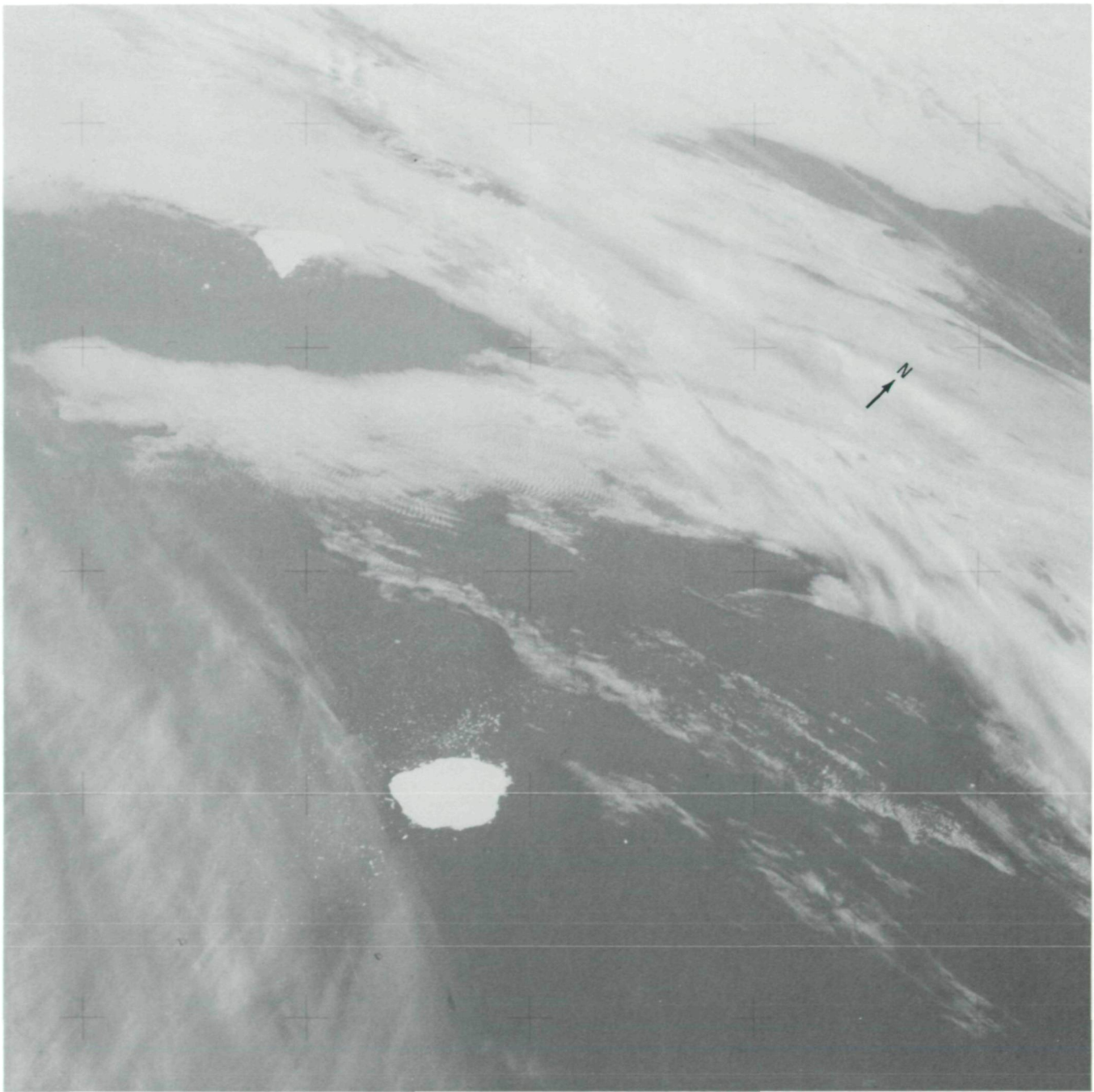


FIGURE 13-26.—Skylab oblique photograph of an area near the Falkland Islands on January 28, 1974, showing two large tabular icebergs (lateral dimensions ≤ 30 km). Note the "cloud" of smaller iceberg fragments, which has been produced by calving (SL4-142-4577).

ICEBERGS

Many tabular icebergs having lateral dimensions of as much as 30 km were identified in the South Pacific and South Atlantic Oceans and were most common in the vicinity of South Georgia and the Falkland Islands. The northernmost iceberg that was sighted, located at latitude 43° S, longitude 37° W, was generally round in plan view and had a diameter of 15 to 20 km. As might be expected, the icebergs farther to the south and near the Antarctic ice sheet have angular shapes. Two icebergs off the Falkland Islands were photographed by the Skylab 4 crewmen (fig. 13-26). One is round and is surrounded by a "cloud" of small iceberg fragments that have been produced by calving, whereas the other large iceberg is more angular.

A more detailed view of the small iceberg fragments "clustered" around the large "source" iceberg is shown in figure 13-27. The pileup of small icebergs along one side of the larger iceberg is caused by the combined action of currents and wind. It appears that the iceberg was transported eastward by the current while surface winds probably acted to transport the fragments to the west of the parent iceberg.

The Skylab 4 crewmen described two isolated clusters of small icebergs (50 to 100 fragments) in the South Atlantic Ocean. These clusters undoubtedly represent the remains of large icebergs that have disintegrated. Observations on the mode of breakup and the disintegration rate of large icebergs that have drifted far north are quite important in appraising the economics of using icebergs as a source of fresh water (ref. 13-2). In any operational scheme for transporting icebergs, a

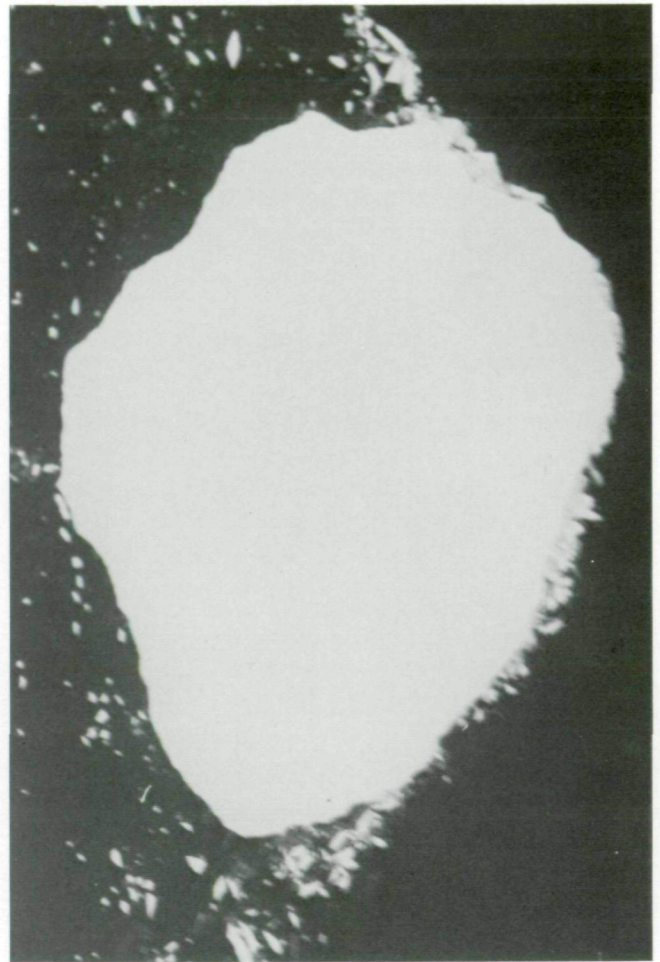


FIGURE 13-27.—Nikon 300-mm Skylab photograph taken on February 6, 1974, of a large, rounded tabular iceberg surrounded by smaller iceberg fragments (SL4-200-7615).

satellite surveillance system would be useful to locate the most appropriate iceberg which has drifted by wind and current as near the delivery site as possible. The difficulty in completing the remainder of the iceberg delivery is directly related to the condition of the iceberg at pickup and to the ice losses during the tow that are caused by melting and calving. If such icebergs can be shown to commonly undergo catastrophic breakups, the attractiveness of such schemes will certainly be decreased.

Another interesting feature noted in some of the photographs consisted of long cloud plumes that occasionally form downwind from the large icebergs. These plumes presumably are caused by the standing wave formed by the air propelled over the iceberg. The plumes commonly extend for distances of 20 times the diameter of the iceberg.

CONCLUSIONS

The Skylab 4 sea and lake ice experiment has resulted in obtaining useful observational and photographic information on a wide variety of topics such as the variability of ice extent, ship routing in ice-infested waters, and iceberg drift and decay. Although many aspects of floating ice can effectively be studied by the use of unmanned satellites, the Skylab 4 results show that the presence of man in space is vital for certain observational tasks. Man has the ability to select and to focus on ice areas that show a high degree of activity.

He can also choose the period and the extent of experimental observations. The objective of the Skylab 4 experiment was accomplished because of the effective data collection by the crewmen over the main designated test sites and because of their ability to recognize and to document other areas of interest. Therefore, it is strongly recommended that in future manned space programs, such as the Space Shuttle Program, visual observations as well as time-sequenced photographs of floating ice be acquired as part of the data collection program.

ACKNOWLEDGMENT

The authors thank Dr. W. D. Forrester and the crew of the COS *Dawson*, Robert J. Weaver and Floyd Kugzruk, for helping to make the ground-truth measurements.

REFERENCES

- 13-1. Tabata, T.: Radar Network for Drift Ice Observation in Hokkaido. *Sea Ice: Proceedings of an International Conference*, P. Carlson, ed., National Research Council, Reykjavik, R.I. '72-4, 1972, pp. 67-79.
- 13-2. Weeks, W. F.; and Campbell, W. J.: Icebergs as a Fresh Water Source: An Appraisal. *J. Glaciol.*, vol. 12, no. 65, 1973, pp. 207-234.

Page Intentionally Left Blank

Quantitative Analysis of Atmospheric Pollution Phenomena

DARRYL RANDESON^a

THE UTILITY of satellite photographs in detecting and evaluating atmospheric pollution has been demonstrated by the author (refs. 14-1 and 14-2), Parmenter (ref. 14-3), Lyons and Pease (ref. 14-4), and others. Imagery from the Skylab 4 mission offers improvements over previous orbital observations of atmospheric pollution because the crewmen were specially trained and equipped to observe, photograph, and describe atmospheric pollution and other meteorological and geophysical features. In particular, the crewmen received several hours of briefings conducted by the members of the multidiscipline Visual Observations Project Team. These briefings and the enthusiasm of the crewmen for the Earth observations program resulted in a very successful mission.

During their 84-day mission, the Skylab 4 crewmen took more than 2000 photographs of Earth with handheld Hasselblad and Nikon cameras. Approximately 75 of these photographs were of air-pollution events (table 14-I). This imagery may be separated into two categories according to the sources of the pollution: (1) natural pollution, which consists of dust generated by wind, naturally induced forest fires, and smoke generated by volcanic activity, and (2) manmade pollution, which includes brush fires, smoke plumes from stacks or open burning, contrails, and ship trails. Results of the analysis of some of the most interesting photographs are discussed in this section.

^aAir Resources Laboratory, Las Vegas, Nevada.

DATA ANALYSIS

Sakura-zima Volcanic Activity

Situated on a small volcanic island in Kagoshima Bay on the Japanese island of Kyūshū, the Sakura-zima Volcano rises 1120 m above sea level. According to the Smithsonian Institution Center for Short-Lived Phenomena, emissions of volcanic smoke began on November 27, 1973. Local reports from Kagoshima, located approximately 10 km west of the volcano, described the eruption as including frequent explosions with detonations, air shocks, and strong emissions of smoke, which reached altitudes of approximately 4000 m. Photographs of the volcanic smoke plume were taken by the Skylab 4 crewmen on December 1, 1973, and on January 7 and 8, 1974. During these three passes, the crewmen photographed the volcano and the emanating smoke plume with both the Hasselblad and the Nikon cameras. A photograph taken on December 1 at approximately 02:00 Greenwich mean time (GMT) is shown in figure 14-1. This photograph is one of five photographs taken sequentially with a 300-mm lens on the Nikon camera. The photograph is underexposed because an f/22 setting was accidentally used in the rush to obtain the photograph, and conditions required an f/11 setting. A map derived from a two-image mosaic of the volcanic plume is shown in figure 14-2. The images of January 7 and 8 are shown in figures 14-3 and 14-4, respectively. A sketch of the January 7 photograph is presented in figure 14-5 to identify geographical

TABLE 14-I.— Pollution Events Observed and/or Photographed by the Skylab 4 Crewmen

| Date | GMT, hr:min | Location | Event ^a |
|---------------|-------------------------|---|--|
| Nov. 17, 1973 | 13:35 | India | "Looks like an oil well fire" |
| Nov. 28 | 13:36 20:07 | Niger River area Near Asunción, Paraguay | "Large number of fires with plumes" "Many, many fires" |
| Nov. 30 | 15:08 18:32 | Off New Jersey coast South America | "Acid stains in water extremely clear" "Lot of fires burning" |
| Dec. 1 | 02:00 | Japan | Sakura-zima Volcano smoke plume |
| Dec. 2 | 15:00 | Flint, Michigan | Contrails |
| Dec. 5 | 00:45 | Approximately 145° E, 20° to 25° N | Erupting volcano |
| Dec. 7 | 14:50 | Off Louisiana coast | Two smoke plumes |
| Dec. 11 | 15:23 | Galapagos Islands | "Fernandina Crater . . . smoking" |
| Dec. 20 | 18:55 | Argentina | Fires and smoke (observation only) |
| Dec. 22 | 18:54 | ≈ 480 km south of Santiago, Chile | Smoke cloud |
| Dec. 28 | 16:49 | Argentina | "Brush fires in the Pampas" |
| Dec. 29 | 12:38 | Central Africa | Slash burning |
| Dec. 30 | 14:45 15:11 23:00 | Argentina Mediterranean Sea Los Angeles | "Fire scar" (observation only) "Wind-blown dust or sand from Sahara over Mediterranean Sea" Pollution pall |
| Jan. 2, 1974 | 01:50 | Near Dubbo, Australia | Brush fire |
| Jan. 5 | 12:34 18:35 | Northern Africa Mexico City | Two very large oil fires Mexico City under smoke |
| Jan. 7 | 03:16 18:04 | Japan Near the South Pole | Sakura-zima Volcano smoke plume Airlow |
| Jan. 8 | 02:46 18:39 | Japan Texas and Mexico | Sakura-zima Volcano smoke plume Haze |
| Jan. 9 | 01:53 | Japan | Sakura-zima Volcano smoke plume |
| Jan. 10 | 02:40 | Japan | Sakura-zima Volcano; cloudy |
| Jan. 13 | 14:35 | | Volcanic smoke (?) (observation only) |
| Jan. 14 | 16:55 | Off southern California coast | Ship trail |
| Jan. 16 | 00:00 22:14 23:45 | Japan Florida Northern Mexico | Sakura-zima Volcano smoke plume "Smoke plumes over Florida" "Smoke plume in northern Mexico" |
| Jan. 19 | 00:54 | Mauritania | "Dust storm over Mauritania; dust blowing 100 miles out to sea" |
| Jan. 20 | 11:38 14:51 | Iran Central Africa | "Dust cloud moving off coast of Iran" "Brush fires in central African republics" |
| Jan. 21 | 13:57 20:29 21:43 | Algeria Venezuela 12° N, 85.5° W | "Oil fires in the Algerian desert" "Smoke plume over Venezuela" Water pollution (?) |
| Jan. 22 | 14:51 16:32 21:51 | Sokoto, Nigeria Coast near Liberia or Guinea Bay of Fonseca | Big fire, large smoke cloud; "stratospheric dust ball" "Wide-reaching dust blowing off coast around Liberia or Guinea." Active volcanoes |
| Jan. 23 | 17:21 18:43 18:50 | Michigan Iowa Cape Hatteras | "Water pollution on northeast shore of Lake Michigan" Snow streak Water pollution |
| Jan. 24 | 14:33 | Central Africa | Brush fires |
| Jan. 25 | 12:50 | Central Africa Central United States | Many fires Contrails over prairie states |
| Jan. 26 | 02:06 13:41 | Nigeria and Chad Nigeria and Chad | "A great, huge patch of fires . . . spectacular night scene." Slash burning (observation only) |
| Jan. 27 | 15:13 | | Slash burning; extensive smoke "Aurora" |
| Jan. 28 | 18:16 | Southwestern United States | Smoke plume |
| Feb. 1 | 02:16 | Japan | Sakura-zima Volcano smoke plume |

^aStatements in quotation marks are excerpts from mission transcripts.



FIGURE 14-1.—Photograph of the Sakura-zima volcanic plume taken at approximately 02:00 GMT on December 1, 1973 (SL4-196-7340).

features, to provide approximate scaling of distances, and to orient the images relative to true north.

Several inferences concerning the smoke plume can be drawn from viewing the Kagoshima atmospheric sounding (fig. 14-6) together with figures 14-1 and 14-2. First, the orientation of the plume in figure 14-1 indicates that it is near the 1700-m level because only the wind directions near this level would transport the plume in the observed direction. In general, winds above the 60-kPa (600 mb) level were westerly. Consequently, figures 14-2 and 14-6 suggest that the volcanic plume is approximately 1700 m above sea level and is flowing through very stable air. Measurements show the length of the plume to be approximately 78 km.

Furthermore, the rather compact nature of the plume supports the contention that it is being transported through a stable atmospheric layer. Initially, the smoke from the volcano was probably trapped near the base of a temperature inversion situated just above the 85-kPa (850 mb) level.

The volcanic plumes in figures 14-3 and 14-4 exhibit a different plume configuration than that in figure 14-1. In figures 14-3 and 14-4, the visible plume appears to spread out at relatively long distances from the source. Atmospheric soundings (figs. 14-7 and 14-8) show the wind and thermal conditions over Kagoshima almost at the time the photographs in figures 14-3 and 14-4 were taken. Sound reasons for the apparent increase in dispersion of the volcanic effluent are difficult to develop

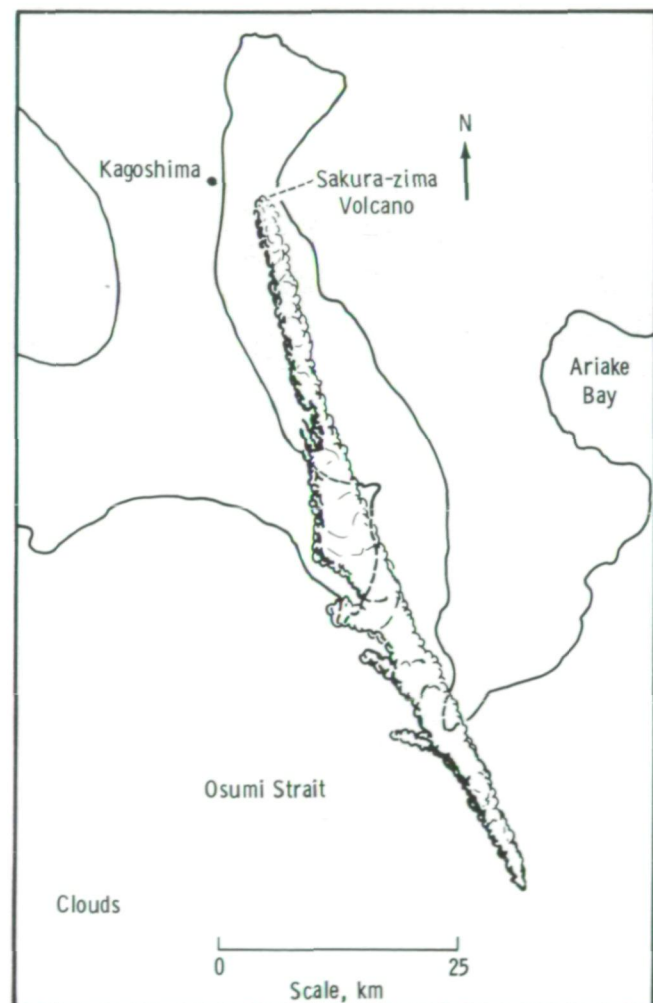


FIGURE 14-2.—Map derived from a two-image mosaic of the Sakura-zima volcanic plume taken on December 1, 1973.



FIGURE 14-3.—Photograph of the Sakura-zima volcanic plume taken on January 7, 1974, at approximately 03:16 GMT (SL4-139-3942).

because of the lack of data and incomplete knowledge of large-scale dispersion processes. Possible explanations for the apparent dispersion in figure 14-3 are as follows.

1. As the plume arrived over the warmer water, convective mixing occurred, dispersing the smoke plume.

2. The plume rose to higher elevations where the atmosphere developed a turbulence regime capable of spreading velocity fluctuations and the smoke through the surrounding air.

3. The volcanic effluent experienced considerable directional shear as it rose vertically.

The apparent dispersion of the visible effluent from the volcano on January 8 is interesting (fig. 14-4). This photograph is one part of a stereophotographic pair; thus, some quantitative information on the elevation of

the top of the smoke is available. Analysis of the stereophotograph revealed that the maximum elevation attained by the visible volcanic effluents was approximately 3200 m (± 150 m) above sea level.¹ The smoke plume appeared to achieve approximately 80 percent of its rise within 50 km of the source, rising to approximately 2500 m above sea level. A center line through the visible smoke is approximately 255 km long. The horizontal area of coverage by the visible volcanic smoke is approximately 20 000 km². The pictured spread of the effluent is postulated to have resulted from the vertical wind shear acting on the smoke as it rose through the lower half of the troposphere.

¹For additional information, see section 5.



FIGURE 14-4.—Oblique view of the Sakura-zima volcanic plume taken on January 8, 1974, at approximately 02:46 GMT (SL4-139-3972).

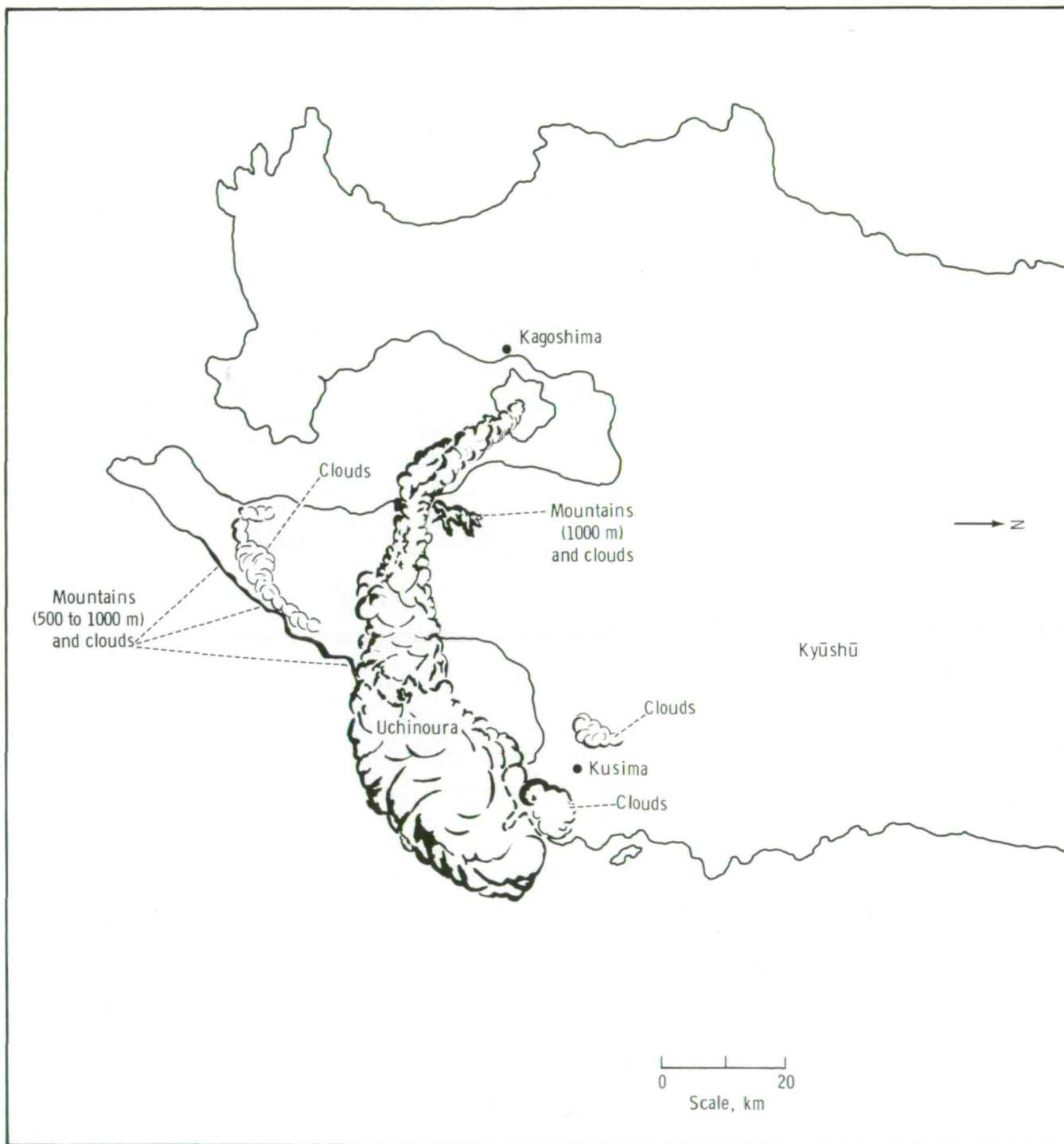


FIGURE 14-5.—Sketch of the photograph in figure 14-3.

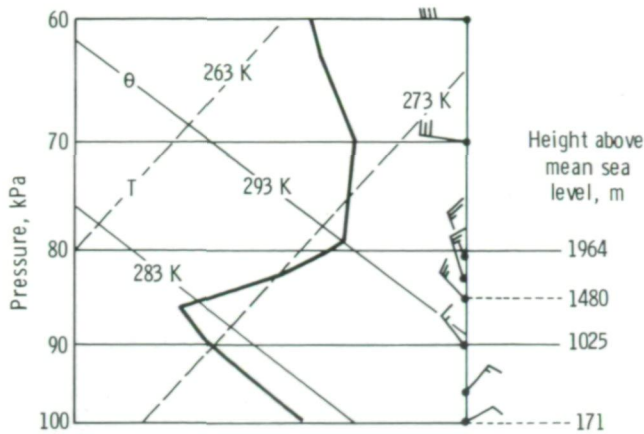


FIGURE 14-6.—Kagoshima atmospheric temperature sounding for 00:00 GMT, December 1, 1973, plotted on a skew-T adiabatic diagram. The lines parallel to the " θ " line are isolines of potential temperature; those parallel to the line labeled "T" are isotherms. Weather symbols are explained in appendix B.

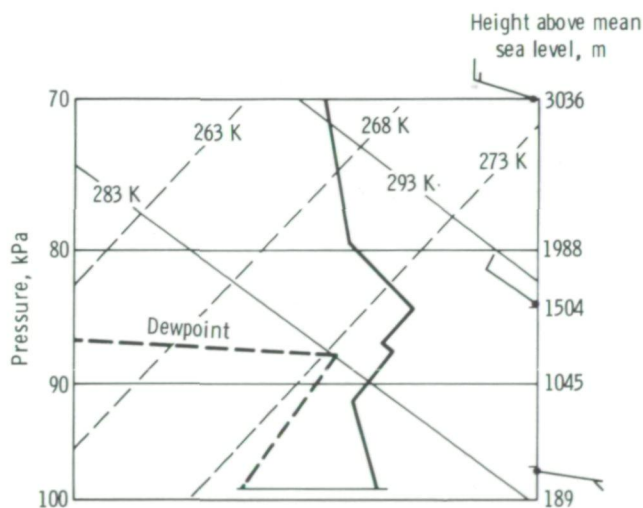


FIGURE 14-7.—Kagoshima temperature sounding taken on January 7, 1974, at 00:00 GMT. Weather symbols are explained in appendix B.

Estimates can be made of the thermal energy released from the Sakura-zima Volcano through use of the handheld-camera imagery, atmospheric soundings, and the plume-rise formulas developed by Briggs (ref. 14-5). For example, from the atmospheric sounding taken at Kagoshima (fig. 14-6) on December 1, a 500-m ascent of the volcanic smoke plume into a stable atmospheric layer can be estimated. This amount of plume rise is suggested by the fact that the plume in

figure 14-1 is oriented parallel to the winds between the 80- and 85-kPa (800 and 850 mb) levels. According to Briggs, the height of rise Δh of a buoyant plume in stable air is given by

$$\Delta h = 5.0 F^{1/4} s^{-3/8} \quad (14-1)$$

where F is a buoyancy flux parameter ($L^4 T^{-3}$, where L is length in meters and T is time in seconds) and s is the restoring acceleration per unit vertical displacement for adiabatic motion in the atmosphere (T^{-2}). After determining F , the heat emission of gases Q_h is given by

$$Q_h = 2.7 \times 10^4 F \quad (14-2)$$

where Q_h is expressed in watts and F is expressed in m^4/sec^3 . With a plume rise of 500 m and an s of approximately $10^{-4}/sec$, this expression yields a thermal energy release of 4×10^7 cal/sec, which is of the order of 10^2 MW. From the stereographic gridding of the plume displayed in figure 14-4, the close-in plume rise caused by buoyancy is approximately 600 m so that the thermal energy release is calculated as approximately 10^2 MW. A similar value is estimated for the plume in figure 14-3. A thermal energy release of 10^2 MW is three orders of magnitude less than that reported by Thorarinnsson and Vonnegut (ref. 14-6) for the Surtsey eruption off the southern coast of Iceland. At least part of this difference can be accounted for by the fact that the Sakura-zima Volcano was not continuously erupting as was the Surtsey Volcano.

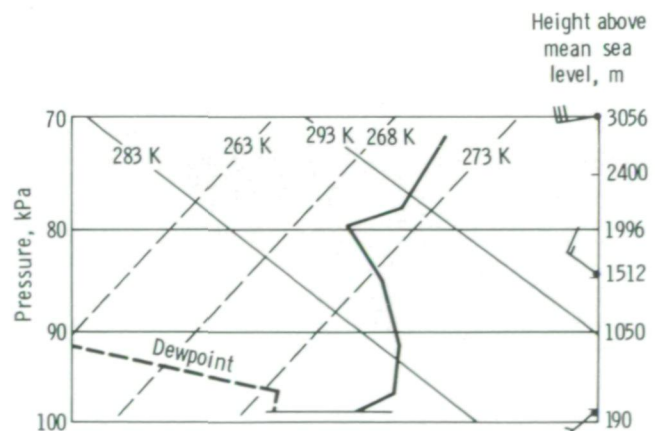


FIGURE 14-8.—Kagoshima temperature sounding taken on January 8, 1974, at 00:00 GMT. Data are missing between 72 and 50 kPa. Weather symbols are explained in appendix B.

Stereophotographs appear to provide a reliable basis for estimating the thermal energy release from volcanic eruptions. These type estimates should contribute to efforts to partition the thermal from the kinetic energy yields of erupting volcanoes. In addition, the imagery and supporting meteorological data indicate that, in all three cases, the eruption cloud did not penetrate the tropopause and create a stratospheric dust veil.

Dust Clouds

On January 20, 1974, at approximately 11:30 GMT, the crewmen photographed a dust cloud over the Arabian Sea (fig. 14-9). The most conspicuous feature in the photograph is the distinct demarcation between the dust cloud and the apparently "dust-free" air. In fact, a frontal-type boundary appears to separate these two air



FIGURE 14-9.—Dust cloud over the Arabian Sea on January 20, 1974 (SI4-141-4280).

masses and to extend southward and curve eastward in the lower half of figure 14-9. The dust cloud appears to extend from Chāh Bahār to the west and beyond Ormara to the east. Based on approximate gridding, the distinct dust line separating the two air masses is approximately 500 km long and extends beyond the image boundaries toward the south and east. The part of the dust cloud that is over water is estimated to cover 130 000 km², an area greater than that of the States of New York or Louisiana or of a country the size of Czechoslovakia.

At least two other significant duststorm episodes

were observed by the crewmen. On December 30, 1973, at approximately 16:30 GMT, the crewmen photographed a dust pall over Algeria and the Mediterranean Sea (fig. 14-10). The crewmen reported that the atmosphere over Algeria was dust free and extremely clear and that a "great arc" or "very sharp line of demarcation," having the appearance of a cirrus cloud, separated clear air to the west from dusty, hazy air to the east. This line of demarcation was described as extending from the southern tip of Sardinia through the strait between Marsala and Tunis to Tripoli and finally southward into central Algeria. The dust pall occupied

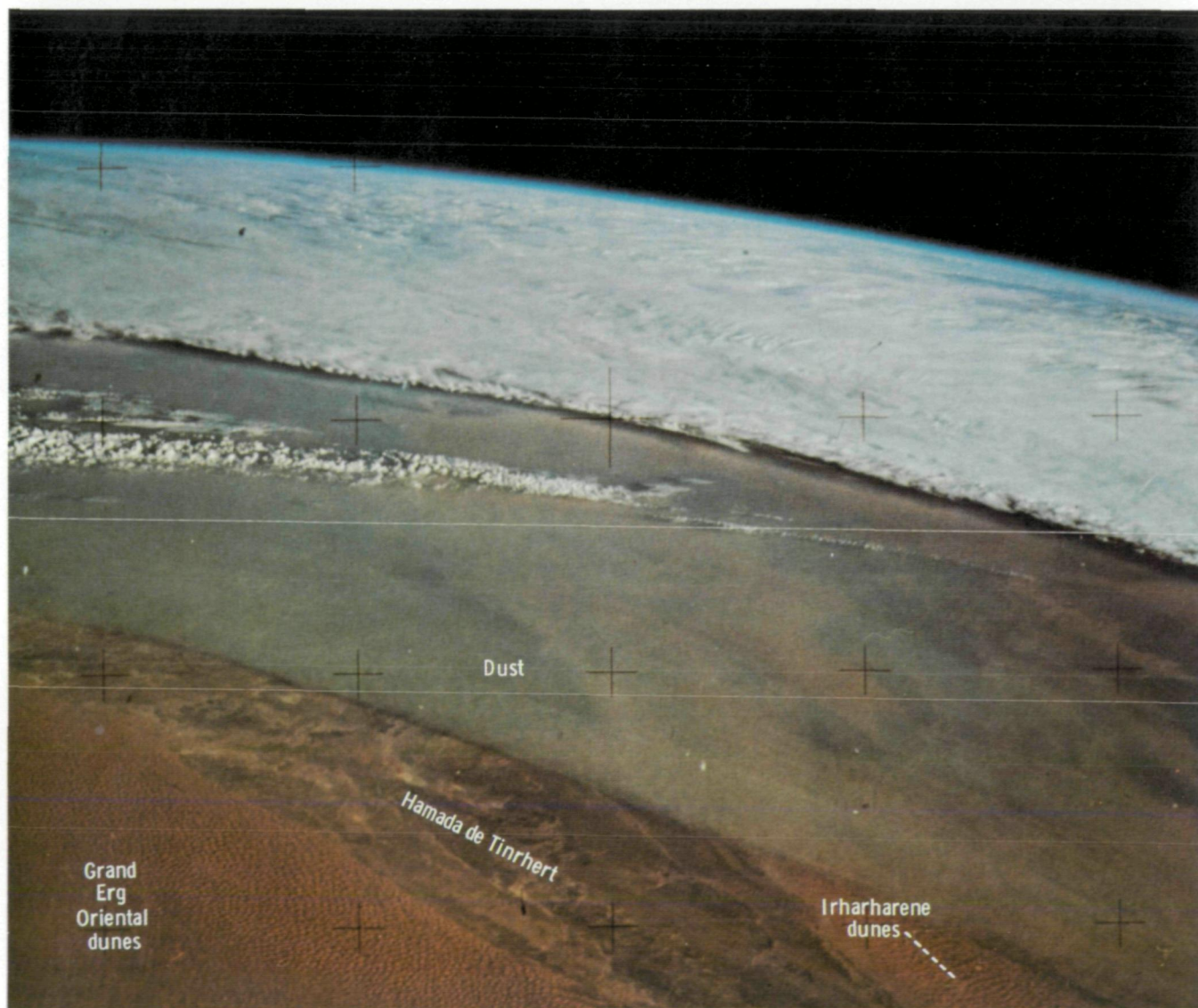


FIGURE 14-10.—Dust pall over eastern Algeria on December 30, 1973, at 16:30 GMT (SL4-138-3793).

the atmospheric region to the "north and east" of this line. Based on this description and figure 14-10, the line of demarcation was approximately 1000 km long, whereas the width of the dust pall was approximately 100 km and yielded a horizontal area of coverage of 100 000 km².

On January 19, 1974, at 01:00 GMT, another dust cloud was observed by the Skylab 4 crewmen. They reported a "duststorm" in progress over Mauritania with dust being blown approximately "100 miles [161 km] out to sea" in the vicinity of Dakar. The dust appeared to be reddish brown and was similar to the color of the ground.

Los Angeles Pollution Pall

A remarkable photograph was taken of the Los Angeles area and the southwestern United States on Sunday, December 30, 1973, at approximately 23:00 GMT (fig. 14-11). The area depicted is cloud free except in the vicinity of the southern San Joaquin Valley where low-cloud ceilings were reported. Snow cover is visible on the Tehachapi Mountains and the southern portion of the Sierra Nevada Mountain Range. All the desert areas appear to be covered by clear air; however, the Los Angeles basin is covered by a whitish pall of pollution. This pall appears to extend southward off the coast near Long Beach, over Santa Catalina Island, east of San Clemente Island, and directly west of the coastline from San Diego to near San Clemente. The pollution pall covers a rectangular area approximately 60 by 50 km (3000 km²) over the Los Angeles basin as seen in figure 14-12. The pall over the Gulf of Santa Catalina envelops an area approximately 140 by 70 km (9800 km²). The entire pollution pall has spread over approximately a 13 000-km² area. Secondary palls seem to exist southeast of Riverside in the Hemet area and to the east of San Bernardino, perhaps over Redlands (fig. 14-11).

A 19:30 GMT atmospheric sounding released from Los Angeles International Airport on December 30 indicated that a strong temperature inversion existed between 820 and 1130 m above sea level. Consequently, the pollution pall pictured in figure 14-11 probably occupied the lowest 820 m of the atmosphere. The pollutants should have been well mixed because the atmosphere below the temperature inversion exhibited a typical afternoon temperature profile with a superadiabatic lapse rate through the first 100 m and

near-neutral conditions to the 820-m level. Limited wind data indicated the macroscale flow in these low atmospheric levels was probably northerly. Such a flow regime seems reasonable in conjunction with the apparent southward extension of the pollution pall into the Gulf of Santa Catalina. The east-west orientation of the dense-appearing pall to the south of the San Gabriel Mountains suggests that this mountain barrier blocked or interfered with the northerly flow and perhaps allowed light, variable winds to develop over the northern portions of the valley.

Surface weather reports from 14 stations in the Los Angeles basin are plotted in standard form in figure 14-13. The data show horizontal visibility to be less than 11 to 13 km (7 to 8 miles) at most of the stations. There are several reports of smoke and haze restricting visibility to 8 km (5 miles) or less. The limited visibilities reported along Interstate Highway (IH) 10 between Ontario and El Monte are particularly noteworthy. The three stations along IH 10 are situated below the densest portion of the pollution pall. However, in the western portion of the basin, there was a pronounced difference in visibility between Burbank and Van Nuys and a noteworthy difference between Los Angeles International Airport and Santa Monica. These data indicate clearer air west of a line from near Burbank to the International Airport, which is confirmed by the photograph in figure 14-11. Also, a 00:00 GMT (December 31) observation from Mount Wilson at an elevation of 1740 m indicated a visibility of 48 km (30 miles), confirming the presence of clear air above the temperature inversion.

Finally, the photographs in figures 14-11 and 14-12 were taken on a Sunday when industrial activity was at a minimum. Thus, the observer could speculate that the pollution pall was probably formed primarily from vehicular exhaust gases.

Long Smoke Plumes

At approximately 14:50 GMT on December 7, 1973, the Skylab 4 crewmen obtained a spectacular photograph (fig. 14-14) of two rather long smoke plumes emanating from sources located on the central Louisiana coast. Investigation of the sources revealed that the plumes were probably the product of open burning of dead marsh grass for wildlife-management purposes. Actually, six or seven individual smoke plumes are visible in the photograph. The longest plume consists of

smoke from two fires located very close together. Smoke plumes from this same area were observed and photographed by the Gemini XII crew on November 14, 1966 (ref. 14-7).

Meteorologically, the eastern half of the United States was dominated by a continental polar air mass centered over Missouri on December 7 at 15:00 GMT. This high-pressure system was causing north-

northeasterly flow in the atmospheric boundary layer over southern Louisiana. In figure 14-15, the 12:00 GMT atmospheric sounding from Lake Charles, Louisiana, for December 7 illustrates the atmospheric flow and thermal structure in the vicinity of the two long plumes pictured in figure 14-14. Lake Charles is located approximately 125 km west-northwest of the plume originating from Marsh Island. The estimated 15:00

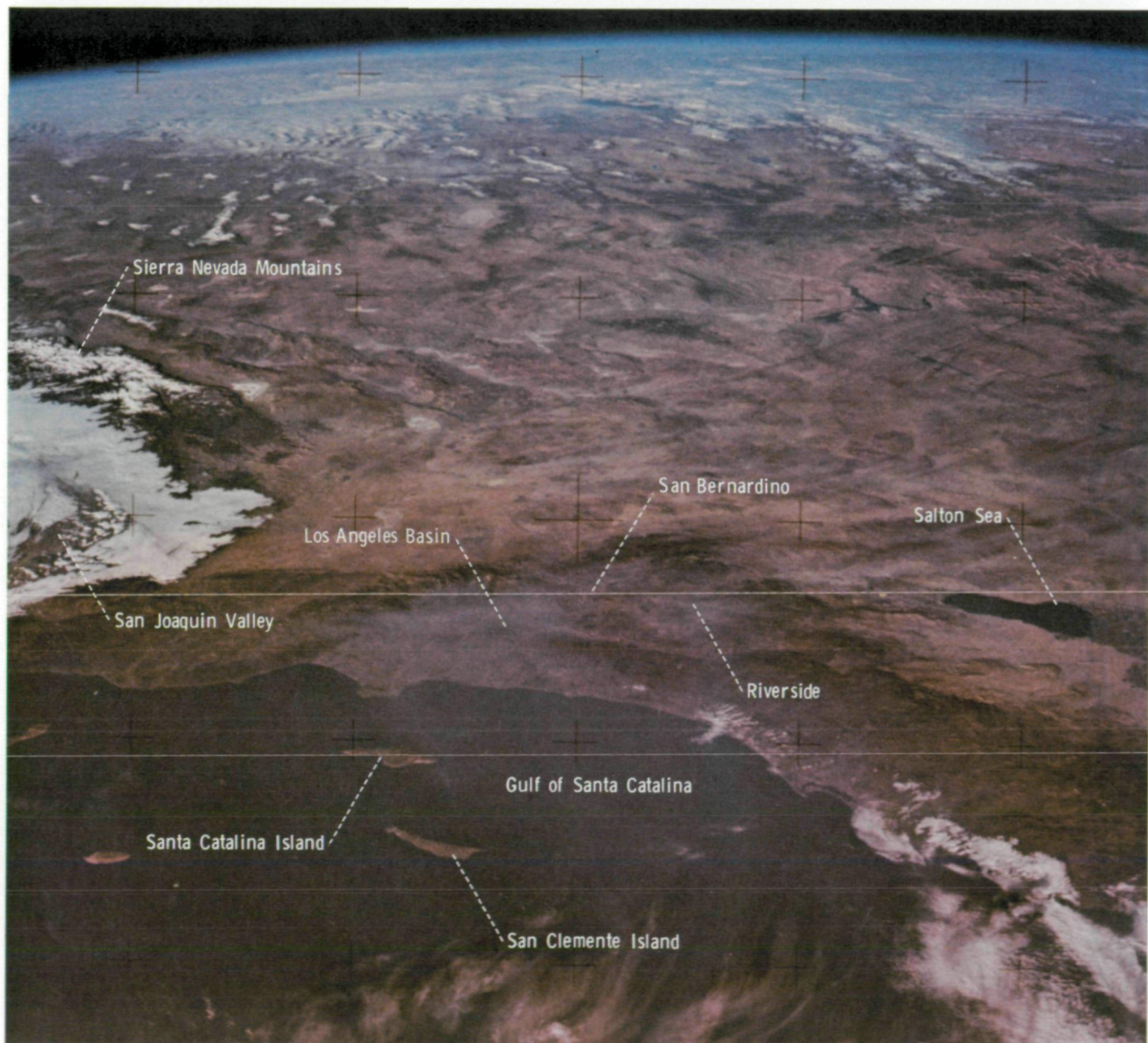


FIGURE 14-11.—Smoke pall over Los Angeles, California, on December 30, 1973, at approximately 23:00 GMT (SI4-138-3808).

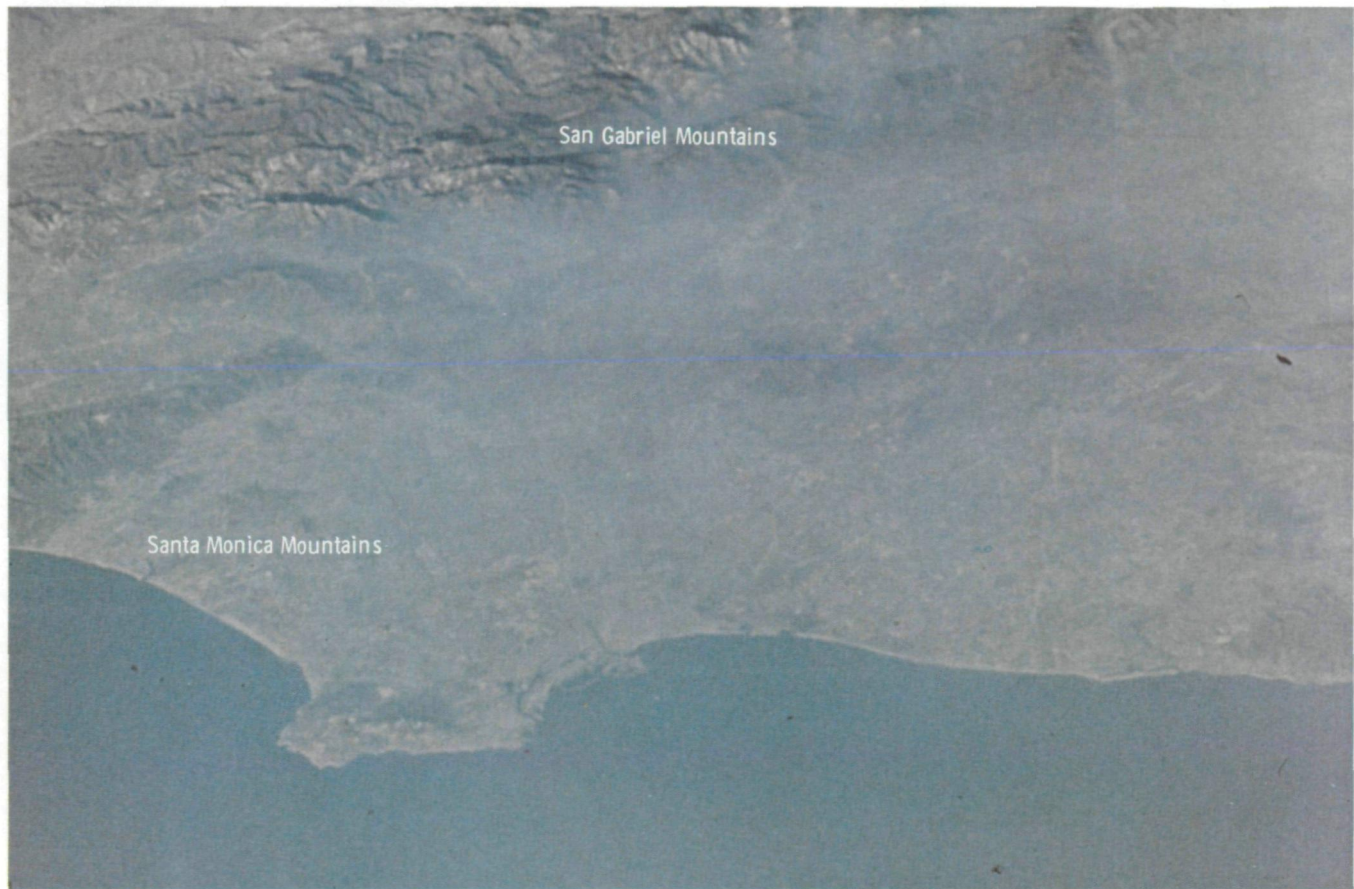


FIGURE 14-12.—Telephotographic image of the Los Angeles basin shown in figure 14-11 (SL4-194-7212).

GMT surface-level air temperature is plotted in figure 14-15 as the atmospheric temperature below the 100-kPa (1000 mb) level. From the sounding data, it can be seen that the thermally stable layer was situated between about the 95- and 90-kPa (950 and 900 mb) levels and a slightly less stable layer was between the 95- and 100-kPa (950 and 1000 mb) levels. The two long plumes in figure 14-14, which originated from ground-level burning of marsh grass, rose an estimated 300 m into the wind field between the 100- and 97-kPa (1000 and 970 mb) levels. Such a rise is confirmed by the fact that the pictured plumes are oriented parallel to the winds in this atmospheric region (035° , 7.7 m/sec (15 knots)). The surface wind was northerly. Water surface temperatures below the smoke plumes should have been approximately 293 K (68° to 70° F), based on climatology.

Figure 14-16 (a sketched enlargement of fig. 14-14) provides orientation with known geographical features

and an appropriate scale for measuring the dimensions of the plumes. From figures 14-14 and 14-16, certain facts can be inferred about the atmospheric structure in the vicinity of the plumes. At first glance, both plumes appear to be rather self-preserving over their entire length and exhibit little or no meandering motion. These features imply the absence of vigorous mixing processes.

The western plume is approximately 145 km long. The horizontal extent of the plume expands to a width of approximately 4 km at a distance of 11 to 12 km from the source, and the plume spreads to a width of approximately 6 km at approximately 50 km from the source. Beyond this point, the visible plume does not appear to spread horizontally. The shorter eastern plume is almost 134 km in length and appears to enlarge horizontally to a maximum width of approximately 5 km at approximately 115 km from the source. For the first 80 km of its length, the plume width is approximately 2 to



FIGURE 14-14.—Imagery of two long smoke plumes originating from sources on the central Louisiana coast at approximately 14:50 GMT on December 7, 1973 (SL4-136-3475). An enlargement of this photograph is presented in National Geographic, vol. 146, no. 4, Oct. 1974, p. 475.

3 km; it expands to 5 km for the last 54 km. The longer plume exhibits no apparent curvature; however, one could speculate that the shorter plume does have a low-amplitude wave mode present with a wavelength of approximately 170 km and a horizontal amplitude of approximately 10 km. The distance between the two plumes ranges from 23 km near the sources to 33 km approximately 110 km from the sources.

If the dimensions of the plumes are known, estimates can be made of the horizontal eddy diffusivity K_y associated with the visible plumes through the equations proposed by Gifford (ref. 14-8) and used by the author (ref. 14-2). Selecting a mean windspeed of 8

m/sec from figure 14-15, a half-plume width of 2.5 km, and a plume length of 145 km, K_y for the longer plume is $2 \times 10^6 \text{ cm}^2/\text{sec}$. For the shorter plume K_y is approximately $6 \times 10^6 \text{ cm}^2/\text{sec}$ when the same windspeed is used with a plume length of 134 km and a half-plume width of 4 km. As an order of magnitude estimate, the eddy diffusivity associated with the pictured plumes is $10^6 \text{ cm}^2/\text{sec}$.

The thickness of the atmospheric boundary layer can be computed through the hypsometric equation by using the data collected by the Lake Charles sounding. These sounding data show the surface pressure to be 103.2 kPa (1032 mb) and the pressure at the base of the stable layer to be 100 kPa (1000 mb), so that the thickness of the atmospheric boundary layer is calculated to be 250 m. Selecting 250 m as the size of the largest possible scale of motion L in the atmospheric boundary layer and assuming that the characteristic velocity u is one-thirtieth of the mean flow (8 m/sec), a crude estimate has been made of the scale of the vertical eddy diffusivity K_z through use of dimensional analysis, which specifies $K_z = uL$. Therefore, K_z is approximately $7 \times 10^5 \text{ cm}^2/\text{sec}$. From figure 14-14, the scale of the internal eddies is estimated to be approximately 1 km, and the characteristic speed of the layer is approximately 0.27 m/sec so that the scale of K_y is approximately $10^6 \text{ cm}^2/\text{sec}$, or slightly larger than K_z . This K_y is consistent with that derived previously from the plume dimensions. Similarly, the characteristic time

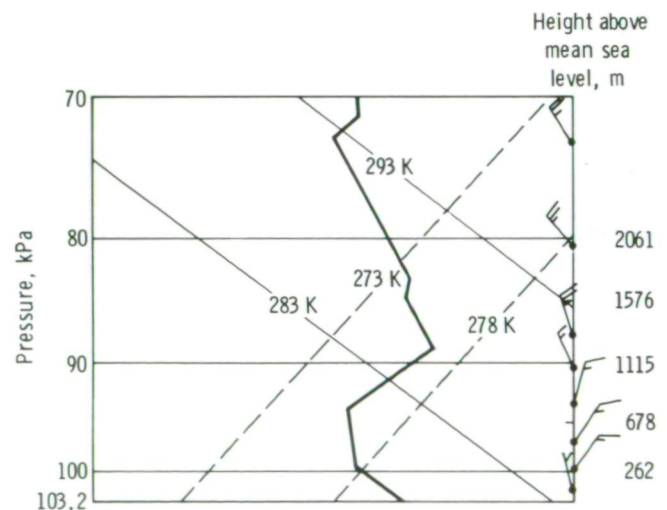


FIGURE 14-15.—Lake Charles, Louisiana, temperature sounding taken on December 7, 1973, at 12:00 GMT. Weather symbols are explained in appendix B.

scale of the motion is given dimensionally as $T = Lu^{-1}$ so that $T = 2600$ seconds. Furthermore, from the visible dimensions of the plumes and the thermal structure of the atmosphere (fig. 14-15), the turbulent scales of motion present in the vicinity of the plumes can be estimated. For example, since the longer plume is approximately 145 km long and displays no apparent curvature, the plume should be embedded in a flow regime with eddies having horizontal wavelengths greater than approximately 290 km. Also, whatever the energy source of the cellular-appearing eddies in the longer plume, the internal structure of the plume seems to consist of eddies with wavelengths on the order of 1 km. That is, the visible plume environment probably contains wind regimes with wavelengths greater than or equal to 290 km, whereas the internal structure of the plume consists of turbulent phenomena with wavelengths less than or equal to 1 km so that eddies with intermediate wavelengths are either relatively weak or not present. Thus, with a mean transport speed of 8 m/sec and a characteristic velocity in the atmospheric boundary layer of 0.27 m/sec, one could infer from figure 14-14 that the atmosphere should be free of turbulent elements with periods ranging from 10 to 1 hours (frequencies between 10^{-1} and 1 hr^{-1}). Spectral analysis of atmospheric windspeeds proves that an energy gap exists for atmospheric waves with frequencies of 10^{-1} to 1 hr^{-1} , so phenomena with these frequencies are not expected to occur generally. The plumes pictured in figure 14-14 tend to confirm the existence of such an energy gap.

The previous analysis assumes, perhaps boldly, the presence of a neutrally stable boundary layer. However, available surface data indicate that this flow regime is meteorologically very dynamic. The moderately strong flow extends from over relatively rough terrain to a water surface that is considerably warmer than the air flowing over it. The surface layer air leaving the coast has a temperature of approximately 280 K (7°C), which should increase to approximately 288 K (15°C) near the end of the plume. This conjecture is based on extrapolations from air temperature reports from two buoys located in the Gulf of Mexico. If a 4 to 5 K (4° to 5°C) excess is allowed for a very low-level superadiabatic lapse rate, the surface layer temperature becomes approximately 293 K (20°C) or close to the water temperature based on climatology. The temperature lapse rate above the surface layer is assumed to be roughly neutral. In this example, stereophotography of the plume might have been helpful in ascertaining

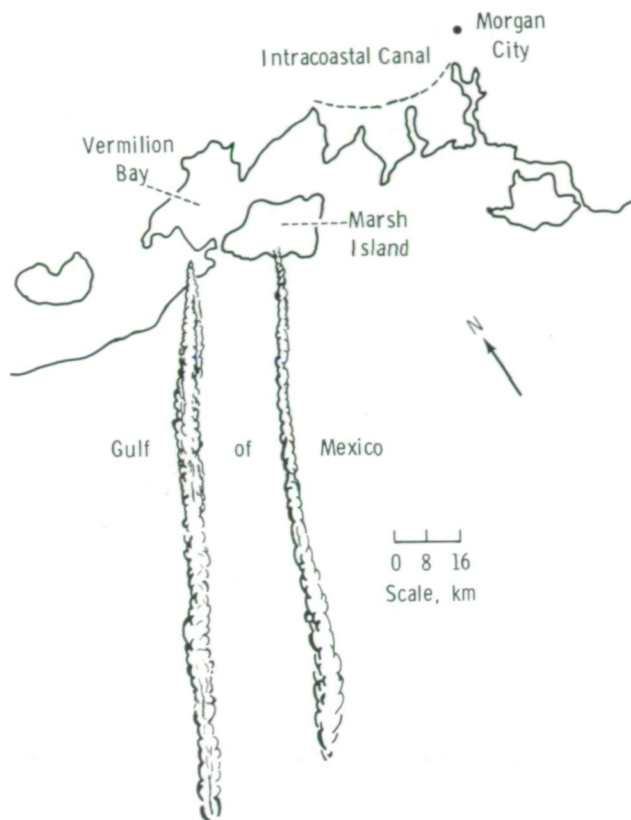


FIGURE 14-16.—Sketch of the imagery shown in figure 14-14.

the height of the atmospheric boundary layer over the Gulf of Mexico and perhaps could have provided more conclusive evidence on the atmospheric thermal structure and flow dynamics.

Finally, the nature of turbulence present in atmospheric flow can be quite different. To emphasize this point, the difference between the structure of the volcanic plumes in figures 14-3 and 14-4 and that of the smoke plumes in figure 14-14 must be noted. Also, considerable difference is apparent between the volcanic plumes in figures 14-3 and 14-4 and the one from the same source shown in figure 14-2 for a different flow regime.

Contrails

The imagery in figure 14-17 was taken on December 2, 1973, at 15:00 GMT and shows a view of Lake Erie

and the State of Michigan. There is considerable distortion of the image toward the west and north. To determine distances, a longitude-latitude grid was constructed and is presented in figure 14-18.

The two freshest jet contrails in figure 14-17 are clearly visible northwest of Lake St. Clair. The longer of the two extends from south of Bay City, Michigan, to near Flint, to approximately 40 km west of Port Huron and is visible for approximately 70 km. Located immediately north of Detroit, the shorter contrail is 48 km

long. Shadows from both contrails are visible on the ground directly to the north of each contrail. Both contrails appear to have a width equal to or slightly less than that of the St. Clair River, which is approximately 1 km wide. In addition, the lengths of these contrails indicate that their atmospheric environment is lacking in wave phenomena with wavelengths less than double the length of the contrails.

An estimate of the altitude of the contrails can be made by measuring the distance from the contrail to the

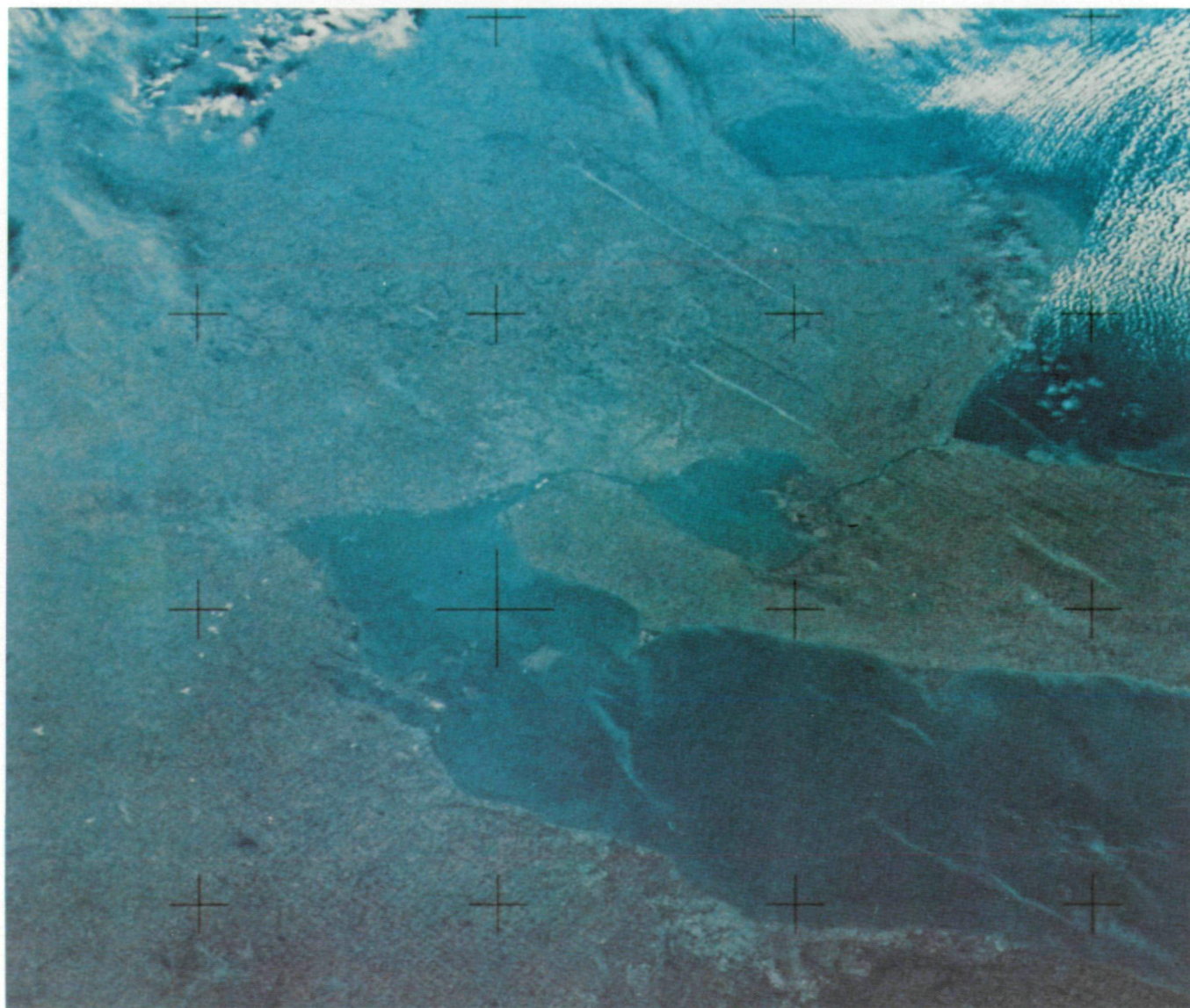


FIGURE 14-17.—Jet contrails in the vicinity of Lake Erie on December 2, 1973 (SL4-136-3405).

shadow and by assuming that the photograph was taken directly over the contrail (obviously a weak assumption). For the given date and time and for a horizontal distance of separation of approximately 15 km, the elevation of the longer contrail is calculated to be near 6680 m. If the photograph had been taken at a 45° angle off vertical (a more realistic assumption), the contrail would be 1.4 times higher, or approximately 9450 m above the ground. Upper-air temperatures in the vicinity of Flint at 12:00 GMT ranged from 230 K (-43° C) at the 9380-m level to 209 K (-64° C) at the 12 070-m level. According to a technique for predicting the occurrence of contrails developed for the U.S. Air Force by Appleman (ref. 14-9), contrails would be expected to form above the 10 600-m level, close to that approximated from figure 14-17 by assuming a 45° angle from vertical. It would appear that, with accurate data on the angle from vertical at which the photograph was taken, the altitude of the contrails could be calculated from the shadows.

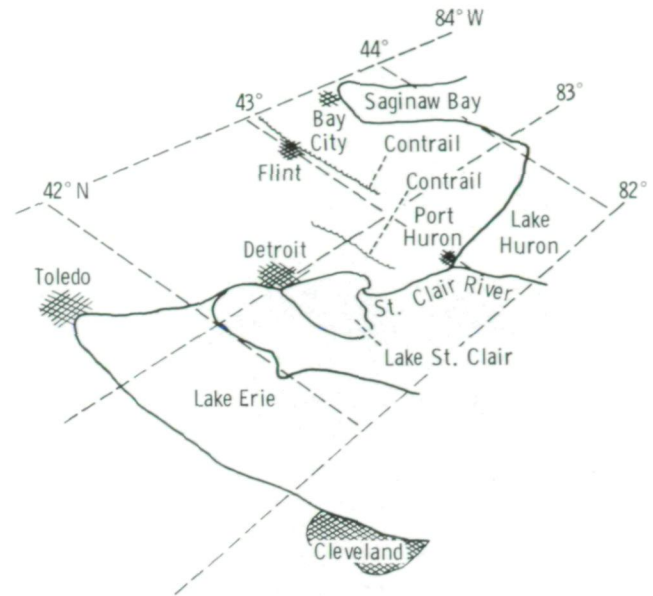


FIGURE 14-18.—Approximate grid for figure 14-17.



FIGURE 14-19.—Jet contrails over midwestern United States on January 25, 1974 (SL4-209-8161).

Examples of the imagery of other contrails are presented in figures 14-19 and 14-20. The contrails pictured over the midwestern United States on January 25, 1974 (fig. 14-19), appear to be in the vicinity of cirrus clouds; however, the contribution of the contrails to the cirrus, if any, cannot be known without supplemental data. Two contrails over Kansas are shown in figure 14-20.



FIGURE 14-20.—Jet contrails over Kansas on February 3, 1974 (SL4-203-7769).

Ship Trail

Sufficient information about camera orientation is not available to permit accurate gridding and location of the plume shown in figure 14-21; however, during debriefing of the crewmen, the plume was identified as a ship trail, a plume of condensed water vapor originating from the exhaust of an ocean-going vessel, located off the coast of southern California on January 14, 1974, at 16:55 GMT. Such anomalous cloud lines were first reported by Conover (refs. 14-10 and 14-11) and more recently by Parmenter (ref. 14-12).

According to Conover, the critical atmospheric conditions that permit the formation of ship trails are (1) the existence of a convectively unstable layer that extends from the surface to a low-level stable layer, (2) saturation or slight supersaturation near the top of the convective layer, and (3) a deficiency of cloud nuclei in the convective layer. From the increased whiteness of clouds along the axis of the plume, one could speculate that nuclei and water vapor in the smoke plume probably enhanced the condensation process and yielded denser-appearing stratocumulus clouds.

African Brush Fires

Numerous brush fires in Africa in the vicinity of Chad and Nigeria are shown in figure 14-22. This photograph, taken on December 29, 1973, at approximately 12:38 GMT, dramatically shows the spatial coverage of manmade smoke from large-scale slash burning in Africa.

Extensive smoke was also observed in this area on January 20 and 24, 1974, and on January 26, when the crewmen reported a "spectacular night scene" with a "huge patch of fires." The area covered by these fires was "a long elliptical area of many, many fires . . . probably 200 to 300 miles [320 to 480 km] long and 50 to 60 miles [80 to 95 km] wide." This observation yields an area coverage of approximately 36 300 km².

Argentine Forest Fires

During the period from December 16, 1973, to January 6, 1974, the worst woodland fires in Argentine history occurred in the sparsely populated area of the central



FIGURE 14-21.—Ship trail photographed off the coast of Southern California on January 14, 1974 (SL4-140-4126).

La Pampa territory. The fires were reported to have consumed 5000 km² of densely forested land. Some of the trees destroyed by the fires were 300 to 400 years old. Also, thousands of cattle were reportedly destroyed on ranches in the area. Weather conditions during the burning were reported to have been very hot; a temperature of 316 K (100° F) was specified in one report. Wind directions were reported as variable with windspeeds estimated at 4 to 9 m/sec. Some thunderstorms were reported in the vicinity of the fires.

The La Pampa territory on December 28, 1973, is shown in figure 14-23. A rather large smoke plume and the accompanying pall are visible across the center of the photograph. Observations by the crewmen on December 20 indicated the spatial coverage by the smoke pall was extensive, "covering an area at least 100 miles in diameter [approximately 20 400 km²] with the smoke visible out to sea 400 to 500 miles [740 to 925 km]." The crewmen also described the smoke to be billowing straight up with a "nimbus buildup" developing with the rising smoke cloud.

Early in the mission, on November 28, 1973, the crewmen observed and photographed many fires burning in northern Argentina west of Asunción, Paraguay (fig. 14-24). The smoke originated as a plume and dispersed into a small cloud or pall of pollution.



FIGURE 14-22.—African brush fires in progress on December 29, 1973 (SL4-138-3768).

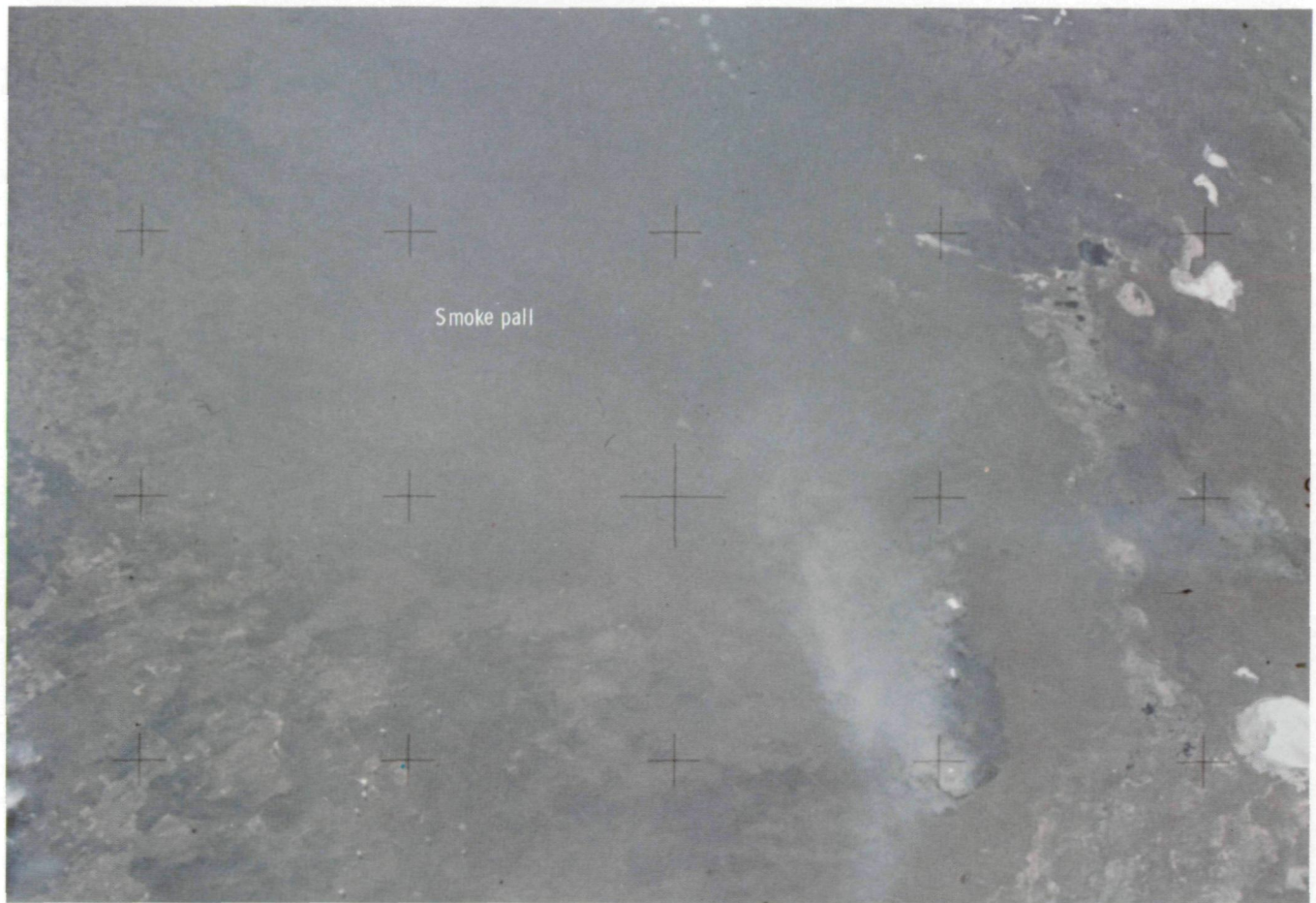


FIGURE 14-23.—Grass fires on the pampas of Argentina (SL4-138-3753).

FIGURE 14-24.—Photograph taken with a 55-mm lens on the Nikon camera of smoke plumes originating from grass fires in northern Argentina on November 28, 1973 (SL4-197-7442).



Atmospheric Phenomena

Cirrus plume.—Parmenter recently reported on the orographic generation of cloudiness downwind of mountain barriers (ref. 14-12). In some of the National Oceanic and Atmospheric Administration NOAA-2 satellite imagery, she recognized some incidents of

large-scale, high cloudiness appearing to generate over mountain ranges and be transported downstream in the midtropospheric flow. In fact, some of the mountain-generated high cloudiness appears to form into long plumes of considerable length (200 to 300 km). Such cloud systems should affect downwind weather by reducing surface heating by depleting the incident solar

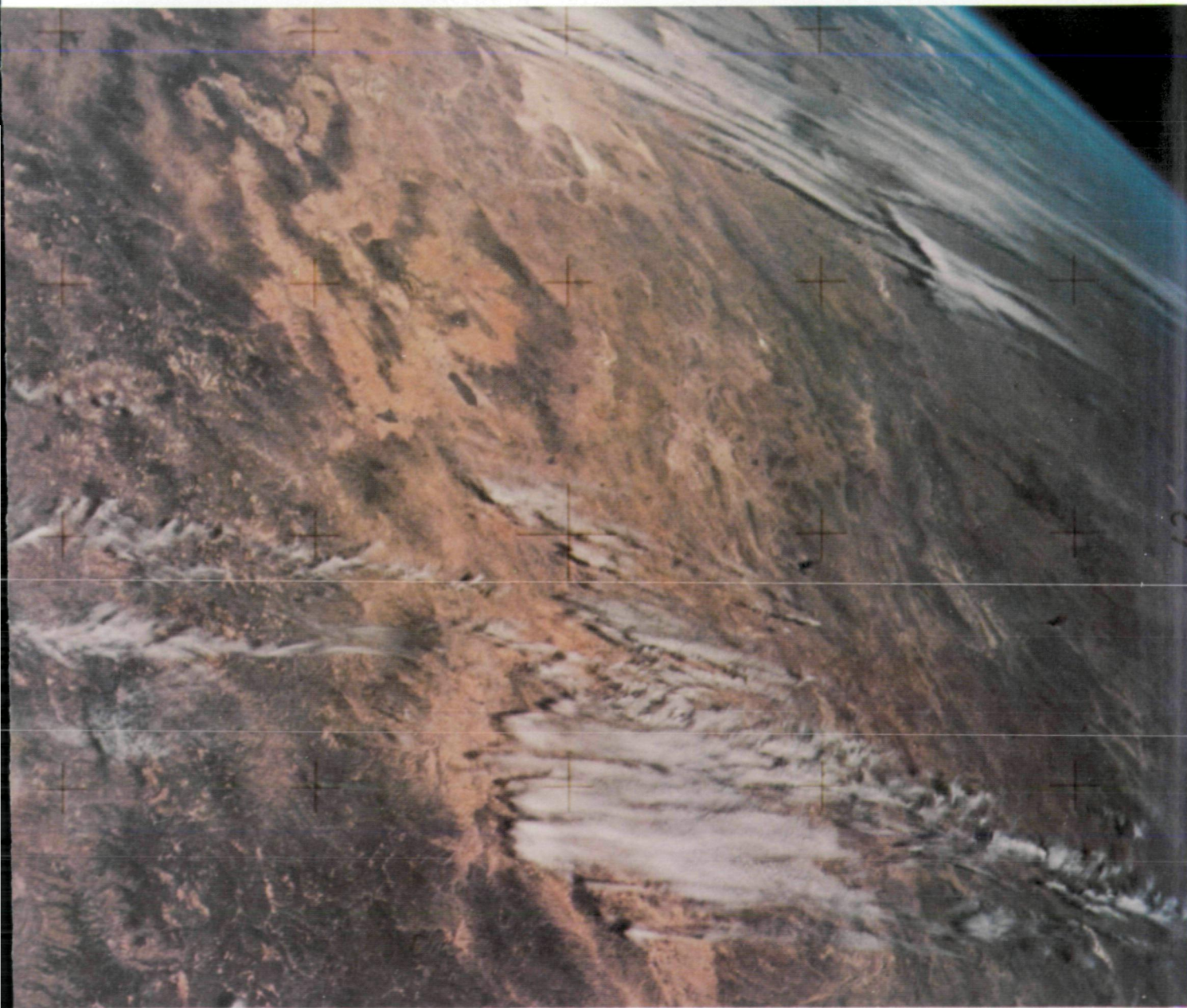


FIGURE 14-25.—Cirrus cloud plumes over Mexico on January 30, 1974, at approximately 18:30 GMT (SL4-143-4606).

radiation, by decreasing the amount of nocturnal cooling, or, possibly, by increasing local precipitation generated by the seeding of underlying supercooled clouds.

An example of cirrus plumes² is presented in the photograph of the northern half of Mexico in figure 14-25, which was taken on January 30, 1974, at 18:30 GMT. Precise gridding of the imagery was not attempted because of the oblique angle at which the photograph was taken and because of the absence of recognizable landmarks. Land areas beneath the plumes should be receiving less insolation than the cloud-free areas. It is possible that the pictured cloud plumes are the anvil tops of thunderstorms; however, considering the season, the dryness of the low-level air mass, and

corresponding imagery from NOAA satellites, the theory that the clouds are cirrus plumes is more plausible.

Knowledge of the impending formation of such mesoscale cloud systems would permit local weather forecasters to make appropriate amendments to their forecasts. However, before the skill can be obtained to forecast the formation of cirrus plumes, meteorologists must discover the atmospheric conditions that create such cloud systems and provide reasons why the clouds expand to cover such large areas. One possible explanation of this phenomenon might be found in the behavior of the flow over wide mountain barriers. With the appropriate wind direction, wide mountain barriers could generate a wide cloud mass or mountain wave with a large amplitude and a long wavelength. Such mountain waves tend to be hydrostatic; consequently, the more typical trapped waves are not observed, and an elongation of the cloud might occur at high altitudes.

² Another possible example of cirrus cloud plumes is visible in figure 18-2 of section 18.



FIGURE 14-26.—Snow streak in the Iowa-Missouri area on January 23, 1974 (SL4-142-4467).

Snow streak.—An interesting streak of snow is shown across the center of the photograph in figure 14-26. This photograph was taken by the crewmen shortly after sunrise on January 23, 1974. Only approximate gridding of the image was possible because of the oblique angle at which the photograph was taken and because of some lens distortion. However, because some prominent geographical features were present, such as the Missouri River, the Platte River, and the Des Moines River, the gridded schematic representation shown in figure 14-27 was derived. Figure 14-27 indicates that the pictured snow streak is approximately 200 km long and extends from immediately north of Falls City, Nebraska, to the vicinity of Chariton, Iowa, where it merges with the large-scale snow cover. The crewmen reported that this “snow streamer” appeared

to originate directly north-northeast of the Tuttle Creek Reservoir, Kansas, approximately 100 km southwest of Falls City, Nebraska. Consequently, this snow streak would be approximately 300 km long. Although the streak is quite apparent in figure 14-26, no surface stations with snow-depth measurements lie within the pictured streak; thus, no surface data were available to provide information on the depth of the snow along the path of the streak. Snow depths from available sites are given in figure 14-27.

The amount of liquid water deposited on the ground may be estimated by assuming (1) that the total snow streak was 300 km long, averaged approximately 10 km in width, and had a snow depth of 2.5 cm (1 in.), and (2) that 25 cm (10 in.) of snow is equivalent to approximately 2.5 cm (1 in.) of liquid water. Using these

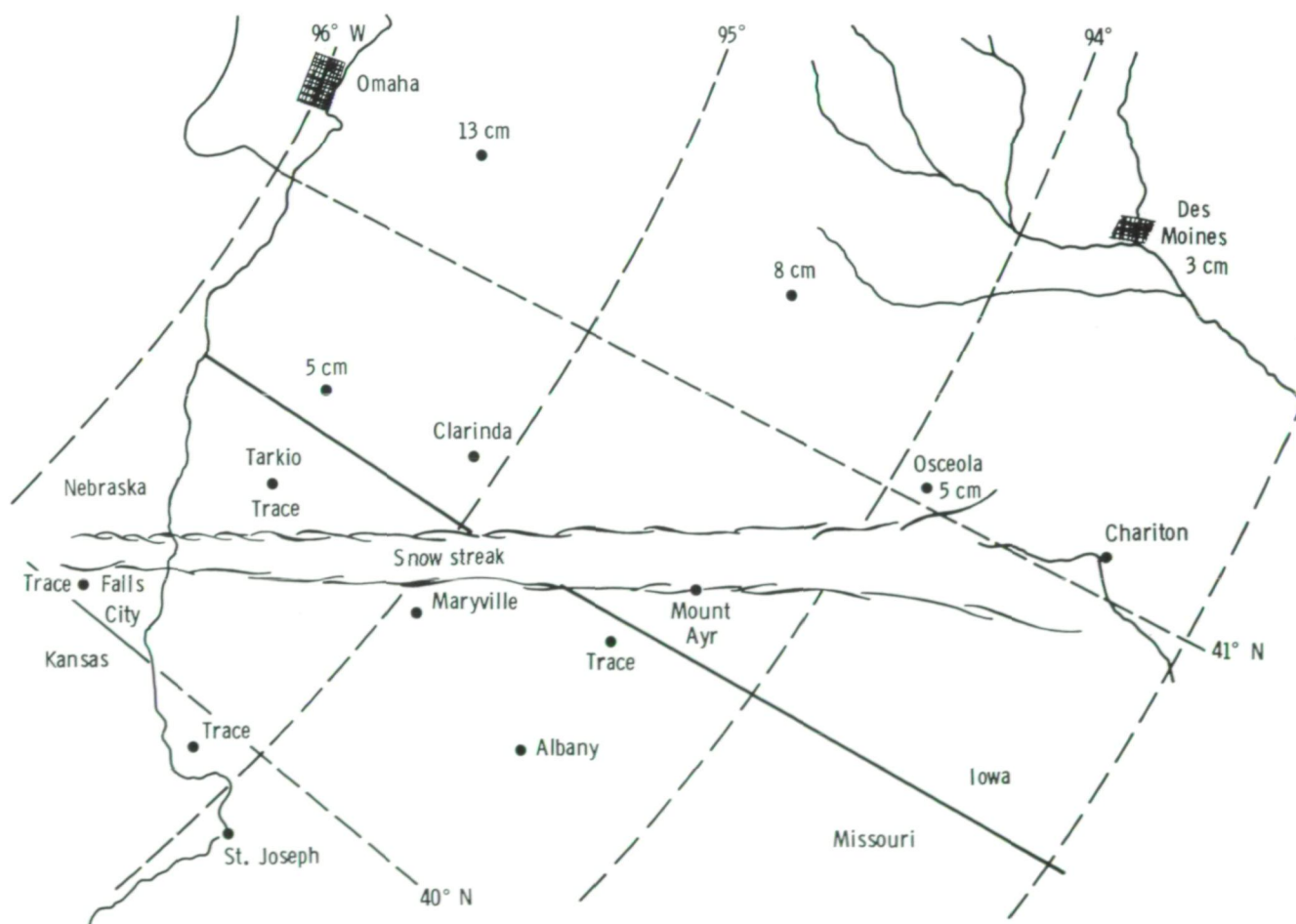


FIGURE 14-27.—Grid for the area shown in figure 14-26. Snow depths are plotted in centimeters from available data for January 23, 1974.

values, 7.6×10^6 m³ of liquid water are calculated to be available to the ground within the snow-streak boundary. The release of this much frozen precipitation would require the release of approximately 4.2×10^{25} J (1×10^{25} cal) of heat to the atmosphere, or the approximate amount of thermal energy generated by the mesoscale storm that produced the pictured snow streak.

CONCLUDING REMARKS

Successful collection of atmospheric pollution imagery during the Visual Observations Project can be traced directly to the special training of the Skylab 4 crewmen in the basic data needs of various scientific disciplines. Direct communication with the crewmen after the mission was particularly useful. The personal accounts given by the Skylab 4 crewmen were especially instrumental in determining the geographic location of the imagery, in obtaining a firsthand assessment of the possible dynamic and kinematic processes involved in smoke-plume formation, and in developing an observations program for future missions. In addition, results of the project confirm that the abilities of humans to reason and to describe provide distinct advantages in making observations. Crew observations (e.g., table 14-I) were very helpful in the search for unusual and new pollution phenomena.

Quantitative analysis of some of the imagery of atmospheric pollution events provided the following useful information.

1. Estimates were obtained of the spatial coverage of both natural and manmade smoke palls and of a wind-generated duststorm. One visible volcanic smoke pall was estimated to cover approximately 20 000 km²;

strong winds blowing over sandy desert soils and generating dust palls covering areas of 100 000 km² were documented. By contrast, a visible manmade smoke pall over the Los Angeles region covered an area of approximately 10 000 km². Such imagery provides a quantitative basis for comparing the scope of regional-scale atmospheric pollution in both its natural and manmade manifestations.

2. Analysis of visible volcanic smoke plumes has provided estimates of the thermal energy level attained by a volcano. Analysis of stereophotographic images and debriefing comments by the crewmen indicate that, in this example, the amount of thermal energy generated (10^2 MW) was apparently too small to permit volcanic effluents to penetrate into the stratosphere. Strong low-level and midtropospheric temperature inversions appeared to dissipate the buoyant momentum of the thermal convective current generated during the observed eruptions.

3. One photograph of some jet contrails revealed that the longest contrail was 70 km in length and approximately 1 km in width. A shadow cast by the contrail was evident on the ground.

4. Further documentation of the occurrence of ship trails was provided by direct observation and concurrent photography by the crewmen.

5. Documentation was provided of the extensive smoke pall generated by large grass fires in the Argentine pampa and by the slash burning of dry grass in Africa. These smoke palls were estimated to cover areas of the order of 20 000 to 40 000 km².

6. Analysis of two long smoke plumes originating on the Louisiana coast provided useful information about smoke plume behavior over long distances (130 to 150 km). In particular, the dimensions of the visible plumes yield a horizontal eddy diffusivity of approximately 10^6

cm²/sec, a value consistent with that obtained independently by dimensional reasoning. Furthermore, the length of the visible plumes also tends to confirm the existence of an energy gap in the atmosphere for wave phenomena with frequencies of 10⁻¹ to 1 hr⁻¹. If stereophotography had been provided, more quantitative information could have been obtained, especially regarding the vertical structure of the plume and the vertical eddy diffusivity.

7. Analysis of some miscellaneous photographs revealed the occurrence of topographically induced cirrus cloud plumes that generated locally cloudy sky conditions in an area that probably would have been forecast to have clear skies. Also, analysis of a snow plume allowed the author to estimate that 4.2×10^{25} J (1×10^{25} cal) of thermal energy were released by the storm system responsible for generating the pictured snow pattern.

ACKNOWLEDGMENTS

Sincere thanks are extended to Dr. H. L. Crutcher and his staff at NOAA/Environmental Data Service National Climatic Center for offering the vital data needed for much of the quantitative information used in this report, and to Dr. Lester Machta, Director of the Air Resources Laboratory, for his approval of the author's participation in this project. The encouragement by the author's colleagues at the Air Resources Laboratory, Las Vegas, Nevada, is gratefully acknowledged.

REFERENCES

- 14-1. Randerson, Darryl: A Study of Air Pollution Sources as Viewed by Earth Satellites. *J. Air Poll. Control Assoc.*, vol. 18, no. 4, Apr. 1968, pp. 249-253.
- 14-2. Randerson, Darryl; Garcia, Joe G.; and Whitehead, Victor S.: Photogrammetric and Photometric Investigation of a Smoke Plume Viewed From Space. *J. Appl. Meteorol.*, vol. 10, no. 6, Dec. 1971, pp. 1122-1131.
- 14-3. Parmenter, Frances C.: Ship Trails or Anomalous Cloud Lines. *Mon. Wea. Rev.*, vol. 100, no. 8, Aug. 1972, pp. 646-647.
- 14-4. Lyons, Walter A.; and Pease, Steven R.: Detection of Particulate Air Pollution Plumes From Major Point Sources Using ERTS-1 Imagery. *American Meteorol. Soc. Bull.*, vol. 54, no. 11, Nov. 1973, pp. 1163-1170.
- 14-5. Briggs, G. A.: Plume Rise — A Critical Survey. Environmental Science Services Administration, AEC Critical Review Series, TID-25075, Springfield, Va., 1969.
- 14-6. Thorarinsson, Sigurdur; and Vonnegut, Bernard: Whirlwinds Produced by the Eruption of Surtsey Volcano. *American Meteorol. Soc. Bull.*, vol. 45, no. 8, Aug. 1964, pp. 440-444.
- 14-7. Earth Photographs From Gemini VI Through XII. NASA SP-171, 1968, pp. 232-238.
- 14-8. Gifford, Frank, Jr.: Smoke Plumes as Quantitative Air Pollution Indices. *Inter. J. Air Poll.* vol. 2, no. 1, 1959, pp. 42-50.
- 14-9. Appleman, Herbert S.: Derivation of Jet Air-Craft Contrail — Formation Curves. U.S. Air Weather Service Technical Report, June 1957, pp. 105-145.
- 14-10. Conover, John H.: Anomalous Cloud Lines. *J. of the Atmos. Sci.*, vol. 23, no. 6, Nov. 1966, pp. 778-785.
- 14-11. Conover, John H.: New Observations of Anomalous Cloud Lines. *J. of the Atmos. Sci.*, vol. 26, no. 5, Part II, Sept. 1969, pp. 1153-1154.
- 14-12. Parmenter, Frances C.: Observing and Forecasting Local Effects From Satellite Data. Proceedings of the Fifth Conference on Weather Forecasting and Analysis, American Meteorol. Soc., 1974, pp. 46-49.

Meteorological Applications of Skylab Handheld-Camera Photographs

W. C. SKILLMAN^a AND WILLIAM E. SHENK^a

ON THE SKYLAB 4 mission, handheld-camera photographs were taken of numerous meteorological phenomena. These photographs, together with the crew descriptions and other data, provide a good source of information for the study of small- and large-scale meteorological circulations. The many stereographic image pairs that were taken provide further quantitative information on the vertical dimension. Specific examples of the value of the photographs for some of the meteorological phenomena are discussed in this section.

EXTRATROPICAL CYCLONE

The high resolution and image contrast of the Skylab 4 color photographs provide an opportunity to see details of the cloud structure associated with extratropical storms that normally cannot be seen in routinely available meteorological satellite images. A well-organized cloud pattern associated with an extratropical

occluded cyclone located near 40° S, 125° W is shown in figure 15-1. Figure 15-1 is oriented so that northeast is at the top of the photograph with the cyclone moving from west to east, or from the lower left to the upper right. The occluded part of the storm covers most of the lower two-thirds of the photograph, and a cold front extends across the top one-third. This cyclone exhibits a spiral configuration that is typical of an occluded storm. The low Sun angle and oblique photographic angle enhance the details of the cloud structure within the main frontal band. There is considerable evidence of convective activity in the band and also near the end of the spiral close to the storm center. Most of the convective activity in the band is near the rear edge of the occluded part of the storm and the cold front. The convection near the center is probably produced by a cold pool of air in the middle troposphere and a sea-surface temperature sufficiently warm to cause a relatively steep lapse rate. Given the same midtropospheric temperatures, the likelihood of this convection would be less if the cyclone were farther south over much colder water. The cloud pattern indicates a new open wave collocated with the intense convection on the front at the upper left portion of the photograph. The same cloud feature is found at approximately 30° S, 127° W in a National Oceanic and Atmospheric Administration satellite (NOAA-2) image (fig. 15-2).

^aNASA Goddard Space Flight Center.

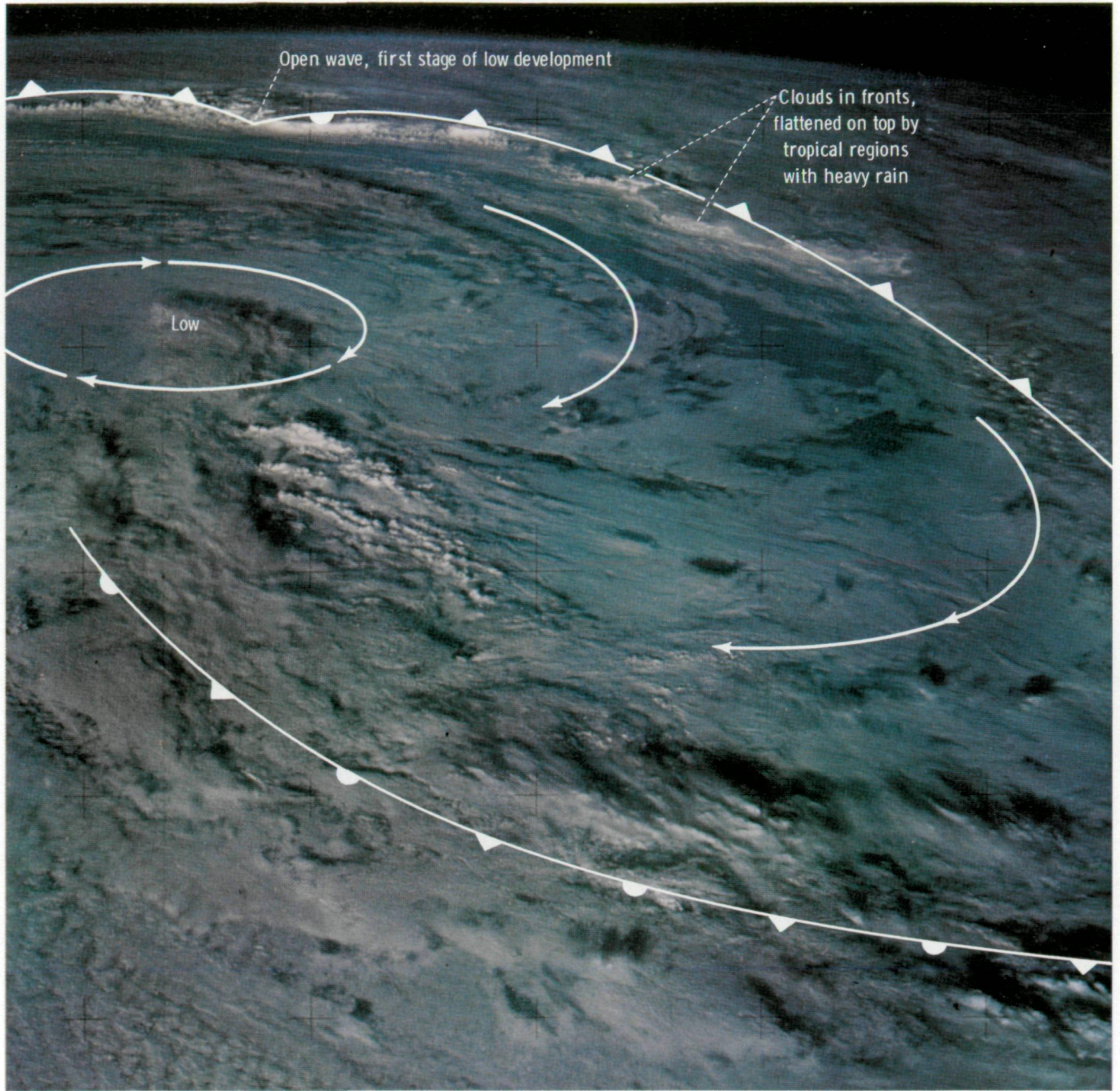
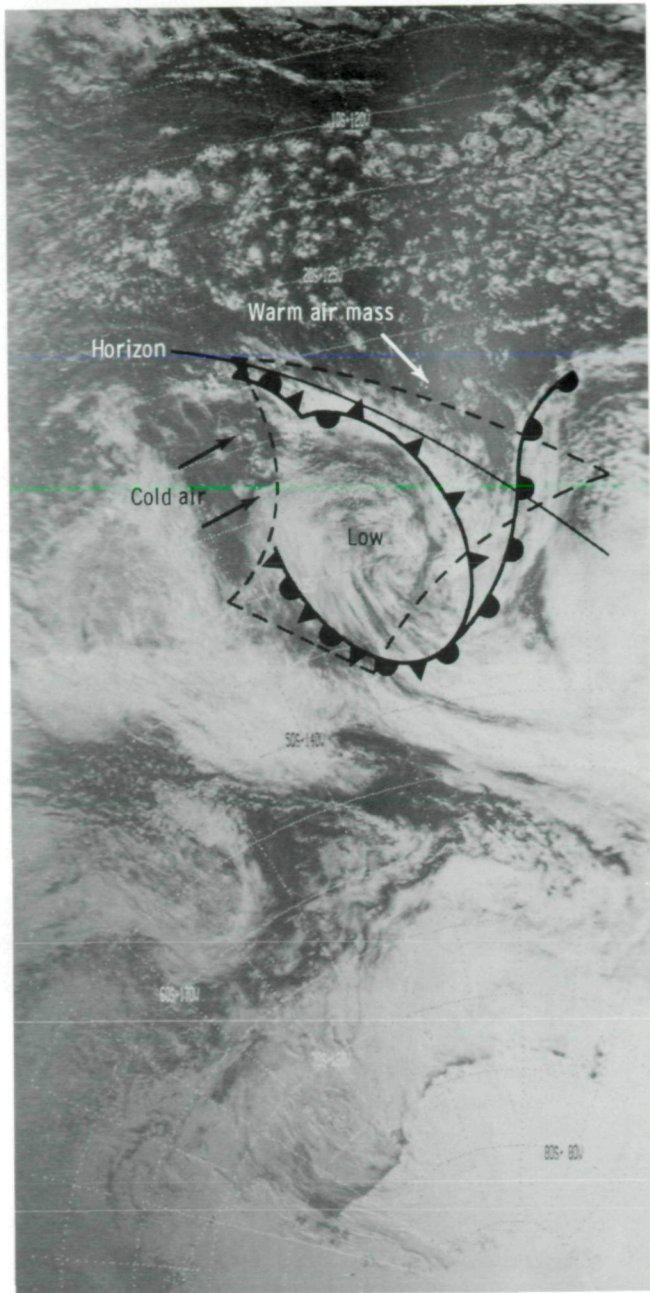


FIGURE 15-1.—Extratropical occluded cyclone near 40° S, 125° W, December 12, 1973 (SL4-137-3565).



JET STREAM CIRRUS

A stereopair taken over southern Arizona and northwestern Mexico east of the Gulf of California on January 21, 1974, is shown in figure 15-3. This stereopair is a good example of cirrus clouds associated with a subtropical jet stream. The surface weather chart (fig. 15-4) for that date shows that a cold front immediately south of the photograph area extended northeastward to a low-pressure area in the Texas Panhandle. The winds aloft are backing from northwest at lower levels to west-southwest at higher levels in the area photographed. A jet stream with west-southwest winds overlies southern Arizona.

When the stereopair in figure 15-3 is viewed through a stereoscope, it is evident that the cirrus clouds are located at many different levels. Thus, errors in estimating the cloud-top height would be made for individual cloud elements if the cirrus cloud tops were assumed to be at uniform height. The problem of height difference shows the value of using stereoscopic techniques for measuring cloud-top heights. Difficulties may also be encountered in trying to use any radiometric technique that depends on temperature or cloud emissivity if these variables cannot be determined. Valuable information concerning the upper troposphere wind profile could be gathered if the cloud motion for each cloud could be obtained from a series of geosynchronous satellite images and if cloud-top heights could be accurately determined by stereoscopic techniques.

FIGURE 15-2.—Composite of NOAA-2 visible scanning radiometer images of the same extratropical occluded cyclone shown in figure 15-1 taken on December 12, 1973.



FIGURE 15-3.—Stereopair of jet stream cirrus over southern Arizona and northwestern Mexico taken at 21:52 GMT, January 21, 1974 (SL4-141-4390 and -4391).

COLD AIR FLOWING OVER WARMER WATER

The effects of cold air flowing over a warmer water surface are shown in figures 15-5 and 15-6. Both photographs were taken near 18:10 Greenwich mean time (GMT) on January 8, 1974. Figure 15-5 shows the eastern half of Lake Erie, Lake Ontario, and the surrounding land, and figure 15-6 shows eastern New York State, the southern New England States, and the adjacent Atlantic Ocean.

The cold northwest flow forming lines of cumulus clouds a short distance off the northern coast of Lake Erie and extending across the lake into western New York State is shown in figure 15-5. The northwest flow was determined from the nearly concurrent surface and upper-air charts (fig. 15-7). Over the eastern Great Lakes, a west-northwest flow was found with pressures between 50 and 85 kPa. Surface data for January 8 show that snow fell beneath these cloud lines, whereas none fell on the adjacent clear areas. Cloud lines seem to

form over particular areas. For example, the line forming south of Toronto, Canada, possibly may have been initiated by industrial pollutants southwest of the city. The location of these sources favorable for the formation of cloud lines could be valuable for predicting areas of locally heavy snowfall along the windward shores of the Great Lakes.

The effects of the northwestern flow of cold and relatively dry air across New England and New York are shown in figure 15-6. Only a short distance offshore, enough moisture, instability, and convergence are created in the lower troposphere for the formation of cumulus clouds. These clouds become more widespread

FIGURE 15-4.—Weather charts for western United States at different altitudes at 00:00 GMT, January 22, 1974. Weather symbols are explained in appendix B. (a) Surface chart. (b) Constant-pressure chart, 85 kPa. (c) Constant-pressure chart, 50 kPa. (d) Constant-pressure chart, 30 kPa. →

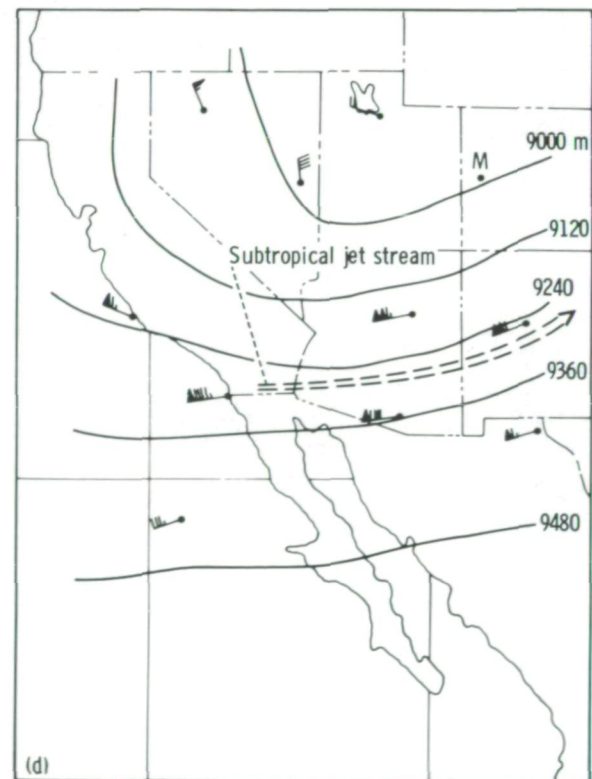
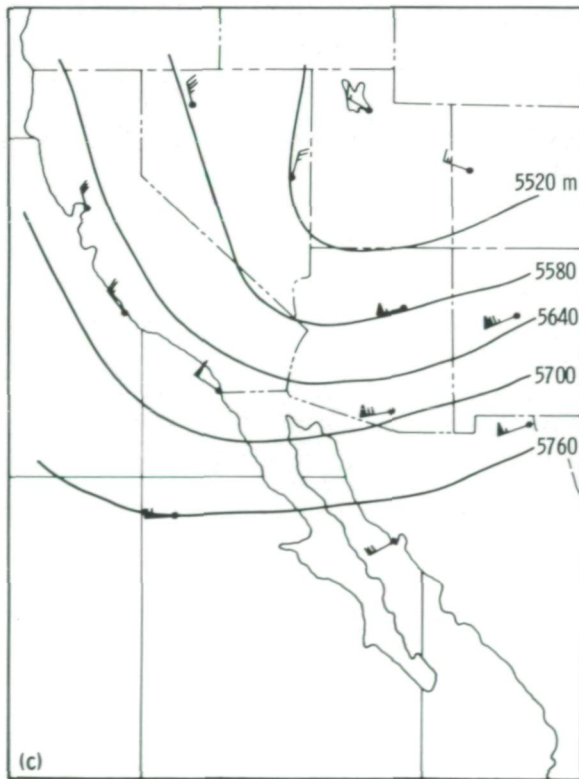
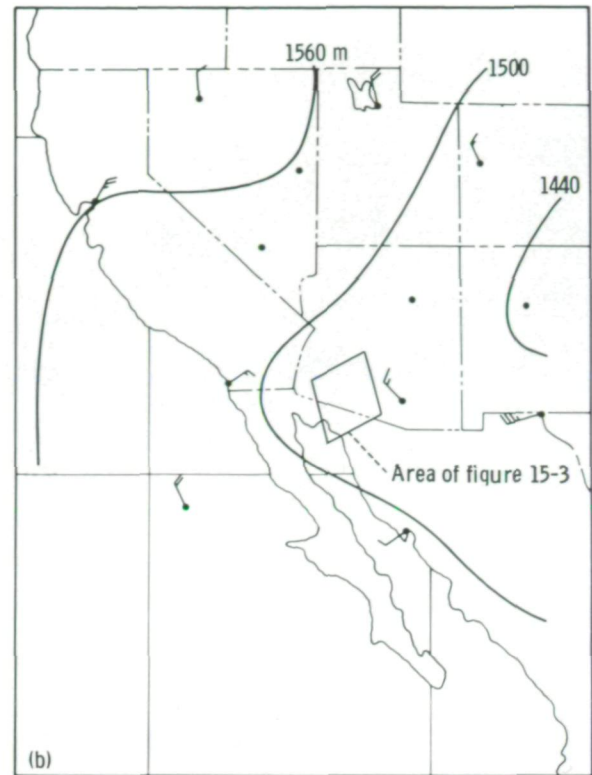
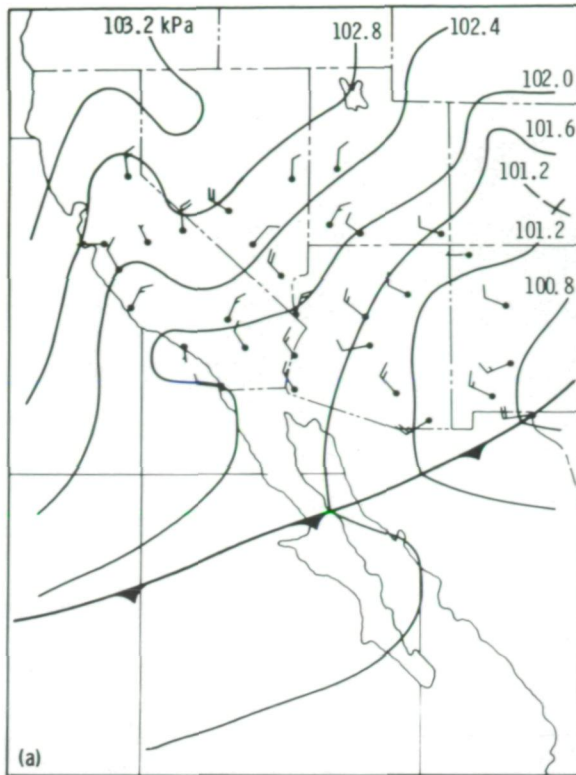




FIGURE 15-5.—Effects of cold air flowing over warmer water off Lake Erie, Lake Ontario, and surrounding land; taken at 18:10 GMT, January 8, 1974 (SL4-139-3989).

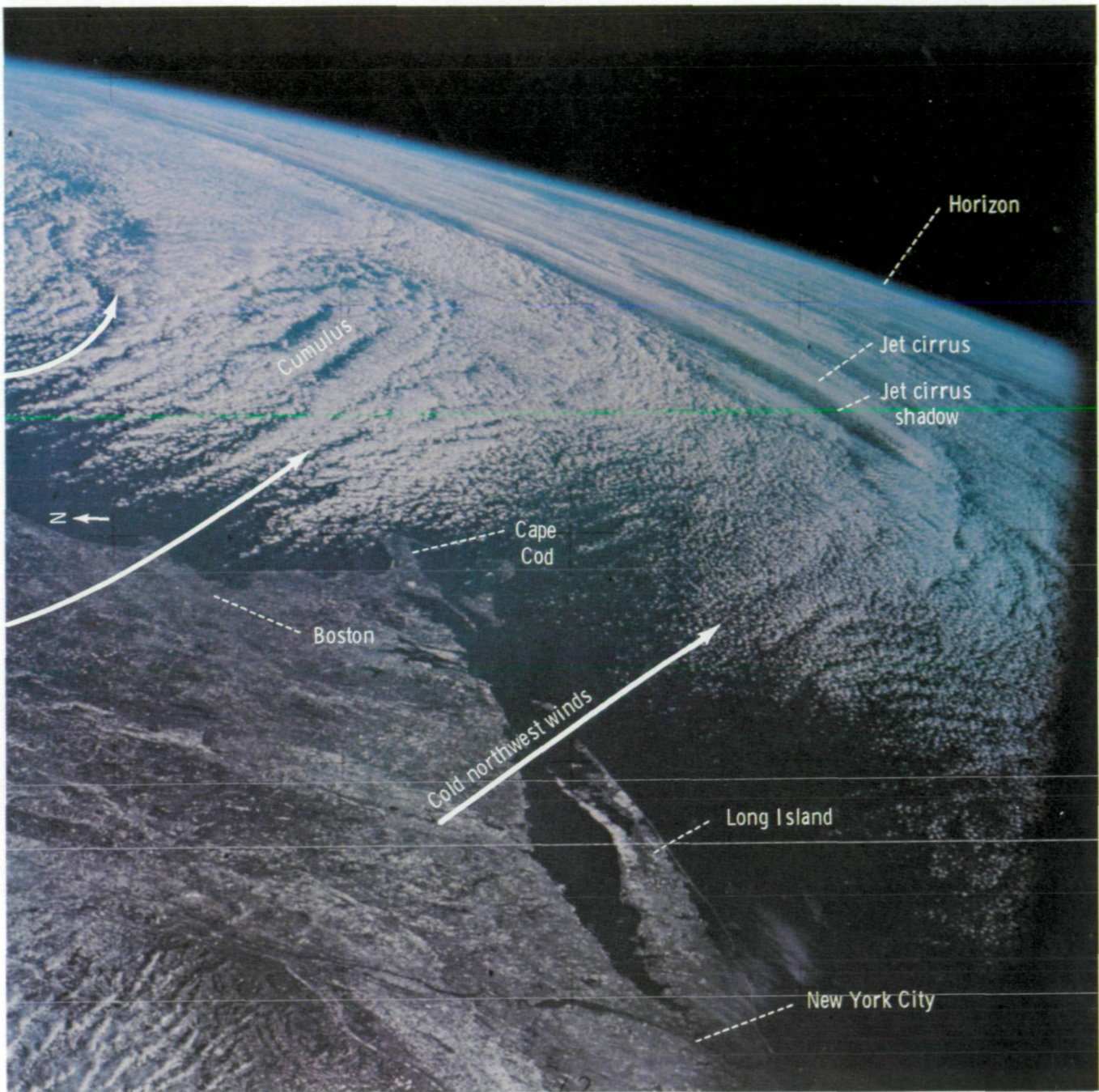


FIGURE 15-6.—Effects of cold air flowing over warmer water off eastern New York State, southern New England, and the Atlantic Ocean; taken at 18:10 GMT, January 8, 1974 (SL4-139-3990).

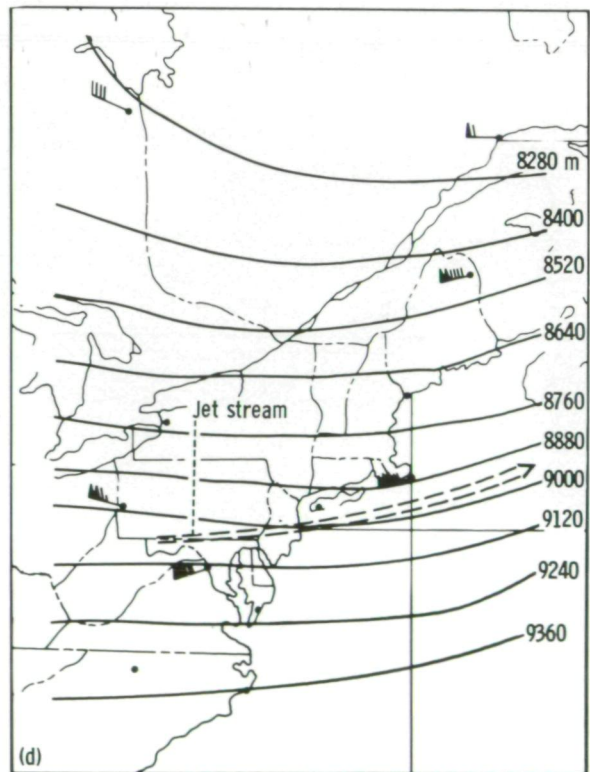
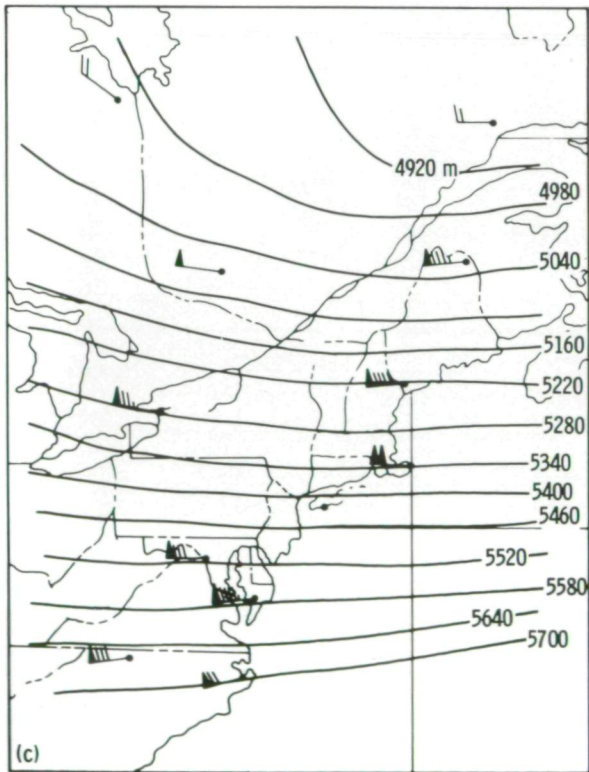
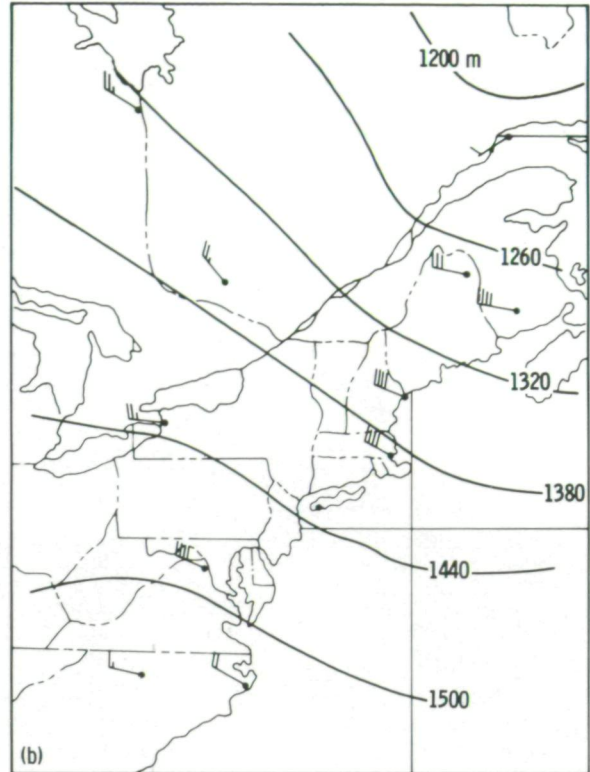
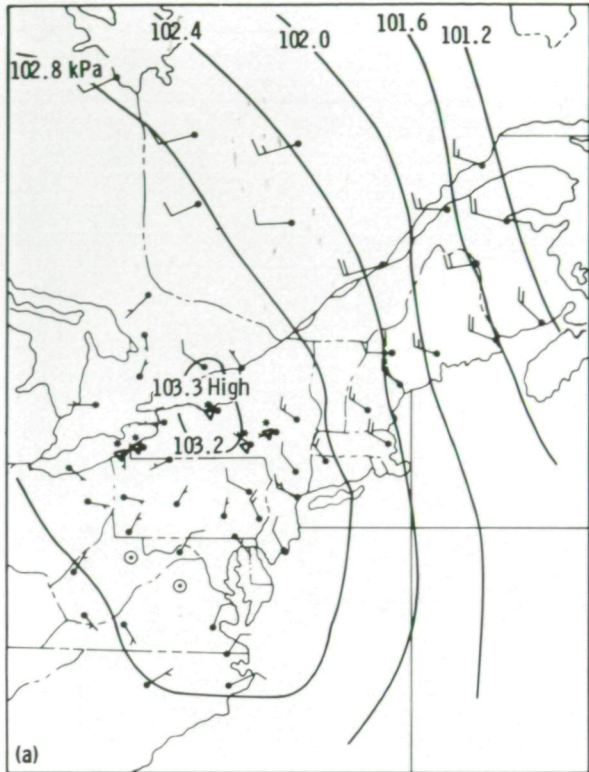


FIGURE 15-7.—Weather charts for eastern United States at different altitudes, January 8, 1974. Weather symbols are explained in appendix B. (a) Surface chart (18:00 GMT). (b) Constant-pressure chart, 85 kPa (12:00 GMT). (c) Constant-pressure chart, 50 kPa (12:00 GMT). (d) Constant-pressure chart, 30 kPa (12:00 GMT).

farther offshore, and the most intense cloudiness appears to be downstream from the clouds that formed nearest the coast. Adjacent to the areas of greatest activity over the ocean, convective overturning within the unstable layer caused sufficient subsidence for the development of clear regions.

Several hundred kilometers southeast of the New England coast in figure 15-6, two long, dark lines representing shadows of higher clouds on the lower cloud formations are clearly visible parallel to and west of the horizon. The shadows are more visible than the clouds. This type of cloudiness is often associated with the jet stream and has been used as a diagnostic tool for locating the position of the jet stream with meteorological satellite data. The upper-air measurements indicate that a jet stream was located approximately in the area of the cloud shadow lines.

The corresponding NOAA-2 image of the same area (fig. 15-8) shows generally similar cloud formations but without the detail recorded in the Skylab photographs.

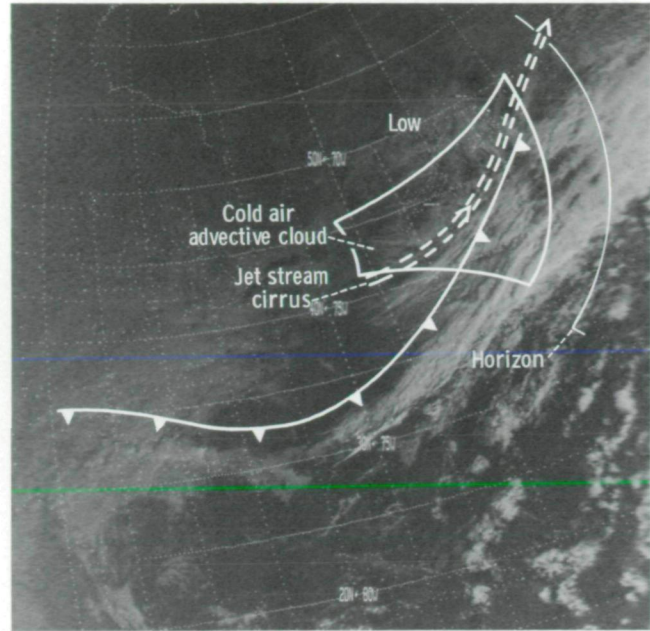


FIGURE 15-8.—Composite of NOAA-2 scanning radiometer images of same area shown in figure 15-6 taken on January 8, 1974.

CONCLUDING REMARKS

Photographs taken from an Earth-orbital satellite are useful in understanding meteorological phenomena. The photographs show the detailed cloud structure of an occluded cyclone and the effects of cold air flowing over warmer water. The stereographic pair demonstrates the height differences of multilayered clouds found in jet stream cirrus that are not discernible in a single meteorological satellite image.

16

Some Aspects of Tropical Storm Structure Revealed by Handheld-Camera Photographs From Space

PETER G. BLACK^a

MANNED SPACE FLIGHT offers a unique opportunity to observe tropical storms. The combination of human judgment and an Earth-orbiting platform enables off-track observations of tropical storms to be made that could not be accomplished by other means. The ability to resolve small-scale features (on the order of hundreds of meters in low-oblique photographs) and to obtain stereopair photographs is unparalleled by other observational techniques.

At the beginning of manned space flight, skills of test pilots were required to develop the complex space-flight technology as evidenced by the successful Gemini and Skylab Programs. Because scientists were part of the Skylab crews, the quantity and quality of scientifically useful photographic data increased. Therefore, it is recommended that, in the Space Shuttle era, professional scientists representing many disciplines participate in the actual data gathering and thereby identify the most significant features for scientific study of tropical storms.

The role of man in space should be recognized realistically as another tool for scientific discovery. Man's primary function therefore should be as a vehicle

of discovery and initial measurement. More precise and detailed measurements would be obtained from unmanned satellites.

Just as the unmanned satellite is a sophisticated scientific tool for gathering data, the human observer in space should be regarded as an equally sophisticated scientific tool. Some circumstances in which manned space observations complemented data from other sources are identified in this report. It should be emphasized that data obtained simultaneously from aircraft and manned and unmanned satellites are complementary and thus greatly enhance the value of each method of observation.

As part of the Skylab Visual Observations Project, handheld-camera photographs of tropical storms obtained during the three manned missions were studied in detail. This study ultimately led to a review of handheld-camera photographs of tropical storms obtained from other manned space flights.

As a result of extensive photographic enhancement and positioning, the following features of tropical storms are apparent.

1. A "hot spot," or persistent convective overshoot region, in the area of a developing tropical storm that generates concentric waves of nearly constant wavelength
2. An outward-tilting eyewall cloud in some quadrants of mature tropical storms

^aNational Oceanic and Atmospheric Administration (NOAA), National Hurricane and Experimental Meteorology Laboratory, Miami, Florida.

3. A variable combination of overshooting convective turrets, internal gravity waves, and transverse shear waves near the inner region of mature tropical storms

Observations relating to these features and their scientific significance are discussed in this report.

PHOTOGRAPHIC ENHANCEMENT TECHNIQUES

The one central fact that has emerged from this study is the presence of many fine-scale (100 to 1000 m) features over the tops of tropical storms. Much of this information has gone unnoticed in the past because manned-space-flight handheld-camera photographs of cloud features generally have been severely overexposed (at least two f-stops) and hence the detail has been obliterated. This detailed information has not been visible from unmanned satellites because, until recently, sensor resolution has not been adequate.¹

An additional problem in identifying features in tropical storm photographs is the lack of natural contrast over the tops of tropical storms. The range of brightness values is nominally only 1 to 5 percent of that found in a standard image. Therefore, the identification of features has been difficult even on underexposed photographs made with color positive film in the past. This problem decreases with decreasing solar elevation angle. Optimum contrast appears to occur at a solar elevation angle of 5° to 15° because cloud height differences and the resulting shadows are accentuated.

For analysis of the Skylab photographs included in this section, an image-enhancement technique developed by T. Fujita and his photographer, B. Ginsburg, of the University of Chicago, was used. For each second-generation black-and-white negative obtained from NASA, a series of five negatives was produced at exposures ranging from two stops below "optimum" to two stops above. For most tropical storms photographed, the negative duplicate underexposed by two f-stops was selected for enhancement and analysis.

In the University of Chicago enhancement process, a trial and error approach was used to produce a third-generation positive and a fourth-generation negative on

¹The U.S. Air Force Defense Meteorological Satellite Program (DMSP) data, which became available to the meteorological community in 1972, and the NASA-NOAA Synchronous Meteorological Satellite (SMS), which became available in the summer of 1974, are capable of resolving scales as small as 0.6 and 1 km, respectively.

high-contrast film (Kodak no. 4154). The slope of the gamma curve (and hence the brightness range) for this film can be regulated by controlling the water temperature during the developing process. In maximizing the slope of the gamma curve, the gray-scale stretch was also maximized. This procedure resulted in a much more critical exposure time necessary to enhance the gray-scale range of interest, namely the very bright end. This method was used successfully to obtain detail that is not visible in the third-generation color transparencies and is greatly subdued in the second-generation black-and-white negatives.

A second method of image enhancement, and one recommended in future work, was explored with Richard J. Blackwell, NASA Jet Propulsion Laboratory (JPL), Pasadena, California. In this technique, similar to those used by JPL for enhancement of lunar and Martian photographs, a flying-spot scanner is used to digitize the photograph into as many as 1024 lines with 1024 samples/line. Each sample represents a brightness intensity, or gray scale, ranging from 0 (white) to 255 (black).

The image is first filtered to eliminate shading and then it is stretched to enhance the contrast. A two-dimensional Fourier transform of the image is then computed in which shapes are represented as a series of trigonometric sine and cosine functions. In this process, the image is represented in terms of the amplitude of a series of frequencies. Unwanted frequencies are identified and filtered out.

In the JPL technique, therefore, any periodicity evident in the photograph is used for the purpose of enhancement together with the concept of gray-scale stretching. Use of digital computers and optical scanning devices can improve upon standard photographic-enhancement techniques by making use of frequency as well as brightness information; by this means, the technique is made more objective and precise.

INTENSE CONVECTION IN DEVELOPING TROPICAL STORMS

Hurricane Ellen: A Case Study

Skylab handheld-camera photographs have documented cloud features in several developing tropical storms. Perhaps the most interesting observations were those obtained by the Skylab 3 crew of developing tropical storm Ellen on September 19, 1973. These data are

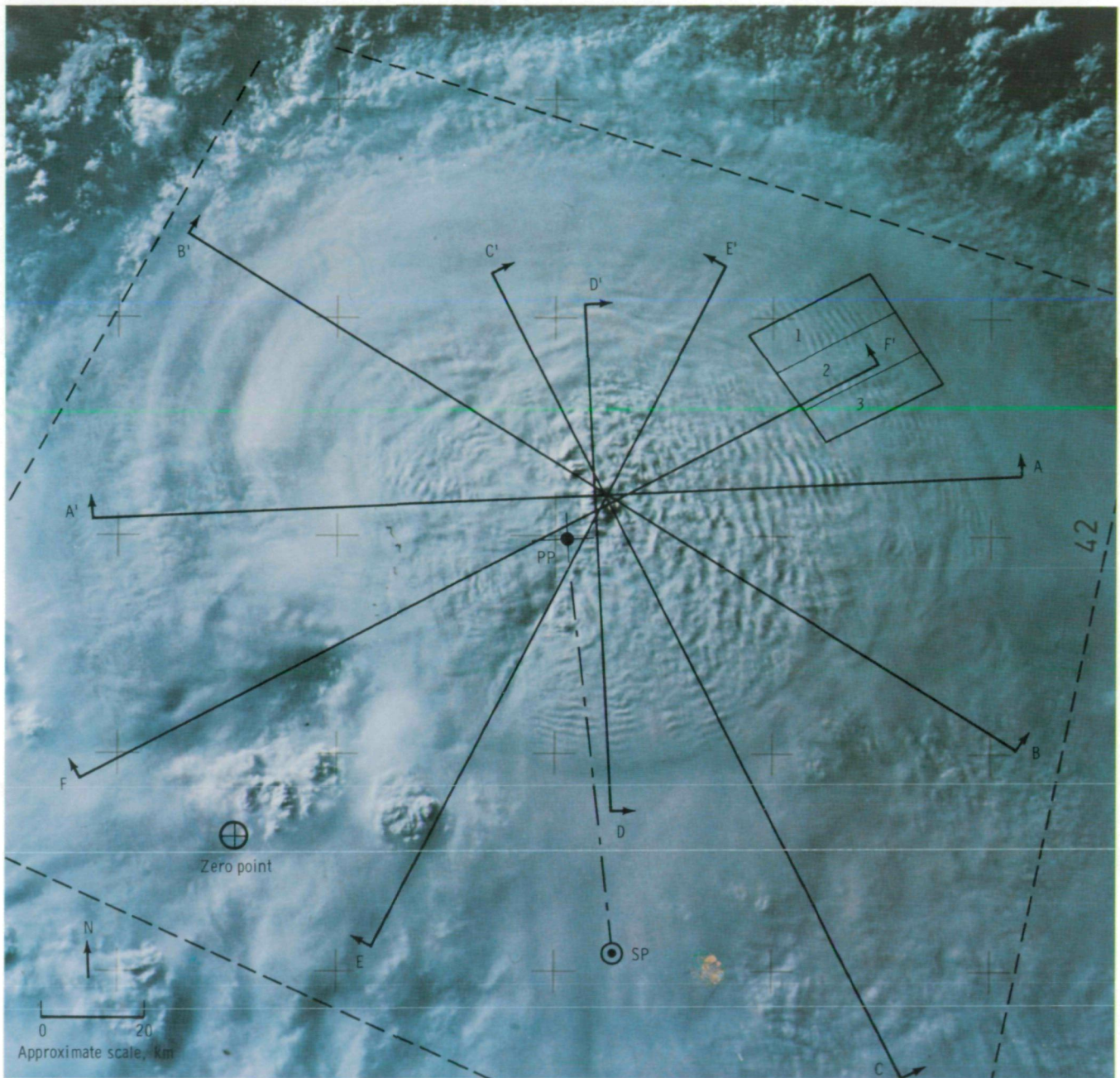


FIGURE 16-1.—Skylab stereophotograph of tropical storm Ellen taken on September 19, 1973, at 20:18:30 Greenwich mean time (GMT). The maximum windspeed was 30 m/sec, and the minimum surface pressure was 98.5 kPa (985 mbar). The storm was located at latitude 27.3° N, longitude 51.1° W. An approximate subsatellite point (SP), the principal point (PP), an elevation reference point (zero point), and the location of cross sections discussed in the section entitled "hurricane Ellen Case: Stereographic Analysis" are shown. The locations of the sectors used for a Fourier transform analysis are shown in the upper right corner. The approximate boundaries of figure 16-2 are indicated by the dashed lines (SL3-122-2572).

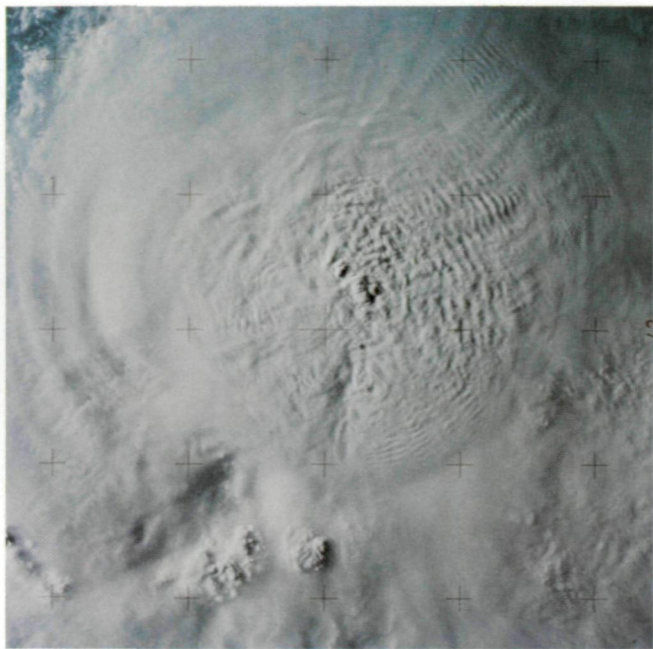


FIGURE 16-2.—Skylab stereophotograph of tropical storm Ellen taken on September 19, 1973, at 20:18:25 GMT (SL3-122-2571).

especially significant because it was the only storm over which usable stereophotographs were obtained to enable determination of cloud heights.

Two stereophotographs of tropical storm Ellen that reveal for the first time the symmetric and wavelike nature of a very large and intense convective event near the center of the storm are shown in figures 16-1 and 16-2. Figure 16-3 is a more oblique photograph taken 15 seconds after figure 16-2 that shows the cloud feature in more perspective with respect to the surroundings. The Skylab flightpath relative to the storm clouds is shown on an NOAA-2 satellite image of the storm (fig. 16-4). The Skylab groundtrack has been shifted so that its location relative to the storm center is indicated. At the time of the Skylab overflight, the storm was approximately 220 km to the west-northwest of its indicated position. As can be seen from the solar elevation angles, the Sun was low in the western sky. The low solar elevation angle was responsible for the high contrast in the Skylab photographs.

The prominent features of the cloud pattern shown in the Skylab photographs are (1) a circular symmetry about a central overshooting region that has three overshooting convective towers and (2) a system of waves with semicircular wave fronts concentric with the

central overshooting region and most prominent on the eastern side of the circular cloud region. These cloud features are produced by strong convection. Convection occurs when certain parcels of air become warmer than their environment; the parcels then become buoyant and accelerate freely. In the hurricane environment, air parcels are sometimes forced upward by low-level convergence and become buoyant only after penetrating a low-level stable layer. The vertical thermodynamic structure of the environment, the initial thermodynamic properties of the parcel, and the magnitude of the forcing event determine the intensity of convection. Air parcels rapidly decelerate when they reach the base of the stratosphere (tropopause), where the temperature stratification is strongly stable (i.e., temperature increases with height). An ascending air parcel rapidly becomes colder (more dense) than the environment, loses its buoyancy, and hence diverges horizontally. In the absence of environmental wind, air parcels diverge uniformly in all directions. The cloud feature is similar to a thunderstorm with an anvil cloud spreading out in a region of weak environmental winds near the tropopause; however, the scale of the central overshooting region in tropical storm Ellen is somewhat larger than that of thunderstorms. For tropical storm Ellen,

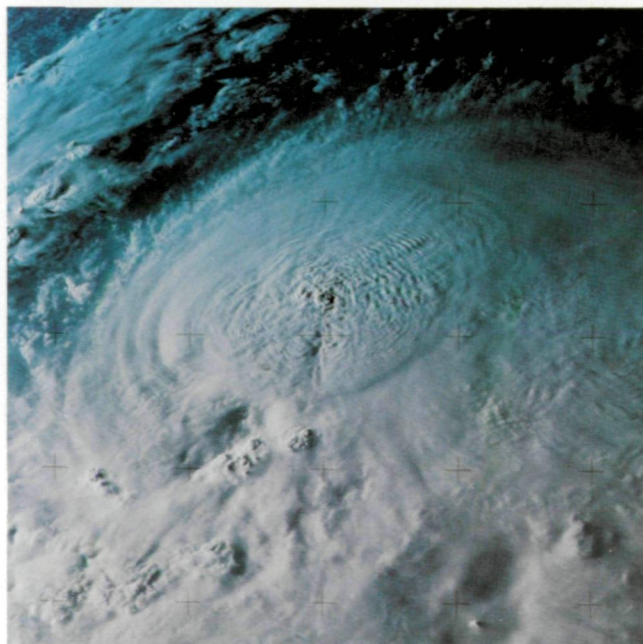


FIGURE 16-3.—Skylab photograph of tropical storm Ellen taken on September 19, 1973, at 20:18:40 GMT (SL3-122-2573).

the circular cloud is nearly 200 km in diameter. This larger scale implies that the convection responsible for the circular cloud must be maintained for a longer time than for thunderstorms.

Figure 16-5 is an enlargement of the eastern semi-circle of the circular cloud feature showing the central overshooting turrets and the concentric waves in greater detail. The upper half of this photograph (northeastern quadrant) was chosen for detailed analysis to determine precise wavelengths and wave orientations. The previously mentioned technique developed by Blackwell (ref. 16-1) was used for this purpose. Based on the results of this analysis, inferences concerning the physical mechanisms responsible for the waves will be made.

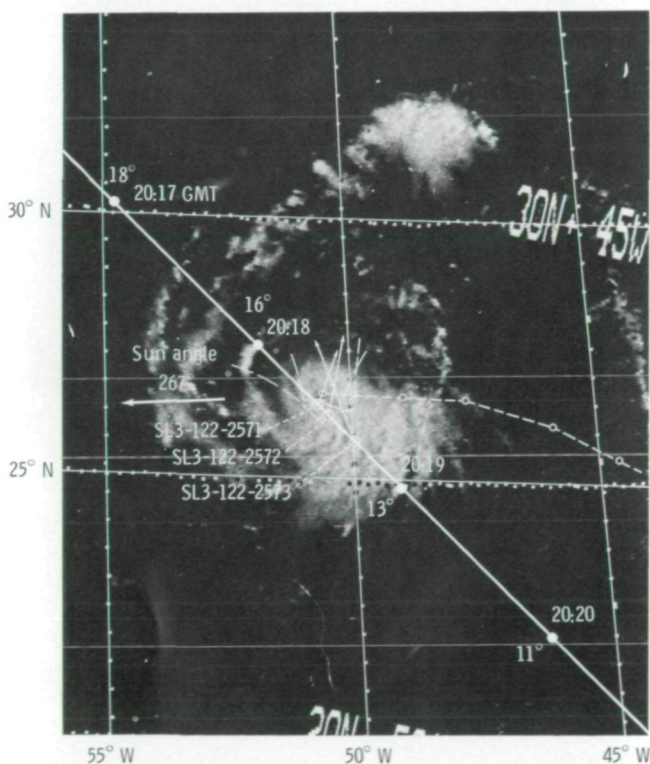


FIGURE 16-4.—An NOAA-2 satellite image of tropical storm Ellen on September 19, 1973, at 11:56:18 GMT. The storm track is indicated by a broken line; the small open circles represent the position of the storm center at 6-hour intervals. Also shown are the Skylab subsatellite points (dots) relative to the storm center at 1-minute intervals with times and solar elevation angles labeled. Approximate Skylab photograph boundaries, principal lines, and subsatellite points (large open circles) are indicated together with Skylab frame numbers. The solar azimuth angle at the time of the Skylab overflight is also indicated (267°).

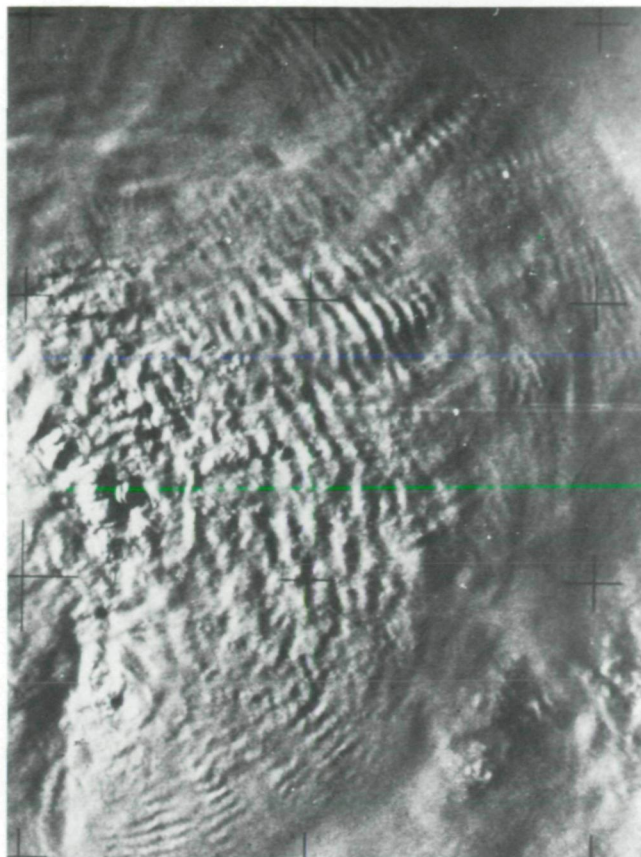


FIGURE 16-5.—Enlargement of a portion of Skylab frame SL3-122-2572 (fig. 16-1) showing the central overshooting turrets and concentric waves of tropical storm Ellen concentrated in the eastern hemisphere and especially the northeastern quadrant.

Results of Digital-Enhancement Process

The northeastern quadrant of the circular cloud feature (fig. 16-2) was scanned by a flying-spot scanner, digitizing the sector into 1024 lines with 1024 samples/line. Resolution was approximately ± 0.05 km. Intensity values ranged from 0 (white) to 255 (black). Figure 16-6(a) is an unprocessed photograph of the region scanned. This and subsequent JPL-enhanced photographs were printed in negative form so that white clouds appear black. The histogram in figure 16-6(a) reveals that brightness values are biased toward the bright end. Furthermore, there is severe shading across the photograph. Figure 16-6(b) shows the effect of removing the bias and the shading with a high-pass filter to obtain a symmetric brightness spectrum. Thus,

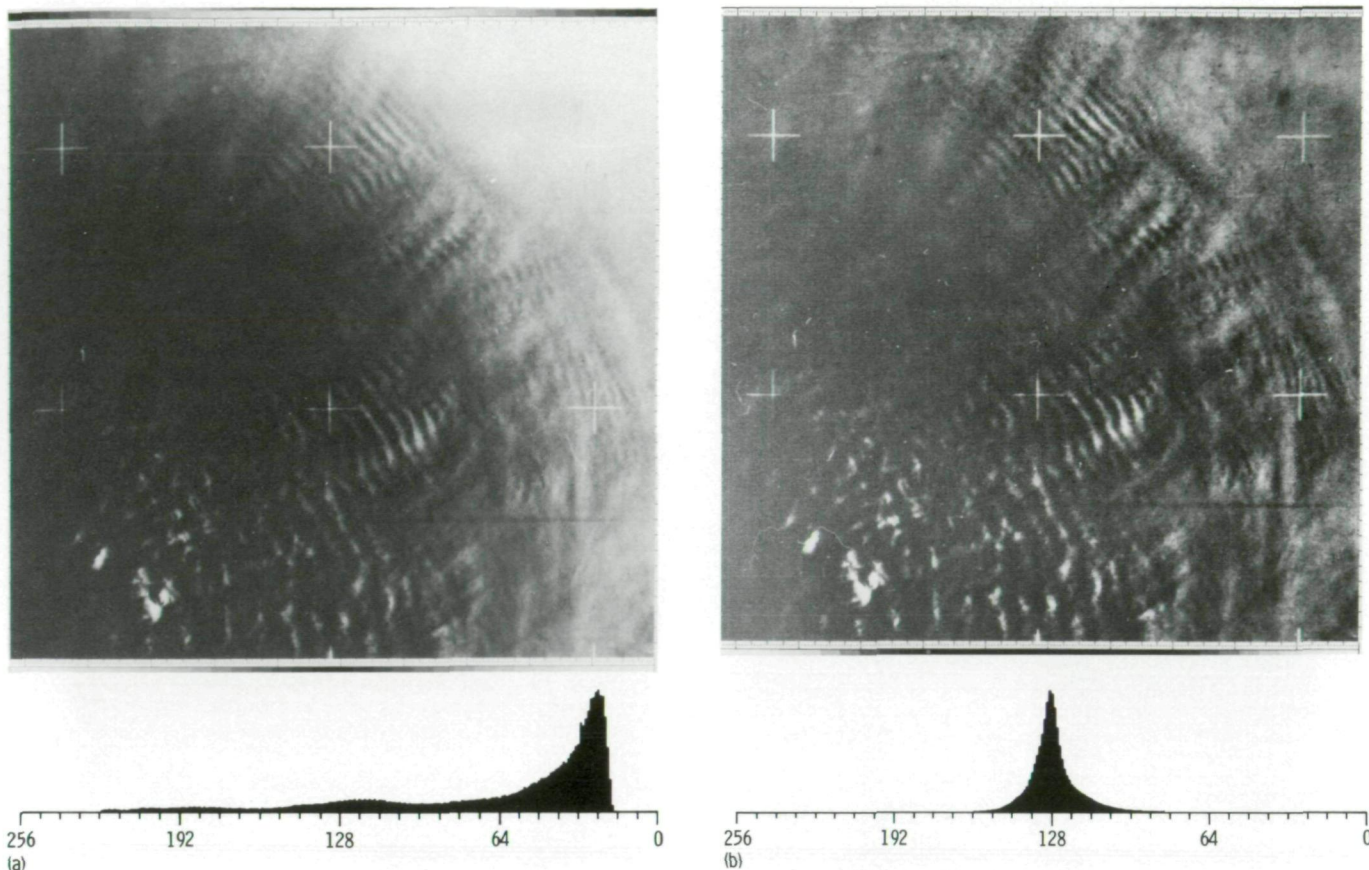


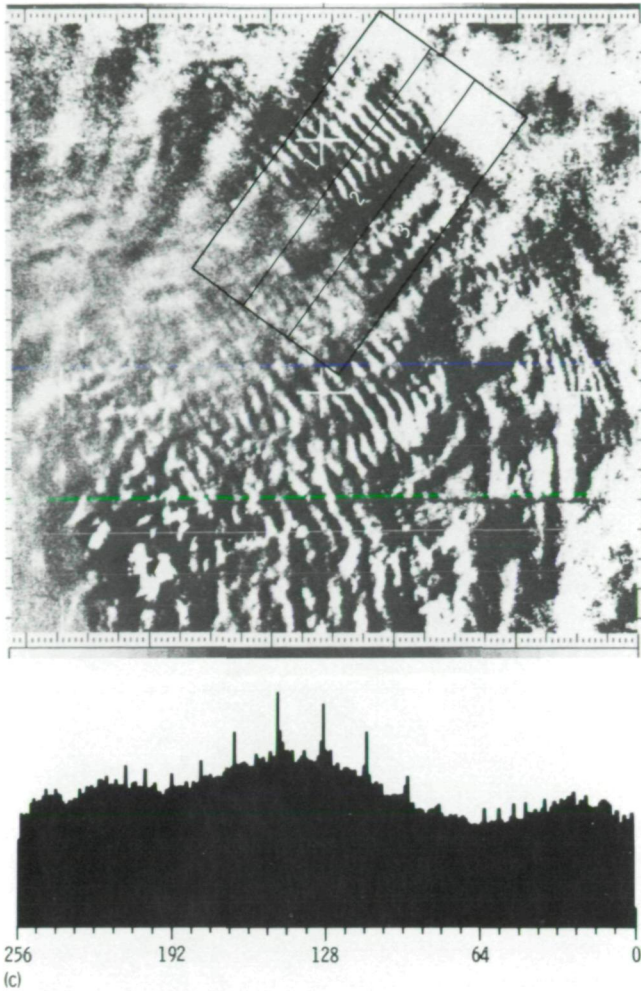
FIGURE 16-6.—Northeastern quadrant of Skylab frame SL3-122-2571 (fig. 16-2) selected for image-enhancement processing. The photograph (printed so that white clouds appear black) and a histogram of gray shades are shown for each step in the JPL process. (a) Before processing; 1024 lines by 1024 samples. Mean is 68.25 and standard deviation σ is 53.14. (b) After removal of bias and shading; 1024 lines by 1024 samples. Mean is 128.02 and σ is 11.16. (c) After gray-scale stretching; 512 lines by 512 samples. Mean is 132.79 and σ is 70.51. The grid denotes an area selected for additional processing. (See fig. 16-9.)

the low-frequency brightness changes are removed and the gray scale extends only over a narrow range of ± 33 gray shades (standard deviation $\sigma = 11.2$) from the mean. These gray shades then were spread over the entire 255-value range to enhance the contrast of the photograph. The results of this process, called gray-scale stretching, are shown in figure 16-6(c) for a digitizing rate reduced by a factor of 2.

Figure 16-7(a) represents a two-dimensional Fourier transform of the gray-scale-stretched photograph shown in figure 16-6(c). The distribution of brightness values in space coordinates has been converted to a distribution of sine wave amplitudes in frequency (wavelength) coordinates. Wavelength (in kilometers) decreases outward from the center as indicated by the overlay. Amplitudes are indicated by the various colors

shown in the color wedge. Note that the left side of the transform is an inverted mirror image of the right side except for a slight distortion introduced by the cathode-ray tube on which the transform was displayed. Figure 16-7(b) is a smoothed version of figure 16-7(a) and illustrates the general features of the transform slightly more clearly because the finer scale details have been smoothed out.

In the interpretation of this transform, the azimuth angle is considered to increase clockwise from 0° at the top to 180° at the bottom. Thus, only the right half of the figure will be discussed. Between azimuths of 0° and 35° , a null exists in the shorter wavelength regime. No waves shorter than approximately 10 km are oriented normal to these azimuths. This fact could be due to either of two reasons. First, the shorter wave fronts



would be nearly parallel to the rays of the Sun over these azimuths, which are located in the northern quadrant of the circular cloud. With the Sun low in the western sky, there would be no shadowing of the waves and hence no contrast between wave crests and troughs. The other explanation is that, in fact, no short-wavelength waves occur in this portion of the cloud. The latter explanation is favored for reasons to be discussed shortly. A peak in the spectrum appears at a wavelength of approximately 2.2 km and extends between azimuths of 35° to 80° . This peak represents the most dominant short waves that appear in figure 16-6(c). The preferred orientation is approximately 45° as indicated by the peak in the spectrum at that azimuth. Note that as the azimuth changes from northeast to east (45° to 90°), the peak in the spectrum shifts gradually to longer wavelengths. This result is significant and will be discussed shortly.

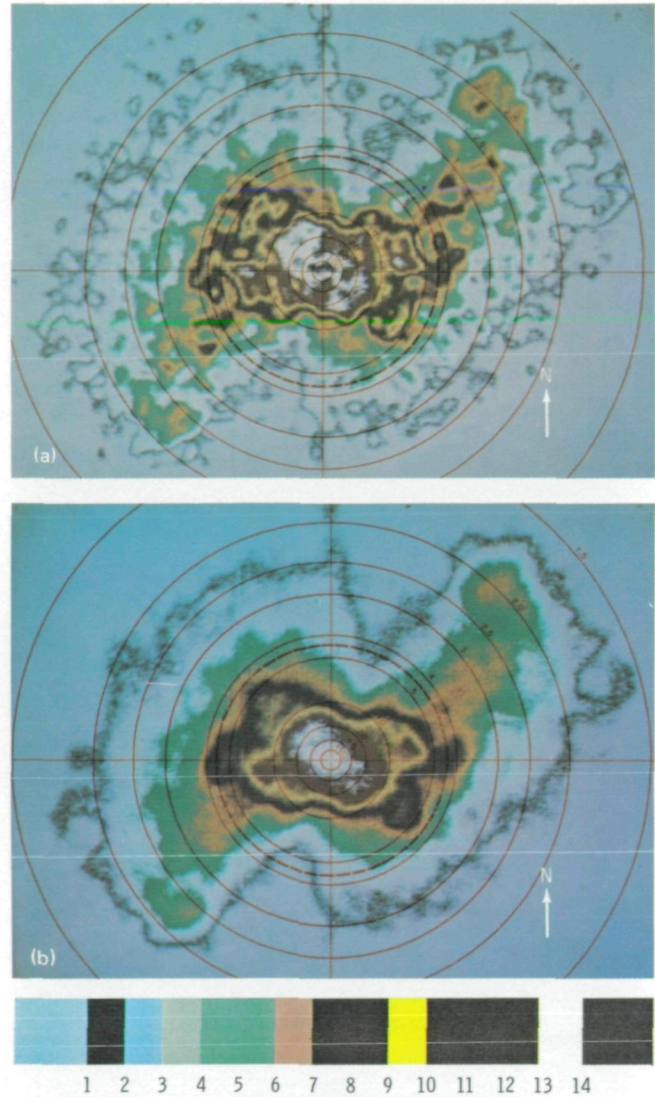


FIGURE 16-7.—Two-dimensional Fourier transform of gray-scale-stretched photograph (fig. 16-6(c)). Wave orientations from 0° (top) to 180° (bottom) are represented in the right half of the figure with azimuth angle increasing in a clockwise sense. The left half of the figure should be an inverted mirror image of the right half with azimuth angle increasing from 0° (bottom) to 180° (top). Because of distortions introduced by the densitometer display unit, exact symmetry is not achieved. The radial coordinate is wavelength, which varies from 100 km near the center to 1.5 km at the outer circle. Relative amplitudes on a scale of 1 to 14 are indicated by the colors shown in the color wedge. The heavy dashed circle indicates the cutoff wavelength (4.5 km) for the high-pass filter used in the analysis. (a) Basic transform. (b) Smoothed version.

The range of azimuths from 60° to 180° generally exhibits spectral peaks at relatively long wavelengths (greater than 4 km). The remaining spectral peaks are located at wavelengths of 4.5 km (extending from 60° to 100°), 7 km (extending from 70° to 135°), 9 km (extending from 70° to 135°), and 18 km (extending from 60° to 170°). Finally, a 50- to 100-km-wavelength wave occurs normal to the 90° azimuth. The 4.5-, 7-, and 9-km-wavelength waves are most dominant in an orientation normal to east and, to a lesser extent, normal to southeast. These waves are not revealed clearly in figure 16-6(c). They must be superimposed on the 2.2-km-wavelength field. The 18-km-wavelength waves are most dominant at azimuths at right angles to the 2.2-km waves. These are the transverse waves, which appear to

radiate outward from the central overshooting dome and to modulate the brightness along the 2.2-km wave fronts. The elongation in the long-wavelength peak near the center in the 090° direction (fig. 16-7(a)) is simply an indication that the brightness contrast across figure 16-6(c) is greater in the east-west direction than in the north-south direction because of the dome shape of the circular cloud and the location of the Sun in the western sky.

The dashed circle at the 4.5-km radius in figure 16-7 represents the outer limit of a high-pass filter that was applied to further isolate the shorter wavelength waves from the longer ones. The result of this filtering is shown in figure 16-8(a), which contains only short-wavelength waves. The low-frequency components that

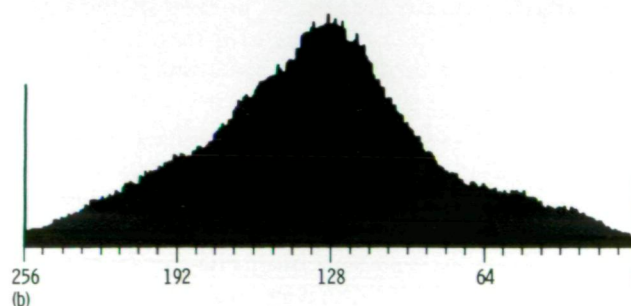
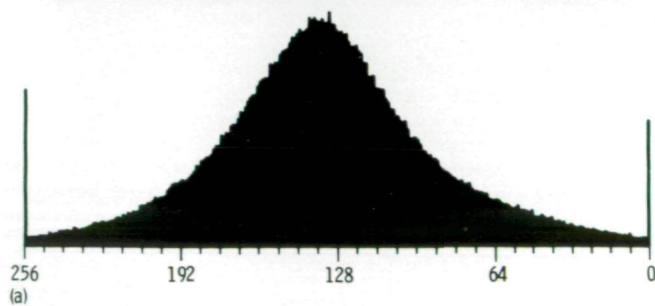
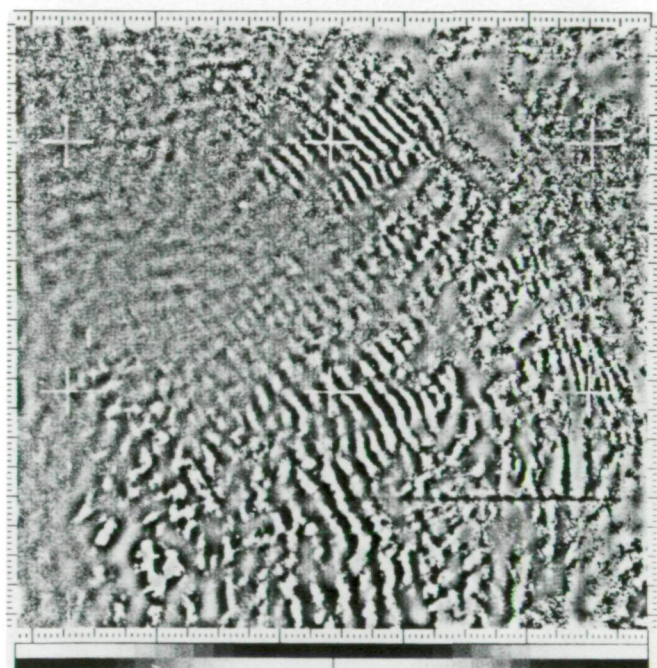


FIGURE 16-8.—Gray-scale-stretched photograph (fig. 16-6(c)) filtered to illustrate enhancement of waves. (a) High-pass filtered using a 4.5-km cutoff wavelength. (b) Low-pass filtered.

were filtered out are shown in figure 16-8(b). Note the appearance of the 4.5-, 7-, and 9-km-wavelength waves, which are oriented nearly parallel to the 2.2-km waves in figure 16-8(a). Note also the distinct appearance of the 18-km-wavelength transverse waves.

As an additional check on the wavelength calculations, a small section of figure 16-6(c) was selected for additional processing, divided into three subsections, and rotated by 49° so that the 2.2-km wave fronts are perpendicular to the scan lines. The subsections are shown in figure 16-9 and also in figures 16-1 and 16-6(c).

Each subsection consists of 50 lines. The brightness values along each group of 50 lines were averaged for each sample. Plots of the average brightness values, after the high-pass filtering described previously, are shown in figures 16-10(a) and 16-10(b) for subsections 1 and 3, respectively. For comparison, relative cloud heights are shown (with respect to the mean cloud surface) along lines within subsections 1 and 3. These values were derived from the stereographic analysis. Note that the wave heights (crest to trough) are on the order of 400 m. With a wavelength of approximately 2 km, this wave height represents a height to length ratio of 1:5. A ratio this small usually is considered to be unstable for gravity wave motion.

Amplitude spectra of the brightness values shown in figures 16-10(a) and 16-10(b) were computed as well as a spectrum of the average of all three subsections; these spectra are shown in figure 16-11. All three spectra show peaks at 2.0 to 2.2 km in agreement with the two-dimensional Fourier transform results. The high-pass filter begins to suppress spectral amplitudes at a wavelength of 3.8 to 4.0 km and completely suppresses wavelengths longer than 4.6 km.

To enable scaling of photographs used in this section, an analysis based on the following information was performed. The Skylab photographs of tropical storm Ellen were made at an altitude of 429.7 km using a Hasselblad camera with a 100-mm focal-length lens. The distance between reseau grid marks on the 70- by 70-mm image plane was 10 mm. Neglecting Earth curvature effects and assuming near-nadir pointing of the camera, the true distance between grid marks is 43.0 km. Independent analysis of the stereophotographs resulted in a calculation of 41.9 km for the grid spacing. A conversion between sample size and distance was accomplished for the JPL analysis by determining that there were 212 samples between reseau grid marks. This value yielded a scale factor of 0.198 km/sample.

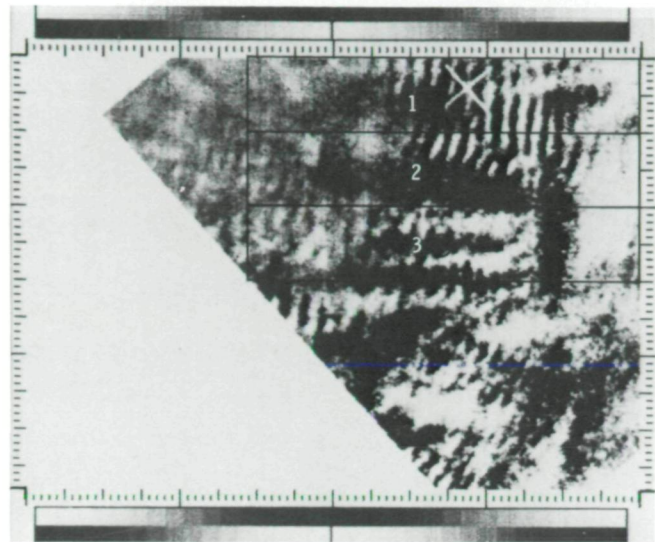
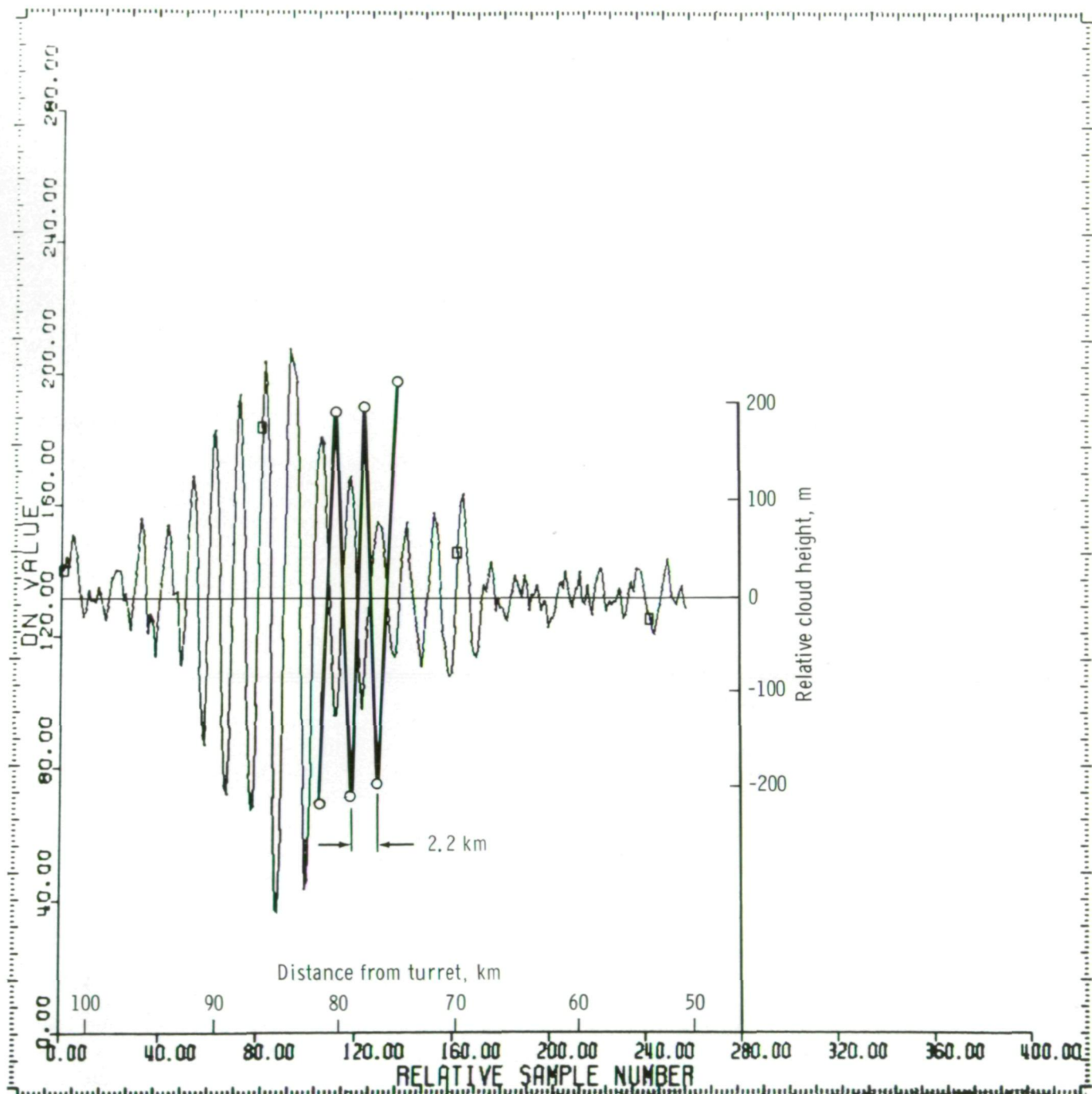


FIGURE 16-9.—Section of gray-scale-stretched photograph (fig. 16-6(c)) rotated for sampling along scan lines perpendicular to 2.2-km wave fronts. Each subsection (1, 2, 3) consists of 50 lines. (See fig. 16-1 for location and original orientation.)

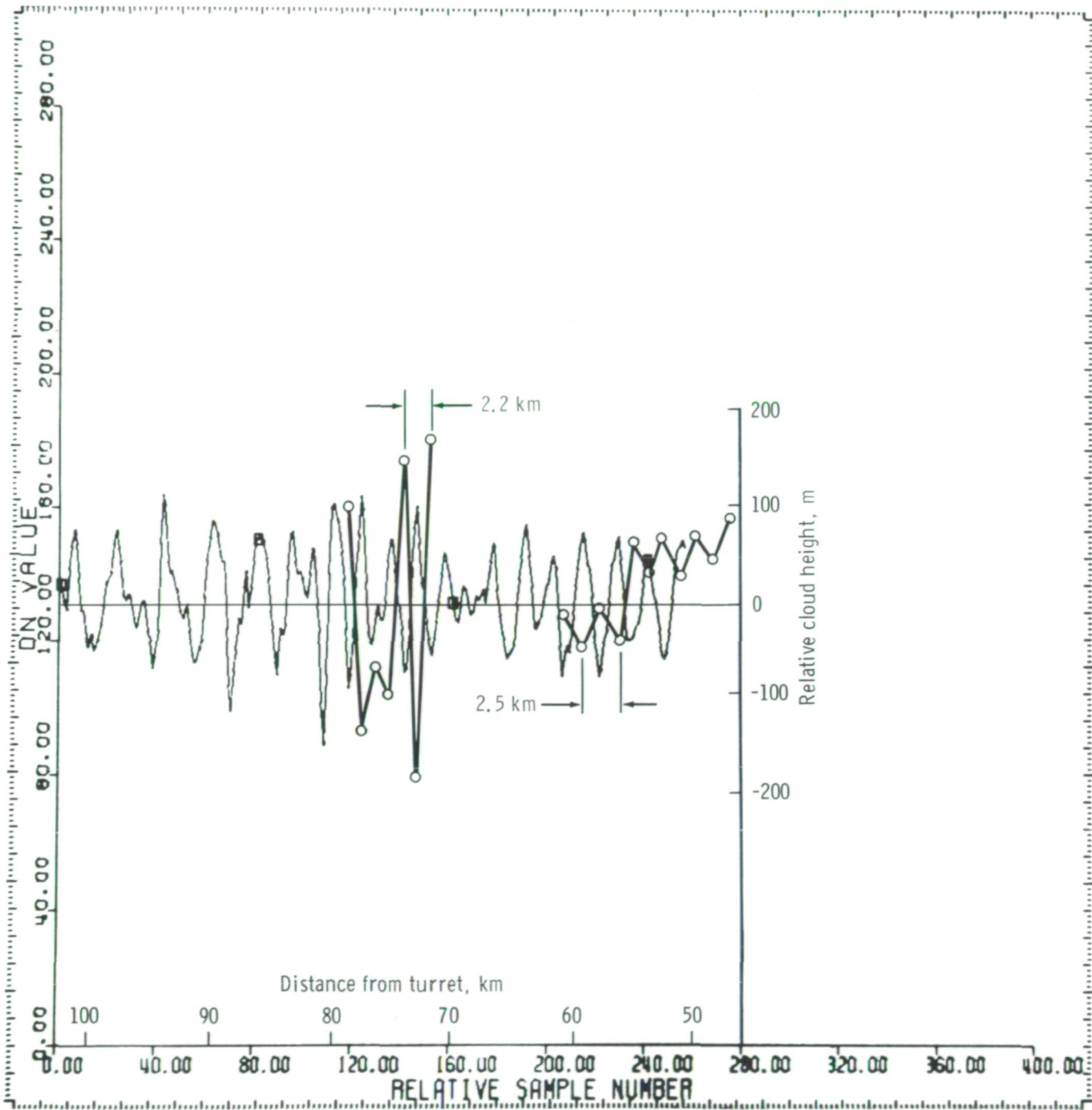
Hurricane Ellen Case: Stereographic Analysis

In addition to the digital enhancement and spectral analysis, a stereographic analysis of figures 16-1 and 16-2 was performed at the Defense Mapping Agency, where relative cloud heights were computed using an AS-11 stereoanalyzer. Because precise photograph times were not known and practically no land or ocean surface was visible over the common field of view, only relative cloud heights were constructed. An elevation reference point (zero point) was established near the periphery of the circular cloud for determining the elevation of control points (fig. 16-1). The lower edge of the circular cloud was assumed to be parallel to the ground. Relative cloud heights were computed along each of six sections labeled A-A' to F-F' (fig. 16-1) and are shown in figure 16-12. Because a correction for nadir angle variations across the photograph was not applied to all sections, the northern portions of the sections, in which the nadir angles are larger than 10° , are shortened. Thus, in figures 16-12(b) to 16-12(f), respectively, B' should extend to approximately 123 km, C' to approximately 65 km, D' to approximately 58 km, E' to approximately 78 km, and F' to 72 km.



(a)

FIGURE 16-10.—Average brightness (DN) values after high-pass filtering for samples contained in rotated section (fig. 16-9). Relative cloud heights and distances from turret are superimposed. (a) Subsection 1. (b) Subsection 3.



(b)

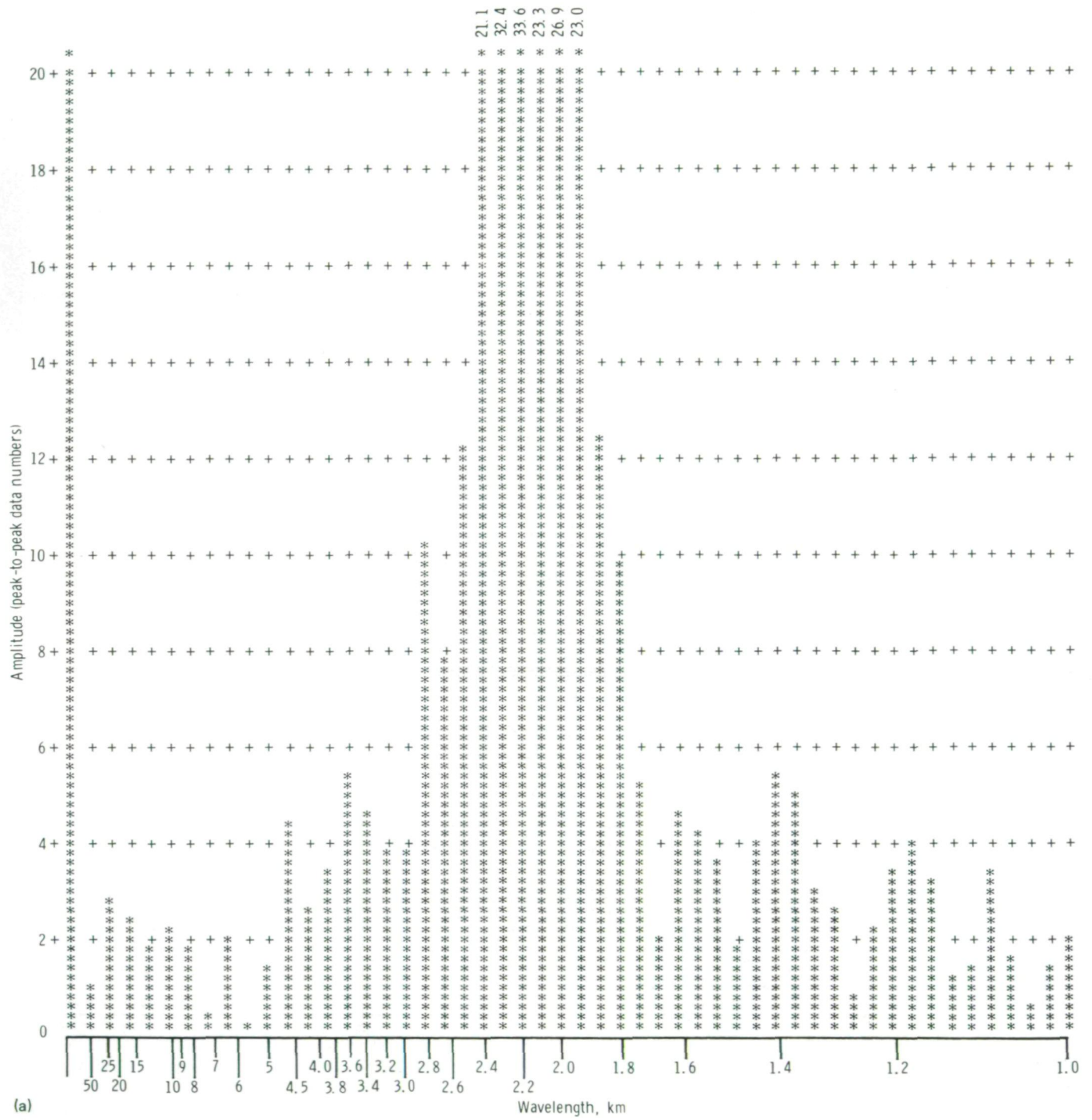


FIGURE 16-11.—Conventional amplitude spectra of average brightness plots. (a) Subsection 1. (b) Subsection 3. (c) Average of subsections 1, 2, and 3.

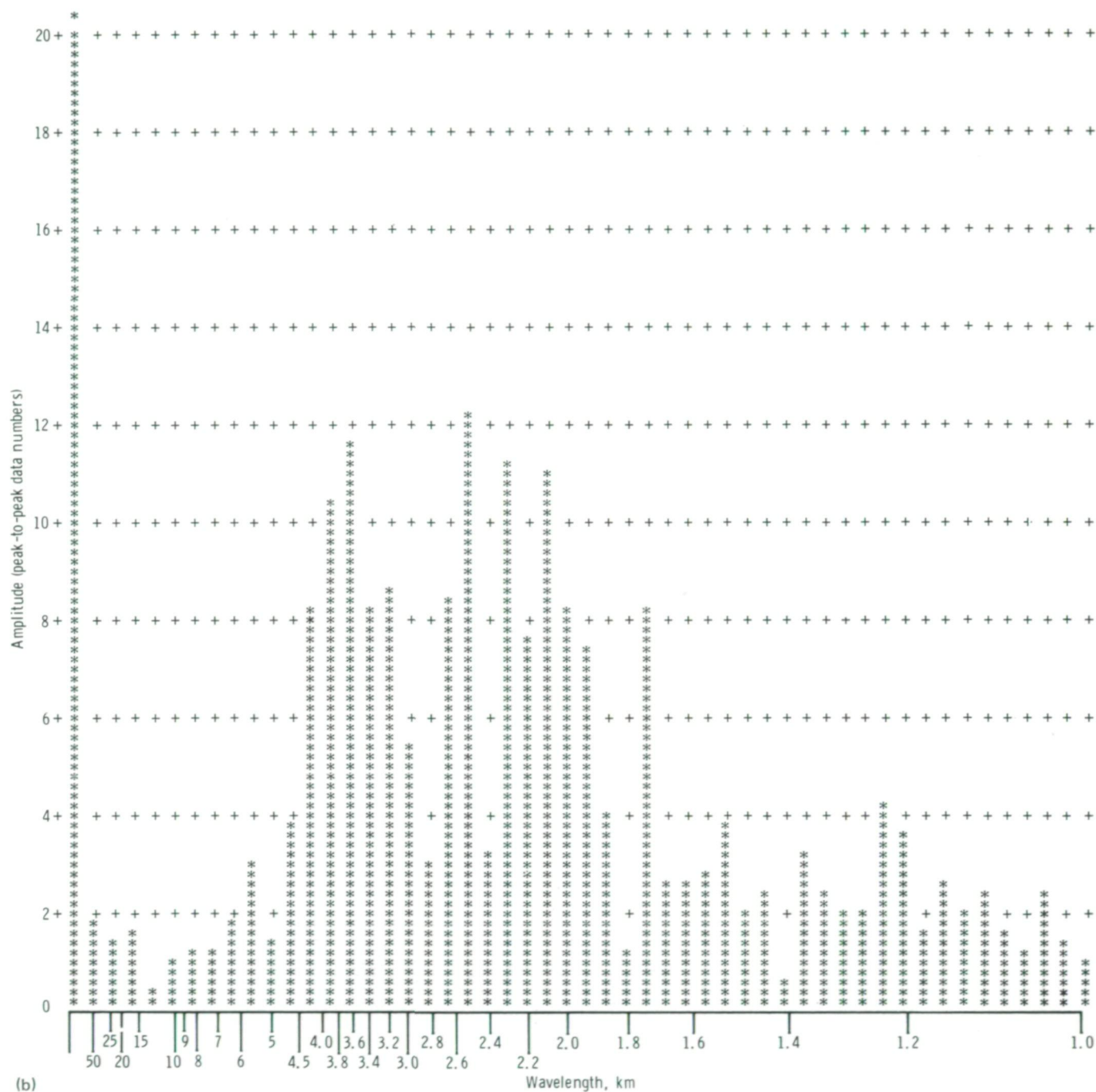


FIGURE 16-11.—Continued.

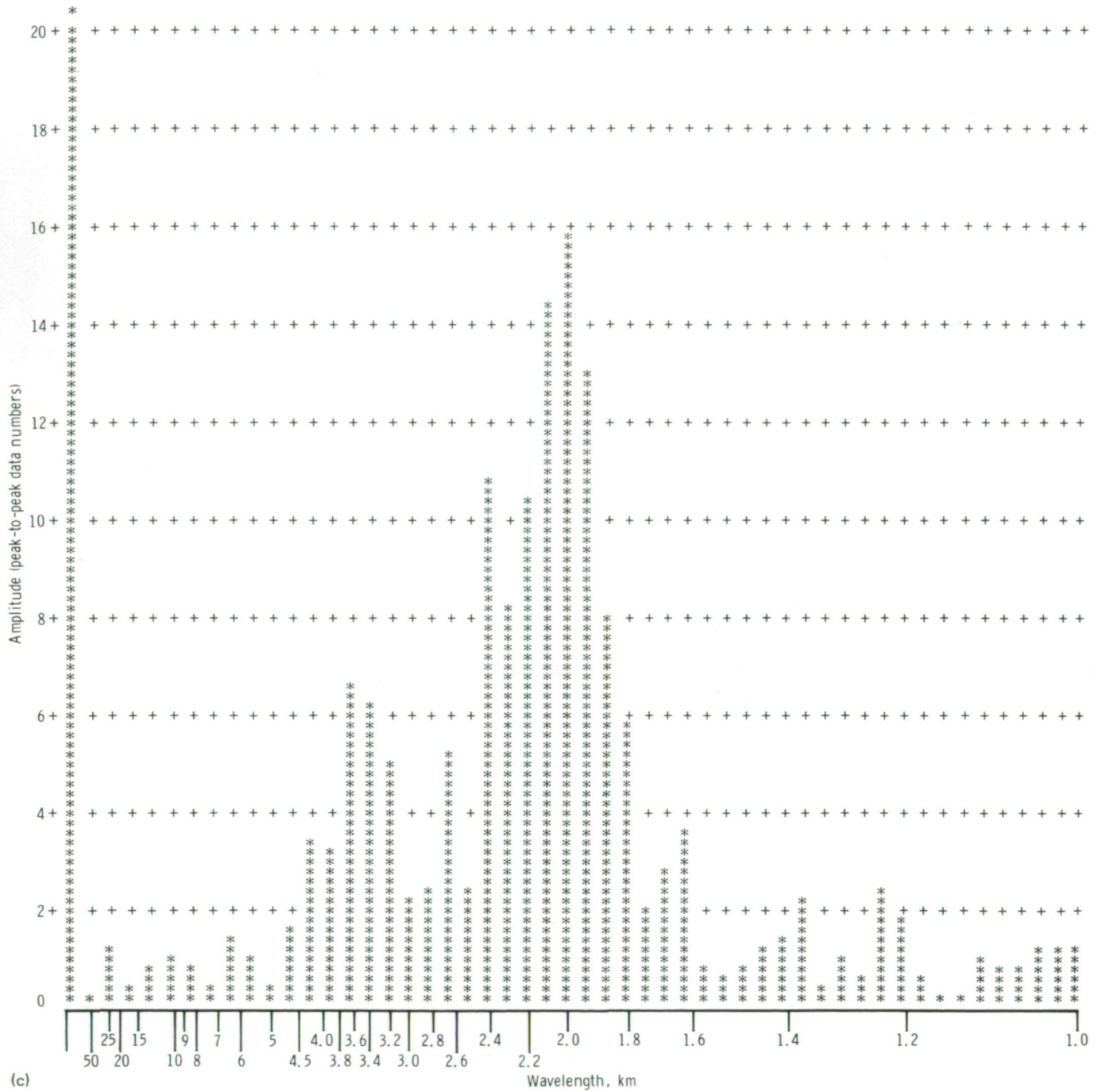


FIGURE 16-11.—Concluded.

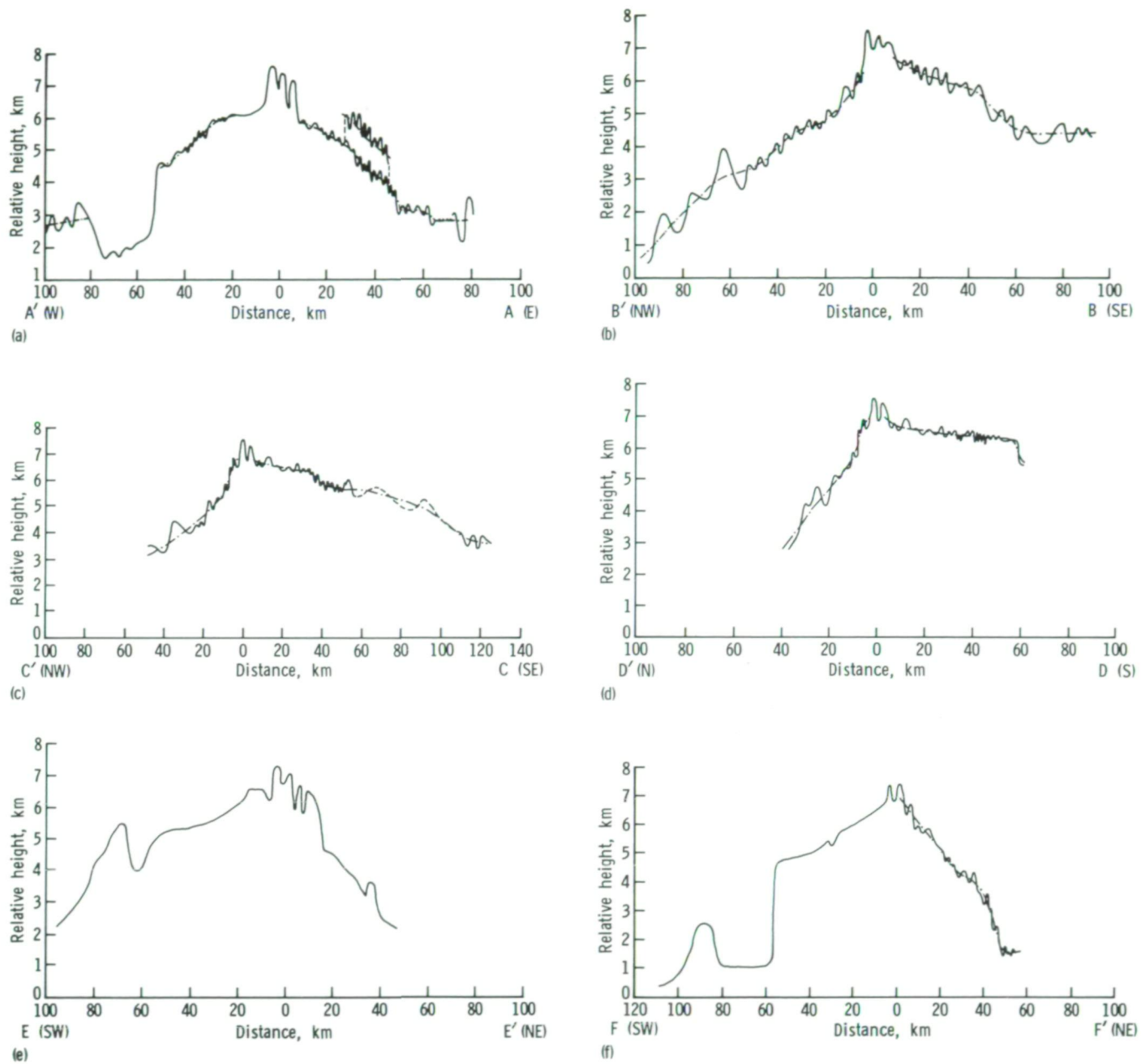


FIGURE 16-12.—Relative cloud heights of tropical storm Ellen. See figure 16-1 for locations of cross-section cutting planes. (a) Section A-A'. (b) Section B-B'. (c) Section C-C'. (d) Section D-D'. (e) Section E-E'. (f) Section F-F'.

The most surprising result of the stereographic analysis is the determination that the circular cloud is a large dome protruding into the stratosphere. If one assumes that a relative height of 3 km corresponds roughly to an "undisturbed" cirrus height near the undisturbed tropopause, then the dome is protruding nearly 3 km above the undisturbed height with smaller scale convective turrets protruding another 1.0 to 1.5 km higher. This result is contrary to the previous concept in which the top of circular cloud features was considered flat with a few protruding turrets overshooting 1 to 2 km above the cirrus clouds.

The mean topography of the dome with the wave motions suppressed is shown in figure 16-13. This analysis was constructed from mean heights on the cross sections (fig. 16-12) and from elevations determined at selected points between cross sections. The analysis shows that the dome is asymmetric and has a steep north side. Long-wavelength waves having lengths of 10 to 12 km and amplitudes of approximately 400 m are prominent on the east and west sides of the circular cloud (fig. 16-13).

Of special interest is the location of the eye with respect to the center of the overshooting area. The eye, indicated by the dashed ellipse (fig. 16-13), is approximately 55 km to the west-southwest of the highest turrets. This location was verified by observations from a U.S. Navy reconnaissance aircraft which flew through the storm 2 hours before the Skylab photograph was taken. The aircraft observers reported a very heavy buildup of clouds east of the eye at a radius from the center of approximately 52 km, which coincided with the maximum wind observation of 35 m/sec. They reported that the eye radius was 22.5 km and that cloud buildups were weak in the western semicircle. This observation corresponds to the cloud buildups to 4.5 km relative height visible in the Skylab photograph at a radius of 22 km to the south and east of the eye center. Thus, the spectacular circular cloud is located in the region of maximum winds 55 km from the eye center.

TABLE 16-I.—Tropical Storm Ellen
Wave Parameters^a

[September 19, 1973]

| Section (b) | Range, km | Wavelength, km | Amplitude, m |
|--------------------|-----------------------------------|--------------------|-------------------|
| Eastern semicircle | | | |
| 0-E' | 70 to 100 | 2.2 | — |
| 0-F' | 10 to 45 45 to 65 | 3.0 2.0 | 300 200 |
| 0-A | 25 to 65 65 to 85 80 to 90 | 2.5 1.5 9.5 | 150 300 650 |
| 0-B | 20 to 50 50 to 90 | 3.5 10.0 | 250 500 |
| 0-C | 35 to 45 45 to 60 | 3.5 1.8 | 250 200 |
| 0-D | 45 to 60 | 1.8 | 150 |
| Western semicircle | | | |
| 0-A' | 25 to 50 50 to 120 | 2.2 11.0 | 150 500 |
| 0-B' | 25 to 40 40 to 65 65 to 120 | 2.6 4.7 12.4 | 200 200 650 |
| 0-C' | 25 to 55 55 to 110 | 4.7 12.0 | 250 600 |
| 0-D' | 25 to 55 | 4.7 | 200 |

^aSee figures 16-1 and 16-2.

^bZeros represent approximate center of circular cloud on respective cloud cross-section cutting plane.

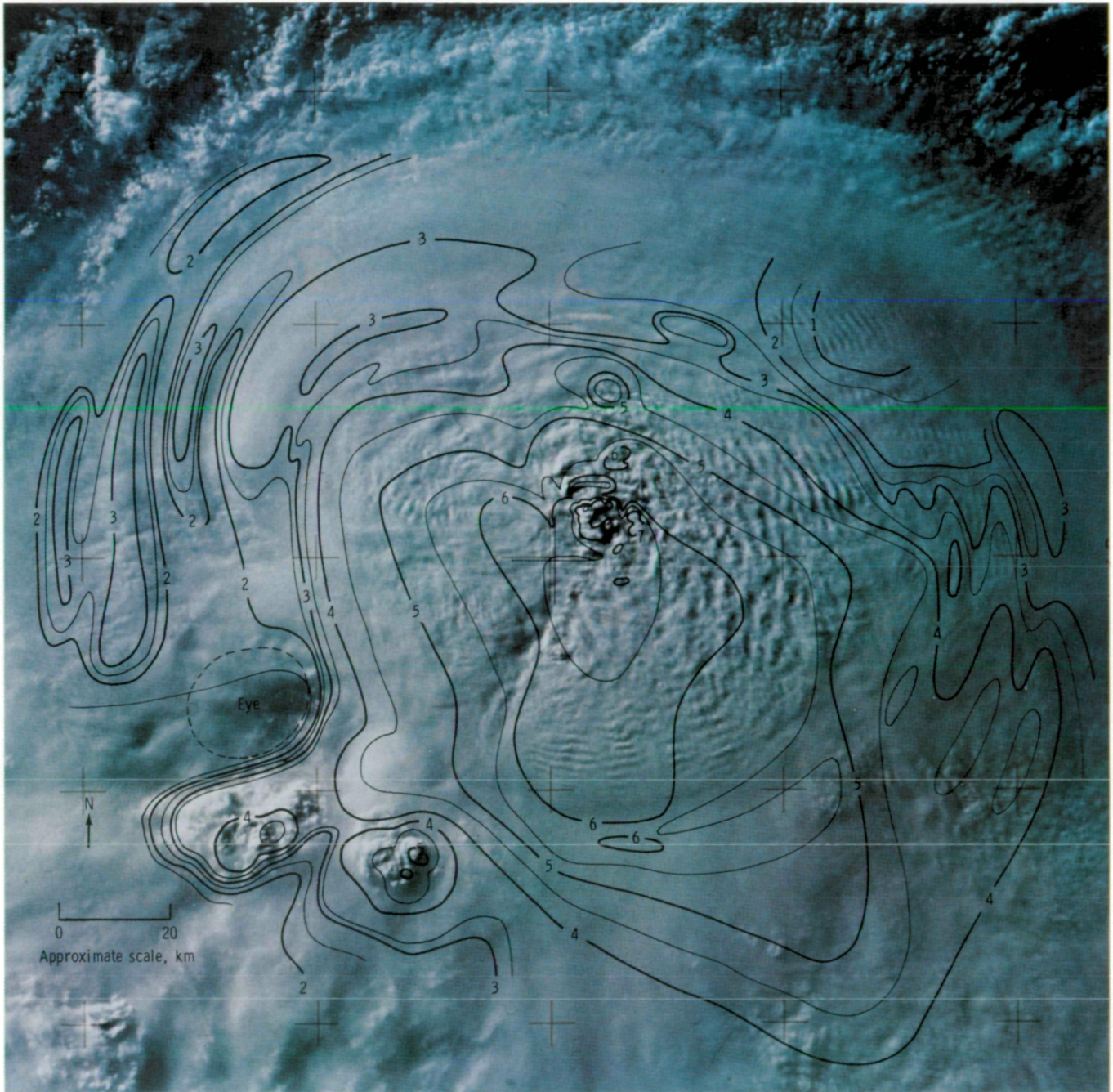


FIGURE 16-13.—Mean cloud height analysis of tropical storm Ellen superimposed on Skylab frame SL3-122-2572 (fig. 16-1). The eye of the storm is located approximately 55 km west-southwest of the highest turrets. Contours are relative height in kilometers.

To clarify the relationship of wavelengths and amplitudes present in the circular cloud, table 16-I, which summarizes the wave measurements based on the stereographic analysis, was prepared. The table indicates that along nearly all sections in the eastern semicircle, there is a tendency for wavelength to decrease as distance from the central turret cluster increases. The waves near the edge of the circular cloud along sections 0-F', 0-A, 0-B, and 0-C and all waves along sections 0-E' and 0-D have wavelengths between 1.5 and 2.2 km, whereas waves located closer to the center of the circular cloud along the former set of sections had wavelengths between 2.5 and 3.5 km. This finding is in agreement with the results of the two-dimensional Fourier transform, which showed that the dominant wavelength increased as azimuth changed from northeast to east.

Two explanations for this behavior are possible. The first is that a change in the mean cloud slope such as might occur near the edge of the circular cloud could cause an apparent change in the wavelength of the waves. If the slope became steeper, the projection of the wave shadows onto a flat image plane would result in closer spacing and thus in an apparent foreshortening of the wavelength. However, this does not appear to be the case according to the cross sections in figure 16-12. A more plausible explanation based on the physical nature of the wave will be discussed in a following subsection.

In contrast to the eastern semicircle, waves in the western semicircle are generally longer and increase in wavelength as distance from the central turret region increases. The wave height to length ratio for these waves is approximately 1:10 in contrast to the 1:5 ratio for the eastern-semicircle waves. The 1:10 ratio suggests that the waves are stable gravity waves.

Other Observations of Circular Cloud Features in Developing Tropical Storms

Circular clouds with wave structure similar to tropical storm Ellen were recently documented by the DMSP satellite (fig. 16-14). The image is of Typhoon Bess on October 11, 1974, at approximately 22:30 GMT (just after sunrise local time). Shading across the circular cloud, especially on the western side, indicates that the feature is dome shaped and is approximately 300 km in diameter compared to 225 km for that of tropical storm Ellen. The wavelength of the waves averages approximately 4.2 km near the center of the dome,

decreases to 3.0 km approximately halfway to the edge of the dome, and remains constant from there to the edge. As in tropical storm Ellen, the waves occur only in the eastern semicircle and decrease in wavelength with distance from the central turrets. The center of the circular cloud appears to be approximately 150 km northeast of the eye (fig. 16-14). Aircraft reconnaissance observations 12 hours earlier indicated that the maximum wind was located 130 km to the east of the eye, which had a diameter of 40 km. From figure 16-14, the eye diameter appears to be nearly 55 km.

From a study of tropical storms having similar circular clouds, Arnold² computed wavelengths of 4.7 km for Typhoon Patsy (Oct. 11, 1973) and 6.0 km for tropical storm Emma (June 16, 1974). Using Arnold's photographs, the author computed a wavelength of 4.2 km for Typhoon Dinah (June 9, 1974). Another case of a similar type of cloud feature was studied by Gentry et al.

²C. P. Arnold, "A Study of Satellite Observed Helmholtz Waves Within A Tropical Cyclone Canopy," term paper, Colorado State University, 1975.

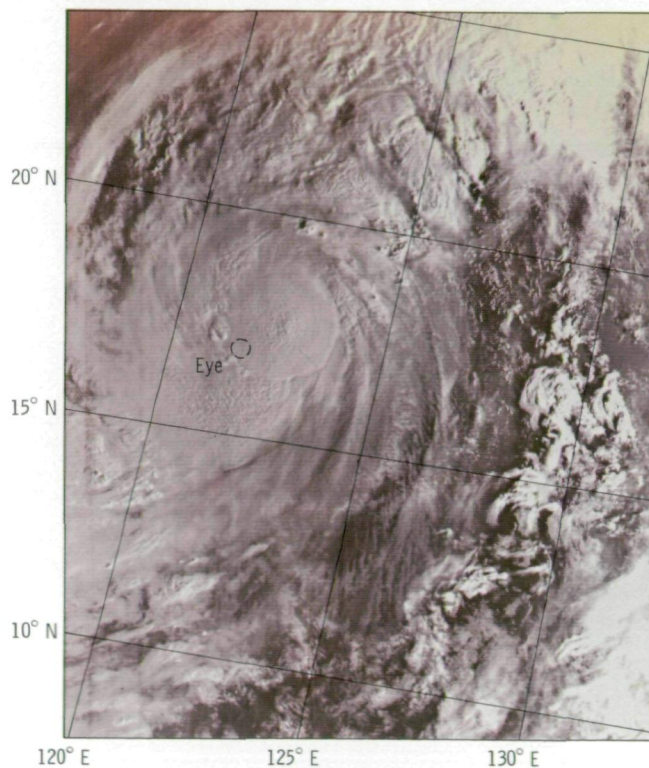


FIGURE 16-14.—A DMSP satellite image of Typhoon Bess taken on October 11, 1974, at approximately 22:30 GMT. The eye is approximately 55 km in diameter and is located approximately 150 km southwest of the circular cloud center.

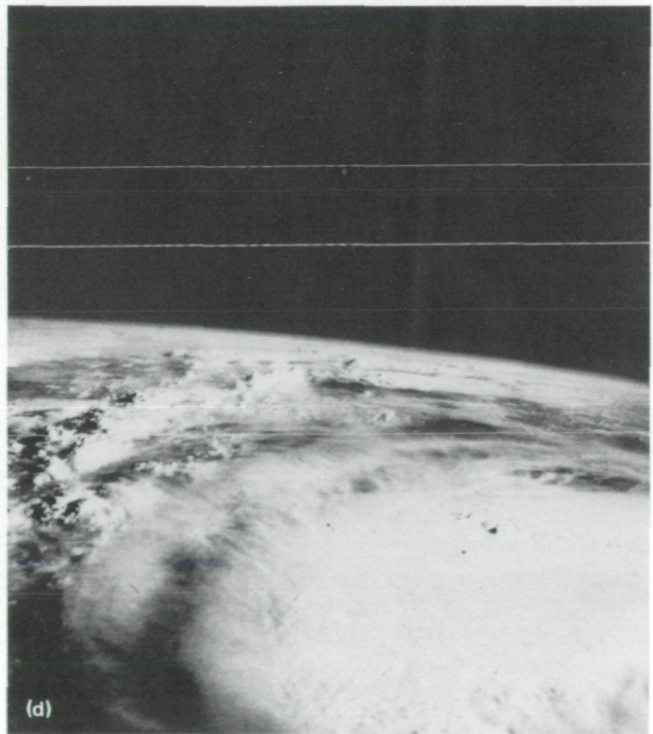
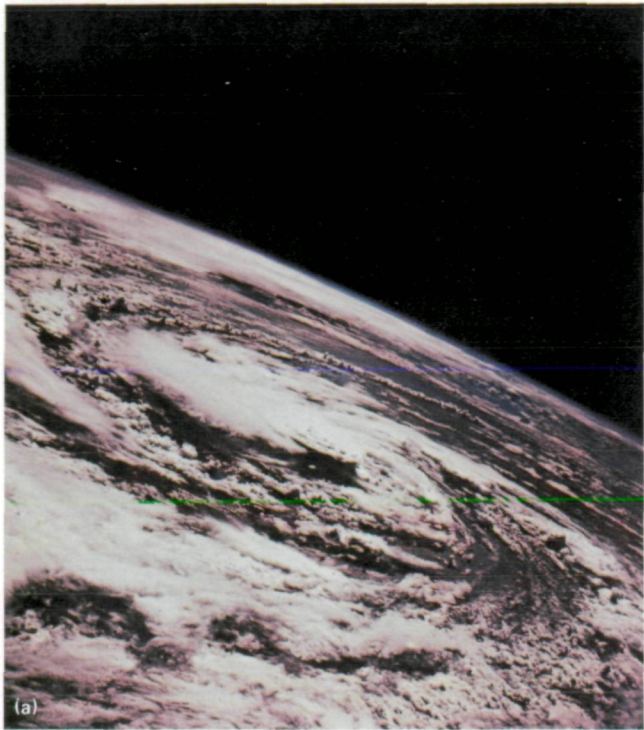


FIGURE 16-15.—Apollo 7 photographs of Hurricane Gladys. (a) Frame AS7-7-1877, October 17, 1968, 15:31 GMT. (b) Frame AS7-8-1891, October 18, 1968, 13:40 GMT. (c) Frame AS7-8-1892, October 18, 1968. (d) Frame AS7-8-1919, October 19, 1968, 13:50 GMT.

(ref. 16-2). This feature, which was called a circular exhaust cloud (CEC), was somewhat smaller than those mentioned previously (55 to 110 km) and did not contain the waves. The feature was located at the radius of maximum wind, approximately 40 km to the north of the storm center. Figure 16-15(a) is an Apollo 7 photograph of Hurricane Gladys taken on October 17, 1968, that illustrates the CEC. Aircraft and radar observations made at about the time of the Apollo overflight were analyzed by Gentry et al., who concluded that (1) the top of the CEC was at an altitude of 12 km at its edge and protruded upward to approximately 14 km at its center, (2) low-level cloud bands converge into the CEC, (3) the only outflow at high levels was that coming from the CEC, (4) the CEC diameter expanded from 55 to 110 km in 4 hours, and (5) the CEC propagation speed was 3 m/sec when the maximum horizontal wind velocity was 32 m/sec.

The Apollo 7 photographs of Hurricane Gladys on October 18 show a circular, dome-shaped (as deduced from shadowing) cloud of approximately 150 km in diameter with embedded waves having a 2-km wavelength (figs. 16-15(b) and 16-15(c)). The waves are still apparent in Apollo 7 photographs taken on October 19 when Hurricane Gladys was off the eastern coast of Florida (fig. 16-15(d)).

A final example of a CEC documented by handheld-camera photography is contained in two Gemini VII photographs of a tropical storm in the eastern Pacific Ocean taken on December 7, 1965, and shown in figure 16-16. The wavelength in this case is approximately 4.5 km.

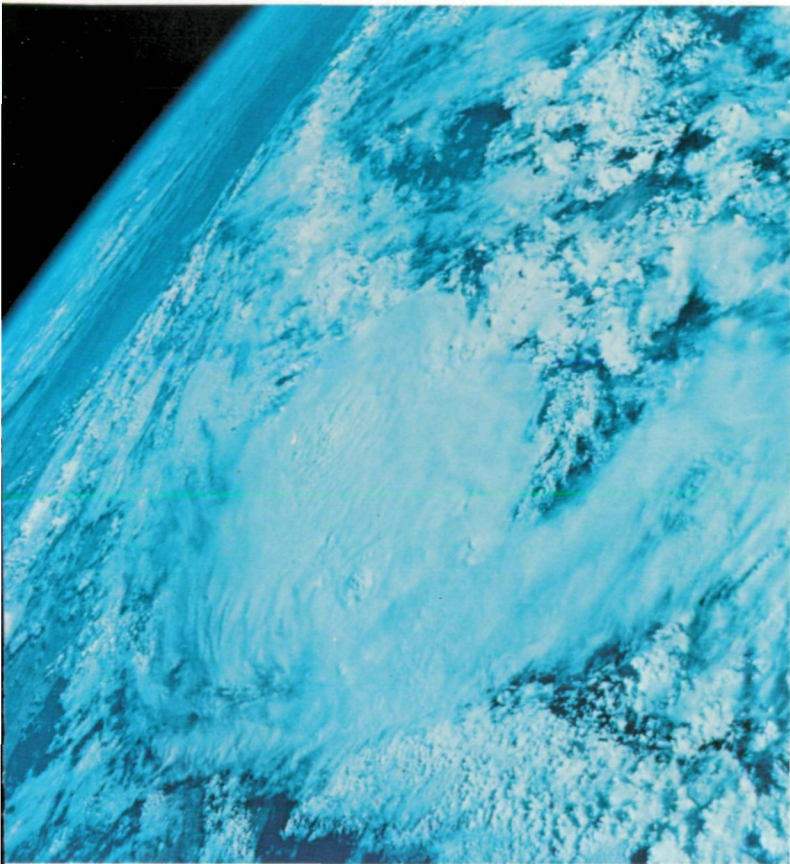
Other cases of large circular convective clouds were photographed from Skylab. Two examples are tropical storm Wanda on January 11, 1974 (fig. 16-17) and tropical storm Christine on September 2, 1973 (fig. 16-18). These photographs do not reveal prominent waves although figure 16-17 of tropical storm Wanda suggests the presence of a few wave fronts.

Comparison of a DMSP image (fig. 16-19) and the Skylab 4 photograph obtained at approximately the

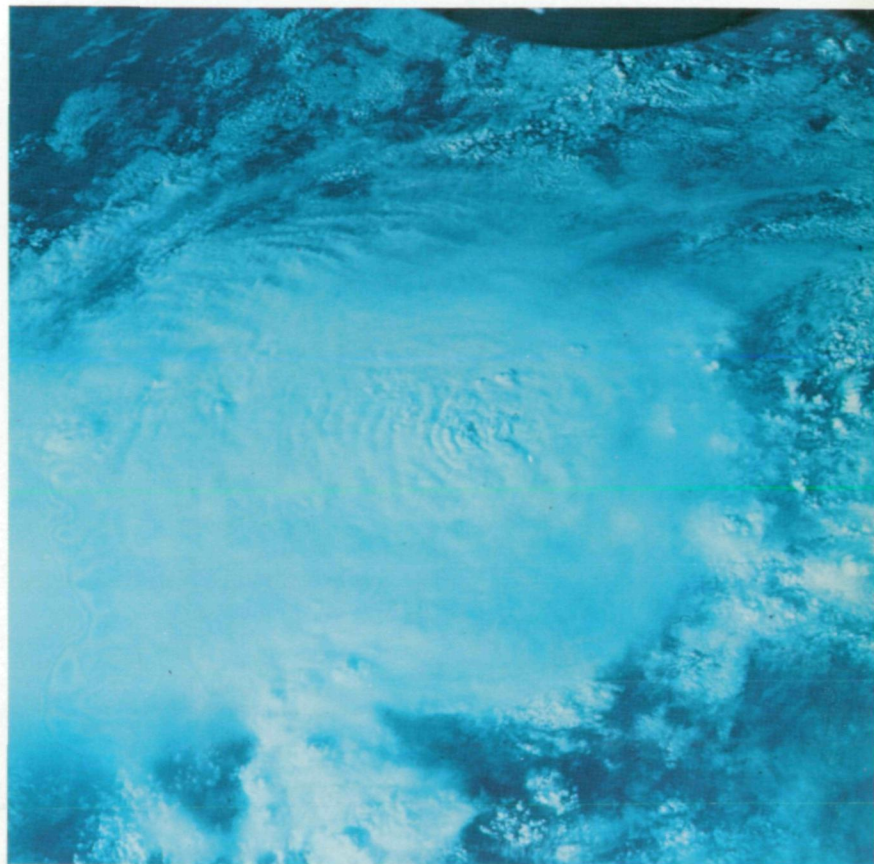
same time (fig. 16-17) demonstrates the relative resolutions of each data source. The DMSP satellite data, when processed to optimize the spatial and gray-scale resolution, provide nearly the same resolution in the overshooting tops that can be obtained from the Skylab handheld-camera photographs.

Circular clouds of the type observed in Hurricane Ellen were photographed with 1-km resolution by SMS within Hurricane Caroline on August 30, 1975, Hurricane Eloise on September 16, 1975, and Hurricane Gladys on September 30, 1975. The maximum cloud diameters were 125, 185, and 220 km, respectively. For Hurricane Eloise, wavelengths of 3.5 km near the center of the cloud disk and 4.9 km near its edge were determined; a wavelength of 8.1 km was observed for Hurricane Gladys.

Circular cloud features similar to those reported here have been observed within developing tropical storms by lower resolution satellites. The details of their structure, however, have been obscured. This type of feature has been referred to as a central dense overcast (CDO) in techniques using satellite cloud morphology to infer tropical storm strength. The CDO is an important parameter in determining intensity classifications with the technique developed by Dvorak (refs. 16-3 and 16-4) and extended for U.S. Air Force use with higher resolution DMSP imagery by Arnold (ref. 16-5). The circular cloud feature described in this report is probably a special case of the CDO described by Dvorak. The case described here refers only to the initial stages of the CDO. The strictly empirical nature of the cloud morphology-intensity relationship recognizes the existence of a nearly circular, well-defined cloud mass that develops near the circulation center as the storm is undergoing steady intensification from tropical storm to hurricane strength. The size of the CDO is postulated by Dvorak to be directly proportional to the storm intensity. According to both Dvorak and Arnold, the center of circulation seems to be located directly beneath the center of the CDO. The following discussion reflects disagreement with this conclusion.



(a)



(b)

FIGURE 16-16.—Gemini VII photographs of unnamed tropical storm in the eastern Pacific Ocean off Baja California on December 7, 1965. (a) Oblique view (S65-63834). (b) Vertical view (S65-63835).

Discussion of Results

Results of the spectral and stereographic analyses of Skylab photographs of Hurricane Ellen on September 19, 1973, are summarized in table 16-II. The observations from space of tropical storms described in this section suggest that circular clouds are not unique events. The feature may be more common than previously

believed and could be representative of a transitory stage in the tropical storm life cycle.

The following discussion is directed to relating the observational data to the physical processes thought to be producing the feature. The horizontal scale of circular clouds implies that large convective updrafts bring air from the surface to the top of the troposphere. Air parcels must expand as they rise in such a manner that

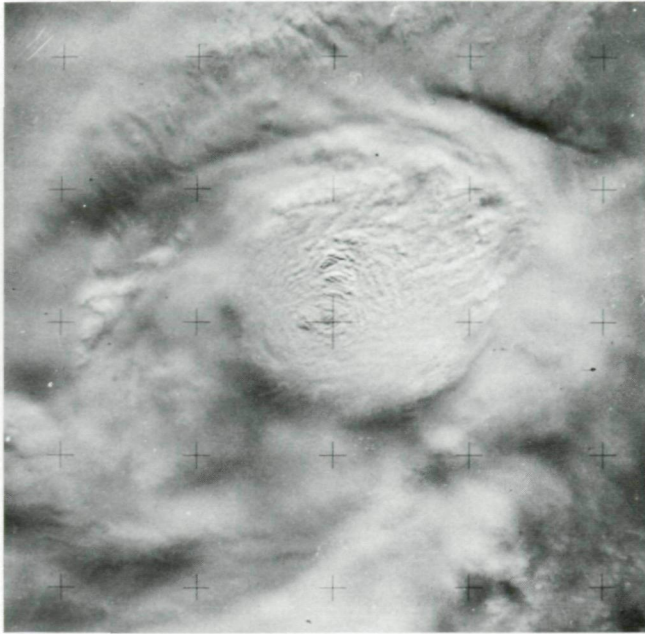


FIGURE 16-17.—Skylab 4 photograph of tropical storm Wanda at 00:16 GMT, January 11, 1974 (SL4-139-4051).

no heat is exchanged with the environment. This is called an adiabatic process and requires that the temperature of the unsaturated parcel decrease at the specified rate of 9.75 K/km. A quantity that is conservative during this process is the potential temperature defined as

$$\theta = T \left(\frac{p_0}{p} \right)^{\frac{R}{c_p}} \quad (16-1)$$

where T is the temperature at pressure p , the reference-level pressure p_0 is 100 kPa (1000 mbar), R is the ideal gas constant, and c_p is the specific heat at constant pressure ($R/c_p = 2/7$). For moist air ascent, the equivalent potential temperature θ_e is defined as the potential temperature of the air after condensation of all moisture by adiabatic processes. In the inner regions of tropical storms, typical θ_e values range from 355 to 360 K but may be higher. Thus, the observations of convective elements overshooting the tropopause by 4.5 km imply adiabatic maintenance of a specific θ_e temperature within the cloud.

The only observational data known to the author of air temperatures measured directly (i.e., from aircraft)

near the top of hurricane eyewalls are shown in figure 16-20. These measurements were recorded over Hurricane Isbell (ref. 16-6) and Hurricane Beulah (ref. 16-7) and showed a tropopause at a pressure of approximately 10 kPa (100 mbar) at an altitude (16 km) that coincided with the top of the cirrus clouds. Both soundings indicated a very intense inversion above the tropopause with a temperature decrease of 10 K in 180 m capped by another adiabatic layer approximately 500 m thick. Above this second layer, the temperature increases at a rate of 7 K/km and then at a slower rate of 4 K/km to a point at which it approaches mean conditions at an altitude of approximately 20 km (6 kPa (60 mbar)). The lapse rate below the tropopause is nearly adiabatic (departures being due to a small amount of mixing), and the potential temperature is approximately 360 K. Average atmospheric soundings for September 18 and 19, 1973, from Bermuda and San Juan, Puerto Rico, both approximately 1500 km from Hurricane Ellen, show a tropopause height at a pressure of approximately 10 kPa (100 mbar). The Bermuda sounding is nearly identical to the mean tropical sounding for September. Thus, if a 4.5-km penetration into the stratosphere by way of a nearly adiabatic process is assumed, the in-cloud temperature at the turret tops should be near 163 K (-110°C). These temperatures

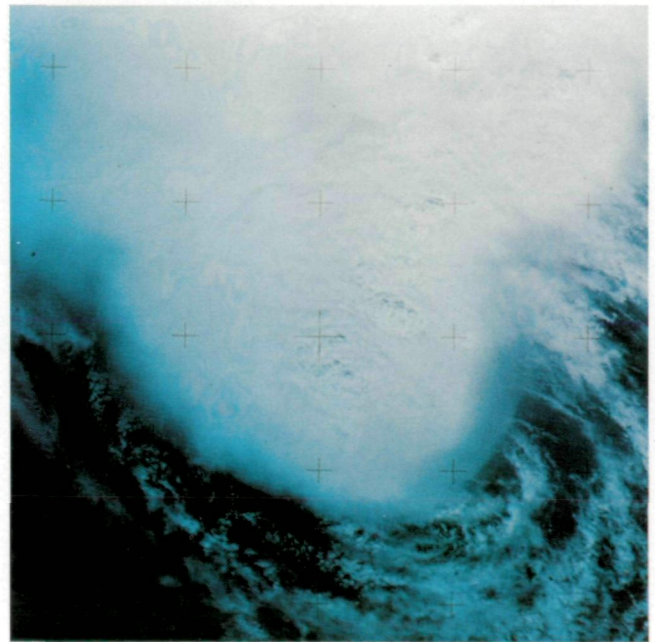


FIGURE 16-18.—Skylab 3 photograph of tropical storm Christine on September 2, 1973 (SL3-121-2322).

TABLE 16-II.—Summary of Hurricane Ellen Measurements

[September 19, 1973]

| | |
|---|------------|
| Storm diameter, km | 400 |
| Cloud disk diameter, km | 225 |
| Dome diameter, km | 12 to 15 |
| Turret diameter, km | 3 to 5 |
| Shorter wavelengths, km | 1.5 to 4.5 |
| Longer wavelengths, km | 9 to 13 |
| Shorter wave amplitude, m | 150 to 300 |
| Longer wave amplitude, m | 500 to 600 |
| Shorter wave height to length ratio | 1:4 to 1:5 |
| Longer wave height to length ratio | 1:10 |
| Undisturbed cirrus height (3-km relative height), km | ≈ 15.5 |
| Cloud disk overshoot, km | 3 |
| Turret overshoot (above cloud disk), km | 1.5 |
| Total maximum overshoot, km | 4.5 |

would occur only over a region several kilometers in diameter. The Beulah and Isbell data lend some credence to this conclusion by revealing that for the non-overshooting conditions in these storms, adiabatic ascent seems to produce the very cold temperatures of 187 and 188 K (−86° and −85° C), respectively, over large areas surrounding the eyewall.

The vertical profile of the east-west component of wind for the San Juan and Bermuda soundings averaged over September 18 and 19 shows an easterly (positive) component above the tropopause the velocity of which increases with height (fig. 16-21). Although the Bermuda winds are weaker than the San Juan winds, the magnitude of the shear indicated by the line slope is nearly identical. The wind in the 5-kPa (50 mbar) layer below the tropopause from 13 to 16 km is weak and thus may allow the outflowing air to expand outward uniformly in all directions and thereby to produce a symmetrical circular cloud. Arnold² also reported easterly winds at the tropopause level for the Typhoon Patsy case (1973) and the tropical storm Emma case (1974).

The atmospheric soundings from San Juan, Puerto Rico, and Turks Island in the vicinity of Hurricane Eloise penetrated the circular cloud that was present in that storm in a region where waves were observed.

²C. P. Arnold, "A Study of Satellite Observed Helmholtz Waves Within A Tropical Cyclone Canopy," term paper, Colorado State University, 1975.

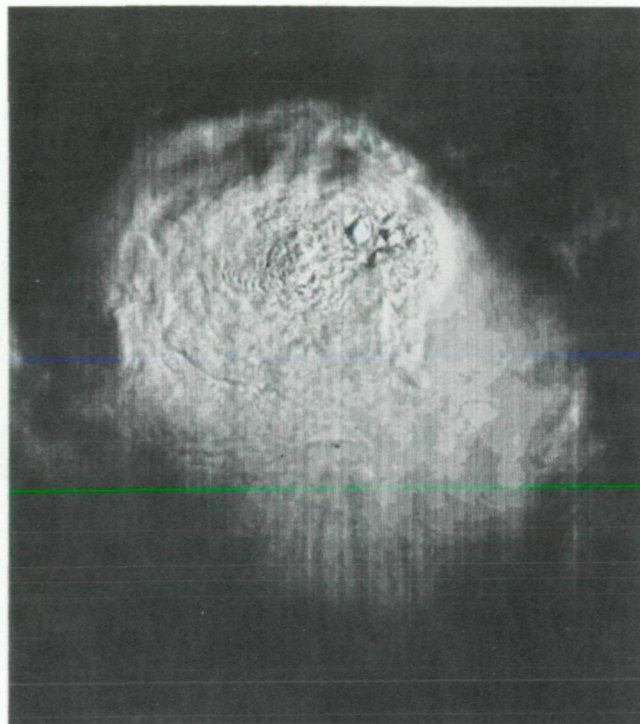


FIGURE 16-19.—Enlargement of DMSP image of tropical storm Wanda at 00:12 GMT, January 11, 1974, in the western Pacific Ocean.

These soundings, shown in figure 16-22, are similar to the Hurricane Ellen proximity soundings (fig. 16-21) in that they reveal nearly calm winds at the tropopause with easterly winds above the tropopause that increase in velocity with height. Figure 16-22 also reveals a very large wind shear just below the cirrus cloud top (coincident with the tropopause). The shears are (30 m/sec)/km and (5 m/sec)/km for the San Juan and Turks Island soundings, respectively.

A discussion of the causes for the observed wave features within the circular cloud follows. An important parameter in this discussion is the Richardson number, which is defined as the ratio of the Brunt-Vaisala frequency N^2 to the square of the wind shear $(\partial u/\partial z)^2$ and is given as

$$R_i = \frac{N^2}{\left(\frac{\partial u}{\partial z}\right)^2} \quad (16-2)$$

where $N^2 = (g/\theta) (\partial\theta/\partial z)$, u is horizontal windspeed along the x-axis (positive from the east), z is the vertical coordinate, and g is acceleration due to gravity. The Brunt-Vaisala frequency is the natural buoyancy frequency of the layer and is a measure of its stability; the larger the value, the more stable the layer. Thus, the

Richardson number is a ratio between buoyancy forces (energy production) and shearing or inertial forces (turbulent dissipation).

When the value of the Richardson number becomes less than approximately 1/4, the layer over which this criterion exists can become unstable when subjected to

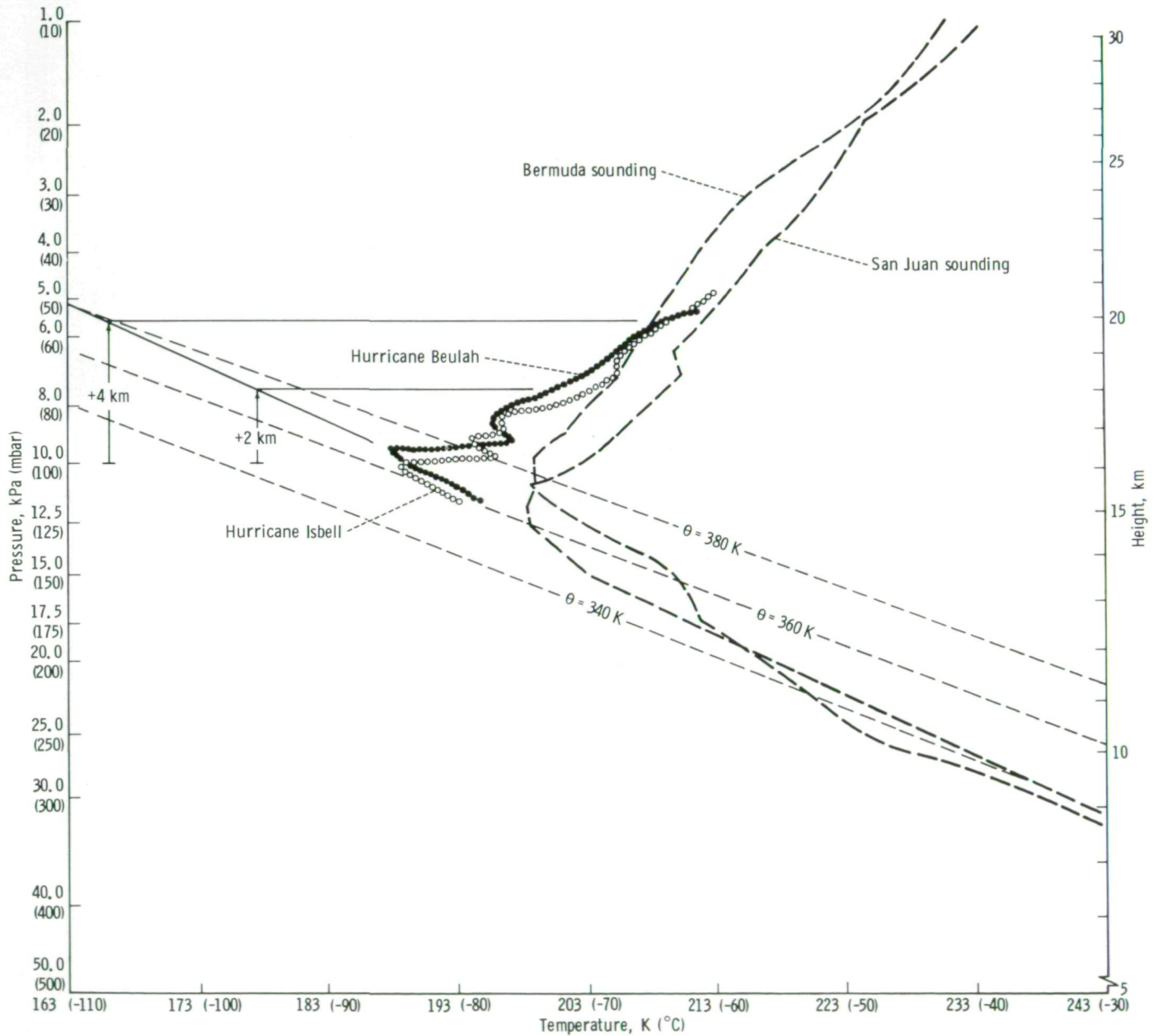


FIGURE 16-20.—Stuve thermodynamic diagram showing temperature as a function of height and pressure for Hurricanes Beulah and Isbell measured by a U-2 aircraft as well as proximity soundings from Bermuda and San Juan, Puerto Rico, for Hurricane Ellen on September 19, 1973.

a perturbation. The vertical profile of potential temperature and wind shear through the layer will determine the dominant wavelengths or scales of the instabilities. In the case of Hurricane Ellen, the intense updrafts penetrating above the circular cloud and forming the turrets near the center provide the perturbation necessary to trigger the instabilities. However, both stable and unstable waves can be excited when an impulsive force strikes a stable layer. If the amplitude of the perturbation is small compared to the depth of the fluid, an analogy can be made with the case of a rock being dropped into a pond. In this case, only stable waves are excited since there is no wind shear and no wind across the density discontinuity (the air-water interface). A continuous spectrum of waves excited by this mechanism disperses outward from the point of

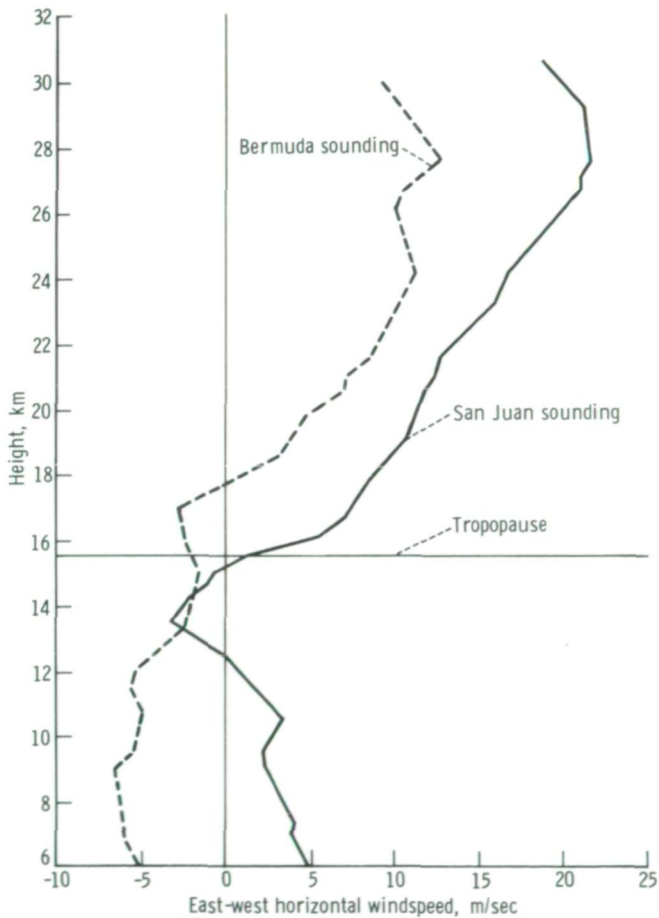


FIGURE 16-21.—Vertical profile of horizontal wind for Bermuda and San Juan, Puerto Rico, averaged over September 18 and 19, 1973. The negative windspeeds are westerly winds; the positive windspeeds are easterly winds.

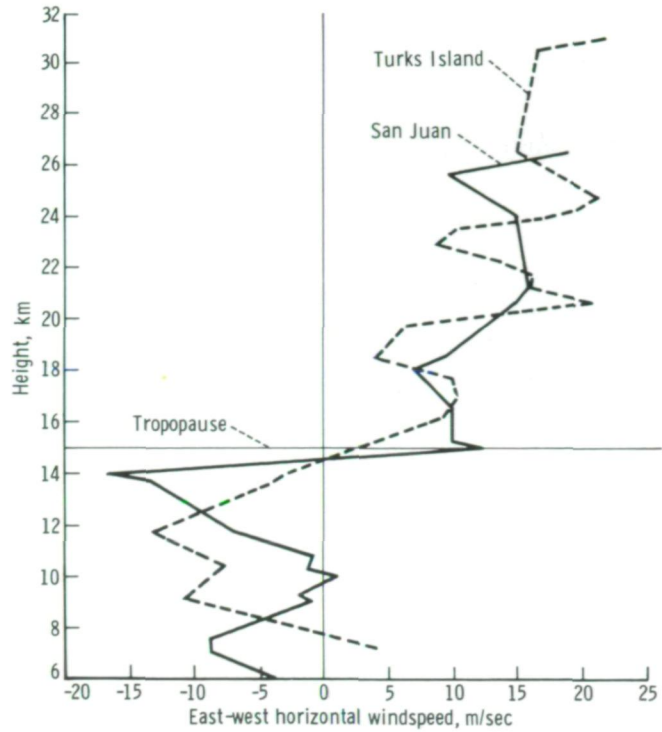


FIGURE 16-22.—Vertical profile of horizontal wind for San Juan, Puerto Rico (12:00 GMT, September 17, 1975), and for the Turks Island (12:00 GMT, September 16, 1975) from soundings taken in the vicinity of Hurricane Eloise. The negative windspeeds are westerly winds; the positive windspeeds are easterly winds.

impact with wave velocity proportional to wavelength. After a period of time, the longest waves, having moved fastest, are farthest from the source, followed by the next longest and so forth. A sorting of wavelengths as a function of distance from the source is thus achieved as shown in figure 16-23. Although this explanation is an oversimplification of the Hurricane Ellen case, it is believed that the longer wavelengths present near the edge of the circular cloud result from a "rock in pond" process.

The more complicated structure thought to be present in the Hurricane Ellen case can be synthesized from figures 16-20 to 16-22. Recall that the maximum circular cloud protrusion above the mean tropopause was 3.0 km at the center (not including the overshooting turrets). An average protrusion in the region of the waves (about halfway between the center and the edge of the circular cloud) of 1.5 km is thus assumed, and an in-cloud temperature of 180 K (-93°C) is implied from figure 16-20. Assuming similarity with the Hurricane Isbell and Beulah profiles, an intense inversion at the

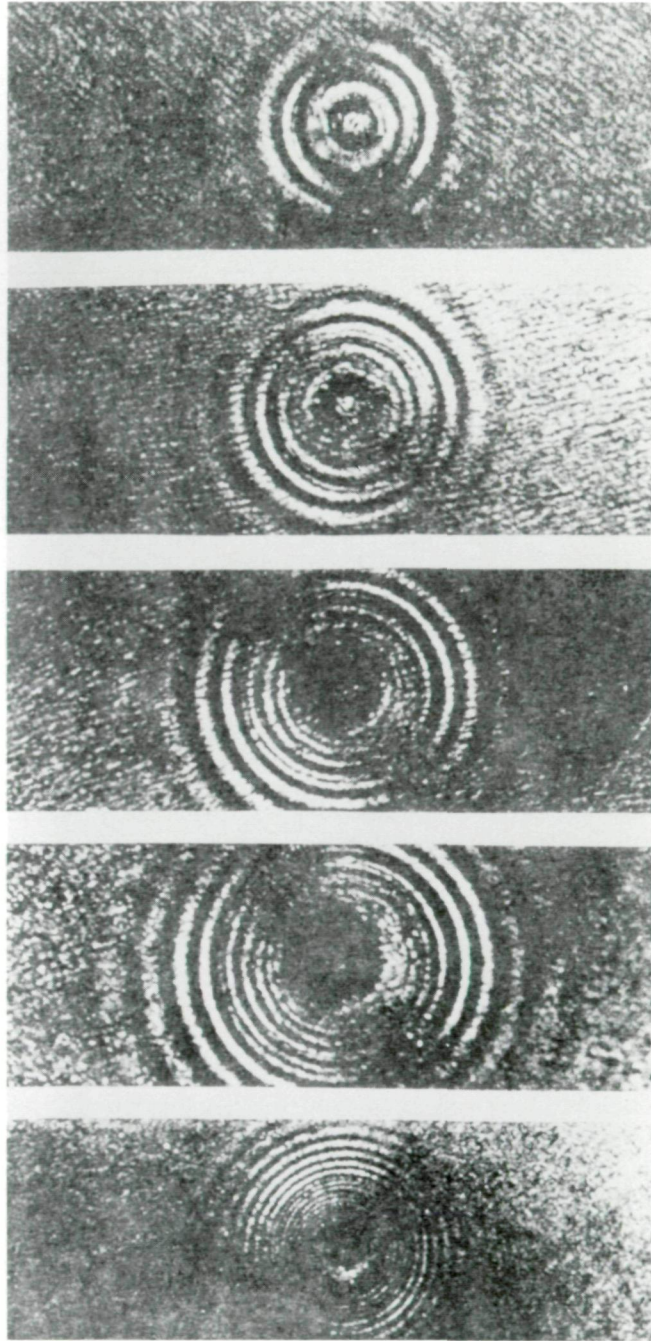


FIGURE 16-23.—Time-sequence photograph of gravity waves radiating outward from the point of impact of a rock dropped into a pan of water showing an increase in wavelength outward from impact. The time sequence begins with the top frame. Reprinted with permission of Interscience Publishers, Inc., New York.

cloud top will then exist. A change in potential temperature $\Delta\theta$ over this approximately 0.5-km-thick layer ΔZ is approximately 40 K, and the average potential temperature $\bar{\theta}$ is approximately 390 K. Thus, assuming $g = 9.8 \text{ m/sec}^2$, the Brunt-Vaisala frequency for the Hurricane Ellen case can be estimated as

$$N^2 \approx \frac{g}{\bar{\theta}} \frac{\Delta\theta}{\Delta Z}$$

$$= 2 \times 10^{-3} \text{ sec}^{-2} \quad (16-3)$$

To estimate the in-cloud air velocity for the Hurricane Ellen case, the following procedure is used. Assuming that $R_i = 1/4$, the westerly component of the windspeed within the cloud at the bottom of the shear layer U_B is calculated as follows.

$$U_T - U_B = 2N\Delta Z \quad (16-4)$$

where the easterly component of the windspeed at the top of the shear layer $U_T = 10 \text{ m/sec}$, $N = 4.47 \times 10^{-2} \text{ sec}^{-1}$, and $\Delta Z = 500 \text{ m}$; thus, $U_B \approx -34.7 \text{ m/sec}$. This estimate is approximately a factor of 2 larger than the maximum in-cloud windspeed measured for Hurricane Eloise. However, considering that the Hurricane Eloise atmospheric sounding was made farther from the circular cloud center than the Hurricane Ellen estimate, the calculation is at least consistent with available observations.

Atmospheric structures similar to that implied for the Hurricane Ellen case have been modeled by various authors (Lindzen (ref. 16-8); Gossard (ref. 16-9); Miles and Howard (ref. 16-10); and Lalas et al. (ref. 16-11)) in an effort to predict the most unstable wavelengths that can be excited. The problem is referred to as the Helmholtz problem, and the resulting instabilities are referred to as Kelvin-Helmholtz waves. Assuming a Richardson number of 1/4, Lindzen (ref. 16-8) derived a relationship for wavelength λ at which the optimum wave-flux generation by Kelvin-Helmholtz waves will occur. This relation is $\lambda_{opt} = 8.89 U/N$, where U is one-half the wind shear across the layer. A relationship stated by Gossard (ref. 16-9) for the most unstable

wavelength is $\lambda_m = 7.85 U/N$, and a similar expression obtained by Miles and Howard (ref. 16-10) is $\lambda_m = 7.5 U/N$. A relation for the largest unstable wavelength given by Lalas et al. (ref. 16-11) is

$$\lambda_x = \frac{2\pi r (2U)^2}{g(1-r)(1+r)}$$

where g is the acceleration of gravity (9.8 m/sec^2) and r is the ratio of potential temperatures in the bottom and top layers. For the Hurricane Ellen case, assuming $U = 22 \text{ m/sec}$ and $r = 0.88$, the preceding wavelength estimates become 4.38, 3.87, 3.70, and 4.8 km, respectively. These values are slightly longer than the wavelengths measured in Hurricane Ellen and Typhoon Bess. This agreement supports the hypothesis that the observed field of short-wavelength waves in the eastern semicircle of the circular cloud is indeed composed of Kelvin-Helmholtz waves.

The importance of these waves in the hurricane energy and momentum budget probably lies in their capability to extract energy from the mean flow in the outflow layer and convert it to turbulent eddies. In other words, the waves comprise a source of energy dissipation in the outflow layer.

Outward-propagating stable gravity waves also appear to be present as suggested by the increase of wavelength with distance from the central turret in the western semicircle of the circular cloud. These waves, especially those with long wavelengths, could be significant in the outward transport of energy and momentum. This would have the effect of enhancing the outward transport through the mean flow in the outflow layer and thus possibly contributing to the development of the storm.

To estimate the contribution of these long waves to the energy flux, the following procedure will be used. The phase velocity C of these waves can be approximated by the deepwater-wave-speed formula corrected for the compressibility of the atmosphere. This relation is

$$C = \left(\frac{1}{2\pi} \epsilon g \lambda \right)^{\frac{1}{2}} \quad (16-5)$$

where $\epsilon = \Delta\theta/\theta$. Groups of waves move with a velocity different from that of individual waves. Since waves tend to travel in groups of slightly different wavelengths (packets), their group velocity C_g differs from the phase velocity C . For deep water, $C_g = C/2$. This relationship is important because wave energy propagates with the group velocity. The amplitude A of these waves should vary with linear distance r from the source according to $A \approx r^{-1}$ since the total energy of the waves around the circular wave front is constant or decaying as the wave front is expanding.

To estimate the energy flux by the long waves visible at the edge of the cirrus shield, the wave-energy density per unit area E is determined by the following:

$$E = \Delta\rho g A^2 \quad (16-6)$$

where $\Delta\rho \approx 10^{-2} \text{ kg/m}^3$, $g = 9.8 \text{ m/sec}^2$, and $A = 500 \text{ m}$ at $r = 100 \text{ km}$. Therefore, $E \approx 25 \times 10^3 \text{ J/m}^2$. The energy flux is expressed by

$$F_E = 2\pi r E C_g \quad (16-7)$$

The group velocity is computed by

$$\begin{aligned} C_g &= \frac{C}{2} \\ &= \left(\frac{1}{8\pi} \epsilon g \lambda \right)^{\frac{1}{2}} \end{aligned} \quad (16-8)$$

where $\epsilon \approx 10^{-2}$ and $\lambda \approx 10 \text{ km}$. Therefore, $C_g = 6.3 \text{ m/sec}$ and $F_E = 10^{11} \text{ J/sec} = 8.6 \times 10^{15} \text{ J/day}$. Hawkins and Rubsam (ref. 16-12) calculated the energy advection within 100 km of Hurricane Hilda as $2 \times 10^{17} \text{ J/day}$. Thus, wave-energy advection approximates 4 percent of the total energy advection and hence could be significant in the energetics of the storm.

The problem of estimating the time and space scales of the convective motion associated with the circular cloud event in Hurricane Ellen will now be discussed. Investigations of severe thunderstorms from a Learjet aircraft by Fujita (ref. 16-13) and Shenk (ref. 16-14)

TABLE 16-III.—Observations of Convective Tower Overshooting^a

| Element diameter <i>D</i> , km | Rise time, sec | Overshoot period <i>P</i> , sec | Overshoot height ΔZ , km | $\frac{\Delta Z}{D}$ | Source |
|-----------------------------------|----------------------|---------------------------------------|--|----------------------|-----------------|
| 0.61 | 48 | 192 | 0.55 | 0.90 | Reference 16-13 |
| ^b 1.32 | — | ^b 333 | — | — | Reference 16-13 |
| 1.85 | 120 | 480 | .93 | .50 | Reference 16-13 |
| 3.00 | 145 | 580 | 2.0 | .67 | Reference 16-15 |
| 4.0 | ^c 180 | ^c 720 | 1.5 | .38 | Hurricane Ellen |
| 6.1 | 240 | 960 | 1.4 | .23 | Reference 16-14 |

^aSee figures 16-24 and 16-25.

^bParameters for Brunt-Vaisala period.

^cComputed from least-squares fit to the observations.

have yielded estimates on two convective scales visible in the Ellen photographs: the dome scale and the turret scale. The dome is typically on the order of 10 km in diameter, whereas the turrets that are superimposed on the dome are generally larger than 1 km in diameter. A smaller feature, the bubble, that is superimposed on the turret ranges from 10 to 100 m across. The rate of production of these features appears to be multiplicative such that a dome may have 5 to 10 turrets superimposed on it and each turret may have several hundred bubbles superimposed on it. Several distinct convective scales are therefore involved in a convective cloud, and each length scale is separated by approximately a decade.

Observations of convective cloud parameters made by Fujita (ref. 16-13), Shenk (ref. 16-14), and Saunders (ref. 16-15) are listed in table 16-III and plotted in figure 16-24. Also shown in figure 16-24 is a least-squares regression line relating the overshoot period *P* to the convective element diameter *D* in kilometers according to $P = 276D^{0.704}$. From this relation, the convective overshoot times *P* (period) for the dome (13.5 km) and turret (4 km) in Hurricane Ellen are 28 and 12 minutes, respectively. The convective length scale associated with the Brunt-Vaisala period P_N is approximately 380 m (fig. 16-24). The ratio of convective overshoot height ΔZ to convective element diameter *D* is plotted as a function of *D* in figure 16-25. The measured ratio for Ellen (open circle) is close to the estimated value from other observations of element size (table 16-III). The quantities in table 16-III are essential parameters for estimating the vertical velocities at the tropopause (ref.

16-15). Based on laboratory experiments, Saunders (ref. 16-15) developed the following relationships.

$$\left. \begin{aligned} \Delta Z &= 1.6 \left(\frac{W'^2 D}{N^2} \right)^{\frac{1}{3}} && \text{for } 0.1 < \frac{\Delta Z}{D} \leq 0.6 \\ \Delta Z &= 2.2 \frac{W'}{N} && \text{for } 0.6 < \frac{\Delta Z}{D} \leq 3 \end{aligned} \right\} \quad (16-9)$$

where *W'* is the rate of ascent of the top of the cloud element. However, the cloud element is composed of an internal circulation such that the vertical air velocity inside the element is given by

$$W \approx 2W' \quad (16-10)$$

Thus, for Hurricane Ellen, the vertical air velocity at the top of the disk (base of the turret) is

$$\begin{aligned} W &= N \left(\frac{\Delta Z^3}{D} \right)^{\frac{1}{2}} \\ &= 41 \text{ m/sec} \end{aligned} \quad (16-11)$$

This is an unusually large vertical velocity and implies

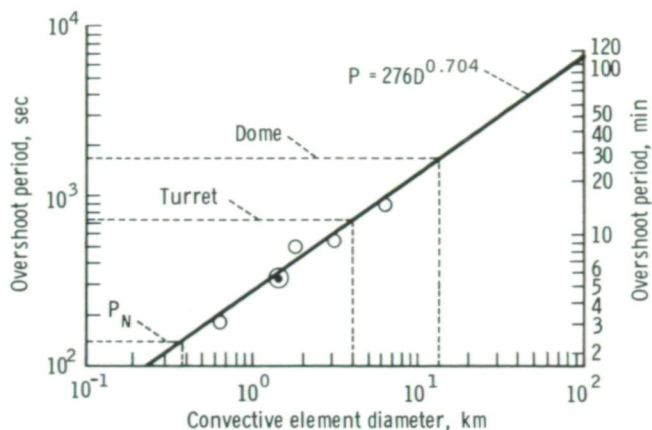


FIGURE 16-24.—Convective time and space scales fitted with a least-squares regression line. Dotted lines indicate the Hurricane Ellen dome, turret, and Brunt-Vaisala period (P_N) scales. The circled data point is the Brunt-Vaisala period plotted from reference 16-13. Additional information on the points is contained in table 16-III and figure 16-25.

very large values for the buoyancy of the air parcels below this level.

The life cycle of the circular cloud itself will now be considered. The approximate life cycle of large circular clouds can be estimated best from analysis of DMSP and SMS data (table 16-IV). For Typhoon Bess, the lifetime of the circular cloud ranges between 12 and 24 hours with a best estimate of approximately 20 hours. For Typhoon Dinah, the lifetime estimate is between 24 and 60 hours with a best estimate of approximately 40 hours. More precise estimates were possible from SMS observations of Hurricanes Eloise and Gladys (1975); their circular cloud lifetimes were 19 and 13 hours, respectively. The circular cloud is present in two Apollo 7 photographs of a previous Hurricane Gladys (fig. 16-15) taken 22 hours apart; thus, a lifetime of approximately 24 hours is indicated. The best estimates, therefore, indicate a CEC life cycle of between 20 and 40 hours.

Because the longest observed period of convective activity is approximately 30 minutes and the life cycle of the circular cloud is on the order of 20 to 40 hours, several convective cycles must occur during the cloud lifetime. This conclusion has been confirmed by the recent SMS observations of Hurricane Eloise during the daytime hours on September 16, 1975, and the SMS-disclosed occurrence of four distinct cycles in Hurricane

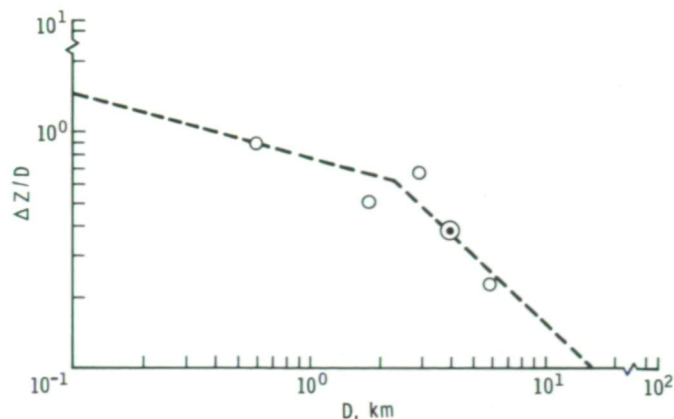


FIGURE 16-25.—Plot of convective element overshoot height to element diameter ratio $\Delta Z/D$ as a function of convective element diameter D . The measured ratio for Hurricane Ellen is indicated by the circled data point. See table 16-III and figure 16-24 for comparative data.

TABLE 16-IV.—Circular Cloud Observations Within Tropical Cyclones From DMSP and SMS Data

| Storm | Date | Time, GMT, hr:min | Observation |
|------------------|----------------|----------------------|------------------|
| DMSP | | | |
| Typhoon Bess | Oct. 10, 1974 | 03:58 | No CEC |
| | | 13:03 | CEC |
| | | 22:27 | CEC ^a |
| | Oct. 11 | 00:02 | Decaying CEC |
| | | 03:39 | No CEC |
| Typhoon Dinah | June 7, 1974 | 02:12 | No CEC |
| | June 8 | 03:25 | CEC |
| | | 11:53 | CEC |
| | 16:07 | CEC | |
| | June 9 | 03:06 | CEC |
| | | 15:58 | Decaying CEC |
| SMS | | | |
| Hurricane Eloise | Sept. 16, 1975 | 03:00 | Beginning CEC |
| | | 22:00 | Decaying CEC |
| Hurricane Gladys | Sept. 30, 1975 | 10:30 | Beginning CEC |
| | | 23:30 | Decaying CEC |

^aFigure 16-14.

TABLE 16-V.—Observed Convective Cycles in Hurricanes Eloise and Gladys

| Storm | Initial time, GMT, hr:min | Interval, hr | Duration, ^a hr |
|----------------------------------|---------------------------|--------------|---------------------------|
| Hurricane Eloise, Sept. 16, 1975 | 09:00 | 2.5 | 2.5 |
| | 11:30 | | — |
| | 16:30 | 5 | 3.5 |
| Hurricane Gladys, Sept. 30, 1975 | 11:00 | 4.5 | 2.5 |
| | 15:30 | 3 | 3 |
| | 18:30 | | 1.5 |
| | 20:30 | 2 | 2 |
| Average | | 2.36 | 2.5 |

^aTime required for circular overshooting anvils to merge with outflow cirrus clouds.

Gladys on September 30, 1975. In both storms, the convection occurred at approximately the same azimuth and radial distance from the storm center during the day despite the 40-m/sec winds near the surface. Table 16-V is a convective cycle summary containing the initial times of each cycle, the time required for the circular overshooting anvils to merge with the outflow cirrus clouds, and the interval between each recurring event. It appears that each convective event successively pushes the tropopause higher and higher. From shadows, it appears that the height of each overshooting turret is the same, but following each cycle, the tropopause is slightly higher than it was initially. This idea is supported by the fact that Kelvin-Helmholtz waves did not appear in Hurricane Eloise until 16 hours after the beginning of the circular cloud. This apparently was the time required for the tropopause to be pushed high enough to encounter sufficiently strong easterly winds in the stratosphere (i.e., easterly windspeeds were increasing with height as in figure 16-21) to destabilize the outflow layer (by means of Kelvin-Helmholtz waves).

Note that for both storms, about twice the time interval has elapsed between 11:00 and 16:00 GMT as had elapsed between cycles at other times of the day. An additional cycle probably occurred at approximately 13:00 to 13:30 GMT but was not observed because of saturation (overexposure) of the photographs due to the high

Sun angle and the lack of compensation for this overexposure in the photographic development process. Assuming that the additional cycle occurred, the average interval between cycles is nearly equal to the length of time between the initial overshoot and the halting of the expansion of the circular anvil. Thus, these analyses indicate that the duration of a distinct convective cycle is approximately 2.5 hours and that six cycles are required to create sufficiently small Richardson numbers ($< 1/4$) at the tropopause to cause dynamic instability and generation of Kelvin-Helmholtz waves. From seven to nine such cycles occur during the life of the circular convective cloud. Because the rise time of the 2.5-hour cycles is 38 minutes and the rise time of the dome events is approximately 7 minutes, it would appear that five or six dome-scale events would make up the active phase of the 2.5-hour cycle. Thus, the circular cloud is actually regenerated seven to nine times by five to six dome-scale events each time.

Further observational evidence for the generation of gravity waves at the tropopause by strong convection was obtained from SMS data for Hurricane Gladys. Four distinct waves in the eastern-hemisphere cirrus clouds were observed to propagate away from the central convective region. The waves had semicircular wave fronts. Table 16-VI contains information on gravity wave speed, time of initial detection t_I , time of dissipation t_F , calculated initial time t_0 , and initial time of the convection cycle t_C for these four waves. The speeds shown are relative to the center of the convective cloud. Each wave can be traced back to an observed convective impulse; therefore, the waves are assumed to be of

TABLE 16-VI.—Summary of Hurricane Gladys Gravity Wave Observations

[September 30, 1975]

| Gravity wave speed, m/sec | | Time, GMT, hr:min | | | |
|---------------------------|--------------------|-------------------|-------|-------|-------|
| NE quadrant | SE quadrant | t_I | t_F | t_0 | t_C |
| 13.5 | 6.4 | 11:30 | 16:30 | 08:30 | 08:30 |
| 8.1 | 4.3 | 14:30 | 18:30 | 08:30 | 08:30 |
| — | 8.1 | 15:30 | 19:30 | 11:30 | 11:00 |
| 10.8 | 8.8 | 19:00 | 21:00 | 15:45 | 15:30 |
| ^a (10.8) | ^a (6.9) | — | — | — | — |

^aAverage speed.

convective origin as proposed for Hurricane Ellen gravity waves. The average wave speed in the northeastern quadrant approximates the 12-m/sec phase speed calculated for Hurricane Ellen waves assuming a wavelength of 10 km. Note that the first two waves listed in table 16-VI appear to come from the same source and that the first wave was observed 3 hours before the slower second wave. This time lapse is in line with the fact that longer waves travel faster and hence would be observed before shorter, slower moving ones.

An important feature of the CEC pointed out by Gentry et al. (ref. 16-2) and confirmed by the SMS observations of Hurricanes Eloise and Gladys is that the CEC moved only very slowly about the storm center and was located to the northeast of the center during most of the period of study. Its velocity as determined from radar was 3 m/sec, whereas that of surrounding echoes was 15 m/sec and that of the low-level wind was 30 m/sec.

Implications for Hurricane Forecasting

The location of each circular exhaust cloud discussed in this report appears to be geographically fixed primarily to the northeast of the circulation center, regardless of the direction of motion of the storm. This location corresponded closely with the location of the

region of maximum wind. Summarized in table 16-VII are parameters of the circular exhaust cloud and their relation to the center of circulation. It appears that the circular clouds develop at a stage of the storm life cycle when the minimum surface pressure has fallen to an average value of 98.3 kPa (983 mbar) ± 0.7 percent (± 0.6 kPa (± 6 mbar)) and the maximum windspeed is 32 m/sec ± 25 percent. On the average, the storm deepens to its minimum pressure 24 to 30 hours after the circular cloud has developed to its maximum size; the average deepening consists of a pressure decrease of 1.4 kPa (14 mbar) ± 50 percent. This conclusion indicates that the average deepening rate following the appearance of the circular cloud is approximately 0.06 kPa/hr (0.6 mbar/hr). Observations of Hurricane Gladys suggest that what actually happens is that storm intensity remains nearly constant during and just following the lifetime of the circular cloud followed by rapid deepening sometime after it disappears.

The mechanism by which rapid storm deepening occurs as a result of intense convective events is uncertain. Recent data from NOAA research flights into tropical storm Eloise at a time when a convective cloud was present reveal a region of intense low-level convergence beneath the cloud together with a significant perturbation in the low-level pressure field. Furthermore, the data indicated a closed middle-level circulation in the immediate vicinity of the cloud rather than

TABLE 16-VII.—Circular Cloud Observations and Tropical Storm Strength

| Storm | Date | β_{storm} | Parameter ^a | | | | | | | |
|------------------------|----------------|------------------------|----------------------------------|-----------------------------|------------------------------|--------------------|----------------------------|---------------------------------|-------------------------------------|----------------------------|
| | | | p_{min} , kPa (mbar) | V_{max} , m/sec | $R_{V_{\text{max}}}$, km | β_V , deg | R_{cloud} , km | β_{cloud} , deg | $\Delta t_{p_{\text{min}}}$, hr | Δp , kPa (mbar) |
| Tropical storm Ellen | Sept. 19, 1973 | NW | 98.5 (985) | 32 | 55 | 090 | 55 | 070 | 30 | 2.3 (23) |
| Tropical storm Gladys | Oct. 17, 1968 | N | 98.6 (986) | 32 | 25 | 045 | 28 | 045 | — | — |
| Hurricane Gladys | Oct. 18, 1968 | NE | 97.8 (978) | 40 | — | — | 20 | 090 | 27 | .8 (8) |
| Typhoon Patsy | Oct. 11, 1973 | WNW | 97.8 (978) | 45 | 10 | 270 | — | — | — | — |
| Tropical cyclone Dinah | June 8, 1974 | WNW | 98.5 (985) | 25 | 78 | 080 | 74 | 120 | — | — |
| Tropical cyclone Dinah | June 9, 1974 | WNW | 97.9 (979) | 28 | 130 | 330 | — | 270 | 41 | 1.1 (11) |
| Tropical storm Emma | June 16, 1974 | N | 99.5 (995) | 20 | 93 | 010 | 83 | 090 | 10 | .7 (7) |
| Tropical cyclone Bess | Oct. 10, 1974 | WNW | 98.1 (981) | 32 | 130 | 050 | 150 | 050 | 14 | 2.1 (21) |
| Hurricane Eloise | Sept. 16, 1975 | W | 99.7 (997) | 35 | 110 | 060 | 120 | 090 | — | — |
| Hurricane Gladys | Sept. 30, 1975 | WNW | 97.7 (977) | 40 | 37 | 020 | 37 | 020 | 45 | 3.7 (37) |

^a β_{storm} = storm direction of motion; p_{min} = minimum sea-level pressure; V_{max} = maximum wind velocity; $R_{V_{\text{max}}}$ = distance from storm center of V_{max} ; β_V = azimuth of $R_{V_{\text{max}}}$; R_{cloud} = distance of CEC from center of circulation; β_{cloud} = azimuth of CEC from center of circulation; $\Delta t_{p_{\text{min}}}$ = approximate time interval from formation of CEC to occurrence of minimum sea-level pressure; and Δp = decrease in pressure following formation of CEC.

over the low-level circulation center. It appears that a significant perturbation is present in the wind and pressure fields because of the large convective cloud. The questions of the nature of the adjustment process between the wind and pressure fields and the chain of events leading to storm deepening are still unanswered.

It is possible to estimate the magnitude of the surface pressure fall to be expected in the eyewall beneath the convective cloud. Neither the length of time required to achieve these falls nor the length of time the lower pressure would be maintained is estimated. The latter presumably would depend on whether the perturbation in the wind field produced the cloud and, hence, the pressure perturbation or the reverse. It is a generally accepted principle that the pressure field will adjust to changes in the wind field on the cloud or hurricane scale, but not the reverse. Therefore, some sort of large-scale interaction with the incipient storm circulation could be presumed to result in the low-level convergence fields needed to support the large convective events. This interaction would begin a sequence of events leading to storm deepening, one stage of which would be a local pressure fall in the maximum wind region.

Estimates of the magnitude of pressure fall to be expected at the base of a circular cloud can be obtained from the following expression.

$$\Delta p = \underbrace{-\hat{g}\bar{\rho} \Delta z}_{\text{I}} - \underbrace{\left(\frac{\bar{v}}{r}\right) \left(\frac{\Delta \bar{w}}{\Delta \phi}\right) \bar{\rho} \Delta z - \bar{w} \Delta \bar{\rho}}_{\text{II}} \quad \underbrace{- \bar{w} \Delta \bar{\rho}}_{\text{III}} \quad (16-12)$$

TABLE 16-VIII.—Estimated Atmospheric Pressure Difference Between Convective Cloud and Environment at Cloud Base

| Atmosphere layer | p - p', kPa (mbar) | | | |
|---------------------------|---------------------|-----------------------------|-----------------------|---------------|
| | Term I ^a | Term II ^a (b) | Term III ^a | Total |
| Lower troposphere | -1.58 (-15.8) | -0.25 (-2.5) | -0.56 (-5.6) | -2.14 (-21.4) |
| Upper troposphere | -0.68 (-6.8) | -0.39 (-3.9) | 0.0 | -0.68 (-6.8) |
| Lower stratosphere | | | | |
| 2-km overshoot | +0.60 (+6.0) | 0.0 | +0.14 (+1.4) | +0.74 (+7.4) |
| 4-km overshoot | +1.80 (+18.0) | 0.0 | +0.14 (+1.4) | +1.94 (+19.4) |
| Totals | | | | |
| Surface to 2-km overshoot | -1.66 (-16.6) | -0.64 (-6.4) | -0.42 (-4.2) | -2.08 (-20.8) |
| Surface to 4-km overshoot | -0.46 (-4.6) | -0.64 (-6.4) | -0.42 (-4.2) | -0.88 (-8.8) |

^aEquation (16-12).

^bTerm II contribution occurs at the edges of the updraft; therefore, Term II values are not reflected in the "Total" column.

where \hat{g} is a reduced gravity, v is horizontal windspeed along the y -axis (positive toward north), w is vertical windspeed, r is the radius of the cloud, ϕ is the azimuthal coordinate, and the overbar denotes an average over a layer. See the appendix for derivation of this relation. Assuming that the equivalent potential temperature of the environment $\hat{\theta}_e$ and of the cloud θ_e as well as the in-cloud vertical velocity are distributed as shown in figure 16-26, then three levels in the vertical are defined: the lower troposphere (0 to 6 km), the upper troposphere (6 to 16 km), and the lower stratosphere (16 to 18 km). Each of the three terms in equation (16-12) has been evaluated for each layer. Term I is the hydrostatic term, Term II is the nonhydrostatic term due to the horizontal shear of the vertical wind, and Term III is the nonhydrostatic term due to the vertical shear of the vertical wind. The calculations are summarized in table 16-VIII.

It should be noted that Term II does not actually contribute to the maximum pressure decrease below the undilute updraft in the convective cloud. Its contribution occurs at the edges of the updraft and hence would tend to spread out the maximum. The nonhydrostatic terms (II and III) would exist only during the active phase of the updraft. The hydrostatic term (I) tends toward zero as the overshooting turrets reach greater heights and as cooling within the overshooting turret increases (i.e., cloud density becomes greater than environment density).

The total pressure decrease for a 2-km overshoot is approximately 2.0 kPa (20 mbar), whereas that for a 4-km overshoot is only approximately 0.4 kPa

(4 mbar). These estimates are based on a large parcel-environment θ_e difference in the lower levels of 10 K (10° C) and a large middle and upper level vertical velocity of 40 m/sec. Therefore, these pressure falls represent a probable extreme case.

As the number of surges increases and the tropopause is pushed higher, the cold dome thus formed should result in the creation of an anticyclonic circulation aloft. The initial radial outflow will thus be transformed to more of an anticyclonic circulation, which will help sustain a vertical circulation in the region of the circular cloud.

FEATURES OF MATURE TROPICAL STORMS REVEALED BY SKYLAB PHOTOGRAPHS

In December 1973, the Skylab 4 crewmen photographed the cloud structures of the mature tropical cyclone Lottie in the South Pacific Ocean. The Skylab groundtrack relative to the storm on December 8 is superimposed on an NOAA-2 image in figure 16-27. The Skylab photograph shown in figure 16-28(a) was taken on December 8 at 23:43:30 GMT (looking toward the north), when tropical cyclone Lottie was 165 km west-southwest of Nandi, Fiji, and moving toward the southeast at a speed of approximately 12 km/hr. Although the photograph was severely overexposed (by approximately three f-stops), detailed cloud features are made visible by photographic enhancement (fig. 16-28(b)). The eyewall region appears to be generally sloping outward from the center and reaches a maximum height at a radius of approximately 36 km (dashed circle). The cloud tops then appear to slope downward and outward until the dark shadow in figure 16-28(b) ringing the overshooting clouds is reached. At this location, the cloud height drops abruptly to the mean cirrus cloud height. The general impression is that the cloud is a giant mushroom with a funnel-shaped hole in the middle. The region of most active convection appears to be in the southwestern and southern quadrants with the least active region in the northern quadrant. Figure 16-28(c) is an enlargement of the southwest eyewall region from figure 16-28(b) and shows the sloping eyewall and many convective turrets. The turrets appear to be oriented along lines that extend radially outward from the eye. In the region of active turrets, there are as many as 100 turrets averaging 1.5 km in diameter and spaced approximately 2.1 km apart. The eastern semicircle of the storm is shown in more

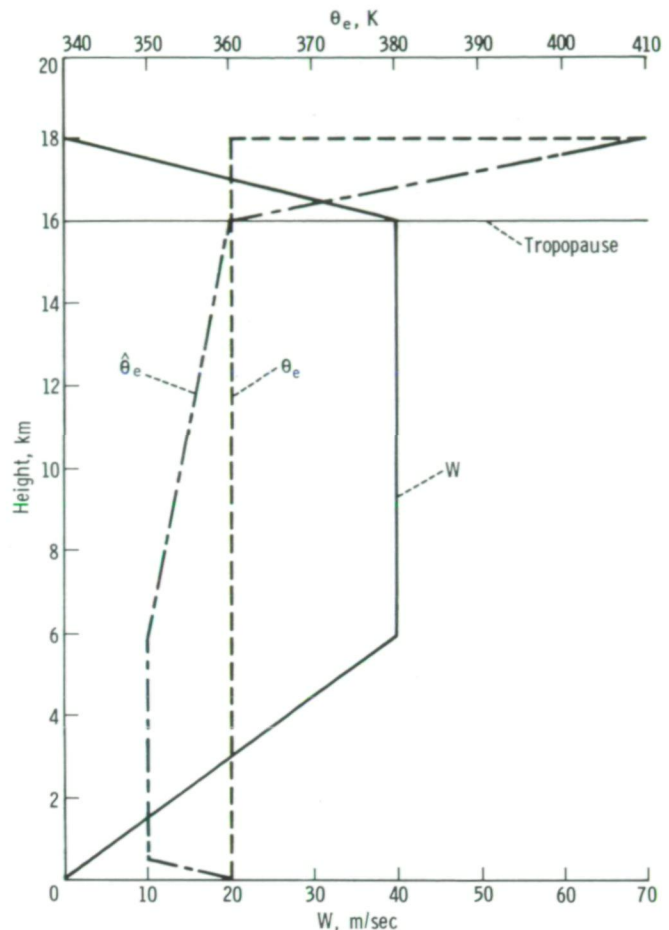


FIGURE 16-26.—Hypothetical distribution of equivalent potential temperature ($\hat{\theta}_e$ for environment, θ_e for cloud) and vertical air velocity W with height within a circular hurricane cloud.

detail in figure 16-29, which is enhanced to show cloud features at a less oblique angle than that of figure 16-28. In this quadrant, the overshooting turrets appear to be slightly less active and the eyewall slope slightly greater. Also, there seems to be an indication of transverse shear waves with a wavelength of 3.6 km.

Figures 16-30(a) and 16-30(b) are Skylab photographs of tropical cyclone Lottie on December 11 when the storm was beginning to decay after reaching its maximum intensity at a wind velocity of 38 m/sec. The eye has disappeared, but there is a region of active convection with a central dome approximately 11 km across. Hundreds of turrets on a scale of 1 to 2 km cover an area approximately 125 km in diameter.

The best documentation of eyewall tilt is in two photographs (figs. 16-31 and 16-32) obtained by the

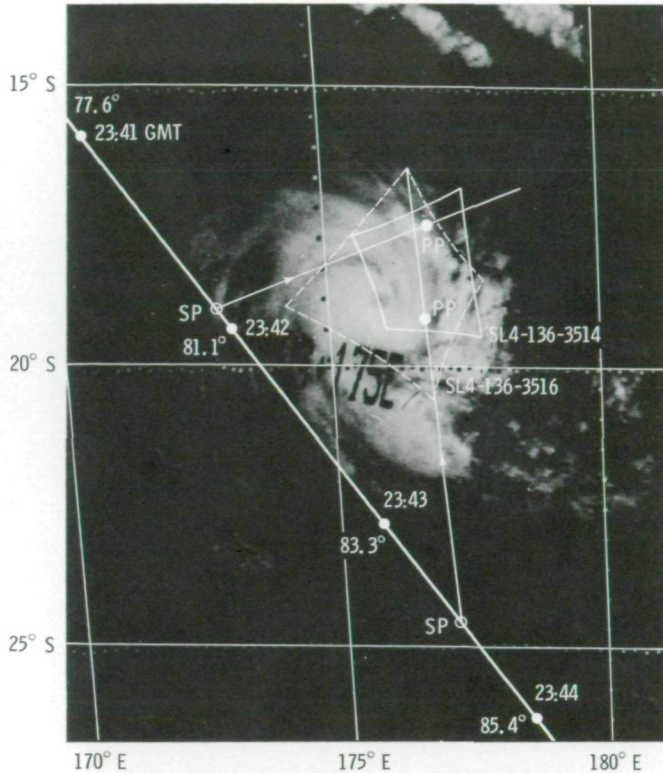
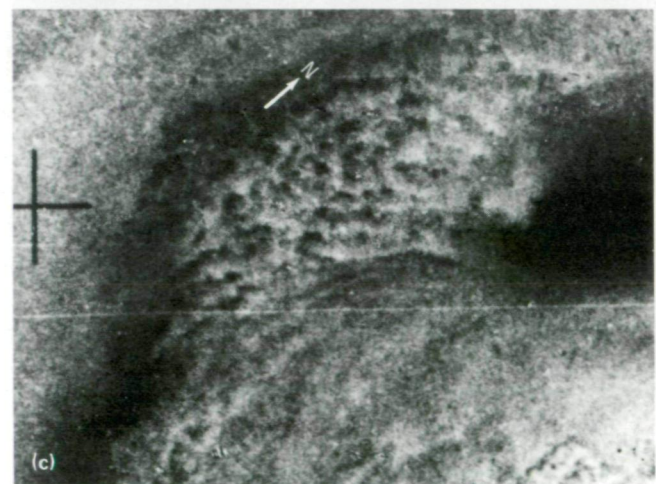
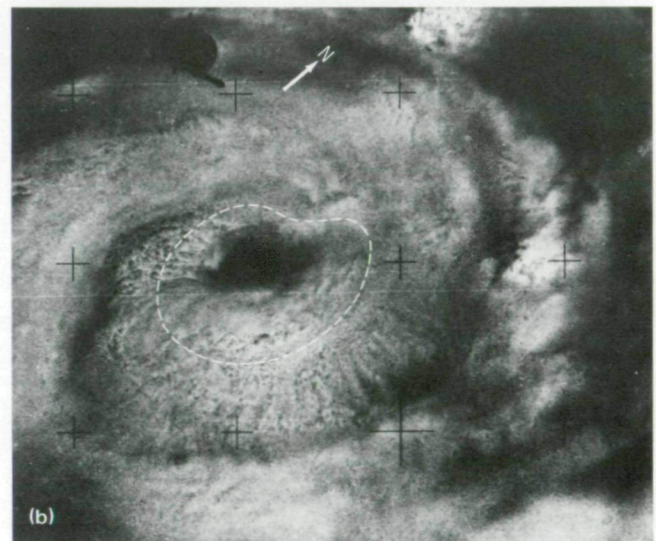
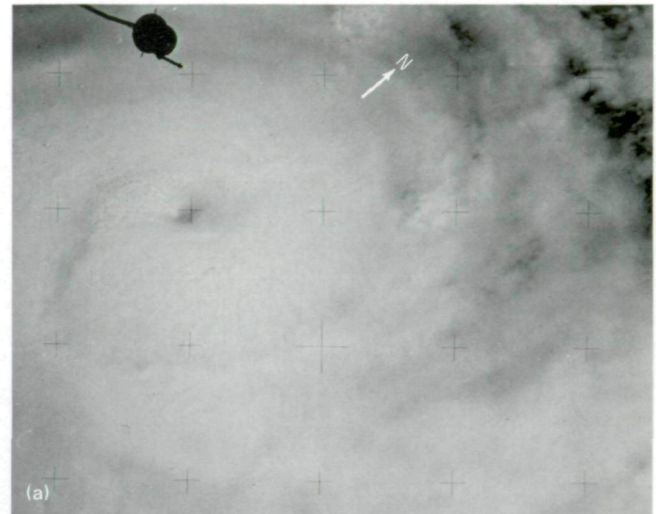


FIGURE 16-27.—An NOAA-2 image of tropical cyclone Lottie on December 8, 1973, at 20:51 GMT. The Skylab groundtrack is shown with subsatellite points plotted at 1-minute intervals and labeled with times and solar elevation angles. Approximate Skylab photograph boundaries, principal lines, subsatellite points (open circles), and principal points also are indicated together with Skylab frame numbers.

Skylab 3 crewmen over Hurricane Irah in the eastern Pacific Ocean at approximately 00:00 GMT on September 24, 1973, when the storm was near the sunset terminator. Figure 16-33 is a Nimbus 5 image of Hurricane Irah taken approximately 7 hours after the Skylab overflight. Because the solar elevation angle was close to zero, the ring of sunlit clouds seen in figure 16-31 indicates the location at which the eyewall clouds begin sloping downward. Figure 16-32 reveals dramatically the cloud structure inside the eye and the intersection of the eyewall clouds with the low-level "scud" clouds at an altitude of approximately 2 km. The wall cloud

FIGURE 16-28.—Skylab photograph of tropical cyclone Lottie taken on December 8, 1973, at 23:43:30 GMT. The maximum windspeed was 35 m/sec; the minimum surface pressure was 97.7 kPa (977 mbar). The storm was located at latitude 18.7° S, longitude 176.0° E (SL4-136-3516). (a) Unenhanced photograph. (b) Enhanced photograph (slightly enlarged) showing the eyewall at maximum height (dashed line). (c) Enlargement of the southwest eyewall region. →



diameter is approximately 15 km at its base and approximately 35 km at its top. The wall cloud tilt varies from approximately 10° on the east side to approximately 45° on the west side.

Another interesting feature seen in figure 16-32 is the series of waves that seem to emanate from the southern edge of the eyewall. Their wavelengths appear to be approximately 1.5 to 2.0 km. Nine distinct wave crests are present. Although the nature of these waves is uncertain, they are quite similar to waves that appear in a DMSP satellite photograph of Hurricane Ava (fig. 16-34).

The tilting eyewall structure appears to be characteristic of many mature hurricanes, and it has been inferred from analysis of aircraft radar data that show the vertical precipitation profiles within convective clouds in hurricane eyewalls. These radar observations, however, were doubted for many years and the outward tilt was ascribed to errors in the radar data. In recent years, more confidence has been gained in the interpretation of the radar data and, with the Skylab photography that shows the eyewall tilt, the old observations may now be viewed with additional insight.

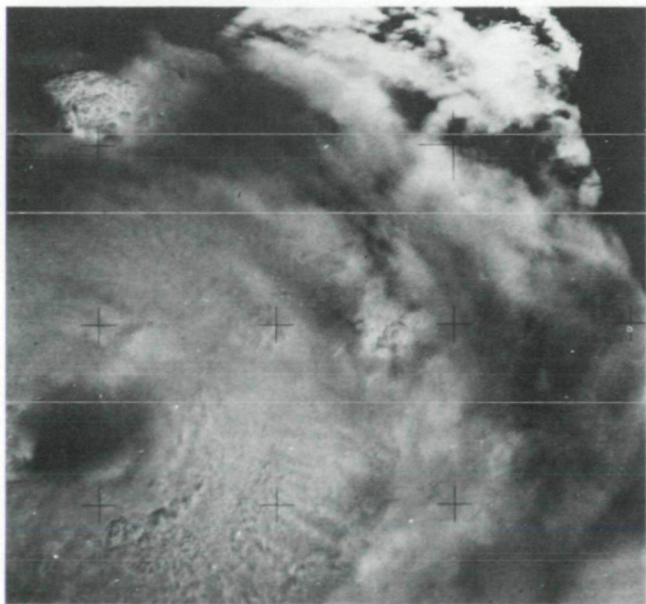


FIGURE 16-29.—Enhanced Skylab photograph of tropical cyclone Lottie taken on December 8, 1973, at 23:41:55 GMT. The windspeed, the pressure, and the geographical coordinates of the storm were approximately the same as those in figure 16-28. The eastern semicircle of the storm is detailed in this frame (SL4-136-3514).

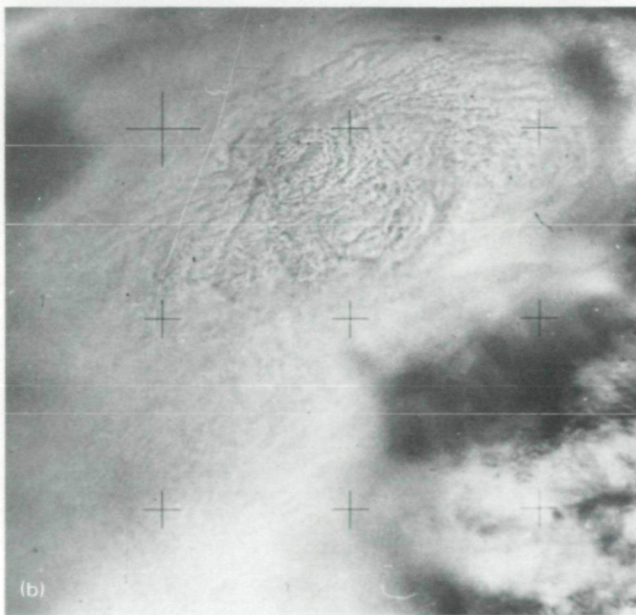
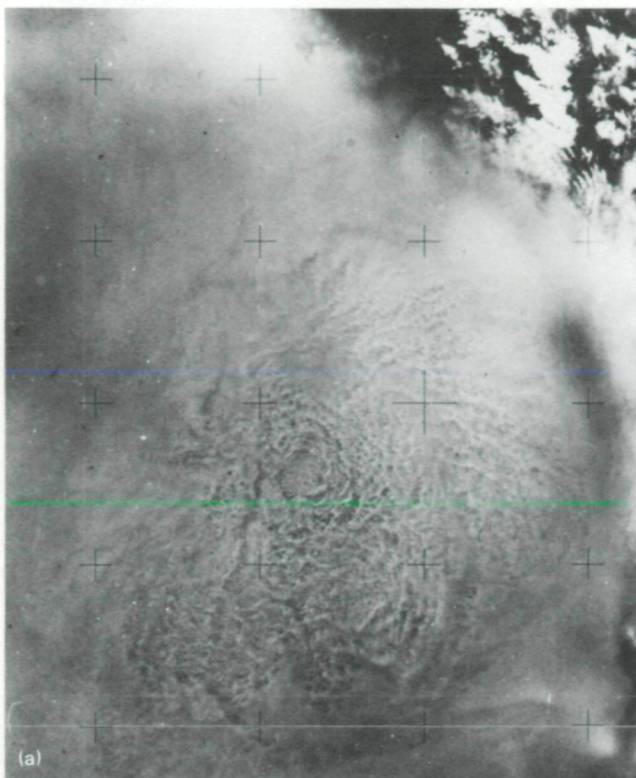


FIGURE 16-30.—Skylab photographs of tropical cyclone Lottie taken on December 11, 1973. The maximum windspeed was 38 m/sec, and the minimum surface pressure was 97.2 kPa (972 mbar). The storm was located at latitude 21.7° S, longitude 175.3° W. (a) Vertical photograph taken at 00:07 GMT (SL4-136-3541). (b) Oblique photograph taken at 00:08 GMT (SL4-136-3543).

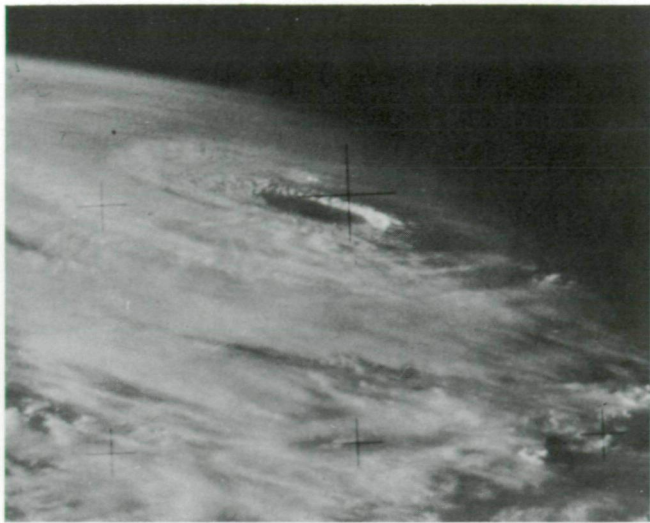


FIGURE 16-31.—Skylab 70-mm Hasselblad photograph of Hurricane Irah taken on September 24, 1973, at 00:00 GMT. The maximum windspeed was 37 m/sec; the minimum surface pressure was 97.7 kPa (977 mbar). The storm was located at latitude 18.0° N, longitude 107.8° W (SL3-122-2627).

Typical examples of eyewall tilts ranging from 20° to 45° were reported in 1960 by Bigler and Hexter (ref. 16-16), in 1961 by Jordan and Schatzle (ref. 16-17), in 1966 by Senn (ref. 16-18), and in 1972 by Black et al. (ref. 16-19). Typical radar images are shown in figure 16-35. The horizontal line across the center of the image is the return from the sea surface. Eyewall tilts of 45° are fairly common, especially above an altitude of 4 km.

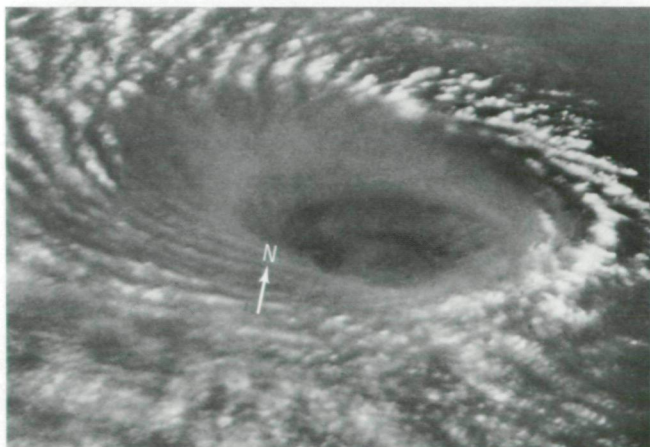


FIGURE 16-32.—Skylab 35-mm Nikon photograph of Hurricane Irah taken with a 135-mm telephotographic lens (SL3-118-2189).

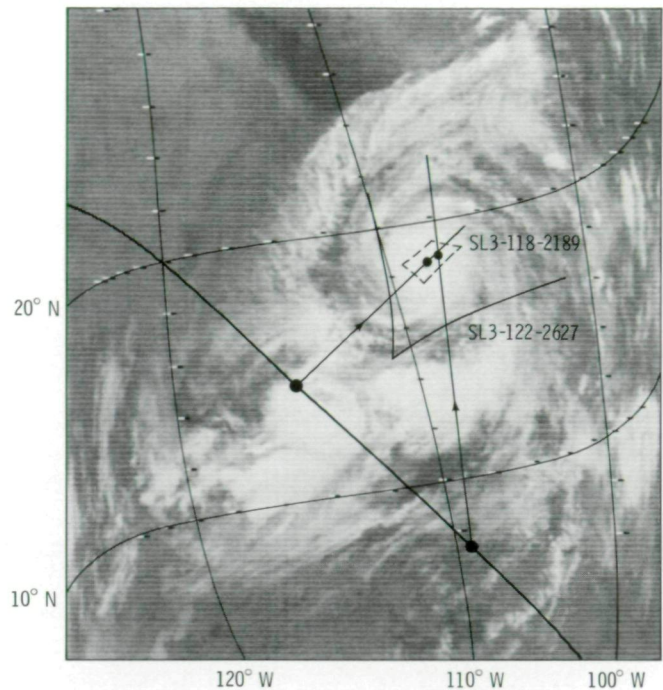


FIGURE 16-33.—A Nimbus 5 image of Hurricane Irah on September 24, 1973, at 06:45 GMT. A medium-resolution infrared radiometer was used at a wavelength of 11.5 μm . The Skylab groundtrack, the approximate locations of the Skylab photographs, and the principal lines, the subsatellite points, and the principal points of the Skylab frames are shown.

Based on these data, the storm structure that seems to be emerging is one in which the eyewall clouds are nearly vertical in quadrants characterized by intense convection. As the convective clouds decay, they tilt outward because of a decrease with height of the horizontal pressure gradient force. The motion of air parcels in a mature hurricane is governed by a balance between pressure gradient and centripetal forces. Because air parcels brought aloft by convective clouds in the eyewall approximately conserve their momentum and hence their centrifugal accelerations, the vertical shear of the horizontal wind is usually small in mature hurricanes. Thus, at the higher altitudes, the outward centripetal force is greater than the pressure gradient force and the parcels spiral outward until a balance is achieved. In the active intense convective clouds, the air parcels are brought aloft very rapidly; thus, there is insufficient time for the forces to achieve balance. As the convective cloud rotates around the eyewall and the updrafts decrease in intensity, the in-cloud air parcels have enough time to achieve a balance of forces. The cloud boundaries then tilt so that they

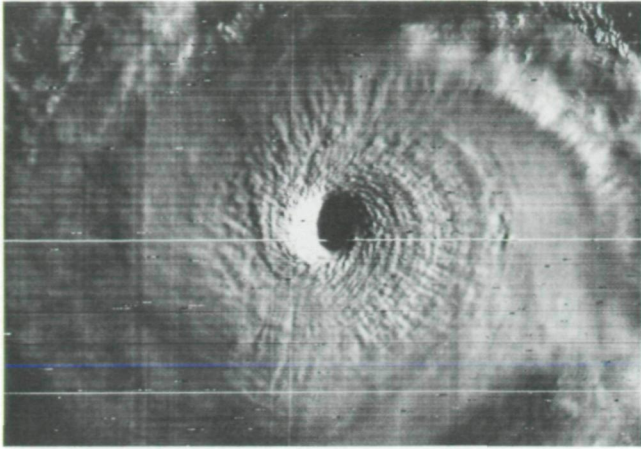


FIGURE 16-34.—A DMSF satellite image of Hurricane Ava obtained on June 7, 1973, at 15:00 GMT.

become parallel to constant absolute angular momentum trajectories. A schematic model of the airflow and cloud structure in a mature hurricane having one region of intense convection is shown in figure 16-36. As the clouds develop and move away from the generating region of intense convection, they decay and tilt outward.

The existence of a significant eyewall tilt in hurricanes has important implications for their structure. Some of the air that is carried aloft by the convective elements converges inward toward the storm center. This mass convergence in the upper layers of the eye forces some air parcels downward. The subsiding air parcels warm adiabatically as they descend. There is thus a subsidence within the eye that causes it to be as much as 15 K (15° C) warmer than the environment outside the storm. Recent analysis by Shea (ref. 16-20) and by Jorgenson³ suggests that on the convective scale, compensating downward vertical velocity is also induced immediately adjacent to the inner eyewall boundary and is superimposed on the eye-scale subsidence. Thus, for many mature storms, the maximum temperatures in the middle levels are observed not at the center of the eye but at the eyewall boundary.

The subsidence warming throughout a large depth of the atmosphere within the eye contributes to the very low surface pressures observed in hurricanes. If the eyewall is tilted, the surface pressure gradient within the eyewall will be determined in part by the degree of tilt. However, with more tilt, the convective cell is less

³Personal communication, 1975.

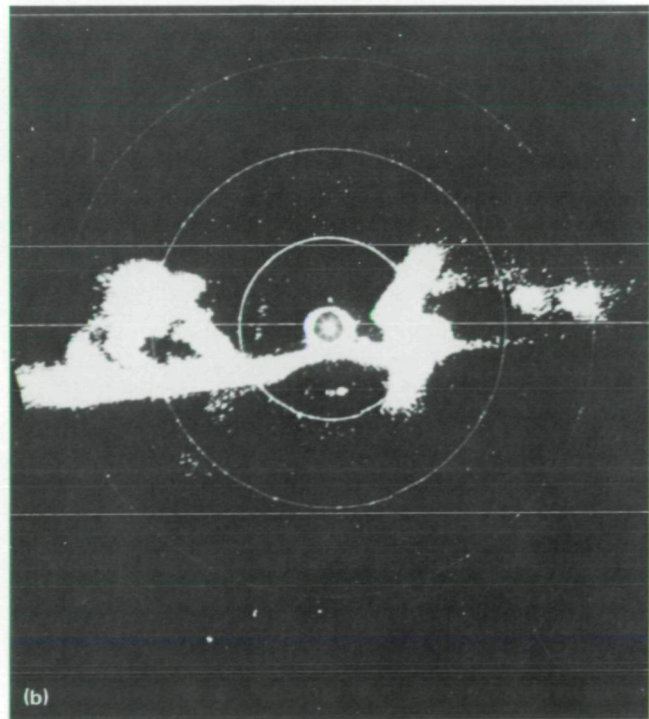
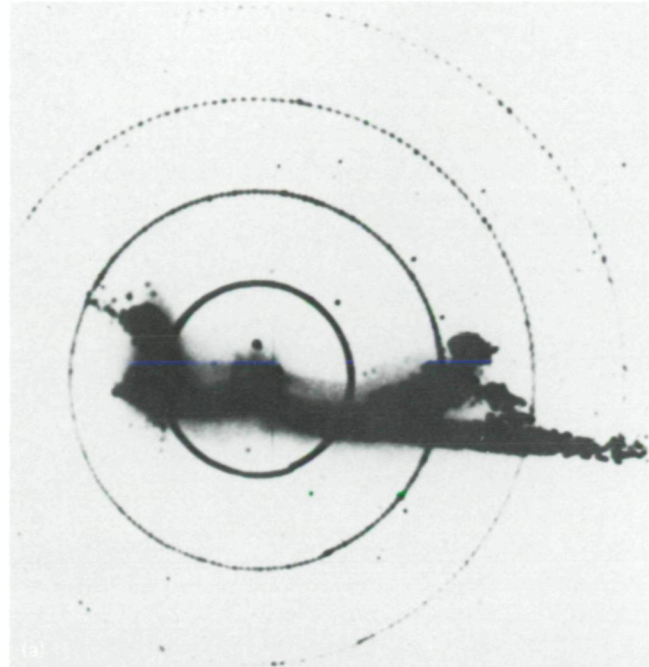


FIGURE 16-35.—Radar vertical sections through a hurricane eye. The horizontal echo at the base is the sea surface. The echo surrounding the aircraft at the center is a false return. Range marks are at 9.25-km intervals. (a) Hurricane Flora, October 3, 1963. Eyewall tilt on the right is 45°; on the left, 30°. (b) Hurricane Cleo, August 23, 1964. Eyewall tilt on the right is 35°; on the left, 40°.

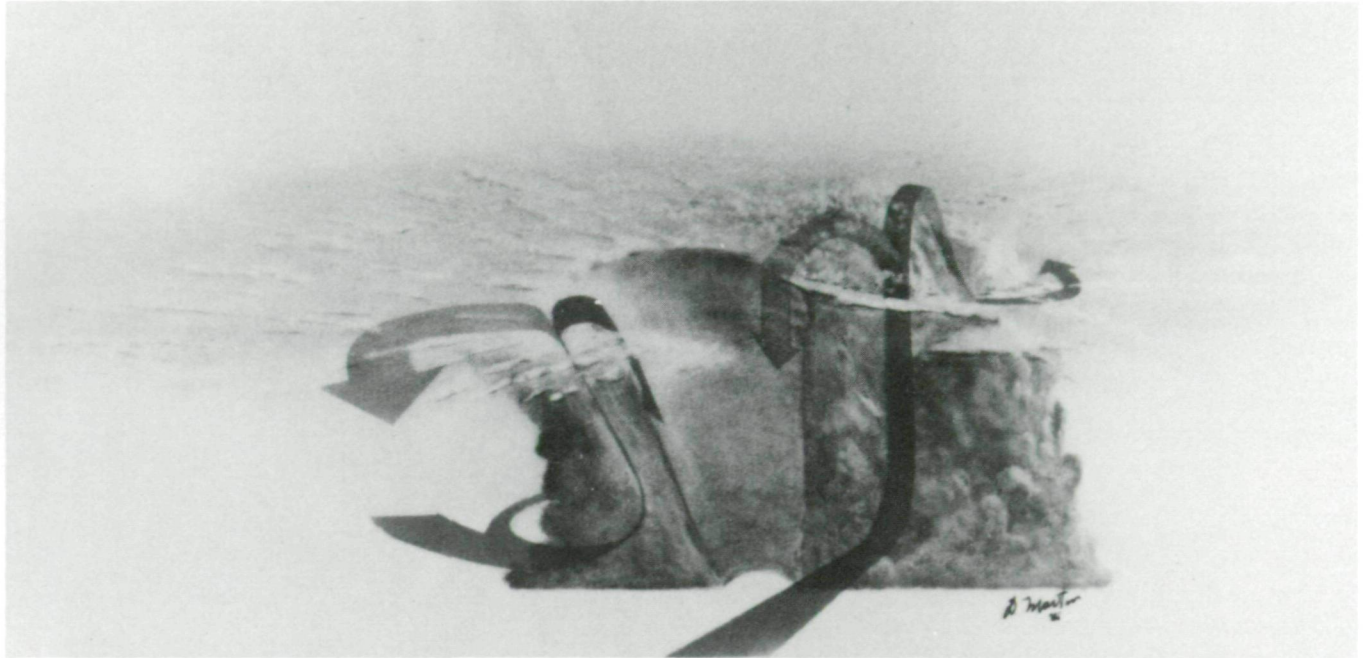


FIGURE 16-36.—Schematic diagram of eyewall cloud structure and airflow in a mature hurricane characterized by a single region of intense convection.

active, the compensating downdraft is weaker, and the increase in eye temperature is less.

In the convective model shown in figure 16-36, most pressure-fall mechanisms within the cloud are in the lower troposphere, whereas the pressure-rise mechanisms are in the upper troposphere. If the eyewall tilts, the surface pressure at the inner edge could fall farther because it would not be canceled by rises aloft.

Another possible effect of eyewall tilt is the extension of the cloud lifetime. In contrast to its behavior in a vertical cloud, rain from the tilted convective cloud would fall adjacent to rather than through the updraft. This lack of suppression would allow a given updraft to be sustained for a longer period.

For some time, there has been a dispute about the mechanism that causes the very low pressures, the strong pressure gradient, and the resulting strong winds in a hurricane. Riehl and Malkus (ref. 16-21) stated that the pressure drop was due to the release of latent heat when water vapor condensed into liquid water in convective clouds. Water vapor and sensible heat were postulated as being continually supplied to the atmosphere from the ocean by evaporation and conduction. Byers (ref. 16-22) cited as proof of the oceanic contribution the observations of Depperman (ref. 16-23)

that the surface air temperature remained nearly constant as the eye approached and the pressure fell. It was reasoned that if the air was not being continually warmed by the ocean, the temperature should fall as the pressure fell. Recently, Carrier et al. (ref. 16-24) suggested that the entire surface pressure fall is due to subsidence aloft and that evaporation from the ocean is not required.

Results of this and other studies have suggested that surface pressure is a function of the heating due to latent heat release within convective clouds coupled with the heating due to subsidence above the sloping eyewall. The asymmetric wind distribution in a hurricane may in part be due to the changing eyewall slope around the circumference of the eyewall. Thus, the maximum winds should occur near the most intense convection and overshooting turrets, where the pressure-fall mechanisms are greatest.

The eyewall structure of Hurricane Ellen is shown in two Skylab photographs obtained on September 21, 1973, 2 days after the circular cloud photographs (figs. 16-1 and 16-2) were taken. Figure 16-37(a) is an NOAA-2 photograph of Hurricane Ellen on September 21 at 12:30 GMT showing the Skylab orbital groundtrack relative to the storm and the location of the

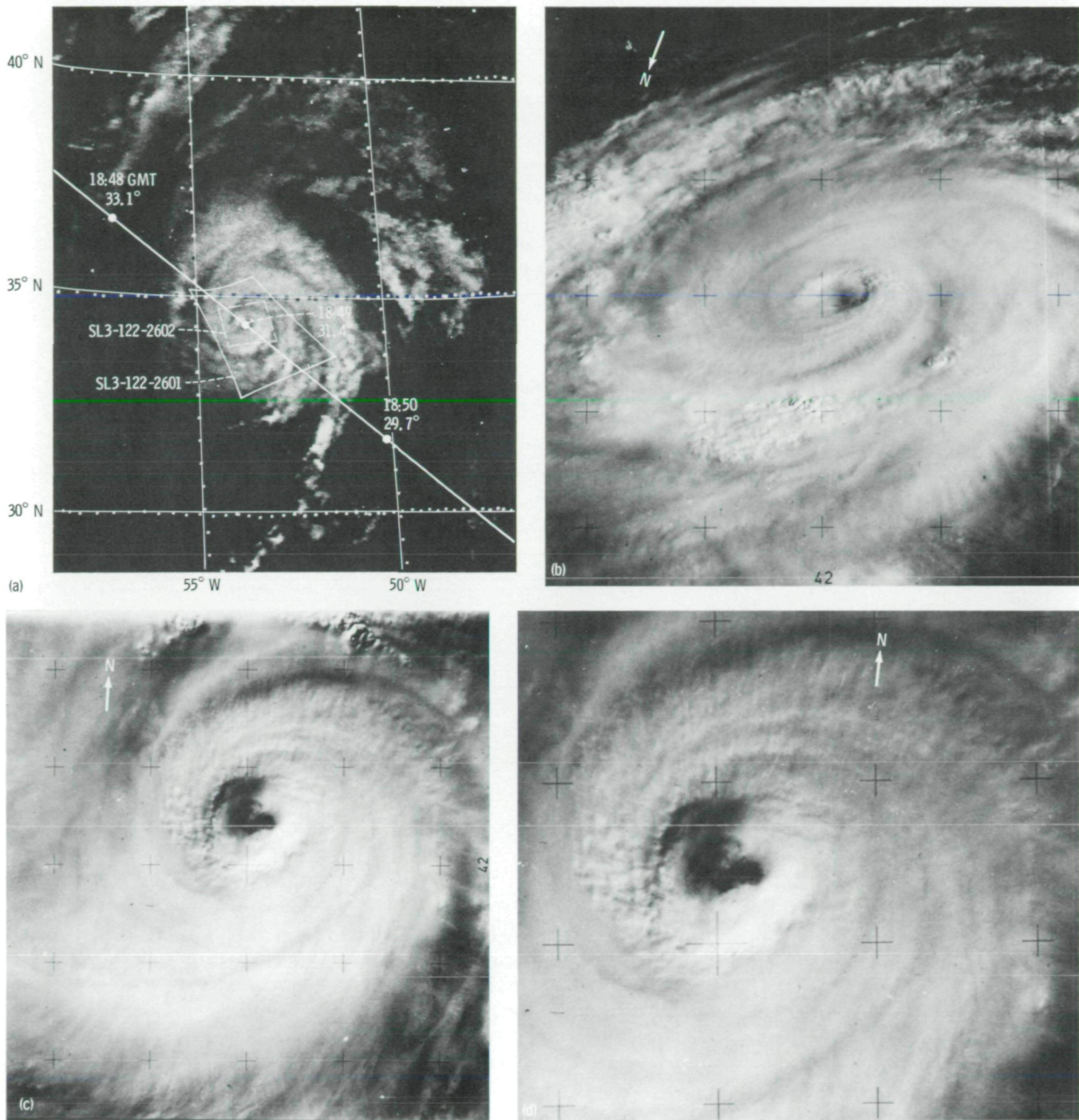


FIGURE 16-37.—Photographs of Hurricane Ellen on September 21, 1973. (a) An NOAA-2 image taken at 12:30 GMT. The Skylab groundtrack has been shifted so that its location relative to the storm center is indicated. Also shown are the approximate boundaries of the Skylab photographs, the Skylab subsatellite points with times and approximate solar elevation angles, and the Skylab frame numbers. (b) Southeastward-looking oblique Skylab photograph obtained at 18:48:20 GMT, when the maximum windspeed was 55 m/sec, the minimum surface pressure was 96.2 kPa (962 mbar), and the storm was located at latitude 36.0° N, longitude 53.0° W (SL3-122-2601). (c) Vertical Skylab photograph obtained at 18:49:00 GMT, when the conditions and location of the storm were approximately the same as those in figure 16-37(b) (SL3-122-2602). (d) Enlargement of figure 16-37(c).

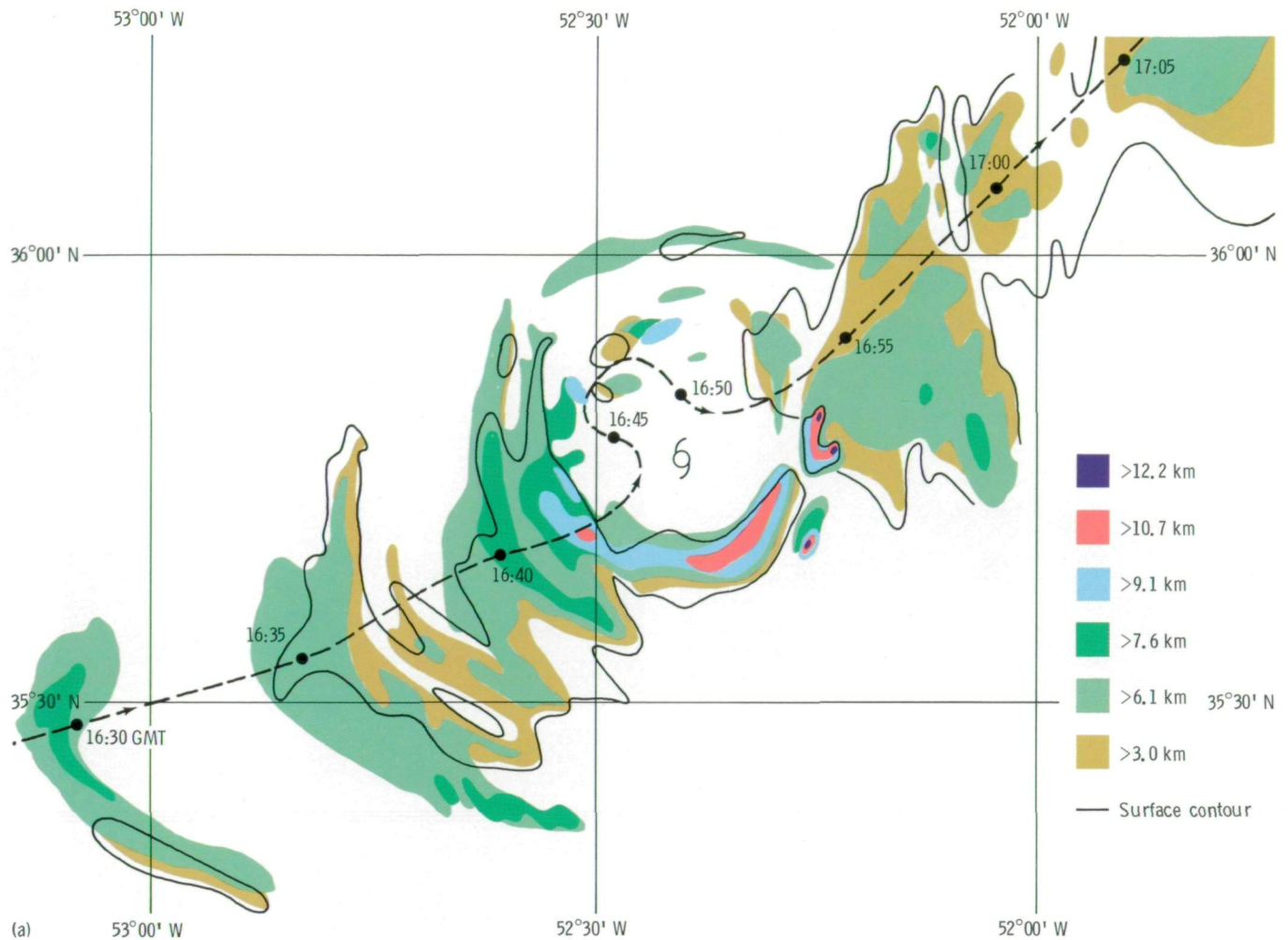


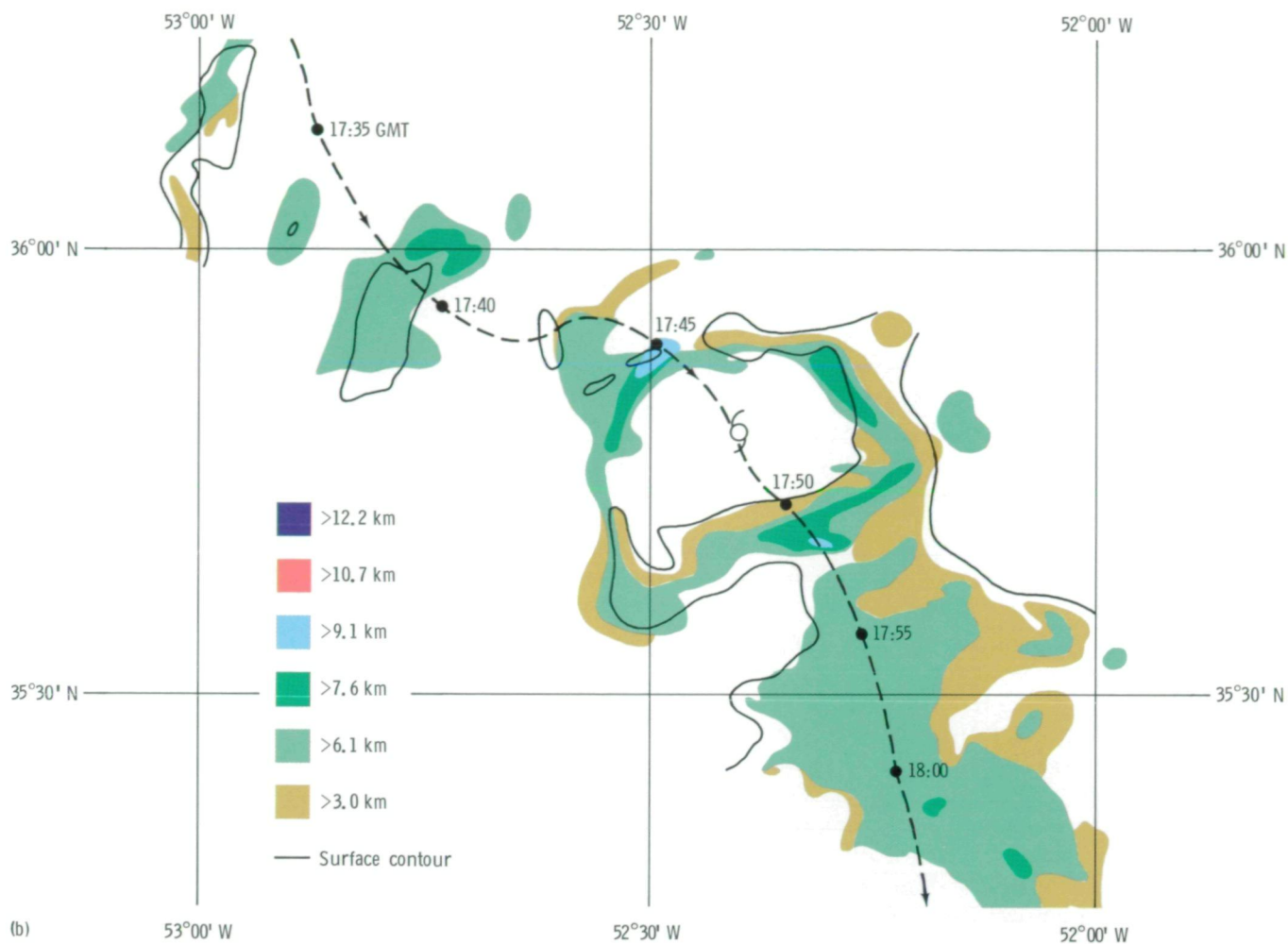
FIGURE 16-38.—Radar echo height analyses within Hurricane Ellen on September 21, 1973, based on NOAA airborne radar for the times noted. (a) 16:30 to 17:05 GMT. (b) 17:35 to 18:05 GMT.

Skylab frames. Figure 16-37(b) is an oblique view, and figure 16-37(c) is a vertical view that shows details of the eyewall cloud region as well as the large, well-developed eye, which is approximately 40 km in diameter. Figure 16-37(d) is an enlargement of figure 16-37(c), in which the eyewall structure resembles that seen in the enhanced photograph of tropical cyclone Lottie (fig. 16-28(b)). Note that each storm has only one region of active, intense convection. For Hurricane Ellen, the intense convective region is in the southern quadrant of the storm. Several turrets having a diameter of approximately 3.1 km are visible in this region. For comparison, figures 16-38(a) and 16-38(b) show radar echo height analyses that were made on the basis of

radar data obtained within 1 hour of the Skylab photographs (figs. 16-37(b) and 16-37(c)). There is good correlation of the cloud features in the eyewall cloud region with the radar echoes. The radar echoes in the southern quadrant are nearly vertical, whereas the echoes in the southwestern quadrant are weaker and tend to tilt outward.

RECOMMENDATIONS FOR THE FUTURE

The most important contribution to the field of tropical storm research by the Skylab Visual Observations Project was the stereophotography of tropical storm



Ellen. This imagery portrays the type of information needed in future research. Because of the significance of this photography to the study of the circular hurricane cloud and related features, there is a need to determine how typical it is of developing storms. Hence, in the future, stereophotographs of developing tropical storms should receive a high priority because, in the judgment of this writer, they will yield significant new information. Stereopairs of mature storms with well-defined eyes should also be obtained in order to determine their use in study of these features. In the future, stereophotography of tropical storms should be the rule and not the exception. Single photographs of tropical storms yield almost no quantitative information compared to that from a stereopair.

This emphasis makes it mandatory that the spacecraft observer be well trained and able to distinguish interesting or little-known features, such as the circular convective cloud, from common or well-known features. This capability is especially pertinent since the emphasis in the future will be on investigation of developing systems. Suspicious areas can be identified from the ground, but the decision as to their significance, in many cases, will have to be made by the astronaut.

The nature of the phenomenon makes it absolutely necessary that crew scheduling be flexible. One of the greatest potential payoffs from handheld-camera photography is the large amount of scientific data return realized by a small amount of crew effort and

preparation. Some sort of flexible system is needed to study variable and moving observation sites such as tropical storms.

Increased opportunities for obtaining stereopair observations will be possible during the Space Shuttle era. By the early 1980's, the meteorological community will have available a worldwide network of operational geostationary satellites that will make possible the monitoring of target areas on a continuous, near-real-time basis for site-planning purposes.

For accurate stereographic analysis of cloud heights (± 10 m), some increase in the sophistication of the camera system will be needed. Absolute time of each photograph to within 1 second and relative time between stereophotographs to within ± 0.1 second is needed for optimum results. Camera-pointing angles accurate to within $\pm 1^\circ$ are required.

The major problem with nearly all tropical storm photographs is that they are consistently overexposed by two to three f-stops. Tropical storm tops are the brightest objects on the face of the Earth and also have a small amount of contrast; these facts must be considered when photographing them. Since the latitude of most films does not extend from the dark shades of the ocean to the bright shades of the storm tops, the former must be sacrificed to document the detail in the latter.

Several suggestions are offered to improve photographs of tropical storms. A fine-grain (low ASA) wide-latitude film appears to be best. The wide latitude is suggested to compensate for exposure errors. If a precise technique for automatically determining exposure can be devised, then use of a narrow-latitude film would be better in order to improve contrast. To further improve contrast, haze filters and especially polarizing filters should be used. Use of a red filter with black-and-white film would also improve contrast.

A selection of cameras with various lenses attached should be available. Because the circular-cloud- and eyewall-scale events are of greatest interest, these scales should nearly fill the field of view for best resolution. Since the scales of these events are on the order of 200 to 300 km, the camera field of view should be 200 to 300 km on a side. Thus, telephotographic, standard, and wide-angle lenses should be available. Depending on spacecraft altitude and camera-pointing angle, the lens

that approximates this field of view should be used. A wide-angle photograph to put the site in perspective with its surroundings is also highly desirable.

The quality of 70-mm photographs was superior to that of 35-mm photographs. Therefore, it would be advisable that three 70-mm single-lens reflex cameras, each equipped with clock data chambers, be carried on future manned missions. One camera should have a wide-angle lens, another a standard lens (e.g., a 90-mm lens), and another a telephotographic lens (e.g., a 200-mm lens).

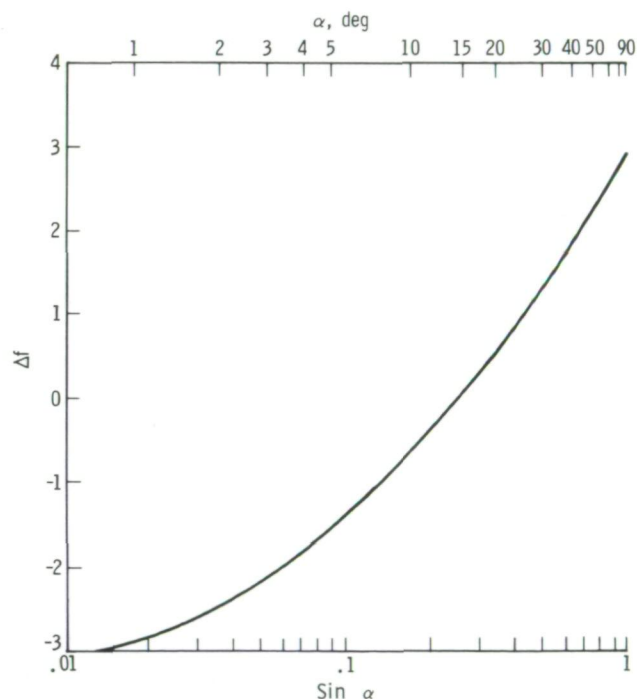


FIGURE 16-39.—Plot of relative exposure Δf based on $f/11$ at $1/250$ second ($\Delta f = 0$) as a function of solar elevation angle α for tropical storm photography using ASA 64 film. The least-squares regression curve (eq. (16-13)) represents the best fit over the entire range of solar elevation angles and is based on estimated exposure error derived from analysis of tropical storm photographs from space (table 16-IX).

TABLE 16-IX.—Exposure Data for Skylab Tropical Storm Photography^a

| Storm | Frame no. | Date | Local time, GMT, hr : min : sec | Geographic coordinates | Sun angle, deg | Exposure, f-stop, sec | Estimated overexposure error, f-stops |
|--------------------------|--------------|----------------|---------------------------------|------------------------|----------------|-----------------------|---------------------------------------|
| Tropical cyclone Lottie | SL4-136-3516 | Dec. 8, 1973 | 23:43:30 | 18.7° S, 176.0° E | 84 | f/11, 1/250 | 3.0 |
| Tropical cyclone Lottie | SL4-136-3541 | Dec. 11, 1973 | 00:07:00 | 21.7° S, 175.3° W | 85 | f/11, 1/250 | 3.0 |
| Tropical storm Ellen | SL3-122-2571 | Sept. 19, 1973 | 20:18:25 | 27.3° N, 51.1° W | 14 | f/5.6, 1/250 | 1.5 |
| Tropical storm Ellen | SL3-122-2572 | Sept. 19, 1973 | 20:18:30 | 27.3° N, 51.1° W | 14 | f/8, 1/250 | .5 |
| Hurricane Ellen | SL3-122-2587 | Sept. 20, 1973 | 19:32:00 | 31.0° N, 54.0° W | 75 | f/11, 1/250 | 1.5 |
| Hurricane Ellen | SL3-122-2601 | Sept. 21, 1973 | 18:48:20 | 36.0° N, 53.0° W | 32 | f/11, 1/250 | 1.5 |
| Tropical storm Christine | SL3-121-2322 | Sept. 2, 1973 | 13:57:00 | 15.3° N, 56.8° W | 57 | f/11, 1/250 | 2.0 |
| Tropical storm Wanda | SL4-139-4051 | Jan. 11, 1974 | 00:16:00 | 12.2° N, 136.0° W | 38 | f/11, 1/250 | 2.0 |
| Typhoon Iris | SL3-116-2053 | Aug. 14, 1973 | 08:43:00 | 25.7° N, 138.5° W | 23 | f/11, 1/250 | 1.0 |
| Hurricane Irah | SL3-118-2189 | Sept. 24, 1973 | 00:00:00 | 18.0° N, 107.8° W | 2 | f/5.6, 1/250 | 0 |
| Hurricane Ava | SL2-6-485 | June 6, 1973 | 12:00:00 | 12.0° N, 107.7° W | 88 | f/11, 1/250 | 3.0 |

^aSee figure 16-39.

The solar elevation angle appears to uniquely define the amount of reflected light (the albedo) from tropical storm tops; however, some azimuth dependence may exist, especially at low Sun angles. As a guide to defining future exposures of tropical storm photographs, an empirical relation has been derived from the well-documented photography of the Skylab 3 crewmen. Their onboard photograph logs contained information on exposures and, from these data, the author estimated the number of f-stops by which each tropical storm photograph was overexposed. The estimated correct exposure was then plotted as a function of the logarithm of the sine of the solar elevation angle, which was estimated from the ephemeris data and the estimated photograph time (fig. 16-39). Because most of the Skylab tropical storm photographs were taken at f/11 and 1/250 second, this setting was used with ASA 64 film as the reference exposure (scale zero in fig. 16-39). The data are shown in table 16-IX.

Several least-squares regression curves were fitted through these data. The best fit over the entire range of

solar elevation angles α for relative exposure Δf was found to be

$$\Delta f = 2.92 + 5.64 \log (\sin \alpha) + 1.33 [\log (\sin \alpha)]^2 \quad (16-13)$$

This equation gave a correlation coefficient of $r = 0.93$. Two linear regression lines were also computed since they are somewhat simpler. They are

$$\Delta f = 2.89 + 4.95 \log (\sin \alpha), \quad \alpha > 5^\circ$$

which gave a correlation coefficient of $r = 0.91$, and

$$\Delta f = -3.21 + 3.11 \log \alpha$$

which gave a correlation coefficient of $r = 0.94$. The preceding relationships could be tested from an RB-57 or U-2 aircraft over a tropical storm or severe thunderstorm by taking photographs at the predicted exposures for a variety of Sun angles.

Appendix

Derivation of the Equation for Estimating Pressure Decrease Beneath a Convective Cloud

The expected surface pressure decrease in the eyewall beneath a convective cloud can be estimated to within an order of magnitude as follows. First, assume that the equivalent potential temperature of the environment $\hat{\theta}_e$ and of the cloud θ_e as well as the in-cloud vertical velocity W are distributed approximately as shown in figure 16-26, which defines three regions in the vertical: the lower troposphere to an altitude of 6 km, the upper troposphere from 6 to 16 km, and the overshooting region in the stratosphere. This model of vertical velocity is based on the calculations of maximum vertical velocity made earlier and the assumption that this value is reached at the 50-kPa (500 mbar) pressure level. The equivalent potential temperature model is based on Sheets' (ref. 16-25) mean soundings and the observation that the in-cloud eyewall θ_e value typically is approximately 360 K. To estimate the surface pressure decrease beneath the circular cloud, Newton's second law of motion in the vertical is written as follows.

$$\frac{dw}{dt} = -g - \frac{1}{\rho} \frac{\partial p}{\partial z} \quad (\text{A1})$$

where w is vertical windspeed, t is time, ρ is air density, p is pressure, and z is the vertical coordinate. This equation is a statement that the vertical acceleration dw/dt of an air parcel is determined by the difference between the acceleration of gravity g and acceleration induced by the vertical pressure gradient term $(1/\rho)(\partial p/\partial z)$. If only small vertical accelerations exist, such as in the environment surrounding the cloud, equation (A1) reduces to the hydrostatic equation

$$\frac{\partial p}{\partial z} = -\rho g \quad (\text{A2})$$

To obtain the surface pressure difference between the environment and the cloud, equation (A2) is subtracted from equation (A1) and integration from the surface to the cloud top is performed. Subtracting, denoting the

environment by primes, and expanding the acceleration term, the following expression is obtained.

$$\begin{aligned} \frac{\partial w}{\partial t} + U \frac{\partial w}{\partial r} + \frac{v}{r} \frac{\partial w}{\partial \phi} + w \frac{\partial w}{\partial z} + \frac{1}{\rho} \frac{\partial}{\partial z} (p - p') &= -\frac{\rho - \rho'}{\rho} g \\ &= -\frac{\theta'_e - \theta_e}{\theta'_e} g \\ &= -\hat{g} \end{aligned} \quad (\text{A3})$$

where U is one-half the wind shear across the layer, r is the radius of the cloud, v is horizontal windspeed along the y -axis (positive toward north), ϕ is the azimuthal coordinate, and \hat{g} is a reduced gravity. Rewriting

$$\frac{\partial}{\partial z} (p - p') = -\rho \hat{g} + \rho \left[\frac{v}{r} \frac{\partial w}{\partial \phi} + w \frac{\partial w}{\partial z} \right] \quad (\text{A4})$$

The pressure deficit is a function of a hydrostatic stability term and a nonhydrostatic acceleration term. The acceleration term is composed of a horizontal and a vertical shear component. To estimate the surface pressure change, the magnitude of these two terms integrated over each of the three layers of the atmosphere is estimated and the contributions from each of the three layers are added.

Approximating the integral, three terms are considered for each layer.

$$\Delta p = \underbrace{-\bar{g}\bar{\rho}}_{\text{I}} \Delta z - \underbrace{\left(\frac{\bar{v}}{r}\right) \left(\frac{\Delta \bar{w}}{\Delta \phi}\right) \bar{\rho}}_{\text{II}} \Delta z - \underbrace{\bar{w} \Delta \bar{w}\bar{\rho}}_{\text{III}} \quad (\text{16-12})$$

where the overbar denotes an average over the layer. Estimates of the pressure difference between cloud and environment for each of the preceding terms for each layer are given in table 16-VIII.

REFERENCES

- 16-1. Blackwell, R. J.; and Crisci, W. A.: Digital Image Processing Technology and Its Application in Forensic Sciences. Paper presented at the American Academy of Forensic Sciences Meeting (Las Vegas, Nev.), Feb. 1973.
- 16-2. Gentry, R. Cecil; Fujita, Tetsuya T.; and Sheets, Robert C.: Aircraft, Spacecraft, Satellite and Radar Observations of Hurricane Gladys, 1968. *J. Appl. Meteorol.*, vol. 9, no. 6, Dec. 1970, pp. 837-850.
- 16-3. Dvorak, V. F.: A Technique for the Analysis and Forecasting of Tropical Cyclone Intensities From Satellite Pictures. NOAA-TM-NESS-45, 1973.
- 16-4. Dvorak, V. F.: Tropical Cyclone Intensity Analysis and Forecasting From Satellite Imagery. *Mon. Weather Rev.*, vol. 103, May 1975, pp. 420-430.
- 16-5. Arnold, C. P.: Tropical Cyclone Position and Intensity Analysis Using Satellite Data. First Weather Wing Pamphlet IWWP105-10, Dept. of the Air Force, 1974.
- 16-6. Gentry, R. C.: Structure of the Upper Troposphere and Lower Stratosphere in the Vicinity of Hurricane Isbell, 1964. *Papers Meteorol. & Geophys.*, Tokyo, vol. 18, no. 4, 1967, pp. 293-310.
- 16-7. Waco, David E.: Temperatures and Turbulence at Tropopause Levels Over Hurricane Beulah (1967). *Mon. Weather Rev.*, vol. 98, no. 10, Oct. 1970, pp. 749-755.
- 16-8. Lindzen, R. S.: Stability of a Helmholtz Velocity Profile in a Continuously Stratified, Infinite Boussinesq Fluid—Applications to Clear Air Turbulence. *J. Atmos. Sci.*, vol. 31, Sept. 1974, pp. 1507-1514.
- 16-9. Gossard, Earl E.: Dynamic Stability of an Isentropic Shear Layer in a Statically Stable Medium. *J. Atmos. Sci.*, vol. 31, no. 2, Mar. 1974, pp. 483-492.
- 16-10. Miles, John W.; and Howard, L. N.: Note on a Heterogeneous Shear Flow. *J. Fluid Mech.*, vol. 20, 1964, pp. 331-336.
- 16-11. Lalas, D. P.; Einaudi, F.; and Fua, D.: The Destabilizing Effect of the Ground on Kelvin-Helmholtz Waves in the Atmosphere. *J. Atmos. Sci.*, vol. 33, no. 1, Jan. 1976, pp. 59-69.
- 16-12. Hawkins, Harry F.; and Rubsam, Daryl T.: Hurricane Hilda, 1964: II. Structure and Budgets of the Hurricane on October 1, 1964. *Mon. Weather Rev.*, vol. 96, no. 9, Sept. 1968, pp. 617-636.
- 16-13. Fujita, T. T.: Overshooting Thunderheads Observed From ATS and Learjet. NASA CR-138595, 1974.
- 16-14. Shenk, W. E.: Cloud Top Height Variability of Strong Convective Cells. *J. Appl. Meteorol.*, vol. 13, Dec. 1974, pp. 917-922.
- 16-15. Saunders, Peter M.: Penetrative Convection in Stably Stratified Fluids. *Tellus*, vol. 14, no. 2, May 1962, pp. 177-194.
- 16-16. Bigler, Stuart G.; and Hexter, Paul L., Jr.: Radar Analysis of Hurricane Debra. Proceedings of the 8th Weather Radar Conference (San Francisco, Calif.), Apr. 11-14, 1960, pp. 25-32.
- 16-17. Jordan, C. L.; and Schatzle, Frank J.: The "Double Eye" of Hurricane Donna. *Mon. Weather Rev.*, vol. 89, no. 9, Sept. 1961, pp. 354-356.
- 16-18. Senn, H. V.: Precipitation Shear and Bright Band Observations in Hurricane Betsy, 1965. Proceedings of the 12th Conference on Radar Meteorology, American Meteorological Society (Boston), 1966, pp. 447-453.
- 16-19. Black, Peter G.; Senn, Harry V.; and Courtright, Charles L.: Airborne Radar Observations of Eye Configuration Changes, Bright Band Distribution, and Precipitation Tilt During the 1969 Multiple Seeding Experiments in Hurricane Debbie. *Mon. Weather Rev.*, vol. 100, no. 3, Mar. 1972, pp. 208-217.
- 16-20. Shea, D. J.: The Structure and Dynamics of the Hurricane's Inner Core Region. Rep. No. 182, Dept. of Atmospheric Sciences, Colorado State University, 1972.
- 16-21. Riehl, Herbert; and Malkus, Joanne: Some Aspects of Hurricane Daisy, 1958. *Tellus*, vol. 13, no. 2, May 1961, pp. 181-213.
- 16-22. Byers, Horace Robert: *General Meteorology*. McGraw-Hill, 1944.
- 16-23. Depperman, C. E.: Wind and Rainfall in Selected Philippine Typhoons. Manila Weather Bureau Central Observatory Report, 1937.
- 16-24. Carrier, G. F.; Hammond, A. L.; and George, O. D.: A Model of the Mature Hurricane. *J. Fluid Mech.*, vol. 47, 1971, pp. 145-170.
- 16-25. Sheets, R. C.: Some Mean Hurricane Soundings. *J. Appl. Meteorol.*, vol. 8, no. 1, 1969, pp. 134-146.

17

Mesoscale Wake Clouds in Skylab Photographs

T. THEODORE FUJITA^a AND JAIME J. TECSON^a

FROM ITS vantage point in space, Skylab provided the crewmembers an excellent opportunity for observing and photographing terrestrial objects. During the last manned mission, some unique and remarkable high-resolution photographs were obtained of mesoscale meteorological phenomena. Analyses of selected photographs are contained in this section.

Mesoscale circulations characterized by wake waves and by vortexes are produced in certain limited areas of the world under favorable conditions. Though these circulations do not affect large areas, the phenomena should significantly affect the synoptic conditions of the local areas and possibly influence conditions of nearby regions.

Remarkably enough, Mariner 9 photographs of the atmosphere of Mars show impressive wave-cloud patterns caused by craters that have been identified by Briggs and Leovy (ref. 17-1). Chopra and Hubert (refs. 17-2 and 17-3) have found a quantitative analog to the island patterns in the vortex streets formed behind a solid cylinder comparable in size to the islands. These researchers have found an apparent resemblance between the meteorological mesoscale eddies and the classical vortex street pattern. Formations of cumulus streets and observance of cloud-free paths under winter monsoon situations in certain areas have been described by Tsuchiya and Fujita (ref. 17-4). Investigation of the high-quality photographs detailing the fine structures of mesoscale phenomena that were obtained from Skylab could yield more meaningful evaluations.

^aThe University of Chicago.

WAKE WAVES OF BOUVET ISLAND IN THE SOUTH ATLANTIC

On December 15, 1973, at 14:23 Greenwich mean time (GMT), the Skylab science pilot described "island wake in stratus; 4° W, 48° S; wake toward the east; 150 miles [241 km] long with 20 to 30 crests and valleys under high Sun angle." He obtained a spectacular sequence of three photographs (SL4-137-3631, SL4-137-3632, and SL4-137-3633) that show a pattern of wake waves such as would be expected to be found behind a moving ship. Figure 17-1 is a semirectified photograph of frame SL4-137-3633 and shows the wave pattern developed behind Bouvet Island in the South Atlantic Ocean. Bouvet Island is located at latitude 54°26' S and longitude 3°24' E. The elevation of the island is 935 m above sea level. The center of the wake (indicated by the wavy dotted line) may represent a sinusoidal fluctuation of the southwesterly flow against the island. The vertex angle of the wake boundaries is computed to be 38°, which is very close to that of a moving ship.

An unusual feature in the wave pattern is the outward extension of the lateral waves, which commonly is seen only inside the vertex angle of a ship wake. Configurations of this form possibly could occur, however. Stoker (ref. 17-5) indicated that the disturbances or surface waves created by a moving ship are not zero outside the region of the disturbance, but rather they are small and of a different order than within. Thus, in water, the waves normally cannot be detected outside the region of disturbance. In the atmosphere, however, the vertical velocity, though small, is nonzero in this

region. In a saturated layer, therefore, a small vertical velocity may be of sufficient magnitude to produce clouds that would reveal the existence of wave clouds extending beyond the region of disturbance. It is difficult to understand how the wave energy could be transported outward into a large vertex angle of approximately 90° .

The half amplitude of the waves (fig. 17-1) is estimated to be approximately 1 km, which is the island elevation. The wavelength varies between 10 and 15 km, which is one order of magnitude larger than the

amplitude. The depth of the atmosphere below the wave is approximately 1 km, indicating that the trough just behind the island might be almost on the ground.

The conclusion drawn from the evidence in figure 17-1 is that the form and occurrence of the atmospheric waves do not correspond to those of deep-water ocean waves, where the kinetic energy of the waves is likely to be lost very quickly. Investigation of the mechanism of wave propagation within and immediately outside the vertex angle behind such an island would be extremely valuable in the study of mesoscale phenomena.

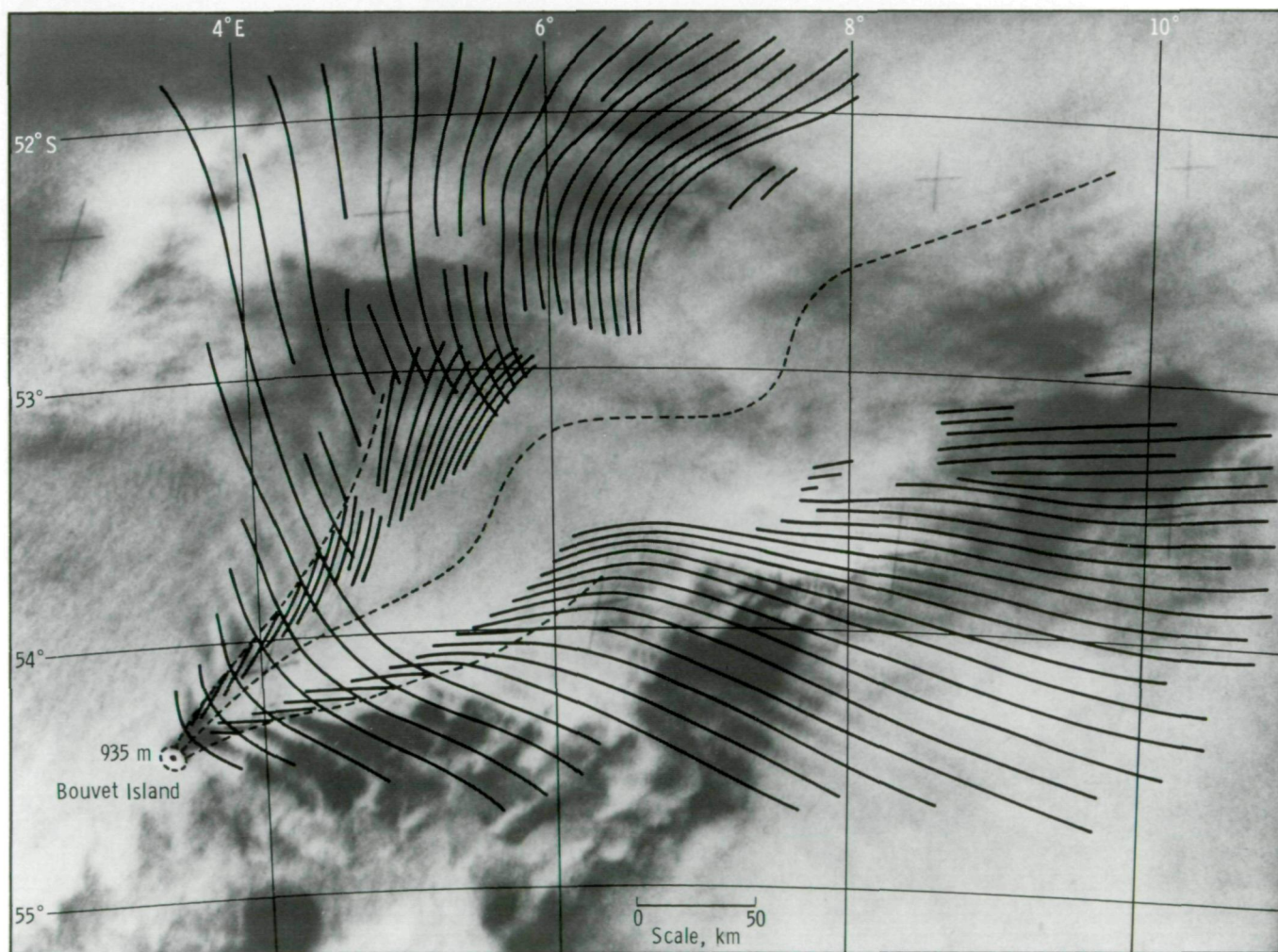


FIGURE 17-1.—Wake waves from Bouvet Island in the South Atlantic; a semirectified photograph taken at 14:23 GMT, December 15, 1973 (SI4-137-3633).

COMPARISON WITH SHIP WAKES

Kelvin's theory (ref. 17-6) of wave patterns created by a moving ship indicates that the V-shaped pattern behind a moving object is similar regardless of the object size as long as the motion is steady along a straight course. When any object, ranging from a duck to a battleship, moves across a water surface, a moving pressure point is created that results in a stationary phase.

The vertical displacement of the water surface at a given point is the integrated effect of the point impulse that moves with an object. When the water is infinite in depth, the point influenced by an object at a specific time moves at the rate of one-half the speed of the object. The instantaneous positions of the influence point are located on a horizontal circle through the ship's position at a specific time. The diameter of the circle coincides with the instantaneous velocity of the ship. The outer boundaries of the V-shaped wake behind the ship are the envelopes of successive circles with increasing diameter in proportion to the distance from the moving ship or obstacle.

The vertex angle is thus expressed by

$$2 \arcsin \frac{1}{3} = 38^{\circ}56' \quad (17-1)$$

which is a constant independent of the object size and speed, as long as the velocity of the object is constant.

Waves caused by a moving pressure point, such as that of a moving ship, are confined to a region of disturbance behind the ship. In particular, two distinct wave sets are apparent in conformity with the fact that

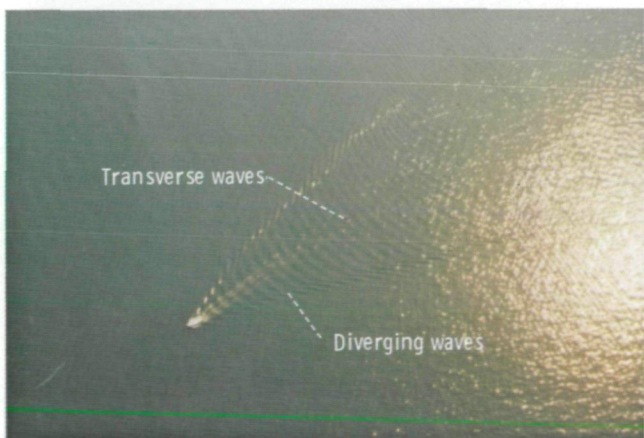


FIGURE 17-2.—Wake waves caused by a slow-moving boat.

each point in the disturbed region corresponds to two influence points. One wave set is arranged roughly at right angles to the course of the ship and designated transverse waves; the other set appears to emanate from the bow of the ship and is called diverging waves. The transverse waves connect the left and right edges of the V-shaped wake. The diverging waves are characterized by the maximum amplitude near the wake boundaries, with amplitudes decreasing to almost zero as they diverge outward.

The wake waves are seen behind moving ships in a lake in figures 17-2 and 17-3. Figure 17-2 is an aerial photograph taken over Lake Michigan, and figure 17-3 was taken over a lake in northern Indiana. Both photographs were taken on July 13, 1974. One of the major differences in the pattern of the wake waves is the existence of the transverse waves in figure 17-2.

Havelock (ref. 17-7) has shown that transverse waves disappear when

$$\frac{c^2}{gh} > 1 \quad (17-2)$$

where c is the ship's speed, g is the gravity, and h is the depth. If the depth of Lake Michigan (fig. 17-2) is assumed to be 30 m and $c = 5$ m/sec, the result is

$$\frac{c^2}{gh} = \frac{25}{9.8 \times 30} \cong 0.1 \quad (17-3)$$

This number would indicate the existence of transverse waves.



FIGURE 17-3.—Wake waves behind a speedboat.

The Indiana lake (fig. 17-3) is very shallow, and the speedboat was moving very fast. If the values $c = 10$ m/sec and $h = 5$ m are used, then

$$\frac{c^2}{gh} = \frac{100}{9.8 \times 5} \cong 2 \quad (17-4)$$

which is considerably larger than 1 when the transverse waves are expected to disappear. As seen in figure 17-3, the wake is characterized by diverging waves only.

This discussion on ship wakes suggests that the wave patterns theoretically are applicable to another fluid—the atmosphere—and occur in two forms.

1. Diverging and transverse waves occur when a ship moves slowly on a deep-water surface; they may occur in slow-moving air with a deep layer below the inversion surface.

2. Diverging waves occur alone when a ship moves fast on a shallow-water surface; they may occur in fast-moving air with a shallow layer below the inversion surface.

A law of similarity between ship wakes in the ocean and island wakes in the atmosphere has not been established. This study of imagery shows evidence to promote a law of similarity. The dimensions of islands must be considered in any study because objects of different sizes and shapes cause dissimilar atmospheric

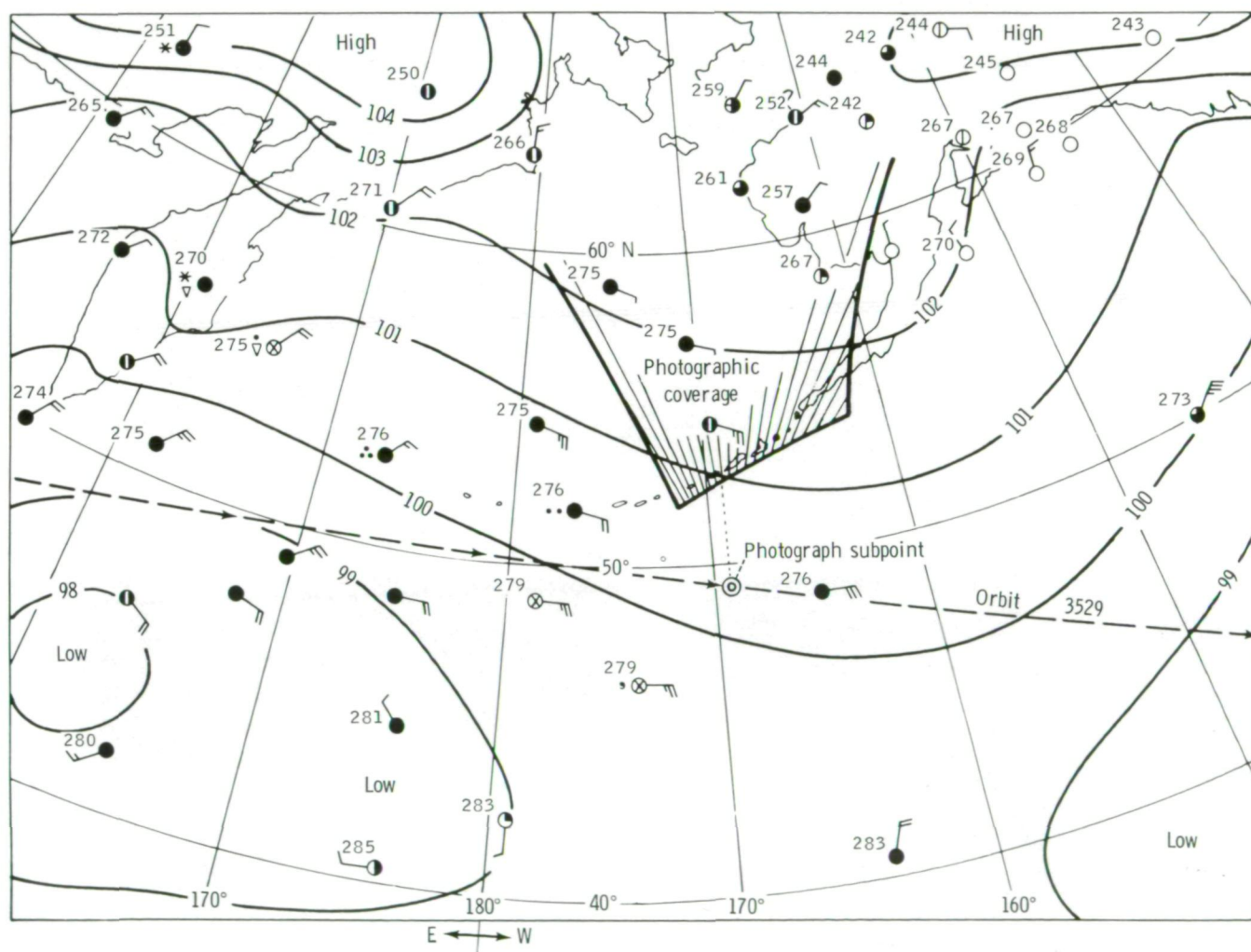


FIGURE 17-4.—The area of the cloud photograph in figure 17-5 superimposed on the surface chart at 00:00 GMT, January 14, 1974. Weather symbols are explained in appendix B.

wakes. For example, the atmospheric wakes downwind from a television tower and from a volcanic island are known to be quite different. Analysis of space photographs must include island size and downwind effects.

WAKE WAVES AND VORTEX STREETS FROM THE ALEUTIAN ISLANDS

On January 14, 1974, the Aleutian Islands were experiencing moderate easterly winds ranging from 10 to 15 m/sec. The upwind side of the island was covered by stratus clouds with tops at approximately 1000 m mean sea level (m.s.l.).

Near the end of orbit 3529, two successive photographs (SL4-140-4111 and SL4-140-4112) of the Aleutian Islands were taken at 01:43 GMT, January 14. Figure 17-4 shows the photograph subpoint, the photographic coverage, and the surface conditions at 00:00 GMT, less than 2 hours before the overflight of Skylab. As seen on the surface map, the flow near the southern

tip of the photograph area is uniform: 12 m/sec from the 120° direction.

Under such a uniform flow, atmospheric waves and eddies were created on the lee or downwind side of the islands. Figure 17-5 is a gridded version of the photo-mosaic of photographs SL4-140-4111 and SL4-140-4112 and covers a 700-km segment of the Aleutian Island chain extending from Amukta Island to Unimak Island.

In figure 17-5, Kármán vortexes are seen to occur predominantly in the wake of large orographic features such as Mount Vsevidof (Umnak), Okmok Crater, Makushin Volcano (Unalaska), and Pogromni Volcano (Unimak). The largest eddy produced in this island chain (marked "P" in fig. 17-5) was formed downwind from the Pavlof Volcano on Pavlof Island (not shown). Wake waves, mostly diverging waves, are found behind small islands and are indicated by solid lines in figure 17-5. Because the characteristics of the flow are uniform, the major factors in producing waves and vortexes are suspected to be the dimensions of the obstacles and velocity of the flow.

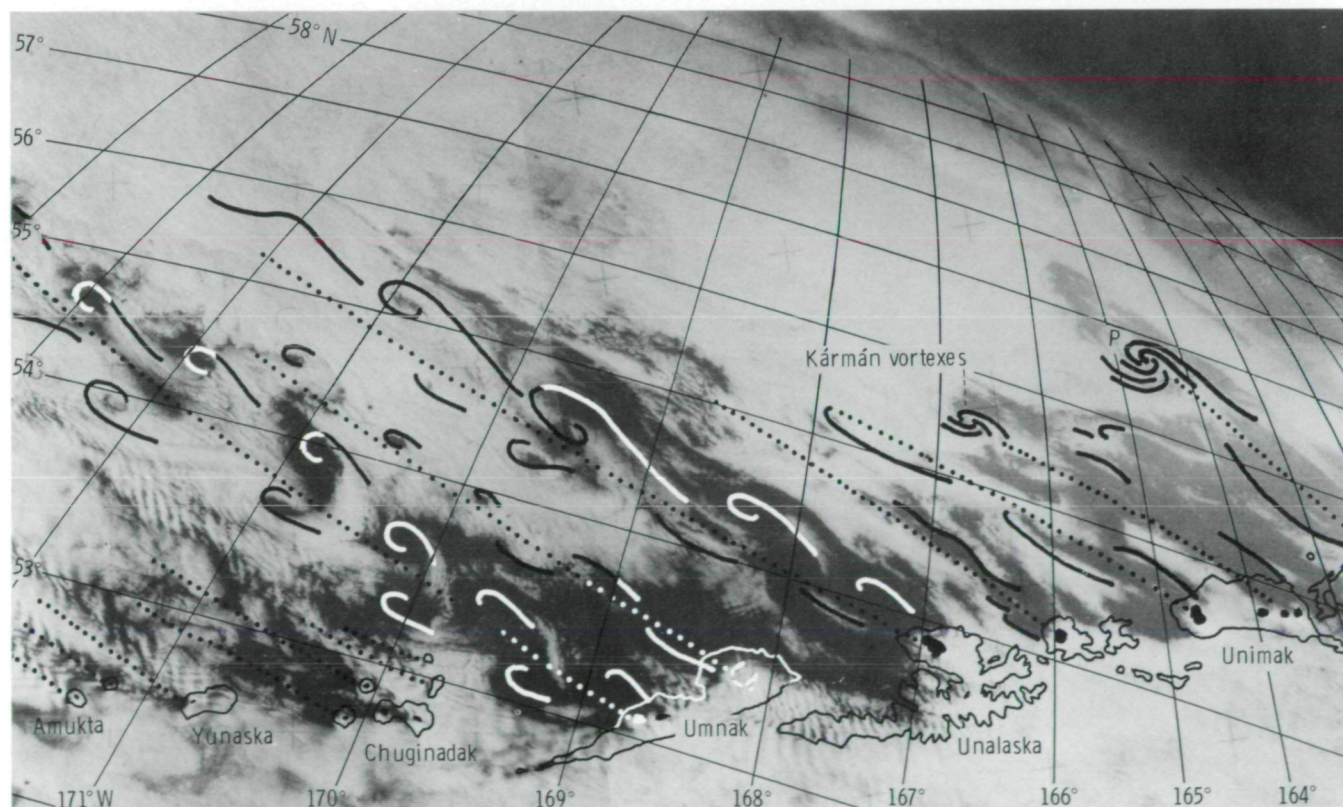


FIGURE 17-5.—Kármán vortex streets and island wakes from the Aleutian Islands at 01:43 GMT, January 14, 1974. Islands are outlined; areas above 1000-m elevation are solid (composite of SL4-140-4111 and -4112).

C-2

Figure 17-6 was constructed by rectifying frame SL4-140-4111 into a 1:1 000 000 scale. It should be noted that small peaks are generating a long wake with diverging waves. Analyses of the photographs in figures 17-5 and 17-6 produced a table of wake characteristics (table 17-I). The width of the obstacles in table 17-I is defined as being the cross-sectional dimension at the 300-m elevation m.s.l. As shown in table 17-I, the critical dimension of the obstacle between the wave and eddy formation is 5 km. If an obstacle is 5 km wide or smaller, diverging waves form in the island wake. The height of the obstacle does not influence the wake characteristics as long as the obstacle extends above the top of the stable layers.

According to laboratory estimates on vortex streets, the Reynolds number Re for the lower limit for stable vortex formation is 35. The kinematic eddy viscosity ν corresponding to the critical diameter of the orographic obstacle can be computed from

$$\nu = \frac{DU}{Re} = 2.4 \times 10^7 \text{ cm}^2/\text{sec} \quad (17-5)$$

where $D = 5000 \text{ m}$ and the geostrophic wind $U = 17 \text{ m/sec}$. This value conforms with that estimated by Chopra and Hubert (ref. 17-2).

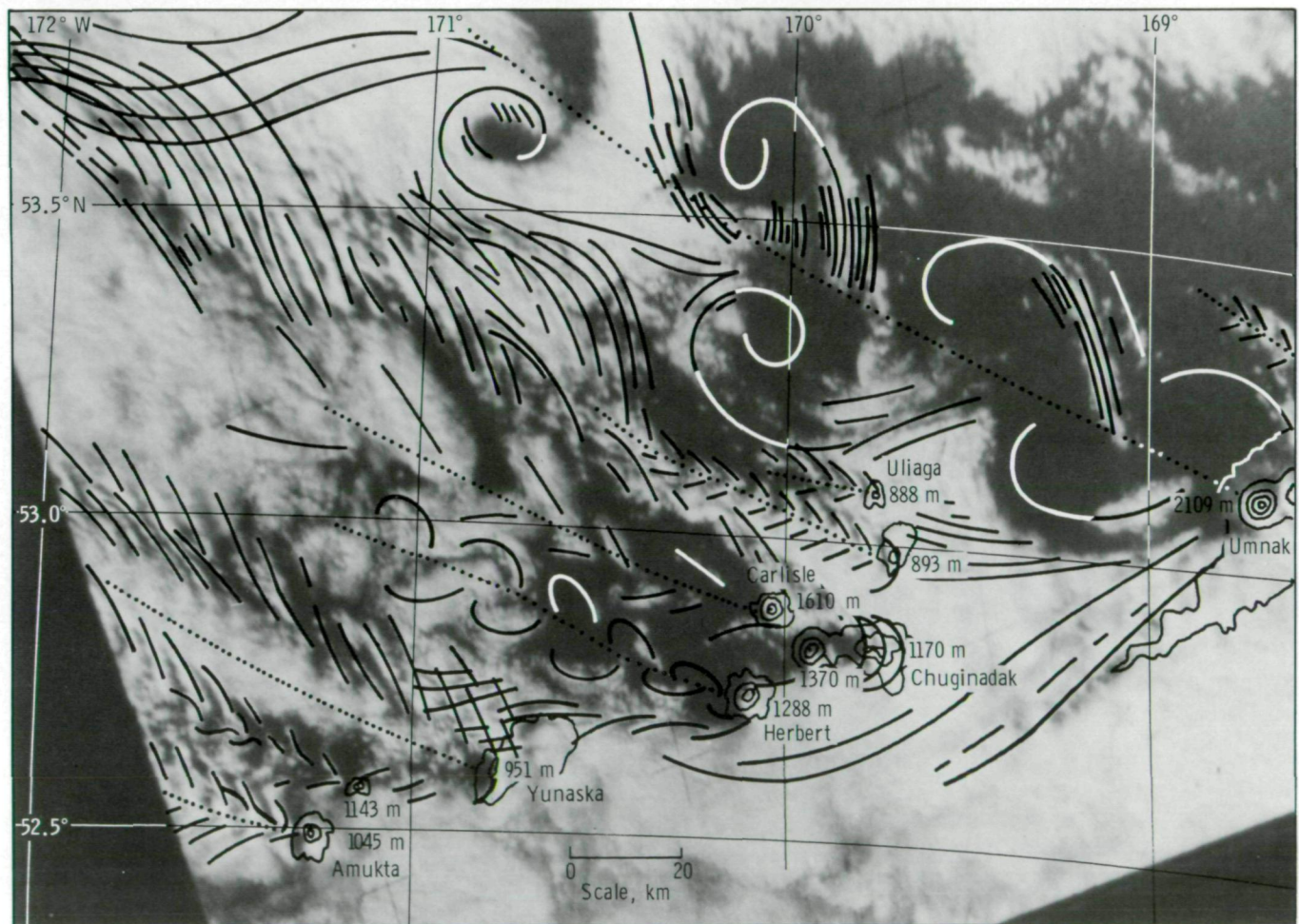


FIGURE 17-6.—Semirectification showing long wakes with diverging waves. Height contours are 500, 1000, and 1500 m m.s.l. (SL4-140-4111).

TABLE 17-I.— Wake Characteristics of Aleutian Islands on January 14, 1974

| Obstacle | Longitude | Height, m | Width, km | Wake type |
|-------------------|-----------|-----------|-----------|------------------|
| Amukta Volcano | 171°15' | 1056 | 4 | Diverging waves |
| Chagulak Island | 171°09' | 1143 | 2 | Diverging waves |
| Yunaska Island | 170°48' | 951 | 5 | Diverging waves |
| Yunaska Island | 170°39' | 600 | 4 | Diverging waves |
| Herbert Island | 170°07' | 1288 | 5 | Waves and eddies |
| Carlisle Island | 170°04' | 1610 | 5 | Waves and eddies |
| Mount Cleveland | 169°57' | 1730 | 5 | Eddies |
| Chuginadak Island | 169°46' | 1170 | 8 | Waves and eddies |
| Uliaga Island | 169°46' | 888 | 2 | Diverging waves |
| Kagamil Island | 169°43' | 893 | 2 | Diverging waves |
| Mount Vsevidof | 168°31' | 1984 | 24 | Vortex street |
| Mount Vsevidof | 168°42' | 2109 | 24 | Vortex street |
| A small peak | 168°18' | 610 | 5 | Diverging waves |
| Tulik Volcano | 168°08' | 1253 | 22 | Vortex street |
| Makushin Volcano | 166°56' | 2036 | 32 | Vortex street |
| Akutan Island | 166°00' | 1303 | 12 | Vortex street |
| Pogromni Volcano | 164°42' | 2002 | 19 | Vortex street |

KÁRMÁN VORTEX STREETS FROM KURIL ISLANDS

A photograph obtained at 00:00 GMT on June 4, 1973, shows that vortex streets under a very weak flow condition developed in the wake of the Kuril Islands. The vortex patterns are shown in the semirectified photograph (fig. 17-7). Of interest is the change in the flow direction within a short distance along the island chain. The weather report from Tōkyō, Japan, indicates that Urup Island at 00:00 GMT was 274 K with 1-m/sec wind velocity from 320°. The large-scale flow as estimated from the wake vortex pattern is anticyclonic with a southerly flow between Iturup and Urup Islands. A small cyclonic eddy is seen northeast of Iturup. The northern coast of Iturup is clear, which indicates a southerly flow there.

The cyclonic eddy to the northeast of Urup suggests the existence of a southwesterly flow along the southeastern coast of the island. Off the southwestern tip of Simushir, a weak northwesterly flow is present. A similar flow prevails across the islands of Ketoy, Rasshua, and Matua.

The sea-surface temperature in June around Matua Island is known to be the coldest in the Kuril chain. Almost every day, low stratus and fog cover the area; this condition indicates the existence of a semipermanent inversion layer. The stratification is therefore

favorable for the development of vortex streets behind the island. It is unusual, however, to observe the significant change in the flow patterns shown in figure 17-7.

BLOCKING OF EVAPORATION CUMULI BY THE ALEUTIAN ISLANDS

Cumulus streets form when dry, cold air of polar-continental origin passes over an ocean. During this process, heat and moisture are transported from the ocean surface to the atmosphere. When the rate of transportation is very fast, the initial formation of cumuli occurs only a few kilometers offshore. Numerous examples of cumulus streets over the Great Lakes, off the coast of Siberia near the Sea of Japan, and off the Atlantic coast of the United States are visible in Skylab photographs.

One of the most striking photographs of such evaporation cumuli was taken at 01:06 GMT on January 17, 1974, looking north toward the Alaska Peninsula (fig. 17-8). As shown in figure 17-9, the center of a well-developed cyclone with a central pressure of 96.5 kPa was located in the Gulf of Alaska. The air temperature at Fort Yukon was 233 K. A strong surge of cold air is seen in the northwestern sector of the cyclone. The windspeed along the Alaskan coast was approximately 10 m/sec from the north.

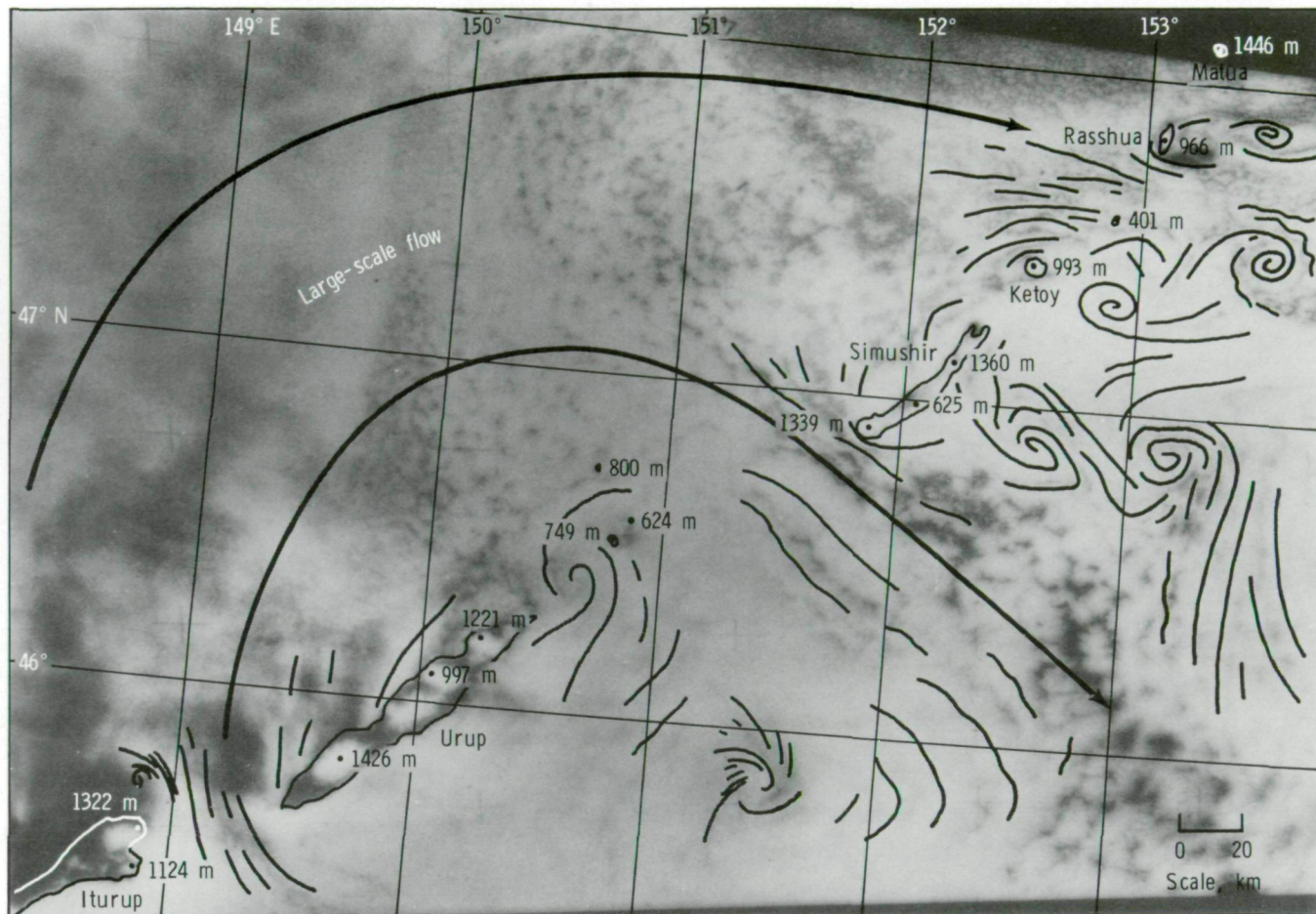


FIGURE 17-7.—Semirectified photograph showing Kármán vortex streets from the Kuril Islands (SL2-5-432).

Figure 17-8 is a gridded photograph that reveals a very narrow cloud-free area along the coast of Kuskokwim Bay, Etolin Strait, and Hazen Bay. The cloud-free path of the cold-air outflow is only several kilometers wide. After the formation of evaporation cumuli, cloud streets develop in the direction parallel to the flow. Numerous streets are seen to extend from the formation points across the Bering Sea toward the Alaska Peninsula. The blocking of these cumulus streets by mountains in the peninsula is similar to a phenomenon frequently seen over Japan under the winter monsoon. However, this phenomenon does not occur in the Atlantic Ocean off the eastern coast of the United States where no blocking mountains exist.

The cloud streets south of the peninsula originate in gaps or low topographic areas where leakage of moisture from the Bering Sea occurs. A most significant

feature in figure 17-8 is the cloud-free dark spot south of Mount Veniaminof, a 2560-m peak. A small eddy street extends downwind from the peak region. Another dark spot is found in the wake of Pavlof Volcano, a 2718-m peak. Coastlines are visible within these dark spots that are cloud free, being dominated by strong downslope winds. Neither waves nor vortexes are present in the wake regions of the Alaska Peninsula. The high peaks in the peninsula block the cumulus streets forming over the Bering Sea. One reason for the absence of waves and vortexes within the obstacle wake on the peninsula appears to be the temperature lapse rate of the air just above the sea surface. If the lapse rate is adiabatic or almost adiabatic, the vertical mixing is stimulated by the eddy transport. Such a mixing process will effectively damp both waves and eddies and thus restrict their transport downwind inside the wake regions.

ORIGINAL PAGE IS
OF POOR QUALITY

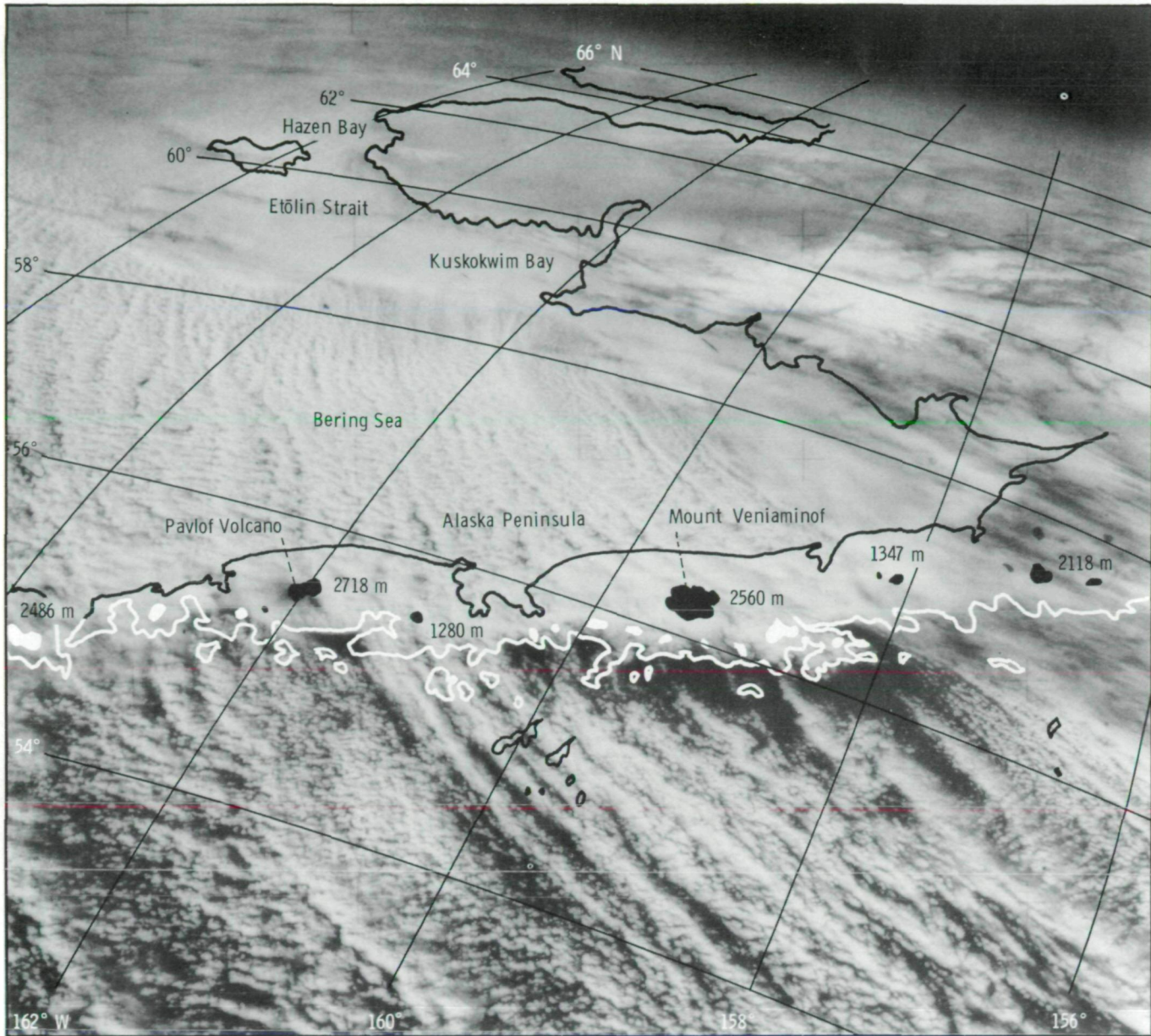


FIGURE 17-8.—Blocking of evaporation cumulus streets by the Aleutian Islands. Grid lines and landmarks placed on photograph taken at 01:06 GMT, January 17, 1974 (SL4-140-4210).

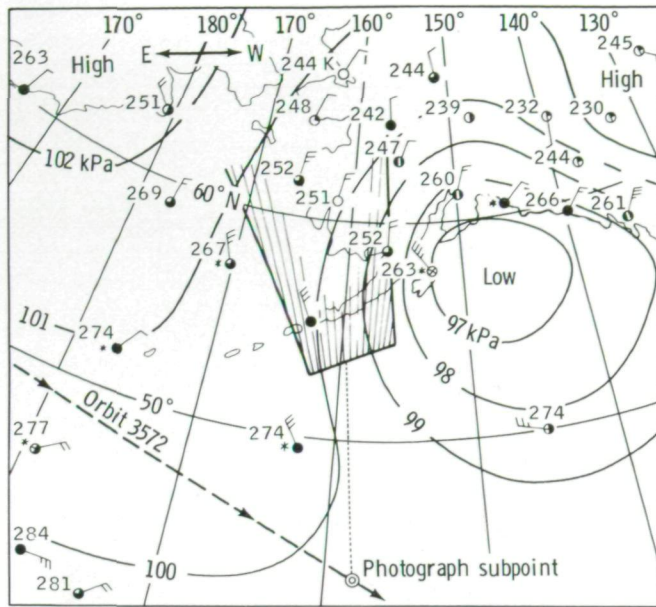


FIGURE 17-9.—Surface map for 00:00 GMT, January 17, 1974, corresponding to the time of figure 17-8. Weather symbols are explained in appendix B.

THERMAL AND MECHANICAL EFFECTS OF SOUTH PACIFIC ISLANDS

During Skylab orbit 3211 on December 23, 1973, an interesting sequence of five photographs (SL4-137-3701 through SL4-137-3705) was taken over the southern end of New Zealand looking toward the south and southeast. Figure 17-10 shows the subpoints and the principal view direction for each photograph and a surface map of the New Zealand area at 00:00 GMT on December 23. The first two photographs were views looking toward the Auckland and Campbell Island areas. Frames 3703 and 3704 show beautiful wake waves extending downwind from Campbell Island. The last photograph shows several cumulus streets or cloud lines forming downwind of Chatham Island.

The cumulus streets that originate over Chatham and Pitt Islands are shown in figure 17-11. The largest street, extending from the northern part of Chatham, originates on the coastline. Because a cloud line often originates over a flat plane downwind from a pointed cape or peninsula, the point of origin of the cloud line could be within the pointed peninsula. Another cloud line originates within the peninsula that extends into Te Whanga Lagoon, the largest lagoon on Chatham Island.

Five cloud lines extend southwestward from high spots of southern Chatham. As the cloud line leaves the source, its direction changes to the southwest, which may mean that the direction changed to that of the gradient wind outside the influence of the island.

Cloud lines from Pitt Island are very important because of their appearance. With the exception of the central line originating from the 296-m peak, the cloud lines take the shape of diverging waves. The microscale pattern of the lines implies that they consist of small cumulus cells. However, the island-scale pattern of the plumes shows a configuration of three diverging waves. Further examination of this photograph would be necessary for a better understanding of the transition between cloud lines and waves.

A small cloud line originates from a spot where no island is shown on the map of the South Pacific region (fig. 17-11). The spot might correspond to an area in which the sea-surface temperature is higher and triggers a conditionally unstable atmosphere. Figure 17-12 shows a vertical profile of air temperature and dewpoint temperature from Chatham Island. The layer from the ocean surface to 1.5 km defines the airspace for cloud development; this layer is conditionally unstable and orographic lift or additional heating would result in cumuliform cloudiness. The plume clouds in figure

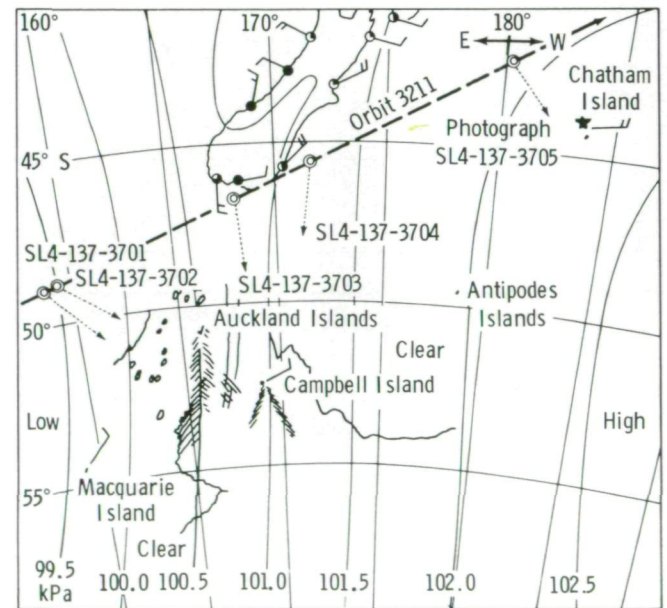


FIGURE 17-10.—Surface map for 00:00 GMT, December 23, 1973. (SL4-137-3701 through SL4-137-3705 were taken at locations of double circles.) Weather symbols are explained in appendix B.

17-11 are embedded in this layer. The stable dry layer between 1.5 and 3 km suppresses cloud development.

An attempt was made to rectify frame SL4-137-3703 for detailed examination of the wake waves from Campbell Island (fig. 17-13). There are two dominant peaks on the island, resulting in the two sources of wake waves in the atmosphere. A minor wake extends from the 465-m peak near the western end of the island. The major wake is originated by the highest (569 m) peak of the island. The combined wake is rather complicated where two sets of waves intersect at acute angles. Unfortunately, no temperature sounding of Campbell Island is available within several hours of the time the photograph was taken.

Winds aloft from Campbell Island show the existence of a significant shear (change in direction and velocity) layer between 1.7 and 2.0 km (fig. 17-14). The advection line of the wake extending toward the 190° direction from the 569-m peak coincides with the flow direction of the lower layer below the shear layer. This may mean that the advection line is the trajectory of the air modified by the island. The center line of the wake obtained by bisecting the V-shaped wake is oriented from the direction 350° to 170°. This orientation is almost the same as the mean value of the windflow direction of the lower layer (10° to 190°) and the upper layer (330° to 150°). These figures indicate that the wake waves propagate with the mean flow of the upper and lower layers.

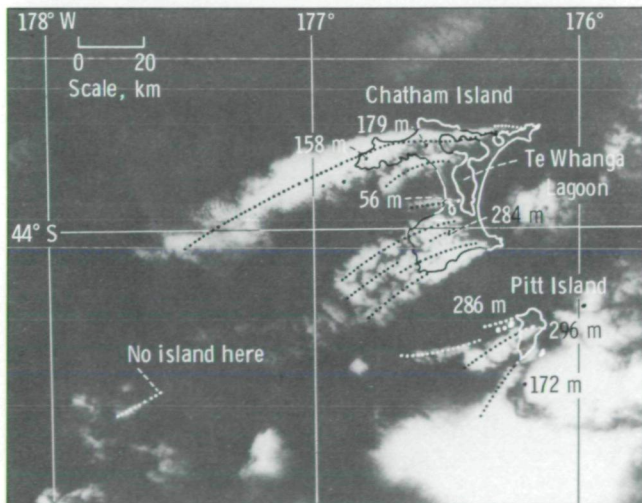


FIGURE 17-11.—Rectified photograph of cumulus streets from Chatham Island taken at 01:14 GMT, December 23, 1973 (SL4-137-3705).

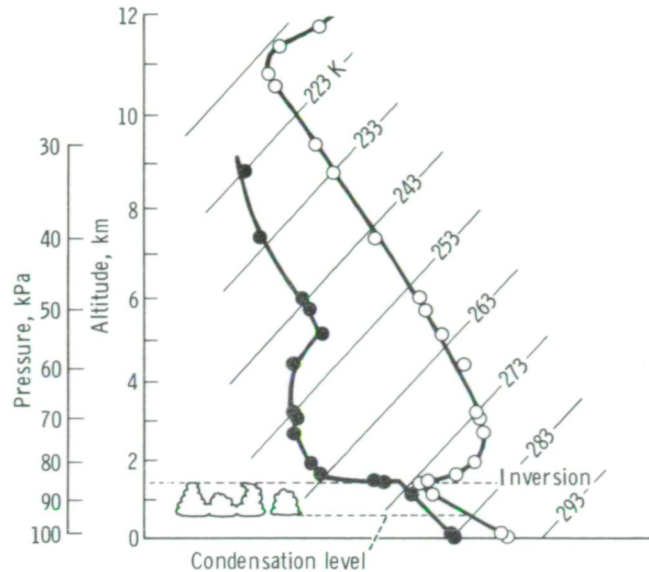


FIGURE 17-12.—Sounding at Chatham Island made at 00:00 GMT, December 23, 1973, 1 hour 14 minutes before figure 17-11 was taken.

DRY AND WET WAKES FROM ANTIPODES ISLANDS

A significant change in the wake of the Antipodes Islands occurred between December 16 and 17, 1973, and was revealed in two Skylab photographs taken 23 hours apart. The photograph taken at 01:13 GMT on December 16 (fig. 17-15) shows small patches of clouds on top of high peaks on the Antipodes Islands southeast of New Zealand. Although a distinct pattern of atmospheric wake waves is visible in figure 17-15, these waves are not characterized by clouds. If cumuliform clouds are embedded inside the waves, their brightness cannot be as low as shown on the photograph.

The authors suspect that the waves were made visible by the differential depth of pollutants trapped beneath the temperature inversion layer. More pollutants are found beneath the crests, whereas fewer pollutants will exist beneath the troughs. Such waves may be identified as "dry waves." Conversely, wake waves with condensed water droplets or clouds may be called "wet waves."

Figure 17-16 is the photograph taken at 00:20 GMT on December 17, 23 hours 07 minutes after figure 17-15 was taken. Significant "wet waves" are seen behind the same island. A considerable change in the flow direction also has occurred.

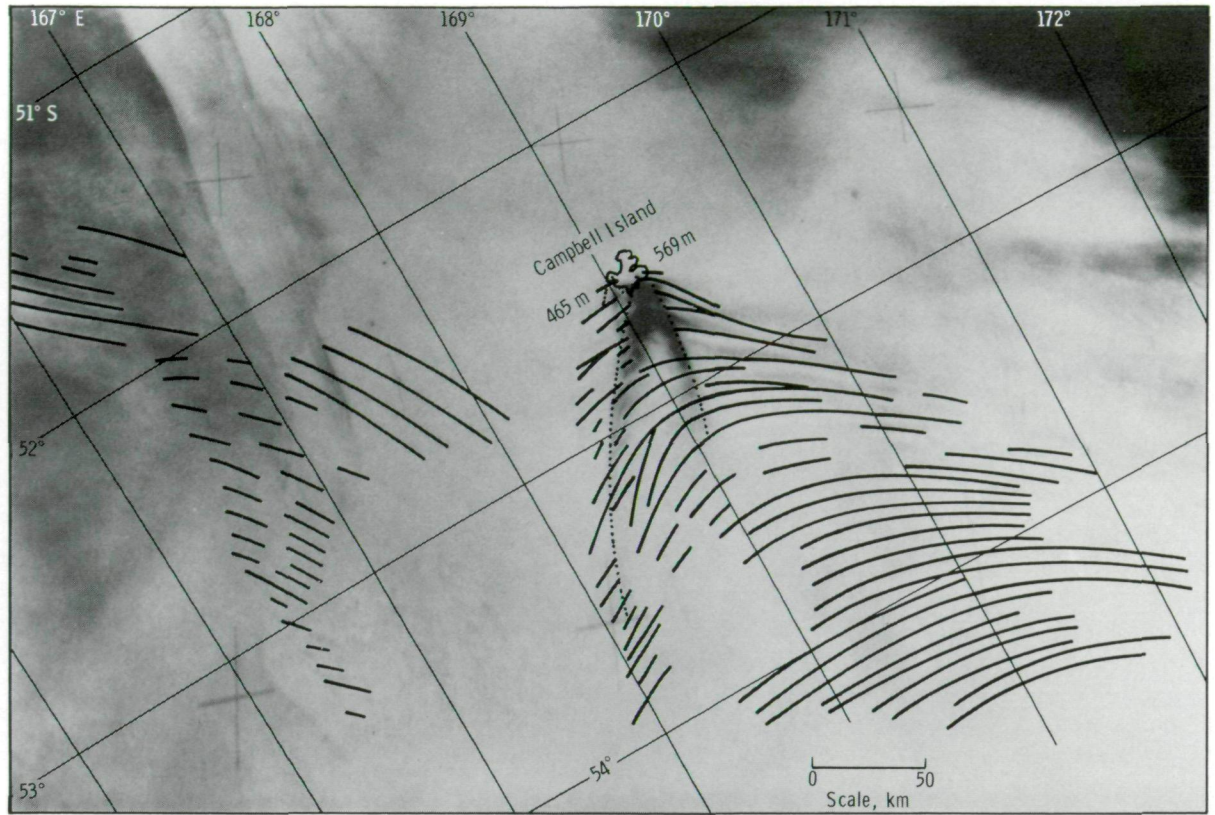


FIGURE 17-13.—Wake waves from Campbell and Auckland Islands south of New Zealand photographed at 01:11 GMT, December 23, 1973 (enlargement of SL4-137-3703).

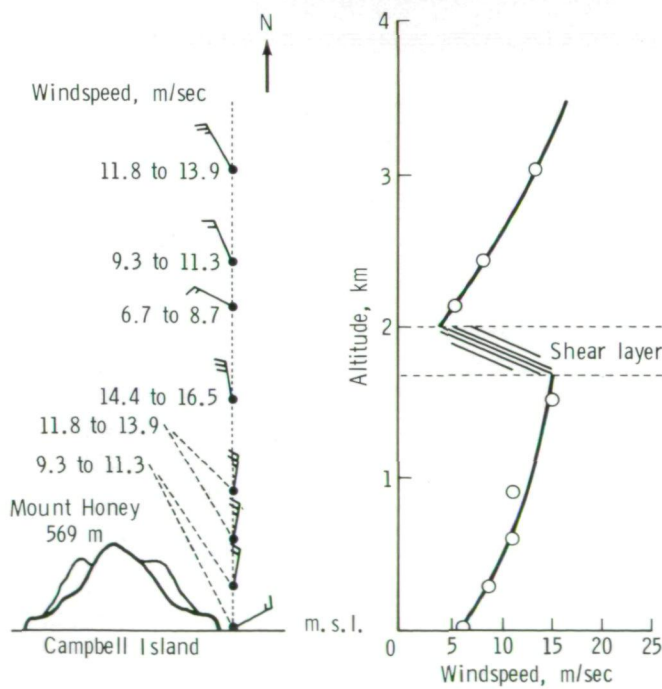


FIGURE 17-14.—Vertical distribution of winds over Campbell Island at 00:00 GMT, December 23, 1973. Weather symbols are explained in appendix B.

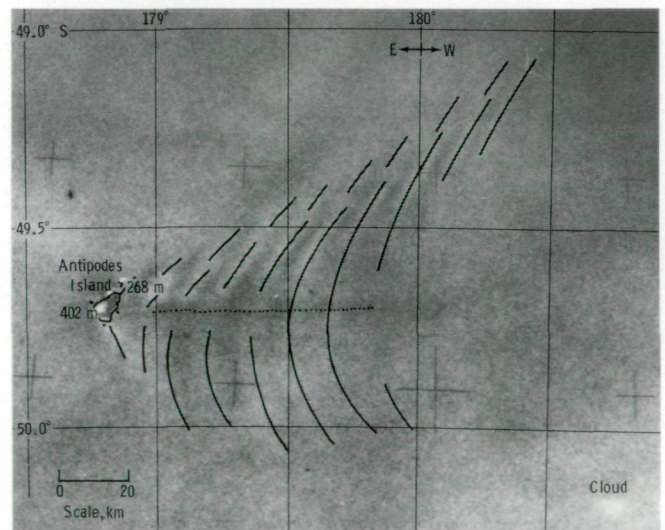


FIGURE 17-15.—Wake waves behind the Antipodes Islands made visible by the differential thickness of air pollution. Dry wakes without clouds are seen in this rectified photograph taken at 01:13 GMT, December 16, 1973 (SL4-137-3655).

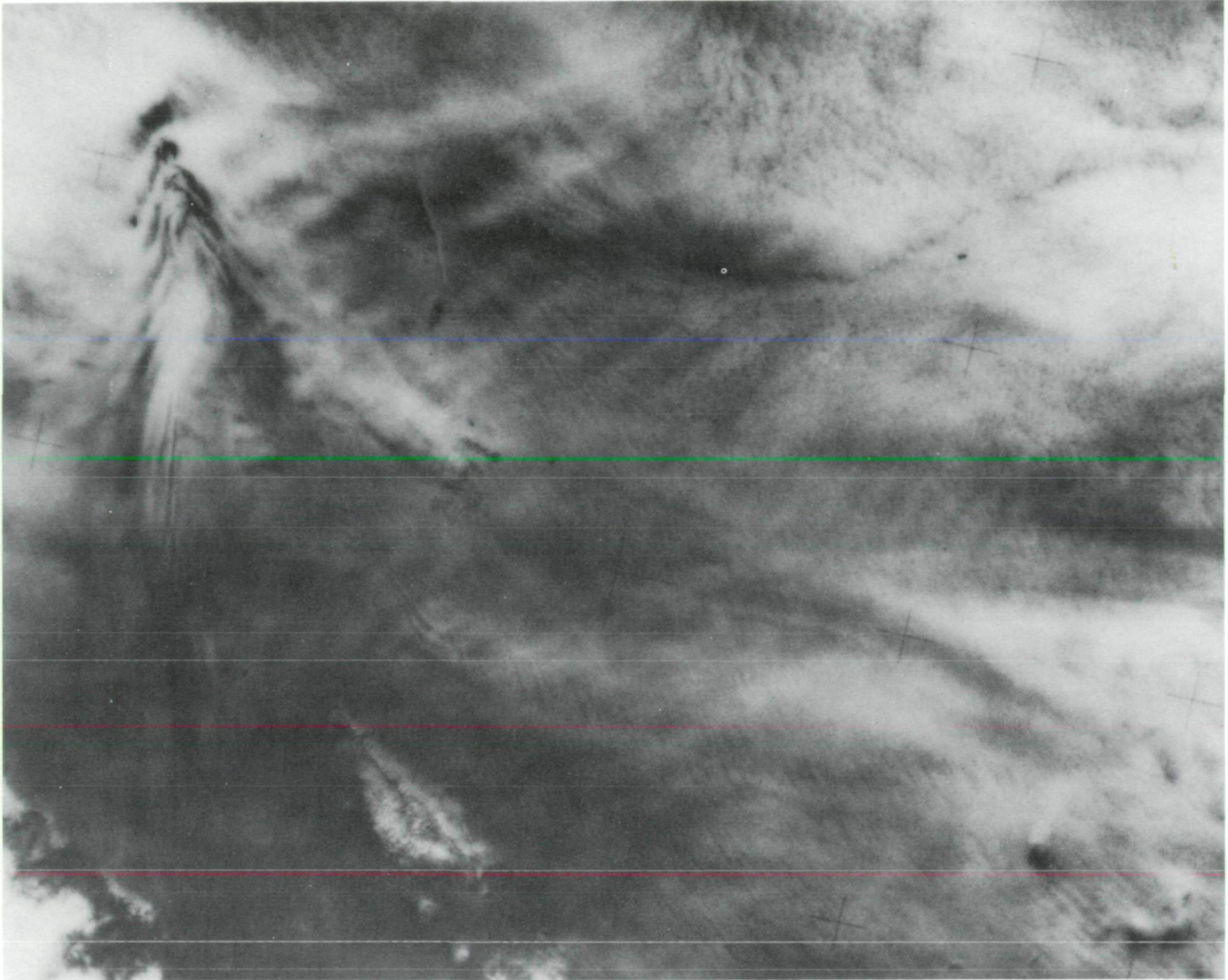


FIGURE 17-16.—Wake waves behind the Antipodes Islands made visible by wave clouds. This photograph of wet wakes with clouds was taken at 00:20 GMT, December 17, 1973 (SL4-137-3668).

The difference in the surface weather maps within 24 hours is shown in figure 17-17. A major change appears to be the advancement of a cyclone toward the east-northeast. The flow direction at the location of the Antipodes Islands shifted from westerly to northerly. Meanwhile, clouds of several types moved into the area. The surface weather maps also indicate that New Zealand was the likely source of the pollution that made wakes in the area of Antipodes (fig. 17-15) easy to see.

A vertical profile of the air temperature, dewpoint temperature, and windspeed as recorded on Campbell

Island December 16, 1973, is given in figure 17-18. The vertical temperature structure indicates the lowest cloud tops at 1 km and a few clouds at 2 km and at 5 km. The isothermal layer from 0.5 to 2.5 km is a mark of low-level stability.

If the characteristics of the stratification at Campbell Island are applied to the Antipodes Islands, the temperature lapse rate is favorable for the atmospheric wave propagation. Such a stable lapse rate will minimize the kinetic energy dissipation through eddy transport of low-level momentum.

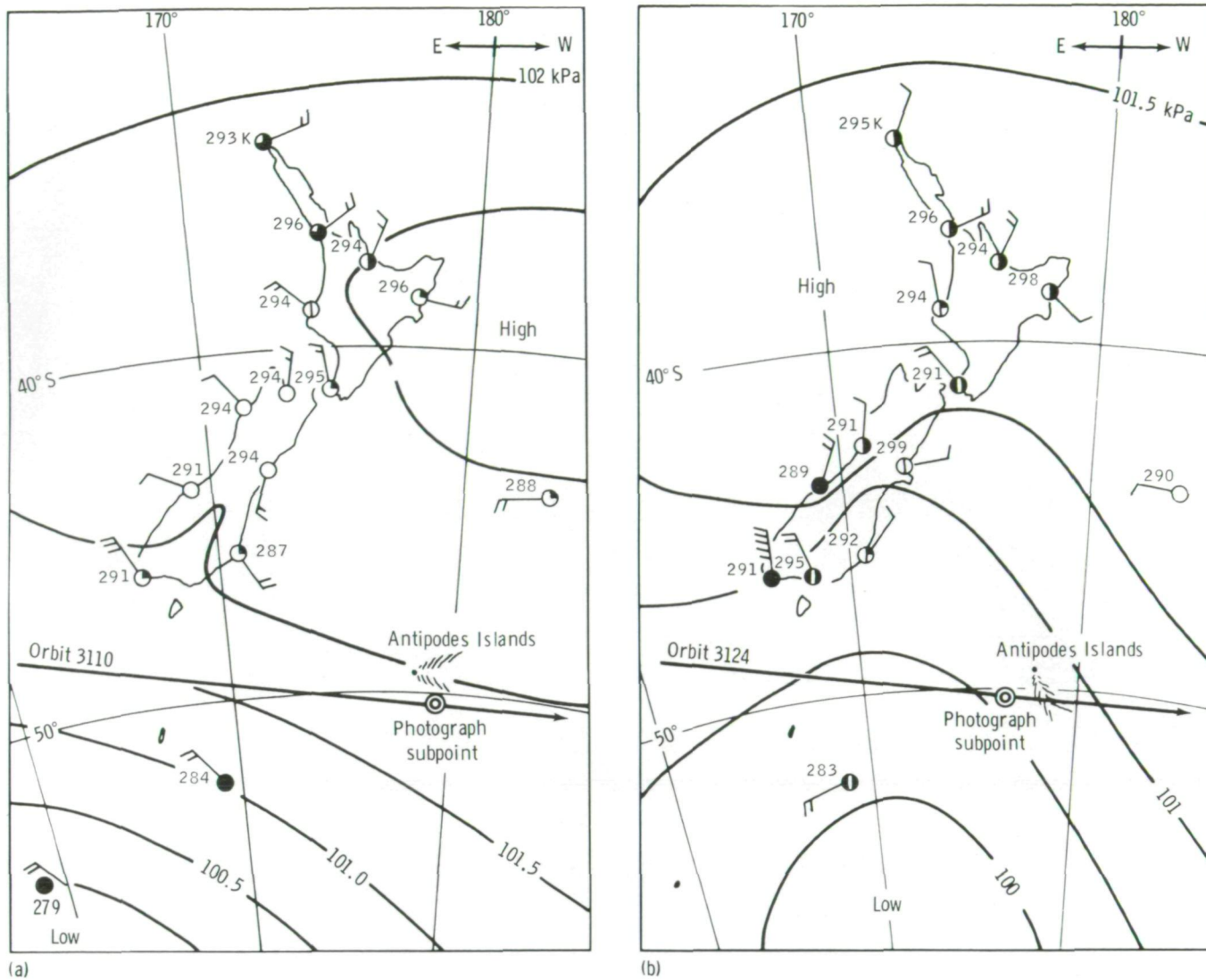


FIGURE 17-17.—Change in the surface flow during the 24-hour period from December 16 to December 17, 1973. Weather symbols are explained in appendix B. (a) 00:00 GMT, December 16. (b) 00:00 GMT, December 17.

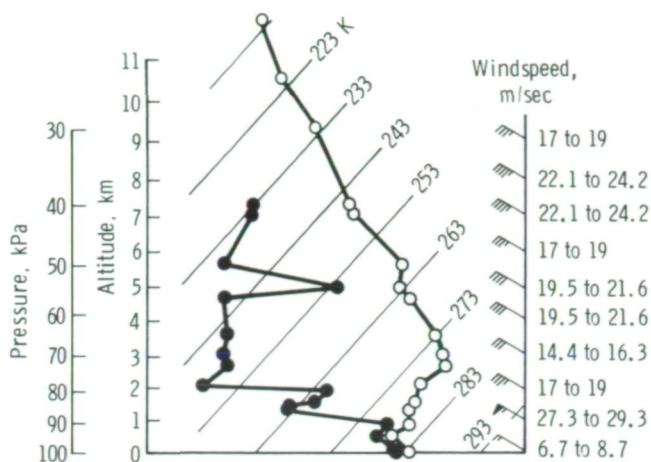


FIGURE 17-18.—Vertical distribution of temperature and wind from Campbell Island at 00:00 GMT, December 16, 1973.

CONCLUSIONS

Examination of mesoscale cloud patterns within the wake of obstacles seen in Skylab photographs reveals the existence of specific types of wake clouds related to meteorological conditions as follows.

1. Cumulus streets occurring when the lapse rate above the surface is adiabatic (a conditionally unstable atmosphere) with a medium to slow flow speed.

2. Kármán vortex streets occurring when the lapse rate above the surface is small, zero, or negative (i.e., a stable atmosphere) with a slow- to medium-speed flow impinging against a relatively large obstacle.

3. Wake waves occurring when the lapse rate above the surface is small (a stable atmosphere) with a medium- to fast-speed flow impinging against a relatively small obstacle. When the flow speed exceeds a critical value, the transverse waves tend to disappear, leaving the diverging waves only.

The human decision in photographing specific phenomena as viewed from a space platform is extremely valuable and important. Skylab photography has demonstrated that new phenomena can be found and photographed efficiently. Such space photography emphasizes the value of human judgment, for which there is no substitute.

REFERENCES

- 17-1. Briggs, Geoffrey A.; and Leovy, Conway B.: Mariner 9 Observations of the Mars North Polar Hood. *Bull. American Meteorol. Soc.*, vol. 55, no. 4, Apr. 1974, pp. 278-296.
- 17-2. Chopra, Kuldip P.; and Hubert, Lester F.: Kármán Vortex Streets in Earth's Atmosphere. *Nature*, vol. 203, no. 4952, Sept. 26, 1964, pp. 1341-1343.
- 17-3. Chopra, Kuldip P.; and Hubert, Lester F.: Kármán Vortex Streets in Wakes of Islands. *J. American Inst. Aeronaut. & Astronaut.*, vol. 3, no. 10, Oct. 1965, pp. 1941-1943.
- 17-4. Tsuchiya, K.; and Fujita, T.: A Satellite Meteorological Study of Evaporation and Cloud Formation Over the Western Pacific Under the Influence of the Winter Monsoon. SMRP Research Paper 55, The University of Chicago, 1966.
- 17-5. Stoker, James Johnston: *Water Waves: The Mathematic Theory With Applications*. Interscience Publishers (New York), 1957.
- 17-6. Kelvin, William Thomson: On the Waves Produced by a Single Impulse in Water of any Depth, or in a Dispersive Medium. *Proc. Roy. Soc. (London)*, ser. A, vol. 42, 1887, pp. 80-85.
- 17-7. Havelock, T. H.: *Wave Resistance Theory and its Application to Ship Problems*. Society of Naval Architects and Marine Engineers, New York, 1950.

18

Mesoscale Cloud Features Observed From Skylab

DAVID E. PITTS,^a J. T. LEE,^b J. FEIN,^c Y. SASAKI,^c
KIT WAGNER,^c AND R. JOHNSON^d

METEOROLOGICAL SATELLITES are an important source of data for the investigation of worldwide weather patterns especially over the oceans where radiosonde and ground stations are absent. Because of the lack of meteorological satellite sensors with spatial resolution on the order of 100 m, local weather forecasting has depended primarily on data from radiosonde and ground stations and aircraft.

Supplementing these data sources, meteorologists have analyzed the photographs of cloud features obtained during the Mercury, Gemini, and Apollo manned space-flight programs. Although some spectacular photographs of weather patterns resulted from these space flights, such information was generally of limited value in research studies of weather phenomena because of the lack of correlative atmospheric measurements and a planned observational program.

When the Skylab 4 mission was projected for 84 days, plans were made to determine the type of photographic and observational data that could be gathered by the crewmen for selected types of cloud features that are related to the development of severe storm systems. The primary tasks were to photograph cloud-street patterns, to estimate the physical dimensions of cloud

streets, and to describe their relationship to other cloud features and to land features. This investigation had two purposes: (1) to observe whether cloud streets manifested moisture convergence and (2) to observe whether cloud-street curvature was an indicator of the source of angular momentum that results in the generation of rotating storms as precursors to tornadoes.

CLOUD STREETS

Cloud streets are long lines of cumuli separated by narrow, clear areas. These clouds usually form at low altitude within 20° of the low-level wind direction, but they occasionally form perpendicular to the wind vector.

The Skylab 4 mission was flown during the winter, and many visible cloud streets were observed over the Great Lakes in the United States and over South America. The cloud streets over the Great Lakes were caused by cold air occurring over warm water, whereas those over South America were caused by thermal convection due to solar heating.

The crewmen photographed and observed many examples of cloud streets, such as those over Honduras, which seemed to terminate abruptly for no apparent reason (fig. 18-1). This condition could be caused by changes in the strength of convection, by a change in windspeed, or by moisture availability. An apparent roll cloud immediately inland on the coast of South America is shown in figure 18-2. This cloud was caused

^aNASA Lyndon B. Johnson Space Center.

^bNational Oceanic and Atmospheric Administration, National Severe Storm Laboratory, Norman, Oklahoma.

^cThe University of Oklahoma, Norman, Oklahoma.

^dLockheed Electronics Co., Houston, Texas.

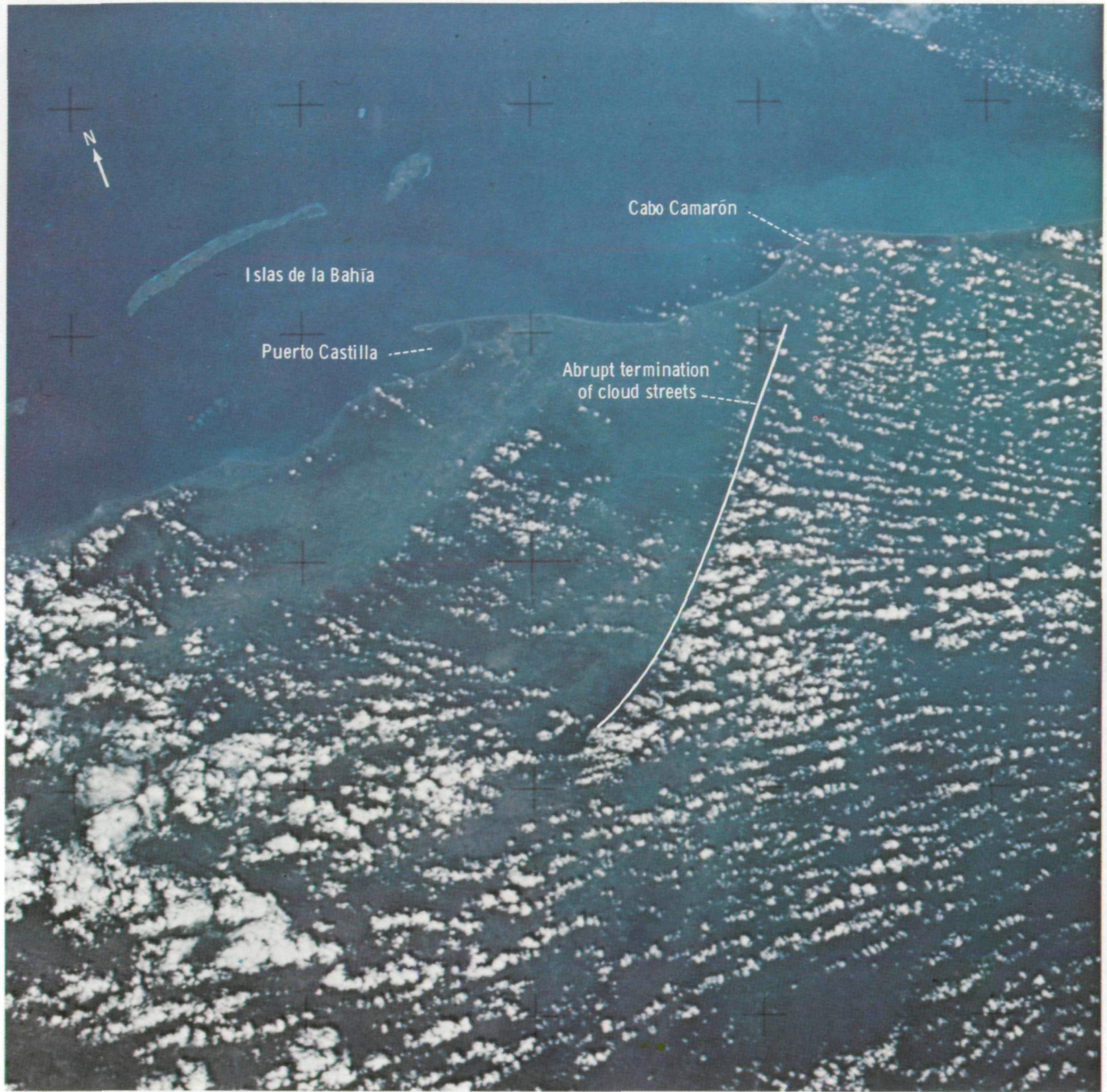


FIGURE 18-1.—Handheld-camera photograph showing distribution of cloud streets over Honduras (SL4-138-3796).

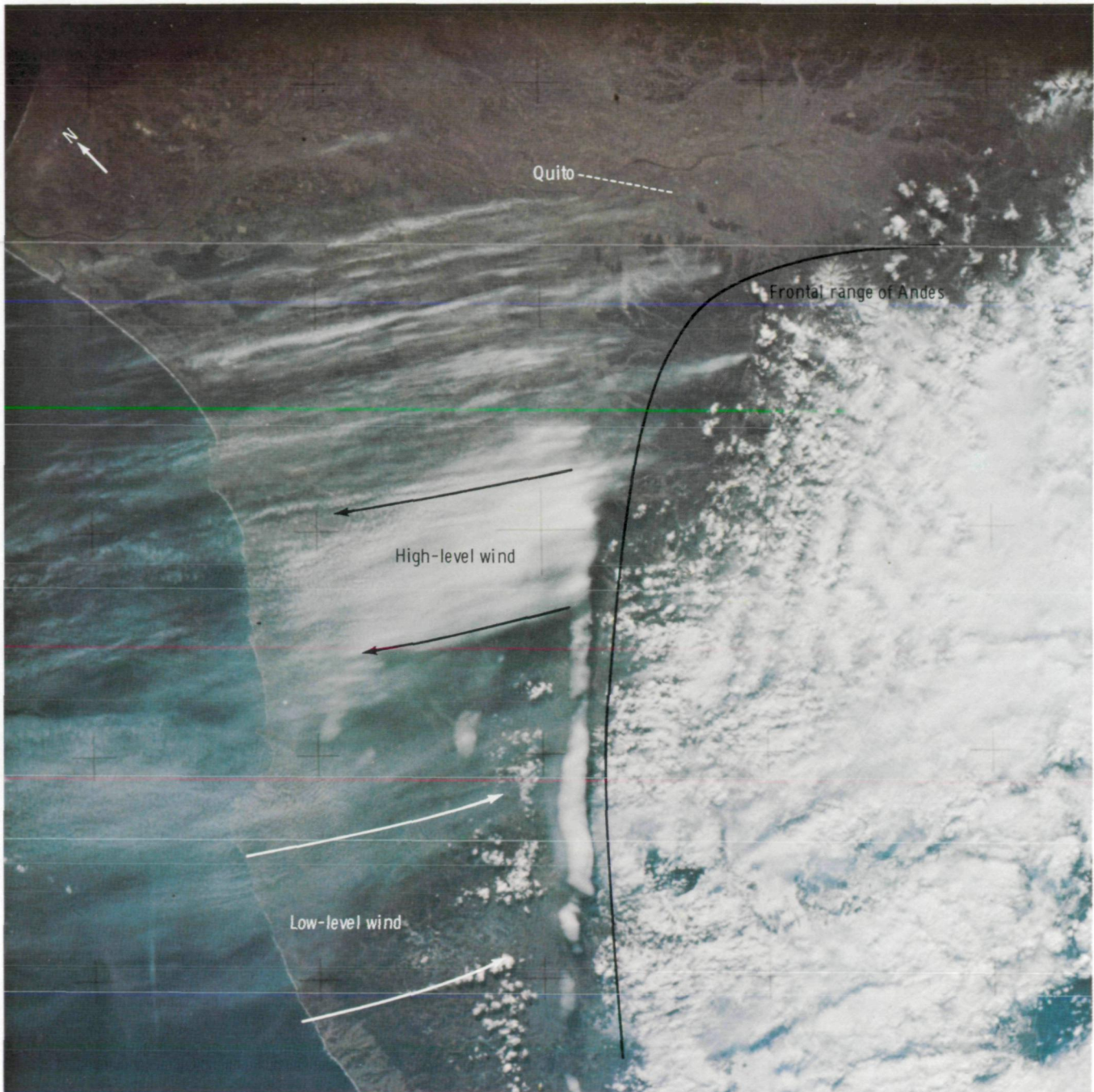


FIGURE 18-2.—A roll-type cloud visible over northern Ecuador (SI4-139-3943).

by the interaction of sea breeze and the 6-km-high Andes Mountains near Quito, Ecuador. Together with this onshore low-level flow is an offshore high-altitude flow that is manifested by the cirri on the left side of the photograph. A photograph of clouds over Cyprus (fig. 18-3) shows the two types of convection clouds that can occur with horizontal winds: the longitudinal roll cloud streets in the upper right, which form along lines within approximately 20° of the wind vector, and the gravity-wave clouds or transverse type, which form perpendicular to the wind vector. Both types are important because they can serve as triggers for the formation of larger convection storm systems.

The crewmen observed, but were unable to photograph, many cloud colors in the down-Sun (antisolar) direction. This glory effect (zero-phase angle), which had not been observed from space before the Skylab missions, seemed to emanate primarily from cirri and strati. The color distribution may possibly be used to distinguish the type of cloud and the droplet size and distribution. On future manned space flights, the relationship of color to the edges of severe storms should be investigated.

PERPENDICULAR CLOUD STREETS

During the Skylab 4 mission, photographs of cloud streets aligned perpendicular to the direction of the mean windflow (i.e., transverse waves) were obtained over Fernando de Noronha, an island 480 km northeast of Recife, Brazil (fig. 18-4). The downwind cloud off the island is oriented perpendicular to the background of cloud streets. In the synoptic photograph of South America (fig. 18-5), the Intertropical Convergence Zone (ITCZ) is north of the island and, as shown in figure 18-4, the transverse cloud streets are oriented north-south, an indication that the wind is flowing from the east. The island lee cloud is therefore west of the island, and the background cloud streets form as transverse waves perpendicular to the mean flow. These transverse waves do not occur as frequently as the longitudinal roll cloud streets, which form parallel to

the mean flow. Figure 18-4 is significant because it shows the breakdown of the metastable transverse cloud streets by a perturbation from the island that resulted in formation of the longitudinal roll cloud street in the lee of the island. Similar small perturbations over land may trigger severe storms because precipipient storm conditions often may exist in metastable equilibrium.

CLOUD STREETS OVER LAKE SUPERIOR

Unusual cloud streets over eastern Lake Superior attracted the crewmen's attention and were photographed at 18:21 Greenwich mean time (GMT) on January 10, 1974 (fig. 18-6), when Lake Superior had little, if any, ice cover. The cloud streets are aligned along a line of convergence in the middle of the lake as manifested by the dense cloud line, which is oriented east-west. The surface meteorological chart at 18:00 GMT showed a shallow east-west high-pressure ridge in southern Canada and extensive frontal weather oriented east-west through the central United States. Over Lake Superior, a mesoscale, thermally induced pressure trough was found coincident with the line of convergence identified in figure 18-6. With the temperature of the unfrozen lake water 11 to 17 K warmer than the adjacent environment over the land, the resulting atmospheric convection initiates a low-level land-to-lake circulation that adds to the pressure-induced circulation. The cloud-street curvature was influenced by the coincident curvature of the surface isobars. Another important feature was the cloud structure and linearity within the line of convergence. An interlinking loop action from cloud cell to cloud cell existed with a wavelength of approximately 15 km. The thermal wind from surface to 1000 m was near 250° at 6.5 m/sec, and cold-air advection, with backing winds, quickly shifted the surface winds to a west-southwest direction at the top of the layer, which contained the cloud streets and the line of convergence.

The rotation of the wind from northerly to west-southwesterly as the convective air rose through a cell

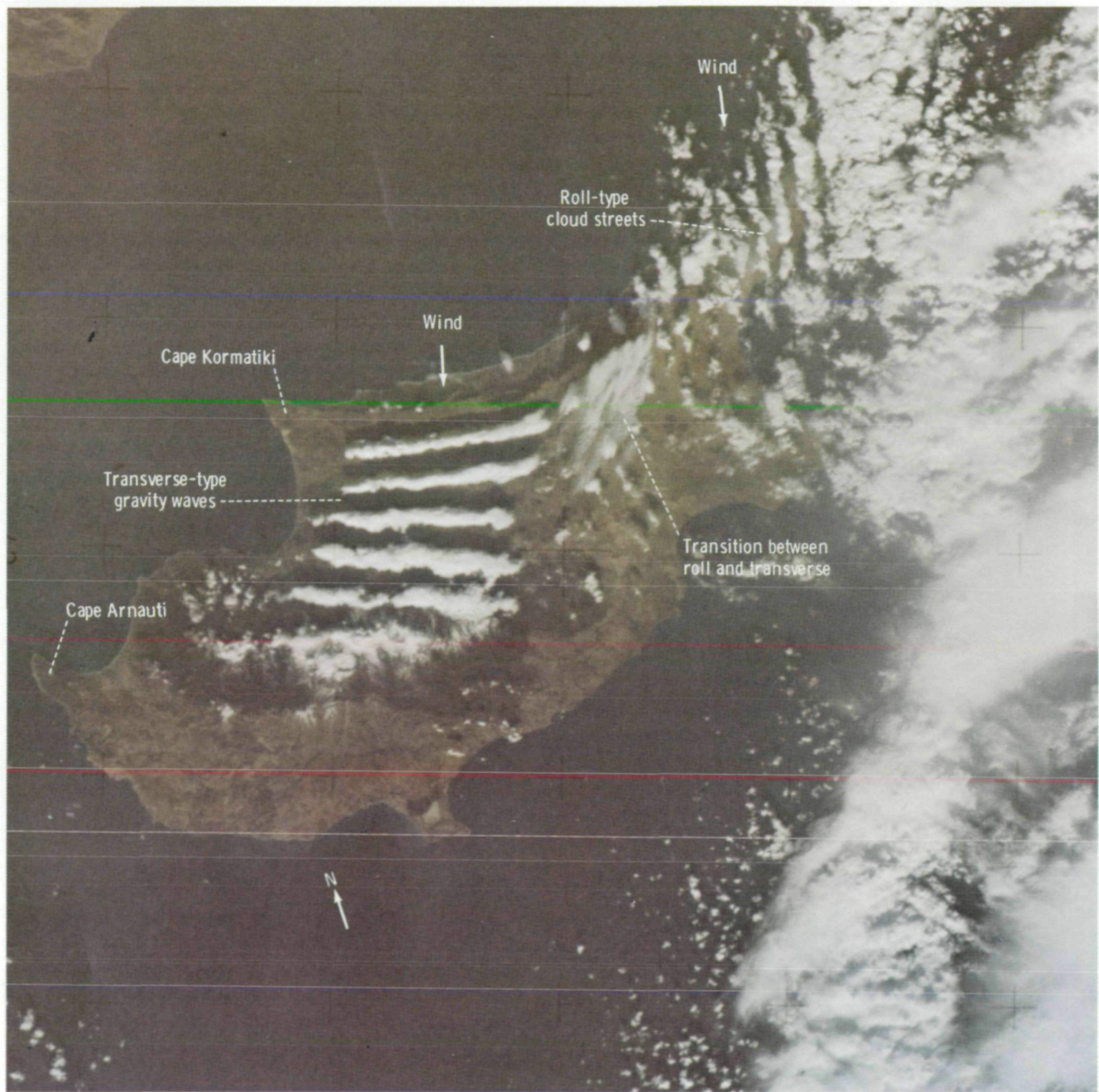


FIGURE 18-3.—Gravity-wave clouds and cloud streets seen over the island of Cyprus (SI4-142-4454).



FIGURE 18-4.—Downwind cloud off the island of Fernando de Noronha photographed January 3, 1974, at 12:27 GMT. The wind direction is from right to left (SL4-138-3874).

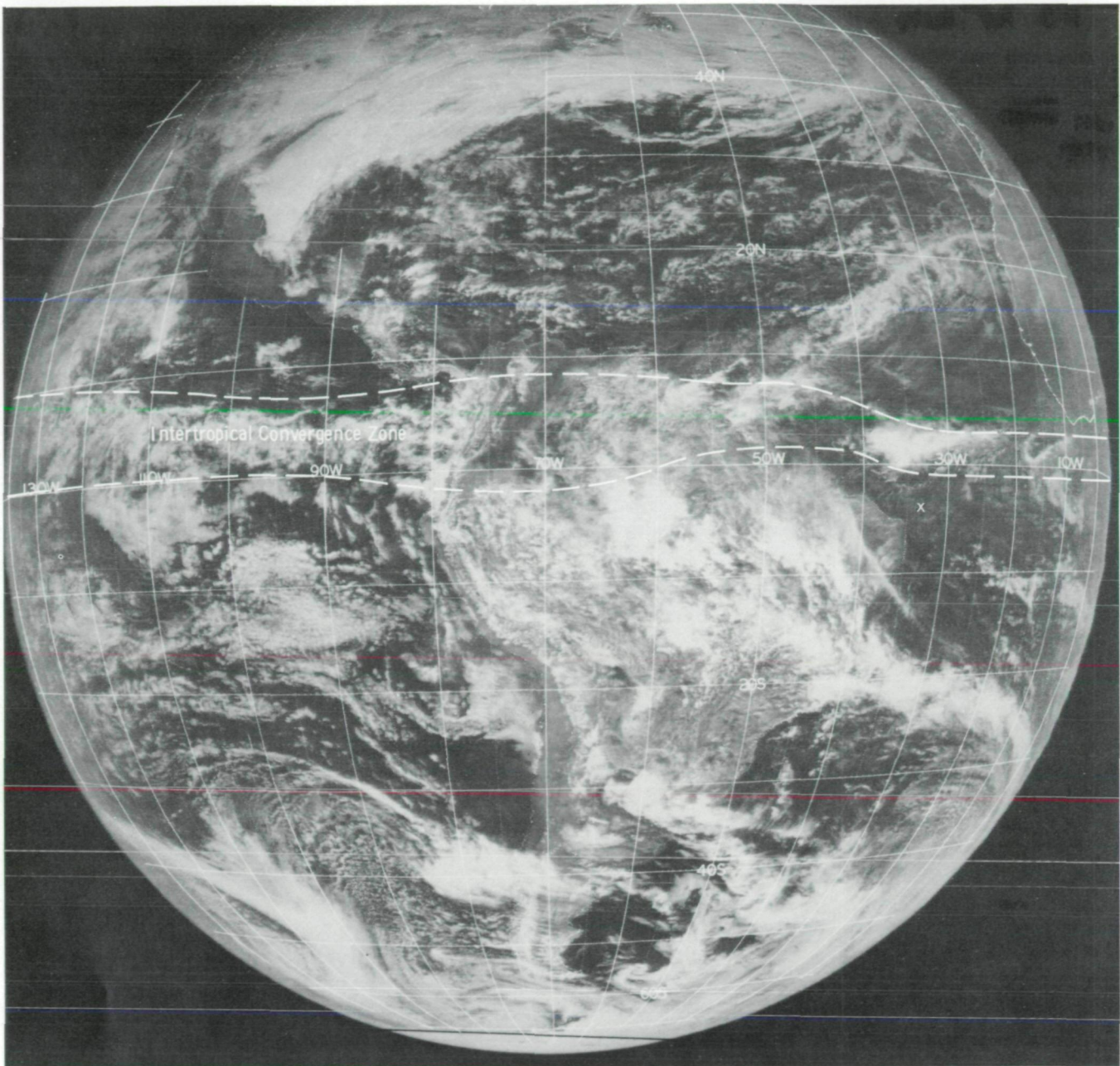


FIGURE 18-5.—Applications Technology Satellite 3 synoptic image obtained on January 3, 1974, at 12:20 GMT.

may have been the source of the angular momentum. This angular momentum caused the apparent cyclonic rotation of the cells in the interlinking loops, a phenomenon that could be similar to the Browning (ref. 18-1) model of a tornado-producing thunderstorm. The line of convergence was also closely related to a dry line, which is oriented east-west in figure 18-6. (Observe the temperature-dewpoint difference.)

In this example, the mesoscale convection was so intense that it dominated the synoptic-scale flow. Thus, under extreme conditions, large heat and moisture sources and sinks in the boundary layer can cause storms to form. Whitehead et al. (ref. 18-2) reported contouring of cloud-top altitudes using Apollo 6 photographs, and one photograph from this set closely resembles the cyclonic convergence in figure 18-6. However, the storm recorded by the Apollo 6 camera occurred in western equatorial Africa (lat. 2° S, long. 15° E) in relatively dry air. This storm was likely caused by solar heating as a result of a general lack of normal cloudiness during most of the day. This particular line also formed along a dry line and exhibited apparent cyclonic rotation. The cloud tops were determined to be above 11 000 m.

Thus, in these two examples, the thermal heating at the surface contributed to the formation of thunderstorms exhibiting apparent rotation. Future investigations should determine whether smaller scale heat sources and sinks contribute to triggering both airmass- and squall-line-type convective storms. Space observers should concentrate on the National Severe Storm Laboratory mesoscale and synoptic-scale networks in central Oklahoma to see formation of cells of this type. The networks are usually operated from mid-April to mid-June.

CLOUD STREETS IN SOUTHWEST OKLAHOMA

From analysis of space images such as those obtained by the Skylab 4 crewmembers for study of cloud streets, the synoptic overview of atmospheric features can be determined. To optimize the use of synoptic photographs, an experiment was performed in southwestern Oklahoma on June 11, 1973, during the Skylab

2 mission. The purpose of the experiment was to obtain radiosonde soundings concurrent with photographic data for comparative analysis with previous studies of cloud streets in the atmospheric boundary layer. In conjunction with photographs from the Skylab multispectral camera system (S190A), radiosonde ascents were made at 1-hour intervals from Fort Sill, Oklahoma, and one sounding balloon was released within 1 minute of the Skylab overflight. Fort Sill is within the 163-km-square Skylab photographic groundtrack (figs. 18-7 and 18-8). In addition, soundings were taken at Norman, Oklahoma, and nearby Tinker Air Force Base.

The surface boundary layer was capped by an inversion, and the upward movement of the inversion base illustrates the boundary-layer growth. Figure 18-9 shows this temporal change above ground at the three stations. When the Skylab photographs were taken, the inversion was rising approximately 100 m/hr. Further evidence of the transitional nature of the boundary layer in the morning is found in figure 18-10. From sunrise until 08:22 central standard time (CST), the wind veered from 185° to 210° and then shifted back past 180° by 11:00 CST. Examination of individual soundings reveals a similar response for the boundary layer and illustrates that the response is not just a result of the inversion rising through a wind profile which changes direction with height (fig. 18-11) but is partly the result of cold-air advection in the lower layer.

Clouds form in this lower layer, and there has been continuing interest in relating orientation of the cloud-street longitudinal axis to boundary-layer wind direction. Plank (ref. 18-3) found cloud-street orientation to be 15° left of the wind direction at the cloud base. Kuettner (ref. 18-4) found the orientation to be within 10° of the convective layer mean wind. For an unstable boundary layer, LeMone (ref. 18-5) found that horizontal roll vortexes associated with cloud streets are 10° to 20° left of the geostrophic wind at the inversion base.

On June 11, 1973, at 15:18:38 GMT when the Fort Sill region was photographed from Skylab (fig. 18-8), the inversion base wind was 8.8 m/sec at 200°. Cloud streets were oriented from 191° to 211° with 205° being the predominant direction. These data indicate that the cloud streets are oriented along the wind direction at the inversion base.

wind direction at 85 kPa (850 mb) on June 11 was approximately 200°, whereas the observed cloud-street axis was approximately 5° to the right of this orientation. This disagreement between Brown's model and the observed orientation (left 20° compared to right 5°) probably results from the assumption in the model of a constant geostrophic wind from surface to 85 kPa. During these observations, apparent cold-air advection produced changing geostrophic wind with height.

Another observable cloud-street feature is spacing between streets. The Skylab photograph (fig. 18-8) shows a 1.2-km average spacing at Fort Sill. Comparisons between occurrences are usually given in terms of horizontal spacing to inversion height ratio. Kuettner (ref. 18-4) and LeMone (ref. 18-5) report a usual ratio range of 2 to 4. The observation of 1.7 in this instance seems to extend the range.

Kuettner mentioned that curvature of the vertical profile of the horizontal windspeed is observed with cloud streets. The value at Fort Sill at 09:17 CST of approximately $-4 \times 10^{-10} \text{ m}^{-1} \text{ sec}^{-1}$ is smaller than the 10^{-8} to 10^{-9} range reported by Kuettner.

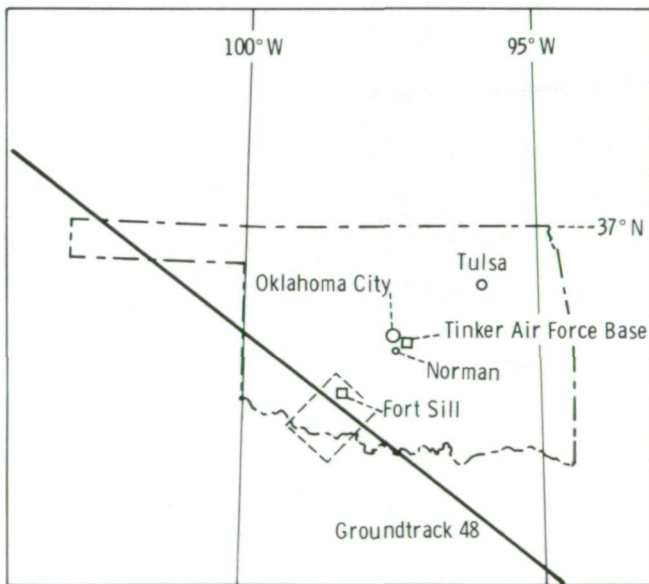


FIGURE 18-7.—Map of Oklahoma showing the Skylab groundtrack. The area outlined is the same as that shown in figure 18-8.

Overall results agree closely with Kuettner's observations. The cloud-street orientation is along the inversion base wind vector, the spacing ratio is 1.7, the windspeed is moderately high in the boundary layer, and some curvature is observed in the wind profile. These observations substantiate the use of cloud-street orientation obtained from satellite photographs as an indicator of low-level windflow in areas lacking radiosonde and surface meteorological observations. This orientation capability is one of the many meteorological uses of satellite photography.

MECHANICAL PROCESSES ASSOCIATED WITH ISLAND PATTERNS

Kármán vortices and lee gravitylike waves commonly occur near islands. Although their features have been observed and studied extensively, the studies are somewhat limited by a lack of surface and upper level meteorological data. Detailed photographs of Kármán vortices were obtained from Skylab; as a result, there is a renewed interest in studying this phenomenon. A typical example of the mechanical generation of Kármán vortices by an island is shown in the Skylab photograph of Guadalupe Island (lat. 29° N, long. 118° W) west of Baja California (fig. 18-13). Other islands observed with Kármán vortices include Cheju Do south of Korea and the Canary Islands off the western coast of Africa. Formation of the vortices requires a windspeed between 5 and 13 m/sec and a strong low-level temperature inversion (ref. 18-7). Laboratory experiments (ref. 18-8) produce vortices that alternate in vorticity, a cyclonic vortex followed by an anticyclonic vortex. Predictions based on theory (ref. 18-8) are that the coriolis forces should not be important in the decay of the vortices and that cyclonically rotating vortices forming along one side of the trail usually do not persist longer than the oppositely rotating vortices on the other side. However, in figure 18-13, three well-defined cyclonic vortices are present with one small remnant of an anticyclonic vortex.

These patterns have been observed regularly during winter months from manned Earth-orbiting satellites and provide supplementary photographic information

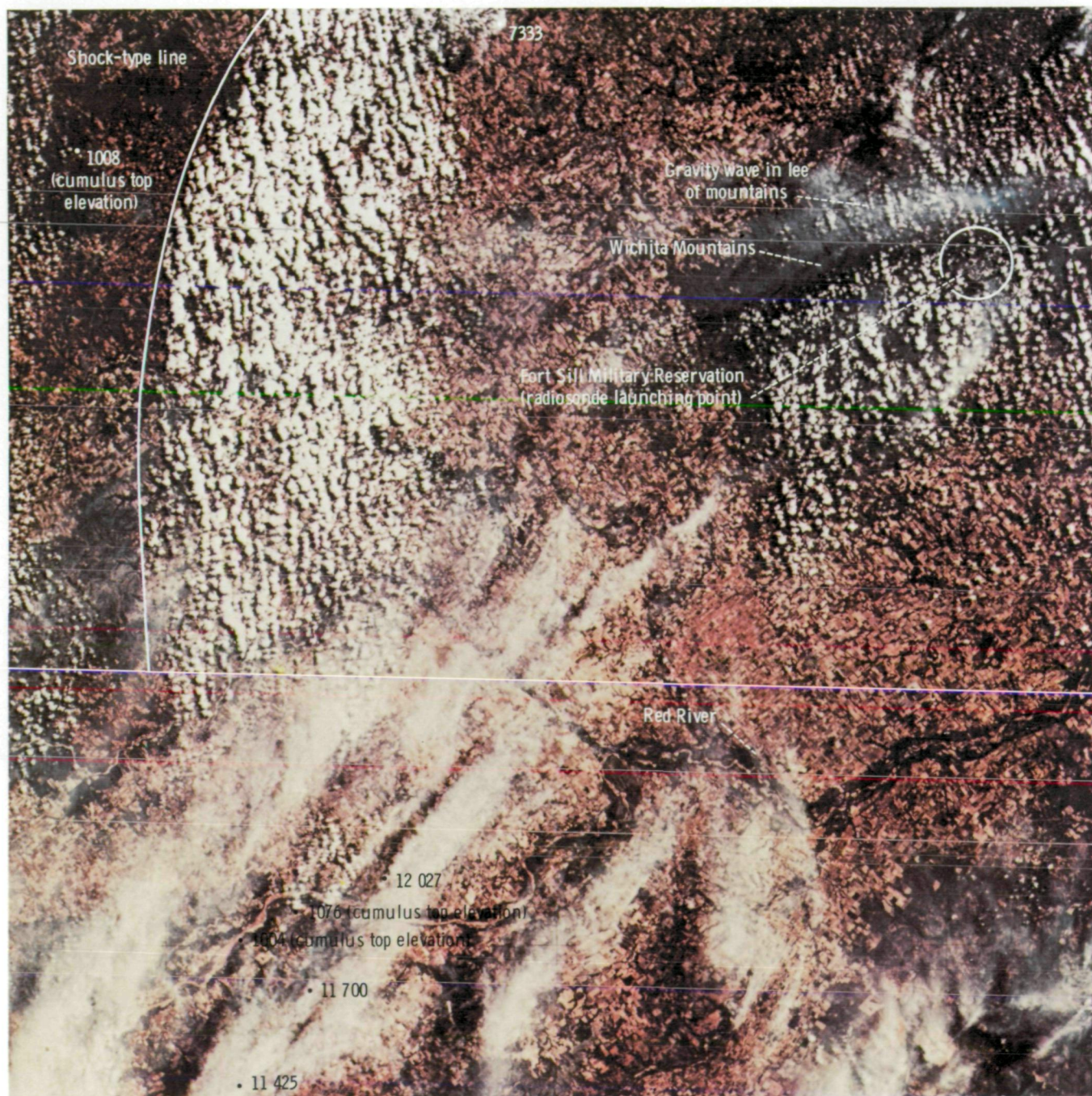


FIGURE 18-8.—Fort Sill, Oklahoma, region (photographed with the Skylab multispectral camera (S190A)) showing cloud formations on June 11, 1973. Cloud heights, determined by using stereographic techniques, are shown in meters above sea level, with an accuracy of ± 50 m (SL2-16-032).

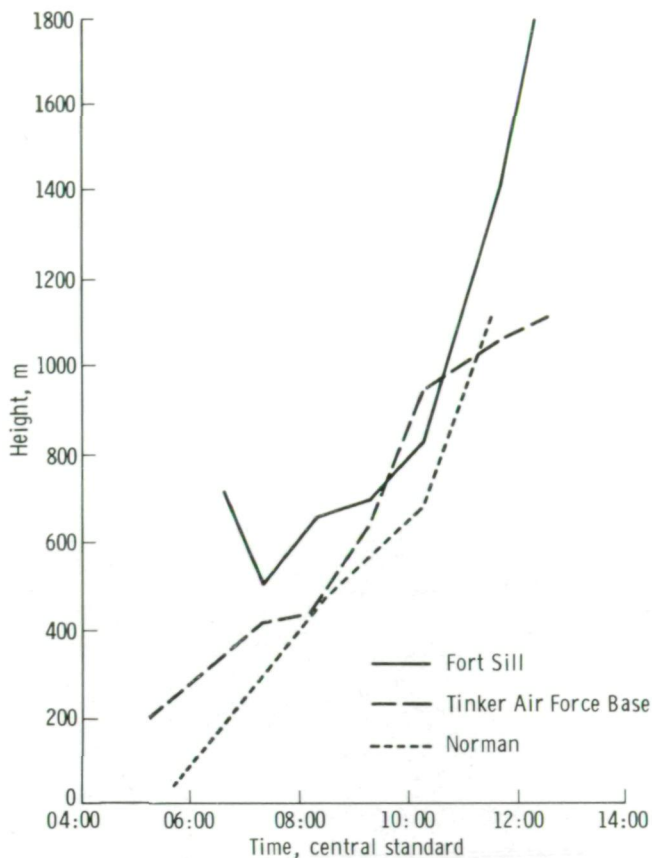


FIGURE 18-9.—Change of the inversion base height on June 11, 1973, is shown for three points in Oklahoma.

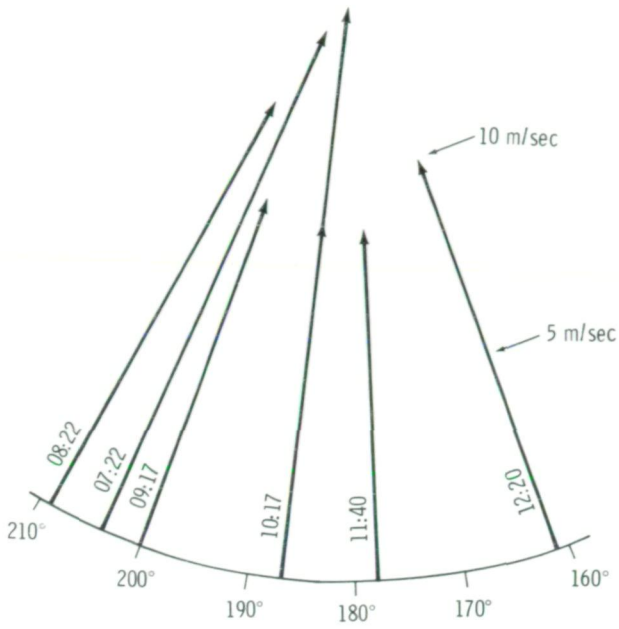
on the occurrence and distribution of vortices in the lee of islands. Analyses of such photographs together with laboratory studies may provide information in understanding turbulent transport processes.

Several unusual bow-shock-type (wake) waves were photographed by the Skylab 4 crewmen. One such photograph (fig. 18-14), taken over Campbell Island (peaks of 569 m and 465 m altitude) approximately 640 km south of New Zealand, shows a well-defined bow-type wave downwind of the island. The complex shock-type wave structure indicates the presence of other energy forces. The photograph of Gough Island (fig. 18-15) (formerly called Diego Alvarez), at approximately latitude 40° S, longitude 10° W, shows both the

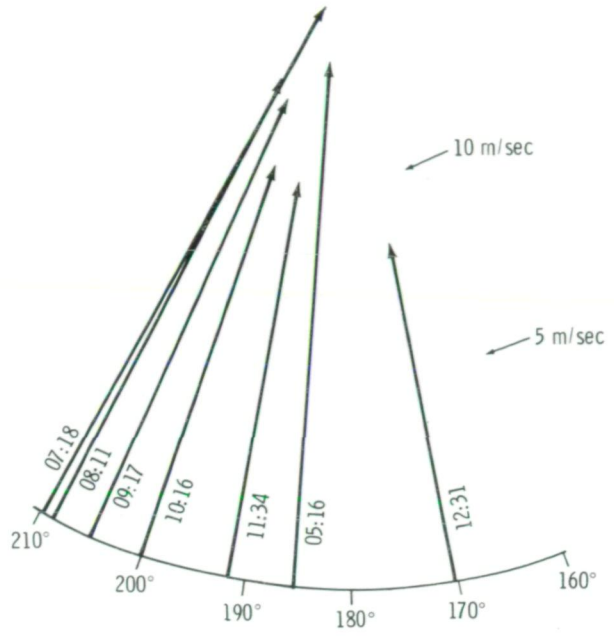
bow-type wave and a well-defined shock-type wave. The crewmembers described the wave as similar to a supersonic flow in which an object causes a diamond shock effect. Gough Island is approximately 13 km long and 6 km wide, and the highest peak, 888 m above sea level, rises from a central plateau bordered by deep valleys and craggy ridges. The wake downwind of the island extends at least 300 km and appears to have a lateral extent of almost the same scale. Preliminary investigations reveal the possibility that these waves may be gravity shock waves that are generated in a neutral or stable planetary boundary layer in which the mean windspeed exceeds the propagation speed of the internal gravity wave. Although Gough Island lies in an area in which little data have been gathered, the temperature profile in the planetary boundary layer was estimated from analysis of vertical-temperature-profiling radiometer data obtained at 08:44 GMT on December 15 by the National Oceanic and Atmospheric Administration satellite NOAA-3. The lapse rate in the stable layer between the surface and 85 kPa (850 mb) permitted calculation of the propagation speed of the internal gravity waves in that layer as approximately 15 m/sec. The shock angle measured from a Skylab photograph (fig. 18-15) implied a mean windspeed in the stable layer of 30 m/sec. A Reynolds number of 40 (ref. 18-9) was determined from the shape of the undulating pattern downwind of the island obstacle. Based on the analytical technique of Wilkins and Sasaki (ref. 18-10), the turbulent diffusion coefficient for the layer was estimated as $5 \times 10^7 \text{ cm}^2/\text{sec}$. These numerical values must be considered as approximations and are based on the hypothesis that the phenomenon observed is a gravity shock wave.

Such phenomena are apparently not confined to Earth atmosphere as indicated by a Mariner 9 image of Mars (fig. 18-16). The wave-cloud pattern is caused by flow over a 100-km crater (ref. 18-11). The wake extends at least 800 km downstream and has a lateral spread of approximately 400 km.

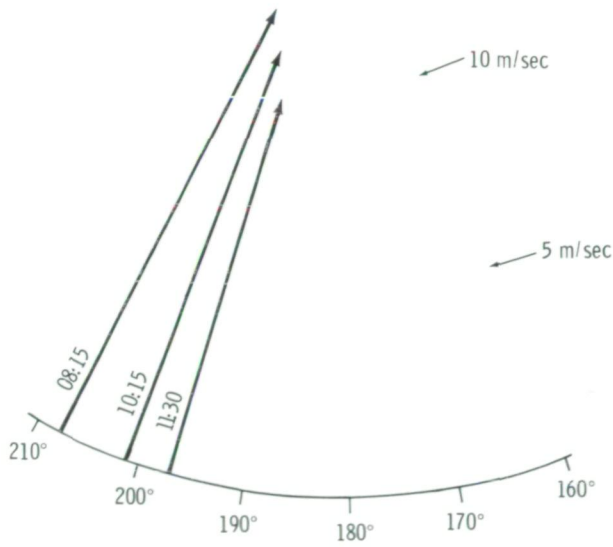
Figure 18-17 is a closeup photograph of a gravitational shock-type wave cloud emanating from one of the Snares Islands southwest of New Zealand at latitude 48° S, longitude 166.5° E. Such gravitational shock



(a)



(c)



(b)

FIGURE 18-10.—Graph of morning wind direction and magnitude as a function of time (CST) on June 11, 1973. Vectors indicate wind velocity at inversion base height. (a) Fort Sill, Oklahoma. (b) Tinker Air Force Base. (c) Norman, Oklahoma.

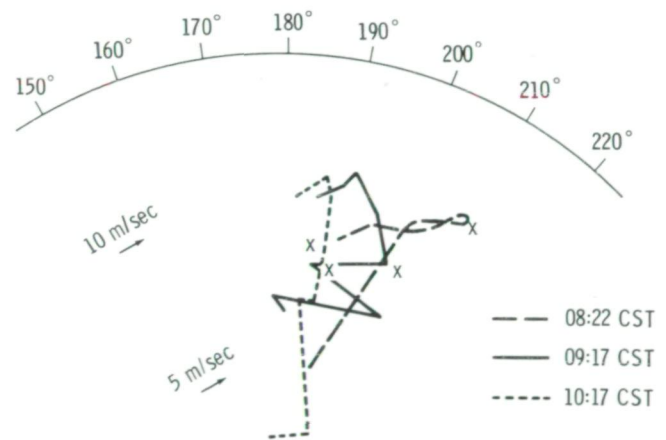


FIGURE 18-11.—Hodographs of wind at Fort Sill, Oklahoma, at different times on June 11, 1973. The inversion base is indicated by "x".

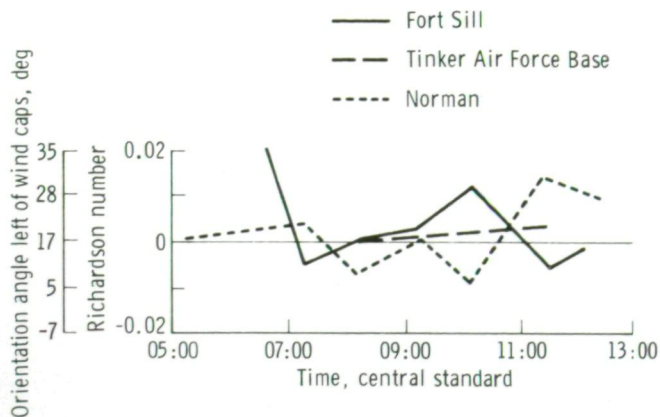


FIGURE 18-12.—Scale showing change in Richardson number with the passage of time. The left scale indicates the relation of the orientation angle of the cloud street to the Richardson number, according to Brown's model (ref. 18-6).

waves occur when the windspeed u exceeds the group velocity C_g .

$$\frac{u}{C_g} > 1 \quad (18-2)$$

The photograph was taken on February 4, 1974, at 04:30 GMT when the Sun was at an elevation of approximately 36° at an azimuth of 286° . The parallel upper and lower clouds can be distinguished because the location of the Sun produces shadows from the high clouds and the detail present enables discernment of the more fibrous nature of the upper clouds. The nadir coverage of the Nikon camera with the 300-mm lens is 34 by 51 km. Although the exact orientation angle of the camera axis is unknown, the lower limit of the altitude of the clouds can be determined if the look angle is assumed to be near nadir. In this photograph, the lower level clouds are estimated to be near 2 km and the upper clouds are near 5 km above the surface of the Earth.

The sounding from Campbell Island (lat. 52.55° S, long. 169.15° E) at 00:00 GMT on February 4, 1974, showed a moist, unstable region from near the surface to approximately 2 km altitude (85 kPa (850 mb)) capped by a dry region and a temperature inversion

with winds at 270° at 4 m/sec. The windspeed became strong with height and was westerly through the entire tropopause. The wind at 5 km altitude was 265° at 23 m/sec. Several other moist regions occurred at higher levels, but none were associated with the temperature inversions. A sounding taken from Invercargill, New Zealand (lat. 46.42° S, long. 168.33° E), shows an entirely different character. The surface temperature is 8 K warmer, the atmosphere is very moist through 30 kPa (300 mb), and the temperature profile is nearly pseudoadiabatic throughout the troposphere. A moist region occurred near 50 kPa (500 mb) (approximately 5.5 km altitude) that was associated with a small temperature inversion. The winds were light easterlies to as high as 7 km, and a 20-m/sec southerly flow developed at 10 km altitude.

The phenomenon photographed is unusual in that the gravity shock wave near 5 km does not have associated transverse (or secondary) bow waves. For these waves to be absent, the stable layer must be very shallow. The stable layer in which the gravity shock wave is occurring in the photograph is approximately 200 m thick, and the wind velocity is approximately 23 m/sec. For the transverse waves to be absent, the wind velocity must be greater than 45 m/sec or the stable layer must be less than 50 m thick. It is also possible that these transverse waves exist but have a wavelength greater than 50 km and therefore fall outside the photograph.

The group velocity of a gravity wave

$$C_g = \sqrt{\frac{\Delta\theta}{\bar{\theta}} \frac{gh}{\bar{\theta}}} \quad (18-3)$$

where $\Delta\theta$ is the vertical potential temperature difference, h is the height of the inversion, and $\bar{\theta}$ is the average potential temperature of the layer, was determined to be 3 m/sec from the shallow inversion in the temperature structure from Invercargill at 54 kPa (540 mb). The average windspeed u between Campbell Island and Invercargill at 5 km was 10 m/sec or a Mach number u/C_g of 3. The angle α of the cloud lines in the upper layer relative to symmetry axis is 20° to 30° , depending on the assumed orientation of the photograph.



FIGURE 18-13.—Handheld-camera photograph showing Kármán vortices in the lee of Guadalupe Island off the coast of Baja California (SL3-122-2497).

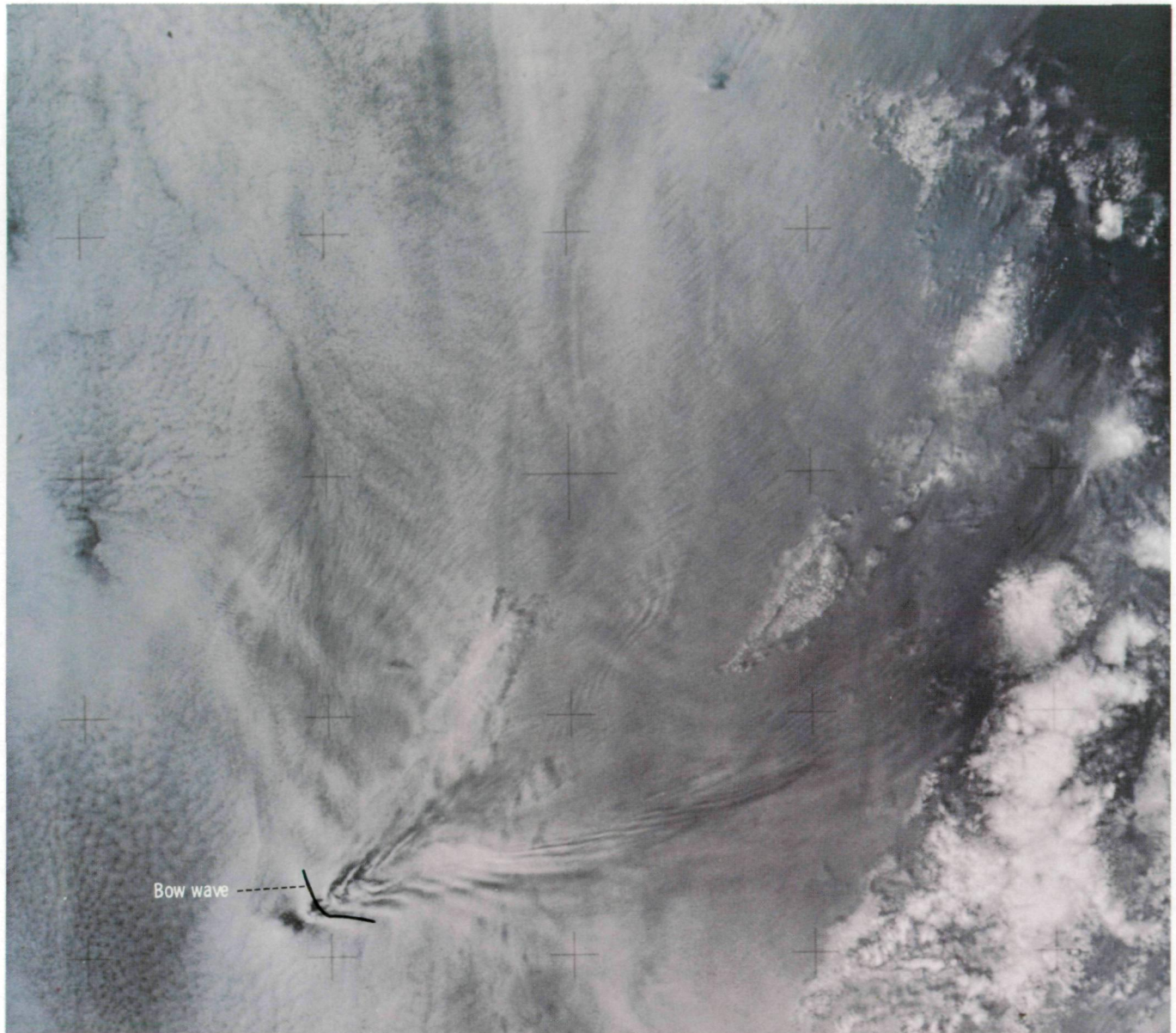


FIGURE 18-14.—A bow-type wave is clearly visible in the lee of Campbell Island (SI4-137-3668).

This angle agrees with the calculated Mach number through the formula

$$\frac{u}{C_g} = \frac{1}{\sin \alpha} \quad (18-4)$$

The lower level clouds appear to be alined with the upper level clouds. From the Campbell Island sounding, a group velocity C_g of approximately 15 m/sec was calculated for a 2-km altitude. The windspeed in the lower layer is 8 m/sec, which gives a Mach number of 0.5 and thus eliminates the possibility of a low-level

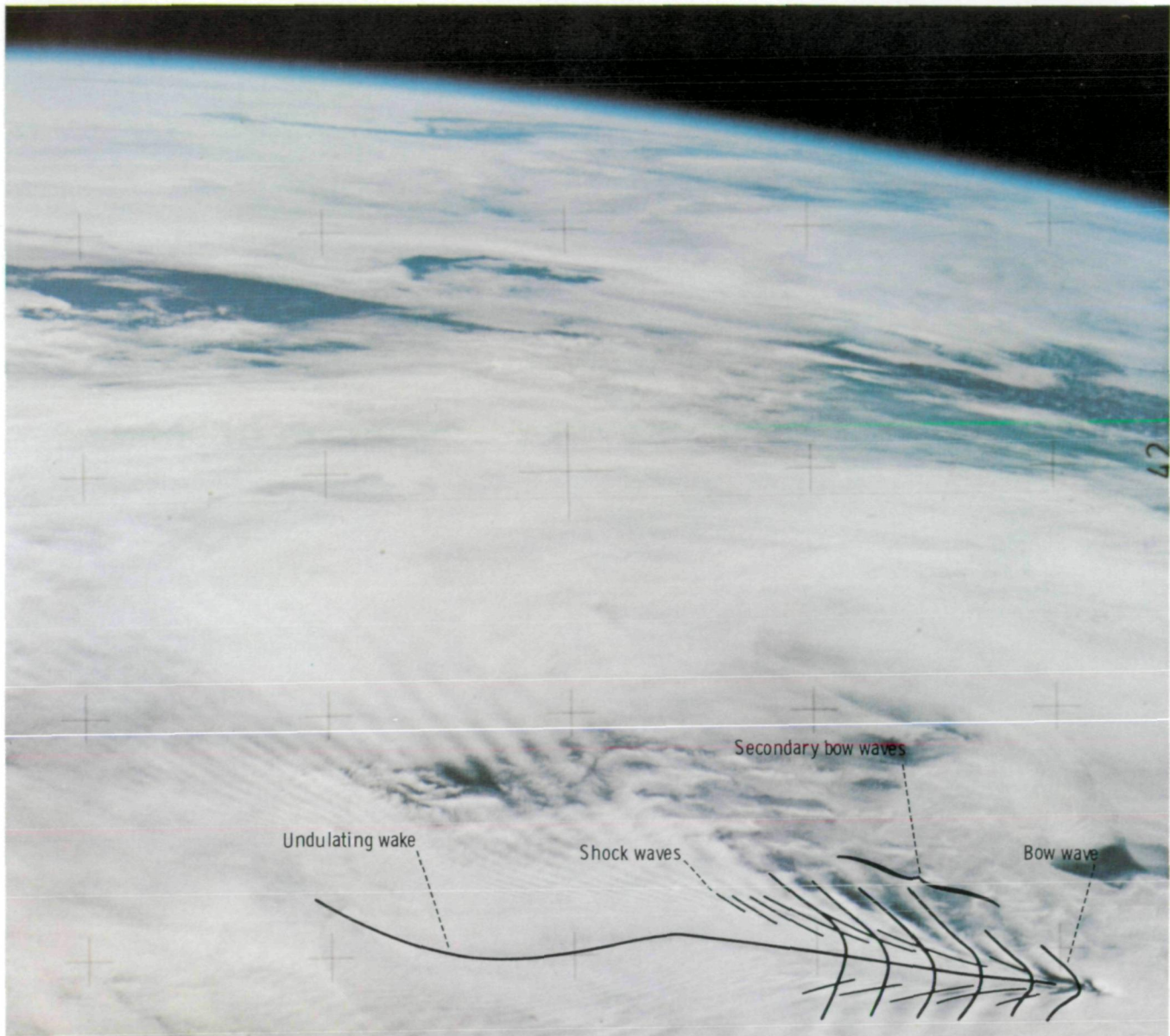


FIGURE 18-15.—This complex atmospheric wave in the lee of Gough Island in the southern Atlantic Ocean was photographed December 15, 1973, at approximately 14:23 GMT. The view is toward the south (SI4-137-3632).

gravity shock wave. However, a cloud-street alinement of this type can occur in the generation of a Kármán vortex. The Reynolds number was calculated to be in the range from 10 to 100, which is a region of prevalent production of vortices. Therefore, this appears to be the result of a gravity shock wave that occurred above Kármán vortices. Indeed, a wide-angle photograph of

this phenomenon may have been as spectacular as the unusual and exciting closeup shown in figure 18-17. The extreme variation in the soundings surrounding this unusual phenomenon demonstrates the importance of the ability of the crewman to measure atmospheric structure near regions that are important to meteorological research.

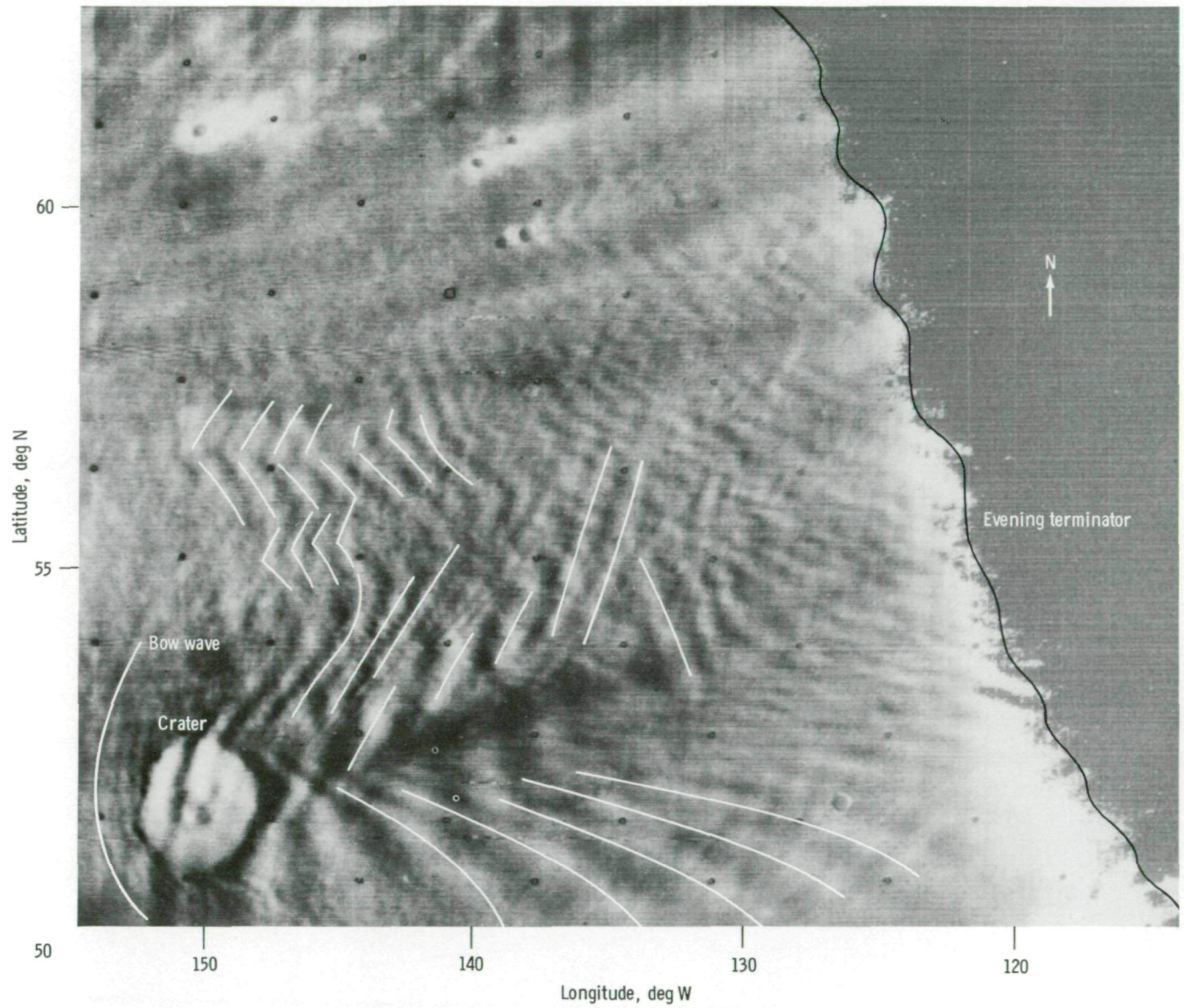


FIGURE 18-16.—Mariner 9 satellite image showing wave clouds in the atmosphere of Mars (S-74-26935).

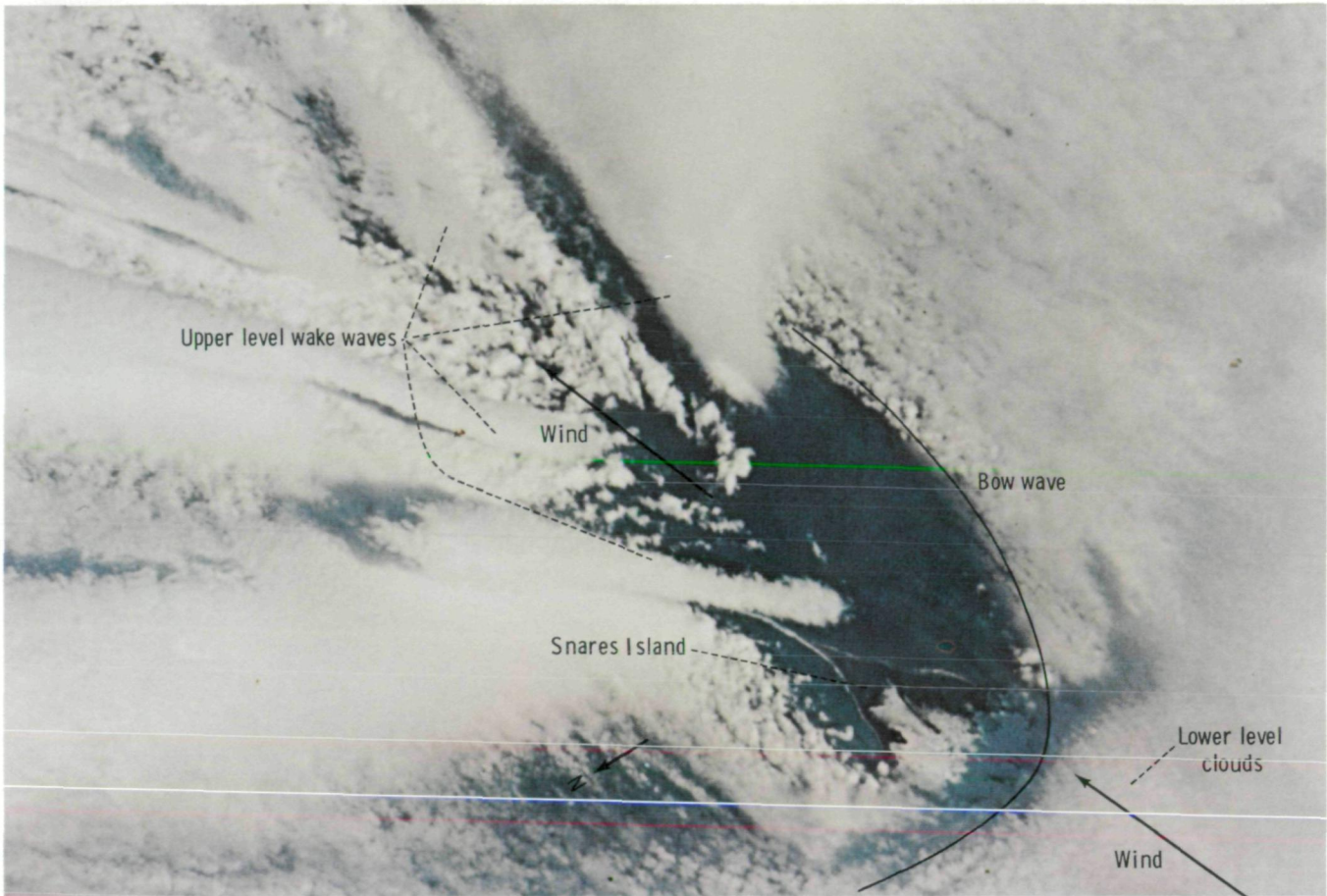


FIGURE 18-17.—Photograph taken at 04:30 GMT on February 4, 1974, with the Nikon camera using a 300-mm lens showing bow and shock-type waves from one of the Snares Islands, located near the southwestern tip of New Zealand (SL4-203-7764).



FIGURE 18-18.—This area of Coro, Venezuela, with cloud streets showing moisture influx into towering cumulus was photographed with the Skylab multispectral camera system (SI4-52-263).

ORIGINAL PAGE IS
OF POOR QUALITY

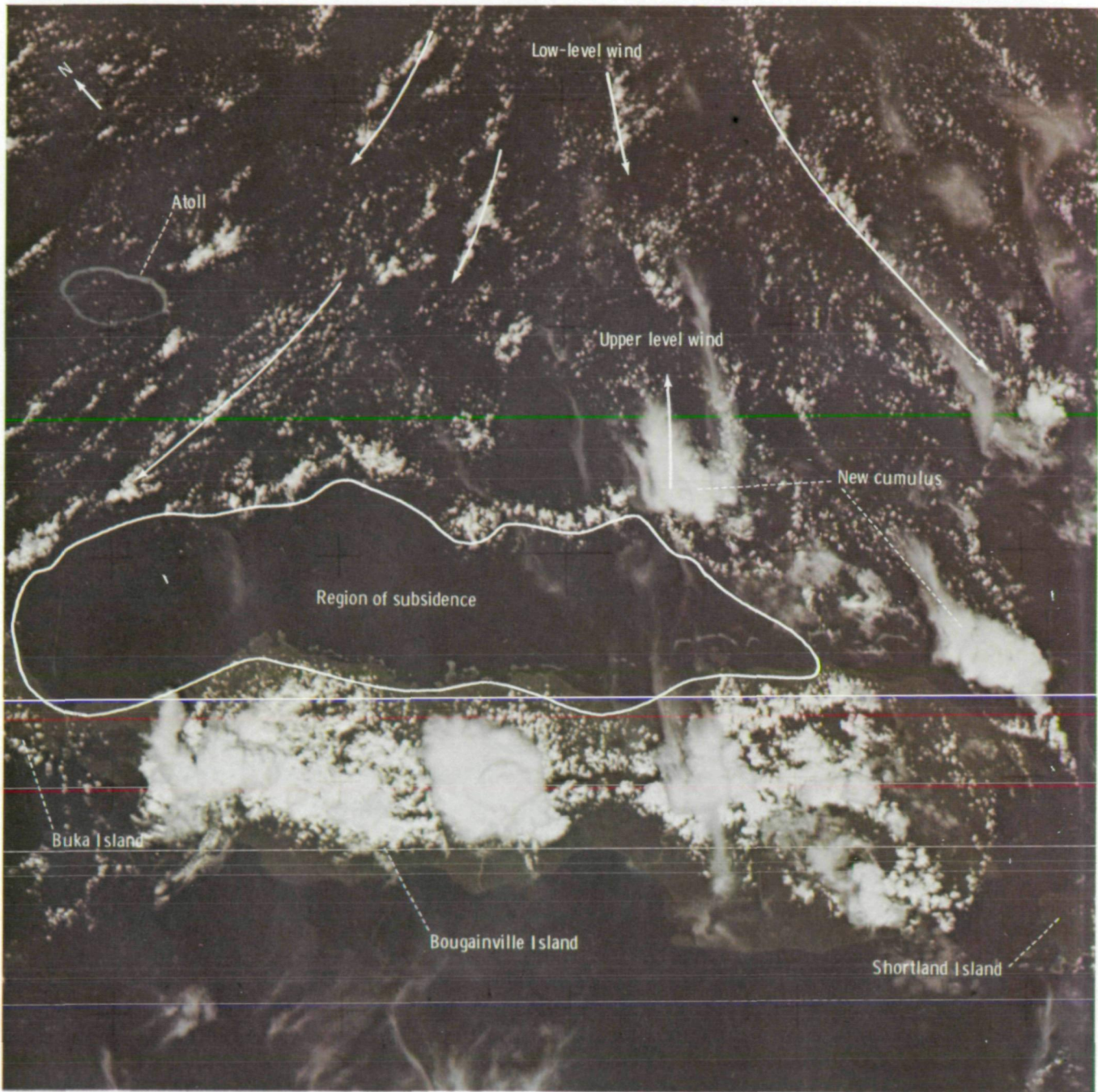


FIGURE 18-19.—Thunderstorms are shown forming as a result of heating and orographic effects from Bougainville Island (SL4-138-3767).



FIGURE 18-20.—This line of cumulus and cumulonimbus in the early stages of forming a squall line was photographed east of Taiwan (SL4-136-3436).

STORM ENVIRONMENTS

Cloud streets commonly form parallel to the wind vector and thus indicate the direction of incoming moisture. Analysis of photographic and observational data obtained by a space observer often provides documentation that aids in determining the importance of regional factors, such as this moisture supply, in the generation of storms. In figure 18-18, cloud streets feed a cumulus, which is associated with cold downdraft, to cause the formation of new cumuli. Figure 18-19 is another example of a region of subsidence adjacent to thunderstorms with new thunderstorm cells forming on the edge of the cold downdraft. This type of cell development is thought to occur often. The ability to predict the location of the subsidence region would aid in short-term prediction of storm genesis. The top of the photograph shows a large amount of cloud-street divergence as an indicator of the low-level windflow. Figure 18-20 shows thunderstorms in an advanced stage of this cycle with the mature cells displaying more cirrus than the younger cells.

RECOMMENDATIONS

Observations by the Skylab 4 crewmen provided information on new and unusual phenomena, especially rare small-scale phenomena. To increase man's capability as an observer, more tools, such as infrared scanners, polarimeters, spectrometers with real-time output, stereopair viewers, and data from weather satellites, should be supplied in the Space Shuttle Program. Other crew aids, such as Polaroid cameras, video tape, or film-developing equipment, should be included to enable performance of temporal studies in orbit. The analysis of some photographs is difficult because time was not recorded automatically for each film frame and a spacecraft ephemeris for visual observations was not available.

A human observer in space has the unique capability to take high-oblique photographs and stereophotographs and to select areas to photograph with a telephotographic lens. This capability should be used to the fullest extent in future missions.

The value of the Apollo 9 photographs to meteorology has been demonstrated by Wooldridge (ref. 18-12) and Wooldridge et al. (ref. 18-13). The

Skylab crewmen, because they were better prepared, further demonstrated the special contribution of man. The valuable information gained from the Skylab visual observations and photographic documentation indicates the value of future manned scientific missions.

REFERENCES

- 18-1. Browning, Keith A.: Air Flow and Precipitation Trajectories Within Severe Local Storms Which Travel to the Right of the Winds. *J. Atmos. Sci.*, vol. 21, no. 6, Nov. 1964, pp. 634-639.
- 18-2. Whitehead, Victor S.; Browne, Ivan D.; and Garcia, Joe G.: Cloud Height Contouring From Apollo 6 Photography. *Bull. American Meteorol. Soc.*, vol. 50, 1969, pp. 522-528.
- 18-3. Plank, V. G.: Wind Conditions in Situations of Patternform and Nonpatternform Cumulus Convection. *Tellus*, vol. 18, 1966, pp. 1-12.
- 18-4. Kuettner, J. P.: Cloud Bands in the Earth's Atmosphere: Observations and Theory. *Tellus*, vol. 23, 1971, pp. 404-425.
- 18-5. LeMone, Margaret Ann: The Structure and Dynamics of Horizontal Roll Vortices in the Planetary Boundary Layer. *J. Atmos. Sci.*, vol. 30, no. 6, Sept. 1973, pp. 1077-1091.
- 18-6. Brown, R. A.: On the Inflection Point Instability of a Stratified Ekman Boundary Layer. *J. Atmos. Sci.*, vol. 29, no. 5, July 1972, pp. 850-859.
- 18-7. Anderson, Ralph K.; and Smith, Arthur H.: Application of Meteorological Satellite Data in Analysis and Forecasting. Supp. 1. ESSA Tech. Rep. NES-51, Nov. 1971.
- 18-8. Wilkins, Eugene M.: Hot-Film Anemometer Measurements of Velocity Decay in Kármán Trail Vortexes. *J. Geophys. Res.*, vol. 75, no. 6, Feb. 20, 1970, pp. 1033-1039.
- 18-9. Goldman, Joseph L.; and Wilkins, Eugene M.: Drag Experiments With Cylinders of Varying Roughness Related to Flow Around Thunderstorm Cells. *J. Geophys. Res.*, vol. 78, no. 6, Feb. 20, 1973, pp. 913-919.
- 18-10. Wilkins, Eugene M.; and Sasaki, Yoshikazu: Resonance Amplification and Viscous Attenuation of Atmospheric Bow Waves. *J. Geophys. Res.*, vol. 74, no. 23, Oct. 1969, pp. 5418-5424.
- 18-11. Briggs, Geoffrey A.; and Leovy, Conway B.: Mariner 9 Observations of the Mars North Polar Hood. *Bull. American Meteorol. Soc.*, vol. 55, no. 4, Apr. 1974, pp. 278-296.
- 18-12. Wooldridge, G. L.: Vertical Momentum Transport Over Mountainous Terrain. Colorado State Univ., Atmospheric Science Paper no. 164, 1970.
- 18-13. Wooldridge, C.; Reiter, E. R.; Vonder Harr, T. H.; and Rasmussen, J. L.: Meteorological Application of Apollo Photography, Final Report. NASA CR-114954, Dec. 1970.

APPENDIX A

Glossary

- adiabatic** — without gain or loss of heat
- akle** — French term for a network pattern of dunes in the western Sahara; a fish-scale pattern of parallel wavy dune ridges
- albedo** — the percentage of incoming radiation reflected by a natural surface such as the ground, ice, snow, or water
- alluvium** — unconsolidated gravel, sand, silt, and clay transported and deposited by water
- altiplano** — a high plateau or plain
- amphibolite** — a crystalloblastic rock consisting mainly of amphibole and plagioclase
- anorthosite** — a granular, plutonic, igneous rock composed almost exclusively of a soda-lime feldspar
- anticyclone** — a system of winds that rotates about a center of high atmospheric pressure clockwise in the Northern Hemisphere and counterclockwise in the Southern Hemisphere, that usually advances at 9 to 13 m/sec, and that usually has a diameter of 2400 to 4000 km
- anticyclonic** — having a sense of rotation about the local vertical opposite to that of the Earth's rotation
- aridification** — the process of human or cultural creation of dry land through removal of vegetation, burning, overgrazing, overcropping, or overurbanization
- ash-flow tuff** — a rock formed of compacted volcanic fragments, generally smaller than 4 mm in diameter
- barchan** — crescent-shaped sand dune in which the horns or arms point downwind
- barchanoid ridge** — asymmetrical wavy dune ridge separated from neighboring wavy dune ridges by open interdune corridors
- batholith** — a stock- or shield-shaped mass (of igneous rock) intruded as the fusion of older formations
- bedrock** — solid rock, usually beneath a veneer of surficial alluvium or eolian sand
- berg wind** — an east wind
- biogenic** — produced by living organisms
- biotite** — a common rock-forming mineral of the mica group
- black ice** — transparent ice formed in rivers and lakes
- breccia** — rock consisting of sharp fragments embedded in a fine-grained matrix
- caldera** — a large basin-shaped volcanic depression more or less circular in form
- calving** — the breaking away of a mass of ice from an ice wall, ice front, or iceberg
- Cartesian coordinate system** — a coordinate system in which the locations of points in space are expressed by reference to three planes, called coordinate planes, no two of which are parallel. The three planes intersect in three straight lines, called coordinate axes. The coordinate planes and coordinate axes intersect in a common point, called the origin.
- clear cutting** — the practice of cutting all the trees in a stand of timber
- climax agriculture (CA)** — agricultural management system in which economic plants (crops) replace the natural vegetation of mature ecosystems
- climax community** — stable organic community that has evolved through successive stages until equilibrium with its physical environment has been attained
- climax environment** — the physical surroundings in which maximum sustained productivity occurs in nature
- columnar ice** — see black ice
- complex dune** — large-scale accumulation of eolian sand formed by the coalescing or combining of individual dunes
- coriolis effect** — the apparent force caused by the Earth's rotation which serves to deflect a moving body on the surface of the Earth to the right in the Northern Hemisphere but to the left in the Southern Hemisphere

craton — a stable, relatively immobile area of the Earth's crust that forms the nuclear mass of a continent or the central basis of an ocean

crescentic dune — see barchan

cyclone — an atmospheric cyclonic circulation, a closed circulation

cyclonic — having a sense of rotation about the local vertical the same as that of the Earth's rotation

desert — an arid or semiarid region characterized by an excess of evaporation over precipitation

desertification — the process of desert formation

desert varnish — surface stain or crust of manganese or iron oxide of brown or black color, usually with a glistening luster, that characterizes many exposed rock surfaces in the desert

discontinuities (in Earth structure) — sudden or rapid changes with depth in one or more of the physical properties of the materials constituting the Earth, as evidenced by seismic data

diverging waves — waves that radiate from a common center and obtain maximum amplitude near the boundaries of a formed wake

draa — Arabic term for large-scale accumulation of eolian sand (see dune complex)

drought — a lack of rainfall or a period of below-normal precipitation during a season in which rainfall normally occurs

dune — an accumulation of windblown sand that usually has a gentle upwind slope and a steep lee slope or slipface (or two slipfaces)

dune complex — an eolian sand accumulation formed from a combination of dunes (locally referred to as draa in parts of North Africa)

dunite — a peridotite consisting almost wholly of olivine and containing accessory pyroxene and chromite

dust veil index — a pure numeric that indicates the magnitude of the stratospheric pall which results from ejection of volcanic dust into the stratosphere as an implicit consequence of paroxysmal eruption

ecosystem — zones of similar ecological phenomena

eddy viscosity — the turbulent transfer of momentum by eddies giving rise to an internal fluid friction, in a manner analogous to the action of molecular viscosity in laminar flow, but taking place on a much larger scale

eolian — borne, deposited, produced, or eroded by the wind

eolian sandstone — sedimentary rock formed of consolidated windblown sand

erg — a desert region with complex dunes where at least 20 percent of the land surface is covered with wind-deposited sediments; a sand sea

ergonomics — biotechnology; the aspect of technology concerned with the application of biological and engineering data to problems relating to man and the machine

eye — in meteorology, usually the "eye of the storm" (hurricane, typhoon); that is, the roughly circular area of comparatively light winds and fair weather found at the center of a severe tropical storm

eyewall — the sides or boundary of the eye of a storm center

fast ice — sea ice that forms and remains fast along the coast where it is attached to the shore, an ice wall, an ice front between shoals, or grounded icebergs

fault — a fracture or fracture zone along which there has been displacement (of a few centimeters or of many kilometers) of the two sides relative to one another parallel to the fracture

flocculation — an aggregation of small lumps, especially of soils and colloids

floe — any relatively flat piece of sea or lake ice 10 m or more across. Floes are subdivided according to horizontal extent as follows: vast, more than 10 km; giant, 5 to 10 km; big, 1 to 5 km; medium, 200 to 1000 m; and small, less than 200 m

fold — a bend in strata or any planar structure

Fourier transform — an analytical transformation of a function $f(x)$ obtained (if it exists) by multiplying the function by e^{-iux} and integrating over all x

$$F(u) = \int_{-\infty}^{\infty} e^{-iux} f(x) dx, \quad -\infty < u < \infty$$

where u is the new variable of the transform $F(u)$ and $i^2 = -1$

fracture — (1) breaks in rocks due to intense folding or faulting, (2) any break or rupture through pack ice or a single floe resulting from the formation processes

frazil ice — fine spicules or plates of ice suspended in water

fumarole — a hole or vent from which fumes or vapors issue; a spring or geyser that emits steam or gaseous vapor; usually found in volcanic areas

gabbro — a plutonic rock consisting of calcic plagioclase and clinopyroxene, with or without orthopyroxene and olivine

gamma — a measure of the processing conditions under which the film was developed

garnetiferous — containing the silicate mineral garnet

Gaussian (or normal) distribution — the fundamental frequency distribution of statistical analysis. A variable x has a Gaussian distribution if its probability of occurrence $f(x)$ (its frequency) is defined according to

$$f(x) = \frac{1}{\sigma\sqrt{2\pi}} \exp \left[-\frac{1}{2} \left(\frac{x - \bar{x}}{\sigma} \right)^2 \right]$$

geostrophic — pertaining to deflective force due to rotation of the Earth

geosynchronous — geostationary; of, relating to, or being an artificial satellite that travels above the Equator and at the same speed as the Earth rotates so that the satellite seems to remain in the same place

giant crescent dune pattern — type of parallel wavy dune pattern where the ridges are composed of coalesced megabarchans with either open or closed interdune hollows

gneiss — a coarse-grained rock in which bands rich in granular minerals alternate with bands rich in schistose minerals

graben — a block, generally long compared to its width, that has been downthrown along faults relative to the rocks on either side

granitic — of, pertaining to, or composed of granite or granitelike rock; coarse- and medium-grained granular igneous rocks

granulite — a metamorphic rock composed of even-sized interlocking granular minerals

gravity wave — a wave disturbance in which buoyancy (or reduced gravity) acts as the restoring force on parcels displaced from hydrostatic equilibrium

gray ice — young ice 10 to 15 cm thick; usually rafts under pressure

gray-white ice — young ice 15 to 30 cm thick; more likely to ridge under pressure than to raft

grid plate — a glass plate on which is etched an accurately ruled grid; sometimes used as a focal plane plate to provide a means of calibrating film distortion; also called a reseau

hogback — a ridge formed by outcroppings of steeply tilted strata

hornblende — one of the common rock-forming minerals of the amphibole group

horns — the pointed ends of a dune, especially the forward-extending arms of a barchan dune or the backward-trailing tails of a parabolic dune

horst — a block of the Earth's crust, generally long compared to its width, that has been uplifted along faults relative to the rocks on either side

hurricane — a severe tropical cyclone in the North Atlantic Ocean, Caribbean Sea, Gulf of Mexico, or eastern North Pacific Ocean off the western coast of Mexico

iceberg — a massive piece of ice of greatly varying shape (more than 5 m above sea level) that has broken away from a glacier; may be either afloat or aground; can be described as tabular, dome shaped, sloping, pinnacled, weathered, or glacier

ice plume — elongated area of slush or small ice floes parallel to the wind direction and existing in open water areas

Intertropical Convergence Zone — a relatively narrow low-latitude zone in which airmasses originating in the two hemispheres converge

intrusive — in petrology, having, while fluid, penetrated into or between other rocks, but solidifying before reaching the surface; said of plutonic igneous rocks and contrasted with effusive or extrusive

isohyet — line on a map connecting points that receive equal amounts of average annual rainfall

joint — a fracture or parting that abruptly interrupts the physical continuity of a rock mass

Kelvin-Helmholtz wave — an unstable wave in a system of two homogeneous fluids with a velocity discontinuity at the surface

khurd — a radial dune

lapse rate — the adiabatic rate of change of a meteorological element (such as temperature) associated with a change in height

lead — any fracture or passageway through sea ice that is navigable by surface vessels

left-lateral fault — a strike-slip fault in which the movement is such that an observer walking toward the fault along an index plane (bed, dike, vein, etc.) must turn left to find the other part of the displaced index plane

linear dunes — parallel straight dunes (also called longitudinal dunes, alab, seifs) that have lengths many times greater than their widths

littoral drift — material moved along a coast under the influence of waves and currents

longitudinal dune — a linear dune ridge that grows or migrates in a direction parallel to its long dimension

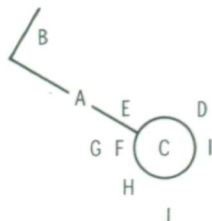
- mafic** — pertaining to or composed dominantly of the magnesian rock-forming silicates
- mangerites** — a special variety of mangonite and manzonite porphyry containing micropertite rich in oligoclase-andesine rather than the usual albite
- maskelynite** — a feldspar found in meteorites
- massif** — a mountainous mass
- mastodons** — radial or star dunes
- megabarchans** — giant crescentic (barchan shaped) complex dunes several hundred meters in height, usually coalescing into chains and forming a parallel wavy dune pattern; each dune complex normally has one major slipface
- mesoscale** — of or relating to a meteorological phenomenon approximately 1 to 100 km in horizontal extent
- metallogenic** — relating to the origin of ores
- metamorphic** — a term used to describe rocks that have formed in a solid state as a result of drastic changes in temperature, pressure, and chemical environment
- metasediments** — partly metamorphosed sedimentary rocks
- metavolcanics** — partly metamorphosed volcanic rocks
- middle-latitude deserts** — deserts that lie between approximately latitudes 30° N and 30° S
- monocline** — strata that dip for an indefinite or unknown length in one direction and that do not apparently form sides of ascertained anticlines or synclines
- monsoon** — a wind system in which wind direction varies with the season of the year
- morphology** — the study of the shape or form of geologic features
- Munsell system** — a system of classifying and designating attributes of opaque surface colors
- oghurd** — a radial or star dune
- orographic** — of or relating to mountains; associated with or induced by the presence of mountains
- pack ice** — general term used to designate any area of sea ice (other than fast ice) regardless of what form it takes or how it is disposed
- pancake ice** — predominantly circular pieces of ice 30 cm to 3 m in diameter and as large as approximately 10 cm in thickness with raised rims due to the pieces striking each other
- parabolic dune** — a U- or V-shaped dune representing a type of blowout in which the middle part has moved forward with respect to the sides or arms, which are usually anchored by vegetation
- parallel straight dune** — a linear ridge of windblown sand with a length much greater than the width; slip-faces usually occur along both sides and move in a lengthwise direction
- parallel wavy dune complex** — an array of crescentic dune segments alined in wavy ridges. Each crescentic segment is approximately as wide as it is long, and the segments are asymmetrical with all segments of a ridge having the major slipfaces oriented in the same direction.
- peak-and-fulje topography** — a pattern of dunes (peaks) and enclosed interdune hollows (fuljes); also known as akle or fish-scale variety of the parallel wavy dune pattern
- piedmont** — lying or formed at the base of mountains
- plagioclase** — a triclinic feldspar, especially one having calcium or sodium in its composition
- playa** — an extremely flat, nonvegetated desert surface formed of clay, silt, and/or evaporite minerals in the bottom of a basin of interior drainage (also known as clay pan, dry lake, inland sebkha, salt pan, or salt flat)
- pluton** — a body of igneous rock that has formed beneath the surface of the Earth by consolidation from magma
- polypyramid** — a radial or star dune
- porphyry** — a rock of feldspar crystals embedded in a compact dark-red or purple groundmass
- potential agricultural zones (PAZ)** — food production zones geographically equivalent to ecosystems
- pseudotachylyte vein** — a black vein rock externally resembling tachylyte but produced by extreme mylonitization
- pyramidal dune** — a radial dune (also known as khurd, oghurd, rhourd, mastodon, polypyramid, or star dune)
- pyroclastic deposits** — indurated deposits of volcanic ejecta, including volcanic agglomerates, breccias, tuff-breccias, tuffs, conglomerates, and sandstones
- pyroxene** — any of a group of igneous-rock-forming silicate minerals that contain calcium, sodium, magnesium, iron, or aluminum, usually occur in short prismatic crystals or massive, are often laminated, and vary in color from white to dark green or black
- radial dune** — a complex, roughly star-shaped dune the segments or arms of which radiate from the high central cone; slipfaces on the dune segments face in at least three directions to resemble a pinwheel

- radiosonde** — a miniature radio transmitter that is carried aloft with instruments for broadcasting the humidity, temperature, and pressure
- rake** — the angle that a line in a plane makes with a horizontal line in that plane
- regional environment** — the physical geography, geology, climate, water resources, and other physiographic features of an area
- Reynolds number** — the nondimensional ratio of the inertial force to the viscous force in fluid motion
- rhourd** — a radial dune
- Richardson number** — a characteristic ratio of work done against gravitational stability to energy transferred from mean to turbulent motion
- ridge (pressure ridge)** — a line or wall of broken ice forced up by pressure; may be fresh or weathered
- rift zone** — a narrow zone of fissures extending down the flanks of a volcano, ordinarily reaching from the summit crater to the foot of the mountain and beyond
- right-lateral fault** — a strike-slip fault in which the movement is such that an observer walking toward the fault along an index plane (bed, dike, vein, etc.) must turn right to find the other part of the displaced index plane
- Sahel** — Arabic word for border
- Sahelian zone** — the broad band of transition from the Sahara to the sub-Saharan savanna
- saltation** — the bouncing movement of sand-sized particles being transported by wind
- salt diapirs** — anticline in which a mobile salt core has injected the more brittle overlying rock
- sand ridge** — a parallel straight or linear dune
- sand rose** — a circular histogram depicting the amount of sand moved by winds of certain speed groups in various compass directions at a given geographic locality
- sand sea** — a region of extensive eolian sand deposits, including dunes and dune complexes that form characteristic patterns (also known as erg, nafud, sand-ridge desert)
- sand sheet or streak** — a flat-surfaced eolian sand deposit without slipfaces but with distinct geographical boundaries
- schist** — rocks that have a foliated structure split up in thin, irregular plates, not by regular cleavage as in clay slate, nor in large flat laminae, as in flagstones
- sea ice** — any form of ice found at sea that has originated from frozen seawater
- seif** — a North African term (meaning sword in Arabic) for a parallel straight (linear) dune
- shatter cone** — structure produced by shear planes outlining a cone several centimeters in diameter which occurs in the rocks of some cryptovolcanic areas
- shear** — an action or stress resulting from applied forces that causes or tends to cause two contiguous parts of a body to slide relative to each other in a direction parallel to their plane of contact
- shear wave** — an unstable type of wave that forms at the boundary between two atmospheric layers moving with different speeds
- slipface** — steep face on the lee side of a dune that is usually at the angle of repose of sand (32° to 34°)
- slush** — snow saturated and mixed with water on land or ice surfaces or a viscous floating mass in water after a heavy snowfall
- snow ice** — ice crust on a water surface formed in considerable part from falling or drifting snow
- solfatara** — all vents emitting sulfurous gases, sodium dioxide, and hydrogen sulfide, usually associated with the approaching extinction of volcanic activity; so called after a small volcano of the same name in the Phlegrean Fields near Naples; cf. "fumarole," which issues mainly steam and water vapor
- spreading zone** — a narrow band of topographically low country dividing two blocks or plates of crustal material that are moving apart; in the midoceanic ridges, the material being added to the spreading blocks or plates is of volcanic origin
- star dune** — a radial dune
- stellate rose** — a radial dune
- stratosphere** — that part of the Earth's atmosphere between the troposphere and the ionosphere
- strike-slip fault** — a transcurrent fault; a fault in which the net slip is practically in the direction of the fault strike
- sunlint** — the bright reflection of sunlight on an expanse of water
- tabular berg** — a flat-topped iceberg; most are formed by calving from an ice shelf and show horizontal banding
- tectonic lineaments** — a linear feature of long geographic extent formed by major structural conditions
- tectonism** — crustal instability; the structural behavior of an element of the crust of the Earth during or between major cycles of sedimentation
- tephra** — a collective term for all clastic volcanic

- materials which during an eruption are ejected from a crater or from some other type of vent and transported through the air, including volcanic dust, ash, cinders, lapilli, scoria, pumice, bombs, and blocks; synonymous with volcanic ejecta
- terrigenic** — produced from or of the Earth; in geology, deposited in or on the Earth's crust
- thermocline** — a layer in a thermally stratified body of water that separates an upper warmer lighter oxygen-rich zone from a lower colder heavier oxygen-poor zone; specifically, a stratum in which temperature declines at least 1 K with each meter increase in depth
- thick/thin first-year ice** — first-year ice more than 120 cm thick
- threshold velocity** — minimum windspeed at which sand grains of 0.25 mm begin to saltate; generally considered to be 16 km/hr
- thunderstorm** — in general, a local storm invariably produced by a cumulonimbus cloud and always accompanied by lightning and thunder, usually with strong gusts of wind, heavy rain, and sometimes hail
- tonalite** — quartz diorite containing hornblende and biotite as chief mafic minerals
- transverse dune** — an asymmetrical dune ridge oriented normal to the dominant wind direction in a particular area (see parallel wavy dunes)
- transverse wave** — a wave in which the direction of propagation of the wave is normal to the displacements of the medium (e.g., a vibrating string)
- troctolite** — a variety of gabbro consisting essentially of labradorite and olivine with little or no pyroxene
- tropical cyclone** — the general term for a cyclone that originates over the tropical oceans
- tropical storm** — the general term for a storm that originates over the tropical oceans
- tropopause** — the upper limit of the troposphere, in middle latitudes generally 10 to 12 km above the Earth's surface
- troposphere** — that portion of the atmosphere next to the Earth's surface in which temperature generally rapidly decreases with altitude, clouds form, and convection is active; in middle latitudes, generally includes the first 10 to 12 km above the Earth's surface
- tsunami** — a long-period sea wave produced by a submarine earthquake or volcanic eruption
- typhoon** — a severe tropical cyclone in the western Pacific Ocean
- U-shaped dune** — a parabolic dune
- ultramafic** — ultrabasic; very low in silica and rich in iron and magnesium minerals
- upsiloidal dune** — a parabolic dune
- vertex** — highest point
- vortex streets** — two parallel rows of alternately placed vortexes along the wake of an obstacle in a fluid of moderate Reynolds number
- vorticity** — a vector measure of local rotation in a fluid flow
- wadi** — a shallow, usually sharply defined depression in a desert region
- wake waves** — waves caused by a moving pressure point, presenting a pattern similar to that formed by a ship moving through the water
- white ice** — thin first-year ice 30 to 70 cm thick
- wind regime** — the pattern of winds characteristic of a particular region
- wind rose** — a circular histogram depicting the percentage occurrence of windspeed groups from a given set of compass directions at a certain geographic locality
- zeolite** — a generic term for a group of hydrous alumino-silicates of sodium, calcium, barium, strontium, and potassium, characterized by their easy and reversible loss of water of hydration and their intumescence when heated strongly

APPENDIX B

Standard Weather Symbols



A, B
Direction and Windspeed

| Symbol | Speed, knots | Speed, m/sec |
|--------|--------------|--------------|
| | Calm | Calm |
| | 1 - 2 | 0.5 - 1 |
| | 3 - 7 | 1.5 - 3.6 |
| | 8 - 12 | 4.1 - 6.2 |
| | 13 - 17 | 6.7 - 8.7 |
| | 18 - 22 | 9.3 - 11.3 |
| | 23 - 27 | 11.8 - 13.9 |
| | 28 - 32 | 14.4 - 16.5 |
| | 33 - 37 | 17 - 19 |
| | 38 - 42 | 19.5 - 21.6 |
| | 43 - 47 | 22.1 - 24.2 |
| | 48 - 52 | 24.7 - 26.7 |
| | 53 - 57 | 27.3 - 29.3 |
| | 58 - 62 | 29.8 - 31.9 |
| | 63 - 67 | 32.4 - 34.5 |
| | 68 - 72 | 35 - 37 |
| | 73 - 77 | 37.6 - 39.6 |
| | 103 - 107 | 53 - 55 |

→ (wind direction)

- A Direction from which wind is blowing (see symbols at left)
- B Windspeed (see symbols at left)
- C Extent of cloud cover (see symbols below)
- D Barometric pressure reduced to sea level, kilopascals (millibars)
- E Air temperature at time of reporting, kelvin
- F Weather condition at time of reporting (see symbols below)
- G Visibility, meters
- H Dewpoint temperature, kelvin
- I Pressure change during the 3 hr period preceding observation, kilopascals (millibars)
- J Height of base of lowest cloud, meters

Missing or unavailable data are indicated by "M" in the proper location.
(Note: Only those codes which appear on maps in this report are listed).

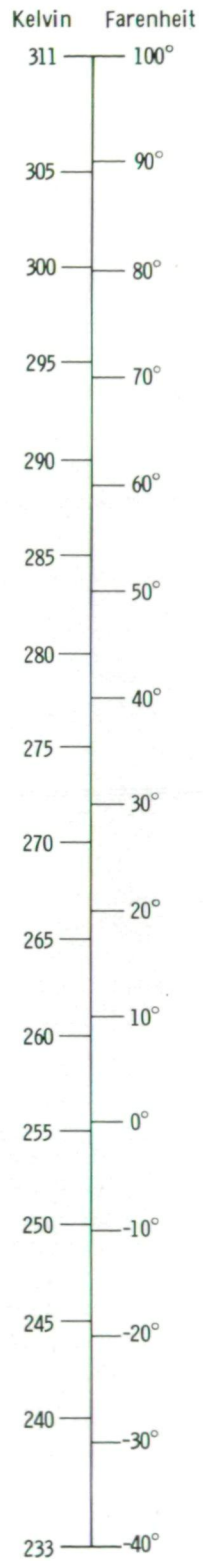
C
Cloud Cover

| Symbol | Percent covered |
|--------|------------------------------|
| | Clear |
| | Up to 10 |
| | 20 to 30 |
| | 40 |
| | 50 |
| | 60 |
| | 70 to 80 |
| | 90 or overcast with openings |
| | Completely overcast |
| | Sky obscured |

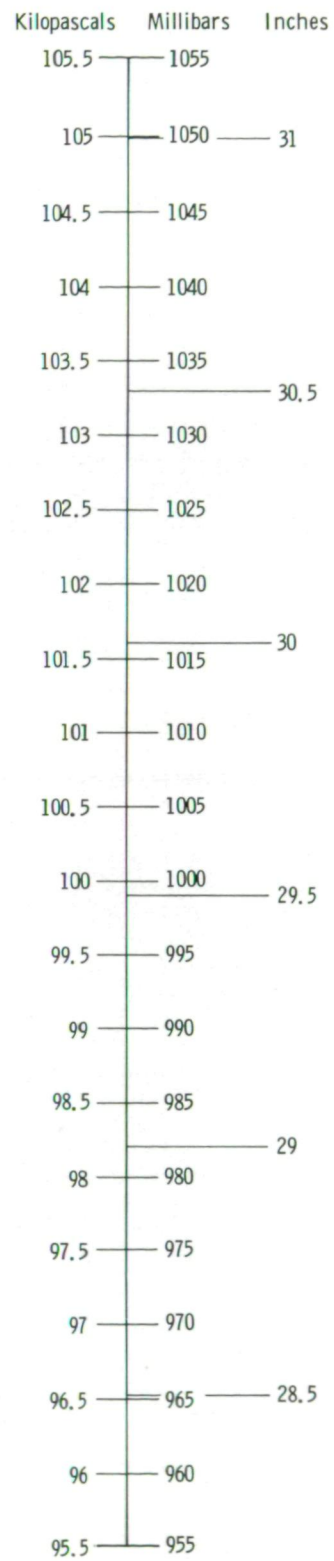
F
Present Weather Conditions

| Symbol | Explanation |
|--------|---|
| | Visibility reduced by smoke |
| | Haze |
| | Intermittent drizzle (not freezing), slight |
| | Continuous rain (not freezing), slight |
| | Continuous rain (not freezing), moderate |
| | Intermittent snow, slight |
| | Slight rain showers |
| | Slight snow showers |

Temperature



Pressure



APPENDIX C

Photograph Index

Reproductions of the Skylab images used as illustrations in this book may be ordered from the EROS Data Center, Sioux Falls, South Dakota 57198, using the EROS Data Center identification number associated with each photograph. Order forms for Skylab photographs are available from the EROS Data Center on request but are not mandatory to place an order.

| <i>Geographic location</i> | <i>Photograph no.</i> | <i>EROS^a Data Center identification no.</i> | <i>Figure no.</i> |
|-------------------------------------|--------------------------|--|-------------------|
| Africa | | | |
| Afar Triangle and African rift zone | SL4-137-3584 | G470137358400 | b3-4(a) |
| | SL4-137-3585 | G470137358500 | |
| Algeria | SL4-139-3900 | G470139390000 | 2-4(a) |
| | SL4-138-3885 | G470138388500 | 2-4(c) |
| | SL4-138-3793 | G470138379300 | 14-10 |
| Chad/Cameroun | SL4-138-3768 | G470138376800 | 14-22 |
| | SL4-138-3789 | G470138378900 | 5-9 |
| Dahomey/Niger | ^c E1487-09350 | | 10-2 |
| Libya | SL4-141-4354 | G470141435400 | 2-3(b) |
| Mali | SL4-141-4361 | G470141436100 | 2-7(b), 10-7 |
| | SL4-136-3381 | G470136338100 | 2-7(c) |
| | SL4-142-4579 | G470142457900 | 10-5 |
| | SL4-142-4497 | G470142449700 | 10-6 |
| Mauritania | SL4-140-4227 | G470140422700 | 2-16, 10-3 |
| Morocco | SL4-139-3910 | G470139391000 | 8-4 |
| Sahara | SL3-28-365 | G30A283650000 | 2-2(c) |
| | SL3-138-3756 | G370138375600 | 2-6(a) |
| Senegal | ^c E1267-10574 | | 10-4 |
| South Africa | SL4-196-7387 | G435196738700 | 12-2 |
| | SL4-196-7389 | G435196738900 | 12-3 |
| South West Africa | SL4-137-3693 | G470137369300 | 2-2(d) |
| | SL4-207-8074 | G435207807400 | 2-4(b) |
| | SL4-207-8073 | G435207807300 | 2-9 |
| Sudan | SL4-208-8140 | G435208814000 | 9-9 |

^aEarth resources observation systems.

^bPhotomosaic.

^cLandsat image.

| <i>Geographic location</i> | <i>Photograph no.</i> | <i>EROS^a Data Center identification no.</i> | <i>Figure no.</i> |
|----------------------------|--------------------------|--|-------------------|
| Asia | | | |
| Bougainville Island | SL4-138-3767 | G470138376700 | 18-19 |
| China | SL4-136-3389 | G470136338900 | 2-3(d) |
| | SL4-197-7423 | G435197742300 | 11-15 |
| Cyprus | SL4-142-4454 | G470142445400 | 18-3 |
| Gulf of Aqaba and Dead Sea | SL4-194-7259 | G435194725900 | 3-6(a) |
| Iran | SL4-141-4251 | G470141425100 | 3-12(a) |
| | SL4-141-4280 | G470141428000 | 14-9 |
| Japan | SL4-196-7340 | G435196734000 | 5-3(a), 14-1 |
| | SL4-139-3942 | G470139394200 | 5-1(a), 14-3 |
| | SL4-139-3972 | G470139397200 | 14-4 |
| | SL4-139-3971 | G470139397100 | 5-4 |
| | SL4-141-4340 | G470141434000 | 13-23 |
| Kuril Islands | SL4-142-4490 | G470142449000 | 13-24 |
| | SL2-5-432 | G20A543200000 | 17-7 |
| Pakistan | SL4-141-4280 | G470141428000 | 14-9 |
| | ^c E1173-05211 | | 2-5(b) |
| Saudi Arabia | SL4-143-4643 | G470143464300 | 2-2(b) |
| | SL4-141-4255 | G470141425500 | 2-3(c) |
| | SL4-138-3751 | G470138375100 | 3-9(a) |
| Sea of Galilee | SL3-46-209 | G30A462090000 | 3-8(a) |
| Taiwan | SL4-136-3436 | G470136343600 | 18-20 |
| U.S.S.R. | SL4-138-3872 | G470138387200 | 3-13(a), 7-30(b) |
| | SL4-138-3871 | G470138387100 | 7-30(a) |
| | SL4-141-4273 | G470141427300 | 5-13 |
| | SL4-141-4336 | G470141433600 | d7-31 |
| | SL4-141-4337 | G470141433700 | |
| | SL4-141-4339 | G470141433900 | 7-32, 13-25 |
| Atlantic Ocean | | | |
| Bermuda Island | SL3-28-050 | G30A280500000 | 11-36 |
| Bouvet Island | SL4-137-3633 | G470137363300 | 17-1 |
| Gough Island | SL4-137-3632 | G470137363200 | 18-15 |
| Falkland Islands area | SL4-142-4577 | G470142457700 | 13-26 |
| | SL4-200-7615 | G435200761500 | 13-27 |
| Falkland Current | SL4-196-7350 | G435196735000 | 11-37 |
| | SL4-137-3721 | G470137372100 | 12-6 |
| | SL4-137-3608 | G470137360800 | 11-23 |
| | SL4-137-3690 | G470137369000 | 12-5 |
| | SL4-143-4610 | G470143461000 | 12-10 |
| South Georgia Island | SL4-138-3782 | G470138378200 | 11-25 |

^aEarth resources observation systems.

^cLandsat image.

^dStereopair.

| <i>Geographic location</i> | <i>Photograph no.</i> | <i>EROS^a Data Center identification no.</i> | <i>Figure no.</i> |
|----------------------------|-------------------------|--|--------------------|
| Atlantic Ocean—Concluded | | | |
| Tropical storm Christine | SL3-121-2322 | G370121232200 | 16-18 |
| Tropical storm Ellen | SL3-122-2572 | G370122257200 | 16-1, 16-5, 16-13 |
| | SL3-122-2571 | G370122257100 | 16-2, 16-6 |
| | SL3-122-2573 | G370122257300 | 16-3 |
| | NOAA-2 image | | 16-4 |
| Hurricane Ellen | NOAA-2 image | | 16-37(a) |
| | SL3-122-2601 | G370122260100 | 16-37(b) |
| | SL3-122-2602 | G370122260200 | 16-37(c), 16-37(d) |
| Australia | | | |
| Kangaroo Island | SL4-137-3564 | G470137356400 | 11-35 |
| New Guinea | SL4-138-3761 | G470138376100 | 11-26 |
| New South Wales | SL4-143-4639 | G470143463900 | 9-3 |
| | SL4-138-3835 | G470138383500 | 9-4 |
| | SL4-200-7638 | G435200763800 | 9-5 |
| Nullarbor Plain | SL4-137-3630 | G470137363000 | 9-8 |
| Simpson Desert | SL4-143-4637 | G470143463700 | 2-2(a) |
| South Australia | SL4-137-3572 | G470137357200 | 8-1 |
| Europe | | | |
| Albania | SL4-141-4408 | G470141440800 | 11-20 |
| Italy | SL4-141-4283 | G470141428300 | 7-29 |
| | SL4-141-4288 | G470141428800 | 5-21(a) |
| Mediterranean Sea | SL4-140-4163 | G470140416300 | 11-38 |
| | SL4-141-4415 | G470141441500 | 11-27 |
| | SL2-5-370 | G20A537000000 | 11-28 |
| Portugal | SL3-34-317 | G30A343170000 | 11-32 |
| Mars | | | |
| | ^e S-74-26935 | | 18-16 |
| New Zealand | | | |
| Auckland Islands | SL4-137-3703 | G470137370300 | 17-13 |
| Antipodes Islands | SL4-137-3655 | G470137365500 | 11-8, 17-15 |
| Campbell Island | SL4-137-3668 | G470137366800 | 17-16, 18-14 |
| Chatham Island | SL4-137-3705 | G470137370500 | 17-11 |
| | SL4-136-3446 | G470136344600 | 11-12, 12-7 |
| Cook Strait | SL4-137-3725 | G470137372500 | 11-10 |
| North Island | SL4-137-3645 | G470137364500 | 11-11 |

^aEarth resources observation systems.

^eMariner 9 satellite image.

| <i>Geographic location</i> | <i>Photograph no.</i> | <i>EROS^a Data Center identification no.</i> | <i>Figure no.</i> |
|------------------------------------|-------------------------|--|---------------------|
| New Zealand—Concluded | | | |
| Snares Island | SL4-203-7764 | G435203776400 | 18-17 |
| South Island | SL4-137-3700 | G470137370000 | 3-19(a), 9-13 |
| | SL4-137-3641 | G470137364100 | 9-12 |
| | SL4-136-3399 | G470136339900 | 3-20(a) |
| | SL4-136-3531 | G470136353100 | 3-21(a) |
| | SL4-137-3646 | G470137364600 | 11-13 |
| North America | | | |
| Caribbean Sea | SL2-10-072 | G20A100720000 | 11-1 |
| | SL4-196-7384 | G435196738400 | 11-2 |
| | SL2-10-181 | G20A101810000 | 11-22 |
| Canada | SL3-122-2628 | G370122262800 | 6-1(a) |
| | SL4-138-3897 | G470138389700 | 6-3(a) |
| | SL4-139-4044 | G470139404400 | 6-4(a) |
| | SL4-140-4101 | G470140410100 | 13-21 |
| | SL4-140-4173 | G470140417300 | 6-2(a) |
| | SL4-140-4206 | G470140420600 | 13-22 |
| | SL4-141-4263 | G470141426300 | 13-7 |
| | SL4-192-7093 | G435192709300 | 6-7 |
| Central America | SL4-201-7666 | G435201766600 | } b3-26 |
| | SL4-201-7667 | G435201766700 | |
| | SL4-201-7668 | G435201766800 | |
| Costa Rica | SL4-142-4567 | G470142456700 | 12-1 |
| Gulf of Mexico | SL3-22-124 | G30A221240000 | 12-9 |
| Hurricane Gladys in Gulf of Mexico | ^f AS7-7-1877 | | 16-15(a) |
| | ^f AS7-8-1891 | | 16-15(b) |
| | ^f AS7-8-1892 | | 16-15(c) |
| | ^f AS7-8-1919 | | 16-15(d) |
| Gulf of St. Lawrence | SL4-139-3934 | G470139393400 | 13-1 |
| | SL4-139-4072 | G470139407200 | 13-5 |
| | SL4-141-4263 | G470141426300 | 13-7 |
| | SL4-141-4326 | G470141432600 | 13-8 |
| | SL4-141-4331 | G470141433100 | 13-9 |
| | SL4-140-4215 | G470140421500 | 13-10 |
| | SL4-141-4321 | G470141432100 | 13-11 |
| | SL4-140-4216 | G470140421600 | 13-12 |
| | SL4-141-4327 | G470141432700 | 13-13 |
| | SL4-141-4366 | G470141436600 | 13-14 |
| Honduras | SL4-138-3796 | G470138379600 | 18-1 |
| Mexico | SL3-40-163 | G30A401630000 | 3-24(a) |
| | SL4-141-4390 | G470141439000 | } ^d 15-3 |
| | SL4-141-4391 | G470141439100 | |
| | SL4-143-4606 | G470143460600 | 14-25 |
| | SL4-140-4131 | G470140413100 | 2-4(d) |
| | SL2-04-155 | G20A041550000 | 3-23(a) |
| | SL4-139-4064 | G470139406400 | 5-14(a) |
| | SL4-207-8056 | G435207805600 | 5-15 |

^aEarth resources observation systems.

^dStereopair.

^bPhotomosaic.

^fApollo 7 photograph.

| <i>Geographic location</i> | <i>Photograph no.</i> | <i>EROS^a Data Center identification no.</i> | <i>Figure no.</i> |
|-----------------------------------|-------------------------|--|-------------------|
| North America – Concluded | | | |
| Baja California | SL4-203-7808 | G435203780800 | 4-10 |
| | SL4-193-7190 | G435193719000 | 4-11 |
| | SL4-203-7809 | G435203780900 | 4-12 |
| Northwestern Mexico | SL4-141-4398 | G470141439800 | 4-13 |
| | SL4-140-4155 | G470140415500 | 4-14 |
| | SL4-194-7236 | G435194723600 | 4-15 |
| | SL4-203-7821 | G435203782100 | 4-16 |
| Guadalupe Island | SL3-122-2497 | G370122249700 | 18-13 |
| Eastern Pacific Ocean | | | |
| 40° S, 125° W | SL4-137-3565 | G470137356500 | 15-1 |
| | NOAA composite | | 15-2 |
| Hurricane Ava | DMSP image | | 16-34 |
| Hurricane Irah | SL3-118-2189 | G335118218900 | 16-32 |
| | SL3-122-2627 | G370122262700 | 16-31 |
| | Nimbus 5 image no. 3852 | | 16-33 |
| Unnamed tropical storm | ^g S65-63834 | | 16-16(a) |
| | ^g S65-63835 | | 16-16(b) |
| West of Galapagos Island (eddies) | SL4-138-3842 | G470138384200 | 11-33 |
| Western Pacific Ocean | | | |
| Typhoon Bess | DMSP image | | 16-14 |
| Tropical cyclone Lottie | SL4-136-3514 | G470136351400 | 16-29 |
| | SL4-136-3516 | G470136351600 | 16-28 |
| | SL4-136-3541 | G470136354100 | 16-30(a) |
| | SL4-136-3543 | G470136354300 | 16-30(b) |
| | NOAA-2 image | | 16-27 |
| Tropical storm Wanda | DMSP image | | 16-19 |
| | SL4-139-4051 | G470139405100 | 16-17 |
| South America | | | |
| Argentina | SL4-143-4608 | G470143460800 | 11-14 |
| | SL4-138-3753 | G470138375300 | 14-23 |
| | SL4-197-7442 | G435197744200 | 14-24 |
| | SL4-197-7443 | G435197744300 | 9-10 |
| Brazil | SL4-197-7416 | G435197741600 | 11-19 |
| Bolivia/Chile | SL4-137-3674 | G470137367400 | } b5-11 |
| | SL4-137-3675 | G470137367500 | |
| | SL4-137-3676 | G470137367600 | |

^aEarth resources observation systems.

^bPhotomosaic.

^gGemini VII photograph.

| <i>Geographic location</i> | <i>Photograph no.</i> | <i>EROS^a Data Center identification no.</i> | <i>Figure no.</i> |
|----------------------------|--------------------------|--|---------------------|
| South America—Concluded | | | |
| Chile | SL4-138-3794 | G470138379400 | 3-15(a) |
| | SL4-137-3711 | G470137371100 | 3-16(a) |
| | SL4-138-3854 | G470138385400 | 11-30 |
| | SL4-138-3858 | G470138385800 | 11-31 |
| Colombia | SL4-139-3914 | G470139391400 | 11-18 |
| Ecuador | SL4-139-3943 | G470139394300 | 18-2 |
| Fernando de Noronha Island | SL4-138-3874 | G470138387400 | 18-4 |
| Galapagos Islands | SL4-195-7299 | G435195729900 | 5-8(a) |
| Venezuela | SL4-52-263 | G40A522630000 | 18-18 |
| United States | | | |
| Alaska | SL4-140-4089 | G470140408900 | 5-18 |
| | SL4-140-4111 | G470140411100 | 17-6 |
| | SL4-140-4111 | G470140411100 | } b17-5 |
| | SL4-140-4112 | G470140411200 | |
| | SL4-140-4210 | G470140421000 | 17-8 |
| Arizona | ^c E1193-17324 | | 2-6(b) |
| | SL4-93-067 | G40B930670000 | 7-10 |
| | SL4-140-4141 | G470140414100 | 7-7 |
| | SL4-141-4390 | G470141439000 | } ^d 15-3 |
| | SL4-141-4391 | G470141439100 | |
| | SL4-142-4435 | G470142443500 | 4-17 |
| | SL4-142-4438 | G470142443800 | 7-8 |
| California | SL4-138-3808 | G470138380800 | 14-11 |
| | SL4-140-4126 | G470140412600 | 14-21 |
| | SL4-141-4374 | G470141437400 | 7-2 |
| | SL4-141-4381 | G470141438100 | } ^d 7-5 |
| | SL4-141-4382 | G470141438200 | |
| | SL4-141-4388 | G470141438800 | 9-1 |
| | SL4-142-4432 | G470142443200 | 9-7 |
| | SL4-142-4434 | G470142443400 | 7-3 |
| | SL4-142-4540 | G470142454000 | 7-4 |
| | SL4-194-7212 | G435194721200 | 14-12 |
| | SL4-196-7354 | G435196735400 | 8-6(a) |
| | SL4-207-8033 | G435207803300 | 9-2 |
| | SL4-142-4540 | G470142454000 | } b4-4 |
| | SL4-142-4541 | G470142454100 | |
| | SL4-142-4543 | G470142454300 | |
| | SL4-142-4545 | G470142454500 | |
| | SL4-142-4547 | G470142454700 | |
| | SL4-142-4548 | G470142454800 | |
| | SL4-142-4549 | G470142454900 | |
| | SL4-142-4545 | G470142454500 | 4-5 |
| SL4-203-7802 | G435203780200 | 4-7 | |
| SL4-203-7804 | G435203780400 | 4-8 | |
| SL4-197-7428 | G435197742800 | 4-9 | |

^aEarth resources observation systems.

^cLandsat image.

^bPhotomosaic.

^dStereopair.

| <i>Geographic location</i> | <i>Photograph no.</i> | <i>EROS^a Data Center identification no.</i> | <i>Figure no.</i> |
|----------------------------|-------------------------|--|-------------------|
| United States—Concluded | | | |
| Colorado | SL2-105-1087 | G235105108700 | 7-15 |
| | SL3-122-2583 | G370122258300 | 7-16 |
| | SL4-138-3875 | G470138387500 | 7-17 |
| | SL4-193-7151 | G435193715100 | 7-25, 8-10(a) |
| Florida | SL4-139-3982 | G470139398200 | 8-7 |
| Great Lakes region | SL4-136-3405 | G470136340500 | 14-17 |
| | SL4-139-3954 | G470139395400 | 7-26, 8-8 |
| | SL4-139-3989 | G470139398900 | 13-15, 15-5 |
| | SL4-139-4041 | G470139404100 | 18-6 |
| | SL4-140-4097 | G470140409700 | 13-16 |
| Hawaii | SL4-138-3865 | G470138386500 | 11-34 |
| | SL4-139-3997 | G470139399700 | 5-17 |
| Iowa | SL4-142-4466 | G470142446600 | 7-22 |
| | SL4-142-4467 | G470142446700 | 7-24, 14-26 |
| Kansas/Oklahoma | SL2-16-032 | G20A160320000 | 18-8 |
| | SL4-203-7769 | G435203776900 | 14-20 |
| | SL4-139-3928 | G470139392800 | 7-21 |
| | SL4-209-8161 | G435209816100 | 14-19 |
| Louisiana | SL4-136-3475 | G470136347500 | 11-16, 14-14 |
| | SL4-139-4032 | G470139403200 | 11-21 |
| | SL4-143-4600 | G470143460000 | 11-17 |
| Nevada | SL4-142-4435 | G470142443500 | 4-17 |
| New York | SL4-139-3990 | G470139399000 | 15-6 |
| | NOAA-2 composite | | 15-8 |
| South Dakota | SL4-139-3994 | G470139399400 | 7-23 |
| | SL4-142-4465 | G470142446500 | 9-6 |
| Texas | SL4-139-3950 | G470139395000 | 8-2 |
| | SL4-203-7773 | G435203777300 | 8-11(a) |
| | ^h AS6-2-1462 | | 8-9 |
| Utah | SL4-139-3992 | G470139399200 | 7-11 |
| | SL4-140-4167 | G470140416700 | 7-12 |
| | SL4-142-4435 | G470142443500 | 4-17 |
| Washington/Oregon | SL2-104-1023 | G235104102300 | 7-18 |
| | SL3-119-2260 | G335119226000 | 7-19 |
| | SL4-139-3935 | G470139393500 | 7-27 |
| | SL4-139-4013 | G470139401300 | 7-28 |
| | SL4-139-4047 | G470139404700 | 5-20 |
| | SL4-139-4048 | G470139404800 | 5-19 |
| | SL4-192-7080 | G435192708000 | 7-20 |
| | SL4-192-7081 | G435192708100 | 9-11 |
| Wyoming | SL2-105-1084 | G235105108400 | 7-14 |
| | SL4-138-3846 | G470138384600 | 7-13 |

^aEarth resources observation systems.

^hApollo 6 photograph.

15W 0 15E 30E 45E 60E 60N 75E 90E



Explanation

-  African drought
-  Deserts
-  Geology
-  Volcanoes
-  Manicouagan impact structure
-  Ice
-  Snow
-  Oceans
-  Coastal sediments
-  Cloud features
-  Atmospheric pollution
-  Cultural features
-  Vegetation patterns
-  Ocean surface circulation
-  Tropical storm

